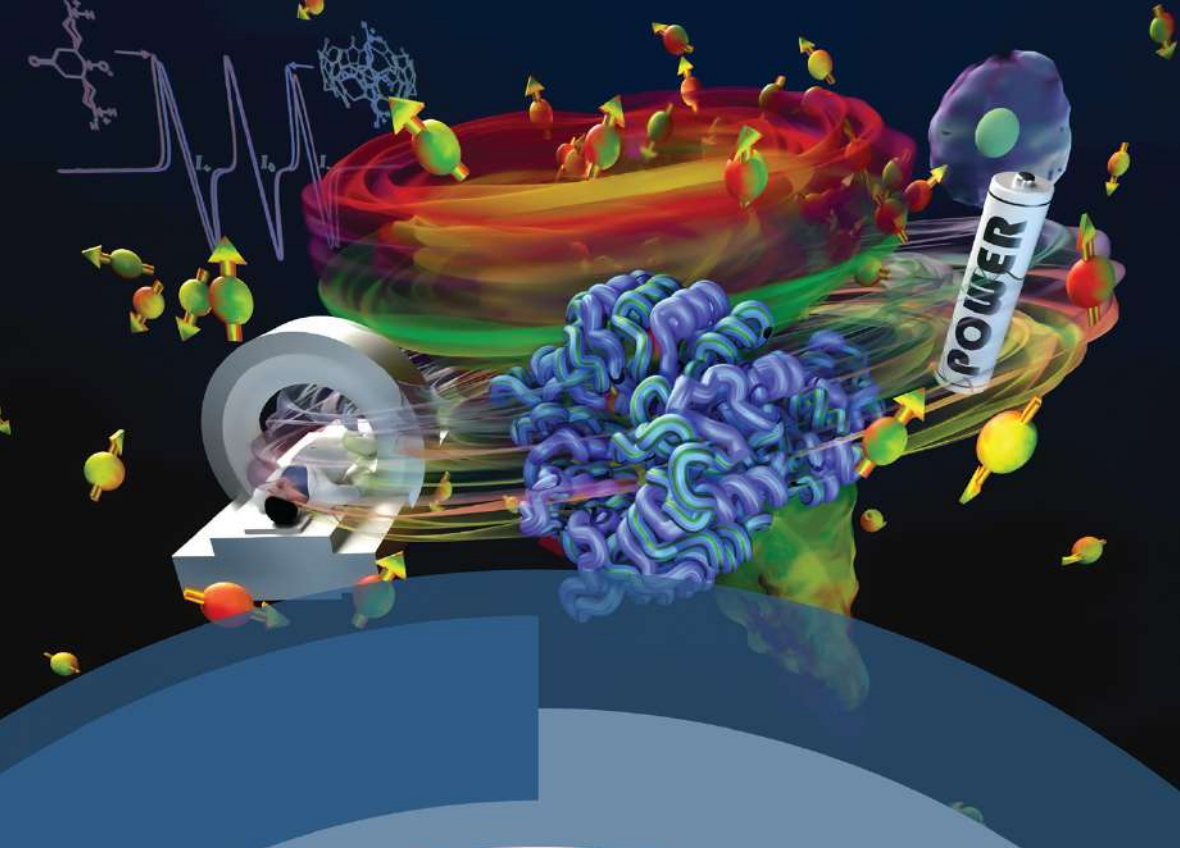

Nitroxides

Synthesis, Properties and Applications

Edited by Olivier Ouari and Didier Gigmes

ROYAL SOCIETY OF CHEMISTRY

Nitroxides

Nitroxides

Edited by

Olivier Ouari
Aix Marseille University, CNRS, ICR UMR7273, Marseille, France
Email: olivier.ouari@univ-amu.fr

and

Didier Gigmes
Aix Marseille University, CNRS, ICR UMR7273, Marseille, France
Email: didier.gigmes@univ-amu.fr

Print ISBN: 978-1-78801-752-7
PDF ISBN: 978-1-78801-965-1
EPUB ISBN: 978-1-78801-966-8

A catalogue record for this book is available from the British Library

The Royal Society of Chemistry is a charity, registered in England and Wales, Number 207890, and a company incorporated in England by Royal Charter (Registered No. RC000524), registered office: Burlington House, Piccadilly, London W1J 0BA, UK, Telephone: +44 (0) 20 7437 8656.

Visit our website at www.rsc.org/books

Printed in the United Kingdom by CPI Group (UK) Ltd, Croydon, CR0 4YY, UK

Preface

O. OUARI* AND D. GIGMES*

Aix Marseille Univ, CNRS, ICR UMR7273, Marseille, France
*Emails: Olivier.ouari@univ-amu.fr; didier.gigmes@univ-amu.fr

The nitroxide field appears to be experiencing endless growth. Innovative applications empowered by new chemistries, physics, biochemistry, materials and nanoscience assembling but also characterization methods are supplying constantly the field enabling both the improvement of established tools and the development of disruptive technologies. Mostly, the particular chemistry and properties of nitroxides underlie the widespread research attention on this class of radical species. High-impact applications are already on the market, such as nitroxide-mediated products used in roof tops of some cars, metal-free and greener oxidation reagents efficient from the laboratory to the industrial scale, including the production of pharmaceuticals, fragrances and nanocellulose, polarizing agents for hyperpolarization techniques, stabilizers and polymerization inhibitors.

All these successes have been made possible by the basic knowledge gained over the last decades but also by the tremendous radical stability and the possible fine tuning of nitroxide properties by designing precise skeletons. Moreover, the electron paramagnetic resonance (EPR) signal of nitroxides contains a remarkable wealth of information on the structure, dynamics, orientation and spin dynamics of the spin system but also on polarity, viscosity, distances, mechanisms, dioxygen (O_2) concentration, pH or redox status in samples.

The diverse chemistry of nitroxides has enabled their widespread use in applications ranging from site-directed spin labeling/electron paramagnetic

Nitroxides
Edited by Olivier Ouari and Didier Gigmes

Published by the Royal Society of Chemistry, www.rsc.org

resonance (EPR) in structural biology,[1–3] polarizing agents for dynamic nuclear polarization (DNP)/hyperpolarization techniques,[4,5] antioxidants in biological studies,[6] redox-active species for energy storage,[7,8] metal-free contrast agents in magnetic resonance imaging (MRI),[9] mediators in radical polymerization,[10] selective and precise probing,[11–13] and catalysts in chemical and oxidation reactions.[14,15]

In this book, we have strived to give a broad coverage to the field of nitroxide radicals, including chemical, biological, materials topics and their study by EPR spectroscopy.

The 'radical' diversity of the application of (poly)nitroxides is reflected in this book by the various contributions in organic synthesis (Szpilman *et al.*), in the methods for the synthesis of different nitroxide skeletons, focusing on the tunability of their structures and properties (Kirilyuk *et al.*), in the use of EPR spectroscopy to reveal detailed local information (Eaton *et al.*), in using nitroxides as spies in probing complex biological and supramolecular systems (Khramtsov, Lucarini *et al.*) and labeling biomolecules to gain precise structural and dynamic information (Klug *et al.*), in energy storage as redox materials for organic lithium batteries (Gohy *et al.*), in the use of nitroxide-mediated polymerization (NMP) to prepare polymers with precise architecture, composition and functionality exhibiting advanced properties (Asua *et al.*), in organic magnetism (Rajca), in paramagnetic liquid crystals (Tamura *et al.*), in using computational tools for investigating and designing new radicals (Coote *et al.*), and in trapping free radicals and characterizing their paramagnetic adducts, notably for reactive oxygen species (ROS) detection (Kalyanaraman *et al.*).

References

1. E. Bordignon, *eMagRes*, 2017, **6**, 235.
2. A. Bonucci, O. Ouari, B. Guigliarelli, V. Belle and E. Mileo, *ChemBioChem*, 2020, **21**, 451.
3. A. Marko, D. Margraf, H. Yu, Y. Mu, G. Stock and T. Prisner, *J. Chem. Phys.*, 2009, **130**, 064102.
4. Q. Z. Ni, E. Daviso, T. V. Can, E. Markhasin, S. K. Jawla, T. M. Swager, R. J. Temkin, J. Herzfeld and R. G. Griffin, *Acc. Chem. Res.*, 2013, **46**, 1933.
5. G. Stevanato, G. Casano, D. J. Kubicki, Y. Rao, L. Esteban Hofer, G. Menzildjian, H. Karoui, D. Siri, M. Cordova, M. Yulikov, G. Jeschke, M. Lelli, A. Lesage, O. Ouari and L. Emsley, *J. Am. Chem. Soc.*, 2020, **142**, 16587.
6. B. P. Soule, F. Hyodo, K. Matsumoto, N. L. Simone, J. A. Cook, M. C. Krishna and J. B. Mitchell, *Free Radicals Biol. Med.*, 2007, **42**, 1632.
7. H. Nishide and K. Oyaizu, *Science*, 2008, **319**, 737.
8. T. Janoschka, N. Martin, M. D. Hager and U. S. Schubert, *Angew. Chem. Int. Ed.*, 2016, **55**, 14427.

9. A. M. Sowers, J. R. McCombs, Y. Wang, J. T. Paletta, S. W. Morton, E. C. Dreaden, M. D. Boska, M. F. Ottaviani, P. T. Hammond, A. Rajca and J. A. Johnson, *Nat. Commun.*, 2014, **5**, 5460.
10. *Nitroxide Mediated Polymerization: From Fundamentals to Applications in Materials Science*, ed. D. Gigmes, The Royal Society of Chemistry, 2015.
11. M. Voinov, I. Rivera-Rivera and A. I. Smirnov, *Biophys. J.*, 2013, **104**, 106.
12. K. L. Chong, B. A. Chalmers, J. K. Cullen, A. Kaur, J. L. Kolanowski, B. J. Morrow, K. E. Fairfull-Smith, M. J. Lavin, N. L. Barnett, E. J. New, M. P. Murphy and S. E. Bottle, *Free Radicals Biol. Med.*, 2018, **128**, 97.
13. M. Lucarini, *Eur. J. Org. Chem.*, 2020, **20**, 2995.
14. S. Wertz and A. Studer, *Green Chem.*, 2013, **15**, 3116.
15. R. Ciriminna and M. Pagliaro, *Org. Process Res. Dev.*, 2010, **14**, 245.

Contents

Nitroxides
Edited by Olivier Ouari and Didier Gigmes

Published by the Royal Society of Chemistry, www.rsc.org

CHAPTER 1

A Brief History and Outlook of Nitroxides

O. OUARI* AND D. GIGMES*

Aix Marseille Univ, CNRS, ICR UMR7273, Marseille, France
*Emails: Olivier.ouari@univ-amu.fr; didier.gigmes@univ-amu.fr

1.1 Brief History

Nitroxides, also named aminoxyl or nitroxyl radicals, constitute a family of versatile organic radical species with rich and diverse properties and reactivity.[1,2] Nitroxides belong to an important class of compounds finding a wide range of applications related to the fields of organic chemistry, physical-chemistry, material science, biology and medicine. Nitroxide compounds have a long history that started in 1845 with the first nitroxide prepared by E. Frémy.[3] Known as Frémy's salt (Scheme 1.1), this radical was initially obtained by oxidation of potassium disulfonate hydroxylamine with lead dioxide and then by reaction of sodium nitrite with sodium bisulfite. The first organic nitroxide, so-called porphyrexide, was then prepared in 1901 by Piloty and Schwerin (Scheme 1.1).[4] Later, in 1914, a nitroxide bearing two aryl groups on the nitrogen atom was obtained for the first time (Scheme 1.1) by Wieland *et al.*[5] In 1959, the synthesis of the first cyclic *N,N*-di-alkyl nitroxide, namely 2,2,6,6-tetramethylpiperidinyl-1-oxyl, better known under the name of TEMPO, was described by Lebedev and Kazarnovskii (Scheme 1.1).[6] Since this report, *N,N*-dialkyl nitroxides have taken on increasing importance over the years. In 1961, the synthesis of non-cyclic di-*tert*-butylnitroxide was described by Hoffmann and Henderson (Scheme 1.1).[7]

Nitroxides
Edited by Olivier Ouari and Didier Gigmes

Published by the Royal Society of Chemistry, www.rsc.org

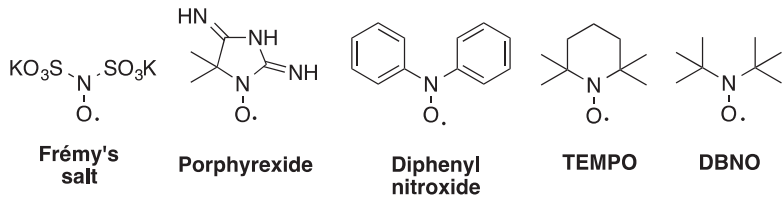

Scheme 1.1 Structures of the early nitroxides.

It has to be mentioned that since the 1960s the development of both efficient methodologies in organic chemistry and electron spin resonance (EPR) spectroscopy has been extremely beneficial for the development of the nitroxide field (Scheme 1.2).[8] Several nitroxide structures such as TEMPO, TOAC, PROXYL, MTSL, DBN, TMIO, AZADO, ABNO and DOXYL are now commercially available and many more have been already described.[2,9,10]

The term stable radical[11] implies that the nitroxide compounds can be safely handled and stored under ambient conditions, without any precaution of temperature, dioxygen (O_2) or moisture exposition. The unusual radical stability and the possible reactions proceeding on the their structure with conservation of the radical properties were early recognized to be a key feature of nitroxide compounds[12–14] explaining the widespread research attention on their reactivity and applications.

1.2 Nitroxide Reactivity

The exceptional properties of nitroxides result from the presence of a three-electron π bond in the aminoxyl group (N–O•). This bond consists in the overlapping of the 2pz orbitals of the nitrogen and oxygen atoms. Hence, the electronic structure of the N–O• group is represented by the contribution of two resonance forms A and B (Scheme 1.3).

Due to the presence of a single electron in the π* orbital (SOMO), the bond index of the N–O bond is 1.5. In addition, the value of the bond energy ($\approx$418 kJ mol^{-1}) and the bond length (1.25 Å $< d_{NO} <$ 1.30 Å) are between those of a single NO bond of an hydroxylamine or alkoxyamine (N–OH $\approx$ 222 kJ mol^{-1} and 1.43 Å, respectively) and those of a NO double bond of a nitroso compound ($\approx$606 kJ mol^{-1} and 1.20 Å, respectively).

In dialkylnitroxides ($R_1 = R_2 =$ alkyl) the spin density is essentially distributed between the nitrogen and oxygen atoms with a slightly larger value on the oxygen atom. The delocalization of the single electron of an aminoxyl group corresponds to an energy gain of approximately 100 kJ mol^{-1}. However, the formation of an O–O bond leads to an energy gain of 170 kJ mol^{-1}. Consequently, the dimerization of nitroxides is not thermodynamically favored because it does not correspond to a gain in bonding electrons. Typically, nitroxides having one or more hydrogen atoms on the α-carbons (C_α) of the nitrogen atom are not stable due to a disproportionation reaction that leads to the formation of the corresponding nitrones and hydroxylamines

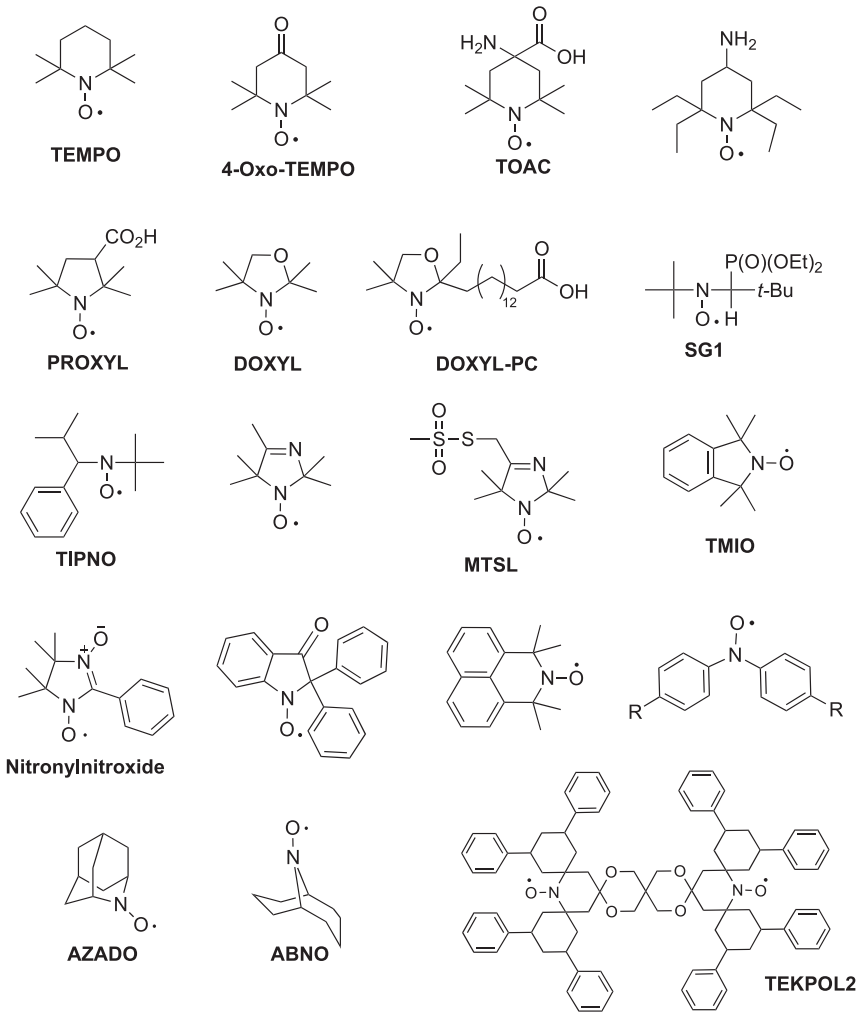

Scheme 1.2 Some examples of the most common nitroxide structures.

(Scheme 1.4).[15] It should be mentioned that very large steric constraints in α-position cause potentially the spontaneous homolytic decomposition of dialkylnitroxides to afford the corresponding nitroso compound and the alkyl radials (Scheme 1.4).[16,17]

However, a few exceptions of stable nitroxides bearing hydrogen atoms on the α-carbons have been reported. For example, due to Bredt's rule we can cite nitroxides containing polycycles (ABNO, AZADO) where the abstraction of the hydrogen in the *alpha* position atom is forbidden.[17] Other examples are related to crowded molecules around the hydrogen to be abstracted or to conformationally constrained nitroxides (TIPNO, SG1, Scheme 1.5) limiting the disproportion reaction to occur.

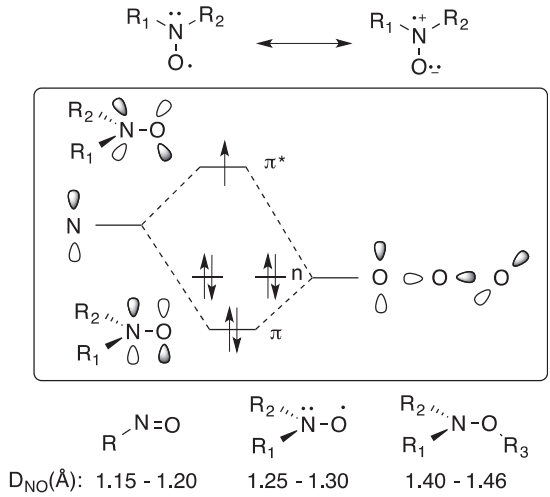

Scheme 1.3 Representation of two resonance structures of nitroxides, a schematic representation of the *n*, π, π* orbitals on the NO• group and the bond length of nitroso, nitroxide and alkoxyamine compounds.

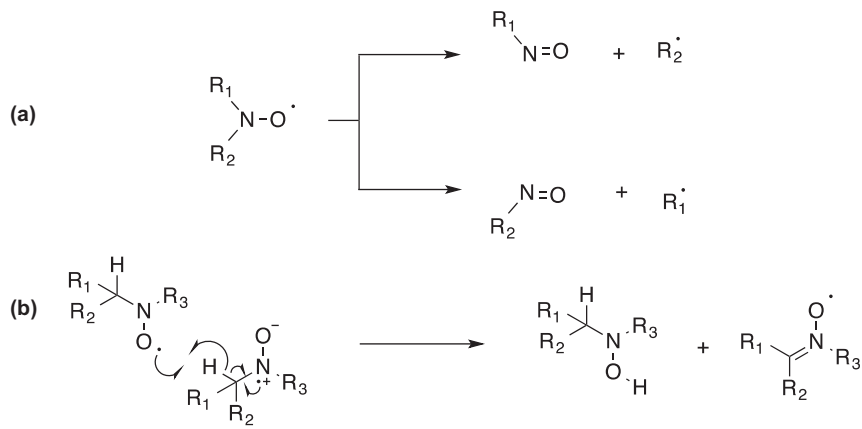

Scheme 1.4 Possible decomposition pathways for nitroxide: (a) fragmentation (b) disproportionation.

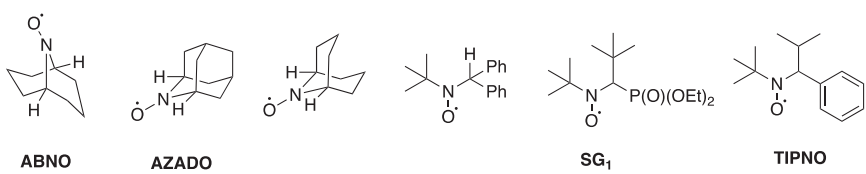

Scheme 1.5 Examples of stable nitroxides bearing hydrogen atom(s) in the α-position.

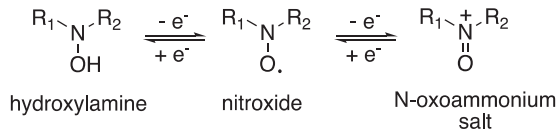

Scheme 1.6 Redox properties of nitroxides.

Interestingly, nitroxides behave as redox amphoters (Scheme 1.6). They can be reversibly oxidized to the corresponding *N*-oxoammonium salt or reduced to the corresponding hydroxylamine in a one-electron process. This property and the tunable redox potentials enable the development of redox probes for biological systems or organic electrodes for lithium batteries or catalytic oxidation reagent in organic synthesis.

N,N-Dialkyl nitroxides such as TEMPO are usually poorly efficient for C–H activation and H-atom abstraction due to the low OH-bond dissociation energy (BDE, 290 kJ mol^{-1}). Nitroxide bearing electron-withdrawing groups such as α,α-diacyl nitroxides are usually employed for reaction with unactivated positions. For comparison, the BDE of NHPI is much larger (367 kJ mol^{-1}) and the corresponding radical is good H-abstracting reagents. In contrast, the reverse process of converting hydroxylamine to nitroxide is usually thermodynamically favorable and the TEMPO hydroxylamine can be used as an antioxidant.

Therefore, the three-electron bond in nitroxides modifies the usual reactivity of the unpaired electron, notably relative to alkyl or peroxyl radicals, *e.g.* with no dimerization, limited H-atom abstraction and no reactivity with air and moisture. Moreover, the relative inertness of the radical center with numerous diamagnetic chemicals and biomolecules provides the possibility to modify other reactive groups of the nitroxide molecules without affecting the paramagnetic center, opening possibilities to tailor the nitroxide structures or bioconjugate the nitroxide spin label.

The reaction of nitroxides with C- and O-centered radicals is usually fast (10^{-6} to 10^{-9} mol s^{-1}). The trapping of C-centered radicals to form alkoxyamines made nitroxides good candidates as radical stabilizers and regulating agents for controlled/living radical polymerization. Also, this feature has been recently employed as a tool to shift a dynamic covalent reaction network out of equilibrium using light-sensitized alkoxyamines,[16] to prepare dynamic assembly of fluorescent hybrid microcrystals[17] and to digitally encode information in polymers.[18] The reaction of short-lived C-centered radicals with stable nitroxides generated at equal rates is at the origin of the persistent radical effect (PRE)[19] that received recently growing interest in organic synthesis because of the high selectivity in the cross-coupling reactions.[20]

1.3 Conclusion

Up to now nitroxide radicals are probably the most studied radical species. They have already proven their importance in various fields. Undoubtedly,

more will arrive in the near future. Indeed, nitroxides and associated compounds will certainly play a key role in the fields of energy storage, metal-free contrast agents for MRI, medicine, material science, advanced EPR, quantum computing and also storage of information.

References

1. L. Tebben and A. Studer, *Angew. Chem., Int. Ed.*, 2011, **50**, 5034.
2. J. F. W. Keana, *Chem. Rev.*, 1978, **1**, 37.
3. E. Fremy, *Ann. Chim. Phys.*, 1845, **Serie 3**, 408.
4. O. Piloty and B. G. Schwerin, *Ber. Dtsch. Chem. Ges.*, 1901, **34**, 1870.
5. H. Wieland and M. Offenbacher, *Ber. Dtsch. Chem. Ges.*, 1914, **47**, 2111.
6. O. L. Lebedev and S. N. Kazarnovskii, *Zh. Obshch. Khim.*, 1960, **30**, 1631.
7. A. K. Hoffmann and A. T. Henderson, *J. Am. Chem. Soc.*, 1961, **83**, 4671.
8. D. Griller and K. U. Ingold, *Acc. Chem. Res.*, 1980, **9**, 317.
9. E. G. Rozantsev and V. D. Sholle, *Synthesis*, 1971, 190.
10. M. M. Haughland, J. E. Lovett and E. A. Anderson, *Chem. Soc. Rev.*, 2016, **47**, 668.
11. D. Griller and K. Ingold, *Acc. Chem. Res.*, 1976, **9**, 13.
12. M. B. Neiman, E. G. Rozantzev and Y. G. Mamedova, *Nature*, 1962, **196**, 472.
13. M. B. Neiman, E. G. Rozantzev, Y. G. Mamedova and G. Yu, *Nature*, 1963, **200**, 256.
14. A. R. Forrester and R. H. Thomson, *Nature*, 1964, **74**, 203.
15. E. G. Rozantsev and V. D. Sholle, *Synthesis*, 1971, 402.
16. M. Herder and J. M. Lehn, *J. Am. Chem. Soc.*, 2018, **140**, 7647.
17. B. Schulte, M. Tsotsalas, M. Becker, A. Studer and L. De Cola, *Angew. Chem., Int. Ed.*, 2010, **49**, 6881.
18. R. K. Roy, A. Meszynska, C. Laure, L. Charles, C. Verchin and J.-F. Lutz, *Nat. Commun.*, 2015, **6**, 7237.
19. H. Fischer, *J. Am. Chem. Soc.*, 1986, **108**, 3925.
20. D. Leifert and A. Studer, *Angew. Chem., Int. Ed.*, 2020, **59**, 74.

CHAPTER 2

General Approaches to Synthesis of Nitroxides

IGOR A. KIRILYUK* AND DMITRII G. MAZHUKIN

N.N.Vorozhtsov Novosibirsk Institute of Organic Chemistry SB RAS,
Pr. Lavrentieva 9, Novosibirsk 630090, Russian Federation
*Email: kirilyuk@nioch.nsc.ru

2.1 What are Nitroxides. Limits of Nitroxide Stability

Nitroxides are a broad family of organic free radicals in which an unpaired electron is localized mainly on a three-electron N–O bond between an oxygen and disubstituted nitrogen atom. They can be represented with resonance structures **1** and **2** (Scheme 2.1).

This very small group is characterized with remarkably high delocalization energy of free electrons. Estimations of this energy by different authors vary in a range from approximately 95[1] to 125[2] kJ mol^{-1}. This provides thermodynamic stability (low energy) of the nitroxide group and makes thermodynamically less favorable reaction pathways leading to free radical decay. This review will focus on nitroxides which at least can be isolated as individual compounds.

The majority of stable nitroxides has two *tert*-alkyl groups at a nitrogen atom or two *gem*-dialkyl moieties in a cyclic structure (Chart 2.1). Many radicals of these types are stable enough to be handled as conventional organic compounds and can be stored for decades in aerobic conditions in a dark place at ambient temperature without any trace of decomposition. Due to the relatively low reactivity of the nitroxide group, various chemical reactions can be used for modification of nitroxide structures with radicals not being affected. However, strongly acidic conditions, strong

Nitroxides
Edited by Olivier Ouari and Didier Gigmes

Published by the Royal Society of Chemistry, www.rsc.org

Scheme 2.1

Chart 2.1 Important types of stable nitroxides.

oxidants and reductants may lead to nitroxide conversion into diamagnetic compounds. Usually, the nitroxide group can be easily recovered after these chemical reactions, alternatively protective groups should be used. The relative simplicity of chemical modification of nitroxide structures resulted in the synthesis of countless numbers of derivatives, allowing for tuning of their spectral parameters and chemical and physical properties for specific applications. Nitroxides can be specifically attached to various molecules or incorporated into complex molecular or supramolecular structures to give various functional materials.[3–5]

Some examples of stable nitroxides with *sec*-alkyl substituents are shown in Chart 2.2. AZADO and Nor-AZADO are powerful catalysts of alcohol oxidation to carbonyl compounds.[6] Nitroxides TIPNO and SG1 are used in nitroxide-mediated polymerization.[7–10] Nitroxide **3** (pK_a 3.6) showed low cytotoxicity and was used to measure acidity in the rat stomach.[11]

Curiously, there is a discrepancy in the numbering of atoms adjacent to N–O$^\bullet$ group in the literature. For example, nitroxides of the type shown in Chart 2.2 in numerous publications are called ''α-hydrogen'',[12,13] which corresponds to UCLA (University of California, Los Angeles) *Illustrated Glossary of Organic Chemistry*,[14] but there is also a number of papers where the same atom is called ''β-hydrogen'' in agreement with traditional terminology in spin trapping/EPR literature (Figure 2.1).[15–17] Moreover, SG1-type nitroxides are usually called ''β-phosphorylated'' but ''α-hydrogen'',[12,18] while nitroxide **4** was called ''β-sulfinyl''.[19] Remarkably, contradictory designations are sometimes used by the same authors. Here we will hold to the terminology used in older spin trapping papers, counting each atom from the first one bound to nitrogen of the N–O$^\bullet$ group.

Nitroxides with β-hydrogen are usually unstable and undergo disproportionation to nitrone and hydroxylamine (Scheme 2.2). This reaction was proposed to proceed *via* β-hydrogen abstraction.[20] X-ray analyses data obtained for some of stable acyclic nitroxides showed that they exist in a conformation with β-hydrogen in *anti*-position to nitroxide oxygen atom and close to the nodal plane of the N–O$^\bullet$ π-system (obviously due to repulsion of bulky substituents).[12] This conformation is unfavorable for hydrogen abstraction in accordance with the suggested mechanism, making the nitroxides persistent. An alternative mechanism does not account for this phenomenon.[21] Disproportionation of bicyclic nitroxides is forbidden by Bredt's rule.

Among the cyclic nitroxides with β-heteroatom(s) in the side chain, the β-phosphorylated nitroxides have by far the greatest importance (Chart 2.3). Radicals **5** and **6** were successfully used for Overhauser-enhanced magnetic resonance imaging of enzymatic activity in tissues.[22,23] Nitroxide **7** was suggested for EPR detection of traces of water in organic solvents.[24]

There is also a large family of stable conjugated nitroxides (Chart 2.4). Various nitronyl- and imino-nitroxides of 2-imidazoline series **8** and **9** are widely used in coordination chemistry as building blocks for assembling

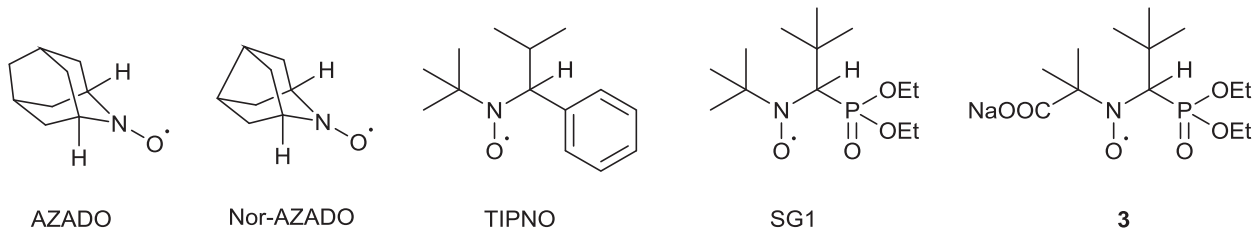

Chart 2.2 Stable nitroxides with hydrogen atom(s) at α-carbon atom(s).

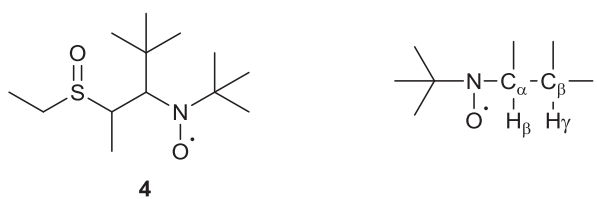

Figure 2.1 Structure of nitroxide **4** and designation of atoms in the nitroxide structure according to ref. 15.

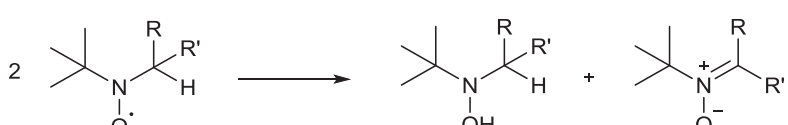

Scheme 2.2 Disproportionation of β-hydrogen nitroxides.

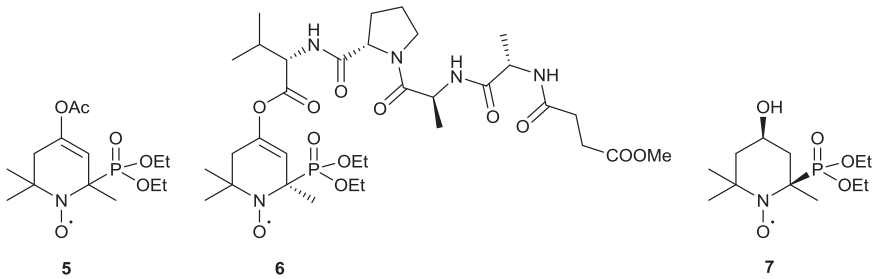

Chart 2.3 β-Phosphorylated nitroxides.

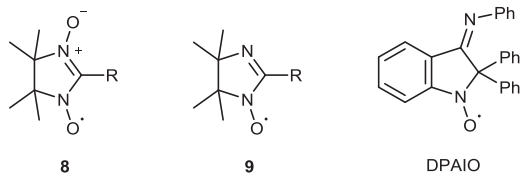

Chart 2.4 Stable conjugated nitroxides.

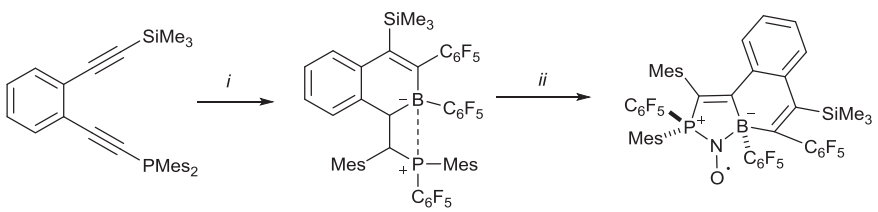

Scheme 2.3 Synthesis of FLPNO nitroxides: (*i*) $B(C_6F_5)_3$, 80 °C; (*ii*) NO (1.5 bar), benzene, rt.[26]

magnetic materials.[5] DPAIO and its derivatives are considered as promising agents for nitroxide-mediated polymerization (NMP).[25]

The number of new nitroxides is rapidly increasing. Recently, a series of new extremely unusual stable nitroxides have been prepared *via* addition of nitric oxide to boron-phosphorus frustrated ionic pairs (Scheme 2.3).[26,27]

Broad diversity in structures of known nitroxides implies strong variation of their stability, chemical properties and spectral parameters. Different peculiarities of nitroxides are exploited in a multitude of applications. Nitroxides are widely used in organic synthesis (specific oxidants, *etc.*).[28–31] Redox properties of nitroxides are used in electric rechargeable batteries (electrode materials, redox active polymers).[32] Being radicals, nitroxides actively scavenge active free radicals produced in living tissues, and their potential as antioxidants, radioprotectors and

therapeutic agents is now well recognized.[33–35] The reversible reaction with carbon-centered free radicals at higher temperatures is used in polymer chemistry (nitroxide-mediated polymerization).[7–10] The simple EPR spectrum of nitroxides is highly sensitive to various properties of their surroundings, and this makes them very useful molecular probes for biophysics (measurement and imaging of pH, oxygen, thiols, *etc.*) and material studies (surface electrostatics and local pH).[36–40] Being uniquely compact stable radicals, they are indispensable spin labels for structural biology (site-directed spin labeling – EPR methods).[41–47] Nitroxide mono-, bi- or polyradicals can transfer spin polarization to magnetic nuclei with efficient enhancement of NMR signal, and this effect is used in dynamic nuclear polarization (DNP) NMR studies of bio-molecules[48] or inorganic materials,[49,50] in magnetic resonance imaging (MRI)[51,52] and Overhauser-enhanced MRI studies *in vivo*.[23,53] A number of efficient profluorescent spin probes have been designed.[54] These compounds showed high efficacy for measurement and visualization of oxidative stress in biological systems, for investigation of degradation and ageing of polymer materials and for estimation of environmental contamination. Nitroxides are used as building blocks for magnetic materials,[5,55] organoelectronic devices and components of quantum computers.[3,4,56–58] The above list is obviously incomplete.

Significant progress has been achieved in nitroxide chemistry in the recent decade. The following options can be mentioned among the most important findings: bioreduction-resistant nitroxides,[59–61] highly efficient DNP agents,[62] fully organic contrast agents for MRI[51,52,63] novel site-directed spin labeling (SDSL) technologies,[43,44,46] profluorescent spin probes and spin labels[64] and advanced NMP regulators.[10,65] Metal-free magnetic nanoemulsions were prepared from nitroxides and suggested for theranostic applications.[66–68] The aim of this review is to give a brief overview of the general methods for preparation of the most demanded types of nitroxides with a focus on the latest publications and modern trends. More information on this subject can be found in recent reviews.[12,16,69–72]

2.2 Nitroxide Group Formation

2.2.1 From Amines

Oxidation of secondary amines is the most common method for nitroxides synthesis. This conversion is usually achieved using hydrogen peroxide with a catalyst or using organic peracids [*m*-chloroperbenzoic acid (*m*CPBA), peracetic acid, *etc.*]. Oxidation with H_2O_2 is usually carried out in aqueous solutions or in mixtures of water and organic solvent (methanol, ethanol, *etc.*) with a large excess of oxidant and with sodium tungstate as a catalyst. Sometimes other catalysts, *e.g.*, phosphotungstic acid or MgO, can also give good yield of a nitroxide (for representative procedures see ref. 73 and 74). Protonation of the amine retards the reaction, therefore basic pH is usually

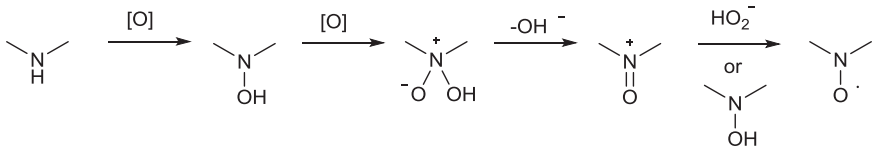

Scheme 2.4 Oxidation of amines to nitroxides.

preferable. Some functional groups, *e.g.*, ester, carboxamide, *etc.*, can undergo hydrolysis in alkaline solutions of hydrogen peroxide.[75] Oxidations with *m*CPBA are performed in organic solvents and can be used for oxidation of hydrolytically unstable substrates, *e.g.*, oxazolidines. Both reactions seem to have similar mechanisms with intermediate formation of hydroxylamine and oxoammonium cation (Scheme 2.4).[16]

The latter is known to be a highly reactive oxidant and may cause destruction or oxidation transformations in the side chain. Hydrogen peroxide is known to react rapidly with oxoammonium cation,[76] retarding oxidation of functional groups in the side chain. As a result, H_2O_2/Na_2WO_4 often gives somewhat higher yields of nitroxides from easily oxidizing amines. Organic peracids are more reactive and afford faster oxidation, but may give lower yields of labile nitroxides. For example, conversion of amines to nitroxides with *m*CPBA may be accompanied by hydroxyalkyl groups oxidation (Scheme 2.5).[70,77] However, it should be noted that the yield of desired nitroxide is strongly dependent on reaction conditions, and literature data are sometimes contradictory.

The H_2O_2/Na_2WO_4 system can be used for oxidation of tertiary *N*-methyl amines to nitroxides, however this conversion requires elevated temperatures (40–50 °C). This procedure was used in the synthesis of pH-sensitive spin probes **16** (Scheme 2.6).[75,80] Tertiary *N*-benzylamines can be oxidized using *m*CPBA, however better yields are achieved *via* hydrogenolysis to secondary amines with subsequent oxidation with H_2O_2/Na_2WO_4 system or *m*CPBA.[69]

2.2.2 From Hydroxylamines

N,*N*-Disubstituted hydroxylamines are of lower accessibility than secondary amines, but some nitroxide precursors of this type can be prepared *via* condensations (especially those of imidazoline series) or *via* nucleophile addition to nitrones (see below). Oxidation of hydroxylamines is generally considered as the easiest way to nitroxides. However, susceptibility of hydroxylamines to oxidation clearly depends on pH. Hydroxylamines are bases with pK_a varying in the range 4–9, depending on the electronic effects of the substituents.[81] Protonation can prevent oxidation of hydroxylamine to nitroxide, *e.g.*, during bromination. Subsequent addition of $NaNO_2$ leads to partial neutralization of the acid and recovery of nitroxide (Scheme 2.7).[60,82–84]

R^1=R^2=Et (**a**), R^1+R^2=$(CH_2)_4$ (**b**), $(CH_2)_5$ (**c**)

Scheme 2.5 Oxidation of secondary amines to nitroxides: (*i*) H_2O_2, Na_2WO_4, MeOH–H_2O 3 : 1, 25 °C, 24 h; (*ii*) *m*CPBA, CH_2Cl_2, 0 °C, 46 min, then rt 3 h; (*iii*) *m*CPBA, $CHCl_3$, −10 °C, then 0 °C.

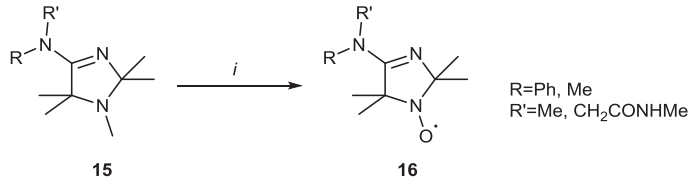

15 **16**

Scheme 2.6 Oxidation of tertiary amines to nitroxides: (*i*) H_2O_2, Na_2WO_4, MeOH 50 °C, 5 h, 50–85%.[75,80]

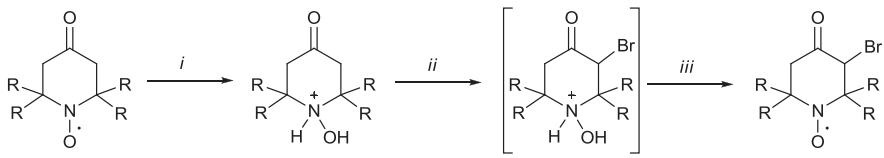

R = Me (56%)[82]; Et (22-44%)[60]
R+R = $(CH_2)_5$ (44-60%)[84]

Scheme 2.7 Bromination of nitroxides: (*i*) HCl, EtOH; (*ii*) Br_2, $CHCl_3$; (*iii*) $NaNO_2$, H_2O.

In aerobic conditions hydroxylamines undergo mild oxidation to nitroxides. The reaction rate is dependent on the redox properties of the hydroxylamine/nitroxide pair. The oxidation of hydroxylamines obviously proceeds faster in strongly basic media. It has been shown that spontaneous aerobic oxidation of hydroxylamines to nitroxides can be suppressed by addition of chelators, capable of binding transition metals.[85] Transition metals ions, which are usually not removed in routine oxidation procedures, can provide efficient single electron transfer on first steps and allow for activation of hydrogen peroxide which does not react with hydroxylamine with a reasonable rate in the absence of a catalyst.[86] The reaction can be accelerated by addition of ammonium–copper complexes. This catalyst provides rapid oxidation due to the high concentration of copper ions and basic pH of the media.

Metal oxides (usually PbO_2 or MnO_2, sometimes HgO, Ag_2O, *etc.*) are efficient oxidants for synthesis of various nitroxides.[16,87] Since oxidation proceeds on the surface of heterogenic oxidant, a large excess of the reagent is necessary. The yield of the nitroxide is dependent on its propensity to oxidative destruction. For oxidation in aqueous solution Na(K)IO_4 or $K_3[Fe(CN)_6]$ can be used.[87,88]

2.2.3 From Alkoxyamines

Alkoxyamines are more often used as protected forms of the nitroxides than as precursors. Methoxyamines can be prepared *via* trapping of methyl radical with nitroxide[89–93] or *via* alkylation of the corresponding

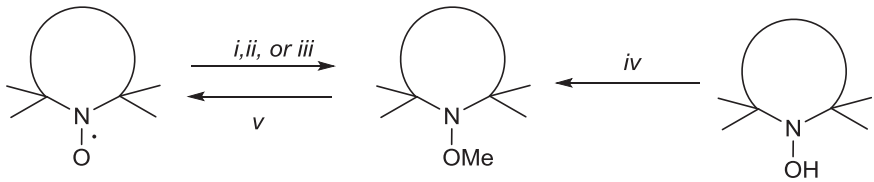

Scheme 2.8 Methoxyamines synthesis and conversion to nitroxides: (*i*) Fe^{2+}, H_2O_2, DMSO, 10 °C, 85–100%;[89] (*ii*) MeCHO, H_2O_2, Cu^+, 70 °C, 72%;[92] (*iii*) Me_2CO, H_2O_2, Cu^+, 10 °C, then rt 12 h, 71%;[91] (*iv*) NaH, DMF, MeI, rt, 72 h, 73%;[94] (*v*) *m*CPBA, CH_2Cl_2, 0.5–8 h, rt, 70–90%.[89]

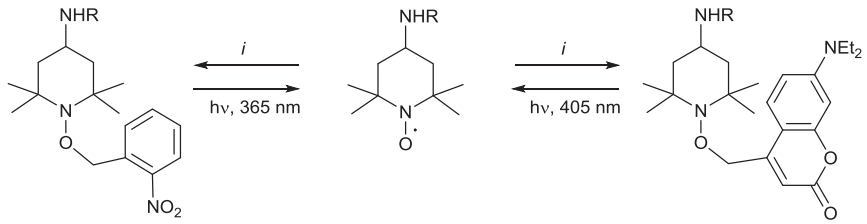

Scheme 2.9 Photolabile protecting groups: (*i*) H_2/Pd/C, then Et_3N, $BrCH_2Ar$ or 4-bromomethyl-7-diethylamino-2*H*-chromen-2-one, 42–98%.[95]

hydroxylamine anion (Scheme 2.8).[94] Nitroxides can be regenerated using *m*-CPBA.[88]

Recently, photolabile protective groups have been described.[95] Corresponding nitroxides can be regenerated from these alkoxyamines with 80–95% yield upon irradiation at 405 or 365 nm (Scheme 2.9).

2.2.4 From Nitrones

Conversion of nitrone into nitroxide requires the introduction of at least one substituent to the α-carbon atom of the nitrone group. Organometallic compounds are by far the most convenient reagents for this purpose. Addition of organometallic reagent (RLi or RMgX) to nitrone affords hydroxylamine, which can be easily oxidized to corresponding nitroxide. This method is widely used for the synthesis of acyclic and cyclic nitroxides of various series.[96–103] Some recent examples are shown in Scheme 2.10.

Addition of Grignard reagents to sterically hindered nitrones may proceed slowly, with a higher contribution of adverse reactions. The yield of nitroxide depends on the basicity of the reagent, because metallation of α-alkylnitrones may lead to autocondensation products or retard/prevent addition.[104] For example, the nucleophilic addition of ethylmagnesium bromide to sterically shielded nitrone **17** does not occur even with a large excess of the reagent, presumably due to complete metallation of the

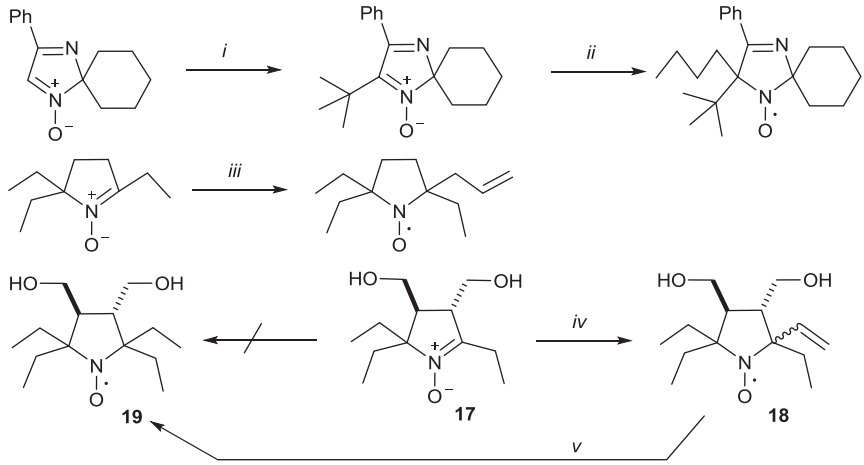

Scheme 2.10 Nitroxides synthesis *via* organometallic compounds addition to nitrones: (*i*) *t*-BuMgCl, Et_2O; H_2O, PbO_2, 70%; (*ii*) BuLi, hexane/benzene; H_2O, PbO_2, 78%;[100] (*iii*) AllMgBr, Et_2O; H_2O, Cu^{2+}, NH_3, O_2, 67%;[98] (*iv*) $CH_2CHMgBr$, THF; H_2O; MnO_2, $CHCl_3$, 70%; (*v*) H_2, Pd/C; O_2, 93%.[59]

ethylnitrone group, while reaction with less basic vinylmagnesium bromide afforded nitroxide **18** which was converted into 2,2,5,5-tetraethyl-substituted nitroxide **19** *via* hydrogenation of the terminal C=C bond (Scheme 2.11).[59] If several substituents must be introduced *via* addition of organometallic compound to nitrone, large ones should be introduced first.[105] Organolithium compounds are generally more reactive both toward addition and metallation, therefore they usually give better yields of nitroxides in reactions with α-aryl- or α-*tert*-alkyl nitrones.[96,100,101]

1,3-Dipolar cycloaddition of alkenes to nitrones is an efficient method of introduction of alkyl substituent to the α-carbon atom of the nitrone group.[106] The reaction of 2,5,5-trisubstituted 1-pyrroline-1-oxides with methylacrylate afforded isoxazolidines and reductive cleavage of N–O bond ring gives aminoalcohols, which then were oxidized to nitroxides with a functional group in the side chain (Scheme 2.11).[107,108]

Intramolecular 1,3-dipolar cycloaddition of nitrones may proceed even with an inactivated C=C bond. The reaction is sensitive to sterical hindrance and highly stereoselective. The starting alkenyl nitrones may be easily prepared *via* addition of Grignard reagent, *e.g.*, pent-4-enylmagnesium bromide, to aldonitrones and oxidation. Isoxazolidine ring opening and oxidation gives spirocyclic nitroxides.[77,79,109] Noteworthily, in this reaction sequence, configuration of the asymmetric center at the hydroxymethyl group is specifically determined producing greater hindrance of nitroxide moiety. An example of stereospecific synthesis of highly strained pyrrolidine nitroxide from optically active nitrone is shown in Scheme 2.12.

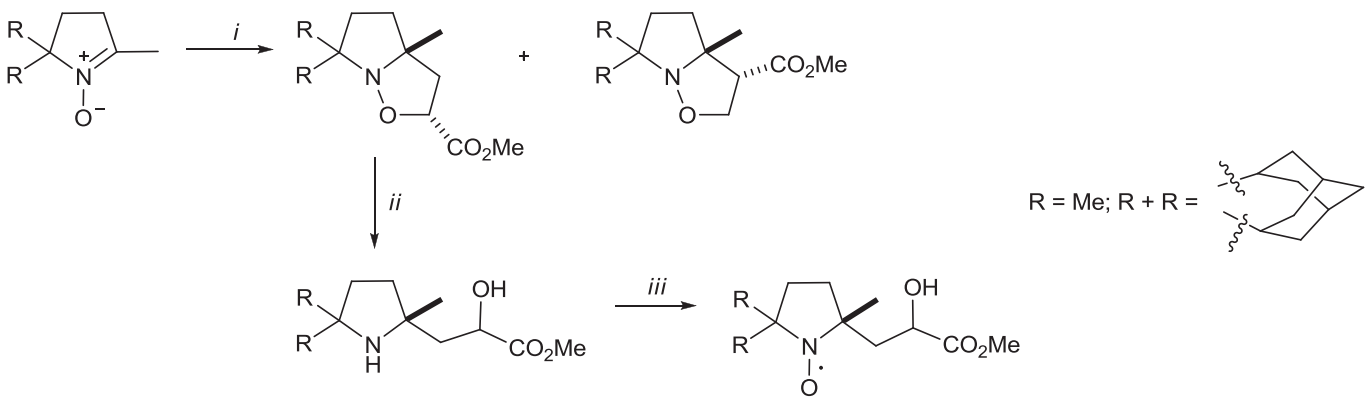

Scheme 2.11 Reagents and conditions: (*i*) methyl acrylate, benzene, 80 °C, 76%; (*ii*) Zn, AcOH, EtOH, 60 °C, 60–74%; (*iii*) H_2O_2, MeOH–H_2O, Na_2WO_4, 24 h, 74%; or *m*-CPBA (2 equiv.), CH_2Cl_2, rt, 5 h, 37%.[107,108]

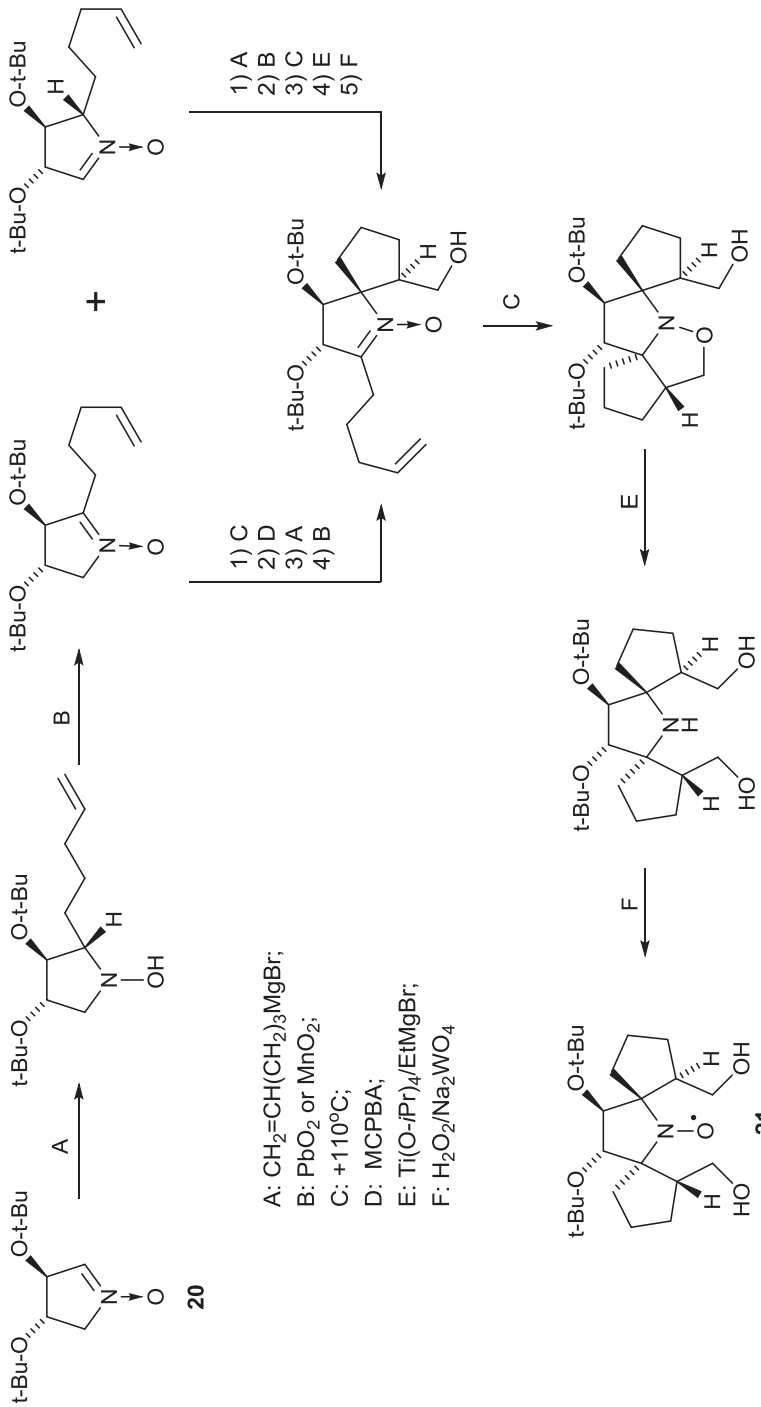

Scheme 2.12 Synthesis of nitroxide **21**.

2.3 Some Contemporary Trends in Nitroxide Chemistry

2.3.1 Influence of Structural Factors upon Redox Properties of Nitroxides: The Fight for Stability in Biological Systems

Redox properties of nitroxides play a very important role and are exploited in various applications. Nitroxides easily undergo one-electron oxidation or reduction to form oxoammonium cation or hydroxylamine, respectively (Scheme 2.13).

These reactions are exploited in synthetic applications of nitroxides, where easy conversion to oxoammonium cation provides nitroxide catalytic activity in oxidation of alcohols into carbonyl compounds[28,29] and in energy-storage devices.[32] The same redox transformations are responsible for superoxide dismutase (SOD) mimetic activity of nitroxides, which plays a major role in their antioxidant and protective properties.[34,110] Nitroxide reduction with redox-active components of living systems determines the decay rates of nitroxide spin probes and labels in biological and biophysical applications.[34,110] The problem of nitroxide bioreduction for many decades was the crucial obstacle to the application of great potential of EPR/spin labeling method to biochemical and biophysical studies *in vivo* and in cells. Recent findings in nitroxide chemistry can open the way for these research.

Five-membered nitroxides, especially those of pyrrolidine, pyrroline and imidazolidine series, are by far more resistant to reduction than nitroxides with smaller or larger ring or acyclic nitroxides, see Chart 2.5.[111–115]

For example, TEMPO shows an almost 50 times higher reduction rate with ascorbate than 2,2,5,5-tetramethylpyrrolidine-1-oxyl.[111] Studies of redox equilibrium in the reversible reaction of various nitroxides with ^{15}N-labeled reference hydroxylamines also revealed a drastic difference between equilibrium constants for five- and six-membered nitroxides (Figure 2.2).[116,117] These equilibrium constants, K, are related to the Gibbs free energy of the reaction with the equation: $\Delta G^{\circ} = -RT\ln K$. The difference between ΔG for each pair of nitroxides (or the ratio of equilibrium constants) is independent of the reference hydroxylamine, characterizing the thermodynamic difference between nitroxide–hydroxylamine redox pairs.

The difference in oxidant properties of nitroxides with different ring sizes obviously arises from conformational peculiarities of different heterocycles, which can stabilize or destabilize sp^2 or sp^3 hybridized nitrogen atoms in

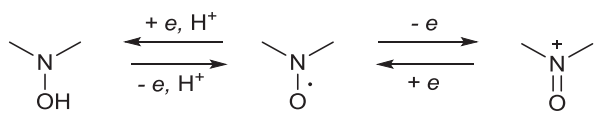

Scheme 2.13 Redox transformations of nitroxides.

Chart 2.5 Various nitroxides ranged in the order of rate of reduction with ascorbate (on the basis of published data).[111,112]

Figure 2.2 Equilibrium in a mixture of nitroxide and reference ^{15}N-hydroxylamine.[116,117]

the ring.[111] Indeed, X-ray analysis data for acyclic nitroxides show that nitrogen of the nitroxide group favors planar geometry.[12] The six-membered rings usually adopt chair conformation and repulsion with equatorial methyl groups leading to deviation of nitroxide moiety from planarity toward pyramidal shape in piperidine nitroxides (this deviation was confirmed by X-ray data[12]) and making hydroxylamine with sp^3 hybridized nitrogen more favorable. In contrast, in five-membered rings, planar conformation of the sp^2 hybridized atom is favorable, while hydroxylamine is strained due to repulsion of the hydroxy group and adjacent methyls.

Remarkably, oxidation of nitroxides to oxoammonium cation does not follow the reverse order to that shown in Chart 2.5 and reveals no significant difference between piperidine and pyrrolidine nitroxides.[116]

Electron-withdrawing substituents expectably increase oxidant activity of nitroxides, increasing their reduction rate. Some authors denote faster reduction of cationic nitroxides compared to anionic ones.[113,118,119] For reactions with ascorbate this effect is sometimes attributed to electrostatic repulsion or attraction with negatively charged ascorbate anion.[61,119] However, the observed reduction rates of nitroxides with the charged groups show good correlation with inductive constants of these substituents,[114] therefore the contribution of electrostatic repulsion (if any) should not be overestimated.

Considering the behavior of nitroxides under the conditions where reversible redox transformations are possible (*e.g.*, in biological systems), one should take into account the pK_a of corresponding hydroxylamines, because protonation of the latter may shift the equilibriums. The ionization state of other functional groups is also important.

In the last decade much attention has been paid to the preparation of various nitroxides which are bulkier than methyl substituents at α-carbons. These nitroxides were called ''sterically shielded'' or ''sterically hindered''. Interestingly, these nitroxides initially attracted more attention in nitroxide-mediated controlled radical polymerization (NMP).[120,121] Bulky substituents may shift back the equilibrium in the reversible reaction of nitroxides with carbon-centered radicals of growing polymer chains with macromolecular alkoxyamine formation and decrease the contribution of side reactions, thereby improving the polymerization process and resulting polymer quality.[78]

The effect of sterical shielding upon the rates of reduction of various nitroxides with ascorbate was studied by several authors.[60,61,75,122–125] It has been shown that replacement of methyl groups at α-carbon atoms of nitroxide moiety with bulkier alkyl substituents leads to an increase of nitroxide stability to reduction. Spiro-cyclohexane moieties at α-carbons are less efficient than geminal ethyl groups.[60] An increase in the lengths of *n*-alkyl substituents produces a minor effect. The ratio of the rate constants of reduction with ascorbate for tetramethyl- to tetraethyl-substituted nitroxides varies greatly depending on the type of heterocycle (see Table 2.1), sometimes exceeding two orders of magnitude. In accordance with the

Table 2.1 Rate constants of reduction with ascorbate $k_{(R=Et)}$ and the ratio of the rate constants $k_{(R=Me)}/k_{(R=Et)}$ for some nitroxides.

	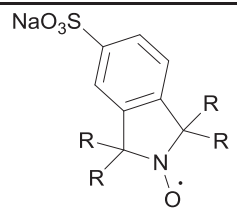	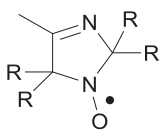	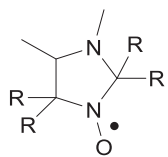	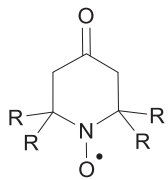	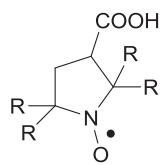	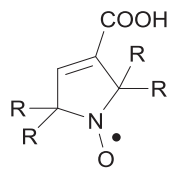	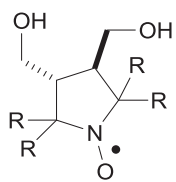
$k_{(R=Et)}$	0.079^{60}	0.5^{126}	0.084^{60} 0.04^{126}	0.066^{60}	0.002^{60}	0.002^{127}	0.00033^{59}
$k_{(R=Me)}/k_{(R=Et)}$	5.6^{60}	11^{126}	20^{126}	87^{60}	40^{60}	140^{127}	600^{59}

aforementioned pattern, five-membered 2,2,5,5-tetraethylpyrrolidine nitroxides demonstrate the highest stability. In the case of nitroxide **19** remote substituents in the positions 3 and 4 *trans* to each other also seem to contribute to nitroxide stability because their repulsion with geminal ethyls produces additional hindrance to the nitroxide group. Some sterically shielded nitroxides demonstrate high lifetimes in living cells, exceeding that of trityl radicals.[61]

Various approaches have been used to investigate the influence of bulky substituents upon redox properties of nitroxides, including kinetic studies and electrochemical measurements to extract thermodynamic parameters characterizing redox properties of different sterically shielded nitroxides.[61,123,124] Kinetics of the reaction of sterically shielded nitroxides with ascorbate deviates from the second-order pattern, leading to quasi-equilibrium with much slower rate constant of decay compared to the initial one. A detailed investigation of the mechanism of this reaction was performed by Bobko *et al.*,[125] who suggested to suppress the reverse reaction of ascorbate radical with hydroxylamine by addition of glutathione. This simplified determination of the rate constants and allowed for quantitative analysis of the observed effects.[123] In addition, equilibrium constants in the reactions of sterically shielded imidazoline and imidazolidine nitroxides with ^{15}N-labeled reference hydroxylamine were determined. Comparison of the equilibrium constants showed that bulky substituents make nitroxide weaker oxidants, *i.e.*, their reduction is thermodynamically less favored. Analysis of all these data by means of multiple regression using the Fujita steric constants E_s and the inductive Hammett constants σ_I of the substituents showed that both the rate and equilibrium constants show satisfactory bi-parameter correlations.[123] This approach allows for simultaneous consideration of both steric and electronic effects of the substituents. Obviously the role of bulky substituents is not limited to hindering access of reductant. Presumably, repulsion with bulky substituents at α-carbons leads to destabilization of pyramidal hydroxylamine, making nitroxide reduction less favorable.

2.3.2 Electron Spin Relaxation

Although spirocyclic moieties provide lower resistance to reduction compared to geminal ethyls, they have an important advantage providing longer spin relaxation times. Studies of spin relaxation for nitroxides of various structures showed that rotation of alkyl substituents enhances spin echo dephasing at temperatures above 60 K, decreasing phase memory time T_m.[128] This parameter is of crucial importance for pulsed double electron–electron resonance (PELDOR or DEER) spectroscopy which is used in structural biology for interspin distance measurements in spin-labeled biomolecules and getting orientational information. Conventional tetramethyl-substituted spin labels are used at temperatures around 50 K, allowing for accurate measurement of 3.5 nm distance.[70,71] Faster spin echo dephasing

rates at higher temperature restrict the measurements to shorter interspin distances and limit the accuracy. The spin labels with spirocyclic moieties at α-carbons demonstrate much lower dephasing rates at 60–180 K than tetramethyl-substituted spin labels,[128,129] allowing PELDOR measurements at liquid nitrogen and even at room temperature.[130]

2.4 The Most Important Nitroxide Classes

2.4.1 Piperidine Nitroxides

Nitroxides of piperidine series have found a large number of applications. Important advantages of TEMPO nitroxides are easy preparation, bulk industrial production (low price) and well-developed functionalization pathways. General methods for synthesis of 2,2,6,6-tetramethylpiperidine-1-oxyl (TEMPO) derivatives including the most useful spin labels have been developed in the early years of nitroxide chemistry starting with triacetonamine.[2,131] Direct condensation of higher ketones to piperidinones is not efficient, except for that with butan-2-one (Scheme 2.14).[132]

The introduction of various substituents into positions 2 and 6 of the piperidine ring can be performed *via* heating of acetonine or *N*-methyl-2,2,6,6-piperidin-4-one with excess of ketone and ammonium chloride.[124,133–137] Depending on the ratio of reagents and conditions, both reactions give mixtures of piperidinones, including those with desired substituents in positions 2 or 2 and 6 of the ring. The resulting amines can be oxidized to corresponding nitroxides. The preparative yields are usually low to moderate, nevertheless numerous 2,2,6,6-tetrasubstituted and 2,6-dispiro-substituted piperidinones have been prepared using this method. Some examples are shown in Scheme 2.15.

To prepare 2,2,6,6-tetraethylpiperidine derivatives the reaction with tetrahydro-4*H*-thiopyran-4-one was used, and thiopyrane moieties in the resulting spiro-tricyclic amine were then subjected to desulfurization with Raney Ni.[138] The carbonyl group may be affected in the reaction conditions,[60] therefore an optimized procedure was suggested with protection of carbonyl group *via* dioxolane formation.[136] Several alternative methods have been suggested,[78,139,140] the most promising of them are shown in Scheme 2.16. It should be noted that all syntheses of 2,2,5,5-tetraethylpiperidin-4-one-1-oxyl imply multistep procedures with low overall yield.

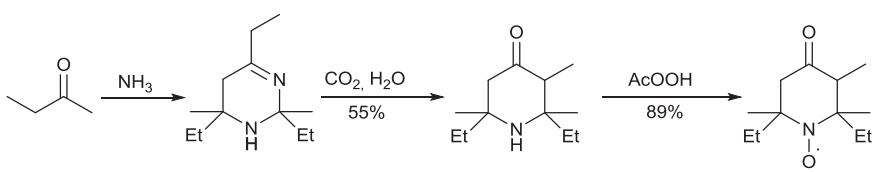

Scheme 2.14 Synthesis of 2,6-diethyl-2,3,6-trimethylpiperidine-4-one-1-oxyl.

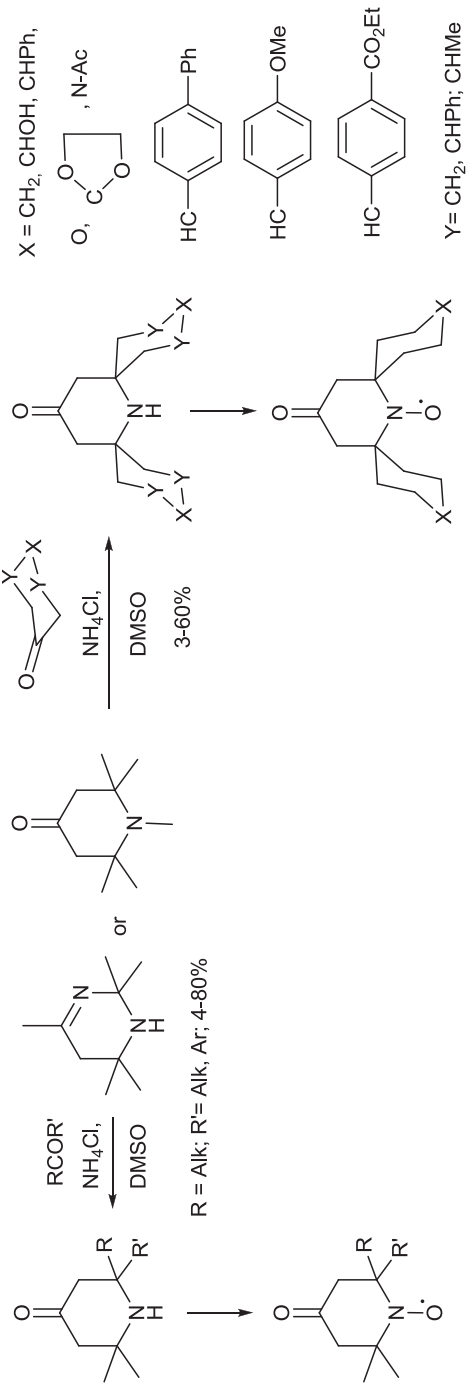

Scheme 2.15 Synthesis of 2,6- and 2-substituted piperidin-4-one-1-oxyls.

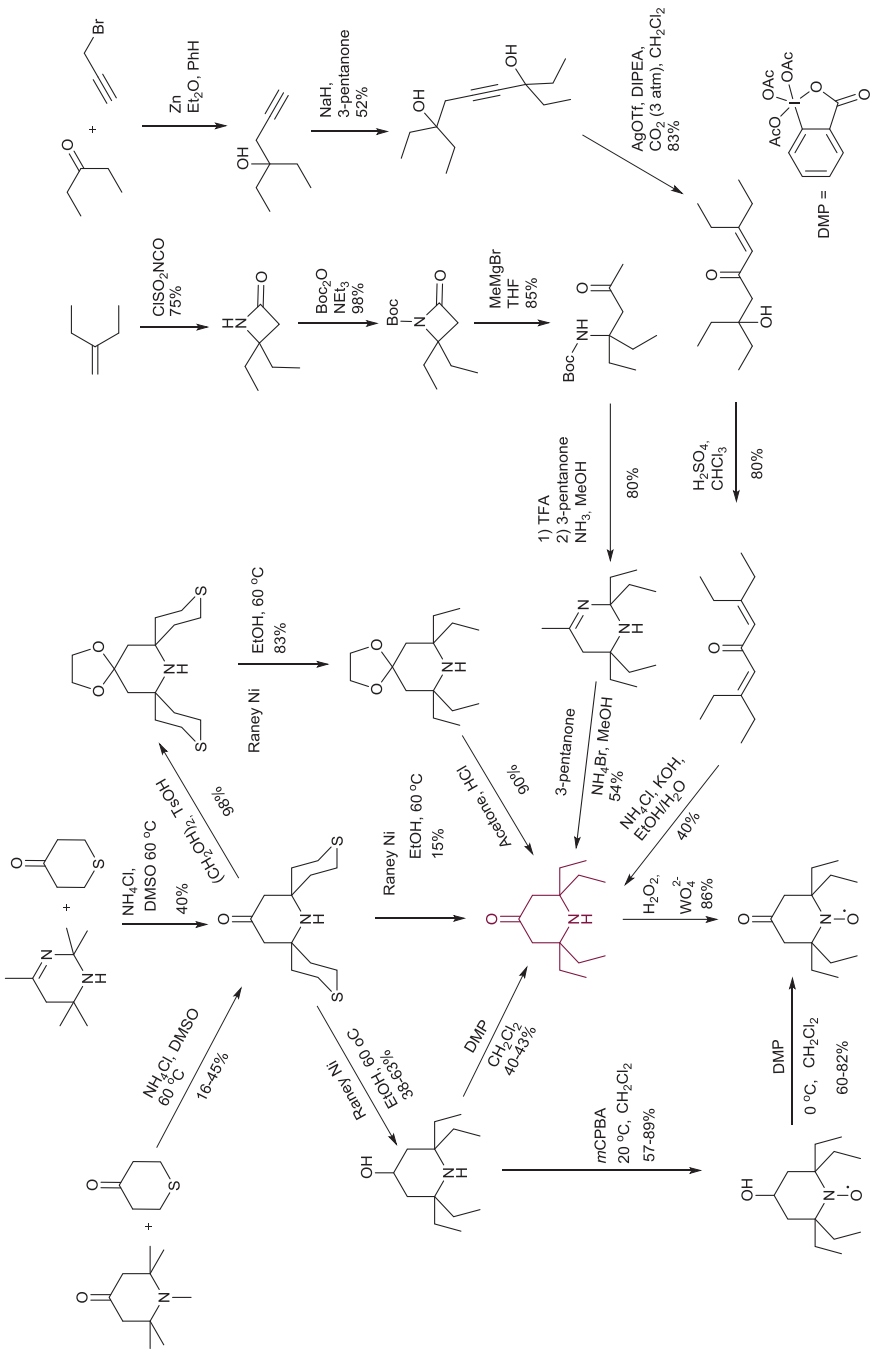

Scheme 2.16 Syntheses of 2,2,5,5-tetraethylpiperidin-4-one-1-oxyl.[60,78,127,136,138,139]

Unless TEMPO derivatives themselves are relatively strong oxidants, they easily undergo one-electron oxidation to oxoammonium cation. The oxoammoinum salts are stable enough to be isolated as individual compounds, provided that the molecule contains no functional groups capable of reacting with oxoammonium cation, *e.g.*, amine, alcohol, *etc.* The low price and easily reversible redox conversions of TEMPO derivatives make them the nitroxides of choice for rechargeable electric batteries[32] and for various catalytic oxidation processes.[28,29] Despite their rapid reduction with biogenic reductants, piperidine nitroxides are often used in biological systems. The redox properties of piperidine nitroxides make them efficient scavengers of superoxide radical, showing pronounced SOD-mimetic and antioxidant activity.[34,35,141,142] Remarkably, sterically shielded piperidine nitroxides showed higher protective activity than TEMPO derivatives,[143] presumably due to the lower electrochemical potential of oxidation and lower reduction rates.[124]

Due to relatively narrow line widths (below 1 G for some non-deuterated TEMPO nitroxides) TEMPO derivatives are considered as potential spin probes for EPR and EPR imaging.[144] Mitochondria-targeted TEMPO derivative, mito-TEMPO, was applied for EPR/EPRI of redox status in mouse brain or tumors.[145,146] 4-Functionalized TEMPO derivatives are achiral, affording no diastereomeric mixtures upon reaction with biomolecules, and can be fruitfully applied in some SDSL-PELDOR studies, see, for example, recent studies of spin-labeled DNA.[147–149]

Recently, several research groups have reported on the syntheses of various paramagnetic nanoparticles with TEMPO incorporated into polymer matrix or attached to the nanocarrier surface (see Scheme 2.17 as an example).[150–153]

2.4.2 Pyrroline Nitroxides

These small radicals with planar achiral structure are the best choice to fulfill the requirement ''to report news, not to make news''. Spin labels of pyrroline series are at the top of the list of the most frequently used spin labels. Pyrroline nitroxides demonstrate slightly lower resistance to reduction compared to pyrrolidine-1-oxyls, but have significantly higher electrochemical potentials of oxidation.

The general method of synthesis of pyrroline nitroxides implies Favorskii rearrangement of brominated piperidin-4-ones.[2,82,127,131,154] Halogenation of piperidin-4-ones in acidic media gives 3,5-dibromo derivatives, which then undergo rearrangement in alkaline media to give corresponding pyrrolines. Depending on the nucleophile present, the rearrangement can give various amides, or esters and carboxylic acid. This sequence gives a high yield of 2,2,5,5-tetramethyl-3-pyrrolines, but the yields of pyrrolines with bulkier substituents in positions 2 and 5 may be significantly lower. Oxidation of resulting pyrrolines affords corresponding nitroxides (Scheme 2.18).

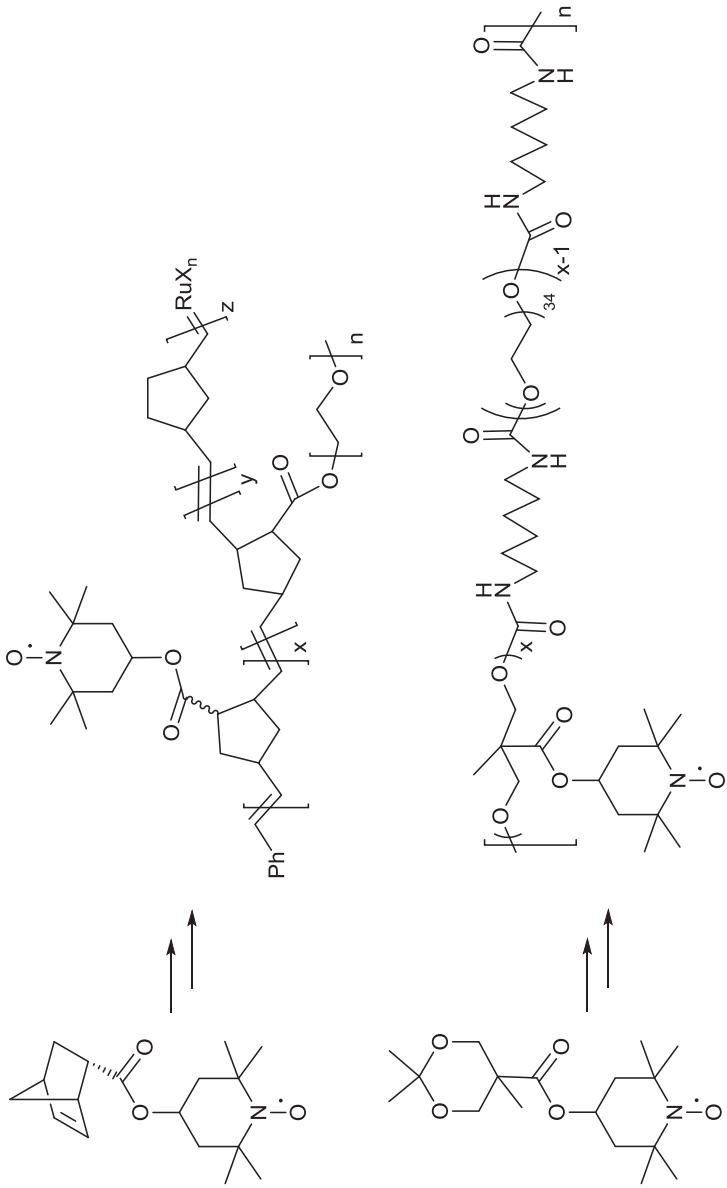

Scheme 2.17

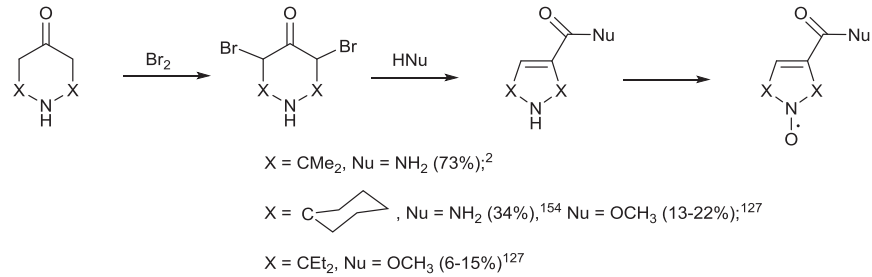

Scheme 2.18

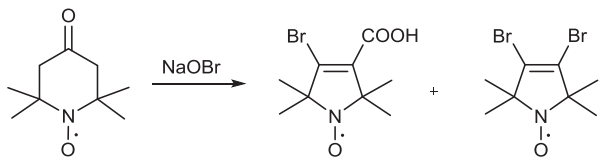

Scheme 2.19

3-Bromopyrroline nitroxides can be prepared in one step from 4-oxo-TEMPO *via* bromination with hypobromite in alkaline media (Scheme 2.19).[131] Remarkably, the few aforementioned pyrroline nitroxides are the key precursors of a huge number of pyrroline spin labels, spin probes and biologically active conjugates. Various methods and efficient procedures for synthesis of numerous 2,2,5,5-tetramethylpyrroline-1-oxyl derivatives have been developed, mainly in Kàlmàn Hideg's laboratory, and can be found in the reviews.[155–158] Current achievements in pyrroline spin labels chemistry were included in recent reviews.[42–44,70,71] Recent syntheses of sterically shielded pyrroline spin labels usually imply similar approaches.[154,159,160]

Recently an original method for synthesis of 2,5-functionalized pyrroline nitroxides was suggested by Rajca *et al.*[161] Reduction of *N*-Boc-2,5-bis-methoxycarbonylpyrrole with Li/di-*tert*-butyl-biphenyl system afforded dianion **22**, which was then quenched with methyl chloroformate or methyl bromoacetate to give 2,2,5,5-tetrasubstituted pyrrolines. Removal of Boc and oxidation afforded nitroxides **23** and **24** (Scheme 2.20). The new nitroxides showed better temperature dependences of electron spin relaxation times T_m and T_1 compared to tetramethyl pyrroline nitroxides,[161] however they are strong oxidants.[162]

2.4.3 Pyrrolidine Nitroxides

Pyrrolidine nitroxides are known to show the highest resistance to bioreduction. For this reason they are widely used in biophysics and biomedical

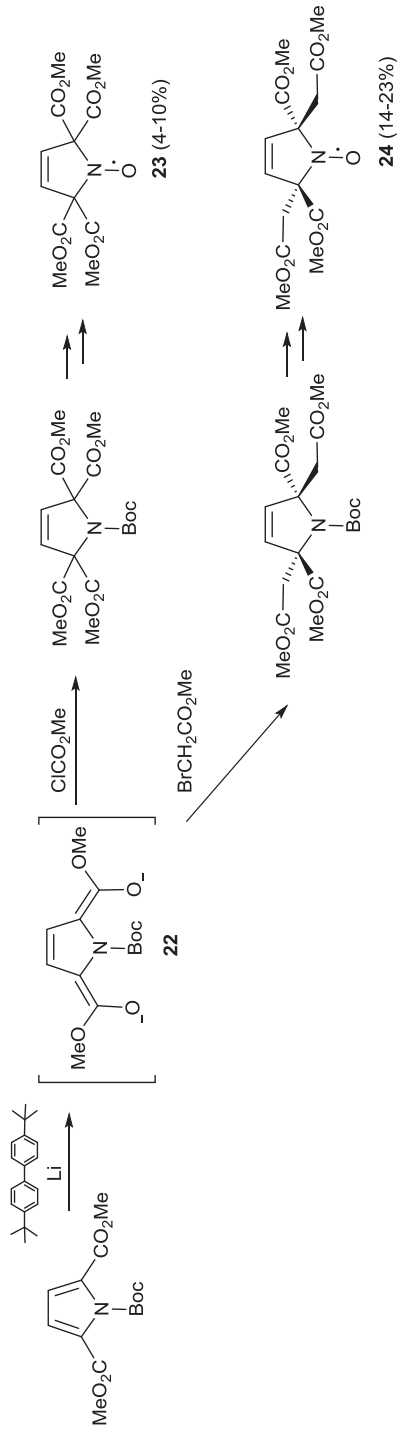

Scheme 2.20

research. Several approaches have been developed for the synthesis of pyrrolidine nitroxides. 3-Functionalized derivatives can be prepared *via* Favorskii rearrangement from 3-bromo-piperidinones.[82,163] This method was successfully used for sterically shielded nitroxides of pyrrolidine series (Scheme 2.21).[60,84] Dispirocyclic nitroxide **25** is a key compound in the synthesis of efficient organic radical contrast agents for MRI.[52,63]

Plenty of 2-functionalized pyrrolidine nitroxides have been prepared from 1-pyrroline 1-oxides *via* addition of organometallic compounds or *via* 1,3-dipolar cycloaddition reaction (see also Schemes 2.11–2.13 in this review). Various methods can be used for preparation of 1-pyrroline 1-oxides. The most commonly used approach implies reductive cyclization of γ-nitroketones or nitroaldehydes (Scheme 2.22).[77,98,105,158]

A series of 1-pyrroline-3-one-1-oxides have been prepared *via* hydrolysis and recyclization of enaminoketones of imidazoline series (Scheme 2.23). Their reaction with organometallic leads to 2-substituted 4-oxopyrrolidine-1-oxyls.[16,100,164,165]

Recently, a convenient synthesis of 2,2,5,5-tetraethyl pyrrolidine nitroxide **19** was published.[59] The pyrrolidine ring was assembled *via* three-component domino reaction of diethyl ketone, α-aminobutyric acid and

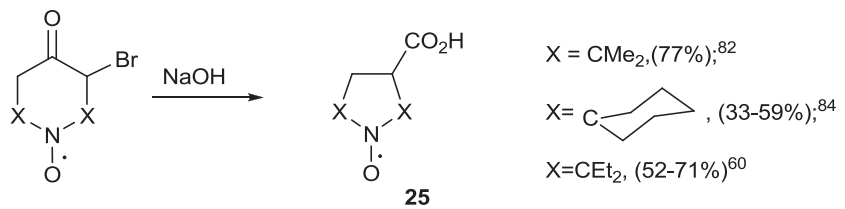

Scheme 2.21

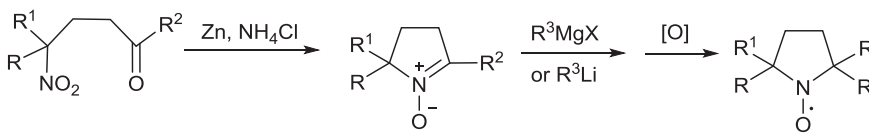

Scheme 2.22

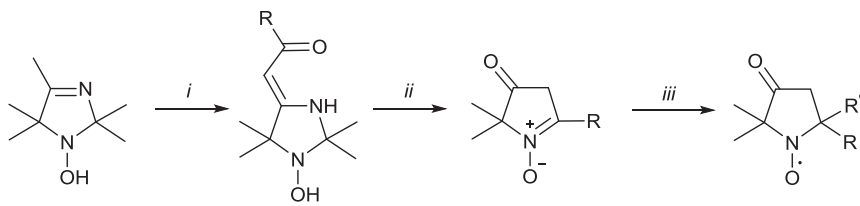

Scheme 2.23 Reagents and conditions: (*i*) LDA or PhLi (2 equiv.)/Ar, RCOOAlk, then H_2O; (*ii*) 10% HCl, 20 °C, 24–72 h, then NaOH to pH 7; (*iii*) R′MgX or R′Li/Ar, then H_2O, MnO_2.

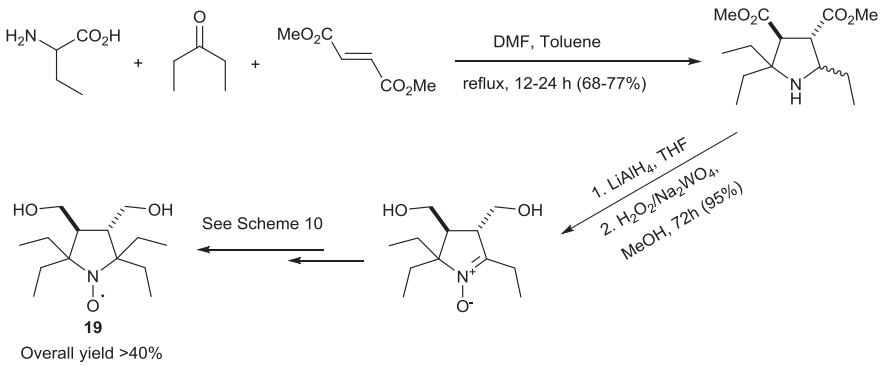

Scheme 2.24

dimethyl fumarate (Scheme 2.24). The reaction implies intermediate azomethine ylide formation from amino acid and ketone with subsequent 1,3-dipolar cycloaddition to fumarate. The following transformations include reduction of ester groups and vinylmagnesium bromide addition. Finally, hydrogenation of the terminal ethylene bond and oxidation afforded the target nitroxide with rather high overall yield (40%).

Pyrrolidine nitroxides can be prepared from pyrroline nitroxides *via* reduction with lithium borohydride[154] or *via* Michael addition to an activated C=C double bond.[166–168] This reaction was used in the synthesis of hydrophilic dicarboxylic acid **26** and diester **27**, which are promising spin probes for EPRI (Scheme 2.25).[167,169–172] Nitroxide **27** was shown to undergo intracellular hydrolysis, leading to accumulation of **26** ($X{=}CMe_2$) inside cells.[173]

Functionalized pyrrolidine nitroxides usually have at least one asymmetric center, therefore their use for spin labeling of chiral biological molecules in PELDOR studies may lead to diastereomeric mixtures. Nevertheless a number of pyrrolidine spin labels are commonly used for spin labeling.[42,70,71,155,158]

Efficient fully organic contrast agents for MRI were assembled *via* attachment of various pyrrolidine spin labels to polyamine dendrimers or *via* polymerization of the nitroxide-containing monomers, including complex structures incorporating sterically shielded pyrrolidine nitroxide, which showed impressive relaxivity parameters and high lifetime in MRI.[51,52,63,174]

2.4.4 Isoindoline Nitroxides

Tetramethyl-substituted nitroxides of isoindoline series are stronger oxidants compared to nitroxides of pyrroline or pyrrolidine series, however their tetraethyl analogs show approximately the same reduction rates as 2,2,5,5-tetramethylpyrrolidine-1-oxyls.[61] Recently, an efficient method for synthesis of 1,1,3,3-tetraethyl-susbstituted isoindoline nitroxides was developed, which opened the way for the broader application of sterically shielded isoindoline nitroxides (Scheme 2.26).[175,176]

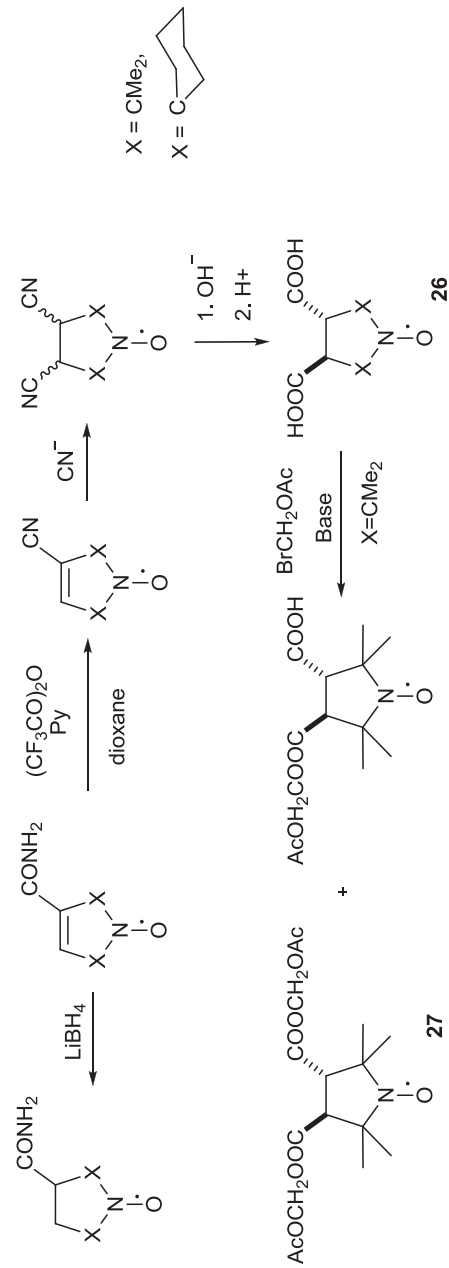

Scheme 2.25 Synthesis of pyrrolidine nitroxides from pyrroline-1-oxyls.

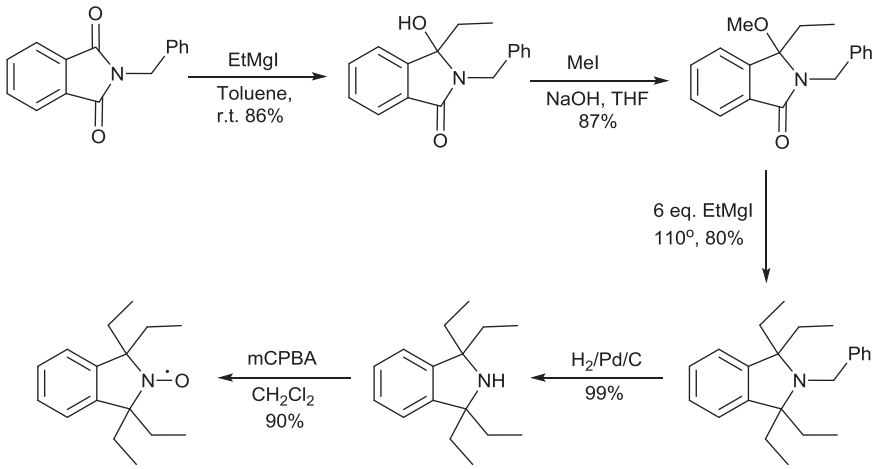

Scheme 2.26 Synthesis of 1,1,3,3-tetraethyl isoindoline nitroxide.

Various approaches to the synthesis of 5,6-disubstituted isoindoline nitroxides have been developed.[177,178] These derivatives were used for assembling annealed heterocyclic systems and synthesis of series of spin labels for rigid attachment to nucleotide moieties of DNA.[70,71]

Isoindoline nitroxides recently attracted much interest due to the synthesis of advanced profluorescent spin probes.[54,64,179–181]

2.4.5 3-Imidazoline and Imidazolidine Nitroxides

Unique properties of this class of nitroxides result from the second nitrogen atom in the heterocycle. This heteroatom is capable of protonation or coordination with metals. Due to close proximity of this basic center to the nitroxide group, protonation at the nitrogen atom in position 3 of the ring produced a high effect upon EPR spectral parameters of these nitroxides. This effect is exploited for local pH measurements in various inhomogeneous media, including living tissues, surfaces of organic and inorganic materials, biomembranes and protein molecules. Nitroxides with pH-dependent spectra are used for investigation of proton transport processes and local electrostatics of surfaces. The general theory and methodology of these measurements can be found in the reviews.[36–40,182–184] A large number of specialized spin probes have been synthesized differing in pK, sensitivity, lipophilicity and stability to reduction.[40,53,99,182,185–187]

The most important pH-sensitive spin probes have been prepared in the series of imidazolidine and 4-amino-3-imidazoline derivatives. Imidazolidine nitroxides represent a fortunate example of minimalistic unification of the basic center and the nitroxide group. Protonation of the N-3 atom leads to localization of the positive charge on two-σ-bonds distance from the

nitroxide group and causes significant electron and spin density redistribution, in particular, in an hfc constant (a_N) decrease by *ca.* 1.3 G. However, close proximity of the nitroxide group to the amino group has an important drawback: due to electron-withdrawing effect of the nitroxide moiety the pK_a of the known imidazolidine nitroxides does not exceed 4.9. The most widely used nitroxides of these series, including spin probes of various lipophilicities **26** and covalently binding spin labels **27** and **28**, were prepared by Reznikov *et al.* (Scheme 2.27).[16,188,189]

In the neutral form a saturated imidazolidine ring nitrogen atom produced a moderate electron-withdrawing effect upon the nitroxide group, therefore these nitroxides show almost the same resistance to reduction as pyrrolines and pyrrolidines.[61,116,123,125,129] Electrochemical oxidation of these nitroxides also occurs at nearly the same potential as oxidation of pyrrolidine nitroxides. However, in contrast to the latter, electrochemical oxidation of imidazolidine nitroxides is irreversible due to the instability of the corresponding oxoammonium cation.[116,190] Similar behavior of imidazolidine nitroxides in reactions with some ROS makes them of potential use for investigation of oxidative stress.[190] However, this effect seems to be responsible for relatively low lifetimes of these nitroxides in biological samples.

Charge delocalization in amidine makes 4-amino-3-imidazoline-1-oxyls much more basic than imidazolidine nitroxides (pK_a varies in the range 5–8), but provides lower sensitivity of the spectral parameters to protonation ($\Delta a_N = 0.8$–1 G). In the 3-imidazoline ring the influence of the neighboring double C=N bond makes oxidant properties of nitroxide group close to those of piperidine nitroxides.[112,116] Relatively high sensitivity to pH changes in a physiologically important region attracted much interest to these spin probes. A convenient pathway to 4-arylamino- and 4-alkyl-amino-2,2,5,5-tetramethyl-3-imidazoline-1-oxyls was developed.[75,186,191,192] The method exploits the 1,3-dipolar cycloaddition reaction of paramagnetic aldonitrone **29** with isocyanates with subsequent scission of oxadiazolone ring with nucleophiles (Scheme 2.28).[186] The overall yield of pH-sensitive nitroxides varies in the range 5–25%. The method allowed for synthesis of various spin probes, including those with p$K_a > 6$. Some of these nitroxides can be used as spin labels, *e.g.*, nitroxide-modified gold nanoparticles have been prepared with pH-dependent EPR spectra.[187]

The most fruitful approach to synthesis of 4-amino-2,5-dihydroimidazole derivatives implies Grignard reagent addition to 5-amino-4*H*-imidazole-3-oxides (Scheme 2.29).[53,99,129,193,194]

The method allows for variation of substituents in positions 2 and 5 of the heterocycle and at the exocyclic nitrogen atom. The titration curves of synthesized nitroxides are shown in Figure 2.3. Remarkably, some of them perfectly fit for measurements of pH in a physiologically important region. Moreover, additional basic centers can be introduced into the side chain, *e.g.*, **31** and **32**, which undergo consecutive protonation upon titration,

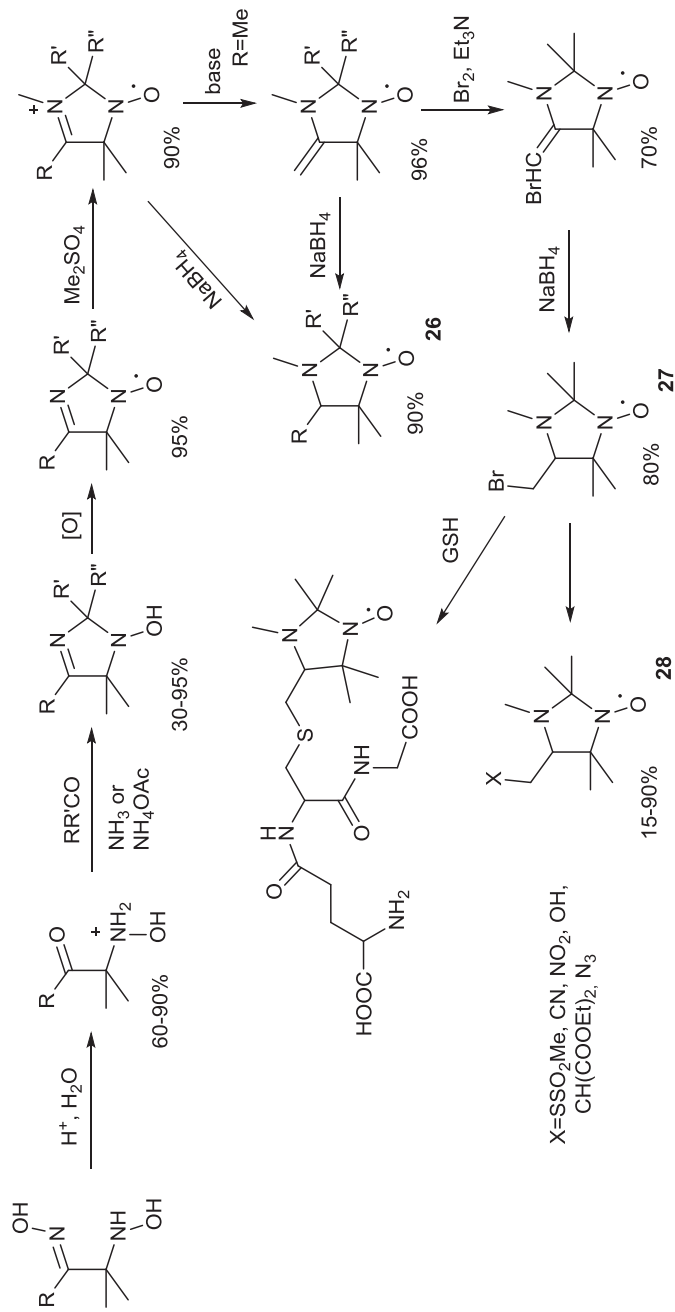

Scheme 2.27 Synthesis of imidazolidine nitroxides.

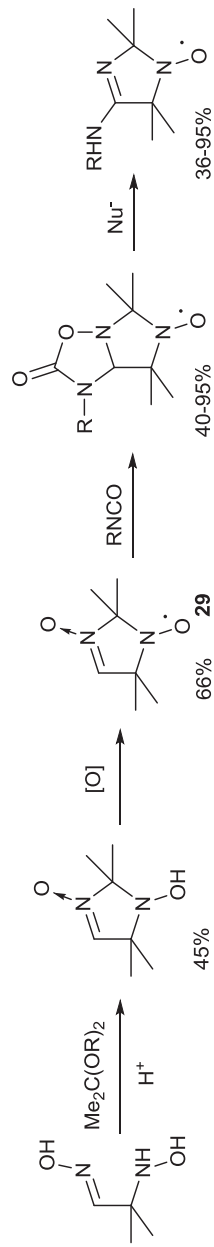

Scheme 2.28 Synthesis of 4-amino-3-imidazolin-3-oxides *via* 1,3-dipolar cycloaddition of isocyanates to paramagnetic aldonitrone **29**.

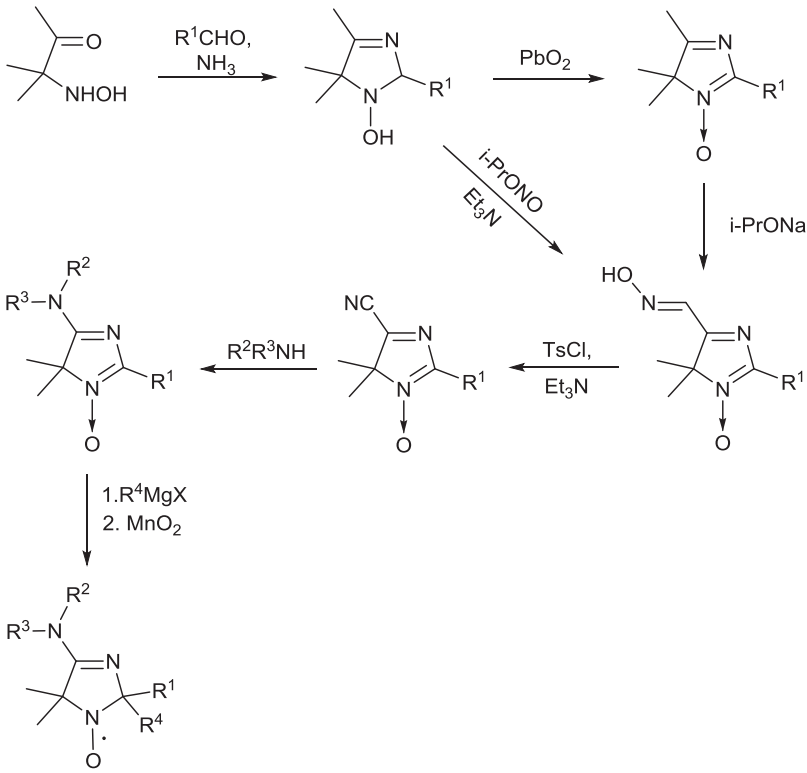

Scheme 2.29 Synthesis of 4-amino-3-imidazolin-1-oxyls *via* Grignard reagent addition to 5-amino-4*H*-imidazole-3-oxides.

making both the range of pH sensitivity and the range of a_N variation broader. The nitroxide **32** was especially useful for investigation of surfaces of various inorganic and organo-inorganic materials.[39]

Nitroxides **35** and **36** were converted into spin labels **37** and **38** (Scheme 2.30). The latter, **38**, was attached to lipid and used for studies of surface electrostatics of biological membranes.[195] The partly deuterated version of **37** was converted into hydrophilic cell-impermeable spin probe **39** which was very efficient in measurement and imaging extracellular pH in living tissues.[53,172,196–198]

Imidazoline nitroxides can be used in nitroxide-mediated polymerization. Protonation of the basic centers in **32** allows for tuning parameters of reversible homolysis of the C–O bond in alkoxyamines of ''sleeping'' polymer chains for successful polymerization of different monomers.[199] Nitroxide **12a** was found suitable for controlled synthesis of methyl methacrylate–styrene block-copolymers.[79] Recently the paramagnetic aldonitrone **29** was used for preparation of alkoxyamine, which is capable of *in situ* activation during polymer synthesis *via* 1,3-dipolar cycloaddition to the monomer.[65]

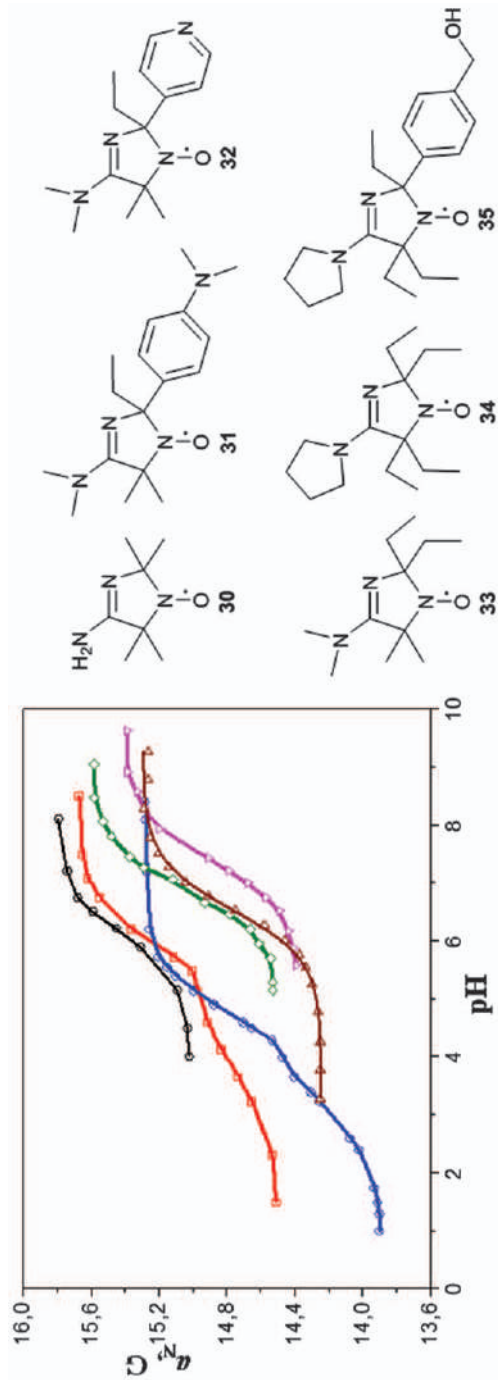

Figure 2.3 Experimental titration curves of hfc constants dependence on pH in X-band EPR spectra of nitroxides **30** (-○-), **31** (-□-), **32** (-○-), **33** (-◇-), **34** (-▽-) and **35** (-▷-).[53,99,129,193]

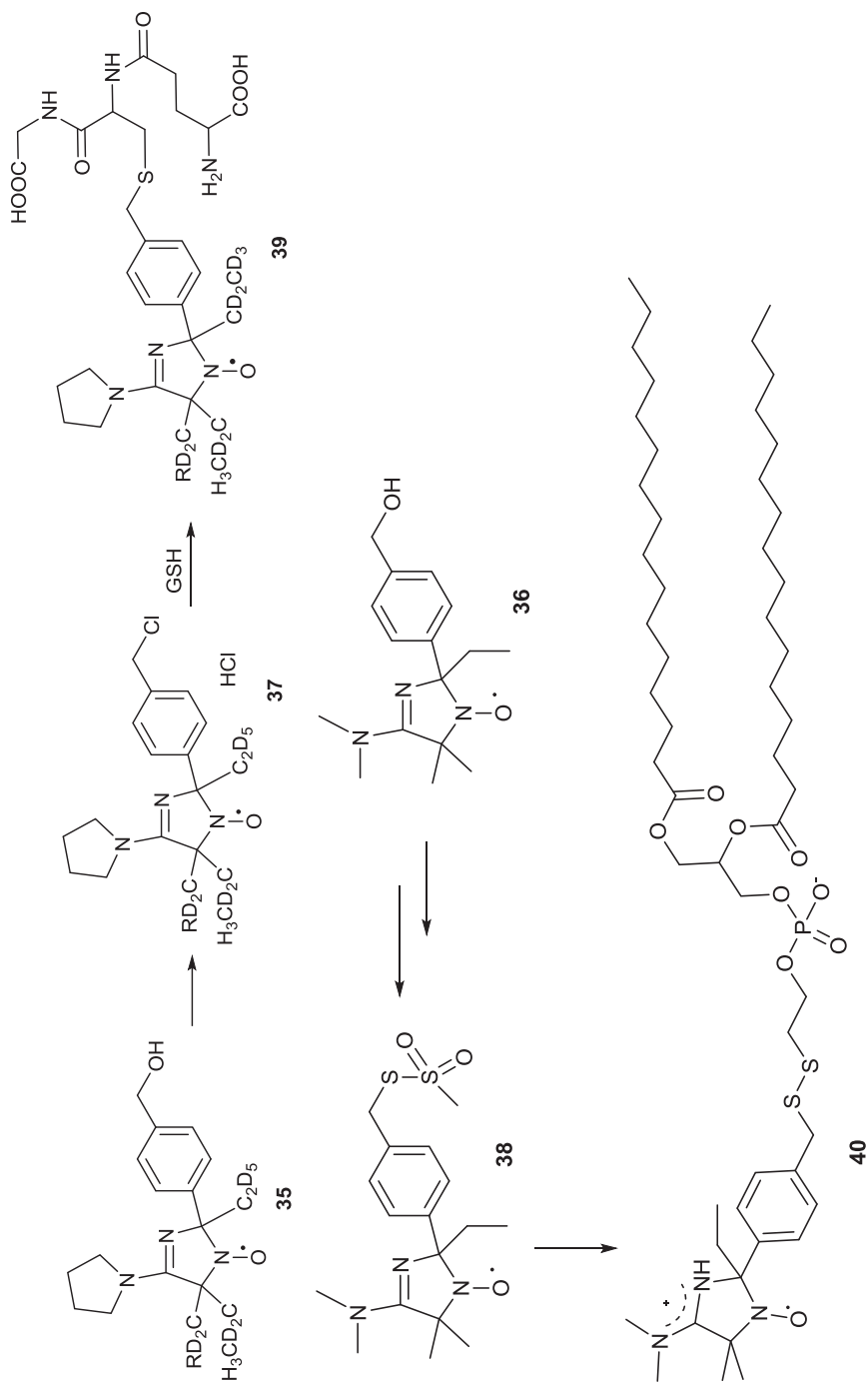

Scheme 2.30 pH-sensitive spin labels and spin probes.

2.5 Cyclic Conjugated Nitroxides

2.5.1 4,5-Dihydroimidazole-1-oxyls

Since its discovery in 1967 by Prof. Edwin F. Ullman *et al.*, a new class of conjugated nitronyl nitroxyl radicals (NNRs) of 4,5-dihydroimidazole-3-oxide-1-oxyl series,[200] these compounds have remained the focus of attention of researchers due to their unique physicochemical characteristics, combining stability with high reactivity. This allowed a variety of functional derivatives to be obtained, equally interesting both for modern materials science (bridging ligands, which are capable of forming 1D magnetic species with different transition-metal and rare-earth ions for single molecular magnets; electroactive components for redox-flow batteries) and for biochemical applications (spin-labeling, powerful NO-regulators, low-toxic contrast agents for MR-tomography, *etc.*). Over the past half century, more than 500 papers, reviews and patents on the synthesis and applications of NNRs have been published.

The general scheme for the synthesis of NNRs has not changed much and usually represents a two-step process involving the condensation of 2,3-bis(hydroxyamino)-2,3-dimethylbutane **41**[201–203] with an aldehyde to form intermediate cyclic 1,3-dihydroxy derivative **42**, which can be rapidly converted into NNRs **43** upon oxidation with $NaIO_4$, MnO_2 or PbO_2. Interestingly, **42** can be obtained by the selective oxidation of cyclic aminal **44** with *m*-CPBA.[203] NNRs **43** can easily lose the oxygen atom upon treatment with nitrous acid or triphenylphosphine, turning into another important class of stable conjugated nitroxyl radicals, iminonitroxides (INRs) **45** (Scheme 2.31).

Plenty of symmetric diradicals, bis-NNRs, have been synthesized in a similar manner over the last two decades *via* condensation of compound **41** with diformyl derivatives of different arenes,[204–209] hetarenes[210–221] and metallocenes.[222] This method was also used to assemble heterodiradical **46** containing nitronyl nitroxyl and benzotriazinyl fragments, which shows unusually high stability, *i.e.*, it does not decompose upon high-temperature sublimation (Scheme 2.32).[223] More recently, similar polycrystalline heterodiradical **47** has been prepared *via* the same method, capable of forming a novel one-dimensional (1D) spin-1 ($S = 1$) chain of organic radicals with intrachain antiferromagnetic coupling of $J'/k = -14$ K, due to the N···N and N···O intermolecular contacts. This type of antiferromagnetic coupling in diradical **47** is by far the strongest among all studied 1D $S = 1$ chains of organic radicals, which also makes 1D $S = 1$ chains of **47** the most isotropic, and therefore an excellent system for studies of low-dimensional magnetism.[224]

Among the principal approaches that have been developed in recent years for the synthesis of functional NNRs, we focus only on those associated either with a change of the environment at the C_α of nitroxyl fragment (C-4, C-5 of imidazoline) or with activation of the substituent at the C-2 atom,

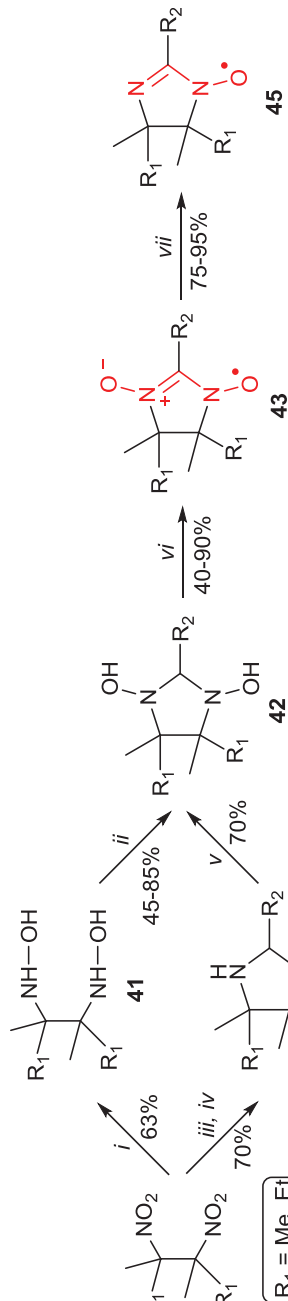

Scheme 2.31 General route to nitronyl nitroxides and iminonitroxides. Reagents and conditions: (*i*) Zn, NH_4Cl, THF–H_2O, Ar, 12 °C (3h) → 5 °C (12 h), then Na_2CO_3, NaCl, Soxlet, DCM; (*ii*) R_2CHO, MeOH (or PhH or THF), rt → Δ; (*iii*) Sn, 37% aq HCl, Δ, 3 h, then NaOH, DCM; (*iv*) R_2CHO, Et_2O, 5 °C, 10 min; (*v*) aq $NaHCO_3$, 2 equiv. *m*-CPBA, DCM, 0 °C, 30 min; (*vi*) MnO_2 (or PbO_2) in MeOH, DCM, $CHCl_3$, rt, 10 min–2 h or $NaIO_4$, H_2O–DCM, 0 °C → 10 °C, 5 min–30 min; (*vii*) $NaNO_2$, H_2O, AcOH, rt.

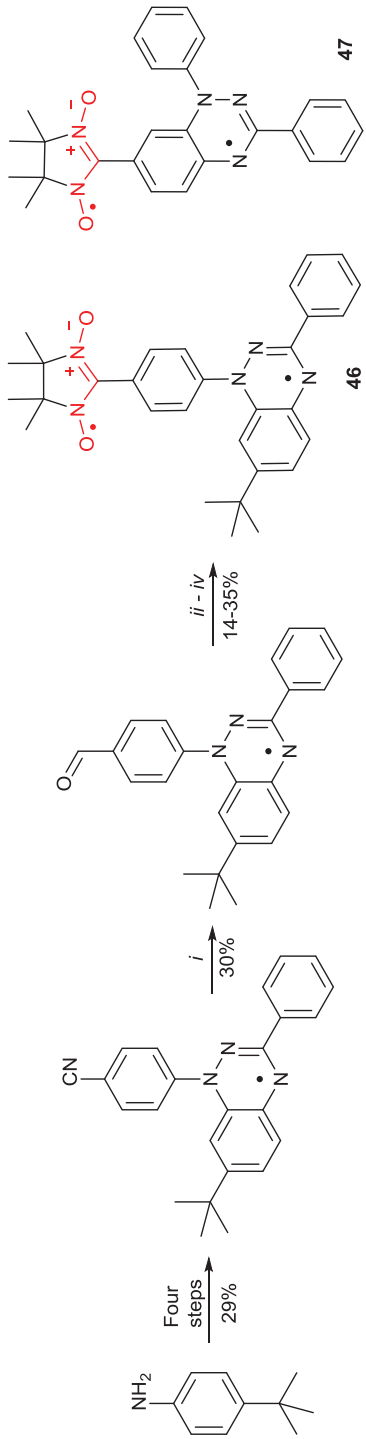

Scheme 2.32 Synthesis of heterodiradicals NNR-benzotriazinyls. Reagents and conditions: (*i*) DIBAL-H, DCM, −78 °C→ rt, then HCl, rt; (*ii*) $Na_2S_2O_4$, $CHCl_3/H_2O$, rt; (*iii*) HOHN–CMe_2–CMe_2–NHOH, MeOH, Δ, 10 h; (*iv*) O_2, TEA, DCM, rt, 12 h.

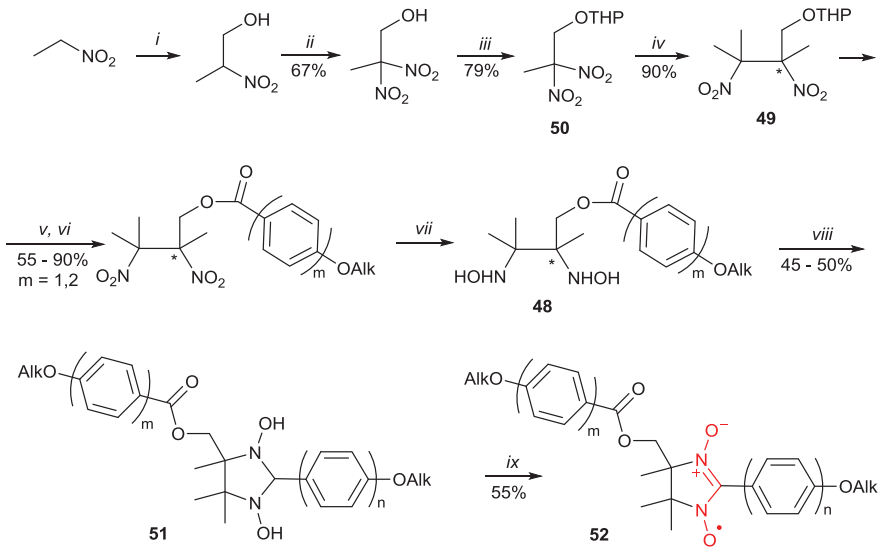

Scheme 2.33 General route to chiral NNRs. Reagents and conditions: (*i*) 37% aq HCHO, NaOH, H_2O, rt, 2 h; (*ii*) $NaNO_2$, $K_3[Fe(CN)_6]$, $Na_2S_2O_8$, THF, 15 °C → rt, 1 h; (*iii*) DHP, PPTS, DCM, rt; (*iv*) $Li^+C^-(Me)_2NO_2$, DMSO, Ar, rt, 15 h; (*v*) I_2, MeOH, 60 °C, 6 h; (*vi*) $AlkO(C_6H_4)_mCOCl$, Et_3N, DMAP, DCM, rt, 22 h; (*vii*) Al, 3% aq $HgCl_2$, THF, H_2O, 0 °C, 20 min; (*viii*) $AlkO(C_6H_4)_nCHO$, 5% mol *p*-TsOH, rt, 4 d; (*ix*) $NaIO_4$, $H_2O/CHCl_3$, rt, 15 min.

allowing the use of NNR-residue as a nucleophilic partner or substrate in palladium-catalyzed cross-coupling reactions.

Tamura *et al.* elaborated an approach for the synthesis of functional 1,2-bis(hydroxylamines) **48** (Scheme 2.33). Asymmetric 1,2-dinitrocompound **49** was prepared from *gem*-dinitro-derivative **50** and the lithium salt of 2-nitropropane *via* the Kornblum reaction[225] and reduced with aluminum amalgam. Condensation of the resulting bis(hydroxylamine) **48** with benzaldehyde[226] or 4-alkoxybenzaldehyde and subsequent oxidation of the intermediate 1,3-dihydroxy derivative **51** leads to a new chiral NNRs **52** bearing a stereogenic center in the imidazolyl framework.[227] It is noteworthy that the authors managed to significantly increase the yield of the condensation product of 1,2-bis(hydroxylamine) with donor type arylaldehyde, by carrying out the reaction without a solvent in the presence of a catalytic amount of *p*-TsOH.

It has been mentioned above that the replacement of geminal methyl groups adjacent to nitroxide group with bulky spirocyclic moieties can produce an increase of nitroxide stability, and alters spin relaxation times. First spirocyclic NNRs were prepared in Ovcharenko lab *via* four-step synthesis starting with cyclopentyl bromide **53** (Scheme 2.34).[228] Nucleophilic substitution of the bromine atom afforded a nitro compound with moderate yield.[229] Remarkably the use of iodine for oxidative dimerization of **54** led to

Scheme 2.34 Synthesis of spirocyclic NNRs. Reagents and conditions: (*i*) ~2 equiv. $NaNO_2$, DMSO (anh.), 15 °C, 3 h; (*ii*) *t*-BuOK, DMF, 50 mol% I_2, 20 °C, 2 h, H_2O; (*iii*) NH_4Cl (4 equiv.), 1 mol% $CdSO_4$, THF, H_2O, Zn (5 equiv.), 15 °C, 90 min, then 20% H_2SO_4 in EtOH, Me_2CO; (*iv*) HetArCHO, H_2O, 20 °C, 1 h; (*v*) MnO_2 (15 equiv.), MeOH, rt, 1 h [*or* $NaIO_4$ (1.5 equiv.), DCM–H_2O, 10 °C, 10 min].

a significant increase of the yield of dinitroalkane **55** (from 17% to 50%) as compared to the earlier described procedure using lead tetraacetate as an oxidant.[230] The reduction of the vicinal dinitro compound **55** by the classical Zn/NH_4Cl system and subsequent condensation of **56** with heteroaromatic aldehydes afforded dispirocyclic NNRs **57**.

NNR **58** is known to exhibit significant C–H acidity upon treatment with *t*-BuOK in DMSO.[231] Treatment with stronger and more sterically hindered base, lithium diisopropylamide (LDA), leads to almost quantitative conversion of **58** into corresponding lithium salt **59**. Further interaction of this stable paramagnetic carbanion **59** with various electrophiles gives 2-substituted derivatives with yields of 43–80% (Scheme 2.35).[232]

Lithium bis(trimethylsilyl)amide (Li-HMDS) is more efficient for generation of carbanion **59**. The latter reacts with various azine-*N*-oxides *via* the S_N^H mechanism affording paramagnetic derivatives of azine *N*-oxides **60** (Scheme 2.36), the reaction being determined solely by kinetic factors. The nucleophilic attack can consecutively target vicinal hydrogens, *e.g.*, reaction with quinoxaline 1,4-dioxide can produce diradicals **61** with topology not accessible within the classic methods of nitronyl nitroxide synthesis.[233–235]

The reaction of carbanion **59** with triazines leads to both substituted NNR and deoxygenated derivatives, iminonitroxides **62**, as a result of either direct oxidation of the intermediate or its dehydration. Interestingly,

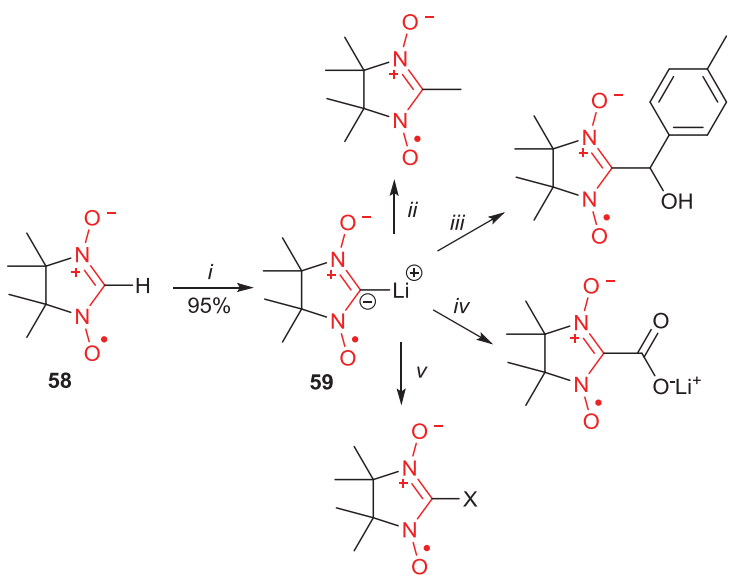

Scheme 2.35 Generation and trapping of carbanion NNR **59**. Reagents and conditions: (*i*) 2 M LDA, THF, −78 °C, 10 min; (*ii*) MeOTf, −78 °C → rt; (*iii*) *p*-tolylaldehyde −78 °C → rt; (*iv*) solid CO_2, −78 °C → rt; (*v*) TMSOTf, *or* S, *or* Se, *or* $Hg(OAc)_2$, −78 °C → rt, X = $SiMe_3$, SLi, SeLi, HgOAc.

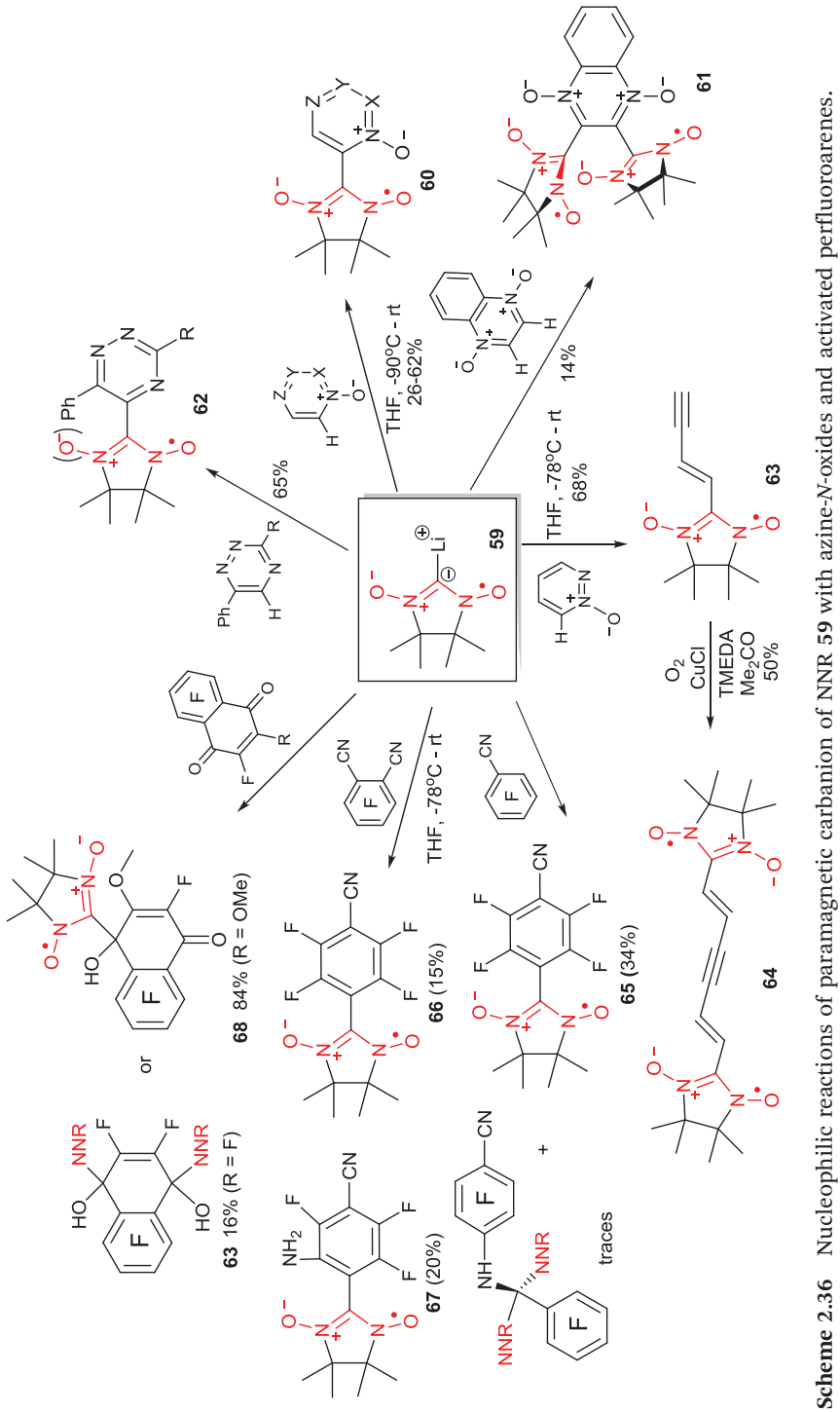

Scheme 2.36 Nucleophilic reactions of paramagnetic carbanion of NNR **59** with azine-*N*-oxides and activated perfluoroarenes.

cinnoline *N*-oxide undergoes the opening of the heterocycle to form 2-enine substituted NNR **63**, which is capable of oxidative transformation to form the diradical **64** with an unusual combination of double and triple bonds (Scheme 2.36).[236]

Activated perfluoroarenes can also react with NNR carbanion **59**. Some examples are shown in Scheme 2.36.[237–239]

The use of paramagnetic synthon **59** proved to be very fruitful for preparation of new conjugated or disjointed homo- and heterodiradicals. For example, the reaction 2-methyl-2-nitrosopropane followed by oxidation with lead(IV) dioxide or manganese(IV) dioxide afforded highly compact nitroxide-substituted nitronyl nitroxide diradical **70**, which was stable in spite of the close proximity of the two radical centers. The di-NNR **70** was quantitatively converted to corresponding di-INR **71** by treatment with nitrous acid (Scheme 2.37).[240,241] These diradicals are stable under aerobic conditions at room temperature and have large positive exchange interactions: $J/k\mathrm{B} = +390$ K ($H = -2J\mathbf{S}_{1/2}\cdot\mathbf{S}_{1/2}$) for NNR **70** and $J/k\mathrm{B} \approx +550$ K for INR **71**.

The silyl derivative of *tert*-butylmethylenenitrone also easily interacts with the paramagnetic carbanion **59**, giving diradical **72**, an analog of 1,1,2,3,3-pentamethylenepropane (PMP) with two nitronyl nitroxide fragments linked through the C(sp^2) atom of the nitrone group. According to magnetic susceptibility measurements, EPR data and *ab initio* calculations diradical **72** have singlet ground state. The singlet–triplet energy splitting ($2J$) is low ($J/k = -7.4$), which comes from the disjointed nature of this diradical.[242] Another reaction of compound **59** with the paramagnetic isomeric cyclic aldonitrone **29** of the 2,5-dihydroimidazole series[243] seems to be the first example of a chemical interaction between two different types of stable radicals, the result of which is not the product of their recombination, but the new stable diradical **73** (Scheme 2.37).[244]

Recently the reaction of **59** with 2,5,5-trimethylpyrroline 1-oxide was studied.[245] The authors succeeded in isolating diradical **74** with a good yield.

Another effective method of functionalizing NNR-H radical was invented by K. Okada and S. Suzuki. Mixing NNR-H **58** and [$Au^I(PPh_3)Cl$] with NaOH in the DCM–MeOH bisolvent (by analogy with the formation of pincer-Pt complexes[246] of NNR) afforded a gold complex of NNR, ([Au^I(NN-2-ido)(PPh_3)]) **75**. This complex is able to react in palladium-catalyzed cross-couplings with various aryl halides to form aryl (hetaryl) substituted NNRs **76**. Iodine derivatives showed the highest activity in these reactions (the yields ranged from 50 to 92%), the most optimal catalyst was $Pd(PPh_3)_4$. Using different diiodo derivatives, corresponding diradicals **77** were obtained (with the exception of *ortho*-substituted diiodobenzene, which under these conditions replaced only one halogen atom, apparently, owing to unfavorable steric factors), as well as a unique triradical **78** (Scheme 2.38).[247]

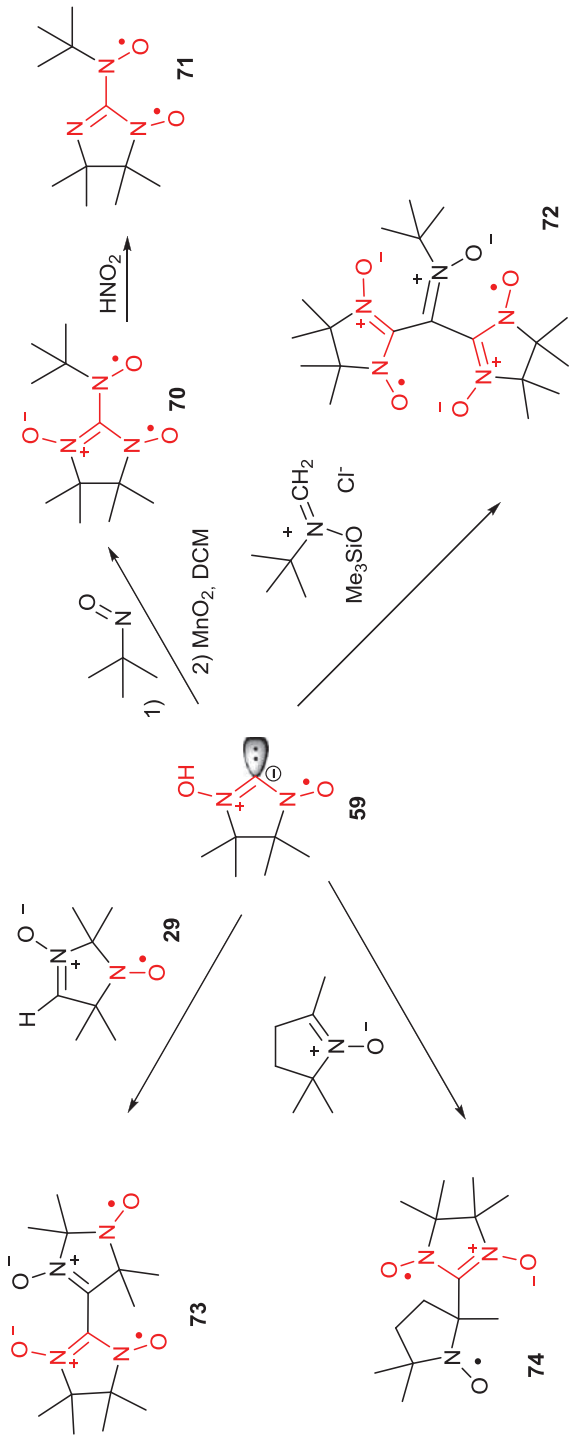

Scheme 2.37 Synthetic approaches for preparation of new types of nitroxide diradicals.

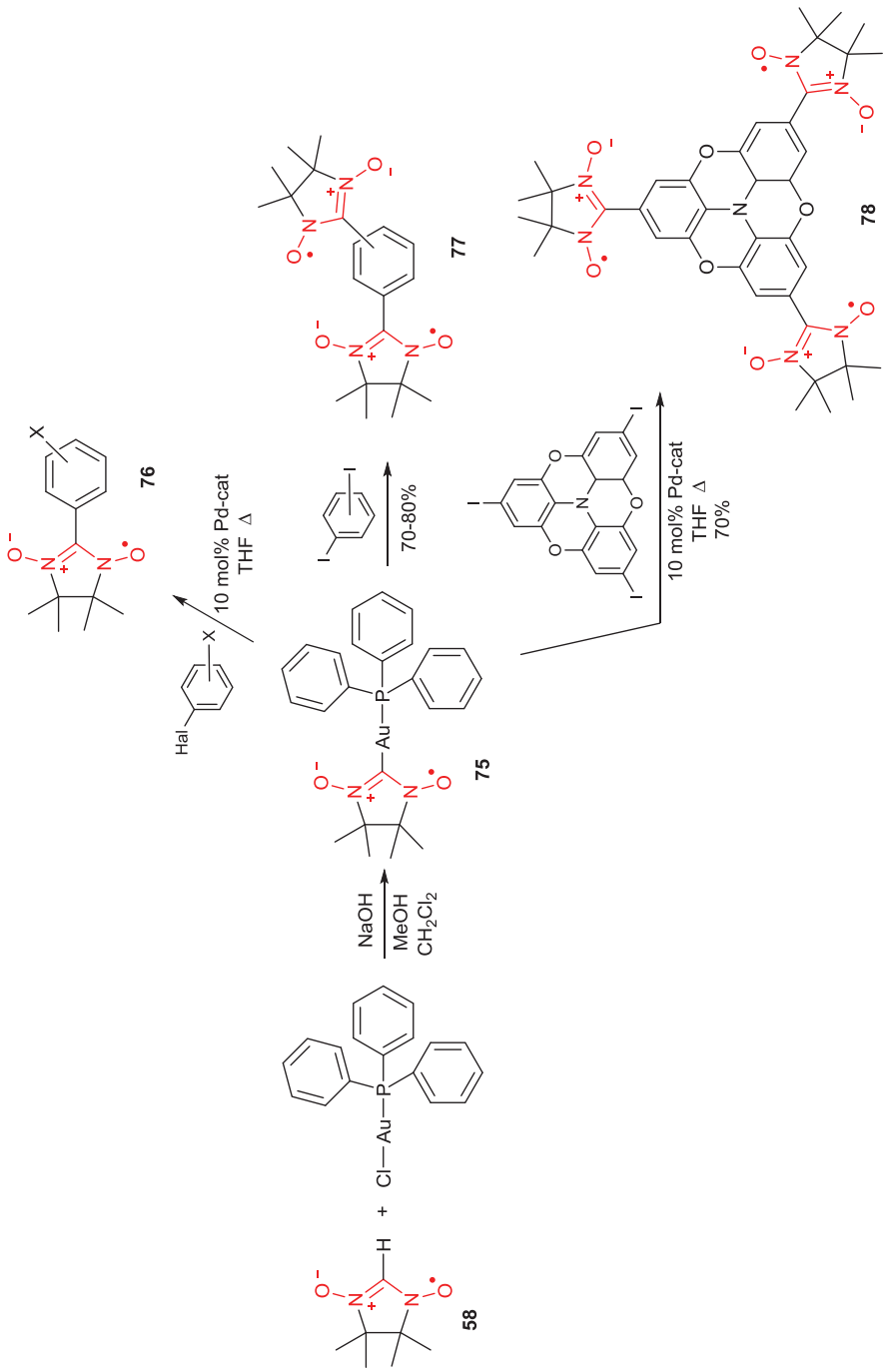

Scheme 2.38 Cross-coupling between gold complex of NNR and Hal-substituted arenes (hetarenes).

2.5.2 Nitronyl Nitroxides of Benzimidazole Series (BenzoNNRs)

Although the first representative of nitronyl nitroxide annelated with the benzene nucleus, 2-phenylbenzimidazol-1-yl *N,N′*-dioxide was synthesized more than 50 years ago,[248] its characterization in the form of stable crystals, for which X-ray structural analysis was performed, magnetic measurements and distribution calculations spin density were made only at the turn of the 21st century.[249]

Two approaches were used in the synthesis of this type of planar nitronyl nitroxides, both are based on the reactions of benzofuroxan (benzo[*c*][1,2,5] oxadiazole 1-oxide) **79** or its derivatives (Scheme 2.39). In the first method, the reduced benzofuroxan derivative, *o*-quinonedioxime **80**,[250] was treated with aromatic aldehyde under acid-catalyzed conditions (cat = HCl, HBr, CCl_3COOH, H_2SO_4 or $HClO_4$); the highest yields of benzimidazoles were observed with four equivalents of 70% $HClO_4$.[251] The resulting 1-hydroxy derivatives **81** were oxidized with a large excess of lead dioxide (~60 equiv.) in DCM to form BenzoNNRs **82** which were isolated in solid form with low to moderate yields.[252] Interestingly, when replacing an aromatic aldehyde with a sterically hindered pivaldehyde, the radical formed during the oxidation of a diamagnetic precursor is stable for some time (about 2 days) only in solution, while attempts to isolate it as a crystals lead only to a diamagnetic oily mixture.[253]

Another approach assumed the reaction of the benzofuroxan **79** with the diarylnitrone obtained by the condensation of *N*-hydroxyaminobenzene with the corresponding aldehyde. 1-Hydroxybenzimidazole-3-oxides, with different heterocyclic residues (*o*- and *m*-pyridyl, 2- and 3-thienyl) in position 2 were obtained. Their oxidation with silver triflate in the presence of tetrabutylammonium hydroxide or using the traditional PbO_2/benzene system resulted in annelated NNRs **82** with moderate yields (~40%).[254] Single crystals of **82** in the form of prisms from dark green to black color were obtained by evaporation of pentane or DCM solution of radical for *ca.* 2 h. Thienyl-substituted benzo-NNRs reveal acceptor–donor interactions, manifested in the appearance of strong broad absorption in near-infrared (NIR) (λ_{max}~1000 nm) and exhibited solvatochromism compatible with charge transfer between the thienyl (donor) and benzonitronyl nitroxide (acceptor) dyads.[255] These studies were supplemented by the publication on the synthesis of a variety of BenzoNNRs and the influence of substituents in the annelated benzene nucleus and in the aryl fragment at the C-2 atom of the BenzoNNRs heterocycle on the distribution of spin density in the radical.[256]

2.5.3 Heterocyclic Vinyl Nitroxides

Vinyl nitroxides **83** can be stabilized with one or two electron-withdrawing groups at the C_β atom. Such radicals were first described by H. G. Aurich *et al.*[257] Usually they are generated by oxidation of the corresponding nitrones **84**, which can readily tautomerize to the enhydroxylamine form due to the

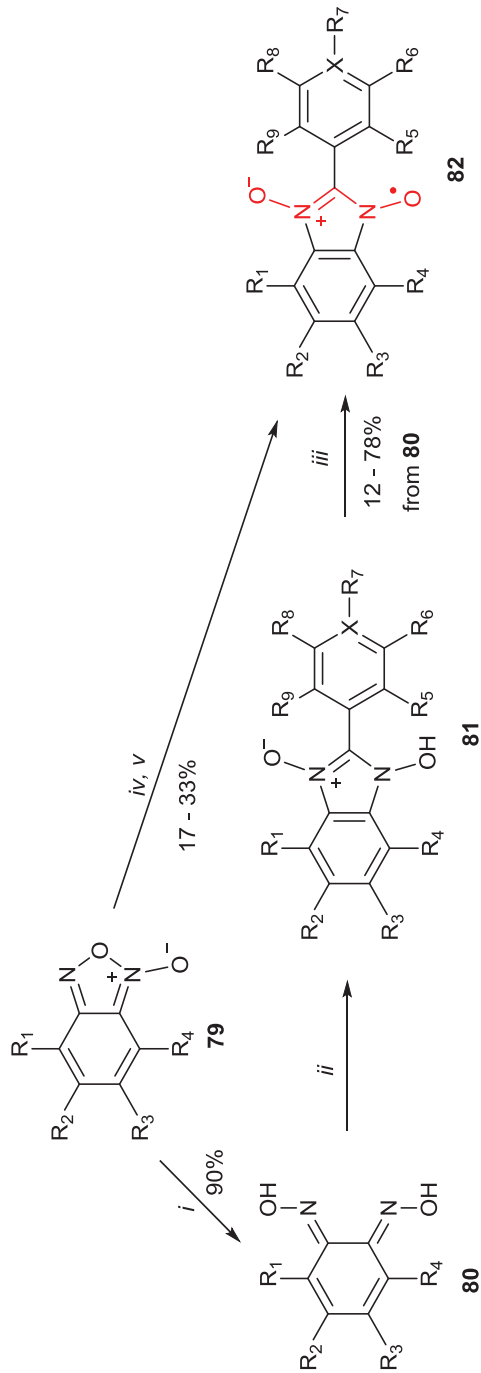

Scheme 2.39 Synthesis of BenzoNNRs. Reagents and conditions: (*i*) 25% aq $N_2H_4 \times H_2O$, 50% aq NaOH, EtOH, 35 °C → 5 °C rt; (*ii*) Ar(Hetar)CHO, EtOH, 4 equiv. of 70% $HClO_4$ (or HBr), Δ, 2 h, then rt, aq NH_4OH; (*iii*) large excess of PbO_2, CH_2Cl_2, 10 min, filtration and repeating process in fresh DCM; (*iv*) Ar(Hetar)CH=N(O)Ph, C_6H_6, Δ, 24 h; (*v*) Bu_4NOH, then AgOTf, toluene, 22 °C, 2 min.

presence of an R_1 substituent possessing the -M effect. Owing to the high degree of delocalization of the spin density over the π system, vinyl nitroxides are extremely highly reactive and, as a rule, could be involved in recombination reactions to form dimers of the C–C or C–O type.[258] Therefore, these radicals cannot be separated in individual form and are referred to as persistent. The typical half-life in the solutions is from 10 min (Scheme 2.40, $R_2 = Ph$) to 2 h (Scheme 2.40, $R_2 = H$, COOMe). According to the authors, monosubstituted vinyl nitroxides are also able to undergo a spin-trapping reaction with their precursor nitrone to give spin adducts.[259]

Significant stabilization of such vinyl nitroxides was achieved when the double C=C bond was incorporated into the five-membered heterocycle, pyrroline, and the β-carbon atom of the multiple endocyclic bond was linked to two electron-withdrawing fragments, the nitrile and carbonyl groups.[260,261] The synthetic scheme for synthesis of these radicals involves the primary functionalization of the 4-methyl group in 1-hydroxy-pentamethylimidazoline **85** by converting it into a lithiated derivative, followed by treatment with an aromatic ester. Under acidic catalysis, the enaminoketone **86** undergoes recyclization with the formation of cyclic β-oxonitrone **87**, a pyrrolinone derivative, which, in its tautomeric enhydroxylamine form, is able to react with *N*-chlorosuccinimide, with the formation of a 3-chloro derivative **88**. The halogen group is easily replaced by a cyano group by the action of cyanide ion in dry DMSO, followed by the final oxidation of the 1-hydroxy derivative which leads to a stable radical **89** (Scheme 2.41).

The radicals **89a,b** are characterized with triplet ESR spectra with the hyperfine interaction constant $a_N = 5.9$ G ($CHCl_3$) and with long-wave absorption maxima in the visible part of the optical spectra at 564–578 nm. They form dark-violet crystals, which could be stored without decomposition in a cool dark place, but are reduced to diamagnetic precursor upon storage in methanolic solution. This reaction proceeded much more rapidly under the action of an alkaline solution of H_2O_2. Interestingly, radical **89a** exists in two crystal modifications, *viz.*, as violet and green modifications. Both these modifications are formed upon crystallization of compound **89a** from hexane. The predominance of a particular form depends on the concentration, the temperature and the crystallization rate. It was found that these modifications possess different magnetic properties. For one of the radicals synthesized, an extremely high energy of intermolecular exchange interaction ($J/k = -101$ K) has been found. It was noted that these types of

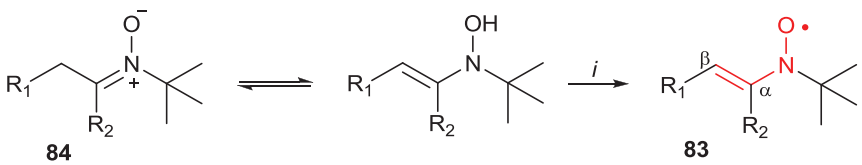

Scheme 2.40 Reagents and conditions: (*i*) NiO_2, $CHCl_3$ (*or* PbO_2, $CHCl_3$), rt, $R_1 = PhSO_2$, COOMe, $R_2 = H$, Ph, COOMe.

Scheme 2.41 Reagents and conditions: (*i*) LDA, Et_2O, rt, 20 min, then R_1COOEt, 0 °C (20 min) → rt (1 h); (*ii*) 10% aq HCl, rt, 24 h; (*iii*) NCS, $CHCl_3$, rt, 1 h; (*iv*) NaCN, DMSO, rt, 45 min, then H_2O, 5% aq HCl; (*v*) 10 equiv. MnO_2, $CHCl_3$, rt, 30 min [R_1 = Ph (**a**), 3-pyridyl (**b**)].

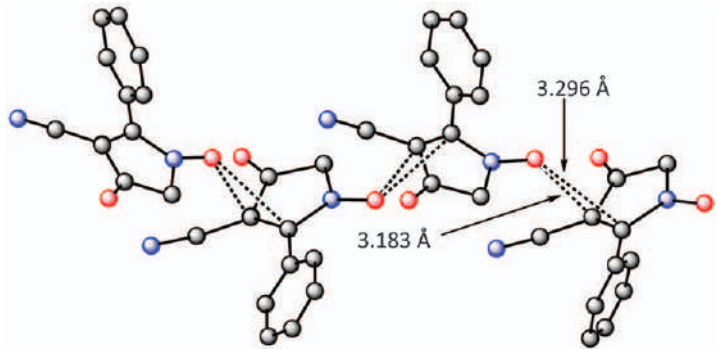

Figure 2.4 Structure of the exchange chain in solid vinyl nitroxide **89a** (H atoms and CH_3 groups are omitted for clarity). Reproduced from ref. 260 with permission from the Royal Society of Chemistry.

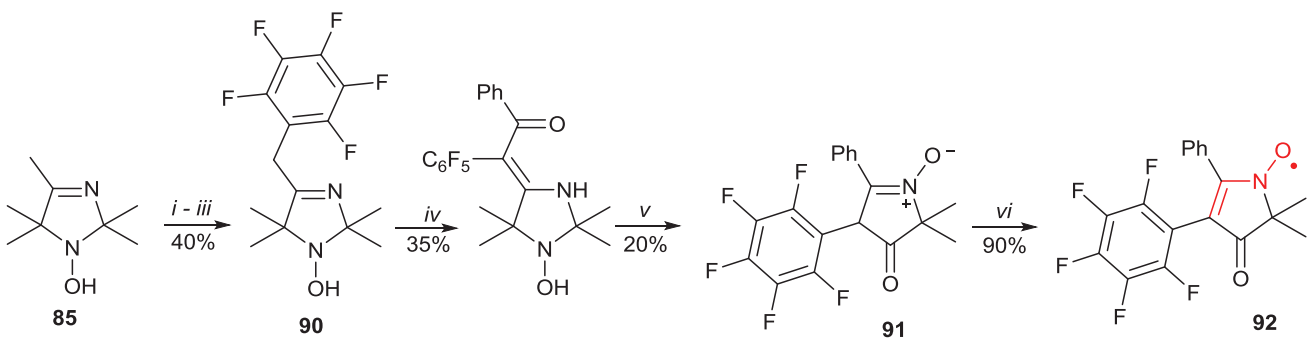

Scheme 2.42 Reagents and conditions: (*i*) LDA, Et_2O, rt, 20 min, then C_6F_6, 0 °C→rt; (*ii*) MnO_2, $CHCl_3$, rt, 1 h; (*iii*) Zn, NH_4Cl, MeOH, rt, 10 min; (*iv*) LDA, Et_2O, rt, 20 min, then PhCOOEt, 0 °C (20 min)→rt (30 min); (*v*) 36% aq HCl–MeOH, 1 : 3, Δ, 2 h; (*vi*) 10 equiv. MnO_2, $CHCl_3$, rt, 30 min.

radicals are able to form magnetic chains with strong interchain exchange interactions at long intermolecular distances (>3 Å) in formally molecular solids (Figure 2.4). The quantum-chemical calculations adequately explain these strong exchange interactions in solid vinylnitroxides. It appeared that these strong interactions are favored by localization of the spin density of the N–O$^{\bullet}$ group of one nitroxide close to the β-carbon of the vinyl group bound to the nitroxyl group of the neighboring nitroxide.

In addition to the nitrile group, other electron-withdrawing substituents, namely the pentafluorophenyl group, can ensure effective stabilization of the unpaired electron. The key pentafluorophenyl derivative **90** was also obtained from carbanion of pentamethyl-substituted imidazoline **85** by reaction with hexafluorobenzene.[262] Re-lithiation, treatment with ethyl benzoate and acid-catalyzed recyclization resulted in a low yield to 3-oxo-4-perfluorophenyl-3,4-dihydro-2*H*-pyrrole 1-oxide **91**, oxidation of which quantitatively gave vinyl nitroxide **92** (Scheme 2.42).

2.6 Conclusion

The broad diversity of known nitroxides can in no way be covered in a short review. Here we have only summarized basic principles, key structures and some current trends in nitroxides chemistry to help the reader in getting a general impression about this rather ''hot'' area of science. Undoubtedly, rapid development of nitroxide chemistry will continue in the coming decades and will result in the synthesis of numerous interesting and useful structures and in discoveries of new areas of application of these radicals in various branches of science and technology.

Acknowledgements

Funding from the Ministry of Science and Higher Education of Russia (project number 14.W03.31.0034) is gratefully acknowledged.

References

1. I. Novak, L. J. Harrison, B. Kovač and L. M. Pratt, *J. Org. Chem.*, 2004, **69**, 7628.
2. E. G. Rozantsev, in *Free Nitroxyl Radicals*, Plenum Press, New York-London, 1970, p. 125.
3. K.-A. Hansen and J. P. Blinco, *Polym. Chem.*, 2018, **9**, 1479.
4. E. P. Tomlinson, M. E. Hay and B. W. Boudouris, *Macromolecules*, 2014, **47**, 6145.
5. V. Ovcharenko, in *Stable Radicals: Fundamentals and Applied Aspects of Odd-electron Compounds*, ed. R. G. Hicks, John Wiley& Sons Ltd., New York, 2010, p. 461.
6. Y. Iwabuchi, *Chem. Pharm. Bull.*, 2013, **61**, 1197.

7. *Nitroxide Mediated Polymerization: From Fundamentals to Applications in Materials Science*, ed. D. Gigmes, RCS Polymer Chemistry Series, No. 19, Croydon, UK, 2016.
8. J. Y. Guillaneuf, C. Lefay, D. Bertin, D. Gigmes and B. Charleux, *Prog. Polym. Sci.*, 2013, **38**, 63.
9. J. Kreutzer and Y. Yagci, *Polymers*, 2018, **10**, 35.
10. M. Edeleva, G. Audran, S. Marque and E. Bagryanskaya, *Materials*, 2019, **12**, 688.
11. S. Thétiot-Laurent, G. Gosset, J.-L. Clément, M. Cassien, A. Mercier, D. Siri, A. Gaudel-Siri, A. Rockenbauer, M. Culcasi and S. Pietri, *ChemBioChem*, 2017, **18**, 300.
12. H. Karoui, F. Le Moigne, O. Ouari and P. Tordo, in *Stable Radicals: Fundamentals and Applied Aspects of Odd-electron Compounds*, ed. R. G. Hicks, Wiley & Sons, New York, 2010, p. 173.
13. H. Toledo, M. Amar, S. Bar, M. A. Iron, N. Fridman, B. Tumanskii, L. J. W. Shimon, M. Botoshansky and A. M. Szpilman, *Org. Biomol. Chem.*, 2015, **13**, 10726.
14. http://www.chem.ucla.edu/~harding/IGOC/B/beta_hydrogen.html.
15. M. Kuvabara, W. Hiraoka and O. Inanami, in *Applications of EPR in Radiation Research*, ed. A. Lund and M. Shiotani, Springer International Publishing, Charm Heidelberg New York Dordrech London, 2014, p. 355.
16. L. B. Volodarsky, V. A. Reznikov and V. I. Ovcharenko, in *Synthetic Chemistry of Stable Nitroxides*, CRC Press Inc., Boca Raton, 1994.
17. F. A. Villamena, M. H. Dickman and D. R. Crist, *Inorg. Chem.*, 1998, **37**, 1454.
18. S. Grimaldi, J.-P. Finet, F. Le Moigne, A. Zeghdaoui, P. Tordo, D. Benoit, M. Fontanille and Y. Gnanou, *Macromolecules*, 2000, **33**, 1141.
19. E. Drockenmuller and J.-M. Catala, *Macromolecules*, 2002, **35**, 2461.
20. D. F. Bowman, T. Gillan and K. U. Ingold, *J. Am. Chem. Soc.*, 1971, **93**, 6555.
21. A. Nilsen and R. Braslau, *J. Polym. Sci., Part A: Polym. Chem.*, 2006, **44**, 697.
22. G. Audran, L. Bosco, P. Brémond, J.-M. Franconi, N. Koonjoo, S. R. A. Marque, P. Massot, P. Mellet, E. Parzy and E. Thiaudière, *Angew. Chem., Int. Ed.*, 2015, **54**, 13379.
23. N. Jugniot, I. Duttagupta, A. Rivot, P. Massot, C. Cardiet, A. Pizzoccaro, M. Jean, N. Vanthuyne, J.-M. Franconi, P. Voisin, G. Devouassoux, E. Parzy, E. Thiaudiere, S. R. A. Marque, A. Bentaher, G. Audran and P. Mellet, *Free Radicals Biol. Med.*, 2018, **126**, 101.
24. G. Audran, L. Bosco, P. Brémond, T. Butscher and S. R. A. Marque, *Org. Biomol. Chem.*, 2016, **14**, 1288.
25. P. Astolfi, L. Greci, P. Stipa, C. Rizzoli, C. Ysacco, M. Rollet, L. Autissier, A. Tardy, Y. Guillaneuf and D. Gigmes, *Polym. Chem.*, 2013, **4**, 3694.

26. R. Liedtke, C. Eller, C. G. Daniliuc, K. Williams, T. H. Warren, M. Tesch, A. Studer, G. Kehr and G. Erker, *Organometallics*, 2016, **35**, 55.
27. M. Sajid, A. Stute, A. J. P. Cardenas, B. J. Culotta, J. A. M. Hepperle, T. H. Warren, B. Schirmer, S. Grimme, A. Studer, C. G. Daniliuc, R. Fröhlich, J. L. Petersen, G. Kehr and G. Erker, *J. Am. Chem. Soc.*, 2012, **134**, 10156.
28. C. Brückner, in *Stable Radicals: Fundamentals and Applied Aspects of Odd-electron Compounds*, ed. R. G. Hicks, John Wiley & Sons Ltd, New York, 2010, p. 433.
29. J. M. Bobbitt, C. Brückner and N. Merbouh, in *Organic Reactions, V. 74*, ed. S. E. Denmark, John Wiley & Sons, Inc., 2009, p. 103.
30. L. Tebben and A. Studer, *Angew. Chem., Int. Ed.*, 2011, **50**, 5034.
31. C. Tansakul and R. Braslau, in *Encyclopedia of Radicals in Chemistry, Biology and Materials*, ed. C. Chatgilialoglua, Wiley, Chichester, 2012, p. 1.
32. T. Suga and H. Nishide, in *Stable Radicals: Fundamentals and Applied Aspects of Odd-electron Compounds*, ed. R. G. Hicks, John Wiley & Sons Ltd, New York, 2010, p. 507.
33. C. Prescott and S. Bottle, *Cell Biochem. Biophys.*, 2017, **75**, 227.
34. B. P. Soule, F. Hyodo, K. Matsumoto, N. L. Simone, J. A. Cook, M. C. Krishna and J. B. Mitchell, *Free Radical Biol. Med.*, 2007, **42**, 1632.
35. M. Lewandowski and K. Gwozdzinski, *Int. J. Mol. Sci.*, 2017, **18**, 2490.
36. V. V. Khramtsov, in *Nitroxides - Theory, Experiment and Applications*, ed. A. I. Kokorin, InTech, Rijeca, Croatia, 2012, p. 317.
37. V. V. Khramtsov and J. L. Zweier, in *Stable Radicals: Fundamentals and Applied Aspects of Odd-electron Compounds*, ed. R. G. Hicks, Wiley, New York, 2010, p. 537.
38. V. V. Khramtsov, *Curr. Org. Chem.*, 2005, **9**, 909.
39. E. Kovaleva and L. Molochnikov, in *Nitroxides: Applications in Chemistry, Biomedicine and Material Science*, ed. G. I. Likhtenshtein, J. Yamauchi, S. Nakatsuji, A. Smirnov and R. Tamura, Wiley-VCH verlag, GmbH & Co. KGaA, Weinheim, 2008, p. 211.
40. M. A. Voinov and A. I. Smirnov, in *Electron Paramagnetic Resonance*, ed. B. C. Gilbert, D. M. Murphy and V. Chechik, RSC Publishing, Cambridge, U.K., vol. 22, 2010, p. 71.
41. W. L. Hubbell, C. J. Lópes, C. Altenbach and Z. Yang, *Curr. Opin. Struct. Biol.*, 2013, **23**, 725.
42. P. Roser, M. J. Schmidt, M. Drescher and D. Summerer, *Org. Biomol. Chem.*, 2016, **14**, 5468.
43. S. A. Shelke and S. T. Sigurdsson, in *Structural Information from Spin-labels and Intrinsic Paramagnetic Centres in the Biosciences*, ed. C. R. Timmel and J. R. Harmer, Springer-Verlag Berlin Heidelberg, Germany, 152, 2014, p. 121.

44. A. J. Fielding, M. G. Consilio, G. Heaven and M. A. Hollas, *Molecules*, 2014, **19**, 16998.
45. K. Zhang and P. Z. Qin, in *Biophysics of RNA Folding: Biophysics for the Life Science 3*, ed. R. Russell, Springer science + Buisiness media, New York, 2013, p. 69.
46. J. P. Klare and H. J. Steinhoff, *Photosynth. Res.*, 2009, **102**, 377.
47. E. G. Bagryanskaya, O. A. Krumkacheva, M. V. Fedin and S. R. A. Marque, in *Methods in Enzymology, Electron Paramagnetic Resonance Investigations of Biological Systems by Using Spin Labels, Spin Probes, and Intrinsic Metal Ions, Part A., V. 563*, ed. P. Z. Qin and K. Warncke, Academic Press, 2015, p. 365.
48. K. Jaudzems, T. Polenova, G. Pintacuda, H. Oschkinat and A. Lesage, *J. Struct. Biol.*, 2019, **206**, 90.
49. P. Berruyer, L. Emsley and A. Lesage, *eMagRes*, 2018, **7**, 93.
50. A. Rankin, J. Trébosc, F. Pourpoint, J.-P. Amoureux and O. Lafon, *Solid State Nucl. Magn. Reson.*, 2019, **101**, 116.
51. C. S. Winalski, S. Shortkroff, E. Schneider, H. Yoshioka, R. V. Mulkern and G. M. Rosen, *Osteoarthr. Cartil.*, 2008, **16**, 815.
52. H. V. T. Nguyen, Q. Chen, J. T. Paletta, P. Harvey, Y. Jiang, H. Zhang, M. D. Boska, M. F. Ottaviani, A. Jasanoff, A. Rajca and J. A. Johnson, *ACS Cent. Sci.*, 2017, **3**, 800.
53. A. Samouilov, O. V. Efimova, A. A. Bobko, Z. Sun, S. Petryakov, T. D. Eubank, D. G. Trofimov, I. A. Kirilyuk, I. A. Grigor'ev, W. Takahashi, J. L. Zweier and V. V. Khramtsov, *Anal. Chem.*, 2014, **86**, 1045.
54. J. P. Blinco, K. E. Fairfull-Smith, B. J. Morrow and S. E. Bottle, *Aust. J. Chem.*, 2011, **64**, 373.
55. X. Meng, W. Shi and P. Cheng, *Coord. Chem. Rev.*, 2019, **378**, 134.
56. P. Franchi, C. Poderi, E. Mezzina, C. Biagini, S. Di Stefano and M. Lucarini, *J. Org. Chem.*, 2019, **84**, 9364.
57. S. Nakazawa, S. Nishida, T. Ise, T. Yoshino, N. Mori, R. D. Rahimi, K. Sato, Y. Morita, K. Toyota, D. Shiomi, M. Kitagawa, H. Hara, P. Carl, P. Höfer and T. Takui, *Angew. Chem., Int. Ed.*, 2012, **51**, 9860.
58. J. Lee, E. Lee, S. Kim, G. S. Bang, D. A. Shultz, R. D. Schmidt, M. D. E. Forbes and H. Lee, *Angew. Chem., Int. Ed.*, 2011, **50**, 4414.
59. S. A. Dobrynin, Y. I. Glazachev, Y. V. Gatilov, E. I. Chernyak, G. E. Salnikov and I. A. Kirilyuk, *J. Org. Chem.*, 2018, **83**, 5392.
60. J. T. Paletta, M. Pink, B. Foley, S. Rajca and A. Rajca, *Org. Lett.*, 2012, **14**, 5322.
61. A. P. Jagtap, I. Krstic, N. C. Kunjir, R. Hänsel, T. F. Prisner and S. T. Sigurdsson, *Free Radical Res.*, 2015, **49**, 78.
62. G. Casano, H. Karoui and O. Ouari, *eMagRes*, 2018, **7**, 195.
63. H. V.-T. Nguyen, A. Detappe, N. M. Gallagher, H. Zhang, P. Harvey, C. Yan, C. Mathieu, M. R. Golder, Y. Jiang, M. F. Ottaviani, A. Jasanoff, A. Rajca, I. Ghobrial, P. P. Ghoroghchian and J. A. Johnson, *ACS Nano*, 2018, **12**, 11343.

64. K. L. Chong, B. A. Chalmers, J. K. Cullen, A. Kaur, J. L. Kolanowski, B. J. Morrow, K. E. Fairfull-Smith, M. J. Lavin, N. L. Barnett, E. J. New, M. P. Murphy and S. E. Bottle, *Free Radicals Biol. Med.*, 2018, **128**, 97.
65. M. Edeleva, D. Morozov, D. Parkhomenko, Y. Polienko, A. Iurchenkova, I. Kirilyuk and E. Bagryanskaya, *Chem. Commun.*, 2019, **55**, 190.
66. K. Nagura, Y. Takemoto, S. Moronaga, Y. Uchida, S. Shimono, A. Shiino, K. Tanigaki, T. Amano, F. Yoshino, Y. Noda, S. Koizumi, N. Komatsu, T. Kato, J. Yamauchi and R. Tamura, *Chem. – Eur. J.*, 2017, **23**, 15713.
67. K. Nagura, Y. Takemoto, F. Yoshino, A. Bogdanov, N. Chumakova, A. K. Vorobiev, H. Imai, T. Matsuda, S. Shimono, T. Kato, N. Komatsu and R. Tamura, *Pharmaceutics*, 2019, **11**, 42.
68. K. Nagura, A. Bogdanov, N. Chumakova, A. K. Vorobiev, S. Moronaga, H. Imai, T. Matsuda, Y. Noda, T. Maeda, S. Koizumi, K. Sakamoto, T. Amano, F. Yoshino, T. Kato, N. Komatsu and R. Tamura, *Nanotechnology*, 2019, **30**, 224002.
69. J. P. Blinco, S. E. Bottle, K. E. Fairfull-Smith, E. M. Simpson and K. Thomas, in *Nitroxide Mediated Polymerization: From Fundamentals to Applications in Materials Science*, ed. D. Gigmes, RSC Publishing, Cambridge, U.K., 2015, p. 114.
70. M. M. Haugland, E. A. Anderson and J. E. Lovett, in *Electron Paramagnetic Resonance, V. 25*, ed. V. Chechik and D. M. Murphy, RSC Publishing, Cambridge, U.K., 2017, p. 1.
71. M. M. Haugland, J. E. Lovett and E. A. Anderson, *Chem. Soc. Rev.*, 2018, **47**, 668.
72. S. Nakatsuji, in *Nitroxides: Applications in Chemistry, Biomedicine, and Materials Science*, ed. G. I. Likhtenshtein, J. Yamauchi, S. Nakatsuji, A. I. Smirnov and R. Tamura, WILEY-VCH Verlag GmbH & Co. KGaA, Weinheim, 2008, p. 161.
73. N. Merbouh, J. M. Bobbitt and C. Brückner, *Org. Prep. Proced. Int.*, 2004, **36**, 1.
74. T. Janoschka, N. Martin, M. D. Hager and U. S. Schubert, *Angew. Chem., Int.,*, 2016, **55**, 14427.
75. J. F. Polienko, T. Schanding, Y. V. Gatilov, I. A. Grigor'ev and M. A. Voinov, *J. Org. Chem.*, 2008, **73**, 502.
76. V. D. Sen', V. A. Golubev, I. V. Kulyk and É. G. Rozantsev, *Russ. Chem. Bull.*, 1976, **25**, 1647.
77. Y. V. Khoroshunova, D. A. Morozov, A. I. Taratayko, P. D. Gladkikh, Y. I. Glazachev and I. A. Kirilyuk, *Beilstein J. Org. Chem.*, 2019, 201937.
78. C. Wetter, J. Gierlich, C. A. Knoop, C. Müller, T. Schulte and A. Studer, *Chem. – Eur. J.*, 2004, **10**, 1156.
79. M. V. Edeleva, D. A. Parkhomenko, D. A. Morozov, S. A. Dobrynin, D. G. Trofimov, B. Kanagatov, I. A. Kirilyuk and E. G. Bagryanskaya, *J. Polym. Sci., Part A: Polym. Chem.*, 2014, **52**, 929.
80. M. A. Voinov, V. V. Martin and L. B. Volodarskii, *Bull. Russ. Acad. Sci. Div. Chem. Sci.*, 1992, **41**, 2091.

81. S. I. Dikalov, Y. F. Polienko and I. Kirilyuk, *Antioxid. Redox Signaling*, 2018, **28**(15), 1433.
82. G. Sosnovsky and Z. Cai, *J. Org. Chem.*, 1995, **60**, 3414.
83. T. Kálai, M. Balog, J. Jekö and K. Hideg, *Synthesis*, 1999, 973.
84. A. Rajca, Y. Wang, M. Boska, J. T. Paletta, A. Olankitwanit, M. A. Swanson, D. G. Mitchell, S. S. Eaton, G. R. Eaton and S. Rajca, *J. Am. Chem. Soc.*, 2012, **134**, 15724.
85. G. M. Rosen, E. Finkelstein and E. J. Rauckman, *Arch. Biochem. Biophys.*, 1982, **215**, 367.
86. S. I. Dikalov and D. G. Harrison, *Antioxid. Redox Signaling*, 2014, **20**, 372.
87. H. G. Aurich, in *Nitrones, Nitronates and Nitroxides*, ed. S. Patai and Z. Rappoport, John Wiley and Sons Ltd., Chichester, 1989, p. 313.
88. S. F. Vasilevsky, S. V. Klyatskaya, O. L. Korovnikova, S. A. Amitina, D. V. Stass, I. A. Grigor'ev and J. Elguero, *Tetrahedron*, 2006, **62**, 4597.
89. B. A. Chalmers, J. C. Morris, K. E. Fairfull-Smith, R. S. Graingerb and S. E. Bottle, *Chem. Commun.*, 2013, **49**, 10382.
90. D. J. Keddie, T. E. Johnson, D. P. Arnold and S. E. Bottle, *Org. Biomol. Chem.*, 2005, **3**, 2593.
91. A. Dichtl, M. Seyfried and K.-U. Schoening, *Synlett*, 2008, 1877.
92. K.-U. Schoening, W. Fischer, S. Hauck, A. Dichtl and M. Kuepfert, *J. Org. Chem.*, 2009, **74**, 1567.
93. G. I. Shchukin, I. A. Grigor'ev and L. B. Volodarskii, *Bull. Acad. Sci. USSR, Div. Chem. Sci.*, 1983, **32**, 2123.
94. V. V. Khramtsov, L. M. Weiner, S. I. Eremenko, O. I. Belchenko, P. V. Schastnev, I. A. Grigor'ev and V. A. Reznikov, *J. Magn. Reson.*, 1985, **61**, 397.
95. I. Seven, T. Weinrich, M. Gränz, C. Grünewald, S. Brüß, I. Krstić, T. F. Prisner, A. Heckel and M. W. Göbel, *Eur. J. Org. Chem.*, 2014, 4037.
96. V. A. Reznikov and L. B. Volodarsky, *Tetrahedron*, 1993, **49**, 10669.
97. M. Balog, C. Abé, T. Kálai, H.-J. Steinhoff, J. Jekő and K. Hideg, *Synthesis*, 2007, 1663.
98. L. Lampp, U. Morgenstern, K. Merzweiler, P. Imming and R. W. Seidel, *J. Mol. Struct.*, 2019, **1182**, 87.
99. I. A. Kirilyuk, T. G. Shevelev, D. A. Morozov, E. L. Khromovskih, N. G. Skuridin, V. V. Khramtsov and I. A. Grigor'ev, *Synthesis*, 2003, 871.
100. M. V. Edeleva, I. A. Kirilyuk, D. P. Zubenko, I. F. Zhurko, S. R. Marque, D. Gigmes, Y. Guillaneuf and E. G. Bagryanskaya, *J. Polym. Sci., Part A: Polym. Chem.*, 2009, **47**, 6579.
101. I. F. Zhurko, S. Dobrynin, A. A. Gorodetskii, Y. I. Glazachev, T. V. Rybalova, E. I. Chernyak, N. Asanbaeva, E. G. Bagryanskaya and I. A. Kirilyuk, *Molecules*, 2020, **25**, 845.
102. T. Kálai, J. Jekő, W. L. Hubbell and K. Hideg, *Synthesis*, 2003, 2084.
103. M. C. López, G. Royal, C. Philouze, P. Y. Chavant and V. Blandin, *Eur. J. Org. Chem.*, 2014, 4884.

104. R. B. Nazarski and R. Skowronski, *J. Chem. Soc., Perkin Trans. 1*, 1989, 1603.
105. J. F. W. Keana, in *Spin Labelling II: Theory and Application*, ed. L. J. Berliner, Academic Press, NY, 1979, p. 115.
106. P. Merino, in *Science of Synthesis*, ed. A. Padwa, Thieme Verlagsgruppe, Stuttgart, 27, 2005, p. 511.
107. C. P. Sár, J. Jekő and K. Hideg, *Synthesis*, 2003, 1367.
108. C. P. Sár, E. Ősz, J. Jekő and K. Hideg, *Synthesis*, 2005, 255.
109. D. A. Morozov, I. A. Kirilyuk, D. A. Komarov, A. Goti, I. Y. Bagryanskaya, N. V. Kuratieva and I. A. Grigor'ev, *J. Org. Chem.*, 2012, **77**, 10688.
110. G. I. Likhtenshtein, in *Nitroxides: Applications in Chemistry, Biomedicine and Material Science*, ed. G. I. Likhtenshtein, J. Yamauchi, S. Nakatsuji, A. Smirnov and R. Tamura, Wiley-VCH, Weinheim, 2008, p. 371.
111. J. F. W. Keana and F. L. Van Nice, *Physiol. Chem. Phys. Med. NMR*, 1984, **16**, 477.
112. V. Yelinova, A. Krainev, A. Savelov and I. Grigor'ev, *J. Chem. Soc., Perkin Trans. 2*, 1993, 2053.
113. W. R. Couet, R. C. Brasch, G. Sosnovsky and T. N. Tozer, *Magn. Reson. Imaging*, 1985, **3**, 83.
114. S. Morris, G. Sosonovsky, B. Hui, C. O. Huber, N. U. M. Rao and H. M. Swartz, *J. Pharm. Sci.*, 1991, **80**, 149.
115. N. Kocherginsky and H. Swartz, in *Nitroxide Spin Labels – Reactions in Biology and Chemistry*, Boca Raton, CRC Press Inc., 1995.
116. G. I. Shchukin and I. A. Grigor'ev in *Imidazoline nitroxides*, ed. L. B. Volodarsky, CRC. Press, Boca Raton, 1988, p. 171.
117. S. A. Dikanov, I. A. Grigoriev, L. B. Volodarskii and Y. D. Tsvetkov, *Russ. J. Phys. Chem. A*, 1982, **50**, 2711.
118. W. R. Couet, R. C. Brasch, G. Sosnovsky, J. Lukszo, I. Preakash, C. T. Gnevuch and T. N. Tozer, *Tetrahedron*, 1985, **41**, 1165.
119. F. Vianello, F. Momo, M. Scarpa and A. Rigo, *Magn. Reson. Imaging*, 1995, **13**, 219.
120. S. Marque, J. Sobek, H. Fischer, A. Kramer, P. Nesvadba and W. Wunderlich, *Macromolecules*, 2003, **36**, 3440.
121. R. D. Puts and D. Y. Sogah, *Macromolecules*, 1996, **29**, 3323.
122. L. Marx, R. Chiarelli, T. Guiberteau and A. Rassat, *J. Chem. Soc., Perkin Trans. 1*, 2000, **8**, 1181.
123. I. A. Kirilyuk, A. A. Bobko, S. V. Semenov, D. A. Komarov, I. G. Irtegova, I. A. Grigor'ev and E. Bagryanskaya, *J. Org. Chem.*, 2015, **80**, 9118.
124. T. Yamasaki, F. Mito, Y. Ito, S. Pandian, Y. Kinoshita, K. Nakano, R. Murugesan, K. Sakai, H. Utsumi and K. Yamada, *J. Org. Chem.*, 2011, **76**, 435.
125. A. A. Bobko, I. A. Kirilyuk, I. A. Grigor'ev, J. L. Zweier and V. V. Khramtsov, *Free Radicals Biol. Med.*, 2007, **42**, 404.
126. I. A. Kirilyuk, A. A. Bobko, I. A. Grigor'ev and V. V. Khramtsov, *Org. Biomol. Chem.*, 2004, **2**, 1025.

127. Y. Wang, J. T. Paletta, K. Berg, E. Reinhart, S. Rajca and A. Rajca, *Org. Lett.*, 2014, **16**, 5298.
128. V. Kathirvelu, C. Smith, C. Parks, M. A. Mannan, Y. Miura, K. Takeshita, S. S. Eaton and G. R. Eaton, *Chem. Commun.*, 2009, 454.
129. A. Rajca, V. Kathirvelu, S. K. Roy, M. Pink, S. Rajca, S. Sarkar, S. S. Eaton and G. R. Eaton, *Chem. – Eur. J.*, 2010, **16**, 5778.
130. V. Meyer, M. A. Swanson, L. J. Clouston, P. J. Boratyński, R. A. Stein, H. S. Mchaourab, A. Rajca, S. S. Eaton and G. R. Eaton, *Biophys. J.*, 2015, **108**, 1213.
131. E. G. Rozantsev, E. S. Kagan and V. D. Sholle, in *Bioactive Spin Labels*, ed. R. I. Zhdanov, Springer-Verlag, Heidelberg, 1992, p. 83.
132. P. Nesvadba, L. Bugnon and R. Sift, *J. Polym. Sci., Part A: Polym. Chem.*, 2004, **42**, 3332.
133. Z. Ma, Q. Huang and J. M. Bobbitt, *J. Org. Chem.*, 1993, **58**, 4837.
134. D. J. Kubicki, G. Casano, M. Schwarzwalder, S. Abel, C. Sauvee, K. Ganesan, M. Yulikov, A. J. Rossini, G. Jeschke, C. Coperet, A. Lesage, P. Tordo, O. Ouari and L. Emsley, *Chem. Sci.*, 2016, **7**, 550.
135. S. Okazaki, M. A. Mannan, K. Sawai, T. Masumizu, Y. Miura and K. Takeshita, *Free Radicals Res.*, 2007, **41**, 1069.
136. K. Sakai, K. Yamada, T. Yamasaki, Y. Kinoshita, F. Mito and H. Utsumi, *Tetrahedron*, 2010, **66**, 2311.
137. Y. Kinoshita, K. Yamada, T. Yamasaki, H. Sadsue, K. Sakai and H. Utsumi, *Free Radical Res.*, 2009, **43**, 565.
138. Y. Kinoshita, K. Yamada, T. Yamasaki, F. Mito, M. Yamato, N. Kosem, H. Deguchi, C. Shirahama, Y. Ito, K. Kitagawa, N. Okukado, K. Sakai and H. Utsumi, *Free Radicals Biol. Med.*, 2010, **49**, 1703.
139. T. Schulte, K. O. Siegenthaler, H. Luftmann, M. Letzel and A. Studer, *Macromolecules*, 2005, **38**, 6833.
140. X. Wang, M. Emoto, A. Sugimoto, Y. Miyake, K. Itto, M. Amasaka, S. Xu, H. Hirata, H. Fujii and H. Arimoto, *Tetrahedron Lett.*, 2014, **55**, 2146.
141. A. E. Dikalova, A. T. Bikineyeva, K. Budzyn, R. R. Nazarewicz, L. McCann, W. Lewis, D. G. Harrison and S. I. Dikalov, *Circ. Res.*, 2010, **107**, 106.
142. R. R. Nazarewicz, A. Dikalova, A. Bikineyeva, S. Ivanov, I. A. Kirilyuk, I. A. Grigor'ev and S. I. Dikalov, *Antioxid. Redox Signaling*, 2013, **19**, 344.
143. T. B. Kajer, K. E. Fairfull-Smith, T. Yamasaki, K. Yamada, S. Fu, S. E. Bottle, C. L. Hawkins and M. J. Davies, *Free Radicals Biol. Med.*, 2014, **70**, 96.
144. S. R. Burks, M. A. Makowsky, Z. A. Yaffe, C. Hoggle, P. Tsai, S. Muralidharan, M. K. Bowman, J. P. Y. Kao and G. M. Rosen, *J. Org. Chem.*, 2010, **75**, 4737.
145. Z. Zhelev, E. Georgieva, D. Lazarova, S. Semkova, I. Aoki, M. Gulubova, T. Higashi and R. Bakalova, *Oxid. Med. Cell. Longevity*, 2019, 6373685.
146. Z. Zhelev, R. Bakalova, I. Aoki, D. Lazarova and T. Saga, *ACS Chem. Neurosci.*, 2013, **4**, 1439.

147. D. B. Gophane and S. T. Sigurdsson, *Beilstein J. Org. Chem.*, 2015, **11**, 219.
148. T. E. Edwards and S. T. Sigurdsson, *Nat. Protoc.*, 2007, **2**, 1954.
149. Y. Sato, H. Hayashi, M. Okazaki, M. Aso, S. Karasawa, S. Ueki, H. Suemunea and N. Koga, *Magn. Reson. Chem.*, 2008, **46**, 1055.
150. L. Xia, C. Zhang, M. Li, K. Wang, Y. Wang, P. Xu and Y. Hu, *Int. J. Nanomed.*, 2018, **13**, 7123.
151. M. Dharmarwardana, A. F. Martins, Z. Chen, P. M. Palacios, C. M. Nowak, R. P. Welch, S. Li, M. A. Luzuriaga, L. Bleris, B. S. Pierce, A. D. Sherry and J. J. Gassensmith, *Mol. Pharmaceutics*, 2018, **15**, 2973.
152. D. Le, M. Dilger, V. Pertici, S. Diabat, D. Gigmes, C. Weiss and G. Delaittre, *Angew. Chem., Int. Ed.*, 2019, **58**, 4725.
153. S. Garmendia, D. Mantione, S. A. Castro, C. Jehanno, L. Lezama, J. L. Hedrick, D. Mecerreyes, L. Salassa and H. Sardon, *Polym. Chem.*, 2017, **8**, 2693.
154. I. A. Kirilyuk, Y. F. Polienko, O. A. Krumkacheva, R. K. Strizhakov, Y. V. Gatilov, I. A. Grigor'ev and E. G. Bagryanskaya, *J. Org. Chem.*, 2012, **77**, 8016.
155. K. Hideg and O. H. Hankovszky, in *Spin Labeling: Theory and Applications*, ed. L. J. Berliner and J. Reuben, Springer Science & Business Media, 2012, p. 427.
156. B. Bognár, G. Úr, C. Sár, O. H. Hankovszky, K. Hideg and T. Kálai, *Curr. Org. Chem.*, 2019, **23**, 480.
157. T. Kálai (Unpublished), 2017, http://real.mtak.hu/id/eprint/56396.
158. K. Hideg, T. Kálai and C. P. Sár, *J. Heterocycl. Chem.*, 2005, **42**, 437.
159. S. Bleicken, T. E. Assafa, H. Zhang, C. Elsner, I. Ritsch, M. Pink, S. Rajca, G. Jeschke, A. Rajca and E. Bordignon, *ChemistryOpen*, 2019, **8**, 1057.
160. G. Karthikeyan, A. Bonucci, G. Casano, G. Gerbaud, S. Abel, V. Thomé, L. Kodjabachian, A. Magalon, B. Guigliarelli, V. Belle, O. Ouari and E. Mileo, *Angew. Chem., Int. Ed.*, 2018, **57**, 1366.
161. S. Huang, J. T. Paletta, H. Elajaili, K. Huber, M. Pink, S. Rajca, G. R. Eaton, S. S. Eaton and A. Rajca, *J. Org. Chem.*, 2017, **82**, 1538.
162. S. Huang, H. Zhang, J. T. Paletta, S. Rajca and A. Rajca, *Free Radical Res.*, 2018, **52**, 327.
163. G. Sosnovsky, N. U. M. Rao, S. W. Li and H. M. Swartz, *J. Org. Chem.*, 1989, **54**, 3667.
164. V. A. Reznikov and L. B. Volodarskii, *Chem. Heterocycl. Compd.*, 1990, **26**, 643.
165. V. A. Reznikov and L. B. Volodarskii, *Bull. Acad. Sci. USSR, Div. Chem. Sci.*, 1990, **39**, 329.
166. A. E. Mathew and J. R. Dodd, *J. Heterocycl. Chem.*, 1985, **22**, 225.
167. M. Miyake, J. Shen, S. Liu, H. Shi, W. Liu, Z. Yuan, A. Pritchard, J. P. Y. Kao, K. J. Liu and G. M. Rosen, *J. Pharmacol. Exp. Ther.*, 2006, **318**, 1187.

168. K. Hideg, O. H. Hankovszky, H. A. Halász and P. Sohár, *J. Chem. Soc., Perkin Trans. 1*, 1988, 2905.
169. T. Yokoyama, A. Taguchi, H. Kubota, N. J. Stewart, S. Matsumoto, I. A. Kirilyuk and H. Hirata, *J. Magn. Reson.*, 2019, **305**, 122.
170. P. Tsai, G. L. Cao, T. J. Merkel and G. M. Rosen, *Free Radical Res.*, 2008, **42**, 4956.
171. H. Kubota, D. A. Komarov, H. Yasui, S. Matsumoto, O. Inanami, I. A. Kirilyuk, V. V. Khramtsov and H. Hirata, *Magn. Reson. Mater. Phys., Biol. Med.*, 2017, **30**, 291.
172. A. A. Gorodetsky, I. A. Kirilyuk, V. V. Khramtsov and D. A. Komarov, *Magn. Reson. Med.*, 2016, **76**, 350.
173. S. I. Dikalov, A. E. Dikalova, D. A. Morozov and I. A. Kirilyuk, *Free Radical Res.*, 2018, **52**, 339.
174. M. A. Sowers, J. R. McCombs, Y. Wang, J. T. Paletta, S. W. Morton, E. C. Dreaden, M. D. Boska, M. F. Ottaviani, P. T. Hammond, A. Rajca and J. A. Johnson, *Nat. Commun.*, 2014, **5**, 5460.
175. V. C. Jayawardena, K. E. Fairfull-Smith and S. E. Bottle, *Aust. J. Chem.*, 2013, **66**, 619.
176. K. S. Chan, X. Z. Li and S. Y. Lee, *Organometallics*, 2010, **29**, 2850.
177. K. E. Fairfull-Smith, F. Brackmann and S. E. Bottle, *Eur. J. Org. Chem.*, 2009, 1902.
178. K. Thomas, B. A. Chalmers, K. E. Fairfull-Smith and S. E. Bottle, *Eur. J. Org. Chem.*, 2013, 853.
179. J. P. Allen, M. C. Pfrunder, J. C. McMurtrie, S. E. Bottle, J. P. Blinco and K. E. Fairfull-Smith, *Eur. J. Org. Chem.*, 2017, 476.
180. C. L. Rayner, S. E. Bottle, G. A. Gole, M. S. Ward and N. L. Barnett, *Neurochem. Int.*, 2016, **92**, 1.
181. V. C. Lussini, J. M. Colwell, K. E. Fairfull-Smith and S. E. Bottle, *Sens. Actuators, B*, 2017, **241**, 199.
182. V. V. Khramtsov and L. B. Volodarsky in *Biological Magnetic Resonance*, ed. L. J. Berliner, Plenum Press, New York, 1998, p. 109.
183. M. A. Voinov and A. I. Smirnov, in *Methods in Enzymology.V. 564*, ed. P. Z. Qin and K. Warncke, Academic Press, Burlington, 2015, p. 191.
184. V. V. Khramtsov, D. Marsh, L. Weiner and V. A. Reznikov, *Biochim. Biophys. Acta*, 1992, **1104**, 317.
185. T. Schanding, P. D. Vogel, W. E. Trommer and J. G. Wise, *Tetrahedron*, 1996, **52**, 5783.
186. Y. F. Polienko, I. A. Grigor'yev and M. A. Voinov, *Chem. Heterocycl. Compd.*, 2009, **45**, 59.
187. V. K. Khlestkin, J. F. Polienko, M. A. Voinov, A. I. Smirnov and V. Chechik, *Langmuir*, 2008, **24**, 609.
188. M. A. Voinov, A. Ruuge, V. A. Reznikov, I. A. Grigor'ev and A. I. Smirnov, *Biochemistry*, 2008, **47**, 5626.
189. A. I. Smirnov, A. Ruuge, V. A. Reznikov, M. A. Voinov and I. A. Grigor'ev, *J. Am. Chem. Soc.*, 2004, **126**, 8872.

190. A. A. Bobko, O. V. Efimova, M. A. Voinov and V. V. Khramtsov, *Free Radical Res.*, 2012, **46**, 1115.
191. T. A. Berezina, V. A. Reznikov and L. B. Volodarsky, *Tetrahedron*, 1993, **49**, 10693.
192. M. Y. Balakirev, V. V. Khramtsov, T. A. Berezina, V. V. Martin and L. B. Volodarsky, *Synthesis*, 1992, 1223.
193. I. A. Kirilyuk, A. A. Bobko, V. V. Khramtsov and I. A. Grigor'ev, *Org. Biomol. Chem.*, 2005, **3**, 1269.
194. D. I. Potapenko, M. A. Foster, D. J. Lurie, I. A. Kirilyuk, J. M. S. Hutchison, I. A. Grigor'ev, E. G. Bagryanskaya and V. V. Khramtsov, *J. Magn. Reson.*, 2006, **182**, 1.
195. M. A. Voinov, C. T. Scheid, I. A. Kirilyuk, D. G. Trofimov and A. I. Smirnov, *J. Phys. Chem. B*, 2017, **121**, 2443.
196. A. A. Bobko, T. D. Eubank, J. L. Voorhees, O. V. Efimova, I. A. Kirilyuk, S. Petryakov, D. G. Trofimiov, C. B. Marsh, J. L. Zweier, I. A. Grigor'ev, A. Samouilov and V. V. Khramtsov, *Magn. Reson. Med.*, 2012, **67**, 1827.
197. D. A. Komarov, I. Dhimitruka, I. A. Kirilyuk, D. G. Trofimiov, I. A. Grigor'ev, J. L. Zweier and V. V. Khramtsov, *Magn. Reson. Med.*, 2012, **68**, 649.
198. D. A. Komarov, Y. Ichikawa, K. Yamamoto, N. J. Stewart, S. Matsumoto, H. Yasui, I. A. Kirilyuk, V. V. Khramtsov, O. Inanami and H. Hirata, *Anal. Chem.*, 2018, **90**, 13938.
199. M. V. Edeleva, I. A. Kirilyuk, I. F. Zhurko, D. A. Parkhomenko, Y. P. Tsentalovich and E. G. Bagryanskaya, *J. Org. Chem.*, 2011, **76**, 5558.
200. J. H. Osiecki and E. F. Ullman, *J. Am. Chem. Soc.*, 1968, **90**, 1078.
201. M. Lamchen and T. W. Mittag, *J. Chem. Soc. C*, 1966, 2300.
202. V. I. Ovcharenko, S. V. Fokin, G. V. Romanenko, I. V. Korobkov and P. Rey, *Russ. Chem. Bull.*, 1999, **48**, 1519.
203. C. Hirel, K. E. Vostrikova, J. Pécaut, V. I. Ovcharenko and P. Rey, *Chem. – Eur. J.*, 2001, **7**, 2007.
204. E. A. Mostovich, Y. Borozdina, V. Enkelmann, K. Removic-Langer, B. Wolf, M. Lang and M. Baumgarten, *Cryst. Growth Des.*, 2012, **12**, 54.
205. Y. B. Borozdina, E. Mostovich, V. Enkelmann, B. Wolf, P. T. Cong, U. Tutsch, M. Lang and M. Baumgarten, *J. Mater. Chem. C*, 2014, **2**, 6618.
206. N. Amaya, T. Ono, Y. Oku, H. Yamaguchi, A. Matsuo, K. Kindo, H. Nojiri, F. Palacio, J. Campo and Y. Hosokoshi, *J. Phys. Soc. Jpn.*, 2017, **86**, 074706.
207. Y. Kanzaki, D. Shiomi, T. Ise, K. Sato and T. Takui, *Polyhedron*, 2007, **26**, 1890.
208. F. Iwahori, T. Suzuki and K. Kato, *Heterocycles*, 2013, **87**, 2031.
209. P. Ravat, Y. Ito, E. Gorelik, V. Enkelmann and M. Baumgarten, *Org. Lett.*, 2013, **15**, 4280.
210. K. Kolanji, L. Postulka, B. Wolf, M. Lang, D. Schollmeyer and M. Baumgarten, *J. Org. Chem.*, 2019, **84**, 140.

211. Z.-X. Xiao, H. Miao, D. Shao, H.-Y. Wei, Y.-Q. Zhang and X.-Y. Wang, *Dalton Trans.*, 2018, **47**, 7925.
212. E. Tretyakov, K. Okada, S. Suzuki, M. Baumgarten, G. Romanenko, A. Bogomyakov and V. Ovcharenko, *J. Phys. Org. Chem.*, 2016, **29**, 725.
213. X. Li, T. Li, L. Tian, Z. Y. Liu and X. G. Wang, *RSC Adv.*, 2015, **5**, 74864.
214. T. Sugano, S. J. Blundell, W. Hayes, P. Day and H. Mori, *Physica B*, 2010, **405**, S327.
215. E. V. Tretyakov, S. E. Tolstikov, G. V. Romanenko, Y. G. Shvedenkov, R. Z. Sagdeev and V. I. Ovcharenko, *Russ. Chem. Bull.*, 2005, **54**, 2169.
216. K. Hayakawa, D. Shiomi, T. Ise, K. Sato and T. Takui, *J. Mater. Chem.*, 2006, **16**, 4146.
217. T. Sugano, S. J. Blundell, W. Hayes and P. Day, *Polyhedron*, 2005, **24**, 2108.
218. E. V. Tretyakov, I. V. Eltsov, S. V. Fokin, Y. G. Shvedenkov, G. V. Romanenko and V. I. Ovcharenko, *Polyhedron*, 2003, **22**, 2499.
219. J. L. Poderoso, A. González-Cabello, O. Jürgens, J. Vidal-Gancedo, J. Veciana, T. Torres and P. Vázquez, *Synth. Met.*, 2001, **121**, 1830.
220. K. Matsuda and M. Irie, *J. Am. Chem. Soc.*, 2000, **122**, 7195.
221. R. Ziessel, G. Ulrich, R. C. Lawson and L. Echegoyen, *J. Mater. Chem.*, 1999, **9**, 1435.
222. C. Sporer, H. Heise, K. Wurst, D. Ruiz-Molina, H. Kopacka, P. Jaitner, F. Köhler, J. J. Novoa and J. Veciana, *Chem. – Eur. J.*, 2004, **10**, 1355.
223. N. M. Gallagher, J. J. Bauer, M. Pink, S. Rajca and A. Rajca, *J. Am. Chem. Soc.*, 2016, **138**, 9377.
224. N. Gallagher, H. Zhang, T. Junghoefer, E. Giangrisostomi, R. Ovsyannikov, M. Pink, S. Rajca, M. B. Casu and A. Rajca, *J. Am. Chem. Soc.*, 2019, **141**, 4764.
225. N. Kornblum and S. D. Boyd, *J. Am. Chem. Soc.*, 1970, **92**, 5784.
226. H. Matsuura, R. Tamura and J. Yamauchi, *Synth. Met.*, 2003, **133–134**, 605.
227. S. Shimono, R. Tamura, N. Ikuma, T. Takimoto, N. Kawame, O. Tamada, N. Sakai, H. Matsuura and J. Yamauchi, *J. Org. Chem.*, 2004, **69**, 475.
228. N. A. Artiukhova, K. Y. Maryunina, S. V. Fokin, E. V. Tretyakov, G. V. Romanenko, A. V. Polushkin, A. S. Bogomyakov, R. Z. Sagdeev and V. I. Ovcharenko, *Russ. Chem. Bull.*, 2013, **62**, 2132.
229. N. Kornblum and J. W. Powers, *J. Org. Chem.*, 1957, **22**, 455.
230. Y. Kai, P. Knochel, S. Kwiatkowski, J. D. Dunitz, J. F. M. Oth, D. Seebach and H.-O. Kalinowski, *Helv. Chim. Acta*, 1982, **65**, 137.
231. D. G. B. Boocock, R. Darcy and E. F. Ullman, *J. Am. Chem. Soc.*, 1968, **90**, 5945.
232. R. Weiss, N. Kraut and F. Hampel, *J. Organomet. Chem.*, 2001, **473**, 617.
233. V. I. Ovcharenko, O. N. Chupakhin, I. S. Kovalev, E. V. Tretyakov, G. V. Romanenko and D. V. Stass, *Russ. Chem. Bull.*, 2008, **57**, 2227.
234. O. N. Chupakhin, I. A. Utepova, M. V. Varaksin, E. V. Tretyakov, G. V. Romanenko, D. V. Stass and V. I. Ovcharenko, *J. Org. Chem.*, 2009, **74**, 2870.

235. M. V. Varaksin, E. V. Tretyakov, I. A. Utepova, G. V. Romanenko, A. S. Bogomyakov, D. V. Stass, R. Z. Sagdeev, V. I. Ovcharenko and O. N. Chupakhin, *Russ. Chem. Bull.*, 2012, **61**, 1469.
236. E. V. Tretyakov, I. A. Utepova, M. V. Varaksin, S. E. Tolstikov, G. V. Romanenko, A. S. Bogomyakov, D. V. Stass, V. I. Ovcharenko and O. N. Chupakhin, *ARKIVOC*, 2011, **2011**(8), 76.
237. E. V. Tretyakov, P. A. Fedyushin, E. V. Panteleeva, D. V. Stass, I. Y. Bagryanskaya, I. V. Beregovaya and A. S. Bogomyakov, *J. Org. Chem.*, 2017, **82**, 4179.
238. P. Fedyushin, E. Panteleeva, I. Bagryanskaya, K. Maryunina, K. Inoue, D. Stass and E. Tretyakov, *J. Fluorine Chem.*, 2019, **217**, 1.
239. S. I. Zhivetyeva, I. A. Zayakin, I. Y. Bagryanskaya, E. V. Zaytseva and E. V. Tretyakov, *Tetrahedron*, 2018, **74**, 3924.
240. S. Suzuki, T. Furui, M. Kuratsu, M. Kozaki, D. Shiomi, K. Sato, T. Takui and K. Okada, *J. Am. Chem. Soc.*, 2010, **132**, 15908.
241. E. V. Tretyakov, S. E. Tolstikov, G. V. Romanenko, A. S. Bogomyakov, D. V. Stass, A. G. Maryasov, N. P. Gritsan and V. I. Ovcharenko, *Russ. Chem. Bull.*, 2011, **60**, 2608.
242. S. Tolstikov, E. Tretyakov, S. Fokin, E. Suturina, G. Romanenko, A. Bogomyakov, D. Stass, A. Maryasov, M. Fedin, N. Gritsan and V. Ovcharenko, *Chem. – Eur. J.*, 2014, **20**, 2793.
243. J. F. Polienko, T. Schanding, M. A. Voinov and I. A. Grigor'ev, *Synth. Commun.*, 2006, **36**, 2763.
244. S. E. Tolstikov, E. V. Tretyakov, D. E. Gorbunov, I. F. Zhurko, M. V. Fedin, G. V. Romanenko, A. S. Bogomyakov, N. P. Gritsan and D. G. Mazhukin, *Chem. – Eur. J.*, 2016, **22**, 14598.
245. H. Tsujimoto, S. Suzuki, M. Kozaki, D. Shiomi, K. Sato, T. Takui and K. Okada, *Chem. – Asian J.*, 2019, **14**, 1801.
246. X. Zhang, S. Suzuki, M. Kozaki and K. Okada, *J. Am. Chem. Soc.*, 2012, **134**, 17866.
247. R. Tanimoto, S. Suzuki, M. Kozaki and K. Okada, *Chem. Lett.*, 2014, **43**, 678.
248. A. T. Balaban, P. J. Halls and A. R. Katritzky, *Chem. Ind.*, 1968, 651.
249. Y. Kusaba, M. Tamura, Y. Hosokoshi, M. Kinoshita, H. Sawa, R. Kato and H. Kobayashi, *J. Mater. Chem.*, 1997, **7**, 1377.
250. F. Pätzold, H.-J. Niclas and H.-J. Förster, *J. Prakt. Chem.*, 1986, **328**, 921.
251. F. Pätzold, H.-J. Niclas and E. Gründemann, *J. Prakt. Chem.*, 1990, **332**, 345.
252. A. Zakrassov, V. Shteiman, Y. Sheynin, B. Tumanskii, M. Botoshansky, M. Kapon, A. Keren, M. Kaftory, T. E. Vosc and J. S. Miller, *J. Mater. Chem.*, 2004, **14**, 1827.
253. D. Shiomi, K. Sato, T. Takui, K. Itoh, M. Tamura, Y. Nishio, K. Kajita, M. Nakagawa, T. Ishida and T. Nogami, *Mol. Cryst. Liq. Cryst.*, 1999, **335**, 359.
254. B. M. Dooley, S. E. Bowles, T. Storr and N. L. Frank, *Org. Lett.*, 2007, **9**, 4781.

255. S. E. Bowles, B. M. Dooley, J. B. Benedict, W. Kaminsky and N. L. Frank, *Polyhedron*, 2009, **28**, 1704.
256. B. Esat, I. Fidan, S. Bahceci, Y. Yerli and L. Sari, *Magn. Reson. Chem.*, 2009, **47**, 641.
257. H. G. Aurich, K. Hahn and K. Stork, *Angew. Chem., Int. Ed.*, 1975, **14**, 551.
258. H. G. Aurich, O. Bubenheim, W. Kessler and K.-D. Mogendorf, *J. Org. Chem.*, 1988, **53**, 4997.
259. H. G. Aurich, M. Schmidt and T. Schwerzel, *Chem. Ber.*, 1985, **118**, 1086.
260. V. A. Reznikov, I. V. Ovcharenko, N. V. Pervukhina, V. N. Ikorskii, A. Grand and V. I. Ovcharenko, *Chem. Commun.*, 1999, 539.
261. V. A. Reznikov, L. B. Volodarsky, T. V. Rybalova and Y. V. Gatilov, *Russ. Chem. Bull.*, 2000, **49**, 106.
262. V. A. Reznikov, L. A. Vishnivetskaya and L. B. Volodarskii, *Russ. Chem. Bull.*, 1993, **42**, 1547.

CHAPTER 3

The Application of Nitroxides in Organic Synthesis

LENIN KUMAR VERDHI AND ALEX. M. SZPILMAN*

Department of Chemical Sciences, Ariel University, Ariel, Israel
*Email: AMSzpilman@gmail.com

3.1 Introduction

Although some nitroxides have been known since 1845 (Figure 3.1),[1] it was the first synthesis of 4-oxo-2,2,6,6-tetramethyl piperidine-*N*-oxyl (4-oxo-TEMPO) (**4**) by Lebedev and Kazarnovsky in 1959,[2] that provided the inspiration and impetus for the successful synthesis and use of other stable nitroxides. Today nitroxides are indispensable tools for a broad range of research areas, including as antioxidants in biology, as mediators in polymer chemistry, as charge carriers in electrochemistry, as spin probes in electron spin resonance studies (ESR) and more importantly as potential oxidation catalysts in organic chemistry. The structure, physical properties and applications of nitroxide radicals in various fields have been highlighted in books and reviews and in the other chapters in this book.[3,4]

Among the many reported nitroxides, the prototypical TEMPO (**5**), 2-azaadamantane-*N*-oxyl (AZADO) (**8**) and 9-azabicyclo[3.3.1]nonane *N*-oxyl (ABNO) (**11**) and their derivatives are currently the most commonly employed nitroxides for chemical transformations. AZADO and ABNO are less sterically encumbered nitroxides, in which the *N*-oxyl functional group is positioned in the bridgehead position of the bicyclic framework (Figure 3.2).

Nitroxides
Edited by Olivier Ouari and Didier Gigmes

Published by the Royal Society of Chemistry, www.rsc.org

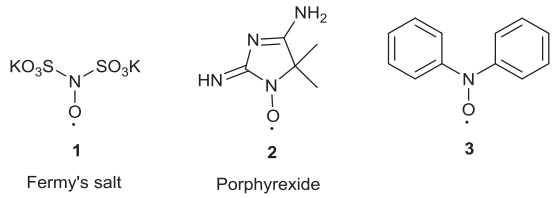

Figure 3.1 Early examples of nitroxides.

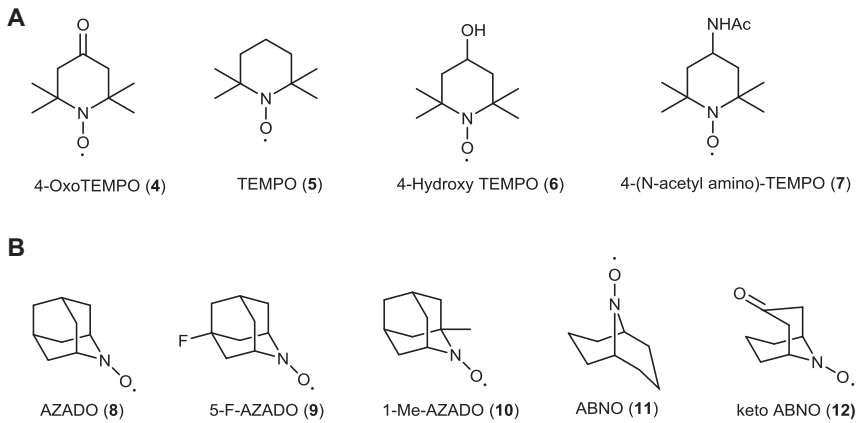

Figure 3.2 Most commonly used nitroxides. (A) TEMPO and its derivatives (B) less sterically hindered nitroxides.

3.2 Nitroxide-catalyzed Oxidation of Alcohols

Oxidation of alcohols to the corresponding aldehydes, ketones and carboxylic acids is the most prolific of all nitroxide-catalyzed reactions. In this regard, a plethora of homogeneous and heterogeneous nitroxide-mediated protocols have been developed. In addition, nitroxides can be employed in two mechanistically distinct ways, as a one-electron oxidant under aerobic conditions or as a two-electron oxidant together with a chemical oxidant (Figure 3.3).

3.2.1 One-electron Pathway using a Nitroxide in Combination with Metal and Oxygen

A nitroxide in conjunction with a one-electron oxidant such as Cu(I) in the presence of oxygen mediates alcohol oxidation in a one-electron pathway. Though not all the details are known of this mechanism, it is postulated that nitroxide TEMPO (**5**) coordinates to Cu(I) to give complex (**15**), which is oxidized to Cu(II) complex (**16**) by molecular oxygen. The resulting Cu(II) complex oxidizes alcohol to the corresponding carbonyl compound *via* a

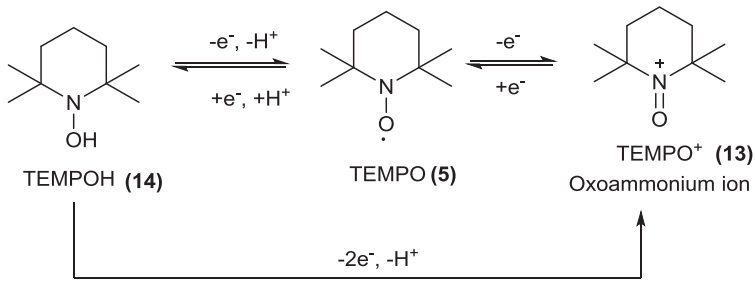

Figure 3.3 Redox chemistry of nitroxide radicals.

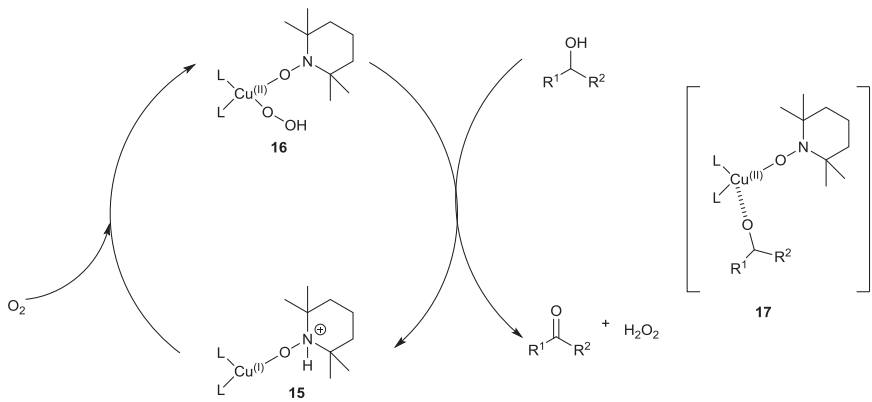

Scheme 3.1 Simplified mechanism of alcohol oxidation *via* a one-electron pathway.

transient intermediate (likely **17**), thus completing the catalytic cycle (Scheme 3.1).[5]

3.2.2 Two-electron Pathway using a Nitroxide in Combination with a Secondary Oxidant

Nitroxide TEMPO (**5**) upon treatment with a secondary oxidant such as bleach generates the strong oxidant oxoammonium ion $TEMPO^+$ (**13**) (Scheme 3.2). The *in situ* formed oxoammonium ion oxidizes the alcohol in a two-electron pathway to the corresponding carbonyl compound and is itself reduced to TEMPOH (**14**).[6] TEMPOH is reoxidized to its oxoammonium cation (**13**) by the secondary oxidant, thus completing the catalytic process (Scheme 3.2). In this two-electron pathway, the secondary oxidant plays a vital dual role by first oxidizing the nitroxide (**5**) to its oxoammonium ion (**13**) and then reoxidizing hydroxylamine (**14**) to the active oxoammonium ion (**13**). In addition, the oxoammonium salt also can be generated by treating nitroxides with strong acids such as *p*-toluene sulfonic acid *via* disproportionation.[7] However, this method requires superstoichiometric amounts of nitroxide for alcohol oxidation.

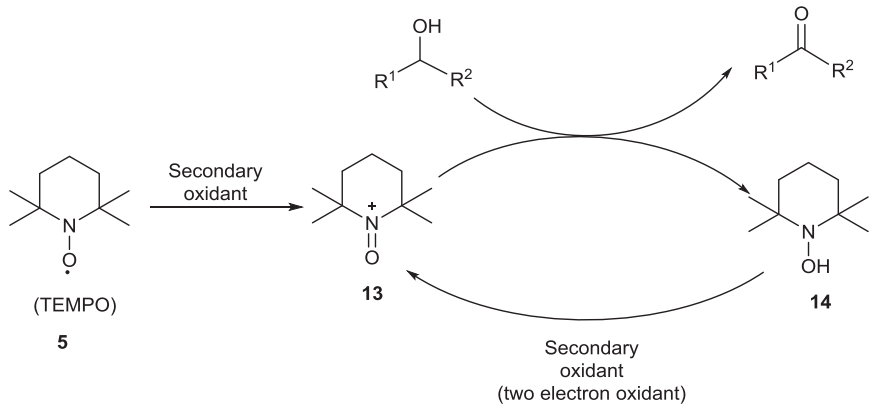

Scheme 3.2 General mechanism of oxidation of alcohols *via* oxoammonium cation.

3.2.3 Nitroxides in Homogeneous Catalysis

3.2.3.1 Nitroxide/Metal-mediated Aerobic Oxidation of Alcohols

In one of the first contributions to the field, the Semmelhack group demonstrated the ability of nitroxides to mediate alcohol oxidation.[8] A catalytic mixture comprised of cuprous chloride (10 mol%) and TEMPO (**5**) or its 4-hydroxy analogue (**6**) (10 mol%) was found to be effective for the aerobic oxidation of allylic and benzylic alcohols in dimethyl formamide (DMF) at 25 °C (Scheme 3.3). Under these conditions, secondary and sterically hindered alcohols were largely unreactive even in the presence of stoichiometric amounts of copper(I) salt and nitroxide. However, switching from cuprous chloride to cupric chloride (110 mol%) did lead to oxidation of secondary alcohols. An early proposed four-step mechanism (see later proposals below) suggests that cupric ion oxidizes TEMPO (**5**) to its oxoammonium form (**13**), which oxidizes alcohols to aldehydes while being reduced to hydroxylamine TEMPOH (**14**). TEMPOH (**14**) undergoes rapid comproportionation with oxoammonium ion (**13**) to regenerate TEMPO (**5**).[9] Finally, copper(I) is oxidized to copper(II) with oxygen.

Sheldon and coworkers reported the combination of $RuCl_2(PPh_3)_3$ (1.5 mol%), TEMPO (**5**) (4.5 mol%) and oxygen for the oxidation of a wide range of activated and unactivated aliphatic primary and secondary alcohols (Scheme 3.4).[10] The oxidation reactions were carried out in a high-pressure reactor with a continuous stream of oxygen–nitrogen gas mixture (8 : 92; v/v), using chlorobenzene or toluene as the solvent at 100 °C for 7 hours. Among other ruthenium compounds tested, $RuCl_3$ gave lower rates, while $RuCl_2(bipy)_2$ and $RuCl_2(DMSO)_2$ were completely unreactive. This catalytic system is not only efficient for the oxidation of alcohols, but also completely suppresses overoxidation of aldehyde products.

Minisci and coworkers disclosed the use of catalytic amounts of Mn(II)–Co(II) or Mn(II)–Cu(II) nitrate salts in combination with TEMPO (**5**) as

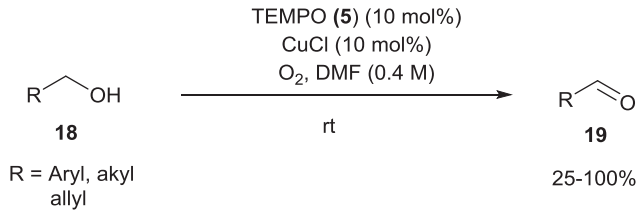

Scheme 3.3 CuCl/TEMPO-catalyzed aerobic oxidation of alcohols.

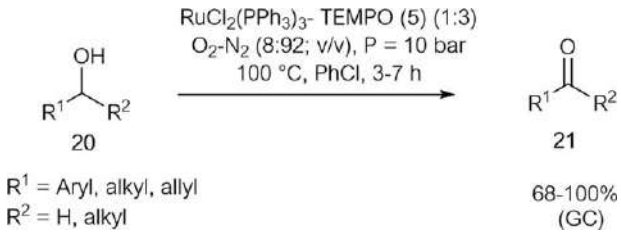

Scheme 3.4 Ru/TEMPO-catalyzed aerobic oxidation of alcohols.

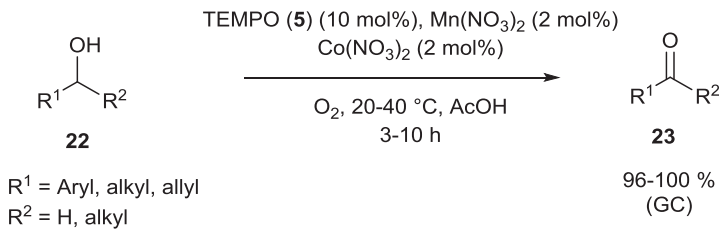

Scheme 3.5 Mn–Co/TEMPO-catalyzed aerobic oxidation of alcohols.

an efficient system for the aerobic oxidation of alcohols to aldehydes and ketones at ambient temperature (Scheme 3.5).[11] A combination of Mn(II) nitrate either with Co(II) or Cu(II) was found to exhibit increased reactivity over the individual metal salts. This oxidation procedure requires the use of acidic reaction medium, which is believed to be essential for the disproportionation of TEMPO (**5**) to the actual oxidant, its oxoammonium salt (**13**). In other solvents such as acetonitrile, no substantial oxidation was observed.

In 2003, Sheldon and coworkers reported a catalytic mixture containing bipyridine (**24**), $CuBr_2$, TEMPO (**5**) and potassium *tert*-butoxide as a base for the chemo-selective oxidation of primary alcohols in the presence of secondary alcohols (Scheme 3.6).[12] An acetonitrile–water (2 : 1) combination was used as the solvent in the presence of air at ambient temperature. No oxidation was observed in the absence of any individual catalytic components. In addition, Sheldon *et al.*, for the first time, proposed a different role for TEMPO (**5**) as a hydrogen acceptor during the reaction. According to

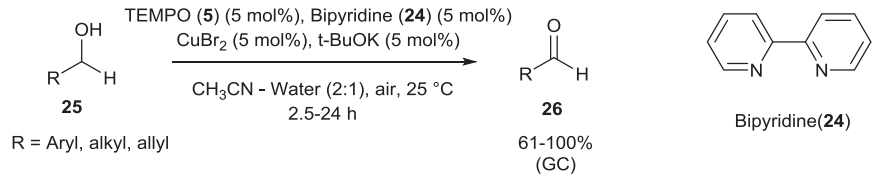

Scheme 3.6 $CuBr_2$/TEMPO-catalyzed aerobic oxidation of alcohols.

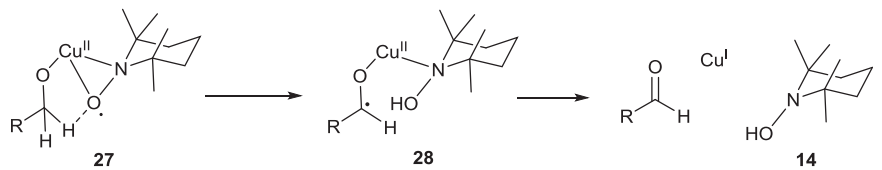

Scheme 3.7 Plausible mechanistic pathway for alcohol oxidation proposed by Sheldon *et al.*[12]

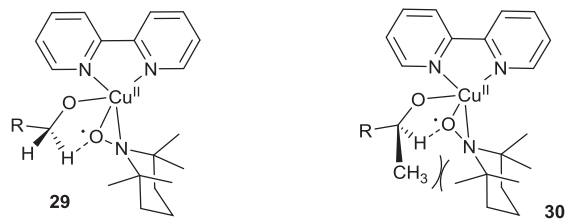

Figure 3.4 Illustration of steric effects in primary and secondary alcohol oxidation.

the proposed mechanism, the TEMPO (**5**) radical coordinates to the Cu(II)–alcoholate complex in an η^2 fashion to afford complex **27**, from which, the H-atom of the alcohol is transferred to TEMPO (**5**). This leads to radical-TEMPOH copper species **28**, which undergoes subsequent intramolecular single-electron transfer affording aldehyde and Cu(I), TEMPOH (**14**) species (Scheme 3.7). The role of *tert*-BuOK was proposed to be to remove the proton from the hydroxy group, thereby facilitating the coordination of the alcoholate to copper. Furthermore, Sheldon *et al.* also explained the lack of reactivity of secondary alcohols. The steric interaction between the methyl groups at the α-position of TEMPO radical (**5**) and alkyl/aryl group of secondary alcohols was postulated as the plausible reason for their unreactivity (Figure 3.4). Due to these steric effects, the barrier for hydrogen atom abstraction from the Cu(II)–alcoholate complex **30** by the nitroxide radical becomes extremely higher, thus retarding the oxidation.

In 2006, Ragauskas *et al.* reported an efficient four-component catalytic system consisting of 4-acetamido TEMPO (**7**), $Cu(ClO_4)_2$, DABCO (**31**) and

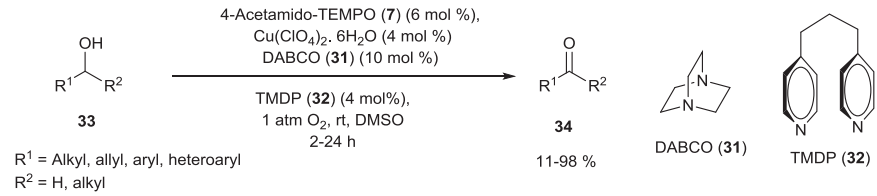

Scheme 3.8 $Cu(ClO_4)_2$/TEMPO-catalyzed aerobic oxidation of alcohols.

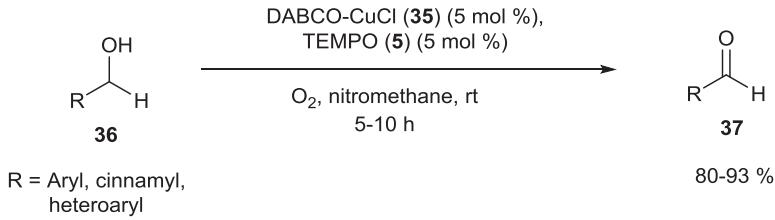

Scheme 3.9 DABCO–CuCl/TEMPO-catalyzed aerobic oxidation of alcohols.

4,4′-trimethylenedipyridine (TMDP) (**32**) as a ligand for room-temperature aerobic oxidation of alcohols in DMSO (Scheme 3.8).[13] This system is applicable for activated and unactivated primary and secondary alcohols. However, secondary alcohols require longer reaction times. More importantly, the catalytic system was recycled and reused two times for oxidation of alcohols without significant loss of activity. Recycling was easily done by simple extraction of the product from the reaction mixture with pentane, leaving the catalytic components in the DMSO solution.

Sekar and coworkers developed a DABCO–CuCl complex (**35**) in combination with TEMPO (**5**) as an active catalytic mixture for the aerobic oxidation of alcohols at room temperature using nitromethane as the solvent (Scheme 3.9).[14] Initial studies were carried out using toluene as the solvent at 100 °C, but the use of nitromethane as a solvent was discovered to be more effective in later studies. Additionally, it was found that DABCO–CuCl complex (**35**) (characterized by single-crystal X-ray analysis) exists in a linear polymeric structure due to strong intermolecular hydrogen bonding. Thus, the use of protic solvent such as nitromethane not only breaks the intermolecular hydrogen bonding, but also enhances catalytic activity. Indeed, all oxidation reactions using nitromethane as the solvent occur at room temperature. DABCO (**31**) was postulated to play a dual role as a base to deprotonate the hydroxy group of alcohol and as an N-donor ligand to CuCl. High selectivities were observed for primary alcohols over secondary alcohols, and no overoxidation of the products was observed.

The Koskinen group performed an extensive investigation into the influence of different catalytic components in the TEMPO–Cu-catalyzed aerobic oxidation of alcohols.[15] Their study revealed that organic amine bases such as 1,4-diazabicyclo[2.2.0]octane (DABCO) (**31**), *N*-methyl imidazole (NMI)

(**38**), *N,N*-dimethyl aminopyridine (DMAP) (**39**), 1,8-diazabicyclo[5.4.0] undec-7-ene [DBU] (**40**) and triethylamine showed better activity compared to inorganic bases KOH and potassium *tert*-butoxide. Among the amine bases DBU (**40**) was found to exhibit the highest activity. In addition, the use of excess base was found to be detrimental.

Although increasing the amount of ligand (bipyridine) slightly increases the rate of the reaction, it was found that ligand stoichiometry does not have a major influence on the reaction. Further studies on TEMPO (**5**) and copper revealed approximately first- and second-order correlations with the reaction rate, respectively. Both TEMPO (**5**) and copper increased the reaction rates when the amount of each individual component was increased. Furthermore, use of air instead of pure oxygen decreased the rate of oxidation and showed first-order kinetics with respect to reaction rate. Based on the collected experimental data, Koskinen *et al.* proposed a binuclear copper(II) complex **41** as a reactive intermediate rather than the one (**29**, Figure 3.4) proposed by Sheldon's group (Scheme 3.10).[12] Hence, oxidations follow second-order dependency on alcohols. A catalytic mixture of $CuBr_2$/bipyridine (**24**)/TEMPO (**5**)/base of ratio 1 : 1 : 1 : 2 in acetonitrile solvent using pure oxygen as the terminal oxidant was found to be the best combination and was used for the oxidation of different aromatic and aliphatic primary and secondary alcohols (Scheme 3.11). Moreover, $Cu(OTf)_2$ was found to effective instead of $CuBr_2$ for more challenging substrates.

The Repo group reported the use of copper(II)–2-*N*-arylpyrrolecarbaldamino complexes **44**(**a–e**) along with TEMPO as an efficient catalytic system for aerobic oxidation of benzylic alcohols in alkaline water solutions at 80 °C (Scheme 3.12).[16] The catalytic activity of synthesized and *in situ* made copper complexes showed similar reactivity. In addition, dioxygen, air or hydrogen peroxide were utilized as terminal oxidants. This catalytic system specifically required alkaline reaction conditions. Hence, reactions were carried out using either NaOH or K_2CO_3 aqueous solutions. Substituents on the R group of the copper complexes had a profound effect on the reactivity. *p*-Chloro **44(c)** and *p*-fluoro **44(d)** phenyl substituents containing complexes showed optimal reactivity, while a hindered 2,6-diisopropyl phenyl substituted complex **44(e)** was barely reactive.

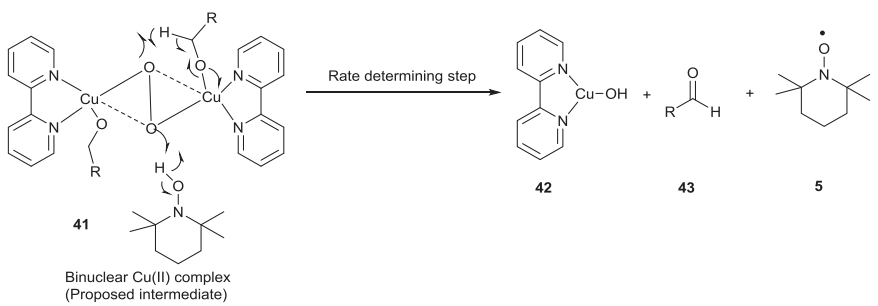

Scheme 3.10 Plausible mechanism for alcohol oxidations, proposed by Koskinen.[11]

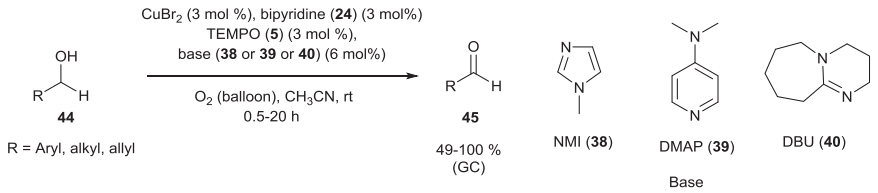

Scheme 3.11 TEMPO-catalyzed aerobic oxidation of alcohols, developed by Koskinen.

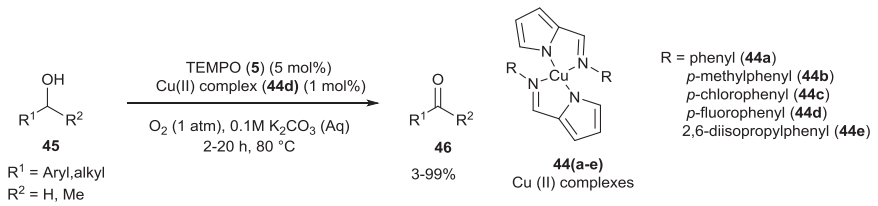

Scheme 3.12 Copper(II)–2-*N*-arylpyrrolecarbaldamino complex/TEMPO-catalyzed oxidation of alcohols.

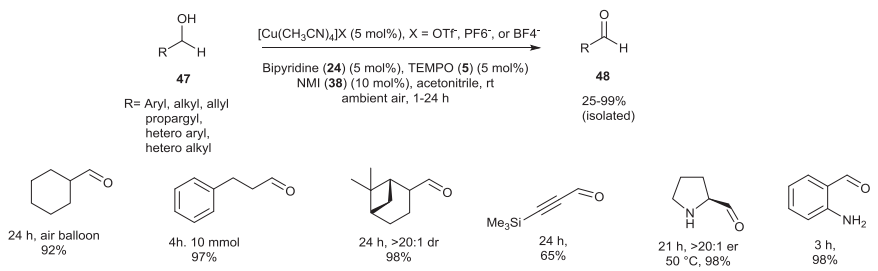

Scheme 3.13 Cu/TEMPO-catalyzed oxidation of alcohols, developed by Stahl's group.[17]

In 2011, a remarkable contribution to the field was reported by the Stahl group. This method employs a highly active bipyridine–Cu(I)–TEMPO–NMI catalyst system allowing oxidation of a wide array of primary alcohols. Benzylic, allylic and aliphatic alcohols are oxidized in acetonitrile at ambient temperature using atmospheric oxygen as terminal oxidant (Scheme 3.13).[17] This system is not only compatible with a broad range of functional groups such as olefins, amines and sulfur-containing alcohols, but also highly selective for primary alcohols over secondary alcohols. Under the developed reaction conditions, though Cu(I)Br and Cu(II)Br_2 were also effective toward oxidations, Cu(I) salts with non-coordinating anions such as $[Cu(CH_3CN)_4]X$ were used as copper sources to maintain reaction mixture homogeneity throughout the reaction. Overall, this effective catalytic mixture was able to overcome most of the limitations that were associated with the previously reported Semmelhack[8] and Sheldon[12] catalytic systems. For example, oxidation of *trans*-4-hexen-1-ol **49** by Semmelhack and Sheldon protocols gave

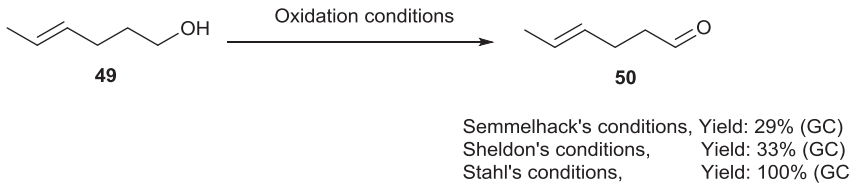

Scheme 3.14 Oxidation of *trans*-4-hexen-1-ol with different oxidative conditions.

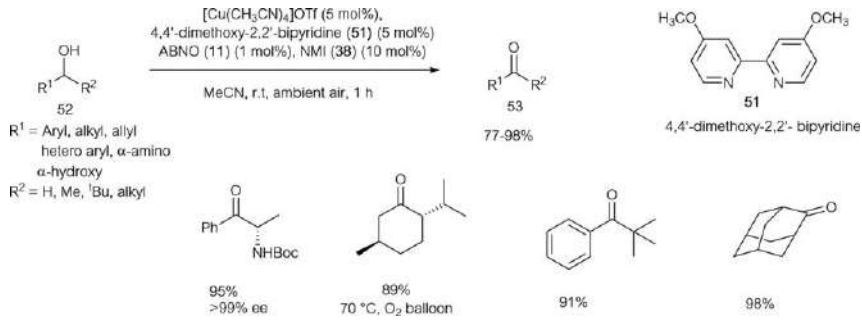

Scheme 3.15 Cu/ABNO-catalyzed aerobic oxidation of alcohols.

only 29% and 33% conversions, respectively, whereas Stahl's conditions gave 100% conversion (GC) (Scheme 3.14). However, this system showed poor or no reactivity towards secondary alcohols, vicinal diols and primary alcohols bearing vicinal chelating groups.

In 2013, Stahl and coworkers resolved the longstanding issue of oxidizing unactivated and aliphatic alcohols, particularly secondary alcohols, by developing a catalytic system comprised of dimethoxy bipyridine (**51**)–Cu(I) and the sterically unencumbered nitroxide ABNO (**11**) instead of commonly used TEMPO (**5**) (Scheme 3.15).[18] In this catalytic system, replacing TEMPO (**5**) with ABNO (**11**) alleviated the steric and electronic constrains of the Cu–TEMPO system. In addition, it was found that electron-rich bipyridine derivatives enhance the rate of the reaction. Most of the oxidation reactions were completed within one hour with 1 mol% of ABNO (**11**) at room temperature using ambient air as the source of oxygen.

As an extension of the oxidation of alcohols, Stalh's group expanded their study on copper–nitroxide catalytic systems to aerobic oxidative lactonization of 1,4-, 1,5-, and 1,6-diols *via* hemiacetal intermediates (Scheme 3.16)[19] as well as oxidative coupling of alcohols and amines to produce amides *via* hemiaminal intermediates (Scheme 3.17).[20] Recently, Stahl and coworkers showed Cu(I)–ABNO mediated synthesis of hetero atom substituted amides. Interestingly, this oxidation process requires neither NMI (**38**) nor any other base (Scheme 3.18).[21]

The Stahl group also carried out mechanistic studies of the copper/TEMPO-catalyzed oxidation reactions.[22] Initially, based on systematic kinetic

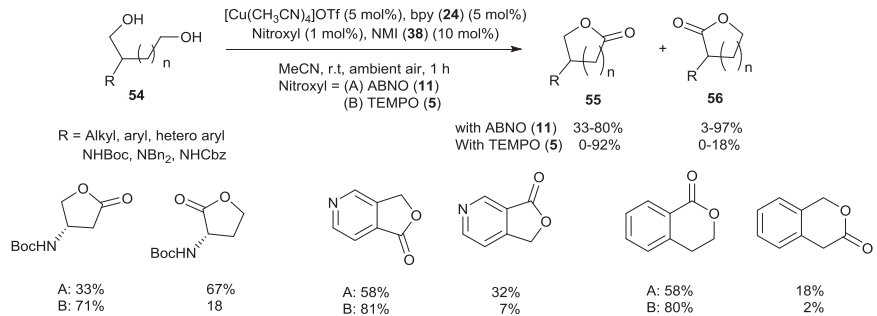

Scheme 3.16 Cu/TEMPO-catalyzed oxidative lactonization of diols.[19]

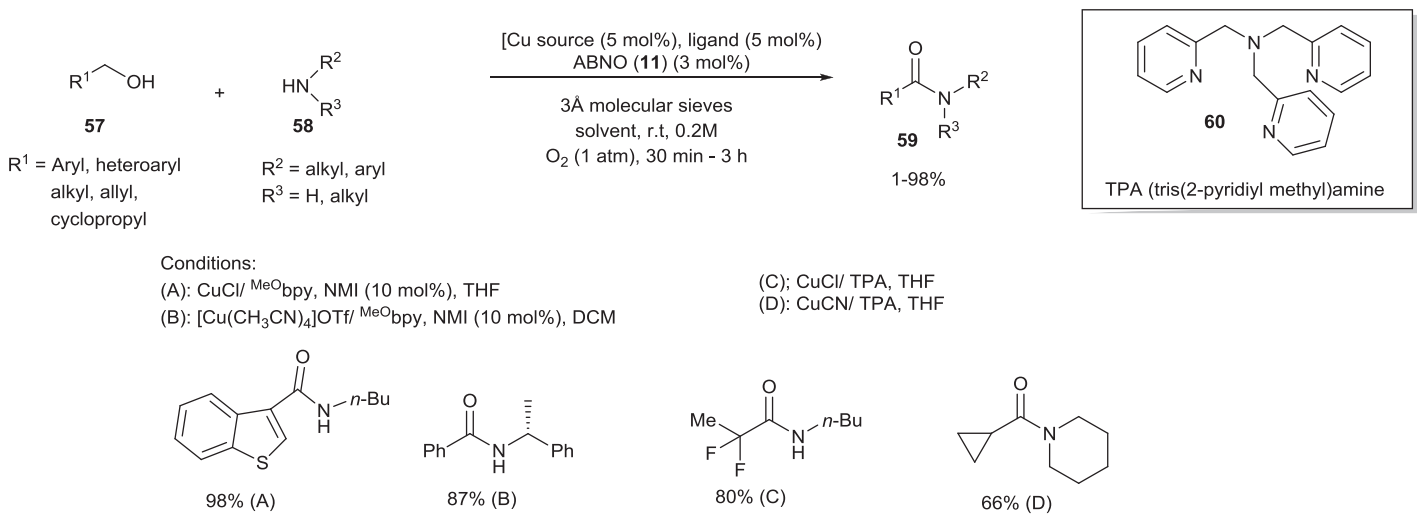

Scheme 3.17 Cu/ABNO-catalyzed oxidative coupling of alcohols and amines.

Scheme 3.18 Cu/ABNO-catalyzed heteroatom substituted amide synthesis.

and spectroscopic studies, they proposed a catalytic mechanism involving bimolecular hydrogen atom transfer between Cu(II)–alkoxy species **64** and TEMPO (**5**) leaving Cu(I) and TEMPOH (**14**) (Scheme 3.19). Molecular oxygen oxidizes Cu(I) and TEMPOH (**14**) to Cu(II)–OH and TEMPO (**5**) radical, which continues the oxidation of alcohol to aldehyde. However, further investigations by Stahl and coworkers using experimental and density functional theory (DFT) studies found that the transition state that involves hydrogen atom transfer *via* bimolecular pathway **67** is higher in energy than hydrogen atom transfer from Cu(II)–alkoxide to a coordinated nitroxyl species **68**,[23] which is in agreement with similar calculations carried out, independently, by Baerendes and coworkers (Figure 3.5).[24] Hence, a pathway involving a closed shell η^1-nitroxyl–Cu adduct **68** was identified to be most favored transition state for alcohol oxidation.

In 2017, Szpilman and Iron described their computational investigations of several possible catalytic cycles for the copper/TEMPO-catalyzed (**5**) oxidation of alcohols to the corresponding carbonyl compounds using density functional methods. A novel catalytic cycle in which TEMPO remains coordinated to copper throughout was found to be the most likely mechanism (Scheme 3.20).[5] According to the proposed mechanism, there are three major steps involved: (1) oxidation of alcohol, in which H-atom transfer from the alkoxy ligand **74** to nitrogen atom of coordinated TEMPO *via* a six-membered intramolecular transition state **68** takes place (Step 6), (2) oxygen activation

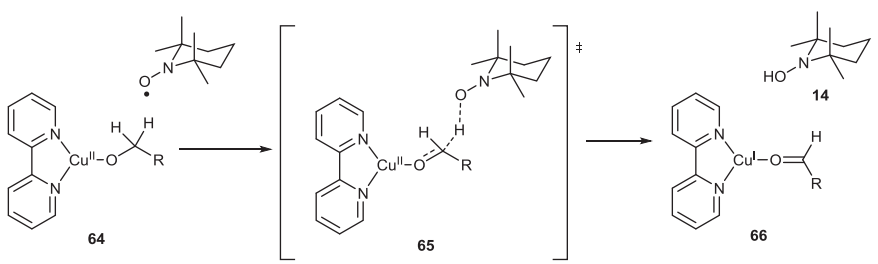

Scheme 3.19 Proposed bimolecular H-atom transfer mechanism.

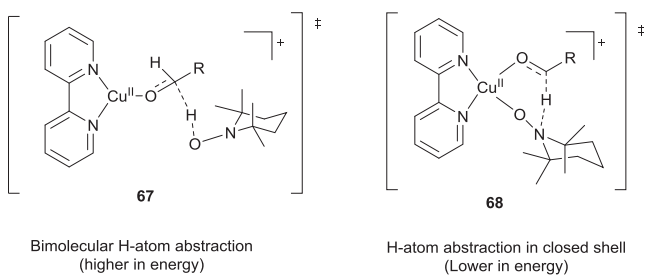

Figure 3.5 Illustration of H-abstraction in bimolecular and closed shell Cu(II) complexes.

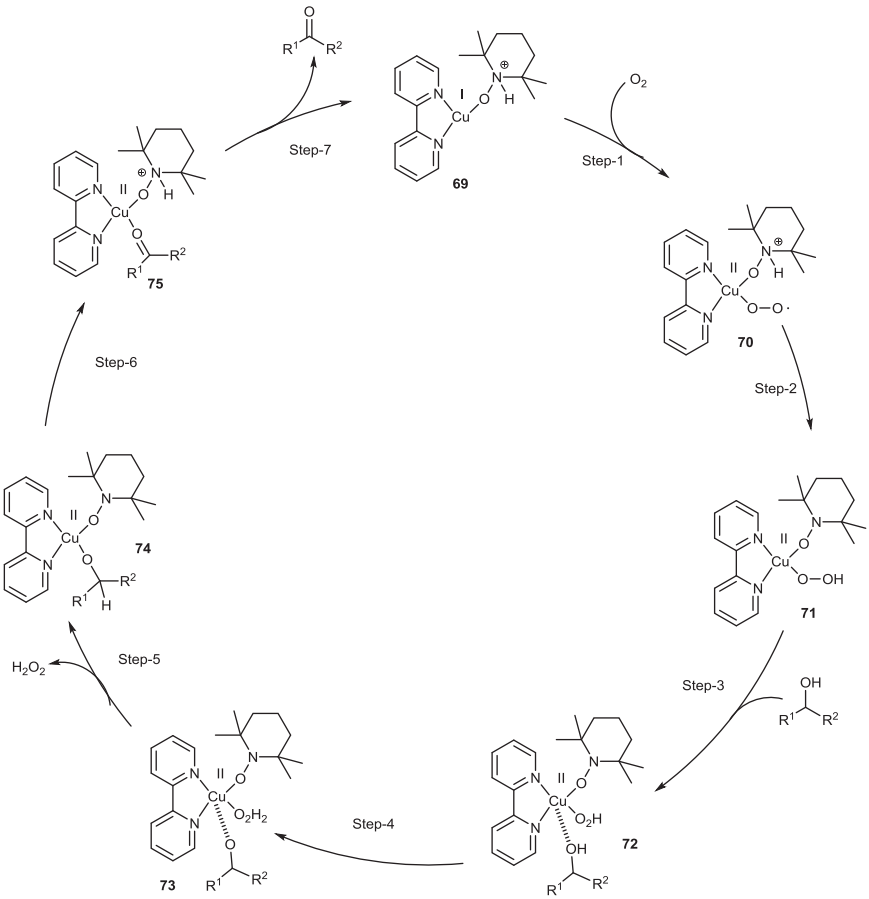

Scheme 3.20 Most likely mechanism for the Cu/TEMPO-catalyzed oxidation of alcohols proposed by the Szpilman group.

with formation of a peroxo complex **70** (Step 1), and (3) alcohol activation with transfer of the O–H proton to the peroxo ligand **72** (Step 4), thereby completing the catalytic cycle. More importantly, activation of oxygen and/or initial activation of alcohol was found to be the rate-determining step rather than the alcohol oxidation step. In addition, in contrast to several previous mechanistic studies, it was identified that NMI (**38**) is not a part of the catalytic cycle. However, it is required to initiate the reaction.

In 2013, Chen and coworkers showed the ability of *in situ* generated Cu–NHC–TEMPO complex **76** to mediate the oxidation of primary alcohols to the corresponding aldehydes (Scheme 3.21).[25] The active catalyst was generated *in situ* by combining TEMPO-anchored imidazolium salt with copper powder. This system is capable of oxidizing aliphatic, allylic, benzylic and propargylic primary alcohols to the respective aldehydes without overoxidation in chlorobenzene at 55 °C. No base is required. Interestingly, upon

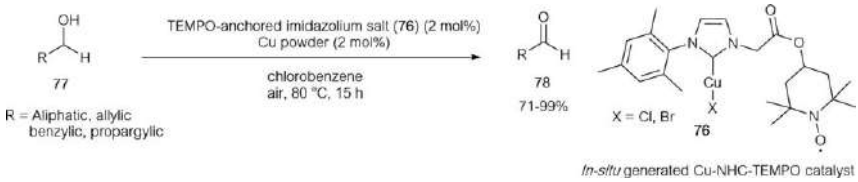

Scheme 3.21 Cu–NHC–TEMPO complex-catalyzed aerobic oxidation of alcohols.

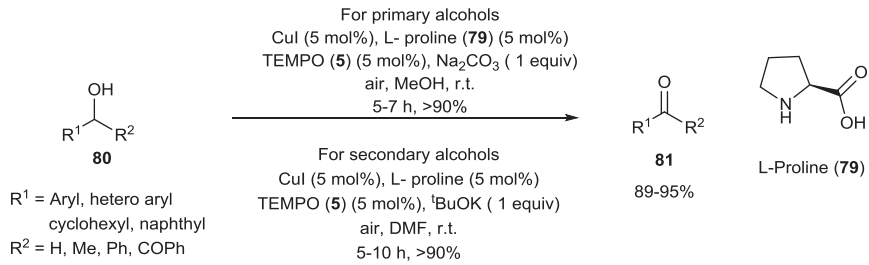

Scheme 3.22 L-proline/Cu/TEMPO-catalyzed aerobic oxidation of alcohols.

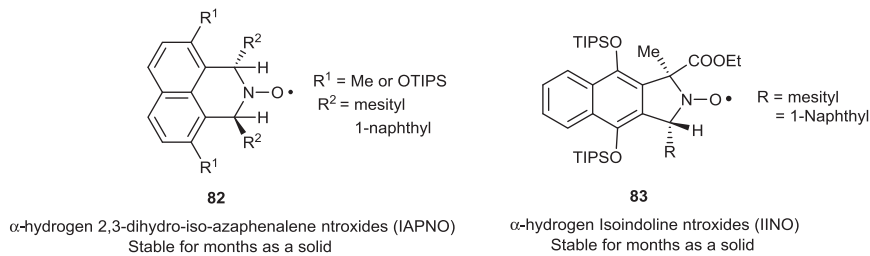

Figure 3.6 Novel α-hydrogen-substituted azaphenalene and isoindoline nitroxides.

the oxidation of 2-phenylethanol and 3-phenylpropan-1-ol, C–C bond cleavage took place affording benzaldehyde as a major product.

Ding *et al.* developed a protocol that involved L-proline (**79**) as an efficient N,O-bidentate ligand, rather than traditionally used bipyridine derivatives, for the Cu/TEMPO catalytic mixture to mediate oxidation of primary and secondary benzyl alcohols to the corresponding aldehyde and ketones (Scheme 3.22).[26] Two distinct set of conditions were used for primary and secondary alcohols. Though this method is applicable to a wide range of activated alcohols, it is ineffective in the case of unactivated alcohols.

In 2015, while the use of nitroxides for various applications was developing at a rapid pace, Szpilman and coworkers designed a novel concept, based on steric and stereo electronic effects, for the preparation of α-hydrogen-substituted nitroxides and accordingly developed two distinct protocols to synthesize the two novel families of cyclic nitroxide radicals possessing α-hydrogens (Figure 3.6).[27] One family of nitroxides, the IAPNO

(**82**) type, has a central piperidine ring and the other IINO (**83**) type has an isoindoline ring in their molecular structure. In addition, the Szpilman group employed the IAPNO (**82**) type of nitroxides as oxidation co-catalyst using the aerobic oxidation conditions developed by Stahl *et al.* This novel nitroxide/copper oxidation system was able to oxidize both activated and unactivated alcohols effectively (Scheme 3.23).[28] Copper bromide was used as the copper source. Oxidation of aliphatic and secondary alcohols required higher temperature (55 °C) due to precipitation of catalyst at room temperature. More importantly, the spent nitroxides were recovered in the form of hydroxylamines and reused. Recently, Szpilman group described the preparation of the first ever α-deuterium-substituted nitroxide radicals of the IAPNO family, which may find a potential application in biomedicine and physical chemistry.[29]

Inspired by enzymatic catalysis, Maayan *et al.* developed a series of unique metallopeptoid intramolecular cooperative catalytic systems, in which the phenanthroline ligand and nitroxide TEMPO are tethered in the same molecular scaffold.[30] These systems proved to be efficient for the oxidation of various benzylic, allylic and aliphatic primary alcohols with turnover number (TON) up to 16 times higher than regular nitroxide-catalyzed oxidation protocols (Scheme 3.24). Among the different metallopeptoids prepared, metallopeptoid trimer BT **88** was found to be more effective. In addition, only 0.5 mol% of catalyst was required for effective oxidation. Maayan's group extended this intramolecular cooperative catalytic system to synthesize different imines from various alcohols *via* alcohol oxidation as a key step.[31]

In 2016, Gao and workers reported the use of the nitroxide ABNO (**11**) in combination with iron nitrate as a metal co-catalyst for the aerobic oxidation of a broad array of activated and unactivated alcohols in acetonitrile at ambient temperature (Scheme 3.25).[32] This efficient protocol requires neither ligand nor base. Gram scale oxidation of benzyl alcohols using only 0.2 mol% of ABNO (**11**) as a catalyst afforded the aldehyde in 95% yield in 16 h.

Iwabuchi and coworkers described the use of the sterically unencumbered nitroxide AZADO (**8**) in combination with a copper source as an effective catalytic mixture for highly chemoselective oxidation of alcohols (**93**) bearing unprotected primary, secondary and tertiary amine substituents (Scheme 3.26).[33] This method proved to be superior to various traditional chemoselective alcohol oxidation reagents and methods. The chemoselectivity of alcohols over amines is attributed to the higher acidity of the O–H group of alcohols relative to the N–H group of amines, which accelerates the formation of copper-alkoxide, an anticipated reactive intermediate during the catalytic cycle. In addition, this method was extended to synthesize nitrogen-containing natural products, myosmine and (–)-mesembrine. Iwabuchi *et al.*, in their further work, applied this protocol to selective oxidation of alcohols in the presence of electron-rich divalent sulfur functionalities (Scheme 3.27).[34]

Scheme 3.23 Cu/IAPNO-catalyzed aerobic oxidation of alcohols.

Scheme 3.24 TEMPO appended metallopeptoid catalyzed oxidation of alcohols.

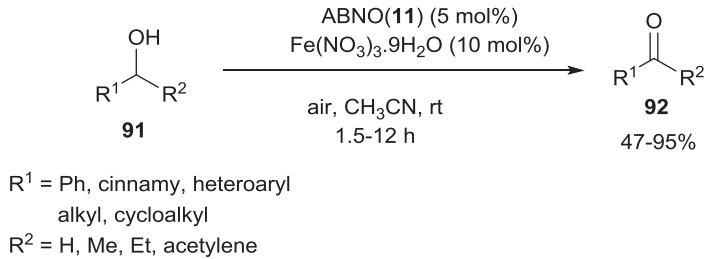

Scheme 3.25 Fe/TEMPO-catalyzed aerobic oxidation of alcohols.

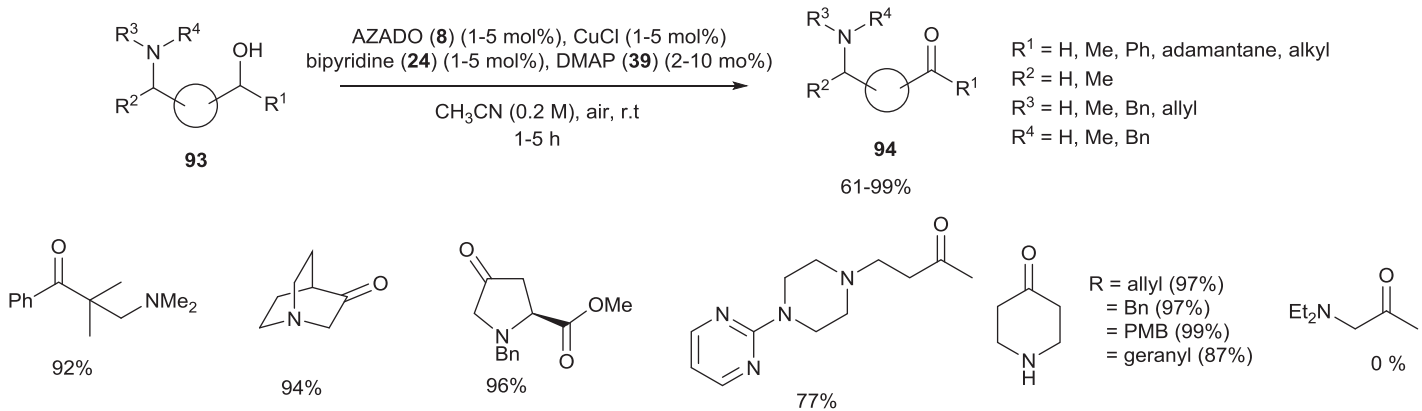

Scheme 3.26 Cu/AZADO-catalyzed chemoselective aerobic oxidation of unprotected amino alcohols to the corresponding amino carbonyl compounds.

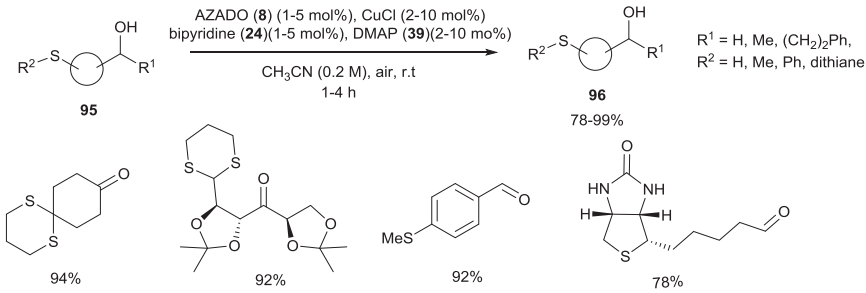

Scheme 3.27 Cu/AZADO-catalyzed chemoselective aerobic oxidation of alcohols bearing sulfur groups.

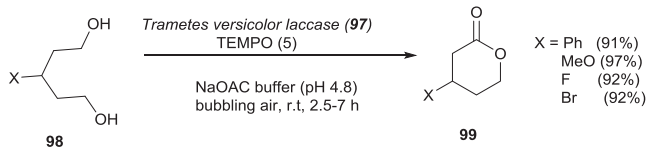

Scheme 3.28 Laccase/TEMPO-catalyzed oxidative lactonization of diols.

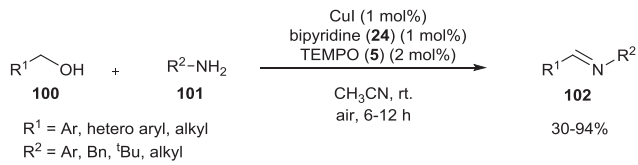

Scheme 3.29 Cu/TEMPO-catalyzed one-pot oxidative condensation of alcohols with amines.

Vicente Gotor-Fernandez *et al.* described the use of the multicopper enzyme laccase (**97**) in combination with TEMPO for the aerobic oxidation of diols to lactones *via* hemiacetal in aqueous medium at room temperature (Scheme 3.28).[35] No base is required for the oxidation, which takes place in sodium acetate buffer (pH 4.8).

Xu and coworkers disclosed a method for preparing imines and α,β-unsaturated imines *via* one-pot oxidative condensation of alcohols with amines, by using TEMPO in combination with a copper salt at room temperature (Scheme 3.29).[36] No base was used in this reaction. This aerobic oxidative system is compatible with a broad range of alcohols and amines.

Huang and coworkers demonstrated the use of a Cu/TEMPO oxidation catalytic system to obtain nitriles directly from alcohols and aqueous ammonia in the presence of oxygen as a terminal oxidant (Scheme 3.30).[37] This double dehydrogenative process is compatible with a wide array of functional groups and afforded good to quantitative yields. In addition, the process of preparing nitriles was coupled to various heterocyclization

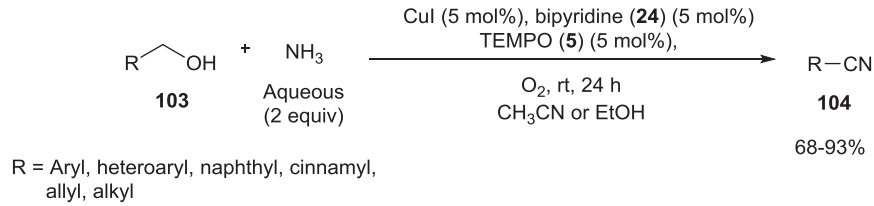

Scheme 3.30 Cu/TEMPO-catalyzed direct synthesis of nitriles from alcohols.

processes to provide a one-pot synthesis of tetrazoles, oxazoline, thiazoline, triazolopyridines and imidazolines. Similar dehydrogenative protocols to prepare nitriles using the Cu/TEMPO catalytic system were developed by Muldoon *et al.*[38] and Tao and coworkers[39] with few modifications. Another similar method was developed by Batra and coworkers by employing TEMPO in combination with iron nitrate as the metal co-catalyst.[40] This method worked well for aliphatic and aromatic alcohols. No ligand or base is required. Interestingly, in the case of reactions of heteroaromatic alcohols to the respective nitriles, prolonged reaction times yielded amide rather than the expected nitrile (Scheme 3.31).

In 2018, Yamaguchi, Jin and coworkers reported the copper/nor-AZADO-catalyzed (**108**) oxidative acylation of amides with alcohols to afford the corresponding imides using molecular oxygen as the terminal oxidant.[41] Interestingly, tetramethylethylenediamine (TMEDA) (**109**) was found to be an efficient ligand for this reaction rather than conventional bipyridine derivatives. A broad range of alcohols were treated with primary and secondary amides under these reaction conditions. Moreover, Evans' imides were also synthesized using this protocol (Scheme 3.32).

Christmann and coworkers demonstrated the ability of Cu/TEMPO (**5**) oxidation catalysts to perform a cascade of oxidation/isomerization of (*Z*)-allylic alcohols (**113**) to (*E*)-α,β-unsaturated aldehydes (**115**) without isolation of the intermediate aldehyde (**114**) (Scheme 3.33).[42] Though NMI (**38**) was effective for the initial oxidation of allylic alcohols, it was found to be less effective in isomerization of the (*Z*)-olefin to (*E*)-olefin. Replacing NMI (**38**) with DMAP (**39**) not only resulted in higher activity in isomerization, but also accelerated the alcohol oxidation. In addition, this protocol was extended to a one-pot oxidation/Diels–Alder protocol (Scheme 3.34). In 2014, Christmann and coworkers developed the one-pot aerobic oxidation of allylic and benzylic alcohols to the corresponding carboxylic acids by merging Cu/TEMPO-catalyzed oxidation with a subsequent chlorite oxidation (Scheme 3.35).[43] Christmann *et al.*, in their further work, reported an efficient one-pot process to prepare 2-chloroalkan-1-ols from alkan-1-ols by combining a Cu/TEMPO oxidation system with an enamine chlorination/reduction. *N*-chlorosuccinimide was used as the chlorinating reagent. The resultant 2-chloroalkan-1-ols can be used to make terminal epoxides (Scheme 3.36).[44]

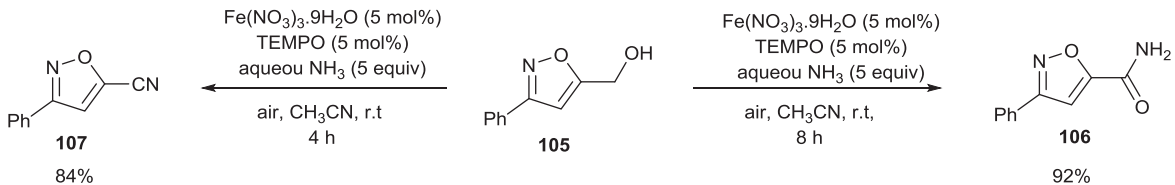

Scheme 3.31 Fe/TEMPO-catalyzed synthesis of nitriles from alcohols.

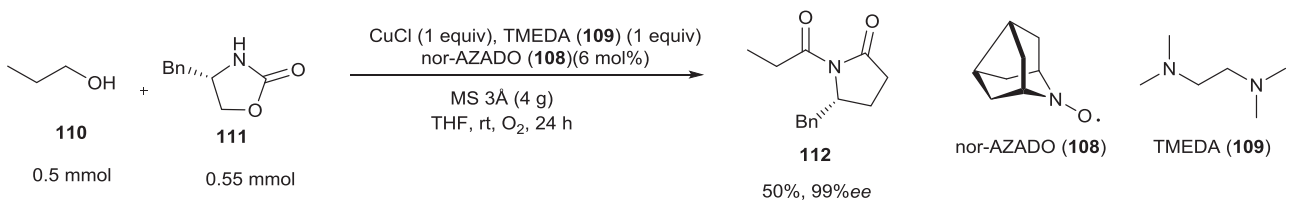

Scheme 3.32 Cu/nor-AZADO-catalyzed oxidative acylation of amides.

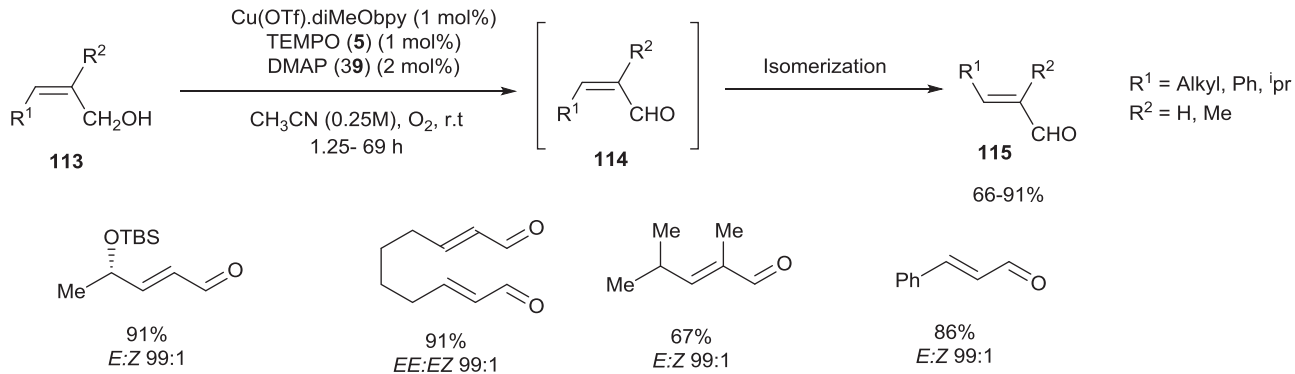

Scheme 3.33 Cu/TEMPO-catalyzed tandem oxidation/isomerization of allylic alcohols.

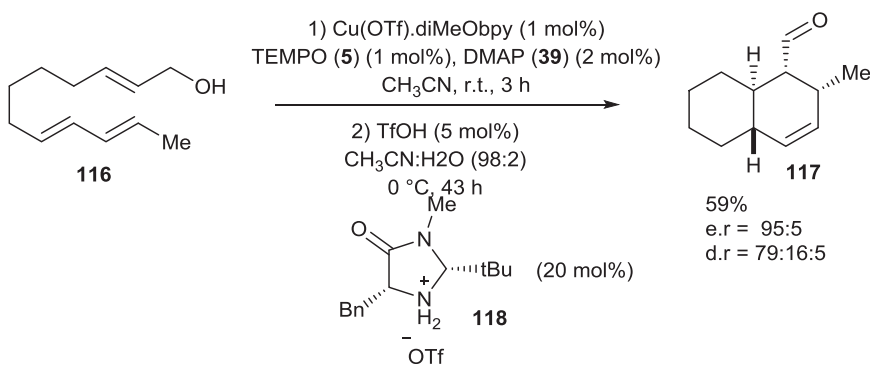

Scheme 3.34 Cu/TEMPO-catalyzed one-pot oxidation/Diels–Alder reaction.

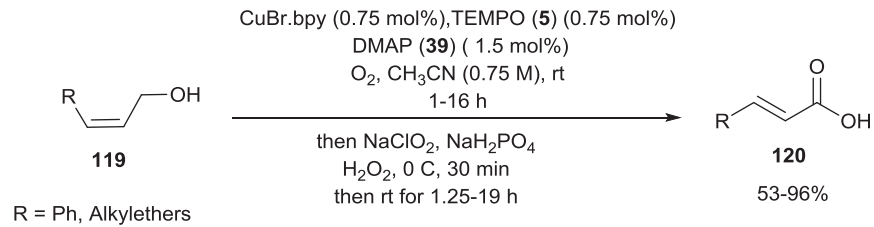

Scheme 3.35 Cu/TEMPO-catalyzed one-pot oxidation–isomerization–oxidation reaction.

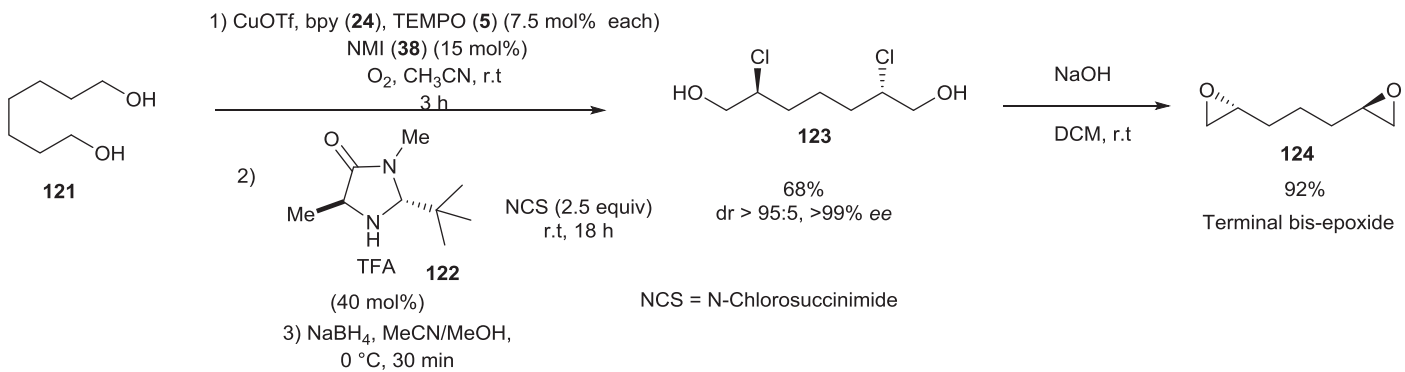

Scheme 3.36 Cu/TEMPO-catalyzed one-pot β-chlorination of alcohol *via* oxidation of alcohols.

Jang and coworkers developed a multicatalytic system composed of a Cu/TEMPO oxidation system and a proline-based chiral organo catalyst (**128**) to prepare β-substituted aldehydes (Scheme 3.37).[45] This one-pot two-step synthesis involves oxidation of allylic alcohols by a Cu/TEMPO aerobic oxidation system to yield the intermediate aldehyde (**126**). Subsequently, addition of a chiral secondary amine and diethyl malonate (**129**) leads to β-substituted aldehydes in high enantioselectivities *via* imine catalysis. Benzoic acid was used as an additive to promote the iminium ion formation, thus improving the yield and enantioselectivity. In addition, this protocol was also applicable to synthesize chiral α,β-substituted aldehydes (**130**) by using excess TEMPO (**5**) (2 equiv.) in the second step to trap the enamine, which is formed during the addition of diethyl malonate to iminium intermediate (Scheme 3.38). For this sequence, adamantane-1-carboxylic acid was used as an additive. Although low yields were obtained in this three-step single-pot reaction, high diastereo- and enantioselectivities were observed. Moreover, in further work, nitromethane was also employed as the Michael donor.[46] A similar method was developed by Da-Ming Du and coworkers to synthesize chiral β-hydrazino alcohols using *N*-Boc-hydrazine as the Michael donor.[47]

Cook and Muldoon disclosed the use of a Cu/TEMPO aerobic catalyst system for the preparation of indoles (**132**) and quinolines (**133**) *via* alcohol oxidation as a key synthetic step (Scheme 3.39).[48] Substituted amino alcohols (**131**) were used as starting materials under the aerobic oxidation conditions developed by Kumpulainen and Koskinen[15] to obtain N-heterocycles. In the case of indole synthesis, longer reaction times led to lower yields. This is likely due to the reported decomposition of the product to unidentified by-products.

Wu and coworkers disclosed a cascade synthesis of quinazolines using a Cu/TEMPO aerobic oxidation system (Scheme 3.40).[49] Reaction of readily available 2-amino benzyl alcohols (**134**) with aldehydes (**135**) in the presence of an ammonia source yielded quinazolines (**136**) in good to excellent yields. Oxidation of alcohols is the key step in this process.

3.2.3.2 *Nitroxide-mediated Oxidation (Two-electron) of Alcohols* via *Oxoammonium Cation*

Since 1960, oxoammonium cations derived from nitroxides have been known to mediate alcohol oxidations as stoichiometric oxidants. A full equivalent or even excess of nitroxide is needed for complete oxidation of alcohols.[50] In 1987, an important contribution to the field was made by Anelli and coworkers, by developing a robust catalytic method for the selective oxidation of primary and secondary alcohols to the corresponding aldehydes and ketones, using *in situ* generated oxoammonium salts from nitroxyl, 4-methoxy TEMPO (**137**), and sodium hypochlorite as a secondary oxidant in a biphasic medium at 0 °C.[51] This method requires only 1 mol%

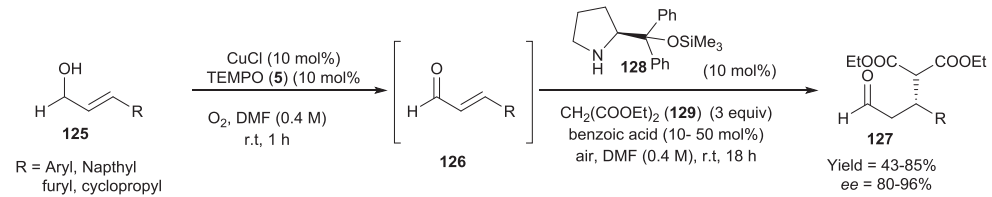

Scheme 3.37 Cu/TEMPO-catalyzed one-pot oxidation–asymmetric Michael addition.

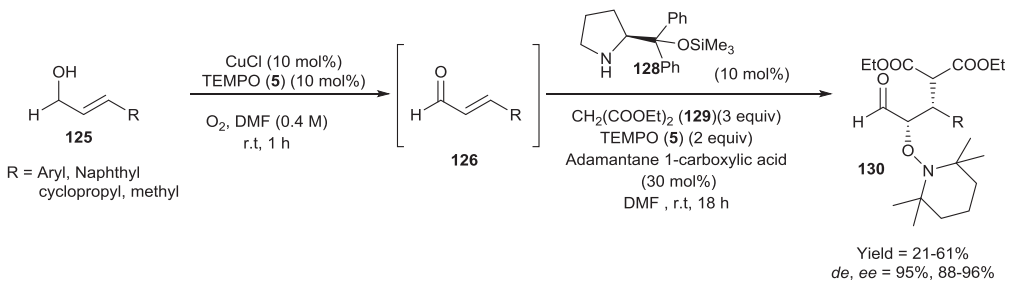

Scheme 3.38 Cu/TEMPO-catalyzed one-pot synthesis of chiral α,β-disubstituted aldehydes.

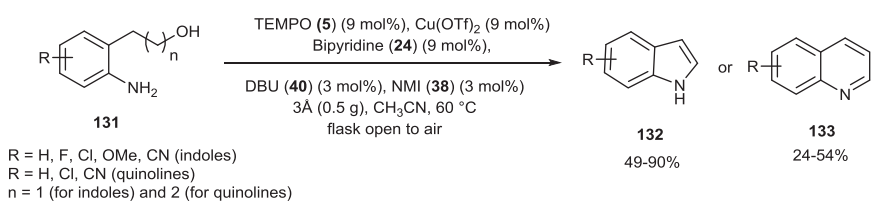

Scheme 3.39 Cu/TEMPO-catalyzed synthesis of indole and quinolines *via* oxidation of alcohols.

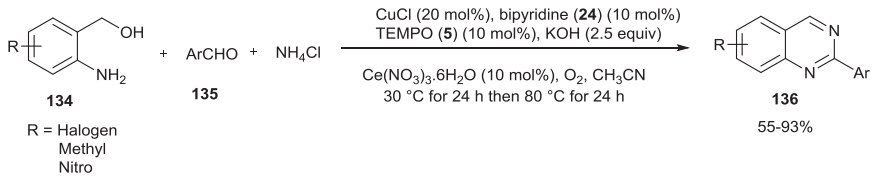

Scheme 3.40 Cu/TEMPO-catalyzed cascade synthesis of quinazolines.

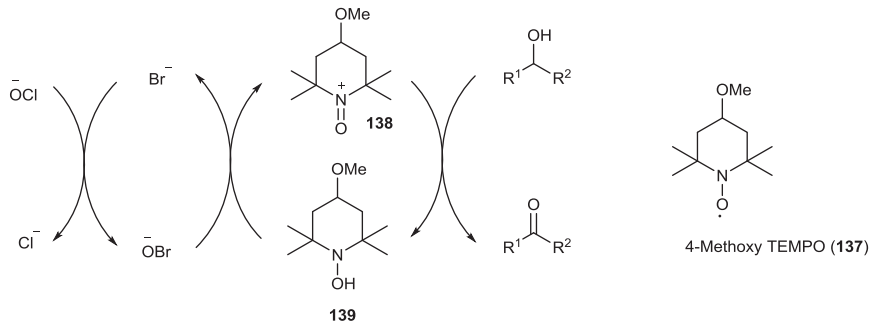

Scheme 3.41 Proposed mechanism for the oxidation of alcohols by Anelli *et al.*

of nitroxide, but a slight excess of sodium hypochlorite solution (1.25 equiv.). In addition, 10 mol% of potassium bromide is also required for efficient oxidations. Moreover, it was found that the pH of the reaction mixture plays an important role, thus, buffering of aqueous solution at pH 8.6 with sodium bicarbonate is necessary. Importantly, only a few minutes are required for the completion of oxidation. Indeed slowing the addition of the stoichiometric oxidant sometimes leads to lower yields due to formation of aldehyde hydrates which are oxidized to carboxylic acids. It is recommended to titrate the bleach before use. Room temperature was found to be detrimental for oxidation. This may be due to decomposition of the oxoammonium salts at higher temperatures. Further oxidation of aldehydes formed upon the oxidation of primary alcohols, to the carboxylic acids is slow under the reaction conditions. However, addition of a catalytic amount of quaternary ammonium salts leads to rapid conversion of aldehydes to the corresponding carboxylic acids. Mechanistically, it is assumed that hypochlorite oxidizes the bromide of KBr to HOBr, which is more soluble in organic solvent. The *in situ* formed HOBr oxidizes both 4-MeO-TEMPO (**137**) and its hydroxylamine (**139**) to the corresponding oxoammonium salt (**138**) (Scheme 3.41). In principle, any co-oxidant with the ability to oxidize nitroxide to its oxoammonium salt can be employed rather than HOCl. Anelli *et al.* extended this effective oxidation method to oxidation of diols. Diol oxidations were carried out using TEMPO (**5**) as the nitroxide, and a pH of 9.5 was maintained at 0–15 °C.[52] Moreover, the potency of this protocol was further showcased by applying it to multigram scale oxidation of (*S*)-(−)-2-methyl butanol (**140**) to (*S*)-(+)-2-methyl butanal (**141**) (Scheme 3.42).[53]

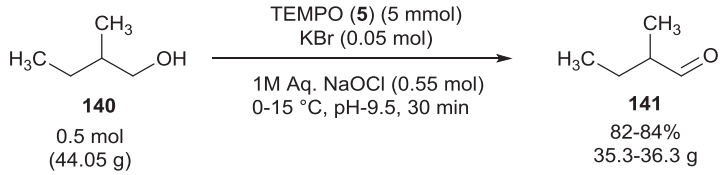

Scheme 3.42 Multigram scale oxidation of (*S*)-(−)-2-methyl butanol to (*S*)-(+)-2-methyl butanal.

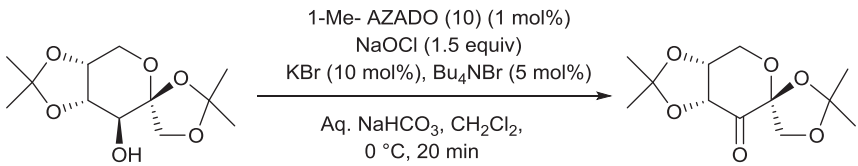

Scheme 3.43 Synthesis of Shi's catalyst by oxidation using 1-Me-AZADO under Anelli's conditions.

Based on Anneli's protocol, several co-oxidants to generate oxoammonium ion *in situ* from nitroxide were developed by other research groups. Notably, *N*-chlorosuccinimide by Einhorn *et al.*,[54a] hypervalent iodine reagent [bis(acetoxy)iodo]benzene (BAIB) by Margarita, Piancatelli *et al.*,[54b] oxone by Bolm *et al.*,[54c] trichloroisocyanuric acid (TCCA) by Giacomelli *et al.*,[54d] molecular iodine by Miller *et al.*,[54e] hydrogen peroxide/HBr in ionic liquid by Ragauskas *et al.*[54f] and pyridine–bromine complexes by Inukochi *et al.*[54g] In all these cases TEMPO was used as the nitroxide, and all the above co-oxidants were effective in generating oxoammonium species in either dichloromethane or toluene.

In 2006, Iwabuchi demonstrated the first ever use of sterically less hindered nitroxides AZADO (**8**) and 1-methyl AZADO (**10**) as catalysts for the oxidation of a wide array of alcohols, including structurally hindered alcohols under Anelli's conditions (Scheme 3.43).[55] Use of this sterically less encumbered nitroxide alleviated the steric constraints that were associated with the more hindered TEMPO and its congeners. This method proved to be superior to other previously developed nitroxides for oxidizing hindered alcohols.

A modification to Anelli's method was developed by Zhao and coworkers, also termed ''Zhao's modification'', in which primary alcohols were directly converted to corresponding carboxylic acids by using catalytic amounts of TEMPO (**5**) and stoichiometric amounts of sodium chlorite (2 equiv.) as secondary oxidant in the presence of catalytic amounts of sodium hypochlorite (Scheme 3.44).[56] Presumably, sodium chlorite oxidizes the intermediate aldehyde to carboxylic acid as in the Lindgren oxidation[56c] by generating sodium hypochlorite, which in turn oxidizes TEMPOH (**14**)

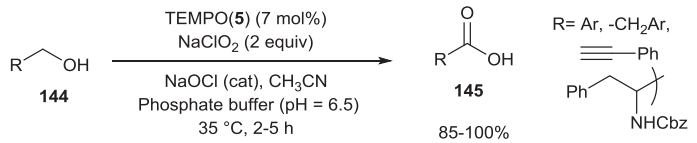

Scheme 3.44 Direct oxidation of primary alcohols to carboxylic acids by Zhao's modification.

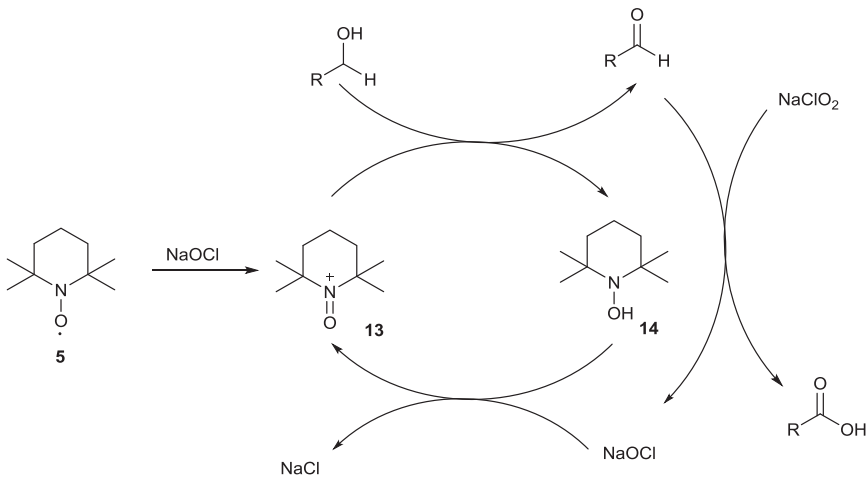

Scheme 3.45 Proposed mechanism of Zhao's oxidation of alcohols to carboxylic acids.

to oxoammonium salt (**13**) (Scheme 3.45). However, to initiate alcohol oxidation, catalytic amounts of hypochlorite are required. Reactions are carried out in acetonitrile phosphate buffer (pH 6.7) biphasic solutions at 35 °C. A similar method was developed by Iwabuchi *et al.*, but using the sterically less hindered nitroxide 1-Me-AZADO (**10**), which showed better activity than prototypical TEMPO (**5**).[57]

Bobbitt *et al.* disclosed a method for the oxidation of alcohols by the *in situ* preparation of oxoammonium salts *via* acid-promoted disproportionation of nitroxides.[7] Two molecules of nitroxide (**7**) in the presence of strong acid undergo disproportionation to produce one molecule of oxoammonium salt (**146**) and a molecule to hydroxyl amine (**147**). The formed oxoammonium oxidizes the alcohol to the carbonyl compounds and gets reduced to the corresponding hydroxyl amine (Scheme 3.46). Though this method is adaptable to a diverse scope of alcohols bearing alkenes and produces high yields, two moles of nitroxides are required to oxidize one mole of substrate. However, hydroxyl amine formed during this reaction can be isolated and recycled by oxidation back to either radical or its oxoammonium form.

A remarkable contribution to the oxoammonium chemistry was reported by Hu and coworkers, who developed the first ever transition metal-free

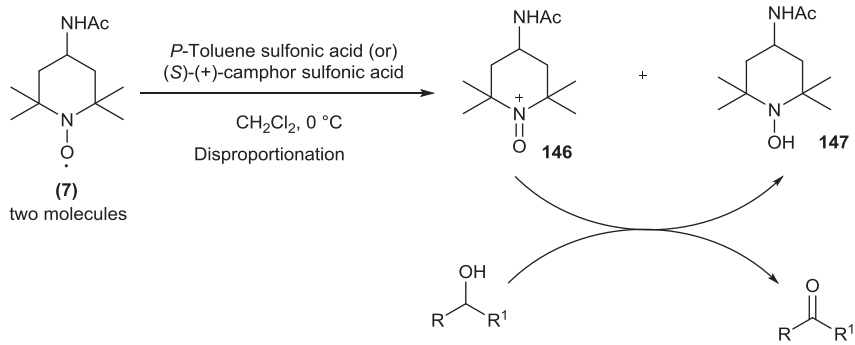

Scheme 3.46 Oxidation of alcohols by oxoammonium salts prepared *via* disproportionation.

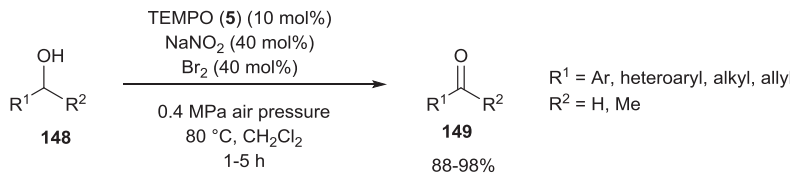

Scheme 3.47 Transition metal-free TEMPO-catalyzed aerobic oxidation of alcohols.

aerobic oxidation of alcohols using TEMPO as a catalyst.[58] An efficient catalytic system composed of TEMPO (**5**), bromine and sodium nitrite as a NO precursor at elevated temperature (80 °C) oxidizes aromatic and aliphatic primary and secondary alcohols to carbonyl compounds under air at 0.1 MPa pressure with the release of water as the only by-product (Scheme 3.47). Mechanistically, the *in situ* formed $TEMPO^+$ (**13**) oxidizes alcohols to carbonyl compounds and gets reduced to TEMPOH (**14**). TEMPOH (**14**) is reoxidized to $TEMPO^+Br^-$ (**150**) and HBr with bromine. The HBr is subsequently oxidized back to bromine by NO_2 leading to formation of NO. NO can be easily oxidized to NO_2 by molecular oxygen (Scheme 3.48). Hu *et al.*, in a further communication, reported the use of 1,3-dibromo-5,5-dimethylhydantoin as a bromine source instead of bromine and water as the solvent in place of dichloromethane. This method was also found to be efficient for the oxidation of all kinds of primary and secondary alcohols.[59] Hu and coworkers further reported on the use of the organic nitrite, *tert*-butyl nitrite as an efficient NO equivalent for the aerobic oxidation of alcohols in the presence of TEMPO.[60]

Based on Hu *et al.*'s aerobic oxidation protocol several other aerobic methods have been developed. Notably, TEMPO (**5**)/HCl/$NaNO_2$ as a catalyst by Liang *et al.*,[61a] a reusable TEMPO and carboxylic acid-functionalized imidazolium salts with $NaNO_2$ by Wang *et al.*,[61b] TEMPO in combination with nitric acid-assisted carbon oxidation system by Kakimoto *et al.*[61c] and hydroxyl amine as a source of NO in the presence of TEMPO by

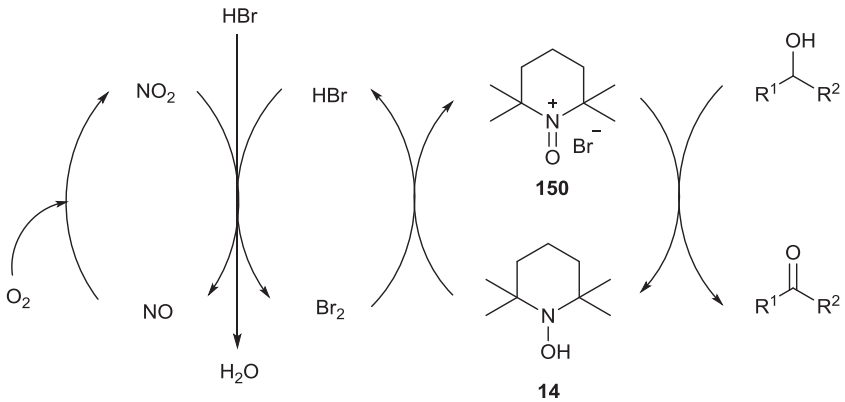

Scheme 3.48 Proposed mechanism for transition metal-free aerobic oxidation of alcohols.

Studer *et al.*[61d] Furthermore, Iwabuchi *et al.* used the less sterically hindered and electrophilic 5-F-AZADO (**9**) in combination with sodium nitrite for the aerobic oxidation of alcohols.[62] A similar aerobic method was developed by the Stahl group, where ABNO (**11**) and keto-ABNO (**12**) were used as nitroxide catalysts in the presence of sodium nitrite and nitric acid and were used for the oxidation of alcohols. In addition, use of sterically unhindered nitroxides exhibited faster reaction rates compared to TEMPO.[63]

Iwabuchi and coworkers described the use of less hindered nitroxide nor-AZADO in combination with diisopropyl azodicarboxylate (DIAD) (**151**) as a secondary oxidant.[64] Addition of acetic acid as an additive was found to enhance the oxidation process. Acetic acid is required to generate the oxoammonium ion by disproportionation of nitroxide radical. A series of primary and secondary alcohols were oxidized under these conditions (Scheme 3.49).

Kawabata and coworkers showed the use of electronically tuned PROXYL-based nitroxide **154c** for the oxidation of alcohols. The electronic tuning of the different nitroxides was done by measuring redox potentials using cyclic voltammetry. From the measured redox potentials, it was found that increasing the number of electron-withdrawing ester groups resulted in an increase of the oxidation potentials (Figure 3.7). Hypervalent iodine reagent phenyl iodonium bis(trifluoroacetate) (PIFA) (**155**) was used as a secondary oxidant (Scheme 3.50).[65] This method was effective for various secondary alcohol oxidations and also used for the chemoselective oxidation of benzylic alcohols in the presence of aliphatic alcohols (so less reactive than TEMPO).

Zhao and coworkers reported an interesting method to oxidize alcohols using a photocatalytic system comprised of dye-sensitized TiO_2 and TEMPO (**5**) under visible light irradiation ($\lambda > 450$ nm) in benzotrifluoride as a solvent. Commercially available anthraquinone dye Alizarin Red (**158**) was used as the sensitizer.[66] According to the proposed three-step catalytic cycle, a dye radical cation (**160**) is formed during an electron transfer from excited state of dye to conduction band of TiO_2. The formed dye radical cation (**160**)

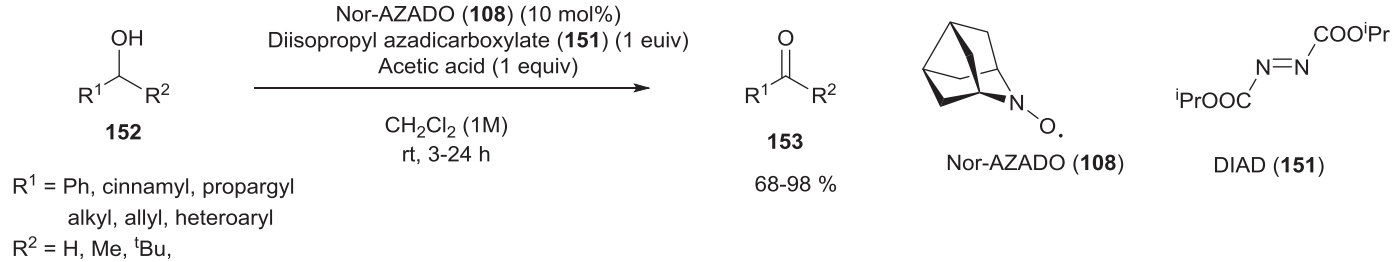

Scheme 3.49 Nor-AZADO-catalyzed oxidation of alcohols using diisopropyl azodicarboxylate as a secondary oxidant.

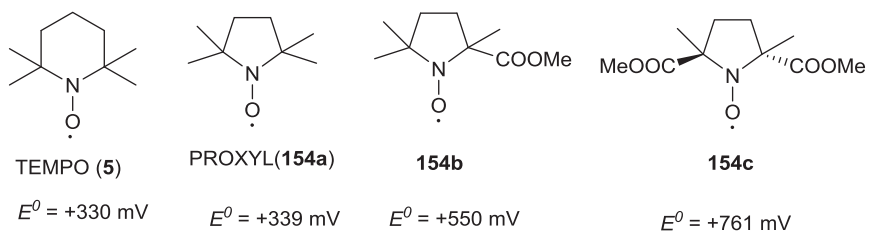

Figure 3.7 Redox potentials of different nitroxides.

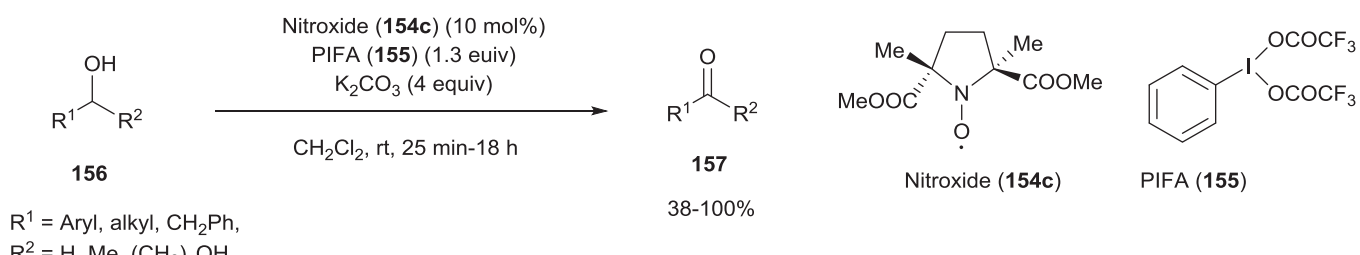

Scheme 3.50 Oxidation of alcohols catalyzed by electronically tuned nitroxide.

then oxidizes TEMPO (**5**) to $TEMPO^+$ (**13**). After alcohol oxidation, the generated TEMPOH (**14**) is oxidized to TEMPO (**5**) by either oxygen or the dye radical cation (**160**) (Scheme 3.51). This method is adaptable to primary and secondary alcohols. A similar method was developed by Li and coworkers but using $Ru(bpy)_3(PF_6)_2$ as a photoredox catalyst in combination with TEMPO (**5**) under visible light in the presence of oxygen.[67] This method is particularly efficient for benzylic alcohols.

Inokuchi and coworkers developed a method to regioselectively oxidize 2-alkylidene-1,3-propanediols (**161**) to (*E*)-2-hydroxymethyl-2-alkenals (**162**) using 4-benzoyloxy TEMPO (**163**) in combination with hypervalent iodine reagent BAIB (**164**) as a co-oxidant in tetrahydropyran solvent (Scheme 3.52).[68] A catalytic amount (1 mol%) of PTSA was also required to promote the oxidation. In addition, the reaction completes in 4 h and produces good yields.

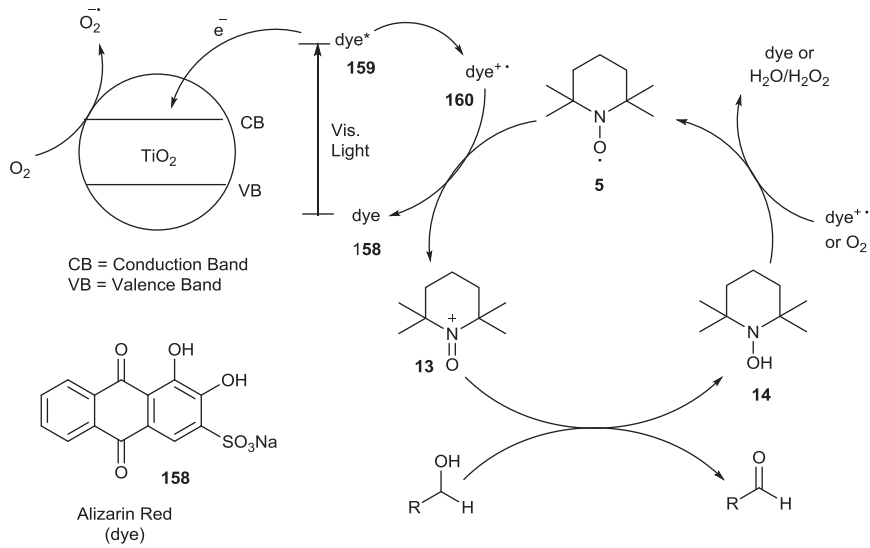

Scheme 3.51 Proposed catalytic cycle for dye-sensitized TiO_2–TEMPO system catalyzed oxidation of alcohols under visible light irradiation.

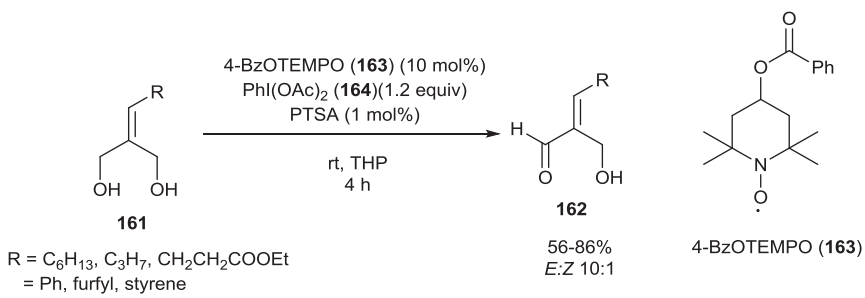

Scheme 3.52 4-BzOTEMPO catalyzed regioselective oxidation of 2-alkylidene-1,3-propane diols.

Iwabuchi and coworkers described the use of 1-Me-AZADO (**10**) in combination with NaOCl and $NaClO_2$ as an efficient catalytic mixture for one-pot oxidative cleavage of terminal diols (**163**) to the corresponding dehomologated carboxylic acids (**165**) (Scheme 3.53).[69] This simple process occurs *via* the oxidative decarboxylation of α-keto-carboxylic acids (**164**). No epimerization was observed during the oxidation of substrates bearing adjacent stereo center. In addition, this protocol was also applied to terminal triols and tetraols to yield the respective carboxylic acids. However, this method is not applicable to internal vicinal diols. Later, Iwabuchi *et al.* resolved the problem associated with internal vicinal diols (**166**) by using AZADO nitroxides in combination with $PhI(OAc)_2$ as a secondary oxidant (Scheme 3.54).[70]

Shibuya *et al.* disclosed a chemoselective oxidation of terminal 1,2-diols (**169**) to α-hydroxy acids (**170**) using TEMPO (**5**), NaOCl and $NaClO_2$ system in biphasic (toluene/water) medium (Scheme 3.55).[71] This method suppresses the concomitant oxidative cleavage to carboxylic acids, which occurs during the oxidation. The use of a biphasic solvent system was found to be essential for successful reaction. Selectivity was derived from solubility control of

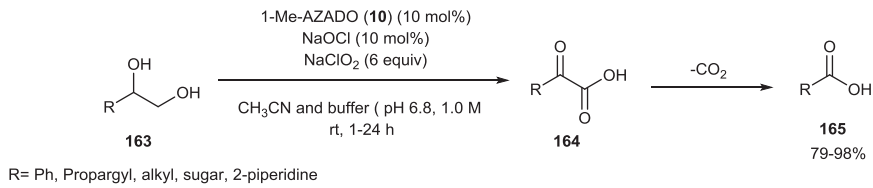

Scheme 3.53 1-Me-AZADO/NaOCl/$NaOCl_2$-mediated one-pot oxidative cleavage of terminal diols to carboxylic acids.

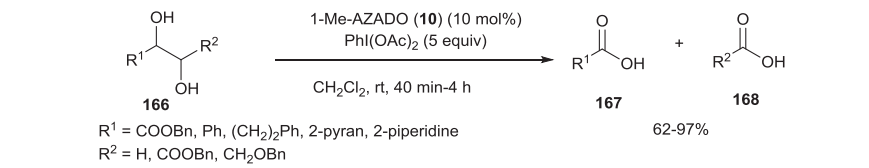

Scheme 3.54 1-Me-AZADO/$PhI(OAc)_2$-mediated one-pot oxidative cleavage of internal diols to carboxylic acids.

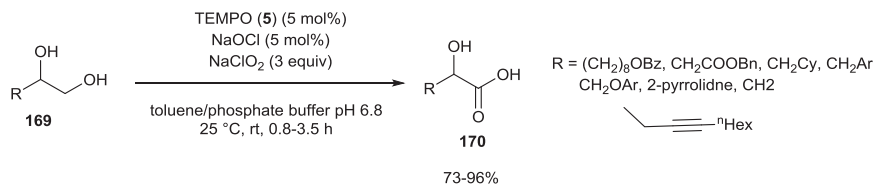

Scheme 3.55 TEMPO/NaOCl/$NaClO_2$-catalyzed chemoselective oxidation of 1,2-diols in biphasic solvent system.

diols and intermediates in toluene. Though *in situ* formed $TEMPO^{+}Cl^{-}$ is hydrophilic in nature, the active species dissolves in hydrophobic toluene, possibly due to a more toluene soluble charge transfer complex between TEMPO–ClO_2 under the reaction conditions, consequently inducing high levels of chemoselectivity. In addition, Shibuya and coworkers in their further work demonstrated the chemoselective aerobic oxidation of α-hydroxy carboxylic acids (**171**) to the corresponding α-keto carboxylic acids (**172**) using ABNO (**11**)/$NaNO_2$ mixture in acetonitrile at ambient temperature (Scheme 3.56).[72] As an extension to this work, Shibuya *et al.* developed an efficient three-step process to synthesize α-amino acids (**174**) from 1,2 diols (**173**).[73] The first two steps of the process involve chemoselective oxidations using nitroxide catalysis to obtain an α-ketoacid, which upon reaction with phenyl glycine (**175**) undergoes transamination to afford an α-amino acid. This method enables the protection-free synthesis of amino acids (Scheme 3.57).

The Landis and Stahl groups described a two-step strategy for the synthesis of α-chiral carboxylic acids *via* asymmetric hydroformylation followed by oxidation.[74] The first step involves rhodium-catalyzed asymmetric hydroformylation of terminal alkene **176** to obtain aldehyde **177**, which undergoes ketoABNO (**12**)/$NaNO_2$-catalyzed aerobic oxidation to the carboxylic acid **178** (Scheme 3.58). No racemization was observed during oxidation, and stereochemical integrity was observed of the *in situ* formed chiral aldehyde **177**.

Bobbitt and coworkers reported the use of 4-acetylamino-2,2,6,6-tetramethylpiperidine-1-oxoammonium tetrafluoroborate (**181**) in combination with pyridine as an oxidant for the oxidative dimerization of primary alcohols to esters.[75] Interestingly, alcohols bearing a β-oxygen gave predominantly esters, whereas alcohols without a β-oxygen produced aldehydes rather than esters. δ-Lactones can also be prepared by this method using

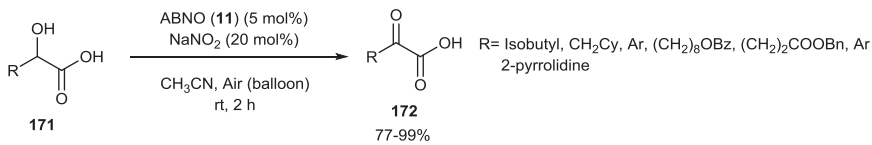

Scheme 3.56 ABNO/$NaNO_2$-catalyzed chemoselective aerobic oxidation of α-hydroxy carboxylic acids to α-keto carboxylic acids.

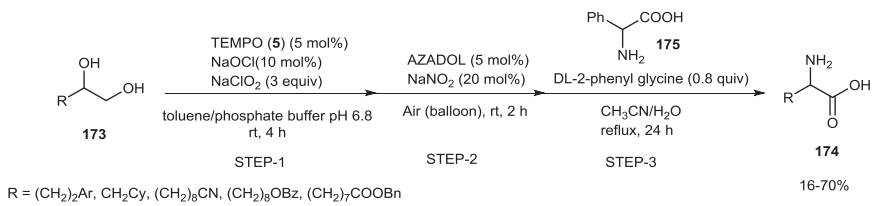

Scheme 3.57 Nitroxide-catalyzed three-step protocol to synthesize amino acids from diols.

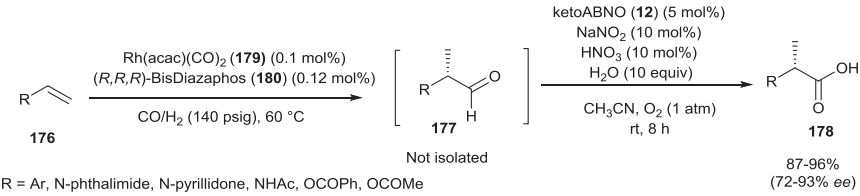

Scheme 3.58 KetoABNO/$NaNO_2$-catalyzed synthesis of α-chiral carboxylic acids from *in situ* generated α-chiral carbaldehydes.

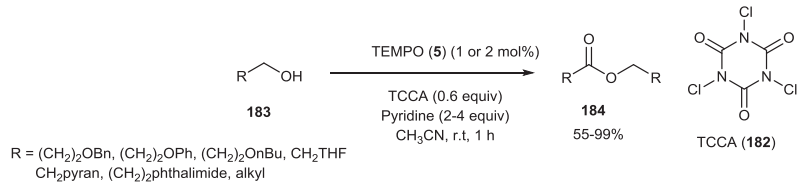

Scheme 3.59 TEMPO-catalyzed oxidative dimerization of alcohols.

diethyl glycol as alcoholic substrates. Although this method is compatible with various substrates and affords good yields, stoichiometric amounts (2.5 equiv.) of oxoammonium ion salt are required to be employed.

In 2012, Szpilman *et al.* described a catalytic method for the oxidative dimerization of alcohols using only 2 mol% of TEMPO (**5**) in combination with environmentally benign TCCA (**182**) as a secondary oxidant and pyridine as base.[76] Slow addition of the oxidant TCCA was found to be critical for esterification (over 1 h). This reaction presumably takes place *via* slow formation of aldehyde hemiacetals. This catalytic method was adaptable to a wide range of primary alcohols. Unlike Bobbitt *et al.*'s method this protocol is compatible with alcohols bearing no β-oxygen (Scheme 3.59). A similar method was developed by Lahiri *et al.* for the synthesis of both self- and cross-esterification of alcohols using TEMPO (**5**) as an oxidant.[77] TEMPO, in combination with oxone, was used for self-esterification of alcohols, whereas TEMPO in combination with iron salts was used for cross-esterification of alcohols.

Szpilman and coworkers also reported on the TEMPO-catalyzed direct oxidation of aldehydes **185** to mixed anhydrides **187** with pivalic acid (**186**).[78] The mixed anhydrides can be converted *in situ* into esters **188** and amides **189** (Scheme 3.60).

Iwabuchi and coworkers described the use of oxoammonium salts derived from TEMPO (**5**) for an efficient oxidative rearrangement of tertiary allylic alcohols **190** to β-substituted α,β-unsaturated carbonyl compounds **191**.[79a] In addition, it was found that oxoammonium salts with counter anions that are poor nucleophiles, such as BF_4^- or SbF_6^-, were crucial for an efficient reaction. Although this method proved to be superior to traditionally employed toxic chromium reagents, it requires stoichiometric amounts

Scheme 3.60 TEMPO-catalyzed direct oxidation of aldehydes to mixed anhydrides.

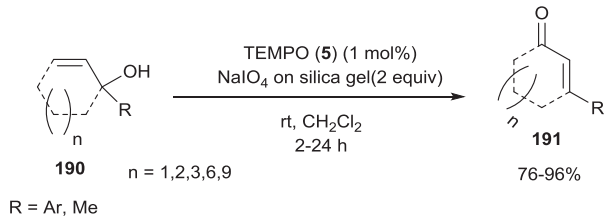

Scheme 3.61 TEMPO-catalyzed oxidative rearrangement of tertiary allylic alcohols.

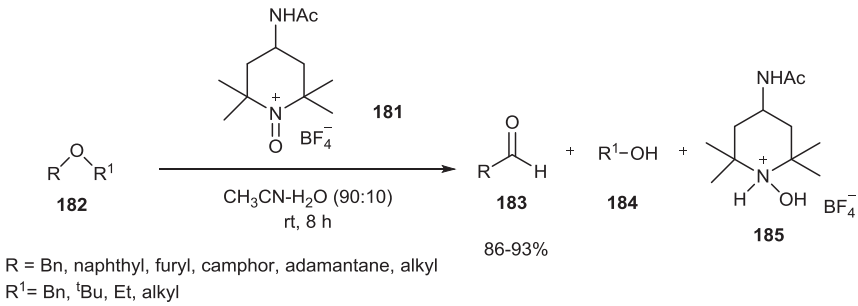

Scheme 3.62 Oxoammonium-mediated oxidative cleavage of benzylic and related ethers.

(1.5 equiv.) of oxoammonium salt. However, the same group developed a catalytic method for oxidative rearrangement of tertiary allylic alcohols using 1 mol% of TEMPO in combination with $NaIO_4$ (2 equiv.) on silica gel in dichloromethane at ambient temperature (Scheme 3.61).[79b]

In 2009, Bobbitt and Bailey described the use of 4-acetamido-2,2,6,6-tetramethylpiperidine-1-oxoammonium tetrafluoroborate (**181**) for the oxidative cleavage of benzylic and related ethers in wet acetonitrile at room temperature to afford the corresponding aldehydes and alcohols. The primary or secondary alcohol products formed in this reaction are further oxidized by **181** to give the respective carboxylic acids and ketones (Scheme 3.62).[80] For the overall process, three equivalents of oxoammonium salt **181** are required. Similarly, in 2015, Leadbeater *et al.* showcased the use of oxoammonium salt **181** for the oxidative cleavage of allyl ethers to the corresponding α,β-unsaturated carbonyl compounds.[81]

3.2.4 Nitroxides in Heterogeneous Catalysis

In 1985, a seminal report by Miyazawa and Endo demonstrated the use of polymer-bound nitroxide as a catalyst in combination with potassium ferricyanide for the oxidation of alcohols in acetonitrile–water biphasic solvent system.[82] Later, Miyazawa and Endo showed the use of Cu(II) salts with polymer nitroxide radical for the oxidation of benzyl alcohols.[83] Following this work, Osa and Bobbitt coworkers disclosed the electrocatalytic oxidation

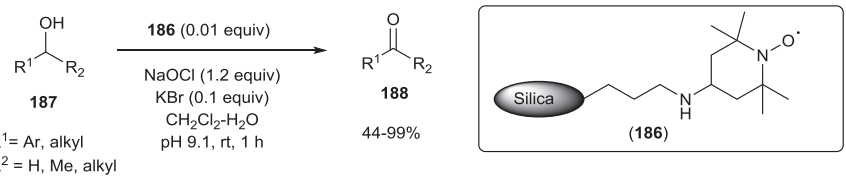

Scheme 3.63 Silica-supported TEMPO-catalyzed oxidation of alcohols.

of the monoterpene Nerol with a polymer-coated electrode using TEMPO as a heterogeneous redox catalyst.[84] In 1995, Tsubokawa *et al.* demonstrated the ability of TEMPO immobilized on ultrafine silica and ferrite surface to function as a catalyst in the presence of Cu(II) salts for the oxidation of primary and secondary alcohols to the corresponding carbonyl compounds.[85] In addition, oxidation of diols under these conditions gave the respective lactones. Moreover, TEMPO immobilized on silicagel can be recovered by simple centrifugation and reused. For example, in the case of benzyl alcohol oxidation, TEMPO–silicagel was recycled 45 times. In all the above cases, it was proposed that oxidation occurs *via* an oxoammonium cation.

Bolm and coworkers developed a recyclable silica-supported TEMPO (**186)** catalyst. Catalyst **186,** in which TEMPO is covalently connected, catalyzed the oxidation of alcohols under Anelli's conditions.[86] Under the developed conditions, primary and secondary alcohols were oxidized effectively over a period of one hour (Scheme 3.63). The catalyst was recovered by filtration and reused 10 times in the case of 1-nonol oxidation without significant loss of activity and yields. In addition, silica-supported TEMPOH also showed similar catalytic reactivity. The silica-supported TEMPO was prepared by reductive amination of 4-oxo TEMPO with commercially available amino propyl-functionalized silica. A similar protocol was developed by Brunel and coworkers, in which TEMPO was covalently immobilized onto mesoporous silica (MCM-41 type).[87] This system was found to be active and reusable in the oxidation of primary alcohols in combination with CuCl in DMF. Similarly, Pagliaro *et al.* developed another method for the oxidation of alcohols using sol–gel ormosils-doped TEMPO as a recyclable catalyst.[88]

Pozzi and coworkers demonstrated the use of poly(ethylene glycol)-supported TEMPO (PEG-TEMPO) (**189**) and sodium hypochlorite as a catalytic mixture for the oxidation of alkyl and aryl alcohols (Scheme 3.64).[89] Though the PEG-TEMPO was soluble in reaction medium, it can be easily recovered by precipitation from diethyl ether, followed by filtration. The recycled catalyst can be reused for oxidations at least six times with no loss of activity. During the same time period, Hayes and coworkers developed several PEG-supported nitroxides and applied them as catalysts using hypochlorite as a secondary oxidant.[90] These supported nitroxides exhibited better activities than TEMPO itself. However, the scope was limited to primary alcohols. Baucherel *et al.* also showed the use of polymer-supported TEMPO as an oxidation catalyst for alcohols, but using molecular oxygen as a terminal

Scheme 3.64 PEG-supported TEMPO-catalyzed oxidation of alcohols.

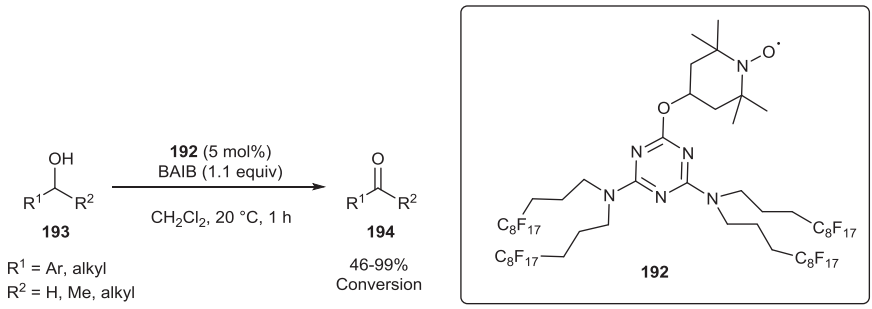

Scheme 3.65 Recyclable fluorous-tagged TEMPO-catalyzed oxidation of alcohols.

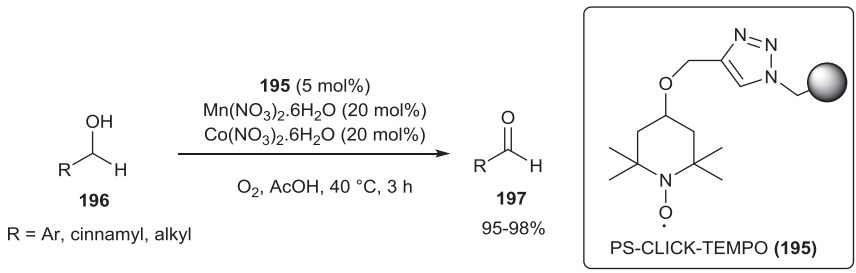

Scheme 3.66 PS-CLICK-TEMPO-catalyzed aerobic oxidation of alcohols.

oxidant in the presence of cobalt nitrate and manganese nitrate as co-catalysts.[91]

Pozzi and coworkers showed the preparation and usage of fluorous-tagged TEMPO radicals (**192**) as catalysts for the oxidation of primary and secondary alcohols (Scheme 3.65).[92] [Bis(acetoxy)iodo] benzene (BAIB) or bleach was used as the terminal oxidants. Though the catalyst was soluble in solvents such as dichloromethane and ethers and forms a homogeneous mixture, fluorous-tagged TEMPO radicals were easily isolated from the reaction products by liquid–liquid extraction with the fluorinated liquid perfluoro-(1,3-dimethyl)cyclohexane. The recovered catalyst was reused up to six times for the oxidation of 1-octanol using BAIB as the terminal oxidant with no significant loss of activity.

Reiser *et al.* developed a protocol to immobilize TEMPO onto a polystyrene resin using Cu(I) catalyzed alkyne–azide cycloaddition.[93] The resulting PS-CLICK-TEMPO (**195**) was used as an oxidation catalyst for aliphatic and aromatic primary and secondary alcohols using either bleach or molecular oxygen as the terminal oxidant. In the case of molecular oxygen as oxidant, a combination of cobalt and manganese nitrates was used as cocatalysts (Scheme 3.66). Moreover, catalyst can be recycled easily by filtration from the products. Reiser *et al.*, in further work, attached multiple triazole moieties and perfluoroalkyl chains to TEMPO, and the resulting TEMPO derivative was used as a catalyst for the oxidation of alcohols with bleach as the terminal oxidant.[94] The derived TEMPO derivative promotes emulsion

formation in dichloromethane/water, thus acting as a surfactant and accelerating the reaction. The supported TEMPO can be easily recovered by filtration of the reaction mixture through a sintered glass funnel.

In 2007, Karimi and coworkers, in their landmark report, showed the transition metal-free aerobic oxidation of alcohols catalyzed by mesoporous silica SBA-15-supported TEMPO (**198**) with air or molecular oxygen as the terminal oxidant.[95a] Reaction conditions were similar to the reaction conditions developed by Hu and coworkers.[58] However, this newly developed protocol requires a lower temperature compared to Hu's method. This method is applicable to alkyl, aryl and heteroaryl alcohols, including highly hindered hydroxy groups (Scheme 3.67). The catalyst can be recovered and recycled. For example, in the case of benzyl alcohol oxidation, catalyst was recovered and reused for 14 subsequent runs without loss of activity with a total turnover number of over 1000. This method is green, efficient and superior to previously developed heterogeneous methods. In 2014, Karimi *et al.* prepared SBA-15-functionalized less sterically hindered nitroxide ABNO (**11**) and used it as a recyclable aerobic oxidation catalyst for activated and unactivated alcohols under metal-free condition.[95b] Moreover, the catalyst was conveniently recovered and reused 14 times with a slight decrease in activity.

Reiser and coworkers demonstrated the preparation and use of recyclable magnetic carbon/cobalt nanoparticles-supported TEMPO (**201**) as an efficient catalyst for the oxidation of alcohols under modified Anelli's protocol (Scheme 3.68).[93b–d,96] TEMPO was grafted on to magnetic support using

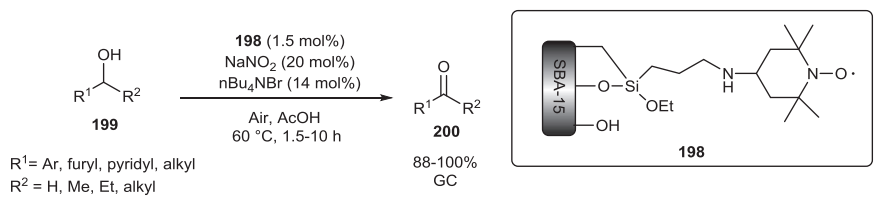

Scheme 3.67 SBA-15-supported TEMPO-catalyzed metal-free aerobic oxidation of alcohols.

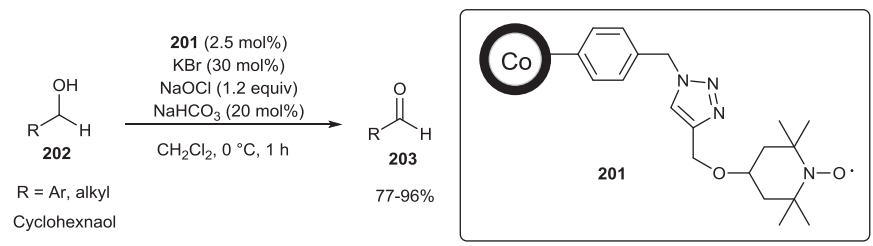

Scheme 3.68 Magnetically separable carbon/cobalt nanoparticle-supported TEMPO-catalyzed oxidation of alcohols.

azide–alkyne cycloaddition. Simple magnetic-assisted decantation is enough to separate the catalyst from the products, and it was shown to be recyclable six times with no loss of activity.

Garrell and Tucker-Schwartz demonstrated the immobilization of TEMPO on iron oxide (Fe_3O_4) superparamagnetic nanoparticles (SPN) and their use as a catalyst for the oxidation of aryl and alkyl alcohols using either bleach or molecular oxygen as the terminal oxidant (Scheme 3.69).[97] For the aerobic oxidation, manganese and cobalt nitrates were used as co-catalysts. In addition, 1,5- and 1,6-diols gave the respective lactones with bleach as oxidant. Immobilization of TEMPO was carried out by employing strong metal-oxide chelating phosphonates and azide/alkyne click chemistry.[93b-d] The catalyst was efficiently recovered from the reaction mixture using a hand-held magnet and recycled 20 times.

Karimi and Farhangi described the use of magnetic core shell nanoparticle-supported TEMPO (MNST) (**207**) as an efficient catalyst for transition metal and halide free aerobic oxidation of aryl and alkyl primary and secondary alcohols in water as the solvent (Scheme 3.70).[98] *tert*-Butyl nitrite was employed as a co-catalyst. In addition, this method is applicable to hindered alcohols. Moreover, the catalyst can be easily separated after the reaction and recycled. In addition, Karimi and Farhangi demonstrated the use of recyclable MNST (**207**) for a one-pot oxidative three-component Passerini reaction of primary and secondary alcohols (**210**) with carboxylic acids (**211**) and isocyanides (**212**) to afford the corresponding α-acyloxy carboxamides (**213**) under transition metal and halogen-free conditions (Scheme 3.71).[99] The catalyst was easily recovered using an external magnet

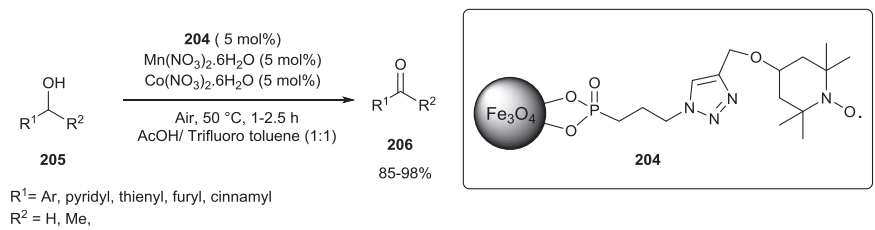

Scheme 3.69 TEMPO-coated superparamagnetic nanoparticle-catalyzed oxidation of alcohols.

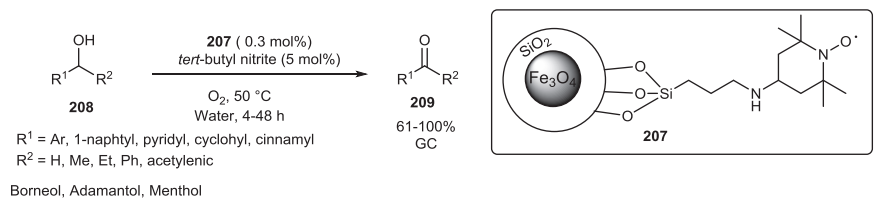

Scheme 3.70 Magnetic core shell nanoparticle-supported TEMPO-catalyzed aerobic oxidation of alcohols in water.

Scheme 3.71 One-pot oxidative three-component Passerini reaction of alcohols catalyzed by MNST catalyst under transition metal- and halogen-free conditions.

and reused for 14 subsequent runs, though there was a slight decrease in the activity. Furthermore, Karimi and coworkers reported the potential use of MNST (**207**) for the selective aerobic oxidation of 5-hydroxymethyl furan (**214**) to the high value-added chemical 2,5-diformyl furan (**215**) in an excellent yield (>99% by GC) under metal- and halide-free conditions (Scheme 3.72).[100] The catalyst was recycled and reused for five consecutive runs.

Gruttadauria and coworkers successfully employed [C60] fullerene as a platform to anchor TEMPO. The resulting nitroxide catalyst (**216**) was employed under Anelli's condition for the oxidation of aliphatic and aromatic primary and secondary alcohols (Scheme 3.73).[101] The catalyst was recycled at least for seven turns without loss of activity. However, EPR studies revealed that the number of radicals decreased during the catalytic cycles.

Chmielewski and Zwoliński reported the preparation of TEMPO-appended zirconium metal–organic frameworks (MOFs) with UiO-66 and UiO-67 (**219**) structures and demonstrated their use as catalysts for the aerobic oxidation

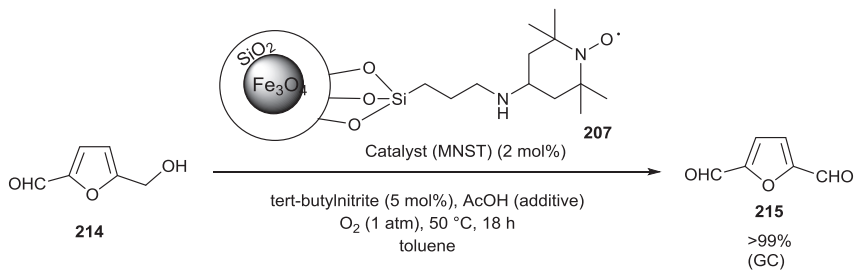

Scheme 3.72 MNST-catalyzed selective oxidation of 5-hydroxymethyl furfural to 5,5-diformylfuran.

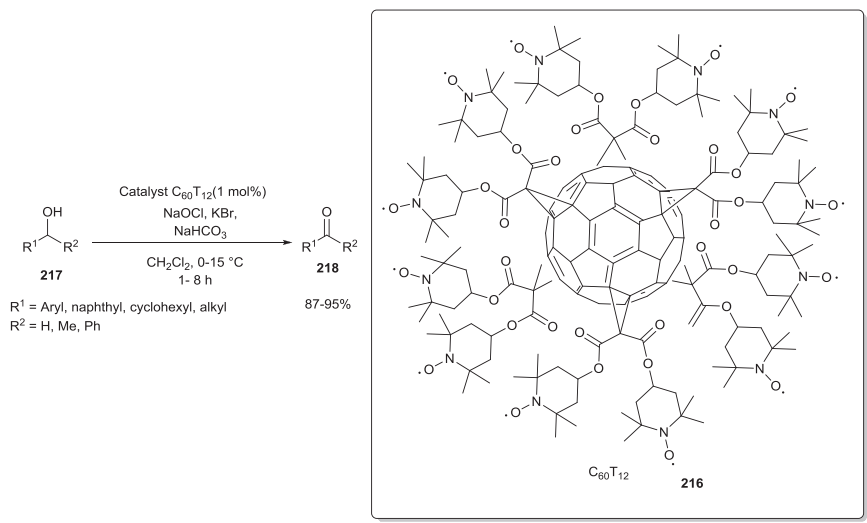

Scheme 3.73 Fullerene-supported TEMPO-catalyzed oxidation of alcohols.

of primary and secondary alcohols (Scheme 3.74).[102] This system is applicable to both primary and secondary alcohols. Moreover, the MOFs can be recycled.

Chen and coworkers demonstrated the direct incorporation of TEMPO onto conjugate microporous polymers (CMPs) (**222**) through four different linkages between TEMPO and carbazole moieties and used these CMPs as catalysts for the oxidation of various alcohols under aerobic conditions (Scheme 3.75).[103] Among the tested catalysts, one with an amide linkage (TEMPO–CMP – **222d**) exhibited the highest activity. Moreover, the

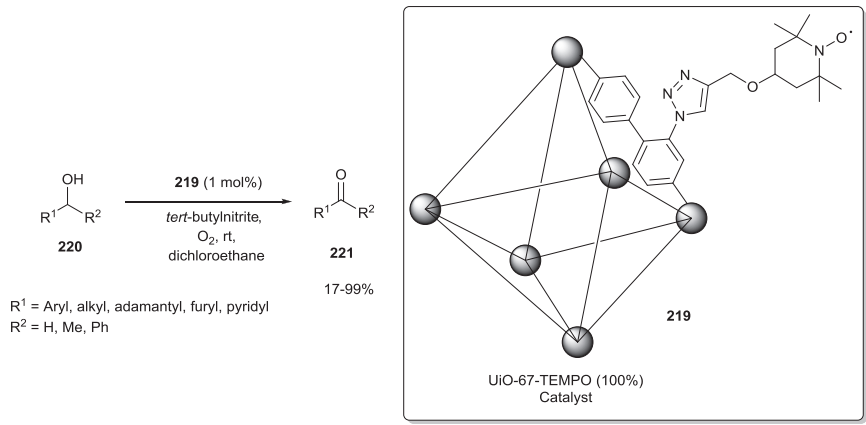

Scheme 3.74 TEMPO-appended zirconium MOFs-catalyzed aerobic oxidation of alcohols.

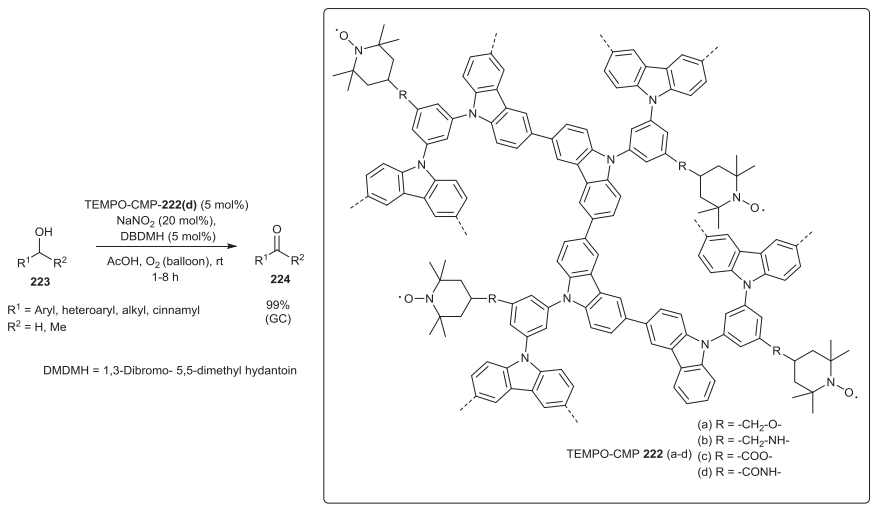

Scheme 3.75 TEMPO-appended conjugate microporous polycarbazole networks-catalyzed oxidation of alcohols.

conjugated microporous polycarbazole networks were easily recovered and reused at least 20 times with no loss of catalytic activity.

Fernandes *et al.* described a method to prepare silica-supported trifunctional heterogeneous TEMPO catalysts (**225**) for the oxidation of benzyl alcohols under aerobic conditions.[104] The trifunctional pyridine triazole (pyta)-Cu/TEMPO/NMI scaffolds linked to alkynes were immobilized on a single azide-functionalized mesoporous silica by Cu(I)-catalyzed alkyne–azide cycloaddition (Figure 3.8).[93b-d] The prepared trifunctional catalysts of different chain lengths were found to catalyze oxidation of benzyl alcohol with superior activity, compared to oxidations carried out by using the individual catalytic components (*i.e.* by homogeneous catalysis). Later, Fernandes and coworkers demonstrated the preparation of a silica-supported Cu/TEMPO/NMI catalytic triad system (**226**), where all the catalytic components were connected in sequence (Figure 3.9) and employed as a catalyst for benzyl alcohol oxidation.[105]

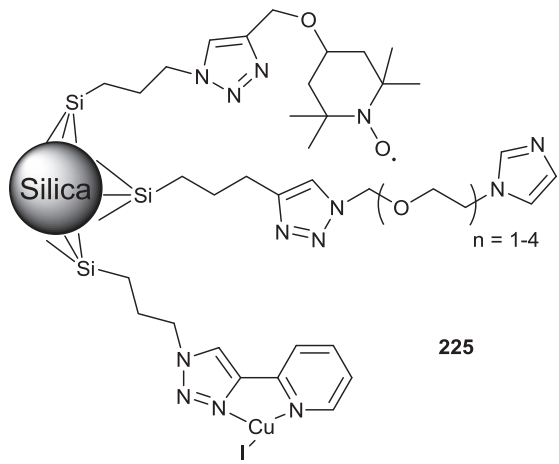

225

Figure 3.8 Silica-supported trifunctionalized catalyst.

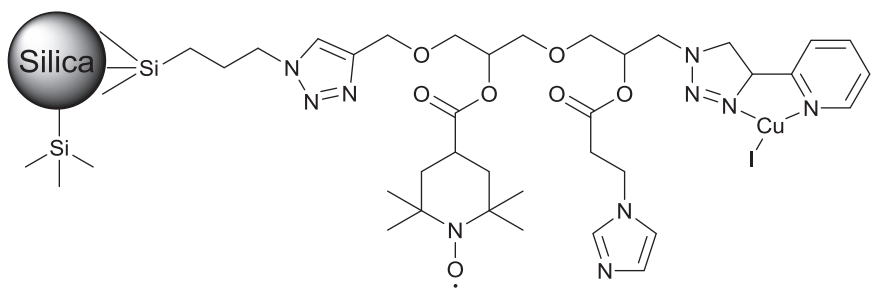

226

Figure 3.9 Recoverable silica-supported sequence-defined catalytic triad for the aerobic oxidation of alcohols.

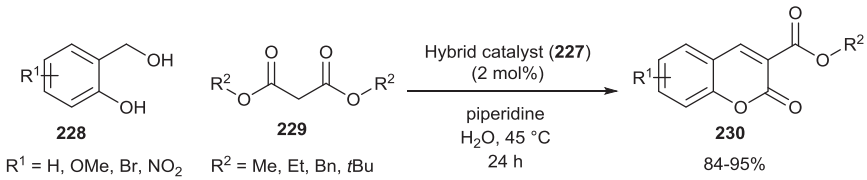

Scheme 3.76 Laccase and TEMPO-immobilized hybrid catalyst SBA-15-catalyzed one-pot synthesis of coumarin-3-carboxyates.

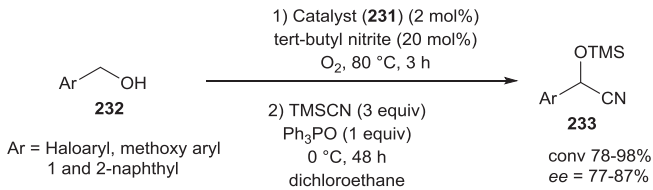

Scheme 3.77 Chiral porous MOF decorated with TEMPO-catalyzed sequential oxidation/asymmetric cyanation.

In 2018, Faramarzi and coworkers synthesized an efficient bifunctional hybrid catalyst (**227**) by co-immobilization of the enzyme laccase and TEMPO (**5**) on mesoporous silica SBA-15, for the one-pot synthesis of coumarins (**230**) using alcohols (**228**) and malonates (**229**) as precursors (Scheme 3.76).[106] Oxidation of alcohols to the corresponding carbonyl compounds is the key step, and the *in situ* formed aldehydes undergo Knoevenagel condensation with malonate to afford coumarin-3-carboxylate **230** derivatives. The catalyst was recovered and reused for 10 cycles with no significant loss of activity.

Cui and coworkers developed a sequential oxidation/asymmetric cyanation protocol using a chiral porous metal organic framework decorated with TEMPO radical (**231**). This one-pot two-step process involves initial oxidation of alcohols (**232**) to aldehydes. Addition of trimethyl cyanide and triphenyl phosphine oxide to the *in situ* prepared aldehyde affords the corresponding chiral products (**233**) in high yields (Scheme 3.77).[107] The chiral MOF was prepared by the reaction of TEMPO-substituted tricarboxylate (**234**) with enantiopure VO(salen) complex (**235**) bearing dipyridine ligands (Scheme 3.78). This heterogeneous method proved to be superior to its homogeneous counterpart.

3.3 Chiral Nitroxide-catalyzed Enantioselective Oxidations

Rychnovsky *et al.* described the first approach towards oxidative kinetic resolution of secondary alcohols using low catalyst loadings (1 mol%) of the BINOL-derived chiral nitroxide (**236**) radical under Anneli's conditions.[108] This system allowed the resolution of racemic benzylic secondary alcohols, but the *S*-values were only 6–7, even for the best substrates (Scheme 3.79).

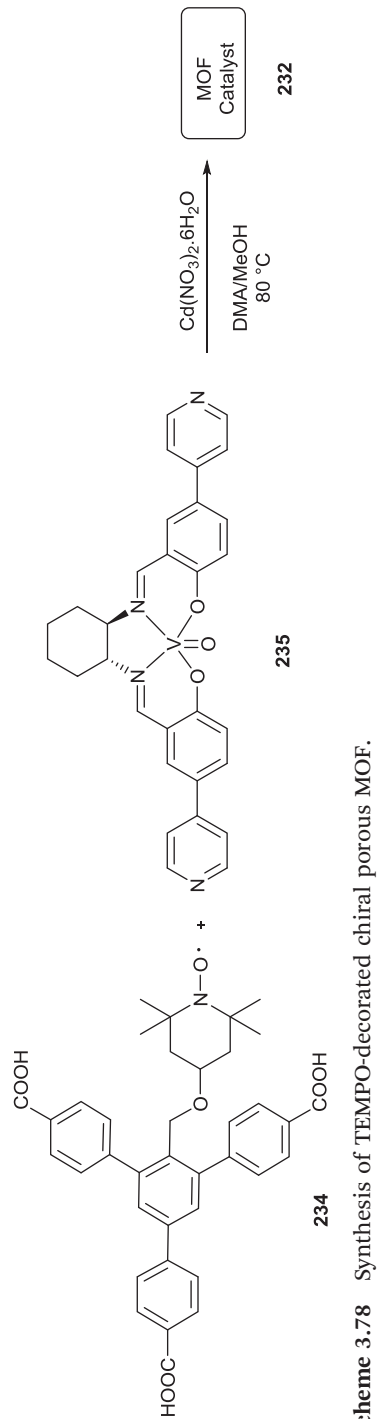

Scheme 3.78 Synthesis of TEMPO-decorated chiral porous MOF.

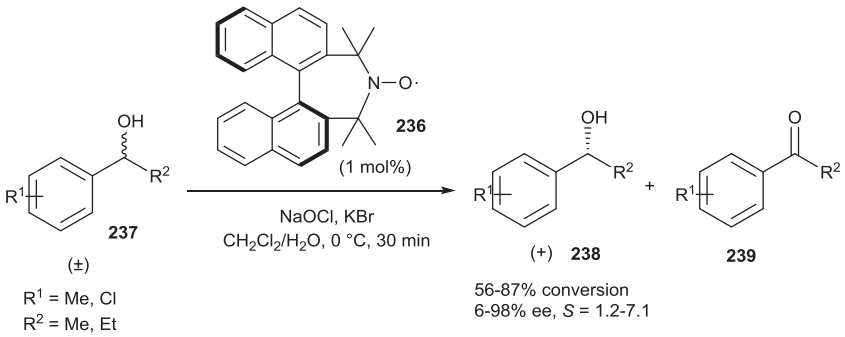

Scheme 3.79 BINOL-derived chiral nitroxide-catalyzed oxidative kinetic resolution (OKR) of alcohols.

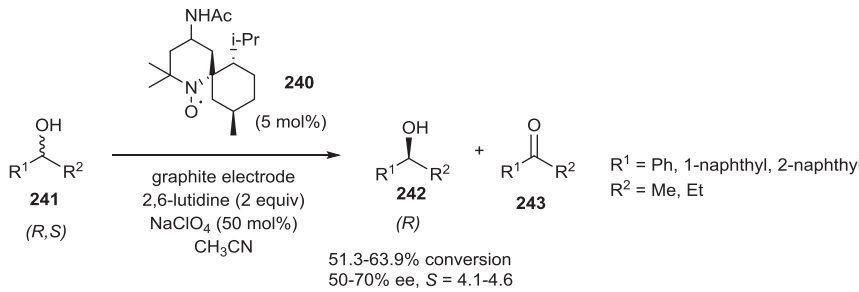

Scheme 3.80 Nitroxide-catalyzed OKR using electrolysis.

Bobbitt and coworkers reported the electrolytic enantioselective oxidation of racemic secondary alcohols using chiral 1-azaspiro[5.5]undecane-*N*-Oxyl (**240**) and a graphite electrode (Scheme 3.80).[109] This method showed modest selectivity for several substrates ($S = 4.1–4.6$). Similar electrolytic enantioselective oxidations using Rychnovsky's BINOL-derived chiral nitroxide (2**36**) was demonstrated by Tanaka *et al.* using platinum as an electrode.[110] This method displayed improved catalytic activity and selectivity.

Onomura *et al.* demonstrated the use of the proline-derived bicyclic chiral nitroxide (**244**) as a catalyst for the enantioselective electro-oxidation of racemic secondary alcohols to afford optically pure alcohols with moderate to high *S* values (up to 21) (Scheme 3.81).[111] Platinum was used as the electrode.

Kawabata *et al.* used the electronically tuned nitroxide radical (**248**) for the oxidative kinetic resolution of aryl alkyl carbinols.[112] This method is particularly effective for the resolution of *tert*-butyl aryl carbinols, and moderate to high selectivity was observed (Scheme 3.82).

In 2014, Iwabuchi *et al.* reported the use of chiral alkoxyamine (**252**) as a precatalyst for organocatalytic oxidative kinetic resolution of secondary alcohols to afford optically active secondary alcohols with high *S* value up to 296 (Scheme 3.83).[113] Catalytically reactive chlorine-containing

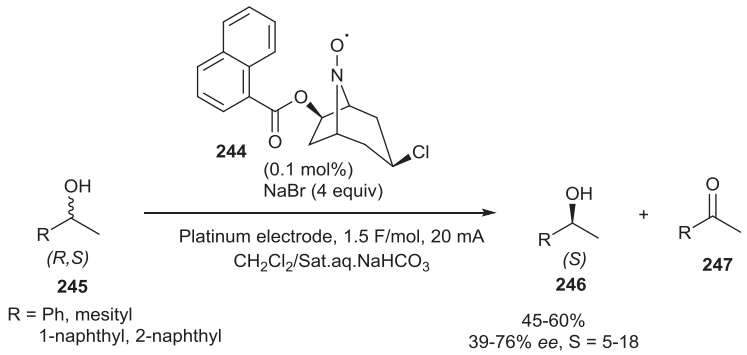

Scheme 3.81 Proline-derived chiral nitroxide-catalyzed resolution of alcohols.

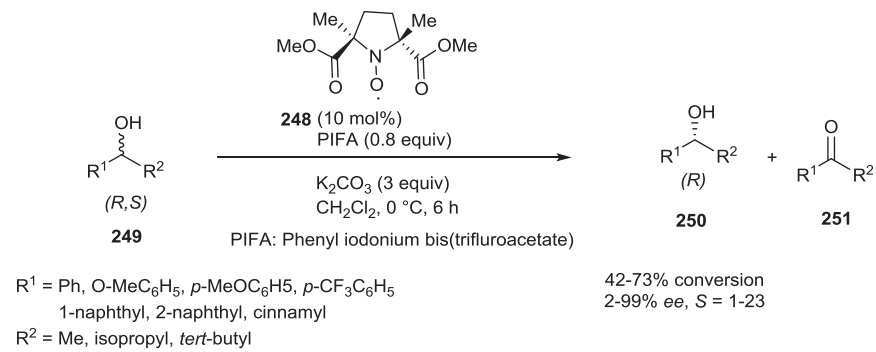

Scheme 3.82 Electronically tuned chiral nitroxide-catalyzed OKR.

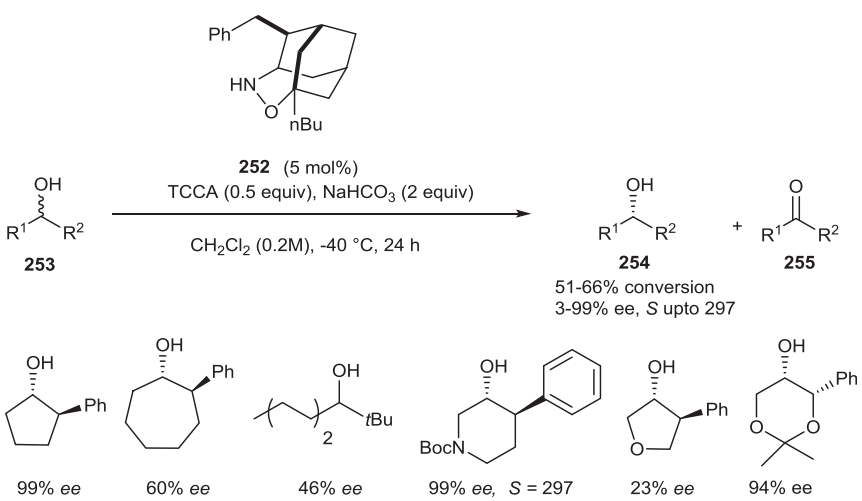

Scheme 3.83 *In situ* generated chiral oxoammonium ion-catalyzed kinetic resolution of alcohols.

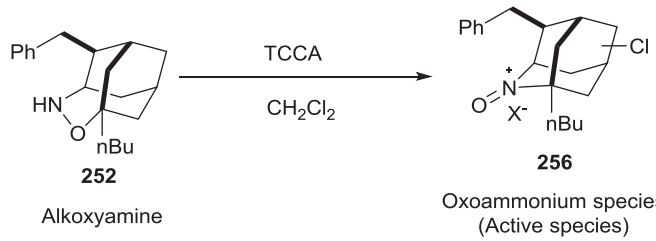

Scheme 3.84 *In situ* generation of chiral oxoammonium salts.

oxoammonium active species (**253**) were generated *in situ* by the reaction of alkoxyamine (**256**) with trichloroisocyanuric acid (TCCA) (Scheme 3.84). In mechanistic studies, it was revealed that the presence of a chlorine atom in the reactive species is crucial for high reactivity and enantioselectivity. Though the effect of the chlorine atom remains unclear, it is believed that the electron-withdrawing chlorine atom increases the electrophilicity of the oxoammonium ion, which in turn increases reaction rates. In addition, the presence of the relatively bulky chlorine atom affects the conformation of *n*-Bu group in the catalyst, which would enhance enantioselectivity. This method is applicable to various unactivated secondary alcohols, including heterocyclic alcohols with high enantioselectivity.

3.4 Nitroxide-catalyzed Oxidation of Amines

In 1983, Semmelhack and Schmid first reported the electrochemical oxidation of amines to nitriles using TEMPO (**5**) as a catalyst in anhydrous acetonitrile (Scheme 3.85).[114] Under the electrochemical conditions, TEMPO (**5**) was oxidized to its oxoammonium cation $TEMPO^+$ (**13**), which in turn oxidizes an amine to an intermediate imine while getting reduced to TEMPOH (**14**). The intermediate imine (**258**) undergoes further oxidative dehydrogenation with another molecule of $TEMPO^+$ (**13**) to yield a nitrile. The formed TEMPOH (**14**) reacts with $TEMPO^+$ (**13**) to generate two molecules of nitroxide radical (**5**), thus completing the catalytic cycle. A series of aromatic and aliphatic amines were oxidized to the corresponding nitriles in good yields. In aqueous reaction media, aldehydes were formed predominantly over nitriles, due to hydrolysis of *in situ* formed imines (**258**). A similar protocol was developed by Walton and coworkers, using poly(TEMPO–acrylate) as an electrocatalyst.[115] In addition, in 1998, Kashiwagi, Osa and coworkers reported the use of TEMPO-modified graphite felt electrode for the selective oxidation of amines to nitriles.[116]

In 2003, Chen *et al.* demonstrated the use of TEMPO (**5**) as a catalyst in combination with TCCA as a secondary oxidant, for the oxidation of primary amines to the corresponding nitriles in dichloromethane (Scheme 3.86).[117] This efficient method is compatible with various amines bearing hydroxy, C–C double bond and dimethyl amino groups. Benzylic amines were oxidized faster and afforded better yields than their aliphatic counterparts.

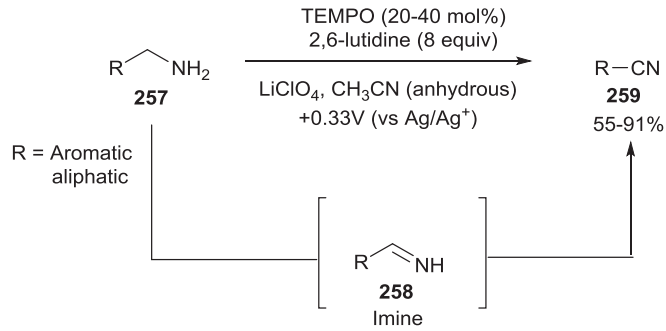

Scheme 3.85 Electrochemical oxidation of amines using TEMPO, by Semmelhack.

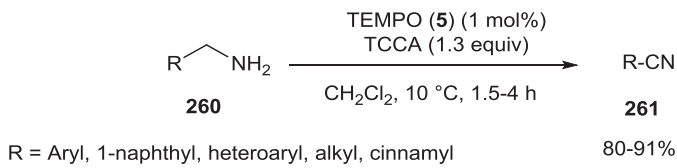

Scheme 3.86 TEMPO/TCCA-catalyzed oxidation of amine to nitriles.

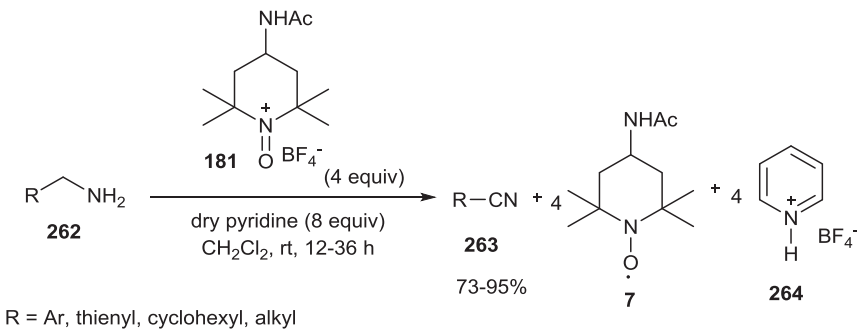

Scheme 3.87 $TEMPO^{+}BF_4^{-}$-catalyzed oxidation of amine to nitriles.

In 2014, Bailey *et al.* described the use of commercially available 4-acetamido-$TEMPO^{+}BF_4^{-}$ salt (**181**) as a stoichiometric oxidant for the oxidation of primary amines to the respective nitriles at room temperature in dichloromethane–pyridine solvent system (Scheme 3.87).[118a] Importantly, slow addition of diluted amines to the reaction mixture was found to be essential to circumvent formation of undesired by-products. This reaction was compatible with aliphatic and aromatic amines. Superstoichiometric amounts (4 equiv.) of oxidant were required for successful oxidation. However, the spent oxidant, TEMPOH, can be recycled and recovered using bleach to regenerate the oxoammonium salt. Furthermore, computational investigations revealed that α-hydride transfer from amine to oxygen of

oxoammonium ion is the rate-determining step. Later, in 2016, Bailey *et al.* developed a catalytic method by using oxone as the terminal oxidant in combination with catalytic amounts of pyridine hydrobromide salt.[118b]

Leadbeater and coworkers described the oxoammonium salt (**181**) mediated synthesis of nitriles (**266**) from aldehydes (**265**). Hexamethyldisilazane (HMDS) was employed as the ammonia source. According to the proposed mechanism, aldehydes react with HMDS to afford silyl-imine (**267**), which undergoes oxidation with 4-NHAc-TEMPO$^{+}BF_4^{-}$ to yield desired nitrile and 4-NHAc-TEMPOH (Scheme 3.88).[119] This method is compatible with numerous aldehyde substrates. Though stoichiometric amounts of oxoammonium salt (2.5 equiv.) were required, the spent oxidant was recycled. A contemporary, but catalytic method for the synthesis of nitriles from aldehydes using 4-acetamido-TEMPO (**7**) (5 mol%) under aerobic conditions was developed by Kim and Noh.[120] Sodium nitrite (10 mol%) and nitric acid (20 mol%) were employed as co-catalysts. Importantly, readily available ammonium acetate was used as the ammonia source. Moreover, alcohols were employed as coupling partners rather than aldehydes to prepare nitriles.

In 2016, Moriyama *et al.* demonstrated the TEMPO (**5**) catalyzed oxidative coupling of amides bearing EWGs (**268**, Scheme 3.89) with silylated nucleophiles (**273**) through activation of amides by *N*-halogenation.[121] According to the proposed mechanism, benzyl amines with EWG (**268**) (*i.e.* sulfonamides or phosphinamides) reacts with *tert*-BuOCl and KBr to form *N*-chloro substituted amides (**269**). Subsequently, TEMPO-catalyzed dissociation of a chlorine atom from the amide affords amidyl radical (**270**) intermediate together with oxoammonium chloride (**271**). Oxoammonium salt **271** oxidizes the amidyl radical (**270**) to the corresponding EWG-protected aldimine (**272**) with simultaneous regeneration of TEMPO (**5**), thus, completing the catalytic cycle. In the second stage of the reaction, the *in situ* formed aldimine (**271**) reacts with the silylated nucleophile in the presence of lithium perchlorate to produce the desired α-substituted amides (**274**) (Scheme 3.89). This method was proven to be efficient for aryl, heteroaryl and alkyl sulfonamides and for a few examples of phosphinamides. In addition, TMSCN, $TMSCF_3$, allylTMS and TMS enolates were employed as silylated nucleophiles to obtain the corresponding α-substituted amides.

Kerton and Hu described the use of TEMPO (**5**) in combination with $CuBr_2$ for the aerobic oxidation of benzylamines (**275**) to the corresponding *N*-benzylidene–benzylamines (277) at ambient temperature (Scheme 3.90).[122] The proposed mechanism states that one equivalent of benzylamine undergoes oxidative dehydrogenation under catalytic conditions to produce aldimine (**276**), which upon transamination with another molecule of benzyl amine leads to the imine **277**. This method was tolerant of a variety of substituents, and thus applicable to various substituted benzylidene benzylamines (**277**). In addition, this catalytic system was also used for oxidative cross-coupling of benzylamines with anilines. Under the catalytic conditions, electron-rich anilines in the absence of benzylamine partners

Scheme 3.88 Oxoammonium salt-mediated direct access to nitriles from aldehydes and its possible mechanism.

Scheme 3.89 TEMPO-catalyzed oxidative coupling of amines bearing EWG with silylated nucleophiles.

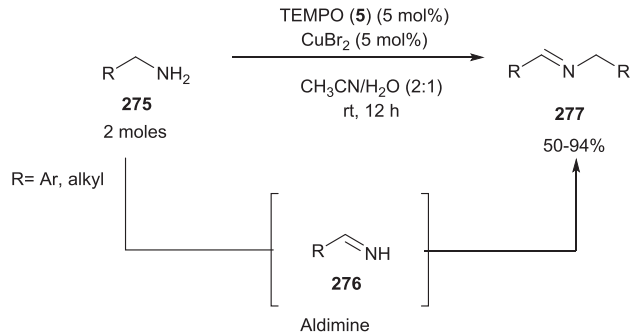

Scheme 3.90 TEMPO/$CuBr_2$-catalyzed oxidative coupling of benzylamines.

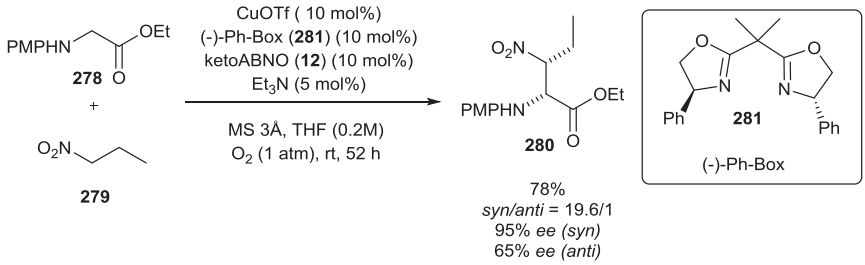

Scheme 3.91 KetoABNO/Cu/(−)-Ph-Box system catalyzed asymmetric cross dehydrogenative coupling.

produced the corresponding azo compounds. Similarly, Kanai *et al.* reported a catalytic system comprised of sterically unencumbered keto ABNO (**12**) and Cu(I) salt for the oxidation amines, particularly secondary amines, to yield the corresponding imines using molecular oxygen as the terminal oxidant.[123] 6,6′-Di-*tert*-butyl-2,2′-bipyridine was employed as the ligand. This efficient protocol was compatible with different secondary benzyl amines. The method was further extended to direct α-derivatization of secondary amines *via* tandem oxidation followed by C–C bond formation. As an example, the asymmetric cross dehydrogenative coupling between glycine ester (**278**) and nitroalkane (**279**) was described (Scheme 3.91).

In 2013, Stahl and Kim developed an efficient method for the aerobic oxidation of amines to nitriles using a catalytic system comprised of (4,4′-*tert*-Bu_2bpy) CuI/ABNO (**11**) and DMAP as a base in acetonitrile at ambient temperature (Scheme 3.92).[124] Interestingly, the use of 4,4′-di-*tert*-butyl-2,2′-bipyridyl as ligand, rather than the traditional bipyridine, suppressed the formation of undesired self-coupled imine. This efficient method was compatible with a broad range of aliphatic, allyl and benzylamines bearing different functionalities and afforded predominantly the nitrile. In addition, preliminary mechanistic studies suggested that oxidation of copper by oxygen is the rate-limiting step of the reaction. In 2017, Ma and coworkers

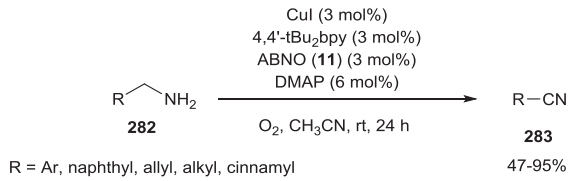

Scheme 3.92 CuI/ABNO-catalyzed oxidation of amines to nitriles.

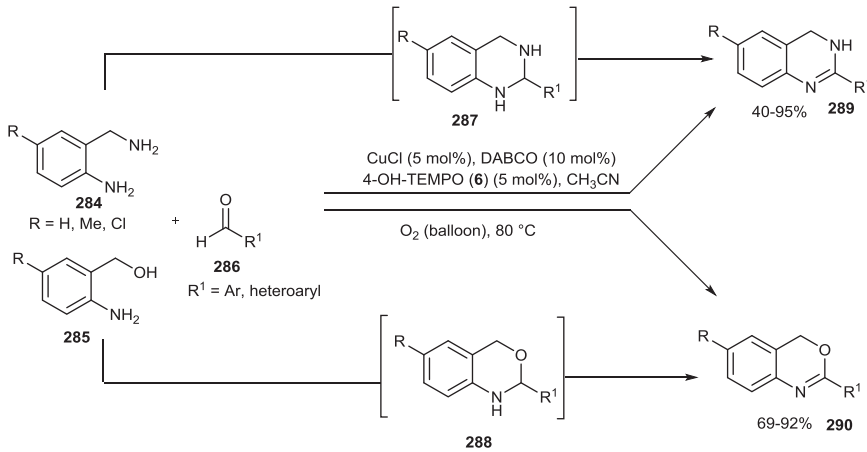

Scheme 3.93 Cu/TEMPO-catalyzed oxidative synthesis of quinazolines and benzoxazines.

developed a similar method using CuCl/TEMPO and *N,N*-dimethylethane-1,2-diamine as a ligand in toluene at 80 °C using air as the oxidant for the conversion of various amines to the corresponding nitriles.[125]

Han *et al.* reported the use of DABCO–CuCl/4-OHTEMPO (**6**) catalytic system for the one-pot synthesis of quinazolines and 4*H*-3,1-benzoxazine heterocycles using oxygen as a terminal oxidant in acetonitrile (Scheme 3.93).[126] 2-Aminobezylamines (**284**) or 2-aminobezylalcohols (**285**) were used as starting materials, which upon condensation with aldehydes (**286**) produced tetrahydroquinazolines (**287**) or tetrahydrobezoxazines (**288**). Subsequent aerobic oxidation with nitroxide **6** afforded the desired products. A similar method was developed by Shen and coworkers, using ABNO (**11**) and KOH as a base in toluene at 80 °C.[127]

3.5 Nitroxide-mediated Sulfide Oxidation

In 1994, Skarzewski and Siedlecka reported the TEMPO (**5**) catalyzed chemo- and diastereoselective oxidation of 1,2- and 1,3-bis(phenylthiol)alkanes and *ortho* bis(phenylthiomethyl)benzene to the corresponding meso disulfoxides

with 90–98% diastereoselectivity under Anelli's biphasic conditions.[128a] Later, in 1996, this elegant method was applied to transform homochiral *N*-protected β-amino sulfides (**291**) to the corresponding chiral sulfoxides (**292**) (Scheme 3.94).[128b] The presence of a stereogenic center induces diastereoselective oxidation and produced diastereomeric sulfoxides in high yield (up to 88% ee). Overoxidation to sulfones was not observed.

In 2005, Punniyamurthy and coworkers reported the use of TEMPO (**5**) in combination with Cu(II)–salan type complex **294** for the selective oxidation of sulfides to sulfoxides. Hydrogen peroxide at 30% was used as a terminal oxidant (Scheme 3.95).[129] Importantly, the Cu(II)–salan complex could be recycled without loss of activity. In 2010, a similar method was described by Reiser *et al.* using TEMPO (**5**) in combination with manganese and cobalt nitrates with molecular oxygen as an oxidant. In addition, recyclable perfluoro alkylated TEMPO derivatives were also shown to mediate sulfide oxidations.[130] In 2018, Wang and coworkers reported TEMPO (**5**) together with $Cu(OAc)_2$ for the aerobic oxidation of sulfides to sulfoxides using pyridine as ligand.[131]

Wang *et al.* described the efficient oxidation of sulfides to sulfoxides with TEMPO-linked metalloporphyrins (**297**) using bleach as a terminal oxidant (Scheme 3.96).[132] Among the prepared iron and manganese porphyrin complexes, the manganese complexes showed better activity and selectivity. Importantly, glycosyl sulfides were selectively oxidized to sulfoxides. These metalloporphyrins were also effective catalysts for the alcohol oxidations.

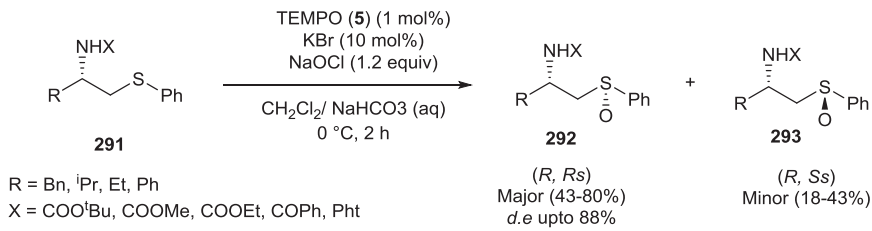

Scheme 3.94 TEMPO-catalyzed oxidation of homochiral sulfides to sulfoxides.

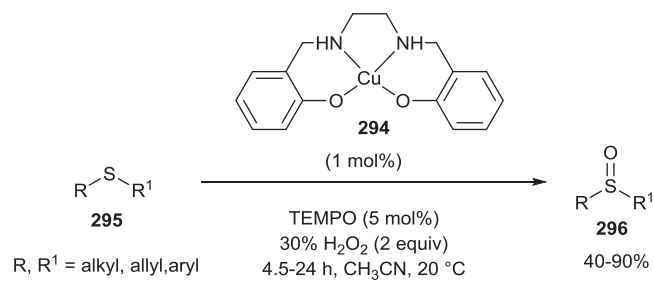

Scheme 3.95 TEMPO/Cu–salan complex catalyzed aerobic oxidation of sulfides.

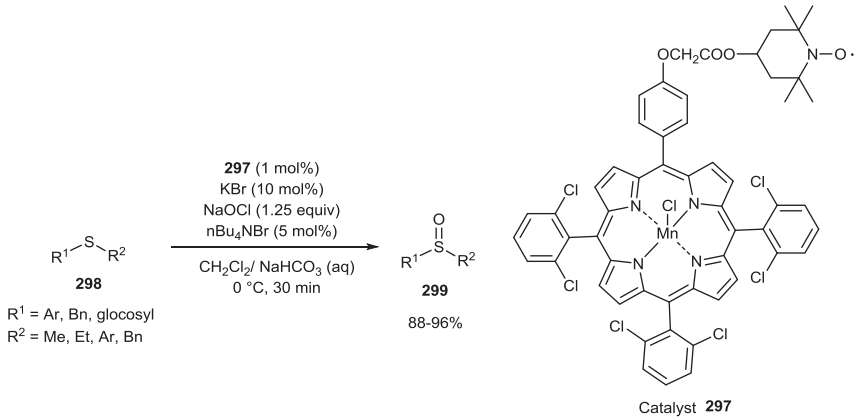

Scheme 3.96 TEMPO-appended manganese porphyrin-catalyzed oxidation of sulfides.

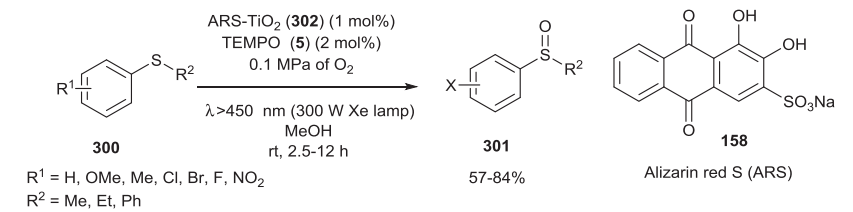

Scheme 3.97 Visible light photoredox catalyst/TEMPO-catalyzed oxidation of sulfides.

Chen *et al.* reported the use of TEMPO (**5**) coupled with a visible light photoredox catalyst for the aerobic oxidation of sulfides to sulfoxides (Scheme 3.97).[133] An organic dye **158** (alizarin red S) anchored to TiO_2 was used as photoredox catalyst (*i.e.* ARS–TiO_2, **302**). Importantly, the use of TEMPO not only enhances the oxidation of sulfides, but also ensures the stability of the ARS–TiO_2 catalyst. A quite similar method was reported by Lang *et al.*, in which the effect of different solvents and efficiency of various TEMPO derivatives were described.[134]

3.6 Nitroxide-mediated C–C Bond Formation Reactions

In 1992, Bobbitt and Ma used stoichiometric amounts of oxoammonium salt $TEMPO^+$ BF_4^- (**181**) for the oxidative coupling of phenols to dihydroxy phenols.[135] In 1993, Osa *et al.* described the electrocatalytic oxidation of naphthols and naphthol ethers to the corresponding binaphthyls using a TEMPO-modified graphite electrode.[136] $TEMPO^+$ was postulated to be generated by electro-oxidation. In 2008, Studer *et al.* reported the use of TEMPO as a stoichiometric oxidant for the homocoupling of aryl, alkenyl and alkynyl Grignard reagents to the corresponding dimers in THF at reflux condition

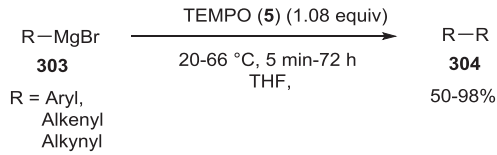

Scheme 3.98 TEMPO-mediated oxidative coupling of aryl, alkenyl and alkynyl Grignard reagents.

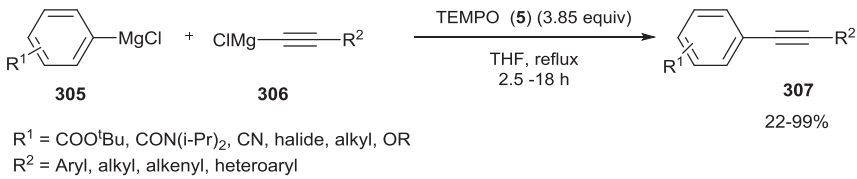

Scheme 3.99 TEMPO-mediated Sonogashira type cross-coupling between aryl and alkynyl Grignard reagents.

(Scheme 3.98).[137] This transition metal-free method was applicable to a wide range of substrates and produced high yields of products. Homocoupling of alkynyl Grignard reagents required longer reaction times in comparison to the alkenyl and aryl counterparts. TEMPO–MgBr was found to be a by-product of the reaction which could be reoxidized to TEMPO with dioxygen in refluxing THF. This crucial observation led to the development of the catalytic method, where 15 mol% of TEMPO in combination with molecular oxygen as the terminal oxidant was used for coupling. Later, this elegant protocol was applied to synthesize conjugate polymers from bis-organomagnesium compounds.[138]

In 2010, Studer and coworkers described a Sonogashira type cross-coupling between *ortho*-substituted aryl and alkynyl Grignard reagents using TEMPO (**5**) as an oxidant (Scheme 3.99).[139] This efficient metal-free protocol was compatible with different functional groups and produced high yields of cross-coupled products. Importantly, installation of *ortho* substituents on aryl Grignard reagents was found to be necessary to suppress homocoupling. Though superstoichiometric amounts of TEMPO (**5**) (3.85 equiv.) were required, the spent oxidant could be easily recycled by purging with oxygen. In 2011, Studer and Murarka demonstrated the TEMPO (**5**) mediated oxidative cross-coupling of nitrones with alkynyl Grignard reagents using molecular oxygen as the terminal oxidant (Scheme 3.100).[140] In addition, the resulting products were transformed to isoxazoles.

Jiao and coworkers reported the construction of C–C bonds between 9,10-dihydroacridine (**311**) and nucleophiles with activated methyl or methylene groups using TEMPO in combination with molecular oxygen as an oxidant (Scheme 3.101).[141] This method was compatible with different nucleophiles, such as nitromethane, malonic ester and malononitrile. Though a clear mechanism was not established, it was assumed that benzyl cations of acridine were involved as reaction intermediates.

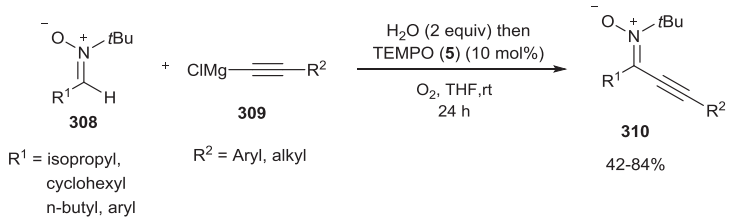

Scheme 3.100 TEMPO-catalyzed oxidative coupling of nitrones with alkynyl-Grignard reagents.

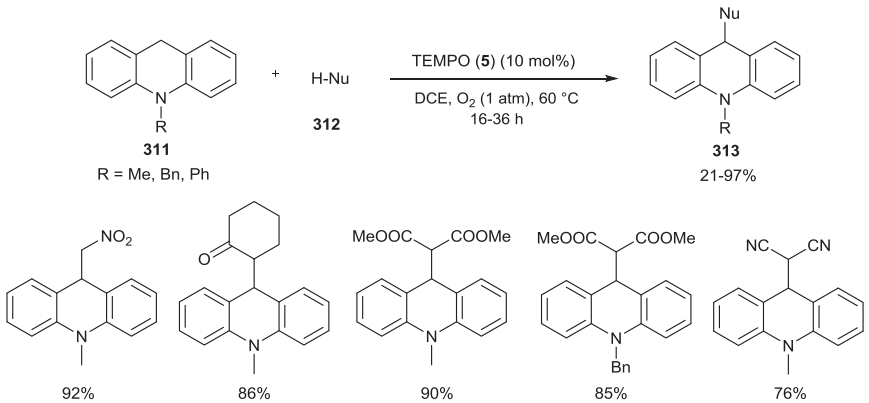

Scheme 3.101 TEMPO-catalyzed oxidative C–C bond formation.

Han and coworkers reported the TEMPO (**5**) mediated aza-Diels–Alder reaction of *in situ* generated azoalkenes (**316**) with olefins to afford tetrahydropyridazines (**317**) (Scheme 3.102).[142] This tandem reaction involves initial formation of azoalkene from ketohydrazones (**314**) *via* hydrazonyl radical, subsequent reaction with an olefin leads to the desired product. This method was compatible with aryl and alkyl ketohydrazones and olefins.

Studer and Vogler reported the use of TEMPO (**5**) as a stoichiometric oxidant in *ortho* directing group mediated C–H arylation of arenes with arylboronic acids catalyzed by rhodium catalyst (Scheme 3.103).[143] 2-Pyridyl and imine functional groups were used as directing groups. According to the proposed mechanism, the main role of TEMPO (**5**) is to oxidize the $L_2Rh(I)Ar$ complex, which is formed during transmetallation with arylboronic acid, to form a $(TEMPO)_2L_2Rh(III)Ar(III)$ complex. The resulting Rh(III) complex undergoes ligand exchange with an arene bearing an *ortho* directing group. Subsequent C–H arylation followed by reductive elimination leads to the desired product. Four equivalents of TEMPO were necessary for the successful reaction. This method is applicable to synthesize different bi-aryl compounds. Later, Studer and Vogler, reported on the Wilkinson's catalyst, catalyzed oxidative homo coupling of aryl and alkenyl boronic acids, where TEMPO (**5**) (4 equiv.) was employed as a stoichiometric oxidant.[144]

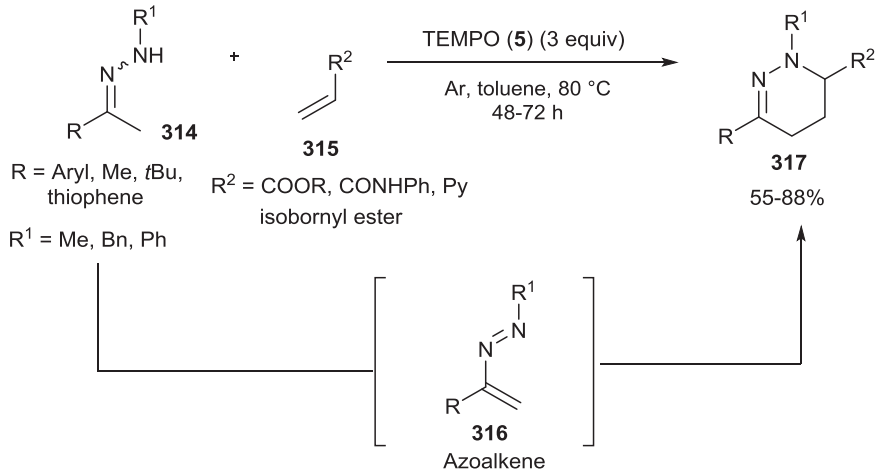

Scheme 3.102 TEMPO-mediated aza-Diels–Alder reaction.

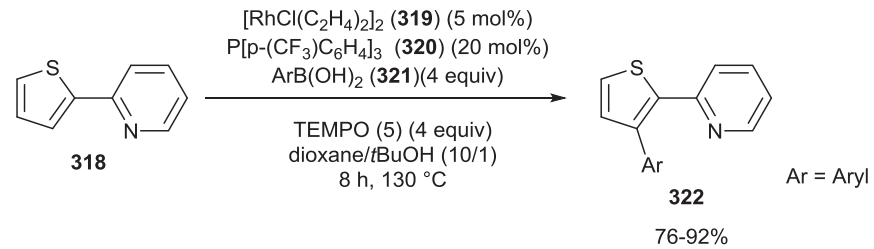

Scheme 3.103 TEMPO as a stoichiometric oxidant for [Rh] catalyzed arylation.

Furthermore, Itami and coworkers demonstrated the palladium-catalyzed oxidative aryl–aryl coupling of thiophenes and thiazoles with employment of TEMPO (**5**) (4 equiv.) as the stoichiometric oxidant.[145] Moreover, in 2012, Studer *et al.* reported a nitroxide (2 equiv.) mediated palladium-catalyzed oxidative Heck arylation for the stereoselective synthesis of tetrasubstituted triarylated alkenes. This elegant method was extended to synthesize *Z*-tamoxifen.[146] In 2014, Forgione *et al.* described the palladium-catalyzed homo coupling of aryl sulfinates to the corresponding bis aryl compounds by using only catalytic amounts of TEMPO (10 mol%) in combination with $CuCl_2 - 2H_2O$ and molecular oxygen as an oxidant.[147]

Studer and coworkers described the palladium-catalyzed arylation and carboaminoxylation of indoles with arylboronic acids using TEMPO (**5**) as an external oxidant.[148] Interestingly, simple indole and *N*-methyl indole afforded 2-aryl substituted indoles (**326**), but installation of protecting groups such as benzoyl, acetyl and Boc groups on the indole nitrogen led to carboaminoxylation (**327**) with high distereoselectivity (*trans*) (Scheme 3.104). In this case TEMPO (**5**) played a dual role as an oxidant to oxidize Pd(0) to Pd(II) and as reagent to trap reactive intermediate formed during the reaction.

Scheme 3.104 Arylation and carboaminoxylation of indoles using TEMPO as the stoichiometric oxidant.

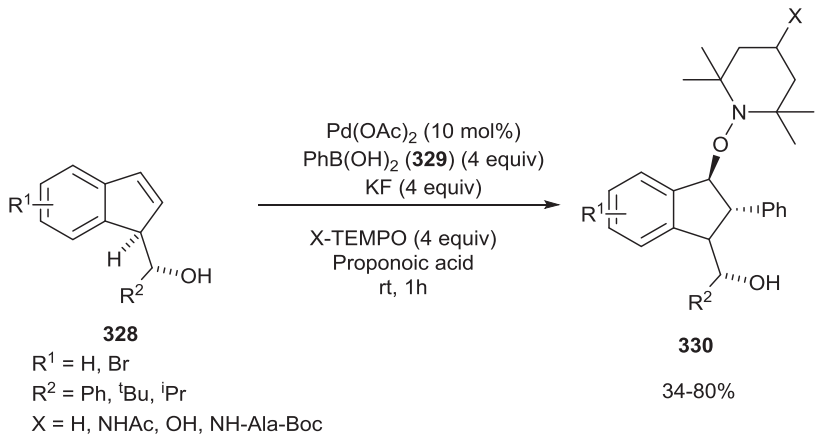

Scheme 3.105 Carboaminoxylation of indenes using TEMPO as the stoichiometric oxidant.

Later, Studer *et al.* extended this protocol for 3-substituted indenes (**328**) to synthesize 1,2,3-substituted indanes (**330**) with high diastereoselectivities (Scheme 3.105).[149]

3.7 Miscellaneous Reactions Mediated by Nitroxides

In 2007, Tanka *et al.* reported the electrochemical oxidative Wacker-type reaction to transform terminal olefins to the corresponding carbonyl compounds using $Pd(OAc)_2$ and TEMPO (**5**) (Scheme 3.106).[150] Though there was no evidence, it was assumed that TEMPO oxidizes Pd(0) to Pd(II) during the reaction process. In the absence of TEMPO, only a trace amount of ketone was formed.

In 2013, Maiti and coworkers disclosed an efficient method for the stereoselective nitration of mono- and di-substituted olefins using silver nitrite as the NO_2 source and TEMPO (**5**) as an oxidant (Scheme 3.107).[151] According to the proposed mechanism, addition of nitro radical to olefin (**333**) generates a carbon-centered radical intermediate (**334**), which upon oxidation with TEMPO (**5**) affords nitro olefin (**335**) with retained stereochemistry. Later, the same group reported a metal-free approach for the synthesis of nitro olefins using *tert*-butyl nitrite (*tert*-BuONO) and TEMPO as an oxidant.[152] Furthermore, this elegant protocol was extended to decarboxylative nitration of α,β-unsaturated carboxylic acids to synthesize nitro olefins using TEMPO as an oxidant.[153]

Wang *et al.* described the synthesis of (*E*)-alkenylphosphonates from olefins using silver nitrate and substoichiometric amount of TEMPO (**5**) (Scheme 3.108).[154] No reaction occurred in the absence of TEMPO. Radical clock experiments revealed that the reaction proceeds *via* a radical pathway.

Jiao and Wang demonstrated a TEMPO (**5**) catalyzed C=C double bond cleavage of cycloalkenes to produce oxo nitriles using TMS azide as the

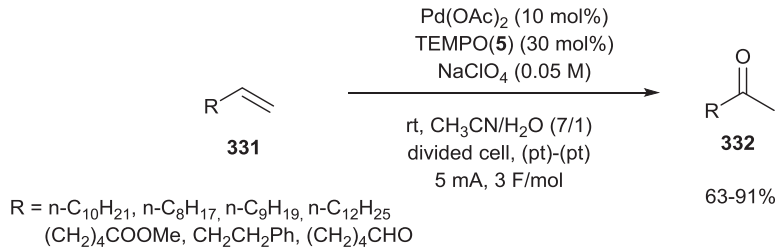

Scheme 3.106 $Pd(OAc)_2$/TEMPO-catalyzed Wacker-type oxidation.

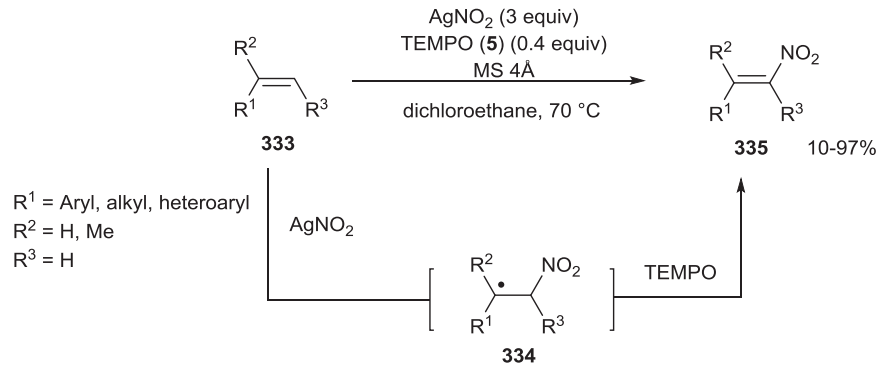

Scheme 3.107 $AgNO_2$/TEMPO-mediated nitration of olefins.

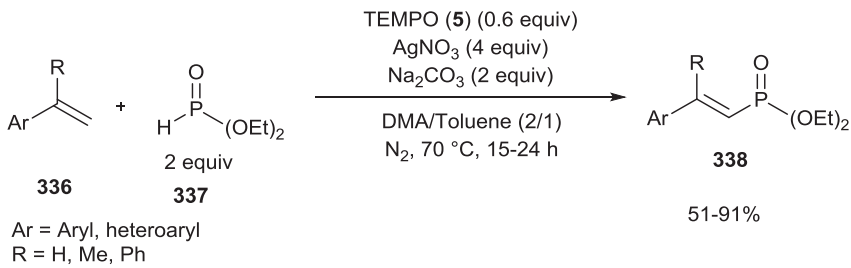

Scheme 3.108 $AgNO_3$/TEMPO-mediated phosphorylation of olefins.

nitrogen source and TEMPO as an oxidant under aerobic conditions (Scheme 3.109).[155] In addition, terminal olefins led to the analog ketones.

Iwabuchi *et al.* demonstrated the direct transformation of cycloalkenes to cycloalkadienes using a stoichiometric amount of oxoammonium salt derived from AZADO (**8**) derivatives (Scheme 3.110).[156] Oxoammonium salts of TEMPO (**5**) derivatives showed almost no reactivity, which is presumably due to its more hindered reactive center. Among the AZADO derivatives tested, 5-fluoro and 4-chloro oxoammonium ions were found to be the best. According to the proposed mechanism, cycloalkene undergoes ene like reaction with 4-Cl-AZADO$^+$ (**342**) to produce *N*-hydroxy ammonium species

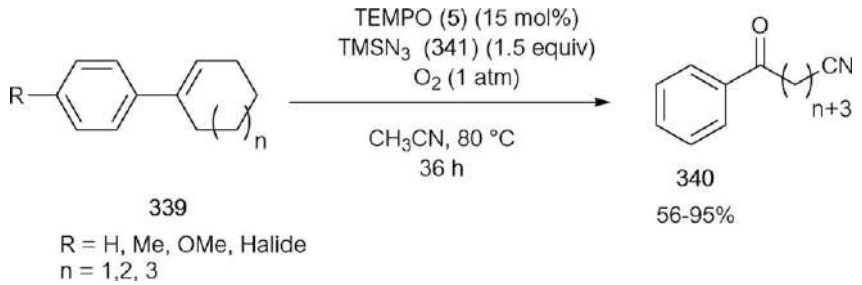

Scheme 3.109 TEMPO catalyzed C=C double bond cleavage to afford oxo nitriles.

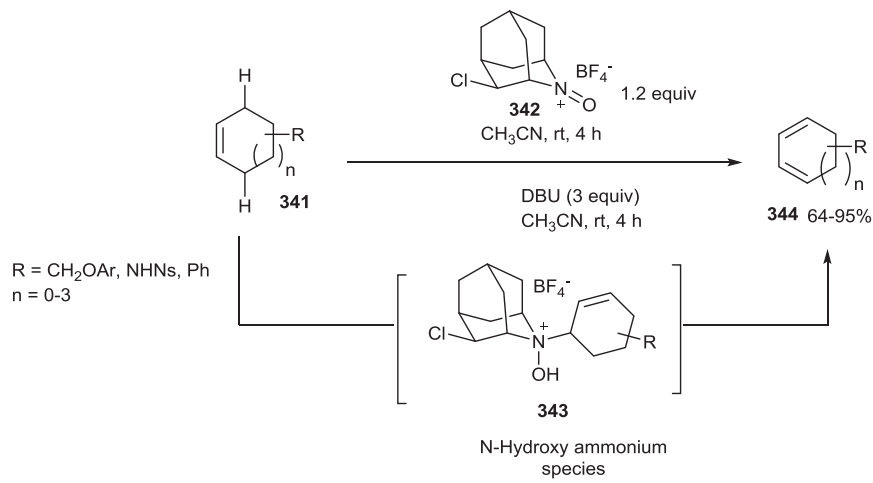

Scheme 3.110 4-Cl-AZADO$^+$ BF_4^--mediated conversion of cycloalkenes to cycloalkadienes.

(**343**), which upon reaction with a base (DBU) affords cycloalkadienes *via* Cope elimination.

Wang and coworkers reported the use of recoverable TEMPO-derived sulfonic salt (**347**) for the aerobic oxidation of benzylic sp^3 C–H bonds (Scheme 3.111).[157] Sodium nitrite and HCl were employed as co-catalysts. This metal-free protocol was applied to synthesize isochromanones and xanthanones from readily accessible alkyl and aromatic precursors.

Yuan *et al.* described the TEMPO-catalyzed oxidative coupling of 2-mecaptobenzothiazoles (**348**) with amines (S–N bond formation) to yield the corresponding sulfonamides (**350**) using molecular oxygen as the terminal oxidant (Scheme 3.112).[158] TEMPO (**5**) is expected to abstract a proton from thiol to afford a thienyl radical, which undergoes further coupling with amines. Unfortunately, this coupling worked only for mercaptobenzothiazoles with various amines. In the case of simple thiols, like phenyl thiols, disulfides were obtained as the products.

Scheme 3.111 Aerobic oxidation of benzylic sp^3 C–H bonds using recoverable TEMPO-derived sulfonate.

Scheme 3.112 TEMPO-catalyzed oxidative coupling of 2-mercaptobenzothiazole with amines.

Knowles *et al.*, in the process of preparing optically pure pyrroloindolines, demonstrated the preparation of alkoxyamine-substituted pyrroloindolines using TEMPO (**5**) as an alkoxyamine precursor with high enantioselectivity *via* proton-coupled electron transfer (PCET) (Scheme 3.113).[159] Treating tryptamine (**351**) and TEMPO (**5**) with an excited state redox catalyst in the presence of chiral phosphoric acid (**355**) leads to alkoxyamine substituted pyrroloindolines (**353**). This process occurs *via* the *in situ* generated radical cation bounded to chiral phosphate base (**352**) thorough H-bonding. In this overall protocol, TEMPO played a dual role. Firstly as a reactant to intercept radical cations and secondly as an oxidant to oxidize the reduced redox catalyst. Importantly, the resulting pyrroloindolines upon single-electron oxidation afforded transient carbocations, which can be trapped by various nucleophiles. Xia and co-workers also reported similar findings with TEMPO.[160]

Lin *et al.* reported the TEMPO–N_3 charge transfer complex (**358**) mediated electrochemical azidooxygenation of olefins (Scheme 3.114).[161] This unique protocol enabled the preparation of vicinal difunctionalized compounds

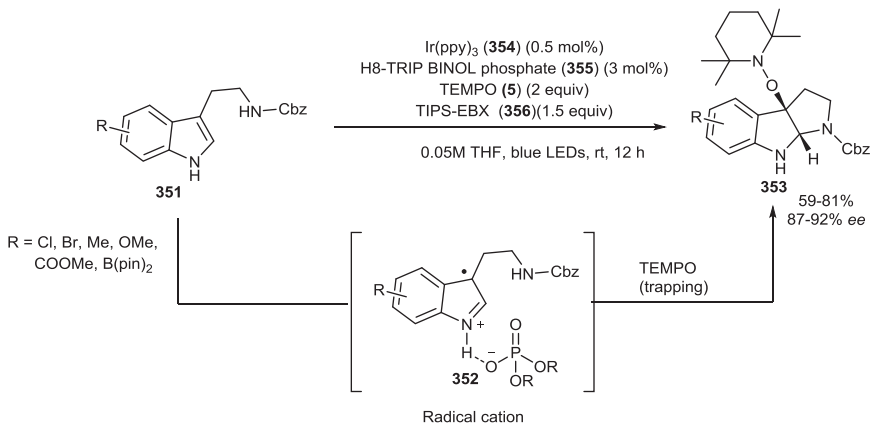

Scheme 3.113 Synthesis of alkoxyamine-substituted enantiopure pyrroloindolines using TEMPO as the alkoxyamine precursor and an oxidant.

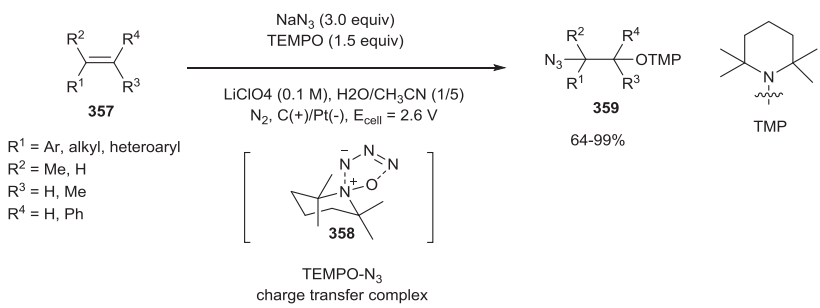

Scheme 3.114 Electrochemical azidooxygenation of alkenes *via* TEMPO–N_3 charge transfer complex.

from alkenes. Mechanistically, the electrochemically generated $TEMPO^+$ presumably promotes the formation of azidyl radical *via* TEMPO–N_3 charge transfer. The resulting azidyl radical initiates the addition of radicals across olefins.

3.8 Conclusion

The use of nitroxides in synthetic chemistry has evolved greatly since the advent of TEMPO. The use of nitroxides as oxidants and catalysts for a diverse range of transformations ranging from alcohol oxidations to C–C bond reactions in both homogeneous and heterogeneous media are proof of their impact and staying power as tools for organic synthesis. The ready availability, stability and unique reaction profile and redox properties have brought nitroxides a special place in the world of chemistry. Undoubtedly, future research in this field will open more exciting avenues for their chemistry.

References

1. (a) E. Fremy, *Ann. Chim. Phys.*, 1845, **15**, 408; (b) O. Piloty and B. G. Schwerin, *Ber. Dtsch. Chem. Ges.*, 1901, **34**, 1870; (c) H. Wieland and M. Offenbächer, *Ber. Dtsch. Chem. Ges.*, 1914, **47**, 2011.
2. O. L. Lebedev and S. N. Kazarnovsky, *Tr. Khim. Khim. Tekhnol.*, 1959, **3**, 649.
3. For books: (a) L. B. Volodarsky, V. A. Reznikov and V. I. Ovcharenko, *Synthetic Chemistry of Stable Nitroxides*, CRC press, 1993; (b) G. I. Likhtenshtein, J. Yamauchi, S. Nakatsuji, A. I. Smirnov and R. Tamura, *Nitroxides: Applications in Chemistry, Biomedicine, and Materials Science*, Wiley-VCH, Weinheim, 2008.
4. For selected reviews on application of nitroxides in synthesis and polymer: (a) R. A. Sheldon and I. W. C. E. Arends, *Adv. Synth. Catal.*, 2004, **346**, 1051; (b) T. Vogler and A. Studer, *Synthesis*, 2008, 1979; (c) L. Tebben and A. Studer, *Angew. Chem., Int. Ed.*, 2011, **50**, 5034; (d) S. Wertz and A. Studer, *Green Chem.*, 2013, **15**, 3116; (e) B. L. Ryland and S. S. Stahl, *Angew. Chem., Int. Ed.*, 2014, **53**, 8824; (f) H. A. Beejapur, Q. Zhang, K. Hu, L. Zhu, J. Wang and Z. Ye, *ACS Catal.*, 2019, **9**, 2777.
5. M. A. Iron and A. M. Szpilman, *Chem. – Eur. J.*, 2017, **23**, 1368.
6. W. F. Bailey, J. M. Bobbitt and K. B. Wiberg, *J. Org. Chem.*, 2007, **72**, 4504.
7. Z. Ma and J. Bobbitt, *J. Org. Chem.*, 1991, **56**, 6110.
8. M. F. Semmelhack, C. R. Schmid, D. A. Cortés and C. S. Chou, *J. Am. Chem. Soc.*, 1984, **106**, 3374.
9. M. F. Semmelhack and C. R. Schmid, *J. Am. Chem. Soc.*, 1983, **105**, 6732.
10. (a) A. Dijksman, I. W. C. E. Arends and R. A. Sheldon, *J. Chem. Soc., Chem. Commun.*, 1999, 1591; (b) A. Dijksman, A. M. González, A. M. i Payeras, I. W. C. E. Arends and R. A. Sheldon, *J. Am. Chem. Soc.*, 2001, **123**, 6826.

11. A. Cecchetto, F. Fontana, F. Minisci and F. Recupero, *Tetrahedron Lett.*, 2001, **42**, 6651.
12. (a) P. Gamez, I. W. C. E. Arends, J. Reedijk and R. A. Sheldon, *Chem. Commun.*, 2003, 2414; (b) P. Gamez, I. W. C. E. Arends, R. A. Sheldon and J. Reedijk, *Adv. Synth. Catal.*, 2004, **346**, 805.
13. N. Jiang and A. J. Ragauskas, *J. Org. Chem.*, 2006, **71**, 7087.
14. S. Mannam, S. K. Alamsetti and G. Sekar, *Adv. Synth. Catal.*, 2007, **349**, 2253.
15. E. T. T. Kumpulainen and A. M. P. Koskinen, *Chem. – Eur. J.*, 2009, **15**, 10901.
16. P. J. Figiel, A. Sibaouih, J. U. Ahmad, M. Nieger, M. T. Räisänen, M. Leskelä and T. Repo, *Adv. Synth. Catal.*, 2009, **351**, 2625.
17. (a) J. M. Hoover and S. S. Stahl, *J. Am. Chem. Soc.*, 2011, **133**, 16901; (b) J. M. Hoover, J. E. Steves and S. S. Stahl, *Nat. Protoc.*, 2012, **7**, 1161.
18. J. E. Steves and S. S. Stahl, *J. Am. Chem. Soc.*, 2013, **135**, 15742.
19. X. Xie and S. S. Stahl, *J. Am. Chem. Soc.*, 2015, **137**, 3767.
20. S. L. Zultanski, J. Zhao and S. S. Stahl, *J. Am. Chem. Soc.*, 2016, **138**, 6416.
21. P. E. Piszel, A. Vasilopoulos and S. S. Stahl, *Angew. Chem., Int. Ed.*, 2019, **58**, 12211.
22. (a) J. M. Hoover, B. L. Ryland and S. S. Stahl, *J. Am. Chem. Soc.*, 2013, **135**, 2357; (b) J. M. Hoover, B. L. Ryland and S. S. Stahl, *ACS Catal.*, 2013, **3**, 2599.
23. B. L. Ryland, S. D. McCann, T. C. Brunold and S. S. Stahl, *J. Am. Chem. Soc.*, 2014, **136**, 12166.
24. (a) C. Michel, P. Belanzoni, P. Gamez, J. Reedijk and E. J. Baerends, *Inorg. Chem.*, 2009, **48**, 11909; (b) P. Belanzoni, C. Michel and E. J. Baerends, *Inorg. Chem.*, 2011, **50**, 11896.
25. X. Liu, Q. Xia, Y. Zhang, W. Chen and C. Chen, *J. Org. Chem.*, 2013, **78**, 8531.
26. G. Zhang, X. Han, Y. Luan, Y. Wang, X. Wen and C. Ding, *Chem. Commun.*, 2013, **49**, 7908.
27. (a) M. Amar, S. Bar, M. A. Iron, H. Toledo, B. Tumanskii, L. J. W. Shimon, M. Botoshansky, N. Fridman and A. M. Szpilman, *Nat. Commun.*, 2015, **6**, 6070; (b) H. Toledo, M. Amar, S. Bar, M. A. Iron, N. Fridman, B. Tumanskii, L. J. W. Shimon, M. Botoshansky and A. M. Szpilman, *Org. Biomol. Chem.*, 2015, **13**, 10726.
28. S. Bar, J. N. Kuamr, M. Amar, H. Toledo, R. J. Batrice and A. M. Szpilman, *ChemCatChem*, 2015, **7**, 1129.
29. H. Toledo, B. Tumanski, D. Sabirov, A. Kaushansky, N. Fridman and A. M. Szpilman, *Org. Biomol. Chem.*, 2019, **17**, 7900.
30. K. J. Pratap and G. Maayan, *Chem. Commun.*, 2015, **51**, 11096.
31. D. C. Mohan, A. Sadhukha and G. Maayan, *J. Catal.*, 2017, **355**, 139.
32. L. Wang, S. Shang, G. Li, L. Ren, Y. Lv and S. Gao, *J. Org. Chem.*, 2016, **81**, 2189.
33. Y. Sasano, S. Nagasawa, M. Yamazaki, M. Shibuya, J. Park and Y. Iwabuchi, *Angew. Chem., Int. Ed.*, 2014, **53**, 3236.

34. Y. Sasano, N. Kogure, S. Nagasawa, K. Kasabata and Y. Iwabuchi, *Org. Lett.*, 2018, **20**, 6104.
35. A. D. Rodrguez, I. Lavandera, S. K. Aksu, R. A. Sheldon, V. Gotar and V. G. Fernandez, *Adv. Synth. Catal.*, 2012, **354**, 3405.
36. H. Tian, X. Yu, Q. Li, J. Wang and Q. Xu, *Adv. Synth. Catal.*, 2012, **354**, 2671.
37. W. Yin, C. Wang and Y. Huang, *Org. Lett.*, 2013, **15**, 1850.
38. L. M. Dornan, Q. Cao, J. C. A. Flanagan, J. J. Crawford, M. J. Cook and M. J. Muldoon, *Chem. Commun.*, 2013, **49**, 6030.
39. C. Tao, F. Liu, Y. Zhu, W. Liu and Z. Cao, *Org. Biomol. Chem.*, 2013, **11**, 3349.
40. S. U. Dighe, D. Chowdhury and S. Batra, *Adv. Synth. Catal.*, 2014, **356**, 3892.
41. K. Kataoka, K. Wachi, X. Jin, K. Suzuki, Y. Sasano, Y. Iwabuchi, J. ya Hasegawa, N. Mizuno and K. Yamaguchi, *Chem. Sci.*, 2018, **9**, 4756.
42. D. Könning, W. Hiller and M. Christmann, *Org. Lett.*, 2012, **14**, 5258.
43. D. Könning, T. Olbrisch, F. D. Sypaseuth, C. C. Tzschucke and M. Christmann, *Chem. Commun.*, 2014, **50**, 5014.
44. J. Swatschek, L. Grothues, J. O. Bauer, C. Strohmann and M. Christmann, *J. Org. Chem.*, 2014, **79**, 976.
45. X. H. Ho, H. J. Oh and H. Y. Jang, *Eur. J. Org. Chem.*, 2012, 5655.
46. J. H. Kim, E. J. Park, H. J. Lee, X. H. Ho, H. S. Yoon, P. Kim, H. Yun and H. Y. Jang, *Eur. J. Org. Chem.*, 2013, 4337.
47. Z. Cui and D. M. Du, *Org. Lett.*, 2016, **18**, 5616.
48. J. C. A. Flanagan, L. M. Dornan, M. G. McLaughlin, N. G. McCreanor, M. J. Cook and M. J. Muldoon, *Green Chem.*, 2012, **14**, 1281.
49. Z. Chen, J. Chen, M. Liu, J. Ding, W. Gao, X. Huang and H. Wu, *J. Org. Chem.*, 2013, **78**, 11342.
50. (a) B. Ganem, *J. Org. Chem.*, 1975, **40**, 1998; (b) T. Miyazawa, T. Endo, S. Shiihashi and M. Okawara, *J. Org. Chem.*, 1985, **50**, 1332; (c) T. Miyazawa and T. Endo, *J. Org. Chem.*, 1985, **50**, 3930.
51. P. L. Anelli, C. Biffi, F. Montanari and S. Quici, *J. Org. Chem.*, 1987, **52**, 2559.
52. P. L. Anelli, S. Banfi, F. Montanari and S. Quici, *J. Org. Chem.*, 1989, **54**, 2970.
53. P. L. Anelli, F. Montanari and S. Quici, *Org. Synth.*, 1990, **69**, 212.
54. (a) J. Einhorn, C. Einhorn, F. Ratajczak and J. L. Pierre, *J. Org. Chem.*, 1996, **61**, 7452; (b) A. De Mico, R. Margarita, L. Parlanti, A. Vescovi and G. Piancatelli, *J. Org. Chem.*, 1997, **62**, 6974; (c) C. Bolm, A. S. Magnus and J. P. Hildebrand, *Org. Lett.*, 2000, **2**, 1173; (d) L. De Luca, G. Giacomelli and A. Porcheddu, *Org. Lett.*, 2001, **3**, 3041; (e) R. A. Miller and R. S. Hoerrner, *Org. Lett.*, 2003, **5**, 285; (f) N. Jiang and A. J. Ragauskas, *Tetrahedron Lett.*, 2005, **46**, 3323; (g) Z. W. Mei, T. Omote, M. Mansour, H. Kawafuchi, Y. Takaguchi, A. Jutand, S. Tsuboi and T. Inokuchi, *Tetrahedron*, 2008, **64**, 10761.

55. M. Shibuya, M. Tomizawa, I. Suzuki and Y. Iwabuchi, *J. Am. Chem. Soc.*, 2006, **128**, 8412.
56. (a) M. Zhao, J. Li, E. Mano, Z. Song, D. M. Tschaen, E. J. J. Grabowski and P. J. Reider, *J. Org. Chem.*, 1999, **64**, 2564; (b) M. M. Zhao, J. Li, E. Mano, Z. J. Song and D. M. Tschaen, *Org. Synth.*, 2005, **81**, 195; (c) B. O. Lindgren and T. Nilsson, *Acta Chem. Scand.*, 1973, **27**, 888.
57. M. Shibuya, T. Sato, M. Tomizawa and Y. Iwabuchi, *Chem. Commun.*, 2009, 1739.
58. R. Liu, X. Liang, C. Dong and X. Hu, *J. Am. Chem. Soc.*, 2004, **126**, 4112.
59. R. Liu, C. Dong, X. Liang, X. Wang and X. Hu, *J. Org. Chem.*, 2005, **70**, 729.
60. (a) Y. Xie, W. Mo, D. Xu, Z. Shen, N. Sun, B. Hu and X. Hu, *J. Org. Chem.*, 2007, **72**, 4288; (b) X. He, Z. Shen, W. Mo, N. Sun, B. Hu and X. Hu, *Adv. Synth. Catal.*, 2009, **351**, 89.
61. (a) X. Wang, R. Liu, Y. Jin and X. Liang, *Chem. – Eur. J.*, 2008, **14**, 2679; (b) C. X. Miao, L. N. He, J. Q. Wang and J. L. Wang, *Adv. Synth. Catal.*, 2009, **351**, 2209; (c) Y. Kuang, H. Rokubuichi, Y. Nabae, T. Hayakawa and M. A. Kakimoto, *Adv. Synth. Catal.*, 2010, **352**, 2635; (d) S. Wertz and A. Studer, *Adv. Synth. Catal.*, 2011, **353**, 69.
62. M. Shibuya, Y. Osada, Y. Sasano, M. Tomizawa and Y. Iwabuchi, *J. Am. Chem. Soc.*, 2011, **133**, 6497.
63. M. B. Lauber and S. S. Stahl, *ACS Catal.*, 2013, **3**, 2612.
64. M. Hayashi, M. Shibuya and Y. Iwabuchi, *J. Org. Chem.*, 2012, **77**, 3005.
65. S. Hamada, T. Furuta, Y. Wada and T. Kawabata, *Angew. Chem., Int. Ed.*, 2013, **52**, 8093.
66. M. Zhang, C. Chen, W. Ma and J. Zhao, *Angew. Chem.*, 2008, **120**, 9876.
67. D. Liu, H. Zhou, X. Gu, X. Shen and P. Li, *Chin. J. Chem.*, 2014, **32**, 117.
68. W. Peng, K. Ashida, T. Hirabaru, L. J. Ma and T. Inokuchi, *Tetrahedron*, 2010, **66**, 9714.
69. M. Shibuya, R. Doi, T. Shibuta, S. Uesugi and Y. Iwabuchi, *Org. Lett.*, 2012, **14**, 5006.
70. M. Shibuya, T. Shibuta, H. Fukuda and Y. Iwabuchi, *Org. Lett.*, 2012, **14**, 5010.
71. K. Furukawa, M. Shibuya and Y. Yamamoto, *Org. Lett.*, 2015, **17**, 2282.
72. K. Furukawa, H. Inada, M. Shibuya and Y. Yamamoto, *Org. Lett.*, 2016, **18**, 4230.
73. H. Inada, M. Shibuya and Y. Yamamoto, *Org. Lett.*, 2019, **21**, 709.
74. K. C. Miles, M. L. Abrams, C. R. Landis and S. S. Stahl, *Org. Lett.*, 2016, **18**, 3590.
75. N. Merbouh, J. M. Bobbitt and C. Brukner, *J. Org. Chem.*, 2004, **69**, 5116.
76. A. Abramovich, H. Toledo, E. Pisarevsky and A. M. Szpilman, *Synlett*, 2012, **23**, 2261.
77. R. Ray, R. D. Jana, M. Bhadra, D. Maiti and G. K. Lahiri, *Chem. – Eur. J.*, 2014, **20**, 15618.
78. H. Toledo, E. Pisarevsky, A. Abramovich and A. M. Szpilman, *Chem. Commun.*, 2013, **49**, 4367.

79. (a) M. Shibuya, M. Tomizawa and Y. Iwabuchi, *J. Org. Chem.*, 2008, **73**, 4750; (b) M. Shibuya, M. Tomizawa and Y. Iwabuchi, *Org. Lett.*, 2008, **10**, 4715.
80. P. P. Pradhan, J. M. Bobbitt and W. F. Bailey, *J. Org. Chem.*, 2009, **74**, 9524.
81. C. B. Kelly, J. M. Ovian, R. M. Cywar, T. R. Gosselin, R. J. Wiles and N. E. Leadbeater, *Org. Biomol. Chem.*, 2015, **13**, 4255.
82. T. Miyazawa and T. Endo, *J. Polym. Sci., Polym. Chem. Ed.*, 1985, **23**, 2487.
83. T. Miyazawa and T. Endo, *J. Mol. Catal.*, 1988, **49**, L31.
84. T. Osa, U. Akiba, I. Segawa and J. M. Bobbitt, *Chem. Lett.*, 1988, 1423.
85. N. Tsubokawa, T. Kimoto and T. Endo, *J. Mol. Catal. A: Chem.*, 1995, **101**, 45.
86. (a) T. Fey, H. Fischer, S. Bachmann, K. Albert and C. Bolm, *J. Org. Chem.*, 2001, **66**, 8154; (b) C. Bolm and T. Fey, *Chem. Commun.*, 1999, 1795.
87. D. Brunel, F. Fajula, J. B. Nagy, B. Deroide, M. J. Verhoef, L. Veum, J. A. Peters and H. van Bekkum, *Appl. Catal., A*, 2001, **213**, 73.
88. R. Ciriminna, C. Bolm, T. Fey and M. Pagliaro, *Adv. Synth. Catal.*, 2002, **344**, 159.
89. G. Pozzi, M. Cavazzini, S. Quici, M. Benaglia and G. Dell'Anna, *Org. Lett.*, 2004, **6**, 441.
90. P. Ferreira, E. Phillips, D. Rippon, S. C. Tsang and W. Hayes, *J. Org. Chem.*, 2004, **69**, 6851.
91. M. Gilhespy, M. Lok and X. Baucherel, *Chem. Commun.*, 2005, 1085.
92. O. Holczknecht, M. Cavazzini, S. Quici, I. Shepperson and G. Pozzi, *Adv. Synth. Catal.*, 2005, **347**, 677.
93. (a) A. Gheorghe, A. Matsuno and O. Reiser, *Adv. Synth. Catal.*, 2006, **348**, 1016; (b) V. V. Rostovtsev, L. G. Green, V. V. Fokin and K. B. Sharpless, *Angew. Chem., Int. Ed.*, 2002, **41**, 2596; (c) C. W Tornøe, C. Christensen and M. Meldal, *J. Org. Chem.*, 2002, **67**, 3057; (d) R. Huisgen, *Pure Appl. Chem.*, 1989, **61**, 613.
94. A. Gheorghe, T. Chinnusamy, E. C. Yañez, P. Hilgers and O. Reiser, *Org. Lett.*, 2008, **10**, 4171.
95. (a) B. Karimi, A. Biglari, J. H. Clark and V. Budarin, *Angew. Chem., Int. Ed.*, 2007, **46**, 7210; (b) B. Karimi, E. Farhangi, H. Vali and S. Vahdati, *ChemSusChem*, 2014, **7**, 2735.
96. A. Schatz, R. N. Grass, W. J. Stark and O. Reiser, *Chem. – Eur. J.*, 2008, **14**, 8262.
97. A. K. Tucker-Schwartz and R. L. Garrell, *Chem. – Eur. J.*, 2010, **16**, 12718.
98. B. Karimi and E. Farhangi, *Chem. – Eur. J.*, 2011, **17**, 6056.
99. B. Karimi and E. Farhangi, *Adv. Synth. Catal.*, 2013, **355**, 508.
100. B. Karimi, H. M. Mirazei and E. Farhangi, *ChemCatChem*, 2014, **6**, 758.
101. H. A. Beejapur, V. Campisciano, P. Franchi, M. Lucarini, F. Giacalone and M. Gruttadauria, *ChemCatChem*, 2014, **6**, 2419.

102. K. M. Zwoliński and M. J. Chmielewski, *ACS Appl. Mater. Interfaces*, 2017, **9**, 33956.
103. M. Liu, B. Zhou, L. Zhou, Z. Xie, S. Li and L. Chen, *J. Mater. Chem. A*, 2018, **6**, 9860.
104. A. E. Fernandes, O. Riant, K. F. Jensen and A. M. Jonas, *Angew. Chem., Int. Ed.*, 2016, **55**, 11044.
105. (a) P. Chandra, A. M. Jonas and A. E. Fernandes, *J. Am. Chem. Soc.*, 2018, **140**, 5176; (b) P. Chandra, A. M. Jonas and A. E. Fernandes, *ACS Catal.*, 2018, **8**, 6006.
106. M. M. Manzari, M. Amini, M. Abdollahi, M. Khoobi, G. Bagherzadeh and M. A. Faramarzi, *ChemCatChem*, 2018, **10**, 1542.
107. Z. Li, Y. Liu, X. Kang and Y. Cui, *Inorg. Chem.*, 2018, **57**, 9786.
108. S. D. Rychnovsky, T. L. McLernon and H. Rajapakse, *J. Org. Chem.*, 1996, **61**, 1194.
109. Y. Kashiwagi, F. Kurashima, C. Kikuchi, J. I. Anzai, T. Osa and J. M. Bobbitt, *Tetrahedron Lett.*, 1999, **40**, 6469.
110. M. Kuroboshi, H. Yoshihisa, M. N. Cortona, Y. Kawakami, Z. Gao and H. Tanaka, *Tetrahedron Lett.*, 2000, **41**, 8131.
111. H. Shiigi, H. Mori, T. Tanaka, Y. Demizu and O. Onomura, *Tetrahedron Lett.*, 2008, **49**, 5247.
112. S. Hamada, Y. Wada, T. Sasamori, N. Tokitoh, T. Furura and T. Kawabata, *Tetrahedron Lett.*, 2014, **55**, 1943.
113. K. Murakami, Y. Sasano, M. Tomizawa, M. Shibuya, E. Kwon and Y. Iwabuchi, *J. Am. Chem. Soc.*, 2014, **136**, 17591.
114. M. F. Semmelhack and C. R. Schmid, *J. Am. Chem. Soc.*, 1983, **105**, 6732.
115. F. MacCorquodale, J. A. Crayston, J. C. Walton and D. J. Worsfold, *Tetrahedron Lett.*, 1990, **31**, 771.
116. Y. Kashiwagi, F. Kurashima, C. Kikuchi, J. Anzai, T. Osa and J. M. Bobbitt, *J. Chin. Chem. Soc.*, 1998, **45**, 135.
117. F. Chen, Y. Kuang, H. Dai, L. Lu and M. Huo, *Synthesis*, 2003, **17**, 2629.
118. (a) K. M. Lambert, J. M. Bobbitt, S. A. Eldirany, K. B. Wiberg and W. F. Bailey, *Org. Lett.*, 2014, **16**, 6484; (b) K. M. Lambert, J. M. Bobbitt, S. A. Eldirany, L. E. Kissane, R. K. Sheridan, Z. D. Stempel, F. H. Sternberg and W. F. Bailey, *Chem. – Eur. J.*, 2016, **22**, 5156.
119. C. B. Kelly, K. M. Lambert, M. A. Mercadante, J. M. Ovian, W. F. Bailey and N. E. Leadbeater, *Angew. Chem., Int. Ed.*, 2015, **54**, 4241.
120. J. H. Noh and J. Kim, *J. Org. Chem.*, 2015, **80**, 11624.
121. K. Moriyama, M. Kuramochi, K. Fujii, T. Morita and H. Togo, *Angew. Chem., Int. Ed.*, 2016, **55**, 14546.
122. Z. Hu and F. M. Kerton, *Org. Biomol. Chem.*, 2012, **10**, 1618.
123. T. Sonobe, K. Oisaki and M. Kanai, *Chem. Sci.*, 2012, **3**, 3249.
124. J. Kim and S. S. Stahl, *ACS Catal.*, 2013, **3**, 1652.
125. X. T. Ma, H. Xu, Y. L. Xiao, C. L. Su, J. P. Liu and Q. Xu, *Chin. Chem. Lett.*, 2017, **28**, 1336.
126. B. Han, X. L. Yang, C. Wang, Y. W. Bai, T. C. Pan, X. Chen and W. Yu, *J. Org. Chem.*, 2012, **77**, 1136.

127. J. Ma, Y. Wan, C. Hong, M. Li, X. Hu, W. Mo, B. Hu, N. Sun, L. Jin and Z. Shen, *Eur. J. Org. Chem.*, 2017, 3335.
128. (a) R. Siedlecka and J. Skarzewski, *Synthesis*, 1994, **1994**, 401; (b) R. Siedlecka and J. Skarzewski, *Synlett*, 1996, **1996**, 757.
129. S. Velusamy, A. V. Kumar, R. Saini and T. Punniyamurthy, *Tetrahedron Lett.*, 2005, **46**, 3819.
130. T. Chinnusamy and O. Reiser, *ChemSusChem*, 2010, **3**, 1040.
131. C. Ren, R. Fang, X. Yu and S. Wang, *Tetrahedron Lett.*, 2018, **59**, 982.
132. J. Y. Huang, S. J. Li and Y. G. Wang, *Tetrahedron Lett.*, 2006, **47**, 5637.
133. X. Lang, J. Zhao and X. Chen, *Angew. Chem., Int. Ed.*, 2016, **128**, 4775.
134. H. Hao, Z. Wang, J.-L. Shi, X. Li and X. Lang, *ChemCatChem*, 2018, **10**, 4545.
135. J. H. Bobbitt and Z. Ma, *Heterocycles*, 1992, **33**, 641.
136. Y. Kashiwagi, H. Ono and T. Osa, *Chem. Lett.*, 1993, 81.
137. (a) M. S. Maji, T. Pfeifer and A. Studer, *Angew. Chem., Int. Ed.*, 2008, **47**, 9547; (b) M. S. Maji and A. Studer, *Synthesis*, 2009, 2467.
138. M. S. Maji, T. Pfeifer and A. Studer, *Chem. – Eur. J.*, 2010, **16**, 5872.
139. M. S. Maji, S. Murarka and A. Studer, *Org. Lett.*, 2010, **12**, 3878.
140. S. Murarka and A. Studer, *Adv. Synth. Catal.*, 2011, **353**, 2708.
141. B. Zhang, Y. Cui and N. Jiao, *Chem. Commun.*, 2012, **48**, 4498.
142. X. L. Yang, X. X. Peng, F. Chen and B. Han, *Org. Lett.*, 2016, **18**, 2070.
143. T. Vogler and A. Studer, *Org. Lett.*, 2008, **10**, 129.
144. T. Vogler and A. Studer, *Adv. Synth. Catal.*, 2008, **350**, 1963.
145. S. Kirchberg, S. Tani, K. Ueda, J. Yamaguchi, A. Studer and K. Itami, *Angew. Chem., Int. Ed.*, 2011, **50**, 2387.
146. Z. He, S. Kirchberg, R. Fröhlich and A. Studer, *Angew. Chem., Int. Ed.*, 2012, **51**, 3699.
147. D. H. Ortgies, F. Chen and P. Forgione, *Eur. J. Org. Chem.*, 2014, 3917.
148. S. Kirchberg, R. Fröhlich and A. Studer, *Angew. Chem., Int. Ed.*, 2009, **48**, 4235.
149. S. Kirchberg, R. Fröhlich and A. Studer, *Angew. Chem., Int. Ed.*, 2010, **49**, 6877.
150. K. Mitsudo, T. Kaide, E. Nakamoto, K. Yoshida and H. Tanaka, *J. Am. Chem. Soc.*, 2007, **129**, 2246.
151. S. Maity, S. Manna, S. Rana, T. Naveen, A. Mallick and D. Maiti, *J. Am. Chem. Soc.*, 2013, **135**, 3355.
152. S. Maity, T. Naveen, U. Sharma and D. Maiti, *Org. Lett.*, 2013, **15**, 3384.
153. S. Manna, S. Jana, T. Saboo, A. Maji and D. Maiti, *Chem. Commun.*, 2013, **49**, 5286.
154. L. Wang, Z. Yang, H. Zhu, H. Liu, S. Lv and X. Xu, *Eur. J. Org. Chem.*, 2019, **2019**, 2138.
155. T. Wang and N. Jiao, *J. Am. Chem. Soc.*, 2013, **135**, 11692.
156. S. Nagasawa, Y. Sasano and Y. Iwabuchi, *Angew. Chem., Int. Ed.*, 2016, **55**, 13189.
157. Z. Zhang, Y. Gao, Y. Liu, J. Li, H. Xie, H. Li and W. Wang, *Org. Lett.*, 2015, **17**, 5492.

158. L. Yang, S. Li, Y. Dou, S. Zhen, H. Li, P. Zhang, B. Yuan and G. Yang, *Asian J. Org. Chem.*, 2017, **6**, 265.
159. E. C. Gentry, L. J. Rono, M. E. Hale, R. Matsuura and R. R. Knowles, *J. Am. Chem. Soc.*, 2018, **140**, 3394.
160. K. Liang, X. Tong, T. Li, B. Shi, H. Wang, P. Yan and C. Xia, *J. Org. Chem.*, 2018, **83**, 10948.
161. J. C. Siu, G. S. Sauer, A. Saha, R. L. Macey, N. Fu, T. Chauviré, K. M. Lancaster and S. Lin, *J. Am. Chem. Soc.*, 2018, **140**, 12511.

CHAPTER 4

Spin Probes and Imaging Using Nitroxides

VALERY V. KHRAMTSOV[a,b]

[a] In Vivo Multifunctional Magnetic Resonance center, Robert C. Byrd Health Science Center, West Virginia University, Morgantown, WV 26506, USA; [b] Department of Biochemistry, West Virginia University School of Medicine, Morgantown, WV 26506, USA
Email: valery.khramtsov@hsc.wvu.edu

4.1 Introduction

Nitroxyl radicals, NRs, represent the most diverse class of stable organic radicals varying in stability, spectral properties and functionality which have been successfully used as spin labels and probes in numerous EPR spectroscopic and imaging applications. In the early 1960s, EPR spectral sensitivities of the NRs to the local environment, including viscosity[1] and polarity,[2] were reported. Later, McConnell and colleagues greatly stimulated NR applications establishing the spin labeling technique with demonstration of the EPR spectra sensitivity of NR labels bound to biologically relevant macromolecules to molecular motion and microenvironment.[3,4] Combination of EPR spin labeling with site-directed mutagenesis reactions originated the site-directed spin labeling technique (SDSL), currently widely used in the study of protein structure and dynamics.[5–7] Sensitivity of the EPR spectra of the NRs to pair-wise Heisenberg spin exchange[8] or magnetic dipole–dipole interactions[9] provides experimental tools for the measurement of intermolecular distances and localization of paramagnetic species such as paramagnetic ions and oxygen. NRs were first paramagnetic probes used for EPR oximetry based on the spin exchange phenomenon between

Nitroxides
Edited by Olivier Ouari and Didier Gigmes

Published by the Royal Society of Chemistry, www.rsc.org

diradical oxygen molecule and NRs.[10–12] The most known reaction of the NRs, their one-electron reduction to EPR-silent hydroxylamines, is largely responsible for the biodegradation of the nitroxides in living tissues[13] and, in general, significantly limits many biological applications of NRs. On the other hand, the rate of NR reduction provides information on redox state of the living tissues[14] overviewed in Chapter 13.

The well-developed chemistry of the NRs[15–17] allows manipulation of their structure and properties, including charge, presence of hydrophilic or hydrophobic groups, various functionalities[18] and ability to be targeted. Small neutral NRs normally easily penetrate cellular membranes and are equally distributed throughout the intracellular and extracellular environments. Conversely, charged NRs will not cross the plasma membrane and thus can be used as extracellular probes.[11,19] NRs encapsulated in liposomes or linked to carrier molecules can be used to achieve organ or tissue selectivity.[20] In general, NRs have low toxicity and can be administered to an animal by infusion or by intraperitoneal, intravenous or intratissue injection.

The stability of the N–O group allows chemical reactions of the NRs which do not destroy the radical center[21,22] and therefore opens the opportunity to study these reactions by EPR.[18,23] They include reactions of the NRs with protons,[24] thiols,[25] nitric oxide (NO),[26–29] as well as enzyme-catalyzed reactions with NR-substrate analogues.[30–32] Recently we described the basic principles of designing functional probes to assess the local chemical microenvironment based on the NRs involved in reversible exchange processes such as spin exchange with diradical oxygen molecule, proton exchange with solvated protons and weak acids, and thiol-disulfide exchange with biological thiols.[18] Introduction into the vicinity of the radical NO fragment of ionizable group, substrate analogues or disulfide link connecting two NR moieties provides a basis for the design of pH-, enzyme- and thiol-sensitive NR probes. In this chapter we overview the basic principles of NR applications as probes to assess the local chemical microenvironment with a focus on their *in vivo* applications.

4.2 NR Oxymetric Probes and EPR Oximetry

4.2.1 Basics of EPR Sensitivity of the Nitroxide Probes to Oxygen

EPR oximetry is one of the most promising noninvasive techniques for measurement of oxygen in living tissues.[33] It is predominantly based on the physical phenomenon of Heisenberg spin exchange between paramagnetic molecules of probe and oxygen, and does not interfere with oxygen metabolism. Both the longitudinal (T_1) and transverse (T_2) relaxation times of the paramagnetic probe are affected by collisions with dissolved diradical molecules of oxygen. The encounter rate, w, is governed by the Smoluchowski equation, $w = 4\pi \cdot r \cdot D \cdot [O_2]$, where r is the interaction distance, and D is the

diffusion constant of oxygen, which is much greater than the diffusion constant of the NR. According to the early work of Pake and Tuttle,[34] the exchange-induced EPR line broadening is proportional to the radical–radical collision rate (for Lorentzian lineshape EPR linewidth in inversely proportional to T_2: $\Delta H_L = 1/(\gamma_e T_2)$, where $\gamma_e = 1.76 \times 10^{11}$ $s^{-1}T^{-1}$ is electron gyromagnetic ratio) and, therefore, to oxygen concentration. Historically, NRs were the first paramagnetic probes used for EPR oximetric measurements.[10,35–39] Backer *et al.*[10] pioneered applications of the continuous wave (CW) EPR T_2 oximetry method based on oxygen-induced line broadening of the NR probe. T_1-sensitive EPR oximetry was developed by Hyde *et al.*[36,39,40] The linewidth of the EPR spectrum and the relaxation times of the unpaired electrons of the probe depend on both probe concentration and the partial pressure of oxygen. T_1-based pulsed EPR oximetry is relatively less sensitive to the concentration of the spin probe than T_2-based CW EPR oximetry.[41]

CW EPR T_2 oximetry based on linewidth broadening exhibits higher sensitivity to oxygen concentration in terms of relative change in linewidths from probes with narrow individual lines. The total EPR linewidth is determined by two components: (i) homogeneous broadening due to transverse relaxation, and (ii) inhomogeneous broadening due to unresolved hyperfine interactions of unpaired electron with neighboring nuclei. In the case of the NRs, hyperfine interactions with ^{14}N ($S_N = 1$) of NO fragment manifest in three nitrogen manifolds, each of them experiencing superhyperfine interactions with neighboring protons. Figure 4.1 demonstrates superhyperfine structures for one of the nitrogen manifolds of the

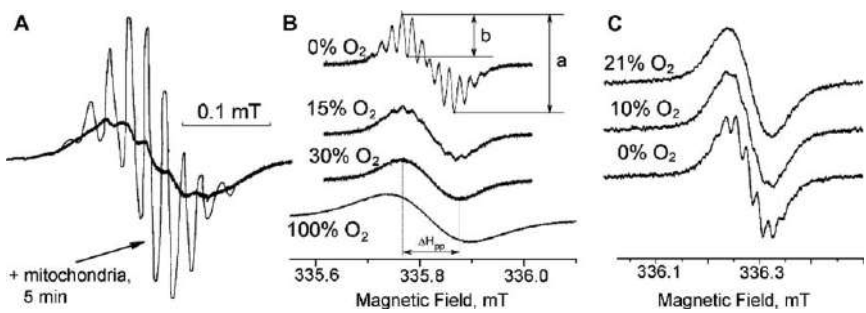

Figure 4.1 X-band EPR spectra of the aqueous solutions of the NR **1–3**. (**A**) Evolution of the EPR spectra of 0.7 mM solution of imidazoline NR **1** upon oxygen consumption by respiring mitochondria that results in linewidth narrowing and increase signal intensity of the individual lines. Reproduced from ref. 10 with permission from Elsevier, Copyright 1977. (**B**) EPR spectra of 0.05 mM pyrroline NR **2** solutions at various oxygen concentrations indicated near the spectra. Reproduced from ref. 44 with permission from John Wiley & Sons, Copyright 2010 John Wiley & Sons, Ltd. (**C**) EPR spectra of 0.5 mM NR **3** solutions at various oxygen concentrations indicated near the spectra. Reproduced from ref. 45 with permission from Springer Nature, Copyright 2002.

five-membered ring imidazoline, pyrroline and isoindoline NRs **1–3** (see Scheme 4.1 for the structures) due to the interactions with 12 protons of the methyl groups in the vicinity to the radical center and additional proton at atom C-4 in the case of NR **2**. Notably, narrow individual line of the resolved superhyperfine structure, typically at the order of 10 μT, provides the basis for the high sensitivity to oxygen, in particular at low oxygen concentrations. Measurement of ''the depth of resolution'' of the NR superhyperfine structure (*e.g.* parameter a/b for the NR **2** shown in the Figure 4.1B) provides excellent sensitivity to oxygen, and has been used for oxygen measurements in cellular and enzymatic systems.[10,35,42] Backer *et al.*[10] used imidazoline NR **1** with the resolved superhyperfine structure to follow mitochondrial respiration in samples containing only about 100 liver cells. While applications of these radicals *in vitro* can be attractive due to high sensitivity,[10,35,43] their potential for *in vivo* oximetric applications, when signal-to-noise ratio (SNR) becomes a critical factor and for imaging applications, which benefit from simple spectrum ideally represented by a single narrow line, is limited due to complex multiline spectra. Halpern *et al.*[12] demonstrated advantages of using partially deuterated analogue of NR **2** with only one hydrogen atom at position C4 of heterocycle, NR **4** (see Scheme 4.1), which exhibits the simplest doublet hyperfine splitting of each nitrogen manifold. In addition to simplification of the spectral pattern and consequent increase in SNR, analysis of lineshape of partially overlapped components of the doublet signal allows for discrimination between oxygen- and concentration-induced contributions in line broadening.[12] In contrast to oxygen-induced effects on the NR EPR spectra, an increase in NR concentration in addition to line broadening results in narrowing of hydrogen hyperfine splitting, therefore allowing for discrimination between oxygen- and concentration-induced line broadening contributions.

Oxygen-induced line-broadening effects vary slightly with the NR structure being about 50 μT/100% oxygen or 45 μT mM^{-1} of oxygen. For most five- and six-membered ring NRs with hydrogen atoms present in the radical heterocycle superhyperfine structure is not resolved contributing to inhomogeneous broadening of nitrogen manifolds. Therefore, the oxygen-induced linewidth changes must be measured across the whole of the nitrogen manifold with relative linewidth changes being consequently smaller. Moreover, large linewidths, typically at the order of 0.1 mT for inhomogeneously broadened nitrogen manifold, limit spatial resolution of

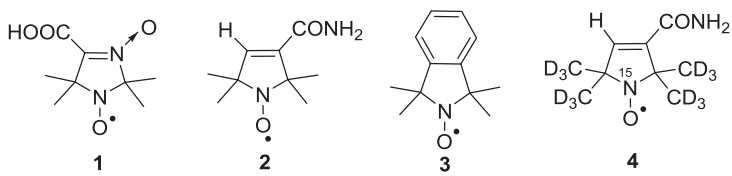

Scheme 4.1 Chemical structures of the NRs of the imidazoline, **1**, pyrroline, **2** and **4**, and isoindoline, **3**, types discussed in the text.

EPR imaging applications. As a consequence, developed by Nycomed Innovation, trityl radicals that exhibit single narrow line,[46,47] were recognized as advanced EPR oximetric probes particularly for *in vivo* applications. On the other hand, a potential disadvantage of the trityl radicals is a bulky and highly charged structure that determines their exclusively extracellular localization. NRs are better suited for more refined targeted EPR oximetry, *e.g.* imaging of intracellular and extracellular environments,[11] penetration through the blood–brain barrier for brain tissue oximetry,[48] *etc.* Therefore, a synthesis of the NRs with narrow linewidth is an important area of research that may significantly broaden EPR oximetric applications.

The lowest values for the peak-to-peak (ΔH_{pp}) linewidth of the nitrogen manifold in anoxic conditions were reported by Rassat and his colleagues for pyrrole NR **5** (Scheme 4.2) and its deuterated derivative NR **6** (40.7 μT and 11.3 μT in benzene, respectively),[49] the latter being comparable with the typical width of the individual line of superhyperfine structure (Figure 4.1A–C). However, attempts to derivatize pyrrol NR **5** to achieve its aqueous solubility were unsuccessful[50] due to instability of the most of the pyrrol radicals. The authors[49] reported extraordinary low nitrogen hyperfine splitting constant of the pyrrol NR **5** ($a_N \approx 0.44$ mT) as a consequence of low spin density residing on NO fragment (*ca.* 0.6), and proposed linear correlation between $(\Delta H_{pp})^{1/2}$ and a_N constant[49] which, however, does not hold for generalization. The most drastic counterexample is provided for piperidine NRs **7** and **8** (Scheme 4.2) with similar values of a_N constants (1.69 mT and 1.59 mT, respectively) but more than three-fold different values of ΔH_{pp} linewidth (158 μT and 47 μT, respectively).[50] The authors[50] proposed that a double-bonded substituent at the 4-position of a piperidine NR heterocycle allows for the dynamic averaging of hydrogen hyperfine couplings *via* fast fluctuations converting axial methyl groups with positive a_H into an equatorial configuration with negative a_H resulting in a narrow linewidth.

Deuteration of the NRs is a commonly used approach to narrow nitrogen manifold linewidth, ΔH_{pp}, resulting in a significant increase of the relative

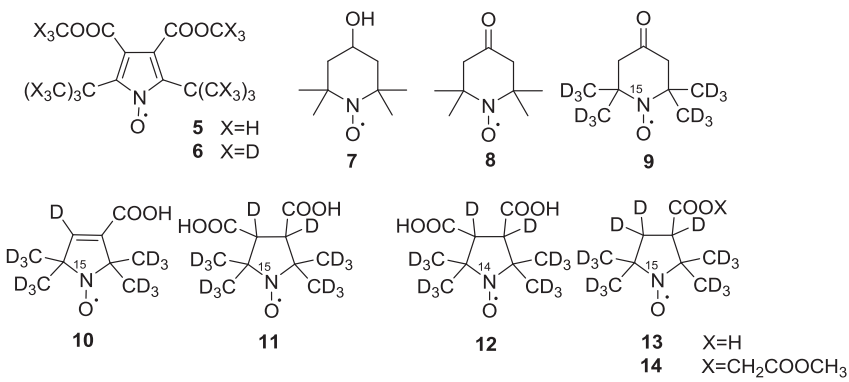

Scheme 4.2 Chemical structures of the NRs **5**–**14** discussed in the text.

sensitivity of the line broadening to pO_2.[51–53] Scheme 4.2 shows chemical structures of several isotopically substituted NRs **9–13** of piperidine, pyrroline and pyrrolidine types with remarkably low linewidths, *e.g.* ΔH_{pp} linewidth being equal to 28 μT for NR **9**[52] and 28–32 μT for NRs **10, 11**[54] (see also Figure 4.2). The decrease in the linewidth upon isotopic substitution is mainly due to the 6.5 times smaller hyperfine interaction constant for the deuteron than that for the proton. In addition, ^{14}N substitution with ^{15}N isotope enhances SNR due to a 1.5 times decrease of the number of nitrogen manifolds and further narrows the linewidth by eliminating quadrupole relaxation mechanisms of the electron spin on ^{14}N nuclei ($I = 1$).[54–56] Note that EPR spectra of ^{15}N- and ^{14}N-substituted NRs do not overlap, therefore combination of cell-permeable lipophilic ^{15}N-substituted NR **9** and cell-impermeable ^{14}N-substituted NR **12** can be used for discriminative intra- and extracellular pO_2 assessment.

For most of the NRs the EPR lineshape of nitrogen manifold can be reasonably described by convolution of Lorentzian function with an effective Gaussian originated from unresolved superhyperfine structure,[57,58] the latter being independent of oxygen concentration. Figure 4.2A illustrates typical dependences of the EPR peak-to-peak (ΔH_{pp}), and Lorentzian $\Delta H_L = 1/(\gamma_e T_2)$, linewidths on the oxygen partial pressure, pO_2, presented for NR **11**. While the measurement of ΔH_{pp} does not require lineshape analysis and can be used for oxygen measurements, only the Lorentzian linewidth ΔH_L is linearly proportional to pO_2 and is a more sensitive and accurate oxygen marker, particularly at low oxygen concentrations. Note that concentration-induced line broadening, being at the order of 10 μT mM^{-1} for the small neutral NRs, can significantly affect EPR lineshape at high NR

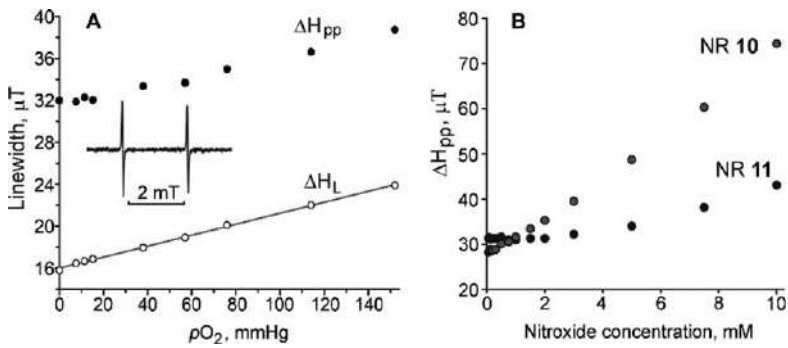

Figure 4.2 (**A**) Dependences of ΔH_{pp} and ΔH_L linewidth on oxygen partial pressure for NR **11**. Insert: EPR spectrum of NR **11** in oxygen-free 50 mM phosphate buffer, pH 7.4. Adapted from ref. 54 with permission from John Wiley & Sons, Copyright 2015 Wiley Periodicals, Inc. (**B**) Dependences of ΔH_{pp} linewidth on radical concentration for the structurally similar NRs **10** and **11** with one and two carboxylic groups, respectively. Reproduced from ref. 54 with permission from John Wiley & Sons, Copyright 2015 Wiley Periodicals, Inc.

concentrations often required to achieve sufficient SNR, therefore interfering with accurate EPR oximetric measurements.[44] An introduction of the charged or ionizable groups in the NR structure may impede interactions between the NR molecules due to electrostatic repulsion and significantly decrease the concentration-induced line-broadening effect as illustrated in Figure 4.2B for two structurally similar NRs (**10** and **11**) with one and two carboxylic groups deprotonated at neutral pH, respectively.[54] The authors noted advanced properties of cell-impermeable NR **11** for measuring tissue extracellular oxygen, including the ability to neglect concentration broadening up to $\approx$1 mM probe concentration, excellent probe stability toward bioreduction, and low toxicity due to its extracellular localization. Recently Hirata *et al.*[56] proposed simultaneous imaging of ^{14}N- and ^{15}N-labeled dicarboxy NRs **11** and **12** to discriminate oxygen- and concentration-induced contributions to line broadening. This discrimination is possible due to the different concentration-induced effects on line broadening of NR **11** and **12** in part due to the different nuclear statistical factors equal to 1/2 and 2/3, respectively, as a consequence of the absence of line broadening for the spin exchange between the NRs with the same projections of nitrogen nuclear spin.[59]

Labile-ester-containing NRs with variable lipophilic, pharmacokinetic and pharmacodynamic properties offer the possibilities to penetrate through the biological membranes and accumulate in intracellular compartments after esterase-catalyzed hydrolysis into corresponding carboxy-nitroxides.[60–64] Weaver *et al.*[48,65] demonstrated advanced properties of ^{15}N, ^{2}H-substituted ester derivative of the pyrrolidine NR **14** (Scheme 4.2), which combines capability to penetrate lipid barriers such as the blood–brain barrier followed by accumulation in the intracellular compartments in the form of carboxy NR **13,** and excellent oxygen sensitivity *in vivo* due to narrow linewidth of the NR **13** due to ^{15}N-, ^{2}H-substitution.

Encapsulation of the NRs in specially designed capsule,[66] micro-[67] and nanoparticles[68] may provide an alternative to isotopic substitution for increasing sensitivity to oxygen, as well as protecting NRs against reduction. For example, encapsulation of the NRs in proteinaceous microspheres filled with an organic liquid greatly increased the sensitivity of the linewidth to oxygen because of higher oxygen solubility in organic solvents.[67]

Summarizing, the structural diversity of the NRs provides the opportunity for targeted EPR oximetry in various *in vitro* and *in vivo* applications.

4.2.2 *In Vivo* EPR Oximetry Using Nitroxide Probes

Measurement of the oxygen concentration in biological tissues is important for understanding both physiological and pathophysiological conditions, including such diseases as myocardial ischemia,[54] cerebral hypoxia[48] and cancer.[69] In particular, under hypoxic conditions tumor tissues are known to be resistant to radiation and chemotherapy.[70–72] A reasonable

radiofrequency penetration depth in tissues makes EPR-based techniques the most appropriate approaches for noninvasive *in vivo* assessment of the tissue oxygenation.

Halpern *et al.*[12] applied low-field 250 MHz EPR imaging to assess the oxygen content in murine FSa and NFSa fibrosarcomas 7 cm deep in tissues of a living animal. As has been mentioned above, to account for the concentration-induced line broadening effect, the authors used selectively deuterated NR **4** with only one hydrogen hyperfine splitting. An oximetric 2D (1 spectral/1 spatial) image of the tumor was obtained allowing, in principle, targeting radiation and chemotherapy adjuvants to tumor hypoxic areas.

Cell-permeable isotopically substituted lipophilic NR **9** was applied in several studies to report on tumor tissue oxygenation and visualize tumor hypoxic areas. Kuppusamy *et al.*[73] used CW L-band EPR spectroscopy and NR **9** probe to measure the averaged oxygenation level in radiation-induced fibrosarcoma (RIF-1) in mice. The authors observed a three-fold lower level of oxygenation of the tumor tissue compared with that of the normal muscle. They also noted that for the accurate data interpretation regarding oxygen concentrations, an apparent distribution of NR **9** into lipophilic compartments with higher oxygen concentrations compared to aqueous compartment has to be taken into account. Hyodo *et al.*[74] performed first pulsed EPR oximetric imaging in mice using NR **9** probe. Strong heterogeneity of tumor oxygenation and significant hypoxic regions (<10 mmHg) characteristic of tumor pathogenesis were observed as illustrated in Figure 4.3 demonstrating the capability of *in vivo* pO_2 tissue imaging using time-domain pulsed EPR of the NRs.

Gorodetsky *et al.*[54] took advantage of the high pO_2 sensitivity and low toxicity of ^{15}N, ^{2}H-substituted dicarboxy NR **11** for mapping the hypoxic area during regional ischemia in an isolated perfused rat heart. The authors did not observe any influence of the presence of 0.5 mM NR **11** in the perfusate on the heart contractile function. Figure 4.4 shows 3D (1 spectral/2 spatial)

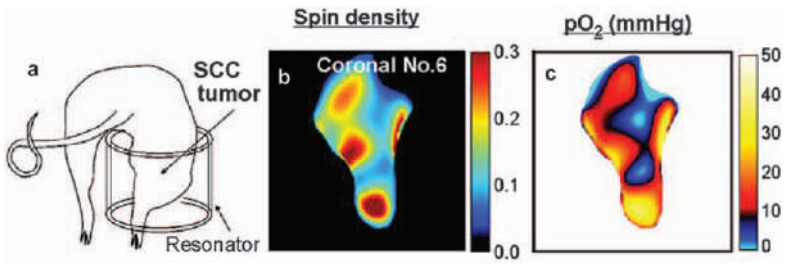

Figure 4.3 3D-pulsed 300 MHz EPR imaging of tumor oxygenation using NR **9**. (a) Schematic illustration of tumor-implanted mouse setting in the smaller parallel coil resonator. (b) Coronal slice view selected from 3D-spin density map of the nitroxide in tumor bearing leg, and (c) corresponding oxygen image calculated from linewidth distribution of NR **9**. Total acquisition time, 2.5 min.
Reproduced from ref. 74 with permission from Elsevier, Copyright 2009.

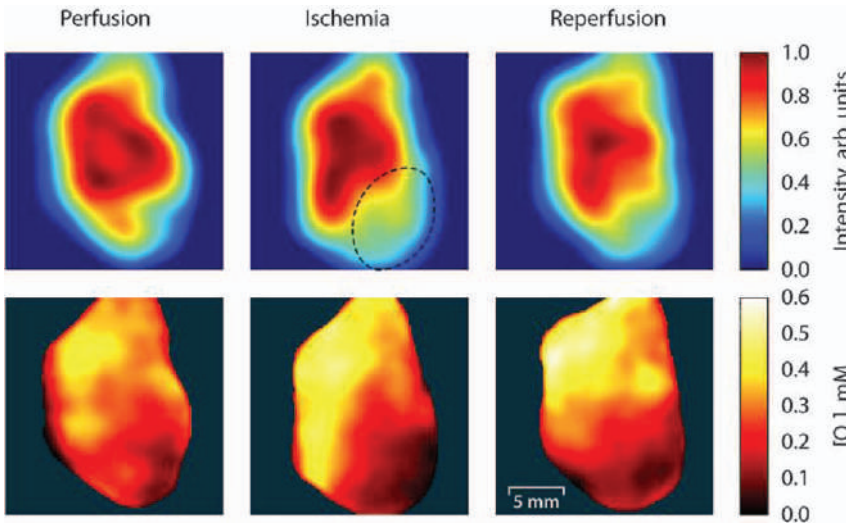

Figure 4.4 Coronal plane 3D (1 spectral/2 spatial) EPR images of an isolated rat heart during normal perfusion, regional ischemia and reperfusion. The heart was perfused in the presence of a 0.5 mM NR **11**. Upper row: Integral intensities of EPR signal. The area indicated by the dashed line is expected to be ischemic. Bottom row: Maps of myocardium oxygenation calculated from spectral data of the images. Acquisition time of a single image, 19 min.
Reproduced from ref. 54 with permission from John Wiley & Sons, Copyright 2015 Wiley Periodicals, Inc.

L-band CW EPR images of isolated rat heart during normal perfusion with NR **11** present in the perfusate, followed by the period of regional ischemia, and then reperfusion. The obtained myocardial pO_2 maps demonstrate strong oxygen depletion in the ischemic region of the heart followed by only partial restoration of tissue oxygenation after reperfusion compared with the preischemic level. The depressed oxygenation on reperfusion is most likely caused by hampered perfusate flow through the compressed vasculature of ischemia-damaged myocardium.

Recently Hirata *et al.*[56,75] reported a method of simultaneous T_2* mapping of dicarboxy pyrrolidine NRs, ^{15}N-substituted NR **11** and ^{14}N-substituted NR **12,** using 750-MHz CW-EPR imaging and demonstrated the feasibility of the approach for potential pO_2 mapping in a mouse tumor model. Simultaneous imaging of two isotopic forms allows to discriminate oxygen- and concentration-induced contribution in line broadening as discussed in Section 4.2.1.

Weaver *et al.*[48,65] demonstrated advanced properties of the esterified ^{15}N-, ^{2}H-substituted pyrrolidine NR **14** for cerebral pO_2 imaging due to its penetration though the blood–brain barrier, accumulation in brain tissue as carboxy NR **13**, and excellent oxygen sensitivity of the latter due to narrow linewidth of isotopically substituted NR.

Subczynski *et al.*[66] introduced the use of an implantable oxygen-permeable capsule filled with NR **9** in light paraffin oil and demonstrated its capability to monitor oxygen concentration in the peritoneal cavity as a function of inhalation mixture. However this method requires the physical insertion of the tube into the animal, and locations in which it can be used are limited. Liu *et al.*[67] applied NRs in proteinaceous microspheres filled with an organic liquid to increase sensitivity to oxygen and demonstrated capability to monitor oxygen concentration *in vivo* for 70 min after intravenous injection of the microspheres into a mouse. However, a concern of this approach is the potential leakage of the organic liquid from the microspheres when they are eventually metabolized, resulting in possible toxicity to the tissue.

The NRs were also explored as oximetric probes for Overhauser-enhanced MRI (OMRI) which combines the advantage of MRI anatomical resolution with the functional sensitivity of EPR. OMRI for myocardium oxygen mapping was first demonstrated in perfused sheep heart using a high concentration, 4 mM, of Fremy's salt nitroxide.[76] However, short relaxation times of the NRs require a high RF power deposition to obtain a good OMRI signal enhancement, therefore recent *in vivo* applications of OMRI oximetry are exclusively based on trityl radicals known for their extraordinary long relaxation times.[77–80]

EPR applications of other oxygen-sensitive paramagnetic materials include soluble trityl radicals[41,81] and particulate probes such as lithium phthalocyanine particles[82,83] and carbonaceous materials (chars, coals, carbon blacks).[84] It should be noted that particulate probes such as lithium phthalocyanine and synthetic char are suitable for measurements of oxygen partial pressure in place of implantation, whereas soluble probes such as NRs and trityl radicals are more suitable for imaging experiments.

4.3 NR pH Probes

4.3.1 Basics of Spectral Sensitivity of the Nitroxides to pH

The presence of the ionizable group in the structure of the NRs in the vicinity of the radical center results in the difference in the EPR spectra of its protonated, RH^+, and unprotonated, R, forms. The first pH effect on EPR spectra of NRs was observed in very strong acids and was related to protonation of the nitroxyl fragment itself.[85–87] To our knowledge, synthesized by Ullman and Osiecki in 1970[88] 2-imidazoline NRs **15** ($pK_a = 6.4$) and **16** ($pK_a = 6.8$) were the first reported stable pH-sensitive radicals with pH sensitivity in the physiological range (see Scheme 4.3). A large pH effect on nitrogen hyperfine splitting ($\Delta a_{N1} \approx 0.3$ mT) was observed upon protonation of imino nitrogen of the radical center. However, 2-imidazoline NRs did not find applications as pH probes, probably due to the relative complexity of their EPR spectra and extremely fast reduction to EPR-silent products in biological fluids.[28,89,90]

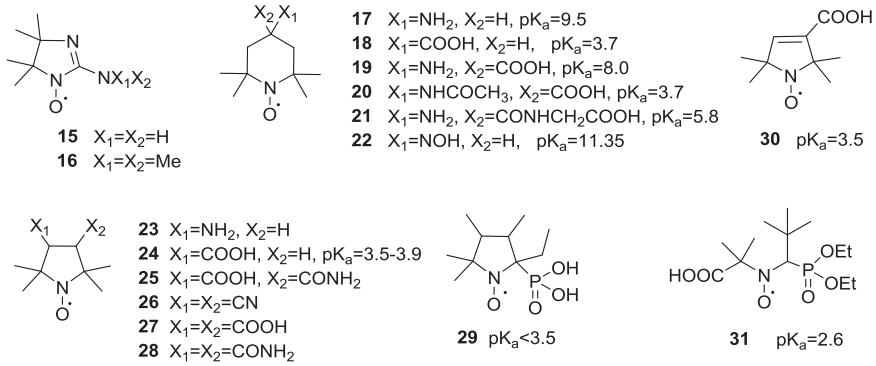

Scheme 4.3 Chemical structures of the pH-sensitive NRs of various types, namely 2-imidazoline NRs **15** and **16**;[88] piperidine NRs **17**,[91,92] **18**,[93] **19–21**[94] and **22**;[95] pyrrolidine NRs **23**,[96] **24**,[93,97] **25–28**[98] and **29**,[99] pyrroline NR **30**[95] and acyclic phosphorylated NR **31**.[100]

The observed pH effects on the EPR spectra of the piperidine, pyrroline and pyrrolidine NRs were impractically small[91–98] due to the long distance between the radical center and ionizable group. The total change in a_N was found to be in the range 15–30 μT for the piperidine NRs **17–22** with ionizable groups at atom C-4 of radical heterocycle and slightly larger in the range of 30–50 μT for the NRs **23–31** with ionizable groups less distant from the NO fragment. Phosphorylated radicals **29** and **31** additionally exhibit significantly larger change in phosphorus hyperfine splitting, a_F (about 260 μT and 190 μT, respectively) at acidic pH < 4, which is not surprising taking into account the large value of $a_F \approx 5$ mT. An application of phosphorylated NRs as pH-sensitive probes in biological systems is attractive due to large pH effects on a_P constant but synthesis of the probes with higher pK_a values is required.

Stable imidazoline and imidazolidine NRs have been proven to be the most useful spin probes for EPR spectroscopy and imaging of pH[18,101–108] due to the large effect of pH on their EPR spectra and a large number of the synthesized probes varied in ranges of pH sensitivity, solubility and stability toward bioreduction. Protonation of the nitrogen atom at β-position of radical heterocycle is schematically illustrated in Scheme 4.4. A positive charge at the N-3 atom stabilizes the nonionic resonance structure of N–O fragment with lower spin density of the unpaired π-electron on the nitrogen atom and, consequently, lower a_N. In Hückel description, the local electric field changes the energy gap between molecular π-orbitals constructed from atomic p-orbitals of N-1 and O atoms, therefore influencing spin density distribution and g-factor (for quantitative description see[93,97,109–112]). Experimentally, protonation of the N-3 atom of the imidazoline and imidazolidine NRs at pH below radical pK_a results in a decrease in hyperfine splitting, $\Delta a_N \approx 100$ μT, and increase in g-factor, $\Delta g \approx 0.0002–0.0003$.[24] The shift of the spectral line positions caused by Δg change linearly increases with an increase in microwave frequency as shown in Figure 4.5 for the

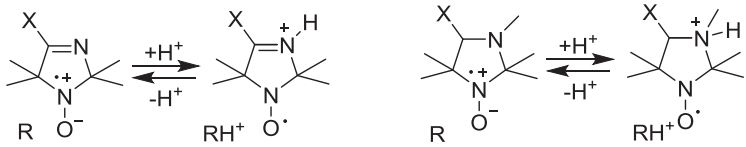

32 X=Me, pK_a=1.3
33 X=NH_2, pK_a=6.1

34 X=Ph, pK_a=3.0
35 X=CH_3, pK_a=4.7

Scheme 4.4 Chemical structures of the representative imidazoline and imidazolidine NRs **32–35** and illustration of the reversible protonation of imino nitrogen of the radical heterocycle. Two main resonance structures are shown suggesting the higher unpaired electron density on nitrogen atom N-1 in the unprotonated form. Strong dependence of pK_a of the NRs **32–35** on the substituent at atom C-4 allows rational design of the pH probes with various range of pH sensitivities.

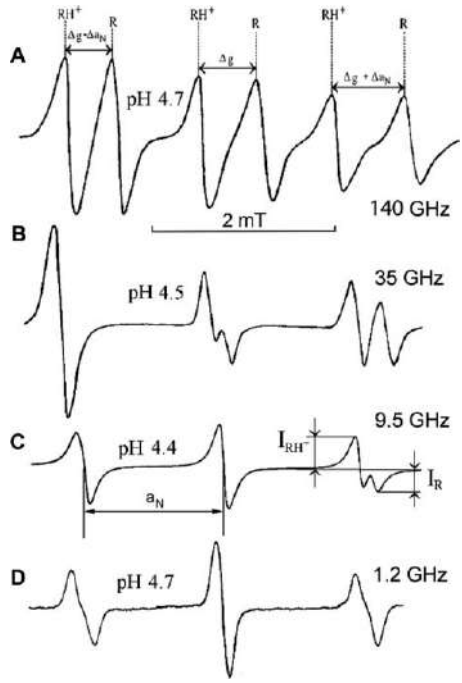

Figure 4.5 The EPR spectra of an aqueous solutions of imidazolidine NR **35** prepared at pH close to pK_a value (pK_a = 4.7) and measured at different EPR bands with EPR frequencies indicated near the spectra: D-band (**A**), Q-band (**B**), X-band (**C**) and L-band (**D**). At D- and Q-bands contributions of g-factor change dominate in observed spectral shifts being about 670 μT and 170 μT, respectively. X-band spectral shift between RH^+ and R forms is observed at high-field component only being equal to $(\Delta g + \Delta a_N) \approx 45$ μT +125 μT = 170 μT. At L-band EPR frequency the contribution of g-factor is negligible, resulting in symmetric L-band EPR spectrum (**D**).
Adapted from ref. 23 with permission from Springer Nature, Copyright 2002.

NR **35** measured at pH close to pK_a of the radical. At high D-band EPR frequency (140 GHz) two triplet spectra of both protonated, R, and deprotonated, RH^+, forms are well resolved, while at low L-band EPR frequency (1.2 GHz) only a slight disturbance of low- and high-field nitrogen manifolds is observed due to superposition of two R and RH^+ forms with different a_N constants, the latter being independent of EPR frequency. For NR with an equilibrium constant K_a, the ratio of concentrations of these two forms is described by the Henderson–Hasselbalch equation, $[H^+] = K_a[RH^+]/[R]$, providing the basis for EPR measurements of pH.

One of the great strengths of the EPR pH-metric technique is its ratiometric character. The pH measurement using NR pH probe does not depend on the probe concentration but on the ratio, $[RH^+]/[R]$, only. In general, spectral simulation is required for accurate determination of the $[RH^+]/[R]$ ratio from the EPR spectra. In practice, two convenient spectral parameters have been often used as pH markers: (i) the ratio of peak intensities of RH^+ and R spectral components resolved upon detection by high-frequency EPR and partially resolved in X-band EPR spectra for high-field nitrogen manifold (see Figure 4.5); and (ii) nitrogen hyperfine splitting, a_N, measured as a distance between unresolved spectral components, and being used almost exclusively as a highly sensitive pH marker in numerous *in vitro* applications using X-band and *in vivo* applications using low-field EPR. Note that the sensitivity of the hyperfine splitting to pH values depends both on EPR frequency and spectrometer settings (*e.g.*, modulation amplitude) and can be optimized.[113,114] Figure 4.6 shows the dependences of a_N on pH for the radical **33** obtained from L-band EPR spectra measured at different modulation amplitudes. Broadening of the EPR linewidth by measurements at modulation amplitude higher than linewidth results in a symmetric spectrum showing a conventional titration curve of the nitrogen hyperfine splitting as well as in significant improvement of SNR, which could be important for applications *in vivo* where fundamental sensitivity is much lower.

Figure 4.7 shows pH dependences of nitrogen hyperfine splitting, a_N, for a representative set of imidazoline and imidazolidine NRs (see Schemes 4.4 and 4.5 for the structures) as molecular pH meters that cover the total pH range of aqueous solutions from 0 to 14. At pH values close to pK_a the X-band EPR spectra of the NRs **33–35, 37–40** with pK_a in the range from 3 to 11 represent superposition of two ionizable forms; the presented a_N splitting was measured as a distance between unresolved low- and central-field nitrogen manifolds as shown in Figure 4.5C. The observed superposition of two ionizable forms is a consequence of slow proton R-RH^+ exchange at EPR time scale due to the low concentration of protons at pH between 3 and 11.[112] In contrast, for the radicals with a value of pK_a <3 such as NR **32** (p$K_a = 1.3$) and **36** ($pK_a^1 \approx 1.1$) the R-RH^+ proton exchange is fast at EPR time scale due to high proton concentration at pH < 3. Interestingly, the fast R-RH^+ exchange was also observed in alkaline medium for the NR **36** ($pK_a^2 \approx 13.25$) due to high concentration of hydroxyl anions, which facilitate proton exchange *via* the mechanism, $RH^+ + OH^- \leftrightarrow R + H_2O$.[23] As a consequence of the fast R-RH^+

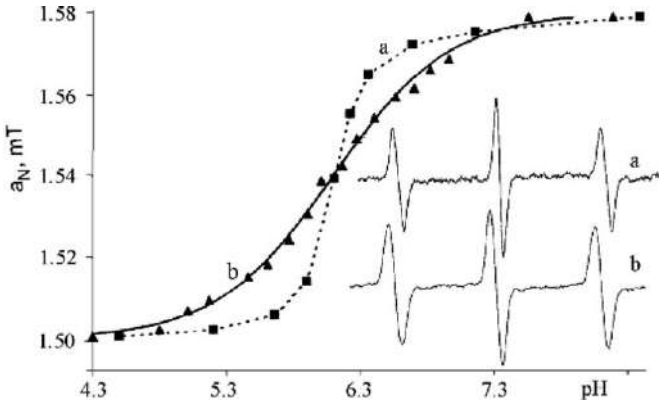

Figure 4.6 The pH dependences of nitrogen hyperfine splitting, a_N, of the L-band EPR spectra of the NR **33** measured at different modulation amplitudes: 50 μT (**a**, ■) and 200 μT (**b**, ▲). *Insert:* The EPR spectra of the 0.5 mM aqueous solutions of the radical R1 detected at pH 6.1, and modulation amplitudes 50 μT (**a**) and 200 μT (**b**). Note that the shift between RH^+ and R forms of the radical at low- and high-field components of the NR **33** EPR spectrum is comparable with the linewidth ($\Delta a_N \approx \Delta H_{pp} \approx 80$ μT), resulting in significant disturbance of the EPR lineshape measured at 50 μT modulation amplitude, and as a consequence, in narrowing the a_N titration curve resulting in compromising sensitivity to pH. Measurements at 200 μT modulation amplitude show a symmetrical EPR spectrum with 2.1 times increase in SNR, and result in a_N dependence on pH described by the conventional titration curve, $a_N(H^+) = (a_N(R) + a_N(RH^+) \times [H^+]/K_a)/(1 + [H^+]/K_a)$ yielding the radical $pK_a = -\log K_a = 6.1$, and the values of hyperfine splitting in two ionizable forms, $a_N(R) = 1.582$ mT and $a_N(RH^+) = 1.501$ mT.
Reproduced from ref. 114 with permission of Mary Ann Liebert, Inc, Copyright 2004.

exchange, the radicals **32** and **36** exhibit simple triplet spectra over the whole pH range with the hyperfine splitting, a_N, dependence on pH being in agreement with the conventional titration curve.

Note that in the presence of buffer in addition to the proton exchange with solvated proton appears the mechanism of proton exchange of the NR with buffer molecules,[18] the latter being the most efficient when dissociation constants of the buffer and NR are close to each other, $pK_a^B \approx pK_a^R$. The rate of buffer-facilitated proton R-RH^+ exchange is linear proportional to the buffer concentration. Therefore, for the radicals with $3 < pK_a < 11$ increase in buffer concentration results in increase of EPR frequency exchange from the slow to fast frequency exchange with corresponding spectral changes illustrated in Figure 4.8 for the ^{15}N, ^{2}H-substituted pH-sensitive NR **41** (see Scheme 4.5 for the structure). Figure 4.8A shows the superposition of two doublet EPR spectra better resolved for the high-field nitrogen manifold due to summation of protonation effects on g-factor and a_N splitting. A narrow line of NR **41** ($\Delta H_{pp} = 33$ μT for nonprotonated form) allows for distinguishing not

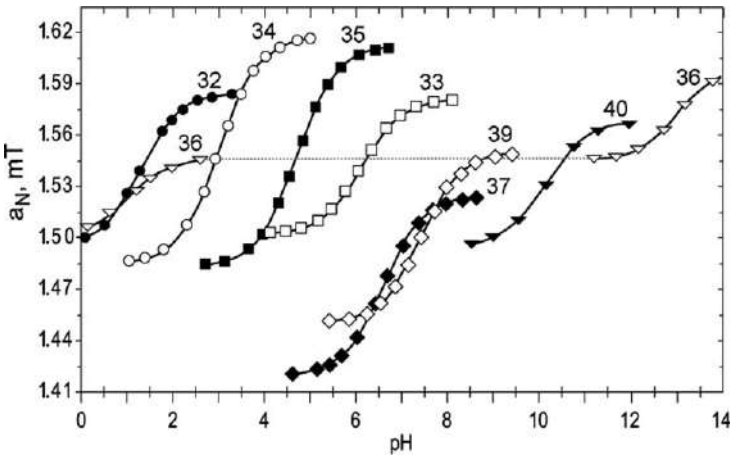

Figure 4.7 A set of imidazoline and imidazolidine NRs as molecular pH meter covering the pH range from 0 to 14. The structures of the NRs are presented in Schemes 4.4 and 4.5. The dependences of a_N on pH were obtained in aqueous solutions using X-band EPR.
The data were summarized from ref. 23, 105, 115 and 116.

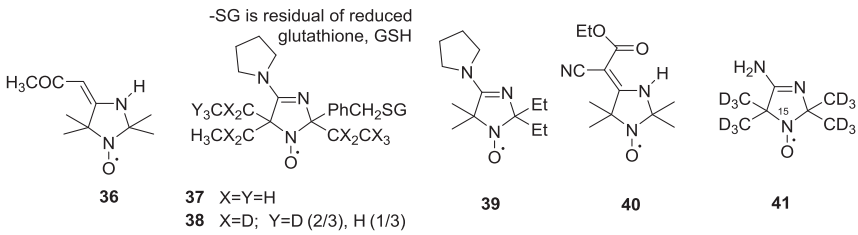

Scheme 4.5 Chemical structures of NRs **36**–**41** discussed in the text.

only R and RH^+ forms but also discriminating two protonated radical forms with different nuclear spin projection of attached proton, RH_α^+ and RH_β^+. An increase in phosphate buffer concentration results first in EPR spectra broadening and then spectral coalescence in a single line. Analysis of EPR spectral shape of the pH-sensitive radical in the case of intermediate buffer-induced exchange allows determination of the rate of exchange, and in principle, provides the opportunity to design EPR probes with sensitivity to the concentration of specific buffer.[18] Recently this approach has been implemented for *in vivo* detection of interstitial phosphate concentration using pH-sensitive monophosphonated trityl radical.[117,118] The narrow line of the trityl probe of about 4 μT and favorable value of phosphono group dissociation constant ($pK_a \approx 6.9$) being close to the pK_a of phosphate provide high spectral sensitivity of this probe to physiologically relevant interstitial phosphate concentrations in the range from 0.1 to 5 mM.[117,119]

pH-sensitive NRs were proposed to be a valuable tool to study the surface electrostatics of biological membranes and proteins.[120] In particular,

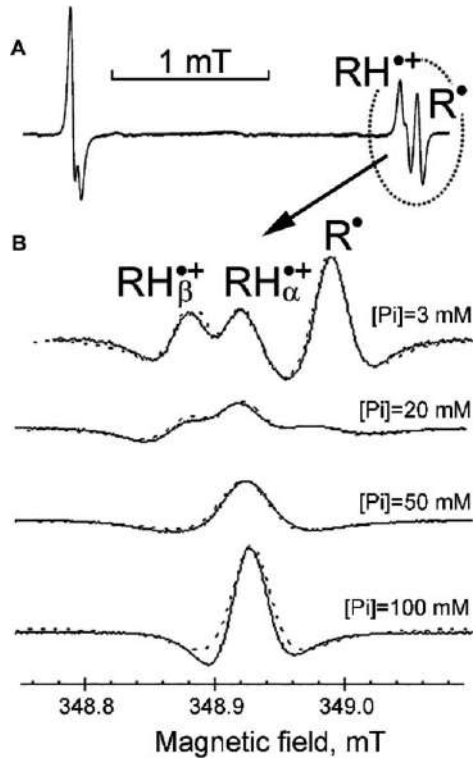

Figure 4.8 First (**A**) and second (**B**) derivatives of the X-band EPR spectra of 0.3 mM aqueous solutions of NR **41** prepared in phosphate buffer of different concentrations indicated near the spectra, pH 5.9. The fitting calculated spectra (dotted lines) to the experimental ones performed as described in ref. 55 provide the values of the rate constants of proton exchange of NR **41** with phosphate.
Adapted from ref. 55 with permission from Springer Nature, Copyright 2001.

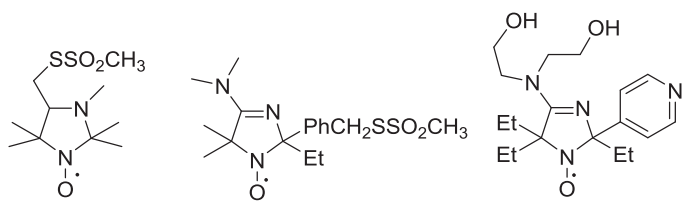

42 **43** **44**

Scheme 4.6 Chemical structures of NRs discussed in the text: thiol-specific pH-sensitive methanesulfonothioate labels **42** and **43**, and ethyl-substituted NR **44** with two ionizable groups.

pH-sensitive thiol-specific methanesulfonothioate NR labels **42** ($pK_a \approx 1.6$)[121] and **43** ($pK_a \approx 5.7$)[122] (Scheme 4.6) were developed and used in biophysical studies of surface electrostatics of lipid bilayers and proteins.[121,123–125]

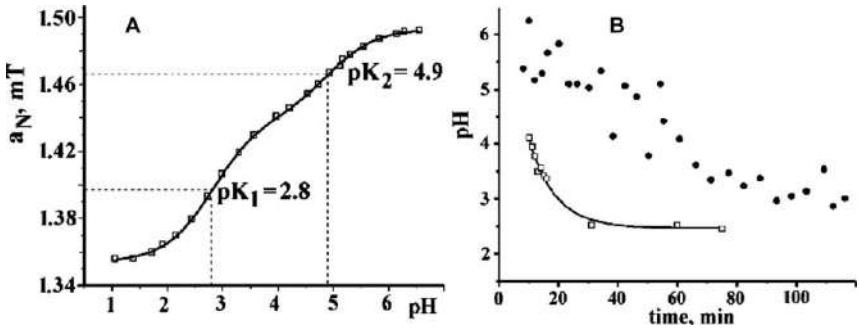

Figure 4.9 *In vivo* EPR monitoring of stomach acidity. (**A**) The pH dependence of hyperfine splitting, a_N, measured from EPR spectra of NR **44**. The solid line was calculated according to the standard titration equation for the compound with two ionizable groups. (**B**) Changes in the stomach acidity of living rat measured by longitudinally detected EPR spectrometer operated at 304 MHz excitation frequency, after giving 3 ml of gavage containing 5 mM NR **44** alone (□) or with 50 mM bicarbonate (●). Reproduced from ref. 135 with permission from Elsevier, Copyright 2006.

Significant efforts were devoted to the synthesis of pH-sensitive NRs for specific applications *in vivo*. Introduction of bulky substituents in α-position to the NO fragment was found to increase NR stability toward reduction, as has been demonstrated for 2,2,5,5-tetraethylimidazole NRs.[115] Further binding of ethyl-substituted NR to highly hydrophilic cell-impermeable tripeptide, glutathione, yields highly hydrophilic NR **37** that does not penetrate cellular membranes and reports specifically on extracellular pH (pH_e),[105] the latter being a prognostic marker in cancer progression. Partial deuteration of the ethyl groups in NR **38** ($\Delta H_{pp} = 1.2$ G) resulted in an about two-fold decrease in the linewidth compared with NR **37** ($\Delta H_{pp} = 2.1$ G) which is of critical importance for applications *in vivo*.[104]

A number of the NRs with two ionizable groups were synthesized to extend the range of pH sensitivity[126] similar to that observed for NR **36** (see a_N titration curve in Figure 4.7). For example, introduction of pyridine in the structure of imidazoline NR **44** results in extended pH sensitivity range from pH 1.5 to pH 6.2, which is useful for monitoring normalization of stomach acidity after the application of antacids (see Figure 4.9).

In summary, up to date a wide variety of pH-sensitive NRs have been developed with different ranges of pH sensitivity, labeling groups, lipophilicity and stability toward bioreduction.[23,102,104,115,126,127]

4.3.2 *In Vivo* Spectroscopy and Imaging of pH Using Nitroxide Probes

The critical role of pH status in physiology and pathophysiology of living organisms is well recognized. Local pH of the tissue microenvironment

critically affects the vital activities of cells. In its turn, intracellular pH is tightly regulated for optimal activities of cellular organelles and enzymes. Spatially and temporarily addressed pH measurements *in vivo* are of considerable clinical relevance. While pH assessment using ^{31}P-NMR of endogenous inorganic phosphate has proven to be the most suitable noninvasive approach, its limitations include lack of resolution (about 0.2–0.3 pH units and even less at lower pH), the fact that P_i concentrations vary with metabolism and ischemia, and its chemical shift dependence on ionic strength.[128,129] Because of these problems, exogenous pH probes are being designed for NMR spectroscopy to improve the detection of myocardial acidosis[128] and extracellular pH in tumors.[130,131] Upon application of exogenous probes, EPR spectroscopy has higher sensitivity compared with NMR for the same probe concentration, and reasonable depth of penetration in living tissues.

The low depth of microwave penetration does not allow X-band application *in vivo* but was found to be very effective for noninvasive pH measurements *in vitro* and *ex vivo*. Spectral-spatial X-band EPR using NR **33** has been applied for non-destructive and localized pH assessment in the microenvironment of biodegradable polymers used as drug delivery systems.[132] X-band EPR imaging of NRs **33** and **35** has been also applied for noninvasive direct and depth-specific measurement of pH within rat and human skin obtained from cosmetic surgery.[133] Phosphorylated NR **31** ($pK_a = 2.6$) was found to be sufficiently stable *in vivo* delivered in rat stomach *via* a thin Teflon cannula.[100] X-band EPR spectroscopy has been used to report pH in gastric fluid drawn from the stomach 30 min afterwards.

The first *in vivo* applications of spin pH probes were performed using L-band EPR spectroscopy in mice.[106,107] Mäder *et al.* demonstrated that L-band EPR spectroscopy is a valuable tool for *in vivo* monitoring of pH-induced degradation of an implanted polymer in mice.[107] Gallez *et al.*[106] demonstrated utility of the L-band EPR-spectroscopy using NR **35** ($pK_a = 4.7$) as a pH probe to monitor stomach acidity in mice after administration of different antacids. NR **35** has been also applied for *in vivo* studies of stomach acidity in rats using longitudinally detected 300 MHz EPR accompanied by mapping radical localization in the stomach using OMRI technique (also termed proton-electron double-resonance imaging, PEDRI).[134] Later, Potapenko *et al.* demonstrated advanced properties of NR **44** for *in vivo* monitoring of stomach acidity,[135] namely an about four-fold increase of radical lifetime *in vivo* compared with NR **35** due to steric protection of the NO fragment against bioreduction, extended range of pH sensitivity from pH 1.5 to pH 6.2 (Figure 4.9A), and highly hydrophilic structure that prevents its penetration through biomembranes and redistribution from the stomach. Figure 4.9B demonstrates real-time monitoring of the stomach acidity of living rats.[135] Long lifetime of NR **44** *in vivo* allows for monitoring drug-induced perturbation of stomach acidity and its normalization afterwards during 1 h or longer periods of time, therefore supporting applicability of pH-sensitive NRs to the studies of drug pharmacology and disease in living animals.

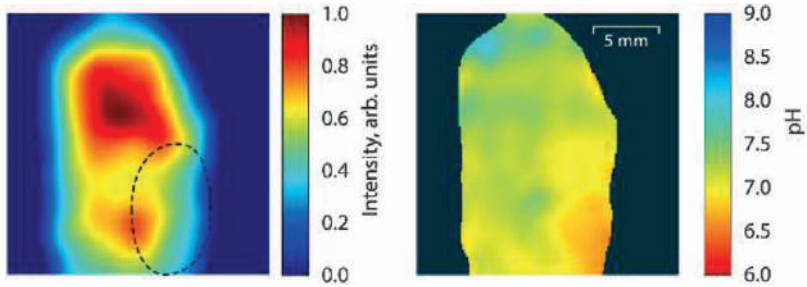

Figure 4.10 Coronal plane 3D (1 spectral/2 spatial) L-band EPR images of an isolated rat heart during regional ischemia. The heart was perfused in the presence of a 1 mM NR **44**. Left: Integral intensity of the EPR signal. The area indicated by the dashed line is expected to be ischemic. Right: pH map calculated from the spectral data of the image. Total image acquisition time, 39 min.
Reproduced from ref. 54 with permission from John Wiley & Sons, Copyright 2015 Wiley Periodicals, Inc.

NRs **37** and **38** ($pK_a = 6.6$) have been proven to be well suited to monitor and map tissue acidic areas in various animal models of diseases, such as ischemic heart disease and cancer.[54,103–105,136–138] Figure 4.10 shows pH mapping of isolated rat heart during regional ischemia obtained using L-band EPR imaging and NR **37**. The observed mean pH values of ischemic tissue were 6.7–6.8, whereas the pH of normally perfused tissue was 7.3–7.4, corresponding to the pH of the perfusate buffer. NR **37** demonstrated high stability in myocardial tissue, did not reveal any cardiotoxicity while providing high functional sensitivity.

NR **37** was applied in several studies to assess acidity of the tumor microenvironment (TME) using low-field EPR techniques. Bobko *et al.*[105,138] demonstrated utility of L-band EPR spectroscopy and NR **37** for *in vivo* monitoring of drug-induced changes in TME pH_e upon therapeutic intervention in various cancer models in mice. Goodwin *et al.*[137] reported changes in pH_e in response to X-ray irradiation in a mouse model of cancer measured using 750 MHz and NR **37**. These spectroscopic studies suggest that low-field EPR spectroscopy in combination with pH-sensitive NRs may offer a useful method for assessment of the physiological change in response to existing and novel cancer therapies.

NR **38**, being deuterated analogue of NR **37**, provides the advantage of narrow linewidth and better SNR, which is of particular importance for imaging application. Figure 4.11 demonstrates a pH map obtained with 750 MHZ EPR imager using NR **38** superimposed with 1.5 T MRI. A pH map obtained on day 5 (Figure 4.11C) reveals small acidic regions with pH_e about 6.6 which became significantly larger on day 8 (Figure 4.11D). The proposed EPR-based pH mapping method enabled quantitative visualization of regional changes in extracellular pH associated with altered tumor metabolism.

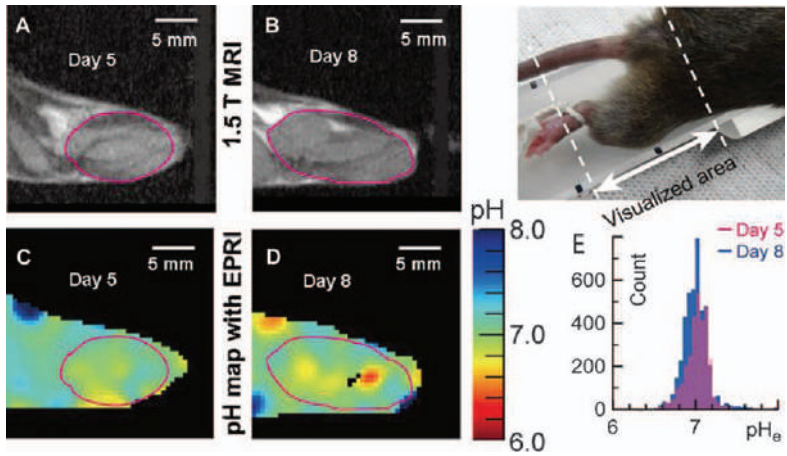

Figure 4.11 EPRI of the progress in acidosis in a SCC VII (murine squamous cell carcinoma) tumor-bearing mouse leg upon tumor growth. NR **38** (10 mg, 0.6 mmol kg^{-1} body weight) was intravenously injected as a bolus over the course of 30 s through a tail vein catheter. EPRI acquisition was started 2 min afterwards; acquisition time, 7.5 min. The photograph shows the mouse leg fixed on the plastic holder. T_2-weighted proton MR anatomical images of the mouse leg in the sagittal plane acquired at days 5 (**A**) and 8 (**B**) after tumor implantation, corresponding pH_e maps (**C** and **D**), and histograms of voxel-wise pH_e data (**E**) measured on days 5 (red) and 8 (blue) for a single mouse, are shown.
Reproduced from ref. 103 with permission from American Chemical Society, Copyright 2018.

Functional Overhauser-enhanced MRI provides an alternative to the EPR imaging approach for *in vivo* pH mapping. OMRI is based on the proton MRI acquired upon EPR irradiation of paramagnetic molecules,[139] the latter providing an enhancement of the NMR signal *via* transfer of polarization from electrons to protons by the Overhauser effect.[140] However, a conventional OMRI approach lacks EPR spectral information. The functional OMRI approaches, namely variable field[141] and variable radio frequency (VRF)[142] OMRI, allow for recovering of essential spectral information and functional mapping. In the case of VRF OMRI, a pH map is obtained from two OMRI acquisitions performed at EPR frequencies of protonated and unprotonated forms of a pH-sensitive probe.[142] Recently, OMRI of NR **38** has been used for extracellular TME pH mapping in mouse model of breast cancer.[104] Comparatively narrow spectral line of the partially deuterated NR **38** allowed for an increase of Overhauser enhancements and reduction in rf power deposition. *In vivo* OMRI pH mapping performed on breast tumor-bearing mice visualizes the areas of tissue acidosis in the TME with a mean pH_e value of about 6.8 ± 0.1 pH units compared to neutral mean pHe 7.1 ± 0.1 of the normal mammary glands. The authors suggest that OMRI pH mapping using NR probes may be a useful tool for spatially resolved

noninvasive extracellular pH monitoring in solid tumors in preclinical studies on small animals, and potentially in larger animals, including humans.

In summary, low-field EPR spectroscopy and imaging of pH in combination with pH-sensitive NRs provides a spatially and temporally addressed method for noninvasive *in vivo* assessment of local tissue microenvironment acidity in various animal models of diseases, including in response to therapeutic interventions.

4.4 NRs as Thiol-sensitive Probes

4.4.1 Basics of GSH Detection Using Nitroxide Probes

The redox state of thiols is an important parameter of prokaryotic and eukaryotic cells and is associated with all major biological processes.[143–147] Among the low-molecular-weight thiols, a ubiquitous thiol-containing tripeptide, glutathione (GSH), presents in virtually all mammalian tissues and plays a central role in cell biology. The intracellular GSH concentrations in mammalian cells are in the range between 1 and 10 mM and are close to half of the total thiol/disulfides in the cells. The redox couple of glutathione and its disulfide form, GSSG, is considered to be a major regulator of the intracellular redox status.[148,149] Reflecting the need to maintain a reduced environment in the nucleocytoplasm, the ratio [GSH]/[GSSG] exceeds 100 in resting cells, whereas in various models of oxidative stress this ratio was reported to be significantly lower.[150] In addition to its role as an intracellular redox regulator, GSH is also considered to be a major intracellular antioxidant. Therefore, substantial effort has been devoted to developing the methods and molecular probes for GSH assessment in biological systems, including *in vivo*.

The reactions of the NRs with GSH are of particular interest for designing GSH-specific NR probes for *in vivo* low-field EPR-based techniques. Appreciable chemical reduction of NRs into EPR-silent hydroxylamines by GSH does not occur over a few hours.[13,25,151–153] However, GSH can significantly contribute to NR reduction in biological systems indirectly by acting as a secondary source of reducing equivalents.[153] Taking into account that GSH is considered as a major intracellular redox buffer, the rate of NR reduction can be used as an indirect method for GSH detection and for *in vivo* evaluation of its role in normal and pathophysiology.[14,154,155] However, this approach has to be justified for each particular application by independent experiments supporting dominant or at least significant contribution of GSH in the reduction of the selected NR probe.

A large number of the NRs with specific reactivity to thiols have been synthesized. The nitroxide spin labels containing in their structures such thiol-reactive functionalities as maleimides,[156] iodoacetates and iodoacetamides,[157] isothiocyanate,[158] alkylhalide,[159] indanedione,[160] organomercurials[159] and alkylthiosulfonates[159,161] were previously synthesized and may

have advantages in some specific applications for the labeling of thiols. The synthesis of the methanethiosulfonate spin label by Hideg *et al.*[161] greatly facilitated the development of an important area of structural EPR, site-directed spin labeling. EPR spectroscopy in combination with thiol-specific NRs allows for determination of the accessible thiol groups in various biological macromolecules, such as human plasma low-density lipoproteins[162] and erythrocyte membranes.[163] This approach normally requires purification of the sample from the unbound label and cannot be used *in vivo*. Moreover, application of thiol-specific mononitroxides for direct EPR measurement of GSH is hardly possible due to insignificant EPR spectral changes of the NR upon binding to low-molecular-weight compounds. The latter limitation was overcome by the development of disulfide nitroxide biradicals,[25,164–166] RSSR (Scheme 4.7).

The RSSR biradicals represent paramagnetic analogues of Ellman's reagent, a chromogenic diaryl disulfide archetype of molecular probe for thiols detection.[167,168] EPR spectra of the RSSR probes are significantly affected by intramolecular spin exchange between two NR fragments resulting in the appearance of "biradical" spectral lines in addition to the conventional triplet of ^{14}N nitrogen manifolds of the mono-NRs (see Figure 4.12A). The appearance of additional lines can be qualitatively explained by contribution of the biradical conformations with intermediate or strong spin exchange between two monoradical fragments characterized by exchange integral, $J \geq a_N$. The EPR spectrum of subensemble of RSSR biradicals with both ^{14}N nuclei of NO fragments having the same spin projections (m_1,m_2: $+1,+1$; 0,0; and $-1,-1$) is not affected by spin exchange, therefore providing conventional triplet spectrum with relative intensities, 1 : 1 : 1. Fast spin exchange in subensembles with different nuclei spin orientations results in line coalescence and appearance of one line in the center for subensembles ($+1,-1$; and $-1,+1$) and two lines shifted by $a_N/2$ in both directions from the center for subensembles ($+1$,0; 0, $+1$; 0, -1; and -1,0), each of these three lines having relative intensity, 2. Therefore, a total superimposed spectrum is represented by the quintet, 1 : 2 : 3 : 2 : 1, with the splitting equal to $a_N/2$. In a general case, the spectrum of the nitroxide biradical is more complex, being represented by the superposition of the conformations with

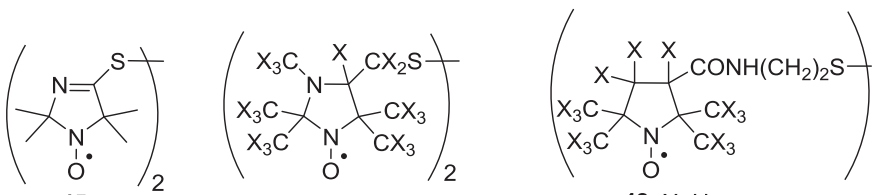

45

46 X=H

47 X=D, N-1=^{15}N

48 X=H

49 X=D, N-1=^{15}N

Scheme 4.7 The chemical structures of the disulfide nitroxide biradicals, RSSR, discussed in the text.

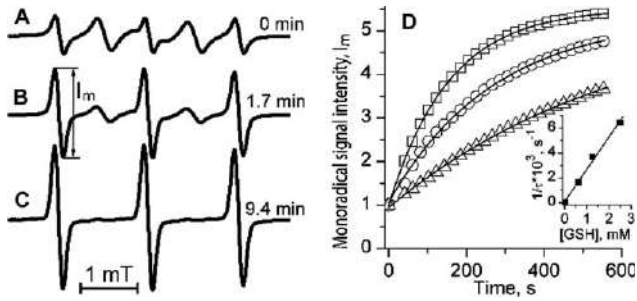

Figure 4.12 (**A–C**) The EPR spectra of 100 μM NR **46** measured at various time points after incubation with 2.5 mM GSH in 0.1 M Na-phosphate buffer, pH 7.2, at 34 °C. (**D**). The kinetics of the increase of amplitude of low-field monoradical component of the EPR spectrum, I_m, after addition of various GSH concentrations: 0.625 mM (Δ), 1.25 mM (○) and 2.5 mM (□). Lines represent the best fit of the experimental kinetics to the monoexponents. Insert: the dependence of inverse time constant of the exponential kinetics, $1/\tau$, on [GSH]. The linear regression ($1/\tau = k_{GSH} \times [GSH]$) provides the observed rate constant value of the reaction between GSH and NR **46**, k_{GSH} (pH 7.2, 34 °C) = 2.8 ± 0.2 $M^{-1} s^{-1}$.
Reproduced from ref. 105 with permission from John Wiley & Sons, Copyright 2011 Wiley Periodicals, Inc.

the different values of exchange integral and dynamics of conformational transitions, *e.g.*, the EPR spectrum of the imidazolidine biradical **46** (Figure 4.12A) is characteristic for the superposition of several biradical conformations with $J \approx a_N$.[164]

As can be seen in Figure 4.12C, the reaction of the disulfide biradical with an excess of GSH results in complete disappearance of biradical components due to splitting of the disulfide bond *via* thiol-disulfide exchange reaction and cancelation of intramolecular spin exchange between two monoradical fragments.[25] Corresponding increase of relative peak intensity of the monoradical components (I_m) is linear proportional to GSH concentration and can be used for the [GSH] measurements using a ''static'' EPR approach. Imidazoline biradical **45** and imidazolidine biradical **46** show three orders of magnitude difference in their observed rate constants with GSH, k_{GSH}, being about 5×10^3 $M^{-1} s^{-1}$ (pH 7.0, room temperature) and 2.8 $M^{-1} s^{-1}$ (pH 7.2, 34 °C), respectively.[25,164] Both probes have a lipophilic structure with the lipophilicity coefficient being equal to 175 for NR **45** and 240 for NR **46** allowing their fast diffusion through lipid bilayers.[164]

Fast-reacting NR **45** has found numerous application for *in vitro* EPR measurement of thiols, in particular GSH presented in cells in millimolar concentrations, using a ''static'' EPR approach. The method relies on application of the access of the probe over GSH and measures the relative increase of the monoradical EPR peak intensity I_m (Figure 4.12B) immediately after probe addition to the sample [the NR **45** easily penetrates cellular membrane and reacts with 1 mM GSH with characteristic time,

$\tau = 1/(k_{GSH} \times [GSH]) \approx 0.2$ s. The sensitivity of the method is sufficiently high to perform the measurements of GSH in a very few (≈ 100) cells.[169] NR **45** has been used to measure GSH in various cells and cellular homogenates,[25,169–171] animal and human blood[172,173] and isolated organs.[174] The described ''static'' EPR approach of GSH assessment has an advantage in its simplicity and represents a fast, highly sensitive, convenient and reliable approach for *in vitro* measurements in optically nontransparent samples. On the negative side, the approach is based on complete consumption of the vital thiols, therefore its application *in vivo* is hardly possible due to corresponding damage to cellular redox functions.

A slow-reacting NR **46** shows a reasonable time window for the reaction with millimolar GSH concentrations at neutral pH ($\tau = 1/(k_{GSH} \times [GSH]) \approx 6$ min at $[GSH] = 1$ mM) allowing for application of a ''kinetic'' EPR approach for GSH detection. Figure 4.12D shows the kinetics of an increase of I_m amplitude of NR **46** in the presence of different GSH concentrations. The inverse time constant of the observed exponential kinetics is proportional to the GSH concentration, and can be used as calibration for the [GSH] measurements. A major advantage of the ''kinetic'' approach is that it allows for using low probe concentration compared to analyte, [GSH], therefore minimizing potential probe toxicity. Isotopic substitution has been used to enhance SNR and functional sensitivity of the approach upon application of the ^{15}N-, ^{2}H-substituted NR **47**.[165]

Recently, pyrrolidine disulfide biradicals **48** and **49** were synthesized.[166] Compared with NRs **45** and **46**, NRs **48** and **49** have higher aqueous solubility (lipophilicity coefficients, 13.5) and longer characteristic time for GSH detection ($k_{GSH} = 0.747$ $M^{-1} s^{-1}$; $\tau = 1/(k_{GSH} \times [GSH]) \approx 20$ min at pH 7.2, 37 °C),[175] the latter allowing for a longer acquisition time of particular importance for imaging applications. Further studies are required to determine their potential for quantitative *in vivo* GSH detection, which strongly depends on the comparative contributions of the various factors into the EPR spectra change, namely the rates of probe reaction with GSH, probe penetration into the cells and probe reduction.

Disulfide trityl biradicals, including trityl-SS-NR and trityl-SS-trityl probes, were recently synthesized.[176] Note that their application for detection of intracellular GSH is hardly possible due to bulky cell-impermeable structure.

4.4.2 *In Vivo* EPR Measurements of Intracellular Glutathione

The methods allowing for assessment of tissue glutathione content *in vivo* might provide a useful indicator of disease risk in humans.[177] Magnetic resonance approaches for GSH detection have great potential for use *in vivo* due to sufficient depth of penetration in living tissue. The NMR approaches were developed to detect endogenous GSH but have limitations due to low sensitivity and difficulties in spectra analysis of numerous overlapping resonances.[178–181] Noninvasive *in vivo* EPR detection of GSH has an advantage over NMR in the absence of the endogenous background signals.

Kuppusamy *et al.* used NR **2** for L-band EPR imaging of tumor redox status of radiation-induced fibrosarcoma (RIF-1) tumor-bearing mice and demonstrated a significant decrease of the NR **2** reduction rate upon GS depletion after animal treatment with L-buthionine sulfoximine (BSO), inhibitor of GSH synthesis.[14] Recently Fujii *et al.* proposed to use 3-methoxycarbonyl-2,2,5,5-tetramethyl-piperidine-1-oxyl (**50**),[154,155] blood–brain barrier permeable NR,[182] for the noninvasive mapping of GSH in mouse brain indirectly through imaging of the NR **50** reduction rates. Pixel-based mapping of brain GSH levels was successfully obtained *in vivo* by using the linear relationship between NR **50** reduction rates in brain, measured by 750 MHz EPR imager, and brain GSH levels, measured by an *in vitro* biochemical assay.[155]

Kinetics-based EPR detection of GSH using nitroxide biradicals **46** and **47** is currently the only available noninvasive tool for direct quantitative measurements of intracellular GSH concentrations, *in vivo*. The method is based on the dominant contribution of GSH in the reaction with the disulfide biradicals, fast diffusion of the probes across cellular membrane and their comparatively low reduction rates.[105,164] Figure 4.13A shows typical *in vivo* L-band EPR spectra measured immediately after NR **46** probe intratumoral injection and 150 s after injection at the time point of maximal monoradical signal amplitude. Comparison of the integral intensities of the spectra shows less than 10% loss of the total EPR signal, supporting an insignificant contribution of the reduction and justifying approximation of

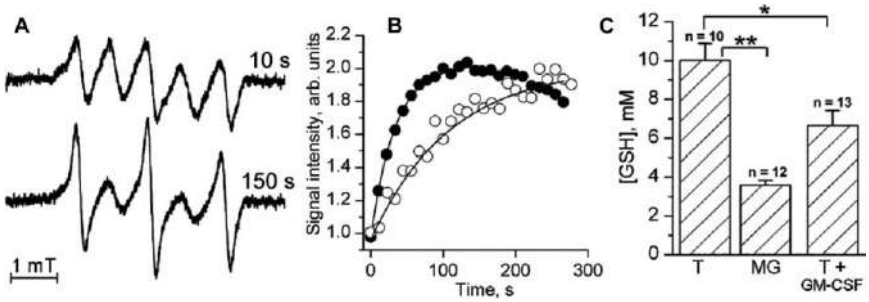

Figure 4.13 (**A**) L-band EPR spectra measured *in vivo* in mammary tumor of female FVB/N mice 10 s and 150 s after intratissue injection of NR **46**. (**B**) Kinetics of the monoradical peak intensity change measured in tumor (●) and normal mammary gland (○). The solid lines are the fits of the initial part of the kinetics by the monoexponent supposing k_{obs} (pH 7.2, 34 °C) = 2.8 M^{-1} s^{-1} and yielding [GSH] = 10.7 mM and 3.3 mM for the tumor and normal mammary gland, respectively. (**C**) Intracellular [GSH] measured using NR **46** *in vivo* in normal mammary glands (MG), mammary tumors (T) of female FVB/N mice and in tumors treated with anticancer agent, granulocyte macrophage colony-stimulating factor (T + GM-CSF) (*$p < 0.01$, **$p < 0.002$).
Reproduced from ref. 105 with permission from John Wiley & Sons, Copyright 2011 Wiley Periodicals, Inc.

the initial exponential signal increase by the reaction of **46** with GSH. Figure 4.13B shows the representative kinetics of the monoradical spectral peak intensity change measured in mammary tumor and normal mammary gland of female FVB/N mice. The analysis of the kinetics yields the values of GSH concentration to be about three-fold higher in tumor compared with that in mammary gland (Figure 4.13C). Treatment with anticancer drug, granulocyte macrophage colony-stimulating factor (GM-CSF) significantly inhibited tumor growth and decreased the GSH level in the tumor microenvironment. High levels of intracellular GSH in tumors are considered to be an important factor in tumor resistance to a variety of commonly used anticancer agents such as cisplatin.[183,184] The ^{15}N, ^{2}H-substituted disulfide NR **47** has been used to compare concentrations of GSH in cisplatin-resistant and cisplatin-sensitive tumors in ovarian tumor-bearing mice.[165] The authors obtained two-fold higher levels of GSH in cisplatin-resistant tumors compared with cisplatin-sensitive ones in agreement with previously reported data[185] supporting the role of GSH in tumor resistance to cisplatin treatment.

Recently, nitroxide biradical **49** was applied for mapping thiol redox status in murine tumors *in vivo* using 250 MHz rapid scan (RS) EPR imaging.[175] Analysis of the spectroscopic data (see Figure 4.14A) shows that only 40%–60% of the overall amount of NR **49** is converted to the monoradical after intratumoral injection, apparently due to significant probe bioreduction and/or binding to tissue components accompanied by spectrum broadening. The simplified kinetic analysis of the time dependences of the biradical and monoradical integral signal intensities of NR **49** yields the value of the pseudo-unimolecular rate constant of the disulfide bond cleavage, k_{obs}, therefore providing the estimate of GSH concentration supposing $k_{obs} \approx k_{GSH}[GSH]$. The estimates of [GSH] of 2.7–4.8 mM were obtained when measured in untreated control tumors and 1.5–2.1 mM when measured 24 h after treating mice with L-buthionine sulfoximine (BSO), an inhibitor of GSH synthesis. In the case of RS EPR imaging, to obtain detailed kinetics data the authors performed 3D spatial imaging of a single spectral point primarily arising from the monoradical component, therefore accelerating the image acquisition time to 35 s. Figure 4.14B shows a sagittal slice and histogram of k_{obs} image in FSa fibrosarcoma tumor of tumor-bearing C3H mice. Because of several factors contributing to the kinetics including disulfide bond cleavage, probe reduction/clearance and decline of thiols and GSH during the reaction due to high probe concentration of about 3–7 mM, the obtained k_{obs} maps provide rather qualitative imaging of thiol redox status of the tumor microenvironment than a quantitative measure of GSH concentrations. Nevertheless, the strong effect of BSO treatment on the rate constants k_{obs} shown in Figure 4.14C suggests a dominant contribution of GSH into observed kinetics.

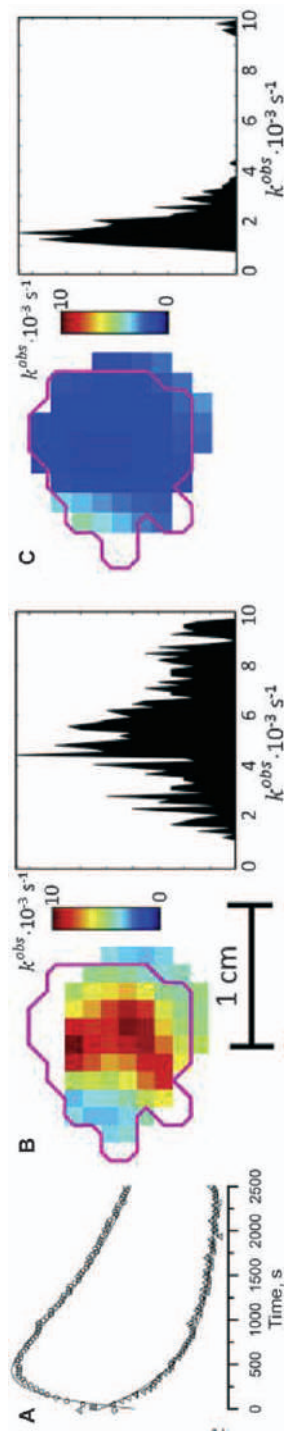

Figure 4.14 *In vivo* 250 MHz rapid scan (RS) EPR spectroscopy (**A**) and imaging (**B**, **C**) of NR **49** after intratumoral injection in FSa fibrosarcoma tumor-bearing C3H mice. (**A**) Time dependence of the biradical (triangles) and monoradical (circles) integral signal intensities obtained using spectra decomposition into biradical and monoradical components. The simplified kinetic analysis yields the value of the pseudo-unimolecular rate constant of the disulfide bond cleavage, k_{obs}, therefore providing the estimate of GSH concentration using approximation, $k_{obs} \approx k_{GSH}$[GSH]. (**B**, **C**) Sagittal slices and histograms of k_{obs} images in FSa tumor before (**B**) and 24 h after application of L-buthionine sulfoximine (BSO), inhibitor of GSH synthesis (**C**). The magenta outline shows the tumor border as obtained from a registered MRI image. The histograms show k_{obs} in all voxels of the tumor.
Reproduced from ref. 175 with permission from Elsevier, Copyright 2016.

4.5 NRs as Probes for Assessment of Enzymatically Catalyzed Reactions

Enzyme activities are important biomarkers of many pathologies, such as cancers, Alzheimer's disease or diabetes.[186–189] While reliable methods have been developed to measure enzyme concentration, expression and activity *in vitro* and *ex vivo*, the direct measurement of enzyme activity *in vivo* remains extremely challenging.[190]

The limited number of radical enzymes[191] and transient character of enzymatically generated radicals[192] dictate the necessity to design a paramagnetic substrate that undergoes EPR-sensitive enzymatic conversion to assess enzymatic activity by EPR. The reported EPR applications of the NR substrate analogues for the enzymatic activity assessment were based on monitoring the time-dependent spectra changes after enzymatic hydrolysis of paramagnetic substrate due to three major factors: (1) the change in rotation correlation time resulting in line broadening or alteration of spectral peak intensity ratio; (2) the canceling of spin exchange and/or dipole–dipole interaction between two radical fragments after bond cleavage resulting in spectral simplification; and (3) the difference in magnetic resonance parameters of the paramagnetic substrate and product. Nakaie *et al.* proposed several paramagnetic substrates of angiotensin I-converting enzyme (ACE), namely angiotensin I[193,194] and bradykinin[195] containing the stable NR amino acid **19**. The authors demonstrated the feasibility of monitoring the ACE activity by following the time-dependent EPR spectral change occurring during the enzymatic hydrolysis of the peptide bond of the NR-substrates. The enzymatic conversion of NR-substrate into a smaller NR-product with shorter rotation correlation time resulted in an increase of the ratio of spectral amplitudes of the central- and high-field components of the triplet EPR spectrum due to a weak linewidth narrowing. A much stronger effect of enzymatic hydrolysis on the motion correlation time and EPR linewidth of NR-substrates has been demonstrated for a number of NR-labeled proteins[196,197] providing a basis for *in vitro*[197] and *in vivo*[198] assessment of proteolytic activity using OMRI.

Hacker *et al.*[199] proposed the use of biradical substrates with two NRs connected *via* an enzyme-cleavable motif for the assessment of the activity of an enzyme of interest. As a proof of concept the authors synthesized an adenosine triphosphate (ATP) analogue, NR-ATP-NR, and demonstrated feasibility of EPR to monitor phosphoanhydride bond cleavage by phosphodiesterase I.

Audran *et al.*[30] proposed a new concept of NR-based assessment of hydrolytic activities of the enzymes based on the synthesis of enzymatically shifting NR-substrate prototype, enol ester of β-phosphorylated NR **51** (see Scheme 4.8). Upon enzymatic hydrolysis of the peptide, the enol ester moiety of NR **51** is converted into a ketone moiety of NR **52** accompanied by a large 400 μT change of the phosphorus hyperfine splitting allowing for EPR monitoring the enzymatic hydrolytic activity. In the following works,

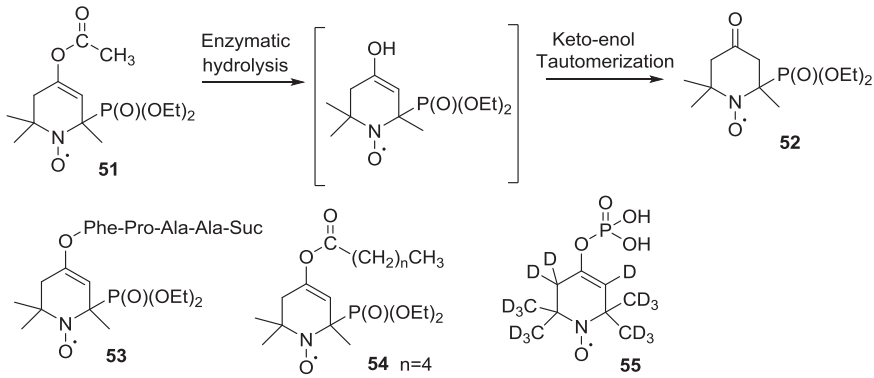

Scheme 4.8 The chemical structures of NRs **51–55** discussed in the text and a schematic illustration of the enzymatic hydrolysis of NR **51**.

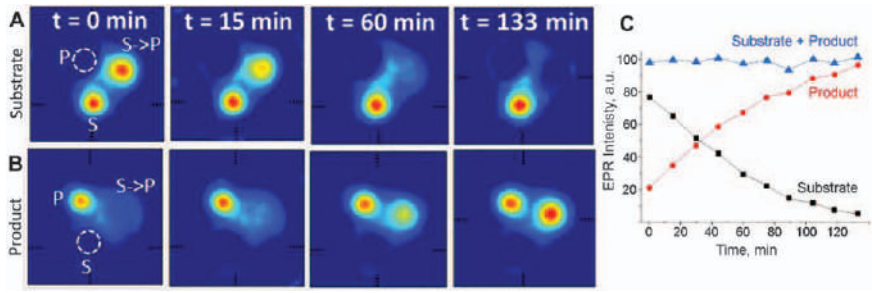

Figure 4.15 *In vitro* 4D spectral-spatial EPR imaging of alkaline phosphatase (ALP) activity. The images of the phantom consisting of the three tubes filled with solutions of substrate, NR **55** (S), its dephosphorylated product (P) and mixture of NR **55** with ALP (S → P) were acquired using an 800 MHz RS EPR imager at room temperature; acquisition time, 10 minutes; field of view, 18 mm; and matrix size, 64×64×64. The slices (*xz*-plane) of the images of EPR signal intensities of the substrate (**A**) and product (**B**) are shown. (**C**) Time evolution of EPR image integral intensities of substrate and product.
Reproduced from ref. 32 with permission from John Wiley & Sons, Copyright 2018 Wiley-VCH Verlag GmbH & Co. KGaA, Weinheim.

NR-labeled peptide **53** specific to the serine proteases chymotrypsin and cathepsin G,[31] and a series of fatty acid enol esters such as NR **54** specific for lipase activities[200] were synthesized.

Sanzhaeva *et al.*[32] proposed a phosphate enol ether of a deuterated NR **55** as paramagnetic substrate prototype for EPR imaging of enzymatic dephosphorylation, one of the key biological processes playing a critical role in physiology and pathophysiology. Dephosphorylation of **NR 55** is accompanied by keto–enol tautomerization similar to that shown for NR **51** in Scheme 4.8. The authors performed first *in vitro* RS EPR imaging of alkaline phosphatase activity with high specificity illustrated in Figure 4.15.

Note that direct monitoring of the enzyme-induced EPR line shift provides high specificity to the detection of the chemical reaction of interest allowing for easy discrimination from the other factors that may affect the motion correlation time or the spin exchange interaction. Audran *et al.*[30] demonstrated a potential of enzyme shifting NRs for mapping of enzymatic activity *in vivo* by OMRI using NR **51**. A mouse was fed with 0.2 ml of 24 mM solution of NR **51**. 3D OMRI images were acquired at 0.2 T at two EPR frequencies, 5425.7 MHz and 5417.5 MHz, corresponding to the EPR resonances of the substrate NR **51** and product of its hydrolysis NR **52**, respectively. The OMRI mapping using two EPR frequencies clearly revealed that digestive enzymes in the stomach and/or in the intestine were able to convert NR **51** into NR **52**. Despite the fact that acetyl nitroxide is a poor protease substrate compared to usual peptidic substrates, these pilot experiments confirm the feasibility of this approach for *in vivo* enzymatic studies.

The ability of EPR and OMRI to image enzymatic activities in non-transparent media, including blood and tissue samples, opens very promising opportunities for biomedical applications.

4.6 Conclusion

In recent decades, functional EPR spectroscopy and imaging have moved closer to biomedical applicability. The bottleneck of *in vivo* EPR-based applications is the requirement of appropriate paramagnetic probes. Due to the well-developed chemistry, the NRs provide a wide range of available structures that vary in solubility and tissue redistribution, spectral and functional sensitivity, ability to be targeted and lifetimes in living tissues. This chapter overviews the development of the NR probes that equip EPR-based spectroscopy and imaging with specific functional sensitivities, describes the backgrounds and recent progress in the NR applications for functional temporally and spatially resolved mapping of oxygen, acidity, glutathione content, and, potentially, specific tissue enzymatic activities. The NRs were the first compounds applied to EPR oximetry and remain a useful tool for *in vivo* tissue oxygen mapping. The imidazoline NR spin pH probes allowed for EPR spectroscopy and imaging of tissue pH in animal models of diseases such as cancer and ischemic heart disease. The developed disulfide NRs, in combination with low-field EPR-based spectroscopy and imaging, represent the only currently available method for *in vivo* noninvasive quantitative assessment of intracellular GSH concentrations. Recent synthesis of enzyme-shifting NRs demonstrates their potential utility to probe specific enzymatic activities in biological systems. A wide range of *in vivo* applications of the NRs as redox-sensitive probes is described in Chapter 13.

In summary, NRs represent a continuously expanding class of soluble paramagnetic probes for functional biomedical EPR spectroscopy and imaging applications.

Acknowledgements

This work was partially supported by NIH grants CA194013, CA192064 and U54GM104942. The WVCTSI is acknowledged for start-up to V.V.K. The content is solely the responsibility of the author and does not necessarily represent the official views of the NIH.

References

1. N. Edelstein, A. Kwok and A. H. Maki, *J. Chem. Phys.*, 1964, **41**, 179–183.
2. A. V. Il'yasov, *J. Struct. Chem.*, 1962, **3**, 84–86.
3. T. J. Stone, T. Buckman, P. L. Nordio and H. M. McConnell, *Proc. Natl. Acad. Sci. U. S. A.*, 1965, **54**, 1010–1017.
4. O. H. Griffith and H. M. McConnell, *Proc. Natl. Acad. Sci. U. S. A.*, 1966, **55**, 8–11.
5. C. Altenbach, S. L. Flitsch, H. G. Khorana and W. L. Hubbell, *Biochemistry*, 1989, **28**, 7806–7812.
6. W. L. Hubbell, D. S. Cafiso and C. Altenbach, *Nat. Struct. Mol. Biol.*, 2000, **7**, 735–739.
7. W. L. Hubbell, H. S. McHaourab, C. Altenbach and M. A. Lietzow, *Structure*, 1996, **4**, 779–783.
8. Y. N. Molin, K. M. Salikhov and K. I. Zamaraev, *Spin Exchange: Principles and Applications in Chemistry and Biology*, Springer-Verlag, Berlin, New York, 1980.
9. M. D. Rabenstein and Y. K. Shin, *Proc. Natl. Acad. Sci. U. S. A.*, 1995, **92**, 8239–8243.
10. J. M. Backer, V. G. Budker, S. I. Eremenko and Y. N. Molin, *Biochim. Biophys. Acta*, 1977, **460**, 152–156.
11. J. F. Glockner, S. W. Norby and H. M. Swartz, *Magn. Reson. Med.*, 1993, **29**, 12–18.
12. H. J. Halpern, C. Yu, M. Peric, E. Barth, D. J. Grdina and B. A. Teicher, *Proc. Natl. Acad. Sci. U. S. A.*, 1994, **91**, 13047–13051.
13. N. Kocherginsky and H. M. Swartz, *Nitroxide Spin Labels: Reactions in Biology and Chemistry*, CRC Press, 1995.
14. P. Kuppusamy, H. Li, G. Ilangovan, A. J. Cardounel, J. L. Zweier, K. Yamada, M. C. Krishna and J. B. Mitchell, *Cancer Res*, 2002, **62**, 307–312.
15. L. B. Volodarsky, V. A. Reznikov and V. I. Ovcharenko, *Synthetic Chemistry of Stable Nitroxides*, CRC Press, Boca Raton, Fla, 1994.
16. K. Hideg, T. Kalai and C. P. Sar, *J. Heterocycl. Chem.*, 2005, **42**, 437–450.
17. H. Karoui, F. Le Moigne, O. Ouari and P. Tordo, in *Stable Radicals: Fundamental and Applied Aspects of Odd-Electron Compounds*, ed. R. G. Hicks, John Wiley & Sons, Ltd., Chichester, UK, 2010, pp. 173–229.
18. V. V. Khramtsov, A. A. Bobko, M. Tseytlin and B. Driesschaert, *Anal. Chem.*, 2017, **89**, 4758–4771.

19. J. E. Baker, W. Froncisz, J. Joseph and B. Kalyanaraman, *Free Radical Biol. Med.*, 1997, **22**, 109–115.
20. B. Gallez, R. Debuyst, R. Demeure, F. Dejehet, C. Grandin, B. Van Beers, H. Taper, J. Pringot and P. Dumont, *Magn. Reson. Med.*, 1993, **30**, 592–599.
21. O. A. Lebedev, M. L. Khidekel and G. A. Razuvaev, *Dokl. Akad. Nauk SSSR*, 1961, **140**, 1327–1331.
22. M. B. Neiman, E. G. Rozatzev and Y. G. Mamedova, *Nature*, 1962, **196**, 472–474.
23. V. V. Khramtsov and L. B. Volodarsky, in *Spin Labeling: The Next Millennium*, ed. L. J. Berliner, Plenum Press, New York, vol. 14, 1998, pp. 109–180.
24. V. V. Khramtsov, L. M. Weiner, I. A. Grigor'ev and L. B. Volodarsky, *Chem. Phys. Lett.*, 1982, **91**, 69–72.
25. V. V. Khramtsov, V. I. Yelinova, L. M. Weiner, T. A. Berezina, V. V. Martin and L. B. Volodarsky, *Anal. Biochem.*, 1989, **182**, 58–63.
26. T. Akaike, M. Yoshida, Y. Miyamoto, K. Sato, M. Kohno, K. Sasamoto, K. Miyazaki, S. Ueda and H. Maeda, *Biochemistry*, 1993, **32**, 827–832.
27. J. Joseph, B. Kalyanaraman and J. S. Hyde, *Biochem. Biophys. Res. Commun.*, 1993, **192**, 926–934.
28. Y. Woldman, V. V. Khramtsov, I. A. Grigor'ev, I. A. Kiriljuk and D. I. Utepbergenov, *Biochem. Biophys. Res. Commun.*, 1994, **202**, 195–203.
29. A. A. Bobko, A. Ivanov and V. V. Khramtsov, *Free Radical Res.*, 2013, **47**, 74–81.
30. G. Audran, L. Bosco, P. Brémond, J. M. Franconi, N. Koonjoo, S. R. A. Marque, P. Massot, P. Mellet, E. Parzy and E. Thiaudière, *Angew. Chem., Int. Ed.*, 2015, **54**, 13379–13384.
31. I. Duttagupt, N. Jugniot, G. Audran, J. M. Franconi, S. R. A. Marque, P. Massot, P. Mellet, E. Parzy, E. Thiaudiere and N. Vanthuyne, *Chem. Eur. J*, 2018, **24**, 7615–7619.
32. U. Sanzhaeva, X. Xu, P. Guggilapu, M. Tseytlin, V. V. Khramtsov and B. Driesschaert, *Angew. Chem., Int. Ed.*, 2018, **57**, 11701–11705.
33. H. M. Swartz, *Antioxid. Redox Signaling*, 2004, **6**, 677–686.
34. G. E. Pake and T. R. Tuttle, *Phys. Rev. Lett.*, 1959, **3**, 423–425.
35. C. S. Lai, L. E. Hopwood, J. S. Hyde and S. Lukiewicz, *Proc. Natl. Acad. Sci. U. S. A.*, 1982, **79**, 1166–1170.
36. W. Froncisz, C. S. Lai and J. S. Hyde, *Proc. Natl. Acad. Sci. U. S. A.*, 1985, **82**, 411–415.
37. G. Bacic, M. J. Nilges, R. L. Magin, T. Walczak and H. M. Swartz, *Magn. Reson. Med.*, 1989, **10**, 266–272.
38. H. C. Chan, J. F. Glockner and H. M. Swartz, *Biochim. Biophys. Acta*, 1989, **1014**, 141–144.
39. J. S. Hyde and W. K. Subszynski, in *Spin Labeling: Theory and Application*, ed. L. J. Berliner and J. Reubens, Plenum Press, New York, vol. 8, 1989, pp. 399–425.

40. J. S. Hyde, J.-J. Jin, J. B. Felix and W. L. Hubbell, *Pure Appl. Chem.*, 1990, **62**, 255–260.
41. B. Epel and H. J. Halpern, *Methods Enzymol.*, 2015, **564**, 501–527.
42. T. Sarna, A. Duleba, W. Korytowski and H. Swartz, *Arch. Biochem. Biophys.*, 1980, **200**, 140–148.
43. N. Khan, J. P. Blinco, S. E. Bottle, K. Hosokawa, H. M. Swartz and A. S. Micallef, *J. Magn. Reson.*, 2011, **211**, 170–177.
44. V. V. Khramtsov and J. L. Zweier, in *Stable Radicals: Fundamentals and Applied Aspects of Odd-Electron Compounds* ed. R. Hicks, John Wiley & Sons, Ltd., Chichester, UK, 2010, pp. 537–566.
45. J. Shen, S. Bottle, N. Khan, O. Grinberg, D. Reid, A. Micallef and H. Swartz, *Appl. Magn. Reson.*, 2002, **22**, 357–368.
46. S. Anderson, K. Golman, F. Rise, H. Wikström and L.-G. Wistrand, *U. S. Pat.*, 5,530,140, 1996.
47. J. H. Ardenkjaer-Larsen, I. Laursen, I. Leunbach, G. Ehnholm, L. G. Wistrand, J. S. Petersson and K. Golman, *J. Magn. Reson.*, 1998, **133**, 1–12.
48. J. M. Weaver and K. J. Liu, *Med. Gas Res.*, 2017, **7**, 56–67.
49. F. Radner, A. Rassat and C. J. Hersvall, *Acta Chem. Scand.*, 1996, **50**, 146–149.
50. S. R. Burks, M. A. Makowsky, Z. A. Yaffe, C. Hoggle, P. Tsai, S. Muralidharan, M. K. Bowman, J. P. Y. Kao and G. M. Rosen, *J. Org. Chem.*, 2010, **75**, 4737–4741.
51. P. Kuppusamy, M. Chzhan, K. Vij, M. Shteynbuk, D. J. Lefer, E. Giannella and J. L. Zweier, *Proc. Natl. Acad. Sci. U. S. A.*, 1994, **91**, 3388–3392.
52. S. S. Velan, R. G. Spencer, J. L. Zweier and P. Kuppusamy, *Magn. Reson. Med.*, 2000, **43**, 804–809.
53. B. Gallez, G. Bacic, F. Goda, J. Jiang, J. A. O'Hara, J. F. Dunn and H. M. Swartz, *Magn. Reson. Med.*, 1996, **35**, 97–106.
54. A. A. Gorodetsky, I. A. Kirilyuk, V. V. Khramtsov and D. A. Komarov, *Magn. Reson. Med.*, 2016, **76**, 350–358.
55. Y. I. Glazachev, I. A. Grigor'ev, E. J. Reijerse and V. V. Khramtsov, *Appl. Magn. Reson.*, 2001, **20**, 489–505.
56. T. Yokoyama, A. Taguchi, H. Kubota, N. J. Stewart, S. Matsumoto, I. A. Kirilyuk and H. Hirata, *J. Magn. Reson.*, 2019, **305**, 122–130.
57. S. N. Dobryakov and Y. S. Lebedev, *Dokl. Akad. Nauk SSSR*, 1968, **182**, 68–70.
58. H. J. Halpern, M. Peric, C. Yu and B. L. Bales, *J. Magn. Reson. Ser. A*, 1993, **103**, 13–22.
59. Y. N. Molin, K. M. Salikhov and K. I. Zamaraev, *Spin Exchange: Principles and Applications in Chemistry and Biology*, Springer-Verlag, New York, 1980.
60. G. Redler, E. D. Barth, K. S. Bauer, J. P. Y. Kao, G. M. Rosen and H. J. Halpern, *Magn. Reson. Med.*, 2014, **71**, 1650–1656.
61. G. M. Rosen, S. R. Burks, M. J. Kohr and J. P. Y. Kao, *Org. Biomol. Chem.*, 2005, **3**, 645–648.

62. M. Miyake, J. G. Shen, S. M. Liu, H. L. Shi, W. L. Liu, Z. R. Yuan, A. Pritchard, J. P. Y. Kao, K. J. Liu and G. M. Rosen, *J. Pharmacol. Exp. Ther.*, 2006, **318**, 1187–1193.
63. J. P. Y. Kao, E. D. Barth, S. R. Burks, P. Smithback, C. Mailer, K. H. Ahn, H. J. Halpern and G. M. Rosen, *Magn. Reson. Med.*, 2007, **58**, 850–854.
64. M. Miyake, S. R. Burks, J. Weaver, P. Tsai, W. L. Liu, D. Bigio, K. S. Bauer, K. J. Liu, G. M. Rosen and J. P. Y. Kao, *J. Pharm. Sci.*, 2010, **99**, 3594–3600.
65. J. Weaver, S. R. Burks, K. J. Liu, J. P. Y. Kao and G. M. Rosen, *J. Magn. Reson.*, 2016, **271**, 68–74.
66. W. K. Subczynski, S. Lukiewicz and J. S. Hyde, *Magn. Reson. Med.*, 1986, **3**, 747–754.
67. K. J. Liu, M. W. Grinstaff, J. Jiang, K. S. Suslick, H. M. Swartz and W. Wang, *Biophys. J.*, 1994, **67**, 896–901.
68. X. A. Qiu, H. L. Zhao, R. H. Yu, J. F. Zhang and M. B. Lan, *Nanomedicine*, 2011, **6**, 225–231.
69. K. Graham and E. Unger, *Int. J. Nanomed.*, 2018, **13**, 6049–6058.
70. M. W. Dewhirst, E. T. Ong, R. D. Braun, B. Smith, B. Klitzman, S. M. Evans and D. Wilson, *Br. J. Cancer*, 1999, **79**, 1717–1722.
71. M. Hockel and P. Vaupel, *J. Natl. Cancer Inst.*, 2001, **93**, 266–276.
72. P. Vaupel, D. K. Kelleher and M. Hockel, *Semin. Oncol.*, 2001, **28**, 29–35.
73. P. Kuppusamy, M. Afeworki, R. A. Shankar, D. Coffin, M. C. Krishna, S. M. Hahn, J. B. Mitchell and J. L. Zweier, *Cancer Res.*, 1998, **58**, 1562–1568.
74. F. Hyodo, S. Matsumoto, N. Devasahayam, C. Dharmaraj, S. Subramanian, J. B. Mitchell and M. C. Krishna, *J. Magn. Reson.*, 2009, **197**, 181–185.
75. H. Kubota, D. A. Komarov, H. B. Yasui, S. Matsumoto, O. Inanami, I. A. Kirilyuk, V. V. Khramtsov and H. S. Hirata, *Magn. Reson. Mater. Phys.*, 2017, **30**, 291–298.
76. D. Grucker and J. Chambron, *Magn. Reson. Imaging*, 1993, **11**, 691–696.
77. M. C. Krishna, S. English, K. Yamada, J. Yoo, R. Murugesan, N. Devasahayam, J. A. Cook, K. Golman, J. H. Ardenkjaer-Larsen, S. Subramanian and J. B. Mitchell, *Proc. Natl. Acad. Sci. U. S. A.*, 2002, **99**, 2216–2221.
78. S. Matsumoto, H. Utsumi, T. Aravalluvan, K. Matsumoto, A. Matsumoto, N. Devasahayam, A. L. Sowers, J. B. Mitchell, S. Subramanian and M. C. Krishna, *Magn. Reson. Med.*, 2005, **54**, 213–217.
79. A. A. Gorodetskii, T. D. Eubank, B. Driesschaert, M. Poncelet, E. Ellis, V. V. Khramtsov and A. A. Bobko, *J. Magn. Reson.*, 2018, **297**, 42–50.
80. S. Kishimoto, M. C. Krishna, V. V. Khramtsov, H. Utsumi and D. J. Lurie, *Antioxid. Redox Signaling*, 2018, **28**, 1345–1364.
81. A. A. Bobko, I. Dhimitruka, T. D. Eubank, C. B. Marsh, J. L. Zweier and V. V. Khramtsov, *Free Radical Biol. Med.*, 2009, **47**, 654–658.
82. K. J. Liu, P. Gast, M. Moussavi, S. W. Norby, N. Vahidi, T. Walczak, M. Wu and H. M. Swartz, *Proc. Natl. Acad. Sci. U. S. A.*, 1993, **90**, 5438–5442.

83. T. Presley, P. Kuppusamy, J. L. Zweier and G. Ilangovan, *Biophys. J.*, 2006, **91**, 4623–4631.
84. R. B. Clarkson, B. M. Odintsov, P. J. Ceroke, J. H. Ardenkjaer-Larsen, M. Fruianu and R. L. Belford, *Phys. Med. Biol.*, 1998, **43**, 1907–1920.
85. V. Malatesta and K. U. Ingold, *J. Am. Chem. Soc.*, 1973, **95**, 6404–6407.
86. R. J. Smith and R. M. Pagni, *J. Org. Chem.*, 1981, **46**, 4307–4309.
87. B. M. Hoffman and T. B. Eames, *J. Am. Chem. Soc.*, 1969, **91**, 2169–2170.
88. E. F. Ullman and J. H. Osiecki, *J. Org. Chem.*, 1970, **35**, 3623–3631.
89. R. F. Haseloff, S. Zollner, I. A. Kirilyuk, I. A. Grigor'ev, R. Reszka, R. Bernhardt, K. Mertsch, B. Roloff and I. E. Blasig, *Free Radical Res.*, 1997, **26**, 7–17.
90. A. A. Bobko, E. G. Bagryanskaya, V. A. Reznikov, N. G. Kolosova, T. L. Clanton and V. V. Khramtsov, *Free Radical Biol. Med.*, 2004, **36**, 248–258.
91. J. C. Hsia and J. M. Boggs, *Biochim. Biophys. Acta*, 1972, **266**, 18–25.
92. A. T. Quintanilha and R. J. Mehlhorn, *FEBS Lett.*, 1978, **91**, 104.
93. G. A. A. Saracino, A. Tedeschi, G. D'Errico, R. Improta, L. Franko, M. Ruzzi, C. Corvaia and V. Barone, *J. Phys. Chem. A*, 2002, **106**, 10700–10706.
94. C. R. Nakaie, G. Goissis, S. Schreier and A. C. Paiva, *Braz. J. Med. Biol. Res.*, 1981, **14**, 173–180.
95. V. V. Khramtsov and L. M. Weiner, in *Imidazoline Nitroxides*, ed. and L. B. Volodarsky, CRC Press, Boca Raton, FL, vol. 2, 1988, pp. 37–80.
96. I. C. P. Smith, in *Biological Applications of Electron Spin Resonance*, ed. H. M. Swartz, J. R. Bolton and D. C. Borg, Wiley-Intersciences, New York, 1972, pp. 483–539.
97. R. N. Schwartz, M. Peric, S. A. Smith and B. L. Bales, *J. Phys. Chem. B*, 1997, **101**, 8735–8739.
98. A. E. Mathew and J. R. Dodd, *J. Heterocycl. Chem.*, 1985, **22**, 225–228.
99. D. L. Haire, E. G. Jansen, G. Chen, V. J. Robinson and I. Hrvoic, *Magn. Reson. Chem.*, 1999, **37**, 251–258.
100. S. Thetiot-Laurent, G. Gosset, J. L. Clement, M. Cassien, A. Mercier, D. Siri, A. Gaudel-Siri, A. Rockenbauer, M. Culcasi and S. Pietri, *Chembiochem*, 2017, **18**, 300–315.
101. V. V. Khramtsov, I. A. Grigor'ev, M. A. Foster, D. J. Lurie and I. Nicholson, *Mol. Cell. Biol.*, 2000, **46**, 1361–1374.
102. V. V. Khramtsov, *Curr. Org. Chem.*, 2005, **9**, 909–923.
103. D. A. Komarov, Y. Ichikawa, K. Yamamoto, N. J. Stewart, S. Matsumoto, H. Yasui, I. A. Kirilyuk, V. V. Khramtsov, O. Inanami and H. Hirata, *Anal. Chem.*, 2018, **90**, 13938–13945.
104. A. Samouilov, O. V. Efimova, A. A. Bobko, Z. Sun, S. Petryakov, T. D. Eubank, D. G. Trofimov, I. A. Kirilyuk, I. A. Grigor'ev, W. Takahashi, J. L. Zweier and V. V. Khramtsov, *Analyt. Chem.*, 2014, **86**, 1045–1052.

105. A. A. Bobko, T. D. Eubank, J. L. Voorhees, O. V. Efimova, I. A. Kirilyuk, S. Petryakov, D. G. Trofimiov, C. B. Marsh, J. L. Zweier, I. A. Grigor'ev, A. Samouilov and V. V. Khramtsov, *Magn. Reson. Med.*, 2012, **67**, 1827–1836.
106. B. Gallez, K. Mader and H. M. Swartz, *Magn. Reson. Med.*, 1996, **36**, 694–697.
107. K. Mader, B. Gallez, K. J. Liu and H. M. Swartz, *Biomaterials*, 1996, **17**, 457–461.
108. V. V. Khramtsov, *Antioxid. Redox Signaling*, 2018, **28**, 1365–1377.
109. R. Improta, G. Scalmani and V. Barone, *Chem. Phys. Lett.*, 2001, **336**, 349–356.
110. A. F. Gulla and D. E. Budil, *J. Phys. Chem. B*, 2001, **105**, 8056–8063.
111. L. N. Ikryannikova, L. Y. Ustynyuk and A. N. Tikhonov, *J. Phys. Chem. A*, 2004, **108**, 4759–4768.
112. V. V. Khramtsov, L. M. Weiner, S. I. Eremenko, O. I. Belchenko, P. V. Schastnev, I. A. Grigorev and V. A. Reznikov, *J. Magn. Reson.*, 1985, **61**, 397–408.
113. V. V. Khramtsov, I. A. Grigor'ev, M. A. Foster, D. J. Lurie, J. L. Zweier and P. Kuppusamy, *Spectroscopy*, 2004, **18**, 213–225.
114. V. V. Khramtsov, I. A. Grigor'ev, M. A. Foster and D. J. Lurie, *Antioxid. Redox Signaling*, 2004, **6**, 667–676.
115. I. A. Kirilyuk, A. A. Bobko, I. A. Grigor'ev and V. V. Khramtsov, *Org. Biomol. Chem.*, 2004, **2**, 1025–1030.
116. V. A. Reznikov, N. G. Skuridin, E. L. Khromovskikh and V. V. Khramtsov, *Russ. Chem. Bull.*, 2003, **52**, 2052–2056.
117. A. A. Bobko, T. D. Eubank, B. Driesschaert, I. Dhimitruka, J. Evans, R. Mohammad, E. E. Tchekneva, M. M. Dikov and V. V. Khramtsov, *Sci Rep*, 2017, **7**, 41233.
118. A. A. Gorodetskii, T. D. Eubank, B. Driesschaert, M. Poncelet, E. Ellise, V. V. Khramtsov and A. A. Bobko, *Sci. Rep.*, 2019, **9**, 12093.
119. A. A. Bobko, I. Dhimitruka, J. L. Zweier and V. V. Khramtsov, *Angew. Chem., Int. Ed.*, 2014, **53**, 2735–2738.
120. V. V. Khramtsov, D. Marsh, L. Weiner and V. A. Reznikov, *Biochim. Biophys. Acta*, 1992, **1104**, 317–324.
121. A. I. Smirnov, A. Ruuge, V. A. Reznikov, M. A. Voinov and I. A. Grigor'ev, *J. Am. Chem. Soc.*, 2004, **126**, 8872–8873.
122. M. A. Voinov, I. A. Kirilyuk and A. I. Smirnov, *J. Phys. Chem. B*, 2009, **113**, 3453–3460.
123. M. A. Voinov, A. Ruuge, V. A. Reznikov, I. A. Grigor'ev and A. I. Smirnov, *Biochemistry*, 2008, **47**, 5626–5637.
124. M. A. Voinov, I. Rivera-Rivera and A. I. Smirnov, *Biophys. J.*, 2013, **104**, 106–116.
125. M. A. Voinov and A. I. Smirnov, *Methods Enzymol.*, 2015, **564**, 191–217.
126. I. A. Kirilyuk, A. A. Bobko, V. V. Khramtsov and I. A. Grigor'ev, *Org. Biomol. Chem.*, 2005, **3**, 1269–1274.

127. M. A. Voinov, J. F. Polienko, T. Schanding, A. A. Bobko, V. V. Khramtsov, Y. V. Gatilov, T. V. Rybalova, A. I. Smirnov and I. A. Grigor'ev, *J. Org. Chem.*, 2005, **70**, 9702–9711.
128. S. Pietri, S. Martel, M. Culcasi, M. C. Delmas-Beauvieux, P. Canioni and J. L. Gallis, *J. Biol. Chem.*, 2001, **276**, 1750–1758.
129. R. J Gillies, J. R. Alger, J. A. den Hollander and R. G. Shulman, in *Intracellular pH: Its Measurement, Regulation and Utilization in Cellular Functions*, ed. R. Nuccitelli and D. W. Deamer, Alan R. Liss, New York, 1982, pp. 79–104.
130. R. J. Gillies, Z. Liu and Z. Bhujwalla, *Am. J. Physiol.*, 1994, **267**, C195–C203.
131. R. J. Gillies, N. Raghunand, M. L. Garcia-Martin and R. A. Gatenby, *IEEE Eng. Med. Biol. Mag.*, 2004, **23**, 57–64.
132. K. Mader, S. Nitschke, R. Stosser and H. H. Borchert, *Polymer*, 1997, **38**, 4785–4794.
133. C. Kroll, W. Hermann, R. Stosser, H. H. Borchert and K. Mader, *Pharm. Res.*, 2001, **18**, 525–530.
134. M. A. Foster, I. A. Grigor'ev, D. J. Lurie, V. V. Khramtsov, S. McCallum, I. Panagiotelis, J. M. Hutchison, A. Koptioug and I. Nicholson, *Magn. Reson. Med.*, 2003, **49**, 558–567.
135. D. I. Potapenko, M. A. Foster, D. J. Lurie, I. A. Kirilyuk, J. M. Hutchison, I. A. Grigor'ev, E. G. Bagryanskaya and V. V. Khramtsov, *J. Magn. Reson.*, 2006, **182**, 1–11.
136. D. A. Komarov, I. Dhimitruka, I. A. Kirilyuk, D. G. Trofimiov, I. A. Grigor'ev, J. L. Zweier and V. V. Khramtsov, *Magn. Reson. Med.*, 2012, **68**, 649–655.
137. J. Goodwin, K. Yachi, M. Nagane, H. Yasui, Y. Miyake, O. Inanami, A. A. Bobko, V. V. Khramtsov and H. Hirata, *NMR Biomed.*, 2014, **27**, 453–458.
138. A. A. Bobko, J. Evans, N. C. Denko and V. V. Khramtsov, *Cell Biochem. Biophys.*, 2017, **75**, 247–253.
139. D. J. Lurie, D. M. Bussell, L. H. Bell and J. R. Mallard, *J. Magn. Reson.*, 1988, **76**, 366–370.
140. A. W. Overhauser, *Phys. Rev.*, 1953, **92**, 411–415.
141. V. V. Khramtsov, G. L. Caia, K. Shet, E. Kesselring, S. Petryakov, J. L. Zweier and A. Samouilov, *J. Magn. Reson.*, 2010, **202**, 267–273.
142. O. V. Efimova, Z. Sun, S. Petryakov, E. Kesselring, G. L. Caia, D. Johnson, J. L. Zweier, V. V. Khramtsov and A. Samouilov, *J. Magn. Reson.*, 2011, **209**, 227–232.
143. L. B. Poole, *Free Radical Biol. Med.*, 2015, **80**, 148–157.
144. C. Kretz-Remy and A. P. Arrigo, *Methods Enzymol.*, 2002, **348**, 200–215.
145. J. S. Stamler and A. Slivka, *Nutr. Rev.*, 1996, **54**, 1–30.
146. Y. M. Go and D. P. Jones, *Crit. Rev. Biochem. Mol. Biol.*, 2013, **48**, 173–181.
147. W. Droge, *Exp. Gerontol.*, 2002, **37**, 1333–1345.
148. F. Q. Schafer and G. R. Buettner, *Free Radical Biol. Med.*, 2001, **30**, 1191–1212.

149. A. Pastore, G. Federici, E. Bertini and F. Piemonte, *Clin. Chim. Acta*, 2003, **333**, 19–39.
150. Y. C. Chai, S. S. Ashraf, K. Rokutan, R. B. Johnston, Jr and J. A. Thomas, *Arch. Biochem. Biophys.*, 1994, **310**, 273–281.
151. J. Glebska, J. Skolimowski, Z. Kudzin, K. Gwozdzinski, A. Grzelak and G. Bartosz, *Free Radical Biol. Med.*, 2003, **35**, 310–316.
152. E. Finkelstein, G. M. Rosen and E. J. Rauckman, *Biochim. Biophys. Acta*, 1984, **802**, 90–98.
153. A. A. Bobko, I. A. Kirilyuk, I. A. Grigor'ev, J. L. Zweier and V. V. Khramtsov, *Free Radical Biol. Med.*, 2007, **42**, 404–412.
154. M. C. Emoto, Y. Matsuoka, K. I. Yamada, H. Sato-Akaba and H. G. Fujii, *Biochem. Biophys. Res. Commun.*, 2017, **485**, 802–806.
155. M. C. Emoto, H. Sato-Akaba, Y. Matsuoka, K. Yamada and H. G. Fujii, *Neurosci Lett*, 2019, **690**, 6–10.
156. O. H. Griffith and H. M. Mcconnell, *Proc. Natl. Acad. Sci. U. S. A.*, 1966, **55**, 8.
157. J. Belagyi, I. Frey and L. Poto, *Eur. J. Biochem.*, 1994, **224**, 215–222.
158. F. Konczol, D. Lorinczy and J. Belagyi, *FEBS Lett.*, 1998, **427**, 341–344.
159. K. Hideg, T. Kalai and C. P. Sar, *J. Heterocycl. Chem.*, 2005, **42**, 437–450.
160. O. Roopnarine, K. Hideg and D. D. Thomas, *Biophys. J.*, 1993, **64**, 1896–1907.
161. L. J. Berliner, J. Grunwald, H. O. Hankovszky and K. Hideg, *Anal. Biochem.*, 1982, **119**, 450–455.
162. M. Kveder, A. Krisko, G. Pifat and H. J. Steinhoff, *Biochim. Biophys. Acta*, 2003, **1631**, 239–245.
163. M. Soszynski and G. Bartosz, *Free Radical Biol. Med.*, 1997, **23**, 463–469.
164. V. V. Khramtsov, V. I. Yelinova, I. Glazachev Yu, V. A. Reznikov and G. Zimmer, *J. Biochem. Biophys. Methods*, 1997, **35**, 115–128.
165. G. I. Roshchupkina, A. A. Bobko, A. Bratasz, V. A. Reznikov, P. Kuppusamy and V. V. Khramtsov, *Free Radical Biol. Med.*, 2008, **45**, 312–320.
166. E. A. Legenzov, S. J. Sims, N. D. A. Dirda, G. M. Rosen and J. P. Kao, *Biochemistry*, 2015, **54**, 6973–6982.
167. G. L. Ellman, *Arch. Biochem. Biophys.*, 1958, **74**, 443–450.
168. G. L. Ellman, *Arch. Biochem. Biophys.*, 1959, **82**, 70–77.
169. L. M. Weiner, H. Hu and H. M. Swartz, *FEBS Lett.*, 1991, **290**, 243–246.
170. A. Balcerczyk, A. Grzelak, A. Janaszewska, W. Jakubowski, S. Koziol, M. Marszalek, B. Rychlik, M. Soszynski, T. Bilinski and G. Bartosz, *Biofactors*, 2003, **17**, 75–82.
171. A. Balcerczyk and G. Bartosz, *Free Radical Res.*, 2003, **37**, 537–541.
172. V. Yelinova, Y. Glazachev, V. Khramtsov, L. Kudryashova, V. Rykova and R. Salganik, *Biochem. Biophys. Res. Commun.*, 1996, **221**, 300–303.
173. V. I. Yelinova, V. V. Khramtsov and A. L. Markel, *Biochem. Biophys. Res. Commun.*, 1999, **263**, 450–453.

174. H. Nohl, K. Stolze and L. M. Weiner, *Methods Enzymol.*, 1995, **251**, 191–203.
175. B. Epel, S. V. Sundramoorthy, M. Krzykawska-Serda, M. C. Maggio, M. Tseytlin, G. R. Eaton, S. S. Eaton, G. M. Rosen, J. P. Y. Kao and H. J. Halpern, *J. Magn. Reson.*, 2017, **276**, 31–36.
176. Y. P. Liu, Y. G. Song, A. Rockenbauer, J. Sun, C. Hemann, F. A. Villamena and J. L. Zweier, *J. Org. Chem.*, 2011, **76**, 3853–3860.
177. R. Franco, O. J. Schoneveld, A. Pappa and M. I. Panayiotidis, *Arch. Physiol. Biochem.*, 2007, **113**, 234–258.
178. J. C. Livesey, R. N. Golden, E. G. Shankland, Z. Grunbaum, M. Wyman and K. A. Krohn, *Int. J. Radiat. Oncol.*, 1992, **22**, 755–757.
179. M. Terpstra, P. G. Henry and R. Gruetter, *Magn. Reson. Med.*, 2003, **50**, 19–23.
180. J. A. Willis and T. Schleich, *Bba-Mol. Cell Res.*, 1995, **1265**, 1–7.
181. A. H. Trabesinger, O. M. Weber, C. O. Duc and P. Boesiger, *Magn. Reson. Med.*, 1999, **42**, 283–289.
182. K. Anzai, K. Saito, K. Takeshita, S. Takahashi, H. Miyazaki, H. Shoji, M. C. I. Lee, T. Masumizu and T. Ozawa, *Magn. Reson. Imaging*, 2003, **21**, 765–772.
183. C. A. Rabik and M. E. Dolan, *Cancer Treat. Rev.*, 2007, **33**, 9–23.
184. A. Bratasz, K. Selvendiran, T. Wasowicz, A. Bobko, V. V. Khramtsov, L. J. Ignarro and P. Kuppusamy, *J. Transl. Med.*, 2008, **6**, 9.
185. F. Y. F. Lee, A. Vessey, E. Rofstad, D. W. Siemann and R. M. Sutherland, *Cancer Res*, 1989, **49**, 5244–5248.
186. K. Gu, Y. Xu, H. Li, Z. Guo, S. Zhu, S. Zhu, P. Shi, T. D. James, H. Tian and W.-H. Zhu, *J. Am. Chem. Soc.*, 2016, **138**, 5334–5340.
187. E. I. Deryugina and J. P. Quigley, *Biochim. Biophys. Acta, Mol. Cell Res.*, 2010, **1803**, 103–120.
188. U. Sharma, D. Pal and R. Prasad, *Indian J. Clin. Biochem.*, 2014, **29**, 269–278.
189. M. Gidh-Jain, J. Takeda, L. Z. Xu, A. J. Lange, N. Vionnet, M. Stoffel, P. Froguel, G. Velho, F. Sun and D. Cohen, *Proc. Natl. Acad. Sci.*, 1993, **90**, 1932–1936.
190. D. V. Hingorani, B. Yoo, A. S. Bernstein and M. D. Pagel, *Chem. - Eur. J.*, 2014, **20**, 9840–9850.
191. G. Jeschke, *Biochim. Biophys. Acta*, 2005, **1707**, 91–102.
192. B. E. Sturgeon, Y. R. Chen and R. P. Mason, *Anal. Chem.*, 2003, **75**, 5006–5011.
193. L. G. de Deus Teixeira, P. A. Bersanetti, S. Schreier, A. K. Carmona and C. R. Nakaie, *FEBS Lett.*, 2007, **581**, 2411–2415.
194. L. G. Teixeira, L. Malavolta, P. A. Bersanetti, S. Schreier, A. K. Carmona and C. R. Nakaie, *PLoS One*, 2015, **10**, e0136608.
195. L. G. Teixeira, L. Malavolta, P. A. Bersanetti, S. Schreier, A. K. Carmona and C. R. Nakaie, *Bioorg. Chem.*, 2016, **69**, 159–166.
196. P. Mellet, P. Massot, G. Madelin, S. R. Marque, E. Harte, J. M. Franconi and E. Thiaudiere, *PLoS One*, 2009, **4**, e5244.

197. E. Parzy, V. Bouchaud, P. Massot, P. Voisin, N. Koonjoo, D. Moncelet, J. M. Franconi, E. Thiaudiere and P. Mellet, *PLoS One*, 2013, **8**, e57946.
198. N. Koonjoo, E. Parzy, P. Massot, M. Lepetit-Coiffe, S. R. Marque, J. M. Franconi, E. Thiaudiere and P. Mellet, *Contrast Media Mol. Imaging*, 2014, **9**, 363–371.
199. S. M. Hacker, C. Hintze, A. Marx and M. Drescher, *Chem. Commun.*, 2014, **50**, 7262–7264.
200. G. Audran, S. Jacoutot, N. Jugniot, S. R. A. Marque and P. Mellet, *Anal. Chem.*, 2019, **91**, 5504–5507.

CHAPTER 5

Nitroxides in Battery-related Applications

B. ERNOULD AND J.-F. GOHY*

Catholic University of Louvain (UCLouvain), Institute of Condensed Matter and Nanosciences (IMCN), Place L. Pasteur 1, 1348, Louvain-la-Neuve, Belgium
*Email: jean-francois.gohy@uclouvain.be

5.1 Context

Regarding our future energy economy, the trend toward more sustainable development is not only affecting energy production and its consumption but also every system found in between, such as portable energy sources. Cleaner energy storage solutions should be developed with the aim of eliminating CO_2 releases during their production. In addition, their design as well as their components should be revisited to rely on renewable raw materials.

Current lithium-ion battery (LIB) technologies mostly rely on the use of electroactive components (*e.g.* $LiCoO_2$, $LiNiO_2$) that could hardly be considered as green, their production and recycling being responsible for significantly high CO_2 releases.[1] The renewability of natural resources is another point of concern as they are relatively scarce, which would render their production even more energy intensive in the future.

In this context, electroactive organic materials may offer intrinsic advantages over their inorganic counterparts,[1] since their syntheses can generally be carried out at lower temperatures, and also they are based on

Nitroxides
Edited by Olivier Ouari and Didier Gigmes

Published by the Royal Society of Chemistry, www.rsc.org

more abundant elements (C, H, O, N, S in particular), that can be potentially generated *via* CO_2 capture or from renewable resources such as biomass. Additionally, owing to their organic nature and the absence of heavy metals, their end-of-life disposal can be facilitated by combustion, for instance.

As other advantages, there are numerous accessible chemical combinations, some of them being multielectron reaction materials. Furthermore, the variety of accessible structures allows to tailor their redox properties *via* the introduction of groups. This can advantageously provide either low- or high-potential materials without altering the underlying chemistry and enables tuning of the resulting battery voltage. As for their performances, high rates are often achievable thanks to the simple redox reactions in contrast, for instance, to complex mechanisms of intercalation compounds.[2] Regarding processing, organic materials of polymeric nature are potentially flexible and compatible with efficient industrial processing such as roll-to-roll techniques. Yet, in order to raise their competitiveness, some of their characteristics are posing challenges that need to be overcome, either *via* the use of original strategies or the development of new materials with more desirable properties. Among the challenges to be faced, organic materials usually display lower thermal stability and lower volumetric energy density. Additionally, they often display a finite solubility in common battery electrolytes for LIBs. This drawback is frequently sought to be mitigated *via* new electrolyte formulation or the incorporation of electrochemical moieties in polymer and organic salts.

Regarding the electroactive compound nature, all organic molecules that undergo reversible redox reactions are in principle suitable candidates for electrode materials. Because of the large assortment and variety of these materials, different classifications can be applied. They can notably be classified according to their chemical functionality or structure and also according to redox reaction directions, *i.e.*, oxidation and/or reduction, that are accessible to the electroactive base material. The former classification will be used in this chapter to provide an overview of a selection of materials. The latter classification is defined here because of the consequences related to the material class properties with respect to its implementation in an actual battery. In this classification (Figure 5.1), three categories of materials are distinguished: p-type organics (P^+/P) yield cations upon oxidation, whereas n-type organics (N/N^-) yield anions upon reduction, and b-type organics ($B^+/B/B^-$) can be both oxidized and reduced.[3]

Organic compounds have mostly their redox potentials ranging roughly between 2 V and 4 V, which makes them usually more suitable as a cathode than anode.[4] Materials of every class can be theoretically used at the positive or the negative electrode, but as a general rule of thumb, p-type organics display higher redox potentials than n-type ones. Whether the active compounds behave as a positive or negative electrode material depends on their redox potential and on that of the particular counter

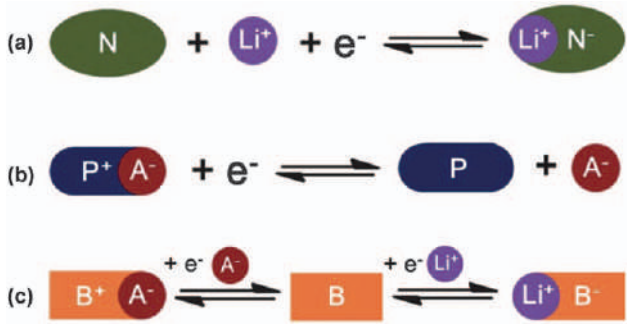

Figure 5.1 The redox reaction of three types of electroactive organics: (a) n-type; (b) p-type; (c) bipolar. A^- stands for an anion of the electrolyte. Li^+ can be replaced by other alkali ions.
Reproduced from ref. 3 with permission from the Royal Society of Chemistry.

electrode. As a large potential difference is commonly desirable, it influences the choice of respective materials to be implemented within the set of electrodes. Most of the electroactive organics are processed in the uncharged state. As for n-type materials, they are potentially Li^+ exchanging materials.

Yet Li^+N^- is most often unstable in an ambient atmosphere because of the spontaneous hydrolysis reaction and oxidation reaction, especially when the N/N^- redox potential is lower than 2.5 V *vs.* Li/Li^+.[3]

Therefore, for implementation with conventional LIB materials, the oxidized uncharged form is more suitable as a negative electrode material, otherwise as a positive electrode material they need to be processed in the reduced state, which may require a pretreatment.[5]

P-type materials in their reduced state are intrinsically compatible with traditional LIB-negative materials. Yet the positive electrode is not exchanging Li^+ cations. In the present case, the mechanism of operation involves both ions from the electrolyte, thus the cell is by definition a dual-ion cell. There lies a major difference with LIBs which are based on the rocking chair principle. Additionally, the resulting hybrid batteries are better called lithium batteries or lithium metal batteries when the negative electrode is lithium metal. Since the electrolyte is not just an ion-transferring medium, a practical consequence is that the salt concentration is decreased upon charging. Because of the charge compensation, this may affect performances of the system under operation and requires an excess of lithium salt that has a non-negligible impact on the volumetric capacity of the cell.[6] In the case of all-organic cells, p-type match well with n-type materials, as positive and negative electrode materials, respectively, provided they are processed in the same state of charge. If both electrodes are of the same type, cell assembly is then carried out so that one electrode material is in the oxidized state, while the other is in the reduced state. This is a common strategy in the case of all-organic cells.

5.2 Organic Batteries Based on Nitroxide Radicals

The purpose of the present section is to focus on oxygen-centered radical compounds and more specifically those involving nitroxide functional groups. Nitroxide-based polymers are widely acknowledged as the most studied radical compounds for electrode applications. Nitroxides are potentially able to undergo reversible reduction to an n-doped aminoxyl anion and/or a reversible oxidation to a p-doped oxoammonium cation (Figure 5.2). To allow stability of the nitroxide group, bulky substituents such as alkyl groups are usually surrounding the radical. The most representative example of stable nitroxides as a small molecule is 2,2,6,6-tetramethylpiperidine-1-oxyl (TEMPO), which has found numerous applications as a probe for biological systems, a radical trap, a catalyst in inorganic oxidation reactions, a mediating species for controlled radical polymerization, *etc.*[7–12]

Studies on nitroxides for energy applications kicked off in 2002 with the first report on their use as positive electrode material by Nakahara *et al.*, which employed poly(2,2,6,6-tetramethylpiperidinyloxy-4-ylmethacrylate) (PTMA). PTMA bears TEMPO units as redox-active side-groups (Figure 5.3).[13] This compound displays a theoretical capacity of 111 mA h g^{-1} and affords flat charge/discharge plateaus centered at 3.6 V *vs.* Li/Li^+. In their report, the group synthesized PTMA starting from its amine precursor, obtained *via* free-radical polymerization of 2,2,6,6-tetramethylpiperidine methacrylate monomer (TMPM), and subsequently oxidized with 3-chloroperoxybenzoic acid into the redox-active form. PTMA later became one of the most studied of its class, and many other groups reported their own synthesis strategies, relying on techniques such as atom transfer radical polymerization (ATRP),[14–16] reversible addition–fragmentation chain-transfer polymerization (RAFT),[16] group-transfer polymerization (GTP),[17] single-electron transfer-living radical polymerization (SET-LRP)[18] and nitroxide-mediated polymerization (NMP).[16]

One of the most distinctive of such nitroxide compounds with respect to other electroactive materials, whether they are organic or inorganic, is the high-rate capability. Kinetic studies have evidenced very fast reaction rates with electron transfer rates constants of about 10^{-1} cm s^{-1},[19] surpassing the value of ferrocene 10^{-2} cm s^{-1},[6] a well-known internal calibrator in electrochemistry. Such high kinetics can be explained by structural aspects; the nitroxide radical hybridized orbital was found to exhibit a character in-between pure sp^2 and sp^3 of oxoammonium cation and amine, respectively.

Figure 5.2 n- and p-Doping mechanism of nitroxide compounds in the presence of a lithium-based electrolyte.

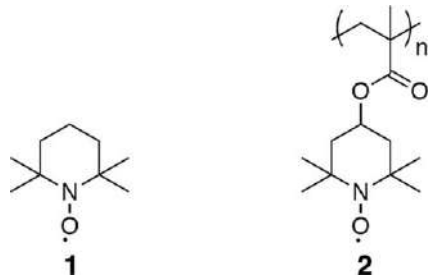

Figure 5.3 Chemical structures of two main representatives of nitroxide radicals: 2,2,6,6-tetramethylpiperidine-1-oxyl (1, TEMPO), and poly(2,2,6,6-tetramethylpiperidinyloxy-4-yl methacrylate) (2, PTMA).

The structure thus experiences minimal structural changes upon oxidation in addition to the absence of bond cleavage/formation, both being beneficial for the reaction rates.

As for the electron transfer within a radical polymer composite, five processes are potentially rate-determining steps: the interfacial charge transfer between the current collector and the conductive filler, the electric conduction in the conductive filler network, the heterogeneous charge transfer at the conductive filler/polymer interface, the electron hopping between redox groups within the bulk polymer layer and the diffusion of electrolyte counter-ions throughout the composite.[6]

As the first two processes are usually smooth, research is more focusing on the last three factors. In particular, owing to their insulating behavior, the charge transfer is regarded as sluggish and can be the rate-limiting step to the propagation of the redox process within the bulk polymer. Therefore, the electrodes typically incorporate conductive fillers – as much as 70 wt% in the earlier reports – to support the redox process,[20] especially at the very high rates that the nitroxide redox kinetics can potentially deliver.

The last electron transfer process, counter-ion diffusion, is another limiting parameter at very high current densities and hence can prevent full material utilization. It is worth noting that from that standpoint the charge process can be slightly less efficient than the discharge process because the concentration of the electrolyte salt drops to a minimum at the fully discharged state.[6] As for the cyclability of nitroxide-based polymer electrodes, the redox species are regarded as offering good long-term cycling stability (>1000 cycles). Nevertheless, even high-molecular-weight polymers of this class are usually soluble in standard organic solutions,[17,20] leading to the so-called shuttle effect – and related self-discharge issues – as well as considerable initial irreversible capacity loss. In that respect, conductive carbon additives generally serve an additional purpose to their charge collection enhancement role, that is, adsorbing soluble species and hence retarding the effects of the slow dissolution of active materials.[21]

5.3 Variations of Nitroxide Polymer Structures and Their Related Properties

Thanks to their many promising properties, nitroxides have enjoyed vivid interest as evidenced by many different related structures proposed in the literature. Some of them were designed to cope with the relatively low theoretical capacity of PTMA (111 mA h g^{-1}) in comparison with common inorganic electrode materials (140 mA h g^{-1} to 170 mA h g^{-1}). This value drops to 70 mA h g^{-1} when the weight of the counter-anion is considered (assuming it to be PF_6^-).

Some of these variations have been designed to simplify the polymer motif or to increase the redox-active group over molecular weight ratio (per repeating unit). An example of such a structure with a higher theoretical capacity is poly(2,2,6,6-tetramethylpiperidine-*N*-oxyl-4-vinyl ether) (Figure 5.4; PTVE, 135 mA h g^{-1}).[22,23]

Other attempts have also been made to improve the rate capabilities. For instance, a conjugated backbone is expected to exhibit semiconductivity and enhance charge transport properties. This strategy has been applied to the design of polyacetylene derivatives such as the one displayed in Figure 5.4.[24,25] Another example is the polyether derivative (Figure 5.4) displaying a flexible and ionophoric backbone obtained from an epoxide-functionalized TEMPO monomer.[26] Structural variations have also been brought to modulate the potential of the redox groups. As for the p-type doping, the tuning can only be achieved over a limited potential window (3.5 V to 3.8 V *vs.* Li/Li^+).[6] The potential of the n-type is more interesting from an application standpoint as it can bring nitroxides to be implemented as negative electrode materials. Furthermore, there is the possibility to assemble an all-polymer cell thanks to a reasonable potential difference (around 1.0 V) accessible with variations of

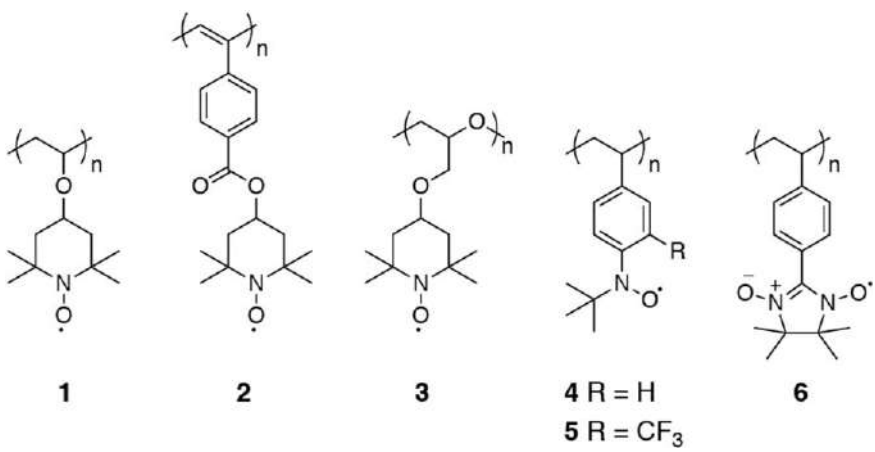

Figure 5.4 Chemical structure variations of nitroxide-based polymers: (1) poly(2,2,6,6-tetramethylpiperidine-*N*-oxyl-4-vinyl ether) (PTVE), (2) polyacetylene derivative, (3) polyether derivative, (4 and 5) poly(nitroxylstyrene) derivatives, and (6) poly(nitronylnitroxide) derivative.

poly(nitroxylstyrenes): one using a structure displaying its p-doping redox activity at a higher redox potential (positive electrode) and the second with a structure bearing trifluoromethyl groups optimized for its n-doping process at lower potential (negative electrode) (Figure 5.4).[27] Another point of interest regarding n-doping is the design of structures that can be both reversibly n-doped and p-doped such as the poly(nitronylnitroxide) reported by Suga *et al.* (Figure 5.4), which displays its redox activity at 2.33 V *vs.* Li/Li^+ and 3.60 V *vs.* Li/Li^+. This n-doping process is then of practical interest for positive electrode applications thanks to its higher overall theoretical capacity of 206 $mA\,h\,g^{-1}$ considering both redox processes.[28]

Density functional theory (DFT) has been used to predict the voltage of PTMA-based radical molecules.[29]

Using this predictive approach, newly designed radicals were investigated. Starting from the PTMA molecule, the methyl groups around the nitroxide center were substituted with various functional groups in order to study their effects on the redox potential.[30] The $-OCH_3$ electron-donating group (EDG) as well as various electron-withdrawing groups (EWGs), –H, $-CH_2OH$, $-CH_2Br$, $-CBr_3$, $-CH_2Cl$, $-CCl_3$, $-NO_2$, $-CH_2F$, $-CHF_2$, $-CF_3$ and –F, were investigated. Since the reference is the methyl group, the –H and $-CH_2OH$ groups were considered in the EDG category. In Figure 5.5a, the four possible positions of the methyl groups are named A, B, C and D. Since the PTMA polymer is modeled with the simpler TEMPO radical, these four

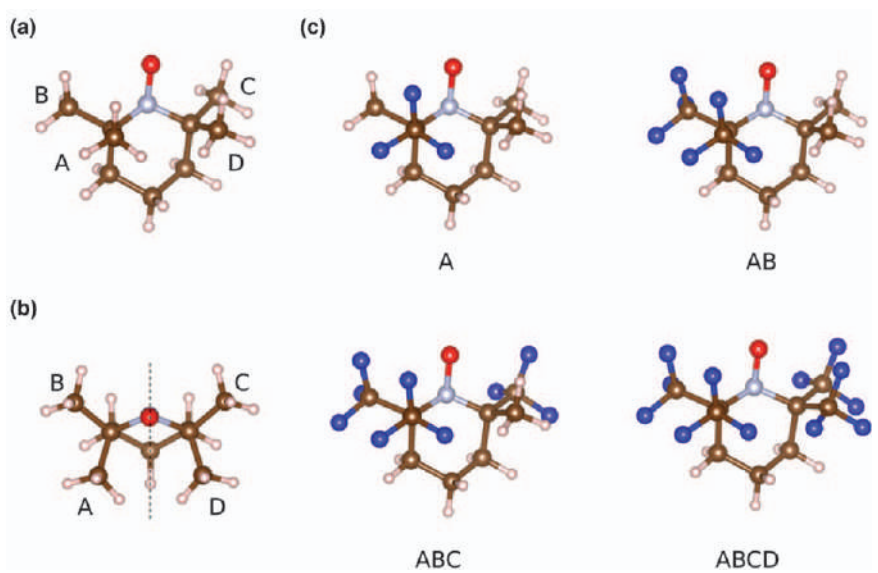

Figure 5.5 (a) TEMPO molecule with the four positions (A, B, C and D) of the methyl groups around the nitroxide center. (b) Top view of the TEMPO radical illustrating the mirror symmetry. (c) Illustration of the substitution of the methyl groups by trifluoromethyl groups: one CF_3 at position A, two CF_3 at AB, three CF_3 at ABC and four CF_3 at ABCD, respectively. Reproduced from ref. 30 with permission from Elsevier, Copyright 2017.

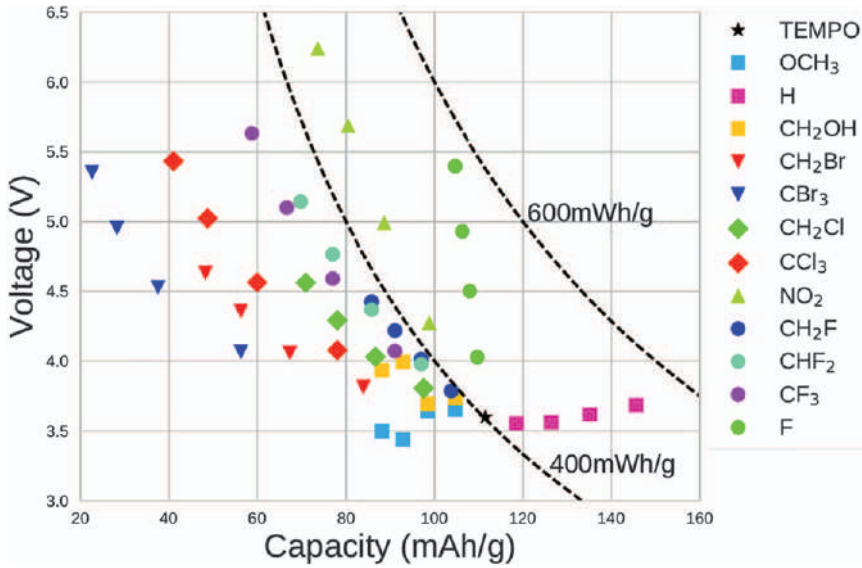

Figure 5.6 Voltage (*vs.* Li^+/Li) *versus* capacity for the newly designed radicals (modified TEMPO radicals). The capacity is calculated by adding the molecular weight of PMMA to allow the comparison with the PTMA (TEMPO attached to PMMA). These values are to be compared to the 3.6 V and the 111 mAh g^{-1} of the Li-ion PTMA battery (indicated by the black star TEMPO). This graph is to be read as follows: for a functional group listed in the legend, the nearest, second nearest, third nearest and the farthest values to the TEMPO black star correspond to one, two, three and four substitutions, respectively.
Reproduced from ref. 30 with permission from Elsevier, Copyright 2017.

positions present a mirror symmetry as illustrated in Figure 5.5b. Position A is equivalent to position D, and B is equivalent to C. On the other hand, position A is not equivalent to position B (or D to C). A and D positions are closer to each other than positions B and C. Consequently, the influence of the functional groups is different at A and D than at the B and C positions. This mirror symmetry allows to reduce the number of simulations, since, for example, the substitution of two methyl groups at positions A and B is equivalent to that at positions C and D (written CD in the following).

For a given functional group, nine newly designed molecules are investigated with substitutions at the following positions: A, B, AB (equivalent to CD), AC (equivalent to BD), AD, BC, ABC (equivalent to BCD), ABD (equivalent to ACD) and ABCD. In Figure 5.5c, the substitutions of the methyl groups by CF_3 are illustrated: from top to bottom, one CF_3 at position A, two CF_3 at AD, three CF_3 at ABC and four CF_3 at ABCD. The geometry of every new molecule created by substitution of functional groups is optimized with the same level of theory as mentioned above. The computed voltages of the newly designed radicals were found to range from 3.4 up to 6.2 V depending on the number and position of the functional groups (see Figure 5.6).[30]

This study paves the way toward the experimental investigation of novel substituted nitroxide radical-containing polymers.

5.4 Nanostructures in Nitroxide Polymer Electrodes

As evidenced earlier in this chapter, a suitable radical polymer electrode should be insoluble in the electrolyte and rely on a minimal amount of conductive additive to achieve the best balance between specific capacity and power performances. Polymers such as PTMA are only partially fulfilling these requirements.

To cope with its slow dissolution in the electrolyte, the traditional solutions are to increase the molar mass or to cross-link the electroactive polymer. A less traditional approach was realized by Lin *et al.* who grafted the electroactive polymer on silica nanoparticles using surface-initiated ATRP (SI-ATRP).[31]

Two other strategies were developed by Hauffman *et al.*, both taking advantage of block copolymer self-assembling properties (Figure 5.7).[15,32] Their strategies relied on the synthesis by ATRP of diblock copolymers combining a PTMA block linked to an insoluble polystyrene (PS) block (PS-*b*-PTMA). In the first strategy, they aimed at obtaining copolymer micelles that were incorporated in relatively classical composite electrodes by blending them with conductive carbon and a binder.[15] In their second report, they used similar block copolymers to realize thin films with phase segregation of PTMA cylindrical domains in a PS matrix. The resulting nanostructured thin film prepared on indium tin oxide demonstrated high rate performances when tested as electrode in an acetonitrile-based electrolyte.[32] Interestingly enough, a perpendicular orientation of the cylindrical PTMA nanodomains was obtained by solvent annealing with a carbonate-containing solvent similar to the solvent used in classical electrolytes for Li-ion batteries.

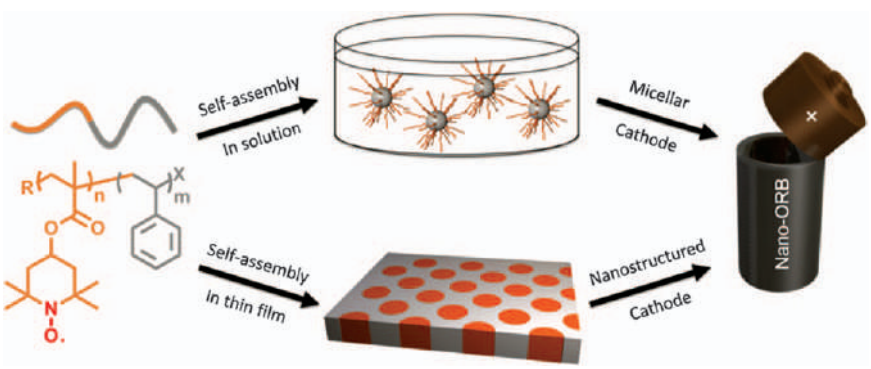

Figure 5.7 Schematic representation of nanostructured organic radical cathodes by self-assembling block copolymers in solution and in bulk with the aim of their application in organic radical batteries (ORBs).

Another interesting strategy to prepare thin-film electrodes was disclosed by Choi *et al.*[33] In their report, they describe a method to individualize single-walled carbon nanotubes (SWCNTs) and wrap them with PTMA at the molecular level. This approach is somewhat similar to the noncovalent grafting of PTMA on CNTs that will be discussed extensively in Section 5.5. The favorable dispersion and the thin-film structure (<200 nm) of this composite material also allowed to reach high rate performances with a very low dead-weight content (4 wt% of SWCNTs) in an acetonitrile-based electrolyte.

Nevertheless, in all the above-mentioned systems, there is a significant dead-weight in the resulting material, and/or the rate performances are demonstrated at the very favorable level of thin films. Furthermore, with the exception of polymer-wrapped SWCNTs, these strategies are not addressing the main downside of traditional approaches which is related to the conductive agent incorporation after all synthetic steps, hence preventing achievement of the formation of an ideal composite structure at the nanoscale. A straightforward approach to circumvent this issue was proposed by Vlad *et al.*[34] The solution that has been adopted consists in incorporating the conductive charge directly during the synthesis of the polymer (*in situ*). To this end, all reagents (monomer, radical initiator and cross-linking agent) are ground and blended together in the solid state in the presence of the SC45 nanocarbon conductive agent. Afterward the reaction mixture is heated up above the monomer melting point in the reactor to form first a slurry where the polymerization process takes place upon further heating (Figure 5.8a). This melt polymerization process possesses the further advantages that it is solvent-free, and that it can potentially be scaled up, as demonstrated by successful preparations at the 100 g scale. Comparisons made with *ex situ* incorporation of carbon after all synthetic steps showed that although conductivity is lower for *in situ* carbon incorporation, the rate performances are higher thanks to the texture of the composite material

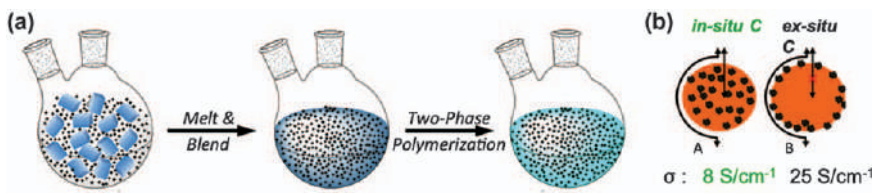

Figure 5.8 (a) Schematic representation of the solvent-free melt-polymerization to synthesize PTMA with *in situ* incorporated carbon. The monomer is melted and blended in the presence of SC45 prior to polymerization. (b) Schematic of various PTMA/C composite morphologies: left, carbon is uniformly dispersed within the polymer matrix as it is better obtained *via* its incorporation during the polymerization; right, carbon primarily coats the surface of polymer particles as usually obtained when incorporation is carried out after all synthetic steps.
Reproduced from ref. 34 with permission from John Wiley & Sons, Copyright 2015 WILEY-VCH Verlag GmbH & Co. KGaA, Weinheim.

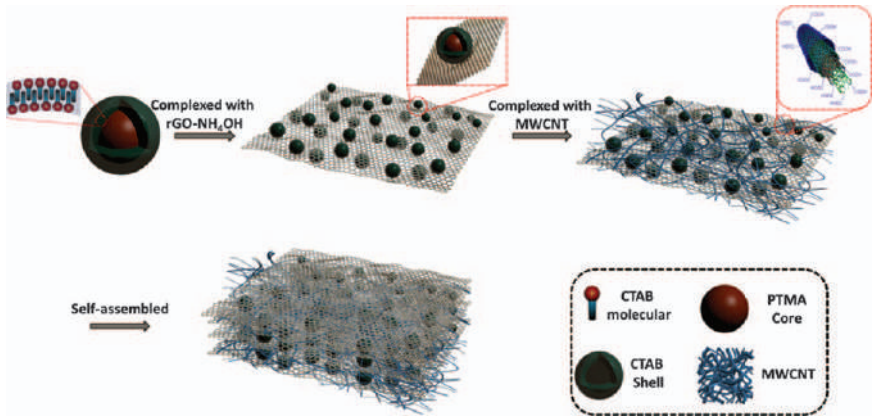

Figure 5.9 Schematic illustration of the procedure used to produce PTMA@CTAB@rGO@CNT free-standing cathode materials. Reproduced from ref. 35 with permission from Elsevier, Copyright 2019.

which is more favorable to the electrochemical reaction propagation upon cycling (Figure 5.8b). In their study, they evidenced that their composites enabled long-term cycling (>1200 cycles) and also that PTMA with 30 wt% of carbon can deliver more than half of its nominal capacity at impressive C-rates higher than 20 C.

Another possibility could be to encapsulate PTMA into semipermeable nanostructures. Those nanosized objects will have to allow the diffusion of the electrolyte in their interior, while the diffusion of PTMA chains out of the nano-objects should be prevented. Full utilization of the PTMA for redox processes is expected to be obtained at the nanoscale, while homogeneous dispersion of the nanosized objects into a conducting network will be required to allow the transfer of electrons. In this respect, PTMA core–shell nanospheres with a cetyl trimethyl ammonium bromide shell (PTMA@CTAB) were prepared as an active component for the preparation of free-standing composite electrodes with functional rGO nanosheets mixed with multi-walled carbon nanotubes (rGO@MWCNTs).[35] As depicted in Figure 5.9, thanks to the flexibility of rGO nanosheets and the electrostatic interactions between the negatively charged rGO and the positively charged PTMA@CTAB nanospheres, the latter ones are dispersed uniformly on the surface of rGO and wrapped one by one without aggregation. With the assistance of van der Waals forces between rGO nanosheets and the bridging connections originating from MWCNTs, free-standing PTMA@CTAB@rGO@MWCNT composite membranes with hierarchical structures are easily obtained through vacuum filtration.[35]

With the protection of rGO shells, the stability of PTMA in the organic electrolyte is significantly improved, and long cycling life has been measured with only 0.03% capacity loss per cycle. At the same time, the uniform dispersion of the nanospheres in the hybrid system leads to a high mass loading of PTMA accompanied by around 100% of active substance

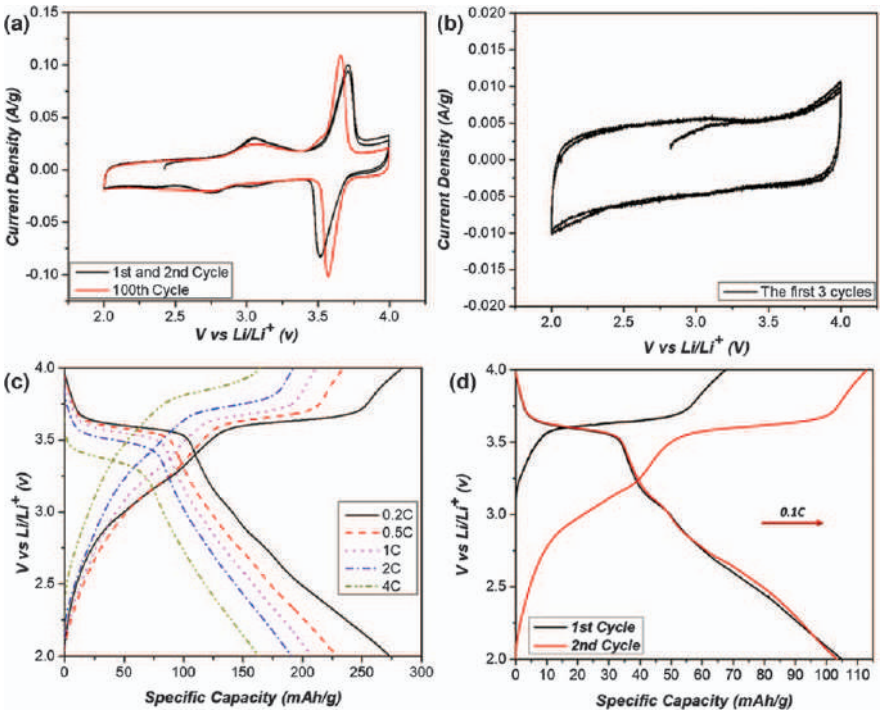

Figure 5.10 (a) Cyclic voltammograms curves of PTMA@CTAB@rGO@MWCNT with the initial two and the 100th scan ($0.05 mV\,s^{-1}$). (b) Cyclic voltammogram curves of rGO@MWCNT with the initial three scans ($0.05 mV\,s^{-1}$). (c) Charge/discharge curves of PTMA@CTAB@rGO@MWCNT at different C rates. (d) Galvanostatic charge/discharge behaviors of PTMA@CTAB@rGO@MWCNT when normalized to the whole electrode weight with two cycles at 0.1C. All of the electrochemical measurements were performed in the 2 to 4 V voltage range.
Reproduced from ref. 35 with permission from Elsevier, Copyright 2019.

utilization. Most importantly, when the cycling voltage range was extended from 2 V to 4 V (Figure 5.10), the composite electrodes show almost the highest reported specific capacity ($105 mA\,h\,g^{-1}$) reported so far for PTMA-based electrodes when normalized to the mass of the whole cathode (no need to consider the quality of the current collector due to the free-standing characteristics), owing to the utilization of Faradaic surface reaction of rGO and the second electron redox reaction of the nitroxide radicals in PTMA to aminoxyl anions.[35] Finally, the entire self-assembly process of the composite membrane is carried out in water without polluting the environment, and the presented approach can be easily extended to other active polymers.

In a related study, porous SiO_2 shells were used to protect PTMA from diffusion into the organic electrolytes. This leads to the improvement of the stability of PTMA, which is further utilized as an effective active component for the preparation of free-standing composite cathode materials with MWCNTs.[36]

5.5 Grafting of Nitroxide-containing Polymers onto Carbon Nanotubes

As stressed above, the incorporation of redox centers into macromolecules inherently presents the advantage of decreasing issues related to the solubility of redox species into standard nonaqueous electrolytes. Yet to be efficient such approaches usually make use of cross-linked polymers. Generally, the electrode formulation based on low conductivity organic macromolecules is thus performed after all synthetic steps, leading to difficulties to obtain a nanoscale homogeneous conducting network. As a consequence, cross-linking is an obstacle that prevents reaching the highest degree of homogeneity. This is where rational design can help by targeting at structures that would permit the combination of facilitated charge transfer and improved robustness. From an application standpoint, an improved charge transfer would bring improvements either in terms of power density or energy density. When it comes to organic electrodes with high carbon content, it is particularly true that these two density parameters can be addressed by a common strategy. For instance, a facilitated charge transfer allows higher power performances at a given carbon content. Conversely, the same power performances can be expected at a lower carbon content, which therefore benefits the energy density. Grafting of nitroxide-containing polymers on CNTs could be an efficient way to meet those expectations. Owing to their inert nature, CNT functionalization presents many challenges to achieve an enhancement or addition of desirable properties without a significant trade-off of others. Indeed, CNTs do not disperse well in most common solvents, hold an important chemical stability and do not present a significant amount of surface chemical functions intrinsically. Designing the best surface chemistry approaches while circumventing these limitations promises to extend the field of applications by improvement of the solubility and compatibility of CNTs in solvents and matrices, tailoring the structure and properties of CNTs and preparation of novel CNT-based devices, composites, biocomplexes and adducts. Surface functionalization methods are classified into two major categories: covalent or noncovalent. For the noncovalent approach, the strategies rely on physisorption. Physisorption is an adsorption mechanism involving physical interactions, therefore relying on electrostatic, van der Waals or hydrogen bond interactions. For the covalent approach (also called grafting), the strategies rely on chemisorption, that is, the creation of chemical bonds as the reactant molecules are modifying the surface of the substrate.

Noncovalent interactions between PTMA and the conductive material have been considered with imidazolium[37] (cation–π interaction) and pyrene[38] (π–π stacking) as anchoring points to immobilize PTMA onto nanostructured carbon derivatives. Zhang *et al.* recently reported a noncovalent interaction between a pyrene-functionalized PTMA and reduced graphene oxide (rGO).[38] In that study, a two-electron redox process promoted by the rGO led to high capacities. Since the PTMA/rGO composites developed by Zhang present a

decrease in capacity (from 1 to 10–20 C) when submitted to variable rates, Hergué *et al.* investigated the importance of the number of pyrene units anchored along the PTMA chain to improve the performance of the corresponding PTMA/CNT nanocomposites.[39] In this report, two pyrene-based PTMA structures were studied and used with multiwalled CNTs (MWCNTs). The first was a PTMA polymer bearing a single pyrene end-group. It was intentionally designed to confer a low steric hindrance and less conformational constraints to the homopolymer when the pyrene interacts with the carbon surface. For the second system, pyrene units were incorporated along the PTMA chain, by copolymerization of a pyrene-substituted methacrylate with the TEMPO-substituted methacrylate. The influence of the macromolecular architecture on the electrochemical response was assessed, focusing on the capacity retention upon cycling and on the cycling rate.[39] To shed light on the nature and stability of the functionalized PTMA/CNT interface, the interactions between the (co)polymer chains and the carbon surface were investigated with molecular modeling techniques. In this report, the controlled synthesis of pyrene-functionalized PTMA-based (co)polymers was achieved *via* atom transfer radical (co)polymerization (ATRP). Since the dangling nitroxide groups of the PTMA can be readily obtained by oxidation of the corresponding secondary amine, 2,2,6,6-tetramethyl-4-piperidyl methacrylate (TMPM) has been used as comonomer in the process. The structure of pyrene-functionalized PTMA-based (co)polymers is depicted in Figure 5.11.[39]

In the following report, Hergué *et al.* synthesized a block copolymer associating poly(3-hexylthiophene) and poly(2,2,6,6-tetramethylpiperidinyloxy-4-yl methacrylate) (P3HT-*b*-PTMA) as active cathode material for batteries.[40] The P3HT blocks were expected to further interact *via* noncovalent interactions with CNTs. While PTMA segments were prepared by ATRP, P3HT blocks were generated by Kumada-catalyst transfer polycondensation

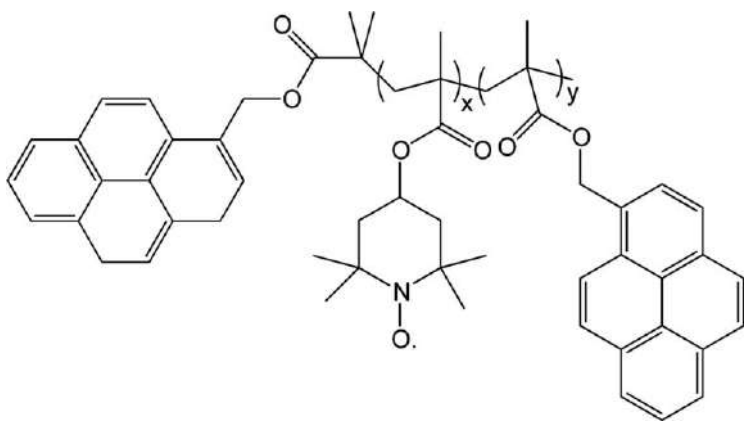

Figure 5.11 Structure of pyrene-functionalized PTMA-based (co)polymers ($y = 0$ for the PTMA polymer bearing a single pyrene end-group).

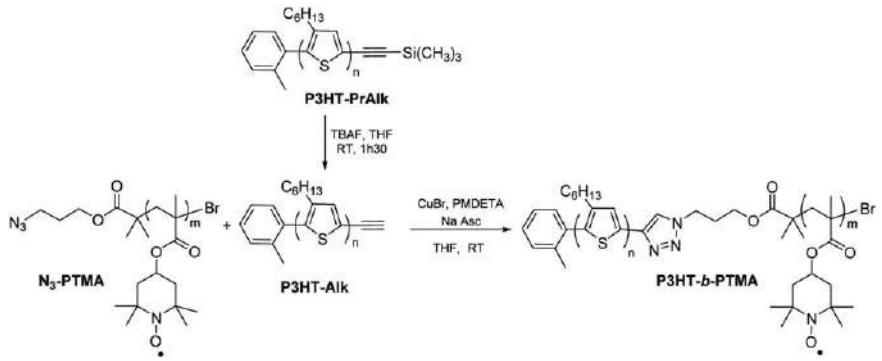

Figure 5.12 Synthesis of poly(3-hexylthiophene-*block*-2,2,6,6-tetramethylpiperidinyloxy-4-yl methacrylate) (P3HT-*b*-PTMA) diblock copolymers by copper azide–alkyne coupling cycloaddition from P3HT–Alk and N_3–PTMA. Reproduced from ref. 40 with permission from the Royal Society of Chemistry.

(KCTP). Both types of blocks were characterized by defined molar masses, narrow dispersities and controlled end-groups. Very efficiently, P3HT-*b*-PTMA diblock copolymers were obtained by a copper azide–akyne coupling cycloaddition of these two end-functionalized blocks (Figure 5.12). Films of P3HT-*b*-PTMA/CNTs/binder (30/60/10 in weight) were used as cathodes, and their performances in half-cells were studied. As compared to homopolymers or physical mixtures of both P3HT and PTMA, the diblock topology allows a real improvement of the capacity cells to be obtained. The electrochemical properties of the half-cells are improved by 25% for $P3HT_{31}$-*b*-$PTMA_{87}$ with a capacity of 60 mA h g^{-1} after 180 cycles (54% of theoretical capacity) and by 60% for $P3HT_{35}$-*b*-$PTMA_{48}$ (85 mA h g^{-1} after 180 cycles, 77% of theoretical capacity).[40] The rate performances recorded between C/10 and 60C show a decrease in capacity from 116 to 75 mA h g^{-1} (67% of the nominal capacity).[48] The initial properties were recovered while using the initial rate at the end of the experiment, confirming the stability of the P3HT-*b*-PTMA electrodes.[40]

Covalent functionalization of CNTs can be performed either by the grafting-from or grafting-onto strategies. Grafting-from processes are typically realized in two steps. The first step consists in the functionalization of the surface with a polymerization initiator.[41] Usually the tethering of initiator moieties is carried out on a reactive site generated or already present at the surface. The second step is the polymerization carried out *in situ* in order to carry the chain growth. During a grafting-from process, the polymerization of the brushes implies the diffusion of the monomer. It turns out that this diffusion of small molecules is an advantage in comparison to the grafting-onto situation where the diffusion process toward the surface involves polymer chains. Consequently, the grafting from allows to aim at higher loading and grafting density.[42] Nevertheless, some considerations regarding steric hindrance are still relevant. In the case of free radical

polymerization (FRP), it has been evidenced that the initiator efficiency is significantly reduced due to its tethering in comparison to its soluble counterpart. This difference could be due to the confinement of the initiator at the surface.[43] Even in the case where the initiator is bound to the surface through a long alkyl chain, its diffusion outside the solvation shell and toward the monomers is hindered. This results in a decrease in the initiator efficiency and possible deactivation of propagating radicals. Furthermore, a decrease in the efficiency is related to the kinetics characterizing every FRP, which are by definition uncontrolled.[43] Such polymerization processes usually exhibit a slow initiation step with respect to propagation. As all the chains are not initiated at the same time, some early-growing chains are already long enough to hinder the diffusion of monomers toward later initiating sites. This phenomenon is even more pronounced as chains are becoming longer and spread on the surface. To circumvent such issues, controlled radical polymerization techniques (CRPs) can be advantageously applied. More specifically, surface-initiated ATRP (SI-ATRP) is particularly suited for the polymerization of 2,2,6,6-tetramethyl-4-piperidyl methacrylate (TMPM), the precursor of PTMA.[31] This strategy has been successfully applied for the synthesis of MWCNT-*g*-PTMA composites, as depicted in Figure 5.13.[44] The first step consists of introducing functionality on the MWCNT surface *via* chemical oxidation, leading, among others, to carboxylic acid functions. Next, the carboxylic acid functions are activated with $SOCl_2$. The accordingly generated acyl chloride subsequently reacts with the alcohol group of 2-hydroxyethyl bromoisobutyrate, affording the MWCNT-initiator for subsequent SI-ATRP.[44]

Extended chemical and morphological analysis confirmed the compact core–shell morphology with a high active material mass loading of 60 wt%. The electrodes made out of these MWCNT-*g*-PTMA composites display good cycling stability (87% of capacity retention after 200 cycles), good rate capabilities and an excellent specific capacity (85% of the theoretical capacity).[44]

The grafting onto consists in the tethering of polymer on a surface by means of a chemical reaction between a reactive functional group belonging to the polymer and a reactive site on the surface to graft. The covalent bond formed between the surface and polymer chain makes the bond robust and resistant to common chemical environmental conditions. From a reactivity standpoint, the grafting is possible as long as the surface chemical sites can interact with the polymer functional groups. Macromolecular chains must diffuse through the existing polymer film to reach the reactive sites on the surface.[41] When the covering of the surface is increasing, the access to residual sites by the subsequent chains to graft becomes hindered. Additionally, the grafted chains may be coiled or even collapsed on the surface, masking neighboring reactive sites. Therefore, to achieve dense and homogeneous grafting of a polymer, the density of reactive sites on the surface and a proper polymer functionalization are important parameters to master as they determine process efficiency. This latter parameter can benefit substantially from the use of controlled polymerization techniques

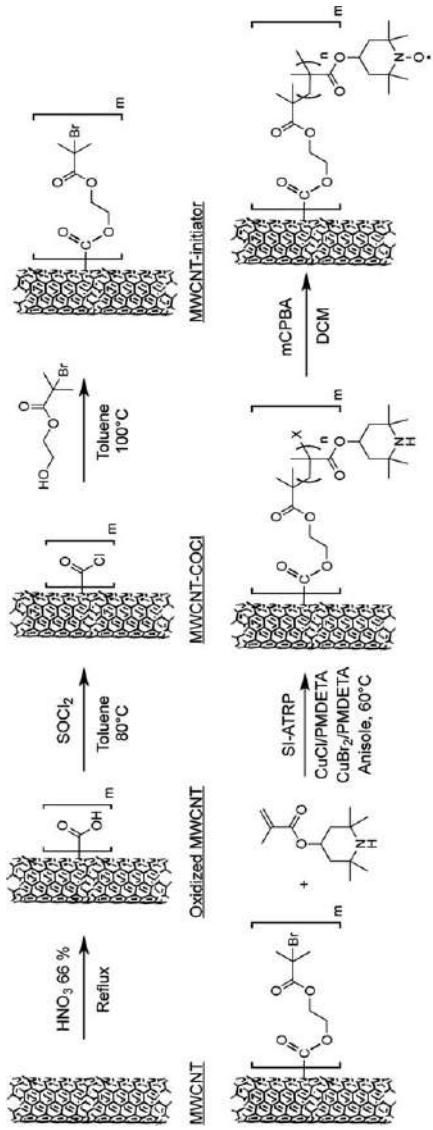

Figure 5.13 Strategy for the "grafting-from" synthesis of PTMA covalently grafted from MWCNTs. Reproduced from ref. 44 with permission from the Royal Society of Chemistry.

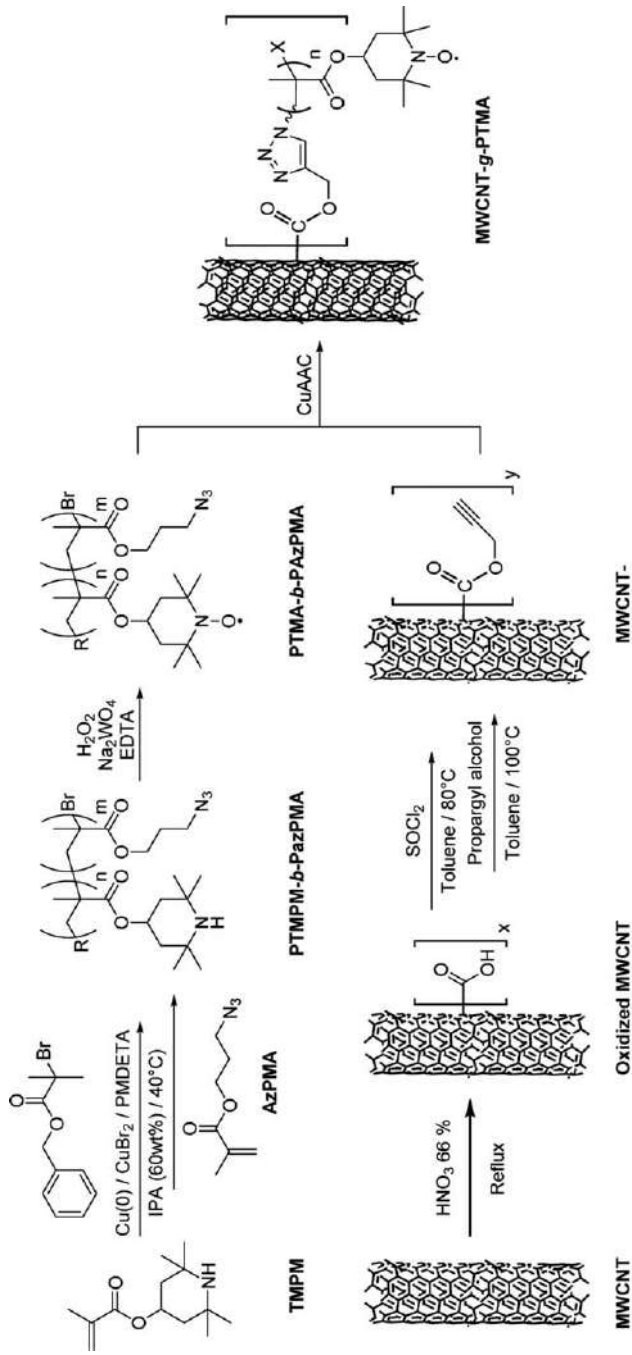

Figure 5.14 Strategy for the "grafting-onto" synthesis of PTMA covalently anchored on MWCNTs. Reproduced from ref. 45 with permission from the Royal Society of Chemistry.

that allow to control precisely the composition of the synthesized polymer chains. MWCNT-*g*-PTMA composites were obtained *via* the grafting-onto methodology.[45] A reactive copolymer incorporating a PTMA sequence along with a sequence bearing azide functional groups was first prepared. Introducing alkyne groups at the MWCNT surface then enables the anchoring of the block copolymer *via* the well-known copper-catalyzed azide–alkyne cycloaddition (CuAAC; Figure 5.14). This strategy yielded the grafted material MWCNT-*g*-PTMA with a PTMA content up to 30 wt% while offering superior electrochemical performance with respect to a more traditional blend of PTMA/MWCNTs.[45]

5.6 Redox Flow Batteries Based on Nitroxide-containing Polymers

Renewable energy sources such as solar, wind and hydroelectric are by definition intermittent. Therefore, there is a time imbalance between production and consumption which could be resolved by decoupling generation from demand. The availability of solutions such as electrochemical energy storage systems could help to eliminate the distinction between base-load and peak generation, allowing loads at any time to be serviced by the lowest energy sources. Redox-flow batteries (RFBs) could fit the position of storage systems in a smart grid environment thanks to their design and characteristics. A main advantage of RFBs is that power (electrode area) and energy (arbitrarily large storage volume) components can be scaled independently, allowing a flexible design owing to the fact that electro-active species are maintained in fluid form.

RFBs have their origins tracing back to the 1960s, with the development of the zinc/chlorine hydrate battery.[46] As a general description, a redox-flow cell uses two circulating fluids containing soluble redox species which are oxidized or reduced to store or deliver energy. The electrolyte fluid containing the positive electrode species is named the catholyte, while the other fluid containing the negative electrode species is named the anolyte. The cell possesses an ion-selective membrane separating the electrode compartments where the fluids are pumped from their respective tanks. The redox species are thus reacting in contact with or in close proximity to the electrodes, while the membrane allows the transport of nonreacting ions (such as H^+ or Na^+) to maintain electroneutrality and electrolyte balance. However, a significant capacity decay is usually affecting those systems due to the lack of satisfactory membranes, inducing a crossover of electroactive species across the utilized anion exchange membrane. Similar difficulties are still of current concern nowadays, that is, the lack of both appropriate and inexpensive membranes with the desirable selectivity. Furthermore, these systems are still of relatively low energy density (25 $W\,h\,kg^{-1}$) due to the limited solubility of species. Consequently, RFBs are better applied to stationary applications and are only mobile in the form of modularized cells in shipping containers. Nevertheless, RFBs display interesting features such as

safety of operation in comparison to classical solid electrode batteries, the possibility to switch between charging and discharging within a fraction of seconds, a better energy density than pumped hydro storage, *etc.* However, wide-scale utilization of RFBs is limited by the abundance and cost of their components, particularly when it comes to systems using redox-active metals and precious metal electrocatalysts.[47] Replacing these metals by electroactive organic compounds is not only offering the advantage of materials that are based on potentially more abundant and inexpensive resources but could also provide solutions to several metal-related problems. In turn, this may lead to more competitive RFBs in the future. Such organic materials can be small molecules (molar mass $<1000\ g\,mol^{-1}$) or macromolecules such as polymers. Noteworthy are the promising systems proposed by Winsberg *et al.*[48,49] and Janoschka *et al.*,[50] which rely on the use of PTMA copolymers. In their copolymers, the redox-active macromolecules were rationally designed so that they bear TEMPO redox-active units combined with water-solubility providing units, the latter preventing the deposition of the copolymer in its reduced state. Such copolymers were then applied as catholyte materials in aqueous electrolytes in combination with Zn^{2+}/Zn^{0} (Figure 5.15)[48,49] or polyviologen anolytes.[50] In these designs of such RFBs, an advantage is made clear. Since they can make use of simple size exclusion membranes, they do not require expensive selective solutions such as Nafion that would increase the ownership costs.

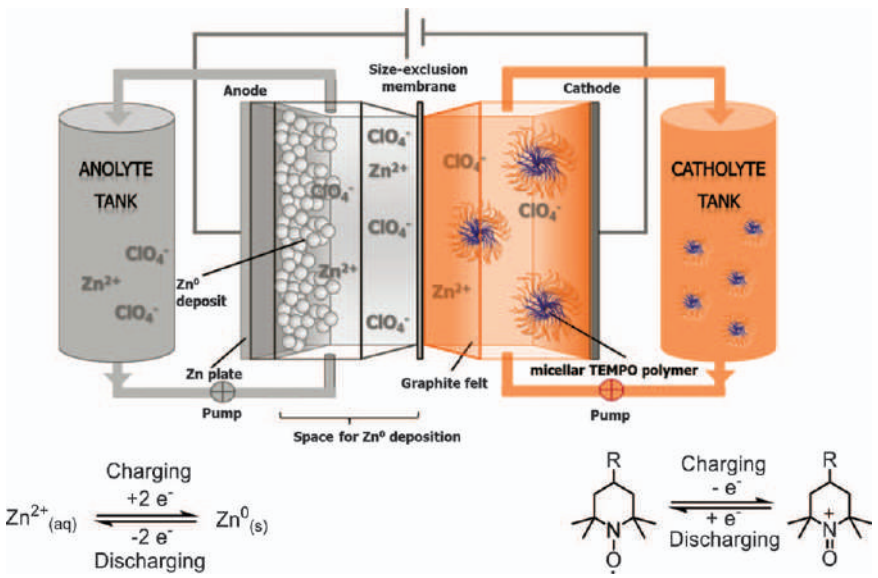

Figure 5.15 An aqueous redox flow battery using a zinc-based anolyte and a PTMA-based catholyte.
Reproduced from ref. 48 with permission from the Royal Society of Chemistry.

5.7 Hybrid Pseudocapacitors Based on Nitroxide Polymers

Batteries and supercapacitors both rely on electrochemical processes that determine the power and energy performance metrics. Whereas batteries rely on bulk reaction properties, supercapacitors, also known as electrical double-layer capacitors (EDLCs), are involved in surface charge storage. Although significant progresses have been made to provide higher power density batteries and higher capacity density supercapacitors, the research is also focusing on electrode materials that combine the best of both worlds. Recognizing that certain electrode materials can display EDLC-like power performances while featuring redox processes that bring their capacity closer to traditional LIB materials, a new classification was proposed for them as pseudocapacitive materials.[51]

A noticeable example of pseudocapacitive materials is PTMA. Nevertheless, for all the reasons presented in their dedicated section in this chapter, there is still a gap between nitroxide-based polymer electrode and LIB materials regarding the specific energy density. A straightforward approach to reach higher capacity for such pseudocapacitive materials would be to combine different energy storage materials within a single device. Such hybrid systems have already been explored with the combination of LIB and EDLC materials,[52] but components only contribute to the performances in a proportional relationship with their composition. Furthermore, power and energy are decoupled. An elegant solution has been provided by Vlad *et al.*, which makes synergistic use of pseudocapacitive and battery components.[53] In their publication, they showed that enhanced battery–capacitor hybrids offering more than the sum of their components can be realized by careful choice of the supercapacitive and battery materials. This idea is exemplified by the choice of $LiFePO_4$ and PTMA as battery and pseudocapacitive materials, respectively. The key design principle of this concept is the rapid electrochemical response in combination with higher working potential of PTMA (Figure 5.16). This allows, at equilibrium, the preferential charging of $LiFePO_4$ at the expense of PTMA. Nonetheless, PTMA is the faster discharge component. Using an appropriate pulse charge sequence, the rapid response of PTMA will ensure fast charge. During the subsequent relaxation, PTMA will charge the $LiFePO_4$ component. Overall, this hybrid system was evidenced to provide high energy and power capacity, over-polarization protection, as well as fast and stable recharge over more than 1500 cycles.[53] Additionally, its unique power-leveling capability could be of particular relevance in solar conversion-storage units.

Applying the same rational, Dolphijn *et al.* designed a system based on the coupling of PTMA with a higher voltage material ($LiMn_2O_4$).[54] The aim here is to obtain hybrid electrodes with enhanced power delivery characteristics, as oxidized $PTMA^+$ will be both the favored and the best rate capable redox species – hence acting as a power buffer (Figure 5.17).

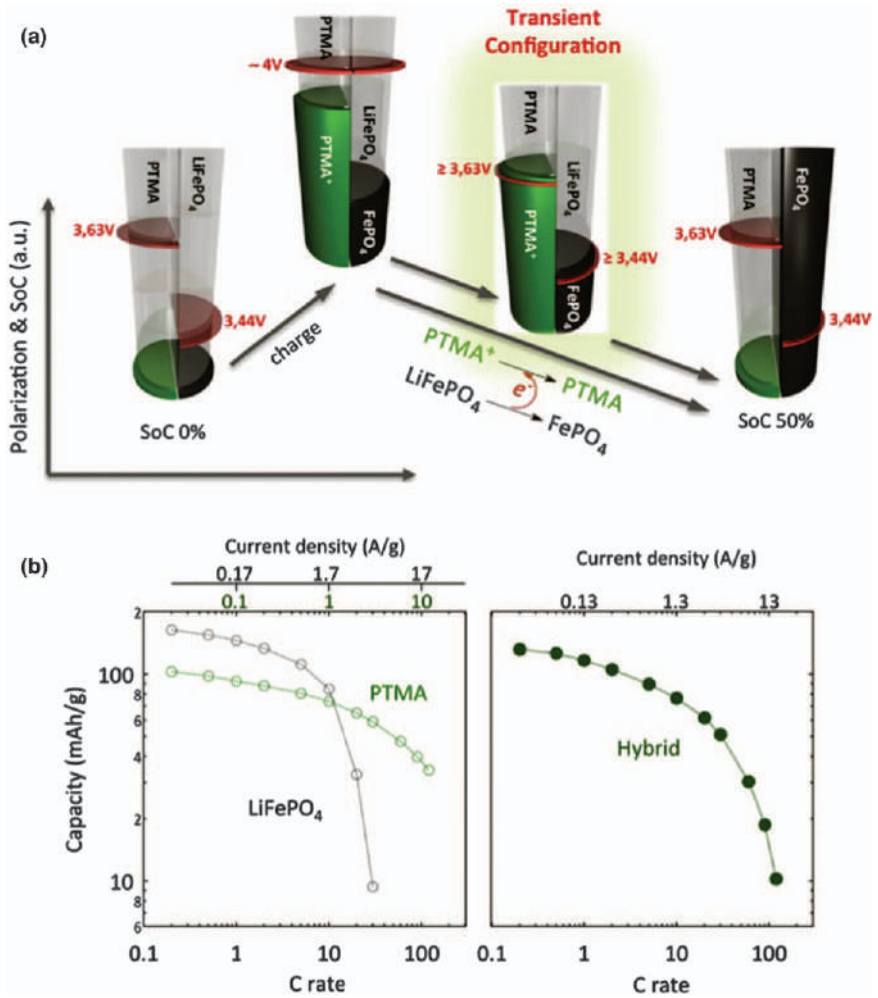

Figure 5.16 (a) Representation of the fast charge/relaxation process. The green and black half-cylinders are indicative of the stored charge in PTMA and $LiFePO_4$, respectively. The relative position of the red disk indicates the polarization of the constituents in the hybrid electrode. Except during the charge, the polarization is the equilibrium open circuit potential for each component. Fast charging leads to a thermodynamically unstable configuration, with evanescent co-existence of high-potential $PTMA^+$ with low-potential $LiFePO_4$ species forcing an internal charge transfer equilibration. The depicted situation is representative of 50% state of charge, *i.e.*, at equilibrium only the $LiFePO_4$ component will be charged, (b) capacity function of C-rate and applied current density (symmetrical charge/discharge conditions) for $LiFePO_4$, PTMA and hybrid electrode. 1C corresponds to 100 $mA\,g^{-1}$, 170 $mA\,g^{-1}$ and 130 $mA\,g^{-1}$ for PTMA, $LiFePO_4$, and hybrid electrode, respectively. Reproduced from ref. 53 with permission from Springer Nature, Copyright 2014.

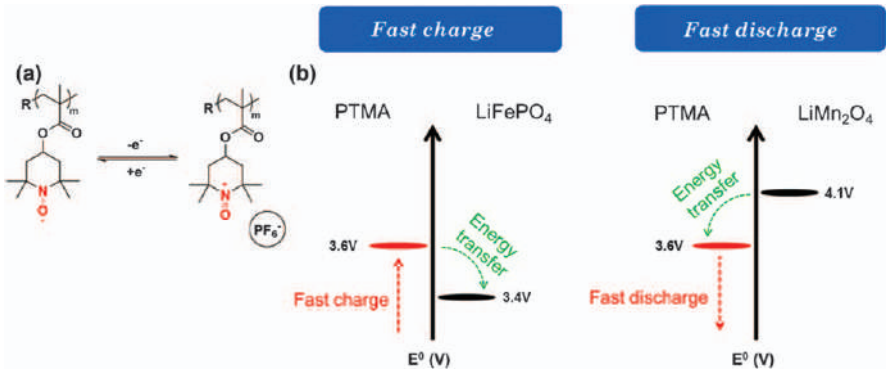

Figure 5.17 (a) Schematic of the one-electron redox in PTMA. The nitroxide radical is the redox-active group, and is transformed into the oxoammonium cation during the oxidation process. (b) Schematic energy levels depiction of the possible configurations. Fast discharge (pulsed, intermittent or continuous) can be enabled whenever the fast component has a lower equilibrium redox potential than the sluggish material. Reproduced from ref. 54 with permission from Elsevier, Copyright 2017.

5.8 Conclusion

This chapter should attract the attention of the community of researchers working on redox organics and more specifically those dedicated to energy storage applications. In this chapter, we have reviewed strategies based on macromolecular engineering and rational design to enable electrochemical performance improvements for energy storage devices incorporating nitroxide-containing polymers and more specifically those based on poly(2,2,6,6-tetramethylpiperidinyloxy-4-yl methacrylate) (PTMA). These improvements target critical parameters relevant toward applications: energy density, power density and cyclability. Additionally, the new chemical structures and pathways as well as the interesting findings that we have reviewed should be found appealing by the broader community of researchers working on batteries and capacitors and also by those working on such diverse topics as conductive and/or electroactive materials. Those researchers are motivated by the context of a challenging era where mankind has to face up to the pressing need for more sustainable, cleaner and yet cost-efficient energy supply chains. While the common thread is dealing with polymeric redox architectures, several axes of developments are presented to push forward their performance metrics.

For example, MWCNT-*g*-PTMA grafted materials display by essence performances that could fill the gap between electrochemical capacitors and LIBs in terms of energy density *vs.* power density, and this is where they could meet application demands. Yet, in terms of implementation, they could find their way by combining them with other electroactive components within a single electrode. For instance, they could advantageously be hybridized with an

inorganic component such as LFP (or LMO) to mitigate their relatively low energy density and also to take advantage of synergistic effects regarding the charge (or discharge) performances of the resulting electrode material. Another possibility would be to take advantage of their enhanced dispersion properties. Since it is often challenging to reach an efficient distribution without dispersing additives, MWCNT-*g*-PTMA could act as a compatibilizing agent to help in the formation of the desired polymer-conductive charge hybrid structure.

From the perspective of enhancing electrode performances of redox organics, nitroxide-containing polymer materials demonstrated here that they allow versatile functional and structural manipulations to tailor their resulting electrochemical properties. This demonstration combined with their contextual advantage of being more environment-friendly than currently used inorganic materials should motivate further developments into more elaborated devices. Nevertheless, this chapter carries messages and perspectives for future developments that should extend beyond the materials and systems presented here. Although this chapter was mainly focused on developments of batteries based on redox organics, projections can be anticipated to other areas of material sciences and electrochemistry where similar concepts and strategies are applicable.

References

1. H. Chen, M. Armand, G. Demailly, F. Dolhem, P. Poizot and J.-P. Tarascon, *ChemSusChem*, 2008, **1**, 348.
2. T. Janoschka, M. D. Hager and U. S. Schubert, *Adv. Mater.*, 2012, **24**, 6397.
3. Z. Song and H. Zhou, *Energy Environ. Sci.*, 2013, **6**, 2280.
4. S. Muench, A. Wild, C. Friebe, B. Häupler, T. Janoschka and U. S. Schubert, *Chem. Rev.*, 2016, **116**, 9438.
5. P. Novák, K. Müller, K. Santhanam and O. Haas, *Chem. Rev.*, 1997, **97**, 207.
6. Y. Liang, Z. Tao and J. Chen, *Adv. Energy Mater.*, 2012, **2**, 742.
7. S. Barriga, *Synlett*, 2001, **2001**, 563.
8. R. Ciriminna and M. Pagliaro, *Org. Process Res. Dev.*, 2010, **14**, 245.
9. J. Nicolas, Y. Guillaneuf, D. Bertin, D. Gigmes and B. Charleux in *Polymer Science: A Comprehensive Reference*, ed. K. Matyjaszewski and M. Möller, Elsevier Ltd, vol. 3, 2012, p. 277.
10. L. Tebben and A. Studer, *Angew. Chem., Int. Ed.*, 2011, **50**, 5034–5068.
11. M. Khodeir, B. Ernould, J. Brassinne, S. Ghiassinejad, H. Jia, S. Antoun, C. Friebe, U. S. Schubert, Z. Kochovski, Y. Lu, E. Van Ruymbeke and J.-F. Gohy, *Soft Matter*, 2019, **15**, 6418.
12. N. Casado, G. Hernández, H. Sardon and D. Mecerreyes, *Prog. Polym. Sci.*, 2016, **52**, 107.
13. K. Nakahara, S. Iwasa, M. Satoh, Y. Morioka, J. Iriyama, M. Suguro and E. Hasegawa, *Chem. Phys. Lett.*, 2002, **359**, 351.

14. G. Hauffman, J. Rolland, J.-P. Bourgeois, A. Vlad and J.-F. Gohy, *J. Polym. Sci. Polym. Chem.*, 2013, **51**, 101.
15. G. Hauffman, Q. Maguin, J. P. Bourgeois, A. Vlad and J. F. Gohy, *Macromol. Rapid Commun.*, 2014, **35**, 228.
16. T. Janoschka, A. Teichler, A. Krieg, M. D. Hager and U. S. Schubert, *J. Polym. Sci. Polym. Chem.*, 2012, **50**, 1394.
17. L. Bugnon, C. J. H. Morton, P. Novak, J. Vetter and P. Nesvadba, *Chem. Mater.*, 2007, **19**, 2910.
18. O. Bertrand, B. Ernould, F. Boujioui, A. Vlad and J.-F. Gohy, *Polym. Chem.*, 2015, **6**, 6067.
19. T. Suga, Y.-J. Pu, K. Oyaizu and H. Nishide, *Bull. Chem. Soc. Jpn.*, 2004, **77**, 2203.
20. K. Zhang, Y. Hu, L. Wang, J. Fan, M. J. Monteiro and Z. Jia, *Polym. Chem.*, 2017, **8**, 1815.
21. S. Yoshihara, H. Isozumi, M. Kasai, H. Yonehara, Y. Ando, K. Oyaizu and H. Nishide, *J. Phys. Chem. B*, 2010, **114**(25), 8335.
22. M. Suguro, S. Iwasa, Y. Kusachi, Y. Morioka and K. Nakahara, *Macromol. Rapid Commun.*, 2007, **28**, 1929.
23. M. Suguro, S. Iwasa and K. Nakahara, *Macromol. Rapid Commun.*, 2008, **29**, 1635.
24. T. Katsumata, M. Satoh, J. Wada, M. Shiotsuki, F. Sanda and T. Masuda, *Macromol. Rapid Commun.*, 2006, **27**, 1206.
25. J. Qu, T. Katsumata, M. Satoh, J. Wada, J. Igarashi, K. Mizoguchi and T. Masuda, *Chem. – Eur. J.*, 2007, **13**, 7965.
26. K. Oyaizu, T. Suga, K. Yoshimura and H. Nishide, *Macromolecules*, 2008, **41**, 6646.
27. T. Suga, Y. J. Pu, S. Kasatori and H. Nishide, *Macromolecules*, 2007, **40**, 3167.
28. T. Suga, S. Sugita, H. Ohshiro, K. Oyaizu and H. Nishide, *Adv. Mater.*, 2011, **23**, 751.
29. N. Dardenne, X. Blase, G. Hautier, J.-C. Charlier and G.-M. Rignanese, *J. Phys. Chem. C*, 2015, **119**, 23373.
30. N. Dardenne, G. Hautier, J.-F. Gohy, J.-C. Charlier and G.-M. Rignanese, *Comput. Mater. Sci.*, 2018, **143**, 27.
31. H. C. Lin, C. C. Li and J. T. Lee, *J. Power Sources*, 2011, **196**, 8098.
32. G. Hauffman, A. Vlad, T. Janoschka, U. S. Schubert and J. F. Gohy, *J. Mater. Chem. A*, 2015, **3**, 19575.
33. W. Choi, S. Ohtani, K. Oyaizu, H. Nishide and K. E. Geckeler, *Adv. Mater.*, 2011, **23**, 4440.
34. A. Vlad, J. Rolland, G. Hauffman, B. Ernould and J.-F. Gohy, *ChemSusChem*, 2015, **8**, 1692.
35. H. Jia, T. Quan, X. Liu, L. Bai, J. Wang, F. Boujioui, R. Ye, A. Vlad, Y. Lu and J.-F. Gohy, *Nano Energy*, 2019, **64**, 103949.
36. H. Jia, C. Friebe, U. S. Schubert, X. Zhang, T. Quan, Y. Lu and J.-F. Gohy, *Energy Technol.*, 2020, **8**, 1901040.
37. R. Peng, Y. Wang, W. Tang, Y. Yang and X. Xie, *Polymers*, 2013, **5**, 847.

38. K. Zhang, Y. Hu, L. Wang, M. J. Monteiro and Z. Jia, *ACS Appl. Mater. Interfaces*, 2017, **9**, 34900.
39. N. Hergué, B. Ernould, A. Minoia, R. Lazzaroni, J.-F. Gohy, P. Dubois and O. Coulembier, *Batteries Supercaps*, 2018, **1**, 102.
40. N. Hergué, B. Ernould, A. Minoia, J. De Winter, P. Gerbaux, R. Lazzaroni, J.-F. Gohy, P. Dubois and O. Coulembier, *Polym. Chem.*, 2019, **10**, 2570.
41. B. Zhao and W. J. Brittain, *Prog. Polym. Sci.*, 2000, **25**, 677.
42. J. Pyun, K. Matyjaszewski, T. Kowalewski, D. Savin, G. Patterson, G. Kickelbick and N. Huesing, *J. Am. Chem. Soc.*, 2001, **123**, 9445.
43. O. Prucker and J. Rühe, *Macromolecules*, 1998, **31**, 602.
44. B. Ernould, M. Devos, J.-P. Bourgeois, J. Rolland, A. Vlad and J.-F. Gohy, *J. Mater. Chem. A*, 2015, **3**, 8832.
45. B. Ernould, O. Bertrand, A. Minoia, R. Lazzaroni, A. Vlad and J.-F. Gohy, *RSC Adv.*, 2017, **7**, 17301.
46. A. Z. Weber, M. M. Mench, J. P. Meyers, P. N. Ross, J. T. Gostick and Q. Liu, *J. Appl. Electrochem.*, 2011, **41**, 1137.
47. K. J. Kim, M.-S. Park, Y.-J. Kim, J. H. Kim, S. X. Dou and M. Skyllas-Kazacos, *J. Mater. Chem. A*, 2015, **3**, 16913.
48. J. Winsberg, S. Muench, T. Hagemann, S. Morgensen, T. Janoschka, G. Hauffman, J.-F. Gohy and U. S. Schubert, *Polym. Chem.*, 2016, **7**, 1711.
49. J. Winsberg, T. Janoschka, S. Morgenstern, T. Hagemann, S. Muench, G. Hauffman, J.-F. Gohy, M. D. Hager and U. S. Schubert, *Adv. Mater.*, 2016, **28**, 2238.
50. T. Janoschka, N. Martin, U. Martin, C. Friebe, S. Morgenstern, H. Hiller, M. D. Hager and U. S. Schubert, *Nature*, 2015, **527**, 78.
51. P. Simon, Y. Gogotsi and B. Dunn, *Science*, 2014, **343**, 1210.
52. D. Cericola and R. Kötz, *Electrochim. Acta*, 2012, **72**, 1.
53. A. Vlad, N. Singh, J. Rolland, S. Melinte, P. M. Ajayan and J.-F. Gohy, *Sci. Rep.*, 2015, **4**, 4315.
54. G. Dolphijn, S. Isikli, F. Gauthy, A. Vlad and J.-F. Gohy, *Electrochim. Acta*, 2017, **255**, 442.

CHAPTER 6

Computational Tools for Nitroxide Design

NICHOLAS S. HILL, BENJAMIN B. NOBLE, FERGUS J. M. ROGERS, ALFRED K. K. FUNG AND MICHELLE L. COOTE*

ARC Centre of Excellence for Electromaterials Science, Research School of Chemistry, Australian National University, Canberra ACT 2601, Australia
*Email: michelle.coote@anu.edu.au

6.1 Introduction

Nitroxides are a class of molecules that exhibit a wide range of chemical properties, the most significant and useful of which is their stability as radical species. This radical stability has been utilised for a wide range of chemical applications, including nitroxide-mediated polymerisations, as fluorescent probes, and in electron paramagnetic resonance spectroscopy. They are also able to undergo reversible oxidation and reduction, which has been harnessed in batteries, solar cells, synthesis and even as medicinal antioxidants. The many and various properties of nitroxides and their applications have been explored throughout this book; this chapter will focus primarily on the methods and considerations for simulating their properties and reactivity.

Computational chemistry is becoming an increasingly powerful tool for modern chemists, as required theoretical insights are often invaluable when rationalising experimental results. Throughout the chapter, emphasis has been placed on utilising modern methods, software packages and literature references to provide an up-to-date overview of how a new computational

Nitroxides
Edited by Olivier Ouari and Didier Gigmes

Published by the Royal Society of Chemistry, www.rsc.org

chemist may begin to tackle the challenges of nitroxide chemistry. Many of the computational lessons taught in this chapter are generally applicable to other areas of organic chemistry; the challenge often with nitroxides is that many of their properties that may be otherwise calculated in isolation are often coupled, for example, combining nitroxide-mediated polymerisations (NMP), with their dependence on accurate kinetic parameters, with photochemistry, and the difficulties when modelling excited states, is necessary to study photo-NMP.

To that end, for a type of model chemistry, different theoretical considerations are explored, such as single- *vs.* multi-reference and combinations thereof, and the impact of different basis sets. Quantitative and qualitative results are also discussed throughout, as are the ability for different approaches to achieve them, and wherever possible recommendations are made. We start with a discussion of the methods needed to model complex spin systems, for which the challenge is the accurate treatment of static correlation without incurring the massive costs of extensive multi-reference calculations. We then examine the methods needed to simulate EPR spectra, which among other things requires specialised basis sets for the correct treatment of core correlation. We then turn to redox chemistry, where the focus shifts to the high-level single-reference methods needed for treating dynamic correlation. For redox chemistry in particular, the treatment of solvent effects also becomes a major potential source of error, due to the participation of charged species. We then examine alkoxyamine dissociation in the context of nitroxide-mediated polymerisation, which uses similar methods to redox chemistry but quite different strategies in structure–reactivity analysis. Finally, we examine methods for the treatment of excited states, particularly in the context of photo-NMP.

6.2 Modelling Complex Spin Systems

Many problems of interest are not adequately handled by conventional methods. Important examples involving nitroxides include their transition metal complexes, polyradicals, many excited-states, as well as the intermediate structures encountered in bond-dissociation events.[1–5] These cases are said to be ''strongly correlated'', meaning that methods based on a *single-reference* wavefunction are a poor approximation of the exact solution. Numerous strategies for dealing with these problems are nonetheless available to the modern chemist, but the functionality is often peculiar and system dependent. We discuss the general theory supported by some recent applications here.

6.2.1 Dynamic *versus* Static Correlation Energy

Quantum-chemical methods differ in their accuracy and complexity primarily through their approaches to modelling the correlation energy (E_c). In

the crudest sense, correlation is the error arising from the Hartree–Fock (HF) approximation to the exact, non-relativistic, time-independent Schrödinger equation within the Born–Oppenheimer approximation:[6,7]

$$E_c = E - E_0 \tag{6.1}$$

where E is the *exact* energy of the system, and E_0 is the energy of the corresponding (HF) wavefunction. Correlation has a somewhat different definition in density functional theory (DFT), however the implications are similar.[8]

In the HF regime, the many-body wavefunction is reduced to a Slater determinant $|\Psi\rangle$ of one-electron molecular spin-orbitals (MO). Each MO is ''independent'', experiencing only the average field generated by all the electrons in the system, such that the explicit many-body nature of the problem is substituted for a coupled set of soluble one-body problems. Indeed, it is from this model that we derive the familiar MO conception of molecular electronic structure.

The ground-state solution to the resultant set of HF equations provides an *upper bound* to the exact ground-state energy such that the error, E_c, is always negative; although this is not necessarily true of the excited states. In general, the complex MOs cannot be determined analytically, so a finite *basis set* of *N basis functions* or atomic orbitals (AO) is introduced, and the MOs are expanded in terms of these. Since the HF equations are nonlinear, the AOs are iteratively mixed together to construct the lowest energy set of N MOs (the self-consistent field method) such that, for an M electron HF system, M MOs are completely occupied and N–M are empty or *virtual*. In this sense HF is a single-reference approximation, as a Slater determinant is evidently based on only one ''configuration'' of occupied MOs.

Correlation energy can be systematically recovered by expanding the total ground-state wavefunction $|\Phi_0\rangle$, as a linear combination of the HF reference $|\Psi_0\rangle$, and its ''excited'' configurations (configuration interaction or CI):

$$|\Phi_0\rangle = c_0|\Psi_0\rangle + \sum_{i>a}^{m} c_a^i|\Psi_a^i\rangle + \sum_{i,j>a,b}^{m} c_{a,b}^{i,j}|\Psi_{a,b}^{i,j}\rangle + \ldots \tag{6.2}$$

where $|\Psi_i^a\rangle$ and $|\Psi_{i,j}^{a,b}\rangle$ are the singly and doubly excited determinants formed by elevating electrons from occupied (i, j *etc.*) to virtual HF MOs (a, b *etc.*). The expansion coefficients c_n, are determined from the CI matrix– an eigenvalue problem – whose solutions correspond to the ground- and excited-states of the system. In the full CI (FCI) limit, where all possible excitations are considered, the exact correlation energy is recovered completely within the bounds of the basis set. Such a calculation is virtually unfeasible however, as the number of determinants in the CI expansion has factorial dependence on the number of AOs. In practical applications, E_c is instead approximated by truncating the expansion or, more commonly, by applying perturbation, coupled pair or Green's function theory. For the interested reader, archetypal methods are discussed in Chapter 4 onwards of ref. 6.

Single-reference post-HF and DFT methods deal directly with so-called dynamical correlation, *i.e.*, the error relating to electronic motion. Static correlation, the focus of this section, arises from errors due to the use of a single-reference wavefunction, and occurs when there is more than one dominant resonance contributor.[9] A simple but illustrative example is the σ-bond dissociation problem. At the equilibrium geometry, the HF reference consisting of the σ^2 configuration, is physically sensible. As the bond is stretched however, the $(\sigma^*)^2$ configuration becomes increasingly important such that at the dissociation limit, both configurations have equal weight in the ground-state wavefunction. In this case, at least two MO configurations are necessary for a valid description of σ-bond dissociation.

Unlike dynamical correlation, static correlation is recovered only slowly by expansions of the type in eqn (6.2). Efficient treatment of statically correlated problems therefore requires instead a more general reference than the single-reference wavefunction. Such a wavefunction can be found in the multireference framework, *i.e.*, where the reference is a superposition of two or more MO configurations. In the multi-configurational self-consistent field (MCSCF) method, the multireference generalisation of SCF, MOs and CI coefficients is varied simultaneously in solving for a particular state. In this way, MCSCF could be thought of as the union of HF, where only MOs of a single determinant are varied, and CI, where the expansion coefficients are varied within a basis set of frozen MOs.[10]

6.2.2 Multireference Methods

MCSCF is most commonly encountered in two related formalisms, namely the complete active space self-consistent field (CASSCF) method, and its reduced analogue, restricted active space self-consistent field (RASSCF). In both schemes, the determinants defined for MCSCF are generated by a full CI treatment of an *active space*, a selection of orbitals generated by an initial HF calculation.[11] CASSCF considers every configuration of the expansion, whilst RASSCF invokes a set of selection criterion to reduce the number of configurations to only the most pursuant contributors. These specifications are denoted $[n, m]$-RAS/CASSCF or RAS/CAS(n, m), where n and m are the number of active space electrons and orbitals, respectively.

The resultant set of configurations grows aggressively with the size of the active space, so the practical challenge occurs in selecting a computable specification which best represents the chemistry of the problem. As a minimum, this must include all MOs that are expected to change significantly during some transformation, as well as those which are partially occupied.[12] Orbital point group symmetry should also be considered, especially in the calculation of spectroscopic properties where selection rules are important; occasionally Rydberg orbitals might also be necessary.[13] All these considerations mean CAS/RASSCF is rather esoteric for the uninitiated, but we stress that orbital selection, which we do not flesh out here, is extremely

important.[14,15] Introductory guides can be found in chapter 4.6 of ref. 7 or chapter 14 of ref. 10.

Like HF, the multireference family is populated by a very large variety of dynamically correlated methods. Common examples include variations on multireference configuration interaction (MRCI) such as difference dedicated configuration interaction (DDCI),[16–21] multireference Moller-Plesset (MRMPn) and restricted/complete active space perturbation theory (RAS/CASPTn),[22,23] as well as multireference coupled cluster theory (MRCC) among others.[24–26] CASPT2, being the most affordable option, is of course most often encountered in the literature, although it should be noted that perturbation theory in general is susceptible to spurious issues, such as intruder states, which are not always foreseeable in the reference wavefunction.[27–30] Other methods have more limited application, but may be the only options capable of satisfactory outcomes for especially difficult problems.

RASSCF and many dynamical correlation methods are not size-consistent, *i.e.*, the energy of a non-interacting dimer is higher than the sum of each monomer considered in isolation. For large problems where this is a concern – typically more than 100 electrons – specialised methods such as second-order *N-Electron Valence State Perturbation Theory* (NEVPT2) and variations of MRCC ought to be considered.[31–33] This said, CASPT2 and MRCI are nearly size-consistent, and so are nonetheless popular options for investigations of multireference nitroxides of moderate size, such as the biradicals studied by Angeli *et al.*[32] and the many polyradicals modelled by Barone *et al.*[34–42]

6.2.3 Single-reference Methods for Strongly Correlated Systems

For predicting ground-state multiplicities and estimating useful properties such as singlet–triplet (*S–T*) energy gaps, one may appeal to one of several single-reference methods which are considerably cheaper.[43] These tend to operate under a similar *modus operandi*, *i.e.*, a strongly correlated low-spin state, such as an open-shell singlet, is estimated by projection or spin excitation from a much less correlated high-spin reference, typically a triplet, quintet, *etc.* for which the single-reference approximation is valid.

The simplest approach can be found in *broken-symmetry* density functional theory (BS-DFT),[44–47] a method which works within the *unrestricted* Kohn–Sham formalism (UDFT), where the spatial components of MOs are allowed to differ. Owing to its computational efficiency, UDFT is often a first approximation for modelling open-shell systems. However, unrestricted wavefunctions suffer from a serious issue known as the *spin contamination error*, the artificial mixing of higher spin states into the wavefunction in such a way that the total spin is greater than its formal value.[48] Strongly correlated problems tend to be highly spin-contaminated, so a direct UDFT calculation on, for

instance, an open-shell singlet, will certainly be erroneous.[49] The BS-DFT method resolves this issue *via* spin projection.[44–47] In the simplest case, a contaminated BS singlet is referenced to the negligibly contaminated triplet state which results in the following expression for the vertical *S*–*T* gap,[50]

$$\Delta_{S-T}^{\text{vert}} = \frac{2(E_{BS} - E_T)}{\langle S_T^2 \rangle - \langle S_{BS}^2 \rangle} \tag{6.3}$$

such that the true singlet energy can be approximated as,

$$E_S = \Delta_{S-T}^{\text{vert}} + E_T \tag{6.4}$$

where E_{BS} is the electronic energy of the contaminated BS singlet, E_T is the energy of the triplet, at the BS singlet geometry, and $\langle S_{BS}^2 \rangle$ and $\langle S_T^2 \rangle$ are the total spin eigenvalues of the BS singlet and triplet states, respectively. Numerical values for these quantities are printed in the output of most quantum chemistry codes. The adiabatic *S*–*T* gap may be written as,

$$\Delta_{S-T}^{\text{adia}} = \frac{2(E_{BS^i} - E_{T^i})}{\langle S_{T^i}^2 \rangle - \langle S_{BS^i}^2 \rangle} + E_{T^i} - E_{T^j} \tag{6.5}$$

or in its approximate form,

$$\Delta_{S-T}^{\text{adia, approx}} = \frac{2(E_{BS^i} - E_{T^j})}{\langle S_{T^j}^2 \rangle - \langle S_{BS^i}^2 \rangle} \tag{6.6}$$

where *i* and *j* indicate the optimised geometries of the BS singlet and triplet states, respectively. A suitable guess for the BS singlet can be accomplished by mixing the HOMO and LUMO orbitals of a closed-shell UDFT singlet (*e.g.*, by invoking the Guess = Mix keyword in Gaussian) thus breaking the spin symmetry of the singlet wavefunction. This method is not limited to singlet–triplet couples and a generalisation can be made for any low-spin, high-spin dimer.[51–56] The quality of the projection is quite sensitive to one's level of theory. Global hybrid functionals such as B3LYP, BMK and M06-2X are recommended,[57,58] although we tend to advise use of the latter for more reliable treatment of organic radicals. Adiabatic gaps are typically improved through the inclusion of zero-point corrections to the energy terms.

A more robust strategy for ground-state calculations is the spin–flip (SF) ansatz of Krylov *et al.*[59] These methods involve an excitation operator whose action is to perform a spin–flip type excitation of an electron from the reference wavefunction, thus changing its multiplicity.[59] In simple terms, a set of low-spin configurations, constituting the strongly correlated problem, are spawned by flipping unpaired electrons in the frozen basis of MOs constituting a high-spin reference. The quality of the resultant wavefunction hinges on the quality of the reference, which in the single-reference framework can be systematically improved forming a familiar hierarchy, *i.e.*, SF-SCF/SF-DFT through to SF-MP2 and high-order SF-EOM-CC, *etc.*[60–64]

The SF operator is perfectly compatible with a UHF, although a *restricted open-shell* (ROHF) reference, where each electron pair is confined to a pair of degenerate MOs, has been shown to benefit predictive power.[65] Several "spin-correct" techniques, that attempt to rectify the spin-contamination problem, have been proposed in recent literature.[66–68]

Another popular addition to the single-reference family is the RAS-SF approach of Casanova *et al.*[69] In this method, the active space is defined under the usual RAS specifications for a ROHF high-spin reference. A larger and more general set of determinants is subsequently generated, describing a wavefunction that is spin-complete and size-consistent.[70] One particular advantage of RAS partitioning is in its regular treatment of polyradicals of arbitrary degree, as these ordinarily pose something of a challenge to single-reference methods. Like RASSCF however, active space specification has a great influence on the quality of the wavefunction, not neglecting the exponential scaling in the number of determinants generated (although scaling with molecular size with a fixed active space is manageable). Recent implementations of RAS-SF also permit a degree of orbital relaxation, admitting this scheme to the multireference family of methods.

6.2.4 Selected Applications

6.2.4.1 Case Study 1: The Role of the Multiconfigurational Character of Nitronyl-nitroxide in the Singlet–triplet Energy Gap of its Diradicals[41]

This recent publication by the Barone group illustrates some of the caveats that must be considered when applying a multireference solution to a typical problem. In this case, the effect of the active space on the quality of calculated *singlet–triplet* (*S–T*) energy gaps for three *nitronyl-nitroxide* (NN)-based diradicals (Figure 6.1) were assessed for the multireference, dynamically correlated DDCI method and its simplified variant, DDCI2. ROHF/6-311G(d) calculations of the triplet states for each species were initially performed on their X-ray crystal structures in the software package GAMESS. For each diradical, an *ad hoc* fragmentation was then undertaken, and the dimensionality of the problem for the multireference component was reduced to the most pertinent features (shown as blue in Figure 6.2), after which the active space was defined. DDCI calculations were then performed in the BALOO code, an in-house program developed independently by Barone for these problems.

Several interesting observations can be made from this work. For reliable treatment of polyradicals involving an NN radical, it was speculated that the CAS reference must include at least three orbitals and electrons for satisfactory agreement with experiment, *i.e.*, one for each N–O fragment and a third for the central carbon. Thus, *S–T* gaps for Ullmann's diradical (see Figure 6.2) were only accurately approximated (*i.e.*, with transition frequencies between 90–110% of experimental values) with a CAS(6,6) reference

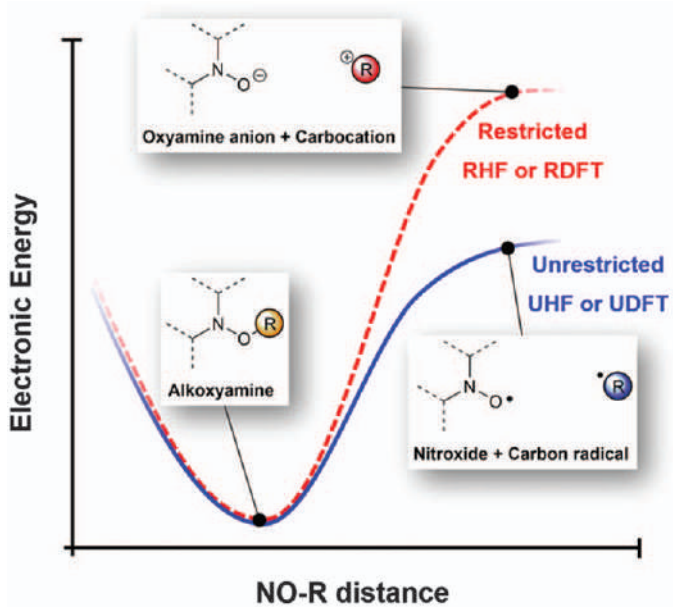

Figure 6.1 Idealised potential energy surfaces for NO–R bond dissociation. Restricted theory (RHF and correlated variants, RDFT) uses the same spatial components for both alpha and beta spin orbitals and consequently it cannot describe bond homolysis. In unrestricted theory (UHF and correlated variants, UDFT) these spatial components are allowed to vary, which provides a better description of homolytic processes (albeit with the introduction spin contamination, see text).

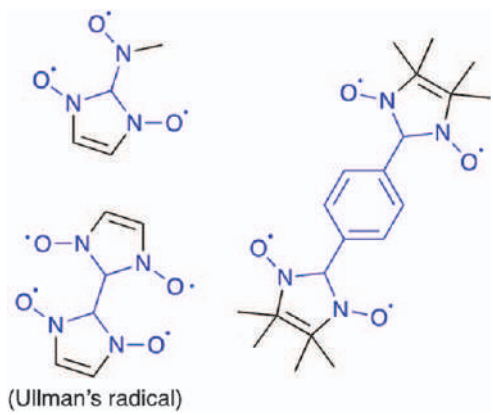

Figure 6.2 Test set in ref. 41. Blue indicates the fragments, whose MOs are considered in the construction of the DDCI space.

involving the LUMO + 2 to HOMO-3 MOs, as these encapsulate both features as well as the linker. The minimal CAS(2,2) reference involving only the magnetic HOMO and HOMO-1 orbitals was woefully inadequate in every

example, resulting in transition frequencies of 10–30% of the experiment. Unsurprisingly, DDCI2 was found to be less reliable than DDCI with the low-quality CAS(2,2) reference. However, the performance became comparable when the (6,6) active space was included. This highlights one of the many subtleties of multireference calculations, namely, the balance between a more complete (read larger) active space, and a more rigorous (read reliable) method for a given allocation of computational resources.

6.2.4.2 *Case Study 2: Spin Coupling Interactions in C=C or B–B-cored Porphyrin-mimetic Graphene Patch Nitroxide Diradicals*[71]

A useful example of both single- and multireference methodologies can be found in this recent article on the *S–T* energy gaps for an isomeric family of C=C and B–B coupled porphyrin-bridged nitroxide diradicals (Figure 6.3). These larger systems are practically out of reach for most multireference methods, but typical of the problems quantified with single-reference approximations in the literature. In this case, gas-phase BS singlet and triplet structures were first optimised in Gaussian with UB3LYP/6-311G(d,p).

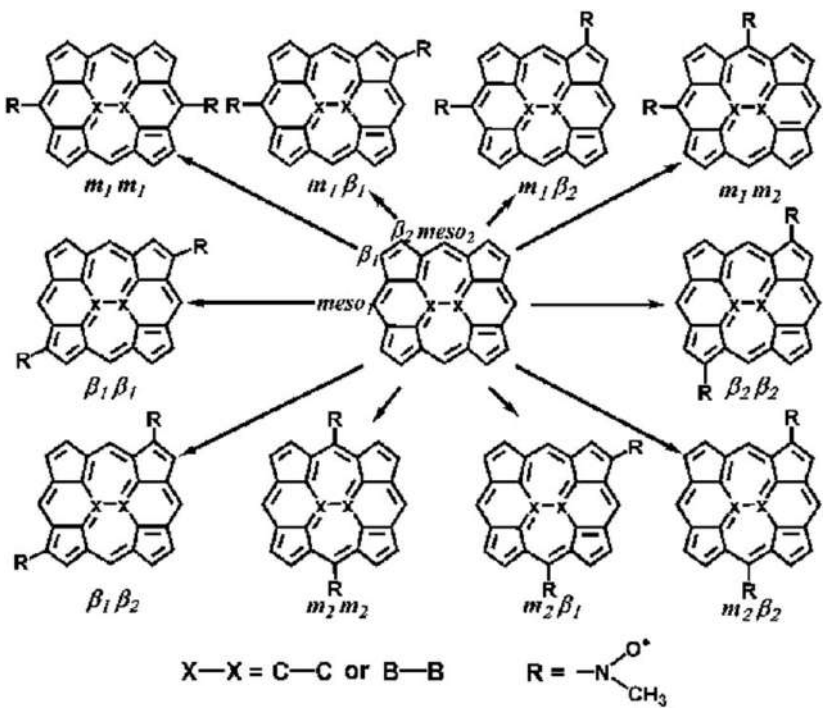

Figure 6.3 Test set of porphyrin-bridged nitroxide diradicals in ref. 71. Reproduced from ref. 71 with permission from the Royal Society of Chemistry.

BS-DFT predictions of the adiabatic *S–T* gap were then estimated using Yamaguchi's approximate expression, with subsequent calculations of the SF-DFT energies obtained from single-point SF-PBE50/6-311G(d,p) and SF-5050/6-311G(d,p) calculations performed in Q-Chem.

The results of this comparison are useful, as they highlight the deficiencies one is likely to encounter when compromising with a single-reference method. Interestingly, both BS- and SF-DFT are in complete agreement as far as predicting the ground-state multiplicities is concerned (*i.e.*, the sign of the *S–T* gap), however the disagreement in the energy itself is quite dramatic (with BS-B3LYP predicting ~30% of the SF-DFT average). The authors complete the remainder of their calculations with BS-B3LYP. However, it is very difficult to comment on which approach is most reliable given the absence of an experimental reference (which is often the case), or a high-level computational reference.

6.2.5 Concluding Remarks

Correct application of multireference methodology is something of an acquired art. The approach used and its accuracy will vary depending of the nature of the problem and/or the resources available to handle it. CAS and RASSCF are available in most quantum chemistry software packages and are useful as a first approximation. However, neglect of the dynamical component will not lead to quantitative agreement with experiment in most cases. For this methods such as MRCI or high-level perturbation theory, up to CASPT3, is required and for these we recommend the licensed packages MOLPRO or MOLCAS. As for MRCC, the powerful implementation of Kallay *et al.*[72] is promising but limited to a stand-alone package of the same name. Fortunately, the code is free for academic use and may be interfaced through the MOLPRO environment. These packages possess somewhat complex input formats that can be unfriendly to the less-experienced user. More agreeable platforms can be found in ORCA or DALTON, the latter of which is also open-source. Any package supporting DFT is suitable for BS calculations, although the SF methods are mostly limited to Q-Chem. In all cases, we advise readers to consult the relevant manual entries before setting any unfamiliar calculations.

6.3 Computation of Electron Paramagnetic Resonance Spectra

Given the range of applications in which nitroxide radicals are formed and take part in chemical reactions, monitoring the formation and presence of the nitroxide radical species can be desirable. To that end, electron paramagnetic resonance (EPR) spectroscopy is an extremely useful technique and one that can be complemented with quantum chemistry simulation to help assign complex spectra and relate that to the underlying structural

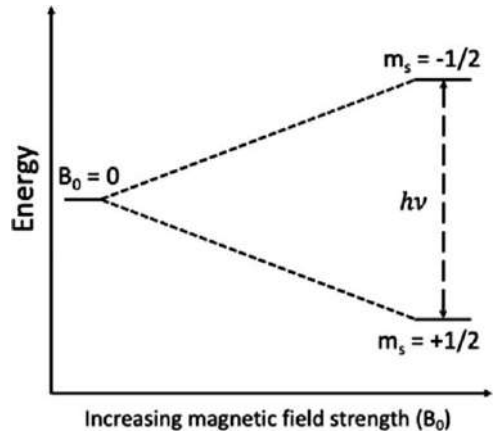

Figure 6.4 Splitting in electron spin states observed upon introduction of a magnetic field.

properties of the radical. Fundamentally, EPR involves measuring the energy at which the magnetic moment of an unpaired electron is flipped in the presence of an external magnetic field (Figure 6.4). To simulate the resulting spectra, one first needs parameters (the *g*-factor and hyperfine splitting constants, defined below) describing the response of the electron to the magnetic field, and one then needs to take into account the experimental environment and aspects such as the tumbling regime and whether the magnetic field is continuous or pulsed. Quantum chemistry can help with the former, and the methodology developed for this purpose is outlined below (Section 6.3.1), while the methodology for the latter is briefly outlined in Section 6.3.2.

6.3.1 Computing *g*-tensors and Hyperfine Coupling Constants with Quantum Chemistry

The main working equation of EPR is given by:

$$\Delta E = h\nu = g_e \mu_B B_0 \tag{6.7}$$

where g_e is the electronic *g*-factor (approximately 2.0 for a free electron), μ_B is the Bohr magneton, and B_0 is the external magnetic field strength. Electrons are not, however, ''free'' in a molecule, as they will interact with both the external magnetic field and internal magnetic fields generated by the nuclei. This generates an effective magnetic field, B_{eff}:

$$B_{\text{eff}} = B_0 \, (1 - \sigma) \tag{6.8}$$

where σ includes local magnetic effects. Eqn (6.8) can then be rewritten as:

$$h\nu = g \mu_B B_0 \tag{6.9}$$

where

$$g = g_e\,(1-\sigma) \tag{6.10}$$

Here, g is referred to as the g-factor. A value of g that is significantly different to the constant g_e term can give information about the molecular orbital in which the unpaired electron resides. In reality the g-factor is a second-rank tensor, selection of an appropriate coordinate system, for example Cartesian coordinates, allows the 3×3 matrix to be diagonalised to give g_{xx}, g_{yy} and g_{zz}. Another consequence of the interaction between an unpaired electron and atomic nuclei is hyperfine splitting, which arises due to coupling between electronic and nuclear spins. This reveals itself in spectra as multiple peaks, centred at $h\nu$, and the so-called ''multiplicity'' of a transition can be complex.

Spectroscopic methods study the response of a system with respect to some external perturbation, and the energy can therefore be expanded as a Taylor series:

$$E(X) = E(0) + \left.\frac{\partial E}{\partial X}\right|_{X=0} \cdot X + \frac{1}{2!}\left.\frac{\partial^2 E}{\partial X^2}\right|_{X=0} \cdot X^2 + \frac{1}{3!}\left.\frac{\partial^3 E}{\partial X^3}\right|_{X=0} \cdot X^3 \ldots \tag{6.11}$$

where X is an external perturbation. The calculation of g-factors is no different in this respect, in that it is the second derivative of the many-electron energy with respect to an external magnetic field and the overall net spin component in a given direction (eqn (6.12)).

$$g_{xx} = \left.\frac{1}{\mu_B}\frac{\partial^2 E}{\partial B_x S_x}\right|_{S=B=0} \tag{6.12}$$

As a result of this well-defined expansion, computation of EPR g-tensors is generally possible by both analytical and numerical methods in most electronic structure packages for a range of quantum chemistry methods, generally HF, DFT and MP2. Traditionally, magnetic property calculations have suffered from gauge invariance; when using an approximate wavefunction the results of the calculation change depending on the orientation of the molecule in the Cartesian frame of reference. This is negated by using, for example, gauge-invariant atom orbitals (GIAO) which ensure exact gauge invariance, or by using a large enough basis set that the invariance becomes negligible. In reality, unless the choice of gauge origin is very poor, the effects of gauge invariance are not large enough to render a calculation useless, however most modern electronic structure packages offer formally invariant methods and their usage is recommended.

The second property of interest is hyperfine splitting constants, arising from the different possible nuclear and electronic spin configurations. For these properties, several terms need to be computed.

The isotropic Fermi contact term, which describes the magnetic interaction between an electron and a nucleus, is required and calculated from:

$$a_{\mathrm{iso}}(N) = \left(\frac{4\pi}{3}\langle S_z\rangle^{-1}\right) g_e g_N \beta_e \beta_N \rho(N) \tag{6.13}$$

where $\langle S_z\rangle$ is the expectation value of the z-component of the total spin, g_e and g_N are the electron and nuclear g-factors, respectively, and β_e and β_N are the electron and nuclear magnetons, respectively. The Fermi contact integral, $\rho(X)$, can be computed as:

$$\rho(N) = \sum_{\mu\nu} P_{\mu\nu}^{\alpha-\beta} \varphi_\mu(r_N)\varphi_\nu(r_N) \tag{6.14}$$

where $P_{\mu\nu}^{\alpha-\beta}$ is the one-electron spin-density-difference matrix, computed as the difference between the spin density matrices of the α and β electrons, and evaluation of the overlap of the φ_μ and φ_ν basis functions is at nuclear position r_x. For brevity, P_N is commonly used in place of $g_e g_N \beta_e \beta_N$.

The spin dipole component, computed as the expectation value over the spin density:

$$A_{kl}^{\mathrm{dip}}(N) = P_N \sum_{\mu,\nu} P_{\mu\nu}^{\alpha-\beta} \langle \varphi_\mu | r_N^{-5} \left(3\vec{r}_k \vec{r}_{N_l} - \delta_{kl} r_N^2\right) | \varphi_\nu \rangle \tag{6.15}$$

where $\vec{r}_N$ is a vector that points from the nucleus of interest to an electron.

The second-order spin–orbit coupling term:

$$A_{\mu\nu}^{\mathrm{orb}}(N) = -\frac{1}{2S} P_N \sum_{\mu\nu} \frac{\partial P_{\mu\nu}^{\alpha-\beta}}{\partial B_k} \langle \varphi_\mu | h_l^{\mathrm{SOC}} | \varphi_\nu \rangle \tag{6.16}$$

Two key points about eqn (6.13) and (6.14) are the computed isotropic contact term is dependent on the quality of the spin-density matrices of α and β electrons, and on the overlap between basis functions at nuclear positions. The quality of the spin-density matrices is generally affected most by the method used to compute them. As all systems with unpaired spins are open shell, restricted MO theory, for example, restricted Hartree–Fock (RHF), is not applicable. Its restricted open-shell counterpart, ROHF, is also found to generally perform poorly as only the singly occupied molecular orbital (SOMO) will contribute to $P_{\mu\nu}^{\alpha-\beta}$, as the spatially identical doubly occupied orbitals will have zero spin-density difference. This can result in the incorrect prediction of zero hyperfine coupling for atoms in the nodal plane of the SOMO. Unrestricted HF (UHF), on the other hand, optimises both α and β orbitals, and can account for spin polarisation. Unfortunately, UHF wavefunctions often suffer from spin contamination, arising from the mixing of higher spin states into the wavefunction, and this too will result in

less accurate spin-density matrices. Projected UHF methods can be used to project out spin contamination to improve results.

Alternatively, one may turn instead to methods that suffer less from spin contamination; indeed, most electronic structure packages offer hyperfine coupling constant calculations with some of the most powerful electronic structure theories, for example, coupled cluster (CC) methods, as well as with DFT. If CC methods are too expensive, DFT methods are generally robust however, as always, it is recommended that the functional of choice is benchmarked for suitability before predictions are made.

The second issue is that of appropriate basis set selection. As the basis set overlap is computed at nuclear positions, those with the largest contributions to the splitting constants describe the core s orbitals. However, the most popular basis sets, for example, those of Pople or Dunning, do not describe the core region with the same flexibility as the valence region. This is due to their emphasis on accurate calculations of bonding phenomena, to which core electrons contribute little. As well as this, atomic s orbitals exhibit an electron cusp at the nucleus, which is not well captured by Gaussian-type orbitals (GTO). To that end, basis sets have been developed that systematically improve the description of the core region of electrons, examples being EPR-II or EPR-III, and their usage is recommended. A second practical consideration when using DFT is to ensure that a large numerical grid is employed, to ensure numerical integration remains accurate.

Although not necessarily common when exploring the chemistry of nitroxide radicals, it is possible one may encounter heavy elements, and under these circumstances relativistic effects may become significant. Unlike if bonding interactions are being studied, in which case the relativistic core electrons can be replaced by an effective core potential (ECP) which may include relativistic effects in its parameterisation, accurate EPR calculations generally require the explicit treatment of electrons. As a result, all-electron approximations are available in most electronic packages, and their use is recommended.

6.3.2 Simulating EPR Spectra

The computational simulation of EPR spectra depends not only on the magnetic properties of the molecule (splitting parameters, spin active nuclei present, linewidth and *g* tensor values) but also on the experimental conditions, such as the type of tumbling regime and whether the spectrum is collected as a continuous-wave (cw) EPR spectrum or under pulsed conditions. Many programs have been developed to simulate spectra, including Easyspin,[73] Winsim,[74] XSophe,[75] and MoSophe.[76] More specialist programs such as WinMOMD[77] for simulation of slow-motional spectra using the MOMD (microscopic order, macroscopic disorder) model, and optimised SLE solvers employed by Freed[78] at the ACERT Center at Cornell have been employed for more targeted systems. Generally speaking, these programs make use of inputted parameters (splitting parameters, spin active nuclei

present, linewidth and *g* tensor values) in order to construct a parameterised spin Hamiltonian. These can be extracted from the experimental spectrum or, if one is trying to make a first principles prediction, these are provided from the quantum-chemical studies described above. A quantum-mechanical approach is then used to simulate the resulting spectrum according to the type of tumbling regime (*i.e.*, isotropic limit, fast motion, slow motion or rigid limit) and whether the spectrum is collected as a continuous-wave (cw) EPR spectrum or under pulsed conditions. Details of how EPR spectra are simulated are covered in Chapter 4.

6.3.3 Selected Applications

6.3.3.1 Case Study 3: DFT Calculations of Isotropic Hyperfine Coupling Constants of Nitrogen Aromatic Radicals: The Challenge of Nitroxide Radicals[79]

In this study, Hermosilla *et al.*[79] assess the performance of DFT for accurately predicting hyperfine coupling constants, using the PBE0 and B3LYP functionals in conjunction with several basis sets; 6-31G(d), N07D, TZVP and EPR-III. The study utilised a test set of 38 nitrogen-containing radical species, with 15 of the species nitroxide radicals (Figure 6.5). As a result of the different coupling environments a total of 165 hyperfine splitting constants for ^{14}N and ^{1}H nuclei were calculated and compared with experimental data. The study highlights the importance of basis sets when calculating EPR properties, as well as the importance of comparing and contrasting DFT results against HF or more advanced wavefunction methods, as the B3LYP results counter-intuitively suggest that 6-31G(d), rather than the larger, EPR-specific EPR-III basis set, was more capable of accurately predicting EPR spectra.

6.3.3.2 Case Study 4: The Temperature Dependence of Nitroxide Spin–label Interaction Parameters: a High-field EPR Study of Intramolecular Motional Contributions[80]

This study used a combination of high-field W-band EPR and density functional theory calculations to study and explain the temperature dependence of the *g* (*anisotropic*), *a* (hyperfine), *q* (quadrupole) tensors of two nitroxides, 3-hydroxymethyl-2,2,5,5-tetramethylpyrrolin-1-oxyl and 4-hydroxy-2,2,6,6-tetramethylpiperidine-N-oxyl, in glass-forming *ortho*-terphenyl solution. The experimental temperature dependencies were attributed to both the averaging of the anisotropies of the EPR parameters in the glassy matrix, and the intramolecular out-of-plane motion of oxygen in the nitroxide group. This latter mechanism was confirmed *via* DFT calculations whereby the B1LYP/SVP level of theory was first used to compute the structures associated with harmonic oxygen out-of-plane vibrations,

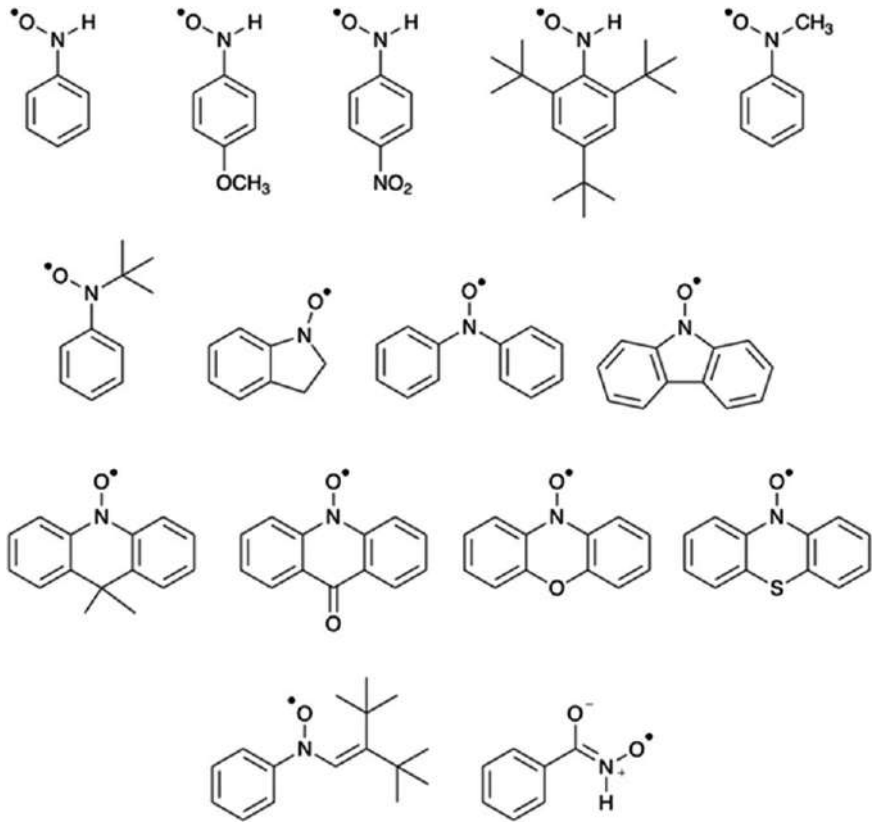

Figure 6.5 Nitroxide radicals studied in ref. 79.

and then the various tensors were calculated at each structure to show how the vibrational motion affected them (Figure 6.6). For this purpose, the SVP basis set was replaced with IGLO-III for computation of the *a*- and *q*-tensors; while for the *g*-tensor LSD/SVP was used in conjunction with RI-SOMF(1X) for the treatment of the spin–orbit coupling operator. Studies such as this highlight the important role of first principles theory in assigning or interpreting complex EPR spectra.

6.4 Predicting Oxidation Potentials

As redox-active molecules possessing unique properties and reactivity, nitroxides are utilised in many applications ranging from energy storage devices[81–85] and oxidation catalysts[86–90] to redox mediators for solar cells[91–94] and superoxide dismutase mimics.[95,96] Nitroxides can typically undergo an electrochemically reversible one-electron oxidation to afford the corresponding oxoammonium cation (see Figure 6.7). In contrast, nitroxide reduction is usually electrochemically irreversible; spontaneous proton

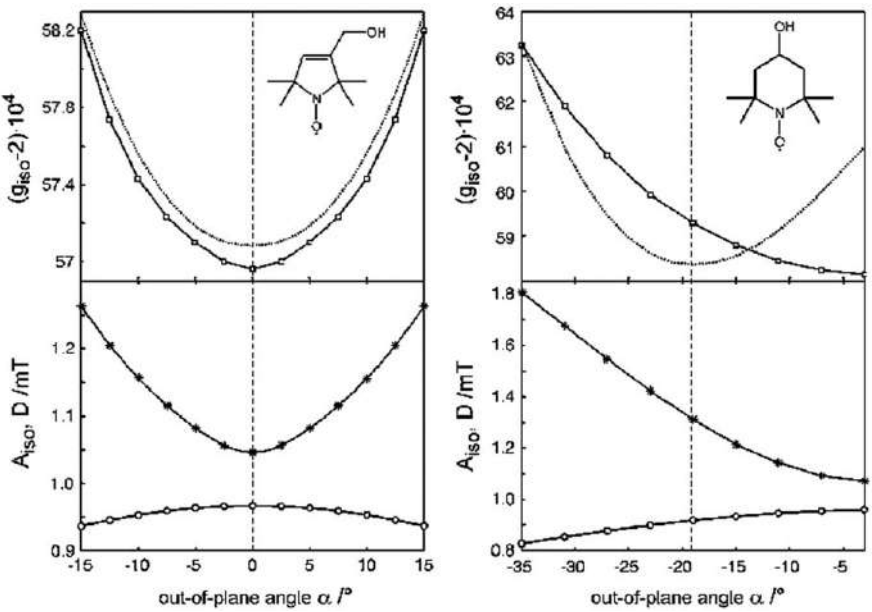

Figure 6.6 The calculated g_{iso} (open square), A_{iso} (asterisk) and D (open circle) values as a function of out-of-plane angle α for 3-hydroxymethyl-2,2,5,5-tetramethylpyrrolin-1-oxyl (left) and 4-hydroxy-2,2,6,6-tetramethylpiperidine-*N*-oxyl (right). The dotted line shows the relaxed energy profile, and the dashed line indicates the minimum energy angle.
Reproduced from ref. 80 with permission from Springer Nature, Copyright 2009.

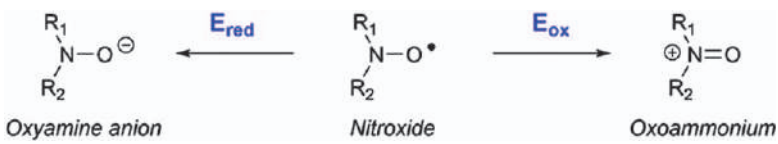

Figure 6.7 The oxidation and reduction of a nitroxide of the general form, $R_1R_2N–O^{\bullet}$.

transfer from protic impurities rapidly quenching the initially formed oxyamine anion as a hydroxylamine. In this latter case, the highly coupled nature of the rate and equilibrium constants for the underlying elementary processes can make the direct experimental measurement of a corresponding potential difficult, and computational chemistry offers a valuable alternative to experiment.

Even when measurement is possible, the accompanying synthesis can be expensive and time-consuming, and as such computational chemistry offers an attractive means of assessing the utility of a given species prior to experiment. In this respect, the success or failure of a given nitroxide hinges on its precise redox properties; including the electrochemical

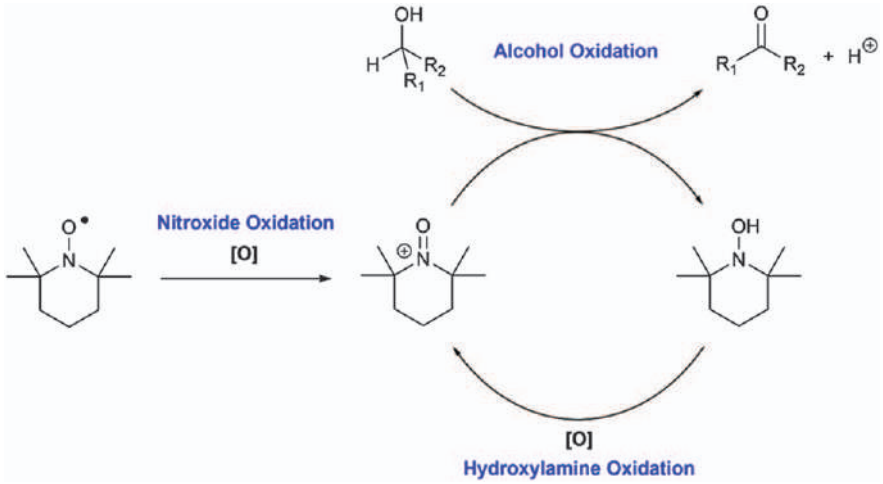

Figure 6.8 The nitroxide-catalysed oxidation of an alcohol to a ketone in the presence of bulk stoichiometric oxidant [O].

reversibility of oxidation/reduction and the respective potentials of these electron transfers. For instance, in alcohol oxidation, nitroxides are frequently employed as catalysts in conjunction with a bulk stoichiometric oxidant, such as sodium hypochlorite or ambient oxygen (see Figure 6.8).[97,98] This bulk oxidant, [O], is used to generate the catalytically active oxoammonium species *in situ*, which in turn oxidises the substrate alcohol to a ketone. If the oxidation potential of the nitroxide is too high, then the bulk oxidant will be unable to oxidise the initial nitroxide into the catalytically active oxoammonium cation. Conversely, if the oxidation potential of the nitroxide is too low, then the oxoammonium cation will be unreactive towards the alcohol substrate. Moreover, in biochemistry nitroxides are of interest as antioxidants; protecting cells against cytotoxic reactive oxygen species.[99,100] *In vivo*, both oxidation and reduction processes involving nitroxides are relevant,[101,102] and so the ability to predict and rationalise the redox potentials of nitroxides is invaluable for screening novel antioxidants.

While other references discuss the theoretical evaluation of redox potentials for organic[103,104] and inorganic[105] species in some detail, we will more briefly outline some of these considerations within the specific context of nitroxide oxidation and reduction. The theoretical calculations of most thermochemical quantities, including oxidation and reduction potentials, usually take advantage of the Born–Oppenheimer approximation, which partitions the electronic and nuclear wavefunction and so separates the calculation into three steps (Figure 6.9). Initially, the electronic energy of the molecule in its oxidised and reduced form is calculated using normal electronic structure calculations. Next, the entropic contribution from nuclear motion is calculated, usually employing harmonic or quasi-harmonic

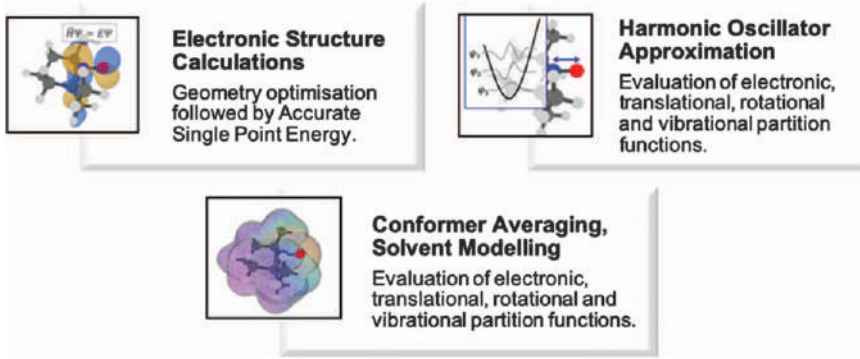

Figure 6.9 The three steps involved in the calculation of oxidation and reduction potentials.

approximation in conjunction with computed frequencies. Finally, statistical averaging of relevant conformations and solvent corrections are applied, usually by assuming Boltzmann distributions and applying continuum solvent models. For computation of redox potentials, the first step affords the gas phase 0 K adiabatic ionisation energy (IE) or electron affinity (EA), the second step computes the (temperature-dependent) entropic corrections, while the third step corrects the resulting gas-phase free energy for solvent effects and appropriately weights these quantities according to the population of the individual conformations.

The main methodological challenges relate to the first and third steps: in the former case, obtaining a sufficiently accurate description of the electronic energies, albeit within a single reference framework; in the latter, modelling the effects of solvation, particularly for the ionic species. In addition, there is the added complication of converting the solution-phase Gibbs free energies for the half reactions into electrode potentials, which entails choosing appropriate values for the reference electrode, treating the electron in a consistent manner, and considering coupled chemical processes where relevant. Below we introduce the methods (and where relevant equations) for each of these steps, before examining some of the applications.

6.4.1 Definitions and Key Equations

The standard reduction potential directly measures the thermodynamic feasibility of the general reduction half-reaction.

$$O\,(\mathrm{s}) + n_\mathrm{e}\,\mathrm{e}^-\,(\mathrm{g}) \leftrightarrow R\,(\mathrm{s}) \tag{6.17}$$

where O refers to an oxidised reagent, R refers to a reduced reagent, n_e is the number of electrons exchanged between the oxidised and reduced species, and ''s'' and ''g'' refer to species in solution and in the gas phase, respectively. Note that the charges of O and R are not shown here but must be

balanced across the reaction. The absolute reduction potential for this reaction is given by the Nernst equation[106,107] as

$$\Delta_r G^\circ(O|R) = -n_e F E^\circ_{\text{abs}} \tag{6.18}$$

where $\Delta_r G^\circ(O|R)$ is the Gibbs free energy change for the half reaction, F is the Faraday constant (96 485 C mol^{-1}), and n_e is the number of electrons transferred in the half-reaction. To facilitate comparison with experiment, this must be converted to a relative (cell) potential measured against a reference electrode (such Fc/Fc$^+$, Ag/Ag$^+$, the standard hydrogen electrode, *etc*.).

$$E^\circ_{\text{rel,REF}}(O|R) = E^\circ_{\text{abs}}(O|R) - E^\circ_{\text{abs}}(\text{REF}) \tag{6.19}$$

Here $E^\circ_{\text{abs}}(\text{REF})$ is the absolute reduction potential of the reference electrode and in principle can be calculated the same way, though in practice literature values are available for most references.[103,104] In choosing a literature value it is important to ensure that the treatment of the electron is consistent in both half reactions so that it cancels from the cell potential. While the electron has no electronic energy as such, it is assumed to have thermal energy and entropy, but the amount differs according to which convention is used. Details of the different conventions are in ref. 103 and 104; ultimately, the choice of convention has no impact on the results provided it is applied consistently.

The values of $E^\circ_{\text{rel,REF}}(O|R)$ yielded from the above equations correspond directly to the experimental half-wave potential for reversible redox processes. However, many species (including nitroxides) can undergo irreversible redox reactions which are often coupled with other spontaneous proton transfer or addition/fragmentation processes. In these situations, experimental cyclic voltammograms (CVs) are complex. One can either fit these experimental CVs with kinetic schemes that take into account the redox processes, the coupled chemical reactions, and diffusion into and out of the double layer. In such cases the computational $E^\circ_{\text{rel,REF}}(O|R)$ can be compared with the fitted potentials obtained for isolated redox processes. Alternatively, one can use computational chemistry to study the coupled processes as well and yield adjusted half-wave potentials. For instance, in aqueous environments reduction of nitroxide radicals is accompanied by rapid protonation (Figure 6.10). As such, formal reduction processes can be represented by different half reactions, which will depend heavily on the nitroxide of interest and on the pH of the solution. Thus, the one-electron reduction of TEMPO$^\bullet$ generates a TEMPO$^-$ oxyamine anion, which is rapidly quenched by water (across a range of pH values) to form the corresponding TEMPOH hydroxylamine. However, the TEMPOH hydroxylamine is itself a weak base (conjugate acid pK_a = 6.9–7.5) and may be protonated depending on the pH of the

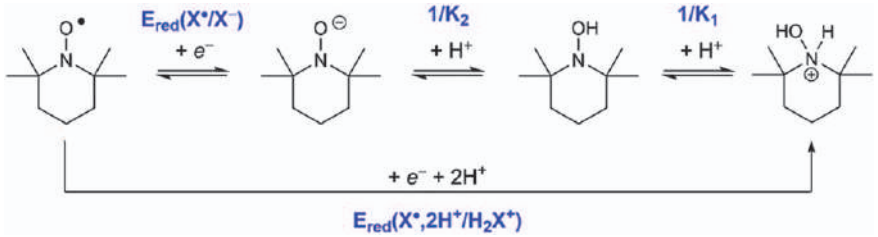

Figure 6.10 Chemical processes associated with the reduction of the TEMPO• radical in water.

solution. As a result, the half-wave reduction potential observed by experimental measurements is given by:

$$E_{1/2} = E_{\mathrm{red}}(X^{\bullet}, 2H^{+}/H_2X^{+}) + \frac{RT}{F}\ln\left(K_1K_2 + K_1[H^{+}] + [H^{+}]^2\right) \qquad (6.20)$$

where E_{red} $(X^{\bullet}, 2H^{+}/H_2X^{+})$, K_1 and K_2 are as defined in Figure 6.9.

6.4.2 Electronic Structure Methods and Gas-phase IEs and EAs

Electronic structure methods are conveniently divided into two categories; wavefunction-based approaches and density functional theory (DFT). Within wavefunction theory there is a hierarchy of different approximations with varying levels of accuracy, some of which were briefly introduced in Section 6.2. For redox potentials, single-reference methods are usually sufficient. There are three main 'families' of correlated single-reference wavefunction methodologies: Møller–Plesset perturbation (MP*n*) theory[108–114] (*e.g.*, second-order Møller–Plesset corrections, MP2), couple cluster (CC) theory[115–117] [*e.g.*, single, double and perturbative triple excitations, CCSD(T)] and finally configurational interaction (CI) theory[117–119] [*e.g.*, quadratic configurational interaction with single, double and perturbative triple excitations, QCISD(T)]. While acceptable accuracy will depend largely on context, a sufficiently accurate treatment of electron correlation is achieved in most chemical systems with CCSD(T) or QCISD(T) used in conjunction with large triple zeta basis sets. Such energies will (usually) only differ from corresponding exact values by 1–2 kJ mol^{-1}.[120,121] Thus, CCSD(T) is frequently labelled the ''gold-standard'' of computational chemistry, as this level of accuracy is sufficiently accurate for most (single-reference) applications.

Composite procedures are a notable subclass of wavefunction-based approaches that pragmatically perform basis set extrapolation schemes and/or combine the results of calculations performed at different levels of theory. These procedures are usually as accurate as the large basis set CCSD(T) (or equivalent) calculations that they are attempting to approximate, but only require a fraction of the computational expense.[122–126] The Gaussian

composite procedures[122–126] (G*n*), originally developed by Curtiss and co-workers are among the most popular, and a popular variant of G3 theory is the less computationally intensive G3(MP2)-RAD procedure.[127] Other well-known *composite procedures* include the CBS methods[128–135] developed by Petersson and co-workers, and the W*n* methods[121,136–138] formulated by Martin and co-workers. Although not strictly a composite procedure, the F12 approximation[139] in its various manifestations also delivers improved accuracy by significantly reducing errors caused by small basis sets.

Density functional theory (DFT) calculates the energy of a molecule or atomic species using its one-electron density and a functional. The Hohenberg-Kohn theorems,[140] which form part of the inspiration for DFT, state:

(1) That the ground-state external potential (and thus total electronic energy of the ground state) is a unique functional of the electron density.
(2) That a density that minimises the total energy of the ground-state is the exact ground-state density.

Using the electron density to obtain the total energy has been touted as a way of circumventing the poor size scaling of wavefunction-based methods. Unfortunately, the first Hohenberg-Kohn theorem is an existence proof rather than a constructive proof. As such, it only establishes that the ground-state external potential is a unique functional of the electron density and provides no insights into its actual mathematical form. Consequently, the exact DFT functional is unknown.

Modern DFT functionals are based on the Kohn–Sham equations,[141] which cleverly consider the Hamiltonian for a fictitious system of *non-interacting electrons* that have an overall ground-state density that is identical to the real atomic or molecular system (where the electrons are allowed to interact). Ideally, DFT would be exact and formulated from fundamental physical and mathematical arguments. However, in practice many popular DFT functionals are heavily parametrised using test sets of experimental and (wave-function-derived) theoretical data. While current DFT functionals offer reasonable accuracy at low computational cost, they can also fail spectacularly and unexpectedly.[142] Many of the most popular functionals, such as B3LYP, have been found to fail dramatically (often to the extent that results are qualitatively incorrect).[142] Moreover, there is no systematic way to improve DFT results and so the choice of functional is quite subjective. Because of this often variable and unpredictable accuracy, DFT should always be employed cautiously in conjunction with appropriate benchmarking.

There are many articles that evaluate the performance of common DFT functions and other wavefunction-based methodology for the calculation of IEs and EAs. For instance, our group examined theoretical procedures for IE and EA calculations on a range of piperidine, pyrrolidine, oxazolidine derivatives, isoindoline and azaphenalene nitroxides.[143] This study revealed

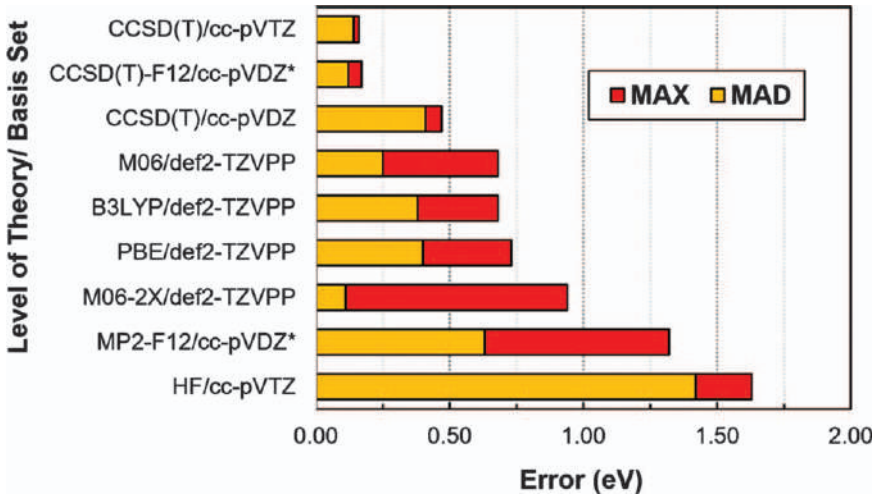

Figure 6.11 Mean absolute error (MAD) and maximum errors (MAX) in adiabatic ionisation energies for the 19 organic species in the Pantazis test set, taken from ref. 144. *Indicates a F12 variant of the standard cc-pVDZ basis set was used.

that low-cost DFT procedures often carried unacceptably large errors, with B3LYP and MPWB1K carrying mean absolute deviations (MAD) for EAs of 0.23 and 0.40 eV, respectively. Interestingly, these errors are primarily associated with the reaction site and can be largely mitigated using an ONIOM partitioning scheme. For instance, B3LYP in conjunction with a G3(MP2)-RAD core affords much smaller deviations (around 0.10 eV). Pantazis and co-workers recently examined the IEs of 19 organic species with several methods using CCSD(T)/CBS data as a reference (see Figure 6.11).[144] Despite its enormous popularity in computational organic chemistry, B3LYP once again performs relatively poorly with mean absolute deviations and maximum deviations (MAX) of around 0.40 and 0.70 eV, respectively. M06-2X performs better with a MAD of only 0.11 eV, although it still suffers an unexpectedly large MAX (for phenol) of nearly 1 eV. CCSD(T)/cc-pVTZ offers excellent accuracy, with MAD and MAX values of 0.14 and 0.16 eV, respectively. However, this accuracy is strongly basis set dependent. If a smaller double-zeta basis set (cc-pVDZ) is employed, the MAD and MAX of CCSD(T) increase dramatically to over 0.4 V. CCSD(T)-F12 offers an excellent compromise, with a double-zeta F12 calculation essentially matching the accuracy of standard triple-zeta CCSD(T).

6.4.3 Solvent Effects and Redox Potentials

To convert gas-phase IEs and EAs to redox potentials, one needs to calculate the Gibbs free energies of solvation, so as to obtain Gibbs free energies in solution. In doing this one also needs to include a term $RT(\ln V)$ to account

for the change of state from 1 atm to 1 M.[145] The simplest and most computationally efficient methods for calculating solvation Gibbs free energies are continuum models, in which each solute molecule is embedded in a cavity surrounded by a dielectric continuum of permittivity ε.[146] Continuum models are designed to reproduce bulk or macroscopic behaviour, and can fare extremely well in certain applications including redox potentials.[147] However, the results obtained using continuum models are highly sensitive to the choice of cavities (which are typically parameterised to reproduce the free energies of solvation for a set of small organic molecules). This reliance on empirical parameterisation means the errors can sometimes be unpredictable. Moreover, their accuracy can suffer if there are explicit solute–solvent interactions such as complex formation or hydrogen bonding.[148] Although this problem can be overcome by including a small number of explicit solvent molecules in the *ab initio* calculation, as in a cluster-continuum model,[149] this adds significantly to the cost of the calculation.

As a result, in small to medium nitroxides (where high-level composite calculations are feasible), the accuracy of redox calculations is usually limited by the accuracy of the continuum solvent model. This is particularly a problem because of the involvement of charged species. For neutral molecules, solvation energies are typically small, and many solvent models are able to compute the solvation energies of neutral molecules with reasonably high accuracy, with errors typically of the order of 5–10 kJ mol^{-1}.[150] However, errors in solvation energies for charged systems can be significantly larger (often above 20 kJ mol^{-1}; see Figure 6.12). This introduces correspondingly large errors into the resulting redox potentials. Fortunately, errors introduced by solvation models are often highly systematic (see Figure 6.13);

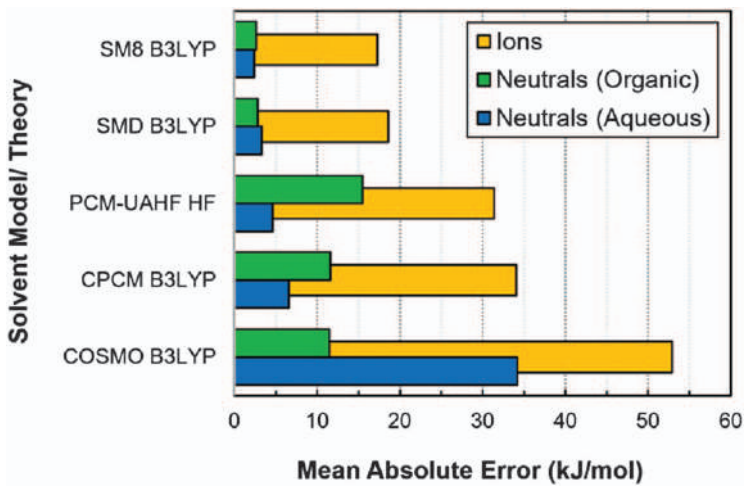

Figure 6.12 Typical errors for ionic and neutral species in popular continuum solvation models.

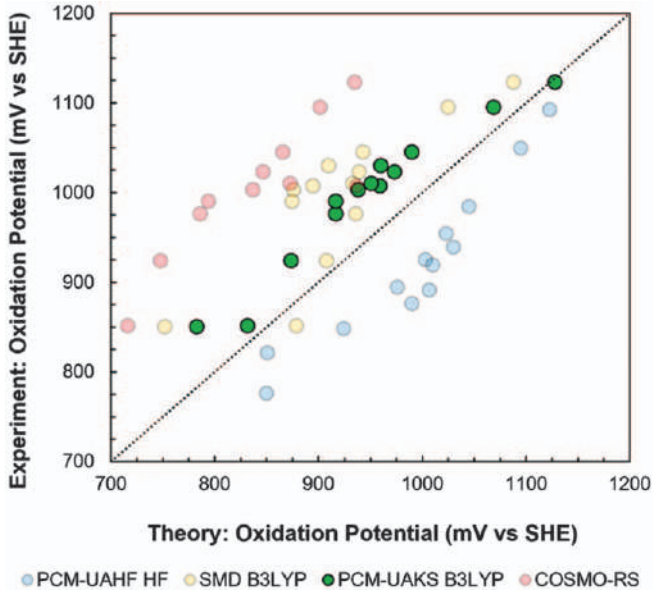

Figure 6.13 The performance of different solvent methodologies for the computational prediction of nitroxide oxidation potentials.

depending on the functionality of the anion or cation in question. Note that in Figure 6.13, the superior absolute performance of PCM-UAKS B3LYP is not a general result for other redox systems, and in other studies of nitroxides or closely related species methods such as SMD or COSMO-RS perform better.[151–156]

Nonetheless, for the most part, errors in solvation energies within a set of related molecules are relatively systematic. As a result, they can be circumvented somewhat by computing redox potentials in an isodesmic fashion, where relative (rather than absolute) potentials are computed against a structurally similar reference system. The potential of the substrate is then determined by using this relative potential in conjunction with an accurate experimental value for the reference couple (see Figure 6.14). This approach exploits systematic error cancelation by offsetting the errors introduced by suboptimal solvation modelling of both charged species. While this approach normally delivers more accurate potentials, it relies on the availability of accurate experimental measurements for the reference couple.

6.4.4 Selected Applications

Computational chemistry offers not only the opportunity to predict kinetics and thermodynamics; it can also be used to help interpret the underlying structure–reactivity trends by providing detailed structural information, dipole and quadrupole moments, and other related properties. This in turn is useful in reagent design, as the case studies below illustrate.

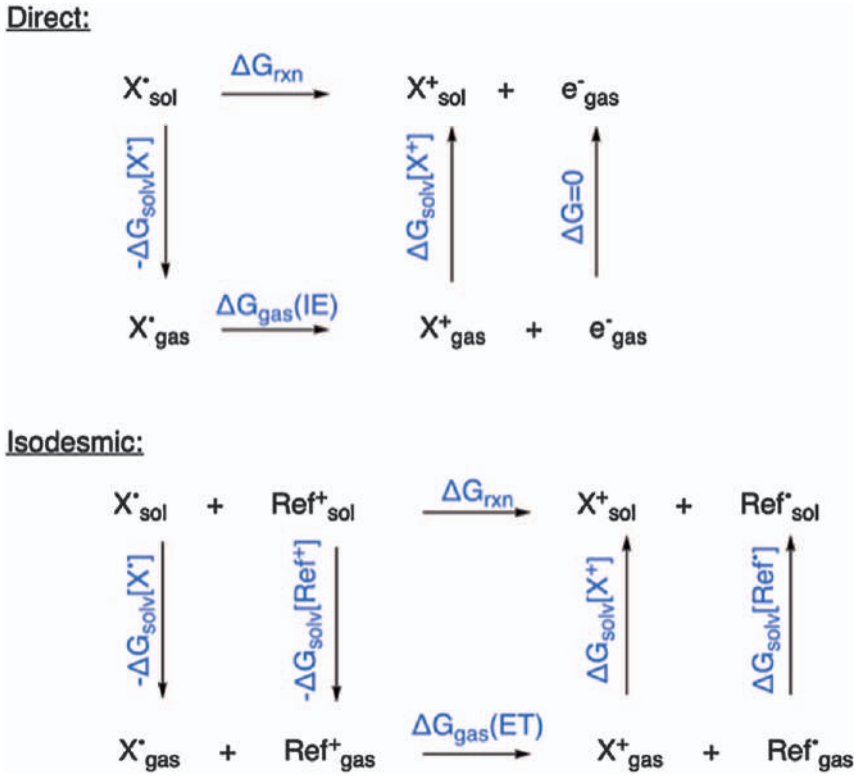

Figure 6.14 Direct *vs.* isodesmic oxidation potential calculations.

6.4.4.1 *Case Study 5: Computational Design of Cyclic Nitroxides as Efficient Redox Mediators for Dye-sensitised Solar Cells*[157]

With decreasing global fossil fuel reserves and increasing energy demand, improving the efficiency and cost-effectiveness of renewable energy is becoming an increasing priority. Dye-sensitised solar cells (DSSCs) are particularly promising, as they are less expensive and more flexible than traditional silicon-based cells. DSSCs are a photoelectrochemical system consisting of two separate electrodes; a mesoporous thin-film semiconductor (usually TiO_2) with a tethered monolayer of sensitising dye and a counter electrode (see Figure 6.15). An electrolyte containing a redox mediator is injected between these two electrodes. Light is first absorbed by a dye, then the photoexcited dye (S*) transfers an electron to TiO_2. The oxidised dye ($S^{+\bullet}$) is reduced by the redox mediator ($Md^{\bullet}$), with the oxidised mediator (Md^{+}) diffusing to the counter electrode. There the oxidised mediator is reduced by current passing through the cell. As it affects the electrochemical potential at the counter electrode and semiconductor, the redox mediator is a crucial component of the cell.

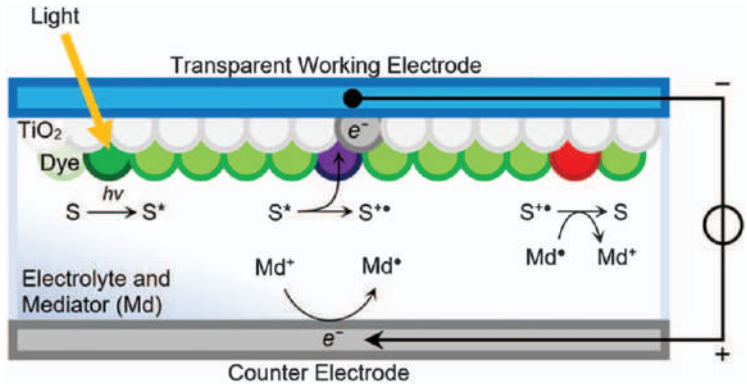

Figure 6.15 A simplified depiction of a dye-sensitised solar cell, showing the principal photoexcitation and electron transfer processes.

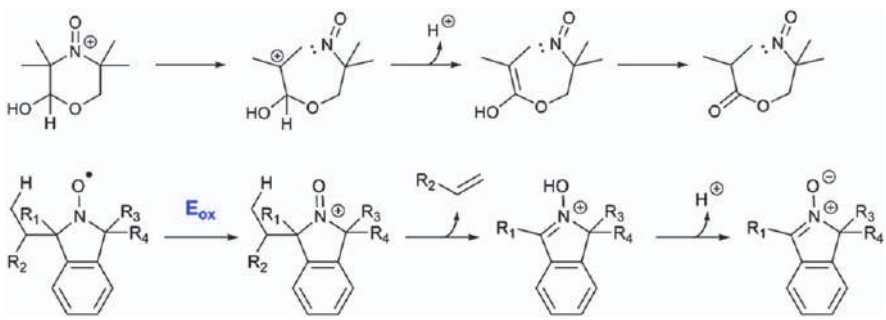

Figure 6.16 (Top) Proposed ring-opening pathway of a hydroxyl-substituted morpholine oxoammonium. The electrochemical oxidation of the corresponding nitroxide is nearly completely irreversible. (Bottom) The generation of isoindoline-derived nitrononones *via* β-fragmentation from the corresponding oxoammonium (with loss of an alkene).

Nitroxides are particularly attractive as redox mediators because of their rapid and (usually) reversible redox chemistry, low toxicity and low corrosivity. They are also characterised by fast rates of both heterogeneous electron-transfer and electron self-exchange reactions. Importantly, their oxidation potentials are also reasonably close to the optimal range of 0.60–0.85 V (*versus* SHE) and can be further optimised through structural modifications. However, this reversibility is fundamentally dependent on their chemical structure with some cyclic nitroxides undergoing irreversible ring-opening processes or fragmentation (Figure 6.16). Experimental cyclic voltammetry measurements can readily establish the oxidation potential of a given nitroxide and its electrochemical reversibility. Synthesis and characterisation of nitroxides is often time-consuming and expensive. Hence, computational screening is particularly attractive; allowing for rapid and accurate prediction of the redox properties of candidate nitroxides.

To address this problem, we studied the nitroxide structural features to help guide experimental optimisation of DSSCs.[157] As redox mediators for DSSCs, nitroxides need to have oxidation potentials of 0.60–0.85 V (*vs.* SHE) and high stability. It was found that most monocyclic nitroxides had potentials in the correct range, but were susceptible to the ring-opening processes of Figure 6.16. These ring-opening processes could be largely suppressed by fusing aromatic rings to piperidine and pyrrolidine nitroxides, leading to azaphenalene and isoindoline ring frameworks. These basic frameworks are resistant to oxidative ring opening, as the initially formed nitroso and carbocation are held near each other by the secondary aromatic scaffold (and rapidly couple). However, their oxidation potentials are too high for DDSCs (1.02 V and 0.98 V, respectively). One possible solution is replacement of the flanking groups with higher alkyls. While calculations indicate this substitution does appreciably lower the oxidation potential of isoindolines, unfortunately it also facilitates a β-fragmentation process that decomposes the oxoammonium species into a nitronone (Figure 6.16). Aside from modification of the flanking alkyl groups, introduction of electron-donating amino substituents onto the aromatic ring also lowered the potential of isoindoline- and azaphenalene-based nitroxides. However, this moiety can also undergo irreversible oxidation with proton loss to form electrochemically inert products. As such, isomers bearing the NH_2 group are unsuitable for the present study.

However, it was shown that there are still nitroxides that possess oxidation potentials within the target range and meet the reversibility criteria outlined above. These included an adamantine-like species, piperidines with α-cyclohexyl groups, TMAO derivatives with alkyl and methoxy substituents, as well a large fused antiaromatic system (Figure 6.17). Later experimental testing by Nishide and co-workers verified that one of these, the 2-azaadamantan-N-oxyl radical was an exceptional redox mediator, consistent with our theoretical predictions.[158] Employing this mediator in a DSSC, Nishide and co-workers set the benchmark efficiency (for organic

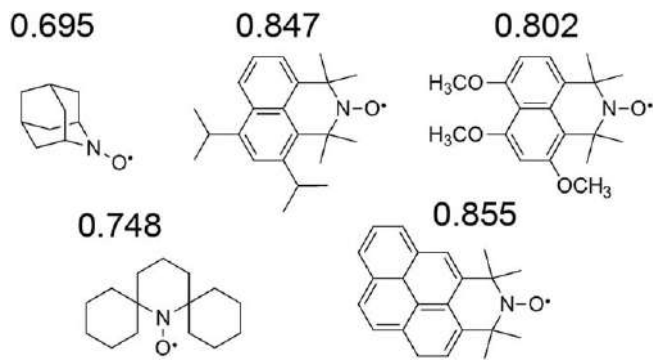

Figure 6.17 Proposed redox mediators showing computed potentials in V *vs.* SHE. Reproduced from ref. 157 with permission from John Wiley & Sons, Copyright 2012 WILEY-VCH Verlag GmbH & Co. KGaA, Weinheim.

radical-based mediators) of 8.6%; significantly improving on the previous efficiency of TEMPO-based DSSCs of 5.4%.

6.4.4.2 *Case Study 6: Effect of Heteroatom and Functionality Substitution on the Oxidation Potential of Cyclic Nitroxide Radicals: Role of Electrostatics in Electrochemistry*[159]

Computing accurate oxidation potentials is undoubtedly helpful, as it enables the prescreening of novel nitroxides for specific applications. However, using theory to deduce quantitative (or semiquantitative) structure–reactivity or structure–property relationships is arguably even more useful because it allows nitroxides to be rationally designed for a specific purpose. Many theoretical and experimental studies rationalise nitroxide oxidation and reduction potentials using strain-arguments based on ring-size and rigidity.[98,143,157,160,161] Normally, the basis for such arguments is that the oxoammonium cation, oxyamine anion and nitroxide radical prefer different degrees of planarity around the nitrogen atom. Thus, attaining the optimal geometric rearrangement is hindered to varying extents by size and rigidity of the primary nitroxide ring. To examine strain-based arguments in more detail, we collated literature[143,157] high-level theoretical predictions of the oxidation and reduction potentials of prototypical nitroxides; separately examining the influence of ring contraction and rigidification.

As Table 6.1 reveals, reduction potentials are significantly lowered by ring-contraction, with a decrease of around 140–180 mV. This indicates the larger piperidine (and azaphenalene) rings are better able to accommodate the geometric changes associated with nitroxide reduction as compared to the smaller pyrrolidine (and isoindoline) rings; consistent with a strain-based argument. Surprisingly, however, ring-size alone does not appreciably influence oxidation potentials; with minimal change moving from piperidine to pyrrolidine (or moving from azaphenalene to isoindoline).

Table 6.1 Relative aqueous oxidation (E_{ox}) and reduction (E_{red}) potentials for piperidine, pyrrolidine, azaphenalene[a] and isoindoline nitroxides. Data taken from ref. 143.

Nitroxide	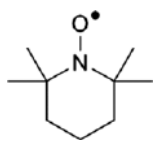	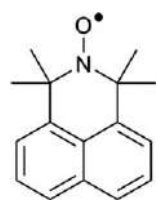	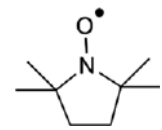	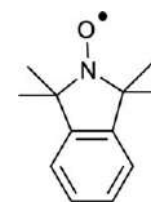
E_{red} (mV)	0.0	+146	−138	−22
E_{ox} (mV)	0.0	+267	+2	+240

[a]Data for the azaphenelene were subsequently corrected in ref. 157 and we show the corrected data here.

While aromatic rigidification does significantly increase oxidation potentials (by 240–260 mV), inexplicably, it also raises the respective reduction potentials (by 120–150 mV). In other words, oxidation potentials are insensitive to ring-size but increase substantially upon rigidification, while reductions potentials are lowered by ring-contraction yet raised by rigidification. Interestingly, rigidification of piperidine through the inclusion of multiple aliphatic frameworks lowers the respective oxidation potential (see Figure 6.17); indicating different effects from aromatic and aliphatic rigidification strategies. Collectively, this behaviour is incompatible with a simple strain-based argument. If attaining the optimal cation or anion geometry is hindered by ring size and rigidity, then why do these parameters appear to operate independently and have unpredictable effects on oxidation and reduction behaviour? Why does rigidification with aromatic (but not aliphatic) frameworks increase nitroxide oxidation potentials?

To address these questions, we recently explored if electrostatics could explain nitroxide oxidation (and reduction) potentials.[159] Electrostatic effects can be described using a multipole expansion, which includes contributions from monopole, dipole, quadrupole and octapole (*etc.*) terms. For electronically uncharged substituents, the dipole term is the first non-zero contributor to this expansion and so formed the basis for our initial investigations. The substituent orientation relative to the >N–O$^{\bullet}$ moiety is crucial, as this axis defines the only component of the dipole moment that will have a non-zero interaction with the charge formed upon oxidation. To decouple the dipole moment of the substituent from that of the >N–O$^{\bullet}$ group, we used analogues in which the >N–O$^{\bullet}$ moiety was replaced with a CH_2 group. This substitution conveniently preserves the relatively fixed orientations of the interacting substituents, as the basic C–C framework of these models is analogous to that of the corresponding nitroxides. Initial investigations revealed that this distance-scaled dipole moment was very well correlated with experimental oxidation potentials. However, three nitroxides from this initial set possessing π-functionality were found to be significant outliers. This led us to investigate if this behaviour, and more generally the effect of aromatic rigidification on redox potentials (as reported in Table 6.1), could be electrostatic in origin.

The importance of quadrupole moments in the electrostatic description of molecules with π systems is well known.[162–164] Moreover, truncating the multipole expansion at the dipole term is only valid if the substituent and $>N^{+}=O$ moiety are sufficiently separated, so at short-range higher order multipole terms may be significant. Inclusion of an appropriately scaled quadrupole term corrects the three previous outliers and simultaneously improves the correlation with the experimental oxidation potential. Moreover, this dipole–quadrupole parameter can be applied successfully to a total test set of 35 different α-tetramethyl substituted nitroxides; comprising of one pyrrolidine, two pyrrolines, 11 isoindolines, 15 piperidines, two morpholines, three azaphenalene and one azepine (Figure 6.18).[159] Despite the structural diversity of these nitroxides (including different ring sizes and rigidity), good correlation was observed between the distance-scaled dipole

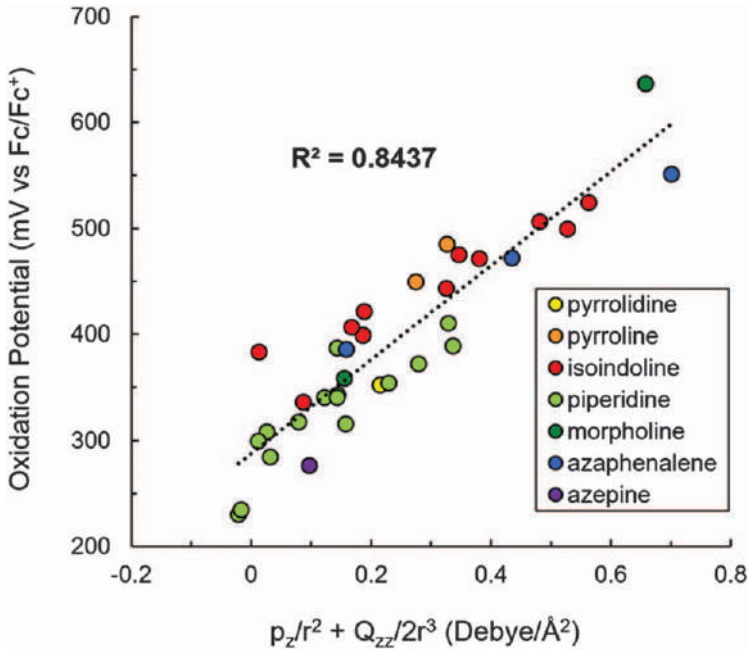

Figure 6.18 The generation of isoindoline-derived nitrononeS *via* β-fragmentation from the corresponding oxoammonium (with loss of an alkene). Data taken from ref. 159.

and quadrupole term and the respective oxidation potential (total $R^2 = 0.84$). Reassuringly, the optimal ratio between the component dipole and quadrupole terms found *via* a two-variable regression (1.78 : 1) is reasonably similar to the theoretical ratio predicted in a multipole expansion (2 : 1). We should caution that due to relatively small separation between the nitroxide moiety and the substituent, higher order multipole moments may also contribute; particularly in more electrostatically complex systems. It is also important to note that this analysis only considers the underlying (gas-phase) electrostatic effects and does not account for other key factors including: induction, ring-strain, through-space orbital overlap and solvent effects. Notwithstanding these considerations, this study highlights how nitroxide oxidation potentials can be rationalised with chemical intuition using substituent-based electrostatic arguments.

Returning briefly to the trends reported in Table 6.1, we can now fully rationalise these redox potentials in terms of strain and electrostatics. Strain-based effects are clearly a factor in the case of nitroxide reduction (where geometry relaxation is normally more significant). However, rigidification through the inclusion of fused aromatic rings introduces a large quadrupole moment. In the case of isoindolines and azaphenalenes, this quadrupole interacts unfavourably with the forming oxoammonium cation, thereby raising the oxidation potential of the corresponding nitroxide. Conversely, this quadrupole interacts favourably with the oxyamine anion

and so also raises the corresponding nitroxide reduction potential. This work highlights the often-underappreciated role that through-space electrostatics has in governing redox behaviour and provides a simple tool for tuning the oxidation behaviour of nitroxide radicals.

6.5 Modelling Nitroxide-mediated Polymerisations

Nitroxide-mediated polymerisation (NMP) was the first successful technique for controlled radical polymerisation.[165] Full details of this process and its achievements are outlined in Chapter 7; for the present purposes it is important to note that the key to control rests with: (a) tuning the equilibrium constant for alkoxyamine dissociation to sit within an ideal range whereby there are enough propagating radicals released to sustain a polymerisation but not enough for significant chain termination; (b) minimising other chain-stopping side reactions. Computational chemistry can assist with both aspects of this design problem and this is illustrated with the case studies outlined below.

6.5.1 Methodology

The computational methods used to study NMP are similar to those used for redox processes: high-level single-reference methods such as G3(MP2)-RAD with appropriate solvation corrections. An example showing agreement of theory and experiment is provided in Figure 6.19, where theory is obtained

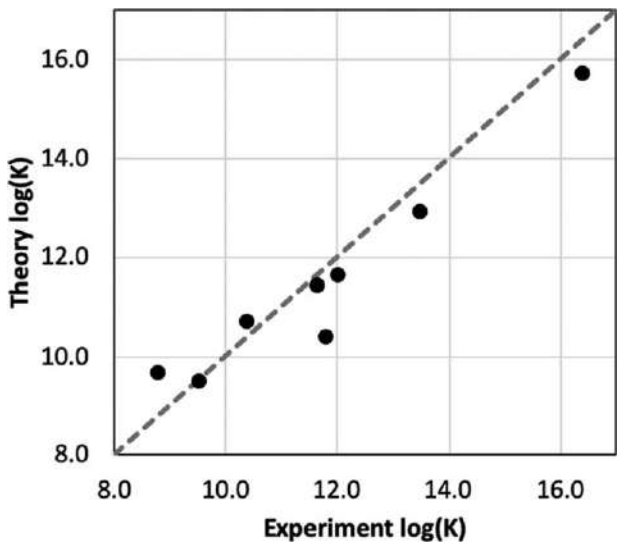

Figure 6.19 Comparison of quantum-chemical and experimental equilibrium constants for alkoxyamine dissociation. Theoretical calculations performed using an ONIOM approximation of G3(MP2)-RAD//B3-LYP/6-31G(d) in conjunction with PCM-UAKS solvation energies at the B3-LYP/6-31G(d) level. Data from ref. 166.

using an ONIOM correction to G3(MP2)-RAD and solvent is modelled using the PCM-UAKS continuum model.[166] In this case the Gibbs free energies of reaction agree to within a mean absolute deviation of 4.5 $kJ\,mol^{-1}$. The kinetics of most of the side reactions in NMP are likewise well described by the same methodology; however, the kinetics of the σ-bond dissociation are, as described in Section 6.2.1, a multireference problem. Fortunately, modelling the kinetics of alkoxyamine bond dissociation is less important for predicting the outcome of an NMP process because the reverse reaction is essentially barrierless and hence the barrier for the forward process is dominated by the thermodynamics.[167]

6.5.2 Selected Applications

6.5.2.1 Case Study 7: Linear-Free Energy Relationships for Modelling Structure–reactivity Trends in Controlled Radical Polymerisation Macromolecules[166,168,169]

A series of theoretical studies used computational chemistry to develop simple equations for predicting the bond dissociation Gibbs free energy (BDFE) and hence equilibrium constant in nitroxide-mediated polymerisation as a function of the leaving group and nitroxide. Key to this work was the identification of appropriate descriptors for the steric, resonance and polar properties of the nitroxide and alkyl radical, and statistical analysis to assess which of these factors were necessary to describe the bond energies. Within a series of alkoxyamines, it was found that the equilibrium constant was well described by the equation[166]

$$\log\,(\mathrm{Keq}) = -0.10\mathrm{IP} - 0.177\mathrm{RSE} - 0.130\mathrm{RSE_{nxd}} + 38.3 \qquad (6.21)$$

In this equation, IP is the vertical ionisation potential of the alkyl radical, RSE is the standard radical stabilisation energy of the alkyl radical, while RSE_{nxd} is a new descriptor for the nitroxide radical, related to the standard radical stabilisation energy, but reflecting in this case the flexibility of the nitroxide to the geometric changes associated with formation of an alkoxyamine. In a follow-up study, the linear-free energy relationship was expanded to cover multiple types of controlled radical polymerisation. The resulting relationship obtained was[168]

$$\mathrm{BDFE[RX]} = 20.8\ \theta\mathrm{[R]} - 9.73\ \mathrm{IP[R]} - 1.10\ \mathrm{RSE[R]} + 192\ \theta\mathrm{[X]} + 57.4$$
$$\mathrm{EA[X]} - 62.0\ \mathrm{Resonance[X]} - 250 \qquad (6.22)$$

where the steric descriptors θ[R] and θ[X] are measured as Tolman's cone angle of Cl-R and CH_3-X, respectively, the polar descriptors IP[R] and EA[X] are the (gas-phase) ionisation energy of $R^\bullet$ and electron affinity of $X^\bullet$, respectively, and the radical stability or resonance descriptors RSE[R] and Resonance[X] are measured as the standard radical stabilisation energy for $R^\bullet$ and the inverse HOMO–LUMO energy gap for $X^\bullet$. Apart from providing a

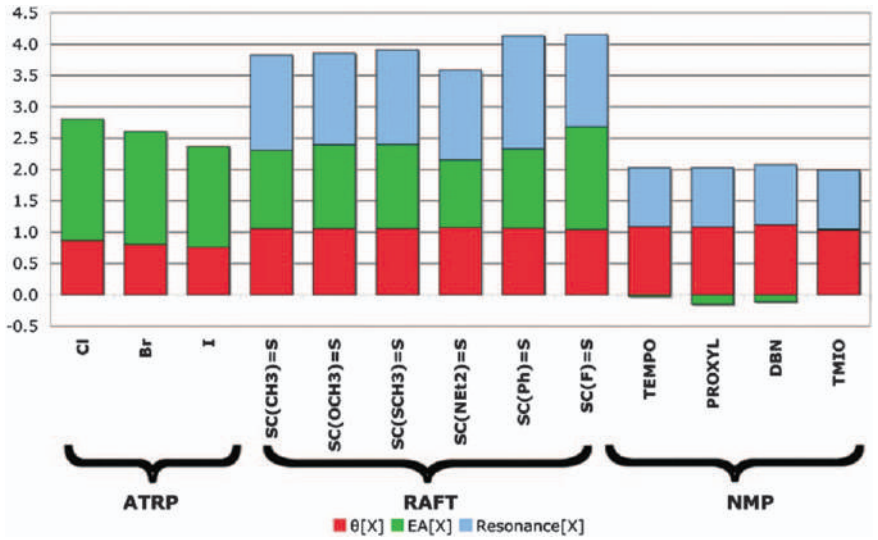

Figure 6.20 Values of each of the X-descriptors in dimensionless units (obtained by dividing each value by the average value for that descriptor across the full data set).
Reproduced from ref. 168 with permission from American Chemical Society, Copyright 2011.

predictive relationship for the bond energy (and hence equilibrium constant for the controlling equilibrium), the analysis of the descriptor values allows for a comparison of the relative importance of polar, steric and resonance effects in NMP *versus* atom transfer radical polymerisation (ATRP) and reversible addition fragmentation chain transfer (RAFT) (Figure 6.20). From Figure 6.20 it is clear that steric effects are relatively consistent across the different processes, while polar effects are important for ATRP and RAFT, and resonance effects are important for NMP and RAFT. This, in turn, gives some guidance as to not only what control agent might be important for a particular type of polymer, but what controlled radical polymerisation process itself might be necessary to target the right equilibrium constant.

6.5.2.2 *Case Study 8: Which Side-reactions Compromise Nitroxide-mediated Polymerisation?*[170]

In this work, a combination of quantum chemistry and kinetic modelling (using the software PREDICI) was used to identify the key side reactions in NMP and study how they varied for different combinations of NMP agents (specifically TEMPO, SG1 and DPAIO) and monomer (styrene, methyl acrylate and methyl methacrylate). A variety of side reactions had been proposed to interfere with NMP (Figure 6.21); through first principles modelling, the study was able to show that the main one was an intramolecular

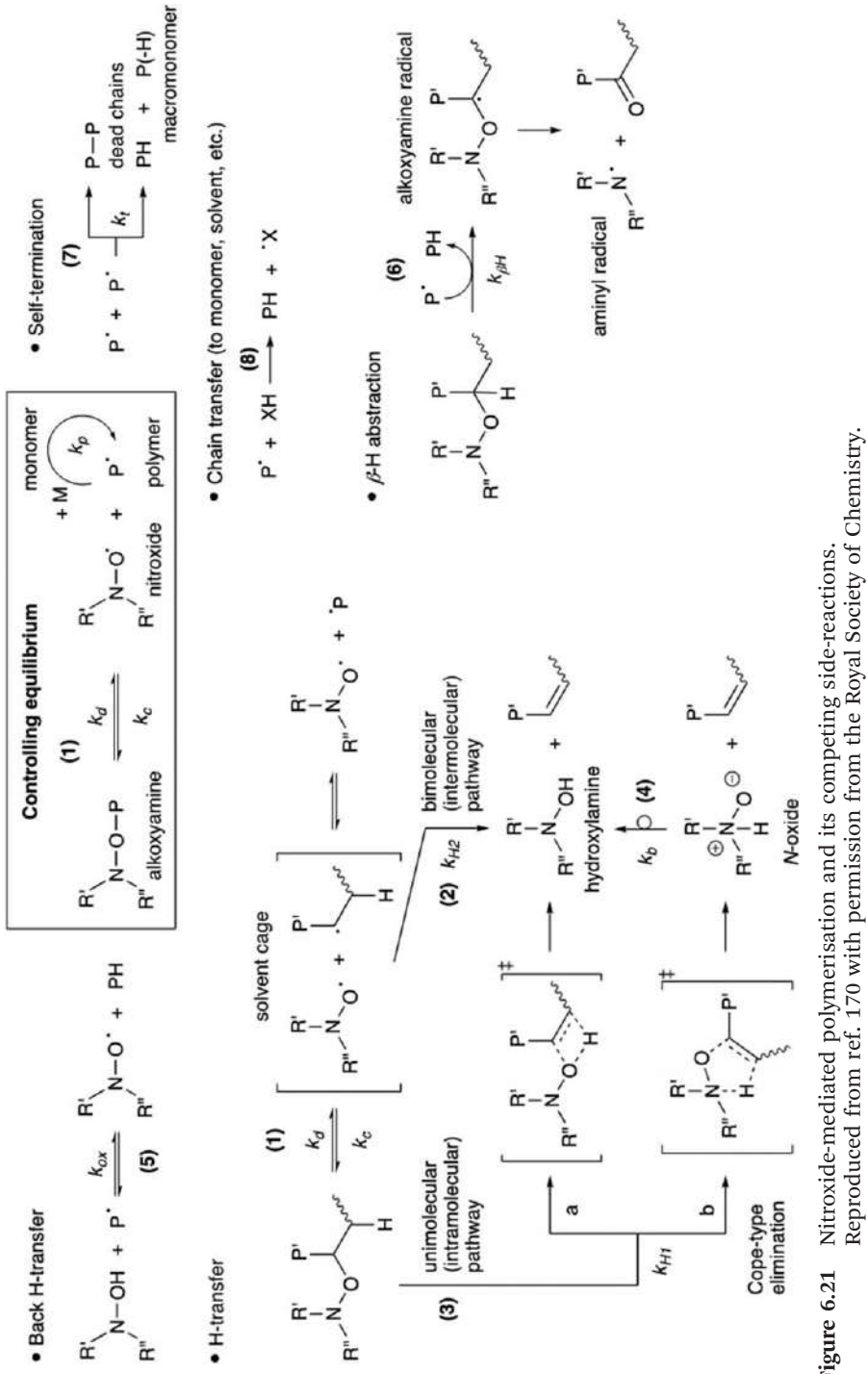

Figure 6.21 Nitroxide-mediated polymerisation and its competing side-reactions.
Reproduced from ref. 170 with permission from the Royal Society of Chemistry.

alkoxyamine decomposition (often referred to as 'disproportionation') *via* a Cope-type elimination, which was kinetically significant for TEMPO- and SG1-mediated polymerisations of MMA, and not significant for the other systems. The β-scission process was also found to be problematic for propagating radicals bearing an abstractable hydrogen. Interestingly, it was also found that, due to penultimate unit effects, the decomposition of alkoxyamines can occur *via* principally different mechanisms between the unimeric and polymeric species.

6.5.2.3 *Case Study 9: Computational Design of pH-switchable Control Agents for Nitroxide-mediated Polymerisation*[155,171–174]

One of the disadvantages of nitroxide-mediated polymerisation is the relatively high temperatures needed for sufficient alkoxyamine dissociation. Not only does this render polymerisation susceptible to side reactions, as seen above, but it also precludes alkoxyamines as a convenient source of carbon-centred radicals in natural product synthesis. Thus, if one could trigger alkoxyamine decomposition under mild conditions in a controlled manner this would be very attractive. One approach is using light and this is outlined below; another is using electrostatic effects. The basic principle behind this latter approach is to take advantage of the dipole associated with the N–O• functionality:

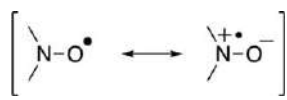

(6.23)

Thus a remote negative charge at the nitrogen side of the nitroxide should stabilise this dipole and in doing so stabilise the radical. Initial computational and experimental studies showed that indeed deprotonation of the carboxylic acid group in 4-carboxy-TEMPO lowered the gas-phase bond dissociation energies of its corresponding alkoxyamines by around 20 kJ mol^{-1}, irrespective of the leaving group.[171,172] Follow-up experimental studies in dichloromethane showed that this "pH-switch" decreased *ca.* 8.5 kJ mol^{-1} due to the increased dielectric constant of the reaction medium and associated decrease in the electrostatic interactions.[174] At that level, while significant, the pH-switch was not large enough to allow 4-carboxy-TEMPO to facilitate NMP at room temperature.[173] Computational studies were thus undertaken to test other nitroxides, known and novel, to see if any would be suitable for room-temperature NMP when charged and would be stable when neutral.[173] Design principles used in choosing the test set included synthetic accessibility, increasing the inherent stability of the nitroxide when uncharged, and placing the charge closer to the nitroxide (but without conjugation). Among the successful designs was a carboxy-TIPNO derivative which is indeed predicted to toggle between stability and radical release at room temperature (Figure 6.22). In this study, computational chemistry provided

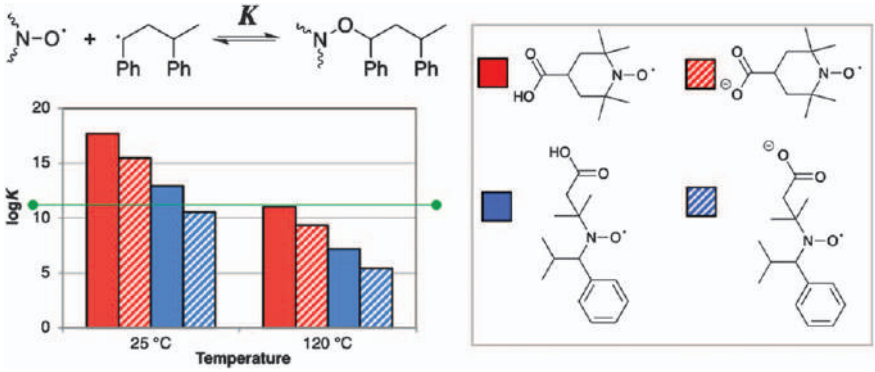

Figure 6.22 Change in equilibrium constant (in bulk styrene at 120 °C and 25 °C) upon deprotonation of 4-carboxy-TEMPO and a TIPNO derivative bearing a remote carboxylic acid group. The green line shows the equilibrium constant of neutral 4-carboxy-TEMPO, which functions well at 120 °C and represents a target value for the deprotonated species at room temperature. Above this line the alkoxyamine is too stable to sustain a polymerisation; below it too many radicals are released for control.
Data taken from ref. 173.

the initial insights behind electrostatic stabilisation and its dependence on chemical structure,[171,172] and subsequently allowed for a large number of molecules to be screened prior to undertaking laborious synthetic work.[173]

6.6 Studying Photoactive Nitroxides

Photoactive nitroxides remain an active area of interest, with potential uses as sensors, probes and as nitroxide-mediated polymerisation agents that can be activated under mild conditions.[175–177] Despite the reasonable amount of literature on photoactive nitroxides, and the well-established quenching of fluorescence upon formation of the nitroxide radical species, there is limited literature on exploring their excited states with computational methods.[178] Photoactive nitroxides do, however, exhibit several properties that can guide our approach to how we might explore their excited states. In this section, the different properties, how these properties can lead to different types of reactivity, and how we can model them, will be described.

6.6.1 Methodological Aspects

6.6.1.1 UV–vis Spectra

Nitroxides like, for example, TEMPO exhibit thermal reactivity in which a stable nitroxide radical is formed, however its σ-bond framework does not lend itself to photoactivity. A widely used approach to increasing light absorption is to introduce highly conjugated chromophore substituents

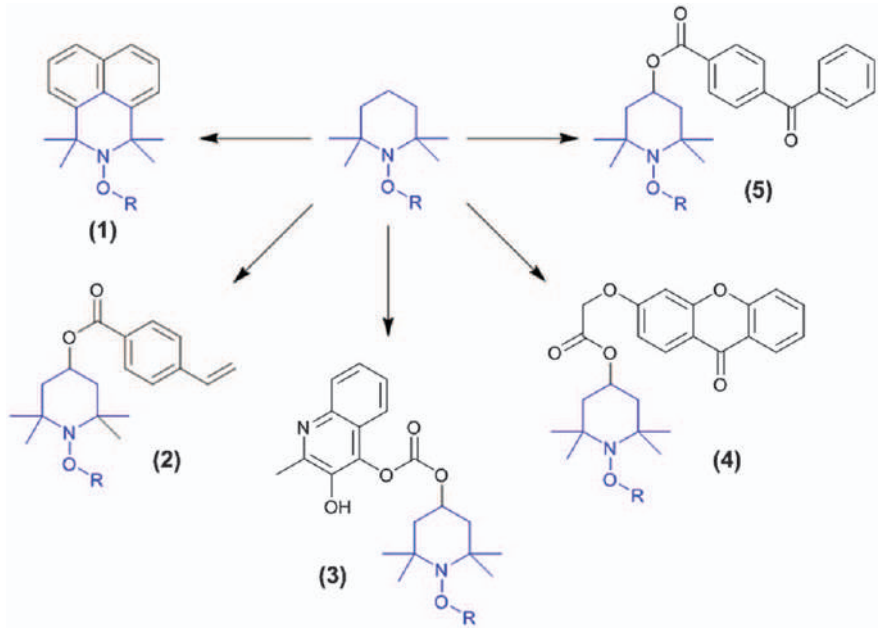

Figure 6.23 Examples of TEMPO-derived, photoactive nitroxide compounds, using naphthalene[179] (1), benzoyloxy[180] (2), quinoline[181] (3), xanthenone[181] (4), and diphenyl-methanone[181] (5) based chromophores.

(Figure 6.23).[179–181] These extended π-systems introduce relatively low energy, bright $\pi\pi^*$ excited states as well as, provided nitrogen and/or oxygen are present, potentially reactive, spectroscopically dark, $n\pi^*$ states. The increased size of the potential molecules of interest can, however, prevent the application of *ab initio* excited-state methods like, for example, Equation-of-Motion Coupled Cluster (EOM-CCSD)[182] or Algebraic Diagrammatic Construction [ADC(n)] methods.[183] The extensive conjugation can also give rise to significant correlation effects, for example, doubly excited states or multiple low-lying excited states. These states are often difficult, or in the case of a doubly excited state impossible, to capture using single-determinant excited-state methods, for example, time-dependent density functional theory (TD-DFT),[184] or time-dependent Hartree–Fock (TD-HF).[185] Ideally, multireference methods (CASSCF, CASPT2)[186] would be employed, which would be capable of capturing the nature of each excited state and any correlation effects. As with most multireference calculations, however, issues will remain with respect to the size of the active space required to accurately model the excited states, as the significant scaling issues will quickly prevent large molecules/large active spaces from being computationally tractable.

Often, the first test of suitability for a particular method is to compute the vertical excitation energies and oscillator intensities for a molecule at its ground-state equilibrium geometry. Comparison of the computed spectrum against its experimental counterpart serves as a benchmark against which

the accuracy of the method can be determined, and can immediately provide insight into the nature of the excited states of interest. When using wavefunction excited-state methods, for example, EOM-CCSD or CASSCF, it is important to ensure a large enough basis set is employed, as such methods exhibit a significant dependence between the calculated vertical excitation energy and basis set.[187,188] At a minimum, a triple-zeta basis set ought to be employed augmented, if possible, with diffuse functions so as to more accurately model the less tightly bound excited-state electrons and charge-transfer states. TD-DFT is found to exhibit a smaller basis set dependence, however its accuracy will also benefit from using a large basis set, if possible.[187]

6.6.1.2 Excited-state Charge Transfer

The introduction of chromophores does not necessarily result in the desired photoreactivity. Sometimes, this can be attributed to the separation of the conjugated chromophore and the reactive species by the nitroxide σ-framework, and can result in orbital localisation, which in turn gives rise to charge-transfer states (Figure 6.24). To fully model these states, any multireference calculations should include the orbitals on each of the moieties, however this can be difficult if the active space becomes too large. If wavefunction calculations are too expensive to run, it is often necessary to turn to TD-DFT, which is much cheaper. In order to assess the best DFT functional to employ for the best accuracy and performance it may be

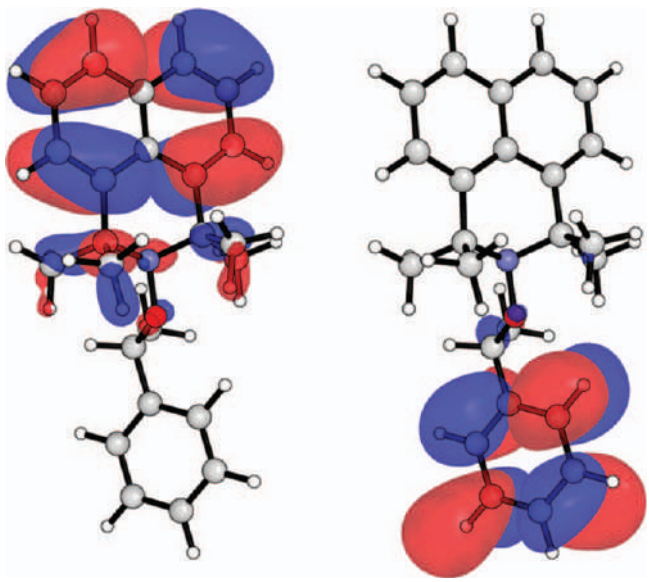

Figure 6.24 Orbital localisation of π-system across the naphthalene moiety (left), and localisation of π*-system across the styrene moiety (right).

necessary to consult existing benchmarking literature,[189] which can provide information about functional accuracy relative to the type of property being investigated. An important issue with TD-DFT is, however, its well-documented failure when attempting to describe charge-transfer states, which precludes the use of traditional, uncorrected functionals (for example BLYP, B3LYP or SVWN).[190] It is necessary instead to employ long-range corrected functionals; for example, LC-ωHPBE or ωB97X-D.[191] These functionals include parameters that mitigate self-interaction error in DFT and TD-DFT, and should correctly predict the $1/R$ asymptotic interaction between the localised charges of the charge-transfer states.

6.6.1.3 *Non-adiabatic Excited-state Behaviour*

Finally, upon excitation it is possible for the nitroxide molecule to undergo complex internal transfer processes like, for example, intersystem crossing (ISC) between different spin states to surfaces that may be highly reactive.[192] An example could be naphthalene TEMPO, which can be used as a photonitroxide-mediated polymerisation agent.[179] Exciting the molecule could result in efficient ISC to a triplet surface; with the electrons unpaired, it is now easier to form the required reactive radical species.

The phenomena that give rise to efficient population of reactive states, for example, conical intersections, can be difficult to model with single-determinant methods; the convergence of two excited-state wavefunctions makes the corresponding regions of molecular geometry inherently multi-determinant, and are best captured with multireference methods such as CASSCF and CASPT2. As mentioned earlier, however, if such methods are inappropriate for a given system it is often necessary to turn again to TD-DFT. Unfortunately, TD-DFT is unable to correctly describe the $3N$-8 dimensionality (where N is the number of atoms) of conical intersections.[193] Despite this, recent work suggests that CAM-B3LYP, M06-2X and BH & HLYP are capable of qualitatively reproducing the geometries at which conical intersections are found.[194] As well as this, M06-2X and BMK are two functionals found to best reproduce singlet–triplet gaps of the excited states of a range of organic molecules,[19] suggesting that the M06-2X functional at least should be applicable to nitroxide excited states and capable of capturing key aspects of nitroxide photoreactivity.

6.6.2 Selected Applications

6.6.2.1 *Case Study 10: Theoretical Study of the Photochemical Initiation in Nitroxide-mediated Photopolymerisation*[178]

In their 2014 paper, Huix-Rotllant *et al.*[178] employed computational methods to explore the photoinitiation mechanism of nitroxide-mediated photopolymerisation. The molecule of interest, shown in Figure 6.25, is expected to exhibit several of the photochemical features described above;

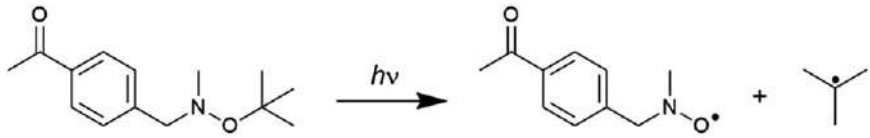

Figure 6.25 Photodissociation mechanism investigated by Huix-Rotllant *et al.*[178]

charge-transfer from the acetophenone to the *tert*-butyl moieties, and excited states of different symmetries, *i.e.*, $\pi\pi^*$ and $n\pi^*$ states originating from the nitrogen and acyl oxygen groups. It is therefore important to select a method capable of at least qualitatively capturing potential states of interest. To that end, Huix-Rotllant *et al.*[178] used two methods, (unrestricted) DFT and the second-order extended multireference quasi-degenerate perturbation theory (XMCQDPT2),[195] to give a balanced description of the most likely photochemical processes taking place. The benefit of this approach is the bulk of the computational work can be performed with relatively cheap DFT, and (qualitative) accuracy is ensured by comparison with multireference methods. The active space employed for the multireference calculations contained the π/π^* and σ/σ^* of interest.

The study examined the changes in several properties: bond dissociation energies, ground- and excited-state equilibrium geometries, and their respective N–O and C–O bond lengths. The study was able to identify the key steps taking place in the photochemical dissociation reaction:

1. Absorption of photon and excitation to $n_O\pi^*$ state, localised on acetophenone moiety
2. Singlet–triplet intersystem crossing, localised still on acetophenone
3. Triplet energy delocalisation across alkoxyamine moiety
4. Bond dissociation of three bonds: σ_{O-C} (desirable), and σ_{N-O} and σ_{N-C}

6.6.3 Concluding Remarks

To conclude, due to their size and complicated photochemical processes, photoactive alkoxyamines present a challenge to current excited-state computational methods. However, appropriate application of single- and multideterminant methods should allow for a reliable, qualitative description of their key features. Single-determinant, ''black-box'' methods should either be correlated wavefunction methods (if possible), or TD-DFT using long-range corrected functionals with some portion of exact exchange. If necessary multireference methods can also be employed, with active spaces consisting of relevant π-, σ- and n-orbitals.

6.7 Further Applications

The applications of computational chemistry described in this chapter are by no means exhaustive. For instance, computational chemistry has played an important role in clarifying the mechanism of the Denisov cycle by which

hindered amine light stabilisers protect polymers from oxidative damage,[196,197] and identified a number of key side reactions in this process.[198,199] These calculations were carried out using high-level single-reference procedures, analogous to those used in studies of nitroxide-mediated polymerisation and similar procedures. More recently, computational chemistry supported by experiment has been used to study the oxidative cleavage of alkoxyamines to produce nitroxide radicals and carbocations, both directly and promoted *via* S_N2 reactions with nucleophiles.[151,152,155] These studies used analogous procedures to those used in studies of nitroxide redox chemistry. On the basis of the mechanistic understanding provided by computational chemistry, a new *in situ* methylation procedure was designed and experimentally demonstrated.[200] This procedure, involving the bench- and air-stable TEMPO-Me reagent, offers major advantages over existing procedures which typically involve reagents with acute toxicity and high volatility. These are just some of the applications of quantum chemistry in studying nitroxide radical chemistry.

As seen in this chapter, the computational methods for studying nitroxides are many and various, and the different types of system and property raise distinct methodological challenges. For instance, high-spin systems and many excited states are invariably multireference in nature, redox potentials and bond energies while single reference usually require high levels of theory, moreover solvation effects are a potentially large source of error in redox systems, while EPR properties have their set of methods and require accurate treatments of core electrons, normally unnecessary in other systems. Nonetheless, in all cases, provided appropriate precautions are taken, methods exist to make chemically useful predictions.

Acknowledgements

MLC gratefully acknowledges support from the Australian Research Council (ARC) Centre of Excellence for Electromaterials Science and an ARC Laureate Fellowship.

References

1. S. Sanvito, *Chem. Soc. Rev.*, 2011, **40**, 3336–3355.
2. T. Sugawara and M. M. Matsushita, *J. Mater. Chem.*, 2009, **19**, 1738–1753.
3. I. Ratera and J. Veciana, *Chem. Soc. Rev.*, 2012, **41**, 303–349.
4. A. J. Wingate and B. W. Boudouris, *J. Polym. Sci., Part A: Polym. Chem.*, 2016, **54**, 1875–1894.
5. M. Abe, *Chem. Rev.*, 2013, **113**, 7011–7088.
6. A. Szabo and N. Ostlund, *Modern Quantum Chemistry: Introduction to Advanced Electronic Structure Theory*, Dover Publications, 1996.
7. F. Jensen, *Introduction to Computational Chemistry*, John Wiley & Sons, Inc., 2006.

8. A. J. Cohen, P. Mori-Sánchez and W. Yang, *Chem. Rev.*, 2012, **112**, 289–320.
9. D. K. W. Mok, R. Neumann and N. C. Handy, *J. Phys. Chem.*, 1996, **100**, 6225–6230.
10. C. J. Cramer, *Essentials of Computational Chemistry: Theories and Models*, Wiley, New York, 2002.
11. P. G. Szalay, T. Müller, G. Gidofalvi, H. Lischka and R. Shepard, *Chem. Rev.*, 2012, **112**, 108–181.
12. V. Veryazov, P. Å. Malmqvist and B. O. Roos, *Int. J. Quantum Chem.*, 2011, **111**, 3329–3338.
13. R. Dawes and S. A. Ndengué, *Int. Rev. Phys. Chem.*, 2016, **35**, 441–478.
14. F. Aiga, *J. Phys. Chem. A*, 2012, **116**, 663–669.
15. F. Krausbeck, D. Mendive-Tapia, A. J. W. Thom and M. J. Bearpark, *Comput. Theor. Chem.*, 2014, **1040–1041**, 14–19.
16. *Recent Advances in Multireference Methods*, ed. K. Hirao, World Scientific, 1999.
17. H. J. Werner and P. J. Knowles, *J. Chem. Phys.*, 1985, **82**, 5053–5063.
18. R. J. Buenker and S. D. Peyerimhoff, *Theor. Chim. Acta*, 1974, **35**, 33–58.
19. J. Miralles, O. Castell, R. Caballol and J.-P. Malrieu, *Chem. Phys.*, 1993, **172**, 33–43.
20. V. M. García, M. Reguero and R. Caballol, *Theor. Chem. Acc.*, 1997, **98**, 50–56.
21. V. M. García, O. Castell, R. Caballol and J. P. Malrieu, *Chem. Phys. Lett.*, 1995, **238**, 222–229.
22. J. Finley, P.-Å. Malmqvist, B. O. Roos and L. Serrano-Andrés, *Chem. Phys. Lett.*, 1998, **288**, 299–306.
23. P. Celani and H.-J. Werner, *J. Chem. Phys.*, 2000, **112**, 5546–5557.
24. C. Li and F. A. Evangelista, *J. Chem. Phys.*, 2016, **144**, 164114.
25. D. I. Lyakh, M. Musiał, V. F. Lotrich and R. J. Bartlett, *Chem. Rev.*, 2012, **112**, 182–243.
26. H.-J. Werner, *Mol. Phys.*, 1996, **89**, 645–661.
27. J. P. Malrieu, R. Caballol, C. J. Calzado, C. de Graaf and N. Guihéry, *Chem. Rev.*, 2014, **114**, 429–492.
28. P. Pulay, *Int. J. Quantum Chem.*, 2011, **111**, 3273–3279.
29. J. P. Zobel, J. J. Nogueira and L. González, *Chem. Sci.*, 2017, **8**, 1482–1499.
30. C. Camacho, H. A. Witek and S. Yamamoto, *J. Comput. Chem.*, 2009, **30**, 468–478.
31. I. Schapiro, K. Sivalingam and F. Neese, *J. Chem. Theory Comput.*, 2013, **9**, 3567–3580.
32. C. Angeli, M. Pastore and R. Cimiraglia, *Theor. Chem. Acc.*, 2007, **117**, 743–754.
33. S. Tolstikov, E. Tretyakov, S. Fokin, E. Suturina, G. Romanenko, A. Bogomyakov, D. Stass, A. Maryasov, M. Fedin, N. Gritsan and V. Ovcharenko, *Chem. – Eur. J.*, 2014, **20**, 2793–2803.
34. V. Barone, C. Boilleau, I. Cacelli, A. Ferretti, S. Monti and G. Prampolini, *J. Chem. Theory Comput.*, 2013, **9**, 300–307.

35. V. Barone, C. Boilleau, I. Cacelli, A. Ferretti and G. Prampolini, *J. Chem. Theory Comput.*, 2013, **9**, 1958–1963.
36. V. Barone, I. Cacelli, P. Cimino, A. Ferretti, S. Monti and G. Prampolini, *J. Phys. Chem. A*, 2009, **113**, 15150–15155.
37. V. Barone, I. Cacelli, A. Ferretti and M. Girlanda, *J. Chem. Phys.*, 2008, **128**, 174303.
38. V. Barone, I. Cacelli, A. Ferretti, S. Monti and G. Prampolini, *Phys. Chem. Chem. Phys.*, 2011, **13**, 4709–4714.
39. V. Barone, I. Cacelli, A. Ferretti, S. Monti and G. Prampolini, *J. Chem. Theory Comput.*, 2011, **7**, 699–706.
40. V. Barone, I. Cacelli, A. Ferretti and G. Prampolini, *Phys. Chem. Chem. Phys.*, 2009, **11**, 3854–3860.
41. V. Barone, I. Cacelli and A. Ferretti, *Phys. Chem. Chem. Phys.*, 2018, **20**, 18547–18555.
42. C. J. Calzado, C. Angeli, C. de Graaf and R. Caballol, *Theor. Chem. Acc.*, 2011, **128**, 505–519.
43. G. M. J. Barca, A. T. B. Gilbert and P. M. W. Gill, *J. Chem. Theory Comput.*, 2018, **14**, 1501–1509.
44. L. Noodleman, C. Y. Peng, D. A. Case and J. M. Mouesca, *Coord. Chem. Rev.*, 1995, **144**, 199–244.
45. L. Noodleman, *J. Chem. Phys.*, 1981, **74**, 5737–5743.
46. K. Yamaguchi, Y. Takahara and T. Fueno, Dordrecht, 1986.
47. K. Yamaguchi, Y. Takahara, T. Fueno and K. N. Houk, *Theor. Chim. Acta*, 1988, **73**, 337–364.
48. A. S. Menon and L. Radom, *J. Phys. Chem. A*, 2008, **112**, 13225–13230.
49. K. Raghavachari and J. B. Anderson, *J. Phys. Chem.*, 1996, **100**, 12960–12973.
50. Y. Kitagawa, T. Saito and K. Yamaguchi, *Symmetry (Group Theory) and Mathematical Treatment in Chemistry*, https://doi.org/10.5772/intechopen.68513, 2018.
51. K. C. Ko, D. Cho and J. Y. Lee, *J. Phys. Chem. A*, 2012, **116**, 6837–6844.
52. K. C. Ko, D. Cho and J. Y. Lee, *J. Phys. Chem. A*, 2013, **117**, 3561–3568.
53. D. Cho, K. C. Ko and J. Y. Lee, *J. Phys. Chem. A*, 2014, **118**, 5112–5121.
54. D. Cho, K. C. Ko and J. Y. Lee, *Int. J. Quantum Chem.*, 2016, **116**, 578–597.
55. M. E. Ali and S. N. Datta, *J. Phys. Chem. A*, 2006, **110**, 2776–2784.
56. M. E. Ali and S. N. Datta, *J. Phys. Chem. A*, 2006, **110**, 10525–10527.
57. E. I. Izgorodina, D. R. B. Brittain, J. L. Hodgson, E. H. Krenske, C. Y. Lin, M. Namazian and M. L. Coote, *J. Phys. Chem. A*, 2007, **111**, 10754–10768.
58. D. Reta Mañeru, A. K. Pal, I. D. P. R. Moreira, S. N. Datta and F. Illas, *J. Chem. Theory Comput.*, 2014, **10**, 335–345.
59. A. I. Krylov, *Chem. Phys. Lett.*, 2001, **338**, 375–384.
60. A. I. Krylov, *Chem. Phys. Lett.*, 2001, **350**, 522–530.
61. A. I. Krylov and C. D. Sherrill, *J. Chem. Phys.*, 2002, **116**, 3194–3203.

62. Y. Shao, M. Head-Gordon and A. I. Krylov, *J. Chem. Phys.*, 2003, **118**, 4807–4818.
63. L. V. Slipchenko and A. I. Krylov, *J. Chem. Phys.*, 2002, **117**, 4694–4708.
64. S. V. Levchenko and A. I. Krylov, *J. Chem. Phys.*, 2003, **120**, 175–185.
65. A. A. Golubeva, A. V. Nemukhin, S. J. Klippenstein, L. B. Harding and A. I. Krylov, *J. Phys. Chem. A*, 2007, **111**, 13264–13271.
66. T. Tsuchimochi, *J. Chem. Phys.*, 2015, **143**, 144114.
67. J. Mato and M. S. Gordon, *Phys. Chem. Chem. Phys.*, 2018, **20**, 2615–2626.
68. X. Zhang and J. M. Herbert, *J. Chem. Phys.*, 2015, **143**, 234107.
69. D. Casanova and M. Head-Gordon, *Phys. Chem. Chem. Phys.*, 2009, **11**, 9779–9790.
70. F. Bell, P. M. Zimmerman, D. Casanova, M. Goldey and M. Head-Gordon, *Phys. Chem. Chem. Phys.*, 2013, **15**, 358–366.
71. M. Song, X. Song and Y. Bu, *Phys. Chem. Chem. Phys.*, 2018, **20**, 8099–8111.
72. Z. Rolik, L. Szegedy, I. Ladjánszki, B. Ladóczki and M. Kállay, *J. Chem. Phys.*, 2013, **139**, 094105.
73. S. Stoll and A. Schweiger, *J. Magn. Reson.*, 2006, **178**, 42–55.
74. D. R. Duling, *J. Magn. Reson., Ser. B*, 1994, **104**, 105–110.
75. D. Wang and G. R. Hanson, *J. Magn. Reson., Ser. A*, 1995, **117**, 1–8.
76. G. R. Hanson, C. J. Noble and S. Benson, in *High Resolution EPR: Applications to Metalloenzymes and Metals in Medicine*, ed. L. Berliner and G. Hanson, Springer New York, New York, NY, DOI: 10.1007/978-0-387-84856-3_4, 2009, pp. 105–173.
77. K. Khairy, D. Budil and P. Fajer, *J. Magn. Reson.*, 2006, **183**, 152–159.
78. D. J. Schneider and J. H. Freed, in *Spin Labeling: Theory and Applications*, ed. L. J. Berliner and J. Reuben, Springer US, Boston, MA, DOI: 10.1007/978-1-4613-0743-3_1, 1989, pp. 1–76.
79. L. Hermosilla, J. M. García de la Vega, C. Sieiro and P. Calle, *J. Chem. Theory Comput.*, 2011, **7**, 1169–1179.
80. A. Savitsky, M. Plato and K. Möbius, *Appl. Magn. Reson.*, 2009, **37**, 415.
81. T. Janoschka, N. Martin, U. Martin, C. Friebe, S. Morgenstern, H. Hiller, M. D. Hager and U. S. Schubert, *Nature*, 2015, **527**, 78.
82. H. Nishide and K. Oyaizu, *Science*, 2008, **319**, 737–738.
83. T. Suga, H. Ohshiro, S. Sugita, K. Oyaizu and H. Nishide, *Adv. Mater.*, 2009, **21**, 1627–1630.
84. T. Janoschka, M. D. Hager and U. S. Schubert, *Adv. Mater.*, 2012, **24**, 6397–6409.
85. K. Zhang, Y. Hu, L. Wang, J. Fan, M. J. Monteiro and Z. Jia, *Polym. Chem.*, 2017, **8**, 1815–1823.
86. J. B. Gerken and S. S. Stahl, *ACS Cent. Sci.*, 2015, **1**, 234–243.
87. A. Badalyan and S. S. Stahl, *Nature*, 2016, **535**, 406.
88. M. Rafiee, K. C. Miles and S. S. Stahl, *J. Am. Chem. Soc.*, 2015, **137**, 14751–14757.

89. Q. Cao, L. M. Dornan, L. Rogan, N. L. Hughes and M. J. Muldoon, *Chem. Commun.*, 2014, **50**, 4524–4543.
90. M. Zhang, C. Chen, W. Ma and J. Zhao, *Angew. Chem., Int. Ed.*, 2008, **47**, 9730–9733.
91. Z. Zhang, P. Chen, T. N. Murakami, S. M. Zakeeruddin and M. Grätzel, *Adv. Funct. Mater.*, 2008, **18**, 341–346.
92. J. Min, J. Won, Y. S. Kang and S. Nagase, *J. Photochem. Photobiol., A*, 2011, **219**, 148–153.
93. T. Murakami, F. Kato, K. Oyaizu and H. Nishide, *J. Photopolym. Sci. Technol.*, 2010, **23**, 353–355.
94. K. Fumiaki, H. Naoki, M. Takaya, O. Chie, O. Kenichi and N. Hiroyuki, *Chem. Lett.*, 2010, **39**, 464–465.
95. B. P. Soule, F. Hyodo, K.-I. Matsumoto, N. L. Simone, J. A. Cook, M. C. Krishna and J. B. Mitchell, *Free Radical Biol. Med.*, 2007, **42**, 1632–1650.
96. T. Offer, A. Russo and A. Samuni, *FASEB J.*, 2000, **14**, 1215–1223.
97. M. B. Lauber and S. S. Stahl, *ACS Catal.*, 2013, **3**, 2612–2616.
98. S. D. Rychnovsky, R. Vaidyanathan, T. Beauchamp, R. Lin and P. J. Farmer, *J. Org. Chem.*, 1999, **64**, 6745–6749.
99. M. Saita, J. Kaneko, T. Sato, S.-S. Takahashi, S. Wada-Takahashi, R. Kawamata, T. Sakurai, M.-C.-I. Lee, N. Hamada, K. Kimoto and Y. Nagasaki, *Biomaterials*, 2016, **76**, 292–301.
100. C. Abe, Y. Uto, A. Kawasaki, C. Noguchi, R. Tanaka, T. Yoshitomi, Y. Nagasaki, Y. Endo and H. Hori, *J. Controlled Release*, 2014, **182**, 67–72.
101. M. C. Krishna, D. A. Grahame, A. Samuni, J. B. Mitchell and A. Russo, *Proc. Natl. Acad. Sci.*, 1992, **89**, 5537–5541.
102. Y. Kinoshita, K.-I. Yamada, T. Yamasaki, F. Mito, M. Yamato, N. Kosem, H. Deguchi, C. Shirahama, Y. Ito, K. Kitagawa, N. Okukado, K. Sakai and H. Utsumi, *Free Radical Biol. Med.*, 2010, **49**, 1703–1709.
103. A. V. Marenich, J. Ho, M. L. Coote, C. J. Cramer and D. G. Truhlar, *Phys. Chem. Chem. Phys.*, 2014, **16**, 15068–15106.
104. J. Ho, M. Coote, C. Cramer and D. Truhlar, in *Organic Electrochemistry: Revised and Expanded*, ed. O. Hammerich and B. Speiser, CRC Press, Taylor and Francis Group, DOI: 10.1201/b19122-8, 2015, pp. 229–259.
105. L. E. Roy, E. Jakubikova, M. G. Guthrie and E. R. Batista, *J. Phys. Chem. A*, 2009, **113**, 6745–6750.
106. R. S. Berry, S. A. Rice and J. Ross, *Physical Chemistry*, Oxford University Press, New York, 2nd edn, 2000.
107. C. G. Zoski, *Handbook of Electrochemistry*, Elsevier, Amsterdam, 2007.
108. C. Møller and M. S. Plesset, *Phys. Rev.*, 1934, **46**, 618–622.
109. M. Head-Gordon, J. A. Pople and M. J. Frisch, *Chem. Phys. Lett.*, 1988, **153**, 503–506.
110. J. A. Pople, J. S. Binkley and R. Seeger, *Int. J. Quantum Chem.*, 1976, **10**, 1–19.
111. R. Krishnan and J. A. Pople, *Int. J. Quantum Chem.*, 1978, **14**, 91–100.

112. P. J. Knowles, J. S. Andrews, R. D. Amos, N. C. Handy and J. A. Pople, *Chem. Phys. Lett.*, 1991, **186**, 130–136.
113. W. J. Lauderdale, J. F. Stanton, J. Gauss, J. D. Watts and R. J. Bartlett, *Chem. Phys. Lett.*, 1991, **187**, 21–28.
114. W. J. Lauderdale, J. F. Stanton, J. Gauss, J. D. Watts and R. J. Bartlett, *J. Chem. Phys.*, 1992, **97**, 6606–6620.
115. G. D. Purvis and R. J. Bartlett, *J. Chem. Phys.*, 1982, **76**, 1910–1918.
116. G. E. Scuseria, C. L. Janssen and H. F. Schaefer, *J. Chem. Phys.*, 1988, **89**, 7382–7387.
117. J. A. Pople, M. Head-Gordon and K. Raghavachari, *J. Chem. Phys.*, 1987, **87**, 5968–5975.
118. J. Gauss and D. Cremer, *Chem. Phys. Lett.*, 1988, **150**, 280–286.
119. E. A. Salter, G. W. Trucks and R. J. Bartlett, *J. Chem. Phys.*, 1989, **90**, 1752–1766.
120. A. Tajti, P. G. Szalay, A. G. Császár, M. Kállay, J. Gauss, E. F. Valeev, B. A. Flowers, J. Vázquez and J. F. Stanton, *J. Chem. Phys.*, 2004, **121**, 11599–11613.
121. A. Karton, E. Rabinovich, J. M. L. Martin and B. Ruscic, *J. Chem. Phys.*, 2006, **125**, 144108.
122. J. A. Pople, M. Head-Gordon, D. J. Fox, K. Raghavachari and L. A. Curtiss, *J. Chem. Phys.*, 1989, **90**, 5622–5629.
123. L. A. Curtiss, C. Jones, G. W. Trucks, K. Raghavachari and J. A. Pople, *J. Chem. Phys.*, 1990, **93**, 2537–2545.
124. L. A. Curtiss, K. Raghavachari, G. W. Trucks and J. A. Pople, *J. Chem. Phys.*, 1991, **94**, 7221–7230.
125. L. A. Curtiss, K. Raghavachari, P. C. Redfern, V. Rassolov and J. A. Pople, *J. Chem. Phys.*, 1998, **109**, 7764–7776.
126. L. A. Curtiss, P. C. Redfern and K. Raghavachari, *J. Chem. Phys.*, 2007, **126**, 084108.
127. D. J. Henry, M. B. Sullivan and L. Radom, *J. Chem. Phys.*, 2003, **118**, 4849–4860.
128. M. R. Nyden and G. A. Petersson, *J. Chem. Phys.*, 1981, **75**, 1843–1862.
129. G. A. Petersson, A. Bennett, T. G. Tensfeldt, M. A. Al-Laham, W. A. Shirley and J. Mantzaris, *J. Chem. Phys.*, 1988, **89**, 2193–2218.
130. G. A. Petersson and M. A. Al-Laham, *J. Chem. Phys.*, 1991, **94**, 6081–6090.
131. G. A. Petersson, T. G. Tensfeldt and J. A. Montgomery, *J. Chem. Phys.*, 1991, **94**, 6091–6101.
132. J. A. Montgomery, J. W. Ochterski and G. A. Petersson, *J. Chem. Phys.*, 1994, **101**, 5900–5909.
133. J. W. Ochterski, G. A. Petersson and J. A. Montgomery, *J. Chem. Phys.*, 1996, **104**, 2598–2619.
134. J. A. Montgomery, M. J. Frisch, J. W. Ochterski and G. A. Petersson, *J. Chem. Phys.*, 1999, **110**, 2822–2827.
135. J. A. Montgomery, M. J. Frisch, J. W. Ochterski and G. A. Petersson, *J. Chem. Phys.*, 2000, **112**, 6532–6542.

136. J. M. L. Martin and G. de Oliveira, *J. Chem. Phys.*, 1999, **111**, 1843–1856.
137. S. Parthiban and J. M. L. Martin, *J. Chem. Phys.*, 2001, **114**, 6014–6029.
138. A. D. Boese, M. Oren, O. Atasoylu, J. M. L. Martin, M. Kállay and J. Gauss, *J. Chem. Phys.*, 2004, **120**, 4129–4141.
139. D. Bednarczyk and J. Bednarczyk, *Phys. Lett. A*, 1978, **64**, 409–410.
140. P. Hohenberg and W. Kohn, *Phys. Rev.*, 1964, **136**, B864–B871.
141. W. Kohn and L. J. Sham, *Phys. Rev.*, 1965, **140**, A1133–A1138.
142. E. I. Izgorodina, M. L. Coote and L. Radom, *J. Phys. Chem. A*, 2005, **109**, 7558–7566.
143. J. L. Hodgson, M. Namazian, S. E. Bottle and M. L. Coote, *J. Phys. Chem. A*, 2007, **111**, 13595–13605.
144. M. Isegawa, F. Neese and D. A. Pantazis, *J. Chem. Theory Comput.*, 2016, **12**, 2272–2284.
145. J. Ho, A. Klamt and M. L. Coote, *J. Phys. Chem. A*, 2010, **114**, 13442–13444.
146. J. Tomasi, *Theor. Chem. Acc.*, 2004, **112**, 184–203.
147. A. V. Marenich, J. Ho, M. L. Coote, C. J. Cramer and D. G. Truhlar, *Phys. Chem. Chem. Phys.*, 2014, **16**, 15068–15106.
148. J. Ho and M. L. Coote, *J. Chem. Theory Comput.*, 2009, **5**, 295–306.
149. J. R. Pliego Jr. and J. M. Riveros, *J. Phys. Chem. A*, 2001, **105**, 7241–7247.
150. A. V. Marenich, C. J. Cramer and D. G. Truhlar, *J. Phys. Chem. B*, 2009, **113**, 6378–6396.
151. C. L. Hammill, B. B. Noble, P. L. Norcott, S. Ciampi and M. L. Coote, *J. Phys. Chem. C*, 2019, **123**, 5273–5281.
152. B. B. Noble, P. L. Norcott, C. L. Hammill, S. Ciampi and M. L. Coote, *J. Phys. Chem. C*, 2019, **123**, 10300–10305.
153. F. J. M. Rogers and M. L. Coote, *J. Phys. Chem. C*, 2019, **123**, 20174–20180.
154. F. J. M. Rogers and M. L. Coote, *J. Phys. Chem. C*, 2019, **123**, 10306–10310.
155. L. Zhang, E. Laborda, N. Darwish, B. B. Noble, J. H. Tyrell, S. Pluczyk, A. P. Le Brun, G. G. Wallace, J. Gonzalez, M. L. Coote and S. Ciampi, *J. Am. Chem. Soc.*, 2018, **140**, 766–774.
156. L. Zhang, Y. B. Vogel, B. B. Noble, V. R. Gonçales, N. Darwish, A. L. Brun, J. J. Gooding, G. G. Wallace, M. L. Coote and S. Ciampi, *J. Am. Chem. Soc.*, 2016, **138**, 9611–9619.
157. G. Gryn'ova, J. M. Barakat, J. P. Blinco, S. E. Bottle and M. L. Coote, *Chem. – Eur. J.*, 2012, **18**, 7582–7593.
158. F. Kato, A. Kikuchi, T. Okuyama, K. Oyaizu and H. Nishide, *Angew. Chem.*, 2012, **124**, 10324–10327.
159. K. Zhang, B. B. Noble, A. C. Mater, M. J. Monteiro, M. L. Coote and Z. Jia, *Phys. Chem. Chem. Phys.*, 2018, **20**, 2606–2614.
160. J. P. Blinco, J. L. Hodgson, B. J. Morrow, J. R. Walker, G. D. Will, M. L. Coote and S. E. Bottle, *J. Org. Chem.*, 2008, **73**, 6763–6771.
161. M. Kavala, R. Boča, L. Dlháň, V. Brezová, M. Breza, J. Kožíšek, M. Fronc, P. Herich, L. Švorc and P. Szolcsányi, *J. Org. Chem.*, 2013, **78**, 6558–6569.

162. K. Daze and F. Hof, in *Encyclopedia of Physical Organic Chemistry*, ed. Z. Wang, U. Wille and E. Juaristi, Wiley, 2016, pp. 1–51.
163. C. R. Martinez and B. L. Iverson, *Chem. Sci.*, 2012, **3**, 2191–2201.
164. A. S. Shetty, J. Zhang and J. S. Moore, *J. Am. Chem. Soc.*, 1996, **118**, 1019–1027.
165. C. J. Hawker, A. W. Bosman and E. Harth, *Chem. Rev.*, 2001, **101**, 3661–3688.
166. J. L. Hodgson, C. Yeh Lin, M. L. Coote, S. R. A. Marque and K. Matyjaszewski, *Macromolecules*, 2010, **43**, 3728–3743.
167. J. L. Hodgson, L. B. Roskop, M. S. Gordon, C. Y. Lin and M. L. Coote, *J. Phys. Chem. A*, 2010, **114**, 10458–10466.
168. C. Y. Lin, S. R. A. Marque, K. Matyjaszewski and M. L. Coote, *Macromolecules*, 2011, **44**, 7568–7583.
169. S. Marque, *J. Org. Chem.*, 2003, **68**, 7582–7590.
170. G. Gryn'ova, C. Y. Lin and M. L. Coote, *Polym. Chem.*, 2013, **4**, 3744–3754.
171. G. Gryn'ova, D. L. Marshall, S. J. Blanksby and M. L. Coote, *Nat. Chem.*, 2013, **5**, 474.
172. G. Gryn'ova and M. L. Coote, *J. Am. Chem. Soc.*, 2013, **135**, 15392–15403.
173. G. Gryn'ova, L. M. Smith and M. L. Coote, *Phys. Chem. Chem. Phys.*, 2017, **19**, 22678–22683.
174. M. Klinska, L. M. Smith, G. Gryn'ova, M. G. Banwell and M. L. Coote, *Chem. Sci.*, 2015, **6**, 5623–5627.
175. J. P. Blinco, K. E. Fairfull-Smith, B. J. Morrow and S. E. Bottle, *Aust. J. Chem.*, 2011, **64**, 373-373.
176. M. Eing, B. T. Tuten, J. P. Blinco and C. Barner-Kowollik, *Chem. – Eur. J.*, 2018, **24**, 12246–12249.
177. K. A. Hansen and J. P. Blinco, *Polym. Chem.*, 2018, **9**, 1479–1516.
178. M. Huix-Rotllant and N. Ferre, *J. Phys. Chem. A*, 2014, **118**, 4464–4470.
179. S. E. Bottle, J.-L. Clement, M. Fleige, E. M. Simpson, Y. Guillaneuf, K. E. Fairfull-Smith, D. Gigmes and J. P. Blinco, *RSC Adv.*, 2016, **6**, 80328–80333.
180. S. Coiai, E. Passaglia and F. Cicogna, *Polym. Int.*, 2019, **68**, 27–63.
181. Y. Guillaneuf, D. Bertin, D. Gigmes, D.-L. Versace, J. Lalevée and J.-P. Fouassier, *Macromolecules*, 2010, **43**, 2204–2212.
182. M. Caricato, *J. Chem. Theory Comput.*, 2012, **8**, 5081–5091.
183. A. Dreuw and M. Wormit, *Wiley Interdiscip. Rev.: Comput. Mol. Sci.*, 2015, **5**, 82–95.
184. R. Ahlrichs and R. Bauernschmitt, *Chem. Phys. Lett.*, 1996, **256**, 454–464.
185. M. A. Ball and A. D. McLachlan, *Mol. Phys.*, 1964, **7**, 501–513.
186. V. Veryazov, P.-A. Malmqvist and B. O. Roos, *Int. J. Quantum Chem.*, 2011, **111**, 3329–3338.
187. A. D. Laurent, A. Blondel and D. Jacquemin, *Theor. Chem. Acc.*, 2015, **134**, 1–11.
188. M. Schreiber, M. R. Silva-Junior, S. P. A. Sauer and W. Thiel, *J. Chem. Phys.*, 2008, **128**, 134110.

189. A. D. Laurent and D. Jacquemin, *Int. J. Quantum Chem.*, 2013, **113**, 2019–2039.
190. A. Dreuw and M. Head-Gordon, *J. Am. Chem. Soc.*, 2004, **126**, 4007–4016.
191. Y. Jiang, Z. Hu, B. Zhou, C. Zhong, Z. Sun and H. Sun, *J. Phys. Chem. C*, 2019, **123**, 5616–5625.
192. W. Domcke and D. R. Yarkony, *Annu. Rev. Phys. Chem.*, 2012, **63**, 325–352.
193. Y. Shu, K. A. Parker and D. G. Truhlar, *J. Phys. Chem. Lett.*, 2017, **8**, 2107–2112.
194. M. Filatov, *J. Chem. Theory Comput.*, 2013, **9**, 4526–4541.
195. A. A. Granovsky, *J. Chem. Phys.*, 2011, **134**, 214113.
196. G. Gryn'ova, K. U. Ingold and M. L. Coote, *J. Am. Chem. Soc.*, 2012, **134**, 12979–12988.
197. J. L. Hodgson and M. L. Coote, *Macromolecules*, 2010, **43**, 4573–4583.
198. M. R. L. Paine, G. Gryn'ova, M. L. Coote, P. J. Barker and S. J. Blanksby, *Polym. Degrad. Stab.*, 2014, **99**, 223–232.
199. D. L. Marshall, M. L. Christian, G. Gryn'ova, M. L. Coote, P. J. Barker and S. J. Blanksby, *Org. Biomol. Chem.*, 2011, **9**, 4936–4947.
200. P. L. Norcott, C. L. Hammill, B. B. Noble, J. C. Robertson, A. Olding, A. C. Bissember and M. L. Coote, *J. Am. Chem. Soc.*, 2019, **141**(38), 15450–15455.

CHAPTER 7

Nitroxide-mediated Polymerization

ALEXANDRE SIMULA,[a] NICHOLAS BALLARD[a,b] AND JOSÉ M. ASUA*[a]

[a] POLYMAT and Kimika Aplikatua Saila, University of the Basque Country UPV/EHU, Joxe Mari Korta Zentroa, Tolosa Hiribidea 72, 20018, Donostia/San Sebastián, Spain; [b] IKERBASQUE, Basque Foundation for Science, 48011 Bilbao, Spain
*Email: jm.asua@ehu.es

7.1 Introduction

Following the pioneering work of Szwarc in "*living*" anionic polymerization,[1] plenty of effort has been devoted to overcoming the intolerances associated with ionic processes by developing radical "*living*" polymerization techniques able to yield macromolecules with predictable molar masses, relatively narrow molar mass distributions (MMD), high end-group(s) fidelity and controlled architectures from a broad range of monomers under mild conditions.[2] This has led to reversible deactivation radical polymerization (RDRP) techniques based on either a reversible activation/deactivation or a degenerative chain transfer process. The main techniques are nitroxide-mediated polymerization (NMP) or stable radical-mediated polymerization (SRMP, as recommended by the IUPAC, though NMP will be utilized throughout this chapter for historical consistency),[3–6] atom transfer radical polymerization (ATRP and derivatives)[7–13] and reversible addition-fragmentation chain transfer (RAFT) polymerization.[14–17] This chapter is devoted to NMP.

Nitroxides
Edited by Olivier Ouari and Didier Gigmes

Published by the Royal Society of Chemistry, www.rsc.org

The 30-year history of NMP has created tremendous interest, with key research groups working on the understanding of the kinetics and features of NMP and the development of new regulators. This research prompted the industrial use of NMP by several companies, such as Ciba (now part of BASF), Xerox, Arkema and others, for applications such as pigment dispersants, pressure-sensitive adhesives, thermoplastic elastomers, nanostructured acrylic glass and coatings.[18–21]

In this chapter, we will give an overview of the polymerization technique, whilst focusing on the recent developments. In the first section, the fundamentals of NMP will be described in order to understand the basics of the polymerization technique, with an overview of the most efficient regulators (*e.g.*, nitroxides/alkoxyamines), the range of monomers that can be polymerized and finally the architectures that can be attained. In the second section, we will focus on the polymerization process and its variations, from bulk/solution to dispersed media and from batch, semibatch to continuous processes. In the last section, the focus will be on the industrial applications of NMP.

7.2 Fundamentals of Nitroxide-mediated Polymerization

7.2.1 Mechanism and Kinetics of Nitroxide-mediated Polymerization

Scheme 7.1 summarizes the main mechanisms involved in NMP. This process is relatively simple and involves initiation, propagation, reversible coupling and termination. The initiation step can be unimolecular, which occurs by decomposition of an alkoxyamine (Scheme 7.1B), or bimolecular, which involves the decomposition of a radical initiator and the presence of a nitroxide *O–N–(R_1)R_2 (Scheme 7.1A; or aminoxyl, as recommended by the IUPAC, though nitroxide will be utilized throughout this chapter). For both types of initiation, an initiating radical R* rapidly reacts with a monomer M, thus yielding a propagating radical P*. The system relies on the presence of nitroxides, acting as persistent radicals, namely they do not ideally terminate and only react through cross-coupling. Under these conditions, the propagating radicals (R* and particularly P* in Scheme 7.1) terminate, decreasing their concentration, and the slight excess of nitroxide shifts the equilibrium toward the dormant macroalkoxyamine. This phenomenon is commonly referred to as the persistent radical effect.[22–24] The decomposition of this macroalkoxyamine can be triggered by moderate to high temperatures (40–200 °C, typically 80–130 °C), UV-light or radiation, which provides sufficient energy to break the labile C–ON bond.

The key aspect of the NMP process is this reversible coupling between a propagating radical P* and a nitroxide *O–N–(R_1)R_2, which allows for the formation of dormant and active polymer chains. For such a system, each

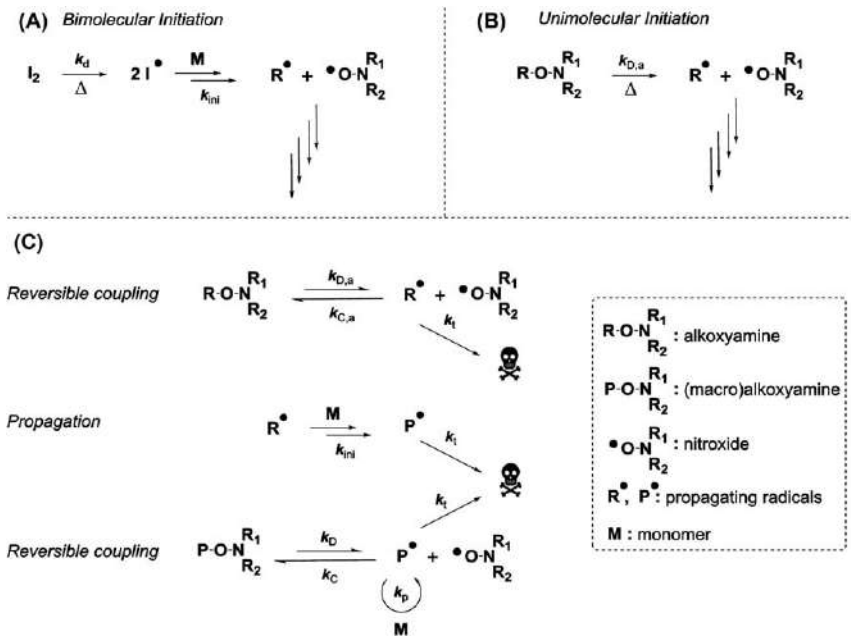

Scheme 7.1 General reaction scheme for nitroxide-mediated polymerization.

growing polymer chain spends most of the time in a dormant state (*i.e.*, as a macroalkoxyamine), and when it becomes a radical (*i.e.*, active), it only adds a few (if any) monomer units before going back to the dormant state. This process is repeated many times, and the statistical distribution of events means that all of the chains have very close chain lengths.

A lot of effort has been dedicated to the understanding and modeling of NMP under idealized conditions (assuming chain length-independent rate coefficients and neglecting the propagation events prior to the equilibrium and side reactions) by the groups of Fischer and Fukuda.[25–27] They derived equations giving the evolution of the monomer concentration over time, as well as the approximation of the polydispersity index value.[23,27–29]

$$\ln\frac{[\mathrm{M}]_0}{[\mathrm{M}]} = \frac{3k_\mathrm{p}}{2}\left(\frac{k_\mathrm{D}[\mathrm{R}-\mathrm{ONR_1R_2}]_0}{3k_\mathrm{t}k_\mathrm{C}}\right)^{1/3} t^{2/3} \tag{7.1}$$

$$\mathrm{PDI}_\infty = 1 + \frac{[\mathrm{R}-\mathrm{ONR_1R_2}]_0}{[\mathrm{M}]_0} + \left(\frac{\pi k_\mathrm{p}^3[\mathrm{R}-\mathrm{ONR_1R_2}]_0}{k_\mathrm{D}k_\mathrm{C}k_\mathrm{t}}\right)^{1/2} \tag{7.2}$$

A look to Scheme 7.1 and eqn (7.1) and (7.2) show that the kinetics of NMP and the extent of control are determined by the relative values of the rate constants of combination k_C, decomposition k_D, termination k_t and propagation k_p.[30–37]

From a practical point of view, it would be valuable to know the control that can be achieved with a certain system (monomer and nitroxide) under given reaction conditions (temperature). Those variables define the values of the rate constant coefficients. Alternatively, it would be desirable to know which nitroxide (this determines k_C and k_D, in part) or which temperature (this affects all parameters) should be used to achieve a desired level of control for a given monomer.[31,38] In both cases, productivity, namely the time needed to implement the polymerization is important. The group of Fischer provided theoretical guidelines to achieve such a goal.[39,40] The control level was defined in terms of Φ_{lim}, the maximum fraction of dead chains ($\Phi_{lim} \rightarrow 0$ means that all chains are "*living*") and δ_{lim}, the maximum residual polydispersity ($\delta_{lim} = Đ - 1 - [R\text{–}ONR_1R_2]_0/[M]_0$; with $Đ = M_w/M_n$). On the other hand, the productivity was characterized by t_{90}, which is the time needed to reach a monomer conversion of 90%. Fischer demonstrated that in order to have "*livingness*", polydispersity and process time lower than Φ_{lim}, δ_{lim} and t_{90}, respectively, k_C and k_D should fulfill the following eqn (7.3)–(7.5).

$$\frac{k_D}{k_C} \leq \frac{k_p[R - ONR_1R_2]_0}{2\log(10)k_t}\Phi_{lim}^2 \tag{7.3}$$

$$k_D k_C \geq \frac{\pi k_p^3[R - ONR_1R_2]_0}{k_t}\frac{1}{\delta_{lim}^2} \tag{7.4}$$

$$\frac{k_D}{k_C} \geq \frac{(2\log(10))^3 k_t}{9[R - ONR_1R_2]_0 k_p^3 t_{90}} \tag{7.5}$$

Figure 7.1 illustrates the implications of eqn (7.3)–(7.5) for a chosen case. In order to have a fraction of dead chains lower than Φ_{lim}, k_D and k_C should have values below the line of eqn (7.3). Similarly, to have a narrow distribution, *i.e.*, polydispersity lower than δ_{lim}, k_D and k_C should have values above the line for eqn (7.4). Finally, to achieve the desired production (process time <= t_{90}), k_D and k_C should have values above the line for eqn (7.5). All conditions can be met within the gray area, defined as the working zone. It is clear that it may be impossible to achieve certain goals. For example, for the system chosen in Figure 7.1, it would be impossible to achieve 90% of "*living*" chains and a monomer conversion of 90% in 10 h because the line of eqn (7.5) will be above that of eqn (7.3).

The polymerization strategy can be modified in order to improve control. Thus, an excess of free nitroxide has been used to achieve lower dispersity values and better "*livingness*" when polymerizing high k_p monomers such as acrylates and acrylamides.[41–43] This strategy is easier to implement in bimolecular initiating systems (though it has also been applied to unimolecular systems),[6] wherein a slightly higher amount of nitroxide is introduced in the reaction medium compared to that of the radical initiator.[44,45]

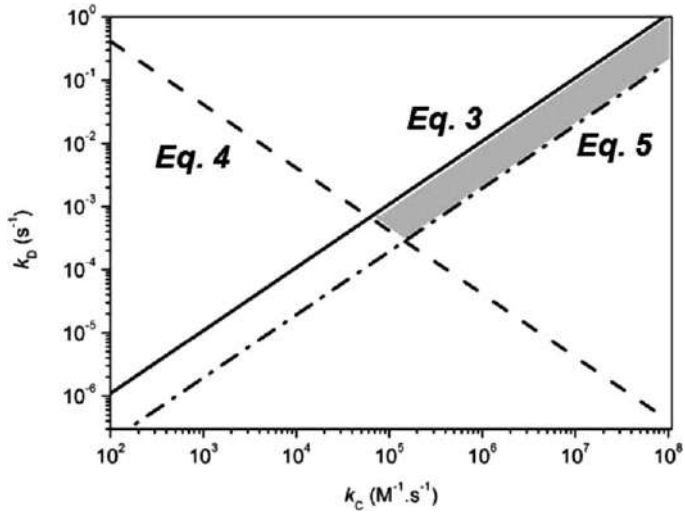

Figure 7.1 Equations and phase diagram for a system with $t_{90} = 20$ h, $k_p = (2.673 \times 10^6) \times \exp(-22.360 \times 10^3/RT)$ $M^{-1} s^{-1}$; $k_t = (1.984 \times 10^8) \times \exp(-5890/RT)$ $M^{-1} s^{-1}$; $[R\text{–}ONR_1R_2]_0 = 2.175 \times 10^{-2}$ M; $\Phi_{lim} = 0.2$; $\delta_{lim} = 0.5$.[39,40]

This stoichiometric imbalance favors a shift of the equilibrium toward the dormant state, thus improving control. It is important to note that the kinetics of polymerization can also be improved by the presence of acids or mild reducing agents, by favoring the polymerization to go toward a dormant state.[46–49] In some cases, extra radical initiators are added to increase productivity,[42,50] but this is at the expense of a decrease in "*livingness*" due to an increase in radical–radical termination. Moreover, the observed molar masses are below the sought ones, as more chains are being produced.[34,44,51,52]

Although eqn (7.1)–(7.5) and Figure 7.1 are valuable to understand nitroxide-mediated polymerization and provide a first guide to achieve a controlled process, they are only limited to rather idealized conditions; *e.g.*, assuming chain length-independent termination, neglecting propagation events prior to the equilibrium and neglecting the presence of side reactions.[53] The importance of both chain length-dependent termination and the initial propagation events has been demonstrated.[32,54,55] Nevertheless, these effects can be easily integrated into polymerization models.[55]

Side reactions can lead to strong deviations with respect to the predictions of eqn (7.1)–(7.5) and control over the polymerization thereof, by disrupting the fine equilibrium between dormant and active chains.[53] Thus, a possible side reaction is the creation of additional propagating radicals due to the thermal self-initiation of monomers such as styrene and *n*-butyl acrylate (BA) at high temperatures.[25,56–58] As discussed above for the case in which the radicals are intentionally generated, this decreases "*livingness*" and reduces the molar masses.[34,44,51,52] The most obvious way of avoiding this problem is

to work at lower temperatures, if adequate nitroxides are available. Nevertheless, this reduction in temperature may strongly increase the polymerization time.

Scheme 7.2 highlights the side reactions associated with the nitroxide itself.[59,60] The loss of a certain quantity of the persistent species shifts the equilibrium toward the active state of the polymerization, thus increasing the rates of polymerization and radical self-termination.[47] A nitroxide can undesirably react with an alkene, leading to a lower level of control, which is the case for 2,2,6,6-tetramethylpiperidine-1-oxyl (TEMPO) during the polymerization of styrene (Scheme 7.2A).[61,62] The persistent radical can also degrade; a process that is favored by the high temperatures typically employed.[63] The mechanism of degradation is specific for each nitroxide, with TEMPO and TIPNO (2,2,5-trimethyl-4-phenyl-3-azahexane-3-oxyl) being prone to oxidation.[64] The nitroxides bearing hydrogen atoms on the C_α bound to the N–O bond that can suffer abstraction of this hydrogen can be abstracted by either a propagating radical (though this is unlikely due to a very low [P*]) or another persistent radical.[60,65] In the latter case, the reaction is referred to as self-disproportionation and yields an hydroxylamine and a nitrone (Scheme 7.2B).[60,66,67] It should be stressed that this reaction can be

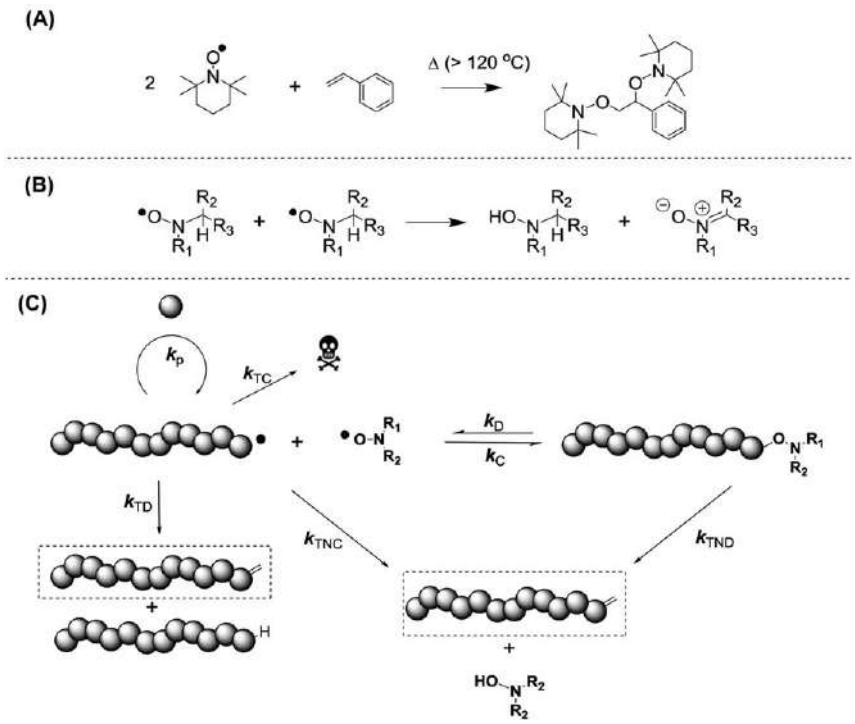

Scheme 7.2 (A) Undesired addition of TEMPO to styrene at high temperatures. (B) Self-disproportionation between two nitroxides. (C) β-H transfer in the NMP of methacrylates.

accelerated in aqueous media. Self-disproportionation occurs with TEMPO and TIPNO, but not with D007 (the nitroxide associated with Disploreg 007; 3-(((2-cyanopropan-2-yl)oxy)(cyclohexyl)amino)-2,2-dimethyl-3-phenylpropanenitrile),[55] SG1 (*N*-*tert*-butyl-*N*-(1-diethylphosphono-2,2-dimethylpropyl)-*N*-oxyl) and some other nitroxides.[68–72] Undesired decomposition of the alkoxyamine has also been evidenced, with the degradation of the CO–N bond being in competition with the desired C–ON in DPAIO (2,2-diphenyl-3-phenylimino-2,3-dihydro-indol-1-yloxyl) and derivatives, thus reducing the control over the polymerization.[73]

In the polymerization of methacrylates, undesired β-hydrogen transfer, also referred to as disproportionation, is usually observed.[74] Disproportionation can either be intramolecular (from the macro-alkoxyamine, with an associated rate constant k_{TND}) or intermolecular between the propagating and persistent radical (with an associated rate constant k_{TNC}), as depicted in Scheme 7.2C, and the relative importance of these reactions cannot be distinguished by chemical analysis.[75] Nevertheless, the nature of the propagating radical and the substituents around the C–O bond have been shown to influence which pathway is more favorable.[76,77] The fraction of disproportionation $f_D = k_{TNC}/(k_C + k_{TNC})$ has been introduced to theoretically predict the evolution of nitroxide concentration and the maximum monomer conversion attainable (C_{max}).[75] Typically, a value of f_D below 5% is necessary to retain sufficient control over the polymerization and high "*livingness*" for various targeted DP_ns.[33] Nevertheless, it should be stressed that the values of f_D and C_{max} are estimated using chain length-independent rate constants and therefore are only approximate indications of the behavior of the system.[55] We recommend that such values are treated with great caution.

Even in the presence of side reactions, control depends on the balance between active and dormant states of the polymerization, which is regulated by the individual values of the rate constants k_D (10^{-10}–10 s^{-1} in between 20 °C and 120 °C) and k_C (10^4–10^8 M^{-1} s^{-1}) and their ratio.[6,33,78] The values of these rate constants are influenced by the nature of the substituents around the breakable C–O bond, *i.e.*, the nature of the initiating (and/or propagating) radical, the nitroxide and its surrounding functional groups.[78] Many manuscripts have been dedicated to studying the influence of substituents on k_D and k_C,[32,63,78–87] hence they will not be described at length herein. Nevertheless, some general trends can be given and are summarized in Figure 7.2. Stabilizations of both the alkyl radical and the nitroxide favor the C–ON bond homolysis (thus increasing k_D).[63,88] Similarly, steric strain on both nitroxide and alkyl fragment tends to increase the value of k_D.[79,89,90] Polarity can have the opposite effects with a more polar alkyl fragment of the alkoxyamine increasing k_D, whilst an increasing polarity in the nitroxide fragment disfavors the C–ON bond cleavage (hence lowers k_D).[83,91–93] Finally, there can be a chain length effect to the value of k_D, which depends on the nature of the propagating radical, with tertiary radicals showing extensive penultimate and antepenultimate effects.[31,79,94–96]

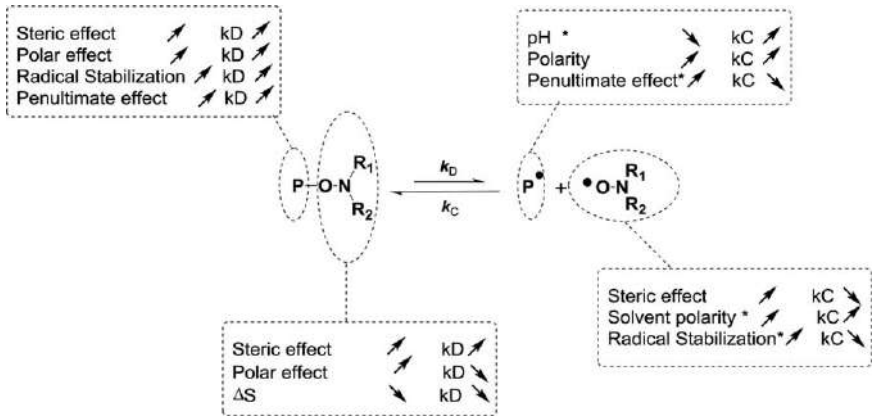

Figure 7.2 Substituents effects on the value of k_D and k_C.
*Those effects affect both nitroxide and radical fragments.[82,84,85]

The effects of the substituents around the N–O bond and the nature of the alkyl radical on the recombination rate constant k_C have been investigated to a lesser extent than those on k_D.[82,84,85] Nevertheless, steric effects tend to decrease the value of k_C, whilst polarity around the N–O bond favors an increase in the rate constant.[97–101] Other parameters may influence the value of k_C, such as enthalpic effect of the alkyl fragment, effects of pH and solvents.[31,95,102,103]

The determination of both rate constants k_D and k_C has been thoroughly investigated, due to their relative importance in the NMP process.[6,85] The rate constant of decomposition k_D can be determined through the decomposition of an alkoxyamine in the presence of a radical scavenger.[63] This can be achieved *via* UV–vis or fluorescence detection,[104] EPR analysis,[63] SEC[105,106] and NMR.[107–109] Estimation of the values of k_D can also be achieved through analysis of the C–ON bond dissociation energy (BDE)[110] utilizing quantum chemical calculations.[55,83,111] The level of quantum calculation can influence the value of the BDE, which will greatly influence the value of k_D.[112,113] Finally, a multiparameter approach relying on high-level *ab initio* calculations has been developed by Coote *et al.*[81] In this method, quantitative linear free-energy relationships are constructed between the structures and properties of the alkoxyamine/nitroxides in order to predict the value of k_D with good accuracy.[79,91]

The experimental determination of k_C can be more arduous,[84] with the necessity to use techniques being able to monitor the rapid reaction between two radicals, such as laser flash photolysis-kinetic absorption spectroscopy (LFP-KAS)[80,97,98] and radical nitroxide recombination-pulsed lamp photolysis size exclusion chromatography (RNR-PLP-SEC).[114] The first technique is more suited to determine the $k_{C,a}$ of an alkoxyamine (small molecules), whilst the second technique is more suited for polymeric species, *i.e.*, for determination of the k_C of the (macro)alkoxyamine. Finally, multiparameter analysis based on stabilization, polarity and steric effects can also be employed to determine the value of k_C.[84,85]

7.2.2 Development of Nitroxides and Alkoxyamines

The development of nitroxides and alkoxyamines has been driven by the need to achieve better control with a larger number of monomers,[6,18,115] as well as a reduction in the occurrence of side reactions.

In the aftermath of numerous investigations on radical trapping, the first patent dealing with NMP emerged in CSIRO.[3] Therein, acylic, five-membered and six-membered ring nitroxides were employed to mediate the NMP of styrene, methyl acrylate (MA) and methyl methacrylate (MMA). Among those nitroxides, TEMPO was later employed to show the viability of the NMP of styrene at high temperatures (>125 °C).[4] In order to reduce both the reaction temperature (to avoid thermal initiation and other side reactions) and the reaction time (24–72 h in the latter case), researchers first investigated TEMPO derivatives (*i.e.*, six-membered ring nitroxides) and their associated alkoxyamines, with various level of success.[86,116–121] The development of many five-, seven- and eight-membered ring nitroxides is worth mentioning, with the size of the ring influencing the decomposition of the resulting alkoxyamine.[96,116,122,123]

A revolutionary stage has been the development of acyclic nitroxides, as depicted in Figure 7.3.[116,124] Some nitroxides bearing hydrogen atoms on the C_α bound to the N–O bond showed good stability,[70–72] which prompted the introduction of TIPNO and its derivatives as good mediators for the polymerization of acrylates and styrene.[44,65,125–128] The next breakthrough was the introduction of heteroatoms in the nitroxide substituents, thus yielding the SG1 nitroxide (and the later BlocBuilder alkoxyamine).[45] These compounds allowed for the well-controlled polymerization of styrene, dienes and acrylates at moderate to high temperatures (40–120 °C).[6] From the last two nitroxides (and derivatives) emerged an extensive amount of alkoxyamines, in order to enhance the polymerization kinetics.[78,79,129] This was achieved by playing with the nature of the initiating radical (the alkyl fragment of the alkoxyamine) in order to increase the value of $k_{D,a}$, thereby improving the kinetics of polymerization.[32,33,96]

The further development of nitroxides and alkoxyamines is closely related to the attempt of many research groups to solve one major issue, the controlled polymerization of methacrylates, which for a long time was a major issue in NMP.[74,130–132] Typically, β-H transfer is observed, resulting in the formation of an ω-unsaturated polymer chain and a hydroxylamine; thus low monomer conversions and steady values of molar masses are observed. To overcome these issues, new nitroxides/alkoxyamines were designed to obtain an optimum dormant/active equilibrium and to avoid an undesired disproportionation events.[31,133] Hence bulky indolinic nitroxides emerged, such as DPAIO (Figure 7.3),[134,135] which was the first nitroxide able to regulate the polymerization of MMA (but not polymerization of styrene at this stage, see Section 7.2.3).[38] The introduction of *N*-phenylalkoxyamines, such as *N*-(1-methyl-(1-(4-nitrophenoxy)carbonyl)ethoxy)-*N*-(1-methyl-(1-(4-nitrophenoxy)carbonyl)ethyl)benzenamine presented a great advance in the field, as they could regulate the polymerization of MMA and styrene partially,

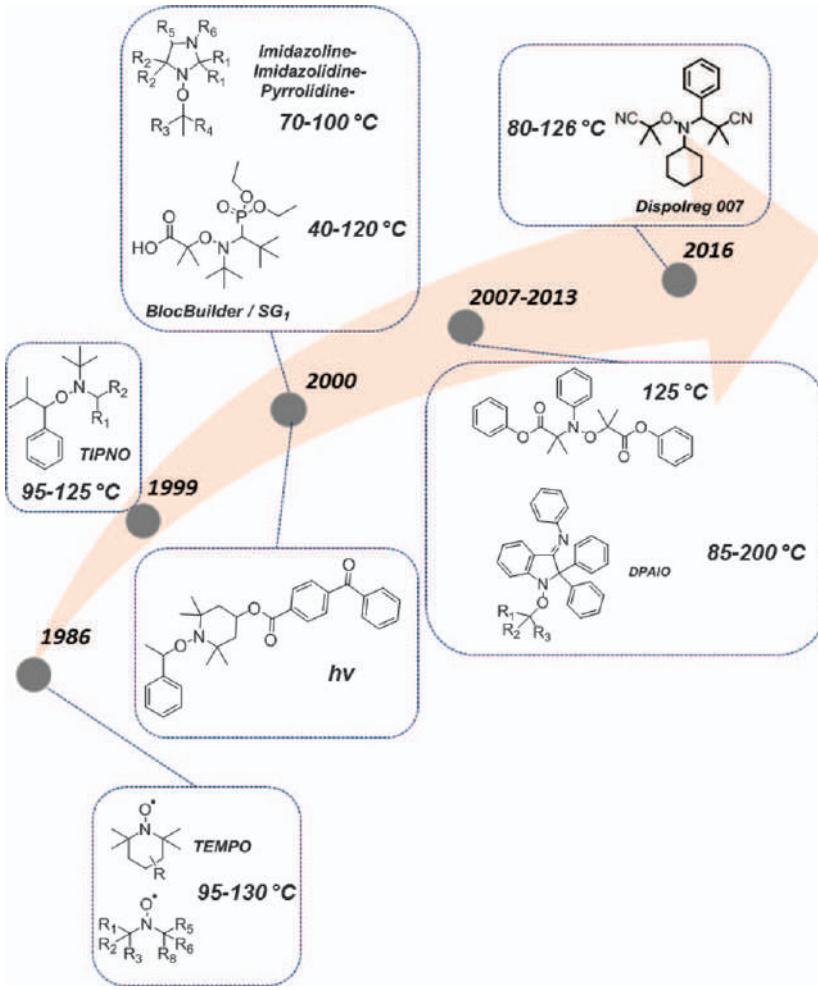

Figure 7.3 Most notable development of nitroxides and alkoxyamines.

whilst their synthesis was less arduous.[136,137] An additional noteworthy advance has been the use of nitrones as precursors for the ''*in situ*'' NMP of styrene, methacrylates, acrylates and dienes.[138,139]

Recently, Dispolreg 007 has emerged as a robust regulator for the controlled polymerization of methacrylates,[55,104,140–143] styrene and acrylates;[52,144] though to a lesser extent for the latter. During the polymerization of methacrylates, Dispolreg 007 shows a low fraction of disproportionation ($f_D = 0.22\%$ at 90 °C), which is not the case for SG1 ($f_D = 7.8\%$ at 70 °C).[55,145] In addition to the good level of control obtained during polymerization, this alkoxyamine became attractive due to the facile three-step synthetic route of amidation, formation of the nitrone and formation of the alkoxyamine, with minimum purification required (through crystallization).

One advance in the development of nitroxides/alkoxyamines lies in the use of UV light to trigger the reversible decomposition/recombination of a (macro)alkoxyamine;[146–150] thus paving the way to nitroxide-mediated photopolymerization (NMP2).[151,152] In order to selectively control the breakage of the C–O bond (instead of the labile N–O bond for instance), chromophores have been introduced as substituents of the alkyl fragment or the nitroxide fragments.[148,153] It should be stressed that for an optimum NMP2 process, the chromophore should be on the nitroxide fragment.[154] This process becomes an elegant tool for surface modifications and/or photo patterning with reactive copolymers.[155–157]

7.2.3 Monomers and Monomers/Regulators Compatibilities

Monomers that can be polymerized by NMP can be segregated into two categories. More activated monomers (MAMs) include vinyl aromatics (namely styrene and derivatives),[3,5,44,45,51,119,158] acrylates,[44,45,159] *N*-substituted and *N,N*-substituted acrylamides,[160–163] methacrylates,[38,104] and acrylonitrile.[44,164] Less activated monomers (LAMs) include dienes,[48,165,166] cyclic ketene acetals[167] or vinyl acetate,[168] *N*-vinylpyrrolidone,[169,170] *N*-vinylcarbazole,[171] vinyl chloride,[172] vinyl ferrocene[173] and azlactones.[174]

The choice of the regulator (*e.g.*, nitroxide or alkoxyamine) is of utmost importance to mediate the polymerization of MAMs and LAMs with good control and good retention of the chain ends (key to the formation of block copolymers, see Section 7.2.4).[5,6] Herein, the focus will be on how to match the reactivity of the monomer to a specific nitroxide or alkoxyamine for an optimum control of the polymerization thereafter (Chart 7.1). The reader should refer to several manuscripts for more details on the breadth of monomers that can be polymerized by NMP.[6]

For instance, TEMPO, TIPNO and BlocBuilder/SG1 can regulate the polymerization of LAMs,[48,166,172] acrylates and styrene but cannot polymerize methacrylates with good control.[44,45,130] In the case of BlocBuilder, this is ascribed to a strong penultimate effect which undesirably affects the values of k_C and k_D, thus favoring undesired β-H transfer.[31,133] The loss of control and "*livingness*" can be overcome by the random copolymerization of methacrylates with a slight amount of a comonomer to modify the value of $\boldsymbol{K} = k_D/k_C$.[175–179] The same strategy has recently been applied to the copolymerization of terpene derivatives.[180–182] More complex alkoxyamine structures can be also utilized at higher temperatures (up to 200 °C) for the polymerization of acrylates and styrene, with relatively good control.[183,184] New nitroxides/alkoxyamines such as DPAIO or *N*-(1-methyl-(1-(4-nitrophenoxy)carbonyl)ethoxy)-*N*-(1-methyl-(1-(4-nitrophenoxy)carbonyl)ethyl)-benzenamine can homopolymerize methyl methacrylate, although with limited monomer conversion and broad molar mass distributions.[38,137] In addition, limited versatility toward other monomers (*e.g.*, acrylates and styrene) is usually observed with these systems, though further modifications of the alkoxyamine structure were shown to improve control in the

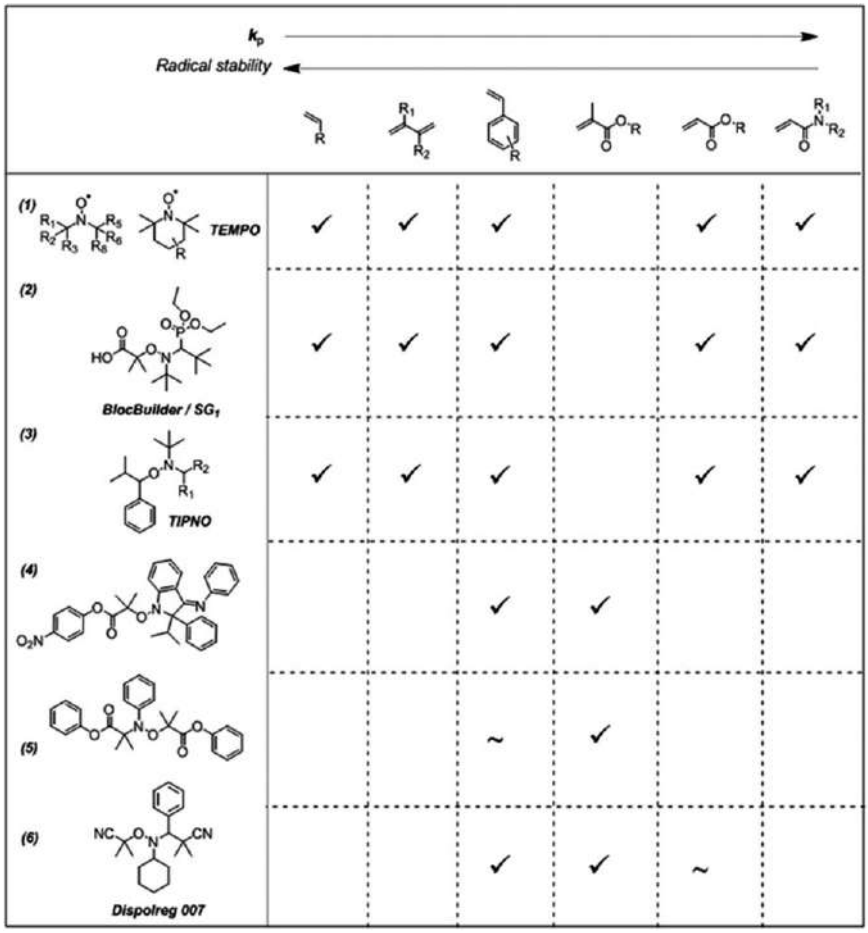

Chart 7.1 Nitroxides/alkoxyamines and monomer compatibility chart. ✓Good control can be achieved. ~ Partial control can be achieved.

case of styrene (Chart 7.1.[4]).[185] This situation has been recently rectified with the development of a new generation of alkoxyamines.[104,138,139] Specifically, Dispolreg 007 has emerged as a robust mediator for the polymerization of MMA and styrene, both in solution and in aqueous dispersion.[52,140–142] Some control over the polymerization of BA was achieved.[144] Good control over the molar mass distributions and good chain end fidelity are obtained with disproportionation being minimal within the time scale of polymerization for MMA.[55]

What emerges from Chart 7.1 is that nitroxides/alkoxyamines capable of regulating the polymerization of methacrylates cannot (in most cases, as described above) control the polymerization of other MAMs and LAMs. This is due to the combination of radical stability, the side reactions inherent to each type of radical (*e.g.*, disproportionation) and the values of k_C and k_D,

which cannot be tuned to a range which can give sufficient control for each monomer. Consequently, the quest for a universal alkoxyamine may be successful if those values of k_D and k_C can be appropriately tuned by means of external stimuli (*e.g.*, pH) and if side reactions are avoided.

7.2.4 Architectures

One of the interests of RDRP lies in the retention of the reactive chain ends, which allows for the formation of a wide range of architectures and functional macrostructures.[186,187] Most of the architectures are summarized in Scheme 7.3. First, functional groups such as –OH,[188–190] –COOH,[32,191] -NHS (*N*-hydroxysuccinimide),[192,193] -SH,[194] -X (X an halogen),[195] H-bonding moieties (*e.g.*, uracil, ureidopyrimidinone),[196,197] chromophores (*e.g.*, pyrene),[148,198,199] alkyne and azide groups can be introduced on the alkyl fragment (α-end) and/or the nitroxide fragment (ω-end) of an alkoxyamine.[195,200] Thus, heterotelechelics and α,ω-telechelic polymers can be produced, paving the way to a myriad of reactive macrostructures, which include (but are not limited to) bioconjugates and organic/inorganic hybrids.[201,202] Some functional groups (*e.g.*, –OH, –COOH, –X) can further initiate polyaddition, polycondensation or step-growth polymerization such as ring-opening polymerization (ROP), RAFT and ATRP.[6,201]

Grafted polymers can be synthesized by NMP,[203,204] through ''grafting from'',[205,206] ''grafting to'' (or ''grafting onto'')[207,208] and ''grafting through'' methods,[209] each leading to different levels of control. Branched or comb copolymers can also be produced by exploiting a side-reaction typically associated with the polymerization of acrylates,[210,211] namely intramolecular chain transfer to polymer (also referred to as backbiting).[212] It is important to stress that backbiting is usually reduced in the presence of a nitroxide.[144,213–215] This effect is also observed in other reversible deactivation radical polymerizations and it has been attributed to the effect of the fast reversible process created by the control agent, which reduces the relative rates of the slowest of the processes involved in parallel competitive

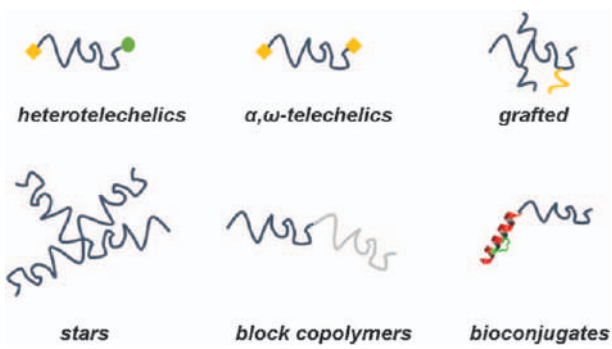

Scheme 7.3 Schematic representation of the architectures attainable by NMP.

reactions (in this case the relative rate of backbiting with respect to propagation is reduced).[215–218] Hyperbranched or dendritic polymers can be synthesized by NMP[219] through the use of inimers [monomers able to (re)initiate polymerization], *i.e.*, bearing a vinyl bond and a pendant nitroxide.[220] A combination of mono- and difunctional monomers can also be utilized.[221] Star polymers have interesting viscosity behaviors and can be synthesized through an ''arm first'' or a ''core first'' approach.[222] An ''outside-in'' strategy utilizing a tris-nitroxide can also be exploited, though moderate control over the desired structure is usually observed.[223] It should be stressed that a ''core first'' approach is preferred to obtain a desired n-arm star structure. In addition, fine tuning of the reaction conditions is required to avoid star–star coupling as a result of radical–radical termination. NMP allows for the formation of cyclic polymers through alkyne/azide coupling post-polymerization (under diluted conditions), though a mixture of cyclic and linear polymer is usually obtained.[224]

The retention of the alkoxyamine chain end(s) can be exploited to synthesize block copolymers. These can be produced from the same monomer families (*e.g.*, styrene–styrene derivatives) or with cross families (*e.g.*, styrene–acrylates or styrene–methacrylates).[225–228] Block copolymers with dienes, such as isoprene (PS-*b*-PI), can also be produced,[229,230] whilst the combination of NMP with other polymerization methods can be useful to yield PE-*b*-PS block copolymers.[231,232] In NMP, the choice of regulators, among other parameters (see below), is crucial to achieve good control over the chain end fidelity and optimum compatibility between monomers.[6] In Chart 7.2, the alkoxyamines/nitroxides able to achieve block copolymers of acrylates, methacrylates and styrene (and derivatives) are listed.

The ability to produce block copolymers depends on several factors. First the structure of the alkoxyamine/nitroxide should promote the control over the polymerization of the monomers (Chart 7.1). In addition, sufficient ''*livingness*'', *i.e.*, the fraction of chains bearing the alkoxyamine end groups, is needed. This ''*livingness*'' depends on the combination of monomer and alkoxyamine/nitroxide selected to produce the first block and on the reaction conditions (temperature, time, bulk, semicontinuous). The concentration of ''*living*'' chains can decrease at high conversions due to the side reactions discussed in Section 7.2.1. Finally, the nature of the monomer will influence the re-initiation step to produce a block copolymer. More specifically, a more stable radical should be preferred for the first block with a less stable radical being utilized for the second block.

This combination explains, in part, the inability of most of the nitroxides/alkoxyamines to produce all types of block copolymers.[6] For instance, the original DPAIO is an efficient regulator for the homopolymerization of methacrylate, though the production of block copolymers from poly(methyl methacrylate) (PMMA) such as PMMA-*b*-PS and PMMA-*b*-PBA is more difficult.[38,130,185] This is due, in part, to undesired CO–N dissociation with acrylates and styrene.[38] A modified DPAIO structure (structure 4 in Chart 7.2) could overcome this issue for styrene.[185] In the case of TIPNO, block

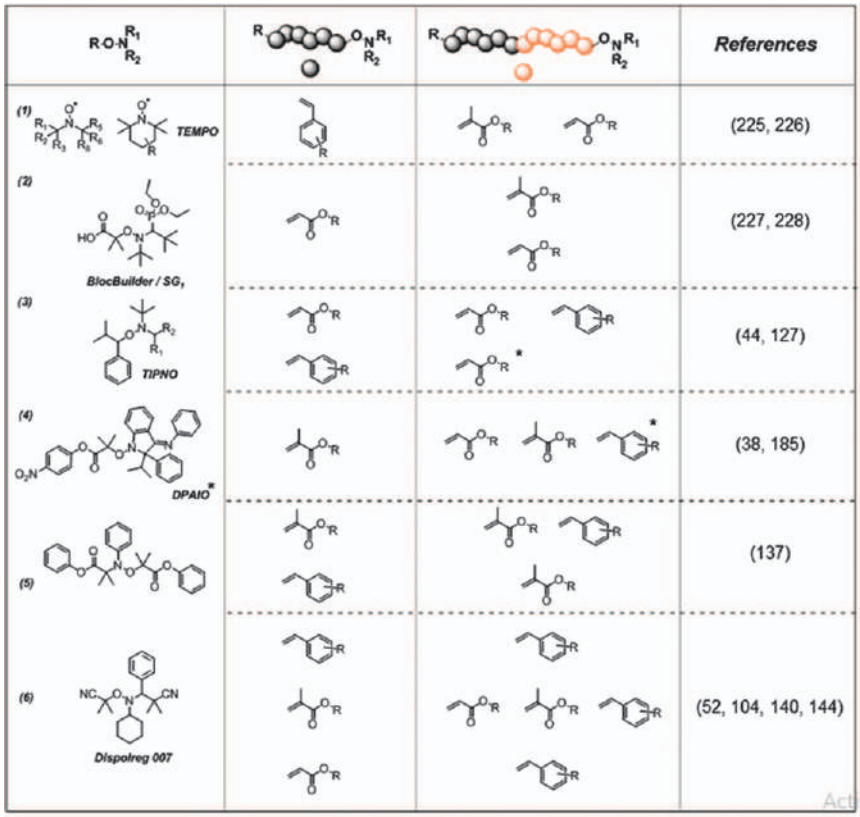

Chart 7.2 Examples of block copolymers produced by nitroxide-mediated polymerization. B1 and B2 correspond to the first and second blocks, respectively. *Modifications on the original alkoxyamine/nitroxide structure were performed.

copolymers containing butyl acrylate and styrene could only be obtained if the poly(butyl acrylate) (PBA) was prepared first.[44] This result was not intuitive, as in terms of radical stability styrene is more stable than butyl acrylate, hence the preparation of PS-*b*-PBA block copolymer should have been preferred. Nonetheless, this was not successful without modification of the nitroxide structure, necessary to enhance the polarity of the nitroxide fragment and change the value of $\boldsymbol{K}$.[127] Pleasingly, Dispolreg 007 allows for the formation of a wide range of block copolymers, including PS-*b*-PMMA, PMMA-*b*-PBMA, PMMA-*b*-PS and PBA-*b*-PS (up to some control of the PBA block).[52,104,142,144]

7.3 Polymerization Processes

A major stumbling block in the commercial development of NMP has been the scaling of the polymerization from the lab scale. As alluded to in the

previous section, this is partly due to the historic difficulty in the synthesis of low-cost nitroxides/alkoxyamines. However, of equal importance is the difficulty in making the transition from batch bulk or solution processes, which are overwhelmingly used in academic literature, to processes that can be conducted at the multi-ton scale.[233] In this section, we will detail the progress that has been made with respect to polymerization processes in the field of NMP.

7.3.1 Bulk/Solution Polymerization

Polymerization in bulk and solution remains the most practical and frequently used method to conduct NMP at the lab scale. In this type of reaction, monomer and alkoxyamine/nitroxide (and optionally solvent) are simply charged to the reaction vessel and heated to the reaction temperature. Since low molecular weights ($M_n < 100\,000$ g mol^{-1}) are typically targeted in NMP, solids contents of 70 wt% are easily achievable before there are significant viscosity issues. It may be noted that higher monomer concentrations are more desirable as, at the same target chain length, the rate is faster whilst minimizing effects of side reactions.[234,235] The use of such batch processes in bulk and solution has provided the vital academic studies that are necessary in order to understand the NMP process as presented in the previous section. However solution/bulk polymerizations in batch are unsuitable for scale up, as they lead to highly viscous/solid reaction mixtures at high conversion which are challenging to use practically and, furthermore, run a serious risk of thermal runaway and explosion.[236] As a result, NMP processes that take place in aqueous dispersed media, as well as in semibatch/continuous processes have been developed, as will be described in the next sections.

7.3.2 Dispersed-phase Polymerization

In conventional free radical polymerization, there are numerous advantages to conducting the polymerization in dispersed media.[237,238] On the one hand, the compartmentalized nature of the reaction media leads to low rates of termination, which allows for faster rates of polymerization and higher molecular weights. The dispersed nature of the reaction also permits high solids contents to be reached before significant changes in the viscosity are observed. Furthermore, in the case of conducting the reaction in water, the low viscosity and the high heat capacity allow for efficient removal of heat generated during the polymerization (and a small effect on the reactor temperature), which is vital in the case of reactions conducted on the industrial scale. In fact, on the industrial scale heat removal is typically a limiting factor in reducing the timescale of the process. Finally, the use of water as the continuous phase omits the use of toxic solvents and improves the sustainability of the process.

For NMP, the "*livingness*" of the polymerization is dependent on limiting termination of growing chains. Therefore, as detailed in Section 7.1, there is a limit on the rate of reaction that can be obtained whilst maintaining control of the polymerization. As a result, the relatively low rate of polymerization required for well-controlled NMP reactions means that many of the beneficial aspects of conducting radical polymerizations in dispersed systems are lost for NMP. Furthermore, as many NMP systems are reliant on temperatures in excess of 100 °C, they must be conducted under pressure when aqueous systems are employed.[6] Although conducting emulsion polymerizations in pressurized vessels is not an issue industrially [large tonnage poly(vinyl chloride) and poly(styrene-*co*-butadiene) are produced under pressure], this has limited the extent of academic research in the area. Despite these drawbacks, the positive aspects of conducting dispersed phase polymerizations have made them the subject of continued interest.[239–241]

Much of the attraction of conducting conventional radical polymerization in dispersed media arises from the compartmentalization of the radical species. This allows for a relatively high radical concentration whilst minimizing termination by effectively segregating two propagating radicals in distinct particles. In NMP, an additional effect of the confined nature of the radicals is observed upon dissociation of the C–ON bond. In this case, both the propagating polymer chain and the nitroxide are generated within the confined space of the polymerizing particle, and this results in a relative increase in recombination.[242–245] This can lower the rate of polymerization (the total radical concentration is lowered) and can also improve the dispersity of the polymer (decrease in number of units added per open cycle).[246–248] On the other hand, in the case of exit of the nitroxide radical from the particle, a significant increase in the rate of polymerization can occur at the cost of some control of the reaction.[249,250] In both cases, the effects of compartmentalization in NMP are typically only observed for particles that are size < 100 nm and in many cases the kinetics of NMP conducted in dispersed media are identical to those conducted in bulk.[244] The confined nature of heterogeneous systems is also attractive in the preparation of novel nanostructured particle morphologies from block copolymers made by NMP due to the effects of nanoconfinement on phase separation.[251,252]

In addition to compartmentalization effects, partitioning of the nitroxide into the aqueous phase can also influence the reaction kinetics in aqueous dispersed polymerizations. In most cases, partitioning has a limited effect on the rate of polymerization as the nitroxide depleted by partitioning into the aqueous phase is regenerated by additional termination reactions until the steady-state concentration of propagating radicals and nitroxide in the particle is reached.[253] For example, comparison of the NMP of styrene in miniemulsion using TEMPO, a hydrophobic nitroxide, and TEMPO-OH, a comparative hydrophilic nitroxide, showed effectively no difference in the rate of polymerization, molecular weight or dispersity value despite the vastly different partitioning behavior.[254] Nitroxide partitioning into the

aqueous phase can however cause significant complications when the nitroxide is unstable in aqueous media. Many nitroxides that contain α-hydrogen atoms, such as SG1, are unstable and undergo disproportionation, particularly at acidic pH.[255] In this case, buffering can be required in order to prevent loss of control of the reaction. It may be noted that decomposition of the nitroxide may in some instances be desirable in order to maintain a relatively high rate of polymerization, and nitroxide scavengers can be added to aid this process.[256–258]

Polymerization reactions in dispersed media can be divided into a number of distinct categories as highlighted in Table 7.1. These include suspension, emulsion, microemulsion and miniemulsion. Dispersion polymerization is also a viable process,[259–263] though it will not be discussed herein. The differences between them give distinct advantages (and disadvantages) when conducting NMP, and therefore in the following section we will detail the different types of dispersed phase polymerizations and how they can be applied in NMP.

Table 7.1 Different polymerization processes used in NMP in dispersed media and their distinguishing features.

Polymerization process	Schematic representation	Notes
Suspension	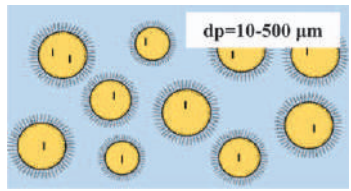	Droplet nucleation Very large particles obtained (not suitable for practical use as a dispersion) No compartmentalization
Miniemulsion	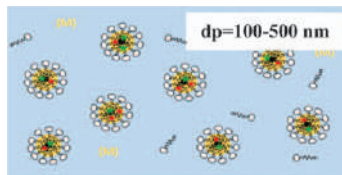	Droplet nucleation Miniemulsion process hard to scale Can be initiated from aqueous or organic phase
Microemulsion	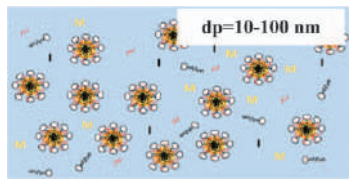	Micellar nucleation High surfactant concentrations, low solids Highly compartmentalized
Emulsion	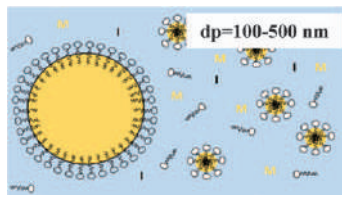	Complications associated with particle nucleation and aqueous phase transport

7.3.2.1 Suspension Polymerization

Suspension polymerization is a technique in which droplets of monomer in the range of 10–100 μm are generated by mechanical agitation in an aqueous surfactant solution, and the reaction occurs with each droplet acting as a miniature reaction mixture.[264] Due to the large particle size, there are no effects of compartmentalization, and the kinetics are typically identical to that of a bulk polymerization but have the advantage of maintaining a low viscosity throughout the process. At the end of the reaction, the polymer can be isolated simply by filtration. Suspension polymerization is particularly advantageous in NMP, as the alkoxyamines that have been designed for bulk/solution systems can be easily translated to the suspension case without the worries of aqueous phase transport or particle nucleation that apply to most dispersed phase techniques.[141] Typical solid content in these polymerizations is up to around 40 wt%.

Most literature reports of NMP in suspension focus on the use of TEMPO-based systems for the polymerization of styrenic monomers at high temperatures (*ca.* 130 °C).[4,265–267] Due to the high cost of TEMPO-based alkoxyamines, in most cases bimolecular initiator systems have been used involving an oil-soluble peroxide and TEMPO.[265–267] In the first step, a TEMPO terminated macroinitiator is formed by bulk polymerization and then subsequently used as a macroinitiator in the suspension polymerization process. This two-step procedure has the advantage that batch-to-batch reproducibility problems in the synthesis of the initial macroalkoxyamine can be avoided.

More recently, the polymerization of methacrylic monomers by suspension polymerization at reduced temperatures ($T = 90$ °C) has also been reported using Dispolreg 007 as alkoxyamine in a unimolecular initiating system leading to spherical particles in the order of 100 μm (see Figure 7.4).[141] When compared to a bulk polymerization under the same conditions, it was noted that significantly faster reaction rates were observed, and high conversions could be reached in the suspension case. This was related to the aqueous phase decomposition of nitroxide. Formation of block copolymers in these reactions can be conducted by simple addition of a second shot of monomer or by isolation of the polymer and redispersion of the microparticles in the presence of the second monomer and subsequent polymerization to form block copolymers.

7.3.2.2 Miniemulsion

Next to suspension polymerization, miniemulsion polymerization offers one of the easiest routes to dispersed systems for NMP.[268] Similar to suspension polymerization, the alkoxyamine/nitroxide is generally dissolved in the organic phase, but in this case high shear is applied to generate droplets in the range of 100 nm. As droplet nucleation is the predominant nucleation mechanism, a final particle size similar to that of the initial miniemulsion is

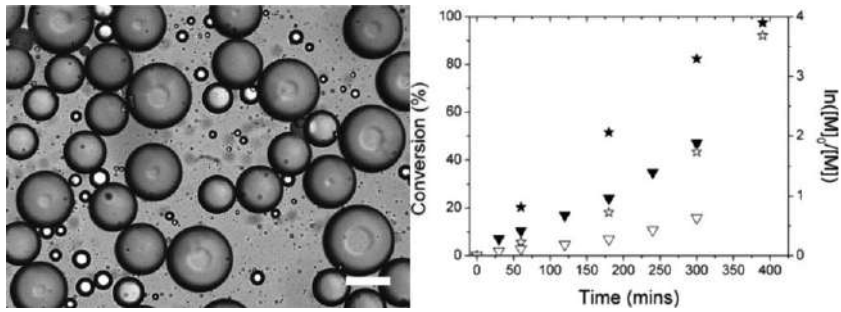

Figure 7.4 Suspension polymerization of methyl methacrylate mediated by Dispolreg 007 leading to spherical particles. The right panel shows the differences in polymerization rate between the reaction in suspension (stars) and the equivalent reaction in bulk (triangles).
Reprinted from ref. 141 with permission from Elsevier, Copyright 2017.

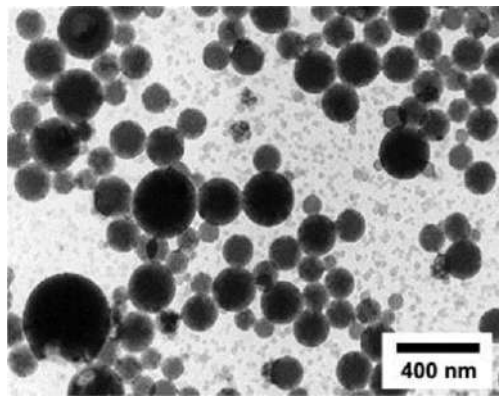

Figure 7.5 Transmission electron microscopy (TEM) image of particles obtained from SG1-mediated miniemulsion polymerization of styrene at 90 °C initiated by azobisisobutyronitrile (AIBN).
Reprinted from ref. 272 with permission from Elsevier, Copyright 2007.

typically obtained leading to particles with size in the range of 100 nm (see Figure 7.5). A costabilizer, *e.g.*, a low-molecular-weight water-insoluble compound (typically hexadecane but more preferably a polymerizable hydrophobic monomer such as stearyl acrylate), is added to prevent Ostwald ripening of the miniemulsion droplets. Unlike suspension polymerization, the significantly reduced droplet size allows for the use of water-soluble initiators in bimolecular systems and water-soluble alkoxyamines (such as BlocBuilder) in unimolecular systems as the higher surface area allows for entry of the radicals from the aqueous phase into the monomer droplets.[269–271]

Similar to the case of suspension polymerization above, most work has been done using TEMPO as a control agent for the miniemulsion polymerization of styrene,[246,257,258,269,273–276] although there are also a number of reports of SG1-based systems for polymerization of both styrene and acrylates.[255,272,277–279] More recently, the polymerization of methacrylic monomers by NMP in miniemulsion using Dispolreg 007 as initiating alkoxyamine has been reported.[142] In the case of TEMPO-based systems and unimolecular SG1-based systems, higher temperatures are typically used and necessitate the use of pressurized reaction vessels. However, in bimolecular SG1-based initiating systems, significantly lower temperatures ($T = 90$ °C) have been used and allowed the reaction to be performed at ambient pressure.[255,272] A downside is that with the use of the bimolecular system at lower temperatures, typically broader molecular weight distributions are observed.[255]

One of the major issues with miniemulsion polymerization is the dispersion step, which requires large amounts of energy and makes scale-up to an industrial scale difficult.[280,281] One potential way to avoid this high energy step has been reported for NMP using surfactants generated *in situ* to spontaneously generate the initial miniemulsion. This miniemulsion can be subsequently polymerized to yield a latex with low particle size (see Figure 7.6).[282,283] These *in situ* surfactants are typically generated by addition of the oil phase containing a long-chain carboxylic acid to the aqueous phase-containing base. Upon contact with the oil and aqueous phase, the carboxylic acid groups are neutralized at the interface to form a surfactant which emulsifies the mixture to form nanometer-sized droplets. While this offers a route around the emulsification step and shows some promise for use in miniemulsion polymerizations,[284,285] typically high volumes of surfactant are required, and there is a limit to the solid content, beyond which a conventional emulsion is formed.[286]

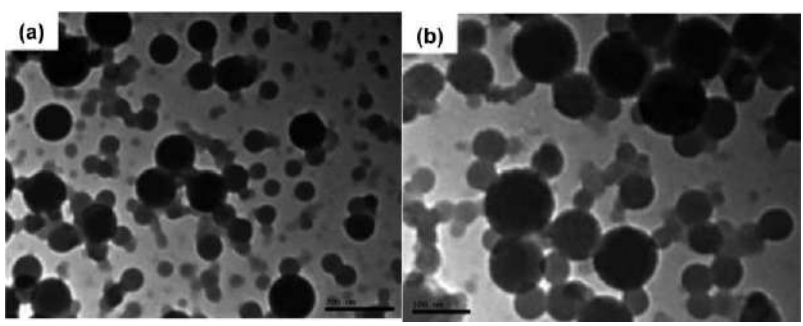

Figure 7.6 Latex produced by miniemulsion polymerization of styrene using an SG1-based macroalkoxyamine. The miniemulsion was produced by *in situ* generation of potassium oleate under low shear.
Reprinted from ref. 282 with permission from American Chemical Society, Copyright 2010.

7.3.2.3 Emulsion Polymerization

Currently, almost all commercial free-radical processes conducted in dispersed media are based on emulsion polymerization.[287] In a conventional emulsion polymerization, the initial reaction mixture consists of an aqueous phase containing monomer swollen surfactant micelles and a dispersed phase of monomer droplets, as in suspension polymerization. However, unlike suspension and miniemulsion polymerization, particles are usually generated either by entry of oligomeric radicals into surfactant micelles *via* a heterogeneous nucleation process or by precipitation of the oligomeric radicals in the aqueous phase (homogeneous nucleation). The large monomer droplets serve as reservoirs of monomer, which is transported through the aqueous phase to the polymer particles where it is consumed. When attempting to translate this to NMP, the complex nucleation process and the need for transport through the aqueous phase severely complicate matters and make emulsion polymerization in NMP far more challenging than miniemulsion or suspension processes.

In an effort to avoid the problems associated with particle nucleation, early experiments focused on the use of seeded polymerizations in which nitroxide and monomer were used to swell a preformed latex and subsequently polymerized.[288] Such a procedure has the obvious disadvantage in the need for a swelling stage as well as the final product containing a significant amount of noncontrolled polymer.

Alternative *ab initio* approaches for NMP in emulsion systems in which no seed is utilized have been adopted using different initiating systems. In the case of both TEMPO- and SG1-based systems, bimolecular *ab initio* emulsion polymerization systems have been developed using persulfates as initiators.[272,289] In addition, unimolecular *ab initio* systems using the deprotonated form of BlocBuilder as well as a difunctional analog of SG1 have been similarly employed to generate radicals in the aqueous phase.[290,291] In general, these systems lead to polymers with broad molecular weight distributions. Moreover, in many cases the dispersions are colloidally unstable due to partitioning of oligomeric alkoxyamines into the large monomer droplets, resulting in undesired droplet nucleation and formation of micron-sized particles (see Figure 7.7). An additional problem is that the high temperatures required for NMP in many cases can result in autoinitiation and the generation of high-molecular-weight polymer in monomer droplets. The polymerization in droplets can be minimized by inclusion of a highly hydrophobic inhibitor in the initial monomer mixture. In this way, the hydrophobicity ensures that transport of the inhibitor is minimized, and only polymerization in the droplets is inhibited.[292] Alternatively, another way to avoid droplet nucleation is to synthesize the macroalkoxyamine at low solids content and subsequently feed monomer to the system to generate a stable latex.[293,294]

An alternative route to *ab initio* emulsion polymerization in NMP systems is through the use of self-assembly of block-copolymers formed during the polymerization process itself. This so-called polymerization-induced self

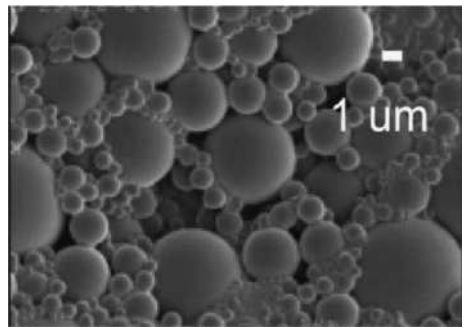

Figure 7.7 SEM image of particles obtained from emulsion polymerization of styrene using TEMPO/KPS initiating system showing both heterogeneous nucleation (small particles) and droplet nucleation (large particles).
Reproduced from ref. 292 with permission from John Wiley & Sons, Copyright 2008 WILEY-VCH Verlag GmbH & Co. KGaA, Weinheim.

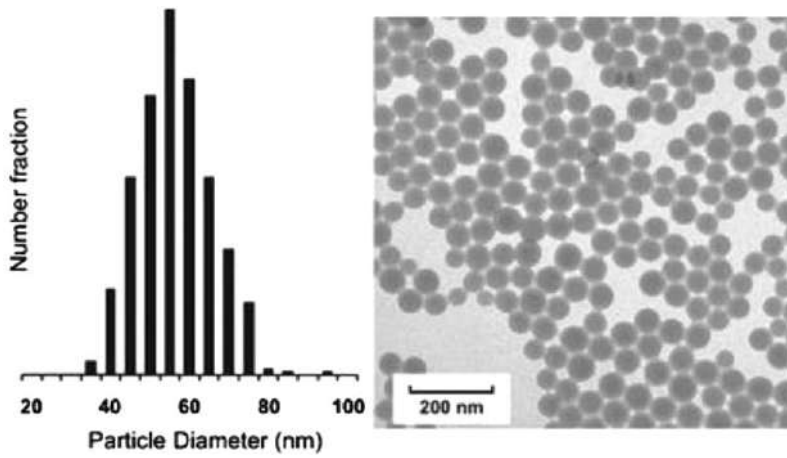

Figure 7.8 TEM image of spherical particles of poly(acrylic acid-*b*-styrene) formed by emulsion polymerization of styrene using a poly(acrylic acid) macroalkoxyamine as initiator.
Reproduced from ref. 296 with permission from the Royal Society of Chemistry.

assembly (PISA) is a technique that takes advantage of the living nature of NMP to direct the formation of dispersed phase structures.[295] In the case of NMP, PISA is typically conducted using a hydrophilic macroalkoxyamine such as an SG1-terminated poly(acrylic acid) that is initially soluble in the aqueous phase.[296–302] Thus radicals are generated within the aqueous phase (as a conventional emulsion polymerization) and are extended with the more hydrophobic monomer that makes up the second block. As the second block grows the block copolymer self-assembles in solution to form spherical particles (see Figure 7.8). A major advantage of this technique is that the

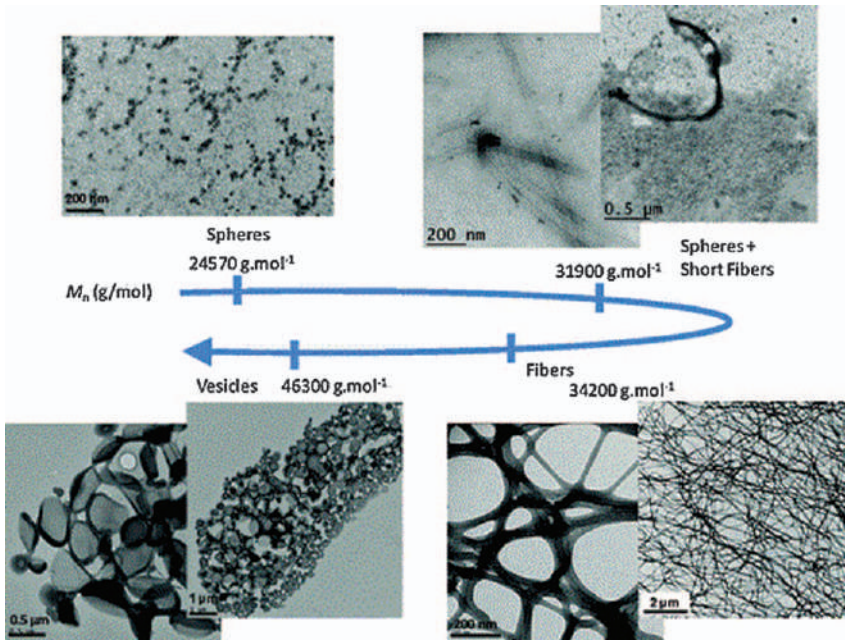

Figure 7.9 TEM images of the final particle morphology obtained from different hydrophobic block molar masses for the same macroinitiator poly(methacrylic acid$_{41}$-*co*-sodium styrene sulfonate$_{10}$)-SG1 (5600 g mol^{-1}). Reprinted from ref. 304 with permission from American Chemical Society, Copyright 2012.

particles are self-stabilizing and do not require additional surfactant, although the presence of a hydrophilic block can be undesirable in many applications of emulsion polymers, such as coatings. A further advantage of the PISA-type systems is that more complex colloidal structures can be obtained.[295] Working on the basis of the framework developed by Isrealachvilli for the self-assembly of amphiphilic molecules,[303] by controlling the relative block length of amphiphilic block copolymers, structures ranging from spheres to worm-like micelles to vesicles can be formed directly in aqueous dispersions (see Figure 7.9).[304–306]

7.3.2.4 Microemulsion

Microemulsion polymerization differs from most dispersed-phase polymerizations because the initial dispersion is in a thermodynamically stable state of monomer swollen micelles dispersed in water. In the case of NMP, this allows the use of hydrophobic biomolecular initiating systems (*i.e.*, AIBN/TEMPO) as well as the use of water-insoluble alkoxyamines, which partition directly into the micelles allowing for micellar nucleation.[307] Typically, microemulsion reactions involve very small particle sizes wherein rapid recombination of the nitroxide and propagating radicals occurs.

Thus a significant reduction in the rate of reaction has been observed compared to the bulk case.[307,308] While such an enhanced rate of recombination can result in slower rates, it can also lead to improvement in the dispersity of the polymer due to a reduced number of monomer additions per open cycle.[248,309] However, the small particle size can also result in differences in the local monomer/alkoxyamine ratio which results in a broadening of the molecular weight distribution.[307]

Oil-in-water microemulsion polymerizations are conducted with low solids content (<5 wt%), and surfactant concentration is high (>10 wt% based on total formulation) making them unattractive from a commercial point of view. In order to overcome this, many microemulsion polymerizations are performed in two stages with a first reaction in batch to produce the macroalkoxymine in discreet polymer particles and subsequent addition of monomer to grow the polymer chains and to increase the solid content.[290,296,310,311] This second stage effectively proceeds as a seeded emulsion polymerization whereby the initial microemulsion polymerization avoids the complications of particle nucleation that have made *ab initio* NMP in emulsion so difficult.

7.3.3 Continuous/Semicontinuous Processes

To date, almost all NMP processes in the open literature have been conducted under batch conditions. However, batch processes are typically difficult to scale-up due to the large enthalpy of polymerization that renders radical polymerizations subject to thermal runaways. An exception is suspension polymerization, which is carried out in batches in large scales. In order to prevent this issue, many conventional commercial radical polymerization processes are done under semibatch or continuous conditions as shown schematically in Table 7.2.

In a semibatch reaction, monomer is continuously fed to the reactor at a certain rate, so that a relatively high instantaneous conversion is maintained, and the concentration of monomer in the reactor at any given time is low. In free-radical polymerizations, this poses little issue, but in NMP it results in a significant increase in the rate of termination relative to propagation, thus leading to relatively low "*livingness*" and high dispersity in semibatch polymerizations when compared to a batch-type system.[140,312,313] Furthermore, low monomer concentrations result in a reduced rate of polymerization, which poses serious issues with regard to commercial viability. As mentioned in previous sections, the use of seeded semibatch reactions in dispersed-phase polymerizations can provide additional advantages as they minimize the challenges in the nucleation step.[252,314]

Similar to semicontinuous processes, while continuous reactors are used commercially for radical emulsion polymerization processes, they provide significant challenges when applied to NMP. Continuous-stirred tank reactors (CSTRs) have been applied to NMP, and while good chain end fidelity can be achieved with such reactors, the distribution of residence times

Table 7.2 Different polymerization processes used in NMP.

Process	Schematic
Batch	
Semibatch	
(Series of) Continuous-stirred tank reactor	
Continuous tubular reactors	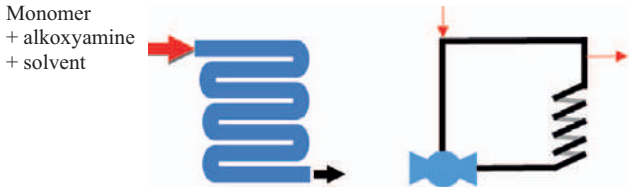 Tubular reactor Continuous loop tubular reactor

results in a dispersity approaching 2.[184] Only in the event that a train of CSTRs is used can the dispersity be significantly reduced with $Đ = 1 + 1/n$ in the best case scenario, where n is the number of reactors in the train.[315,316]

An alternative to the use of CSTRs is the use of continuous tubular reactors. The high surface area to volume ratio of such tubular systems allows heat to be removed efficiently and allows better control of the polymerization process.[317,318] In the ideal case, such tubular reactors operate with plug-flow, and thus the reaction behaves as in a regular batch polymerization, avoiding the continually high instantaneous monomer conversion that makes semibatch reactions challenging. For example, in miniemulsion NMP conducted in a tubular reactor, it has been shown that there are negligible differences between batch and tubular reactions.[319,320] Block-copolymers can also be synthesized by connecting two tubular reactors in series.[318] Unfortunately, while they provide good control of the polymerization compared to other continuous/semicontinuous techniques, tubular reactors require fairly long

residence times and are hard to implement commercially in solution processes, as the viscosity of the reaction mixture leads to many operational difficulties. Similarly, in dispersed-phase systems clogging of the reactor walls is often a major issue.

7.4 Industrial Applications

Since the first report on NMP in the CSIRO 1983 patent, there has been a tremendous interest in implementing the polymerization technique in an industrial set-up.[3] Several major companies have been involved in the development of NMP and regulators thereof in an industrial context, to introduce novel materials and/or additives in the market. IBM, CIBA (now part of BASF), Xerox, Arkema, Symyx, Elf Atochem (now Arkema), Atofina and Bayer were amongst the major patent applicants regarding the use of NMP in an industrial context. The applications are diverse, ranging from pigments dispersing agents in coatings, oil dispersant in cosmetic formulations, additives in thermoset resins, additives in laundry detergents, additives for lubricant modifications and others.[19,20]

Moad and coworkers have recently regrouped all 76 patent applications in NMP since 1983 until the year 2000 (listed in priority dates), whilst elegantly describing the innovations within.[18] The reader is kindly referred to this book chapter for further information. From 2000 onwards, the main actor in the industrial development of NMP has been Arkema. The company first focused on the commercialization of regulators, namely the SG1 nitroxide and the BlocBuilder® alkoxyamine.[321,322] Derivatives from those regulators were also developed.[323] Then, they exploited the versatility of the alkoxyamine/nitroxide to synthesize acrylic block copolymers, later formulated in the commercial products Nanostrength® and Flexibloc®.[21] The company demonstrated the scalability of their innovative polymers by producing block copolymers on the ton scale in Mont (France). The various types of Nanostrength® products that were developed differ in ''hard'' and ''soft'' fractions, molar mass and functionality. This allows multiple usages, such as pressure-sensitive adhesives, thermoplastic elastomers, toughened thermoset resins and nanostructured PMMA.[324–328] The BlocBuilder® regulator was recently utilized to improve the mechanical properties and chemical resistance of a nanostructured PMMA glass.[329,330] This was later commercialized as Altuglas® ShieldUp grade, to be applied in automotive and aeronautic glazing.[330,331]

BlocBuilder® was also utilized in a joined patent between Arkema and Daikin Industries to synthesize block copolymers for applications as water and oil repellent resins.[332] The acrylic block copolymers contained fluorinated and non-fluorinated blocks.

Lubrizol has taken advantage of the NMP process to design star polymers, which were later employed as viscosity modifier in lubricating oils.[333] They utilized TEMPO to mediate the polymerization of acrylics to yield the star ''arms''.

BASF has patented the synthesis of various alkoxyamines (NOR regulators) which could mediate the NMP of acrylates and styrene.[20] Subsequently, they utilized those regulators to prepare amphiphilic block copolymers and comb copolymers for applications as soil antiredeposition and soil release agents in laundry detergent formulations.[334,335] The NOR regulators were also employed in the synthesis of block copolymers that were later applied as additives to improve the flow of polymer melts.[336] The company also designed functional alkoxyamines, bearing isocyanate groups, in order to prepare poly(acrylates) which can be further reacted with α,ω-hydroxy poly(dimethylsiloxanes).[337] The resulting block copolymers were later employed as additives in ink and/or paints aqueous formulations.

In spite of these developments, it seems that there is a dichotomy between the rich academic research and the relatively modest industrial developments. In two recent manuscripts, Destarac discussed the difficulties of successfully implementing RDRP techniques in an industrial set-up.[19,20] One reason for the poor translation from academic research to industrial applications is the overall cost of a final product made by NMP. Industrial implementation requires the cost-effective and consistent production of high-quality products under safe, environmentally friendly conditions. The cost of the regulators (nitroxides and/or alkoxyamines) is particularly important because most of the aimed products are additives made out of block copolymers of relatively low molecular weight. Besides, as at least a molecule of alkoxyamine/nitroxide is needed per polymer chain, the amount of regulator needed is substantial. Therefore, there is a need for cheaper control agents (nitroxides/alkoxyamines), and in this regard the development of cheap and robust alkoxyamines such as Dispolreg 007 offers a step in the right direction. Another aspect that increases the production cost of high-purity polymers is the need for post-polymerization purifications. Industrial implementation will require a balance to be reached between purity and performance, so that post-polymerization purifications are avoided.

7.5 Conclusions

The need for synthetic procedures able to yield polymers with well-controlled microstructures under mild reaction conditions has been the driving force for the development of reversible deactivation radical polymerization (RDRP) techniques. Among these, nitroxide-mediated polymerization (NMP) is appealing because it is not affected by some of the drawbacks of the main competing techniques (presence of copper in ATRP, odor due to the presence of sulfur in RAFT and residual coloring in both).

The intensive research in academia and industry has led to a good understanding of the fundamental mechanisms of NMP. As a result, nitroxides/alkoxyamines have emerged that are able to regulate the polymerization of most monomer families including acrylates, acrylamides, methacrylates, styrene, and dienes among others. However, no general-purpose control agent, namely an agent able to control all monomer

families, is yet available. A wide range of architectures (including but not limited to block copolymers) can be produced, but some combinations of monomers are difficult if not impossible to obtain, due to the lack of a universal nitroxide/alkoxyamine.

NMP can be implemented in homogeneous (bulk, solution) and dispersed (suspension, emulsion, miniemulsion and microemulsion) media, the latter being more suitable for industrial implementation. Among the different polymerizations in dispersed media, suspensions and miniemulsions are easier to implement because they do not require extensive mass transport through the aqueous phase due to the formation of particles by droplet nucleation. In principle, NMP is not limited to any type of reactor (stirred tank and tubular) or operation mode (batch, semibatch and continuous), but stirred tank reactors operating under batch conditions for suspension and semibatch conditions for other dispersion processes are likely the most promising for industrial implementation.

Products produced by NMP are slowly but steadily entering the market. One of the reasons for the slow industrialization is the cost of nitroxides/alkoxyamines required. This is particularly an issue as most target products are low-molecular-weight additives and, as at least one molecule of control agent per polymer chain is needed, this requires large amounts of nitroxide (or alkoxyamine). In this regard, the development of cheap and robust alkoxyamines such as Dispolreg 007 offers a step toward scalable NMP-based polymerization processes.

References

1. M. Szwarc, 'Living' Polymers, *Nature*, 1956, **178**(4543), 1168–1169.
2. R. P. Quirk and B. Lee, Experimental Criteria for Living Polymerizations, *Polym. Int.*, 1992, **27**(4), 359–367.
3. D. H. Solomon, E. Rizzardo, and P. Cacioli, inventors; Commonwealth Scientific And Industrial Research Organization, assignee. Polymerization process and polymers produced thereby, *U. S. Pat.*, US4581429 A, 1986.
4. M. K. Georges, R. P. N. Veregin, P. M. Kazmaier and G. K. Hamer, Narrow molecular weight resins by a free-radical polymerization process, *Macromolecules*, 1993, **26**(11), 2987–2988.
5. C. J. Hawker, A. W. Bosman and E. Harth, New Polymer Synthesis by Nitroxide Mediated Living Radical Polymerizations, *Chem. Rev.*, 2001, **101**(12), 3661–3688.
6. J. Nicolas, Y. Guillaneuf, C. Lefay, D. Bertin, D. Gigmes and B. Charleux, Nitroxide-mediated polymerization, *Prog. Polym. Sci.*, 2013, **38**(1), 63–235.
7. M. Kato, M. Kamigaito, M. Sawamoto and T. Higashimura, Polymerization of Methyl Methacrylate with the Carbon Tetrachloride/Dichlorotris(triphenylphosphine)ruthenium(II)/Methylaluminum Bis(2,6-di-tert-butylphenoxide) Initiating System: Possibility of Living Radical Polymerization, *Macromolecules*, 1995, **28**(5), 1721–1723.

8. J.-S. Wang and K. Matyjaszewski, ''Living''/Controlled Radical Polymerization. Transition-Metal-Catalyzed Atom Transfer Radical Polymerization in the Presence of a Conventional Radical Initiator, *Macromolecules*, 1995, **28**(22), 7572–7573.
9. K. Matyjaszewski and J. Xia, Atom Transfer Radical Polymerization, *Chem. Rev.*, 2001, **101**(9), 2921–2990.
10. K. Matyjaszewski, Atom Transfer Radical Polymerization (ATRP): Current Status and Future Perspectives, *Macromolecules*, 2012, **45**(10), 4015–4039.
11. M. Ouchi, T. Terashima and M. Sawamoto, Transition Metal-Catalyzed Living Radical Polymerization: Toward Perfection in Catalysis and Precision Polymer Synthesis, *Chem. Rev.*, 2009, **109**(11), 4963–5050.
12. A. Anastasaki, V. Nikolaou, G. Nurumbetov, P. Wilson, K. Kempe and J. F. Quinn, *et al.*, Cu(0)-Mediated Living Radical Polymerization: A Versatile Tool for Materials Synthesis, *Chem. Rev.*, 2016, **116**(3), 835–877.
13. X. Pan, M. Fantin, F. Yuan and K. Matyjaszewski, Externally controlled atom transfer radical polymerization, *Chem. Soc. Rev.*, 2018, **47**(14), 5457–5490.
14. J. Krstina, G. Moad, E. Rizzardo, C. L. Winzor, C. T. Berge and M. Fryd, Narrow Polydispersity Block Copolymers by Free-Radical Polymerization in the Presence of Macromonomers, *Macromolecules*, 1995, **28**(15), 5381–5385.
15. J. Chiefari, Y. K. Chong, F. Ercole, J. Krstina, J. Jeffery and T. P. T. Le, *et al.*, Living Free-Radical Polymerization by Reversible Addition–Fragmentation Chain Transfer: The RAFT Process, *Macromolecules*, 1998, **31**(16), 5559–5562.
16. G. Moad, E. Rizzardo and S. H. Thang, Living Radical Polymerization by the RAFT Process – A Third Update, *Aust. J. Chem.*, 2012, **65**(8), 985–1076.
17. S. Perrier, 50th Anniversary Perspective: RAFT Polymerization—A User Guide, *Macromolecules*, 2017, **50**(19), 7433–7447.
18. G. Moad and E. Rizzardo, The History of Nitroxide-mediated Polymerization, *Nitroxide Mediated Polymerization: From Fundamentals to Applications in Materials Science*, The Royal Society of Chemistry, ch. 1, 2016, pp. 1–44.
19. M. Destarac, Controlled Radical Polymerization: Industrial Stakes, Obstacles and Achievements, *Macromol. React. Eng.*, 2010, **4**(3–4), 165–179.
20. M. Destarac, Industrial development of reversible-deactivation radical polymerization: is the induction period over?, *Polymer Chemistry*, 2018, **9**(40), 4947–4967.
21. P. Gerard, L. Couvreur, S. Magnet, J. Ness and S. Schmidt, Controlled Architecture Polymers at Arkema: Synthesis, Morphology and Properties of All-Acrylic Block Copolymers. *Controlled/Living Radical Polymerization: Progress in RAFT, DT, NMP & OMRP*, ACS Symposium Series. 1024, American Chemical Society, 2009, pp. 361–373.

22. T. Kothe, S. Marque, R. Martschke, M. Popov and H. Fischer, Radical reaction kinetics during homolysis of N-alkoxyamines: verification of the persistent radical effect, *J. Chem. Soc., Perkin Trans. 2*, 1998, (7), 1553–1560.
23. H. Fischer, The persistent radical effect in controlled radical polymerizations, *J. Polym. Sci., Part A: Polym. Chem.*, 1999, **37**(13), 1885–1901.
24. H. Fischer, The Persistent Radical Effect: A Principle for Selective Radical Reactions and Living Radical Polymerizations, *Chem. Rev.*, 2001, **101**(12), 3581–3610.
25. T. Fukuda, A. Goto and K. Ohno, Mechanisms and kinetics of living radical polymerizations, *Macromol. Rapid Commun.*, 2000, **21**(4), 151–165.
26. A. Goto and T. Fukuda, Kinetics of living radical polymerization, *Prog. Polym. Sci.*, 2004, **29**(4), 329–385.
27. M. Souaille and H. Fischer, Kinetic Conditions for Living and Controlled Free Radical Polymerizations Mediated by Reversible Combination of Transient Propagating and Persistent Radicals: The Ideal Mechanism, *Macromolecules*, 2000, **33**(20), 7378–7394.
28. W. Tang, N. V. Tsarevsky and K. Matyjaszewski, Determination of Equilibrium Constants for Atom Transfer Radical Polymerization, *J. Am. Chem. Soc.*, 2006, **128**(5), 1598–1604.
29. W. Tang, T. Fukuda and K. Matyjaszewski, Reevaluation of Persistent Radical Effect in NMP, *Macromolecules*, 2006, **39**(13), 4332–4337.
30. D. Greszta and K. Matyjaszewski, Mechanism of Controlled/''Living'' Radical Polymerization of Styrene in the Presence of Nitroxyl Radicals. Kinetics and Simulations, *Macromolecules*, 1996, **29**(24), 7661–7670.
31. Y. Guillaneuf, D. Gigmes, S. R. A. Marque, P. Tordo and D. Bertin, Nitroxide-Mediated Polymerization of Methyl Methacrylate Using an SG1-Based Alkoxyamine: How the Penultimate Effect Could Lead to Uncontrolled and Unliving Polymerization, *Macromol. Chem. Phys.*, 2006, **207**(14), 1278–1288.
32. F. Chauvin, P.-E. Dufils, D. Gigmes, Y. Guillaneuf, S. R. A. Marque and P. Tordo, *et al.*, Nitroxide-Mediated Polymerization: The Pivotal Role of the kd Value of the Initiating Alkoxyamine and the Importance of the Experimental Conditions, *Macromolecules*, 2006, **39**(16), 5238–5250.
33. D. Gigmes, D. Bertin, C. Lefay and Y. Guillaneuf, Kinetic Modeling of Nitroxide-Mediated Polymerization: Conditions for Living and Controlled Polymerization, *Macromol. Theory Simul.*, 2009, **18**(7–8), 402–419.
34. M. Roa-Luna, A. Nabifar, M. P. Díaz-Barber, N. T. McManus, E. Vivaldo-Lima and L. M. F. Lona, *et al.*, Another Perspective on the Nitroxide Mediated Radical Polymerization (NMRP) of Styrene Using 2,2,6,6-Tetramethyl-1-piperidinyloxy (TEMPO) and Dibenzoyl Peroxide (BPO), *J. Macromol. Sci., Part A*, 2007, **44**(3), 337–349.
35. E. Saldívar-Guerra, J. Bonilla, G. Zacahua and M. Albores-Velasco, Incubation period in the 2,2,4,4-tetramethyl-1-piperidinyloxy-mediated thermal autopolymerization of styrene: Kinetics and simulations, *J. Polym. Sci., Part A: Polym. Chem.*, 2006, **44**(24), 6962–6979.

36. L. Wang and L. J. Broadbelt, Kinetics of Segment Formation in Nitroxide-Mediated Controlled Radical Polymerization: Comparison with Classic Theory, *Macromolecules*, 2010, **43**(5), 2228–2235.
37. D. R. D'hooge, P. H. M. Van Steenberge, M.-F. Reyniers and G. B. Marin, The strength of multi-scale modeling to unveil the complexity of radical polymerization, *Prog. Polym. Sci.*, 2016, **58**, 59–89.
38. Y. Guillaneuf, D. Gigmes, S. R. A. Marque, P. Astolfi, L. Greci and P. Tordo, *et al.*, First Effective Nitroxide-Mediated Polymerization of Methyl Methacrylate, *Macromolecules*, 2007, **40**(9), 3108–3114.
39. H. Fischer and M. Souaille, The Persistent Radical Effect in Living Radical Polymerization – Borderline Cases and Side-Reactions. CHIMIA International Journal for, *Chemistry*, 2001, **55**(3), 109–113.
40. H. Fischer, Criteria for Livingness and Control in Nitroxide-Mediated and Related Radical Polymerizations, *Advances in Controlled/Living Radical Polymerization*, ACS Symposium Series. 854, American Chemical Society, 2003, pp. 10–23.
41. M. Souaille and H. Fischer, Rate Enhancement and Retardation Strategies in Living Free Radical Polymerizations Mediated by Nitroxides and Other Persistent Species: A Theoretical Assessment, *Macromolecules*, 2002, **35**(1), 248–261.
42. D. Greszta and K. Matyjaszewski, TEMPO-mediated polymerization of styrene: Rate enhancement with dicumyl peroxide, *J. Polym. Sci., Part A: Polym. Chem.*, 1997, **35**(9), 1857–1861.
43. P. Lacroix-Desmazes, J.-F. Lutz, F. Chauvin, R. Severac and B. Boutevin, Living Radical Polymerization: Use of an Excess of Nitroxide as a Rate Moderator, *Macromolecules*, 2001, **34**(26), 8866–8871.
44. D. Benoit, V. Chaplinski, R. Braslau and C. J. Hawker, Development of a Universal Alkoxyamine for ''Living'' Free Radical Polymerizations, *J. Am. Chem. Soc.*, 1999, **121**(16), 3904–3920.
45. D. Benoit, S. Grimaldi, S. Robin, J.-P. Finet, P. Tordo and Y. Gnanou, Kinetics and Mechanism of Controlled Free-Radical Polymerization of Styrene and n-Butyl Acrylate in the Presence of an Acyclic β-Phosphonylated Nitroxide, *J. Am. Chem. Soc.*, 2000, **122**(25), 5929–5939.
46. E. Malmström, R. D. Miller and C. J. Hawker, Development of a new class of rate-accelerating additives for nitroxide-mediated 'living' free radical polymerization, *Tetrahedron*, 1997, **53**(45), 15225–15236.
47. M. K. Georges, R. P. N. Veregin, P. M. Kazmaier, G. K. Hamer and M. Saban, Narrow Polydispersity Polystyrene by a Free-Radical Polymerization Process-Rate Enhancement, *Macromolecules*, 1994, **27**(24), 7228–7229.
48. B. Keoshkerian, M. Georges, M. Quinlan, R. Veregin and B. Goodbrand, Polyacrylates and Polydienes to High Conversion by a Stable Free Radical Polymerization Process: Use of Reducing Agents, *Macromolecules*, 1998, **31**(21), 7559–7561.

49. M. K. Georges, J. L. Lukkarila and A. R. Szkurhan, TEMPO-Mediated n-Butyl Acrylate Polymerizations, *Macromolecules*, 2004, **37**(4), 1297–1303.
50. A. Goto and T. Fukuda, Effects of Radical Initiator on Polymerization Rate and Polydispersity in Nitroxide-Controlled Free Radical Polymerization, *Macromolecules*, 1997, **30**(15), 4272–4277.
51. M. Lansalot, Y. Guillaneuf, B. Luneau, S. Acerbis, P.-E. Dufils and A. Gaudel-Siri, *et al.*, A Step Towards High-Molecular-Weight Living/Controlled Polystyrene Using SG1-Mediated Polymerization, *Macromol. React. Eng.*, 2010, **4**(6–7), 403–414.
52. A. Simula, M. Aguirre, N. Ballard, A. Veloso, J. R. Leiza and S. van Es, *et al.*, Novel alkoxyamines for the successful controlled polymerization of styrene and methacrylates, *Polym. Chem.*, 2017, **8**(10), 1728–1736.
53. G. Gryn'ova, C. Y. Lin and M. L. Coote, Which side-reactions compromise nitroxide mediated polymerization?, *Polym. Chem.*, 2013, **4**(13), 3744–3754.
54. C. Barner-Kowollik and G. T. Russell, Chain-length-dependent termination in radical polymerization: Subtle revolution in tackling a long-standing challenge, *Prog. Polym. Sci.*, 2009, **34**(11), 1211–1259.
55. A. Simula, F. Ruipérez, N. Ballard, J. R. Leiza, S. van Es and J. M. Asua, Why can Dispolreg 007 control the nitroxide mediated polymerization of methacrylates?, *Polym. Chem.*, 2019, **10**(1), 106–113.
56. S. Srinivasan, M. W. Lee, M. C. Grady, M. Soroush and A. M. Rappe, Self-Initiation Mechanism in Spontaneous Thermal Polymerization of Ethyl and n-Butyl Acrylate: A Theoretical Study, *J. Phys. Chem. A*, 2010, **114**(30), 7975–7983.
57. W. Devonport, L. Michalak, E. Malmström, M. Mate, B. Kurdi and C. J. Hawker, *et al.*, ''Living'' Free-Radical Polymerizations in the Absence of Initiators: Controlled Autopolymerization, *Macromolecules*, 1997, **30**(7), 1929–1934.
58. G. Moad and D. H. Solomon, Initiation, in *The Chemistry of Radical Polymerization*, ed. Solomon G. M. H., 2nd edn, Elsevier Science Ltd, Amsterdam, ch. 3, 2005, pp. 49–166.
59. K. Adamic, D. F. Bowman and K. U. Ingold, Self-reaction of diethylnitroxide radicals, *J. Am. Chem. Soc.*, 1970, **92**(4), 1093–1094.
60. D. F. Bowman, T. Gillan and K. U. Ingold, Kinetic applications of electron paramagnetic resonance spectroscopy. III. Self-reactions of dialkyl nitroxide radicals, *J. Am. Chem. Soc.*, 1971, **93**(24), 6555–6561.
61. T. J. Connolly and J. C. Scaiano, Reactions of the ''stable'' nitroxide radical TEMPO. Relevance to ''living'' free radical polymerizations and autopolymerization of styrene, *Tetrahedron Lett.*, 1997, **38**(7), 1133–1136.
62. F. Aldabbagh, W. K. Busfield, I. D. Jenkins and S. H. Thang, The reactivity of nitroxides towards alkenes, *Tetrahedron Lett.*, 2000, **41**(19), 3673–3676.

63. S. Marque, C. Le Mercier, P. Tordo and H. Fischer, Factors Influencing the C–O–Bond Homolysis of Trialkylhydroxylamines, *Macromolecules*, 2000, **33**(12), 4403–4410.
64. A. Nilsen and R. Braslau, Nitroxide decomposition: Implications toward nitroxide design for applications in living free-radical polymerization, *J. Polym. Sci., Part A: Polym. Chem.*, 2006, **44**(2), 697–717.
65. A. Studer, K. Harms, C. Knoop, C. Müller and T. Schulte, New Sterically Hindered Nitroxides for the Living Free Radical Polymerization: X-ray Structure of an α-H-Bearing Nitroxide, *Macromolecules*, 2004, **37**(1), 27–34.
66. D. F. Bowman, J. L. Brokenshire, T. Gillan and K. U. Ingold, Kinetic applications of electron paramagnetic resonance spectroscopy. II. Self-reactions of N-alkyl nitroxides and N-phenyl nitroxide, *J. Am. Chem. Soc.*, 1971, **93**(24), 6551–6555.
67. K. U. Ingold, K. Adamic, D. F. Bowman and T. Gillan, Kinetic applications of electron paramagnetic resonance spectroscopy. I. Self-reactions of diethyl nitroxide radicals, *J. Am. Chem. Soc.*, 1971, **93**(4), 902–908.
68. S. Grimaldi, D. Siri, J.-P. Finet and P. Tordo, *N* - *tert* -Butyl- *N* -(1-dibenzylphosphono-2,2-dimethylpropyl)nitroxide, *Acta Cryst*, 1998, **C54**, 1712–1714.
69. M. Iwamura and N. Inamoto, Novel Radical 1,3-Addition to Nitrones, *Bull. Chem. Soc. Jpn.*, 1967, **40**(3), 702.
70. M. Iwamura and N. Inamoto, Reactions of Nitrones with Free Radicals. II. Formation of Nitroxides, *Bull. Chem. Soc. Jpn.*, 1970, **43**(3), 860–863.
71. V. A. Reznikov and L. B. Volodarsky, Stable nitroxides with hydrogen at α-carbon of the nitroxyl group, *Tetrahedron Lett.*, 1994, **35**(14), 2239–2240.
72. V. A. Reznikov, I. A. Gulorov, Y. V. Gatilov, T. V. Rybalova and L. B. Volodarsky, Stable nitroxyl radicals with a hydrogen atom at α-carbon atom of nitroxyl group, *Russ. Chem. Bull.*, 1996, **45**(2), 384–392.
73. D. Gigmes, A. Gaudel-Siri, S. R. A. Marque, D. Bertin, P. Tordo and P. Astolfi, *et al.*, Alkoxyamines of Stable Aromatic Nitroxides: N–O vs. C–O Bond Homolysis, *Helv. Chim. Acta*, 2006, **89**(10), 2312–2326.
74. G. Moad, A. G. Anderson, F. Ercole, C. H. J. Johnson, J. Krstina and C. L. Moad, *et al.*, Controlled-Growth Free-Radical Polymerization of Methacrylate Esters: Reversible Chain Transfer versus Reversible Termination. *Controlled Radical Polymerization*, ACS Symposium Series. 685, American Chemical Society, 1998, pp. 332–360.
75. M. Souaille and H. Fischer, Living Free Radical Polymerizations Mediated by the Reversible Combination of Transient Propagating and Persistent Nitroxide Radicals. The Role of Hydroxylamine and Alkene Formation, *Macromolecules*, 2001, **34**(9), 2830–2838.
76. D. Parkhomenko, E. G. Bagryanskaya, S. R. A. Marque and D. Siri, Intramolecular proton transfer (IPT) in alkoxyamine: a theoretical investigation, *Phys. Chem. Chem. Phys.*, 2013, **15**(33), 13862–13871.

77. M. V. Edeleva, I. A. Kirilyuk, D. P. Zubenko, I. F. Zhurko, S. R. A. Marque and D. Gigmes, *et al.*, Kinetic study of H-atom transfer in imidazoline-, imidazolidine-, and pyrrolidine-based alkoxyamines: Consequences for nitroxide-mediated polymerization, *J. Polym. Sci., Part A: Polym. Chem.*, 2009, **47**(23), 6579–6595.
78. D. Bertin, D. Gigmes, S. R. A. Marque and P. Tordo, Kinetic subtleties of nitroxide mediated polymerization, *Chem. Soc. Rev.*, 2011, **40**(5), 2189–2198.
79. D. Bertin, D. Gigmes, S. R. A. Marque and P. Tordo, Polar, Steric, and Stabilization Effects in Alkoxyamines C–ON Bond Homolysis: A Multiparameter Analysis, *Macromolecules*, 2005, **38**(7), 2638–2650.
80. J. Lalevée, D. Gigmes, D. Bertin, X. Allonas and J. P. Fouassier, Interaction of monomer radicals with nitroxides: A new access to the radical-radical combination rate constants, *Chem. Phys. Lett.*, 2007, **449**(1), 231–235.
81. J. L. Hodgson, C. Yeh Lin, M. L. Coote, S. R. A. Marque and K. Matyjaszewski, Linear Free-Energy Relationships for the Alkyl Radical Affinities of Nitroxides: A Theoretical Study, *Macromolecules*, 2010, **43**(8), 3728–3743.
82. G. Audran, P. Bremond and S. R. A. Marque, Labile alkoxyamines: past, present, and future, *Chem. Commun.*, 2014, **50**(59), 7921–7928.
83. P. Nkolo, G. Audran, R. Bikanga, P. Brémond, S. R. A. Marque and V. Roubaud, C–ON bond homolysis of alkoxyamines: when too high polarity is detrimental, *OOrg. Biomol. Chem.*, 2017, **15**(29), 6167–6176.
84. E. G. Bagryanskaya and S. R. A. Marque, Scavenging of Organic C-Centered Radicals by Nitroxides, *Chem. Rev.*, 2014, **114**(9), 5011–5056.
85. E. G. Bagryanskaya and S. R. A. Marque, Kinetic Aspects of Nitroxide Mediated Polymerization, *Nitroxide Mediated Polymerization: From Fundamentals to Applications in Materials Science*, The Royal Society of Chemistry, ch. 2, 2016, pp. 45–113.
86. H. Fischer, A. Kramer, S. R. A. Marque and P. Nesvadba, Steric and Polar Effects of the Cyclic Nitroxyl Fragment on the C–ON Bond Homolysis Rate Constant, *Macromolecules*, 2005, **38**(24), 9974–9984.
87. D. A. Parkhomenko, M. V. Edeleva, V. G. Kiselev and E. G. Bagryanskaya, pH-Sensitive C–ON Bond Homolysis of Alkoxyamines of Imidazoline Series: A Theoretical Study, *J. Phys. Chem. B*, 2014, **118**(20), 5542–5550.
88. E. Beaudoin, D. Bertin, D. Gigmes, S. R. A. Marque, D. Siri and P. Tordo, Alkoxyamine C–ON Bond Homolysis: Stereoelectronic Effects, *Eur. J. Org. Chem.*, 2006, **2006**(7), 1755–1768.
89. S. Acerbis, E. Beaudoin, D. Bertin, D. Gigmes, S. Marque and P. Tordo, Leveled Steric Effect in Alkoxyamines of SG1-Type, *Macromol. Chem. Phys.*, 2004, **205**(7), 973–978.
90. G. Audran, R. Bikanga, P. Brémond, J.-P. Joly, S. R. A. Marque and P. Nkolo, Normal, Leveled, and Enhanced Steric Effects in

Alkoxyamines Carrying a β-Phosphorylated Nitroxyl Fragment, *J. Org. Chem.*, 2017, **82**(11), 5702–5709.
91. S. Marque, Influence of the Nitroxide Structure on the Homolysis Rate Constant of Alkoxyamines: A Taft–Ingold Analysis, *J. Org. Chem.*, 2003, **68**(20), 7582–7590.
92. M. Mazarin, M. Girod, S. Viel, T. N. T. Phan, S. R. A. Marque and S. Humbel, *et al.*, Role of the Adducted Cation in the Release of Nitroxide End Group of Controlled Polymer in Mass Spectrometry, *Macromolecules*, 2009, **42**(6), 1849–1859.
93. M. V. Edeleva, I. A. Kirilyuk, I. F. Zhurko, D. A. Parkhomenko, Y. P. Tsentalovich and E. G. Bagryanskaya, pH-Sensitive C–ON Bond Homolysis of Alkoxyamines of Imidazoline Series with Multiple Ionizable Groups As an Approach for Control of Nitroxide Mediated Polymerization, *J. Org. Chem.*, 2011, **76**(14), 5558–5573.
94. O. Guerret, J.-L. Couturier, F. Chauvin, H. El-Bouazzy, D. Bertin and D. Gigmes, *et al.*, Influence of Solvent and Polymer Chain Length on the Hemolysis of SG1-Based Alkoxyamines. *Advances in Controlled/Living Radical Polymerization*, ACS Symposium Series. 854, American Chemical Society, 2003, pp. 412–423.
95. D. Bertin, P.-E. Dufils, I. Durand, D. Gigmes, B. Giovanetti and Y. Guillaneuf, *et al.*, Effect of the Penultimate Unit on the C—ON Bond Homolysis in SG1-Based Alkoxyamines, *Macromol. Chem. Phys.*, 2008, **209**(2), 220–224.
96. E. Bagryanskaya, D. Bertin, D. Gigmes, I. Kirilyuk, S. R. A. Marque and V. Reznikov, *et al.*, Can the First Addition of Alkyl Radicals Play a Role in the Fate of NMP?, *Macromol. Chem. Phys.*, 2008, **209**(13), 1345–1357.
97. V. W. Bowry and K. U. Ingold, Kinetics of nitroxide radical trapping. 2. Structural effects, *J. Am. Chem. Soc.*, 1992, **114**(13), 4992–4996.
98. J. Sobek, R. Martschke and H. Fischer, Entropy Control of the Cross-Reaction between Carbon-Centered and Nitroxide Radicals, *J. Am. Chem. Soc.*, 2001, **123**(12), 2849–2857.
99. S. Marque, J. Sobek, H. Fischer, A. Kramer, P. Nesvadba and W. Wunderlich, Steric Effects of Ring Substituents on the Decay and Reformation Kinetics of Piperazinone-Based Alkoxyamines, *Macromolecules*, 2003, **36**(9), 3440–3442.
100. H. Fischer, S. R. A. Marque and P. Nesvadba, Re-formation Reaction of Cyclic Nitroxide-Based Alkoxyamines: Steric and Polar/Stabilization Effects, *Helv. Chim. Acta*, 2006, **89**(10), 2330–2340.
101. D. Zubenko, Y. Tsentalovich, N. Lebedeva, I. Kirilyuk, G. Roshchupkina and I. Zhurko, *et al.*, Laser Flash Photolysis and CIDNP Studies of Steric Effects on Coupling Rate Constants of Imidazolidine Nitroxide with Carbon-Centered Radicals, Methyl Isobutyrate-2-yl and tert-Butyl Propionate-2-yl, *J. Org. Chem.*, 2006, **71**(16), 6044–6052.
102. A. L. J. Beckwith, V. W. Bowry and K. U. Ingold, Kinetics of nitroxide radical trapping. 1. Solvent effects, *J. Am. Chem. Soc.*, 1992, **114**(13), 4983–4992.

103. E. G. Bagryanskaya, S. R. A. Marque and Y. P. Tsentalovich, Alkoxyamine Re-Formation Reaction. Effects of the Nitroxide Fragment: A Multiparameter Analysis, *J. Org. Chem.*, 2012, **77**(11), 4996–5005.
104. N. Ballard, M. Aguirre, A. Simula, A. Agirre, J. R. Leiza and J. M. Asua, *et al.*, New Class of Alkoxyamines for Efficient Controlled Homopolymerization of Methacrylates, *ACS Macro Lett.*, 2016, 1019–1022.
105. T. Fukuda and A. Goto, Gel permeation chromatographic determination of activation rate constants in nitroxide-controlled free radical polymerization, 2. Analysis of evolution of polydispersities, *Macromol. Rapid Commun.*, 1997, **18**(8), 683–688.
106. O. G. Ballesteros, L. Maretti, R. Sastre and J. C. Scaiano, Kinetics of Cap Separation in Nitroxide-Regulated ''Living'' Free Radical Polymerization: Application of a Novel Methodology Involving a Prefluorescent Nitroxide Switch, *Macromolecules*, 2001, **34**(18), 6184–6187.
107. D. Bertin, D. Gigmes, S. Marque and P. Tordo, 31P NMR measurement of the homolysis rate constant of the C-ON bond of β-phosphorylated alkoxyamines, *e-Polymers*, 2003, **3**, 1.
108. L. Li, G. K. Hamer and M. K. Georges, A Quantitative 1H NMR Method for the Determination of Alkoxyamine Dissociation Rate Constants in Stable Free Radical Polymerization. Application to Styrene Dimer Alkoxyamines, *Macromolecules*, 2006, **39**(26), 9201–9207.
109. P. Kelemen, J. Lugtenburg and B. Klumperman, 15N NMR Spectroscopy of Labeled Alkoxyamines. 15N-Labeled Model Compounds for Nitroxide-Trapping Studies in Free-Radical (Co)polymerization, *J. Org. Chem.*, 2003, **68**(19), 7322–7328.
110. M. V. Ciriano, H.-G. Korth, W. B. van Scheppingen and P. Mulder, Thermal Stability of 2,2,6,6-Tetramethylpiperidine-1-oxyl (TEMPO) and Related N-Alkoxyamines, *J. Am. Chem. Soc.*, 1999, **121**(27), 6375–6381.
111. A. Gaudel-Siri, D. Siri and P. Tordo, Homolysis of N-alkoxyamines: A Computational Study, *ChemPhysChem*, 2006, **7**(2), 430–438.
112. E. I. Izgorodina, D. R. B. Brittain, J. L. Hodgson, E. H. Krenske, C. Y. Lin and M. Namazian, *et al.*, Should Contemporary Density Functional Theory Methods Be Used to Study the Thermodynamics of Radical Reactions?, *J. Phys. Chem. A*, 2007, **111**(42), 10754–10768.
113. B. Chan, M. L. Coote and L. Radom, G4-SP, G4(MP2)-SP, G4-sc, and G4(MP2)-sc: Modifications to G4 and G4(MP2) for the Treatment of Medium-Sized Radicals, *J. Chem. Theory Comput.*, 2010, **6**(9), 2647–2653.
114. Y. Guillaneuf, D. Bertin, P. Castignolles and B. Charleux, New Experimental Procedure To Determine the Recombination Rate Constants between Nitroxides and Macroradicals, *Macromolecules*, 2005, **38**(11), 4638–4646.
115. A. C. Greene and R. B. Grubbs, Current Methods for *N*-Alkoxyamine Synthesis. *Controlled/Living Radical Polymerization: Progress in RAFT, DT, NMP & OMRP*, ACS Symposium Series. 1024, American Chemical Society, 2009, pp. 81–93.

116. G. Moad and E. Rizzardo, Alkoxyamine-Initiated Living Radical Polymerization: Factors Affecting Alkoxyamine Homolysis Rates, *Macromolecules*, 1995, **28**(26), 8722–8728.
117. N. A. Listigovers, M. K. Georges, P. G. Odell and B. Keoshkerian, Narrow-Polydispersity Diblock and Triblock Copolymers of Alkyl Acrylates by a ''Living'' Stable Free Radical Polymerization, *Macromolecules*, 1996, **29**(27), 8992–8993.
118. C. Wetter, J. Gierlich, C. A. Knoop, C. Müller, T. Schulte and A. Studer, Steric and Electronic Effects in Cyclic Alkoxyamines—Synthesis and Applications as Regulators for Controlled/Living Radical Polymerization, *Chem. Eur. J.*, 2004, **10**(5), 1156–1166.
119. C. A. Knoop and A. Studer, Hydroxy- and Silyloxy-Substituted TEMPO Derivatives for the Living Free-Radical Polymerization of Styrene and n-Butyl Acrylate: Synthesis, Kinetics, and Mechanistic Studies, *J. Am. Chem. Soc.*, 2003, **125**(52), 16327–16333.
120. K. O. Siegenthaler and A. Studer, Nitroxide-Mediated Radical Polymerization/Increase of Steric Demand in Nitroxides. How Much Is Too Much?, *Macromolecules*, 2006, **39**(4), 1347–1352.
121. G. Audran, E. G. Bagryanskaya, P. Brémond, M. V. Edeleva, S. R. A. Marque and D. A. Parkhomenko, *et al.*, Trityl-based alkoxyamines as NMP controllers and spin-labels, *Polym. Chem.*, 2016, **7**(42), 6490–6499.
122. Y. K. Chong, F. Ercole, G. Moad, E. Rizzardo, S. H. Thang and A. G. Anderson, Imidazolidinone Nitroxide-Mediated Polymerization, *Macromolecules*, 1999, **32**(21), 6895–6903.
123. S. Miele, P. Nesvadba and A. Studer, 1-tert-Butyl-3,3,5,5-tetraalkyl-2-piperazinon-4-oxyls: Highly Efficient Nitroxides for Controlled Radical Polymerization, *Macromolecules*, 2009, **42**(7), 2419–2427.
124. S. O. Hammouch and J.-M. Catala, ''Living radical'' polymerization of styrene in the presence of a nitroxide compound, *Macromol. Rapid Commun.*, 1996, **17**(10), 683–691.
125. O. Lagrille, N. R. Cameron, P. A. Lovell, R. Blanchard, A. E. Goeta and R. Koch, Novel acyclic nitroxides for nitroxide-mediated polymerization: Kinetic, electron paramagnetic resonance spectroscopic, X-ray diffraction, and molecular modeling investigations, *J. Polym. Sci., Part A: Polym. Chem.*, 2006, **44**(6), 1926–1940.
126. R. Nicolaÿ, L. Marx, P. Hémery and K. Matyjaszewski, Synthesis and Evaluation of a Functional, Water- and Organo-Soluble Nitroxide for ''Living'' Free Radical Polymerization, *Macromolecules*, 2007, **40**(17), 6067–6075.
127. L. Marx and P. Hemery, Synthesis and evaluation of a new polar, TIPNO type nitroxide for ''living'' free radical polymerization, *Polymer*, 2009, **50**(13), 2752–2761.
128. R. Braslau, G. O'Bryan, A. Nilsen, J. Henise, T. Thongpaisanwong and E. Murphy, *et al.*, The Synthesis and Evaluation of New α-Hydrogen Nitroxides for 'Living' Free Radical Polymerization, *Synthesis*, 2005, **2005**(09), 1496–1506.

129. C. Le Mercier, S. Acerbis, D. Bertin, F. Chauvin, D. Gigmes and O. Guerret, *et al.*, Design and use of β-phosphorus nitroxides and alkoxyamines in controlled/''living'' free radical polymerizations, *Macromol. Symp.*, 2002, **182**(1), 225–247.
130. E. Guégain, Y. Guillaneuf and J. Nicolas, Nitroxide-Mediated Polymerization of Methacrylic Esters: Insights and Solutions to a Long-Standing Problem, *Macromol. Rapid Commun.*, 2015, **36**(13), 1227–1247.
131. C. Burguière, M.-A. Dourges, B. Charleux and J.-P. Vairon, Synthesis and Characterization of ω-Unsaturated Poly(styrene-b-n-butyl methacrylate) Block Copolymers Using TEMPO-Mediated Controlled Radical Polymerization, *Macromolecules*, 1999, **32**(12), 3883–3890.
132. C. Dire, J. Belleney, J. Nicolas, D. Bertin, S. Magnet and B. Charleux, β-Hydrogen transfer from poly(methyl methacrylate) propagating radicals to the nitroxide SG1: Analysis of the chain-end and determination of the rate constant, *J. Polym. Sci., Part A: Polym. Chem.*, 2008, **46**(18), 6333–6345.
133. R. McHale, F. Aldabbagh and P. B. Zetterlund, The role of excess nitroxide in the SG1 (N-tert-butyl-N-[1-diethylphosphono-(2,2-dimethylpropyl)] nitroxide)-mediated polymerization of methyl methacrylate, *J. Polym. Sci., Part A: Polym. Chem.*, 2007, **45**(11), 2194–2203.
134. C. Berti, M. Colonna, L. Greci and L. Marchetti, Stable nitroxide radicals from phenylisatogen and arylimino-derivatives with organometallic compounds, *Tetrahedron*, 1975, **31**(15), 1745–1753.
135. M. Edeleva, S. R. A. Marque, D. Bertin, D. Gigmes, Y. Guillaneuf and S. V. Morozov, *et al.*, Hydrogen-transfer reaction in nitroxide mediated polymerization of methyl methacrylate: 2,2-Diphenyl-3-phenylimino-2,3-dihydroindol-1-yloxyl nitroxide (DPAIO) vs. TEMPO, *J. Polym. Sci., Part A: Polym. Chem.*, 2008, **46**(20), 6828–6842.
136. A. C. Greene and R. B. Grubbs, Synthesis and Evaluation of N-Phenylalkoxyamines for Nitroxide-Mediated Polymerization, *Macromolecules*, 2009, **42**(13), 4388–4390.
137. A. C. Greene and R. B. Grubbs, Nitroxide-Mediated Polymerization of Methyl Methacrylate and Styrene with New Alkoxyamines from 4-Nitrophenyl 2-Methylpropionat-2-yl Radicals, *Macromolecules*, 2010, **43**(24), 10320–10325.
138. V. Sciannamea, R. Jérôme and C. Detrembleur, In-Situ Nitroxide-Mediated Radical Polymerization (NMP) Processes: Their Understanding and Optimization, *Chem. Rev.*, 2008, **108**(3), 1104–1126.
139. C. Detrembleur, C. Jerome, J. De Winter, P. Gerbaux, J.-L. Clement and Y. Guillaneuf, *et al.*, Nitroxide mediated polymerization of methacrylates at moderate temperature, *Polym. Chem.*, 2014, **5**(2), 335–340.
140. N. Ballard, A. Simula, M. Aguirre, J. R. Leiza, S. van Es and J. M. Asua, Synthesis of poly(methyl methacrylate) and block copolymers by semibatch nitroxide mediated polymerization, *Polym. Chem.*, 2016, **7**(45), 6964–6972.

141. N. Ballard, M. Aguirre, A. Simula, J. R. Leiza, S. van Es and J. M. Asua, Nitroxide mediated suspension polymerization of methacrylic monomers, *Chem. Eng. J.*, 2017, **316**, 655–662.
142. N. Ballard, M. Aguirre, A. Simula, J. R. Leiza, S. van Es and J. M. Asua, High solids content nitroxide mediated miniemulsion polymerization of n-butyl methacrylate, *Polym. Chem.*, 2017, **8**(10), 1628–1635.
143. E. Mehravar, A. Agirre, N. Ballard, S. van Es, A. Arbe and J. R. Leiza, *et al.*, Insights into the Network Structure of Cross-Linked Polymers Synthesized via Miniemulsion Nitroxide-Mediated Radical Polymerization, *Macromolecules*, 2018, **51**(23), 9740–9748.
144. A. Simula, N. Ballard, M. Aguirre, J. R. Leiza, S. van Es and J. M. Asua, Nitroxide Mediated Copolymerization of acrylates, methacrylates and styrene: The importance of side reactions in the polymerization of acrylates, *Eur. Polym. J.*, 2018.
145. S. K. Fierens, P. H. M. Van Steenberge, F. Vermeire, M.-F. Reyniers, G. B. Marin and D. R. D'Hooge, An evaluation of the impact of SG1 disproportionation and the addition of styrene in NMP of methyl methacrylate, *AIChE J.*, 2018, **64**(7), 2545–2559.
146. J. C. Scaiano, T. J. Connolly, N. Mohtat and C. N. Pliva, Exploratory study of the quenching of photosensitizers by initiators of free radical ''living'' polymerization, *Can. J. Chem.*, 1997, **75**(1), 92–97.
147. S. Hu, J. H. Malpert, X. Yang and D. C. Neckers, Exploring chromophore tethered aminoethers as potential photoinitiators for controlled radical polymerization, *Polymer*, 2000, **41**(2), 445–452.
148. M. Baron, J. C. Morris, S. Telitel, J.-L. Clément, J. Lalevée and F. Morlet-Savary, *et al.*, Light-Sensitive Alkoxyamines as Versatile Spatially- and Temporally- Controlled Precursors of Alkyl Radicals and Nitroxides, *J. Am. Chem. Soc.*, 2018, **140**(9), 3339–3344.
149. M. Herder and J.-M. Lehn, The Photodynamic Covalent Bond: Sensitized Alkoxyamines as a Tool To Shift Reaction Networks Out-of-Equilibrium Using Light Energy, *J. Am. Chem. Soc.*, 2018, **140**(24), 7647–7657.
150. B. B. Noble, P. L. Norcott, C. L. Hammill, S. Ciampi and M. L. Coote, The Mechanism of Oxidative Alkoxyamine Cleavage: The Surprising Role of Solvent and Supporting Electrolyte, *J. Phys. Chem. C*, 2019, **123**(16), 10300–10305.
151. Y. Guillaneuf, D. Bertin, D. Gigmes, D.-L. Versace, J. Lalevée and J.-P. Fouassier, Toward Nitroxide-Mediated Photopolymerization, *Macromolecules*, 2010, **43**(5), 2204–2212.
152. M. Chen, M. Zhong and J. A. Johnson, Light-Controlled Radical Polymerization: Mechanisms, Methods, and Applications, *Chem. Rev.*, 2016, **116**(17), 10167–10211.
153. M. Huix-Rotllant and N. Ferré, Theoretical Study of the Photochemical Initiation in Nitroxide-Mediated Photopolymerization, *J. Phys. Chem. A*, 2014, **118**(25), 4464–4470.
154. Y. Guillaneuf, D.-L. Versace, D. Bertin, J. Lalevée, D. Gigmes and J.-P. Fouassier, Importance of the Position of the Chromophore Group

on the Dissociation Process of Light Sensitive Alkoxyamines, *Macromol. Rapid Commun.*, 2010, **31**(21), 1909–1913.
155. S. Telitel, S. Telitel, J. Bosson, A. Spangenberg, J. Lalevée and F. Morlet-Savary, *et al.*, Nitroxide Mediated Photopolymerization: A Versatile Tool for the Fabrication of Complex Multilayer Polyfunctional Copolymer Nanostructures, *Adv. Mater. Interfaces*, 2014, **1**(5), 1400067.
156. J. Morris, S. Telitel, K. E. Fairfull-Smith, S. E. Bottle, J. Lalevée and J.-L. Clément, *et al.*, Novel polymer synthesis methodologies using combinations of thermally- and photochemically-induced nitroxide mediated polymerization, *Polym. Chem.*, 2015, **6**(5), 754–763.
157. M. Edeleva, G. Audran, S. Marque and E. Bagryanskaya, Smart Control of Nitroxide-Mediated Polymerization Initiators' Reactivity by pH, Complexation with Metals, and Chemical Transformations, *Materials*, 2019, **12**(5), 688.
158. N. B. Kannan and B. H. Lessard, Copolymerization of 2,3,4,5,6-Pentafluorostyrene and Methacrylic Acid by Nitroxide-Mediated Polymerization: The Importance of Reactivity Ratios, *Macromol. React. Eng.*, 2016, **10**(6), 600–610.
159. N. R. Cameron and A. J. Reid, n-Butyl Acrylate Polymerization Mediated by a PROXYL Nitroxide, *Macromolecules*, 2002, **35**(27), 9890–9895.
160. B. Grassl, G. Clisson, A. Khoukh and L. Billon, Nitroxide-mediated radical polymerization of acrylamide in water solution, *Eur. Polym. J.*, 2008, **44**(1), 50–58.
161. J. Rigolini, B. Grassl, L. Billon, S. Reynaud and O. F. X. Donard, Microwave-assisted nitroxide-mediated radical polymerization of acrylamide in aqueous solution, *J. Polym. Sci., Part A: Polym. Chem.*, 2009, **47**(24), 6919–6931.
162. T. Diaz, A. Fischer, A. Jonquières, A. Brembilla and P. Lochon, Controlled Polymerization of Functional Monomers and Synthesis of Block Copolymers Using a β-Phosphonylated Nitroxide, *Macromolecules*, 2003, **36**(7), 2235–2241.
163. T. M. Eggenhuisen, C. R. Becer, M. W. M. Fijten, R. Eckardt, R. Hoogenboom and U. S. Schubert, Libraries of Statistical Hydroxypropyl Acrylate Containing Copolymers with LCST Properties Prepared by NMP, *Macromolecules*, 2008, **41**(14), 5132–5140.
164. C. Tang, T. Kowalewski and K. Matyjaszewski, Preparation of Polyacrylonitrile-block-poly(n-butyl acrylate) Copolymers Using Atom Transfer Radical Polymerization and Nitroxide Mediated Polymerization Processes, *Macromolecules*, 2003, **36**(5), 1465–1473.
165. J.-L. Pradel, B. Ameduri and B. Boutevin, Use of controlled radical polymerization of butadiene with AIBN and TEMPO for the determination of the NMR characteristics of hydroxymethyl groups, *Macromol. Chem. Phys.*, 1999, **200**(10), 2304–2308.
166. S. Harrisson, P. Couvreur and J. Nicolas, SG1 Nitroxide-Mediated Polymerization of Isoprene: Alkoxyamine Structure/Control

Relationship and α,ω–Chain-End Functionalization, *Macromolecules*, 2011, **44**(23), 9230–9238.
167. Y. Wei, E. J. Connors, X. Jia and C. Wang, Controlled free radical ring-opening polymerization and chain extension of the ''living'' polymer, *J. Polym. Sci., Part A: Polym. Chem.*, 1998, **36**(5), 761–771.
168. E. Yoshida, Nitroxide-mediated photo-living radical polymerization of vinyl acetate, *Colloid Polym. Sci.*, 2009, **288**(1), 73.
169. P. Bilalis, M. Pitsikalis and N. Hadjichristidis, Controlled nitroxide-mediated and reversible addition–fragmentation chain transfer polymerization of N-vinylpyrrolidone: Synthesis of block copolymers with styrene and 2-vinylpyridine, *J. Polym. Sci., Part A: Polym. Chem.*, 2006, **44**(1), 659–665.
170. N. Handké, T. Trimaille, E. Luciani, M. Rollet, T. Delair and B. Verrier, *et al.*, Elaboration of densely functionalized polylactide nanoparticles from N-acryloxysuccinimide-based block copolymers, *J. Polym. Sci., Part A: Polym. Chem.*, 2011, **49**(6), 1341–1350.
171. M. Nowakowska, S. Zapotoczny and A. Karewicz, Polymeric photosensitizers. Part 4. Synthesis of poly(sodium styrenesulfonate-block-N-vinylcarbazole) by nitroxide-mediated free radical polymerization, *Polymer*, 2001, **42**(5), 1817–1823.
172. C. M. R. Abreu, A. C. Fonseca, N. M. P. Rocha, J. T. Guthrie, A. C. Serra and J. F. J. Coelho, Poly(vinyl chloride): current status and future perspectives via reversible deactivation radical polymerization methods, *Prog. Polym. Sci.*, 2018, **87**, 34–69.
173. M. Baumert, J. Fröhlich, M. Stieger, H. Frey, R. Mülhaupt and H. Plenio, Styrene-vinylferrocene random and block copolymers by TEMPO-mediated radical polymerization, *Macromol. Rapid Commun.*, 1999, **20**(4), 203–209.
174. D. C. Tully, M. J. Roberts, B. H. Geierstanger and R. B. Grubbs, Synthesis of Reactive Poly(vinyl oxazolones) via Nitroxide-Mediated ''Living'' Free Radical Polymerization, *Macromolecules*, 2003, **36**(12), 4302–4308.
175. B. Charleux, J. Nicolas and O. Guerret, Theoretical Expression of the Average Activation–Deactivation Equilibrium Constant in Controlled/Living Free-Radical Copolymerization Operating via Reversible Termination. Application to a Strongly Improved Control in Nitroxide-Mediated Polymerization of Methyl Methacrylate, *Macromolecules*, 2005, **38**(13), 5485–5492.
176. W. Mei and M. Maric, Nitroxide-Mediated Polymerization of 2-Hydroxyethyl Methacrylate (HEMA) Controlled with Low Concentrations of Acrylonitrile and Styrene, *Macromol. React. Eng.*, 2017, **11**(3), 1600067.
177. J. Nicolas, C. Dire, L. Mueller, J. Belleney, B. Charleux and S. R. A. Marque, *et al.*, Living Character of Polymer Chains Prepared via Nitroxide-Mediated Controlled Free-Radical Polymerization of Methyl Methacrylate in the Presence of a Small Amount of Styrene at Low Temperature, *Macromolecules*, 2006, **39**(24), 8274–8282.

178. J. Nicolas, L. Mueller, C. Dire, K. Matyjaszewski and B. Charleux, Comprehensive Modeling Study of Nitroxide-Mediated Controlled/Living Radical Copolymerization of Methyl Methacrylate with a Small Amount of Styrene, *Macromolecules*, 2009, **42**(13), 4470–4478.
179. X. G. Qiao, Z. Zhou, X. C. Pang, M. Lansalot and E. Bourgeat-Lami, Nitroxide-mediated polymerization of methacrylates in the presence of 4-vinyl pyridine as controlling comonomer, *Polymer*, 2019, **172**, 330–338.
180. A. Métafiot, Y. Kanawati, J.-F. Gérard, B. Defoort and M. Marić, Synthesis of β-Myrcene-Based Polymers and Styrene Block and Statistical Copolymers by SG1 Nitroxide-Mediated Controlled Radical Polymerization, *Macromolecules*, 2017, **50**(8), 3101–3120.
181. A. Métafiot, J.-F. Gérard, B. Defoort and M. Marić, Synthesis of β-myrcene/glycidyl methacrylate statistical and amphiphilic diblock copolymers by SG1 nitroxide-mediated controlled radical polymerization, *J. Polym. Sci., Part A: Polym. Chem.*, 2018, **56**(8), 860–878.
182. A. Métafiot, L. Gagnon, S. Pruvost, P. Hubert, J.-F. Gérard and B. Defoort, *et al.*, β-Myrcene/isobornyl methacrylate SG1 nitroxide-mediated controlled radical polymerization: synthesis and characterization of gradient, diblock and triblock copolymers, *RSC Adv.*, 2019, **9**(6), 3377–3395.
183. K. A. Payne, P. Nesvadba, J. Debling, M. F. Cunningham and R. A. Hutchinson, Nitroxide-Mediated Polymerization at Elevated Temperatures, *ACS Macro Lett.*, 2015, **4**(3), 280–283.
184. K. A. Payne, J. Debling, P. Nesvadba, M. F. Cunningham and R. A. Hutchinson, NMP of styrene in batch and CSTR at elevated temperatures: Modeling experimental trends, *Eur. Polym. J.*, 2016, **80**, 186–199.
185. P. Astolfi, L. Greci, P. Stipa, C. Rizzoli, C. Ysacco and M. Rollet, *et al.*, Indolinic nitroxides: evaluation of their potential as universal control agents for nitroxide mediated polymerization, *Polym. Chem.*, 2013, **4**(13), 3694–3704.
186. R. K. Iha, K. L. Wooley, A. M. Nyström, D. J. Burke, M. J. Kade and C. J. Hawker, Applications of Orthogonal "Click" Chemistries in the Synthesis of Functional Soft Materials, *Chem. Rev.*, 2009, **109**(11), 5620–5686.
187. D. J. Lunn, E. H. Discekici, J. Read de Alaniz, W. R. Gutekunst and C. J. Hawker, Established and emerging strategies for polymer chain-end modification, *J. Polym. Sci., Part A: Polym. Chem.*, 2017, **55**(18), 2903–2914.
188. P.-E. Dufils, N. Chagneux, D. Gigmes, T. Trimaille, S. R. A. Marque and D. Bertin, *et al.*, Intermolecular radical addition of alkoxyamines onto olefins: An easy access to advanced macromolecular architectures precursors, *Polymer*, 2007, **48**(18), 5219–5225.
189. M. Bothe and G. Schmidt-Naake, An Improved Catalytic Method for Alkoxyamine Synthesis – Functionalized and Biradical Initiators for Nitroxide-Mediated Radical Polymerization, *Macromol. Rapid Commun.*, 2003, **24**(10), 609–613.

190. V. Poirier, M. Duc, J.-F. Carpentier and Y. Sarazin, One-Pot Synthesis of Lactide–Styrene Diblock Copolymers via Catalytic Immortal Ring-Opening Polymerization of Lactide and Nitroxide-Mediated Polymerization of Styrene, *ChemSusChem*, 2010, **3**(5), 579–590.
191. Y. Miura, K. Hirota, H. Moto and B. Yamada, High-Yield Synthesis of Alkoxyamine Initiators Carrying a Functional Group by Reaction of Ethylbenzenes with Di-tert-butyl Diperoxalate in the Presence of Nitroxides, *Macromolecules*, 1998, **31**(14), 4659–4661.
192. M. Chenal, C. Boursier, Y. Guillaneuf, M. Taverna, P. Couvreur and J. Nicolas, First peptide/protein PEGylation with functional polymers designed by nitroxide-mediated polymerization, *Polym. Chem.*, 2011, **2**(7), 1523–1530.
193. J. Vinas, N. Chagneux, D. Gigmes, T. Trimaille, A. Favier and D. Bertin, SG1-based alkoxyamine bearing a N-succinimidyl ester: A versatile tool for advanced polymer synthesis, *Polymer*, 2008, **49**(17), 3639–3647.
194. N. L. Hill, J. L. Jarvis, F. Pettersson and R. Braslau, Synthesis of thiol-derivatized initiators for nitroxide-mediated radical polymerization: Reversible disulfide formation, *React. Funct. Polym.*, 2008, **68**(1), 361–368.
195. J. Dao, D. Benoit and C. J. Hawker, A versatile and efficient synthesis of alkoxyamine LFR initiators via manganese based asymmetric epoxidation catalysts, *J. Polym. Sci., Part A: Polym. Chem.*, 1998, **36**(12), 2161–2167.
196. B. D. Mather, J. R. Lizotte and T. E. Long, Synthesis of Chain End Functionalized Multiple Hydrogen Bonded Polystyrenes and Poly(alkyl acrylates) Using Controlled Radical Polymerization, *Macromolecules*, 2004, **37**(25), 9331–9337.
197. U. Mansfeld, A. Winter, M. D. Hager, R. Hoogenboom, W. Gunther and U. S. Schubert, Orthogonal self-assembly of stimuli-responsive supramolecular polymers using one-step prepared heterotelechelic building blocks, *Polym. Chem.*, 2013, **4**(1), 113–123.
198. E. E. Malmström and C. J. Hawker, Macromolecular engineering via 'living' free radical polymerizations, *Macromol. Chem. Phys.*, 1998, **199**(6), 923–935.
199. J. Su, X. Liu, J. Hu, Q. You, Y. Cui and Y. Chen, Photo-induced controlled radical polymerization of methyl methacrylate mediated by photosensitive nitroxides, *Polym. Int.*, 2015, **64**(7), 867–874.
200. R. Vukićević, U. Schwadtke, S. Schmücker, P. Schäfer, D. Kuckling and S. Beuermann, Alkyne–azide coupling of tailored poly(vinylidene fluoride) and polystyrene for the synthesis of block copolymers, *Polym. Chem.*, 2012, **3**(2), 409–414.
201. M. A. Tasdelen, M. U. Kahveci and Y. Yagci, Telechelic polymers by living and controlled/living polymerization methods, *Prog. Polym. Sci.*, 2011, **36**(4), 455–567.
202. D. Vinciguerra, J. Tran and J. Nicolas, Telechelic polymers from reversible-deactivation radical polymerization for biomedical applications, *Chem. Commun.*, 2018, **54**(3), 228–240.

203. N. Hadjichristidis, S. Pispas, M. Pitsikalis, H. Iatrou and D. J. Lohse, Graft Copolymers, *Encyclopedia of Polymer Science and Technology*, John Wiley & Sons, Inc., 2002.
204. N. Hadjichristidis, H. Iatrou, M. Pitsikalis and J. Mays, Macromolecular architectures by living and controlled/living polymerizations, *Prog. Polym. Sci.*, 2006, **31**(12), 1068–1132.
205. S. Flakus and G. Schmidt-Naake, Synthesis of Graft Copolymers by Nitroxide Mediated Radical Polymerization of Styrene and n-Butylacrylate Using Alkoxyamine-Functionalized Copolymers as Macroinitiators, *Macromol. Symp.*, 2009, **275–276**(1), 43–51.
206. C. J. Hawker, Architectural Control in ''Living'' Free Radical Polymerizations: Preparation of Star and Graft Polymers, *Angew. Chem., Int. Ed. Engl.*, 1995, **34**(13–14), 1456–1459.
207. J. Su, Y. Amamoto, M. Nishihara, A. Takahara and H. Otsuka, Reversible cross-linking of hydrophilic dynamic covalent polymers with radically exchangeable alkoxyamines in aqueous media, *Polym. Chem.*, 2011, **2**(9), 2021–2026.
208. Z. Ma, C. Zheng, Z. Shen, D. Liang and X. Fan, Synthesis and properties of comb polymers with semirigid mesogen-jacketed polymers as side chains, *J. Polym. Sci., Part A: Polym. Chem.*, 2012, **50**(5), 918–926.
209. C. J. Hawker, D. Mecerreyes, E. Elce, J. Dao, J. L. Hedrick and I. Barakat, *et al.*, ''Living'' free radical polymerization of macromonomers: Preparation of well defined graft copolymers, *Macromol. Chem. Phys.*, 1997, **198**(1), 155–166.
210. N. Ballard and J. M. Asua, Radical polymerization of acrylic monomers: An overview, *Prog. Polym. Sci.*, 2018, **79**, 40–60.
211. N. M. Ahmad, B. Charleux, C. Farcet, C. J. Ferguson, S. G. Gaynor and B. S. Hawkett, *et al.*, Chain Transfer to Polymer and Branching in Controlled Radical Polymerizations of n-Butyl Acrylate, *Macromol. Rapid Commun.*, 2009, **30**(23), 2002–2021.
212. C. Plessis, G. Arzamendi, J. R. Leiza, H. A. S. Schoonbrood, D. Charmot and J. M. Asua, A Decrease in Effective Acrylate Propagation Rate Constants Caused by Intramolecular Chain Transfer, *Macromolecules*, 2000, **33**(1), 4–7.
213. L. Hlalele and B. Klumperman, In Situ1H NMR Studies of High-Temperature Nitroxide-Mediated Polymerization of n-Butyl Acrylate, *Macromolecules*, 2011, **44**(18), 7100–7108.
214. L. Hlalele and B. Klumperman, In Situ NMR and Modeling Studies of Nitroxide Mediated Copolymerization of Styrene and n-Butyl Acrylate, *Macromolecules*, 2011, **44**(17), 6683–6690.
215. N. Ballard, J. I. Santos and J. M. Asua, Reevaluation of the Formation and Reactivity of Midchain Radicals in Nitroxide-Mediated Polymerization of Acrylic Monomers, *Macromolecules*, 2015, **48**(9), 2909–2915.
216. N. Ballard, S. Rusconi, E. Akhmatskaya, D. Sokolovski, J. C. de la Cal and J. M. Asua, Impact of Competitive Processes on Controlled Radical Polymerization, *Macromolecules*, 2014, **47**(19), 6580–6590.

217. N. Ballard, M. Salsamendi, J. I. Santos, F. Ruipérez, J. R. Leiza and J. M. Asua, Experimental Evidence Shedding Light on the Origin of the Reduction of Branching of Acrylates in ATRP, *Macromolecules*, 2014, **47**(3), 964–972.
218. N. Ballard, J. C. de la Cal and J. M. Asua, The Role of Chain Transfer Agent in Reducing Branching Content in Radical Polymerization of Acrylates, *Macromolecules*, 2015, **48**(4), 987–993.
219. M. R. Leduc, C. J. Hawker, J. Dao and J. M. J. Fréchet, Dendritic Initiators for ''Living'' Radical Polymerizations: A Versatile Approach to the Synthesis of Dendritic-Linear Block Copolymers, *J. Am. Chem. Soc.*, 1996, **118**(45), 11111–11118.
220. C. J. Hawker, J. M. J. Frechet, R. B. Grubbs and J. Dao, Preparation of Hyperbranched and Star Polymers by a ''Living'', Self-Condensing Free Radical Polymerization, *J. Am. Chem. Soc.*, 1995, **117**(43), 10763–10764.
221. A. Khan, M. Malkoch, M. F. Montague and C. J. Hawker, Synthesis and characterization of hyperbranched polymers with increased chemical versatility for imprint lithographic resists, *J. Polym. Sci., Part A: Polym. Chem.*, 2008, **46**(18), 6238–6254.
222. J. M. Ren, T. G. McKenzie, Q. Fu, E. H. H. Wong, J. Xu and Z. An, *et al.*, Star Polymers, *Chem. Rev.*, 2016, **116**(12), 6743–6836.
223. J. Li, Z. Zhang, X. Zhu, J. Zhu and Z. Cheng, Nitroxide-mediated polymerization of styrene in the presence of a novel trinitroxide, *e-Polymers*, 2010, **10**, 1.
224. G. O'Bryan, N. Ningnuek and R. Braslau, Cyclization of α, ω heterotelechelic polystyrene prepared by nitroxide-mediated radical polymerization, *Polymer*, 2008, **49**(24), 5241–5248.
225. Z. Yousi, L. Jian, Z. Rongchuan, Y. Jianliang, D. Lizong and Z. Lansun, Synthesis of Block Copolymer from Dissimilar Vinyl Monomer by Stable Free Radical Polymerization, *Macromolecules*, 2000, **33**(13), 4745–4749.
226. K. Tortosa, J. A. Smith and M. F. Cunningham, Synthesis of Polystyrene-block-poly(butyl acrylate) Copolymers Using Nitroxide-Mediated Living Radical Polymerization in Miniemulsion, *Macromol. Rapid Commun.*, 2001, **22**(12), 957–961.
227. K. Bian and M. F. Cunningham, Nitroxide-Mediated Living Radical Polymerization of 2-Hydroxyethyl Acrylate and the Synthesis of Amphiphilic Block Copolymers, *Macromolecules*, 2005, **38**(3), 695–701.
228. A.-V. Ruzette, S. Tencé-Girault, L. Leibler, F. Chauvin, D. Bertin and O. Guerret, *et al.*, Molecular Disorder and Mesoscopic Order in Polydisperse Acrylic Block Copolymers Prepared by Controlled Radical Polymerization, *Macromolecules*, 2006, **39**(17), 5804–5814.
229. D. Benoit, E. Harth, P. Fox, R. M. Waymouth and C. J. Hawker, Accurate Structural Control and Block Formation in the Living Polymerization of 1,3-Dienes by Nitroxide-Mediated Procedures, *Macromolecules*, 2000, **33**(2), 363–370.
230. C. Ott, B. G. G. Lohmeijer, D. Wouters and U. S. Schubert, Terpyridine-Terminated Homo and Diblock Copolymer LEGO Units by

Nitroxide-Mediated Radical Polymerization, *Macromol. Chem. Phys.*, 2006, **207**(16), 1439–1449.
231. S. M. Banik, B. L. Monnot, R. L. Weber and M. K. Mahanthappa, ROMP-CT/NMP Synthesis of Multiblock Copolymers Containing Linear Poly(ethylene) Segments, *Macromolecules*, 2011, **44**(18), 7141–7148.
232. R. G. Lopez, C. Boisson, F. D'Agosto, R. Spitz, F. Boisson and D. Bertin, *et al.*, Synthesis and Characterization of Macroalkoxyamines Based on Polyethylene, *Macromolecules*, 2004, **37**(10), 3540–3542.
233. X. Li, E. Mastan, W.-J. Wang, B.-G. Li and S. Zhu, Progress in reactor engineering of controlled radical polymerization: a comprehensive review, *React. Chem. Eng.*, 2016, **1**(1), 23–59.
234. A. Veloso, W. Garcia, A. Agirre, N. Ballard, F. Ruiperez and J. C. de la Cal, *et al.*, Determining the effect of side reactions on product distributions in RAFT polymerization by MALDI-TOF MS, *Polym. Chem.*, 2015, **6**(30), 5437–5450.
235. B. Lessard, C. Tervo and M. Marić, High-Molecular-Weight Poly(tert-butyl acrylate) by Nitroxide-Mediated Polymerization: Effect of Chain Transfer to Solvent, *Macromol. React. Eng.*, 2009, **3**(5–6), 245–256.
236. R. A. Hutchinson and A. Penlidis, Free-Radical Polymerization: Homogeneous Systems, *Polym. React. Eng.*, 2007, 118–178.
237. R. G. Gilbert, *Emulsion Polymerization: A Mechanistic Approach*, Academic Press, 1995.
238. M. J. Barandiaran, J. C. d. l. Cal and J. M. Asua, Emulsion Polymerization, *Polym. React. Eng.*, 2007, 233–272.
239. P. B. Zetterlund, Y. Kagawa and M. Okubo, Controlled/Living Radical Polymerization in Dispersed Systems, *Chem. Rev.*, 2008, **108**(9), 3747–3794.
240. P. B. Zetterlund, S. C. Thickett, S. Perrier, E. Bourgeat-Lami and M. Lansalot, Controlled/Living Radical Polymerization in Dispersed Systems: An Update, *Chem. Rev.*, 2015, **115**(18), 9745–9800.
241. M. F. Cunningham, Controlled/living radical polymerization in aqueous dispersed systems, *Prog. Polym. Sci.*, 2008, **33**(4), 365–398.
242. P. B. Zetterlund and M. Okubo, Compartmentalization in Nitroxide-Mediated Radical Polymerization in Dispersed Systems, *Macromolecules*, 2006, **39**(26), 8959–8967.
243. P. B. Zetterlund, Nitroxide-Mediated Radical Polymerization in Dispersed Systems: Compartmentalization and Nitroxide Partitioning, *Macromol. Theory Simul.*, 2010, **19**(1), 11–23.
244. P. B. Zetterlund, Controlled/living radical polymerization in nanoreactors: compartmentalization effects, *Polym. Chem.*, 2011, **2**(3), 534–549.
245. H. Tobita, Kinetics of Stable Free Radical Mediated Polymerization inside Submicron Particles, *Macromol. Theory Simul.*, 2007, **16**(9), 810–823.
246. H. Maehata, C. Buragina, M. Cunningham and B. Keoshkerian, Compartmentalization in TEMPO-Mediated Styrene Miniemulsion Polymerization, *Macromolecules*, 2007, **40**(20), 7126–7131.

247. T. Tanaka, M. Okayama, Y. Kitayama, Y. Kagawa and M. Okubo, Preparation of ''Mushroom-like'' Janus Particles by Site-Selective Surface-Initiated Atom Transfer Radical Polymerization in Aqueous Dispersed Systems, *Langmuir*, 2010, **26**(11), 7843–7847.
248. S. Tomoeda, Y. Kitayama, J. Wakamatsu, H. Minami, P. B. Zetterlund and M. Okubo, Nitroxide-Mediated Radical Polymerization in Microemulsion (Microemulsion NMP) of n-Butyl Acrylate, *Macromolecules*, 2011, **44**(14), 5599–5604.
249. Y. Sugihara and P. B. Zetterlund, Synergistic Effects of Compartmentalization and Nitroxide Exit/Entry in Nitroxide-Mediated Radical Polymerization in Dispersed Systems, *ACS Macro Lett.*, 2012, **1**(6), 692–696.
250. Y. Guo and P. B. Zetterlund, Rate-Enhanced Nitroxide-Mediated Miniemulsion Polymerization, *ACS Macro Lett.*, 2012, **1**(6), 748–752.
251. J. Jennings, G. He, S. M. Howdle and P. B. Zetterlund, Block copolymer synthesis by controlled/living radical polymerisation in heterogeneous systems, *Chem. Soc. Rev.*, 2016, **45**(18), 5055–5084.
252. J. Nicolas, B. Charleux and S. Magnet, Multistep and semibatch nitroxide-mediated controlled free-radical emulsion polymerization: A significant step toward conceivable industrial processes, *J. Polym. Sci., Part A: Polym. Chem.*, 2006, **44**(13), 4142–4153.
253. P. B. Zetterlund and M. Okubo, Nitroxide-Mediated Radical Polymerization in Miniemulsion at Stationary State: Rationale for Independence of Polymerization Rate on Nitroxide Partitioning Using Oil-Phase Initiation, *Macromol. Theory Simul.*, 2005, **14**(7), 415–420.
254. J. W. Ma, J. A. Smith, K. B. McAuley, M. F. Cunningham, B. Keoshkerian and M. K. Georges, Nitroxide-mediated radical polymerization of styrene in miniemulsion: model studies of alkoxyamine-initiated systems, *Chem. Eng. Sci.*, 2003, **58**(7), 1163–1176.
255. C. Farcet, M. Lansalot, B. Charleux, R. Pirri and J. P. Vairon, Mechanistic Aspects of Nitroxide-Mediated Controlled Radical Polymerization of Styrene in Miniemulsion, Using a Water-Soluble Radical Initiator, *Macromolecules*, 2000, **33**(23), 8559–8570.
256. M. F. Cunningham, K. Tortosa, M. Lin, B. Keoshkerian and M. K. Georges, Influence of camphorsulfonic acid in nitroxide-mediated styrene miniemulsion polymerization, *J. Polym. Sci., Part A: Polym. Chem.*, 2002, **40**(16), 2828–2841.
257. M. Cunningham, M. Lin, C. Buragina, S. Milton, D. Ng and C. C. Hsu, *et al.*, Maximizing polymer livingness in nitroxide-mediated miniemulsion polymerizations, *Polymer*, 2005, **46**(4), 1025–1032.
258. M. F. Cunningham, D. C. T. Ng, S. G. Milton and B. Keoshkerian, Low temperature TEMPO-mediated styrene polymerization in miniemulsion, *J. Polym. Sci., Part A: Polym. Chem.*, 2006, **44**(1), 232–242.
259. M. Hölderle, M. Baumert and R. Mülhaupt, Comparison of Controlled Radical Styrene Polymerizations in Bulk and Nonaqueous Dispersion, *Macromolecules*, 1997, **30**(11), 3420–3422.

260. L. I. Gabaston, R. A. Jackson and S. P. Armes, Living Free-Radical Dispersion Polymerization of Styrene, *Macromolecules*, 1998, **31**(9), 2883–2888.
261. R. McHale, F. Aldabbagh, P. B. Zetterlund, H. Minami and M. Okubo, Nitroxide-Mediated Radical Dispersion Polymerization of Styrene in Supercritical Carbon Dioxide Using a Poly(dimethylsiloxane-b-methyl methacrylate) Stabilizer, *Macromolecules*, 2006, **39**(20), 6853–6860.
262. P. B. Zetterlund, F. Aldabbagh and M. Okubo, Controlled/living heterogeneous radical polymerization in supercritical carbon dioxide, *J. Polym. Sci., Part A: Polym. Chem.*, 2009, **47**(15), 3711–3728.
263. B. Grignard, T. Phan, D. Bertin, D. Gigmes, C. Jérôme and C. Detrembleur, Dispersion nitroxide mediated polymerization of methyl methacrylate in supercritical carbon dioxide using in situ formed stabilizers, *Polym. Chem.*, 2010, **1**(6), 837–840.
264. E. Vivaldo-Lima, P. E. Wood, A. E. Hamielec and A. Penlidis, An Updated Review on Suspension Polymerization, *Ind. Eng. Chem. Res.*, 1997, **36**(4), 939–965.
265. C. Taube and G. Schmidt-Naake, TEMPO-controlled radical suspension polymerization of poly(styrene)-block-poly(styrene-co-acrylonitrile) and poly(styrene)-block-poly(styrene-co-butyl methacrylate), *Macromol. Mater. Eng.*, 2000, **279**(1), 26–33.
266. M. K. Lenzi, M. F. Cunningham, E. L. Lima and J. C. Pinto, Producing Bimodal Molecular Weight Distribution Polymer Resins Using Living and Conventional Free-Radical Polymerization, *Ind. Eng. Chem. Res.*, 2005, **44**(8), 2568–2578.
267. E. García-Leal, M. A. Ordaz-Quintero, E. Saldívar-Guerra, M. E. Albores-Velasco and E. Vivaldo-Lima, Nitroxide-Mediated Controlled Radical Styrene Polymerization Via a Mass-Suspension Process, *Macromol. React. Eng.*, 2013, **7**(12), 699–712.
268. M. F. Cunningham, Recent progress in nitroxide-mediated polymerizations in miniemulsion, *C. R. Chim*, 2003, **6**(11), 1351–1374.
269. M. F. Cunningham, M. Xie, K. B. McAuley, B. Keoshkerian and M. K. Georges, Nitroxide-Mediated Styrene Miniemulsion Polymerization, *Macromolecules*, 2002, **35**(1), 59–66.
270. J. W. Ma, M. F. Cunningham, K. B. McAuley, B. Keoshkerian and M. Georges, Nitroxide mediated living radical polymerization of styrene in miniemulsion—modelling persulfate-initiated systems, *Chem. Eng. Sci.*, 2003, **58**(7), 1177–1190.
271. J. Nicolas, B. Charleux, O. Guerret and S. Magnet, Novel SG1-Based Water-Soluble Alkoxyamine for Nitroxide-Mediated Controlled Free-Radical Polymerization of Styrene and n-Butyl Acrylate in Miniemulsion, *Macromolecules*, 2004, **37**(12), 4453–4463.
272. B. Charleux and J. Nicolas, Water-soluble SG1-based alkoxyamines: A breakthrough in controlled/living free-radical polymerization in aqueous dispersed media, *Polymer*, 2007, **48**(20), 5813–5833.

273. T. Prodpran, V. L. Dimonie, E. D. Sudol and M. S. El-Aasser, Nitroxide-mediated living free radical miniemulsion polymerization of styrene, *Macromol. Symp.*, 2000, **155**(1), 1–14.
274. G. Pan, E. D. Sudol, V. L. Dimonie and M. S. El-Aasser, Nitroxide-Mediated Living Free Radical Miniemulsion Polymerization of Styrene, *Macromolecules*, 2001, **34**(3), 481–488.
275. B. Keoshkerian, P. J. MacLeod and M. K. Georges, Block Copolymer Synthesis by a Miniemulsion Stable Free Radical Polymerization Process, *Macromolecules*, 2001, **34**(11), 3594–3599.
276. K. Tortosa, J.-A. Smith and M. F. Cunningham, Synthesis of Polystyrene-block-poly(butyl acrylate) Copolymers Using Nitroxide-Mediated Living Radical Polymerization in Miniemulsion, *Macromol. Rapid Commun.*, 2001, **22**(12), 957–961.
277. C. Farcet, B. Charleux and R. Pirri, Poly(n-butyl acrylate) Homopolymer and Poly[n-butyl acrylate-b-(n-butyl acrylate-co-styrene)] Block Copolymer Prepared via Nitroxide-Mediated Living/Controlled Radical Polymerization in Miniemulsion, *Macromolecules*, 2001, **34**(12), 3823–3826.
278. C. Farcet, J. Nicolas and B. Charleux, Kinetic study of the nitroxide-mediated controlled free-radical polymerization of n-butyl acrylate in aqueous miniemulsions, *J. Polym. Sci., Part A: Polym. Chem.*, 2002, **40**(24), 4410–4420.
279. C. Farcet, J. Belleney, B. Charleux and R. Pirri, Structural Characterization of Nitroxide-Terminated Poly(n-butyl acrylate) Prepared in Bulk and Miniemulsion Polymerizations, *Macromolecules*, 2002, **35**(13), 4912–4918.
280. J. M. Asua, Challenges for industrialization of miniemulsion polymerization, *Prog. Polym. Sci.*, 2014, **39**(10), 1797–1826.
281. M. Manea, A. Chemtob, M. Paulis, J. C. de la Cal, M. J. Barandiaran and J. M. Asua, Miniemulsification in high-pressure homogenizers, *AIChE J.*, 2008, **54**(1), 289–297.
282. Y. Guo, J. Liu and P. B. Zetterlund, Nitroxide-Mediated Radical Polymerization in Miniemulsion On the Basis of in Situ Surfactant Formation without Use of Homogenization Device, *Macromolecules*, 2010, **43**(14), 5914–5916.
283. Y. Guo and P. B. Zetterlund, Particle formation mechanism in radical polymerization in miniemulsion based on in situ surfactant formation without high energy homogenization, *Polymer*, 2011, **52**(19), 4199–4207.
284. U. El-Jaby, M. Cunningham and T. F. L. McKenna, Miniemulsions via in situ Surfactant Generation, *Macromol. Chem. Phys.*, 2010, **211**(12), 1377–1386.
285. U. El-Jaby, M. Cunningham and T. F. L. McKenna, The Advantages of In Situ Surfactant Generation for Miniemulsions, *Macromol. Rapid Commun.*, 2010, **31**(6), 558–562.
286. N. Ballard, M. Salsamendi, P. Carretero and J. M. Asua, An investigation into the nature and potential of in-situ surfactants for low energy miniemulsification, *J. Colloid Interface Sci.*, 2015, **458**, 69–78.

287. J. M. Asua, Emulsion polymerization: From fundamental mechanisms to process developments, *J. Polym. Sci., Part A: Polym. Chem.*, 2004, **42**(5), 1025–1041.
288. S. A. F. Bon, M. Bosveld, B. Klumperman and A. L. German, Controlled Radical Polymerization in Emulsion, *Macromolecules*, 1997, **30**(2), 324–326.
289. C. Marestin, C. Noël, A. Guyot and J. Claverie, Nitroxide Mediated Living Radical Polymerization of Styrene in Emulsion, *Macromolecules*, 1998, **31**(12), 4041–4044.
290. J. Nicolas, B. Charleux, O. Guerret and S. Magnet, Nitroxide-Mediated Controlled Free-Radical Emulsion Polymerization of Styrene and n-Butyl Acrylate with a Water-Soluble Alkoxyamine as Initiator, *Angew. Chem., Int. Ed.*, 2004, **43**(45), 6186–6189.
291. J. Nicolas, B. Charleux, O. Guerret and S. Magnet, Nitroxide-Mediated Controlled Free-Radical Emulsion Polymerization Using a Difunctional Water-Soluble Alkoxyamine Initiator. Toward the Control of Particle Size, Particle Size Distribution, and the Synthesis of Triblock Copolymers, *Macromolecules*, 2005, **38**(24), 9963–9973.
292. H. Maehata, X. Liu, M. Cunningham and B. Keoshkerian, TEMPO-Mediated Emulsion Polymerization, *Macromol. Rapid Commun.*, 2008, **29**(6), 479–484.
293. M. E. Thomson, A.-M. Manley, J. S. Ness, S. C. Schmidt and M. F. Cunningham, Nitroxide-Mediated Surfactant-Free Emulsion Polymerization of n-Butyl Methacrylate with a Small Amount of Styrene, *Macromolecules*, 2010, **43**(19), 7958–7963.
294. M. E. Thomson, J. S. Ness, S. C. Schmidt, N. Macy, T. F. L. McKenna and M. F. Cunningham, Particle nucleation in high solids nitroxide mediated emulsion polymerization of n-butyl acrylate with a difunctional alkoxyamine initiator, *Polym. Chem.*, 2013, **4**(6), 1803–1814.
295. B. Charleux, G. Delaittre, J. Rieger and F. D'Agosto, Polymerization-Induced Self-Assembly: From Soluble Macromolecules to Block Copolymer Nano-Objects in One Step, *Macromolecules*, 2012, **45**(17), 6753–6765.
296. G. Delaittre, J. Nicolas, C. Lefay, M. Save and B. Charleux, Surfactant-free synthesis of amphiphilic diblock copolymer nanoparticles via nitroxide-mediated emulsion polymerization, *Chem. Commun.*, 2005, **5**, 614–616.
297. G. Delaittre, J. Nicolas, C. Lefay, M. Save and B. Charleux, Aqueous suspension of amphiphilic diblock copolymer nanoparticles prepared in situ from a water-soluble poly(sodium acrylate) alkoxyamine macroinitiator, *Soft Matter*, 2006, **2**(3), 223–231.
298. C. Dire, S. Magnet, L. Couvreur and B. Charleux, Nitroxide-Mediated Controlled/Living Free-Radical Surfactant-Free Emulsion Polymerization of Methyl Methacrylate Using a Poly(methacrylic acid)-Based Macroalkoxyamine Initiator, *Macromolecules*, 2009, **42**(1), 95–103.
299. S. Brusseau, J. Belleney, S. Magnet, L. Couvreur and B. Charleux, Nitroxide-mediated copolymerization of methacrylic acid with sodium

4-styrene sulfonate: towards new water-soluble macroalkoxyamines for the synthesis of amphiphilic block copolymers and nanoparticles, *Polym. Chem.*, 2010, **1**(5), 720–729.
300. S. Brusseau, F. D'Agosto, S. Magnet, L. Couvreur, C. Chamignon and B. Charleux, Nitroxide-Mediated Copolymerization of Methacrylic Acid and Sodium 4-Styrenesulfonate in Water Solution and One-Pot Synthesis of Amphiphilic Block Copolymer Nanoparticles, *Macromolecules*, 2011, **44**(14), 5590–5598.
301. A. Darabi, A. R. Shirin-Abadi, J. Pinaud, P. G. Jessop and M. F. Cunningham, Nitroxide-mediated surfactant-free emulsion copolymerization of methyl methacrylate and styrene using poly(2-(diethyl)aminoethyl methacrylate-co-styrene) as a stimuli-responsive macroalkoxyamine, *Polym. Chem.*, 2014, **5**(21), 6163–6170.
302. A. Darabi, A. R. Shirin-Abadi, P. G. Jessop and M. F. Cunningham, Nitroxide-Mediated Polymerization of 2-(Diethylamino)ethyl Methacrylate (DEAEMA) in Water, *Macromolecules*, 2015, **48**(1), 72–80.
303. J. N. Israelachvili, Thermodynamic Principles of Self-Assembly, in *Intermolecular and Surface Forces,* ed. J. N. Israelachvili, 3rd edn, Academic Press, Boston, ch. 19, 2011, pp. 503–534.
304. E. Groison, S. Brusseau, F. D'Agosto, S. Magnet, R. Inoubli and L. Couvreur, *et al.*, Well-Defined Amphiphilic Block Copolymer Nanoobjects via Nitroxide-Mediated Emulsion Polymerization, *ACS Macro Lett.*, 2012, **1**(1), 47–51.
305. X. G. Qiao, M. Lansalot, E. Bourgeat-Lami and B. Charleux, Nitroxide-Mediated Polymerization-Induced Self-Assembly of Poly(poly(ethylene oxide) methyl ether methacrylate-co-styrene)-b-poly(n-butyl methacrylate-co-styrene) Amphiphilic Block Copolymers, *Macromolecules*, 2013, **46**(11), 4285–4295.
306. X. G. Qiao, P. Y. Dugas, B. Charleux, M. Lansalot and E. Bourgeat-Lami, Nitroxide-mediated polymerization-induced self-assembly of amphiphilic block copolymers with a pH/temperature dual sensitive stabilizer block, *Polym. Chem.*, 2017, **8**(27), 4014–4029.
307. J. Wakamatsu, M. Kawasaki, P. B. Zetterlund and M. Okubo, Nitroxide-Mediated Radical Polymerization in Microemulsion, *Macromol. Rapid Commun.*, 2007, **28**(24), 2346–2353.
308. P. B. Zetterlund, J. Wakamatsu and M. Okubo, Nitroxide-Mediated Radical Polymerization of Styrene in Aqueous Microemulsion: Initiator Efficiency, Compartmentalization, and Nitroxide Phase Transfer, *Macromolecules*, 2009, **42**(18), 6944–6952.
309. Y. Kitayama, S. Tomoeda and M. Okubo, Experimental Evidence and Beneficial Use of Confined Space Effect in Nitroxide-Mediated Radical Microemulsion Polymerization (Microemulsion NMP) of n-Butyl Acrylate, *Macromolecules*, 2012, **45**(19), 7884–7889.
310. M. E. Thomson, J. S. Ness, S. C. Schmidt and M. F. Cunningham, High Solids Nitroxide-Mediated Microemulsion Polymerization of MMA with

a Small Amount of Styrene and Synthesis of (MMA-co-St)-block-(BMA-co-St) Polymers, *Macromolecules*, 2011, **44**(6), 1460–1470.
311. W. S. J. Li and M. F. Cunningham, Nitroxide-mediated microemulsion polymerization of n-butyl acrylate: decoupling of target molecular weight and particle size, *Polym. Chem.*, 2014, **5**(12), 3804–3816.
312. Y. Wang, R. A. Hutchinson and M. F. Cunningham, A Semi-Batch Process for Nitroxide Mediated Radical Polymerization, *Macromol. Mater. Eng.*, 2005, **290**(4), 230–241.
313. Y. Fu, M. F. Cunningham and R. A. Hutchinson, Modeling of Nitroxide-Mediated Semibatch Radical Polymerization, *Macromol. React. Eng.*, 2007, **1**(2), 243–252.
314. R. González-Blanco, M. F. Cunningham and E. Saldívar-Guerra, High solids TEMPO-mediated radical semibatch emulsion polymerization of styrene, *J. Polym. Sci., Part A: Polym. Chem.*, 2016, **54**(1), 49–62.
315. M. Zhang and W. H. Ray, Modeling of ''living'' free-radical polymerization processes. I. Batch, semibatch, and continuous tank reactors, *J. Appl. Polym. Sci.*, 2002, **86**(7), 1630–1662.
316. F. Joseph Schork and W. Smulders, On the molecular weight distribution polydispersity of continuous living-radical polymerization, *J. Appl. Polym. Sci.*, 2004, **92**(1), 539–542.
317. C. Rosenfeld, C. Serra, C. Brochon and G. Hadziioannou, High-temperature nitroxide-mediated radical polymerization in a continuous microtube reactor: Towards a better control of the polymerization reaction, *Chem. Eng. Sci.*, 2007, **62**(18), 5245–5250.
318. C. Rosenfeld, C. Serra, C. Brochon, V. Hessel and G. Hadziioannou, Use of micromixers to control the molecular weight distribution in continuous two-stage nitroxide-mediated copolymerizations, *Chem. Eng. J.*, 2008, **135**, S242–S246.
319. T. E. Enright, M. F. Cunningham and B. Keoshkerian, Nitroxide-Mediated Polymerization of Styrene in a Continuous Tubular Reactor, *Macromol. Rapid Commun.*, 2005, **26**(4), 221–225.
320. T. E. Enright, M. F. Cunningham and B. Keoshkerian, Nitroxide-Mediated Bulk and Miniemulsion Polymerization in a Continuous Tubular Reactor: Synthesis of Homo-, Di- and Triblock Copolymers, *Macromol. React. Eng.*, 2010, **4**(3–4), 186–196.
321. J. P. Gillet, O. Guerret and P. Tordo, WO2000040526A2, 1999, Elf Atochem S.A. WIPO (PCT).
322. J. L. Couturier, O. Guerret and D. Bertin, FR2843393A1, 2004, Atofina. Fr. Pat.
323. T. Buergel and A. Pfeil, Wo2013156356, 2012, Hilti. WIPO (PCT).
324. P. A. Callais, S. C. Schmidt, B. L. Stainbrook, N. Passade Boupat, P. Gerard and S. Magnet, WO2007016499, 2005, Arkema. WIPO (PCT).
325. S. C. Schmidt, P. A. Callais, N. E. Macy, J.-M. Corpart, J. S. Ness and J. J. Cernohous, WO2007078819, 2005, Arkema. WIPO (PCT).

326. O. Guerret, P. Gerard, J.-P. Pascault and A. Bonnet, WO2006077153A2, 2005, Arkema. WIPO (PCT).
327. N. M. Martyak, N. E. Macy, M. D. Gernon, S. C. Schmidt and C. M. Dowling, WO2008154558, 2007, Arkema. WIPO (PCT).
328. M. O. Wells and S. C. Schmidt, US2009065737, 2007, Arkema. U.S. Pat.
329. P. Gerard, FR2936524A1, 2008, Arkema. Fr. Pat.
330. J.-M. Boutilier and J.-P. Disson, WO2012136941, 2011, Arkema. WIPO (PCT).
331. M. Rouby, WO2018001481A1, 2017, Saint-Gobain. WIPO (PCT).
332. I. Yamamoto, K. Sakami, E. Masuda, S. Bourrigaud, H. Hediger and S. Cazaumayou, *et al.*, EP3357946A1, 2017, Arkema and Daikin Industries. Eur. Pat.
333. D. C. Visger and R. M. Lange, US6369162B1, 2000, The Lubrizol Corporation. U.S. Pat.
334. H. Kou, F. Pirrung, R. Ettl, B. U. von Vacano, D. Perera-Diez and P. Barraleiro, *et al.*, US20160032224, 2014, BASF S.E. and Henkel A.G. U.S. Pat.
335. M. Hazenkamp, F. O. H. Pirrung, D. Perera and P. Barreleiro, C. Junkes and W. von Rybinski, WO2013060708A1, 2011, BASF S.E. WIPO (PCT).
336. R. Dabbous, S. Onclin and H. Roemling, WO2012000992, 2010, BASF S.E. WIPO (PCT).
337. L. Engelbrecht, F. Pirrung, C. Auschra, R. Knischka and R. Kranwetvogel, US2015337086, 2013, BASF S.E. U.S. Pat.

CHAPTER 8

Nitroxides in Supramolecular Chemistry

ELISABETTA MEZZINA* AND MARCO LUCARINI*

Alma mater Studiorum – University of Bologna, Department of Chemistry ''Giacomo Ciamician'', Via San Giacomo 11, Bologna I-40136, Italy
*Emails: elisabetta.mezzina@unibo.it; marco.lucarini@unibo.it

8.1 Introduction

With the advance of supramolecular chemistry, the need for diverse analytical methodologies as a tool to exploit basic principles for the rational design of the building blocks used to assembly supramolecular aggregates is continuously increasing. In this respect, electron paramagnetic resonance (EPR)[1] and related methods offer particular opportunities to study supramolecular systems. The main advantages of EPR are the sensitivity of the method; the possibility of obtaining kinetic information in the submicrosecond time range; the ability to measure tumbling rates on the nanosecond timescale and distances between spin labels in the 0–100 Å range. The strength of EPR lies also in its possible application to heterogeneous and solid samples.

Because of these EPR favourable features, in recent years spin probing and labelling methodologies have largely expanded beyond the classical context of biology and structural biochemistry and are now commonly used in the characterization of supramolecular assemblies.[2]

Both spin probe and spin label terminology refer to the methodology in which one (or more) paramagnetic species (in most cases a nitroxide radical) is used to report EPR information on the chemical environment experienced by the radical itself. Generally speaking, nitroxides are considered spin

Nitroxides
Edited by Olivier Ouari and Didier Gigmes

Published by the Royal Society of Chemistry, www.rsc.org

probes when they are introduced noncovalently in the sample under investigation, while they act as a spin label when covalently bound to the chemical entity.

The use of nitroxide radicals as spin probes in supramolecular chemistry has been reviewed regularly in recent years.[2–7] Here, we shall review selected examples to show the main features in using nitroxide radicals in supramolecular chemistry. Most of this chapter will be devoted to the description of spin-labelled building blocks used to assemble mechanically interlocked molecules (MIMs),[8] which represents a very promising field of application of nitroxide probes.

8.2 Nitroxide Spin Probes in Host–guest Chemistry

The complexation of organic radicals by host systems has been studied from time to time by EPR spectroscopy during the last 40 years. Different types of host families have been investigated (see Figure 8.1) the mostly used being cyclodextrins (CD),[9] cucurbiturils (CB),[10,11] calixarenes (CX),[12] molecular capsules (MC)[13] and monolayer-protected nanoparticles (MPN).[14]

8.2.1 Sterically Hindered Nitroxides

Most of these reports have been concerned with sterically protected nitroxides, and some selected structures are reported in Figure 8.2.

The use of the nitroxide spin probe in host–guest chemistry derives from the responsiveness of isotropic nitrogen hyperfine splitting constant (a_N, comprised between 13.5 G and 18 G) to the nature of the environment surrounding the nitroxide probe. In particular, the greater the polarity and/or the hydrogen-bonding capability of the medium surrounding the radical centre, the more important is the dipolar structure (Structure B, Figure 8.3) having both a larger spin density on the nitrogen and a larger value of the nitrogen hyperfine coupling. Thus, the partitioning of nitroxide probes in the hydrophobic environment of the water-soluble host container is expected to give rise to a reduction in the value of nitrogen splitting. As an example (Figure 8.3), inclusion of the TEMPO radical by cryptophane molecular capsule or cucurbituril hosts reduces a_N (17.3 G in water) to 15.9 G or 16.2 G, respectively, with the result that the resonance fields for the included probes are significantly different from those for the free nitroxide.

As clearly evident in the EPR spectra reported in Figure 8.3, a helpful aspect in using nitroxide spin probe relies on the relatively short time scale of EPR compared to NMR, which in many cases allows to detect separate signals for the complexed and uncomplexed radicals. When differences in the resonance fields of the EPR lines of the complexed and free nitroxide are sufficiently large, the determination of their relative concentrations, and therefore of the equilibrium constants for the formation of the paramagnetic complex, can be done easily by simulating the corresponding EPR spectrum.

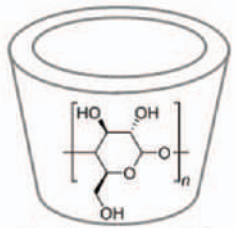

α-, β- and γ-Cyclodextrins (CD) are cyclic oligosaccharides made up of six, seven or eight D-glucose units, respectively. The oligosaccharide ring forms a torus, with the primary OH groups located at the narrower end, while the secondary OH groups are located around the larger opening. The chiral internal cavity is hydrophobic, while the external surface is hydrophilic. In water solution, CDs can form a broad range of 1:1 inclusion complexes.

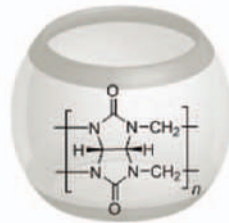

Cucurbit[n]urils (CB) are a family of cyclic pumpkin-shaped molecules consisting of 5 to 10 glycoluril units characterized by the presence of a hydrophobic cavity that is accessible through two identical carbonyl-fringed portals. In water solution, CBs can form a broad range of 1:1 inclusion complexes.

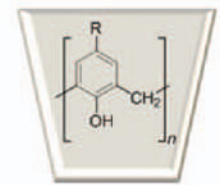

Calixarenes (CX) are basket shaped macromolecules which can be obtained by base-catalyzed condensation of *p-tert*-butyl phenol with formaldehyde. The name, derived from the Latin "calix", exemplifies the cuplike shape of the macrocycles when they assume the conformation in which all four aryl groups are oriented in the same direction.

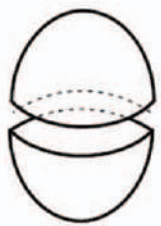

Self-assembling molecular capsules (MC) are receptors with enclosed cavities that are formed by reversibly noncovalent interactions of two or more subunits like cyclodextrins, cucurbiturils, calixrenes, resorcinares, etc.

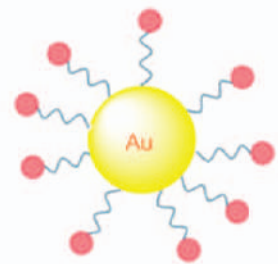

Gold nanoparticles (AuNP) passivated by organic ligands, form a self-assembled monolayer (SAM) on a curved surface. These systems are, usually named monolayer-protected clusters (MPCs). SAMs on NPs simultaneously stabilize the reactive metal and present organic functional groups at the particle–solvent interface.

Figure 8.1 Some representative host systems.

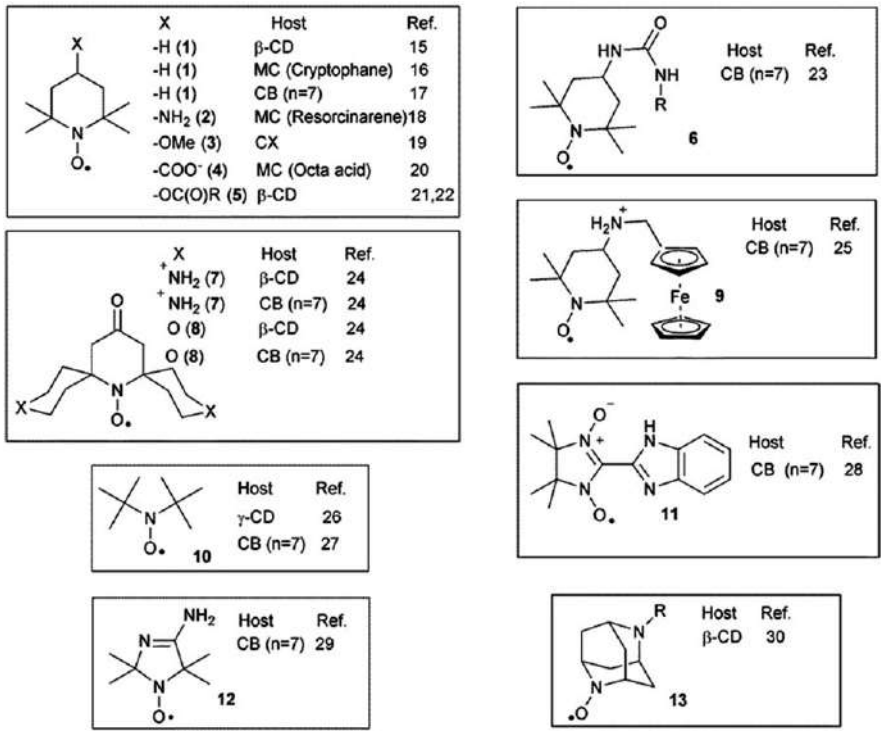

Figure 8.2 Some representative nitroxide spin probes.[15–30]

8.2.2 Nitroxide Probes with Non-zero Spin Atom at β-position

When a non-zero spin atom X is present at the β-position of dialkyl nitroxide, further information on the nature of the paramagnetic complex can be obtained by measurement of the X coupling constant.

According to the Heller–McConnell relationship, the coupling of β-position in dialkyl nitroxides strongly depends on the dihedral angle θ between the SOMO on the nitrogen atom and the C–X bond (see Figure 8.4 with X=H).[31] Thus, any variation of the conformation adopted by the nitroxide when complexed will be reflected in a significant change to the β-coupling constants.

As an example, by using both unsubstituted[32] and substituted[33] diphenylmethyl *tert*-butyl nitroxides it was possible to detect bimodal inclusion complex of cyclodextrins from the *tert*-butyl or phenyl side. In this case the probe experiences both different polarities and conformational influences depending on the direction of the inclusion, and these differences are large enough to be detected by EPR spectroscopy (see Figure 8.4).

Examples when X=P have also been reported in the literature (see Scheme 8.1). However the phosphorus splitting constants, a_P, do not

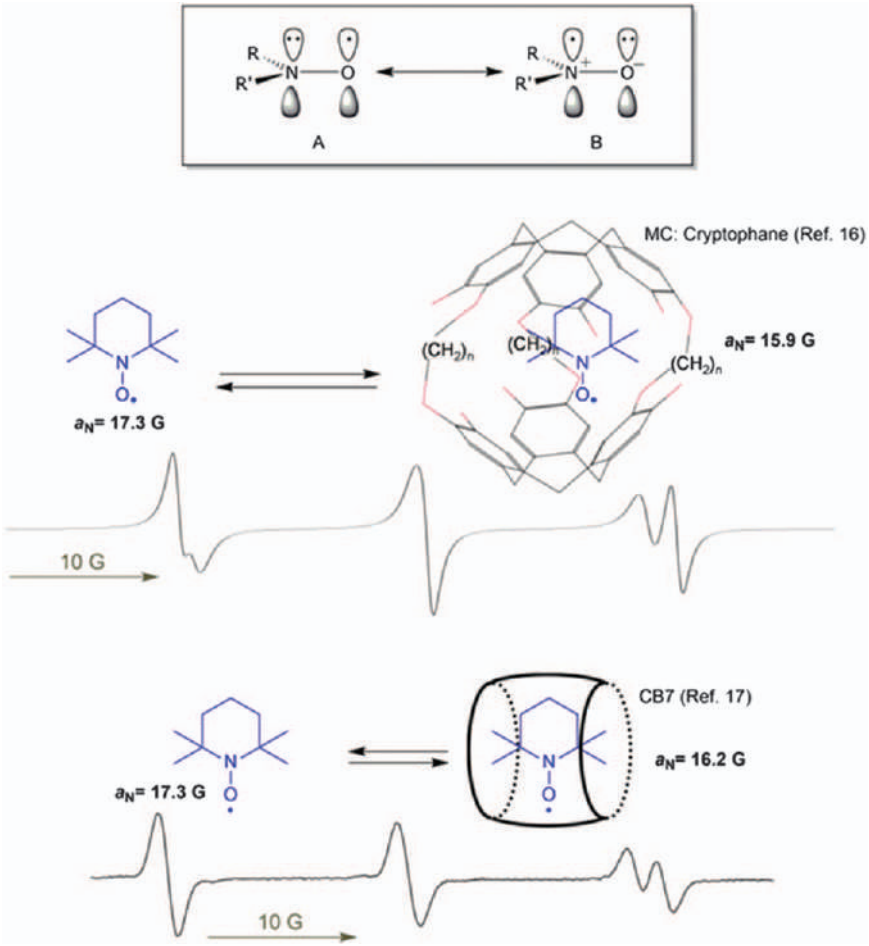

Figure 8.3 Resonance structures of nitroxides and EPR spectra of TEMPO recorded in the presence of cryptophane and CB7 in water.

significantly change upon inclusion as reported for the DEPMPO adduct of superoxide[34] or the capsular inclusion complex of *para*-hexanoyl calix[4]arene with stable nitroxyl radical DEPN.[35]

When a β-methylene group is present, the conformational behaviour of the dialkyl nitroxide is more complicated. Different conformations having a large value for a_H are possible, and even small variation in the averaged geometry adopted by the radical probe could result in a significant variation of β-coupling.

This was actually the case of the benzyl *tert*-butyl nitroxide family, containing two H-atoms at the β-position (see Scheme 8.2).

Because of their ability to disproportionate into the corresponding hydroxylamine and nitrone (see Scheme 8.2), these nitroxide probes are

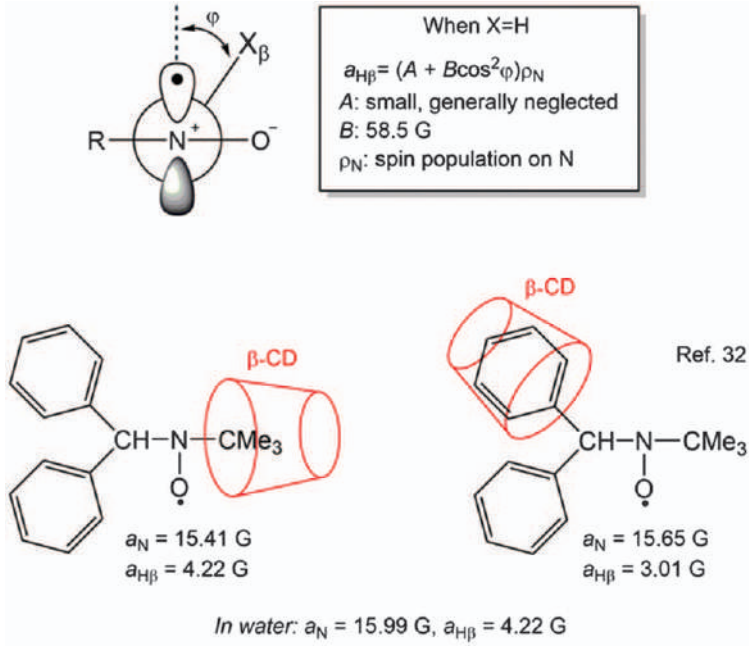

Figure 8.4 Dependence of β-coupling on the conformation adopted by nitroxide radicals and schematic representation of bimodal inclusion of diphenylmethyl *tert*-butyl nitroxide.

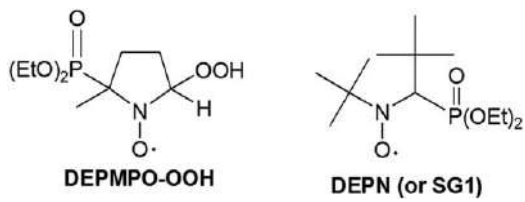

Scheme 8.1 Some representative phosphorylated nitroxide radicals.

characterized by a reduced lifetime when compared to sterically hindered nitroxides and must be generated *in situ* by reaction of the corresponding amine with a proper oxidant. A steady-state concentration of nitroxide is, thus, observed inside the EPR tube when the rates of formation and destruction are approximately equal. This condition is reached a few minutes after mixing the reagents in the oxidation step, allowing the easy recording of several EPR spectra before the complete loss of the EPR signal.

If the presence of the oxidant (commonly an organic peracid) is tolerated by the supramolecular assembly under investigation, the use of BTBN has several advantages compared to sterically hindered nitroxide: (i) different recognition units can be introduced in the aromatic ring by relatively simple synthetic procedure; (ii) the EPR spectrum of the complexed nitroxide

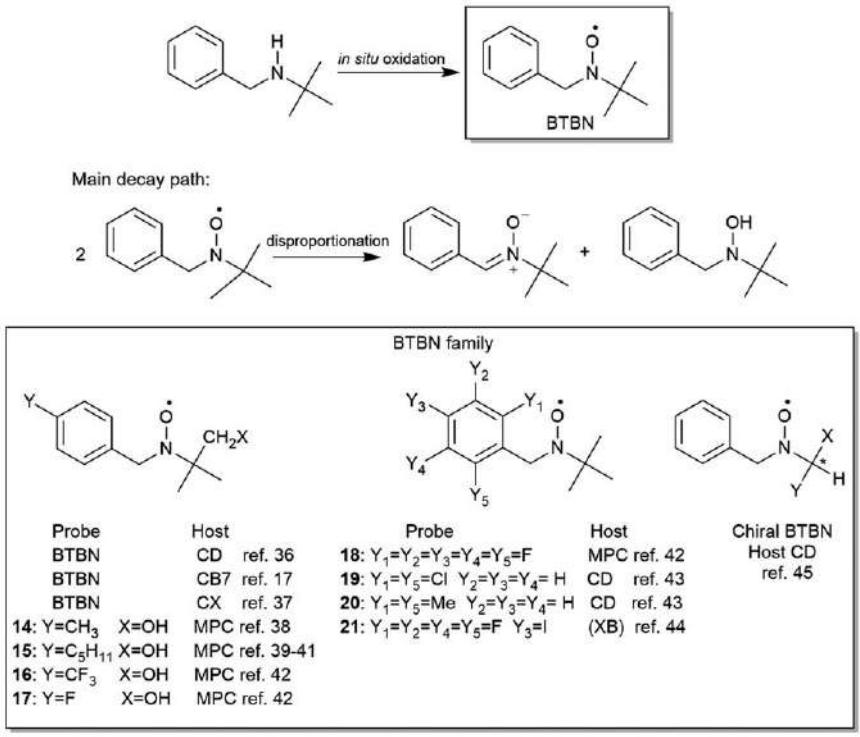

Scheme 8.2 Spin probes of the BTBN family.[17,36–45]

generally shows much larger differences in the resonance fields of the spectral lines compared to the uncomplexed radical in solution; (iii) because of these significant differences in the resonance field of the wing lines of each beta-proton triplet of the included and free species, with several host systems investigated the EPR spectra of BTBN family show strong linewidth dependence on temperature, indicating that the lifetime, t, of formation and dissociation of the supramolecular complexes is in the range characteristic of the EPR spectroscopy.[46,47] This favourable feature allows the measurement of the rate constants for the exchange process (k_{in} and k_{out}, see Figure 8.5) by analysing line shape variations.

A weak noncovalent interaction can also be monitored by the BTBN nitroxide family. As an example, the formation of a halogen bond (XB) complex[48] between nitroxide **21** and several XB acceptors was recently evidenced by a sizeable change in the value of the benzylic hyperfine splitting upon complexation (see Scheme 8.3).[44] In this case, the rate of formation and breaking of the halogen bond is very large on the time scale of EPR, and the experimental spectrum represents the concentration-weighted average of the spectra due to the free and halogen-bonded species. Thermodynamic parameters for the formation of XB complex with quinuclidine were obtained by recording EPR spectra at different temperatures. In addition, competitive

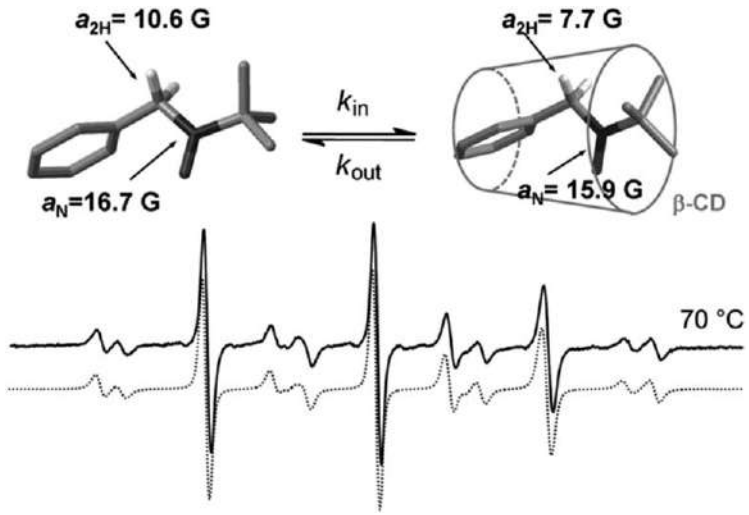

Figure 8.5 Schematic representation of the equilibrium taking place in the presence of β-CD and EPR spectrum of BTBN recorded in water at 70 °C in the presence of β-CD with the corresponding theoretical simulation (dotted line).

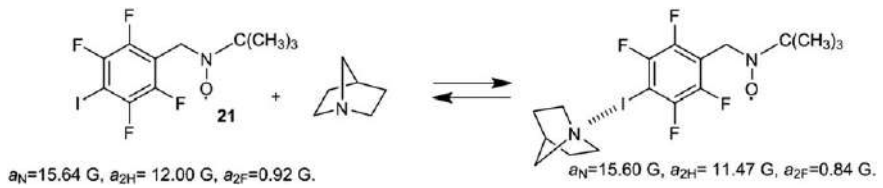

Scheme 8.3 EPR parameters of the free and the halogen-bonded probe **21** in $CHCl_3$.

experiments allowed for the measurement of the equilibrium constant of the XB complex with a chloride anion. The proposed procedure constitutes the first direct EPR methodology, providing a reliable determination of the strength of the XB bond in solution.

8.2.3 Nitroxide Probes Showing Spin–spin Interaction

Structures containing two or more nitroxide radicals relatively close in space are particularly interesting because their continuous-wave EPR spectra contain information on the degree of through-space spin exchange coupling (J) between the two nitroxides.[49] Because through-space spin exchange interaction is distance dependent, variations of the conformation of the polynitroxide (and thus a change in the distance between the spin centres) upon the binding event can be revealed by EPR. Actually, modulation of exchange interaction in di- or polynitroxides was observed by adding CD[50–52] or CB[52–56] hosts to the solution containing the spin probe (see Figure 8.6).

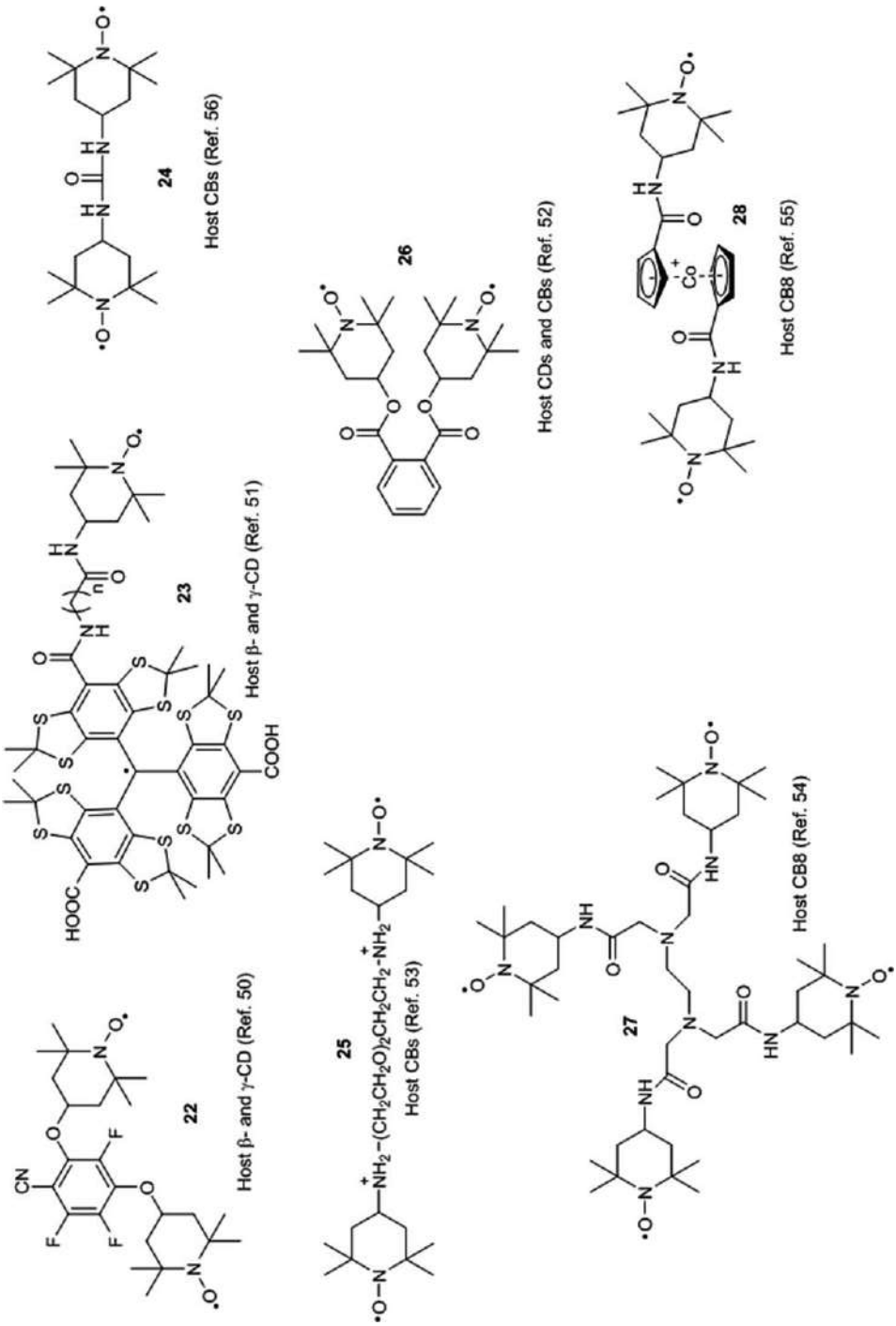

Figure 8.6 Some representative nitroxide probes showing modulation of the spin–spin interaction after complexation by a macrocyclic host.[50–56]

In all examples reported, when the nitroxide guest fits into the hydrophobic cavity of the host, the addition of a macrocycle is able to suppress the spin–spin exchange interaction, and the EPR spectra shift from a multiline pattern (>3) to the conventional three-line pattern.

8.2.4 Mechanically Interlocked Nitroxide Probes

The concept of host–guest chemistry was further developed with the idea of kinetically trapped guests inside the cavity of macrocyclic molecules. This means that the inclusion complex cannot be separated without breaking any covalent bond, while no covalent bond is present between the components, and this can be achieved by mechanically interlocking the molecular components (MIMs) of the inclusion complex by using sterically hindered groups or by exploiting the topology of the complex itself.[8] The two main examples of MIMs are represented by rotaxanes and catenanes (see Figure 8.7).[8] A rotaxane consists of a linear molecule which is threaded through a ring with the ends of the thread, or axle, capped in such a manner that the ring cannot slip off. Another example of topologically connected species is represented by catenanes that are mechanically interlocked macrocycles akin to links in a chain.

The first example of nitroxide spin-labelled [2]catenane was reported in 2003,[57] while the preparation of a spin-labelled dumbbell-shaped [2]rotaxane containing α-CD as the wheel (**Rot-1**, Figure 8.8) was reported in 2006.[58] The latter example represented the first paramagnetic mechanically interlocked molecule (MIM) in which the entrapment of the incorporated alkyl chain axle was realized using persistent nitroxide radicals as stoppers. This was possible by reacting in water sebacoyl chloride in the presence of α-CD with 4-amino-TEMPO.

In this MIM the effect of rotaxanation was highlighted comparing the EPR spectrum of the bis-TEMPO axle with that of its interlocked rotaxane **Rot-1** (Figure 8.8). Actually, the five-line signals of the dumbbell, typical of a flexible, magnetically coupled diradical, change to a three-line spectrum as expected for a noninteracting biradical in the extended conformation with TEMPO fragments behaving as two single nitroxides.[49,59]

Similarly, the synthesis and characterization of a [2]rotaxane based on cyclobis(paraquat-*p*-phenylene) tetracation, $CBPQT^{4+}$, containing a spirocyclic nitroxide spin label as stopper (**Rot-2**) have been described (see Figure 8.9).[60]

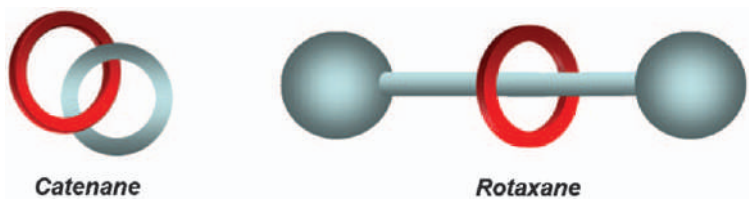

Figure 8.7 Graphical representations of a catenane (left) and a rotaxane (right), which comprise the two main classes of mechanomolecules (MIMs).

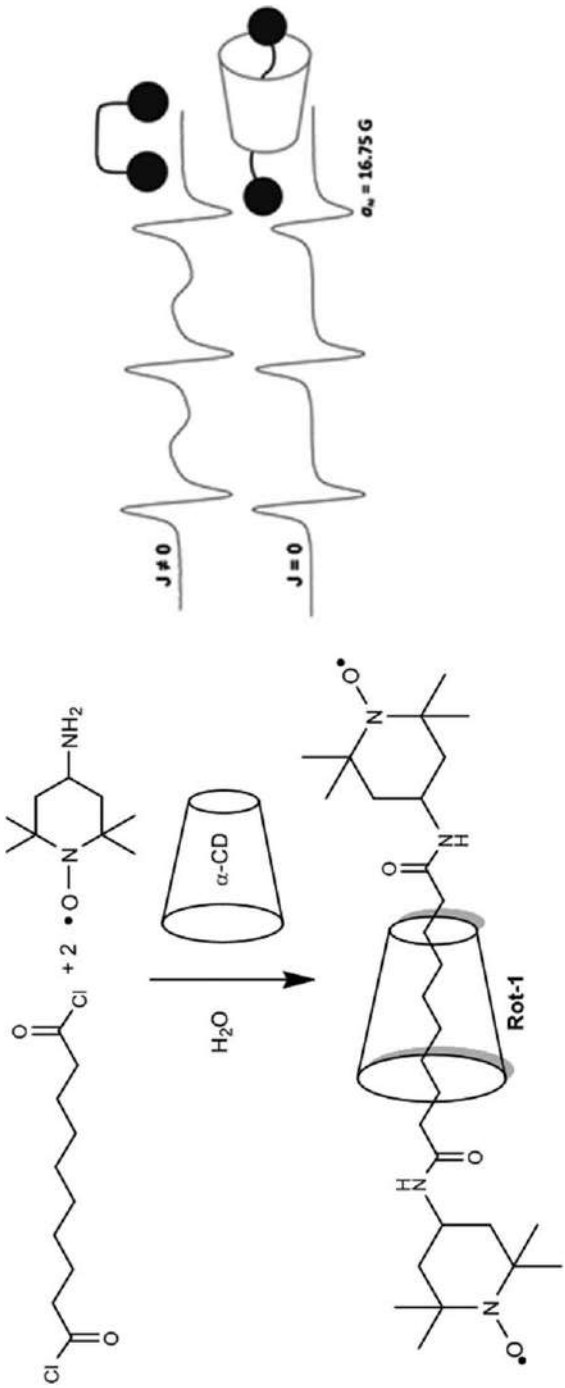

Figure 8.8 Reaction scheme for the preparation of **Rot-1** and its EPR spectrum recorded in water (bottom). The EPR spectrum of the corresponding free thread is also shown (top).

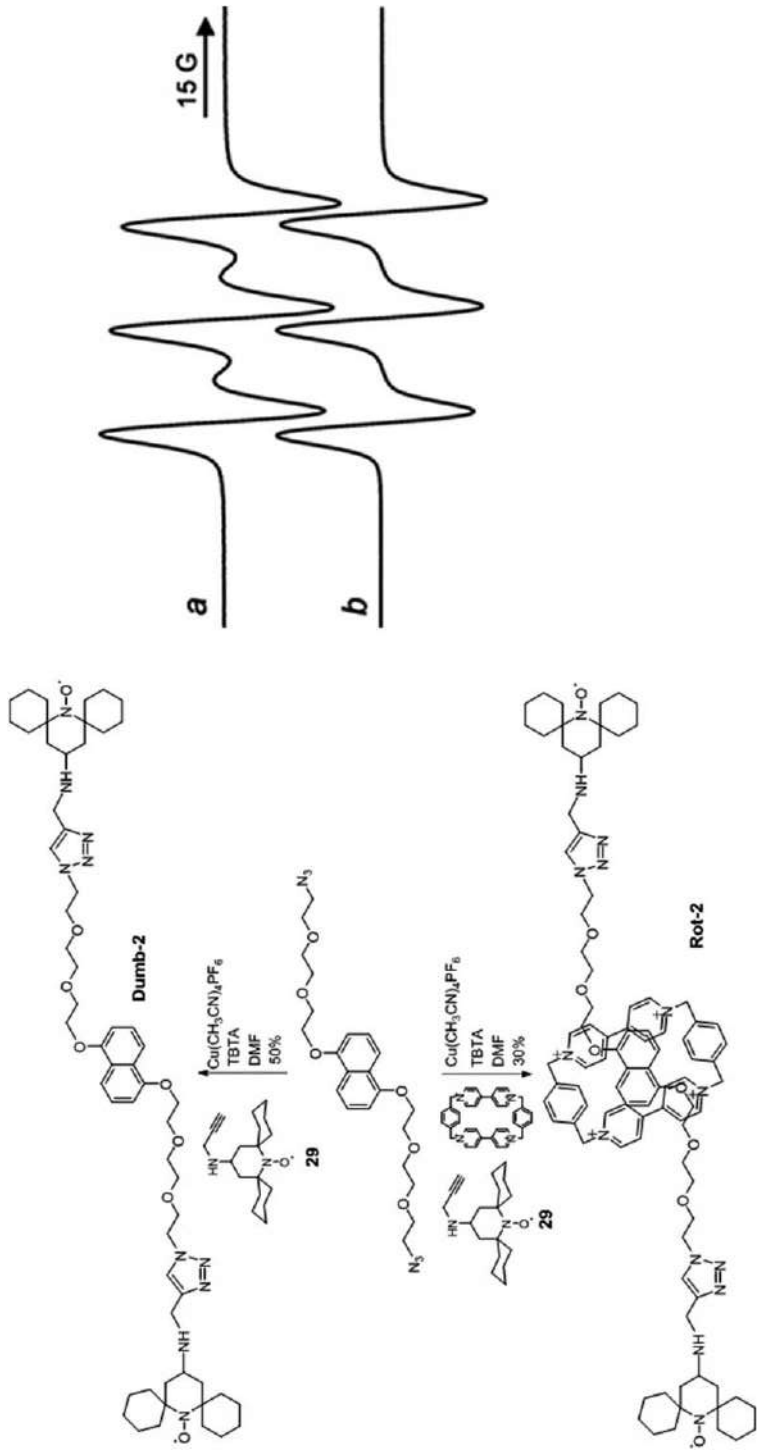

Figure 8.9 Synthesis of dumbbell **Dumb-2**, rotaxane **Rot-2** and their EPR spectra (**Dumb-2** *a*; **Rot-2** *b*) in CH_3CN at 338 K.

Rot-2 was prepared following the threading-and-stoppering approach developed by Stoddard and coworkers.[61] An alkyne azide copper-catalysed cycloaddition was performed *in situ* after the complexation of $CBPQT^{4+}$ with 1,5-dioxynaphtalene (DNP) axial derivatives carrying at both ends an azide group (Figure 8.9). Because the TEMPO unit is not large enough to be used as the end-cap group in CBPQT-based rotaxanes, a sterically hindered nitroxide (**29**) containing spirocyclohexyl substituents at the 2 and 6 positions of the piperidine-*N*-oxyl ring was used as a terminal radical unit.

Once again, EPR was used to provide evidence of the formation of the interlocked structure. Because of the exchange interaction between the paramagnetic fragments linked by the polyether chain, the EPR spectrum of the dumbbell **Dumb-2** is characterized by five lines (Figure 8.9a). On the contrary, that obtained from rotaxane **Rot-2** (Figure 8.9b) consists of only three lines as expected for a nitroxide biradical in which single radical units do not interact with each other. This implies that rotaxanation by the aromatic wheel $CBPQT^{4+}$ significantly reduces the probability of having conformations where the nitroxide stoppers are close to each other. Similar EPR results were also observed for a similar rotaxane containing a tetrathiafulvalene (TTF) unit in place of DNP (**Rot-3**, Scheme 8.4).[60]

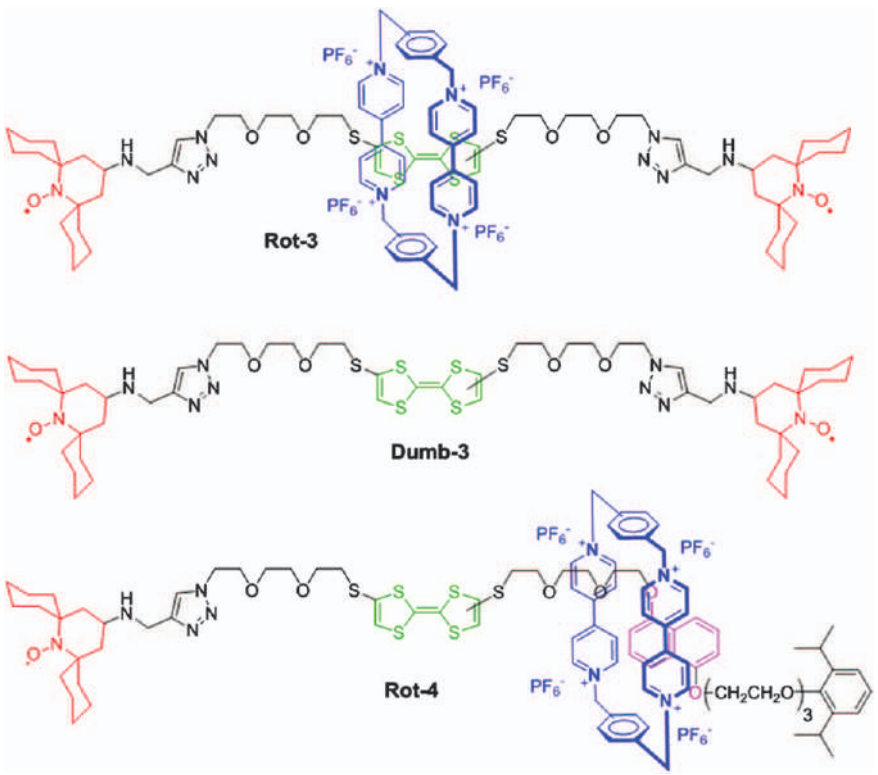

Scheme 8.4 Spin-labelled dumbbell and rotaxanes containing a TTF unit.

Rotaxane threads can be designed in such a manner that they contain two different binding sites for the macrocycle. The preference for the macrocycle to bind to one site or the other can then be influenced by external factors, either chemically, electrochemically or photochemically.[8] The ring can therefore be moved back-and-forth along the axle, and such functional assemblies are known as a molecular shuttle.[8]

Owing to the well-known redox properties of the TTF (TTF moiety can be easily oxidized reversibly to the $TTF^{\bullet+}$ radical cation and then subsequently to the TTF^{2+} dication), the rotaxane **Rot-4** (Scheme 8.4) containing simultaneously the TTF and DNP binding sites was the object of a more detailed study.[62] The oxidation of TTF station in **Dumb-3** determined the formation of a heterotriradical derivative characterized by spin exchanges between the three unpaired electrons (see Figure 8.10a). Because of the high number of σ bonds in the linker between the spin labels, the predominant exchange mechanism between the radical centres must have through-space character. Actually, spin-exchange is completely suppressed by rotaxanation in **Rot-3** as indicated by the corresponding EPR spectrum (Figure 8.10b), which shows superimposed signals of a nonexchanging dinitroxide (1 : 1 : 1 triplet) and

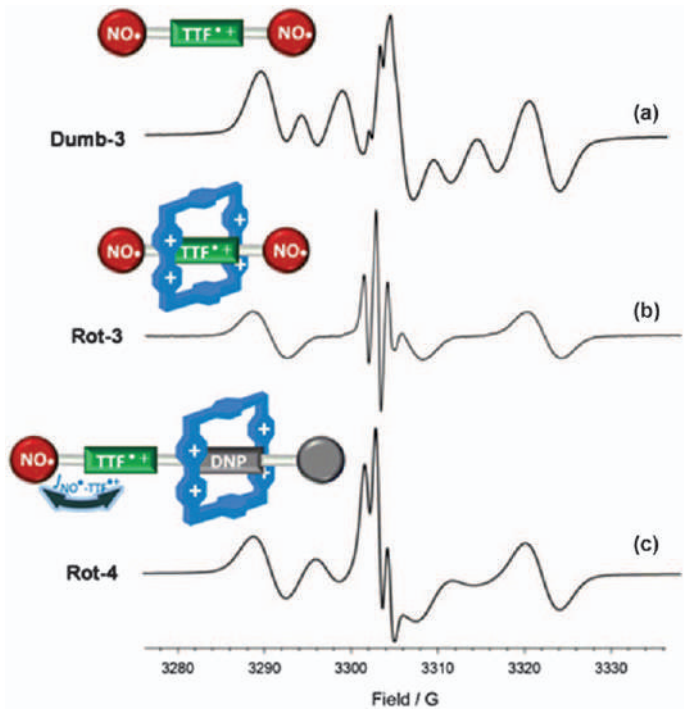

Figure 8.10 EPR spectra recorded in ACN at 298 K at a concentration of 0.2 mM: (a) the free thread **Dumb-3**; (b) the [2]rotaxane **Rot-3** in the presence of 0.5 equiv. of $Fe(ClO_4)_3$; (c) the [2]rotaxane **Rot-4** in the presence of 0.5 equiv of $Fe(ClO_4)_3$.

the TTF radical cation (1 : 2 : 1 triplet). The loss of interactions between the different radical units suggests that the $CBPQT^{4+}$ ring is acting as an ''attenuator'' of spin exchange.

EPR investigation on the bistable spin-labelled [2]rotaxane **Rot-4**, incorporating the TTF and DNP moieties as recognition sites and only one nitroxide spin label as terminal unit (Scheme 8.4) indicated that $CBPQT^{4+}$ preferentially encircled the DNP unit as expected on the basis of the greater affinity of the host for this station.[61] When $TTF^{\bullet+}$ radical cation is formed, the corresponding EPR spectrum (Figure 8.10c) shows a strong spin–exchange interaction between the nitroxide stopper unit and $TTF^{\bullet+}$, suggesting that the macrocycle position was preserved also after the TTF oxidation.[62]

The synthesis and characterization of a dinitroxide cucurbit[6]uril-based [3]rotaxane (**Rot-5**) having the structure reported in Scheme 8.5 have also been reported.[53] This bis-spin-labelled mechanically interlocked molecule allowed for the first time measurement of the end-to-end distance in a rotaxane by PELDOR experiments and to extract information on the intrinsic flexibility of the thread.[63a] As expected, the rotaxane is characterized by a very narrow distribution of the end–end distance between the two TEMPO groups because of the presence of two CB6.

More recently pulsed EPR spectroscopy was also used to measure the interaction between two inequivalent spins in a hybrid rotaxane molecule containing a nitroxide unit and a $\{Cr_7Ni\}$ ring.[63b]

8.2.5 Supramolecular Polynitroxides

While modulation of spin–spin coupling between nitroxide fragments covalently bonded in supramolecular assemblies has been thoroughly investigated, examples of strong through-space spin interactions between nitroxide radicals ordered by a supramolecular architecture have been seldom reported.

The formation of a supratriradical based on protonated 4-amino-TEMPO (**2**),[64] 4-methoxy-TEMPO (**3**),[65] NMe_3^+-TEMPO[66] and CB8 was demonstrated to occur in a water solution. The EPR seven-line pattern observed in all three cases corresponded to a triangular assembly of a 1 : 1 CB@nitroxide complex whose structure has been determined by X-ray analysis (Figure 8.11).[65]

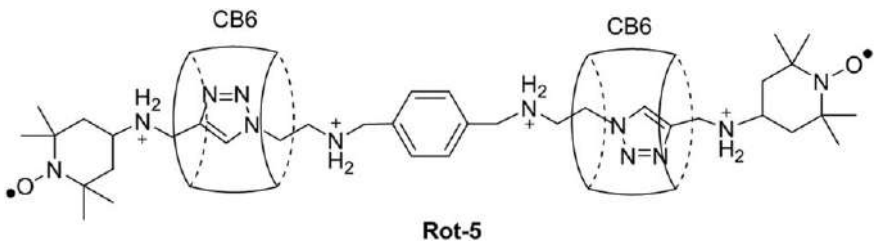

Scheme 8.5 Structure of [3]rotaxane **Rot-5**.

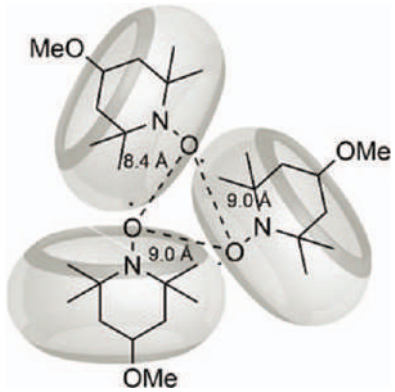

Figure 8.11 Structure of the 3·CB8 inclusion complex showing a three-spin-system interaction.

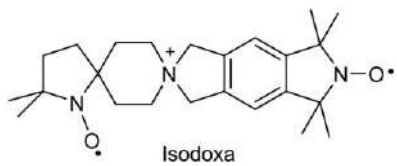

Scheme 8.6 Structure of the Isodoxa spin probe.

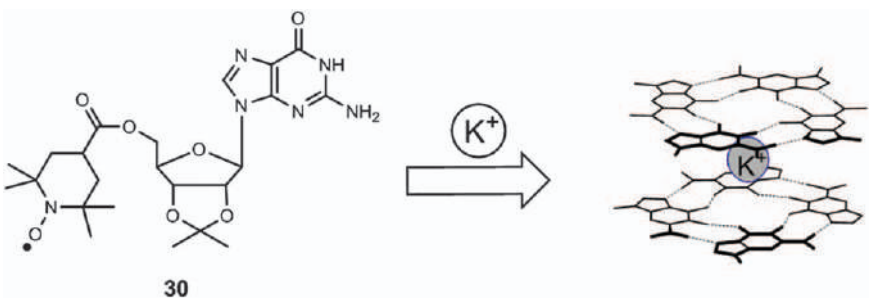

Scheme 8.7 Schematic representation of the octamer formed from paramagnetic guanosine **30**.

More recently a new supramolecular hexaradical based on the trimerization of Isodoxa·CB8 1 : 1 complexes was reported (Scheme 8.6).[67] The presence of two sodium ions was systematically observed in the trimer structures, and the presence of Na^+ triggered or strengthened the triangulation of CB[8]:guest 1 : 1 complexes in solution.

A different example of nitroxide moieties ordered by a supramolecular architecture based on lipophilic guanosines has also been reported.[68] In this example, the guanosine derivative **30** containing 4-carbonyl-2,2,6,6-tetramethylpiperidine-1-oxyl unit forms an octameric polynitroxide by its K^+-templated self-assembly (see Scheme 8.7).

8.2.6 Fluorescent Nitroxide Spin Probes

The complexation by β-CD of a series of dual molecular probes bearing fluorescent (pyrene or dansyl fluorophores) and nitroxide moieties linked by flexible short polyether chains was described in the literature (see Scheme 8.8).[69,70] These molecular probes offer the possibility to investigate host–guest systems, by using EPR and fluorescence spectroscopies concertedly.

8.3 Nitroxide Spin Labelling of Macrocycles for the Investigation of Supramolecular Assemblies

As mentioned in the Introduction, the spin-labelling approach consists in covalently linking a specific nitroxide label to a supramolecular aggregate whose EPR paramagnetic spectral properties make it possible to collect new information on the system under investigation. Specifically this section will be focused on the synthesis of selected organic hosts grafted to a nitroxide radical centre and on the use of the corresponding paramagnetic macrocycles in host–guest recognition or in mechanical bonded assemblies to explore new properties by EPR analysis.

8.3.1 Spin-labelled Cyclodextrins

In 1970, Paton and Kaiser[71] reported the first example of spin-labelled cyclodextrin containing a nitroxide arm covalently bound to the macrocycle rim. However, only 35 years later a systematic EPR study of the properties of paramagnetic CDs was realized by Ionita and Chechik.[72] CDs were tagged with commercially available substituted 4-Y-TEMPO derivatives (Y=NH_2, $NHCOCH_2Br$, maleimide unit) by forming a covalent link at the edge of a suitably monofunctionalized ring. In particular the 6-position of the β-cyclodextrin (β-CD) was spin functionalized by treating monotosylated β-CD (**6-OTs-β-CD**) with 4-amino-TEMPO.[72] (**β-CD-1**) Alternatively, 4-(2-bromoacetamido)-TEMPO or 4-maleimido-TEMPO undergo nucleophilic substitution with 6-mercapto-β-cyclodextrin in alkaline water to afford the corresponding monosubstituted cyclodextrins **β-CD-2** and **β-CD-3**,

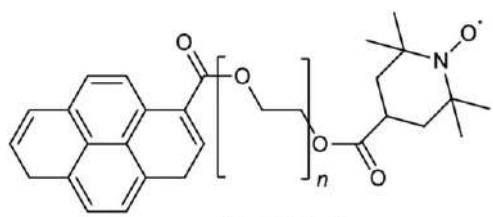

Py(EG)$_n$T
n=1-6

Scheme 8.8 Structure of fluorescent spin probes.

respectively (Figure 8.12).[72] In a similar manner, a nitronylnitroxide containing a phenolic functionality was also introduced in a permethylated-monotosylated β-CD in alkaline medium (**β-CD-4**).[73]

The ability of **β-CD-1–3** to recognize dendrimers,[72] polymers[74] or hydrogels[75] was demonstrated by observing a significant decrease in the tumbling rate of the assemblies through the broadening of EPR high field spectral line of the nitroxide involved in the complexation with these large guest molecules.

Later, the same authors described the EPR data of a bis-nitroxide CDs[76] having close or far distances between TEMPO radicals. By monitoring the different degree of spin–spin interaction between the two nitroxides it was possible to observe different conformations adopted by the hosts in dichloromethane and in water solutions. These results were exploited to study the recognition process of these macrocycles with adamantane-capped diethylene glycol by EPR.[76]

In 2006, Tordo's group reported the attachment of a persistent nitroxide (1,1-dimethylethyl-2-methyl-1-phenylpropyl nitroxide, TIPNO) on permethyl-β-cyclodextrin (**β-CD-5**, Figure 8.13).[77] The interest in the synthesis of such derivatives was related to the fact that they represent a good model for an improved class of nitrone spin traps conjugated with cyclodextrin cavity.[77] This promising spin trap strategy relies on the selective inclusion of the generated spin adducts inside the CD cavity such as to physically protect nitroxide moiety from bioreductants. Simulation of the EPR spectrum of **β-CD-5** recorded in aqueous solution evidenced the co-existence of two fast-exchanging species, one having the nitroxide moiety outside, and the other displaying a weak self-inclusion of the aromatic group inside the cavity.

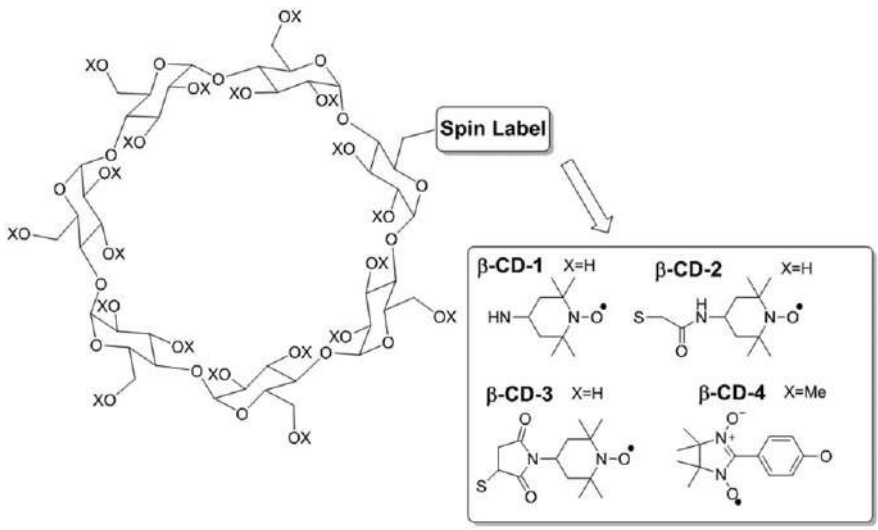

Figure 8.12 Spin-labelled cyclodextrins at the 6-position.

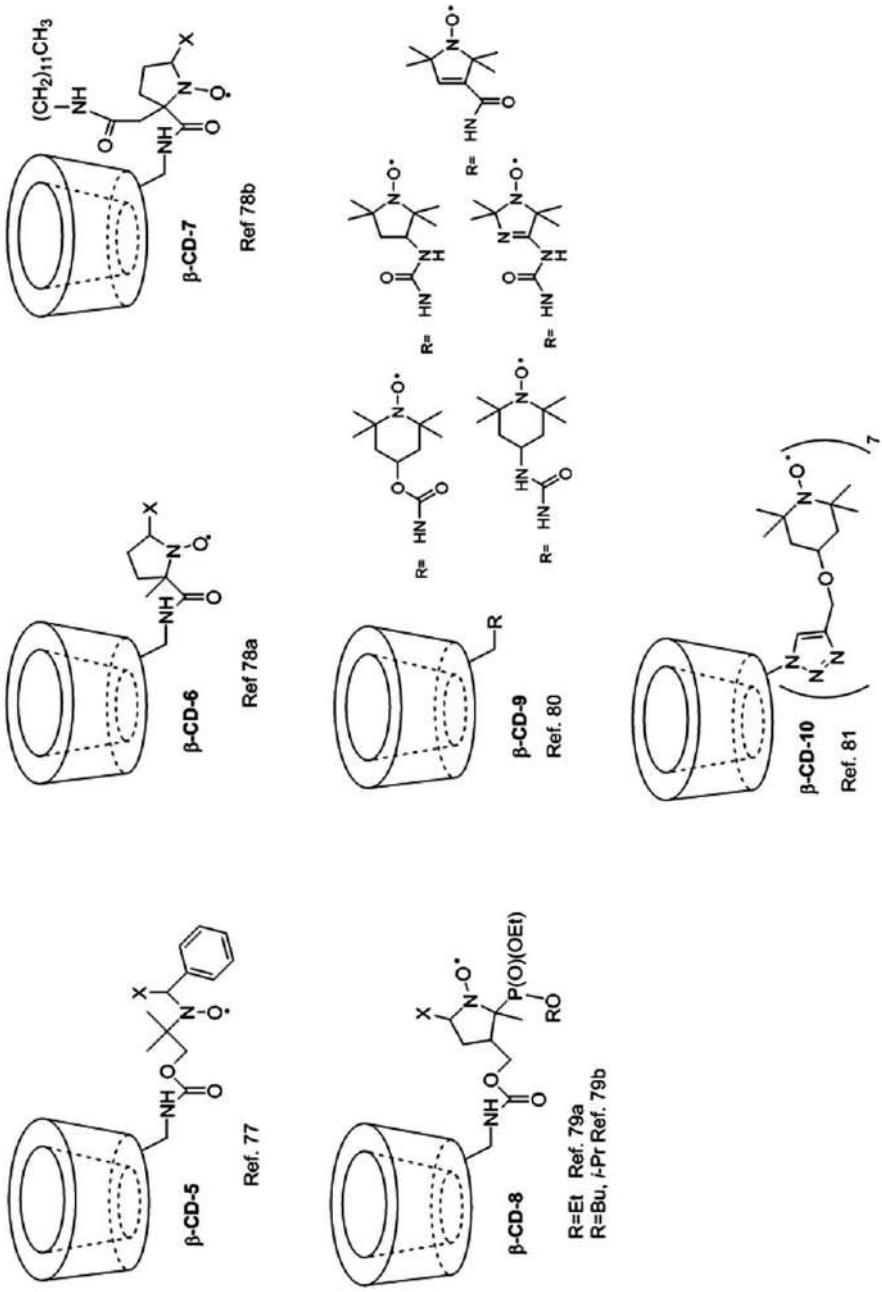

Figure 8.13 Structures of **β-CD-5–10.**

Other groups described the synthesis of β-CD–cyclic nitrone conjugate 5-*N*-β-cyclodextrin-carboxamide-5-methyl-1-pyrroline *N*-oxide (**β-CD-6**) and a nitrone spin trap, **β-CD-7**, that is tethered *via* amide bonds to β-CD and dodecyl chain.[78] In both cases, their superoxide adducts showed improved resistance to reduction and were characterized by EPR spectroscopy.

Different examples of β-CD–nitrone conjugates containing a phosphorus atom at β-position have also been reported.[79] These new DEPMPO-based spin traps have been designed and synthesized for improved superoxide detection, each carrying a CD moiety but with a different alkyl chain on the phosphorus atom or with a long spacer arm (Figure 8.13).

Pulsed EPR has been employed to study a series of new complexes based on fully methylated cyclodextrin (Figure 8.13) covalently bound to the piperidine, pyrroline, pyrrolidine and pH-sensitive imidazoline type nitroxides.[80] Using the electron spin echo envelope modulation technique (ESEEM), the accessibility of the nitroxide unit to solvent molecules in different complexes was investigated as a function of the structure and length of the linkers connecting the radical centre to the macrocycle.

Strong spin–spin interactions were observed in a β-CD connected to seven TEMPO units at the secondary hydroxylic unit of the smaller rim (**β-CD-10**).[81] Combining EPR, DC-SQUID magnetometry and relaxivity measurements was possible to show that the spin–spin interaction in **β-CD-10** cannot be described by the symmetrical arrangement of the seven nitroxide units on the CD rim.

8.3.2 Mechanically Interlocked Spin-labelled Cyclodextrins

In 2008, the first example of a self-included [1]rotaxane-type[82] nitroxide-appended β-cyclodextrin was synthesized. In the molecule, the aminoxyl functionality was mechanically trapped inside the cavity of CD by a covalent link occurring on one of the CD rims. To date, this remains the only example of a ''genuine'' [1]rotaxane containing a nitroxide unit included in the cavity of the macrocycle. The synthesis outlined in Scheme 8.9 showed distinct behaviours upon treatment of nitroxide **31a** and **31b** with 6-mercapto-β-cyclodextrin in alkaline water. The self-included species was isolated only using the bromo ester TEMPO **31b** as the reactant.

The noncomplexed TEMPO fragment was characterized by $a_N = 17.00$ G in water, and when involved in the interlocked *lasso*-type complex the value decreased to $a_N = 16.55$ G (Figure 8.14). By this method it was also possible to distinguish the intermolecular complexation with a second β-CD ring ($a_N = 16.48$) and the partial self-complexation of the radical through the upper rim of the CD ($a_N = 16.80$). In competitive experiments, addition of sodium dodecyl sulphate (SDS) to [1]-rotaxane did not cause any variation of the spectrum of **β-CD-12**, thus confirming the irreversible nitroxide trapping inside the CD cavity.

In 2012, a double spin-labelled α-CD-based [2]rotaxane characterized by the presence of two nitroxidic fragments both at the wheel and at the dumbbell was reported.[83] The CD wheel was labelled by employing Cu(I)-catalysed click

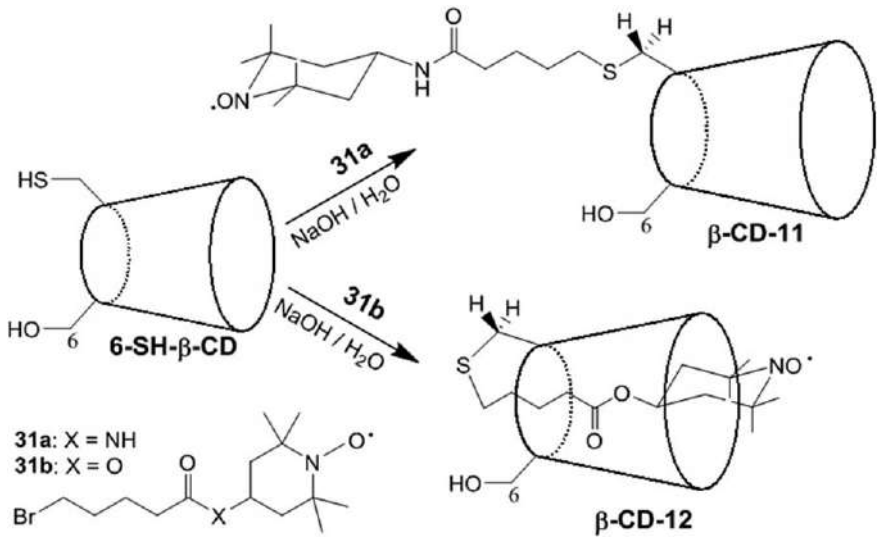

Scheme 8.9 Synthesis and structure of **β-CD-11** and **β-CD-12**.

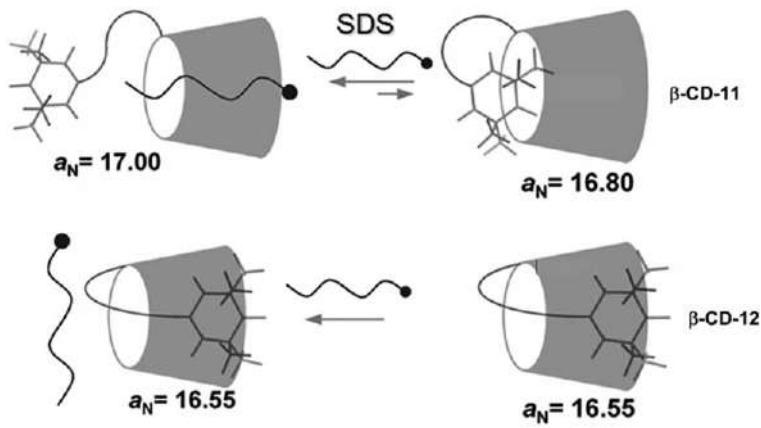

Figure 8.14 Schematic representation of equilibria involving **β-CD-11** and **β-CD-12**.

azide–alkyne reaction (CuAAC).[84] TEMPO-monofunctionalized α-CDs, both at the primary rim (**α-CD-1**, Scheme 8.10) or at the larger secondary one (3 position, **α-CD-2**, Scheme 8.10),[83] were prepared starting from mono-azidodeoxy-α-cyclodextrin (6-N_3-α-CD, 3-N_3-α-CD), obtained by the corresponding tosylated α-CD after tosyl displacement with sodium azide,[85] with 4-propargyloxy-TEMPO.[86]

Then the bis-labelled MIM, prepared following the approach reported by Fort and coworkers,[85] was obtained treating an α-CD pseudorotaxane (**pseudo-Rot-6a**, Scheme 8.11) consisting of a lactose-blocked C-10 half thread carrying an azido group with an alkyne-TEMPO stopper.

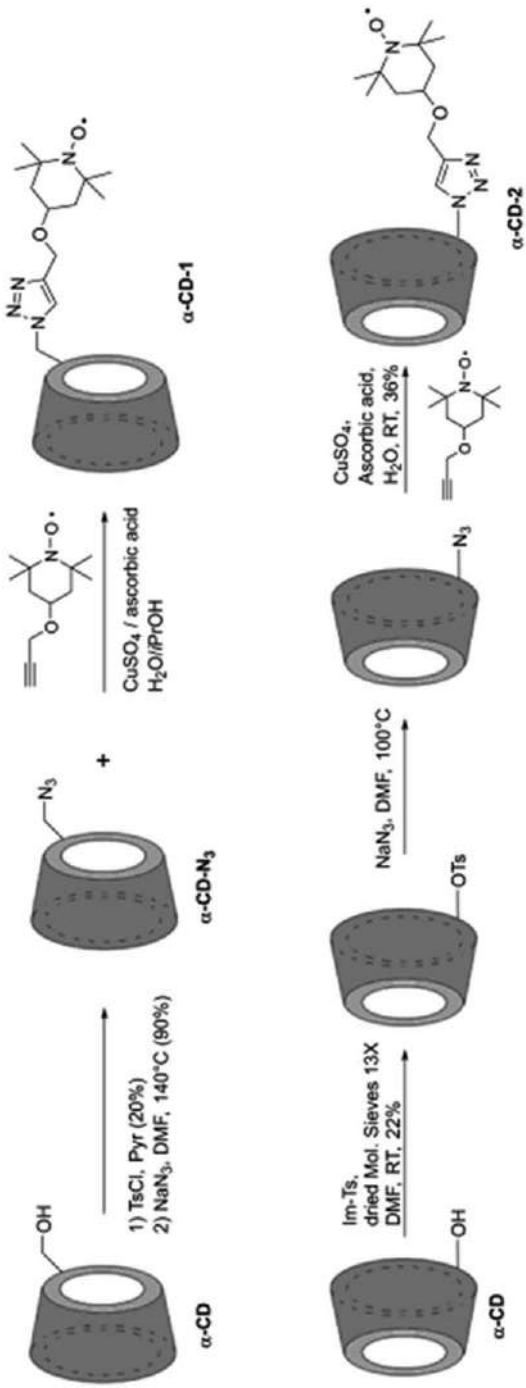

Scheme 8.10 Synthesis and structures of the spin-labelled α-cyclodextrin **α-CD-1** and **α-CD-2**.

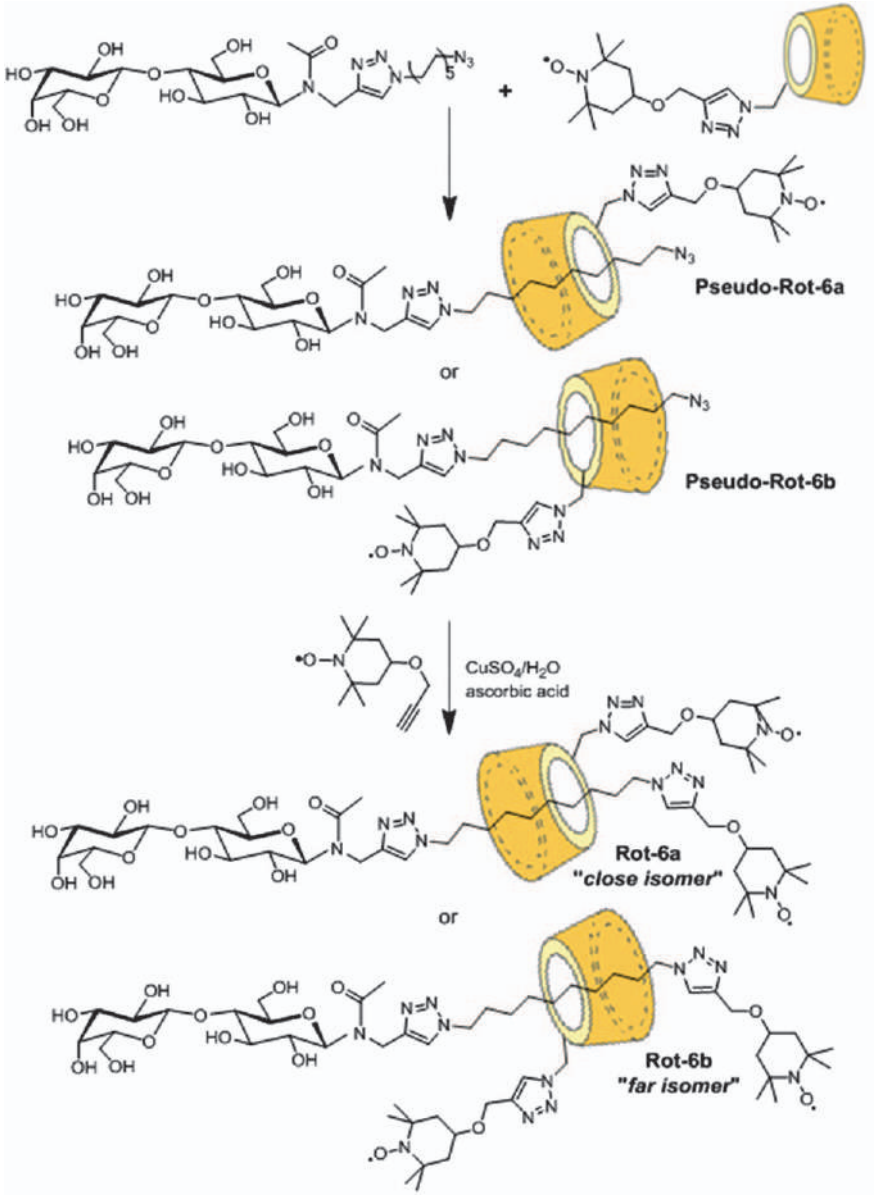

Scheme 8.11 Synthesis and structure of bis-labelled rotaxanes **Rot-6a** and **Rot-6b**.

Because of the unsymmetrical structure of both the ring and the axle, a mixture of isomers could be predicted on the base of the orientation of the CD along the thread. By combining the information extracted from the EPR spectrum (characterized by the presence of spin exchange) and molecular dynamic calculations it was possible to identify the isolated isomer as the ''*close isomer*'' (**Rot-6a**, Figure 8.15).

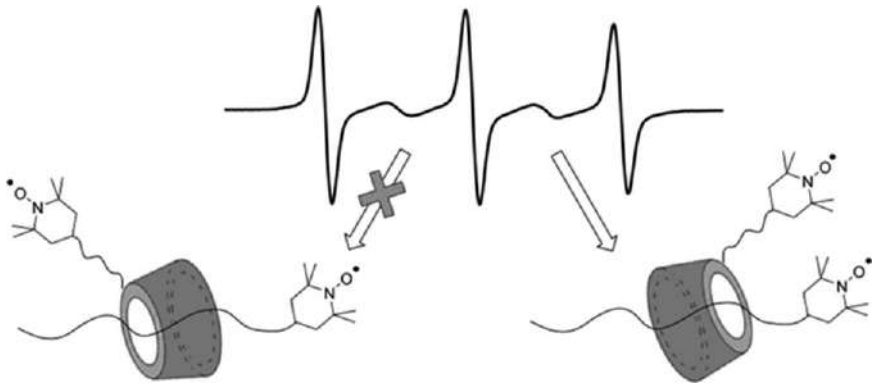

Figure 8.15 EPR spectrum of **Rot-6a** recorded in water at 328 K.

8.3.3 Spin-labelled CBPQT Tetracation

In all examples illustrated before, the spin label was inserted in a pre-established macrocyclic structure. An alternative scheme consists in the synthesis of a spin label fragment that successively undergoes a cyclization reaction to form the ring structure. This was the case of mono- and bis-spin-labelled π-electron-deficient tetracationic cyclophane ring, cyclobis(paraquat-*p*-phenylene) ($CBPQT^{4+}$), one of the most versatile hosts involved in the preparation of artificial molecular machines (AMM) proposed by Stoddart's group.[87] To realize this, the bis-pyridinium precursors salts, either in the unsubstituted (**pre-CBPQT-1**) or in the one-armed (**pre-CBPQT-2**) form, have been reacted with a TEMPO-substituted benzyl dibromide (Scheme 8.12).[88]

In a recent work,[89] the electrochemical behaviour of a bis spin-labelled "Stoddart–Heath type" bistable [2]rotaxane, **Rot-7**$^{2\cdot4+}$ (Figure 8.16) exploiting oxidation of the TTF to its EPR active radical cation $TTF^{\bullet+}$ was investigated. The molecular machine consisted of a double-station (1,5-dioxynaphthalene) DNP/TTF dumbbell (**Dumb-7**$^{\bullet}$) and the macrocycle (**CBPQT-1**, Scheme 8.12) both labelled with nitroxide radicals. The bulky spirocyclohexyl piperidine-*N*-oxyl was used as a stoppering unit for the axle. The single-station rotaxanes as well as the corresponding dumbbells were synthesized (Figure 8.16) for comparison studies.

The EPR spectra of **Rot-9**$^{2\cdot4+}$ and **Rot-10**$^{2\cdot4+}$ (Figure 8.17a and b) were composed by five spectral lines due to strong spin exchange $J_{NO^{\bullet}-NO^{\bullet}}$ between the nitroxide units (through space spin exchange mechanism). Conversely, the bistable rotaxane **Rot-7**$^{2\cdot4+}$ presents only a three-line spectrum with a nonsymmetrical shape due to the superimposition of the signals of both the wheel and the dumbbell radical labels, that contributes to the overall spectra in a 1 : 1 ratio (Figure 8.17c). The two radicals do not display spin exchange so confirming that **CBPQT-1** encircles preferentially the TTF station which is expected to be far from the paramagnetic stopper unit.

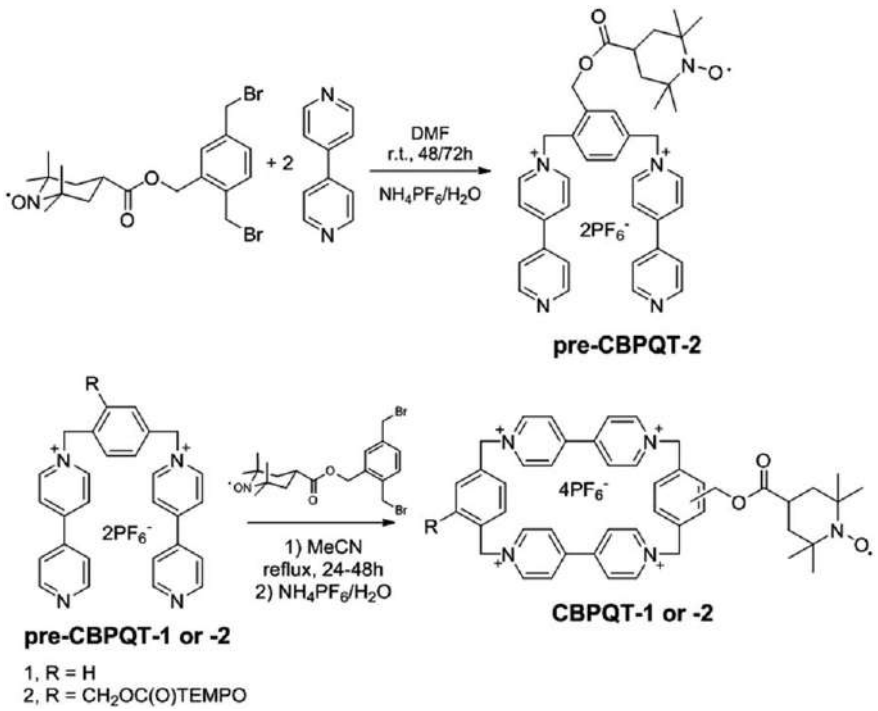

Scheme 8.12 Synthesis and structures of the paramagnetic macrocycles **CBPQBT-1** and **-2**.

Due to the flexibility of the glycolic chains, one-electron oxidation with $Fe(ClO_4)_3$ of **Rot-7**$^{2\cdot4+}$ produces EPR exchange signals between N–O$^{\bullet}$ and TTF$^{\bullet+}$. This result was the proof of the movement of the wheel onto the DMP station after addition of $Fe(ClO_4)_3$. Actually, the formation of the TTF radical cation is expected to destabilize the mechanically interlocked molecule and to lower the effective barrier for the shuttling of the CBPQT^{4+} ring onto the DNP recognition unit producing exchange signals between N–O$^{\bullet}$ and TTF$^{\bullet+}$. If the oxidation is performed in an electrochemical EPR cell, the inversion of the sign of the current reduced TTF$^{\bullet+}$ to its neutral form and the starting EPR spectra of **Rot-7**$^{2\cdot4+}$ was restored. These experiments were repeated in many cycles confirming the reversible nature of the switching process.

8.3.4 Spin-labelled Pillarenes

Click conditions were employed also to introduce spin labels in a pillar[5]-arene macrocycle,[90] a member of a family of electron rich pillar-shaped symmetrical hosts.[91] Following the synthetic approach reported by Stoddart *et al.*[92] (Scheme 8.13) a pillar[5]arene monofunctionalized with an azide

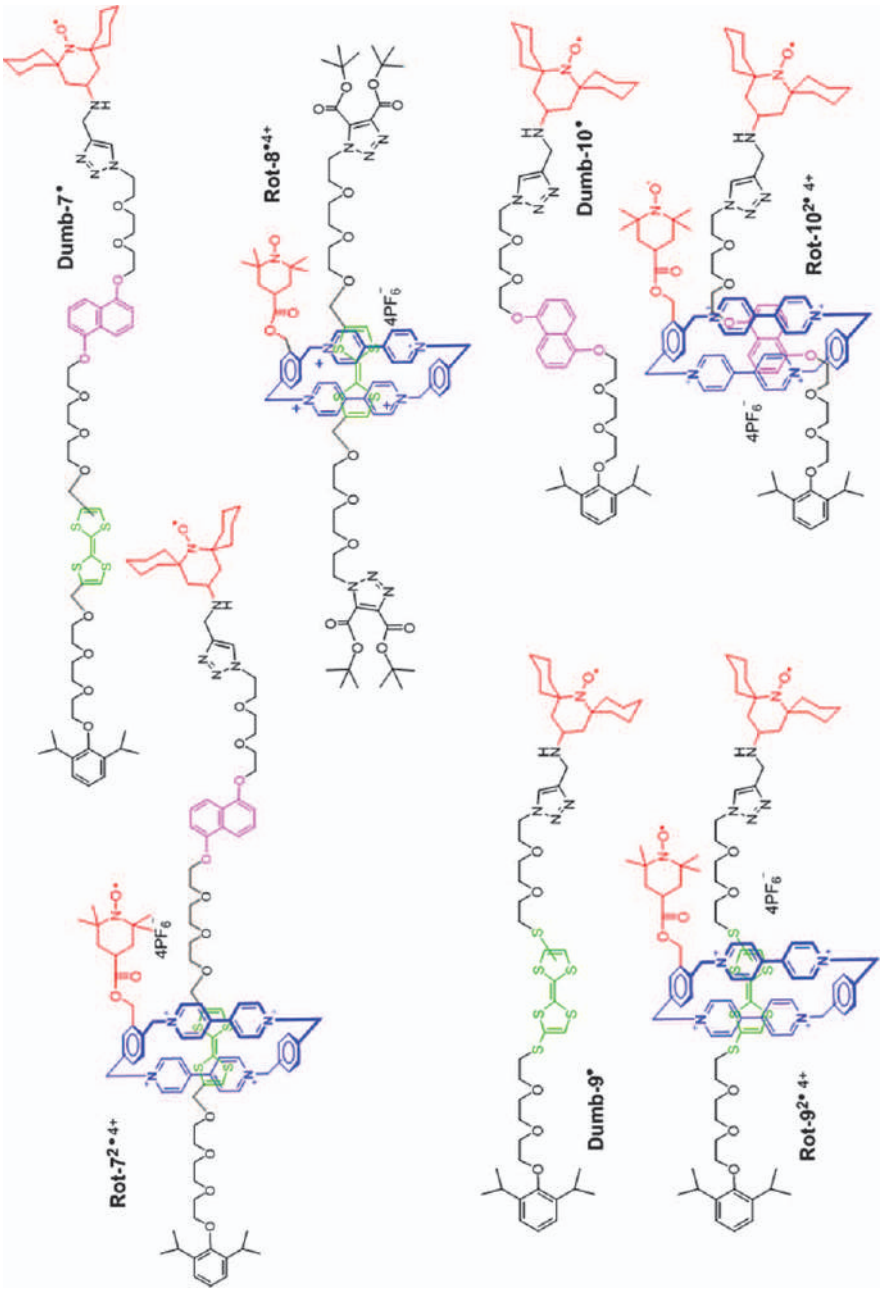

Figure 8.16 Structures of the bis-labelled [2]rotaxanes and the corresponding dumbbells.

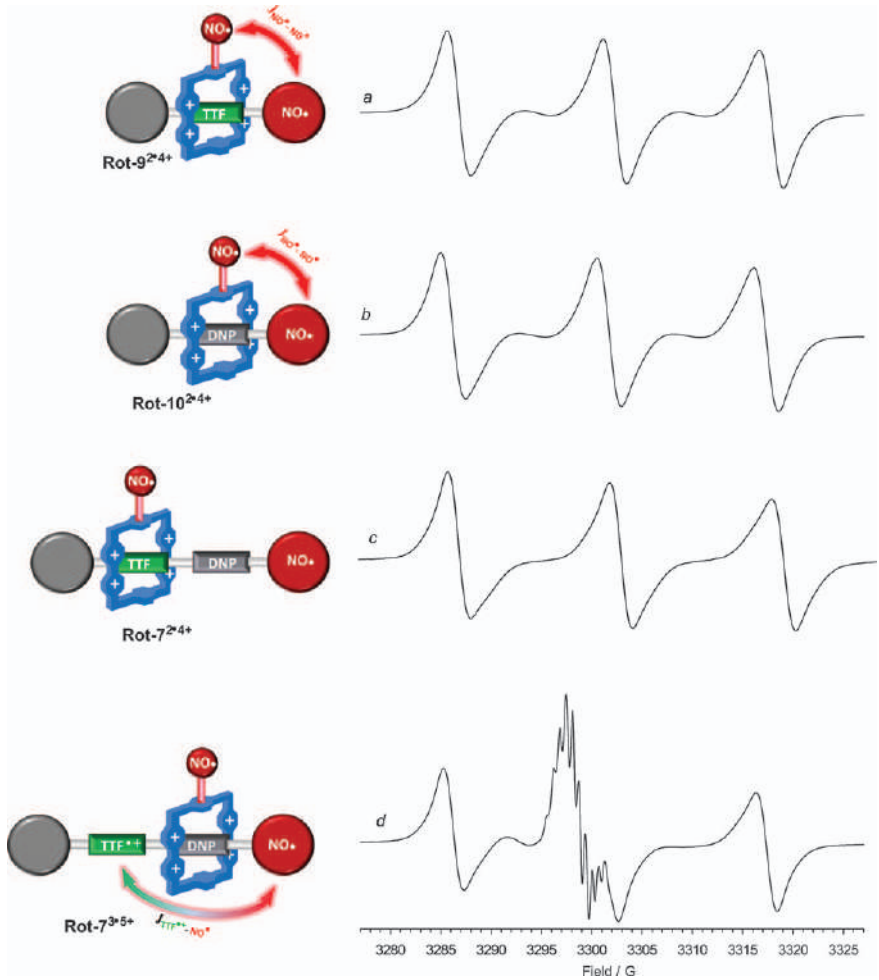

Figure 8.17 EPR spectra of the spin-labelled rotaxanes: (a) **Rot-9**$^{2•4+}$, (b) **Rot-10**$^{2•4+}$ and **Rot-7**$^{2•4+}$ before (c) and after (d) oxidation with 1 equivalent of $Fe(ClO_4)_3$, at 328 K in ACN.

group (**N_3-P5A**) was reacted through CuAAC by reaction with alkyne nitroxide to afford the first example of spin-labelled pilla[5]arene (**P5A-1**).[93]

Pillar[n]arenes show an electron-donating cavity and interesting host–guest properties with electron-accepting molecules such as viologen and pyridinium derivatives,[90,94] imidazolium cations[95] and bis(imidazolium) dications[96] in organic media. The inclusion complexes of such compounds with pillar[5]-arene are characterized by relatively high binding constants (*ca.* 10^3–10^4 M^{-1}).

To test the host properties of paramagnetic **P5A-1** (Scheme 8.13), the complexation of 4-methyl-*N*-butylpiridinum–PF_6 salt as a model guest was investigated by ^{1}H NMR titration in $CDCl_3$. The experiment could be easily

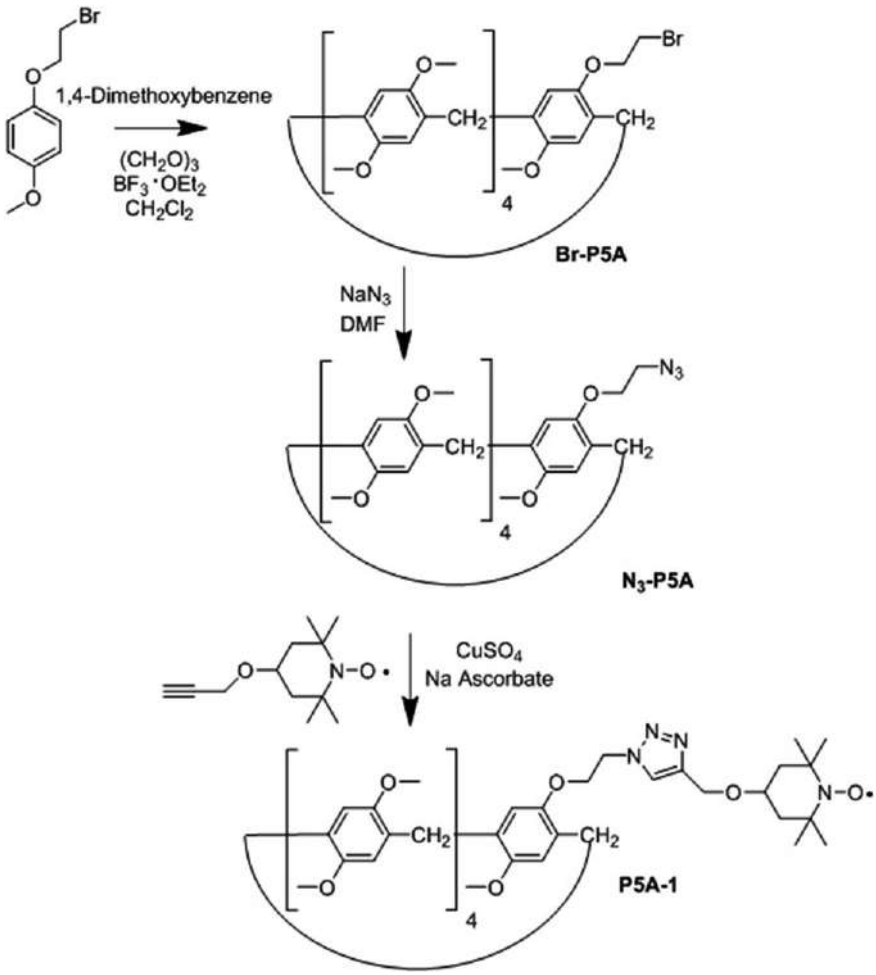

Scheme 8.13 Synthesis of the spin-labelled pillar[5]arene **P5A-1**.

performed in the presence of the paramagnetic centre by following the remarkable upfield shifts of both the aromatic protons and the methylene protons of the guest after the complexation process.

An association constant of 2572 M^{-1} in $CDCl_3$ was calculated from a curve-fitting analysis of the data. These values, compared with the value of 2197 M^{-1} measured in $CDCl_3$ with the unfunctionalized pillar[5]arene under the same experimental conditions show that the paramagnetic arm does not hinder complexation processes.[93]

8.3.5 Spin-labelled Crown Ethers and Cryptands

Several examples of spin-labelled crown ethers and cryptands have been reported in the past (Figure 8.18).[97–102] They were used to monitor the

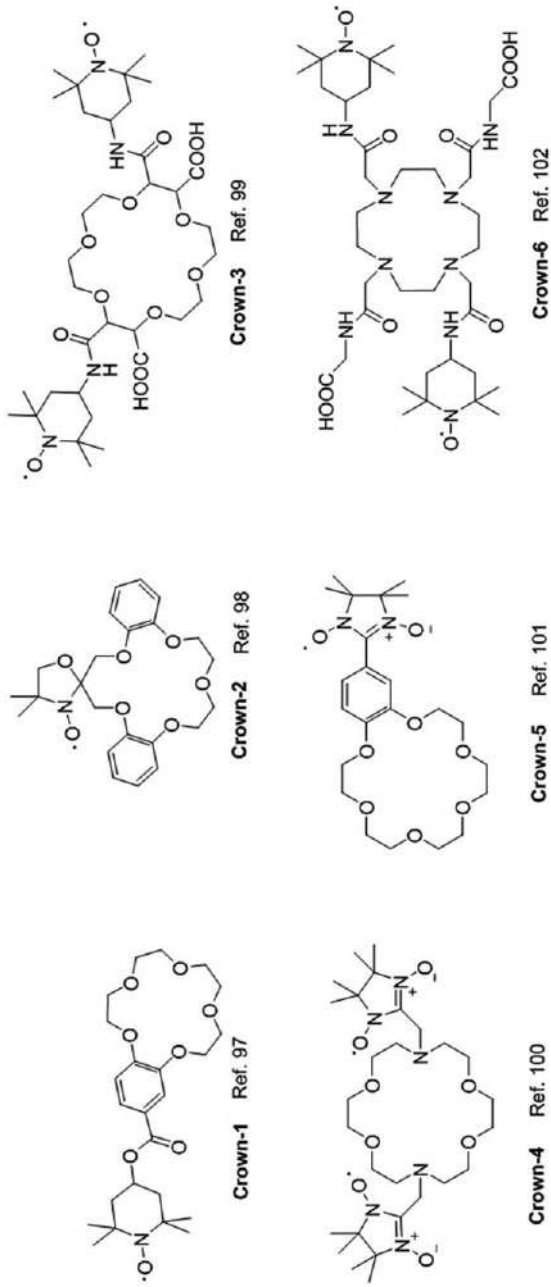

Figure 8.18 Structures of spin-labelled crown ethers.

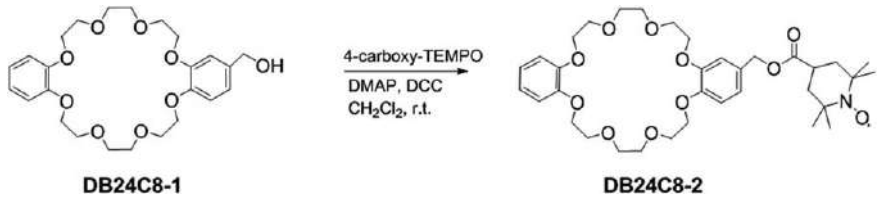

Scheme 8.14 Synthesis and structure of the paramagnetic crown ether **DB24C8-2**.

formation of complexes with cations by EPR spectroscopy in an organic solvent. As a selected example, diazacrown **Crown-4** showed a remarkable sensitivity to the presence of alkali metal cations as a consequence of the change in the degree of spin exchange between the two aminoxyl units after metal complexation.

More recently, the first example of a [2]rotaxane incorporating a spin-labelled crown ether has been reported.[103] The paramagnetic crown ether **DB24C8-2** was prepared in good yield by using 4-carboxy-TEMPO and dibenzo[24]crown-8 ring alcohol derivative (**DB24C8-1**) in the presence of *N,N′*-dicyclohexylcarbodiimide (DCC) and 4-dimethylaminopyridine (DMAP) as the condensing reagents (Scheme 8.14).

The spin-labelled crown ether **DB24C8-2** was then rotaxanated by incorporating a dumbbell containing a terminal TEMPO unit (**Rot-11H**$^{3+}$, Figure 8.19).[103] The dumbbell component possesses a dialkylammonium and a 4,4′-bipyridinium (BPY^{2+}) recognition site.

Deprotonation of the rotaxane NH_2^+ groups results in a quantitative displacement of the DB24C8 ring to the BPY^{2+} recognition site, a process that can be reversed by acid treatment. Interaction between TEMPO radicals connected to the ring and dumbbell components could be switched reversibly several times between noncoupled (three-line ESR spectrum) and coupled (five-line ESR spectrum) upon displacement of the spin-labelled **DB24C8-2** macrocycle, without an appreciable loss of ESR signal, indicating that this molecular machine is capable of switching on/off magnetic interactions by chemically driven reversible mechanical effects.

In order to limit conformational changes, which can interfere with the primary motion of the molecular machine (the ring shuttling),[104] a methylene unit connecting the aromatic ring and the probe was removed from **DB24C8-2** affording the **DB24C8-3** macrocycle (Figure 8.20).[105]

By using **BDC24C8-3** as a more rigid labelled wheel, the novel rotaxane **Rot-12H**$^{3+}$ was prepared (Figure 8.21). In this case, conformational changes on the crown ether induced by the shuttling process were demonstrated by performing PELDOR experiments supported by molecular dynamics (MD) calculations.[105]

In particular, the PELDOR constrains to the MD calculations allowed to have a reliable picture of the structural changes promoted by the chemical switching between the **Rot-12H**$^{3+}$ and **Rot-12**$^{2+}$ molecules. The macrocycle goes from a Z-shaped geometry in **Rot-12H**$^{3+}$ (ring on the ammonium site) to

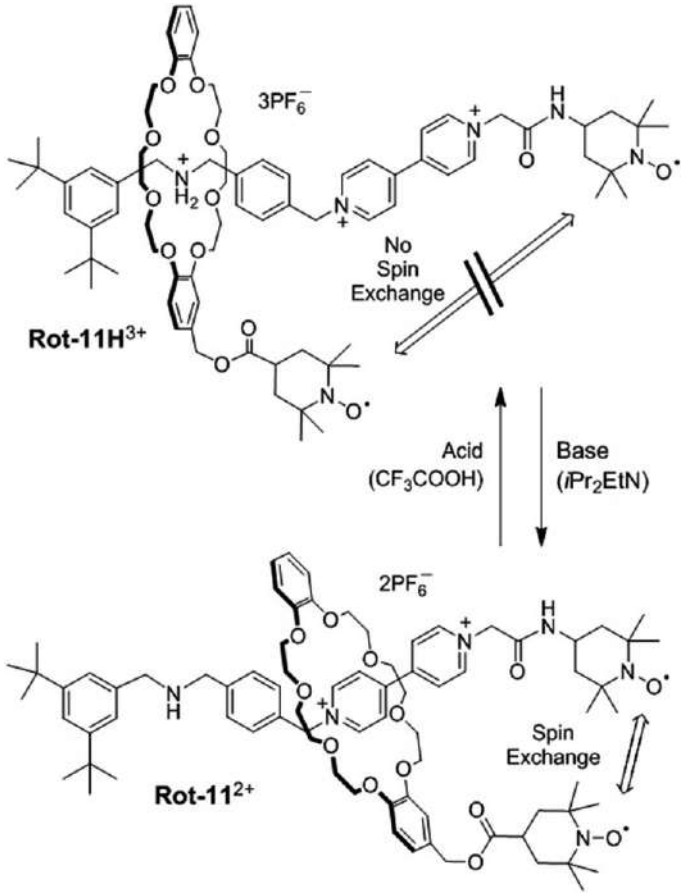

Figure 8.19 Acid–base controlled shuttling in the rotaxane **Rot-11H^{3+}** and schematic representation of the consequent change of distance between the two TEMPO radicals.[103]

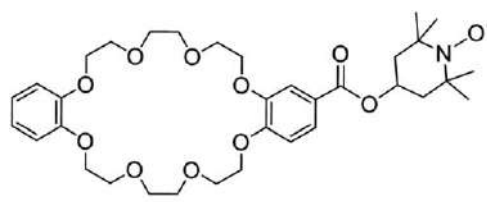

DB24C8-3

Figure 8.20 Structure of spin-labelled **DB24C8-3**.

a V-shaped geometry in **Rot-12^{2+}** (ring on the bipyridinium site). As a result, the distance between the nitroxide labels (Figure 8.22) is not significantly affected by ring shuttling and remains quite large (22.6 Å and 24.2 Å for

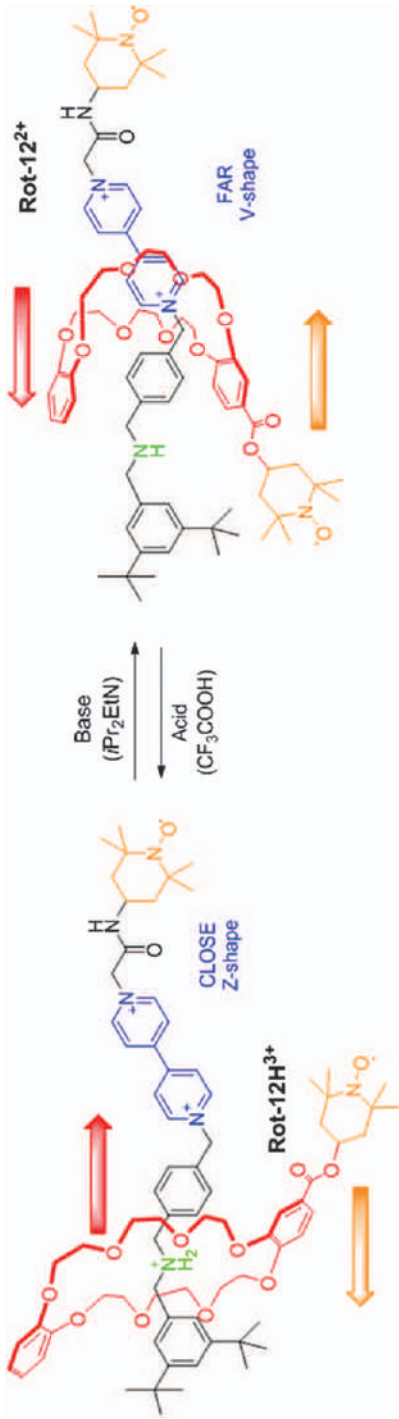

Figure 8.21 Conformational change of the crown ether in the chemical-induced shuttling of the ring in **Rot-12H**$^{3+}$.

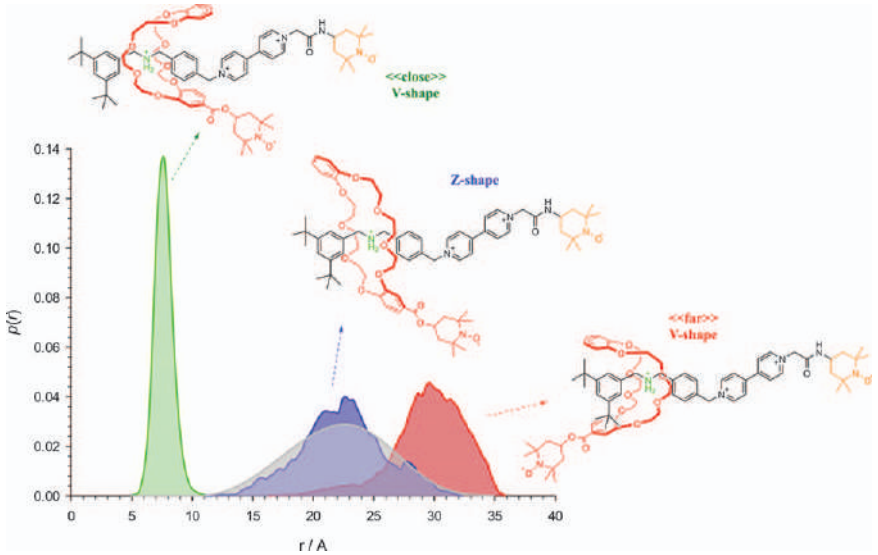

Figure 8.22 Experimental (determined by PELDOR, grey) and theoretical (MD calculations) label-to-label distance distributions of the [2]rotaxane **Rot-12H**$^{3+}$ (when the ring is on NH_2^+ station) in frozen ACN solution.

Rot-12H^{3+} and **Rot-12**$^{2+}$, respectively), so that through-space electron exchange interactions are largely prevented as shown by continuous-wave EPR spectra.[105]

The possibility to afford dialkyl nitroxide radicals bringing a DB24C8 group was recently investigated.[106] These wheels (**DB24C8-4**, Scheme 8.15), that can be easily generated by *in situ* oxidation of the corresponding amine precursor with 3-chloroperbenzoic acid (MCPBA), provide favourable EPR features as previously described for the related benzyl *tert*-butyl nitroxide. In particular EPR coupling constants of benzylic protons are affected by cationic binding, which leads to distinguishing between different cationic guests. The amount of cations in the order of mM concentrations can easily be detected by this method.

The general good agreement with quantitative data previously determined suggests that EPR can be usefully employed to study complexation by crown ethers even in supramolecular systems of higher complexity when traditional methods based on NMR or fluorescence cannot be applied.

By adapting the original procedure proposed by Keana *et al.*[107] a new crown-ether wheel incorporating a dialkyl nitroxide functionality (**34**, Scheme 8.16) inside a ring has been recently proposed as a novel paramagnetic macrocycle.[108] An important step of this synthesis concerns the reaction of nitrone **32** with MeLi that provided hydroxylamine derivative **33** in quantitative yield as a mixture of *cis* and *trans* isomers in 6.5 : 3.5 molar ratio, as assessed by ^{1}H NMR. The prevalence of *cis* isomer was attributed to the less hindered attack of the organometallic reagent to the nitrone **32** opposite to the bulky phenyl group.

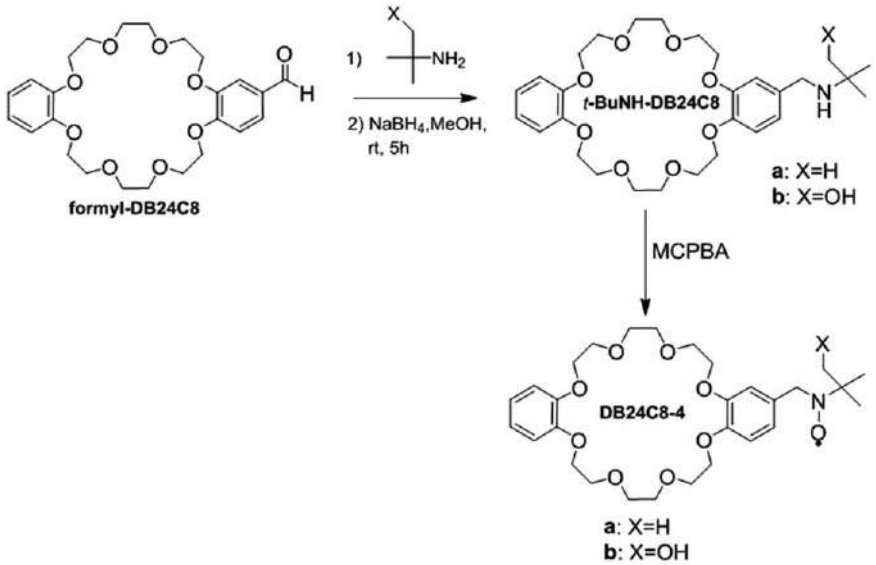

Scheme 8.15 Reaction scheme for the preparation of the paramagnetic macrocycle **DB24C8-4.**

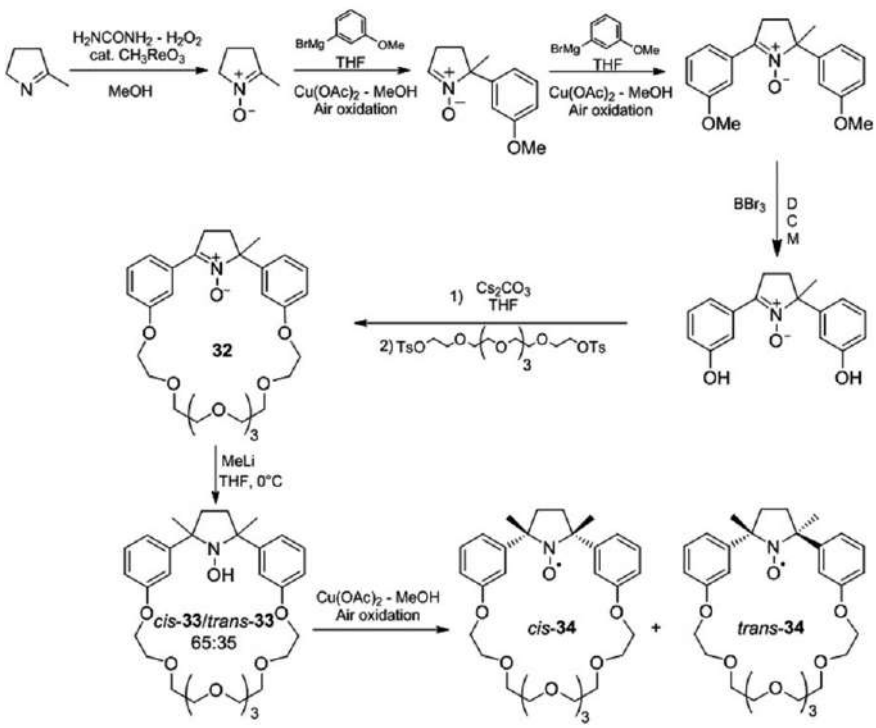

Scheme 8.16 Reaction scheme for the preparation of the paramagnetic macrocycle **34.**

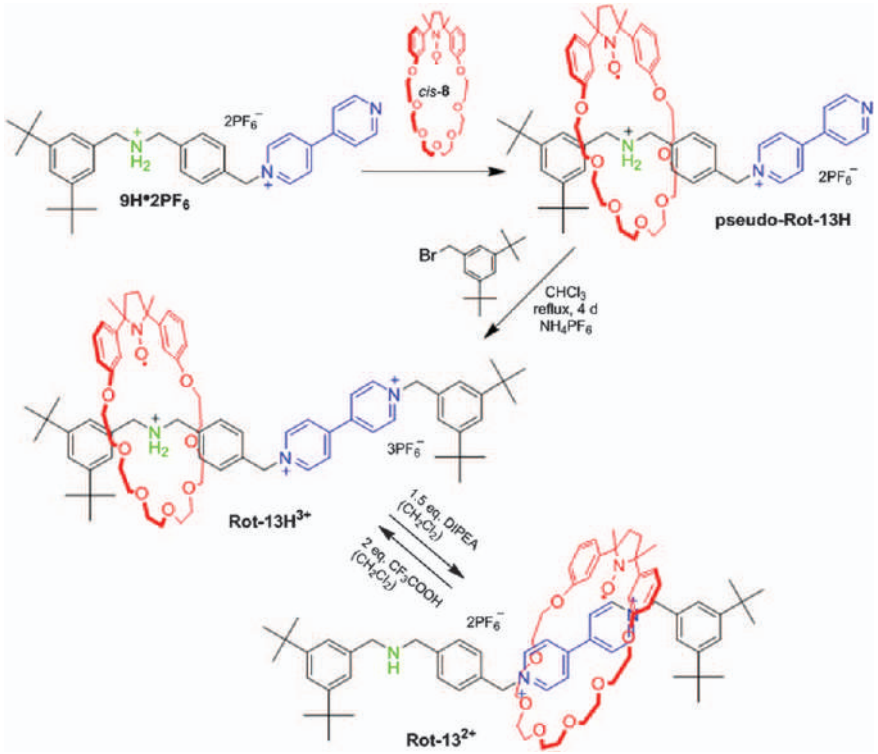

Scheme 8.17 Reaction scheme for the preparation of the rotaxane **Rot-13H**$^{3+}$ and the switching process between **Rot-13H**$^{3+}$ and **Rot-13**$^{2+}$.

The subsequent oxidation of the *cis*/*trans*-**33** gave mainly the *cis* crown ether **34** that was used as the wheel in a novel paramagnetic bistable [2]rotaxane containing dialkylammonium and 4,4′-bipyridinium recognition sites in the dumbbell component (**Rot-13H**$^{3+}$, see Scheme 8.17).

While in all previously reported examples the shuttling process was detected by EPR because of switching between noncoupled (three-line EPR spectrum) and coupled (five-line EPR spectrum) states of nitroxide radicals connected to the ring and dumbbell,[103] in **Rot-13H**$^{3+}$, for the first time, the nitroxide unit acts not only as an EPR probe for the switching, but also interacts with the bipyridinium recognition site of the thread by charge–dipolar interaction. This allows to probe the movement of the macrocycle between the two molecular stations of the [2]rotaxane after addition of a base simply by measuring the nitrogen hyperfine splittings a_N in the corresponding EPR spectra.

8.3.6 Calixarenes and Resorcinarenes

Calixarene macrocycles containing two, four or six nitroxide labels have also been described in the literature.[109] Similar to crown ether, modulation of

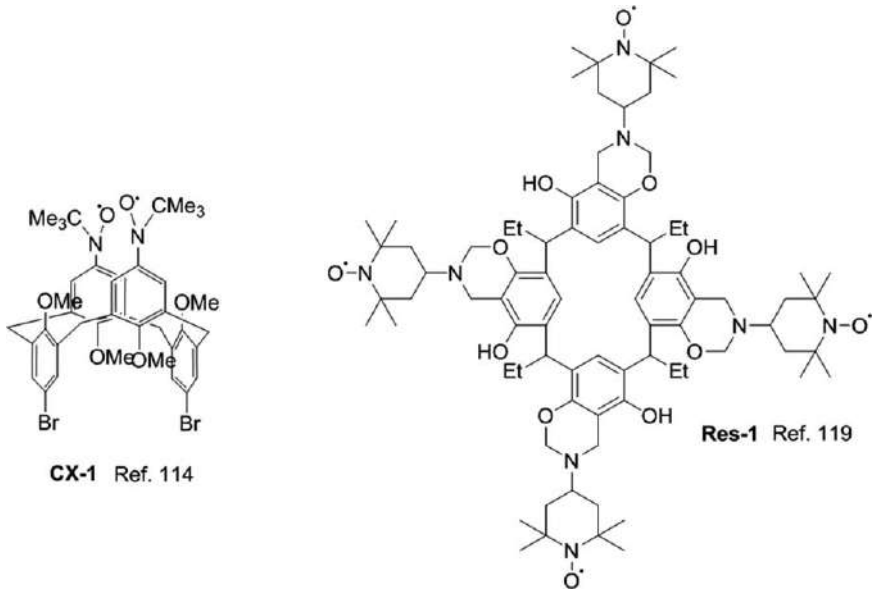

Scheme 8.18 Structure of a representative spin-labelled calixarene and resorcinarene.

spin exchange between aminoxyl units was used to prove complexation of alkali metal,[109] Zn[110] and Ag cations.[111] The presence of spin labels was also used to monitor the exchange process between different macrocycle conformations.[112–114]

Finally, spin-labelled calixarenes were found to have accessible high-spin states, this being an important property for the applications of these macrocycles as molecular magnetic materials.[115–118]

Examples of condensation reactions to introduce nitroxide spin labels were reported for resorcinares. As a selected example, when four equivalents of 4-amino-TEMPO and eight equivalents of formaldehyde are used, complete spin labelling of the four aromatic rings is observed with resorcin[4]arene (**Res-1**, Scheme 8.18).[119]

8.4 Conclusion

The reported examples showed that nitroxides represent useful probes for the investigation of noncovalent assemblies, and we expect that these open-shell molecules, in conjunction with EPR spectroscopy, will continue to represent a valuable tool in the field of supramolecular chemistry. In particular, the development of mechanically interlocked paramagnetic molecules in which the nitroxide moiety behaves as a recognition site for the formation of supramolecular assembly, the development of sophisticated spin traps based on the coupling of nitrones with macrocyclic compounds and applications of host–guest chemistry to tune nitroxide properties (like in

bioimaging or dynamic nuclear polarization/NMR) will be the subject of significant improvements in the next few years. The combined use of nitroxides and PELDOR or multifrequency EPR experiments (at the moment rarely explored) can also be expected to be particularly useful for the characterization of host–guest complexes.

Acknowledgements

This work was supported by the University of Bologna.

References

1. *Electron Paramagnetic Resonance: a Practitioner's Toolkit*, ed. M. Brustolon and E. Giamello, John Wiley & Sons Inc., Hoboken, New Jersey, 2009.
2. M. Lucarini and E. Mezzina, *Electron Paramagn. Reson.*, 2010, **22**, 41.
3. P. Franchi, M. Lucarini and G. F. Pedulli, *Curr. Org. Chem.*, 2004, **8**, 1831.
4. M. Lucarini in *Encyclopedia of Radicals in Chemistry, Biology and Materials*, ed. C. Chatgilialoglu and A. Studer, Wiley, Chichester, Vol. 2, 2012, p. 229.
5. D. Bardelang, M. Hardy, O. Ouari and P. Tordo, in *Encyclopedia of Radicals in Chemistry, Biology and Materials*, ed. C. Chatgilialoglu and A. Studer, Wiley, Chichester, Vol. 4, 2012, p. 1.
6. E. Mezzina, R. Manoni, F. Romano and M. Lucarini, *Asian J. Org. Chem.*, 2015, **4**, 296.
7. E. G. Bagryanskaya and S. R. A. Marque, *Electron Paramagn. Reson.*, 2017, **25**, 180.
8. C. J. Bruns and J. F. Stoddart, *The Nature of the Mechanical Bond: From Molecules to Machines*, John Wiley & Sons, Inc., Hoboken, New Jersey, 2017.
9. G. Crini, *Chem. Rev.*, 2014, **114**, 10940.
10. S. J. Barrow, S. Kasera, M. J. Rowland, J. del Barrio and O. A. Scherman, *Chem. Rev.*, 2015, **115**, 12320.
11. O. Ouari and D. Bardelang, *Isr. J. Chem.*, 2018, **58**, 343.
12. *Calixarenes and Beyond*, ed. P. Neri, J. L. Sessler and M.-X. Wang, Springer, 2016.
13. M. M. Conn and J. Rebek, *Chem. Rev.*, 1997, **97**, 1647.
14. M. Lucarini and L. Pasquato, *Nanoscale*, 2010, **2**, 668.
15. J. Martinie, J. Minchon and A. Rassat, *J. Am. Chem. Soc.*, 1975, **97**, 1818.
16. L. Gare, H. Vezin, J.-P. Dutasta and A. Collet, *Chem. Commun.*, 1996, 719.
17. E. Mezzina, F. Cruciani, G. F. Pedulli and M. Lucarini, *Chem. - Eur. J.*, 2007, **13**, 7223.
18. E. Mileo, S. Yi, P. Bhattacharya and A. E. Kaifer, *Angew. Chem., Int. Ed.*, 2009, **48**, 5337.

19. E. G. Bagryanskaya, D. N. Polovyanenko, M. V. Fedin, L. Kulik, A. Schnegg, A. Savitsky, K. Möbius, A. W. Coleman, G. S. Ananchenko and J. A. Ripmeester, *Phys. Chem. Chem. Phys.*, 2009, **11**, 6700.
20. J. Y.-C. Chen, N. Jayaraj, S. Jockusch, M. F. Ottaviani, V. Ramamurthy and N. J. Turro, *J. Am. Chem. Soc.*, 2008, **130**, 7206.
21. G. Ionita, A. Caragheorgheopol, H. Caldararu, L. Jones and V. Chechik, *Org. Biomol. Chem.*, 2009, **7**, 598.
22. B. Dzikovski, D. Tipikin, V. Livshits, K. Earle and J. Freed, *Phys. Chem. Chem. Phys.*, 2009, **11**, 6676.
23. G. Ionita, A. M. Madalan, A. M. Ariciu, A. Medvedovici and P. Ionita, *New J. Chem.*, 2016, **40**, 503.
24. G. Casano, F. Poulhe's, T. K. Tran, M. M. Ayhan, H. Karoui, D. Siri, A. Gaudel-Siri, A. Rockenbauer, G. Jeschke, D. Bardelang, P. Tordo and O. Ouari, *Nanoscale*, 2015, **7**, 12143.
25. S. Yi, B. Captain and A. E. Kaifer, *Chem. Commun.*, 2011, **47**, 5500.
26. M. P. Eastman, B. Freiha, C. C. Hsu and C. Allen Chang, *J. Phys. Chem.*, 1988, **92**, 1682.
27. M. Spulber, S. Schlick and F. A. Villamena, *J. Phys. Chem. A*, 2012, **116**, 8475.
28. E. V. Peresypkina, V. P. Fedin, V. Maurel, A. Grand, P. Rey and K. E. Vostrikova, *Chem. - Eur. J.*, 2010, **16**, 12481.
29. I. Kirilyuk, D. Polovyanenko, S. Semenov, I. Grigor'ev, O. Gerasko, V. Fedin and E. G. Bagryanskaya, *J. Phys. Chem. B*, 2010, **114**, 1719.
30. S. S. Eaton, A. Rajca, Z. Yang and G. R. Eaton, *Free Radical Res.*, 2018, **52**, 319.
31. C. Heller and H. M. McConnell, *J. Chem. Phys.*, 1960, **32**, 1535.
32. Y. Kotake and E. G. Janzen, *J. Am. Chem. Soc.*, 1988, **110**, 3699.
33. K. Miyazono, T. Hanaya and Y. Sueishi, *J. Inclusion Phenom. Macrocyclic Chem.*, 2015, **83**, 193.
34. H. Karoui, A. Rockenbauer, S. Pietri and P. Tordo, *Chem. Commun.*, 2002, 3030.
35. G. S. Ananchenko, K. A. Udachin, A. W. Coleman, D. N. Polovyanenko, E. G. Bagryanskaya and J. A. Ripmeester, *Chem. Commun.*, 2008, 223.
36. M. Lucarini and B. P. Roberts, *Chem. Commun.*, 1996, 1577.
37. P. Franchi, M. Lucarini, G. F. Pedulli and D. Sciotto, *Angew. Chem., Int. Ed.*, 2000, **39**, 263.
38. M. Lucarini, P. Franchi, G. F. Pedulli, P. Pengo, P. Scrimin and L. Pasquato, *J. Am. Chem. Soc.*, 2004, **126**, 9326.
39. M. Lucarini, P. Franchi, G. F. Pedulli, C. Gentilini, P. Polizzi, P. Pengo, P. Scrimin and L. Pasquato, *J. Am. Chem. Soc.*, 2005, **127**, 16384.
40. C. Gentilini, F. Evangelista, P. Rudolf, P. Franchi, M. Lucarini and L. Pasquato, *J. Am. Chem. Soc.*, 2008, **130**, 15678.
41. C. Gentilini, P. Franchi, E. Mileo, S. Polizzi, M. Lucarini and L. Pasquato, *Angew. Chem., Int. Ed.*, 2009, **48**, 3060.
42. M. Boccalon, S. Bidoggia, F. Romano, L. Gualandi, P. Franchi, M. Lucarini, P. Pengo and L. Pasquato, *J. Mater. Chem. B*, 2015, **3**, 432.

43. P. Franchi, C. Casati, E. Mezzina and M. Lucarini, *Org. Biomol. Chem.*, 2011, **9**, 6396.
44. L. Gualandi, E. Mezzina, P. Franchi and M. Lucarini, *Chem. - Eur. J.*, 2016, **22**, 16017.
45. P. Franchi, M. Lucarini, E. Mezzina and G. F. Pedulli, *J. Am. Chem. Soc.*, 2004, **126**, 4343.
46. M. Lucarini, B. Luppi, G. F. Pedulli and B. P. Roberts, *Chem. - Eur. J.*, 1999, **5**, 2048.
47. E. Mileo, P. Franchi, R. Gotti, C. Bendazzoli, E. Mezzina and M. Lucarini, *Chem. Commun.*, 2008, 1311.
48. G. Cavallo, P. Metrangolo, R. Milani, T. Pilati, A. Priimagi, G. Resnati and G. Terraneo, *Chem. Rev.*, 2016, **116**, 2478.
49. M. Abe, *Chem. Rev.*, 2013, **113**, 7011.
50. M. Porel, M. F. Ottaviani, S. Jockusch, N. J. Turro and V. Ramamurthy, *RSC Adv.*, 2013, **3**, 427.
51. X. Tan, Y. Song, H. Liu, Q. Zhong, A. Rockenbauer, F. A. Villamena, J. L. Zweier and Y. Liu, *Org. Biomol. Chem.*, 2016, **14**, 1694.
52. M. Porel, M. F. Ottaviani, S. Jockusch, N. Jayaraj, N. J. Turro and V. Ramamurthy, *Chem. Commun.*, 2010, 7736.
53. E. Mileo, C. Casati, P. Franchi, E. Mezzina and M. Lucarini, *Org. Biomol. Chem.*, 2011, **9**, 2920.
54. D. Bardelang, G. Casano, F. Poulhe's, H. Karoui, J. Filippini, A. Rockenbauer, R. Rosas, V. Monnier, D. Siri, A. Gaudel-Siri, O. Ouari and P. Tordo, *J. Am. Chem. Soc.*, 2014, **136**, 17570.
55. S. Yi, B. Captain, M. F. Ottaviani and A. E. Kaifer, *Langmuir*, 2011, **27**, 5624.
56. G. Ionita, A. M. Madalan, A. M. Ariciu, A. Medvedovici and P. Ionita, *New J. Chem.*, 2016, **40**, 503.
57. G. Jeschke and A. Godtwhile, *ChemPhysChem*, 2003, **4**, 1328.
58. E. Mezzina, M. Fanì, F. Ferroni, P. Franchi, M. Menna and M. Lucarini, *J. Org. Chem.*, 2006, **71**, 3773.
59. V. N. Parmon, A. I. Kokorin, G. M. Zhidomirov and K. I. Zamarev, *Mol. Phys.*, 1975, **30**, 695.
60. R. Manoni, F. Romano, C. Casati, P. Franchi, E. Mezzina and M. Lucarini, *Org. Chem. Front.*, 2014, **1**, 477.
61. A. C. Fahrenbach, C. J. Bruns, D. Cao and J. F. Stoddart, *Acc. Chem. Res.*, 2012, **45**, 1581.
62. F. Romano, R. Manoni, P. Franchi, E. Mezzina and M. Lucarini, *Chem. - Eur. J.*, 2015, **21**, 2775.
63. (a) R. Pievo, C. Casati, P. Franchi, E. Mezzina, M. Bennati and M. Lucarini, *ChemPhysChem*, 2012, **13**, 2659; (b) M.-E. Boulon, A. Fernandez, E. M. Pineda, N. F. Chilton, G. Timco, A. J. Fielding and R. E. P. Winpenny, *Angew. Chem., Int. Ed.*, 2017, **56**, 3876.
64. E. Mileo, E. Mezzina, F. Grepioni, G. F. Pedulli and M. Lucarini, *Chem. - Eur. J.*, 2009, **15**, 7859.

65. D. Bardelang, K. Banaszak, H. Karoui, A. Rockenbauer, M. Waite, K. Udachin, J. A. Ripmeester, C. I. Ratcliffe, O. Ouari and P. Tordo, *J. Am. Chem. Soc.*, 2009, **131**, 5402.
66. N. Jayaraj, M. Porel, M. F. Ottaviani, M. V. S. N. Maddipatla, A. Modelli, J. P. Da Silva, B. R. Bhogala, B. Captain, S. Jockusch, N. J. Turro and V. Ramamurthy, *Langmuir*, 2009, **25**, 13820.
67. S. Combes, K. T. Tran, M. M. Ayhan, H. Karoui, A. Rockenbauer, A. Tonetto, V. Monnier, L. Charles, R. Rosas, S. Viel, D. Siri, P. Tordo, S. Clair, R. Wang, D. Bardelang and O. Ouari, *J. Am. Chem. Soc.*, 2019, **141**, 5897.
68. C. Graziano, S. Pieraccini, S. Masiero, M. Lucarini and G. P. Spada, *Org. Lett.*, 2008, **10**, 1739.
69. M. Vasilescu, E. Pincu, V. Meltzer and G. Ionita, *New J. Chem.*, 2012, **36**, 2128.
70. S. Mocanu, I. Matei, S. Ionescu, V. Tecuceanu, G. Marinescu, P. Ionita, D. Culita, A. Leonties and G. Ionita, *Phys. Chem. Chem. Phys.*, 2017, **19**, 27839.
71. R. M. Paton and E. T. Kaiser, *J. Am. Chem. Soc.*, 1970, **92**, 4723.
72. G. Ionita and V. Chechik, *Org. Biomol. Chem.*, 2005, **3**, 3096.
73. R. K. Strizhakov, E. V. Tretyakov, A. S. Medvedeva, V. V. Novokshonov, V. G. Vasiliev, V. I. Ovcharenko, O. A. Krumkacheva, M. V. Fedin and E. G. Bagryanskaya, *Appl. Magn. Reson.*, 2014, **45**, 1087.
74. V. Chechik and G. Ionita, *Org. Biomol. Chem.*, 2006, **4**, 3505.
75. (a) G. Ionita and V. Chechik, *Chem. Commun.*, 2010, **46**, 8255; (b) G. Ionita, M. Florent, D. Goldfarb and V. Chechik, *J. Phys. Chem. B*, 2009, **113**, 5781.
76. V. Chechik and G. Ionita, *New J. Chem.*, 2007, **31**, 1726.
77. (a) D. Bardelang, A. Rockenbauer, L. Jicsinszky, J.-P. Finet, H. Karoui, S. Lambert, S. R. A. Marque and P. Tordo, *J. Org. Chem.*, 2006, **71**, 7657; (b) D. Bardelang, J.-P. Finet, L. Jicsinszky, H. Karoui, S. R. A. Marque, A. Rockenbauer, R. Rosas, L. Charles, V. Monnier and P. Tordo, *Chem. – Eur. J.*, 2007, **13**, 9344; (c) E. G. Bagryanskaya, D. Bardelang, S. Chenesseau, J. P. Finet, L. Jicsinszky, H. Karoui, S. R. A. Marque, K. Möbius, D. Polovyanenko, A. Savitsky and P. Tordo, *Appl. Magn. Reson.*, 2009, **36**, 181.
78. (a) Y. Han, B. Tuccio, R. Lauricella and F. A. Villamena, *J. Org. Chem.*, 2008, **73**, 7108; (b) Y. Han, Y. Liu, A. Rockenbauer, J. L. Zweier, G. Durand and F. A. Villamena, *J. Org. Chem.*, 2009, **74**, 5369.
79. (a) M. Hardy, D. Bardelang, H. Karoui, A. Rockenbauer, J.-P. Finet, L. Jicsinszky, R. Rosas, O. Ouari and P. Tordo, *Chem. – Eur. J.*, 2009, **15**, 11114; (b) F. Poulhès, E. Rizzato, P. Bernasconi, R. Rosas, S. Viel, L. Jicsinszky, A. Rockenbauer, D. Bardelang, D. Siri, A. Gaudel-Siri, H. Karoui, M. Hardy and O. Ouari, *Org. Biomol. Chem.*, 2017, **15**, 6358.
80. O. A. Krumkacheva, M. V. Fedin, D. N. Polovyanenko, L. Jicsinszky, S. R. A. Marque and E. G. Bagryanskaya, *J. Phys. Chem. B*, 2013, **117**, 8223.

81. F. Caglieris, L. Melone, F. Canepa, G. Lamura, F. Castiglione, M. Ferro, L. Malpezzi, A. Mele, C. Punta, P. Franchi, M. Lucarini, B. Rossi and F. Trotta, *RSC Adv.*, 2015, **5**, 76133.
82. P. Franchi, M. Fanì, E. Mezzina and M. Lucarini, *Org. Lett.*, 2008, **10**, 1901.
83. C. Casati, P. Franchi, R. Pievo, E. Mezzina and M. Lucarini, *J. Am. Chem. Soc.*, 2012, **134**, 19108.
84. (a) H. C. Kolb, M. G. Finn and K. B. Sharpless, *Angew. Chem., Int. Ed.*, 2001, **40**, 2004; (b) V. V. Rostovtsev, L. G. Green, V. V. Fokin and K. B. Sharpless, *Angew. Chem., Int. Ed.*, 2002, **41**, 2596.
85. M. Chwalek, R. Auzély and S. Fort, *Org. Biomol. Chem.*, 2009, **7**, 1680.
86. J. Luo, C. Pardin, W. D. Lubell and X. X. Zhu, *Chem. Commun.*, 2007, 2136.
87. V. Balzani, A. Credi, F. M. Raymo and J. F. Stoddart, *Angew. Chem., Int. Ed.*, 2000, **39**, 3349.
88. A. Margotti, C. Casati, M. Lucarini and E. Mezzina, *Tetrahedron Lett.*, 2008, **49**, 4784.
89. V. Bleve, P. Franchi, L. Gualandi, F. Romano, E. Mezzina and M. Lucarini, *Org. Chem. Front.*, 2018, **5**, 1579.
90. T. Ogoshi, S. Kanai, S. Fujinami, T. A. Yamagishi and Y. Nakamoto, *J. Am. Chem. Soc.*, 2008, **130**, 5022.
91. (a) M. Xue, Y. Yang, X. Chi, Z. Zhang and F. Huang, *Acc. Chem. Res.*, 2012, **45**, 1294; (b) P. J. Cragg and K. Sharma, *Chem. Soc. Rev.*, 2012, **41**, 597; (c) T. Ogoshi and T. A. Yamagishi, *Eur. J. Org. Chem.*, 2013, 2961.
92. N. L. Strutt, R. S. Forgan, J. M. Spruell, Y. Y. Botros and J. F. Stoddart, *J. Am. Chem. Soc.*, 2011, **133**, 5668.
93. R. Manoni, P. Neviani, P. Franchi, E. Mezzina and M. Lucarini, *Eur. J. Org. Chem.*, 2014, 147.
94. (a) C. Li, Q. Xu, J. Li, Y. Feina and X. Jia, *Org. Biomol. Chem.*, 2010, **8**, 1568; (b) T. Ogoshi, D. Yamafuji, T. Aoki and T. A. Yamagishi, *J. Org. Chem.*, 2011, **76**, 9497.
95. T. Ogoshi, S. Tanaka, T. A. Yamagishi and Y. Nakamoto, *Chem. Lett.*, 2011, **40**, 96.
96. C. Li, L. Zhao, J. Li, X. Ding, S. Chen, Q. Zhang, Y. Yu and X. Jia, *Chem. Commun.*, 2010, **46**, 9016.
97. K. Ishizu, H. Kohama and K. Mukai, *Chem. Lett.*, 1978, 227.
98. M. P. Eastman, D. E. Patterson, R. A. Bartsch, Y. Liu and P. G. Eller, *J. Phys. Chem.*, 1982, **86**, 2052.
99. H. Dugas and M. Ptak, *J. Chem. Soc., Chem. Commun.*, 1982, 710.
100. G. Ulrich, P. Turek, R. Ziessel, A. De Cian and J. Fischer, *Chem. Commun.*, 1996, 2461.
101. Y. Kanzaki, T. Ise, D. Shiomi, K. Sato and T. Takui, *Synth. Met.*, 2005, **154**, 293.
102. S. J. Ratnakar, T. C. Soesbe, L. Laporca Lumata, Q. Do, S. Viswanathan, C.-Y. Lin, A. D. Sherry and Z. Kovacs, *J. Am. Chem. Soc.*, 2013, **135**, 14904.

103. V. Bleve, C. Schäfer, P. Franchi, S. Silvi, E. Mezzina, A. Credi and M. Lucarini, *ChemistryOpen*, 2015, **4**, 18.
104. (a) S. Saha, A. H. Flood, J. F. Stoddart, S. Impellizzeri, S. Silvi, M. Venturi and A. Credi, *J. Am. Chem. Soc.*, 2007, **129**, 12159; (b) M. Woźny, J. Pawłowska, A. Osior, P. Świder, R. Bilewicz and B. Korybut-Daszkiewicza, *Chem. Sci.*, 2014, **5**, 2836.
105. P. Franchi, V. Bleve, E. Mezzina, C. Schäfer, G. Ragazzon, M. Albertini, D. Carbonera, A. Credi, M. Di Valentin and M. Lucarini, *Chem. – Eur. J.*, 2016, **22**, 8745.
106. L. Gualandi, P. Franchi, A. Credi, E. Mezzina and M. Lucarini, *Phys. Chem. Chem. Phys.*, 2019, **21**, 3558.
107. J. F. W. Keana, J. Cuomo, L. Lex and S. E. Seyedrezai, *J. Org. Chem.*, 1983, **48**, 2647.
108. V. Bleve, P. Franchi, E. Konstanteli, L. Gualandi, S. M. Goldup, E. Mezzina and M. Lucarini, *Chem. - Eur. J.*, 2018, **24**, 1198.
109. K. Araki, R. Nakamura, H. Otsuka and S. Shinkai, *J. Chem. Soc., Chem. Commun.*, 1995, 2121.
110. G. Ulrich, P. Turek and R. Ziessel, *Tetrahedron Lett.*, 1996, **37**, 8755.
111. X. Hu, H. Yang and Y. Li, *Spectrochim. Acta, Part A*, 2008, **70**, 439.
112. Q. Wang, Y. Li and G.-S. Wu, *Chem. Commun.*, 2002, 1268.
113. X. Hu, Y. Li, H. Yang and Y. Luo, *Tetrahedron Lett.*, 2006, **47**, 7463.
114. Y. Li and H. Yang, *Chem. Lett.*, 2010, **39**, 796.
115. T. Sawai, K. Sato, T. Ise, D. Shiomi, K. Toyota, Y. Morita and T. Takui, *Angew. Chem., Int. Ed.*, 2008, **47**, 3988.
116. A. Rajca, M. Pink, T. Rojsajjakul, K. Lu, H. Wang and S. Rajca, *J. Am. Chem. Soc.*, 2003, **125**, 8534.
117. A. Rajca, S. Mukherjee, M. Pink and S. Rajca, *J. Am. Chem. Soc.*, 2006, **128**, 13497.
118. A. Rajca, M. Pink, S. Mukherjee, S. Rajca and K. Das, *Tetrahedron*, 2007, **63**, 10731.
119. L. Kröck, A. Shivanyuk, D. B. Goodin and J. Rebek, Jr, *Chem. Commun.*, 2004, 272.

CHAPTER 9

Magnetism of Nitroxides

ANDRZEJ RAJCA

University of Nebraska, Department of Chemistry, Lincoln,
Nebraska 68588, USA
Email: arajca1@unl.edu

9.1 Introduction

Nitroxides are organic radicals with excellent stability that enable a wide range of applications in polymer science, synthesis, catalysis, organic materials, biophysics and biomedicine. While the radicals are mostly stabilized by steric shielding of the unpaired electron, nitroxide stability is imparted by the resonance delocalization of the unpaired electron over the N–O bond. In nitroxides, the paramagnetic N–O moiety is very much tolerant to various conditions that enable the practical use of the radicals. Because their structural and functional diversity can be achieved by organic synthesis, nitroxides are attractive for studying molecular magnetism. Nitroxides are perhaps the most investigated organic radicals in the development of molecule-based magnets. This chapter provides an overview of the molecular design and characterization of high-spin nitroxide radicals, with strong through-bond ferromagnetic exchange couplings, in relation to organic magnetism.

9.2 High-spin Diradicals and Polyradicals

Organic molecules with high-spin ground states (total spin quantum number $S \geq 1$) are of interest as basic building blocks for organic magnets[1–5] and for potential applications in spintronics,[6–8] dynamic nuclear polarization (DNP) NMR[9] and organic paramagnetic relaxation reagents,[10] including

Nitroxides
Edited by Olivier Ouari and Didier Gigmes

Published by the Royal Society of Chemistry, www.rsc.org

contrast agents in magnetic resonance imaging (MRI).[11–14] These applications emanate from the enhanced paramagnetic properties, which scale with the $S(S+1)$ factor, but to realize the potential of high-spin molecules, the following two conditions must be fulfilled:

(1) the high-spin ground state is at least a couple of kcal mol^{-1} [$\gg$0.6 kcal mol^{-1} $\approx$ thermal energy (RT) at room temperature] below the nearest low-spin excited state,[15,16]
(2) the molecule should be persistent at room temperature or better, at ambient conditions and at elevated temperature.

9.3 Design and Characterization of High-spin Nitroxide Diradicals and Polyradicals

Organic radicals, which possess one unpaired electron, may be viewed as the primary organic spin-bearing units or spin centers (SCs) with $S = 1/2$. For nitroxides, the two-atom N–O moiety may be viewed as an SC, as the spin densities at both O and N atoms are positive and about equal.[17] In the molecular design of high-spin organic molecules, the goal is to conjugate multiple SCs, in such a way that the spins couple ferromagnetically, to provide a high-spin ($S \geq 1$) ground state. This ferromagnetic interaction should ideally be sufficiently strong to produce a large separation in energy between the high-spin ground state and low-spin excited states. In a diradical, the singlet triplet energy gap (ΔE_{ST}) is determined by the exchange coupling constant (J), which is given by a simplified Heisenberg–Hamiltonian for two electrons,[18,19] typically expressed as

$$H = -2JS_1 \times S_2 \tag{9.1}$$

where the singlet–triplet energy gap, $\Delta E_{ST} = 2J$.

In planar π-conjugated diradicals, the through-bond exchange couplings between SCs are dominant. The coupling can be either ferromagnetic ($J > 0$) or antiferromagnetic ($J < 0$). Ferromagnetic *vs.* antiferromagnetic exchange coupling between SCs is a function of the π-connectivity and can be qualitatively predicted using Ovchinnikov parity models, where each spin in the π-system is assumed to possess the opposite spin of its nearest neighbor (Figure 9.1).[20] (Similar parity models apply to polyradicals for prediction of through-bond ferromagnetic *vs.* antiferromagnetic exchange coupling between the nearest neighbor SCs.)

We consider non-Kekulé molecules, for which the simplest examples may be illustrated using methyl radicals as SCs and ethylene as a coupling unit. Trimethylenemethane (TMM), the molecule with 1,1-connection of ethylene to methyl radicals, possesses a triplet ($S = 1$) ground state with relatively large $\Delta E_{ST} \approx 16$ kcal mol^{-1}.[21] The nitroxide analogs of TMM, such as Okada's diradicals **1** and **2**, have triplet ground states with smaller $\Delta E_{ST} \approx 1.6$ and 2.2 kcal mol^{-1}, respectively.[22] For non-Kekulé molecule such as

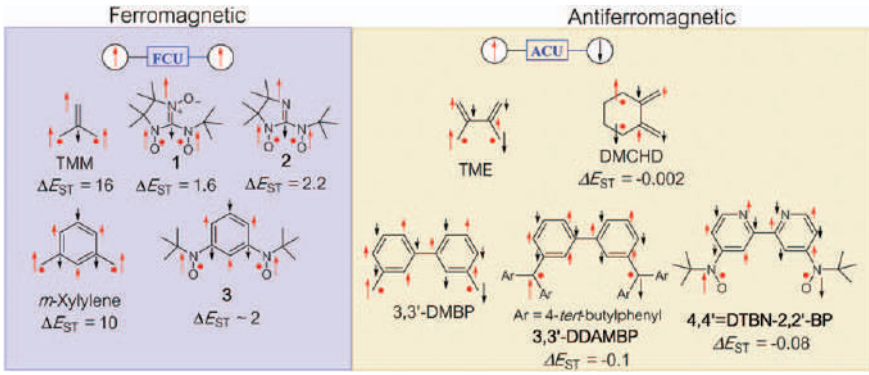

Figure 9.1 Ferromagnetic and antiferromagnetic exchange coupling predicted using parity models in planar π-conjugated non-Kekulé molecules; ΔE_{ST} in kcal mol^{-1}.

tetramethylenethane (TME), the parity models predict a singlet ground state (with a very small $|\Delta E_{ST}|$), which is in agreement with the experimental finding of $\Delta E_{ST} \approx -1$ K $= -0.002$ kcal mol^{-1} for its analogs 2,3-dimethylenecyclohexane-1,4-diyl (DMCHD).[23]

The best-known non-Kekulé molecule, *m*-xylylene, in which the methyl radicals are connected to the *m*-phenylene coupling unit, possesses a triplet ground state with relatively large $\Delta E_{ST} \approx 10$ kcal mol^{-1}.[24] However, analogous nitroxide diradical **3** possesses a much smaller, very approximate $\Delta E_{ST} \approx 2$ kcal mol^{-1}.[25,26] 3,3′-Dimethylenebiphenylene (3,3′-DMBP) diradical, in which two radicals are linked through a 3,3′-biphenylene unit, possesses a singlet ground state with a small $|\Delta E_{ST}|$, as evidenced by the experimental findings of $\Delta E_{ST} \approx -0.1$ and -0.08 kcal mol^{-1} for 3,3′-di[(diaryl)methylene]-biphenylene (**3,3′-DDAMBP**) and 4,4′-di(*tert*-butylnitroxide)-2,2′-bispyridilene (**4,4′-DTBN-2,2′-BP**), respectively.[27,28]

In the parity model, the coupling units that mediated the ferromagnetic coupling between SCs (*e.g.*, *m*-phenylene and 1,1-connected ethylene) are defined as ferromagnetic coupling units (FCUs) and those that mediated antiferromagnetic coupling (*e.g.*, 3.3′-biphenyl, *o*-phenylene, *p*-phenylene) are defined as antiferromagnetic coupling units (ACUs).[29–31]

The simple parity models are a convenient, effective approach for predicting the ground state qualitatively, but they do not address the strength of the exchange coupling, especially in non-Kekulé molecules. The Pauli exclusion principle dictates the electron exchange interactions in organic molecules that lead to either ferromagnetic or antiferromagnetic coupling. Very strong antiferromagnetic coupling is nearly ubiquitous in organic molecules, as they mostly possess a large HOMO–LUMO energy gap. In the case of Kekulé molecules in which the HOMO energy is significantly lower than that of the LUMO, the electron spins of the two electrons that occupy the HOMO must be antiparallel, as dictated by the Pauli exclusion principle. For non-Kekulé diradicals, the energies of frontier MOs are approximately

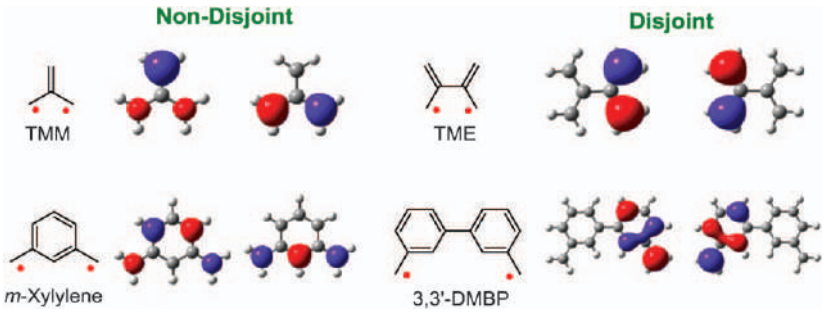

Figure 9.2 Singly occupied MOs (SOMOs) of triplet states for nondisjoint and disjoint non-Kekulé diradicals at the UB3LYP/6-311+G(d,p) level.

equal (near-degenerate MOs), leading to two singly occupied MOs (SOMOs). Borden and Davidson classified the SOMOs that are spatially coinciding at some atoms as ''non-disjoint'' and those that are not spatially coinciding at any atoms as ''disjoint,'' as illustrated for TMM (and *m*-xylylene) and TME (and 3,3′-DMBP) (Figure 9.2).[32]

Very weak exchange coupling is typical for the disjoint SOMOs, which gives rise to a small $|\Delta E_{ST}|$. Presumably, the small exchange coupling through σ-bonds is the origin of a singlet ground state.[29,32] On the other hand, exchange coupling is strong and ferromagnetic for non-disjoint SOMOs. It is apparent that when the two electrons spins are aligned parallel, they introduce a node in the spatial part of the wave function. As a consequence, the Coulombic repulsion within the area of spatial coincidence diminishes, as in the case of an extension of the Pauli exclusion principle to multielectron wavefunctions.[29–32]

Electron paramagnetic resonance (EPR) spectroscopy and superconducting quantum interference device (SQUID) magnetometry are the two common techniques that are used to characterize high-spin organic diradicals. It is essential that the samples are diluted in frozen glassy matrices, to minimize the intermolecular interactions.

EPR spectroscopy provides important information concerning the unpaired electrons in the $S = 1$ state. Among the valuable parameters are the zero-field splitting (D and E), g-tensor and nuclear hyperfine coupling tensor. To observe hyperfine coupling, nuclei must have a significant electron spin density and at least one abundant isotope with nonzero nuclear spin (I), such as ^{14}N with an $I = 1$.[30,33]

SQUID magnetometry is a powerful technique for measuring magnetization (or closely related paramagnetic susceptibility, χ) as a function of temperature and external magnetic field. These measurements require a careful background correction for diamagnetism of the sample. It is important to keep in mind that the existing diamagnetism in the sample and sample holder/matrix can dominate the magnetization (or susceptibility), especially for dilute samples in matrices at high temperature (T) or at high magnetic field (H). At low temperatures, the curvature of the normalized

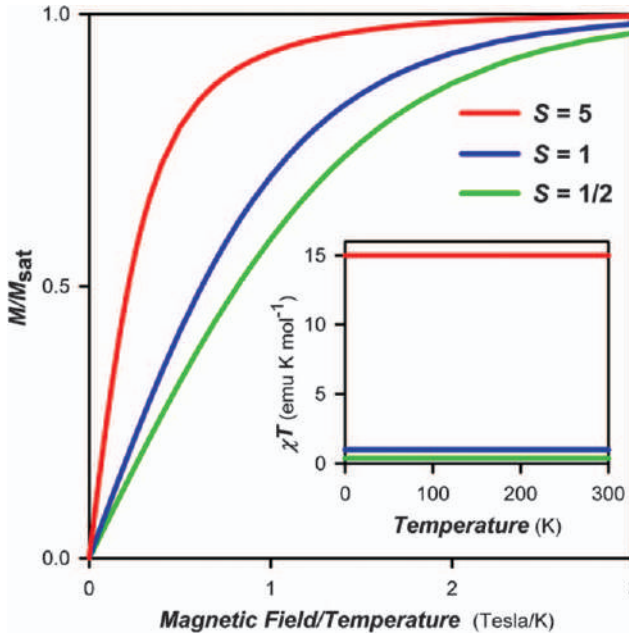

Figure 9.3 SQUID magnetometry of paramagnets: the normalized magnetization (M/M_{sat}) *vs.* H/T plots; inset: χT *vs.* T plots for infinite values of ΔE_{ST}.

magnetization (M/M_{sat}) *vs.* H/T plot provides the ground-state spin multiplicity, based upon thermal population of m_S-states.[30] This approach is independent of sample concentration (or weight) (Figure 9.3). The value of M_{sat} (in Bohr magnetons, μ_B) provides a fraction of unpaired electrons present in the sample, with $M_{sat} = 1\ \mu_B$ corresponding to a spin concentration of 100%.

In special cases in which ΔE_{ST} is comparable to RT (where T corresponds to the temperature range of the measurement), thermal population of the low-spin excited states at a higher temperature diminishes the χT. The amplitude of the decreased χT can be used to assess ΔE_{ST}.[30,31] In those cases in which the ΔE_{ST} significantly exceeds RT (*e.g.*, 0.6 kcal mol^{-1} at $T = 298$ K), an experimental assessment of ΔE_{ST} becomes difficult, allowing only for determination of a lower limit for ΔE_{ST} (Figure 9.4).

Variable-temperature EPR spectroscopy may analogously be used to assess $\Delta E_{ST} \sim RT$ *via* the amplitude of the decreased IT at higher temperatures, where I is the EPR intensity. (The NMR-based paramagnetic shift method may also be utilized in a similar way.[30,34]) Quantitative EPR spectroscopy provides a powerful method, where χ or χT of the sample are determined by comparison with the reference consisting of a stable $S = 1/2$ radical. In a typical implementation, the sample and reference are prepared as solutions (or glassy matrices) of a comparable concentration in an identical solvent (matrix). Especially for the variable-temperature EPR experiments, it is

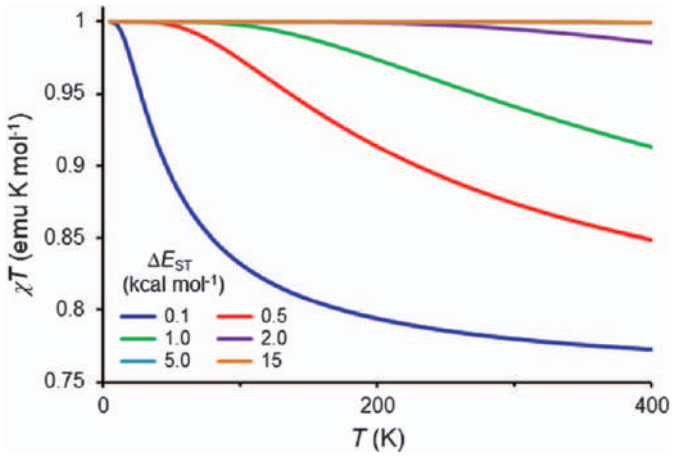

Figure 9.4 SQUID magnetometry and quantitative EPR spectroscopy: determination of ΔE_{ST} in a triplet ground state diradical based on χT *vs.* T plots. For a diradical, triplet occupancy (%) is equal to χT * 100%.

important to avoid microwave saturation at low temperatures – both for the sample and the reference. Determination of χ or χT by quantitative EPR spectroscopy has an advantage over SQUID magnetometry, because the diamagnetic background in an insulating solid or liquid sample is not detected in EPR spectroscopy, *i.e.*, paramagnetic χ is measured directly without a need for diamagnetic background correction.[35–37]

There are various theoretical approaches that aim at accurate prediction of the ΔE_{ST}. The density functional theory, employing Noodleman's broken symmetry approach (BS-DFT),[38–40] has found widespread use. However, the relatively lower computational cost of BS-DFT, compared to other more sophisticated approaches, is offset by lower accuracy; that is, the common density functionals such as B3LYP or M06-2X typically overestimate the ΔE_{ST} of high-spin diradicals.[41,42] The more complex post Hartree–Fock methods, such as the Difference Dedicated Configuration Interaction (DDCI or DDCI2) and Complete Active Space Self-Consistent Field (CASSCF) implemented with the Complete Active Space Second-order Perturbation Theory (CASPT2), are much more accurate.[42–45] The CASSCF/CASPT2 method combines the Configuration Interaction (CI) techniques with many-body perturbation theory (up to the second order) to account for electron correlation.[46,47] The DDCI approach is based on direct computation of energy differences between the electronic states of interest by CI techniques.[48] In the DDCI approach, it is essential to select judiciously only those determinants from the multireference wave function by single and double replacements, that are likely to contribute to the energy difference between the states.[49] The DDCI can be considered as one of the most reliable methods for estimating spin energy gaps in systems of synthetic interest at reasonable expense.[42,43,50]

9.4 *m*-Phenylene Alkyl–Aryl Nitroxide Diradicals

Numerous alkyl–aryl *m*-phenylene-based nitroxide diradicals have been prepared and studied. The design of this class of diradical is directed at promoting delocalization of spin density into the *m*-phenylene FCU to maximize the spin density within the FCU. The design strategy evolved from the evidence that the spin density of the *m*-phenylene diaryl diradicals significantly delocalizes into the neighboring aryl substituents (see Section 9.5). Examples of high spin, $S = 1$ ground state alkyl–aryl nitroxide diradicals **3–11** are shown in Figure 9.5.[11,25,26,51–61] Magnetism of these radicals can be elaborated using SQUID magnetometry and computations.

For diradical **3**, a fit to SQUID χT *vs.* T data (up to $T = 300$ K) apparently gives $\Delta E_{ST} \approx 2$ kcal mol^{-1} (Figure 9.6).[25,26] However such an amazing result must have a huge standard error, especially in the absence of exact correction for diamagnetism, and thus the reliability is low. One of the reasons is that, because of the thermal population of the lowest excited singlet state, such high ΔE_{ST} corresponds to minuscule lowering of the χT value. That is, even at 300 K, χT decreases by 0.5% only and the diamagnetic contribution is relatively large at this high temperature (Figure 9.4).

The more reliable result would be $\Delta E_{ST} \gg RT \sim 0.6$ kcal mol^{-1} for nitroxides **3**, **5** and **8**.[26,54,55] Similarly, $\Delta E_{ST} > 0.7$ kcal mol^{-1} and $\Delta E_{ST} \approx 1.3$ kcal mol^{-1}, obtained from the fit to the SQUID χT *vs.* T data for **7** and **9**,[11,56] should be reported as $\Delta E_{ST} \gg RT \sim 0.6$ kcal mol^{-1}. Both nitroxides **4** and **6** have lower ΔE_{ST} because their *ortho*-substituents (CF_3 and *tert*-butyl phenyl) cause the NO moieties to twist out-of-coplanarity with the *m*-phenylene coupling unit.[52,54] These values of ΔE_{ST} may be compared with the upper bound estimates by BS-DFT (UB3LYP/6-31G(d,p)): ~3.0, 0.18, 3.4 and 1.5 kcal mol^{-1} for **3–6.** Note that the X-ray geometries for **4–6** were used in these computations.[52,54] The estimated ΔE_{ST} for **5** is the largest because of its constrained conformation enforcing approximate co-planarity of nitroxides with *m*-phenylene FCU. Barone and coworkers used the accurate DDCI method to compute $\Delta E_{ST} = 0.84$, 0.077, 0.86, 0.98 kcal mol^{-1} for **3**, **4**, **9** and the model diradical **7a**, respectively.[59]

Barone and coworkers also studied a simplified diradical **3a** (Figure 9.5) using both BS-DFT (UB3LYP) and a highly accurate DDCI2 method.[60] The computations provided the $\Delta E_{ST} = 1.58$ kcal mol^{-1} (*vs.* 1.87 kcal mol^{-1} by BS-DFT) for the global minimum corresponding to planar conformation of **3a**. For the twisted conformation with ONCC torsional angles $\theta = 45^\circ$ (and $\theta = 135^\circ$), $\Delta E_{ST} \approx 0.51$ kcal mol^{-1} was obtained. In addition, it was noticed that ΔE_{ST} varied as $\cos^2(\theta)$,[60] *i.e.*, revealing Karplus–Conroy-type relationship.

Barone and coworkers also carried out a conformational study of diradical **4** using DDCI and CAS(2,2) approaches.[61] The goal of the study was rationalizing experimental results of slow increase of χT upon rapid freezing of **4** in 2-MeTHF, ultimately reaching the value consistent with the triplet ground state. This goal was not attained, presumably because computations were carried out in the gas phase,[61] and the experimental results were highly specific to 2-MeTHF.[52]

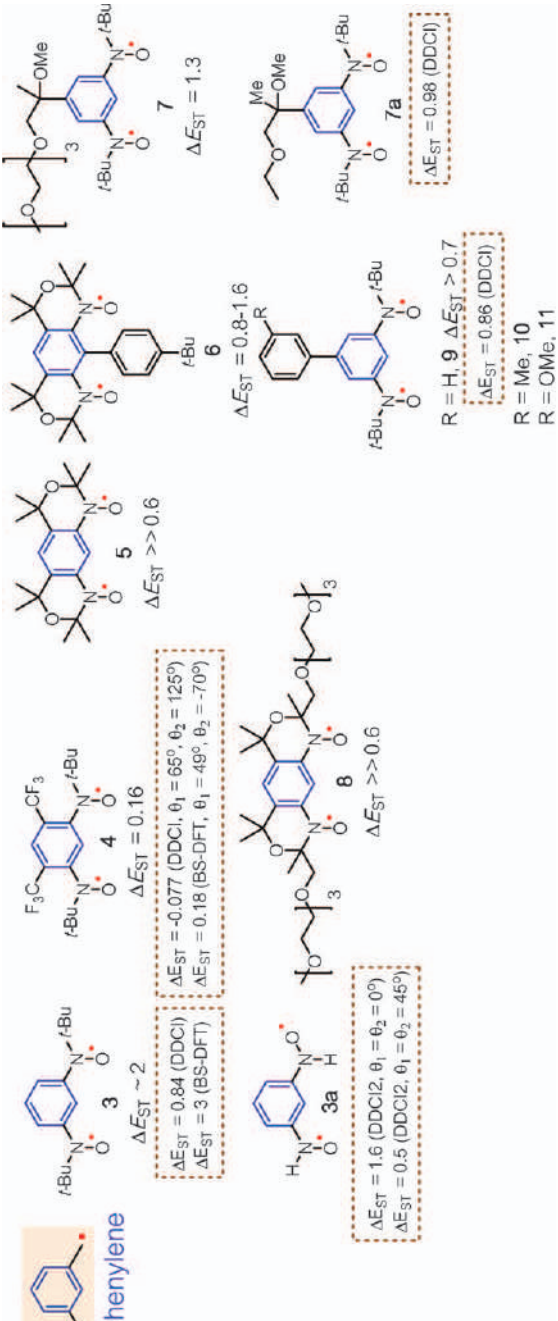

Figure 9.5 Selected alkyl–aryl *m*-phenylene based high-spin nitroxide diradicals: experimental values of ΔE_{ST} (in kcal mol^{-1}) are shown as well as those computed by DDCI and BS-DFT (UB3LYP) methods.

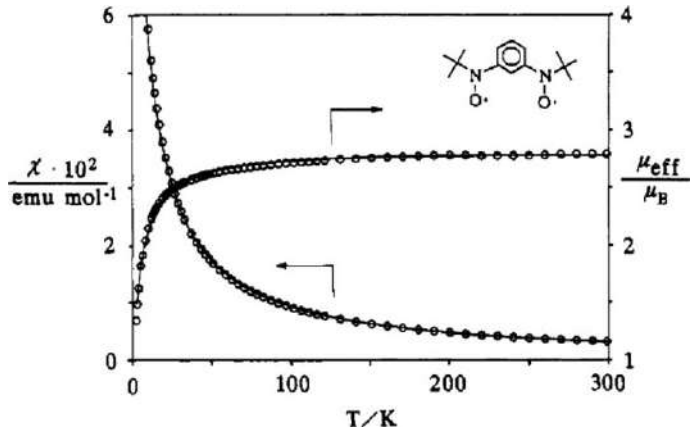

Figure 9.6 Temperature dependencies of molar magnetic susceptibility (χ) and effective magnetic moment (μ_{eff}/μ_B). Solid lines are theoretical curves with $J/k = 500$ K, computed analogously as shown in Figure 9.4. Please note that $\mu_{eff}/\mu_B \approx 2.83(\chi T)^{1/2}$.
Adapted from ref. 26 with permission from American Chemical Society, Copyright 1991.

Stability of the *m*-phenylene alkyl–aryl nitroxide diradicals depends on their substitution pattern. Nitroxide diradical **3** decomposes in solution to the corresponding aminoquinone imine *N*-oxide within a few hours,[51] however diradicals **4–11** are relatively persistent at ambient conditions. Diradical **5** is observed to be stable in the crystalline state for several months and pure samples of **5** are stable in solution at room temperature for at least two days.[54] Despite the additional steric shielding of the *ortho* position in the case of diradical **6**, it slowly decomposes in solution at ambient conditions – perhaps, not surprising in view of its strained structure as revealed by X-ray crystallography.[54]

Water-soluble diradical **7** provides the first example of a high-spin diradical studied in aqueous solutions and matrices.[11] However, the measured ^{1}H water relaxivities are a bit disappointing, most likely, because of inadequate water access to the NO moieties within the hydrophobic moiety of the diradical.[11,13] A similar phenomenon is observed for aminyl-based radicals.[62,63]

Conformationally restrained nitroxide diradical **8** is an example of a high-spin diradical that is soluble in biologically friendly matrices. Electron spin relaxation times of **8** are comprehensively studied in the temperature range $T = 10$–300 K. Both electron spin T_1 and T_m are strongly affected by modulation of anisotropic magnetic dipole–dipole interactions in **8** and in diradicals with similar interspin distances.[55]

Nitroxide diradicals **9–11** show interesting magnetic properties in the solid state,[56–58] with **9** crystallizing in two phases. The α-phase consists of NO-dimers with short N–O = 2.321 and 2.359 Å contacts within one-dimensional chain, thus leading to a diamagnetic state; the β-phase

consists of much longer intermolecular N–O > 5.4 Å contacts, thus leading to a strongly paramagnetic state of magnetically independent $S = 1$ diradicals. Interestingly, the diamagnetic α-phase undergoes an irreversible phase transition to the paramagnetic β-phase at about 350 K. In the α-phase at $T < 230$ K, the crystalline structures of diradicals **10** and **11** with diamagnetic properties resemble diradical **9** in the α-phase. At $T > 350$ K, the structures of **10** and **11** with strong paramagnetic properties of $S = 1$ diradical are analogous to that of **9** in the β-phase. Interestingly, an intermediate phase corresponding to magnetically isolated dimers of diradicals, in which only one nitroxide in each diradical possesses short intermolecular N–O contacts, is detected in the intermediate temperature range, $230 < T < 350$ K. This intermediate phase corresponds to two magnetically independent $S = 1/2$ nitroxide radicals per each dimer (Figure 9.7). The solid–solid phase transitions in **10** and **11** are single-crystal-to-single-crystal type and associated with a change of color of crystals. However, there is no hysteresis for the χT *vs.* T (or χ *vs.* T) data.

The solid–solid phase transition in nitroxides is quite an appealing phenomenon, especially when it associates with magnetism. Some interesting phase transition phenomena of nitroxides are illustrated in **AZADO** radical and **NN_2–DT*m*BDT** diradical.[64,65] Photochromic behavior, with the hysteresis in the χ *vs.* T data between 280 and 305 K, is observed for **AZADO** nitroxide radical (Figure 9.7) in the solid state. The low-temperature ($T < 280$ K) phase crystal has a yellow color and corresponds to the diamagnetic $S = 0$ NO π-dimers with short N–O ≈ 2.3 Å contacts. The high-temperature ($T > 305$ K) phase, reddish-brown color solid, for which a single-crystal X-ray structure could not be obtained, displays paramagnetic $S = 1/2$ behavior.[64] Similar results were obtained for the methyl derivative of AZADO (1-methyl-2-azaadamantane *N*-oxyl).[66]

For **NN_2–DT*m*BDT** diradical,[65] the differential scanning calorimetry (DSC) and integration of selected IR bands (*vs.* temperature) show a reversible phase transition with hysteresis in the temperature range 275–284 K and an

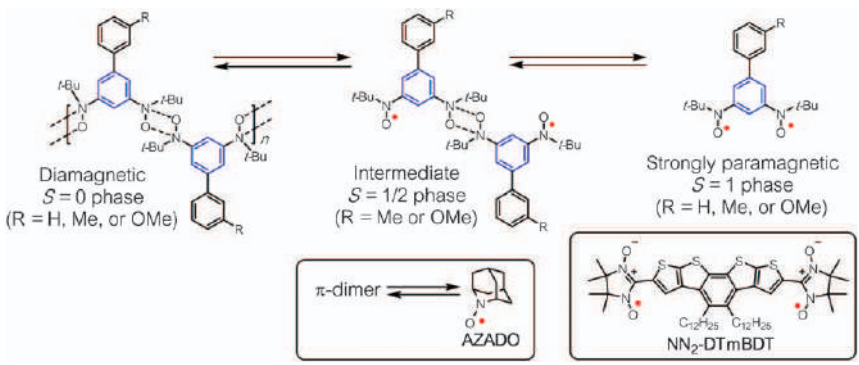

Figure 9.7 Selected nitroxide radicals exhibiting solid–solid phase transitions: $S = 1$ diradicals **9** – **11**, $S = 1/2$ **AZADO** radical and **NN_2–DT*m*BDT** diradical.

irreversible phase transition near 408 K. However, no single-crystal X-ray structure could be obtained for the high-temperature phase (at $T = 303$ K). At low temperatures, the X-ray structure shows moderately short O–O = 3.5–3.6 Å contacts between nitronyl nitroxide moieties, which the BS-DFT computation predicts to be relatively weak antiferromagnetic couplings of $|J| < 25$ K. These antiferromagnetic J values are similar to those computed for intramolecular exchange coupling; the ΔE_{ST} is not determined experimentally.[65]

9.5 *m*-Phenylene Diaryl Nitroxide Diradicals

Polyradicals with alternating connectivity of radicals and *m*-phenylene are potential building blocks for high-spin polyradicals that could be useful in the development of organic magnetic materials.[2,3,30] However, there are only a few known diaryl nitroxide radicals, and most of them are monoradicals.[67] Some attempts have been made to prepare diaryl nitroxide polymer and oligomers, including our work on diaryl nitroxide diradicals **12–14** (Figure 9.8),[68–71] which reveals why these trials were destined to be failures.

Preparations of diradicals **12** and **13** are enabled by the development of the low-temperature method for oxidation of secondary diaryl amines by dimethyldioxirane (DMDO) in dichloromethane. The progress of the oxidation is monitored by magnetic resonance spectroscopy (EPR and ^{1}H NMR) and by magnetic studies in solution using SQUID magnetometry, with the reaction mixture strictly maintained at low temperature (−80 °C or below).[68]

Oxidation of a simple 4,4′-di-*tert*-butyl-diphenylamine provides the well-known 4,4′-di-*tert*-butyl-diphenylnitroxide (**DTBDPN**) radical[67,68] in 40–60% isolated yields. (These yields are significantly lower than the nearly quantitative yields reported for oxidation of sterically hindered secondary dialkylamines with DMDO to the corresponding dialkylnitroxide radicals such as TEMPO.[72]) Interestingly, polycrystalline **DTBDPN**, crystallized from ethanol,

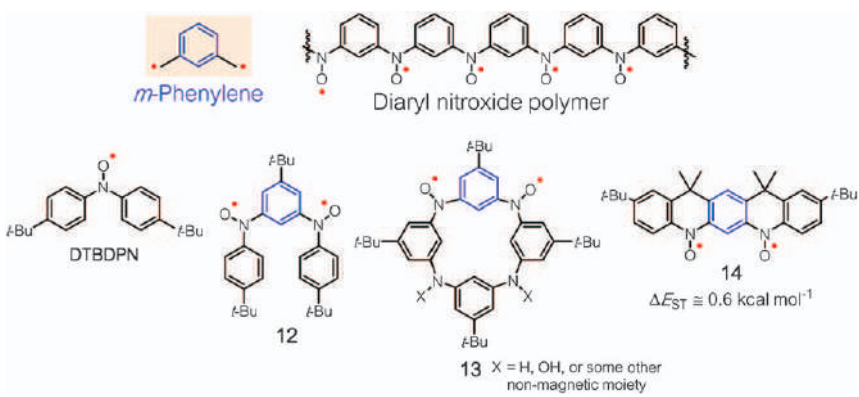

Figure 9.8 Diaryl *m*-phenylene-based high-spin nitroxide diradicals **12–14** and diaryl nitroxide radical **DTBDPN**.

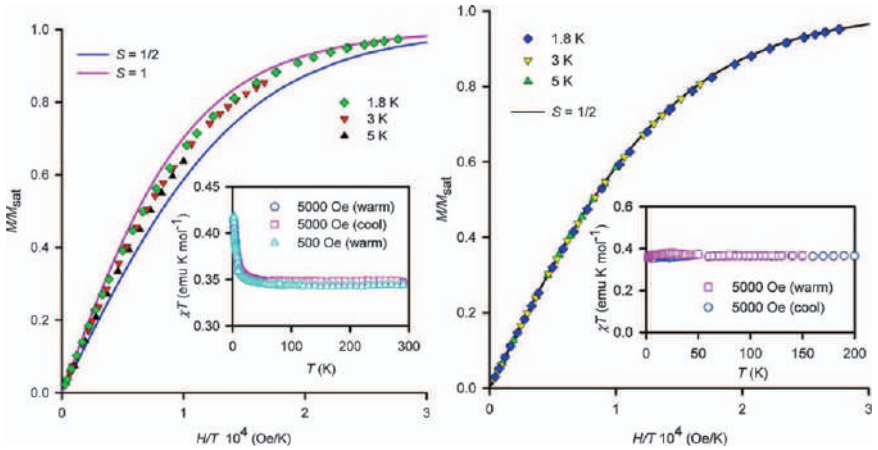

Figure 9.9 SQUID magnetometry of $S = 1/2$ monoradical **DTBDPN** in the solid state (left panel) and in 2-MeTHF (right panel).
Adapted from ref. 68 with permission from American Chemical Society, Copyright 2008.

shows intermolecular ferromagnetic interactions as evidenced by the increasing curvatures ($S > 1/2$) of the M/M_{sat} *vs.* H/T plots at 5, 3 and 1.8 K, corresponding to $S = 0.67$, 0.80 and 0.85, respectively. The χT *vs.* T plot shows an upward turn, from $\chi T \approx 0.35$ emu K mol^{-1} at $T = 50$ K to $\chi T \approx 0.42$ emu K mol^{-1} at $T = 1.8$ K. On the other hand, SQUID magnetometry for 0.1 M **DTBDPN** in 2-methyltetrahydrofuran (2-MeTHF) gives the data consistent with a perfect $S = 1/2$ paramagnet (Figure 9.9).

Diaryl nitroxide diradicals **12** and **13** are prepared by the low-temperature oxidation of the corresponding diaryl diamine and aza[1_4]metacyclophane[69] using DMDO as oxidant. Two conformers of **12** are detected by EPR spectroscopy. EPR spectra of the reaction mixture at 140 K show side bands that represent the dipolar coupling patterns of two $S = 1$ dinitroxide conformers with smaller and larger spectral widths ($|2D/hc|$). The major conformer with smaller $|2D/hc|$ corresponds to the structure with longer interspin distances between nitroxides. The relative intensities of the side bands (for triplet state) and the center peaks (for an $S = 1/2$ radical impurity) in the EPR spectra, taken before and after the SQUID magnetometry, are in qualitative agreement with the average values $1 > S > 1/2$ obtained from the curvature of the M/M_{sat} *vs* H/T Brillouin plots. In particular, the spin-average S-value, $S_s \approx 0.7$,[73] indicates a triplet ground state for **12**. For diradical **13**, the reaction mixture shows a rather weak EPR spectrum such that the spectral intensity is too low to permit determination of its ground state. In addition, neither triradical nor tetraradical is detected.

Diradical **14** is designed with increased steric shielding of the *para*-positions of the *m*-phenylene FCU, and the nitroxide moieties are annelated with the FCU ring structure to enforce coplanarity.[70] As a result, diradical **14** is more stable and could be isolated as polycrystalline solid at ambient

conditions, though, in concentrated solutions, it undergoes slow decomposition at room temperature. Because of the enforced coplanarity of nitroxide moieties with *m*-phenylene FCU, **14** is expected to possess a larger ΔE_{ST} compared to **12**. BS-DFT estimates of ΔE_{ST} for **12** and **14** are 1.8 and 2.0 kcal mol^{-1}, respectively.[68,70] The accurate DDCI computation by Barone and coworkers provides $\Delta E_{ST} \approx 0.6$ kcal mol^{-1} for **14**,[74,75] in good agreement with the experimental value. The SQUID magnetometry of polycrystalline **14** provides the χT *vs.* T plot that corresponded to a lower bound $\Delta E_{ST} \geq 0.6$ kcal mol^{-1}.[70] Notably, the hydrocarbon (polyarylmethyl) analog of **14** is also stable at room temperature (under inert atmosphere) and is a triplet ground state;[76] its $\Delta E_{ST} \approx 6$ kcal mol^{-1}, as estimated by BS-DFT, is much higher than that for **14**.

Although **14** is sufficiently stable to be isolated as solid, crystals of sufficient quality for an X-ray crystallography could not be obtained. Therefore, the structure of **14** is largely established by correlation between the experimental and DFT-computed EPR spectra as illustrated in Figure 9.10.[71] Experimental EPR spectrum for diradical **14** in glassy toluene at 140 K shows six symmetrically positioned side bands associated with a triplet state with the following values of zero-field splitting (zfs) parameters, $|D| = 12.25 \times 10^{-3}$ cm^{-1} and $|E| = 1.40 \times 10^{-3}$ cm^{-1}. The DFT computations (UB3LYP/EPR-II), based upon spin–spin only approximation (magnetic dipole–dipole interaction between unpaired electrons), somewhat overestimate the spacing of the outer *Z*-bands ($2|D|$) and the spacings of the inner X- and Y-bands (approximately $3|E|$) by giving $D = -17.7 \times 10^{-3}$ cm^{-1} and $E = -4.22 \times 10^{-3}$ cm^{-1} (Figure 9.10).[77–79] As expected for the planar

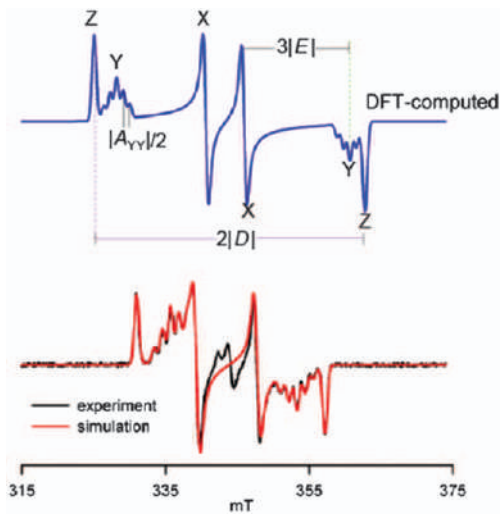

Figure 9.10 EPR spectra for nitroxide diradical **14**. Top: DFT-computed spectrum at the UB3LYP/EPR-II level of theory. Bottom: experimental spectrum in toluene at 140 K and spectral simulation.

nitroxide–*m*-phenylene–nitroxide π-system in **14**, ^{14}N hyperfine coupling of two nitrogens splits the Y-bands into quintets, analogously to those for nitroxide diradicals **5** and **8**.[53–55] The spacings within the quintet should correspond to $|A_{YY}|/2$, where A_{YY} is the largest principal value of the ^{14}N *A*-tensor oriented parallel to the direction of the $2p_\pi$ orbital on the nitrogens (*Y*-axis). The DFT-computed values of $A_{YY}/2 = 0.837\times10^{-3}\,cm^{-1}$ and $0.892\times10^{-3}\,cm^{-1}$ at the UB3LYP/EPR-II and UB3LYP/EPR-III levels slightly underestimate the experimental value of $1.06\times10^{-3}\,cm^{-1}$. The positions of ''centers of gravity'' for each pair of the bands, labeled by X, Y and Z, are determined by the corresponding principal values of the *g*-tensor: g_{XX}, g_{YY}, g_{ZZ}. The DFT-computed values of $g_{XX} = 2.0083$, $g_{YY} = 2.0022$, $g_{ZZ} = 2.0055$, using coupled-perturbed Kohn–Sham (CP-KS) theory at the UB3LYP/EPR-II level,[80] are in good agreement with the corresponding experimental values, $g_{XX} = 2.0076$, $g_{YY} = 2.0020$, $g_{ZZ} = 2.0047$.

9.6 TMM Nitroxide Diradicals

Numerous diradicals with 1,1-connection of ethylene to nitroxides have been prepared and studied. The TMM-based nitroxide diradical **17** was reported by Iwamura and coworkers in 1992.[81] Polycrystalline diradical **17** was characterized by SQUID magnetometry, for which triplet ground state with a small $\Delta E_{ST} = 0.030$ kcal mol^{-1} was determined (Figure 9.11).[81] Diradicals **15** and **16** were subsequently reported; their $\Delta E_{ST} = 1.28$ kcal mol^{-1} (**15**) and $\Delta E_{ST} = 0.43$ kcal mol^{-1} (**16**) were quite substantial.[82,83] In 2010, Okada and coworkers reported the synthesis and characterization of the triplet ground-state diradicals **1** and **2** with relatively larger $\Delta E_{ST} \approx 1.6$ and 2.2 kcal mol^{-1}, respectively, as determined by SQUID magnetometry of polycrystalline diradicals.[22] These ΔE_{ST} values are of a similar magnitude to those of the ''planarized'' *m*-phenylene-based nitroxide diradicals **5** and **8**. Notably, both diradicals are sterically encumbered, as indicated by the values of torsion angles (θ) between the NO moiety and C = N FCU: $\theta = 76^\circ$ and 40° in **1** and **2**, respectively.[22] This may explain the phenomenon that the ΔE_{ST} for **1** is smaller than that for **2**, whilst the ΔE_{ST} for **15** is larger than that for **16**. Both diradicals **1** and **2** are stable at ambient conditions and they may be sublimed at 55–70 °C without decomposition.[22]

Shultz and coworkers reported a series of TMM-based nitroxide diradicals,[84–86] including diradicals with singlet (**18**, **19** and **22**) and triplet (**20** and **21**) ground states; their values of ΔE_{ST} were measured for the samples in polyvinyl chloride (PVC)-matrices (and in polycrystalline solids) by SQUID magnetometry. For nitroxides **18**–**21**, the ΔE_{ST} value is correlated with the average torsion angle (θ) between the phenyl rings and TMM moiety, as determined by X-ray crystallography, using a simple Karplus–Conroy-type relation: $\Delta E_{ST} = 0.25\ \cos^2(\theta) - 0.097$ (kcal mol^{-1}).[86] This correlation establishes through-bond ferromagnetic exchange coupling for nearly coplanar diradicals with small θ and through-space antiferromagnetic exchange coupling for sterically encumbered diradicals with large θ.

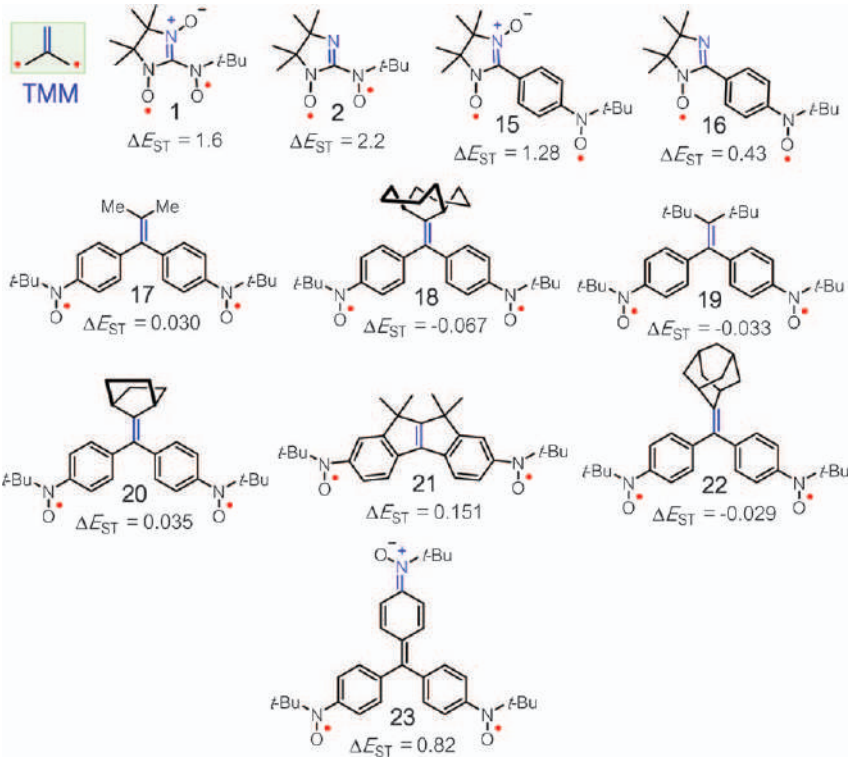

Figure 9.11 TMM nitroxide diradicals.

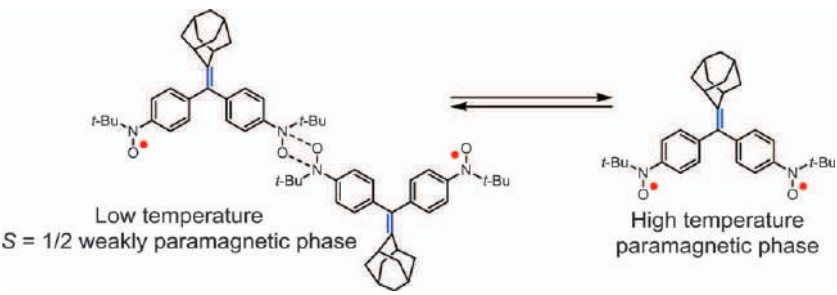

Figure 9.12 Solid–solid phase transition for diradical **22**.

Nitroxide **22** could not be included in the Karplus–Conroy correlation because it exhibits structural phase transition in the crystal, associated with magnetic hysteresis in χT *vs.* T data between 60 and 85 K (Figure 9.12).[85]

The low-temperature X-ray structure at 25 K shows the NO π-dimer of the diradical molecules that formed between one of the nitroxides with the N–O contacts of 2.450 Å. The nitroxide moieties within the NO dimer are in the singlet ($S = 0$) ground state with a large $|\Delta E_{ST}|$ (strong antiferromagnetic coupling), while the other two nitroxides are magnetically independent

$S = 1/2$ radicals. In the high temperature phase, the N–O contacts within the NO dimer increase to 5.37 Å, based on the X-ray structure obtained at 158 K, thus weakening the antiferromagnetic coupling to be practically negligible, especially at the elevated temperatures. This observation provides the rationale for the magnetic phase transition observed for polycrystalline **22**.[86] It should be noted that the low-temperature $S = 1/2$ phase for diradical **22** is both structurally and magnetically equivalent to the intermediate $S = 1/2$ phase for diradicals **10** and **11** (Figures 9.5 and 9.7).

Another example of notable TMM-based nitroxide diradical is the "quinoidal-TMM" nitroxide diradical **23**, which was reported by Iwamura and coworkers in 1996.[87,88] Diradical **23** possesses a modest $\Delta E_{ST} = 0.82$ kcal mol^{-1}.[87,88] The hydrocarbon (polyarylmethyl) analog of **23** also possesses triplet ground state and is stable at room temperature (under inert atmosphere).[89]

9.7 High-spin Nitroxide Triradicals

Because of the highly challenging design and synthesis, there are only a few examples of high-spin nitroxide triradicals. Triradicals **24**–**27** (Figure 9.13) were prepared and studied by Iwamura and coworkers.[26,90] Notably, **24** is the only example of a high-spin nitroxide triradical based on *m*-phenylene FCUs. The nature of the problem in preparation of this class of high-spin polyradical is discussed in Section 9.5 (*m*-Phenylene diaryl nitroxide diradicals), though

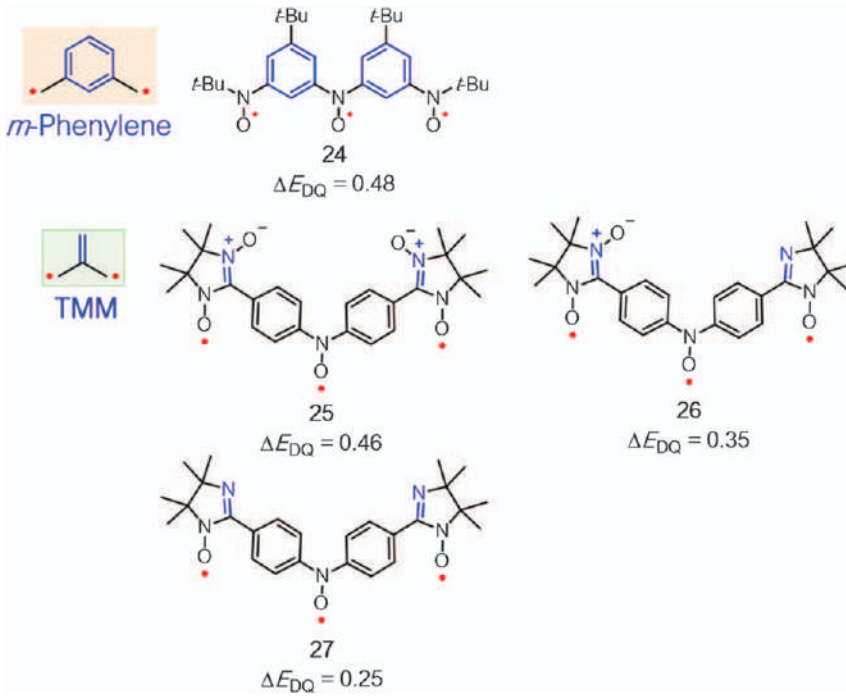

Figure 9.13 High-spin ($S = 3/2$) nitroxide triradicals.

24 consists of only a single diaryl mononitroxide moiety. The other examples are TMM-based nitroxides, in which the more stable nitroxides, *e.g.*, nitronyl nitroxides, are adopted as SCs to enhance overall stability. Polycrystalline triradicals are characterized by SQUID magnetometry, for which the χT *vs.* T data provide the values of doublet–quartet energy gap, ΔE_{DQ}. The *m*-phenylene based triradical **24** has the highest values of $\Delta E_{DQ} = 0.48$ kcal mol^{-1}.[26] The bis(nitronyl nitroxide) triradical **25** has a similar $\Delta E_{DQ} = 0.46$ kcal mol^{-1} to that of **24**. The fact that **26** and **27** have lower $\Delta E_{DQ} = 0.35$ and 0.25 kcal mol^{-1} is expected,[90] based on the values of $\Delta E_{ST} = 1.28$ and 0.43 kcal mol^{-1} for TMM-type diradicals **15** and **16** (Figure 9.11).

m-Phenylene triradical **24** is stable under ambient conditions in solution and as polycrystalline solid for weeks.[26] Triradicals **25** and **26** are sufficiently persistent to be purified by chromatography on neutral alumina.[90]

9.8 High-spin Nitroxide-based Hybrid Diradical Cations and Triradical Cations

Organic radical cations with excellent stability are of interest in the design of high-spin molecules. An intriguing case is the molecular designs derived from the nitronyl nitroxides linked to the electron-rich π-conjugated system, for which Sugawara and coworkers observed the notable phenomenon of SOMO–HOMO energy level inversion (Figure 9.14).[6] The energy level of the SOMO is below that of the HOMO because the coefficients of the SOMO are localized to the nitronyl nitroxide moiety, which consists of electronegative heteroatoms such as oxygen and nitrogen. Furthermore, the on-site Coulomb repulsion of the SOMO is large because the addition of an extra electron to the spatially restricted SOMO requires a large amount of energy. Therefore, the half-occupied SOMO is preserved even though the doubly occupied HOMO is at the higher energy.[6]

Recently, it has been shown that the SOMO–HOMO energy level inversion could also be found in radicals and radical cations delocalized within helical and double-helical π-conjugated systems, which upon one-electron oxidation would form triplet ground-state diradical cations and diradical dications with a significant ΔE_{ST}.[37,91] This unique phenomenon of coinciding SOMO–HOMO inversion and high-spin ground states is of general interest because it demonstrates a violation of the Aufbau principle[92,93] and it may be exploited for preparation of materials with cooperative conductivity and magnetism.[6]

The cooperative conductivity and magnetism in a molecule have been observed. For example, a giant negative magnetoresistance is detected for nitronyl nitroxide-linked benzoTTF **28**,[94] for which the first (benzoTTF) and second (nitronyl nitroxide) redox potentials are at 0.82 and 0.90 V in acetonitrile *versus* Ag/AgCl. At $T = 2$ K and external magnetic field of $H = 5$ Tesla, the ratio of magnetoresistance, *i.e.*, $100\% \times (R_H - R_0)/R_0$, where R_H is the resistance under the magnetic field and R_0 is the resistance under an ambient field, reaches −70%.[94] The mechanism of the magnetoresistance phenomenon is proposed based on the formation of triplet ground-state diradical cations when

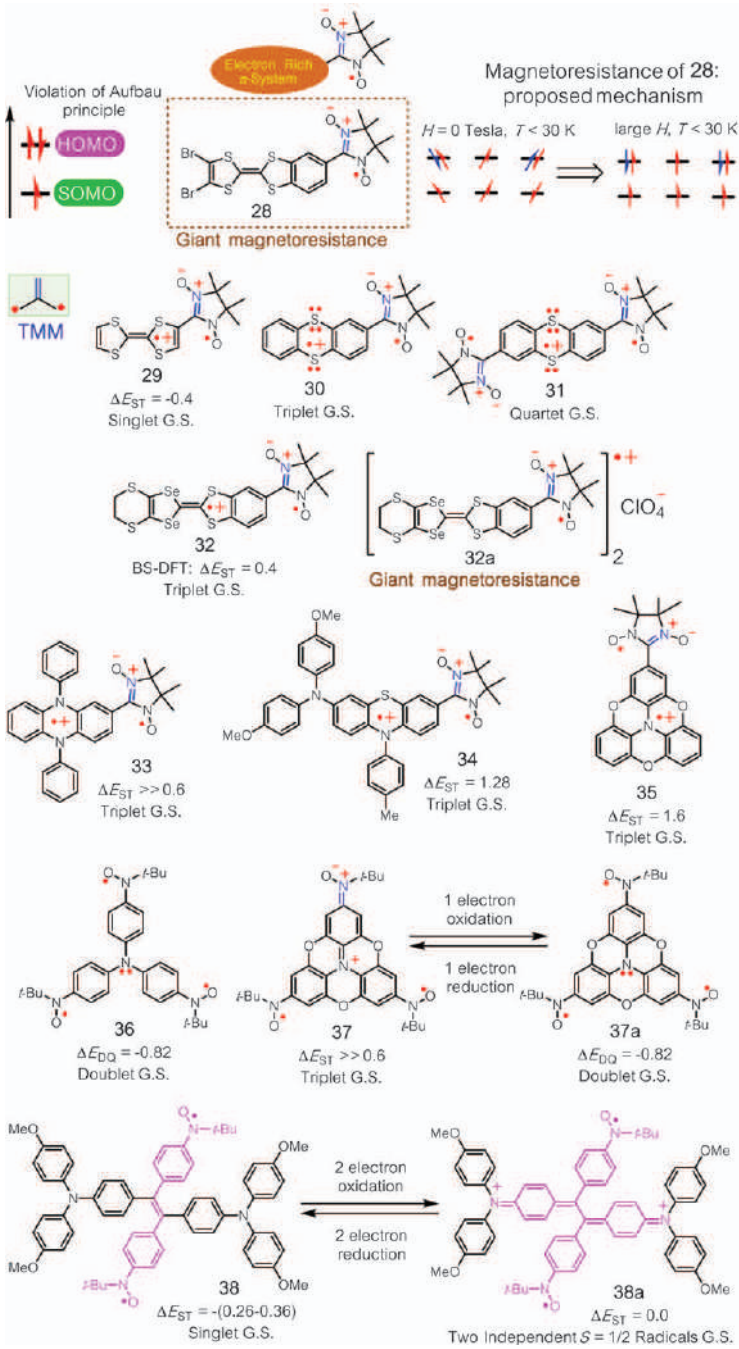

Figure 9.14 (Nitronyl) nitroxide-radical cation hybrid diradicals.

the crystal of **28** is hole-doped through the positive electrode. In the proposed mechanism, at $H = 0$ Tesla, conduction electrons, which move along the columnar donor stack, are scattered by the thermally fluctuating paramagnetic spins of the radical sites. As the H increases, the localized spins align parallel to the external field. Therefore, on the basis of the double-exchange mechanism, only a conduction electron of the opposite spin could be transferred (Figure 9.14A); in other words, the spin down (blue spin in Figure 9.14) would readily transfer to the adjacent hole site if the antiparallel red spin is available. Onset of magnetoresistance at 30 K provides an estimate for the strength of exchange coupling between localized unpaired nitronyl nitroxide moieties and delocalized (itinerant) conduction electrons in the crystal.[94]

For **28**, $S = 1$ ground-state diradical cation is formed *via* hole doping upon applied electric field. Alternatively, the hole doping can be achieved *via* chemical oxidation of the π-system. In one of the earliest attempts, in 1994, nitronyl nitroxide-linked TTF diradical cation **29** does not provide the anticipated triplet ground state; that is, singlet ground state with negative value of $\Delta E_{ST} = -0.4$ kcal mol^{-1} is determined by variable-temperature EPR spectroscopy. The singlet ground state is obtained presumably because of large out-of-plane twisting of nitronyl nitroxide with respect to the TTF moiety.[95] Diradical and triradical cations of nitronyl nitroxide-linked phenanthrene **30** and **31** (as well as its regioisomer), with apparently less susceptibility to out-of-plane twisting nitronyl nitroxide moieties, were characterized as high-spin ground-state molecules by pulsed EPR spectroscopy at low temperatures, but the energy gaps, ΔE_{ST} and ΔE_{DQ}, were not determined.[96]

Sugawara and coworkers investigated the diradical cation **32**, an analog of **28**. The BS-DFT computations predict that diradical cation **32** is a triplet ground state with $\Delta E_{ST} = 0.4$ kcal mol^{-1}.[6,97] They find that the ion-radical salt **32a**, obtained by electrocrystallization of neutral **32**, exhibits giant negative magnetoresistance. The ratio of magnetoresistance $100\% \times (R_H - R_0)/R_0 = -70\%$ is obtained at $T = 2$ K and at $H = 9$ Tesla. The magnetic field dependence of the ratio of the magnetoresistance is correlated with H (0–9 or 9–0 Tesla), resulting in a bell-shaped curve. The proposed mechanism for magnetoresistance is identical to that for **28** (Figure 9.12), with the onset at a relatively lower temperature of 20 K.[97]

Okada and coworkers[98] designed a highly stable nitronyl nitroxide-linked *N*,*N*-diphenylphenazine diradical cation **33**, which they were able to isolate as a tetrafluoroborate salt. Room-temperature stability of the diradical cation salt, enables determination of its $\Delta E_{ST} \gg 0.6$ kcal mol^{-1} using the SQUID χT *vs.* T data of the polycrystalline **33**. In addition, when tetrabromoferrate ($FeBr_4^-$) is used as a counter anion for diradical cation **33**, they observe a three-dimensional, long-range ferrimagnetic ordering at $T_c = 6.7$ K, based upon measurements of dc and ac magnetic susceptibilities and heat capacity.[99] More recently, Okada and coworkers reported additional examples of analogous stable nitronyl nitroxide-based diradical cations such as **34** and **35**.[100,101] Notably, **35** shows a weak ferromagnetic ordering with transition

temperature of $T_N = 2.85$ K, as determined by ac susceptibility and magnetization studies and heat capacity measurements.[101]

The electron-rich π-conjugated system also offers additional intriguing observations. Oxidation of the electron donor in a system composed of radicals and a π-donor could alter the π-conjugation network, affecting the magnetic interaction. In 1999, Iwamura and coworkers synthesized trinitroxide-substituted triphenylamine **36** and determined that it is a doublet ground state with $\Delta E_{DQ} < -0.2$ kcal mol^{-1}.[102] Its diradical cation could be viewed as a TMM-type π-conjugated system with a triplet ground state, analogous to the isoelectronic diradical **23** (Figure 9.11). Although cyclic voltammetry of **36** shows a reversible one-electron oxidation wave, the related diradical cation could not be isolated.[102]

In 2012, Okada and coworkers[103] prepared an analogous radical cation **37**, by replacing triphenylamine with trioxytriphenylamine, a much easier way to oxidize moiety (Figure 9.14). Both **37** and **37a** could be readily isolated and characterized by X-ray crystallography. Large energy gaps between the high- and low-spin state for **37** and **37a** were determined. This is a fascinating example of a multiplicity redox switching that is effective at ambient conditions.

In 2005, Tanaka and coworkers[104] reported the switchable ground-state multiplicity system that is effective at low temperatures. Diradical **38** possesses singlet ground state with $\Delta E_{ST} = -0.26$ and -0.36 kcal mol^{-1} (depending on conformation). Upon two-electron oxidation, diradical dication **38a** possessed two magnetically independent $S = 1/2$ nitroxide radicals ($\Delta E_{ST} \approx 0.0$ kcal mol^{-1}). More recently, they prepared the nitroxide- and nitronyl nitroxide-linked phenyldiamine diradicals and the corresponding triradical cations, but the energy gaps between the high- and low-spin states were not reported.[105,106]

9.9 Thermally Robust High-spin Nitronyl Nitroxide–Blatter Diradicals

In the search to enhance the thermal stability of high-spin diradicals, various structural designs based on an exceptionally robust *N*-centered Blatter radical have been explored. Feasible synthesis of the radicals is among the chief considerations that dictate the design of diradicals to the hybrid nitronyl nitroxide–Blatter radicals. The BS-DFT computational survey reveals that only the diradicals derived from a nitronyl nitroxide-linked to Blatter radical are likely to possess a significant ΔE_{ST} (Figure 9.15).[36,107] It can be recognized that these radicals are the TMM-based diradicals, and therefore the relative values of computed ΔE_{ST} are as expected for the diradicals of this type, *e.g.*, **15** and **16** (Figure 9.11).

The synthesis of these diradicals relies on the resilience of the Blatter radical toward chemical transformations. The starting materials, cyano-substituted Blatter radicals **39a** and **41a**, are prepared by adopting literature procedures for Blatter monoradicals.[108] The reduction of cyano group with DIBAL-H at low temperature is followed by hydrolysis of the resultant

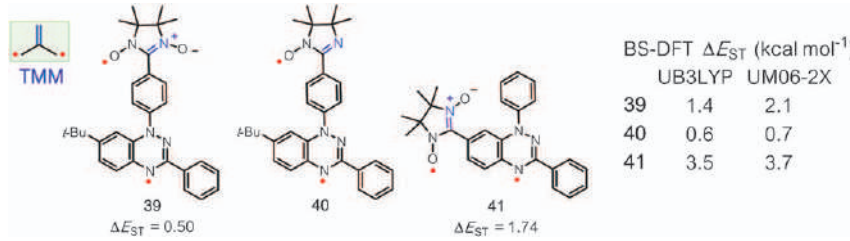

Figure 9.15 High-spin Blatter–nitroxide diradicals.

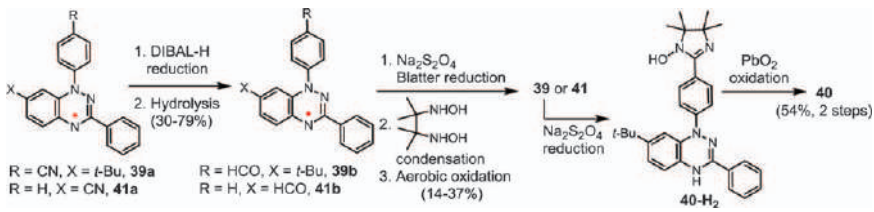

Figure 9.16 Synthesis of diradicals **39**–**41**.

imine to the aldehyde group, to provide Blatter radicals **39b** and **41b**. Subsequently, reduction of Blatter radical, condensation with dihydroxylamine and oxidation in air, in the presence of a base such as triethylamine, give diradicals **39** and **41**. Reduction of both nitronyl nitroxide and Blatter radical using sodium dithionite provides intermediate **40–H$_2$**, which upon re-oxidation with lead(IV) oxide furnishes diradical **40** (Figure 9.16). Diradicals **39** and **41** are free of diamagnetic and paramagnetic impurities, as determined by SQUID magnetometry and EPR spectroscopy.

All three diradicals **39**–**41** are very stable and can be purified on normal-phase silica gel without taking special precautions. Especially, diradicals **39** and **41** are thermally robust, showing onsets of decomposition in thermal gravimetry analyses (TGAs) at 175 and 160 °C, respectively. On the other hand, diradical **40** decomposes much more readily, with a TGA onset of decomposition at about 70 °C. Diradical **39** can be sublimed without decomposition at 140 °C under medium vacuum ($p \approx 6 \times 10^{-6}$ mbar).[36]

Diradical **41** crystallizes in space group P-1. The crystal consists of two nonequivalent molecules, A and B, and one molecule of dichloromethane (solvent of crystallization). In molecules A and B, the nitronyl nitroxide radical moiety is nearly coplanar and out-of-plane twisted with the Blatter radical π-system, respectively. The corresponding N–C8A–C1A–C torsions are in the −13 to −15° range in molecule A, while in molecule B, the corresponding torsions are in the 28–30° range. In the crystal, molecules A and B pack in an alternating fashion into one-dimensional chains (along the crystallographic *a*-axis) with close intermolecular N···N and O···N contacts. Two types of short N2A···N3B = 3.509 Å and O4B···N1A = 3.335 contacts between molecules A and B are identified. Because all nitrogens and oxygens

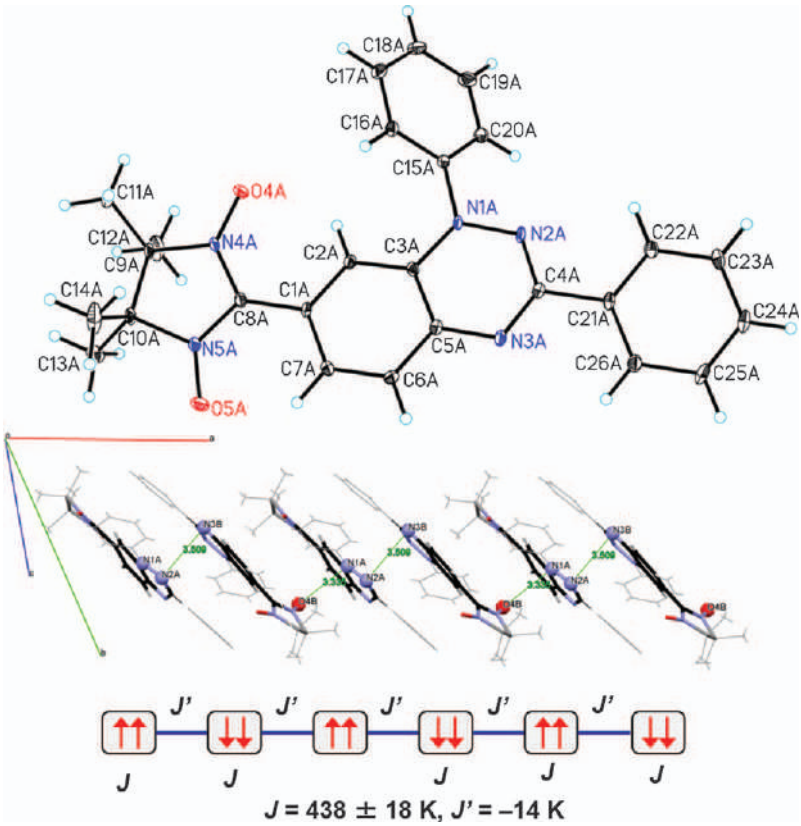

Figure 9.17 Top panel: Single crystal X-ray structure of diradical **41** with molecule A shown only; thermal ellipsoids for C, N and O are set at the 50% probability level. Bottom panel: Packing of molecules A and B into a one-dimensional $S = 1$ antiferromagnetic chain; nitrogens and oxygens with large positive-spin densities and close intermolecular contacts, N2A···N3B = 3.509 Å and O4B···N1A = 3.335 Å, are displayed as ball-and-stick.

in diradical **41** possess large positive-spin densities, such contacts are anticipated to give rise to intermolecular antiferromagnetic coupling between pairs of molecules A and B within the 1D chain, thus providing the 1D antiferromagnetic chain of weakly coupled $S = 1$ diradicals (Figure 9.17). In fact, the SQUID χ *vs.* T data, which show a characteristic broad maximum at about 20 K, give an excellent fit to 1D antiferromagnetic chain model with $J' = -14$ K. The 1D chain of **41** is the most isotropic, with very weak local anisotropy, $|D/2J'| \approx 4 \times 10^{-4}$,[54,109] and thus could potentially be an excellent system for studies of low-dimensional magnetism.[110]

SQUID magnetometry of polycrystalline **39** and **41** provides $\Delta E_{ST} = 0.50 \pm 0.02$ and 1.74 ± 0.07 kcal mol^{-1}, respectively.[107] The value of

$\Delta E_{ST} = 0.47 \pm 0.07$ kcal mol^{-1} for **37** is similar to that obtained by quantitative EPR spectroscopy in dilute solutions/matrices.[36,107] The triplet, $S = 1$ ground states of **39** and **41** are unequivocally established by SQUID magnetometry of the dilute samples in glassy polystyrene matrices, based on the curvature of normalized magnetization (M/M_{sat}) *vs.* $H/(T - \theta)$ plots, where $|\theta| \leq 0.05$ K is a mean-field correction for very weak antiferromagnetic interactions in dilute matrix.[107] The experimental values of ΔE_{ST} for **39** and **41** are well reproduced by computations at the CAS(10,10) level of theory.[111]

Diradical **41** is evaporated intact under ultra-high vacuum (UHV) at about 100 °C to form thin films on a silicon, SiO_2/Si(111), substrate, and it can be kept at room temperature. The film nominal thickness is about 1.5 nm. High-resolution C 1s and N 1s core-level XPS spectra provide evidence for structural integrity of **41** on the silicon surface. In particular, the spectra show four types of nitrogen atoms with relative intensities of 1 : 1: 1: 2, with the most intense peak assigned to the nitronyl nitroxide moiety. In addition, the less resolved XPS spectra of polycrystalline **41** show nearly identical spectral envelopes to those of the films. AFM images (Figure 9.16) and the line profiles, obtained by averaging the AFM signal, reveal islands of different lateral size.[107]

The molecular orientation of diradicals **41** with respect to the substrate is determined by NEXAFS spectra, by using two different polarization directions of the incident light, giving rise to NEXAFS dichroism (Figure 9.19). This dichroism clearly indicates that the island aggregation that is detected by AFM (Figure 9.18) is crystalline (not amorphous). An average orientation of the molecules in the film is comparable to the one adopted in the single crystals, with the crystallographic *a*-axis of the unit cell almost perpendicular to the substrate.[107] One of the remaining questions to answer is whether the films consist of 1-D antiferromagnetic chains as suggested by the orientation of diradical molecules in the film.

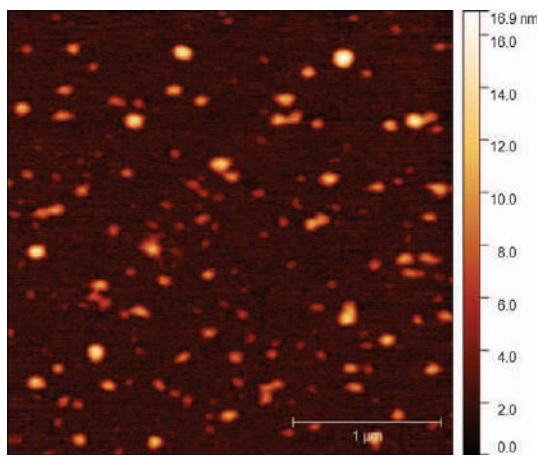

Figure 9.18 A typical AFM image of a 1.4 nm nominally thick film of **41**.

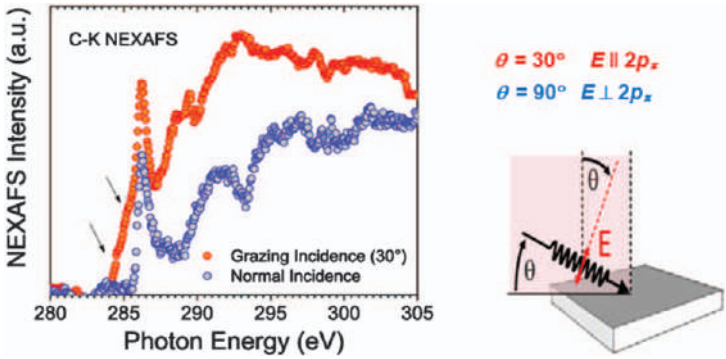

Figure 9.19 C–K NEXAFS spectra of **41** obtained from a 1.5 nm nominally thick film and geometry of the experiment. The spectra were taken in grazing incidence and in normal incidence as indicated. Two low-energy shoulders at $\theta = 30^{\circ}$ are indicated with the arrows.

9.10 Conclusion

Significant advances have been made in the field of high-spin nitroxide radicals – primarily based upon the development of hybrid high-spin diradicals (and triradicals). The ingenious molecular designs derived from the nitroxide or nitronyl nitroxides linked to electron-rich π-conjugated system have provided high-spin radicals with remarkable and novel properties. The hybrid radicals that consist of an electron-rich π-system that can be readily oxidized to radical cation have provided the robust radicals with SOMO–HOMO energy level inversion, which upon chemical oxidation or *in situ* electrode doping, readily produce high-spin diradical cations with relatively large singlet–triplet energy gaps. For selected diradical cations, a giant magnetoresistance was observed. Such hybrid radicals have also provided redox-switchable high-spin diradical cations that are effective at ambient conditions. Lastly, the hybrid radical derived from nitronyl nitroxides linked to a Blatter radical provided high-spin diradicals that are exceedingly thermally robust, including the magnetically and thermally robust diradical, for which thin films can be formed under ultra-high vacuum; the films are stable under UHV and are well characterized structurally. Along with the design of high-spin molecules, improvement of experimental and computational methods for determination of the energy gaps between the high-spin ground state and low-spin excited state is important for further advances in organic magnetism.

Acknowledgements

I thank all the current and former Rajca group students and postdoctoral associates who contributed to the research on high-spin molecules and whose names appear in the references. My special thanks go to

Dr. Suchada Rajca who helped me to improve the manuscript. I thank the National Science Foundation (NSF), Chemistry Division for support of this research under Grant Numbers: CHE-1665256 and CHE-1955349; and the National Institutes of Health (NIH) under Grant Numbers: NIGMS #R01GM124310-01 and NIBIB #R01EB-019950-01A1. The content of this work is solely the responsibility of the author and does not necessarily represent the official views of the NSF or NIH.

References

1. N. Mataga, Possible ''Ferromagnetic States'' of Some Hypothetical Hydrocarbons, *Theor. Chim. Acta*, 1968, **10**, 372–376.
2. A. Rajca, J. Wongsriratanakul and S. Rajca, Magnetic Ordering in an Organic Polymer, *Science*, 2001, **294**, 1503–1505.
3. A. Rajca, From High-Spin Organic Molecules to Polymers with Magnetic Ordering, *Chem. – Eur. J.*, 2002, **8**, 4834–4841.
4. P. M. Lahti, Structure–property relationships for metal-free organic magnetic materials, *Adv. Phys. Org. Chem.*, 2011, **45**, 93–169.
5. I. Ratera and J. Veciana, Playing with organic radicals as building blocks for functional molecular materials, *Chem. Soc. Rev.*, 2012, **41**, 303–349.
6. T. Sugawara, H. Komatsu and K. Suzuki, Interplay between magnetism and conductivity derived from spin-polarized donor radicals, *Chem. Soc. Rev.*, 2011, **40**, 3105–3118.
7. C. Herrmann, G. C. Solomon and R. A. Ratner, Organic Radicals as Spin Filters, *J. Am. Chem. Soc.*, 2010, **132**, 3682–3684.
8. S. Shil, D. Bhattacharya, A. Misra and D. J. Klein, A high-spin organic diradical as a spin filter, *Phys. Chem. Chem. Phys.*, 2015, **17**, 23378–23383.
9. S. Fujiwara, M. Hosoyamada, K. Tateishi, T. Uesaka, K. Ideta, N. Kimizuka and N. Yanai, Dynamic Nuclear Polarization of Metal–Organic Frameworks Using Photoexcited Triplet Electrons, *J. Am. Chem. Soc.*, 2018, **140**, 15606–15610.
10. G. M. Clore and J. Iwahara, Theory, Practice, and Applications of Paramagnetic Relaxation Enhancement for the Characterization of Transient Low-Population States of Biological Macromolecules and Their Complexes, *Chem. Rev.*, 2008, **109**, 4108–4139.
11. G. Spagnol, K. Shiraishi, S. Rajca and A. Rajca, Triplet Ground State ($S = 1$) Pegylated Bis(aminoxyl) Diradical: Synthesis and the Effect of Water on Magnetic Properties, *Chem. Commun.*, 2005, 5047–5049.
12. R. M. Davis, A. L. Sowers, W. Degraff, M. Bernardo, A. Thetoford, M. C. Krishna and J. B. Mitchell, A novel nitroxide is an effective brain redox imaging contrast agent and *in vivo* radioprotector, *Free Radical Biol. Chem.*, 2011, **51**, 780–790.
13. A. Rajca, Y. Wang, M. Boska, J. T. Paletta, A. Olankitwanit, M. A. Swanson, D. G. Mitchell, S. S. Eaton, G. R. Eaton and S. Rajca,

Organic Radical Contrast Agents for Magnetic Resonance Imaging, *J. Am. Chem. Soc.*, 2012, **134**, 15724–15727.
14. H. V.-T. Nguyen, Q. Chen, J. T. Paletta, P. Harvey, Y. Jiang, H. Zhang, M. D. Boska, M. F. Ottaviani, A. Jasanoff, A. Rajca and J. A. Johnson, Nitroxide-based macromolecular contrast agents with unprecedented transverse relaxivity and stability for magnetic resonance imaging of tumors, *ACS Cent. Sci.*, 2017, **3**, 800–811.
15. M. Abe, Diradicals, *Chem. Rev.*, 2013, **113**, 7011–7088.
16. W. C. Lineberger and W. T. Borden, The synergy between qualitative theory, quantitative calculations, and direct experiments in understanding, calculating, and measuring the energy differences between the lowest singlet and triplet states of organic diradicals, *Phys. Chem. Chem. Phys.*, 2011, **13**, 11792–11813.
17. H. G. Aurich, K. Hahn, K. Stork and W. Weiss, Aminyl oxides (nitroxides). XXIV. Empirical determination of the spin density distribution in aminyl oxides, *Tetrahedron*, 1977, **33**, 969–975.
18. E. Merzbacher, *Quantum Mechanics*, Wiley, New York, 1970, p. 528.
19. I. Ciofini, C. Adamo, V. Barone, G. Berthier and A. Rassat, Mapping the many-electron generalised spin-exchange Hamiltonian to accurate post-HF calculations, *Chem. Phys.*, 2005, **309**, 133–141.
20. A. A. Ovchinnikov, Multiplicity of the ground state of large alternant organic molecules with conjugated bonds (do organic ferromagnets exist?), *Theor. Chim. Acta*, 1978, **47**, 297–304.
21. P. G. Wenthold, J. Hu, R. R. Squires and W. C. Lineberger, Photoelectron Spectroscopy of the Trimethylenemethane Negative Ion. The Singlet–Triplet Splitting of Trimethylenemethane, *J. Am. Chem. Soc.*, 1996, **118**, 475–476.
22. S. Suzuki, T. Furui, M. Kuratsu, M. Kozaki, D. Shiomi, K. Sato, T. Takui and K. Okada, Nitroxide-substituted nitronyl nitroxide and iminonitroxide, *J. Am. Chem. Soc.*, 2010, **132**, 15908–15910.
23. K. Matsuda and H. Iwamura, Demonstration of the degeneracy of the singlet and triplet states in 2,3-dimethylenocyclohehexane-1,4-diyl by measurement of its magnetic properties, *J. Chem. Soc., Perkin Trans. 2*, 1998, 1023–1026.
24. P. G. Wenthold, J. B. Kim and W. C. Lineberger, Photoelectron Spectroscopy of m-Xylylene Anion, *J. Am. Chem. Soc.*, 1997, **119**, 1354–1359.
25. M. Kazuo, N. Hiroshi and I. Kazuhiko, The Proof of a Triplet Ground State in the *N*,*N*′-Di-*t*-butyl-*m*-phenylenebinitroxide Biradical, *Bull. Chem. Soc. Jpn.*, 1975, **48**, 2381–2382.
26. T. Ishida and H. Iwamura, Bis[3-*tert*-butyl-5-(*N*-oxy-*tert*-butylamino)-phenyl] nitroxide in a quartet ground state: a prototype for persistent high-spin poly[(oxyimino)-1,3-phenylenes], *J. Am. Chem. Soc.*, 1991, **113**, 4238–4241.
27. A. Rajca and S. Rajca, Intramolecular antiferromagnetic vs ferromagnetic spin coupling through the biphenyl unit, *J. Am. Chem. Soc.*, 1996, **118**, 8121–8126.

28. A. Sakane, H. Kumada, S. Karasawa, N. Koga and H. Iwamura, Molecular Structures and Magnetic Properties of the Mixed-Ligand Complexes of Bis(hexafluoroacetylacetonato)manganese(II), -copper(II), and -zinc(II) with 4,4′-Bis(N-tert-butyl-N-oxylamino)-2,2′-bipyridine. Isosceles Triangular Hetero-Three-Spin Systems Consisting of Aminoxyls and Metal Ions, *Inorg. Chem.*, 2000, **39**, 2891–2896.
29. D. A. Dougherty, Spin control in organic molecules, *Acc. Chem. Res.*, 1991, **24**, 88–94.
30. A. Rajca, Organic Di- and Polyradicals. From Spin Coupling to Magnetism? *Chem. Rev.*, 1994, **94**, 871–893.
31. N. M. Gallagher, A. Olankitwanit and A. Rajca, High-Spin Organic Molecules, *J. Org. Chem.*, 2015, **80**, 1291–1298.
32. W. T. Borden and E. R. Davidson, Effects of electron repulsion in conjugated hydrocarbon diradicals, *J. Am. Chem. Soc.*, 1977, **99**, 4587–4594.
33. J. R. Morton, Electron Spin Resonance Spectra of Oriented Radicals, *Chem. Rev.*, 1964, **64**, 453–471.
34. P. W. Kopf and R. W. Krellick, Magnetic resonance studies of some phenoxy and nitroxide biradicals, *J. Am. Chem. Soc.*, 1969, **91**, 6569–6573.
35. A. Olankitwanit, M. Pink, S. Rajca and A. Rajca, Synthesis of Aza-*m*-Xylylene Diradicals with Large Singlet-Triplet Energy Gap and Statistical Analyses of their EPR Spectra, *J. Am. Chem. Soc.*, 2014, **136**, 14277–14288.
36. N. M. Gallagher, J. J. Bauer, M. Pink, S. Rajca and A. Rajca, High-Spin Organic Diradical with Robust Stability, *J. Am. Chem. Soc.*, 2016, **138**, 9377–9380.
37. S. Chan, H. Zhang, A. Olankitwanit, S. Rajca and A. Rajca, High-Spin Diradical Dication of Chiral π-Conjugated Double Helical Molecule, *J. Am. Chem. Soc.*, 2019, **141**, 17287–17294.
38. L. Noodleman and J. G. Norman, The Xα valence bond theory of weak electronic coupling. Application to the low-lying states of $Mo_2Cl_8^{4-}$, *J. Chem. Phys.*, 1979, **70**, 4903–4906.
39. L. Noodleman, Valence bond description of antiferromagnetic coupling in transition metal dimers, *J. Chem. Phys.*, 1981, **74**, 5737–5743.
40. K. Yamaguchi, F. Jensen, A. Dorigo and K. N. Houk, A spin correction procedure for unrestricted Hartree-Fock and Møller-Plesset wavefunctions for singlet diradicals and polyradicals, *Chem. Phys. Lett.*, 1988, **149**, 537–542.
41. D. R. Maneru, A. K. Pal, I. de, P. R. Moreira, S. N. Datta and F. Illas, The Triplet–Singlet Gap in the *m*-Xylylene Radical: A Not So Simple One, *J. Chem. Theory Comput.*, 2014, **10**, 335–345.
42. G. Trinquier, N. Suaud and J.-P. Malrieu, Theoretical Design of High-Spin Polycyclic Hydrocarbons, *Chem. – Eur. J.*, 2010, **16**, 8762–8772.

43. V. Barone, I. Cacelli, A. Ferretti and G. Prampolini, Quantitative prediction and interpretation of spin energy gaps in polyradicals: the virtual magnetic balance, *Phys. Chem. Chem. Phys.*, 2017, **19**, 9039–9044.
44. W. T. Borden, With a Little Help from My Friends: Forty Years of Fruitful Chemical Collaborations, *J. Org. Chem.*, 2011, **76**, 2943–2964.
45. W. T. Borden and E. R. Davidson, The Importance of Including Dynamic Electron Correlation in *ab Initio* Calculations, *Acc. Chem. Res.*, 1996, **29**, 67–75.
46. K. Anderson, R. A. Malmqvist and B. O. Roos, Second-order perturbation theory with a complete active space self-consistent field reference function, *J. Chem. Phys.*, 1992, **96**, 1218–1226.
47. K. Anderson, R. A. Malmqvist, B. O. Roos, A. J. Sadlej and K. Wolinski, Second-order perturbation theory with a CASSCF reference function, *J. Chem. Phys.*, 1990, **94**, 5483–5488.
48. J. Miralles, J. P. Daudey and R. Caballol, Variational calculation of small energy differences. The singlet-triplet gap in $[Cu_2Cl_6]^{2-}$, *Chem. Phys. Lett.*, 1992, **198**, 555–562.
49. J.-P. Malrieu, Cancellations occurring in the calculation of transition energies by a perturbation development of configuration interaction matrices, *J. Chem. Phys.*, 1967, **47**, 4555–4558.
50. C. Sousa, C. de Graaf, F. Illas and G. Pacchioni, Excited States in Metal Oxides by Configuration Interaction and Multireference Perturbation Theory, in *Progress in Theoretical Chemistry and Physics*, ed. J. Maruani, C. Minot and R. McWeeny, Kluwer Academic Publishers, vol. 2, 2002, pp. 221–245, DOI: 10.1007/0-306-46950-2_13.
51. A. Calder, A. R. Forrester, P. G. James and G. R. Luckhurst, Nitroxide radicals. V. *N,N′*-Di-tert-butyl-m-phenylenebinitroxide, a stable triplet, *J. Am. Chem. Soc.*, 1969, **91**, 3724–3727.
52. A. Rajca, K. Lu, S. Rajca and C. Ross, II, Singlet-triplet bistability in a 1,3-phenylene-based bis(aminoxyl) diradical, *Chem. Commun.*, 1999, 1249–1250.
53. A. Rassat and U. Sieveking, A Stable Aromatic Diradical with Strong Dipolar Electronic Interaction, *Angew. Chem., Int. Ed. Engl.*, 1972, **11**, 303–304.
54. A. Rajca, M. Takahashi, M. Pink, G. Spagnol and S. Rajca, Conformationally Constrained, Stable, Triplet Ground State ($S=1$) Nitroxide Diradicals. Antiferromagnetic Chains of $S=1$ Diradicals, *J. Am. Chem. Soc.*, 2007, **129**, 10159–10170.
55. H. Sato, V. Kathirvelu, G. Spagnol, S. Rajca, A. Rajca, S. S. Eaton and G. R. Eaton, Impact of electron-electron spin interaction on electron spin relaxation of nitroxide diradicals and tetraradical in glassy solvents between 10 and 300 K, *J. Phys. Chem. B*, 2008, **112**, 2818–2828.
56. H. Nishimaki, S. Mashiyama, M. Yasui, T. Nogami and T. Ishida, Bistable Polymorphs Showing Diamagnetic and Paramagnetic States of an Organic Crystalline Biradical Biphenyl-3,5-diyl Bis(*tert*-butylnitroxide), *Chem. Mater.*, 2006, **18**, 3602–3604.

57. G. Kurokawa, T. Ishida and T. Nogami, Remarkably strong intermolecular antiferromagnetic couplings in the crystal of biphenyl-3,5-diyl bis(*tert*-butyl nitroxide), *Chem. Phys. Lett.*, 2004, **392**, 74–79.
58. H. Nishimaki and T. Ishida, Organic Two-Step Spin-Transition-Like Behavior in a Linear $S = 1$ Array: 3′-Methylbiphenyl-3,5-diyl Bis(*tert*-butylnitroxide) and Related Compounds, *J. Am. Chem. Soc.*, 2010, **132**, 9598–9599.
59. V. Barone, I. Cacelli, A. Ferretti, S. Monti and G. Prampolini, An Integrated Protocol for the Accurate Calculation of Magnetic Interactions in Organic Magnets, *J. Chem. Theory Comput.*, 2011, **7**, 699–706.
60. V. Barone, I. Cacelli, P. Cimino, A. Ferretti, S. Monti and G. Prampolini, Magnetic Interactions in Phenyl-Bridged Nitroxide Diradicals: Conformational Effects by Multireference and Broken Symmetry DFT Approaches, *J. Phys. Chem. A*, 2009, **113**, 15150–15155.
61. V. Barone, C. Boilleau, I. Cacelli, A. Ferretti and G. Prampolini, Conformational Effects on the Magnetic Properties of an Organic Diradical: A Computational Study, *J. Chem. Theory Comput.*, 2013, **9**, 1958–1963.
62. Y. Wang, S. Rajca and A. Rajca, PEGylated, Water-Soluble, Stable Aminyl Radical, *J. Org. Chem.*, 2017, **82**, 7512–7518.
63. Y. Wang, A. Olankitwanit, S. Rajca and A. Rajca, Intramolecular Hydrogen Atom Transfer in Aminyl Radical at Room Temperature with Large Kinetic Isotope Effect, *J. Am. Chem. Soc.*, 2017, **139**, 7144–7147.
64. S. Matsumoto, T. Higashiyama, H. Akutsu and S. Nakatsuji, A Functional Nitroxide Radical Displaying Unique Thermochromism and Magnetic Phase Transition, *Angew. Chem., Int. Ed.*, 2011, **50**, 10879–10883.
65. E. Tretyakov, A. Keerthi, M. Baumgarten, S. Veber, M. Fedin, D. Gorbunov, I. Shundrina and N. Gritsan, The Design of Radical Stacks: Nitronyl-Nitroxide-Substituted Heteropentacenes, *ChemistryOpen*, 2017, **6**, 642–652.
66. A. Dragulescu-Andrasi, A. S. Filatov, R. T. Oakley, X. Li, K. Lekin, A. Huq, C. Pak, S. M. Greer, J. McKay, M. Jo, J. Lengyel, I. Hung, E. Maradzike, A. E. DePrince III, S. A. Stoian, S. Hill, Y.-Y. Hu and M. Shatruk, Radical Dimerization in a Plastic Organic Crystal Leads to Structural and Magnetic Bistability with Wide Thermal Hysteresis, *J. Am. Chem. Soc.*, 2019, **141**, 17989–17994.
67. T. V. Magdesieva and O. A. Levitskiy, Molecular design of stable diarylnitroxides, *Russian Chem. Rev.*, 2018, **87**, 707–725.
68. A. Rajca, M. Vale and S. Rajca, Diarylnitroxide Diradicals: Low-Temperature Oxidation of Diarylamines to Nitroxides, *J. Am. Chem. Soc.*, 2008, **130**, 9099–9105.
69. M. Vale, M. Pink, S. Rajca and A. Rajca, Synthesis, Structure, and Conformation of Aza[1n]metacyclophanes, *J. Org. Chem.*, 2008, **73**, 27–35.
70. A. Rajca, K. Shiraishi and S. Rajca, Stable diarylnitroxide diradical with triplet ground state, *Chem. Commun.*, 2009, 4372–4374.

71. A. Rajca, K. Shiraishi, P. J. Boratyński, M. Pink, M. Miyasaka and S. Rajca, Oxidation of Annelated Diarylamines: Analysis of Reaction Pathways to Nitroxide Diradical and Spirocyclic Products, *J. Org. Chem.*, 2011, **76**, 8447–8457.
72. R. W. Murray and M. Singh, Chemistry of dioxiranes. II. A convenient high yield synthesis of nitroxides, *Tetrahedron Lett.*, 1988, **29**, 4677–4680.
73. A. Rajca, S. Rajca and J. Wongsriratanakul, Very High-Spin Organic Polymer: π-Conjugated Hydrocarbon Network with Average Spin of $S \geq 40$, *J. Am. Chem. Soc.*, 1999, **121**, 6308–6309.
74. V. Barone, I. Cacelli, A. Ferretti, S. Monti and G. Prampolini, Singlet–triplet energy gap of a diarylnitroxide diradical by an accurate many-body perturbative approach, *Phys. Chem. Chem. Phys.*, 2011, **13**, 4709–4714.
75. V. Barone, C. Boilleau, I. Cacelli, A. Ferretti, S. Monti and G. Prampolini, Structure-Properties Relationships in Triplet Ground State Organic Diradicals: A Computational Study, *J. Chem. Theory Comput.*, 2013, **9**, 300–307.
76. A. Rajca and S. Utamapanya, π-Conjugated Systems with Unique Electronic Structure: A Case of ''Planarized'' 1,3-Connected Polyarylmethyl carbodianion and Stable Triplet Hydrocarbon Diradical, *J. Org. Chem.*, 1992, **57**, 1760–1767.
77. S. Sinnecker and F. Neese, Spin–Spin Contributions to the Zero-Field Splitting Tensor in Organic Triplets, Carbenes and Biradicals – A Density Functional and Ab Initio Study, *J. Phys. Chem. A*, 2006, **110**, 12267–12275.
78. A. Rajca, A. Olankitwanit and S. Rajca, Triplet Ground State Derivative of Aza-*m*-Xylylene Diradical with Large Singlet-Triplet Energy Gap, *J. Am. Chem. Soc.*, 2011, **133**, 4750–4753.
79. A. Rajca, A. Olankitwanit, Y. Wang, P. J. Boratynski, M. Pink and S. Rajca, High-Spin $S = 2$ Ground State Aminyl Tetraradicals, *J. Am. Chem. Soc.*, 2013, **135**, 18205–18215.
80. F. Neese, Prediction of electron paramagnetic resonance *g*-values using coupled perturbed Hartree–Fock and Kohn–Sham theory, *J. Chem. Phys.*, 2001, **115**, 11080–11096.
81. T. Matsumoto, T. Ishida, N. Koga and H. Iwamura, Intramolecular magnetic coupling between two nitrene or two nitroxide units through 1,1-diphenylethylene chromophores. Isomeric dinitrenes and dinitroxides related in connectivity to trimethylenemethane, tetramethyleneethane, and pentamethylenepropane, *J. Am. Chem. Soc*, 1992, **114**, 9952–9959.
82. K. Inoue and H. Iwamura, 2-[p(N-tert-butyl-N-oxyamino)phenyl]-4,4,5,5-tetramethyl-4,5-dihydroimidazol-3-oxide-1-oxyl, a Stable Diradical with a Triplet Ground State, *Angew. Chem., Int. Ed. Engl.*, 1995, **34**, 927–928.
83. Y. Hosokoshi, K. Takizawa, H. Nakano, T. Goto, M. Takahashi and K. Inoue, Construction of spin-1 Heisenberg ferromagnetic-antiferromagnetic alternating chains with various exchange couplings, *J. Magn. Magn. Mater.*, 1998, **177–181**, 634–635.

84. D. A. Shultz, A. K. Boal, H. Lee and G. T. Farmer, Structure–Property Relationships in Trimethylenemethane-Type Biradicals. 2. Synthesis and EPR Spectral Characterization of Dinitroxide Biradical, *J. Org. Chem.*, 1999, **64**, 4386–4396.
85. D. A. Shultz, R. M. Fico, P. D. Boyle and J. W. Kampf, Observation of a Hysteretic Phase Transition in a Crystalline Dinitroxide Biradical That Leads to Magnetic Bistability, *J. Am. Chem. Soc.*, 2001, **123**, 10403–10404.
86. D. A. Shultz, R. M. Fico, Jr., H. Lee, J. W. Kampf, K. Kirschbaum, A. A. Pinkerton and P. D. Boyle, Mechanisms of Exchange Modulation in Trimethylenemethane-type Biradicals: The Roles of Conformation and Spin Density, *J. Am. Chem. Soc.*, 2003, **125**, 15426–15432.
87. T. Itoh, K. Matsuda, H. Iwamura and K. Hori, Tris[*p*-(*N*-oxyl-*N*-*tert*-butylamino)phenyl]amine, -methyl, and -borane Have Doublet, Triplet, and Doublet Ground States, Respectively, *J. Am. Chem. Soc.*, 2000, **122**, 2567–2576.
88. D. C. Oniciu, K. Matsuda and H. Iwamura, Synthesis and EPR characterisation of triphenylmethane derivatives carrying N-tert-butyl nitroxide radical moieties: use of the diradical as a ligand for a complex with $Mn^{II}(hfac)_2$, *J. Chem. Soc., Perkin Trans. 2*, 1996, 907–913.
89. A. Rajca, K. Shiraishi, M. Vale, H. Han and S. Rajca, Stable Hydrocarbon Diradical, An Analogue of Trimethylenemethane, *J. Am. Chem. Soc.*, 2005, **127**, 9014–9020.
90. M. Tanaka, K. Matsuda, T. Itoh and H. Iwamura, Syntheses and Magnetic Properties of Stable Organic Triradicals with Quartet Ground States Consisting of Different Nitroxide Radicals, *J. Am. Chem. Soc.*, 1998, **120**, 7168–7173.
91. Y. Wang, H. Zhang, M. Pink, A. Olankitwanit, S. Rajca and A. Rajca, Radical Cation and Neutral Radical of Aza-thia[7]helicene with SOMO–HOMO Energy Level Inversion, *J. Am. Chem. Soc.*, 2016, **138**, 7298–7304.
92. G. Gryn'ova and M. L. Coote, Origin and Scope of Long-Range Stabilizing Interactions and Associated SOMO–HOMO Conversion in Distonic Radical Anions, *J. Am. Chem. Soc.*, 2013, **135**, 15392–15403.
93. P. Franchi, E. Mezzina and M. Lucarini, SOMO–HOMO Conversion in Distonic Radical Anions: An Experimental Test in Solution by EPR Radical Equilibration Technique, *J. Am. Chem. Soc.*, 2014, **136**, 1250–1252.
94. H. Komatsu, M. M. Matsushita, S. Yamamura, Y. Sugawara, K. Suzuki and T. Sugawara, Influence of Magnetic Field upon the Conductance of a Unicomponent Crystal of a Tetrathiafulvalene-Based Nitronyl Nitroxide, *J. Am. Chem. Soc.*, 2010, **132**, 4528–4529.
95. R. Kumai, M. M. Matsushita, A. Izuoka and T. Sugawara, Intramolecular Exchange Interaction in a Novel Cross-Conjugated Spin System Composed of π-Ion Radical and Nitronyl Nitroxide, *J. Am. Chem. Soc.*, 1994, **116**, 4523–4524.

96. A. Izuoka, M. Hiraishi, T. Abe, T. Sugawara, K. Sato and T. Takui, Spin Alignment in Singly Oxidized Spin-Polarized Diradical Donor: Thianthrene Bis(nitronyl nitroxide), *J. Am. Chem. Soc.*, 2000, **122**, 3234–3235.
97. M. M. Matsushita, H. Kawakami, T. Sugawara and M. Ogata, Molecule-based system with coexisting conductivity and magnetism and without magnetic inorganic ions, *Phys. Rev. B*, 2008, **77**, 195208-1-6.
98. S. Hiraoka, T. Okamoto, M. Kozaki, D. Shiomi, K. Sato, T. Takui and K. Okada, A Stable Radical-Substituted Radical Cation with Strongly Ferromagnetic Interaction: Nitronyl Nitroxide-Substituted 5,10-Diphenyl-5,10-dihydrophenazine Radical Cation, *J. Am. Chem. Soc.*, 2004, **126**, 58–59.
99. Y. Masuda, M. Kuratsu, S. Suzuki, M. Kozaki, D. Shiomi, K. Sato, T. Takui, Y. Hosokoshi, X.-Z. Lan, Y. Miyazaki, A. Inaba and K. Okada, A New Ferrimagnet Based on a Radical-Substituted Radical Cation Salt, *J. Am. Chem. Soc.*, 2009, **131**, 4670–4673.
100. T. Tahara, S. Suzuki, M. Kozaki, D. Shiomi, K. Sugisaki, K. Sato, T. Takui, Y. Miyake, Y. Hosokoshi, H. Nojiri and K. Okada, Triplet Diradical-Cation Salts Consisting of the Phenothiazine Radical Cation and a Nitronyl Nitroxide, *Chem. – Eur. J.*, 2019, **25**, 7201–7209.
101. M. Kuratsu, S. Suzuki, M. Kozaki, D. Shiomi, K. Sato, T. Takui, T. Kanzawa, Y. Hosokoshi, X.-Z. Lan, Y. Miyazaki, A. Inaba and K. Okada, (Nitronyl nitroxide)-substituted trioxytriphenylamine radical cation tetrachlorogallate salt: a 2p-electron-based weak ferromagnet composed of a triplet diradical cation, *Chem. – Asian J.*, 2012, **7**, 1604–1609.
102. T. Itoh, K. Matsuda and H. Iwamura, A Triphenylamine Derivative with Three p-(N-tert-Butyl-N-oxylamino)phenyl Radical Units and Yet a Doublet Ground State, *Angew. Chem., Int. Ed.*, 1999, **38**, 1791–1793.
103. S. Suzuki, A. Nagata, M. Kuratsu, M. Kozaki, R. Tanaka, D. Shiomi, K. Sugisaki, K. Toyota, K. Sato, T. Takui and K. Okada, Trinitroxide-Trioxytriphenylamine: Spin-State Conversion from Triradical Doublet to Diradical Cation Triplet by Oxidative Modulation of a π-Conjugated System, *Angew. Chem., Int. Ed.*, 2012, **51**, 3193–3197.
104. A. Ito, Y. Nakano, T. Kato and K. Tanaka, Tetraarylethylene having two nitroxide groups: redox-switching of through-bond magnetic interaction by conformation change, *Chem. Commun.*, 2005, 403–405.
105. A. Ito, Y. Nakano, M. Urabe, T. Kato and K. Tanaka, Triradical Cation of *p*-Phenylenediamine Having Two Nitroxide Radical Groups: Spin Alignment Mediated by Delocalized Spin, *J. Am. Chem. Soc.*, 2006, **128**, 2948–2953.
106. A. Ito, R. Kurata, D. Sakamaki, S. Yano, Y. Kono, Y. Nakano, K. Furukawa, T. Kato and K. Tanaka, Redox Modulation of *para*-Phenylenediamine by Substituted Nitronyl Nitroxide Groups and Their Spin States, *J. Phys. Chem. A*, 2013, **117**, 12858–12867.

107. N. Gallagher, H. Zhang, T. Junghoefer, E. Giangrisostomi, R. Ovsyannikov, M. Pink, S. Rajca, M. B. Casu and A. Rajca, Thermally and Magnetically Robust Triplet Ground State Diradical, *J. Am. Chem. Soc.*, 2019, **141**, 4764–4774.
108. C. P. Constantinides and P. A. Koutentis, Stable N- and N/S-Rich Heterocyclic Radicals: Synthesis and Applications, *Adv. Heterocycl. Chem.*, 2016, **119**, 173–207.
109. W. Wang, C. Chen, C. Shu, S. Rajca, X. Wang and A. Rajca, $S = 1$ Tetraazacyclophane Diradical Dication with Robust Stability: a Case of Low Temperature One-Dimensional Antiferromagnetic Chain, *J. Am. Chem. Soc.*, 2018, **140**, 7820–7826.
110. K. Wierschem and P. Sengupta, Quenching the Haldane gap in spin-1 Heisenberg antiferromagnets, *Phys. Rev. Lett.*, 2014, **112**, 247203.
111. A. Bajaj and Md. E. Ali, First-Principle Design of Blatter's Diradicals with Strong Ferromagnetic Exchange Interactions, *J. Phys. Chem. C*, 2019, **123**, 15186–15194.

CHAPTER 10

Applications of Nitroxide Spin Labels to Structural Biology

C. S. KLUG,* M. T. LERCH AND J. B. FEIX

Medical College of Wisconsin, Department of Biophysics, 8701 Watertown Plank Road, Milwaukee, WI 53226, USA
*Email: candice@mcw.edu

10.1 Introduction

Nitroxide spin labeling was introduced by McConnell and co-workers in the mid-1960s with the goals of using electron paramagnetic resonance (EPR) spectroscopy to investigate conformational changes in proteins[1,2] and the biophysical properties of lipid bilayer membranes.[3–5] A nitroxide spin label contains a paramagnetic aminoxyl radical that is stabilized by protecting groups and is sensitive to motion and polarity, with the electron density sufficiently localized to be useful as a point for distance measurements. Early protein spin labeling relied on maleimide or iodoacetamide spin labels to modify naturally occurring cysteine residues. A major advance in the application of EPR spin labeling occurred when Hubbell and co-workers developed the site-directed spin labeling (SDSL) methodology[6–9] based on the revolutionary advances in molecular biology that followed the introduction of polymerase chain reaction methods. SDSL and improvements in cloning methodology allowed the introduction of a spin label at a position of choice in virtually any protein, vastly expanding the scope of EPR spin labeling. The methanethiosulfonate (MTS) spin label was introduced in 1982[10] followed by numerous derivatives, many of which were first synthesized by Hideg and co-workers.[11,12] Significant technological advances occurred concomitant with the progress in biological and biochemical methods, notably the introduction

Nitroxides
Edited by Olivier Ouari and Didier Gigmes

Published by the Royal Society of Chemistry, www.rsc.org

of loop-gap resonators by Froncisz and Hyde[13] and the development of pulse EPR methods such as dead-time free double electron–electron resonance (DEER, also known as pELDOR [pulsed electron–electron double resonance])[14] and double quantum coherence (DQC) spectroscopy.[15] Dozens of protein structure and functional dynamics studies are published each year using the SDSL EPR spectroscopy technique (also referred to as SDSL-EPR) with nitroxide spin labels as the reporter molecules (*e.g.*, ref. 16–206). An array of developments have been made in the synthesis and application of novel nitroxide-based spin labels specific to the study of protein structure and functional dynamics since their introduction. Future advances are likely to focus on improved methods for the selective introduction of spin labels into proteins, new spin labels with increased stability in intact cells and improved relaxation properties, continued development of pulse and time-resolved instrumentation technologies and improvements in computational methods of analysis and the integration of EPR data with molecular modeling and dynamics calculations. In this chapter, we discuss the current state of the art of nitroxide-based SDSL EPR spectroscopy, including the development and use of novel nitroxide spin labels over the past five years, with a primary emphasis on their application to protein structure and dynamics.

10.2 Nitroxide Spin Labels for Protein Structural Biology Studies

A variety of nitroxide-based spin labels is used in EPR for structural biology studies. The nitroxide is typically integrated into a five-membered pyrrolidine or six-membered piperidine ring structure (*e.g.*, Figure 10.1). The labels are often attached to the free sulfhydryl group of a cysteine residue within a protein or peptide to form a disulfide bond by inclusion of an MTS leaving group to the spin label; the resulting disulfide linkage is reversible through cleavage by a reducing agent. Alternatively, the labels can be attached to the free sulfhydryl group of a cysteine residue through a noncleavable covalent bond by inclusion of a maleimide (*e.g.*, MAL-6, MSL) or iodoacetamide (*e.g.*, IASL, IAP) leaving group to the spin label. Additionally, labels are available that covalently attach to noncysteine residues, such as lysine (*e.g.*, 1-oxyl-2,2,5,5-tetramethylpyrroline-3-carboxylate *N*-hydroxysuccinimide ester), tyrosine (*e.g.*, 4-amino-2,2,5,5-tetramethyl-3-imidazoline-1-yloxy) or methionine [*e.g.*, 3-(2-iodoacetamido)-2,2,5,5-tetramethyl-1-pyrrolidinyloxy at low pH], to unnatural amino acids through click chemistry (*e.g.*, K1, Az-TEIO), to RNA or to DNA (*e.g.*, aliphatic isocyanate nitroxides, R5p), or that integrate into the backbone of a synthesized peptide (*e.g.*, TOAC, TOPP) or lipid (*e.g.*, 12-phosphatidylcholine spin label [12-PCSL], cholesterol spin label [CSL]).

By far the most commonly used label for protein structural biology studies is the sulfhydryl-specific MTSL spin label, which forms the R1 side chain upon attaching to a cysteine amino acid (Figure 10.1). However, a number of modifications of MTSL and other newly designed labels have been specifically created for specialized uses and are becoming more mainstream.

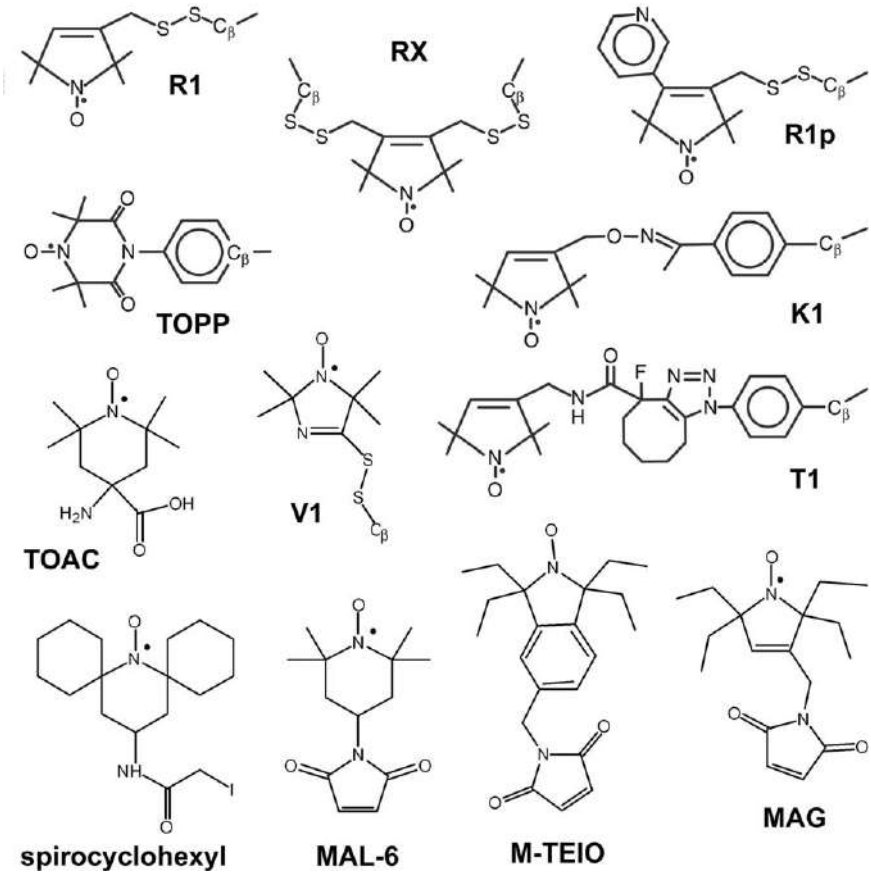

Figure 10.1 Example nitroxide spin label and side chain structures. Structures of side chains that are formed upon covalent attachment of a spin label to a protein through the C_α or C_β atom (*i.e.*, R1, RX, R1p, K1, T1, V1, TOPP). Structures of spin labels (with reactive groups still attached; *i.e.*, TOAC, spirocyclohexyl, MAL-6, M-TEIO, MAG).
Some elements reproduced from ref. 269 with permission from Elsevier, Copyright 2013.

In the subsequent sections, we describe many of the nitroxide-based labels used for SDSL EPR spectroscopy studies of proteins and lipids, along with their specific strengths, weaknesses, useful properties and limitations; this is an extensive, but not exhaustive, list. The labels are commercially available unless otherwise stated.

10.2.1 MTSL

The 1-oxyl-2,2,5,5-tetramethyl-Δ3-pyrroline-3-methyl methanethiosulfonate spin label (MTSL or MTSSL) has been the go-to spin label for decades. The R1 group that is formed upon reaction of MTSL with the free sulfhydryl

of a cysteine residue (Figure 10.1) is comparatively small in that it has approximately the same volume as one of the larger amino acids such as tryptophan and thus does not typically disrupt the protein structure. MTSL readily reacts with free sulfhydryl groups through its MTS moiety, which is easily removed from the sample after the reaction. Its major strength is that it very effectively reports motion on the nanosecond timescale, and thus it remains the universal label for continuous-wave (CW) EPR spectroscopy studies that rely on motional analysis of side chain motion. It has been very well characterized, including numerous crystal structures of proteins containing R1 (*e.g.*, ref. 207), and extensive rotamer libraries and motional analyses have been published. The motional states represented by the spectra of this side chain are well recognized by EPR spectroscopists. Disadvantages include the need for cryogenic temperatures for DEER experiments due to the short spin–lattice relaxation (T_1) and phase-memory (T_m) times at room temperature (*e.g.*, ref. 208) and the ready reduction of the nitroxide under reducing conditions such as those inside cells (*e.g.*, ref. 189). In addition, its side chain flexibility due to the five rotatable bonds that attach the nitroxide ring to the protein backbone can add to the width of the distance distribution in DEER experiments. Also, it is cleavable under reducing conditions or in the presence of other free sulfhydryls, which is true for any label attached through a disulfide bond, yet this can also be an advantage in cases where removal of the label is desirable. Addressing the weaknesses of R1 has motivated the development of several new labels, including many described in the following sections.

10.2.2 MTSL with 4′ Modifications

An array of labels has been synthesized where the 4′ hydrogen of the nitroxide ring has been replaced with a larger molecule or group.[12] For example, substitutions include bromine (R7),[209] methyl (R1b),[12] phenyl (R1f)[12] and pyridyl (R1p; Figure 10.1)[210] that are intended to slow down the motion of the spin label side chain to either report on protein backbone motions without contributions from spin label side chain motion or obtain narrower DEER distance distributions. With the exception of Br-MTSL to create R7, most modified labels are not commercially available.

10.2.3 Bifunctional Spin Labels

The bifunctional 3,4-bis-(methanethiosulfonylmethyl)-2,2,5,5-tetramethyl-2,5-dihydro-1*H*-pyrrol-1-yloxy spin label (BSL) (*e.g.*, ref. 160) or HO-1944[211] is composed of MTSL with an additional linker such that the nitroxide ring attaches to two cysteine residues simultaneously to create the RX side chain (Figure 10.1).[211] This spin label requires the introduction of two cysteine residues at i and i + 3 or i + 4 on a helix or at i and i + 2 within a β-strand. The double attachment results in a highly constrained nitroxide, effectively eliminating spin label side chain motion. The major advantage of this label

is that DEER distance distributions are narrower (*e.g.*, a 6.5 Å distribution width for double R1 labels narrows to 2.8 Å with RX labels),[211] as it effectively represents the distance between two immobile points on the protein without motion from spin label side chain flexibility; widths in the distance distributions using RX represent the flexibility of the protein backbone rather than spin label motion. In addition, the rigidity of the label allows microsecond timescale motions of the protein or protein domains to be studied using ELDOR (electron–electron double resonance) spectroscopy.[211] The disadvantages of this label include the need for prior structural information to appropriately place the spin labels in a stable helix or β-strand and the need for the introduction of two cysteine mutations per labeling site into the protein of interest.

10.2.4 Imidazoline Spin Labels

Bis(2,2,5,5-tetramethyl-3-imidazoline-1-oxyl-4-il)-disulfide spin label (IDSL) forms the V1 side chain upon reaction with a free sulfhydryl group[212] and a similar label (Rn) forms the same side chain.[106] V1 contains one less bond than MTSL in the linker between the nitroxide ring and the disulfide bond, and the nitroxide ring contains an extra nitrogen (Figure 10.1). Spectral and crystallographic evidence indicates the internal motion of the V1 side chain is ordered, with only one or two preferred rotameric states, making it a highly attractive choice for DEER spectroscopy.[212] Computational analysis suggests this side chain may be more sensitive to faster motion than R1 and thus useful for monitoring high-amplitude protein backbone fluctuations and motional studies on the low nanosecond timescale using CW EPR spectroscopy.[106,212] The main disadvantage of the V1 label is that it is prone to dissociation, particularly for partially buried sites or where the label is otherwise sterically constrained, which may limit its utility in CW and SR EPR studies but has a negligible effect on DEER data analysis.

10.2.5 Maleimide Spin Labels

4-Maleimido-2,2,6,6-tetramethylpiperidine-1-oxyl spin label (4-maleimido TEMPO [MAL-6, MSL or 4-MT]) contains a six-membered nitroxide ring; thus, it has the nickname MAL-6 even though the maleimide group is attached to the 4′ carbon position of the ring (Figure 10.1). Similarly, 3-maleimido-2,2,5,5-tetramethyl-1-pyrrolidinyloxy spin label (3-maleimido PROXYL or 5-MSL) contains a five-membered nitroxide ring. When attached to a cysteine residue, MAL-6 has a longer linker than R1 but exhibits slower motion, so it is not as useful as R1 for CW EPR spectroscopy motional studies. An advantage of MAL-6 is that the maleimide group allows it to be used in the presence of reducing agents such as dithiothreitol because it forms a stable carbon–sulfur covalent bond. This is beneficial for increasing the labeling efficiency of cysteine residues by keeping the sulfhydryl group in the reduced state until spin labeled.

10.2.6 Tetraethyl Spin Labels

The tetraethylpiperidinyloxy (TETPO), tetraethylisoindoline (TEIO) and maleimide-functionalized *gem*-diethyl (MAG) spin labels contain geminyl ethyl groups rather than the traditional methyl groups found on MTSL, MAL-6 and MTSL derivatives. Maleimide-TETPO (M-TETPO), maleimide-TEIO (M-TEIO), azide-TEIO (Az-TEIO) and MAG labels were recently developed to protect the stability of the nitroxide in the reducing environment found within cells.[137,161,164,213] Their intended use is for *in vivo* (or in-cell) spin labeling of proteins for CW and DEER spectroscopy studies. These labels are based on a similar strategy that was developed for labeling RNA for DEER spectroscopy studies.[214] The benefits include increased stability of the nitroxide under reducing conditions (*i.e.*, the TETPO and TEIO nitroxides are stable in ascorbate or cell lysate or oocyte extract for hours compared with minutes for methyl-protected pyrrolidine labels such as MTSL)[137,164] and the ability to label specific sites within the cell using Az-TEIO even in the presence of background cysteines. Disadvantages include the lack of specificity to a particular cysteine *in vivo*, need for introduction of the Az-TEIO *via* click chemistry through an unnatural amino acid and low labeling efficiency. The slightly larger size of TEIO compared with TETPO or MTSL and their limited modeling and simulation data are potential current limitations. These labels were each custom synthesized and are not yet commercially available.

10.2.7 Spirocyclohexyl Iodoacetamide Spin Label

The nitroxide for the spirocyclohexyl iodoacetamide spin label is integrated into a piperidine ring containing two six-membered rings on either side of the nitroxide as protecting groups (Figure 10.1).[44] The overall goal of this design is to allow room-temperature DEER experiments by increasing the T_m of the spin label at room temperature. The intent is to enable DEER spectroscopy on proteins at temperatures >80 K. A significant benefit is that this nitroxide is much smaller than triarylmethyl spin labels, which are non-nitroxides developed for a similar goal. A disadvantage is that it is not yet commercially available. Another design to increase the T_m resulted in the aza-adamantyl spin label, which also eliminates the *gem*-methyl groups.[215]

10.2.8 Unnatural Amino Acid Spin Labels

Some spin labels can be selectively introduced into a protein (*e.g.*, K1 or T1; Figure 10.1) through reaction with an unnatural amino acid (noncanonical amino acid), which is incorporated *in vivo* through a specialized tRNA, or by direct incorporation of a spin-labeled amino acid *in vivo*.[163] The major advantage of this approach is that the spin label is targeted to a specific site without the concern that other reactive groups are present *in vivo* or *in vitro*; that is, proteins with a large number of native cysteines or functionally required cysteines or cystines can be selectively labeled. Disadvantages

currently include the need for specialized *in vivo* expression reagents; low protein yields, inefficient unnatural amino acid incorporation and labeling yields; and an increased flexibility of the spin label due to the long linkers attaching the nitroxides to the protein backbone.

10.2.9 TOAC and TOPP Spin Labels

2,2,6,6-Tetramethyl-piperidine-1-oxy-4-amino-4-carboxylic acid (TOAC) and 4-(3,3,5,5-tetramethyl-2,6-dioxo-4-oxylpiperazin-1-yl)-L-phenylglycine (TOPP)[65,216] are amino acid replacements that are directly incorporated during solid-phase peptide synthesis to introduce the nitroxide ring at a specific location within a synthesized peptide. The nitroxide ring is integrated into the peptide backbone for TOAC and semirigidly attached through a planar phenyl ring for TOPP (Figure 10.1). Their rigid attachment to a peptide backbone is advantageous for DEER spectroscopy studies of peptides. TOPP is especially well suited for membrane peptide studies by DEER, but it is not yet commercially available.[65,200] The main disadvantage is that these spin labels are only applicable to synthesized protein fragments and peptides because currently they cannot be incorporated into recombinantly expressed proteins.

10.2.10 Other Spin Labels

Covalent and noncovalent nitroxide-based labels for RNA and DNA have been developed in parallel to those for SDSL of proteins (*e.g.*, ref. 217–226). A variety of spin-labeled lipids also exist for the study of lipid membranes important in structural biology; for example, the classic 5-, 7-, 10-, 12-PCSLs where a nitroxide is attached to the corresponding acyl chain carbon atom of a phosphatidylcholine lipid, labeled cholesterol and other lipid-analog labels (*e.g.*, ref. 227–231). In addition, a number of spin labels that do not contain a nitroxide moiety are being successfully developed and utilized for protein structure and function studies (*e.g.*, Cu(II),[202,232,233] Fe(III)[234] and Gd(III) complexes,[195,235–237] and triarylmethyls [TAM, trityl][87,238–241]) using EPR spectroscopy techniques. Further, nitroxides are being utilized in structural biology studies for non-EPR biophysical approaches such as paramagnetic relaxation enhancement nuclear magnetic resonance spectroscopy[79,242–245] and dynamic nuclear polarization,[173,246] and as magnetic resonance imaging contrast agents.[247]

10.3 Applications of Nitroxide Spin Labels in Structural Biology

Examples of specific applications of nitroxide spin labels to protein structural biology studies can be found in hundreds of publications over the past five years alone. The field continues to grow as EPR instrumentation

technology evolves and new labels are created to enable additional systems and biomedically relevant questions to be investigated by nitroxide-based SDSL EPR spectroscopy. In addition to the hundreds of experiments using nitroxide spin labels to study protein structure and functional dynamics published in the last five years (*i.e.*, 2014–2019; *e.g.*, ref. 16–206), a variety of how-to guides and reviews were published in this timeframe that aid in selecting spin labels for specific experiments and showcasing examples of their use in EPR spectroscopy experiments (*e.g.*, ref. 18, 21, 24, 40, 48, 49, 51, 81, 101, 122, 148, 161, 163, 248). In this chapter, a small subset of nitroxide spin-labeling experiments on membrane and soluble proteins is highlighted to exemplify applications using various nitroxide spin labels in three major classes of EPR experiments: DEER spectroscopy, saturation recovery (SR) EPR and EPR spectroscopy of protein structures in intact cells.

10.3.1 DEER Applications

DEER spectroscopy is a large and actively growing field of EPR, with novel labels being most commonly applied to this powerful experimental approach. An example of the evolution of labels for DEER spectroscopy can be found in the much-studied field of G-protein-coupled receptors (GPCRs). GPCRs are a large and important family of signal transduction proteins responsible for regulating nearly every aspect of human physiology.[249] SDSL EPR spectroscopy is particularly useful for characterizing structure and dynamics in large membrane-bound proteins and protein complexes,[18,122,248] and the membrane-bound protein that has been studied most extensively by SDSL EPR is the prototypical GPCR rhodopsin.[49,250] Rhodopsin is a photoreceptor found in the rod cells of the retina and is responsible for dim-light vision.[251] Early SDSL EPR studies of rhodopsin utilized CW-based methods such as lineshape analysis, solvent accessibility and dipolar broadening. More recently, as pulse EPR instrumentation and methods have advanced and become more widely accessible, efforts have shifted to the use of DEER spectroscopy to determine structural information about this receptor. SDSL in combination with DEER spectroscopy provides high-resolution, long-range (~20–80 Å) distance distributions between pairs of spin labels introduced into a single protein or into different subunits of a protein–protein complex.[252] The ability of DEER to provide a distribution of distances, rather than the average distance, means that each structure present in the conformational ensemble is reported along with its relative population.

In a recent DEER study of rhodopsin, intermolecular distance constraints between rhodopsin and inhibitory G protein G_i generated a model of the complex, revealing differences in the interactions of G_i and G_s that provided insights into G protein specificity.[156] A study of rhodopsin in nanodiscs demonstrated that in a native-like lipid environment both the inactive and light-activated receptor exist in a manifold of conformational substates in equilibrium.[114] The intramolecular structure and dynamics of GPCR interaction partners arrestin[94,119] and G protein[27,50] have also been characterized.

DEER has proven to be a useful technique in studies of other GPCRs as well, including providing insight into the structural basis for agonist-mediated signaling in the β_2 adrenergic receptor[42] and resolving a dimerization equilibrium and interface in the neurotensin receptor 1.[126] The information provided by SDSL-EPR techniques such as DEER is highly complementary to the structures solved by cryo-electron microscopy (cryo-EM) and X-ray crystallography, and it is becoming increasingly common to use DEER experiments to corroborate key features of new GPCR cryo-EM and crystal structures.[253–257]

A notable new study on the angiotensin II type 1 receptor benefited from the use of a disulfide-linked imidazoline nitroxide side chain referred to as V1.[201] This spin label side chain exhibits highly constrained internal motion resulting from an intra-side chain interaction of the sulfur atoms with both the protein backbone and the 3-nitrogen of the imidazoline ring.[212] The reduced rotameric space of V1 decreases the contribution of spin label side chain flexibility to the width of DEER distributions, allowing more precise information about protein flexibility to be obtained.[53] In the most detailed mapping of the activation states of GPCRs by DEER reported to date, data were collected for 10 V1-labeled angiotensin receptor mutants bound to a panel of ligands including antagonists, balanced agonists, β-arrestin-biased agonists and G protein-biased agonists, as well as for the unliganded receptor. Individual receptors can signal through multiple G proteins and arrestins, and the goal of this study was to uncover the molecular mechanisms underlying the ability of ligands to selectively activate a particular signaling pathway over others (*i.e.*, biased agonism). It is immediately apparent from the DEER distance distributions that significant conformational heterogeneity exists in all liganded and unliganded states, rather than a single, well-defined conformation being adopted under each condition. Additionally, distinct patterns of distance changes are populated by each class of ligand (Figure 10.2), and an analysis of the complete DEER dataset yielded models for four distinct conformations. In this study, the ability to resolve multiple states was likely enhanced by the greater resolution afforded by the V1 label. Functional roles for each conformation were assigned by comparing the ligand-specific patterns of conformational changes with the pathway-specific impact of the ligands on signaling. The data are consistent with a model in which the G protein requires an open receptor conformation (Figure 10.2E) for binding, whereas arrestin binding is more promiscuous and can occur through either the open conformation or two different occluded conformations (Figure 10.2C–D). The V1 side chain enabled these distinct populations to be identified, and this study showcases the power of the SDSL EPR spectroscopy approach to identify biologically important conformations of large membrane proteins using nitroxide spin labels.

In other applications, a number of different labeling strategies coupled nitroxide-based spin labels with non-nitroxide labels for distance measurements. For example, nitroxide–Cu(II)[193,202] and nitroxide–Gd(III),[204] as well as triple labeling with two metals and a nitroxide,[116] recently have been utilized to determine distances between a spin-labeled site and a paramagnetic metal

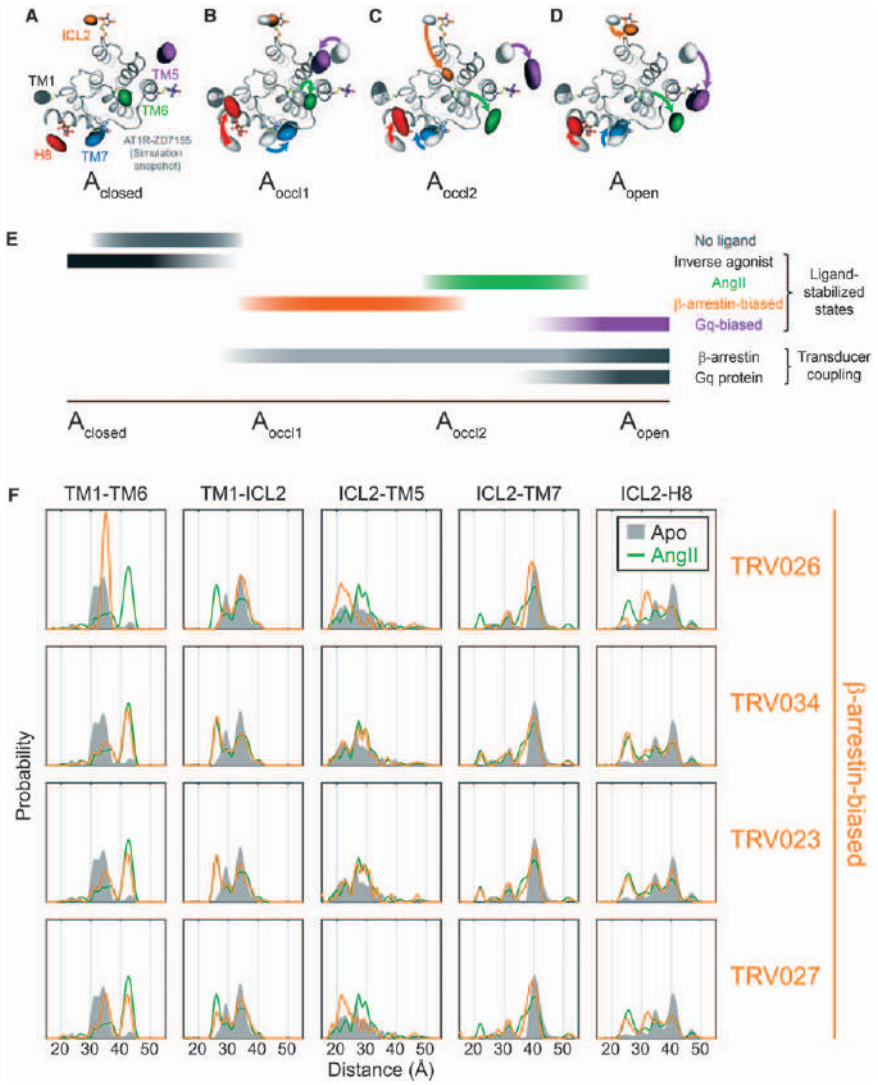

Figure 10.2 DEER distance mapping reveals conformational signatures of biased agonism in the angiotensin II type 1 receptor. (A–D) Analysis of the data identified four distinct conformations where the spin density of labels placed at the cytoplasmic ends of transmembrane (TM) helices 1, 5, 6 and 7 as well as helix 8 (H8) and intracellular loop 2 (ICL2) are shown using color-coded clouds. (E) Extensive knowledge of the signaling impact of the ligands used in this study enabled functional assignments to be made for each of the four conformations identified. (F) A subset of the distance distributions from the study are shown, highlighting differences in distances populated in the unliganded receptor (Apo, gray), angiotensin II-bound receptor (AngII, green) and receptor bound to a panel of β-arrestin-biased ligands (orange).
Adapted from ref. 201 with permission from Elsevier, Copyright 2018.

ion chelate by DEER spectroscopy, as well as ^{19}F–nitroxide pairs for electron nuclear double resonance (ENDOR)-determined distances up to 15 Å.[258]

10.3.2 SR EPR Applications

SR is conceptually the simplest of the pulsed EPR methods and a powerful approach capable of providing room-temperature distance measurements, accessibility of spin labels to relaxation agents, phase separations in membranes and protein conformational equilibria. The theory and application of SR EPR have been considered in a number of book chapters and reviews,[51,259,260] including a recent discussion on the application of SR to spin labels.[51] This section showcases how SR can be used to investigate proteins labeled with R1 and how labels with reduced motion or intrinsically longer T_1 values are beneficial for room-temperature distance measurements.

Using nitroxide spin labels and SR, it is possible to determine the exchange rate (*e.g.*, in the 10 kHz–1 MHz range) between spin-labeled protein conformational populations with different rotational correlation times (*i.e.*, observable as multicomponent X-band CW EPR spectra representing the different motional states). The rate of exchange is determined by SR by measuring the difference between the T_1 values of each population. This was explored for T4 lysozyme and fatty-acid-binding protein mutants labeled with MTSL to quantify the equilibrium exchange rates between the two conformational populations, which are related to the functional states of the proteins.[92,261] A single T_1 results when the multicomponent spectrum is due to R1 rotamer exchange rather than protein conformational exchange; that is, SR can readily distinguish between two-component spectra arising from a single protein conformation with two different rotamers of the spin label side chain (which exchange rapidly on the T_{1e} time scale and give single-exponential recoveries) from two-component spectra arising from an equilibrium between protein conformations (which exchange at slow-to-intermediate rates on the T_{1e} time scale and give multicomponent recoveries).[51,92,261] Thus, SR can be an important complimentary method for CW studies where MTSL is often the label of choice due to its sensitivity to the local environment. Using the uniform penalty (UPEN) method of data analysis, it is possible to extract both relative populations and exchange rates for proteins in conformational equilibria.[92] SR studies to investigate conformational equilibria using labels other than R1 remain to be explored.

Nitroxide T_1 values are acutely sensitive to the presence of diffusible paramagnetic relaxation agents. As an example, SR has been used to show that a C-terminal amphipathic helix of the influenza A M2 protein labeled with MTSL populates at least two conformations in POPC:POPG bilayers[36] and was used to characterize membrane penetration of the wild-type M2 protein and a budding defective mutant based on collision rates for spin-labeled sites with O_2.[100] SR measurements on O_2 collision rates with lipid-analog labels have been used extensively to study domain formation in lipid bilayers (*e.g.*, ref. 262–265). A recent study showcases the use

of a stretched exponential function to analyze SR data that allowed characterization of heterogeneity in membrane fluidity.[265] This, and other advanced methods of data analysis such as the UPEN approach,[92] are particularly valuable for complex biological samples.

Nitroxide T_1 values are also influenced by the presence of nearby paramagnetic metal ions, providing a basis for room-temperature distance measurements.[51,266] Although SR gives an average distance rather than a distance distribution, measurement at room temperature makes it an attractive complimentary approach to DEER and DQC, especially where there is concern about the effects of sample freezing. Relaxation enhancement depends on the T_{1e} of the nitroxide, relaxation times (T_1 and T_2) of the fast-relaxing metal ion and rotational correlation time of the nitroxide–metal interspin vector.[51,266] A number of recent advances have been reported for site-specific introduction of Cu^{2+} as the metal ion,[233,266–268] with distance measurements up to 36 Å reported in T4 lysozyme using a variety of nitroxide spin labels with excellent agreement between the SR distances and the average distances obtained by Cu^{2+}–nitroxide DEER.[266] A key result of this study is that the maximum measurable distance depends strongly on immobilization of the nitroxide. Decreasing the rotational correlation time of the spin label increases the intrinsic T_{1e} of the nitroxide, making it possible to measure longer distances. For example, R1p and RX have longer intrinsic T_{1e} values than R1 due to their greater immobilization, and thus enabled measurement of longer distances than with R1 (Figure 10.3).[51,266]

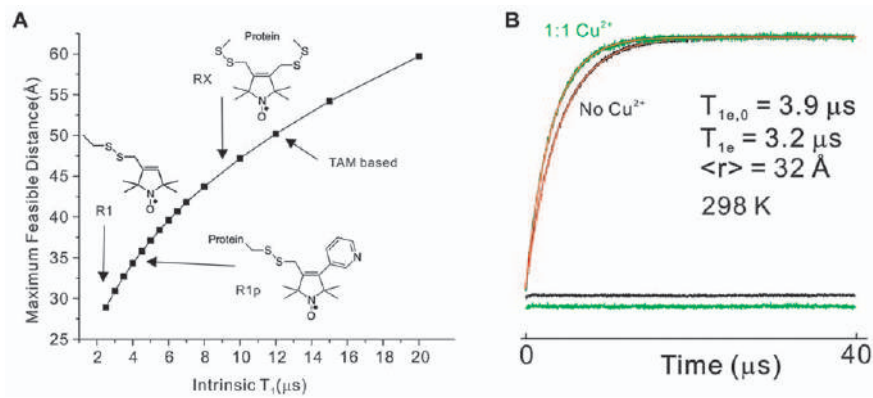

Figure 10.3 (A) Correlation between the intrinsic T_{1e} of the nitroxide and the maximum distance measurable by SR EPR spectroscopy. (B) SR signals fit to single exponentials with residuals demonstrating the relaxation enhancement of the nitroxide due to the presence of Cu^{2+}. The T_{1e} values and mean distance measured at 298 K are shown.
Adapted from ref. 51 with permission from Elsevier, Copyright 2015 and from ref. 266 https://doi.org/10.1021/ja5083206 with permission from American Chemical Society, Copyright 2014. Further permissions related to the material excerpted should be directed to the American Chemical Society.

Even longer distances can be measured if T_{1e} of the radical can be further lengthened, such as with the non-nitroxide label TAM as the spin label paired with Cu^{2+}; distances in T4 lysozyme up to 40 Å were measured using TAM and Cu^{2+}.[87] Additional novel labels with longer intrinsic T_{1e} values will further enhance the utility of SR for long-range distance measurements in proteins at room temperature.

10.3.3 *In Vivo* EPR Applications

Novel labeling strategies have also continued to evolve for the application of SDSL EPR spectroscopy *in vivo*. For example, a novel set of spin labels was recently developed to protect the nitroxide against reduction in a cellular environment.[164] M-TEIO and Az-TEIO contain an isoindoline ring attached to the nitroxide pyrrolidine ring, as well as the tetraethyl groups of the MAG (TETPO) spin label to protect the nitroxide (Figure 10.1). Experimental X-band CW EPR data for the *in vitro* TEIO-labeled thioredoxin protein, introduced either through maleimide reaction with cysteine residues or *via* click chemistry with the genetically encoded unnatural amino acid *para*-ethynyl-L-phenylalanine, show that these modifications indeed increase the stability of the radical from minutes to hours when in the presence of ascorbate, *E. coli* lysate and HEK (human embryonic kidney) lysate compared with a traditional tetramethyl proxyl group.[164] Further, TEIO labels were incorporated and tested for DEER distance distributions; the labeling efficiency was less than stoichiometric for the click chemistry reaction (60%) but was still sufficient for accurate analysis of distance distributions. The longer linker for Az-TEIO compared with M-TEIO is evident in the slightly longer distance observed in the distance distributions (42 Å *vs.* 40 Å), though both distributions align fairly well with the predicted 40 Å mean distance distribution.[164] Coupled with the approach described below, where proteins are labeled *in vivo* and not purified, this new label has high potential for enabling *in vivo* experiments on proteins to study their native structure, conformational changes and environment.

To date, *in vivo* spin labeling generally entailed labeling purified proteins *in vitro* and then injecting them back into the cell or studying spin-labeled proteins localized on the cell surface.[28,35,68,137,164] An exciting new advance is the use of nitroxide-based spin labels for true *in vivo* DEER spectroscopy. A recent development shows successful *in vivo* spin labeling of overexpressed proteins with traditional labels (*i.e.*, MTSL) through the use of genetically modified cells.[189] Mutant strains of *E. coli* containing deletions of the genes encoding the proteins DsbA or DsbB, which are members of the Dsb (disulfide bond) family of enzymes, improve the spin-labeling efficiency with MTSL of introduced cysteine pairs located on overexpressed proteins inside cells (Figure 10.4). This *in vivo* labeling technique enabled periplasmic-facing cysteine pairs on an outer-membrane protein, BtuB, to be labeled with a nitroxide spin label in intact cells at a level sufficient for accurate DEER analysis.[189] BtuB was found to exhibit different structures and

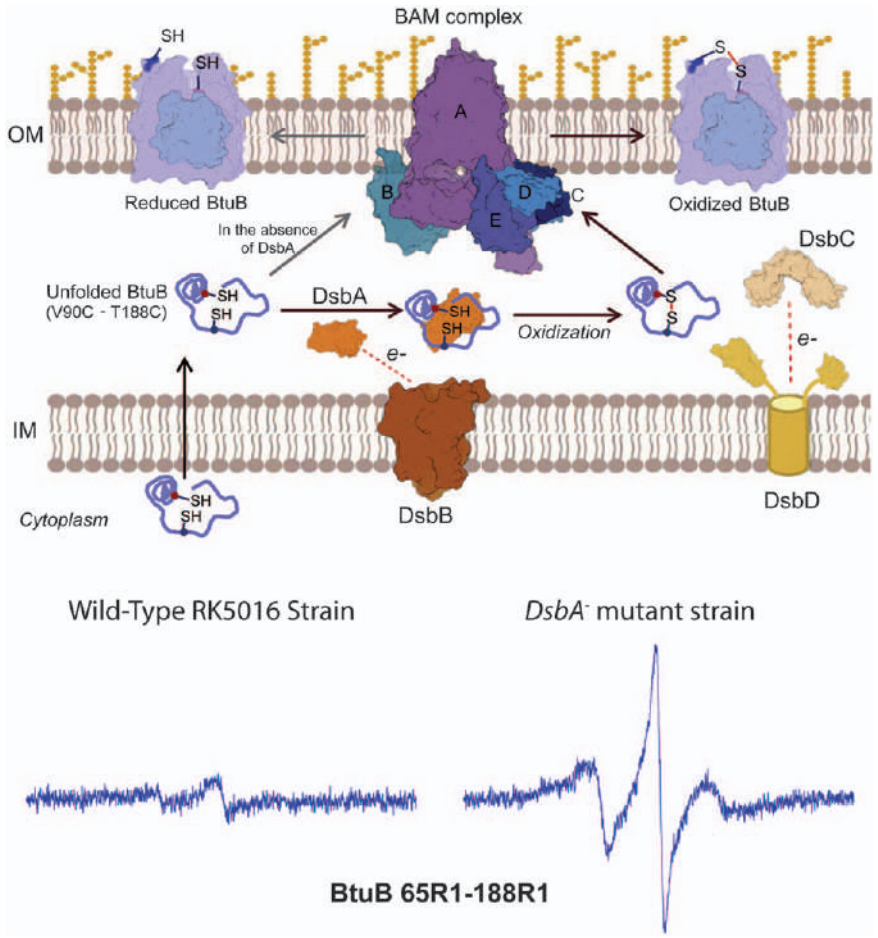

Figure 10.4 (Top) Illustration of the Dsb system that cross-links pairs of cysteine residues in proteins (such as BtuB) that are destined for the outer membrane of Gram-negative bacteria. (Bottom) Single scan CW X-band EPR spectra of *in vivo* labeled 65R1-188R1 BtuB in wild-type RK5016 and RK5016 *dsbA*- cells. The *dsbA* knockout prevents cross-linking of the introduced cysteines in BtuB, enabling effective *in vivo* spin labeling for DEER studies.
Reproduced from ref. 189 with permission from Elsevier, Copyright 2019.

conformational changes within the cell than when studied in isolated outer membranes or reconstituted into liposomes. This is an exciting advance that allows proteins naturally expressed and folded *in vivo* to be studied in their native environment. Further studies may showcase the combination of this technique with more redox-stable labels to obtain even higher labeling efficiencies or specifically directed incorporation through unnatural amino acids as described earlier.

10.4 Future Directions

The evolution of the design of nitroxide spin labels will undoubtedly continue to provide novel labels that expand the scope of SDSL EPR spectroscopy. We expect that major advances are likely to continue to occur for DEER spectroscopy applications and *in vivo* spin-labeling studies. Rigid labels that do not add width to the distance distributions in DEER data due to spin label side chain motion, label efficiently and specifically and do not disrupt the protein structure are still needed. Labels that can eliminate the need for data acquisition at cryogenic temperatures are also of current and future interest. Further, labels that can enter and survive in the cellular environment to specifically label a protein *in vivo* and are resistant to reduction are still emerging. These labels will have a tremendous impact on the ability to study the structure and function of proteins expressed, folded and functioning in their native environment.

Acknowledgements

Editorial support from Lydia Washechek and financial support from NIH grants GM108817 (to CSK), GM135581 (to MTL) and GM114234 (to JBF) to fund our nitroxide-based SDSL EPR spectroscopy experiments are gratefully acknowledged.

References

1. T. J. Stone, T. Buckman, P. L. Nordio and H. M. McConnell, *Proc. Natl. Acad. Sci. U. S. A.*, 1965, **54**, 1010–1017.
2. S. Ogawa and H. M. McConnell, *Proc. Natl. Acad. Sci. U. S. A.*, 1967, **58**, 19–26.
3. W. L. Hubbell and H. M. McConnell, *Proc. Natl. Acad. Sci. U. S. A.*, 1968, **61**, 12–16.
4. W. L. Hubbell and H. M. McConnell, *J. Am. Chem. Soc.*, 1971, **93**, 314–326.
5. R. D. Kornberg and H. M. McConnell, *Proc. Natl. Acad. Sci. U. S. A.*, 1971, **68**, 2564–2568.
6. C. Altenbach, S. L. Flitsch, H. G. Khorana and W. L. Hubbell, *Biochemistry*, 1989, **28**, 7806–7812.
7. C. Altenbach, W. Froncisz, J. S. Hyde and W. L. Hubbell, *Biophys. J.*, 1989, **56**, 1183–1191.
8. A. P. Todd, J. Cong, F. Levinthal, C. Levinthal and W. L. Hubbell, *Proteins*, 1989, **6**, 294–305.
9. C. Altenbach, D. A. Greenhalgh, H. G. Khorana and W. L. Hubbell, *Proc. Natl. Acad. Sci. U. S. A.*, 1994, **91**, 1667–1671.
10. L. J. Berliner, J. Grunwald, H. O. Hankovszky and K. Hideg, *Anal. Biochem.*, 1982, **119**, 450–455.
11. H. S. Mchaourab, T. Kalai, K. Hideg and W. L. Hubbell, *Biochemistry*, 1999, **38**, 2947–2955.

12. L. Columbus, T. Kalai, J. Jeko, K. Hideg and W. L. Hubbell, *Biochemistry*, 2001, **40**, 3828–3846.
13. W. Froncisz and J. S. Hyde, *J. Magn. Reson.*, 1982, **47**, 515–521.
14. M. Pannier, S. Veit, A. Godt, G. Jeschke and H. W. Spiess, *J. Magn. Reson.*, 2000, **142**, 331–340.
15. P. P. Borbat and J. H. Freed, in *Biological Magnetic Resonance*, ed. L. J. Berliner, S. S. Eaton and G. R. Eaton, Kluwer Academic/Plenum Publishers, New York, vol. 19, 2000, pp. 383–459.
16. B. J. Gaffney, *Acc. Chem. Res.*, 2014, **47**, 3588–3595.
17. D. Akhmetzyanov, J. Plackmeyer, B. Endeward, V. Denysenkov and T. F. Prisner, *Phys. Chem. Chem. Phys.*, 2015, **17**, 6760–6766.
18. C. Altenbach, C. J. Lopez, K. Hideg and W. L. Hubbell, *Methods Enzymol.*, 2015, **564**, 59–100.
19. B. P. Binder, S. Cornea, A. R. Thompson, R. J. Moen and D. D. Thomas, *Proc. Natl. Acad. Sci. U. S. A.*, 2015, **112**, 7972–7977.
20. D. E. Budil, *Methods Enzymol.*, 2015, **563**, 143–170.
21. D. Burdette and A. Gross, *Methods Enzymol.*, 2015, **564**, 389–400.
22. J. P. Campbell, J. T. Ryan, P. R. Shrestha, Z. Liu, C. Vaz, J. H. Kim, V. Georgiou and K. P. Cheung, *Anal. Chem.*, 2015, **87**, 4910–4916.
23. T. M. Casey and G. E. Fanucci, *Methods Enzymol.*, 2015, **564**, 153–187.
24. S. Chakrapani, *Methods Enzymol.*, 2015, **557**, 279–306.
25. T. F. Cunningham, M. D. Shannon, M. R. Putterman, R. J. Arachchige, I. Sengupta, M. Gao, C. P. Jaroniec and S. Saxena, *J. Phys. Chem. B*, 2015, **119**, 2839–2843.
26. H. A. DeBerg, J. R. Bankston, J. C. Rosenbaum, P. S. Brzovic, W. N. Zagotta and S. Stoll, *Structure*, 2015, **23**, 734–744.
27. R. O. Dror, T. J. Mildorf, D. Hilger, A. Manglik, D. W. Borhani, D. H. Arlow, A. Philippsen, N. Villanueva, Z. Yang, M. T. Lerch, W. L. Hubbell, B. K. Kobilka, R. K. Sunahara and D. E. Shaw, *Science*, 2015, **348**, 1361–1365.
28. S. Dunkel, L. P. Pulagam, H. J. Steinhoff and J. P. Klare, *Phys. Chem. Chem. Phys.*, 2015, **17**, 4875–4878.
29. S. S. Eaton and G. R. Eaton, *Methods Enzymol.*, 2015, **563**, 37–58.
30. E. G. Evans and G. L. Millhauser, *Methods Enzymol.*, 2015, **563**, 503–527.
31. P. Fajer, M. Fajer, M. Zawrotny and W. Yang, *Methods Enzymol.*, 2015, **563**, 623–642.
32. L. Garbuio, B. Lewandowski, P. Wilhelm, L. Ziegler, M. Yulikov, H. Wennemers and G. Jeschke, *Chemistry*, 2015, **21**, 10747–10753.
33. R. Guzzi and R. Bartucci, *Arch. Biochem. Biophys.*, 2015, **580**, 102–111.
34. S. M. Islam and B. Roux, *J. Phys. Chem. B*, 2015, **119**, 3901–3911.
35. B. Joseph, A. Sikora, E. Bordignon, G. Jeschke, D. S. Cafiso and T. F. Prisner, *Angew. Chem., Int. Ed. Engl.*, 2015, **54**, 6196–6199.
36. S. S. Kim, M. A. Upshur, K. Saotome, I. D. Sahu, R. M. McCarrick, J. B. Feix, G. A. Lorigan and K. P. Howard, *Biochemistry*, 2015, **54**, 7157–7167.

37. A. W. Kittell and J. S. Hyde, *J. Magn. Reson.*, 2015, **255**, 68–76.
38. N. Le Breton, M. Martinho, E. Mileo, E. Etienne, G. Gerbaud, B. Guigliarelli and V. Belle, *Front. Mol. Biosci.*, 2015, **2**, 21.
39. M. T. Lerch, C. J. Lopez, Z. Yang, M. J. Kreitman, J. Horwitz and W. L. Hubbell, *Proc. Natl. Acad. Sci. U. S. A.*, 2015, **112**, E2437–E2446.
40. M. T. Lerch, Z. Yang, C. Altenbach and W. L. Hubbell, *Methods Enzymol.*, 2015, **564**, 29–57.
41. Q. Li, R. Shen, J. S. Treger, S. S. Wanderling, W. Milewski, K. Siwowska, F. Bezanilla and E. Perozo, *Proc. Natl. Acad. Sci. U. S. A.*, 2015, **112**, E5926–E5935.
42. A. Manglik, T. H. Kim, M. Masureel, C. Altenbach, Z. Yang, D. Hilger, M. T. Lerch, T. S. Kobilka, F. S. Thian, W. L. Hubbell, R. S. Prosser and B. K. Kobilka, *Cell*, 2015, **161**, 1101–1111.
43. D. Marsh, *J. Phys. Chem. A*, 2015, **119**, 919–921.
44. V. Meyer, M. A. Swanson, L. J. Clouston, P. J. Boratynski, R. A. Stein, H. S. McHaourab, A. Rajca, S. S. Eaton and G. R. Eaton, *Biophys. J.*, 2015, **108**, 1213–1219.
45. I. D. Sahu, A. F. Craig, M. M. Dunagan, K. R. Troxel, R. Zhang, A. G. Meiberg, C. N. Harmon, R. M. McCarrick, B. M. Kroncke, C. R. Sanders and G. A. Lorigan, *Biochemistry*, 2015, **54**, 6402–6412.
46. M. J. Schmidt, A. Fedoseev, D. Bucker, J. Borbas, C. Peter, M. Drescher and D. Summerer, *ACS Chem. Biol.*, 2015, **10**, 2764–2771.
47. V. N. Syryamina, A. G. Maryasov, M. K. Bowman and S. A. Dzuba, *J. Magn. Reson.*, 2015, **261**, 169–174.
48. A. R. Thompson, B. P. Binder, J. E. McCaffrey, B. Svensson and D. D. Thomas, *Methods Enzymol.*, 2015, **564**, 101–123.
49. N. Van Eps, L. N. Caro, T. Morizumi and O. P. Ernst, *Photochem. Photobiol. Sci.*, 2015, **14**, 1586–1597.
50. N. Van Eps, C. J. Thomas, W. L. Hubbell and S. R. Sprang, *Proc. Natl. Acad. Sci. U. S. A.*, 2015, **112**, 1404–1409.
51. Z. Yang, M. Bridges, M. T. Lerch, C. Altenbach and W. L. Hubbell, *Methods Enzymol.*, 2015, **564**, 3–27.
52. D. Abdullin, G. Hagelueken and O. Schiemann, *Phys. Chem. Chem. Phys.*, 2016, **18**, 10428–10437.
53. A. R. Balo, H. Feyrer and O. P. Ernst, *Biochemistry*, 2016, **55**, 5256–5263.
54. S. Basak, S. Chatterjee and S. Chakrapani, *J. Visualized Exp.*, 2016, **113**, 54127.
55. M. G. Concilio, A. J. Fielding, R. Bayliss and S. G. Burgess, *Theor. Chem. Acc.*, 2016, **135**, 97.
56. T. F. Cunningham, S. Pornsuwan, W. S. Horne and S. Saxena, *Protein Sci.*, 2016, **25**, 1049–1060.
57. D. R. Davydov, Z. Yang, N. Davydova, J. R. Halpert and W. L. Hubbell, *Biophys. J.*, 2016, **110**, 1485–1498.
58. D. Dawidowski and D. S. Cafiso, *Structure*, 2016, **24**, 392–400.
59. H. A. DeBerg, P. S. Brzovic, G. E. Flynn, W. N. Zagotta and S. Stoll, *J. Biol. Chem.*, 2016, **291**, 371–381.

60. M. Di Valentin, M. Albertini, M. G. Dal Farra, E. Zurlo, L. Orian, A. Polimeno, M. Gobbo and D. Carbonera, *Chemistry*, 2016, **22**, 17204–17214.
61. J. M. Esquiaqui, E. M. Sherman, J. D. Ye and G. E. Fanucci, *Biochemistry*, 2016, **55**, 4295–4305.
62. E. G. Evans, M. J. Pushie, K. A. Markham, H. W. Lee and G. L. Millhauser, *Structure*, 2016, **24**, 1057–1067.
63. E. R. Georgieva, P. P. Borbat, K. Grushin, S. Stoilova-McPhie, N. J. Kulkarni, Z. Liang and J. H. Freed, *Front. Physiol.*, 2016, **7**, 317.
64. C. M. Grytz, A. Marko, P. Cekan, S. T. Sigurdsson and T. F. Prisner, *Phys. Chem. Chem. Phys.*, 2016, **18**, 2993–3002.
65. K. Halbmair, J. Wegner, U. Diederichsen and M. Bennati, *Biophys. J.*, 2016, **111**, 2345–2348.
66. C. Her, J. E. McCaffrey, D. D. Thomas and C. B. Karim, *Biophys. J.*, 2016, **111**, 2387–2394.
67. C. Hintze, D. Bucker, S. Domingo Kohler, G. Jeschke and M. Drescher, *J. Phys. Chem. Lett.*, 2016, **7**, 2204–2209.
68. B. Joseph, A. Sikora and D. S. Cafiso, *J. Am. Chem. Soc.*, 2016, **138**, 1844–1847.
69. B. Joseph, V. M. Tormyshev, O. Y. Rogozhnikova, D. Akhmetzyanov, E. G. Bagryanskaya and T. F. Prisner, *Angew. Chem., Int. Ed. Engl.*, 2016, **55**, 11538–11542.
70. P. Kaur, Y. Li, J. Cai and L. Song, *Biophys. J.*, 2016, **110**, 1789–1799.
71. N. Le Breton, T. Adrianaivomananjaona, G. Gerbaud, E. Etienne, E. Bisetto, A. Dautant, B. Guigliarelli, F. Haraux, M. Martinho and V. Belle, *Biochim. Biophys. Acta*, 2016, **1857**, 89–97.
72. S. Ling, W. Wang, L. Yu, J. Peng, X. Cai, Y. Xiong, Z. Hayati, L. Zhang, Z. Zhang, L. Song and C. Tian, *Sci. Rep.*, 2016, **6**, 20025.
73. L. Liu, J. Hess, I. D. Sahu, P. G. FitzGerald, R. M. McCarrick and G. A. Lorigan, *J. Phys. Chem. B*, 2016, **120**, 12321–12326.
74. L. Liu, I. D. Sahu, R. M. McCarrick and G. A. Lorigan, *J. Phys. Chem. B*, 2016, **120**, 633–640.
75. Z. Liu, T. M. Casey, M. E. Blackburn, X. Huang, L. Pham, I. M. de Vera, J. D. Carter, J. L. Kear-Scott, A. M. Veloro, L. Galiano and G. E. Fanucci, *Phys. Chem. Chem. Phys.*, 2016, **18**, 5819–5831.
76. T. Mandal, S. Shin, S. Aluvila, H. C. Chen, C. Grieve, J. Y. Choe, E. H. Cheng, E. J. Hustedt and K. J. Oh, *Sci. Rep.*, 2016, **6**, 30763.
77. D. Marsh, *J. Magn. Reson.*, 2016, **272**, 172–180.
78. D. Marsh, *J. Magn. Reson.*, 2016, **272**, 166–171.
79. E. Matei and A. M. Gronenborn, *Angew. Chem., Int. Ed. Engl.*, 2016, **55**, 150–154.
80. J. Petrlova, S. Hilt, M. Budamagunta, J. Domingo-Espin, J. C. Voss and J. O. Lagerstedt, *Biopolymers*, 2016, **105**, 683–692.
81. P. Roser, M. J. Schmidt, M. Drescher and D. Summerer, *Org. Biomol. Chem.*, 2016, **14**, 5468–5476.

82. T. Schmidt, M. A. Walti, J. L. Baber, E. J. Hustedt and G. M. Clore, *Angew. Chem., Int. Ed. Engl.*, 2016, **55**, 15905–15909.
83. T. F. Segawa, M. Doppelbauer, L. Garbuio, A. Doll, Y. O. Polyhach and G. Jeschke, *J. Chem. Phys.*, 2016, **144**, 194201.
84. A. Sikora, B. Joseph, M. Matson, J. R. Staley and D. S. Cafiso, *Biophys. J.*, 2016, **111**, 1908–1918.
85. L. Song, Z. Liu, P. Kaur, J. M. Esquiaqui, R. I. Hunter, S. Hill, G. M. Smith and G. E. Fanucci, *J. Magn. Reson.*, 2016, **265**, 188–196.
86. B. M. Stadtmueller, K. E. Huey-Tubman, C. J. Lopez, Z. Yang, W. L. Hubbell and P. J. Bjorkman, *eLife*, 2016, **5**, e10640.
87. Z. Yang, M. D. Bridges, C. J. Lopez, O. Y. Rogozhnikova, D. V. Trukhin, E. K. Brooks, V. Tormyshev, H. J. Halpern and W. L. Hubbell, *J. Magn. Reson.*, 2016, **269**, 50–54.
88. S. Basak, N. Schmandt, Y. Gicheru and S. Chakrapani, *eLife*, 2017, **6**, e23886.
89. N. Bavi, C. D. Cox, E. Perozo and B. Martinac, *Channels*, 2017, **11**, 91–93.
90. N. Bavi, A. D. Martinac, D. M. Cortes, O. Bavi, P. Ridone, T. Nomura, A. P. Hill, B. Martinac and E. Perozo, *Sci. Rep.*, 2017, **7**, 17229.
91. L. Bottorf, S. Rafferty, I. D. Sahu, R. M. McCarrick and G. A. Lorigan, *J. Phys. Chem. B*, 2017, **121**, 2961–2967.
92. M. D. Bridges, Z. Yang, C. Altenbach and W. L. Hubbell, *Appl. Magn. Reson.*, 2017, **48**, 1315–1340.
93. K. J. Chang, Y. H. Kuo and Y. W. Chiang, *J. Phys. Chem. B*, 2017, **121**, 4355–4363.
94. Q. Chen, N. A. Perry, S. A. Vishnivetskiy, S. Berndt, N. C. Gilbert, Y. Zhuo, P. K. Singh, J. Tholen, M. D. Ohi, E. V. Gurevich, C. A. Brautigam, C. S. Klug, V. V. Gurevich and T. M. Iverson, *Nat. Commun.*, 2017, **8**, 1427.
95. A. Collauto, H. A. DeBerg, R. Kaufmann, W. N. Zagotta, S. Stoll and D. Goldfarb, *Phys. Chem. Chem. Phys.*, 2017, **19**, 15324–15334.
96. A. W. Fischer, D. M. Anderson, M. H. Tessmer, D. W. Frank, J. B. Feix and J. Meiler, *ACS Omega*, 2017, **2**, 2977–2984.
97. C. Gmeiner, G. Dorn, F. H. T. Allain, G. Jeschke and M. Yulikov, *Phys. Chem. Chem. Phys.*, 2017, **19**, 28360–28380.
98. C. Gmeiner, D. Klose, E. Mileo, V. Belle, S. R. A. Marque, G. Dorn, F. H. T. Allain, B. Guigliarelli, G. Jeschke and M. Yulikov, *J. Phys. Chem. Lett.*, 2017, **8**, 4852–4857.
99. E. A. Golysheva, G. Y. Shevelev and S. A. Dzuba, *J. Chem. Phys.*, 2017, **147**, 064501.
100. A. L. Herneisen, I. D. Sahu, R. M. McCarrick, J. B. Feix, G. A. Lorigan and K. P. Howard, *Biochemistry*, 2017, **56**, 5955–5963.
101. C. E. Jones and L. J. Berliner, *Cell Biochem. Biophys.*, 2017, **75**, 195–202.
102. S. Kucher, S. Korneev, S. Tyagi, R. Apfelbaum, D. Grohmann, E. A. Lemke, J. P. Klare, H. J. Steinhoff and D. Klose, *J. Magn. Reson.*, 2017, **275**, 38–45.
103. D. Marsh, *J. Magn. Reson.*, 2017, **277**, 86–94.

104. S. Mittal and D. Shukla, *J. Phys. Chem. B*, 2017, **121**, 9761–9770.
105. A. Nalepa, M. Malferrari, W. Lubitz, G. Venturoli, K. Mobius and A. Savitsky, *Phys. Chem. Chem. Phys.*, 2017, **19**, 28388–28400.
106. V. S. Oganesyan, F. Chami, G. F. White and A. J. Thomson, *J. Magn. Reson.*, 2017, **274**, 24–35.
107. A. Pavicevic, J. Luo, A. Popovic-Bijelic and M. Mojovic, *Eur. Biophys. J.*, 2017, **46**, 773–787.
108. C. Pliotas, *Methods Enzymol.*, 2017, **594**, 203–242.
109. P. R. Potluri, J. Chamoun, J. A. Cooke, M. Badr, J. A. Guse, R. Rayes, N. M. Cordina, D. McCamey, P. G. Fajer and L. J. Brown, *J. Struct. Biol.*, 2017, **200**, 376–387.
110. K. M. Schultz and C. S. Klug, *Appl. Magn. Reson.*, 2017, **18**, 1341–1353.
111. K. M. Schultz, T. J. Lundquist and C. S. Klug, *Protein Sci.*, 2017, **26**, 1517–1523.
112. M. Suliman, V. Santosh, T. C. M. Seegar, A. C. Dalton, K. M. Schultz, C. S. Klug and W. A. Barton, *PLoS One*, 2017, **12**, e0184271.
113. M. H. Tessmer, D. M. Anderson, A. Buchaklian, D. W. Frank and J. B. Feix, *J. Biol. Chem.*, 2017, **292**, 3411–3419.
114. N. Van Eps, L. N. Caro, T. Morizumi, A. K. Kusnetzow, M. Szczepek, K. P. Hofmann, T. H. Bayburt, S. G. Sligar, O. P. Ernst and W. L. Hubbell, *Proc. Natl. Acad. Sci. U. S. A.*, 2017, **114**, E3268–E3275.
115. M. A. Walti, T. Schmidt, D. T. Murray, H. Wang, J. E. Hinshaw and G. M. Clore, *Proc. Natl. Acad. Sci. U. S. A.*, 2017, **114**, 9104–9109.
116. Z. Wu, A. Feintuch, A. Collauto, L. A. Adams, L. Aurelio, B. Graham, G. Otting and D. Goldfarb, *J. Phys. Chem. Lett.*, 2017, **8**, 5277–5282.
117. J. Yang, Y. Zong, J. Su, H. Li, H. Zhu, L. Columbus, L. Zhou and Q. Liu, *Nat. Commun.*, 2017, **8**, 1201.
118. M. Asada, T. Nishimura, K. Ifuku and H. Mino, *Biochim. Biophys. Acta, Bioenerg.*, 2018, **1859**, 394–399.
119. A. Bandyopadhyay, N. Van Eps, B. T. Eger, S. Rauscher, R. S. Yedidi, T. Moroni, G. M. West, K. A. Robinson, P. R. Griffin, J. Mitchell and O. P. Ernst, *J. Mol. Biol.*, 2018, **430**, 4102–4118.
120. L. A. Bergdoll, M. T. Lerch, J. W. Patrick, K. Belardo, C. Altenbach, P. Bisignano, A. Laganowsky, M. Grabe, W. L. Hubbell and J. Abramson, *Proc. Natl. Acad. Sci. U. S. A.*, 2018, **115**, E172–E179.
121. A. Bieber, D. Bucker and M. Drescher, *J. Magn. Reson.*, 2018, **296**, 29–35.
122. E. Bordignon and S. Bleicken, *Biochim. Biophys. Acta, Biomembr.*, 2018, **1860**, 841–853.
123. L. Bottorf, I. D. Sahu, R. M. McCarrick and G. A. Lorigan, *Biochim. Biophys. Acta, Biomembr.*, 2018, **1860**, 1447–1451.
124. S. Chatterjee, R. Vyas, S. V. Chalamalasetti, I. D. Sahu, J. Clatot, X. Wan, G. A. Lorigan, I. Deschenes and S. Chakrapani, *J. Gen. Physiol.*, 2018, **150**, 1333–1347.
125. D. P. Claxton, K. L. Jagessar, P. R. Steed, R. A. Stein and H. S. McHaourab, *Proc. Natl. Acad. Sci. U. S. A.*, 2018, **115**, E6182–E6190.

126. P. M. Dijkman, O. K. Castell, A. D. Goddard, J. C. Munoz-Garcia, C. de Graaf, M. I. Wallace and A. Watts, *Nat. Commun.*, 2018, **9**, 1710.
127. J. B. Feix, S. Kohn, M. H. Tessmer, D. M. Anderson and D. W. Frank, *Cell Biochem. Biophys.*, 2019, **77**, 79–87, DOI: 10.1007/s12013-018-0851-8.
128. A. Flores, J. C. Quon, A. F. Perez and Y. Ba, *Eur. Biophys. J.*, 2018, **47**, 611–630.
129. A. Giannoulis, K. Ackermann, P. E. Spindler, C. Higgins, D. B. Cordes, A. M. Z. Slawin, T. F. Prisner and B. E. Bode, *Phys. Chem. Chem. Phys.*, 2018, **20**, 11196–11205.
130. A. Giannoulis, C. L. Motion, M. Oranges, M. Buhl, G. M. Smith and B. E. Bode, *Phys. Chem. Chem. Phys.*, 2018, **20**, 2151–2154.
131. X. Gu, M. D. Bridges, Y. Yan, P. W. de Waal, X. E. Zhou, K. M. Suino-Powell, H. E. Xu, W. L. Hubbell and K. Melcher, *J. Biol. Chem.*, 2018, **293**, 16994–17007.
132. J. H. Guo, R. W. Jiang, J. L. Andersen, M. Esmann and N. U. Fedosova, *FEBS J.*, 2018, **285**, 2292–2305.
133. M. M. Haugland, J. E. Lovett and E. A. Anderson, *Chem. Soc. Rev.*, 2018, **47**, 668–680.
134. J. M. Hays, M. K. Kieber, J. Z. Li, J. I. Han, L. Columbus and P. M. Kasson, *Angew. Chem., Int. Ed. Engl.*, 2018, **57**, 17110–17114.
135. J. P. Hines, M. R. Dent, D. J. Stevens and J. N. Burstyn, *Protein Sci.*, 2018, **27**, 1670–1679.
136. F. Hsu, G. Park and Z. Guo, *ACS Omega*, 2018, **3**, 8401–8407.
137. G. Karthikeyan, A. Bonucci, G. Casano, G. Gerbaud, S. Abel, V. Thome, L. Kodjabachian, A. Magalon, B. Guigliarelli, V. Belle, O. Ouari and E. Mileo, *Angew. Chem., Int. Ed. Engl.*, 2018, **57**, 1366–1370.
138. S. Lim, G. Roseman, I. Peshenko, G. Manchala, D. Cudia, A. M. Dizhoor, G. Millhauser and J. B. Ames, *PLoS One*, 2018, **13**, e0193947.
139. L. Liu, I. D. Sahu, L. Bottorf, R. M. McCarrick and G. A. Lorigan, *J. Phys. Chem. B*, 2018, **122**, 4388–4396.
140. D. Marsh, *J. Phys. Chem. B*, 2018, **122**, 6129–6133.
141. D. Marsh, *Appl. Magn. Reson.*, 2018, **49**, 97–106.
142. P. D. Martin, Z. M. James and D. D. Thomas, *Biophys. J.*, 2018, **114**, 2573–2583.
143. M. Martinho, D. Allegro, I. Huvent, C. Chabaud, E. Etienne, H. Kovacic, B. Guigliarelli, V. Peyrot, I. Landrieu, V. Belle and P. Barbier, *Sci. Rep.*, 2018, **8**, 13846.
144. D. J. Mayo, I. D. Sahu and G. A. Lorigan, *Chem. Phys. Lipids*, 2018, **213**, 124–130.
145. B. Nforneh, A. M. Bovell and K. Warncke, *Free Radical Res.*, 2018, **52**, 307–318.
146. S. B. Nyenhuis and D. S. Cafiso, *Protein Sci.*, 2018, **27**, 1008–1012.
147. I. Sadowska-Bartosz, I. Stefaniuk, B. Cieniek and G. Bartosz, *Free Radical Res.*, 2018, **52**, 335–338.
148. I. D. Sahu and G. A. Lorigan, *BioMed Res. Int.*, 2018, **2018**, 3248289.

149. J. L. Sarver, M. Zhang, L. Liu, D. Nyenhuis and D. S. Cafiso, *Biochemistry*, 2018, **57**, 1045–1053.
150. K. M. Schultz, M. A. Fischer, E. L. Noey and C. S. Klug, *Protein Sci.*, 2018, **27**, 1407–1417.
151. K. M. Schultz and C. S. Klug, *Protein Sci.*, 2018, **27**, 381–389.
152. B. Selmke, P. P. Borbat, C. Nickolaus, R. Varadarajan, J. H. Freed and W. E. Trommer, *Biochemistry*, 2018, **57**, 5507–5512.
153. B. M. Stadtmueller, M. D. Bridges, K. M. Dam, M. T. Lerch, K. E. Huey-Tubman, W. L. Hubbell and P. J. Bjorkman, *Immunity*, 2018, **49**, 235–246, e234.
154. V. N. Syryamina, M. De Zotti, C. Toniolo, F. Formaggio and S. A. Dzuba, *Phys. Chem. Chem. Phys.*, 2018, **20**, 3592–3601.
155. M. H. Tessmer, D. M. Anderson, A. M. Pickrum, M. O. Riegert, R. Moretti, J. Meiler, J. B. Feix and D. W. Frank, *Proc. Natl. Acad. Sci. U. S. A.*, 2018, **115**, 525–530.
156. N. Van Eps, C. Altenbach, L. N. Caro, N. R. Latorraca, S. A. Hollingsworth, R. O. Dror, O. P. Ernst and W. L. Hubbell, *Proc. Natl. Acad. Sci. U. S. A.*, 2018, **115**, 2383–2388.
157. G. M. Warren, R. A. Stein, H. S. McHaourab and B. F. Eichman, *Int. J. Mol. Sci.*, 2018, **19**, 3049.
158. D. M. Yin, D. Hammler, M. F. Peter, A. Marx, A. Schmitz and G. Hagelueken, *Chemistry*, 2018, **24**, 6665–6671.
159. S. Anankanbil, J. H. Mose, B. Perez, W. Cheng, J. N. Pedersen and Z. Guo, *Food Chem.*, 2019, **275**, 474–479.
160. B. P. Binder, A. R. Thompson and D. D. Thomas, *Biophys. J.*, 2019, **117**, 319–330.
161. A. Bonucci, O. Ouari, B. Guigliarelli, V. Belle and E. Mileo, *ChemBioChem*, 2020, **21**, 451–460.
162. E. Bordignon, S. Kucher and Y. Polyhach, *Methods Mol. Biol.*, 2019, **2003**, 493–528.
163. T. Braun, M. Drescher and D. Summerer, *Int. J. Mol. Sci.*, 2019, **20**, 373.
164. T. S. Braun, P. Widder, U. Osswald, L. Gross, L. Williams, M. Schmidt, I. Helmle, D. Summerer and M. Drescher, *ChemBioChem*, 2020, **21**(7), 958–962.
165. M. Brodrecht, K. Herr, S. Bothe, M. de Oliveira, Jr, T. Gutmann and G. Buntkowsky, *ChemPhysChem*, 2019, **20**, 1475–1487.
166. M. Burger, S. Rein, S. Weber, P. Graber and S. Kacprzak, *Eur. Biophys. J.*, 2020, **49**, 1–10.
167. R. Carloni, N. Sanz Del Olmo, P. Ortega, A. Fattori, R. Gomez, M. F. Ottaviani, S. Garcia-Gallego, M. Cangiotti and F. J. de la Mata, *Biomolecules*, 2019, **9**, 540.
168. M. G. Dal Farra, S. Richert, C. Martin, C. Larminie, M. Gobbo, E. Bergantino, C. R. Timmel, A. M. Bowen and M. Di Valentin, *ChemPhysChem*, 2019, **20**, 931–935.
169. Y. Ding, V. Kathiresan, X. Zhang, I. S. Haworth and P. Z. Qin, *J. Phys. Chem. A*, 2019, **123**, 3592–3598.

170. D. L. Drew, Jr, T. Ahammad, R. A. Serafin, B. J. Butcher, K. R. Clowes, Z. Drake, I. D. Sahu, R. M. McCarrick and G. A. Lorigan, *Anal. Biochem.*, 2019, **567**, 14–20.
171. M. A. Ehrenberger, A. Vieyra, J. M. Esquiaqui and G. E. Fanucci, *Biochem. Biophys. Res. Commun.*, 2019, **516**, 839–844.
172. J. B. Feix, S. Kohn, M. H. Tessmer, D. M. Anderson and D. W. Frank, *Cell Biochem. Biophys.*, 2019, **77**, 79–87.
173. J. M. Franck and S. Han, *Methods Enzymol.*, 2019, **615**, 131–175.
174. D. D. Gae, M. S. Budamagunta, J. F. Hess, R. M. McCarrick, G. A. Lorigan, P. G. FitzGerald and J. C. Voss, *Structure*, 2019, **27**, 1547–1560, e1544.
175. L. Galazzo, L. Nogara, F. LoVerso, A. Polimeno, B. Blaauw, M. Sandri, C. Reggiani and D. Carbonera, *Am. J. Physiol.: Cell Physiol.*, 2019, **316**, C722–C730.
176. D. Goldfarb, *J. Magn. Reson.*, 2019, **306**, 102–108.
177. E. A. Golysheva, R. I. Samoilova, M. De Zotti, C. Toniolo, F. Formaggio and S. A. Dzuba, *J. Magn. Reson.*, 2019, **309**, 106621.
178. Y. P. Hervis, A. Valle, S. Dunkel, J. P. Klare, L. Canet, M. E. Lanio, C. Alvarez, I. F. Pazos and H. J. Steinhoff, *J. Struct. Biol.*, 2019, **208**, 30–42.
179. B. Joseph, E. A. Jaumann, A. Sikora, K. Barth, T. F. Prisner and D. S. Cafiso, *Nat. Protoc.*, 2019, **14**, 2344–2369.
180. E. Kachooei, N. M. Cordina and L. J. Brown, *Biophys. Rev.*, 2019, **11**, 621–639.
181. C. Kapsalis, B. Wang, H. El Mkami, S. J. Pitt, J. R. Schnell, T. K. Smith, J. D. Lippiat, B. E. Bode and C. Pliotas, *Nat. Commun.*, 2019, **10**, 4619.
182. A. Kugele, T. S. Braun, P. Widder, L. Williams, M. J. Schmidt, D. Summerer and M. Drescher, *Chem. Commun.*, 2019, **55**, 1923–1926.
183. A. Kugele, B. Silkenath, J. Langer, V. Wittmann and M. Drescher, *ChemBioChem*, 2019, **20**, 2479–2484.
184. N. Le Breton, S. Longhi, A. Rockenbauer, B. Guigliarelli, S. R. A. Marque, V. Belle and M. Martinho, *Phys. Chem. Chem. Phys.*, 2019, **21**, 22584–22588.
185. V. Leone, I. Waclawska, K. Kossmann, C. Koshy, M. Sharma, T. F. Prisner, C. Ziegler, B. Endeward and L. R. Forrest, *J. Gen. Physiol.*, 2019, **151**, 381–394.
186. T. Mandal, E. J. Hustedt, L. Song and K. J. Oh, *Methods Mol. Biol.*, 2019, **1877**, 257–303.
187. P. D. Martin, B. Svensson, D. D. Thomas and S. Stoll, *J. Phys. Chem. B*, 2019, **123**(48), 10131–10141.
188. S. Milikisiyants, M. A. Voinov, A. Marek, M. Jafarabadi, J. Liu, R. Han, S. Wang and A. I. Smirnov, *J. Magn. Reson.*, 2019, **298**, 115–126.
189. T. D. Nilaweera, D. A. Nyenhuis, R. K. Nakamoto and D. S. Cafiso, *Biophys. J.*, 2019, **117**, 1476–1484.
190. S. B. Nyenhuis, A. Thapa and D. S. Cafiso, *Biophys. J.*, 2019, **117**, 247–257.

191. M. F. Peter, A. T. Tuukkanen, C. A. Heubach, A. Selsam, F. G. Duthie, D. I. Svergun, O. Schiemann and G. Hagelueken, *Structure*, 2019, **27**, 1416–1426, e1413.
192. Y. Qi, J. Lee, X. Cheng, R. Shen, S. M. Islam, B. Roux and W. Im, *J. Comput. Chem.*, 2020, **41**(5), 415–420.
193. I. Ritsch, D. Klose, H. Hintz, A. Godt, G. Jeschke and M. Yulikov, *Chimia*, 2019, **73**, 268–276.
194. Y. Savich, B. P. Binder, A. R. Thompson and D. D. Thomas, *J. Gen. Physiol.*, 2019, **151**, 1007–1016.
195. A. Shah, A. Roux, M. Starck, J. A. Mosely, M. Stevens, D. G. Norman, R. I. Hunter, H. El Mkami, G. M. Smith, D. Parker and J. E. Lovett, *Inorg. Chem.*, 2019, **58**, 3015–3025.
196. K. Singewald, M. J. Lawless and S. Saxena, *J. Magn. Reson.*, 2019, **299**, 21–27.
197. T. I. Springer, T. E. Reid, S. L. Gies and J. B. Feix, *J. Biol. Chem.*, 2019, **294**(50), 19012–19021.
198. S. Tachon, E. Fournier, C. Decroos, P. Mansuelle, E. Etienne, M. Maresca, M. Martinho, V. Belle, T. Tron and A. J. Simaan, *Mol. Biotechnol.*, 2019, **61**, 650–662.
199. M. Teucher, H. Zhang, V. Bader, K. F. Winklhofer, A. J. Garcia-Saez, A. Rajca, S. Bleicken and E. Bordignon, *Sci. Rep.*, 2019, **9**, 13013.
200. J. Wegner, G. Valora, K. Halbmair, A. Kehl, B. Worbs, M. Bennati and U. Diederichsen, *Chemistry*, 2019, **25**, 2203–2207.
201. L. M. Wingler, M. Elgeti, D. Hilger, N. R. Latorraca, M. T. Lerch, D. P. Staus, R. O. Dror, B. K. Kobilka, W. L. Hubbell and R. J. Lefkowitz, *Cell*, 2019, **176**, 468–478, e411.
202. J. L. Wort, K. Ackermann, A. Giannoulis, A. J. Stewart, D. G. Norman and B. E. Bode, *Angew. Chem., Int. Ed. Engl.*, 2019, **58**, 11681–11685.
203. C. Xia, A. L. Shen, P. Duangkaew, R. Kotewong, P. Rongnoparut, J. Feix and J. P. Kim, *Biochemistry*, 2019, **58**, 2408–2418.
204. E. H. Yardeni, T. Bahrenberg, R. A. Stein, S. Mishra, E. Zomot, B. Graham, K. L. Tuck, T. Huber, E. Bibi, H. S. McHaourab and D. Goldfarb, *Sci. Rep.*, 2019, **9**, 12528.
205. C. Zhao, T. Somiya, S. Takai, S. Ueki and T. Arata, *Sci. Rep.*, 2019, **9**, 15259.
206. E. Zurlo, I. Gorrono Bikandi, N. J. Meeuwenoord, D. V. Filippov and M. Huber, *Phys. Chem. Chem. Phys.*, 2019, **21**, 25187–25195.
207. R. Langen, K. J. Oh, D. Cascio and W. L. Hubbell, *Biochemistry*, 2000, **39**, 8396–8405.
208. G. Jeschke and Y. Polyhach, *Phys. Chem. Chem. Phys.*, 2007, **9**, 1895–1910.
209. C. Altenbach, K. J. Oh, R. J. Trabanino, K. Hideg and W. L. Hubbell, *Biochemistry*, 2001, **40**, 15471–15482.
210. N. L. Fawzi, M. R. Fleissner, N. J. Anthis, T. Kalai, K. Hideg, W. L. Hubbell and G. M. Clore, *J. Biomol. NMR*, 2011, **51**, 105–114.

211. M. R. Fleissner, M. D. Bridges, E. K. Brooks, D. Cascio, T. Kalai, K. Hideg and W. L. Hubbell, *Proc. Natl. Acad. Sci. U. S. A.*, 2011, **108**, 16241–16246.
212. D. Toledo Warshaviak, V. V. Khramtsov, D. Cascio, C. Altenbach and W. L. Hubbell, *J. Magn. Reson.*, 2013, **232**, 53–61.
213. S. Bleicken, T. E. Assafa, H. Zhang, C. Elsner, I. Ritsch, M. Pink, S. Rajca, G. Jeschke, A. Rajca and E. Bordignon, *ChemistryOpen*, 2019, **8**, 1057–1065.
214. S. Saha, A. P. Jagtap and S. T. Sigurdsson, *Chem. Commun.*, 2015, **51**, 13142–13145.
215. S. S. Eaton, A. Rajca, Z. Yang and G. R. Eaton, *Free Radical Res.*, 2018, **52**, 319–326.
216. S. Stoller, G. Sicoli, T. Y. Baranova, M. Bennati and U. Diederichsen, *Angew. Chem., Int. Ed. Engl.*, 2011, **50**, 9743–9746.
217. E. S. Babaylova, A. V. Ivanov, A. A. Malygin, M. A. Vorobjeva, A. G. Venyaminova, Y. F. Polienko, I. A. Kirilyuk, O. A. Krumkacheva, M. V. Fedin, G. G. Karpova and E. G. Bagryanskaya, *Org. Biomol. Chem.*, 2014, **12**, 3129–3136.
218. B. A. Chalmers, S. Saha, T. Nguyen, J. McMurtrie, S. T. Sigurdsson, S. E. Bottle and K. S. Masters, *Org. Lett.*, 2014, **16**, 5528–5531.
219. K. Wawrzyniak-Turek and C. Hobartner, *Methods Enzymol.*, 2014, **549**, 85–104.
220. S. Saha, A. P. Jagtap and S. T. Sigurdsson, *Methods Enzymol.*, 2015, **563**, 397–414.
221. N. S. Tangprasertchai, X. Zhang, Y. Ding, K. Tham, R. Rohs, I. S. Haworth and P. Z. Qin, *Methods Enzymol.*, 2015, **564**, 427–453.
222. M. Granz, N. Erlenbach, P. Spindler, D. B. Gophane, L. S. Stelzl, S. T. Sigurdsson and T. F. Prisner, *Angew. Chem., Int. Ed. Engl.*, 2018, **57**, 10540–10543.
223. N. R. Kamble and S. T. Sigurdsson, *Chemistry*, 2018, **24**, 4157–4164.
224. T. Weinrich, E. A. Jaumann, U. M. Scheffer, T. F. Prisner and M. W. Gobel, *Beilstein J. Org. Chem.*, 2018, **14**, 1563–1569.
225. T. Weinrich, E. A. Jaumann, U. Scheffer, T. F. Prisner and M. W. Gobel, *Chemistry*, 2018, **24**, 6202–6207.
226. B. Endeward, A. Marko, V. P. Denysenkov, S. T. Sigurdsson and T. F. Prisner, *Methods Enzymol.*, 2015, **564**, 403–425.
227. B. Dzikovski, V. Livshits and J. Freed, *J. Phys. Chem. B*, 2015, **119**, 13330–13346.
228. K. Tsuda, *Heart Vessels*, 2016, **31**, 1724–1730.
229. M. A. Voinov, C. T. Scheid, I. A. Kirilyuk, D. G. Trofimov and A. I. Smirnov, *J. Phys. Chem. B*, 2017, **121**, 2443–2453.
230. L. Mainali, W. J. O'Brien and W. K. Subczynski, *Exp. Eye Res.*, 2019, **178**, 72–81.
231. A. N. Tikhonov and W. K. Subczynski, *Cell Biochem. Biophys.*, 2019, **77**, 47–59.

232. Z. Yang, M. Ji, T. F. Cunningham and S. Saxena, *Methods Enzymol.*, 2015, **563**, 459–481.
233. G. E. Merz, P. P. Borbat, A. R. Muok, M. Srivastava, D. N. Bunck, J. H. Freed and B. R. Crane, *J. Phys. Chem. B*, 2018, **122**, 9443–9451.
234. D. Abdullin, P. Brehm, N. Fleck, S. Spicher, S. Grimme and O. Schiemann, *Chemistry*, 2019, **25**, 14388.
235. D. Goldfarb, *Phys. Chem. Chem. Phys.*, 2014, **16**, 9685–9699.
236. M. C. Mahawaththa, M. D. Lee, A. Giannoulis, L. A. Adams, A. Feintuch, J. D. Swarbrick, B. Graham, C. Nitsche, D. Goldfarb and G. Otting, *Phys. Chem. Chem. Phys.*, 2018, **20**, 23535–23545.
237. Y. Yang, F. Yang, X. Y. Li, X. C. Su and D. Goldfarb, *J. Phys. Chem. B*, 2019, **123**, 1050–1059.
238. J. J. Jassoy, A. Berndhauser, F. Duthie, S. P. Kuhn, G. Hagelueken and O. Schiemann, *Angew. Chem., Int. Ed. Engl.*, 2017, **56**, 177–181.
239. A. Giannoulis, Y. Yang, Y. J. Gong, X. Tan, A. Feintuch, R. Carmieli, T. Bahrenberg, Y. Liu, X. C. Su and D. Goldfarb, *Phys. Chem. Chem. Phys.*, 2019, **21**, 10217–10227.
240. O. A. Krumkacheva, I. O. Timofeev, L. V. Politanskaya, Y. F. Polienko, E. V. Tretyakov, O. Y. Rogozhnikova, D. V. Trukhin, V. M. Tormyshev, A. S. Chubarov, E. G. Bagryanskaya and M. V. Fedin, *Angew. Chem., Int. Ed. Engl.*, 2019, **58**, 13271–13275.
241. K. Sato, R. Hirao, I. Timofeev, O. Krumkacheva, E. Zaytseva, O. Rogozhnikova, V. M. Tormyshev, D. Trukhin, E. Bagryanskaya, T. Gutmann, V. Klimavicius, G. Buntkowsky, K. Sugisaki, S. Nakazawa, H. Matsuoka, K. Toyota, D. Shiomi and T. Takui, *J. Phys. Chem. A*, 2019, **123**, 7507–7517.
242. L. Columbus and B. Kroncke, *Methods Enzymol.*, 2015, **557**, 329–348.
243. M. Sjodt and R. T. Clubb, *Bio-Protoc.*, 2017, **7**, e2207.
244. M. E. Dempsey, H. D. Marble, T. L. Shen, N. L. Fawzi and E. M. Darling, *Bioconjugate Chem.*, 2018, **29**, 335–342.
245. P. R. Potluri, N. M. Cordina, E. Kachooei and L. J. Brown, *Biochemistry*, 2019, **58**, 908–917.
246. A. N. Smith, U. T. Twahir, T. Dubroca, G. E. Fanucci and J. R. Long, *J. Phys. Chem. B*, 2016, **120**, 7880–7888.
247. S. Hilt, T. Tang, J. H. Walton, M. Budamagunta, I. Maezawa, T. Kalai, K. Hideg, V. Singh, H. Wulff, Q. Gong, L. W. Jin, A. Louie and J. C. Voss, *J. Alzheimer's Dis.*, 2017, **55**, 1667–1681.
248. D. S. Cafiso, *Acc. Chem. Res.*, 2014, **47**, 3102–3109.
249. M. C. Lagerstrom and H. B. Schioth, *Nat. Rev. Drug Discovery*, 2008, **7**, 339–357.
250. W. L. Hubbell, C. Altenbach, C. M. Hubbell and H. G. Khorana, *Adv. Protein Chem.*, 2003, **63**, 243–290.
251. S. T. Menon, M. Han and T. P. Sakmar, *Physiol. Rev.*, 2001, **81**, 1659–1688.
252. G. Jeschke, *Annu. Rev. Phys. Chem.*, 2012, **63**, 419–446.

253. Y. Kang, X. E. Zhou, X. Gao, Y. He, W. Liu, A. Ishchenko, A. Barty, T. A. White, O. Yefanov, G. W. Han, Q. Xu, P. W. de Waal, J. Ke, M. H. Tan, C. Zhang, A. Moeller, G. M. West, B. D. Pascal, N. Van Eps, L. N. Caro, S. A. Vishnivetskiy, R. J. Lee, K. M. Suino-Powell, X. Gu, K. Pal, J. Ma, X. Zhi, S. Boutet, G. J. Williams, M. Messerschmidt, C. Gati, N. A. Zatsepin, D. Wang, D. James, S. Basu, S. Roy-Chowdhury, C. E. Conrad, J. Coe, H. Liu, S. Lisova, C. Kupitz, I. Grotjohann, R. Fromme, Y. Jiang, M. Tan, H. Yang, J. Li, M. Wang, Z. Zheng, D. Li, N. Howe, Y. Zhao, J. Standfuss, K. Diederichs, Y. Dong, C. S. Potter, B. Carragher, M. Caffrey, H. Jiang, H. N. Chapman, J. C. Spence, P. Fromme, U. Weierstall, O. P. Ernst, V. Katritch, V. V. Gurevich, P. R. Griffin, W. L. Hubbell, R. C. Stevens, V. Cherezov, K. Melcher and H. E. Xu, *Nature*, 2015, **523**, 561–567.

254. X. E. Zhou, Y. He, P. W. de Waal, X. Gao, Y. Kang, N. Van Eps, Y. Yin, K. Pal, D. Goswami, T. A. White, A. Barty, N. R. Latorraca, H. N. Chapman, W. L. Hubbell, R. O. Dror, R. C. Stevens, V. Cherezov, V. V. Gurevich, P. R. Griffin, O. P. Ernst, K. Melcher and H. E. Xu, *Cell*, 2017, **170**, 457–469, e413.

255. Y. Kang, O. Kuybeda, P. W. de Waal, S. Mukherjee, N. Van Eps, P. Dutka, X. E. Zhou, A. Bartesaghi, S. Erramilli, T. Morizumi, X. Gu, Y. Yin, P. Liu, Y. Jiang, X. Meng, G. Zhao, K. Melcher, O. P. Ernst, A. A. Kossiakoff, S. Subramaniam and H. E. Xu, *Nature*, 2018, **558**, 553–558.

256. H. Zhang, A. Qiao, L. Yang, N. Van Eps, K. S. Frederiksen, D. Yang, A. Dai, X. Cai, H. Zhang, C. Yi, C. Cao, L. He, H. Yang, J. Lau, O. P. Ernst, M. A. Hanson, R. C. Stevens, M. W. Wang, S. Reedtz-Runge, H. Jiang, Q. Zhao and B. Wu, *Nature*, 2018, **553**, 106–110.

257. D. Y. Zhao, M. Poge, T. Morizumi, S. Gulati, N. Van Eps, J. Zhang, P. Miszta, S. Filipek, J. Mahamid, J. M. Plitzko, W. Baumeister, O. P. Ernst and K. Palczewski, *J. Biol. Chem.*, 2019, **294**, 14215–14230.

258. A. Meyer, S. Dechert, S. Dey, C. Hobartner and M. Bennati, *Angew. Chem., Int. Ed. Engl.*, 2020, **59**, 373.

259. B. H. Robinson, D. A. Haas and C. Mailer, *Science*, 1994, **263**, 490–493.

260. S. S. Eaton and G. R. Eaton, in *Biomedical EPR, Part B: Methodology, Instrumentation, and Dynamics*, ed. S. R. Eaton, G. R. Eaton and L. J. Berliner, Springer US, Boston, MA, vol. 24, 2005, pp. 3–18.

261. M. D. Bridges, K. Hideg and W. L. Hubbell, *Appl. Magn. Reson.*, 2010, **37**, 363.

262. M. Raguz, L. Mainali, W. J. O'Brien and W. K. Subczynski, *Exp. Eye Res.*, 2015, **132**, 78–90.

263. W. K. Subczynski, L. Mainali, M. Raguz and W. J. O'Brien, *Exp. Eye Res.*, 2017, **156**, 79–86.

264. L. Mainali, T. G. Camenisch, J. S. Hyde and W. K. Subczynski, *Appl. Magn. Reson.*, 2017, **48**, 1355–1373.

265. N. Stein, L. Mainali, J. S. Hyde and W. K. Subczynski, *Appl. Magn. Reson.*, 2019, **50**, 903–918.
266. Z. Yang, G. Jimenez-Oses, C. J. Lopez, M. D. Bridges, K. N. Houk and W. L. Hubbell, *J. Am. Chem. Soc.*, 2014, **136**, 15356–15365.
267. T. F. Cunningham, M. R. Putterman, A. Desai, W. S. Horne and S. Saxena, *Angew. Chem., Int. Ed. Engl.*, 2015, **54**, 6330–6334.
268. S. Ghosh, M. J. Lawless, G. S. Rule and S. Saxena, *J. Magn. Reson.*, 2018, **286**, 163–171.
269. W. L. Hubbell, C. J. Lopez, C. Altenbach and Z. Yang, *Curr. Opin. Struct. Biol.*, 2013, **23**, 725–733.

CHAPTER 11

Nitroxides in Liquid Crystals

RUI TAMURA,*[a] YOSHIAKI UCHIDA[b] AND KOTA NAGURA[a]

[a] Kyoto University, Graduate School of Human and Environmental Studies, Kyoto 606-8501, Japan; [b] Osaka University, Graduate School of Engineering Science, Toyonaka, Osaka 560-8531, Japan
*Email: tamura.rui.45x@st.kyoto-u.ac.jp

11.1 Introduction

Thanks to the outstanding thermodynamic stability of nitroxide radicals (NRs) that is ascribed to the delocalization of the unpaired electron over the N–O bond and thereby no dimerization, sterically protected NR structures have found various applications in the field of materials science, *e.g.*, as the spin source for metal-free organic magnetic materials[1] and spintronic devices[2] and as the redox species for catalytic chemical oxidation reactions[3] and polymer buttery devices.[4] The landmark with respect to the former spin source was the discovery of the first purely organic ferromagnet ($Tc = 0.6$ K) for one of several polymorphs of a nitronyl nitroxide, 2-(4-nitrophenyl)-4,4,5,5-tetramethylimidazoline-1-3-oxide (**1**) in 1991 (Figure 11.1).[5] Since then, more than 20 NR-based organic ferromagnets were documented by the end of twentieth century.[1] However, the *Tc* of 1.48 K recorded for one of the polymorphs of 1,3,5,7-tetramethyl-2,6-diazaadamane-*N*,*N*′-dioxyl (**2**) in 1993 is still a champion data of organic radical crystals examined (Figure 11.1).[6] In other words, these ferromagnet crystals exhibit an ordinary paramagnetic behaviour at temperatures above these low *Tc*'s.

In order to develop unique NR-based magnetic materials that can show strong magnetic interactions even at room temperature or higher, we paid attention to liquid crystalline (LC) phases which are defined as a thermal mesophase between crystalline and isotropic phases and have various layer

Nitroxides
Edited by Olivier Ouari and Didier Gigmes

Published by the Royal Society of Chemistry, www.rsc.org

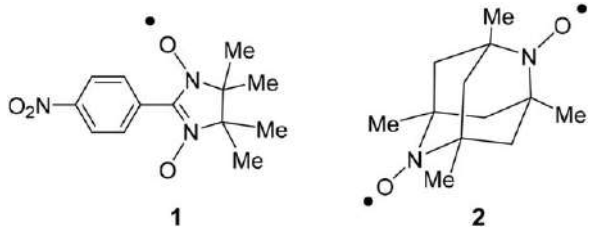

Figure 11.1 Representative NR-based organic ferromagnets.

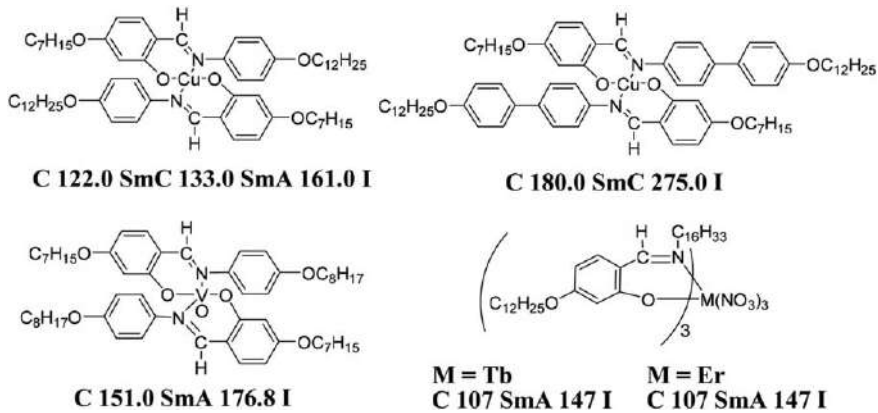

Figure 11.2 Representative metallomesogens and their LC temperatures.

and domain structures.[7] From a different viewpoint, LC phases can be considered to be a sort of 'complexity' system consisting of non-equilibrium dynamic states due to the molecular motion (rotation and translation) and the coherent collective properties of molecules in the LC domains.[8] Accordingly, they are so sensitive to external stimuli, such as temperature, light, pressure, electric or magnetic field, or added chiral dopants, that the molecular orientation and LC superstructure can be easily controlled.[9]

Magnetic LC materials had attracted great interest as soft materials to enhance the effect of magnetic fields on the electric and optical properties of liquid crystals; they were anticipated to exhibit unique magnetic interactions and thereby unconventional magneto-electric[10–13] or magneto-optical properties in the LC state.[14–16] However, there had been no prominent study on this interesting topic, because the majority of magnetic LCs were highly viscous transition (d-block) or lanthanide (f-block) metal-containing metallomesogens (Figure 11.2),[17,18] which were not appropriate for investigating the swift molecular motion and reorientation in the LC phases under low magnetic fields. At present, no appreciable intermolecular ferromagnetic nor superparamagnetic interaction has been observed in the LC state of d- or f-block metallomesogens. Meanwhile, only a few all-organic radical LC compounds were prepared until 2003 (Figure 11.3),[19–24] because

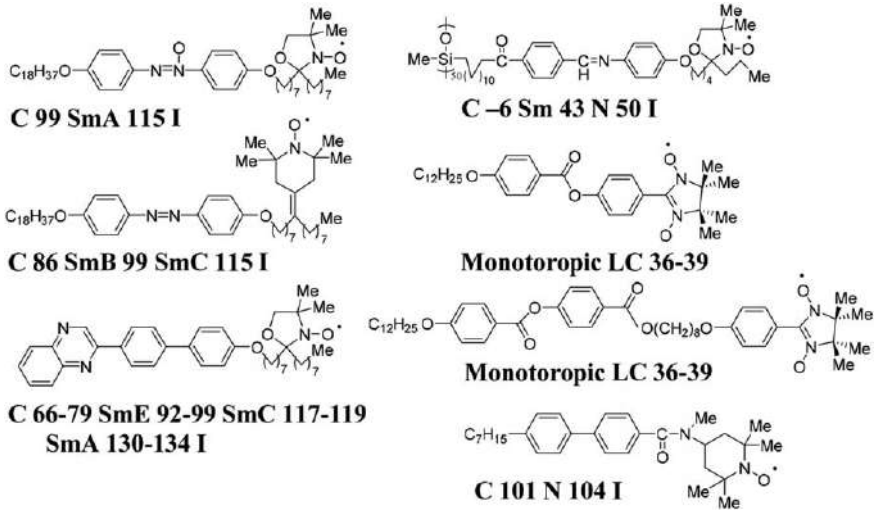

Figure 11.3 Representative NR-based organic rod-like LC compounds reported until 2003 and their LC temperatures.

the geometry and bulkiness of the radical-stabilizing substituents had been considered to be detrimental to the stability of liquid crystals, which requires molecular linearity or planarity.[25] Neither did they show appreciable intermolecular ferromagnetic nor superparamagnetic interaction.

With this situation in mind, in 2003 we designed and prepared novel metal-free magnetic LC compounds with low viscosity which were expected to afford the following two possibilities; (i) formation of magnetic domains (or order) in applied magnetic fields and (ii) occurrence of coupling between magnetic dipole and electric dipole moments (magneto-electric effect) in the ferroelectric LC phase.[26–28] Consequently, we discovered that all-organic rod-like LC compounds (**3** and the derivatives) with a stable NR unit in the central core position and thereby a negative dielectric anisotropy ($\Delta\varepsilon < 0$) exhibit a unique superparamagnetic behaviour under low magnetic fields in the various chiral and achiral LC phases (Figure 11.4).[29–31] This observation was interpreted in terms of the generation of spin glass (SG)-like inhomogeneous superparamagnetic interactions (the average spin–spin exchange interaction constant $\bar{J} > 0$) induced by low magnetic fields at high temperatures, since it was proved that this phenomenon was independent of the molecular reorientation effects arising from the very small molecular magnetic anisotropy ($\Delta\chi$)[32] and did not result from the contamination by extrinsic magnetic metal or metal ion impurities.[33] This unique superparamagnetic phenomenon was referred to as the 'positive magneto-LC effect'.[34] Thus far such a superparamagnetic behaviour has not been observed for analogous non-LC NR compounds.

Furthermore, by making the most of such superparamagnetic properties of LC NR compounds, we have successfully prepared stable redox-resistant (i) W/O/W (water-in-oil-in-water) type of metal-free magnetic microemulsions

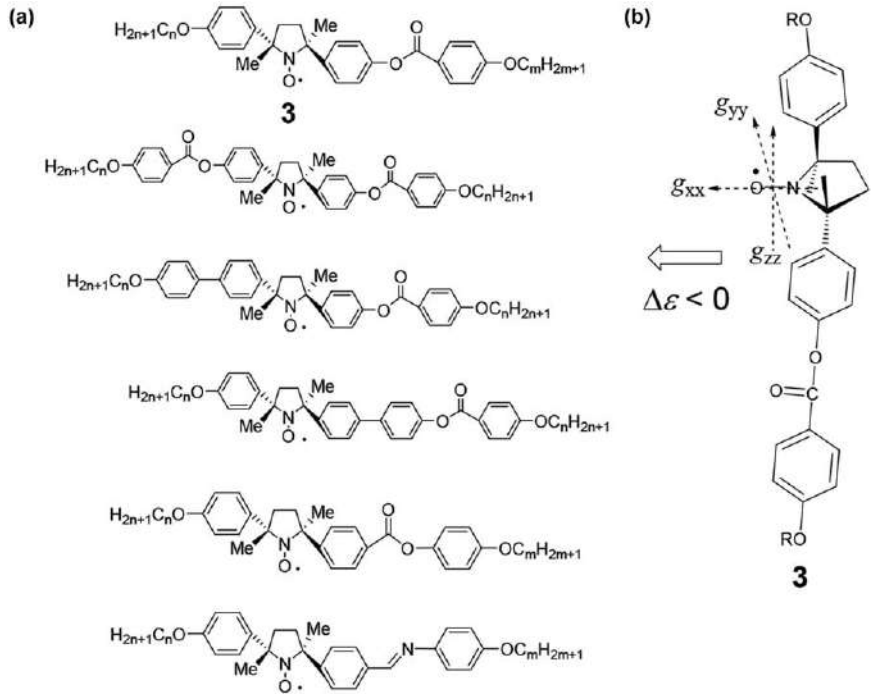

Figure 11.4 (a) PROXYL-based organic rod-like LC compounds synthesized. (b) Principal *g*-values and negative dielectric anisotropy ($\Delta\varepsilon < 0$) of **3**.

to use as a magnetic carrier for nanolitre cargoes[35] and (ii) O/W type of nano-sized mixed micelles to use as an effective theranostic nanomedicine directed towards the development of targeted drug delivery system (DDS) carriers visible by magnetic resonance imaging (MRI).[36–38]

As the latest comprehensive review as well as database-like article on the preparation, characterization and magnetic properties of a wide array of all-organic radical LC compounds synthesized thus far, an excellent one entitled ''Liquid crystalline derivatives of heterocyclic radicals'' by Kaszynski is strongly recommended.[39]

11.2 Rod-like LC NR Compounds

11.2.1 Molecular Design

First described is the design of compounds **3** containing a 2,2,5,5-tetra-substituted pyrrolidine-*N*-oxyl (PROXYL) radical structure in the central core position (Figure 11.4) which satisfied the following four requirements:

(1) **Spin source**: A nitroxyl group with a large electric dipole moment (*ca*. 3 Debye) and known principle *g*-values (g_{xx}, g_{yy}, g_{zz}) is the best choice, because (i) the dipole moment is large enough for the source of

spontaneous polarization (*Ps*) to show ferroelectricity and (ii) the principal *g*-values are useful to determine the molecular orientation in each LC phase by electron paramagnetic resonance (EPR) spectroscopy.

(2) **High thermal and photochemical stability**: The PROXYL radical structure is stable enough for repeated heating and cooling cycles below 170 °C (453 K) and visible light irradiation in the air.

(3) **Molecular structure**: The geometrically fixed chiral PROXYL radical unit should be incorporated into the rigid core of LC molecule (i) to avoid the free rotation of the nitroxyl group inside the molecule so as to make use of the EPR *g*-value and the dielectric anisotropy($\Delta\varepsilon$) and (ii) to obtain a slightly zigzag molecular structure and a negative dielectric anisotropy($\Delta\varepsilon < 0$) necessary for the appearance of a chiral smectic C (SmC*) phase to show ferroelectricity.

(4) **Synthesis**: It is better to synthesize both racemic and enantiomerically enriched samples for each chiral molecule, because the magnetic properties can be compared between the corresponding achiral and chiral LC phases.

11.2.2 SG-like Superparamagnetic Behaviour (*i.e.*, Positive Magneto-LC Effect)

Although the possibility of strong intermolecular magnetic interactions in rod-like LC radical materials had been considered unrealistic due to the inaccessibility of the McConnell type of long-range spin–spin exchange interactions between rotating molecules (10^8–10^{10} s^{-1}) in the LC state,[25] we observed a nonlinear relationship between the applied magnetic field (H) and the observed magnetization (M) in the chiral and achiral LC phases of **3** ($m = n = 13$) (Figure 11.5a and b) by SQUID magnetometry.[31] This result implied the generation of superparamagnetic interactions in the LC phases. Furthermore, the SQUID measurement of the temperature dependence of molar magnetic susceptibility (χ_M) for (*S*,*S*)-enriched **3** ($m = n = 13$) indicated an increase in the χ_M at the crystal-to-LC phase transition temperature in the first heating run and the increased χ_M (12%) was preserved in the isotropic phase by further heating and in the crystalline phase in the first cooling run from the isotropic phase (Figure 11.5c). Such a thermal effect was quite similar to that observed for metallic spin glass materials.[40] In fact, these radical LC droplets floating on hot water were attracted by a permanent magnet and moved quickly and freely on the hot water under the influence of the magnet. Furthermore, to gain an insight into the origin of the positive magneto-LC effect, the temperature dependence of EPR line-width (ΔH_{pp}) was compared with that of χ_M by SQUID measurement. As a result, a large ΔH_{pp} increase was noted in accordance with the χ_M increase at the crystal-to-LC phase transition in the heating run (Figure 11.5d), indicating that the generation of strong ferromagnetic spin–spin dipole interactions as well as exchange interactions were responsible for the superparamagnetic 'positive magneto-LC effect ($\bar{J} > 0$)' (Figure 11.5e).[31,34]

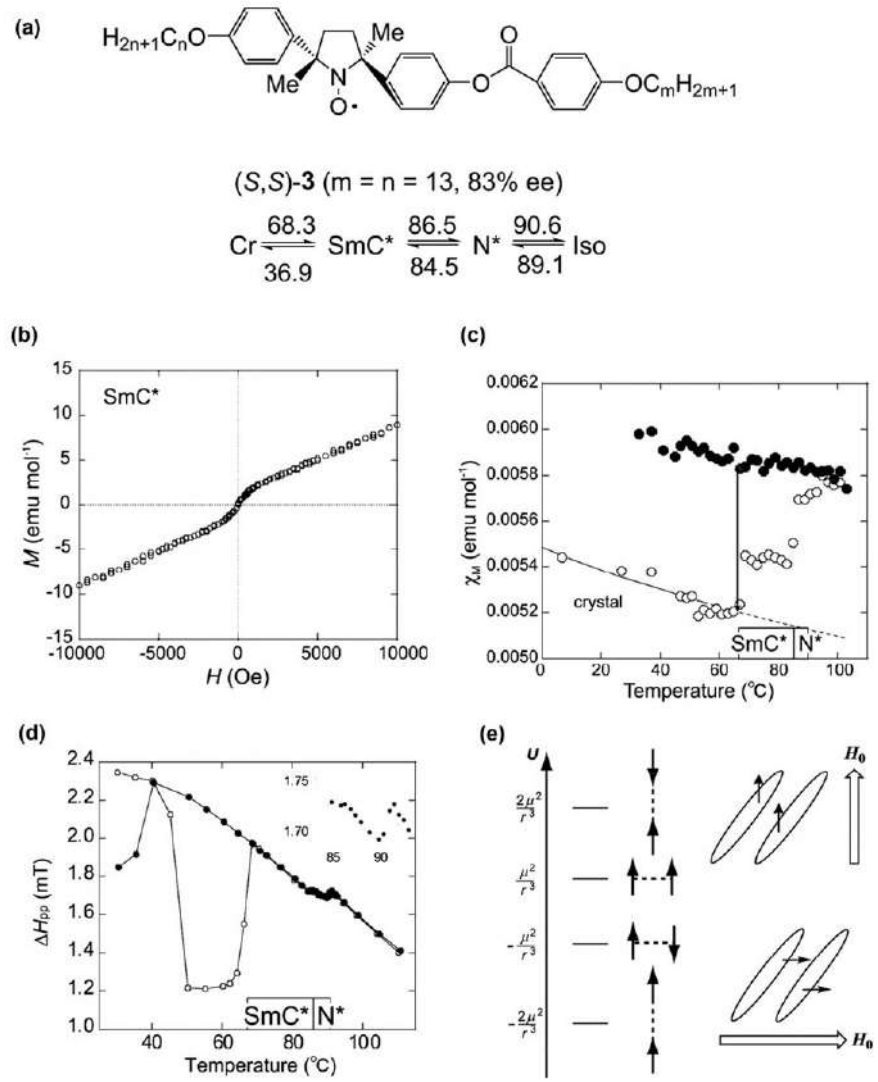

Figure 11.5 (a) LC temperature, (b) magnetic field (H) dependence of molar magnetization (M), (c) temperature dependence of molar magnetic susceptibility (χ_M) measured at 0.05 T, (d) temperature dependence of EPR line-width (ΔH_{pp}) measured at around 0.33 T, and (e) relative stability of four possible anisotropic spin–spin dipole interactions between two spins (left side) and expected spin–spin interactions between spins localized in radical moieties in each layer of SmC* phase (right side) for (*S*,*S*)-**3** ($m = n = 13$). Open and filled circles represent the first heating and cooling runs, respectively.
Reproduced from ref. 31 with permission from American Chemical Society, Copyright 2010.

Thus, it was suggested that the positive magneto-LC-effect resulted mesoscopically from (i) the generation of spin glass-like superparamagnetic interactions ($\bar{J}>0$) due to the formation of inhomogeneous magnetic domains and microscopically from (ii) the preferential formation of a head-to-tail type of ferromagnetic spin–spin dipole interactions in each magnetic domain.

11.2.3 Conditions for Increasing 'Positive Magneto-LC Effect' in Rod-like Liquid Crystals

An enhancement of the positive magneto-LC effect was observed in the following five different types of liquid crystals, which are chiral or have a low order parameter and/or a small domain size.

Chiral neutral monoradical liquid crystals: With respect to LC compounds **3** and the derivatives with a negative dielectric anisotropy ($\Delta\varepsilon<0$), enantiomerically enriched samples always showed a larger positive magneto-LC-effect ($\bar{J}>0$) at the crystal-to-LC phase transition than the corresponding racemic samples (Figure 11.6b).[31] Meanwhile, regarding analogous LC compounds **4** with a positive dielectric anisotropy ($\Delta\varepsilon>0$), the racemic sample showed a negative magneto-LC effect ($\bar{J}<0$) at the crystal-to-LC phase transition (Figure 11.6a and c).[34] Although the addition of chiral dopants to racemic **4** could change an achiral nematic (N) phase to a chiral nematic (N*) one, the sign and magnitude of negative magneto-LC effect were not affected, indicating a strong centrosymmetric dimer formation between (*R*,*R*) and (*S*,*S*) molecules due to the $\Delta\varepsilon>0$, which results in the generation of weak antiferromagnetic interactions arising from the local SOMO-SOMO overlapping by the strong side-by-side spin–spin dipole interaction (Figure 11.6c). In contrast, the (*S*,*S*)-enriched **4** showing an N* or chiral smectic A (SmA*) phase displayed a large positive magneto-LC effect, similar to the case of (*S*,*S*)-enriched **3**. For (*S*,*S*)-enriched **4**, the higher the ee value, the larger the positive magneto-LC effect. Thus, highly enantiomerically enriched samples turned out to show a large positive magneto-LC effect, irrespective of the sign of $\Delta\varepsilon$.

Chiral neutral biradical liquid crystal:[41] The measurement of the temperature dependence of molar magnetic susceptibility (χ_M) by both the SQUID magnetometry and the EPR spectroscopic analysis using a double-integration method indicated that the positive magneto-LC effect (38% χ_M increase) at the crystal-to-N* phase transition noted for the biradical (*S*,*S*,*S*,*S*)-**5** (>99% ee) was much larger than those of other chiral neutral monoradical liquid crystals (Figure 11.7a–d). This χ_M increase also was kept in the cooling run until low temperatures. The temperature dependence of EPR ΔH_{pp} suggested that this large positive magneto-LC effect originated from the increased intermolecular ferromagnetic spin–spin dipole and exchange interactions due to the inhomogeneous intermolecular short contact in the N* phase (Figure 11.7e).

Hydrogen-bonded liquid crystal:[42] Racemic or highly (*S*,*S*)-enriched hydrogen-bonded compounds **8** with a low-order parameter, which was comprised of chiral radical carboxylic acid **6** and achiral pyridine derivative **7**

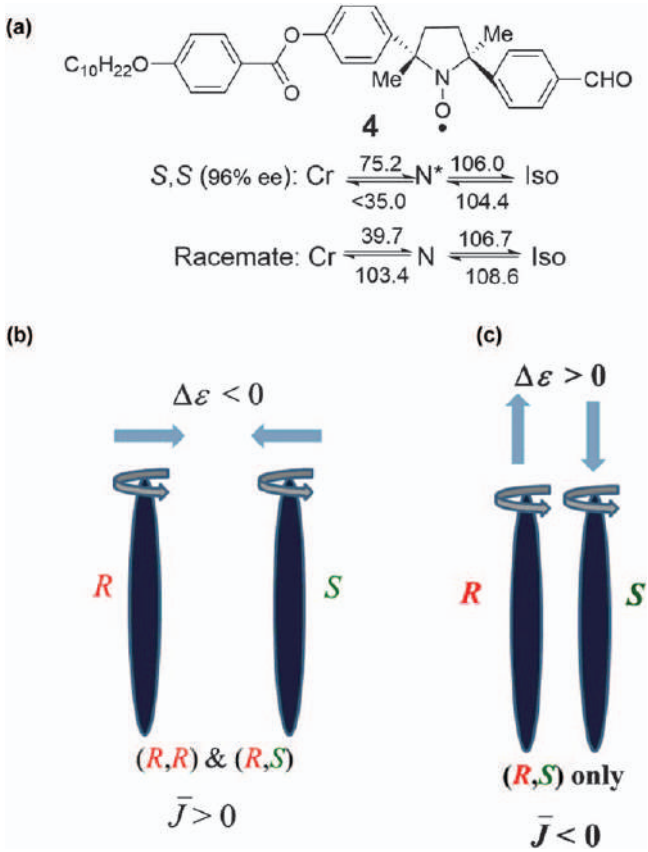

Figure 11.6 (a) LC temperature of (*S*,*S*)-enriched and racemic **4** with positive Δε. (b) Positive magneto-LC effect observed in the case of samples with $\Delta\varepsilon < 0$, irrespective of the chirality of LC phases. (c) Negative magneto-LC effect observed in the case of racemic samples with $\Delta\varepsilon > 0$.

and displayed an N or N* phase, respectively, exhibited a larger positive magneto-LC effect than the corresponding covalent-bonded LC compounds with a higher order parameter, due most likely to the more inhomogeneous intermolecular short contacts in the hydrogen-bonded LC phases (Figure 11.8). In this case, (*S*,*S*)-enriched **8** also showed a larger positive magneto-LC effect than racemic **8**.

Ionic liquid crystal:[43] Referring to the molecular structure of racemic imidazolium ionic liquid (IL) mono NR compound **9** which served as an excellent spin probe for the investigation of the local structure or the molecular shape anisotropy of diamagnetic IL solvents,[44] ionic liquid crystalline (ILC) racemic and (*S*,*S*)-enriched **10** were synthesized and subjected to SQUID magnetometry and EPR spectroscopy. As a consequence, racemic **10** exhibited a distinctly large χ_M value due to the superparamagnetic behaviour under a low magnetic field ($H < 0.1$ T) even in the original solid phase of the as-synthesized sample,

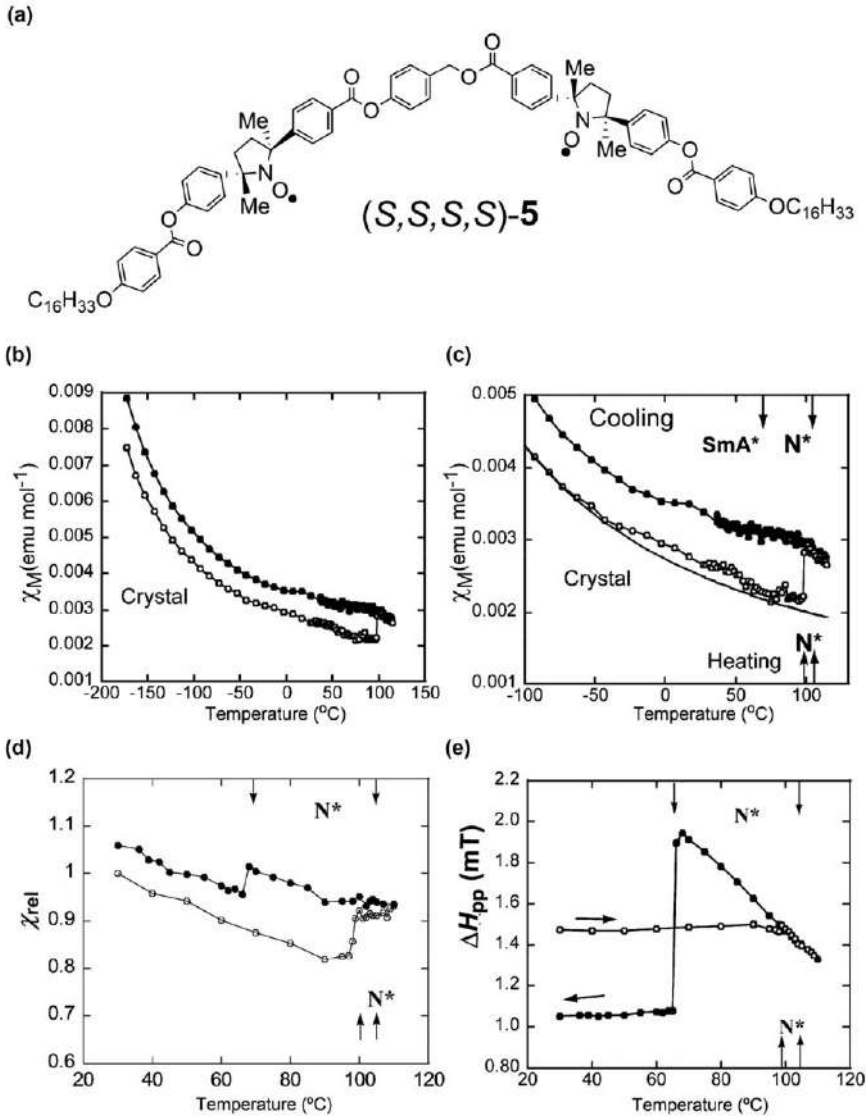

Figure 11.7 (a) Molecular structure of (*S*,*S*,*S*,*S*)-**5**. (b) Temperature dependence of molar magnetic susceptibility (χ_M) by SQUID magnetometry between −170 and +120 °C measured at 0.05 T, (c) magnification of (b) between −100 and +120 °C, (d) temperature dependence of relative molar paramagnetic susceptibility (χ_{rel}) by EPR spectroscopic analysis using a double integration method at around 0.33 T, and (e) temperature dependence of EPR line-width (ΔH_{pp}) for (*S*,*S*,*S*,*S*)-**5**. Open and filled circles represent the first heating and cooling runs, respectively. The solid line in (c) shows the Curie–Weiss fitting curve.
Reproduced from ref. 41 with permission from the Royal Society of Chemistry.

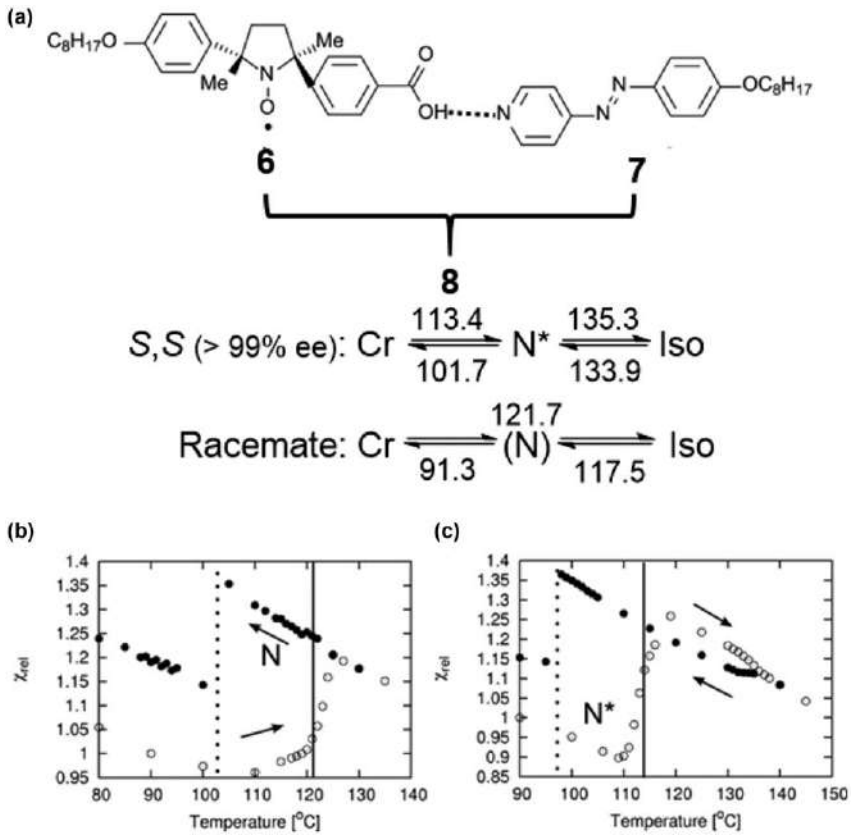

Figure 11.8 (a) Molecular structure of the hydrogen-bonded LC compound **8** composed of **6** and **7**. Temperature dependence of χ_{rel} for (b) racemic **8** and (c) (*S*,*S*)-**8** by EPR spectroscopy at around 0.33 T. Open and filled circles represent the first heating and cooling runs, respectively.
Reproduced from ref. 42 with permission from American Chemical Society, Copyright 2012.

an additional 27% χ_M increase (positive magneto-LC effect) at the solid-to-SmA phase transition and a preservation of this overall large χ_M value not only in the isotropic phase by the first heating and in the solid phase by the first cooling until cryogenic temperatures, but also in the SmA and isotropic phases by the second heating (Figure 11.9 and see Section 11.4). In this case, (*S*,*S*)-enriched **10** showed a larger positive magneto-LC effect at the solid-to-SmA* phase transition than the racemic **10**, too.

LC physical gels:[45] LC physical gels were prepared by heating a mixture of racemic nitroxide monoradical compound **3** ($m = 8$, $n = 7$) and a small amount of diamagnetic organic gelator (*R*,*R*)-**11** followed by cooling to investigate the effects of the gelator on the positive magneto-LC effect for racemic **3**. Consequently, as the LC domain size decreased by increasing the

(a)

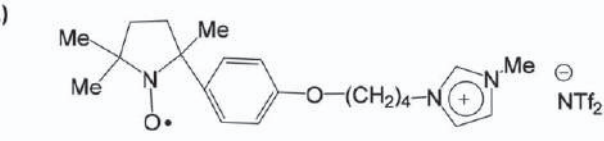

9

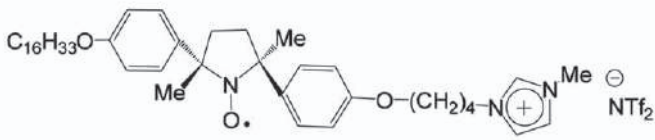

10

(b)

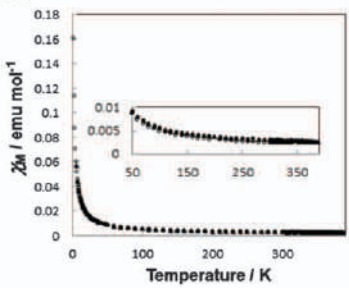

(c)

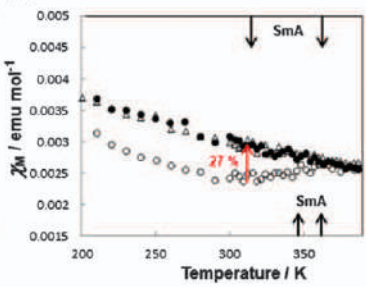

(d)

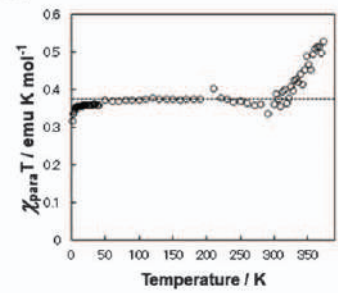

(e)

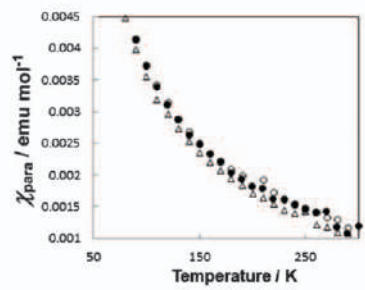

(f)

	$\chi_{dia} + \chi_{TIM}$ / emu mol^{-1}	Curie constant C / emu K mol^{-1}	χ_{TIM} / emu mol^{-1}
1st heating	$+1.22\times10^{-3}$	0.37	$+1.8\times10^{-3}$
1st cooling	$+1.90\times10^{-3}$	0.37	$+2.5\times10^{-3}$
2nd heating	$+1.99\times10^{-3}$	0.36	$+2.6\times10^{-3}$

amount of (*R*,*R*)-**11** up to 10 mol%, the positive magneto-LC effect increased in the resulting fine domains structure manipulated by self-assembled fibres composed of organic gelator molecules (Figure 11.10).

11.2.4 Observation of 'Magneto-electric Effect' in a Ferroelectric LC Phase at High Temperature

The magneto-electric effect (or coupling) had been observed only for inorganic multiferroic materials such as $YMnO_3$, $TbMnO_3$ and so forth, which showed both ferroelectricity and magnetic order (ferromagnetism or antiferromagnetism) at cryogenic temperatures.[10–13] Therefore, it was expected that the unique magneto-electric effect might occur in the ferroelectric LC (FLC) phase of the (*S*,*S*)-enriched **3** ($m = n = 13$) which displayed both an excellent ferroelectricity [$P_S = 24$ nC cm^{-2}, $\tau_{10-90} = 213$ μs, $\theta = 29°$, $\eta = 73.0$ m Pa s at 74 °C by the triangle wave method using a sandwich cell (4 μm thickness)] in a surface-stabilized liquid crystal cell[27] and superparamagnetic interactions (positive magneto-LC effects) in the bulk SmC* phase.[31]

Such was indeed the case. The temperature dependence of relative paramagnetic susceptibility ($\chi_{rel,E}$) was measured by EPR spectroscopy using a handmade 4-μm-tick sandwich cell (50×5 mm) in which the inner surface of two glass substrates with indium tin oxide (ITO) electrode was coated with polyimide polymer and then only one inner surface in the cell was rubbed with a velvet roller (Figure 11.11). The most appropriate sample of (*S*,*S*)-**3** ($m = n = 13$) of 65% ee was loaded into the lower tip of the cell. Then the cell tip was inserted into the EPR cavity (Figure 11.11).

The DC electric field dependence of relative paramagnetic susceptibility ($\chi_{rel,E}$), *g*-value, and ΔH_{pp} was measured between +25 V and −25 V at 75 °C in the two cases; the applied magnetic field ($H = ca.$ 0.33 T) was either perpendicular or parallel to the direction of the electric field. In the case of the perpendicular application of the magnetic field, a hysteresis loop was observed regarding all of $\chi_{rel,E}$, *g*-value and ΔH_{pp} (Figure 11.12a–c), indicating successful observation of the magneto-electric effect in the FLC state at 75 °C for the first time.[46] In contrast, in the case of the parallel application of magnetic field, no hysteresis loop was observed (Figure 11.12d–f).

11.3 Discotic Columnar LC NR Compounds

Since 2008, five NRs (**12**–**16**) -based,[33,47–50] a lot of π-delocalized oxoverdazyl (**17**)[51] and benzotriazynyl (**18**)[52] radicals-based, and several π-delocalized triarylmethyl (**19**)[53] radicals-based columnar LC compounds have been prepared (Figure 11.13).[39] Among them, only two non-π-delocalized NR

Figure 11.9 (a) Molecular structures of imidazolium mono NR IL compound **9** and ILC compound **10**. Temperature dependence of (b) χ_M in the first heating and cooling runs, and the second heating run, (c) χ_M by magnification (between 200 and 400 K) of (b), (d) $\chi_{para}T$ in the first heating run, (e) χ_{para} in the first heating and cooling runs, and the second heating run, measured for racemic **10** at 0.05 T. The open circles, filled circles and open triangles indicate plots in the first heating, first cooling and second heating runs, respectively. (f) Magnetic constants and superparamagnetic χ_{TIM} values obtained between 100 and 180 K in the first heating and cooling runs, and the second heating run.

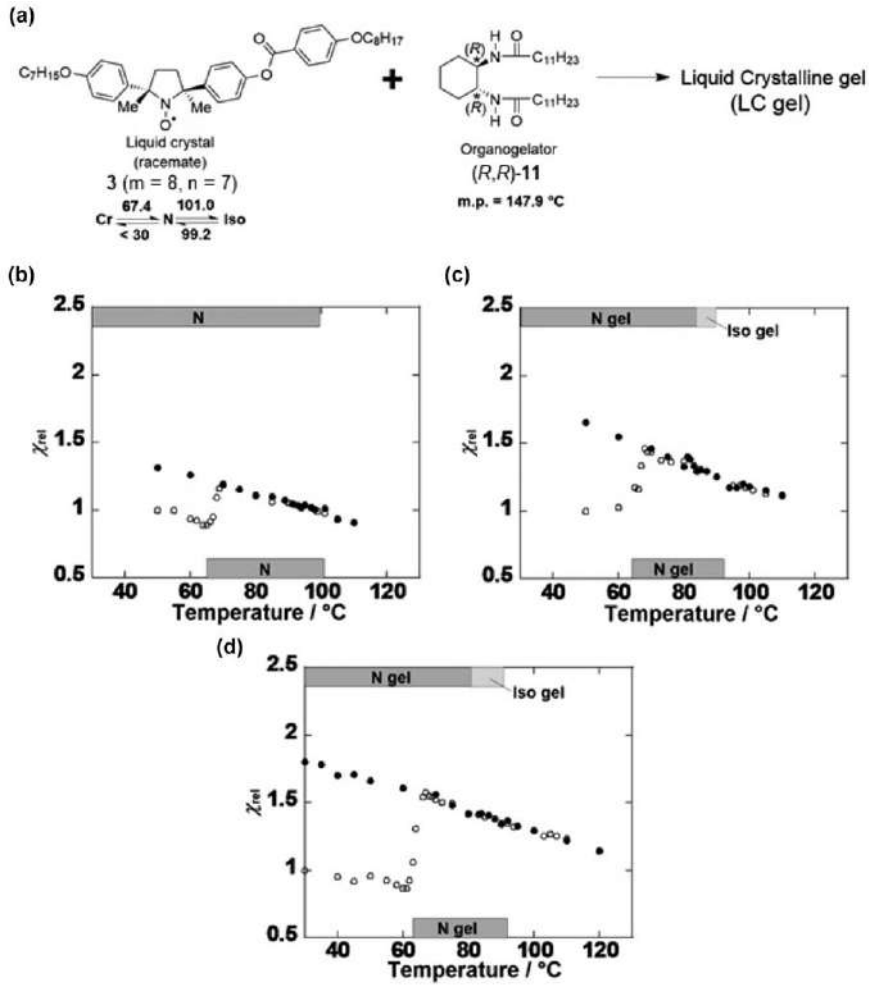

Figure 11.10 (a) Preparation of LC gels. Temperature dependence of χ_{rel} for (b) free racemic **3** (m = 8, n = 7), and (c) 5 wt.% and (d) 10 wt.% N gel mixtures, measured at round 0.33 T. Open and filled circles represent the first heating and cooling runs, respectively.

compounds **15**[50] and **16**[33] were confirmed to show a distinct positive magneto-LC effect in the hexagonal columnar (Col_h) LC phase by full characterization of the magnetic properties by SQUID magnetometry and EPR spectroscopy, whereas other radical compounds **17–19** did not show a positive magneto-LC effect in the columnar LC phase, most likely because of the π–π dimer formation that usually results in the antiferromagnetic interactions.

11.3.1 Monoradicals

12:[47] In 2008, Yelamaggad and Nakatsuji *et al.* reported the first stable discotic all-organic mono NR compounds **12**, which had a nitroxide unit

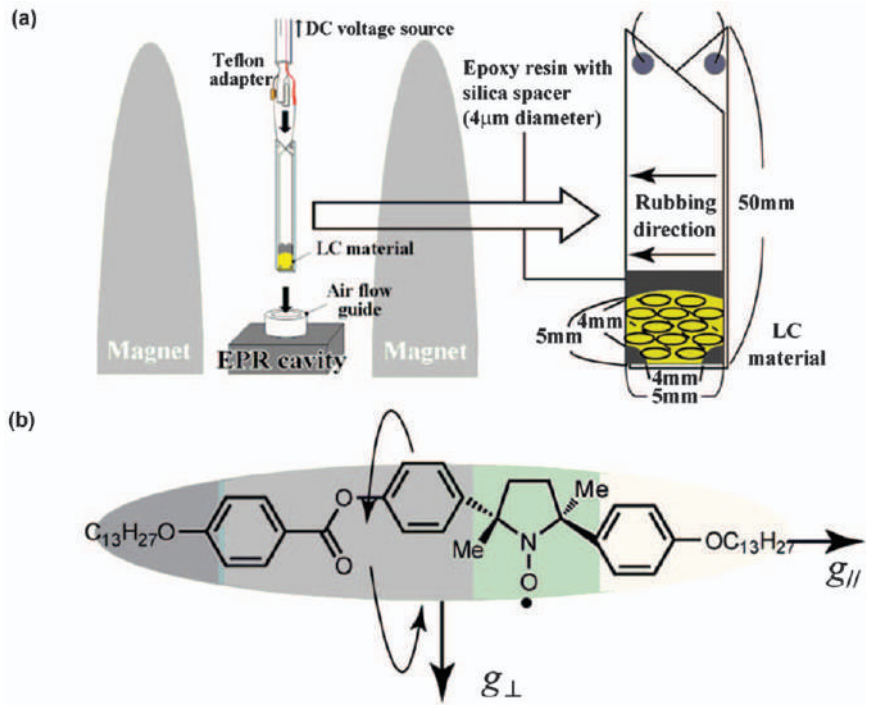

Figure 11.11 (a) Experimental setup to monitor the variable-temperature or electric field-dependent EPR spectra of (*S*,*S*)-**3** ($m = n = 13$) confined in a long 4 mm thick sandwich cell and (b) the principal axes of inertia and *g*-values.
Reproduced from ref. 46 with permission from the Royal Society of Chemistry.

(TEMPO or PROXYL group) at the peripheral position in the molecule and showed an enantiotropic columnar phase over a wide temperature range. However, weak antiferromagnetic interactions were observed in the crystalline, columnar LC and supercooled phases by SQUID magnetometry.

13:[48] In 2014, Ravat *et al.* reported that the hexabenzocoronene derivative **13** carrying a conjugated *tert*-butyl nitroxide moiety showed the positive magneto-LC effect in the hexagonal columnar phase by EPR spectroscopic analysis. However, there was no report for the data obtained by SQUID magnetometry, which is essential to verify this interesting result.

14:[49] In 2016, Bajzikova and Kohout *et al.* reported the magnetic properties of all-organic paramagnetic bent-core LC compounds having a TEMPO radical unit at the terminal position and exhibiting rich polymorphism including columnar phases (B_{1Rev} and $B_{1Rev'}$) at high temperatures were reported. However, these compounds did not show a positive magneto-LC effect in the LC phases.

15:[50] In 2018, we reported that both racemic **15** or (*R*,*R*)-**15** which formed intermolecular hydrogen bonds between the NO and OH groups in the condensed phases exhibited the glass state-to-hexagonal columnar LC phase

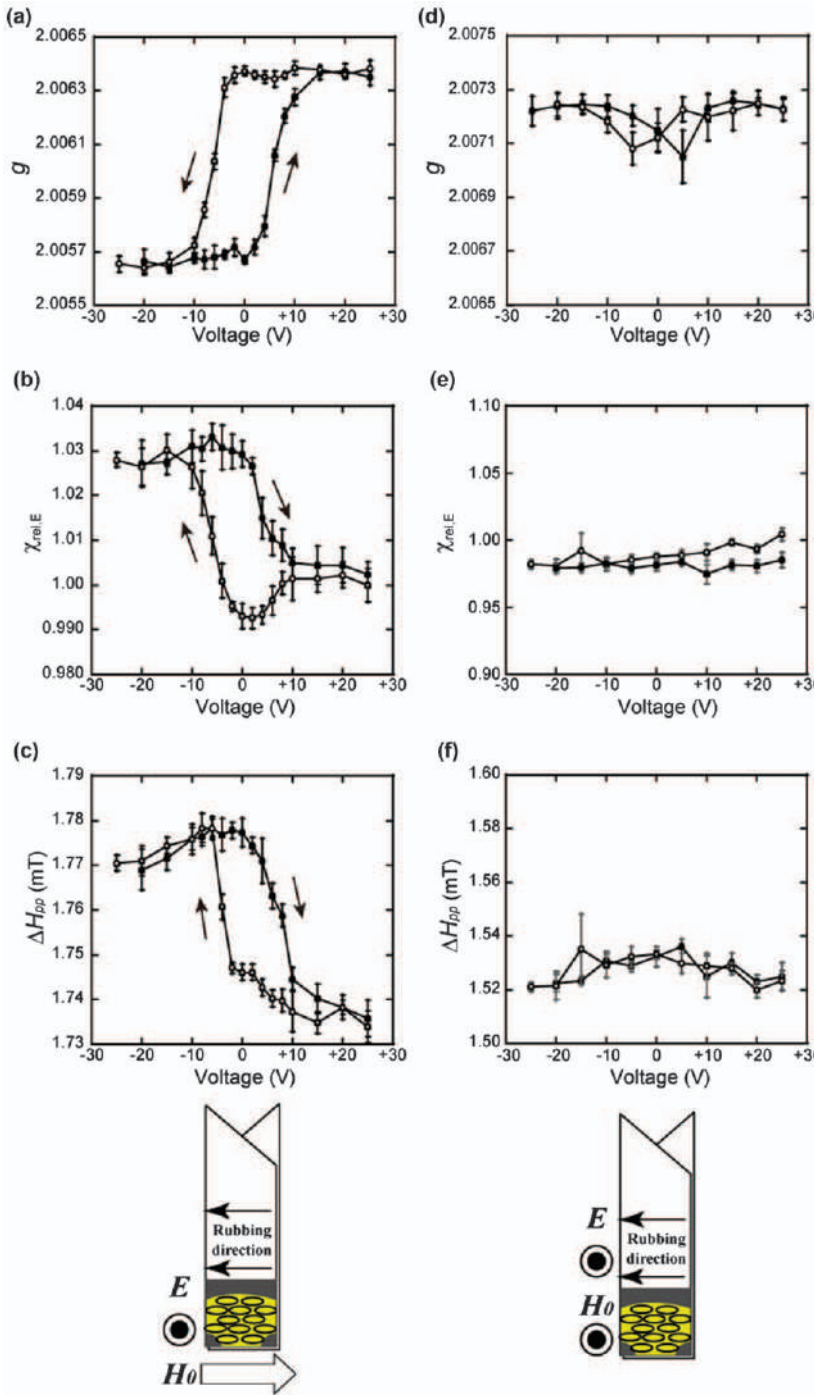

transition below room temperature. Both SQUID magnetometry and EPR spectroscopic analysis revealed that a large positive magneto-LC effect was observed in the LC and isotropic phases in the first heating run at both 0.05 and 0.5 T (Figure 11.14); this is likely due to the molecular flow, in contrast to our expectation that it generally disrupts magnetic orderings.

11.3.2 Diradical

16:[33] An achiral meso diradical compound (*R*,*S*)-**16** was synthesized and subjected to the measurement of the temperature dependence of χ_M by SQUID magnetometry and EPR spectroscopic analysis (Figure 11.15 and see Section 11.4). As a result, although (*R*,*S*)-**16** showed an ordinary paramagnetic behaviour in the original solid, a mixture of (*R*,*S*)-**16** and a small amount (5 mol%) of racemic diastereomers [a 1 : 1 mixture of (*R*,*R*)-**16** and (*S*,*S*)-**16**] exhibited superparamagnetic behaviour in the original solid phase, an additional χ_M increase (positive magneto-LC effect) at the crystal-to-Col_h phase transition by the first heating and a preservation of this χ_M increase not only in the isotropic phase by further heating and in the solid phase by the first cooling until cryogenic temperatures, but also in the Col_h and isotropic phases by the second heating, under low magnetic field ($H < 0.1$ T) (Figure 11.15a–g). In this instance, when the content of the racemic diastereomers was increased up to 20 mol%, a substantial χ_M increase was observed in all phases in the first heating run and more in the first cooling run (Figure 11.15h). Furthermore, the fact that the formation of a chiral helical columnar structure in the presence of a magnetic field (<0.5 T) was confirmed for achiral meso **16** by the temperature-resolved second harmonic generation (TR-SHG) microscopy deserves mention.

11.4 Origin of Superparamagnetic Phenomenon 'Positive Magneto-LC Effect'

First, the origin of superparamagnetic behaviour observed in all-organic LC NR compounds is discussed mesoscopically on the basis of the properties of metallic spin glass materials as stated by Fischer and Hertz: "A spin glass is i) a collection of spins (*i.e.*, magnetic moments) whose low-temperature state is a frozen disordered one, rather than the kind of uniform or periodic pattern we are accustomed to finding in conventional magnets, ii) observed

Figure 11.12 Electric field dependence of (a and d) *g*-value, (b and e) $\chi_{rel,E}$, and (c and f) ΔH_{pp} for the ferroelectric phase of (*S*,*S*)-**3** ($m = n = 13$, 65% ee) confined in a thin rubbed sandwich cell at 75 °C by EPR spectroscopy at around 0.33 T. The magnetic field was applied perpendicular (a, b and c) or parallel (d, e and f) to the electric field. Open and filled circles represent the application of electric fields from +25 V to −25 V and then −25 V to +25V, respectively.
Reproduced from ref. 46 with permission from the Royal Society of Chemistry.

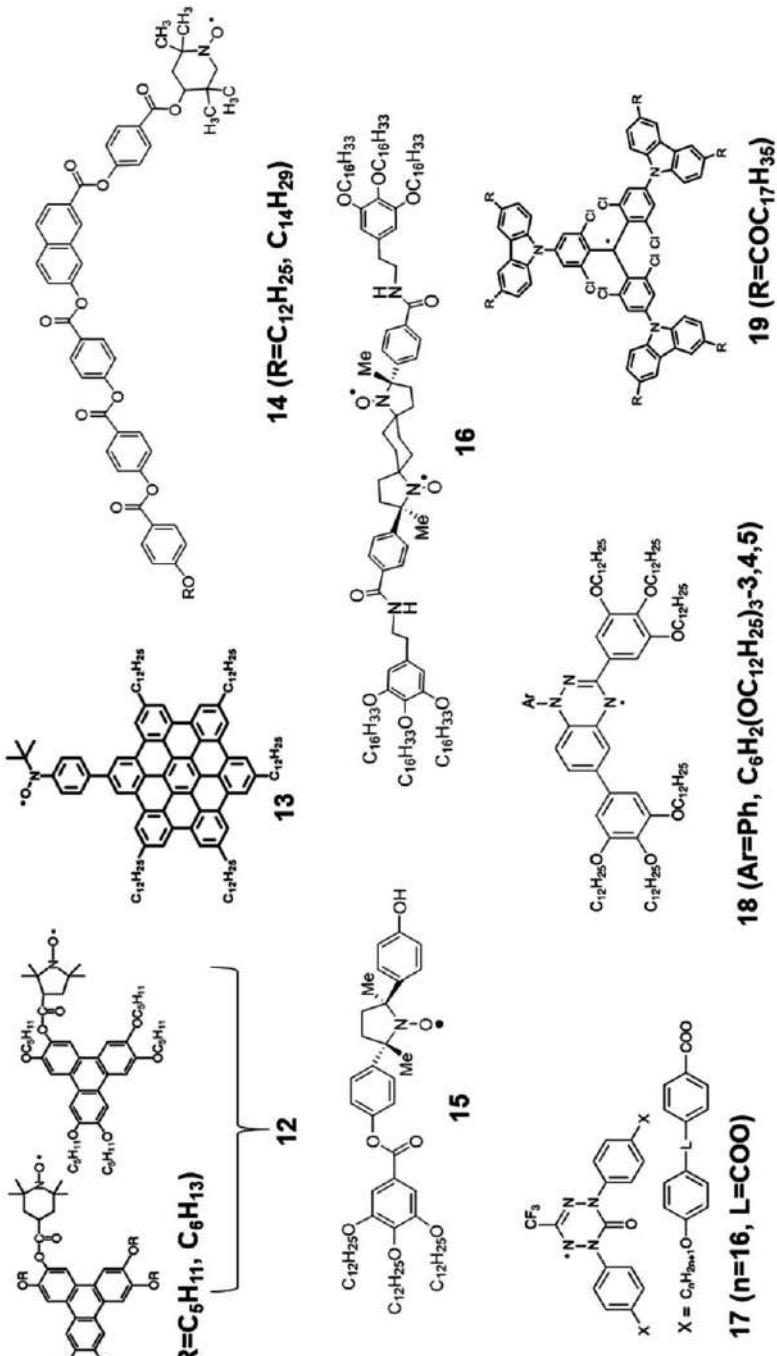

Figure 11.13 Molecular structures of organic radical-containing discotic columnar LC compounds.

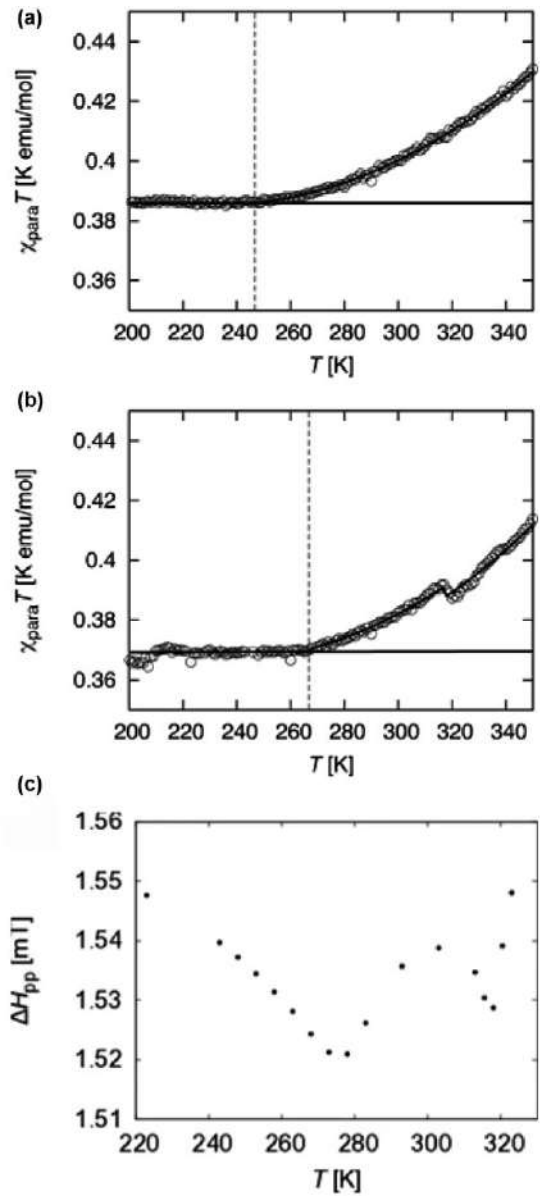

Figure 11.14 Temperature dependences of $\chi_{para}T$ for (a) racemic **15** and (b) (*R*,*R*)-**15** at 0.5 T by SQUID magnetometry, and of (c) EPR ΔH_{pp} for racemic **15** at around 0.33 T. The circles denote the experimental data in the heating run, and the horizontal solid lines denote the Curie–Weiss fitting curves for the LC glass state. The vertical broken lines denote the estimated glass state-to-LC phase transition temperatures, and the solid lines on the circles to the right of the broken lines denote the fitting curves for LC and isotropic phases.
Reproduced from ref. 50 with permission from American Chemical Society, Copyright 2018.

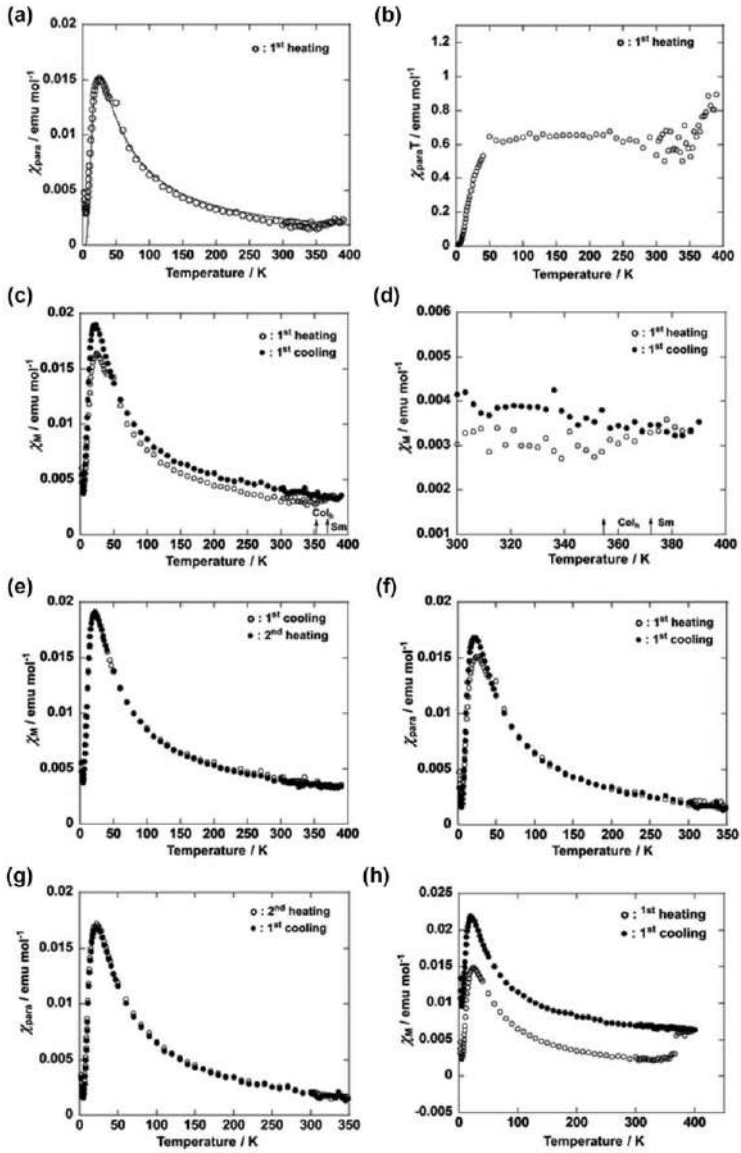

(i)

	$\chi_{dia} + \chi_{TIM}$ / emu mol^{-1}	Curie constant C / emu K mol^{-1}	χ_{TIM} / emu mol^{-1}
1st heating	$+1.24\times10^{-3}$	0.64	$+2.8\times10^{-3}$
1st cooling	$+2.14\times10^{-3}$	0.65	$+3.7\times10^{-3}$
2nd heating	$+1.90\times10^{-3}$	0.65	$+3.5\times10^{-3}$

in magnetic metal alloys such as Cu(Mn) and Au(Fe), and iii) induced by thermal processing or the presence of impurity".[40]

The analysis of the experimental results on the temperature dependence of χ_M for the LC NR compounds showing the positive magneto-LC effect indicated that the χ_M should be defined as the sum of temperature-dependent paramagnetic susceptibility ($\chi_{para} > 0$), a temperature-independent diamagnetic one ($\chi_{dia} < 0$) and a unique temperature-independent magnetic one ($\chi_{TIM} > 0$) (eqn (11.1)).[33,43]

$$\chi_M = \chi_{para} + \chi_{dia} + \chi_{TIM} \tag{11.1}$$

Since only the sum of χ_{dia} and χ_{TIM} values could be experimentally obtained as the temperature-independent component by χ_M-T^{-1} plots according to the Curie–Weiss law (eqn (11.2)), the χ_{TIM} value was derived by using the theoretical χ_{dia} value calculated according to the Pascal's constants.

$$\chi_{para} = C/(T - \theta) \tag{11.2}$$

The generation of this χ_{TIM} value, which corresponds to the χ_M increase at the crystal-to-LC phase transition in the first heating run for compounds **3**–**5**, **8** and **15**, is responsible for the positive magneto-LC effect (or the superparamagnetic interactions). In the case of ILC monoradical **10** or meso Col_h diradical **16** containing the racemic diastereomers, the χ_{TIM} value already existed in the original solid and increased at the solid-to-LC phase transition by the first heating. This increased χ_{TIM} value was kept in the isotropic phase by further heating, in the LC and solid phases by the first cooling from the isotropic phase, and in the LC and isotropic phases by the second heating. For example, the χ_{TIM} value between 100 and 180 K observed in the first cooling run from the isotropic phase for racemic **10** was as large as $+2.5\times10^{-3}$ emu mol^{-1} (Figure 11.9f),[43] and that between 100 and 200 K observed for **16** containing 5 or 20 mol% of racemic diastereomers was also as large as $+3.7\times10^{-3}$ or $+4.4\times10^{-3}$ emu mol^{-1}, respectively (Figure 11.15i).[33] These results imply that the total area of superparamagnetic spin domains is comparable to that of paramagnetic spins.

Thus, the origin of such unique magnetic properties observed in all phases of racemic **10** or meso **16** containing the racemic diastereomers can

Figure 11.15 Temperature dependence of (a) χ_{para} in the first heating run (the solid line calculated by using the Bleany-Bowers equation with $2J/k_B = -39.6$ K), (b) χ_{para} T in the first heating, (c) χ_M in the first heating and cooling runs, (d) χ_M by magnification (between 300 and 400 K) of (c), (e) χ_M in the first cooling and second heating runs, (f) χ_{para} in the first heating and cooling runs and (g) χ_{para} in the first cooling and second heating runs, measured for **1**(95 : 5), and (h) χ_M in the first heating and cooling runs measured for **1**(80 : 20), at 0.05 T in the temperature range between 2 and 390 K. (i) Obtained magnetic constants and χ_{TIM} values in the first heating and cooling runs, and the second heating run for **1**(95 : 5).

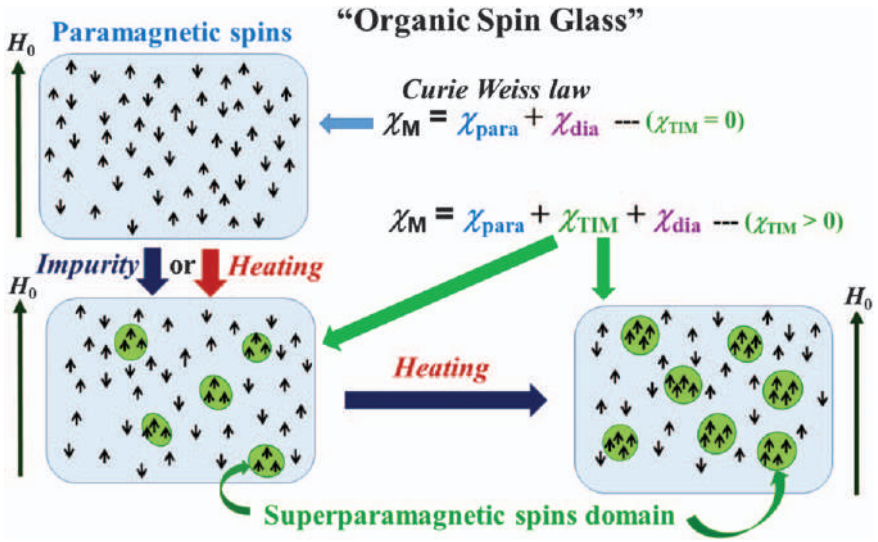

Figure 11.16 Schematic representation of organic spin glass. The formation of superparamagnetic spin domains surrounded by paramagnetic spins by heating or the presence of impurity, and additional enlargement of the size and/or number of the domains by heating.

be rationalized mesoscopically in terms of (i) the preferential formation of spin glass-like inhomogeneous magnetic domains consisting of superparamagnetic spin domains surrounded by paramagnetic spins in the original solid phase, (ii) the subsequent enlargement of the size and/or number of superparamagnetic spin domains by thermal processing, and (iii) preservation of the overall increased superparamagnetic spin domains in the solid phase by cooling until cryogenic temperatures, under low magnetic fields (<0.1 T) (Figure 11.16).

Meanwhile, to gain a microscopic insight into the origin of the intermolecular ferromagnetic interactions operating in each superparamagnetic domain, the extent of anisotropic spin–spin dipole interactions can be evaluated by the measurement of the temperature dependence of EPR peak-to-peak line width (ΔH_{pp}). Generally, it is known that the change in ΔH_{pp} reflects the following two competing factors: (i) anisotropic spin–spin dipole interaction; the stronger the interactions are, the more the ΔH_{pp} increase is and (ii) isotropic spin–spin exchange interaction; the stronger the interactions are, the greater the ΔH_{pp} decrease is. Accordingly, by comparing the EPR ΔH_{pp} value with the SQUID χ_M change (increase or decrease) at the solid-to-LC phase transition, one can judge whether either ferromagnetic or antiferromagnetic spin–spin dipole interactions dominate in the LC phases. Therefore, the fact that all of the LC NR compounds **3**–**5**, **8**, **10**, **15** and **16** showed both a ΔH_{pp} increase and a χ_M increase at the solid-to-LC phase transition indicated the occurrence of ferromagnetic spin–spin dipole and

exchange interactions in the LC phases (Figure 11.5e). This is because the LC superstructural anisotropy could induce the anisotropy of the spin–spin dipole interaction, eventually leading to the generation of the anisotropic and inhomogeneous magnetic interactions in the LC domains.

As the mechanism of ferromagnetic spin–spin dipole and exchange interactions operating in each superparamagnetic domain, Vorobiev *et al.* suggested that the intermolecular spin polarization operating between the central paramagnetic centre of one molecule and the aromatic ring of another molecule in the centrosymmetric dimer, rather than the direct through-space interactions between the spin centres, contributes to the occurrence of a positive magneto-LC effect by the DFT calculations of spin density distribution in the interacting molecules based on the crystal structure of (*S*,*S*)-**3** ($m = n = 4$) (Figure 11.17a and b).[54] Furthermore, we speculated that in the case of non-centrosymmetric chiral LC phases, additional intermolecular CH/O and/or CH/π interactions, which are very often observed in the crystal structures, might contribute to the spin polarization mechanism (Figure 11.17c).

11.5 Application to Metal-free Magnetic Microemulsions, Mixed Micelles and Nanoemulsions

Considering the proposed spin polarization mechanism including CH/O and/or CH/π interactions regarding the generation of superparamagnetic interactions in the LC NR compounds, we predicted that it might be possible to observe such a unique magnetic phenomenon in other organic NR soft-materials, if simple NR compounds could be densely confined in a capsule. In fact, sonication of a mixture of oily racemic 2,2,5-trimethyl-5-phenylpyrrolinine-*N*-oxyl radical **20** (Figure 11.18a), which was confirmed to show a distinctly alternating spin polarization on each atom in the molecule by DFT calculations, and one of surfactants such as SDS (sodium dodecyl sulfate) in water at 25 °C gave several emulsions with a particle size of 1–2 mm ϕ at the bottom in the glass vial. These emulsions were attracted by a permanent magnet approaching from the outside bottom and moved quickly and smoothly under the influence of the magnet. This observation encouraged us to prepare NR microcapsules and nano-sized mixed micelles.

11.5.1 Microemulsions[35]

We prepared stable NR liquid microcapsules (diameter 300 μm) consisting of monodispersed core–shell W/O/W double emulsion droplets (Figure 11.18) using a microfluidic device. These emulsions were magnetically transportable and served as flexible antioxidative magnetic carriers for on-demand cargo-transport system and droplet-based sensors. In addition, if the NR compound can show an LC phase at room temperature, LC NR

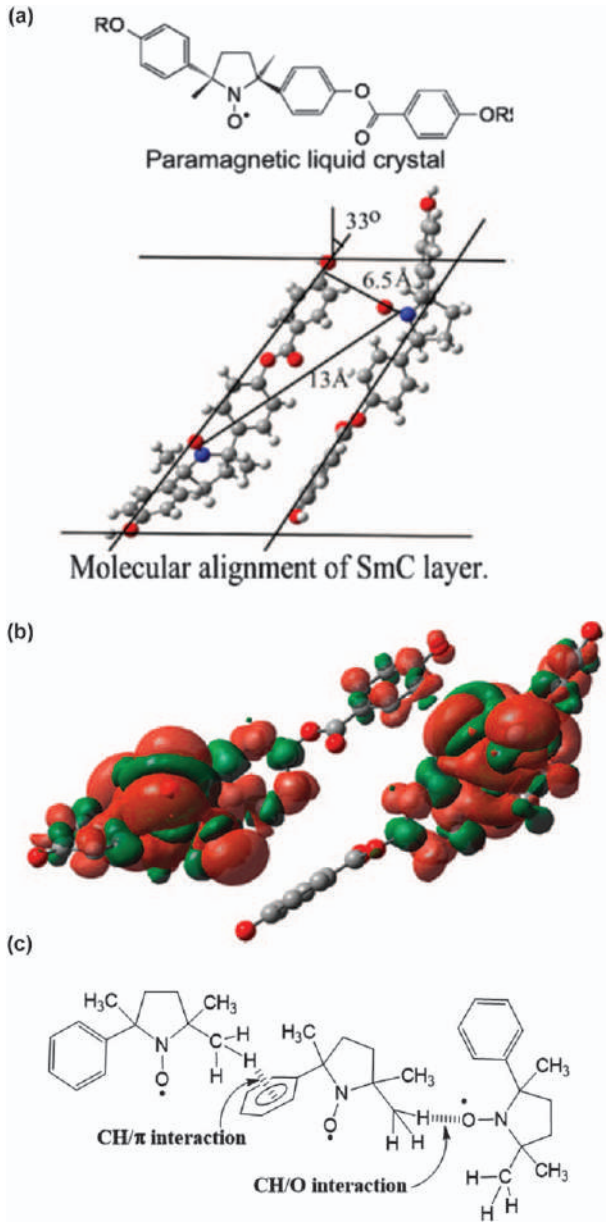

Figure 11.17 (a) Relative position of a pair of molecules in the crystal structure of (*S*,*S*)-**3** ($m = n = 4$) and (b) spin density distribution in the same pair by DFT calculations. (c) Expected intermolecular CH/O and CH/π interactions.
Reproduced from ref. 54 with permission from American Chemical Society, Copyright 2014.

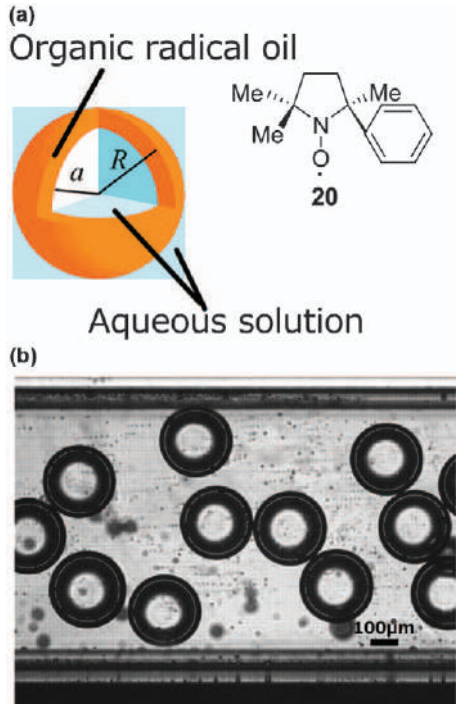

Figure 11.18 (a) Schematic of a W/O/W emulsion droplet with an organic radical oil shell consisting of radical compound **20**. The W/O/W emulsion has inner and outer aqueous phases and a middle organic radical oil phase. (b) Bright-field microphotographs of the mono-dispersed W/O/W emulsion droplets ($R = 135$ μm, $a = 110$ μm).
Reproduced from ref. 35 with permission from the Royal Society of Chemistry.

microcapsules with much more functions will be able to be fabricated using microfluidic devices.[55]

11.5.2 Nano-sized Mixed Micelles and Drug or Fluorescence Agent-loaded Nanoemulsions[36–38,56]

With a view to developing theranostic nanomedicines for targeted drug delivery systems (DDS) visible by MRI, robust metal-free magnetic nano-sized mixed micelles (mean particle size less than 20 nm) consisting of a biocompatible non-ionic surfactant Brij58 or Tween80 and low-molecular-weight 2,2,5-trimethyl-5-(4-alkoxy)phenylpyrrolidine-*N*-oxyl radicals (**21**) were prepared in pH 7.4 phosphate-buffered saline (PBS) (Figure 11.19). The particle sizes were determined by small-angle neutron-scattering (SANS) and dynamic light-scattering (DLS) measurements. The resulting mixed micelles showed high colloidal stability, low cytotoxicity, enough reduction resistance

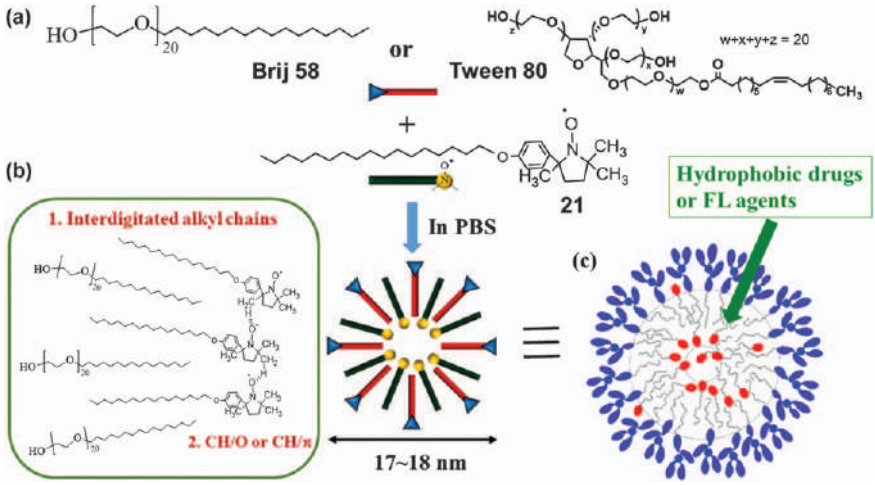

Figure 11.19 (a) Preparation of mixed micelles (17–18 nm ϕ) from NR **21** and Brij58 or Tween 80 in PBS. (b) Formation of stable mixed micelles owing to the interdigitated layer structure of long alkyl chains and CH/O and/or CH/π interactions between neighbouring cyclic NR moieties. (c) An expected mixed micelle structure. Hydrophobic drugs and/or fluorescence agents can be easily incorporated into the mixed micelles to form stable nanoemulsions.[56]

to excess ascorbic acid, and sufficient contrast enhancement in the proton longitudinal relaxation time (T_1) weighted MR images in PBS *in vitro* and *in vivo* (Figure 11.20). Furthermore, hydrophobic anticancer drugs and/or fluorescence agents could be encapsulated into the mixed micelles to give stable nanoemulsions (Figure 11.19c). The resulting anticancer drug paclitaxel-loaded nanoemulsions were efficiently incorporated into HeLa cancer cells to suppress cell growth.

11.6 Conclusions

In 2015, we predicted in ref. 57 that the positive magneto-LC effect should be induced in discotic columnar LC phases, too, by introducing chirality or bulky substituent into the molecule so as to avoid the strong π–π dimer formation. Indeed, this prediction has become reality. As described in Section 11.3, the distinct positive magneto-LC effect was observed in non-π-delocalized LC NR compounds **15** and **16** showing a Col_h LC phase. Interestingly, the Col_h phase of achiral meso **16** was SHG-active in the presence of a magnetic field, indicating the formation of a chiral helical columnar structure. Furthermore, SQUID magnetometry and EPR spectroscopic analysis of novel ILC compound **10** as well as discotic LC compound **16** proved that they displayed typical spin glass-like superparamagnetic features such as thermal (and impurity) effects which were observed in metallic spin glass materials. The mesoscopical origin of such a

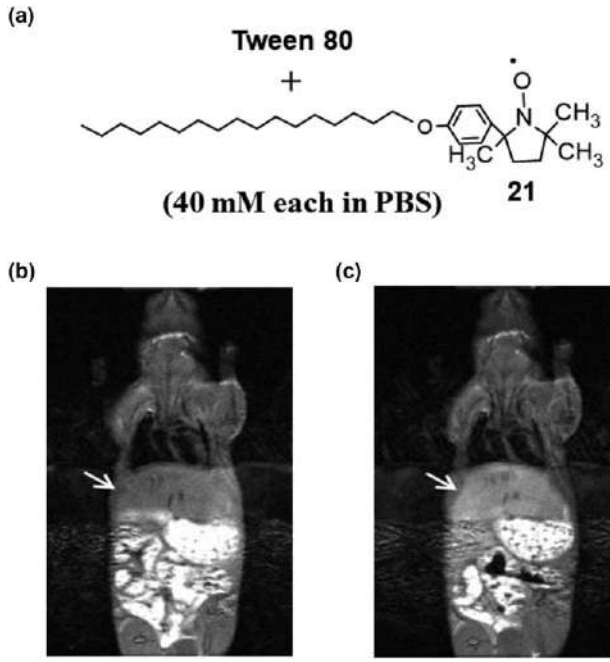

Figure 11.20 A solution (200 μL) of mixed micelles prepared from (a) NR **21** and Tween 80 (final concentration 40 mM each) in PBS was intravenously injected into a male ICR mouse: coronal T_1-weighted MR images for the liver (b) before injection and (c) 23 min after injection. Distinct contrast enhancement was observed in the liver in (c) (indicted by white arrows[56]).

superparamagnetic behaviour could be explained in terms of the preferential formation of superparamagnetic spins domains surrounded by paramagnetic spins in the presence of organic impurity and/or the enlargement of the size and/or number of the superparamagnetic spin domains by thermal processing. In each superparamagnetic spin domain, ferromagnetic microscopic spin–spin dipole and exchange interactions were suggested to operate by the intermolecular spin polarization mechanism including intermolecular CH/O and CH/π interactions. Thus, the definition of the term 'positive magneto-LC effect' should be extended to all phases of LC NR compounds which showed such a superparamagnetic behaviour. In contrast, thus far such a magnetic behaviour has not been observed with respect to analogous non-LC NR compounds.

In order to extend the generation of superparamagnetic interactions to other organic NR soft-materials systems, we prepared (i) a stable NR liquid microcapsule which can serve as flexible antioxidative magnetic carriers for on-demand cargo-transport system and droplet-based sensors and (ii) robust redox-resistant magnetic nano-sized mixed micelles to use as the theranostic nanomedicines for targeted DDS visible by MRI.

Acknowledgements

Support from JSPS KAKENHI (Grant number 26248024 for RT, and 17H04896 and 17K19032 for YU) is acknowledged.

References

1. D. B. Amabilino and J. Veciana, in *Magnetism: Molecules to Materials II*, ed. J. S. Miller and M. Drillon, Wiley-VCH, Weinheim, 2001, pp. 1–60.
2. T. Sugawara, H. Komatsu and K. Suzuki, *Chem. Soc. Rev.*, 2011, **40**, 3105–3118.
3. C. Tansakul and R. Braslau, in *Encyclopedia of Radicals in Chemistry, Biology and Materials, Vol. 2: Synthetic Strategies and Applications*, ed. C. Chatgilialoglu and A. Studer, Johan Wiley & Sons, Chichester, 2012, pp. 1096–1129.
4. T. Suga and H. Nishide, in *Stable Radicals: Fundamentals and Applied Aspects of Odd-Electron Compounds*, ed. R. G. Hicks, John Wiley & Sons, Chichester, 2010, pp. 507–520.
5. M. Tamura, Y. Nakazawa, D. Shiomi, K. Nozawa, Y. Hosokoshi, M. Ishikawa, M. Takahashi and M. Kinoshita, *Chem. Phys. Lett.*, 1991, **186**, 401–404.
6. R. Chiarelli, M. A. Novak, A. Rassat and J. L. Tholence, *Nature*, 1993, **363**, 147–149.
7. I. Dierking, *Textures of Liquid Crystals*, Wiley-VCH, Weinheim, 2003.
8. K. Mainzer, *Symmetry and Complexity: The Sprit and Beauty of Nonlinear Science*, World Scientific, 2005.
9. *Handbook of Liquid Crystals*, ed. J. W. Goodby, P. J. Collings, T. Kato, C. Tschierske, H. F. Gleeson and P. Raynes, Wiley-VCH, Weinheim, 2nd edn, vol. 1–8, 2014.
10. W. Eerenstein, N. D. Mathur and J. F. Scott, *Nature*, 2006, **442**, 759–765.
11. C. N. R. Rao and C. R. Serrao, *J. Mater. Chem.*, 2007, **17**, 4931–4938.
12. C. Felser, G. H. Fecher and B. Balke, *Angew. Chem., Int. Ed.*, 2007, **46**, 668–699.
13. S. Seki, *Magnetoelectric Response in Low-Dimensional Frustrated Spin Systems*, Springer, Tokyo, 2012.
14. G. L. J. A. Rikken and E. Raupach, *Nature*, 1997, **390**, 493–494.
15. G. L. J. A. Rikken and E. Raupach, *Nature*, 2000, **405**, 932–935.
16. C. Train, R. Gheorghe, V. Krsic, L.-M. Chamoreau, N. S. Ovanesyan, G. L. J. A. Rikken, M. Grussele and M. Verdaguer, *Nat. Mater.*, 2008, **7**, 729–734.
17. K. Binnemans and C. Gröller-Walrand, *Chem. Rev.*, 2002, **102**, 2302–2345.
18. R. Tamura, Y. Uchida and K. Suzuki, in *Handbook of Liquid Crystals*, ed. J. W. Goodby, P. J. Collings, T. Kato, C. Tschierske, H. F. Gleeson and P. Raynes, Wiley-VCH, Weinheim, 2nd edn, vol. 8, 2014, pp. 837–864.
19. M. Dvolaitzky, J. Billard and F. Poldy, *C. R. Acad. Sci.*, 1974, **279C**, 533–535.

20. M. Dvolaitzky, C. Taupin and F. Poldy, *Tetrahedron Lett.*, 1976, **18**, 1469–1472.
21. M. Dvolaitzky, J. Billard and F. Poldy, *Tetrahedron*, 1976, **32**, 1835–1838.
22. J. Allgaier and H. Finkelmann, *Macromol. Chem. Phys.*, 1994, **195**, 1017–1030.
23. S. Greve, V. Vill and W. Friedrichsen, *Z. Naturforsch.*, 2002, **57b**, 677–684.
24. S. Nakatsuji, M. Mizumoto, H. Ikemoto, H. Akutsu and J. Yamada, *Eur. J. Org. Chem.*, 2002, 1912–1918.
25. P. Kaszyński, in *Magnetic Properties of Organic Materials*, ed. P. M. Lahti, Marcel Dekker, New York, 1999, pp. 325–344.
26. N. Ikuma, R. Tamura, S. Shimono, N. Kawame, O. Tamada, N. Sakai, J. Yamauchi and Y. Yamamoto, *Angew. Chem. Int. Ed.*, 2004, **43**, 3677–3682.
27. N. Ikuma, R. Tamura, S. Shimono, Y. Uchida, K. Masaki, J. Yamauchi, Y. Aoki and H. Nohira, *Adv. Mater.*, 2006, **8**, 477–480.
28. N. Ikuma, R. Tamura, K. Masaki, Y. Uchida, S. Shimono, J. Yamauchi, Y. Aoki and H. Nohira, *Ferroelectrics*, 2006, **343**, 119–125.
29. R. Tamura, Y. Uchida and N. Ikuma, *J. Mater. Chem.*, 2008, **18**, 2872–2876.
30. Y. Uchida, N. Ikuma, R. Tamura, S. Shimono, Y. Noda, J. Yamauchi, Y. Aoki and H. Nohira, *J. Mater. Chem.*, 2008, **18**, 2950–2952.
31. Y. Uchida, K. Suzuki, R. Tamura, N. Ikuma, S. Shimono, Y. Noda and J. Yamauchi, *J. Am. Chem. Soc.*, 2010, **132**, 9746–9752.
32. Y. Uchida, R. Tamura, N. Ikuma, S. Shimono, J. Yamauchi, Y. Shimbo, H. Takezoe, Y. Aoki and H. Nohira, *J. Mater. Chem.*, 2009, **19**, 415–418.
33. Y. Takemoto, E. Zaytseva, K. Suzuki, N. Yoshioka, Y. Takanishi, M. Funahashi, Y. Uchida, T. Akita, J. Park, S. Sato, S. Clevers, G. Coquerel, D. G. Mazhukin, S. Shimono, M. Sugiyama, H. Takahashi, J. Yamauchi and R. Tamura, *Chem. – Eur. J.*, 2018, **24**, 17293–17302.
34. K. Suzuki, Y. Uchida, R. Tamura, S. Shimono and J. Yamauchi, *J. Mater. Chem.*, 2012, **22**, 6799–6806.
35. Y. Uchida, Y. Iwai, T. Akita, T. Mitome, K. Suzuki, R. Tamura and N. Nishiyama, *J. Mater. Chem. B*, 2014, **2**, 4130–4133.
36. K. Nagura, Y. Takemoto, S. Moronaga, Y. Uchida, S. Shimono, A. Shiino, K. Tanigaki, T. Amano, F. Yoshino, Y. Noda, S. Koizumi, N. Komatsu, T. Kato, J. Yamauchi and R. Tamura, *Chem. – Eur. J.*, 2017, **23**, 15713–15720.
37. K. Nagura, A. Bogdanov, N. Chumakova, A. K. Vorobiev, S. Moronaga, H. Imai, T. Matsuda, Y. Noda, T. Maeda, S. Koizumi, K. Sakamoto, T. Amano, F. Yoshino, T. Kato, N. Komatsu and R. Tamura, *Nanotechnology*, 2019, **30**, 224002, (8pp).
38. K. Nagura, Y. Takemoto, F. Yoshino, A. Bogdanov, N. Chumakova, A. K. Vorobiev, H. Imai, T. Matsuda, S. Shimono, T. Kato, N. Komatsu and R. Tamura, *Pharmaceutics*, 2019, **11**, 42, (9pp).

39. P. Kaszyński, S. Kapusciński and S. Ciastek-Iskrzycka, *Adv. Heterocycl. Chem.*, 2019, **128**, 263–331.
40. K. H. Fischer and J. A. Hertz, *Spin Glasses*, Cambridge University Press, Cambridge, 1991.
41. K. Suzuki, Y. Takemoto, S. Takaoka, K. Taguchi, Y. Uchida, D. G. Mazhukin, I. A. Grigor'ev and R. Tamura, *Chem. Commun.*, 2016, **52**, 3935–3938.
42. Y. Uchida, K. Suzuki and R. Tamura, *J. Phys. Chem. B*, 2012, **116**, 9791–9795.
43. Y. Uchida, T. Sakaguchi, S. Oki, S. Shimono, J. Park, M. Sugiyama, S. Sato, E. Zaytseva, D. G. Mazhukin and R. Tamura, the manuscript submitted.
44. Y. Uchida, S. Oki, R. Tamura, T. Sakaguchi, K. Suzuki, K. Ishibashi and J. Yamauchi, *J. Mater. Chem.*, 2009, **19**, 6877–6881.
45. Y. Takemoto, Y. Uchida, S. Shimono, J. Yamauchi and R. Tamura, *Mol. Cryst. Liq. Cryst.*, 2017, **647**, 279–289.
46. K. Suzuki, Y. Uchida, R. Tamura, Y. Noda, N. Ikuma, S. Shimono and J. Yamauchi, *Soft Matter*, 2013, **9**, 4687–4692.
47. C. V. Yelamaggad, A. S. Achalkumar, D. S. S. Rao, M. Nobusawa, H. Akutsu, J. Yamada and S. Nakatsuji, *J. Mater. Chem.*, 2008, **18**, 3433–3437.
48. P. Ravat, T. Marszalek, W. Pisula, K. Müllen and M. Baumgaten, *J. Am. Chem. Soc.*, 2014, **136**, 12860–12863.
49. K. Bajziková, M. Kohout, J. Tarábek, J. Svoboda, V. Novotná, J. Vejpravová, D. Pociecha and E. Gorecka, *J. Mater. Chem. C*, 2016, **4**, 1154–11547.
50. S. Nakagami, T. Akita, D. Kiyohara, Y. Uchida, R. Tamura and N. Nishiyama, *J. Phys. Chem. B*, 2018, **122**, 7409–7415.
51. M. Jasiński, D. Pociecha, H. Monobe, J. Szczytko and P. P. Kaszyński, *J. Am. Chem. Soc.*, 2014, **216**, 14658–14661.
52. M. Jasiński, J. Szczytko, D. Pociecha, H. Monobe and P. Kaszyński, *J. Am. Chem. Soc.*, 2016, **138**, 9421–9424.
53. S. Castellano, F. Lopez-Calahorra, E. Brillas, L. Julia and D. Velasco,, *Angew. Chem., Int. Ed.*, 2009, **48**, 6516–6519.
54. A. K. Vorobiev, N. Chumakova, D. A. Pomogailo, Y. Uchida, K. Suzuki, Y. Noda and R. Tamura, *J. Phys. Chem. B*, 2014, **118**, 1932–1942.
55. T. Akita, H. Kouno, Y. Iwai, Y. Uchida and N. Nishiyama, *J. Mater. Chem. C*, 2017, **5**, 1303–1307.
56. K. Nagura, *Development of All-Organic Magnetic Mixed Micelles Aiming at Biomedical Application*, Doctor thesis, Kyoto University, March 2019.
57. R. Tamura, Y. Uchida and K. Suzuki, in *Advances in Organic Crystal Chemistry: Comprehensive Reviews 2015*, ed. R. Tamura and M. Miyata, Springer, Tokyo, 2015, pp. 689–706.

CHAPTER 12

Nitroxide Intervention in Oxidative and Free Radical Damage in Biology and Disease

STEVEN E. BOTTLE,*[a] GRACE ENG,[a] PAUL WITTING[b] AND BELAL CHAMI[b]

[a] School of Chemistry and Physics, Queensland University of Technology, (QUT), Australia; [b] Discipline of Pathology, School of Medical Sciences, Faculty of Medicine and Health, University of Sydney, Australia
*Email: s.bottle@qut.edu.au

12.1 Introduction: Reactive and Stable Free Radicals in Biological Systems

Free radicals, more often simply called 'radicals', are broadly recognised as being highly reactive, extremely short-lived species. Radicals typically undergo relatively non-selective atom abstraction reactions and undertake rapid combination reactions at near-diffusion-controlled rates. As an odd-electron radical species is statistically most likely to encounter an even-electron, non-radical species, any subsequent reaction must in turn therefore generate yet another radical. Consequently, considerable chemical change can be induced by the generation of only a small number of reactive free radicals. When produced in unregulated quantities the impact of such radicals on biological systems can be severe, meaning that radicals can pose a serious threat to cellular health.[1] Surprisingly, however, radicals are constantly being produced in cells and tissues under physiological conditions through normal biochemical processes such as cellular respiration, and there is a raft of

Nitroxides
Edited by Olivier Ouari and Didier Gigmes

Published by the Royal Society of Chemistry, www.rsc.org

endogenous antioxidant systems that regulate free radical production. Indeed, radicals also play critically important and beneficial roles in signal transduction pathways that underpin cellular function.[2] Endogenous radicals, even those involved in essential signal cascades, are still highly reactive species and consequently are short-lived and have limited selectivity. This reactivity can promote, or directly cause, oxidation of important structural or functional components of cells, such as proteins, carbohydrates, lipids and even DNA nucleotides.[3] Such damage can easily lead to cell death, either directly due to loss of function, by promoting pro-apoptotic pathways leading to decreased cellular viability, or through uncontrolled proliferation leading to cancer.[4]

Nitroxide free radicals, on the other hand, are not typical radicals in that they can be highly stable and kinetically persistent. Nitroxides persist as stable free radicals[5,6] due to delocalisation of the unpaired electron over the nitrogen–oxygen bond and the energetically unfavourable homo-dimerisation that would form a peroxy-type bond. Nitroxides that are used in research studies are usually low-molecular-weight, membrane-permeable species and the presence of the unpaired electron generates paramagnetic properties and enables their monitoring using electron paramagnetic resonance (EPR) spectroscopy. In the more than 60 years since the first reports describing stable dialkyl-substituted nitroxide free radicals,[7–9] these species have been employed in a wide variety of applications, including as stabilisers in plastics and as radical spin-traps in radical-mediated polymerisation processes.[10–12] Nitroxides have also been used as contrast agents for magnetic resonance imaging[13,14] and spin labels and probes in EPR spectroscopy to study key biophysical and biochemical parameters such as oxygen concentration,[15–17] membrane fluidity,[18,19] pH,[20] temperature[21] and the structural properties of membrane transport proteins.[22,23] Furthermore, as spin probes and contrast agents, nitroxides have been shown to be useful tools for non-invasively monitoring cellular and tissue redox status *in vivo* using whole animal models[24–29] (Figure 12.1).

Despite their overall stability, nitroxides can rapidly react with certain other free radicals and in this context they have been successfully used in the study of, and intervention in, experimental models of oxidative stress. Oxidative stress is a broad term that encompasses a range of critical issues pertaining to cellular health that arise from an imbalance in the levels of damaging free radicals and redox-active species in the cellular environment. The term ''reactive oxygen species'' (ROS) is typically used to categorise the many forms of these species that can be associated with promoting dysfunction and ultimately disease progression. The antioxidant properties of nitroxides and their reactivity towards ROS clearly suggest a therapeutic role in intervening in a number of important diseases, including cancer, which involve redox imbalances characterised by heightened levels of oxidative stress.

When assessing the potential of nitroxides as novel drugs, it is important to note that physiologically most nitroxides are rapidly reduced,[30] and plasma half-lives can be impractically short. Clearance rates for nitroxides are often very high[31] (which suggests low toxicity), which has also been seen

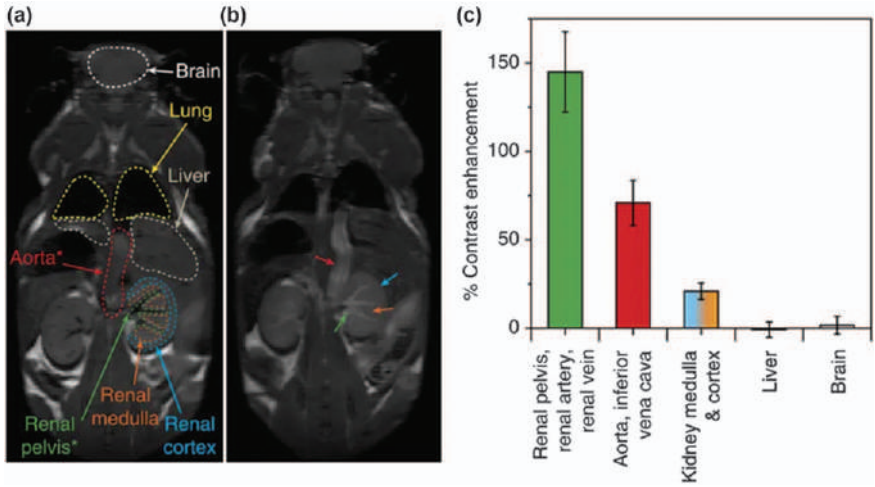

Figure 12.1 An example of magnetic resonance imaging enhancement made possible with a nitroxide nanoparticle. (a) Magnetic resonance (MR) image of whole mouse with specific organs/tissues highlighted for clarity. (b) MR image of the same mouse 30 min after injection with a combination of MR/fluorescent/EPR-responsive nitroxide nanoparticle. (c) Indication of the degree of MR image contrast enhancement possible using the nitroxide contrast agent.
Reproduced from ref. 13 with permission from Springer Nature, Copyright 2014.

as a limitation[32] for drug development. Recent developments have seen the evolution of sterically stabilised nitroxides and new modes of delivery of nitroxides that have seen improved biological half-life for this group of drugs. Despite these conditions however, this chapter outlines some of the recent findings where nitroxides have provided a significant therapeutic effect or an important mechanistic insight into diseases involving heightened levels of oxidative stress. Much of the efficacy of the approaches described is dependent on the cyclic bio-reduction and oxidative regeneration of nitroxides under physiological conditions. It is therefore worth noting then that new tetra-ethyl and related increased steric bulk nitroxides, which display far greater resistance to bio-reduction,[33] hold significant potential to deliver even more important results as they are applied to the study and intervention in the diseases and disorders described herein.

12.2 Antioxidants as Potential Therapeutics in Diseases such as Cancer and the Role of Nitroxide Free Radicals

Cancer arises from changes in cellular DNA that either enhance cellular proliferation or decrease cellular death pathways. As free radicals are able to induce such changes to DNA it follows that antioxidants that can remove free

radicals should therefore lower cancer risk. Indeed, promising results from a number of early epidemiological and laboratory investigations suggested that dietary antioxidants such as vitamin E, selenium and lycopene could be beneficial in preventing cancer.[34] These results prompted several large-scale clinical trials including the *Alpha-Tocopherol, Beta-Carotene prevention* (ATBC) study, the *Heart Outcome Prevention Evaluation – The Ongoing Outcomes* (HOPE-TOO) study, the *Prostate, Lung, Colorectal and Ovarian* (PLCO) cancer screening trial and the *SELenium and vitamin E Cancer prevention Trial* (SELECT).[35–39] Surprisingly, the results from these clinical studies demonstrated limited, if any, impact from the use of such antioxidants and in some trials were halted due to adverse impacts. For example, overall risk for prostate cancer, for instance, is unaffected by dietary antioxidant supplements.[39–41] In fact, in a 2011 follow-up study, updated data from the SELECT trial showed a significantly *increased* risk of prostate cancer among healthy men taking vitamin E (400 IU per day).[42] Furthermore, men with higher levels of selenium at the start of the trial had doubled the risk of developing high-grade prostate cancer by taking selenium supplements. The findings from epidemiological studies are themselves conflicting, with some reporting an inverse association between dietary antioxidant intake (*e.g.*, vitamin A, β-carotene, lycopene, selenium) and prostate cancer risk,[4,43–45,47] while others have found no association or some degree of protection.[48,49] Yet other clinical studies have provided further conflicting results.[46,50–52]

The lack of clear efficacy observed with antioxidant combinations for improving cancer patient outcomes may perhaps be attributed to these agents only being able to interact with ROS accumulated within the cells and having limited impact on the underlying processes that lead to ROS generation. Thus, compartmentalisation of ROS generation within the complex cell cytoplasm may be the reason that some antioxidants fail to inhibit ROS production sufficiently to provide a benefit. Supporting this hypothesis is the finding that ROS production rather than accumulation plays an important role in the aggressive phenotypic behaviour of cancer cells.[53]

Consequently, as well as studies where antioxidants are used for broad-spectrum protection in some diseases, alternative approaches using these species are increasingly being explored for a number of diseases including cancer and metabolic disease. Malignant cancer cells are under intrinsic oxidative stress, and there is evidence from studies with 3D cell cultures that the central region of the cancer sphere is hypoxic. Recognising this, an alternative approach can be to actually impose a degree of additional oxidative stress, rather than attempt to protect all cells using antioxidants. This approach would specifically induce toxicity to already stressed cancer cells. By increasing ROS levels to a point that overwhelms the antioxidant capacity,[54–56] irreversible oxidative damage could be induced that leads to apoptosis. Indeed, increased formation of ROS has been shown to contribute to the antitumour effects of radiotherapy and is in part responsible for the cytotoxicity of many chemotherapeutic agents.[57] Exploiting the metabolic differences between cancer cells and normal cells therefore represents a potential therapeutic strategy to

selectively kill cancer cells. Nitroxides deliver unique capability in this regard, as apart from rapidly scavenging reactive free radicals and acting as superoxide dismutase mimics capable of reducing superoxide radical anion to hydrogen peroxide,[58,59] their unusual chemistry also allows for both oxidation or reduction to be achieved under appropriate physiological conditions. Despite being recognised and having an established role as antioxidants, the overall metabolic fate of nitroxides in cells and tissues is chemical reduction to the corresponding hydroxylamine. Introduction of nitroxides therefore leads to oxidation of the cellular components that produce this reduction. Accordingly, if delivered in the right context nitroxides might be used to deliver an additional, mild, oxidative insult to the cell.

One recent study that exploits this approach is the combination use of TEMPOL with the chemotherapeutic drug cisplatin, which when used in conjunction proved to be effective in inducing apoptosis in ovarian cancer cells.[60] Furthermore, a third means by which nitroxides can impact on diseases and disorders is thorough interference with kinases[61] and signalling cascades driven by redox-active agents. Nitroxides, for instance, can access alternative chemo-preventative pathways unavailable to the more standard antioxidants employed in the large-scale clinical trials described above. One example of the established impacts of nitroxides in this context is their interaction with known tumour suppressor genes such as p53.[62]

The broader impact of nitroxides outside of direct antioxidant action and radical scavenging has clear consequences in physiological processes and diseases outside of cancer, including most notably the process of inflammation.

12.3 The Role of Nitroxides in Moderating Inflammation and Diseases Involving Inflammation Including Heart Disease

Inflammation is an important hallmark of cancer, but can also be linked to a range of other diseases and conditions including atherosclerosis, physical trauma and ischaemia. Inflammation is a protective response initiated to directly combat the primary injury, however it also serves to subsequently remove necrotic cells and tissues created during this initial response. Furthermore, inflammation also serves a third purpose to ultimately induce tissue repair in the damaged area and promote a process termed resolution. The complex balance of host tissue/cell destruction and growth triggered by inflammation intertwines these cellular responses with carcinogenesis, proliferation and migration. Consequently, inflammation can be directly linked to a number of cancers,[63,64] however inflammation, particularly chronic inflammation, is also critically important in a larger number of disorders with symptoms ranging from mild to severe, of which heart disease is arguably the most important. With heart disease, the predominant immediate treatment strategies to mitigate the acute damage of an infarct focus on rapid reperfusion as the most effective therapy to reduce the size of the infarct.

However, reperfusion itself can induce long-term cardiomyocyte damage through the recruitment of circulating pro-inflammatory cells to the site of damage, which can lead to increased tissue damage.[65,66] Acting as anti-oxidants, nitroxides have the potential to intervene in many of the processes initiated by the oxidative burst that follows reperfusion,[67–70] but their broader role in controlling inflammation in this context has received less attention.

Post-myocardial infarction-mediated inflammation in the damaged tissues coupled with reperfusion injury and dysregulated key enzymes (such as the haem enzyme, myeloperoxidase, MPO) increases the progression from heart attack to heart failure.[71–73] MPO is a critically important peroxidase enzyme present in the neutrophils generated in the inflammatory response to infection. The iron in the MPO enzyme exists natively in its ferric Fe^{3+} form. However, the reaction between ferric MPO and H_2O_2 (typically elevated in the ischaemic myocardium follow heart attack) yields the highly reactive MPO Fe^{4+} compound I.[74] MPO compound I can subsequently catalyse the oxidation of chloride, bromide or thiocyanate anions to the corresponding hypohalous acids (HOX, X = Cl-, Br- or SCN-) and the MPO compound I is reduced back to the native Fe^{3+} MPO form, thus recycling the enzyme for further redox activity. In the absence of exogenous pathogens hypohalous acids subsequently damage a wide range of biomolecules in cardiac myocytes and elicit further pro-inflammatory pathways.[75] Nitroxides have been shown to limit the formation of ROS including HOCl that damage the heart,[76] as they convert MPO compound I to the less reactive compound II form.[77–79] Nitroxides have also been shown to limit MPO-mediated inflammation caused by other agents.[80] Therefore, this class of drugs has some potential as an adjunctive therapy for heart attack where recruitment of inflammatory cells that contain MPO is a characteristic of the recovery phase.

As well as preventing MPO-catalysed oxidative damage, nitroxides also affect the activity of protein disulphide isomerase (PDI) and downregulate pro-inflammatory cytokines that otherwise attract/recruit more inflammatory cells to the site of injury.[81–84] Nitroxides can also control the release of leukocytes that occurs during inflammation and decrease endotoxin-related disease in animals.[85] Nitroxides also hold clear therapeutic potential in a range of other diseases and injuries where inflammation can be a factor, especially age-related diseases[86] and neurodegeneration,[87,88] as well as diseases of the respiratory[89,90] and digestive tracts.[91,92] In the case of neurodegenerative disorders, nitroxides can impart direct neuron protection[93] as well as through decreasing neuro-inflammation[94] but may also intervene in the nitric oxide signalling pathways activated in brain injury.[95,96] Neuroprotection in Alzheimer's disease may arise through effects on amyloid formation.[97–99] However, nitroxides are also more broadly implicated in therapies to improve neuronal mitochondrial function,[100–103] pain and neuropathy[104] and to recover from nerve damage and traumatic brain injury.[105,106]

There is also increasing attention being placed on the potential role of nitroxides in diseases of the gastrointestinal tract as they can alter bile acid

components that in turn inhibit key receptors in the intestine and lower fat production thus helping non-alcoholic fatty liver disease and other disorders of the gut,[107–110] which has implications in the treatment of inflammatory bowel disease.[111] Some of the efficacies in the gut may be interlinked with the effects nitroxides can have on biofilms, bacteria and gut microbiota.[112,113] The impact of nitroxides on biofilms[114,115] suggests nitroxides play a role mimicking and competing with nitric oxide-mediated processes.[116,117] The degree of bio-reduction and its role are yet to be established in this context, but clearly it has the potential to be an important parameter.[118]

12.4 The Metabolism of Nitroxides – Bioreduction and Regeneration

It has long been determined that in cells and tissues, nitroxides are readily reduced to their corresponding hydroxylamines through both enzymatic and non-enzymatic pathways.[119–121] The primary site of these one-electron reductions occurs at the level of ubiquinone in the mitochondrial respiratory chain.[30,122–124] However, in cells rich in ascorbate, such as erythrocytes, hepatocytes and kidney cells, ascorbate may be the principal reducing agent.[120,125–127] The low-molecular-weight antioxidant glutathione, on the other hand, contributes significantly to the reduction of nitroxides indirectly by acting as a secondary source of reducing equivalents.[26,128]

The bioreduction of nitroxides depends on a range of factors including their physicochemical properties, in particular, the nature of the ring containing the nitroxide moiety[129–131] and the lipophilicity or hydrophilicity of the nitroxide[132,133] (and the charge on the molecule[134,135]). In addition, cells under different oxygen concentrations,[133] pH[136] or having different cellular redox metabolic state may have different rates of nitroxide metabolism.

Initially, the short half-life of nitroxides[32] was seen as a limitation, as it reduces their effectiveness as antioxidants and imaging agents in biological systems. Consequently, long- term exposure to these compounds or higher concentrations of nitroxides is required to effectively inhibit tumour growth[137] and to achieve a therapeutic dose *in vivo*.[138,139] Nevertheless, because the reduction of a nitroxide to the hydroxylamine results in a loss of magnetic resonance intensity, monitoring the rate of nitroxide reduction has enabled the evaluation of cellular and tissue redox status[29,140–142] and ROS generation *in vivo*.[28] Likewise, oxidation of the hydroxylamine back to the nitroxide radical has been used for measuring intracellular ROS levels and oxygen concentration.[143,144] These approaches clearly highlight the importance of the reversible nature of nitroxide reduction – in the presence of oxygen or oxidising agents, cells can oxidise hydroxylamines back to the nitroxides.[133] Under reducing conditions however, such as those found in hypoxic tumours, re-oxidation of the hydroxylamine to the nitroxide is less efficient, resulting in increased (overall) nitroxide decay rates.[25,145] This provides a rationalisation for why treatment with nitroxides selectively protects normal tissues and not the tumour against radiation damage[146] and

rationalises the finding that nitroxide radicals provide greater radioprotection than their corresponding hydroxylamines.[147] Interestingly however, when TEMPOL hydroxylamine (Tempol-H) was administered to C3H mice, significant protection was observed against whole-body irradiation, suggesting Tempol-H is oxidised back to the active radioprotective nitroxide *in vivo*.[148] Therefore, it may be concluded that regardless of which form the nitroxide is administered in, a distribution of nitroxide radical or non-radical hydroxylamine will be achieved *in vivo*, depending on the oxygen status and the reducing equivalents available[149] and that both these species undertake some interaction with ROS.

12.5 Dual Nature of Nitroxides – Cytotoxic and Protective Anti- and Pro-oxidants

During the past decades, the protective antioxidant action of nitroxides has been established for a diverse range of oxidative damage induced at the cellular, isolated organ or systemic level, including through reperfusion injury,[150,151] mechanical trauma to the brain,[152] chemically induced gastric mucosal damage,[153] ROS,[151,154,155] ionising radiation[139,146] and chemotherapeutic drugs.[156,157]

Several mechanisms have been proposed to account for the antioxidant activity of nitroxides. Nitroxides are most widely recognised as able to detoxify oxygen metabolites[158,159] and carbon-centred radicals[160,161] catalytically through their action as SOD mimics.[162] In this regard the role of nitroxides in catalytically converting superoxide into less reactive species has been long established,[163] and the rates of this dismutation have been estimated to be at least 10^7 M^{-1} s^{-1}, depending on the pH. At high concentrations and more aggressive conditions it has also been suggested that TEMPOL, at least, can also react with human SOD1 (hSOD1) to remove ROS, but to also be consumed in the process. The enzyme hSOD1 reacts with H_2O_2 to produce carbonate radical, which in turn is thought to oxidise the enzyme to carbonylated and covalently dimerised forms. TEMPOL was shown to not inhibit hSOD1 turnover, but rather to decrease subsequent oxidation, probably by scavenging the carbonate radical produced and by recombining with hSOD1-derived radicals. As a result, TEMPOL was consumed nearly stoichiometrically with hSOD1 monomers under these conditions.[164]

By undergoing one-electron transfer reactions, nitroxides are readily reduced to hydroxylamines (reduction) or oxidised to oxoammonium cations (oxidation).[30,165] Consequently, nitroxides can afford protection either as reducing agents or as oxidants, while continuously being recycled.[166] Another example of their SOD mimetic activity is their ability to maintain transition metals at higher oxidised states, thereby pre-empting Fenton or metal-catalysed Haber–Weiss reactions that lead to the generation of free radicals and in turn damage DNA and proteins.[167,168] Moreover, nitroxides can stimulate catalase-like activity in haem proteins,[169] as well as participate in radical–radical recombination and chain-breaking reactions.

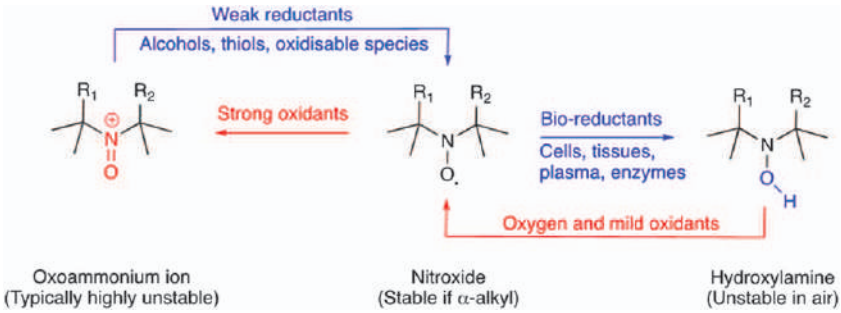

Figure 12.2 Available oxidation and reduction states of nitroxides. Redox cycling ability of nitroxides, shuttling from fully oxidised (non-stable, non-radical) oxoammonium ion to (stable radical) nitroxide and to (non-stable, non-radical) hydroxylamine. Further reduction to the secondary amine (R_2NH) is also possible *in vivo*.

Nitroxides may interact with glutathione, not directly, but following the reaction of glutathione with ROS to give more reactive glutathionyl radicals (G-S$^\bullet$). Glutathione can be present in high (milliMolar) concentrations in cells where it represents a primary antioxidant defence. However the resultant G-S$^\bullet$ radicals generated through reactions with ROS may themselves become detrimental as their concentrations build. The reaction of G-S$^\bullet$ radicals with nitroxides may explain the formation of secondary amines from nitroxides under physiological conditions (Figure 12.2).[170]

Developing a detailed understanding of the mode of action of nitroxides in biological systems is confounded by the influence of side chains, ring size and overall chemical structure, as well as by different responses to specific dose and treatment regimes.[171,172] The measured antioxidant effects of nitroxides have been shown to strongly correlate with the specific structure and rates of bio-reduction and re-oxidation. The cytotoxic effects of the TEMPO class of nitroxides towards tumour cells may be influenced by the presence or type of substituent(s) at position-4 of the piperidine ring.[173] There have also been differences in the levels of radioprotection and *in vivo* distribution demonstrated among 3-substituted pyrrolidine-*N*-oxyls,[174] suggesting that the effect of both substituent structure and ring size impacts on nitroxide potency.

Surprisingly, and depending on the specific nitroxide employed, the concentration employed can also be a major factor, with bell-shaped dose–response curves frequently generated.[175] At lower concentrations for instance, TEMPOL protected the proteolytic enzyme papain from oxidative inactivation induced by xanthine/xanthine oxidase, however this protection was lost at higher concentrations.[175] Similarly, TEMPOL at relatively low concentrations (5–50 μM) protected against metal-induced cyto- and geno-toxicity in human lymphocytes,[176] although at higher concentrations (100–1000 μM and above), it induced adverse effects on the cells (Figure 12.3).[177,178]

One drug that has been investigated at therapeutically relevant (nM to μM) concentrations is HO-3867, a compound which combines a curcumin

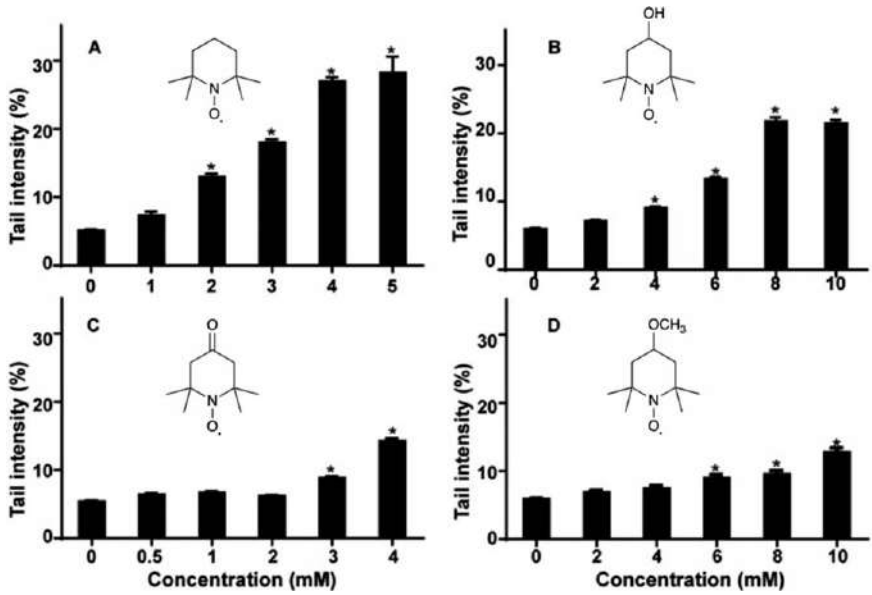

Figure 12.3 High concentration of TEMPO and derivatives cause DNA-strand breaks in mouse lymphoma cells. DNA strand breaks induced by nitroxides as detected using the Comet assay. (A) TEMPO; (B) 4-hydroxy-TEMPO; (C) 4-oxo-TEMPO; (D) 4-methoxy-TEMPO.
Reproduced from ref. 177 with permission from Oxford University Press, Copyright 2018.

analogue with a pyrroline nitroxide precursor.[179] Exploiting the severely hypoxic environment present in the fibrotic tumours of pancreatic cancer, the hydroxylamine of HO-3867 is not readily converted to the nitroxide by oxygen and oxidising conditions, thereby allowing the curcumin pharmacophore to induce reducing environment-specific toxicity. Similar tumour-specific toxicity has been seen with ovarian cancers, however for pancreatic cancer these authors attribute the efficacy to redox-derived impacts on Signal Transducer and Activator of Transcription (STAT3) signalling. STAT3 is constitutively active in human pancreatic cancer and is associated with poor prognosis (Figure 12.4).[180]

Potent side pharmacophores and redox cycling are clearly important, but seemingly not essential, factors to deliver differentiated therapeutic responses. For instance, despite their close structural similarity, the nitroxides TEMPOL and TEMPO can deliver different mechanisms of action at the molecular level, as evidenced by the induction of divergent signal transduction pathways in MDA-MB 231 breast cancer cells.[181] TEMPOL stimulated extracellular signal-regulated kinase 1 activity, whereas an equimolar albeit high (10 mM) concentration of TEMPO induced ceramide generation, stress-activated protein kinase activation and ultimately stimulated apoptotic cell death pathways. The ability of these nitroxides to elicit distinct

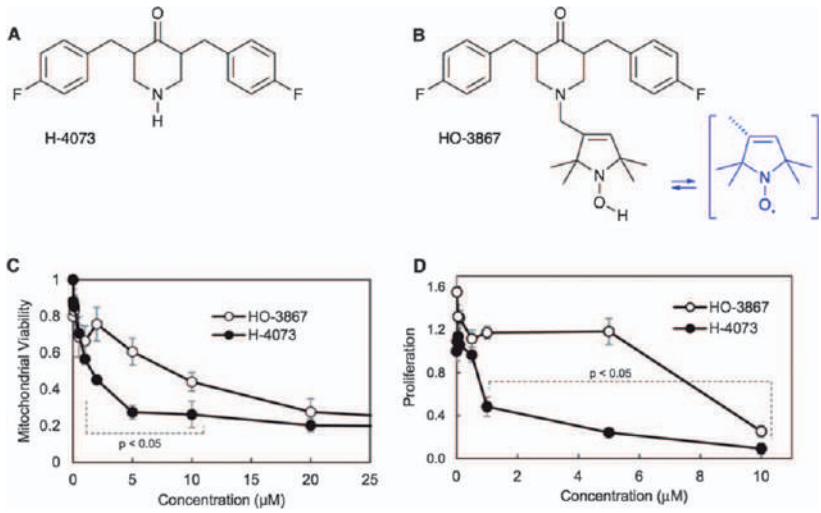

Figure 12.4 The effect on mitochondrial viability, proliferation and colony-forming ability of AsPC-1 cells exposed to a nitroxide derived from the reduced hydroxylamine analogue. (A) Molecular structure of H-4073. (B) Molecular structure of HO-3867, with a *N*-hydroxypyrroline group attached to the *N*-terminal of piperidone. (C) Mitochondrial viability data (mean ± SD; $N = 5$) obtained from AsPC-1 cells treated with the compounds in the concentration range 0–20 μM for 24 h. (D) Cell proliferation data (mean ± SD; $N = 3$) obtained from AsPC-1 cells treated with the compounds in the concentration range 0–10 μM for 24 h.
Reproduced from ref. 180 with permission from Springer Nature, Copyright 2019.

signalling pathways in the absence of environmental oxidative stress is perhaps triggered by secondary radicals and ROS associated with cellular metabolism, and differentially regulated by early events, such as the control of protein tyrosine phosphorylation and the generation of ceramide. The localisation of TEMPOL and TEMPO within different subcellular compartments could be a contributing factor to these results. Although both nitroxides readily cross the cell membrane, the more lipophilic nature of TEMPO compared to TEMPOL leads to its greater accumulation in the cell membrane. In contrast, TEMPOL, being more water soluble, is more broadly dispersed throughout the cell. Furthermore, this nitroxide has been shown to stimulate the expression of the urokinase receptor protein UPAR, which has both physiological and pathophysiological roles, and to reduce superoxide levels in human prostate cancer cells.[182]

12.6 The Role of Nitroxides in Cancer and Related Diseases *In Vitro* and *In Vivo*

The interlinked roles of nitroxide structure and dose have been demonstrated in cancer, but are also evident with other cancer-related diseases

both *in vitro* and *in vivo*. TEMPOL represses levels of hypoxia-inducible factor-2α (HIF2α) in mouse models of Chuvash polycythaemia and has potential as a therapeutic for altitude sickness in non-adapted individuals.[183] The significance of this reaction may be wide ranging as this transcription factor activates a number of downstream molecular pathways that have been linked to the growth of cancers, such as angiogenesis. The chemopreventative effects of TEMPOL have been demonstrated in C3H mice prone to age-related spontaneous tumour incidence[184] and mice with Faconi anaemia.[185] Chemical modification of nitroxides to enhance specific organelle targeting has been used as a strategy to enhance nitroxide bioactivity. For example, when a mitochondrially targeted nitroxide was used[185] the efficacy towards Faconi anaemia was shown to arise through repression of the transforming growth factor cytokine TGF-β. A mitochondrially targeted nitroxide improves the symptoms of a mouse model of Huntington's disease,[186] which is significant as there is currently no effective therapeutic intervention for this progressively debilitating disease.

Another disease with progressively debilitating symptoms, that involves both carcinogenesis and neuronal damage and in which nitroxides have shown promise, is ataxia telangiectasia (A-T), an autosomal recessive disorder characterised by a pleiotropic phenotype. The neurodegenerative phenotype in this disease has been proposed to arise as a consequence of oxidative stress due to observations of significantly reduced total antioxidant capacity in A-T patients[187] and increased levels of oxidative stress both in A-T cells[188] and in the cerebellum of *Atm*-deficient mice.[189,190]

Treatment with TEMPOL has been shown to extend the life-span of *Atm* mutant mice by increasing latency to tumorigenesis, which was associated with a reduction in oxidative stress and damage.[191] However much more potent effects were observed with a different nitroxide, the aryl-fused ring isoindoline-based nitroxide (CTMIO; see Figure 12.5), particularly in regards to neuroprotection. Purkinje neurons from *Atm*-deficient mice demonstrate poor survival and markedly reduced dendritic branching and elongation in culture compared to cells from their wild-type littermates.[192] Remarkably,

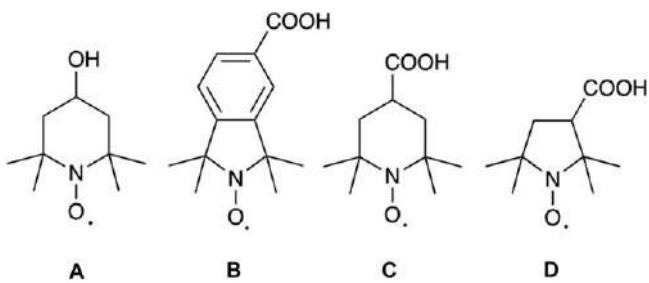

Figure 12.5 The structure of four nitroxides that have shown impact on the disease ataxia telangiectasia. See ref. 191, 193 and 195. (A) TEMPOL; (B) CTMIO (CarboxyTMIO); (C) TEMPO (CarboxyTEMPO); (D) CPROXYL (CarboxyPROXYL).

treatment with the nitroxide CTMIO protected against Purkinje cell death *in vitro* and enhanced dendritogenesis back to wild-type levels. Likewise, administration of this nitroxide antioxidant throughout pregnancy improved the survival of Purkinje cells from Atm-mutant offspring, and reduced oxidative stress and damage in the cerebellum of older animals, as evidenced by an increase in catalase activity and reduced levels of nitrotyrosine.[192] CTMIO also corrected for the neuro-behavioural abnormalities observed in Atm-deficient mice.[193]

The predisposition of A-T patients to lymphoid tumours is recapitulated in *Atm*-disrupted mice, with almost all animals succumbing to thymic lymphomas within five months of birth.[194] CTMIO dramatically increased the longevity of *Atm*-deficient mice by delaying the onset of thymic lymphomas, although this did not appear to be *via* a mechanism involving the induction of apoptosis.[193] Notably, the extent of tumour protection exhibited by CTMIO was much greater than that previously observed with TEMPOL[191] and the salen-manganese antioxidant EUK-189.[190] The effectiveness of the nitroxide CTMIO in protecting against tumour development was further substantiated by its lack of toxicity and efficacy at micromolar doses. Promising results were also reported in another study where A-T cells that were pre-incubated with CTMIO and other carboxy nitroxides had greater survival rates post-irradiation and presented fewer chromosomal aberrations compared to untreated cells.[195] In contrast, the antioxidant vitamin E and its water-soluble analogue Trolox had little impact on the survival of irradiated A-T cells, suggesting differences in the mechanism of antioxidant action of nitroxides[196] compared to vitamin E.[197]

Alternatively, nitroxides may indirectly cause damage to biomolecules by generating other ROS while performing SOD mimetic[167] and complex 1-inhibiting actions.[198,199] Increases in intracellular oxidative stress arising from treatment with relatively high doses of nitroxides led to the impairment of oxidative phosphorylation and were accompanied by glutathione depletion and a decrease in mitochondrial membrane potential. These changes resulted in the induction of apoptosis in the HL60 human leukaemia cell line.[199] Such a mechanism of action is of interest given that mitochondrial events play a crucial role in the apoptotic process. By-passing activation of the p53 pathway, which is a major pathway in DNA damage-induced apoptosis, could be beneficial if nitroxides were to act primarily on the mitochondrion to elicit the intrinsic pathway of apoptosis. This could potentially explain the dose-dependent increase in $p21^{WAF1/CIP1}$ levels in C6 glioma cells even in the absence of detectable p53 protein, following exposure to Tempol.[137] Furthermore, TEMPO and a related analogue, 4-ferrocenecarboxyl-TEMPO, have been shown to inhibit cancer cell viability through activation of caspase 3, a key player in the mitochondrial-related intrinsic apoptotic pathway, providing further evidence that nitroxide-induced cell death can occur through mitochondrial-mediated events.[138,200] Besides activation of potent cell death effectors, TEMPO treatment is also known to induce cell cycle arrest, decrease cell proliferation and increase ceramide levels, which

in turn enhances oxidative damage.[137,138] TEMPO has also been shown to induce oxidative stress[201] and at high doses activates the critically important c-Jun *N*-terminal kinase (JNK), which regulates key mitogen-activated protein kinase (MAPK)-signalling pathways linked to toxicity.[202] Thus, it appears that under specific conditions TEMPO at least can induce multifactorial cell death responses involving oxidative stress.

More importantly, the antitumour activity of TEMPO has also been observed *in vivo*, where it is effective against both hormone-responsive and hormone-refractory prostate cancer xenografts grown in athymic mice.[138] In addition to this, nitroxides can act as chemosensitisers to enhance the cytotoxic effects of chemotherapeutic agents, such as cisplatin, mitoxantrone and doxorubicin, in cancer cells.[138,203,204]

The results described above indicate that nitroxides not only exert antioxidant activity in protecting biological systems against diverse oxidative insults, but are also capable of inducing cytotoxicity depending on their specific microenvironment, treatment dose and exposure times. Nitroxides that activate apoptotic pathways by modulating the intracellular redox state therefore represent attractive candidates as leads for new chemotherapeutic agents, particularly if cell death occurs *via* p53-independent mechanisms, since many tumours lack functional p53. Furthermore, their efficacy in late stage cancer, *e.g.*, in breast cancer cells exhibiting loss of hormone receptors, together with their ability to selectively kill tumour cells *versus* normal cells and sensitise cancer cells to chemotherapeutic drugs, confer significant potential for clinical application. A common theme underpinning many of the effects of nitroxides is their influence on mitochondrial chemistry, and this is becoming an increasingly important focus of attention in the development of nitroxides as biologically active agents.

12.7 The Role of Nitroxides in Mitochondrial Chemistry and Cell Signalling and the Impact on Disease

The mitochondrion is such an integral part of cellular function that any dysfunction leads to significant and wide-ranging health impacts. Many diseases, including Alzheimer's disease, muscular dystrophy, Lou Gehrig's disease, diabetes and cancer, involve poorly functioning mitochondria. There are also a group of genetically linked disorders broadly categorised under the term "mitochondrial disease" where insufficient energy production from the mitochondria can impact virtually any of the body's organs and tissues, although the conditions are worst with cells with the highest energy demands such as muscle, brain and nerve cells. Mitochondrial complex 1 deficiency disorders, for example, represent a group of such diseases where poorly functioning mitochondrial complex 1 (arising from nuclear or mitochondrial DNA mutations) has been identified as the most common defect in childhood-onset mitochondrial OXPHOS disorders such as Leber hereditary optic neuropathy

(LHON), Kearns-Sayre syndrome and Leigh disease amongst others. Currently there are no effective therapeutic interventions to combat the pathology of mitochondrial disease. However, a recent result with a mitochondrially targeted nitroxide[205] demonstrated the value of decreasing superoxide production within the organelle, as this leads to enhanced mitochondrial bio-energetics and therefore suggests a potential therapeutic approach (Figure 12.6).

Mitochondrial metabolism is also a crucial element in cancer development, progression and metastasis. Targeting the more negative membrane potentials of cancer cell mitochondria represents an attractive chemotherapeutic approach and in this context, interfering with energy metabolism with mitochondrially targeted nitroxides has recently been shown to induce mitophagy in colon cancer.[206] The use of phosphonium ion-linked nitroxides as well as other nitroxides with mitochondrially targeting chemistries opens up a new field of control and influence on signalling pathways regulated by ROS as well as a number of other important biochemical processes. Compounds targeted to the mitochondria can induce antiproliferative and cytotoxic effects in tumour cells without a significant impact on the surrounding normal cells.[207,208] This approach has also proven to be effective in skin cancer and melanoma,[209–211] as well as Alzheimer's disease[212] and other conditions affecting the central nervous system;[213] as well as diseases related to fatty acid metabolism[214] and radiation treatments.[215–218]

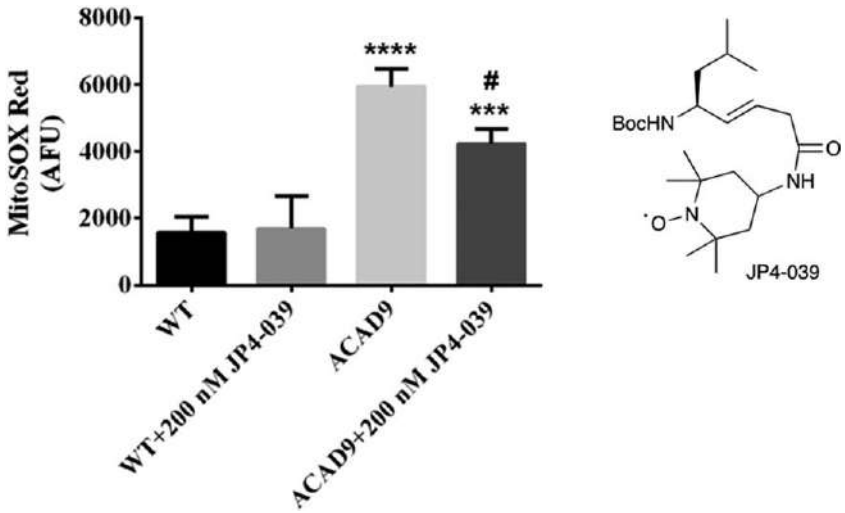

Figure 12.6 The effect of a mitochondrially targeted nitroxide on superoxide production. The effect of 200 nM mitochondrially targeted nitroxide JP4-039 on superoxide production as measured through response to a MitoSox Red assay over 24 hours for fibroblasts deficient in a protein related to complex 1 deficiency.
Reproduced from ref. 205, https://doi.org/10.1038/s41598-018-19543-3, under the terms of the CC BY 4.0 license, http://creativecommons.org/licenses/by/4.0/.

In conclusion, the use of structural variation and side-chain properties to control subcellular delivery and bio-activity of nitroxides is opening up major new opportunities to exploit the antioxidant and redox activity of nitroxides for therapeutic advantage in a wide range of human disorders. Targeted localisation, coupled with new approaches to moderate nitroxide reduction rates as well as control oxidation chemistry, promises to deliver new understanding and influence over the key enzymatic and biochemical processes underpinning a broad range of important diseases.

References

1. B. Commoner, J. Townsend and G. E. Pake, Free Radicals in Biological Materials, *Nature*, 1954, **174**, 689–691.
2. H. M. Lander, An Essential Role for Free Radicals and Derived Species in Signal Transduction, *FASEB J.*, 1997, **11**, 118–124.
3. T. Finkel and N. J. Holbrook, Oxidants, Oxidative Stress and the Biology of Ageing, *Nature*, 2000, **408**, 239–247.
4. S. P. Hussain, L. J. Hofseth and C. C. Harris, Radical Causes of Cancer, *Nat. Rev. Cancer*, 2003, **3**, 276–285.
5. B. J. Gaffney, The Stability of the Paramagnetic Nitroxide Group, in *Spin labelling Theory and Applications*, ed. L. J. Berliner, New York, Academic Press, ch. 5, 1976, pp. 183–238.
6. S. M. Hahn, L. Wilson, C. M. Krishna, J. Liebmann, W. DeGraff, J. Gamson, A. Samuni, D. Venzon and J. B. Mitchell, Identification of Nitroxide Radioprotectors, *Radiat. Res.*, 1992, **132**(1), 87–93.
7. O. L. Lebedev and S. N. Kazarnovskii, Intermediate Oxidation Products of Amines by Tungstate, *Tr. Khim. Khim. Tekhnol.*, 1959, **2**, 649–665.
8. M. B. Neiman, E. G. Rosantsez and Y. G. Mamedova, Free Radical Reactions Involving No Unpaired Electrons, *Nature*, 1962, **196**, 472–474.
9. A. K. Hoffmann and A. T. Henderson, A New Stable Free Radical: Di-t-ButylNitroxide, *J. Am. Chem. Soc.*, 1961, **83**, 4671–4672.
10. G. Moad and E. Rizzardo, Alkoxyamine-Initiated Living Radical Polymerization: Factors Affecting Alkoxyamine Homolysis Rates, *Macromolecules*, 1995, **28**(26), 8722–8728.
11. O. G. Ballesteros, L. Maretti, R. Sastre and J. C. Scaiano, Kinetics of Cap Separation in Nitroxide-Regulated ''Living'' Free Radical Polymerization: Application of a Novel Methodology Involving a Profluorescent Nitroxide Switch, *Macromolecules*, 2001, **34**(18), 6184–6187.
12. C. Coenjarts, O. Garcia, L. Llauger, J. Palfreyman, A. L. Vinette and J. C. Scaiano, Mapping Photogenerated Radicals in Thin Polymer Films: Fluorescence Imaging Using a Profluorescent Radical Probe, Coenjarts, *J. Am. Chem. Soc.*, 2003, **125**(3), 620–621.
13. M. A. Sowers, J. R. McCombs, Y. Wang, J. T. Paletta, S. W. Morton, E. C. Dreaden, M. D. Boska, M. F. Ottaviani, P. T. Hammond, A. Rajca and J. A. Johnson, Redox-responsive Branched-bottlebrush Polymers for in vivo MRI and Fluorescence Imaging, *Nat. Commun.*, 2014, **5**, 5460–5465.

14. H. M. Swartz, Interaction Between Cells and Nitroxides and their Implications for their Uses as Biophysical Probes and as Metabolically Responsive Contrast Agents for In Vivo NMR, *J. Magn. Reson.*, 1986, **8**, 172–175.
15. P. D. Morse and H. M. Swartz, Measurement of Intracellular Oxygen Concentration Using the Spin Label TEMPO, *Magn. Reson. Med.*, 1985, **2**, 114–127.
16. H. Hu, G. Sosnovsky and H. M. Swartz, Simultaneous Measurements of the Intra- and Extra-cellular Oxygen Concentration in Viable Cells, *Biochim. Biophys. Acta, Biomembr.*, 1992, **1112**(2), 161–166.
17. J. F. Glockner, S. W. Norby and H. M. Swartz, Simultaneous Measurement of Intracellular and Extracellular Oxygen Concentrations Using a Nitroxide-Liposome System, *Magn. Reson. Med.*, 1993, **29**(1), 12–18.
18. C.-S. Lai, L. E. Hopwood and H. M. Swartz, ESR Studies on Membrane Fluidity of Chinese Hamster Ovary Cells Grown on Microcarriers and in Suspension, *Exp. Cell Res.*, 1980, **130**(2), 437–442.
19. M. R. Edgcomb, S. Sirimanne, B. J. Wilkinson, P. Drouin and R. Morse, Electron Paramagnetic Resonance Studies of the Membrane Fluidity of the Foodborne Pathogenic Psychrotroph Listeria Monocytogenes, *Biochim. Biophys. Acta, Biomembr.*, 2000, **1463**(1), 31–42.
20. B. Gallez, K. Mader and H. M. Swartz, Noninvasive Measurement of the pH inside the Gut by Using pH-Sensitive Nitroxides. An In Vivo EPR Study, *Magn. Reson. Med.*, 1996, **36**(5), 694–697.
21. J. J. Eckburg, J. C. Chato, K. J. Liu, M. W. Grinstaff, H. M. Swartz, K. S. Suslick and F. P. Auteri, The Measurement of Temperature with Electron Paramagnetic Resonance Spectroscopy, *J. Biomech. Eng.*, 1996, **118**(2), 193–200, DOI: 10.1115/1.2795959.
22. P. J. Spooner, L. M. Veenhoff, A. Watts and B. Poolman, Structural Information on a Membrane Transport Protein from Nuclear Magnetic Resonance Spectroscopy Using Sequence-Selective Nitroxide Labelling, *Biochemistry*, 1999, **38**(30), 9634–9639.
23. A. T. Yordanov, K.-I. Yamada, M. C. Krishna, A. Russo, J. Yoo, S. English, J. B. Mitchell and M. W. Brechbiel, Acyl-Protected Hydroxylamines as Spin Label Generators for EPR Brain Imaging, *J. Med. Chem.*, 2002, **45**(11), 2283–2288.
24. L. J. Berliner and X. Wan, In Vivo Pharmacokinetics by Electron Magnetic Resonance Spectroscopy, *Magn. Reson. Med.*, 1989, **9**(3), 430–434.
25. G. Ilangovan, H. Li, J. L. Zweier and P. Kuppusamy, In Vivo Measurement of Tumor Redox Environment using EPR Spectroscopy, *Mol. Cell. Biochem.*, 2002, **234**(1), 393–398.
26. P. Kuppusamy, H. Li, G. Ilangovan, A. J. Cardounel, J. L. Zweier, K. Yamada, M. C. Krishna and J. B. Mitchell, Noninvasive Imaging of Tumor Redox Status and its Modification by Tissue Glutathione Levels, *Cancer Res.*, 2002, **62**(1), 307–313.
27. K. I. Yamada, P. Kuppusamy, S. English, J. Yoo, A. Irie, S. Subramanian, J. B. Mitchell and M. C. Krishna, Feasibility and Assessment of Non

Invasive In Vivo Redox Status using Electron Paramagnetic Resonance Imaging, *Acta Radiol.*, 2002, **43**(4), 433–440.
28. K. Kasazaki, K. Yasukawa, H. Sano and H. Utsumi, Non-Invasive Analysis of Reactive Oxygen Species Generated in NH4OH-Induced Gastric Lesions of Rats Using a 300 MHz In Vivo ESR Technique, *Free Radical Res.*, 2003, **37**(7), 757–766.
29. F. Hyodo, K.-I. Matsumoto, A. Matsumoto, J. B. Mitchell and M. C. Krishna, Probing the Intracellular Redox Status of Tumors with Magnetic Resonance Imaging and Redox-Sensitive Contrast Agents, *Cancer Res.*, 2006, **66**(20), 9921–9928.
30. H. M. Swartz, Principles of the Metabolism of Nitroxides and their Implications for Spin Trapping, *Free Radical Res.*, 1990, **9**(3–6), 399–405.
31. X. Wan, T.-C. Fu, A. Funk and R. E. London, Differential Clearance of Nitroxide MRI Contrast Agents from Rat Cerebral Ventricles, *Brain Res. Bull.*, 1995, **36**(1), 91–96.
32. A. M. Komarov, J. Joseph and C.-S. Lai, In Vivo Pharmacokinetics of Nitroxides in Mice, *Biochem. Biophys. Res. Commun.*, 1994, **201**(2), 1035–1042.
33. T. Kajer, K. Fairfull-Smith, T. Yamasaki, K. Yamada, S. E. Bottle and M. J. Davies, *et al.*, Inhibition of Neutrophil-Mediated Oxidants by Tetraethyl/Tetramethyl Nitroxides, *Free Radicals Biol. Med.*, 2014, **70**, 96–105.
34. N. E. Fleshner and L. H. Klotz, Diet, Androgens, Oxidative Stress and Prostate Cancer Susceptibility, *Cancer Metastasis Rev.*, 1998, **17**(4), 325–330.
35. O. P. Heinonen, L. Koss, D. Albanes, P. R. Taylor, A. M. Hartman, B. K. Edwards, J. Virtamo, J. K. Huttunen, J. Haapakoski and N. Malila, Prostate Cancer and Supplementation with α-Tocopherol and β-Carotene: Incidence and Mortality in a Controlled Trial, *J. Natl. Cancer Inst.*, 1998, **90**(6), 440–442.
36. J. K. Gohagan, P. C. Prorok, R. B. Hayes and B.-S. Kramer, The Prostate, Lung, Colorectal and Ovarian (PLCO) Cancer Screening Trial of the National Cancer Institute: History, Organization and Status, *Controlled Clin. Trials*, 2000, **21**(6), 251S–272S.
37. E. Lonn, J. Bosch, S. Yusuf, P. Sheridan, J. Pogue, J. Arnold, C. Ross, A. Arnold, P. Sleight and J. Probstfield, Effects of Long-Term Vitamin E Supplementation on Cardiovascular Events and Cancer: A Randomized Controlled Trial, *JAMA, J. Am. Med. Assoc.*, 2005, **293**(11), 1338–1347.
38. V. A. Kirsh, R. Z. Hayes, S. T. Mayne, N. Chatterjee, A. F. Subar, L. B. Dixon, D. Albanes, G. L. Andriole, D. A. Urban and U. Peters, Supplemental and Dietary Vitamin E, β-Carotene and Vitamin C Intakes and Prostate Cancer Risk, *J. Natl. Cancer Inst.*, 2006, **98**(4), 245–254.
39. S. M. Lippman, E. A. Klein, P. J. Goodman, M. S. Lucia, I. M. Thompson, L. G. Ford, H. L. Parnes, L. M. Minasian, J. M. Gaziano and J. A. Hartline, Effect of Selenium and Vitamin E on Risk of Prostate

Cancer and Other Cancers: The Selenium and Vitamin E Cancer Prevention Trial (SELECT), *JAMA, J. Am. Med. Assoc.*, 2009, **301**(1), 39–51.
40. C. H. Hennekens, J. E. Buring, J. E. Manson, M. Stampfer, B. Rosner, N. R. Cook, C. Belanger, F. LaMotte, J. M. Gaziano and P. M. Ridker, Lack of Effect of Long-Term Supplementation with Beta Carotene on the Incidence of Malignant Neoplasms and Cardiovascular Disease, *N. Engl. J. Med.*, 1996, **334**(18), 1145–1149.
41. G. S. Omenn, G. E. Goodman, M. D. Thornquist, J. Balmes, M. R. Cullen, A. Glass, J. P. Keogh, F. L. Meyskens, B. Valanis and J. H. Williams, Risk Factors for Lung Cancer and for Intervention Effects in CARET, the Beta- Carotene and Retinol Efficacy Trial, *J. Natl. Cancer Inst.*, 1996, **88**(21), 1550–1559.
42. E. A. Klein, I. M. Thompson, C. M. Tangen, J. J. Crowley, M. S. Lucia, P. J. Goodman, L. M. Minasian, L. G. Ford, H. L. Parnes and J. M. Gaziano, Vitamin E And The Risk Of Prostate Cancer: The Selenium And Vitamin E Cancer Prevention Trial (SELECT), *JAMA, J. Am. Med. Assoc.*, 2011, **306**(14), 1549–1556.
43. S. Graham, B. Haughey, J. Marshall, R. Priore, T. Byers, T. Rzepka, C. Mettlin and J. E. Pontes, Diet in the Epidemiology of Carcinoma of the Prostate Gland, *J. Natl. Cancer Inst.*, 1983, **70**(4), 687–692.
44. M. Y. Heshmat, L. Kaul, J. Kovi, M. A. Jackson, A. G. Jackson, G. W. Jones, M. Edson, J. P. Enterline, R. G. Worrell and S. L. Perry, Nutrition and Prostate Cancer: A Case-Control Study, *Prostate*, 1985, **6**(1), 7–17.
45. L. N. Kolonel, C. N. Yoshizawa and J. H. Hankin, Diet and Prostatic Cancer: A Case-Control Study in Hawaii, *Am. J. Epidemiol.*, 1988, **127**(5), 999–1012.
46. D. W. West, M. L. Slattery, L. M. Robison, T. K. French and A. W. Mahoney, Adult Dietary Intake and Prostate Cancer Risk in Utah: A Case-Control Study with Special Emphasis on Aggressive Tumors, *Cancer, Causes Control*, 1991, **2**(2), 85–94.
47. R. Talamini, S. Franceschi, C. La Vecchia, D. Serraino, S. Barra and E. Negri, Diet and Prostatic Cancer: A Case-Control Study in Northern Italy, *Nutr. Cancer*, 1992, **18**(3), 277–286.
48. Y. Ohno, O. Yoshida, K. Oishi, K. Okada, H. Yamabe and F. H. Schroeder, Dietary -Carotene and Cancer of the Prostate: A Case-Control Study in Kyoto, Japan, *Cancer Res.*, 1988, **48**(5), 1331–1336.
49. C. Mettlin, S. Selenskas, N. Natarajan and R. Huben, Beta-Carotene and Animal Fats and their Relationship to Prostate Cancer Risk. A Case—Control Study, *Cancer*, 1989, **64**(3), 605–612.
50. A. Paganini-Hill, A. Chao, R. K. Ross and B. E. Henderson, Vitamin A, - Carotene and the Risk of Cancer: A Prospective Study, *J. Natl. Cancer Inst.*, 1987, **79**(3), 443–448.
51. A. W. Hsing, J. K. McLaughlin, L. M. Schuman, E. Bjelke, G. Gridley, S. Wacholder, H. T. C. Chien and W. J. Blot, Diet, Tobacco Use, and Fatal Prostate Cancer: Results from the Lutheran Brotherhood Cohort Study, *Cancer Res.*, 1990, **50**(21), 6836–6840.

52. M. L. Daviglus, A. R. Dyer, V. Persky, N. Chavez, M. Drum, J. Goldberg, K. Liu, D. K. Morris, R. B. Shekelle and Stamler, Dietary Beta-Carotene, Vitamin C, and Risk of Prostate Cancer: Results from the Western Electric Study, *J. Epidemiol.*, 1996, **7**(5), 472–477.
53. L. Khandrika, B. Kumar, S. Koul, P. Maroni and H. K. Koul, Oxidative Stress in Prostate Cancer, *Cancer Lett.*, 2009, **282**(2), 125–136.
54. Q. Kong, J. Beel and K. Lillehei, A Threshold Concept for Cancer Therapy, *Med. Hypotheses*, 2000, **55**(1), 29–35.
55. Y. Zhou, E. O. Hileman, W. Plunkett, M. J. Keating and P. Huang, Free Radical Stress in Chronic Lymphocytic Leukemia Cells and its Role in Cellular Sensitivity to ROS-Generating Anticancer Agents, *Blood*, 2003, **101**(10), 4098–4104.
56. H. Pelicano, D. Carney and P. Huang, ROS Stress in Cancer Cells and Therapeutic Implications, *Drug Resist. Updates*, 2004, **7**(2), 97–110.
57. B. Halliwell, Oxidative Stress and Cancer: Have We Moved Forward? *Biochem. J.*, 2007, **401**, 1–11.
58. I. Batinic-Haberle, J. S. Reboucas and I. Spasojevic, Superoxide Dismutase Mimics: Chemistry, Pharmacology, and Therapeutic Potential, *Antioxid. Redox Signaling*, 2010, **13**(6), 877–918.
59. A. Dhanasekaran, S. Kotamraju, C. Karunakaran, S. V. Kalivendi, S. Thomas, J. Joseph and B. Kalyanaraman, Mitochondria Superoxide Dismutase Mimetic Inhibits Peroxide-Induced Oxidative Damage and Apoptosis: Role of Mitochondrial Superoxide, *Free Radical Biol. Med.*, 2005, **39**(5), 567–583.
60. M. Wang, K. Li, Z. Zou, L. Li, L. Zhu, Q. Wang, W. Gao, Y. Wang, W. Huang, R. Liu, K. Yao and Q. Liu, Piperidine Nitroxide TEMPOL Enhances Cisplatin-Induced Apoptosis in Ovarian Cancer Cells, *Oncol. Lett.*, 2018, **16**, 4847–4854.
61. G. B. Santos, A. C. Ribeiro, S. N. Lima, A. Trostchansky, C. D. Cerdeira and M. R. Brigagao, Nitroxide TEMPOL Down-Regulates Kinase Activities Associated with NADPH Oxidase Function in Phagocytic Cells and Potentially Decreases their Fungicidal Response, *Chem.-Biol. Interact.*, 2018, **279**, 203–209.
62. L. Erker, R. Schubert, H. Yakushiji, C. Barlow, D. Larson, J. B. Mitchell and A. Wynshaw-Boris, Cancer Chemoprevention by the Antioxidant TEMPOL acts partially via the P53 Tumor Suppressor, *Hum. Mol. Genet.*, 2005, **14**(12), 1699–1708.
63. A. Mantovani, P. Allavena, A. Sica and F. Balkwill, Cancer-related Inflammation, *Nature*, 2008, **454**(7203), 436–444.
64. S. Kawanishi, S. Ohnishi, N. Ma, Y. Hiraku and M. Murata, Crosstalk between DNA Damage and Inflammation in the Multiple Steps of Carcinogenesis, *Int. J. Mol. Sci.*, 2017, **18**(8), 1808.
65. B. R. Slegtenhorst, F. J. Dor, H. Rodriguez, F. J. Voskuil and S. G. Tullius, Ischemia/reperfusion Injury and its Consequences on Immunity and Inflammation, *Curr. Transplant. Rep.*, 2014, **1**(3), 147–154.

66. A. Gregg, S. E. Bottle, S. M. Devine, H. Figler, J. Linden, P. White, C. W. Pouton, V. Urmaliya and P. J. Scammells, Dual Acting Antioxidant A1 Adenosine Receptor Agonists, *Bioorg. Med. Chem. Lett.*, 2007, **17**(19), 5437–5441.
67. W. Bi, Y. Bi, P. Li, S. Hou, X. Yan, C. Hensley, Y. Zhang, S. Jockusch, T. D. Legalley, K. M. Gibson and L. Lanrong Bi, Cardioprotection Effects of LPTC-5 Involve Mitochondrial Protection and Dynamics, *ACS Omega*, 2019, **46**, 9868–9877.
68. N. E. Hausler, S. M. Devine, F. M. McRobb, L. Warfe, C. W. Pouton, J. M. Haynes, S. E. Bottle, P. J. White and P. J. Scammells, Synthesis and Pharmacological Evaluation of Dual Acting Antioxidant A2A Adenosine Receptor Agonists, *J. Med. Chem.*, 2012, **55**(7), 3521–3534.
69. J. R. Walker, K. E. Fairfull-Smith, K. Anzai, S. Lau, P. J. White, P. J. Scammells and S. E. Bottle, Edaravone Containing Isoindoline Nitroxides for the Potential Treatment of Cardiovascular Ischaemia, *Med. Chem. Commun.*, 2011, **2**(5), 436–441.
70. S. M. Devine, A. D. Gregg, H. Figler, K. McIntosh, V. Urmaliya, J. Linden, C. W. Pouton, P. White, S. E. Bottle and P. J. Scammells, Synthesis and Evaluation of New N6 - Substituted Adenosine-5'-*N*-Methylcarboxamides as A3 Adenosine Receptor Agonists, *Bioorg. Med. Chem.*, 2010, **18**(9), 3078–3087.
71. M. Neri, I. Riezzo, N. Pascale, C. Pomara and E. Turillazzi, Ischemia/Reperfusion Injury following Acute Myocardial Infarction: A Critical Issue for Clinicians and Forensic Pathologists, *Mediators Inflammation*, 2017, 7018393.
72. R. S. Velagaleti, M. J. Pencina, J. M. Murabito, T. J. Wang, N. I. Parikh, R. B. D'agostino, D. Levy, W. B. Kannel and R. S. Vasan, Long-term trends in the incidence of heart failure after myocardial infarction, *Circulation*, 2008, **118**, 2057–2062.
73. A. Ding, P. Kalaignanasundaram, S. D. Ricardo, A. Abdelkader, P. K. Witting, B. R. Broughton, H. B. Kim, B. F. Wyse, J. K. Phillips and R. G. Evans, Chronic Treatment with TEMPOL does not significantly Ameliorate Renal Tissue Hypoxia or Disease Progression in a Rodent Model of Polycystic Kidney Disease, *Clin. Exp. Pharmacol. Physiol.*, 2012, **39**(11), 917–929.
74. M. J. Davies, Myeloperoxidase-Derived Oxidation: Mechanisms of Biological Damage and its Prevention, *J. Clin. Biochem. Nutr.*, 2011, **48**, 8–19.
75. B. Chami, G. Jeong, A. Varda, A. M. Maw, H. B. Kim, G. M. Fong, M. Simone, B. S. Rayner, X. S. Wang, J. M. Dennis and P. K. Witting, The Nitroxide 4-methoxy TEMPO inhibits neutrophil-stimulated kinase activation in H9c2 cardiomyocytes, *Arch. Biochem. Biophys.*, 2017, **629**, 19–35.
76. X. S. Wang, H. B. Kim, A. Szuchman-Sapir, A. McMahon, J. M. Dennis and P. K. Witting, Neutrophils Recruited to the Myocardium After Acute Experimental Myocardial Infarct Generate Hypochlorous Acid that Oxidizes Cardiac Myoglobin, *Arch. Biochem. Biophys.*, 2016, **612**, 103–114.

77. M. D. Rees, S. E. Bottle, K. E. Fairfull-Smith, E. Malle, J. M. Whitelock and M. J. Davies, Inhibition of Myeloperoxidase-Mediated Hypochlorous Acid Production by Nitroxides, *Biochem. J.*, 2009, **421**, 79–86.
78. T. B. Kajer, K. E. Fairfull-Smith, T. Yamasaki, K. Yamada, S. Fu, S. E. Bottle, C. L. Hawkins and M. J. Davies, Inhibition of Myeloperoxidase- and Neutrophil-Mediated Oxidant Production by Tetraethyl and Tetramethyl Nitroxides, *Free Radical Biol. Med.*, 2014, **70**, 96–105.
79. R. F. Queiroz, S. M. Vaz and O. Augusto, Inhibition of the Chlorinating Activity of Myeloperoxidase by Tempol: Revisiting the Kinetics and Mechanisms, *Biochem. J.*, 2011, **439**(3), 423–431.
80. R. F. Queiroz, A. K. Jordao, A. C. Cunha, V. F. Ferreira, M. R. Brigagao, A. Malvezzi, A. T. Amaral and O. Augusto, Nitroxides Attenuate Carrageenan-Induced Inflammation in Rat Paws by Reducing Neutrophil Infiltration and the Resulting Myeloperoxidase-Mediated Damage, *Free Radical Biol. Med.*, 2012, **53**(10), 1942–1953.
81. C. H. J. Kim, J. B. Mitchell, C. A. Bursill, A. L. Sowers, A. Thetford, J. A. Cook, D. M. van Reyk and M. J. Davies, The Nitroxide Radical TEMPOL Prevents Obesity, Hyperlipidaemia, Elevation of Inflammatory Cytokines, and Modulates Atherosclerotic Plaque Composition in Apoe-/- Mice, *Atherosclerosis*, 2015, **240**(1), 234–241.
82. G. B. Santos, L. Gonzalez-Perilli, M. Mastrogiovanni, A. Aicardo, C. D. Cerdeira, A. Trostchansky and M. R. Brigagao, Nitroxide 4-Hydroxy-2,2,6,6-Tetramethylpiperidine-1-Oxyl (Tempol) Inhibits the Reductase Activity of Protein Disulfide Isomerase via Covalent Binding to the Cys400 Residue on CXXC Redox Motif at the A' Active Site, *Chem.-Biol. Interact.*, 2017, **272**, 117–124.
83. M. H. Tsuhako, O. Augusto, E. Linares, G. Chadi, S. Giorgio and C. A. Pereira, TEMPOL Ameliorates Murine Viral Encephalomyelitis by Preserving the Blood-Brain Barrier, Reducing Viral Load, and Lessening Inflammation, *Free Radical Biol. Med.*, 2010, **48**(5), 704–712.
84. M. M. Khattab, TEMPOL, A Membrane-Permeable Radical Scavenger, Attenuates Peroxynitrite- And Superoxide Anion-Enhanced Carrageenan-Induced Paw Edema And Hyperalgesia: A Key Role For Superoxide Anion, *Eur. J. Pharmacol.*, 2006, **548**(1–3), 167–173.
85. S. N. P. Lima, C. D. Cerdeira, G. B. Santos, M. Fernandes, M. de, A. Giusti-Paiva and M. R. Brigagao, TEMPOL Modulates The Leukocyte Response To Inflammatory Stimuli And Attenuates Endotoxin-Induced Sickness Behaviour In Mice, *Arch. Physiol. Biochem.*, 2018, DOI: 10.1080/13813455.2018.1538247. Ahead of Print.
86. J. A. Zarling, V. E. Brunt, A. K. Vallerga, W. Li, A. Tao, D. A. Zarling and C. T. Minson, Nitroxide Pharmaceutical Development for Age-Related Degeneration and Disease, *Front. Genet.*, 2015, **6**, 325/1–325/9.
87. G. J. McBean, M. G. Lopez and F. K. Wallner, Redox-Based Therapeutics in Neurodegenerative Disease, *Br. J. Pharmacol.*, 2017, **174**(12), 1750–1770.
88. P. Boonruamkaew, B. Long, S. Sakaue, Y. Tomidokoro, K. Ishii, A. Tamaoka and Y. Nagasaki, Chronic Treatment With a Smart

Antioxidative Nanoparticle for Inhibition of Amyloid Plaque Propagation in TG2576 Mouse Model of Alzheimer's Disease, *Sci. Rep.*, 2017, **7**(1), 1–13.

89. S. Goldstein, A. Samuni and Berkman, Nitroxide Radicals for the Treatment of Diseases of the Respiratory Tract Neville PCT Int. Appl., WO 2016151591 A1 20160929, 2016.
90. M. Assayag, S. Goldstein, A. Samuni and N. Berkman, Cyclic Nitroxide Radicals Attenuate Inflammation and Hyper-Responsiveness in a Mouse Model of Allergic Asthma, *Free Radical Biol. Med.*, 2015, **87**, 148–156.
91. B. Chami, N. J. J. Martin, J. M. Dennis and P. K. Witting, Myeloperoxidase in the inflamed colon: A novel target for treating inflammatory bowel disease, *Arch. Biochem. Biophys.*, 2018, **645**, 61–71.
92. B. Chami, P. T. San Gabriel, S. Kum-Jew, X. Wang, N. Dickerhof, J. M. Dennis and P. K. Witting, The Nitroxide 4-Methoxy-TEMPO Inhibits the Pathogenesis of Dextran Sodium Sulfate-Stimulated Experimental Colitis, *Redox Biol.*, 2020, e101333.
93. T. Lipman, R. Tabakman and P. Lazarovici, Neuroprotective Effects of the Stable Nitroxide Compound TEMPOL on 1-Methyl-4-Phenylpyridinium Ion-Induced Neurotoxicity in the Nerve Growth Factor-Differentiated Model of Pheochromocytoma PC12 Cells, *Eur. J. Pharmacol.*, 2006, **549**(1–3), 50–57.
94. M. H. Tsuhako, O. Augusto, E. Linares, G. Chadi, S. Giorgio and C. A. Pereira, TEMPOL Ameliorates Murine Viral Encephalomyelitis by Preserving the Blood-Brain Barrier, Reducing Viral Load, and Lessening Inflammation, *Free Radical Biol. Med.*, 2010, **48**(5), 704–771.
95. M. A. Zorrilla-Zubilete, D. G. Maur, M. L. Palumbo and A. M. Genaro, Role of Nitric Oxide Signalling Pathways in Brain Injuries, *Curr. Chem. Biol.*, 2010, **4**(3), 250–261.
96. C.-T. Lee, L.-E. Yu and J.-Y. Wang, Nitroxide Antioxidant as a Potential Strategy to Attenuate the Oxidative/Nitrosative Stress Induced by Hydrogen Peroxide Plus Nitric Oxide in Cultured Neurons, *Nitric oxide*, 2016, **54**, 38–50.
97. J. Petrlova, T. Kalai, I. Maezawa, R. Altman, G. Harishchandra, H.-S. Hong, D. A. Bricarello, A. N. Parikh, G. A. Lorigan and L.-W. Jin, *et al.*, The Influence of Spin-Labeled Fluorene Compounds on the Assembly and toxicity of the Aβ Peptide, *PLoS One*, 2012, **7**(4), e35443.
98. S. Hilt, R. Altman, T. Kalai, I. Maezawa, Q. Gong, S. Wachsmann-Hogiu, L.-W. Jin and J. C. Voss, A Bifunctional Anti-Amyloid Blocks Oxidative Stress and the Accumulation of Intraneuronal Amyloid-Beta, *Molecules*, 2018, **23**(8), 2010/1–2010/22.
99. T. Kalai, J. Petrlova, M. Balog, H. H. Aung, J. C. Voss and K. Hideg, Synthesis and Study of 2-Amino-7-Bromofluorenes Modified with Nitroxides and their Precursors as Dual Anti-Amyloid and Antioxidant Active Compounds, *Eur. J. Med. Chem.*, 2011, **46**(4), 1348–1355.
100. S. Sifuentes-Franco, F. P. Pacheco-Moises, A. D. Rodriguez-Carrizalez and A. G. Miranda-Diaz, The Role of Oxidative Stress, Mitochondrial

Function, and Autophagy in Diabetic Polyneuropathy, *J. Diabetes Res.*, 2017, 1673081/1–1673081/15.
101. P. K. Samaiya, G. Narayan, A. Kumar and S. Krishnamurthy, TEMPOL (4 hydroxy-tempo) Inhibits Anoxia-induced Progression of Mitochondrial Dysfunction and Associated Neurobehavioral Impairment in Neonatal Rats, *J. Neurol. Sci.*, 2017, **375**, 58–67.
102. T. Manabe, A. Matsumura, K. Yokokawa, T. Saito, M. Fujikura, N. Iwahara, T. Matsushita, S. Suzuki, S. Hisahara and J. Kawamata, *et al.*, Evaluation of Mitochondrial Oxidative Stress in the Brain of a Transgenic Mouse Model of Alzheimer's Disease by In Vitro Electron Paramagnetic Resonance Spectroscopy, *J. Alzheimer's Dis.*, 2019, **67**(3), 1079–1087.
103. P. Cassina, A. Cassina, M. Pehar, R. Castellanos, M. Gandelman, A. de Leon, K. M. Robinson, R. P. Mason, J. S. Beckman and L. Barbeito, *et al.*, Mitochondrial Dysfunction in SOD1G93A-Bearing Astrocytes Promotes Motor Neuron Degeneration: Prevention by Mitochondrial-Targeted Antioxidants, *J. Neurosci.*, 2008, **28**(16), 4115–4122.
104. L. Zhan, R. Li, Y. Sun, M. Dou, W. Yang, S. He and Y. Zhang, Effect of Mito-TEMPO, a Mitochondria-Targeted Antioxidant, in Rats with Neuropathic Pain, *NeuroReport*, 2018, **29**(15), 1275–1281.
105. S. P. Patel, P. G. Sullivan, J. D. Pandya and A. G. Rabchevsky, Differential Effects of the Mitochondrial Uncoupling Agent, 2,4-Dinitrophenol, or the Nitroxide Antioxidant, TEMPOL, on Synaptic or Nonsynaptic Mitochondria after Spinal Cord Injury, *J. Neurosci. Res.*, 2009, **87**(1), 130–140.
106. E. D. Hall, R. A. Vaishnav and A. G. Mustafa, Antioxidant Therapies for Traumatic Brain Injury, *Neurotherapeutics*, 2010, **7**(1), 51–61.
107. C. Jiang, C. Xie, F. Li, L. Zhang, R. G. Nichols, K. W. Krausz, J. Cai, Y. Qi, Z.-Z. Fang and S. Takahashi, *et al.*, Intestinal Farnesoid X Receptor Signalling Promotes Nonalcoholic Fatty Liver Disease, *J. Clin. Invest.*, 2015, **125**(1), 386–402.
108. H. Deguchi, K. Yasukawa and T. Yamasaki, *et al.*, Nitroxides Prevent Exacerbation of Indomethacin-Induced Gastric Damage in Adjuvant Arthritis Rats, *Free Radical Biol. Med.*, 2011, **51**, 1799–1805.
109. L. Wei, B. L. Leibowitz, M. Epperly, C. Bi, A. Li, J. Steinman, P. Wipf, S. Li, L. Zhang, J. Greenberger and J. Yu, The GS-Nitroxide JP4-039 Improves Intestinal Barrier and Stem Cell Recovery in Irradiated Mice, *Sci. Rep.*, 2018, **8**, 1–12, (2072).
110. B. Chami, A. Vallejo, G. Jeong, A. Varda and P. K. Witting, 4-Methoxy TEMPO Attenuates Murine Experimental Colitis, *Free Radical Biol. Med.*, 2016, **100**, S94–S95.
111. B. Chami, N. J. Martin, J. M. Dennis and P. K. Witting, Myeloperoxidase in the Inflamed Colon: A Novel Target for Treating Inflammatory Bowel Disease, *Arch. Biochem. Biophys.*, 2018, **645**, 61–71.
112. J. Cai, R. G. Nichols, I. Koo, Z. A. Kalikow, L. Zhang, Y. Tian, J. Zhang, P. B. Smith and A. D. Patterson, Multiplatform Physiologic and

Metabolic Phenotyping Reveals Microbial Toxicity, *mSystems*, 2018, **3**(6), e00123-18.
113. J. Cai, L. Zhang, R. A. Jones, J. B. Correll, E. Hatzakis, P. B. Smith, F. J. Gonzalez and A. D. Patterson, Antioxidant Drug TEMPOL Promotes Functional Metabolic Changes in the Gut Microbiota, *J. Proteome Res.*, 2016, **15**(2), 563–571.
114. H. Woehlk, M. J. Trimble, S. C. Mansour, D. Pletzer, V. Trouillet, A. Welle, L. Barner, R. E. W. Hancock, C. Barner-Kowollik and K. E. Fairfull-Smith, Controlling Biofilm Formation with Nitroxide Functional Surfaces, *Polym. Chem.*, 2019, **10**(31), 4252–4258.
115. C. de la Fuente-Nunez, F. Reffuveille, K. E. Fairfull-Smith and R. E. W. Hancock, Effect of Nitroxides on Swarming Motility and Biofilm Formation, Multicellular Behaviors in Pseudomonas Aeruginosa, *Antimicrob. Agents Chemother.*, 2013, **57**(10), 4877–4881.
116. M. A. Lam, D. I. Pattison, S. E. Bottle, D. J. Keddie and M. J. Davies, Nitric Oxide and Nitroxides can act as Efficient Scavengers of Protein-Derived Free Radicals, *Chem. Res. Toxicol.*, 2008, **21**(11), 2111–2119.
117. C. Lee, L. E. Yu and J. Y. Wang, Nitroxide Antioxidant as a Potential Strategy to Attenuate the Oxidative/Nitrosative Stress Induced by Hydrogen Peroxide Plus Nitric Oxide in Cultured Neurons, *Nitric oxide*, 2016, **54**, 38–50.
118. T. B. Kajer, K. E. Fairfull-Smith, T. Yamasaki, K.-I. Yamada, S. Fu, S. E. Bottle, C. L. Hawkins and M. J. Davies, Inhibition of Myeloperoxidase- and Neutrophil-Mediated Oxidant Production by Tetraethyl and Tetramethyl Nitroxides, *Free Radical Biol. Med.*, 2014, **70**, 96–105.
119. K. U. Schallreuter and J. M. Wood, The Role of Thioredoxin Reductase in the Reduction of Free Radicals at the Surface of the Epidermis, *Biochem. Biophys. Res. Commun.*, 1986, **136**(2), 630–637.
120. J. F. W. Keana, S. Pou and G. M. Rosen, Nitroxides as Potential Contrast Enhancing Agents for MRI Application: Influence of Structure on the Rate of Reduction by Rat Hepatocytes, Whole Liver Homogenate, Subcellular Fractions, and Ascorbate, *Magn. Reson. Med.*, 1987, **5**(6), 525–536.
121. K. Chen and H. M. Swartz, Oxidation of Hydroxylamines to Nitroxide Spin Labels in Living Cells, *Biochim. Biophys. Acta*, 1988, **970**(3), 270–277.
122. A. Iannone, A. Bini, H. M. Swartz, A. Tomasi and V. Vannini, Metabolism in Rat Liver Microsomes of the Nitroxide Spin Probe Tempol, *Biochem. Pharmacol.*, 1989, **38**(16), 2581–2586.
123. A. Iannone, A. Tomasi, V. Vannini and H. M. Swartz, Metabolism of Nitroxide Spin Labels in Subcellular Fraction of Rat Liver I: Reduction by Microsomes, *Biochim. Biophys. Acta, Gen. Subj.*, 1990, **1034**(3), 285–289.
124. A. Iannone, A. Tomasi, V. Vannini and H. M. Swartz, Metabolism of Nitroxide Spin Labels in Subcellular Fractions of Rat Liver IIz; Reduction in the Cytosol, *Biochim. Biophys. Acta, Gen. Subj.*, 1990, **1034**(3), 290–293.

125. E. Rauckman, G. Rosen and L. Griffeth, Enzymatic Reactions of Spin Labels, in *Spin Labelling in Pharmacology*, 1984, pp. 175–190.
126. U. G. Eriksson, R. C. Brasch and T. N. Tozer, Nonenzymatic Bioreduction In Rat Liver And Kidney Of Nitroxyl Spin Labels, Potential Contrast Agents In Magnetic Resonance Imaging, *Drug Metab. Dispos.*, 1987, **15**(2), 155–160.
127. O. Saphier, T. Silberstein, A. Shames, G. Likhtenshtein, E. Maimon, D. Mankuta, M. Mazor, M. Katz, D. Meyerstein and N. Meyerstein, The Reduction of a Nitroxide Spin Label as a Probe of Human Blood Antioxidant Properties, *Free Radical Res.*, 2003, **37**(3), 301–308.
128. J. Glebska, J. Skolimowski, Z. Kudzin, K. Gwozdzinski, A. Grzelak and G. Bartosz, Pro-Oxidative Activity of Nitroxides in their Reactions with Glutathione, *Free Radical Biol. Med.*, 2003, **35**(3), 310–316.
129. J. Keana and F. Van Nice, Influence of Structure on the Reduction of Nitroxide MRI Contrast-Enhancing Agents by Ascorbate, *Physiol. Chem. Phys. Med. NMR*, 1984, **16**(6), 477–487.
130. S. Belkin, R. J. Mehlhorn, K. Hideg, O. Hankovsky and L. Packer, Reduction and Destruction Rates of Nitroxide Spin Probes, *Arch. Biochem. Biophys.*, 1987, **256**(1), 232–243.
131. S. Morris, G. Sosnovsky, B. Hui, C. Huber and H. Swartz, Chemical and Electrochemical Reduction Rates of Cyclic Nitroxides (Nitroxyls), *J. Pharm. Sci.*, 1991, **80**(2), 149–152.
132. M. Sentjurc, P. Morse and H. Swartz, Influence of Metabolic Inhibitors on the Nitroxide Reduction in Cells, *Period. Biol.*, 1986, **88**, 202–203.
133. K. Chen, J. F. Glockner, P. D. Morse and H. M. Swartz, Effects of Oxygen on the Metabolism of Nitroxide Spin Labels in Cells, *Biochemistry*, 1989, **28**(6), 2496–2501.
134. A. H. Ross and H. M. McConnell, Permeation of a Spin-Label Phosphate into the Human Erythrocyte, *Biochemistry*, 1975, **14**(13), 2793–2798.
135. U. G. Eriksson, T. N. Tozer, G. Sosnovsky, J. Lukszo and R. C. Brasch, Human Erythrocyte Membrane Permeability and Nitroxyl Spin-Label Reduction, *J. Pharm. Sci.*, 1986, **75**(4), 334–337.
136. H. M. Swartz and G. S. Timmins, The Metabolism of Nitroxides in Cells and Tissues, in *Toxicology of the Human Environment: The Critical Role of Free Radicals*, ed. C. J. Rhodes, Taylor and Francis, London, 2000, pp. 91–111.
137. M. B. Gariboldi, R. Ravizza, C. Petterino, M. Castagnaro, G. Finocchiaro and E. Monti, Study of In Vitro and In Vivo effects of the piperidine nitroxide Tempol-A potential new therapeutic agent for Gliomas, *Eur. J. Cancer*, 2003, **39**(6), 829–837.
138. S. Suy, J. B. Mitchell, A. Samuni, S. Mueller and U. Kasid, Nitroxide TEMPO, a small molecule, induces apoptosis in Prostate carcinoma cells and suppresses tumor growth in Athymic Mice, *Cancer*, 2005, **103**(6), 1302–1313.
139. J. B. Mitchell, W. DeGraff, D. Kaufman, M. C. Krishna, A. Samuni, E. Finkelstein, M. S. Ahn, S. M. Hahn, J. Gamson and A. Russo,

Inhibition of Oxygen-Dependent Radiation-Induced Damage by the Nitroxide Superoxide Dismutase Mimic, Tempol, *Arch. Biochem. Biophys.*, 1991, **289**(1), 62–67.

140. K. L. Chong, B. A. Chalmers, J. K. Cullen, A. Kaur, J. L. Kolanowski, B. J. Morrow, K. E. Fairfull-Smith, M. J. Lavin, N. L. Barnett and E. J. New, *et al.*, Pro-Fluorescent Mitochondria-Targeted Real-Time Responsive Redox Probes Synthesised from Carboxy Isoindoline Nitroxides: Sensitive Probes Of Mitochondrial Redox Status in Cells, *Free Radical Biol. Med.*, 2018, **128**, 97–110.
141. B. J. Morrow, D. J. Keddie, N. Gueven, M. F. Lavin and S. E. Bottle, A Novel Profluorescent Nitroxide as a Sensitive Probe for the Cellular Redox Environment, *Free Radical Biol. Med.*, 2010, **49**(1), 67–76.
142. K. I. Yamada, D. Inoue, S. Matsumoto and H. Utsumi, In Vivo Measurement of Redox Status in Streptozotocin-Induced Diabetic Rat using Targeted Nitroxyl Probes, *Antioxid. Redox Signaling*, 2004, **6**(3), 605–611.
143. S. Dikalov, M. Skatchkov, B. Fink and E. Bassenge, Quantification of Superoxide Radicals and Peroxynitrite in Vascular Cells Using Oxidation of Sterically Hindered Hydroxylamines and Electron Spin Resonance, *Nitric oxide*, 1997, **1**(5), 423–431.
144. S. I. Dikalov, Y. F. Polienko and I. Kirilyuk, Electron Paramagnetic Resonance Measurements of Reactive Oxygen Species by Cyclic Hydroxylamine Spin Probes, *Antioxid. Redox Signaling*, 2018, **28**(15), 1433–1443.
145. S. Ishida, H. Kumashiro, N. Tsuchihashi, T. Ogata, M. Ono, H. Kamada and E. Yoshida, In Vivo Analysis of Nitroxide radicals injected into small animals by L-Band ESR Technique, *Phys. Med. Biol.*, 1989, **34**, 1317–1327.
146. A. P. Cotrim, F. Hyodo, K. I. Matsumoto, A. L. Sowers, J. A. Cook, B. J. Baum, M. C. Krishna and J. B. Mitchell, Differential Radiation Protection of Salivary Glands Versus Tumor by TEMPOL with Accompanying Tissue Assessment of TEMPOL by Magnetic Resonance Imaging, *Clin. Cancer Res.*, 2007, **13**(16), 4928–4939.
147. S. Xavier, K.-I. Yamada, A. M. Samuni, A. Samuni, W. DeGraff, M. C. Krishna and J. B. Mitchell, Differential Protection by Nitroxides and Hydroxylamines to Radiation-Induced and Metal Ion-Catalyzed Oxidative Damage, *Biochim. Biophys. Acta, Gen. Subj.*, 2002, **1573**(2), 109–120.
148. S. M. Hahn, M. C. Krishna, A. M. DeLuca, D. Coffin and J. B. Mitchell, Evaluation of the Hydroxylamine Tempol-H as an In Vivo Radioprotector, *Free Radical Biol. Med.*, 2000, **28**(6), 953–958.
149. M. C. Krishna, W. DeGraff, O. H. Hankovszky, C. P. Sar, T. Kalai, J. Jeko, A. Russo, J. B. Mitchell and K. Hideg, Studies of Structure-Activity Relationship of Nitroxide Free Radicals and their Precursors as Modifiers Against Oxidative Damage, *J. Med. Chem.*, 1998, **41**(18), 3477–3492.

150. D. Gelvan, P. Saltman and S. R. Powell, Cardiac Reperfusion Damage Prevented by a Nitroxide Free Radical, *Proc. Natl. Acad. Sci. U. S. A.*, 1991, **88**(11), 4680–4684.
151. A. Samuni, D. Winkelsberg, A. Pinson, S. M. Hahn, J. B. Mitchell and A. Russo, Nitroxide Stable Radicals Protect Beating Cardiomyocytes Against Oxidative Damage, *J. Clin. Invest.*, 1991, **87**(5), 1526–1530.
152. E. Beit-Yannai, R. Zhang, V. Trembovler, A. Samuni and E. Shohami, Cerebroprotective Effect of Stable Nitroxide Radicals in Closed Head Injury in the Rat, *Brain Res.*, 1996, **717**(1–2), 22–28.
153. D. Rachmilewitz, F. Karmeli, E. Okon and A. Samuni, A Novel Anti-ulcerogenic Stable Radical Prevents Gastric Mucosal Lesions in Rats, *Gut*, 1994, **35**(9), 1181.
154. W. G. Degraff, M. C. Krishna, A. Russo and J. B. Mitchell, Anti-mutagenicity of a Low Molecular Weight Superoxide Dismutase Mimic Against Oxidative Mutagens, *Environ. Mol. Mutagen.*, 1992, **19**(1), 21–26.
155. J. Reddan, M. Sevilla, F. Giblin, V. Padgaonkar, D. Dziedzic, V. Leverenz, I. Misra and J. Peters, The Superoxide Dismutase Mimic TEMPOL Protects Cultured Rabbit Lens Epithelial Cells from Hydrogen Peroxide Insult, *J. Exp. Eye Res.*, 1993, **56**(5), 543–554.
156. M. C. Krishna, W. DeGraff, S. Tamura, F. J. Gonzalez, A. Samuni, A. Russo and J. B. Mitchell, Mechanisms of Hypoxic and Aerobic Cytotoxicity of Mitomycin C in Chinese Hamster V79 Cells, *Cancer Res.*, 1991, **51**(24), 6622–6628.
157. E. Monti, D. Cova, E. Guido, R. Morelli and C. Oliva, Protective Effect of the Nitroxide TEMPOL Against the Cardiotoxicity of Adriamycin, *Free Radical Biol. Med.*, 1996, **21**(4), 463–470.
158. B. P. Soule, F. Hyodo, K.-I. Matsumoto, N. L. Simone, J. A. Cook, M. C. Krishna and J. B. Mitchell, The Chemistry and Biology of Nitroxide Compounds, *Free Radical Biol. Med.*, 2007, **42**(11), 1632–1650.
159. S. Dikalov, M. Skatchkov and E. Bassenge, Spin Trapping of Superoxide Radicals and Peroxynitrite by 1-Hydroxy-3-Carboxy-Pyrrolidine and 1-Hydroxy-2,2,6,6-Tetramethyl-4-Oxo-Piperidine and the Stability of Corresponding Nitroxyl Radicals Towards Biological Reductants, *Biochem. Biophys. Res. Commun.*, 1997, **231**(3), 701–704.
160. A. Beckwith, V. Bowry and K. Ingold, Kinetics of Nitroxide Radical Trapping 1: Solvent Effects, *J. Am. Chem. Soc.*, 1992, **114**(13), 4983–4992.
161. V. Bowry and K. Ingold, Kinetics of Nitroxide Radical Trapping 2: Structural Effects, *J. Am. Chem. Soc.*, 1992, **114**(13), 4992–4996.
162. A. Samuni, M. C. Krishna, P. Riesz, E. Finkelstein and A. Russo, A Novel Metal-Free Low Molecular Weight Superoxide Dismutase Mimic, *J. Biol. Chem.*, 1988, **263**(34), 17921–17927.
163. M. C. Krishna, A. Russo, J. B. Mitchell, S. Goldstein, H. Dafni and A. Samuni, Do Nitroxide Antioxidants act as Scavengers of O2-. or as SOD Mimics? *J. Biol. Chem.*, 1996, **271**(42), 26026–26031.
164. R. F. Queiroz, V. Paviani, F. R. Coelho, E. F. Marques, P. Di Mascio and O. Augusto, The Carbonylation and Covalent Dimerization of Human

Superoxide Dismutase 1 Caused by its Bicarbonate-Dependent Peroxidase Activity is Inhibited by the Radical Scavenger TEMPOL, *Biochem. J.*, 2013, **455**(1), 37–46.

165. M. C. Krishna, D. A. Grahame, A. Samuni, J. B. Mitchell and A. Russo, Oxoammonium Cation Intermediate in the Nitroxide-Catalyzed Dismutation of Superoxide, *Proc. Natl. Acad. Sci. U. S. A.*, 1992, **89**(12), 5537–5541.
166. Y. Aronovitch, D. Godinger, A. Israeli, M. C. Krishna, A. Samuni and S. Goldstein, Dual Activity of Nitroxides as Pro- and Antioxidants: Catalysis of Copper-Mediated DNA Breakage and H2O2 Dismutation, *Free Radical Biol. Med.*, 2007, **42**(9), 1317–1325.
167. J. B. Mitchell, A. Samuni, M. C. Krishna, W. G. DeGraff, M. S. Ahn, U. Samuni and A. Russo, Biologically Active Metal-Independent Superoxide Dismutase Mimics, *Biochemistry*, 1990, **29**(11), 2802–2807.
168. A. Samuni, D. Godinger, J. Aronovitch, A. Russo and J. B. Mitchell, Nitroxides Block DNA Scission and Protect Cells from Oxidative Damage, *Biochemistry*, 1991, **30**(2), 555–561.
169. M. C. Krishna, A. Samuni, J. Taira, S. Goldstein, J. B. Mitchell and A. Russo, Stimulation by Nitroxides of Catalase-Like Activity of Hemeproteins, *J. Biol. Chem.*, 1996, **271**(42), 26018.
170. H. Yu, L. Cao, F. Li, Q. Wu, Q. Li, S. Wang and Y. Guo, The Antioxidant Mechanism of Nitroxide TEMPO: Scavenging with Glutathionyl Radicals, *RSC Adv.*, 2015, **5**(78), 63655–63661.
171. G. Durand, F. Choteau, R. A. Prosak, A. Rockenbauer, F. A. Villamena and B. Pucci, Synthesis, Physical-Chemical and Biological Properties of Amphiphilic Amino Acid Conjugates of Nitroxides, *New J. Chem.*, 2010, **34**(9), 1909–1920.
172. S. I. Dikalov, A. E. Dikalova, D. A. Morozov and I. A. Kirilyuk, Cellular Accumulation and Antioxidant Activity of Acetoxymethoxycarbonyl Pyrrolidine Nitroxides, *Free Radical Res.*, 2018, **52**(3), 339–350.
173. D. Metodiewa, A. Kochman, J. Skolimowski, L. Gebicka and C. Koska, Metexyl (4-Methoxy-2,2,6,6-Tetramethylpiperidine-1-Oxyl) as an Oxygen Radicals Scavenger and Apoptosis Inducer In Vivo, *Anticancer Res.*, 1999, **19**(6B), 5259–5264.
174. K. Anzai, M. Ueno, A. Yoshida, M. Furuse, W. Aung, I. Nakanishi, T. Moritake, K. Takeshita and N. Ikota, Comparison of Stable Nitroxide, 3- Substituted 2,2,5,5-Tetramethylpyrrolidine-N-Oxyls, with respect to Protection from Radiation, Prevention of DNA Damage and Distribution in Mice, *Free Radical Biol. Med.*, 2006, **40**(7), 1170–1178.
175. T. Offer, A. Russo and A. Samuni, The Pro-Oxidative Activity of SOD and Nitroxide SOD Mimics, *FASEB J.*, 2000, **14**(9), 1215–1220.
176. A. Lewinska, M. Wnuk, E. Slota and G. Bartosz, The Nitroxide Antioxidant TEMPOL affects Metal-Induced Cyto- and Genotoxicity in Human Lymphocytes In Vitro, *Mutat. Res., Genet. Toxicol. Environ. Mutagen.*, 2008, **649**(1), 7–14.

177. X. Guo, J. E. Seo, S. M. Bryce, J. A. Tan, Q. Wu, S. L. Dial, M. M. Moore and N. Mei, Comparative Genotoxicity of TEMPO and 3 of its Derivatives in Mouse Lymphoma Cells, *Toxicol. Sci*, 2018, **163**(1), 214–225.
178. Z. Zhang, Z. Ren, S. Chen, X. Guo, F. Liu, L. Guo and N. Mei, ROS Generation and JNK Activation contribute to 4-Methoxy-TEMPO-Induced Cytotoxicity, Autophagy, and DNA Damage in HepG2 Cells, *Arch. Toxicol.*, 2018, **92**, 717–728.
179. K. Selvendiran, S. Ahmed, A. Dayton, M. L. Kuppusamy, M. Tazi, A. Bratasz, L. Tong, B. K. Rivera, T. Kalai, K. Hideg and P. Kuppusamy, Safe and Targeted Anticancer Efficacy of a Novel Class of Antioxidant-Conjugated Difluorodiarylidenyl Piperidones: Differential Cytotoxicity in Healthy and Cancer Cells, *Free Radical Biol. Med.*, 2010, **48**(9), 1228–1235.
180. J. M. Mast, D. Tse, K. Shee, M. L. Kuppusamy, M. M. Kmiec, T. Kálai and P. Kuppusamy, Diarylidenylpiperidones, H-4073 and HO-3867, Induce G2/M Cell-Cycle Arrest, Apoptosis and Inhibit STAT3 Phosphorylation in Human Pancreatic Cancer Cells, *Cell Biochem. Biophys.*, 2019, **77**, 109–119.
181. S. Suy, J. B. Mitchell, D. Ehleiter, A. Haimovitz-Friedman and U. Kasid, Nitroxides TEMPOL and TEMPO Induce Divergent Signal Transduction Pathways in MDA-MB 231 Breast Cancer Cells, *J. Biol. Chem.*, 1998, **273**(28), 17871–17878.
182. D. Lejeune, M. Hasanuzzaman, A. Pitcock, J. Francis and I. Sehgal, The Superoxide Scavenger TEMPOL Induces Urokinase Receptor (Upar) Expression in Human Prostate Cancer Cells, *Mol. Cancer*, 2006, **5**(1), 21.
183. M. C. Ghosh, D. L. Zhang, H. Ollivierre, M. A. Eckhaus and T. A. Rouault, Translational Repression of HIF2α Expression in Mice with Chuvash Polycythemia Reverses Polycythemia, *J. Clin. Invest.*, 2018, **128**(4), 1317–1325.
184. J. B. Mitchell, S. Xavier, A. M. DeLuca, A. L. Sowers, J. A. Cook, M. C. Krishna, S. M. Hahn and A. Russo, A low molecular weight antioxidant decreases weight and lowers tumor incidence, *Free Radical Biol. Med.*, 2003, **34**(1), 93–102.
185. M. W. Epperly, B. H. Rhieu, D. Franicola, T. Dixon, S. Cao, X. Zhang, D. Shields, H. Wang, J. S. Greenberger and P. Wipf, Induction of TGF-β by Irradiation or Chemotherapy in Fanconi Anemia (FA) Mouse Bone Marrow is Modulated by Small Molecule Radiation Mitigators JP4-039 and MMS350, *In Vivo*, 2017, **31**(2), 159–168.
186. A. A. Polyzos, N. I. Wood, P. Williams, P. Wipf, A. J. Morton and C. T. McMurray, XJB-5-131-Mediated Improvement in Physiology and Behaviour of the R6/2 Mouse Model of Huntington's Disease is Age- and Sex- Dependent, *PLoS One*, 2018, **13**(4), e0194580.
187. J. Reichenbach, R. Schubert, C. Schwan, K. Müller, H. Böhles and S. Zielen, Anti-Oxidative Capacity in Patients with Ataxia Telangiectasia, *Clinical and Experimental Immunology*, 1999, **117**, 535–539.

188. M. Gatei, D. Shkedy, K. K. Khanna, T. Uziel, Y. Shiloh, T. K. Pandita, M. F. Lavin and G. Rotman, Ataxia-Telangiectasia: Chronic Activation of Damage-Responsive Functions is Reduced by Alpha-Lipoic Acid, *Oncogene*, 2001, **20**(3), 289–294.
189. D. J. Watters, Oxidative Stress in Ataxia Telangiectasia, *Redox Rep.*, 2003, **8**(1), 23–29.
190. S. E. Browne, L. J. Roberts, P. A. Dennery, S. R. Doctrow, M. F. Beal, C. Barlow and R. L. Levine, Treatment with a Catalytic Antioxidant Corrects the Neurobehavioral Defect in Ataxia-Telangiectasia Mice, *Free Radical Biol. Med.*, 2004, **36**(7), 938–942.
191. R. Schubert, L. Erker, C. Barlow, H. Yakushiji, D. Larson, A. Russo, J. B. Mitchell and A. Wynshaw-Boris, Cancer Chemoprevention by the Antioxidant TEMPOL in Atm-Deficient Mice, *Hum. Mol. Genet.*, 2004, **13**(16), 1793–1802.
192. P. Chen, C. Peng, J. Luff, K. Spring, D. Watters, S. Bottle, S. Furuya and M. F. Lavin, Oxidative Stress is Responsible for Deficient Survival and Dendritogenesis in Purkinje Neurons from Ataxia-Telangiectasia Mutated Mutant Mice, *J. Neurosci.*, 2003, **23**(36), 11453–11460.
193. N. Gueven, J. Luff, C. Peng, K. Hosokawa, S. E. Bottle and M. F. Lavin, Dramatic Extension of Tumor Latency and Correction of Neurobehavioral Phenotype in Atm-Mutant Mice With a Nitroxide Antioxidant, *Free Radical Biol. Med.*, 2006, **41**(6), 992–1000.
194. C. Barlow, S. Hirotsune, R. Paylor, M. Liyanage, M. Eckhaus, F. Collins, Y. Shiloh, J. N. Crawley, T. Ried, D. Tagle and A. Wynshaw-Boris, Atm-Deficient Mice: A Paradigm of Ataxia Telangiectasia, *Cell*, 1996, **86**(1), 159–171.
195. K. Hosokawa, P. Chen, F. M. Lavin and S. E. Bottle, The Impact of Carboxy Nitroxide Antioxidants on Irradiated Ataxia Telangiectasia Cells, *Free Radical Biol. Med.*, 2004, **37**(7), 946–952.
196. S. Goldstein, G. Merenyi, A. Russo and A. Samuni, The Role of Oxoammonium Cation in the SOD-Mimic Activity of Cyclic Nitroxides, *J. Am. Chem. Soc.*, 2003, **125**(3), 789–795.
197. E. Herrera and C. Barbas, Vitamin E: Action, Metabolism and Perspectives, *J. Physiol. Biochem.*, 2001, **57**(1), 43–56.
198. E. E. Voest, E. van Faassen, B. S. van Asbeck, J. P. Neijt and J. J. Marx, Increased Hydrogen Peroxide Concentration in Human Tumor Cells Due to a Nitroxide Free Radical, *Biochim. Biophys. Acta*, 1992, **1136**(2), 113–118.
199. E. Monti, R. Supino, M. Colleoni, B. Costa, R. Ravizza and M. B. Gariboldi, Nitroxide TEMPOL Impairs Mitochondrial Function and Induces Apoptosis in HL60 Cells, *J. Cell. Biochem.*, 2001, **82**(2), 271–276.
200. Y. Wu, W. Tang, C. L. Li, J. W. Liu, L. D. Miao, J. Han and M. B. Lan, Cytotoxicity of a newly synthesized Nitroxide Derivative of 4-Ferrocenecarboxyl-2,2,6,6-Tetramethylpiperidine-1-Oxyl in High Metastatic Lung Tumor Cells, *Pharmazie*, 2006, **61**(12), 1028–1033.

201. X. Guo, R. A. Mittelstaedt, L. Guo, J. G. Shaddock, R. H. Heflich, A. H. Bigger, M. M. Moore and N. Mei, Nitroxide TEMPO: A Genotoxic and Oxidative Stress Inducer in Cultured Cells, *Toxicol. In Vitro*, 2013, **27**, 1496–1502.
202. X. Guo, S. Chen, Z. Zhang, V. N. Dobrovolsky, S. L. Dial, L. Guo and N. Mei, Reactive Oxygen Species and C-Jun N-Terminal Kinases Contribute to TEMPO-Induced Apoptosis in L5178Y Cells, *Chem.-Biol. Interact.*, 2015, **235**, 27–36.
203. M. Wang, K. Li, Z. Zou, L. Li, L. Zhu, Q. Wang, W. Gao, Y. Wang, W. Huang, R. Liu, K. Yao and Q. Liu, Piperidine Nitroxide TEMPOL Enhances Cisplatin-Induced Apoptosis in Ovarian Cancer Cells, *Oncol. Lett.*, 2018, **16**, 4847–4854.
204. M. B. Gariboldi, F. Terni, R. Ravizza, S. Meschini, M. Marra, M. Condello, G. Arancia and E. Monti, The Nitroxide TEMPOL Modulates Anthracycline Resistance in Breast Cancer Cells, *Free Radical Biol. Med.*, 2006, **40**(8), 1409–1418.
205. G. Leipnitz, A.-W. Mohsen, A. Karunanidhi, B. Seminotti, V. Y. Roginskaya, D. M. Markantone, M. Grings, S. J. Mihalik, P. Wipf, B. Van Houten and J. Vockley, Evaluation of Mitochondrial Bioenergetics, Dynamics, Endoplasmic Reticulum- Mitochondria Crosstalk, and Reactive Oxygen Species in Fibroblasts from patients with Complex I Deficiency, *Sci. Rep.*, 2018, **8**(1165), 1–14.
206. K. A. Boyle, J. Van Wickle, R. B. Hill, A. Marchese, B. Kalyanaraman and M. B. Dwinell, Mitochondria-Targeted Drugs Stimulate Mitophagy and Abrogate Colon Cancer Cell Proliferation, *J. Biol. Chem.*, 2018, **293**(38), 14891–14904.
207. G. Cheng, J. Zielonka, D. McAllister, M. Hardy, O. Ouari, J. Joseph, M. B. Dwinell and B. Kalyanaraman, Antiproliferative Effects of Mitochondria-Targeted Cationic Antioxidants and Analogs: Role of Mitochondrial Bioenergetics and Energy-Sensing Mechanism, *Cancer Lett.*, 2015, **365**, 96–106.
208. J. Zielonka, J. Joseph, A. Sikora, M. Hardy, O. Ouari, J. Vasquez-Vivar, G. Cheng, M. Lopez and B. Kalyanaraman, Mitochondria-Targeted Triphenylphosphonium-Based Compounds: Syntheses, Mechanisms of Action, and Therapeutic and Diagnostic Applications, *Chem. Rev.*, 2017, **117**, 10043–10120.
209. R. M. Brand, P. Wipf, A. Durham, M. W. Epperly, J. S. Greenberger and L. D. Falo, Targeting Mitochondrial Oxidative Stress to Mitigate UV-Induced Skin Damage, *Front. Pharmacol.*, 2018, **9**(920), 1–10.
210. S.-K. Hong, D. Starenki, P.-K. Wu and J.-I. Park, Suppression of B-Raf^{v600e} Melanoma Cell Survival by Targeting Mitochondria Using Triphenyl-Phosphonium-Conjugated Nitroxide Or Ubiquinone, *Cancer Biol. Ther.*, 2017, **18**(2), 106–114.
211. R. M. Brand, M. W. Epperly, J. M. Stottlemyer, E. M. Skoda, X. Gao, S. Li, S. Huq, P. Wipf, V. E. Kagan and J. S. Greenberger, *et al.*, A Topical Mitochondria-Targeted Redox-Cycling Nitroxide Mitigates Oxidative

Stress-Induced Skin Damage, *J. Invest. Dermatol.*, 2017, **137**(3), 576–586.

212. T. Manabe, A. Matsumura, K. Yokokawa, T. Saito, M. Fujikura, N. Iwahara, T. Matsushita, S. Suzuki, S. Hisahara, J. Kawamata, H. Suzuki, M. C. Emoto, H. G. Fujii and S. Shimohama, Evaluation of Mitochondrial Oxidative Stress in the Brain of a Transgenic Mouse Model of Alzheimer's Disease by in vitro Electron Paramagnetic Resonance Spectroscopy, *J. Alzheimer's Dis.*, 2019, **67**(3), 1079–1087.
213. J. Park, J.-S. Min, B. Kim, U.-B. Chae, J. W. Yun, M.-S. Choi, I.-K. Kong, K.-T. Chang and D.-S. Lee, Mitochondrial ROS govern the LPS-Induced Pro-Inflammatory response in Microglia Cells by regulating MAPK and NF-Kb Pathways, *Neurosci. Lett.*, 2015, **584**, 191–196.
214. B. Seminotti, G. Leipnitz, A. Karunanidhi, C. Kochersperger, V. Y. Roginskaya, S. Basu, Y. Wang, P. Wipf, B. Van Houten, A.-W. Mohsen and J. Vockley, Mitochondrial Energetics is impaired in very Long-Chain Acyl-CoA Dehydrogenase Deficiency and can be rescued by treatment with Mitochondria-Targeted Electron Scavengers, *Hum. Mol. Genet.*, 2019, **28**(6), 928–941.
215. A. Shinde, H. Berhane, B. H. Rhieu, R. Kalash, K. Xu, J. Goff, M. W. Epperly, D. Franicola, X. Zhang and T. Dixon, *et al.*, Intraoral Mitochondrial-Targeted GS-Nitroxide, JP4-039, Radioprotects Normal Tissue in Tumor-Bearing Radiosensitive Fancd2-/- (C57BL/6) Mice, *Radiat. Res.*, 2016, **185**(2), 134–150.
216. J. Steinman, M. Epperly, W. Hou, J. Willis, H. Wang, R. Fisher, T. McCaw, M. S. Huq, J. S. Greenberger and B. Liu, *et al.*, Improved Total-Body Irradiation Survival by delivery of two radiation Mitigators that target distinct cell death pathways, *Radiat. Res.*, 2018, **189**(1), 68–83.
217. M. W. Epperly, R. Fisher, H. Wang, J. S. Greenberger, J. R. Sacher, T. Krainz, X. Zhang, P. Wipf, M. Liang and J. R. Sacher, *et al.*, Effectiveness of Analogs of the GS-Nitroxide, JP4-039, as Total Body Irradiation Mitigators, *In Vivo*, 2017, **31**(1), 39–43.
218. C. P. Feliciano and Y. Nagasaki, Antioxidant nanomedicine protects against ionizing radiation-induced life-shortening in C57BL/6J mice, *ACS Biomater. Sci. Eng.*, 2019, **5**, 5631–5636.

CHAPTER 13

Spin Trapping

J. ZIELONKA,[a] M. HARDY[b] AND B. KALYANARAMAN*[a]

[a] Department of Biophysics, Medical College of Wisconsin, 8701 Watertown Plank Road, Milwaukee, WI 53226, USA; [b] Aix Marseille Univ, CNRS, ICR, UMR 7273, Marseille 13013, France
*Email: balarama@mcw.edu

13.1 Introduction

Radicals, defined as chemical species bearing unpaired electron(s), are important intermediates in chemistry and biology.[1] Although their reactivity and stability in solution vary significantly depending on their chemical structure and chemical surroundings, in most cases their lifetimes are relatively short, making their detection and quantitative analyses a challenging task. Time-resolved pulse techniques, including pulse radiolysis and laser flash photolysis, provide an opportunity to selectively generate and directly detect many radical species and to study their chemical reactivity and reaction kinetics.[2] Analyses of nonradical end products of the chemical or biochemical process may be also used to point to the involvement of the radical species. Chemical probes are typically used to provide more direct evidence of the involvement of a radical in a process of interest. When the probe reacts with the radical species, it is converted to a more stable product, which can accumulate over the time of incubation and cross the detection limit of the method of choice. Among the chemical probes, spin traps are especially well suited to detect unstable free radicals, as their products – typically nitroxides – are not only more stable, even in complex biological systems, but also in many cases carry a spectroscopic ''footprint'' of the trapped radical when coupled to electron paramagnetic resonance (EPR)-based analysis.[3]

Nitroxides
Edited by Olivier Ouari and Didier Gigmes

Published by the Royal Society of Chemistry, www.rsc.org

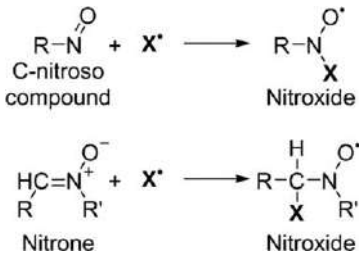

Scheme 13.1 Trapping of the X• radical by nitroso and nitrone spin traps to form nitroxide spin adducts.

In the late 1960s, a series of papers reported the addition reaction of free radicals to nitroso compounds and nitrones, forming more stable nitroxides (Scheme 13.1) detectable by EPR spectroscopy.[4–13] This discovery coincided with the discovery of the superoxide dismutase enzyme, one of the most important breakthroughs in the field of free radical biology.[14,15] The potential of using nitrones and nitroso compounds to trap, detect and identify the radicals formed in chemically and biologically relevant systems was soon realized.[12,16]

Among the several advantages of EPR spin trapping for the detection of free radicals, the formation of a covalent bond between the probe and the radical, with the formation of a more stable, EPR-active product, seems most important. The covalent bond between the radical and the spin traps results in the formation of the product, which is unique for the radical trapped. In many cases, this results in a highly characteristic and species-specific EPR spectrum, enabling identification of the radical species by EPR spectroscopy. Other techniques, where a covalent bond between the probe and the radical is formed, typically involve further transformations of the primary radical adduct to a nonradical product and require separation and identification of the product by chromatographic techniques coupled to highly sensitive detection modalities, including electrochemical or mass spectrometric detectors. EPR spin trapping provides nondestructive, real-time monitoring of the accumulation of the spin adduct(s), and in many cases spectra of the mixture of several different spin adducts can be deconvoluted, and the kinetic profiles of each radical adduct established.[17]

Two major classes of spin traps have been developed: C-nitroso compounds and nitrones (Scheme 13.1).[18] In each case, the radical addition results in the formation of the nitroxide product, typically of sufficient stability to be detected by EPR spectrometry.

The most popular nitroso spin traps include 2-methyl-2-nitrosopropane (MNP, Scheme 13.2) and the aromatic nitroso analogs NB (nitrosobenzene),[19,20] ND (nitrosodurene)[21] and water-soluble 3,5-dibromo-4-nitrosobenzene sulfonate (DBNBS).[22]

The advantage of the C-nitroso spin traps lies in the direct attachment of the radical to the nitrogen atom of the nitroxide moiety, resulting in significant perturbance of the nitroxide EPR spectrum, revealing hyperfine

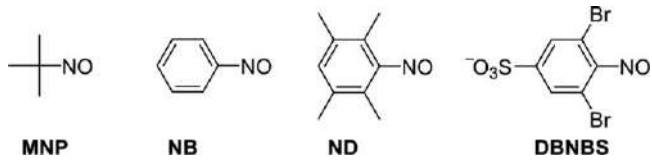

Scheme 13.2 Examples of C-nitroso spin traps.

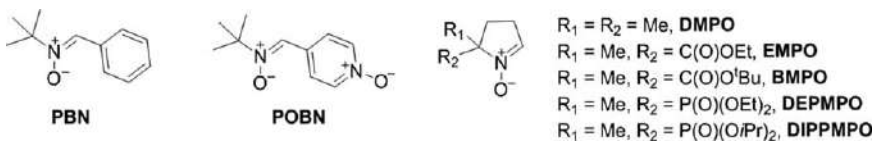

Scheme 13.3 General structures of linear and cyclic nitrones.

splittings from the nuclei of the trapped radical and allowing more straightforward identification of the radical trapped.

Two classes of nitrone spin traps are widely used: (i) the linear nitrones, including phenyl-*N*-*tert*-butylnitrone (PBN) and POBN (α-[4-pyridyl 1-oxide]-*N*-*tert*-butylnitrone), and (ii) the pyrroline-based cyclic nitrones, including 5,5-dimethyl-1-pyrroline-*N*-oxide (DMPO), 5-ethoxycarbonyl-5-methyl-1-pyrroline-*N*-oxide (EMPO), 5-*tert*-butoxycarbonyl-5-methyl-1-pyrroline *N*-oxide (BMPO), 5-(diethoxyphosphoryl)-5-methyl-1-pyrroline *N*-oxide (DEPMPO) and 5-(diisopropoxyphosphoryl)-5-methyl-1-pyrroline-*N*-oxide (DIPPMPO, Scheme 13.3).

In the case of nitrone spin traps, the spectrum-based assignment of the radicals trapped is not obvious and requires the reference spectrum obtained under a controlled reaction of the radical of interest with the spin trap. However, much wider application of nitrones has been found in biological sciences, due to their superior applicability to detect oxygen-derived/centered radicals.

The advantage of most spin traps is their relatively wide electrochemical window,[23–26] resulting in their resistance to relatively strong one-electron oxidizing and reducing agents in electron transfer reactions. Many of those radical species add to the double bond of the spin trap rather than accepting or donating an electron or hydrogen atom. Therefore, under most conditions, the detection of a spin adduct provides unequivocal proof for the occurrence of the radical of interest. Although uncommon, under specific conditions, the EPR-active nitroxide may be potentially formed *via* other mechanisms, including (i) addition of nucleophilic substrate followed by one-electron oxidation of the resulting hydroxylamine (Forrester–Hepburn reaction, Scheme 13.4a) or (ii) one-electron oxidation followed by reaction of the resulting spin trap radical cation with water or other nucleophiles (inverted spin trapping, Scheme 13.4b). Several experimental approaches have been developed to identify the occurrence of those reactions.[27–30]

Since the spin-trapping technique was established, significant progress in spin trap development has been made, which has provided a better understanding of the spin-trapping reaction chemistry and of the kinetics and

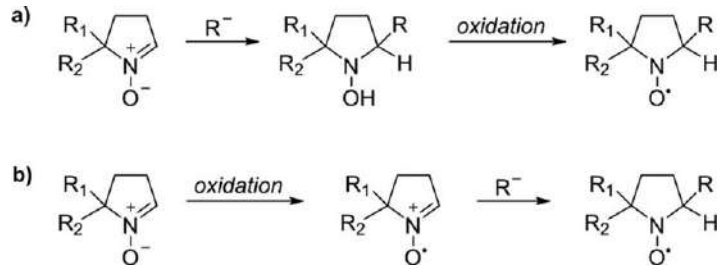

Scheme 13.4 Nitroxide formation from spin traps not involving radical addition.

stability of the spin adduct in chemical and biological systems.[31–35] The spin-trapping technique has been instrumental in studying the formation of free radicals in numerous chemical reactions and has likely made the greatest impact in redox biochemistry, enzymology and free radical biology, toxicology and medicine.[34–42] Although the spin-trapping technique has existed for over half a century, it is still evolving, with new structures being designed and tested,[18] and new (bio)analytical approaches to detect the adducts in biological systems *in vitro* and in animals *in vivo* continuing to be developed.

In this chapter, we provide examples of how the spin-trapping technique can be used to study the chemical mechanisms of the oxidation of redox probes, we provide the chemical aspects of the detection of different biologically relevant radicals, and we show recent advances in spin trap development and extension of the technique to non-EPR detection modalities.

13.2 Application of the Spin-trapping Technique in the Mechanistic Studies of Redox Probes

13.2.1 Mechanism of the Reaction of Boronate Probes with Peroxynitrite

Aromatic boronates undergo oxidation to the corresponding phenols upon reaction with hydrogen peroxide (H_2O_2), peroxyacids, hypohalogenous acids, amino acid hydroperoxides and peroxynitrite ($ONOO^-$).[43–48] This has been utilized in the development of redox probes for detection of such oxidants in cell-free and cellular systems. In the case of the reaction of boronates with $ONOO^-$, the phenolic product, as well as minor products including nitrobenzene, is formed (Scheme 13.5).[44,49]

EPR spin-trapping experiments were performed to explore the role of radical species in the formation of the nitrobenzene-type product. In fact, application of the MNP nitroso spin trap (Scheme 13.2) allowed the detection of the spin adduct, whose EPR spectrum was sensitive to the actual substituent on the phenyl ring of the phenylboronic acid (Figure 13.1), consistent with the formation of phenyl-type radicals during the reaction of phenylboronates with $ONOO^-$.

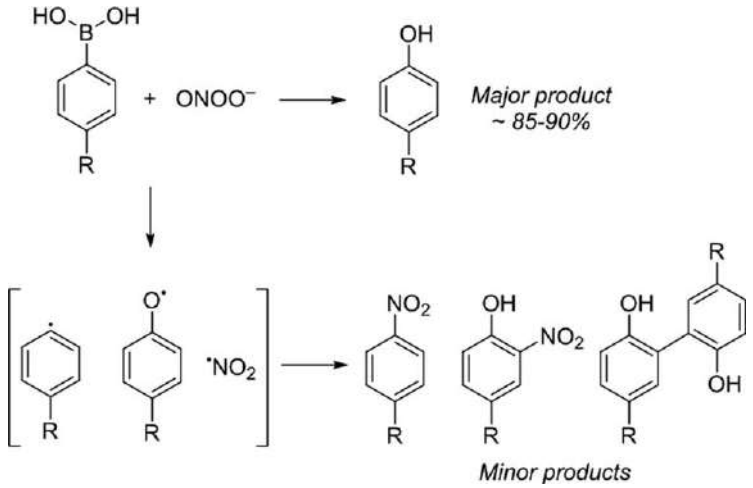

Scheme 13.5 Major and minor products formed during the reaction of aromatic boronic acids with $ONOO^-$.
Adapted and reprinted with permission from A. Sikora, J. Zielonka, M. Lopez, A. Dybala-Defratyka, J. Joseph, A. Marcinek, B. Kalyanaraman. Reaction between peroxynitrite and boronates: EPR spin-trapping, HPLC analyses and quantum mechanical study of the free radical pathway. Chemical research in toxicology. Reproduced from ref. 49 with permission from American Chemical Society, Copyright 2011.

Moreover, the addition of the spin trap led to decreased yield of the minor products, further confirming the involvement of the radical intermediate(s) in their formation. Also, DEPMPO cyclic nitrone was used to detect the intermediate radical formed during the reaction, and, again, a spectrum consistent with a carbon-centered radical adduct (12 lines, $a_H = 22.8$, $a_P = 44.8$ G) has been detected. These data, together with product analyses and DFT calculation, pointed to the mechanism of boronate oxidation by $ONOO^-$ occurring *via* two pathways of the decomposition of the $ONOO^-$ adduct to boronates: major heterolytic cleavage of the O–O bond leading to the phenolic product and minor (10–15% yield) homolytic cleavage of the O–O bond leading to the formation of the phenyl and nitrogen dioxide ($^\bullet NO_2$) radicals (Scheme 13.6).

EPR spin trapping was also used to probe free radical formation during the reaction of $ONOO^-$ with a bioluminescent boronate probe, peroxy-caged luciferin (PCL-1, Figure 13.2A).[50] Upon oxidation, the primary phenolic product formed eliminates quinone methide to form luciferin, a substrate for luciferase. In the presence of spin traps, the reaction between PCL-1 and $ONOO^-$ leads to the formation of spin adducts of a carbon-centered radical, both for MNP and DIPPMPO spin traps (Figure 13.2B,C). Liquid chromatography–mass spectrometry-based analyses of the spin adducts confirmed the trapping of the phenyl radical formed during the reaction (Figure 13.2D,E).[50]

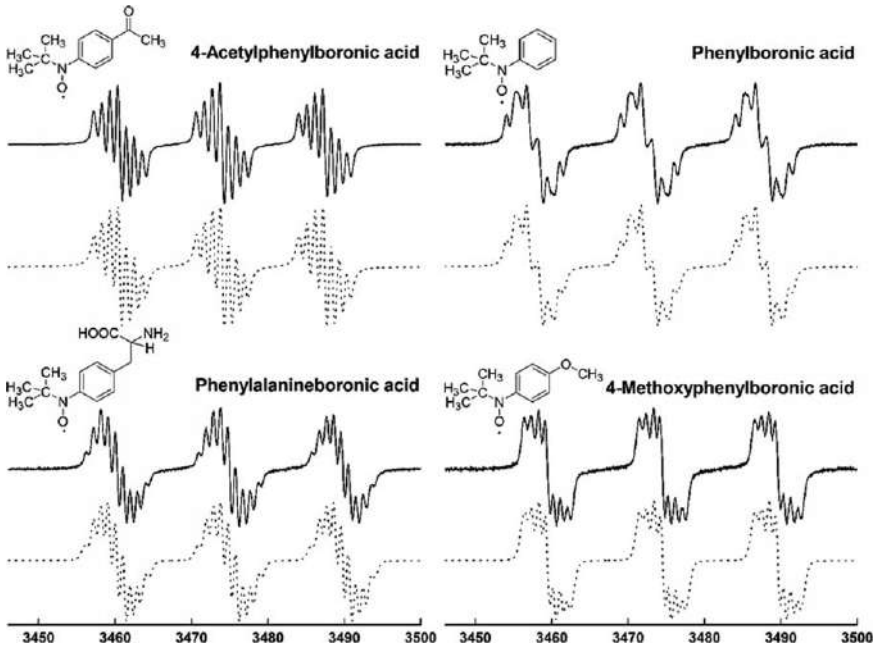

Figure 13.1 Experimental (solid lines) and simulated (dashed lines) EPR spectra of the spin adducts to MNP of phenyl radical produced during the reaction of different phenylboronates with $ONOO^-$.
Reproduced from ref. 49 with permission from American Chemical Society, Copyright 2011.

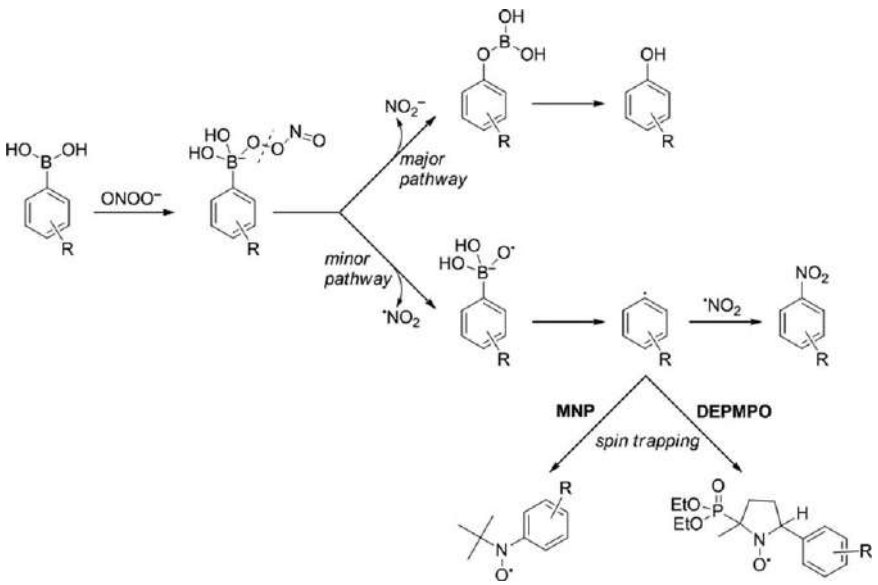

Scheme 13.6 Formation and trapping of the phenyl radical in the minor pathway of the reaction of boronic acids with $ONOO^-$.

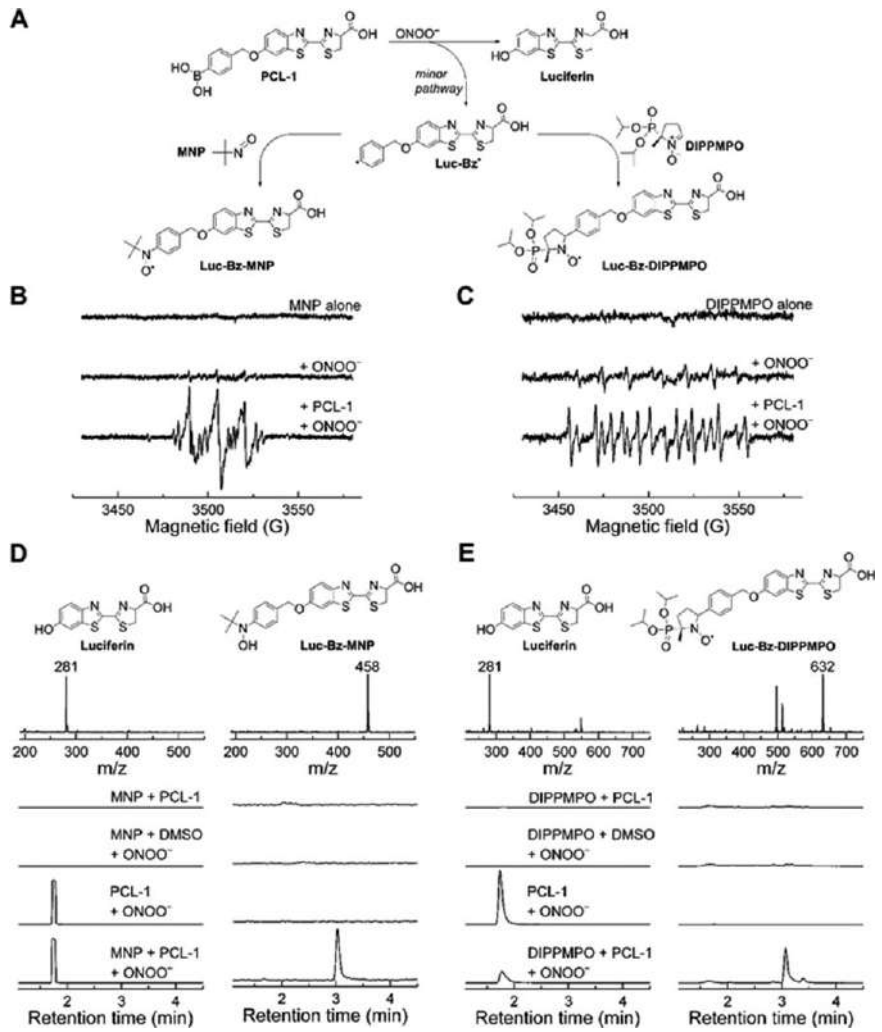

Figure 13.2 Studies of the mechanism of the reaction between PCL-1 and $ONOO^-$, using EPR spin trapping in combination with liquid chromatography–mass spectrometry analyses of the spin adducts.
Reproduced from ref. 50 with permission from Elsevier, Copyright 2016.

When spin-trapping experiments using the MNP spin trap were performed on phenylboronates bearing the bulky triphenylphosphonium moiety, attached to the phenyl ring *via* a methylene group in positions *ortho*-, *meta*- and *para*- to the boronate group, the spin-trapping results were significantly affected by the relative position of both groups (Figure 13.3).

In the case of the *para* position, a spectrum of the spin adduct displayed an additional hyperfine splitting due to the spin interaction with the phosphorus atom; however, no such splitting was observed in the case of the *meta*

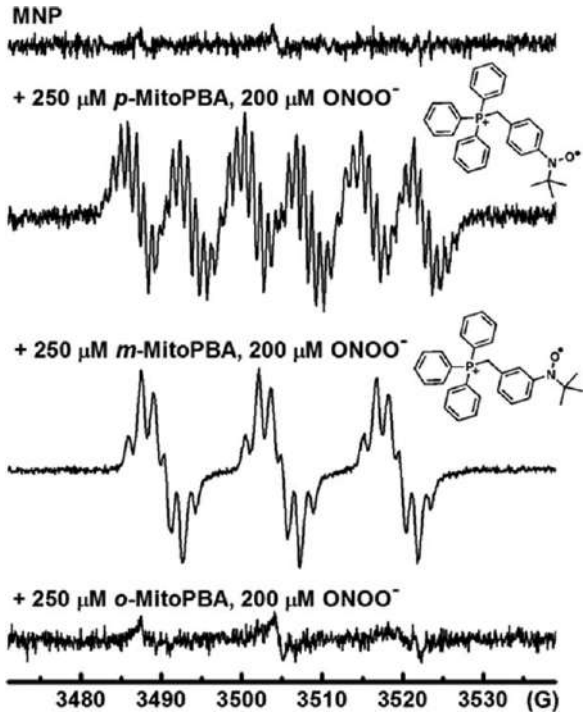

Figure 13.3 EPR spectra of the spin adducts formed during the reaction between *ortho*-, *meta*- and *para*-isomers of MitoPhB(OH)$_2$ (MitoPBA) probes and $ONOO^-$ in the presence of the MNP spin trap. Reproduced from ref. 51 with permission from American Chemical Society, Copyright 2013.

isomer, and no EPR signal was detected in case of the *ortho* isomer (Figure 13.3). Because the yield of the phenyl radical was similar for all three isomers, the lack of trapping of the phenyl radical in the case of the *ortho* isomer must be due to steric hindrance, resulting in a slower trapping reaction and rapid intramolecular scavenging of the phenyl radical *via* a cyclization reaction.[51] In fact, the identification and quantitation of the products of the reaction indicate that the nitrobenzene type product (*o*MitoPhNO$_2$) is formed with only 0.5% yield, and the predominant minor product (10.5% yield) is *cyclo*-*o*MitoPh (Scheme 13.7).[52]

The DEPMPO spin trap was used to detect phenyl radicals during the reaction of 4-acetylphenylboronic acid (APBA) with $ONOO^-$ produced *in situ* from co-generated fluxes of superoxide radical anion ($O_2^{\bullet -}$) and nitric oxide radical ($^\bullet$NO, Figure 13.4). Incubation of DEPMPO with an enzymatic superoxide-generating system (xanthine/xanthine oxidase, X/XO) led to the formation of the superoxide spin adduct, and the signal was completely inhibited in the presence of superoxide dismutase (SOD). The addition of an $^\bullet$NO-donor resulted in the appearance of the EPR spectrum attributable to the hydroxyl radical adduct, consistent with the spontaneous decomposition of $ONOO^-$

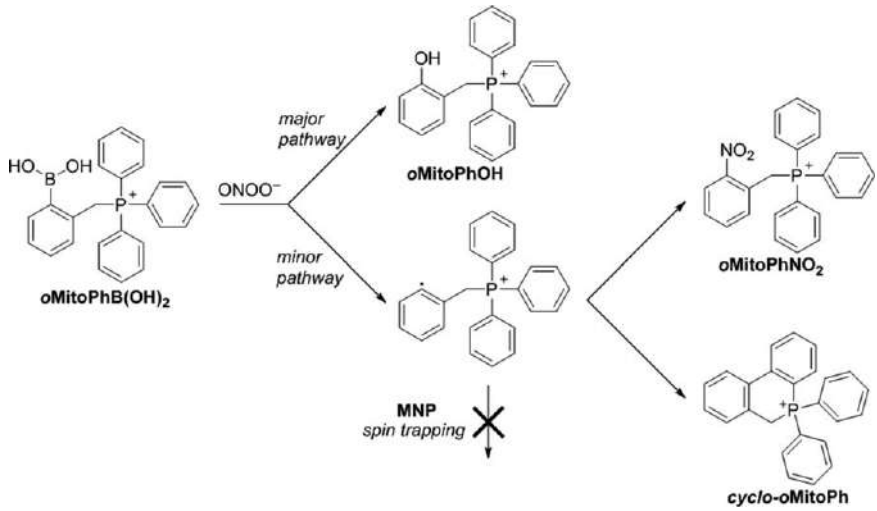

Scheme 13.7 Phenyl radical formed from *o*MitoPhB(OH)$_2$ probe undergoes rapid cyclization, and no EPR signal can be detected using the MNP spin trap.

with the formation of the hydroxyl radical, HO$^{\bullet}$. Similar to the reaction with bolus ONOO$^-$, the APBA reaction with ONOO$^-$ generated *in situ* leads to the appearance of the 12-line spectrum attributed to the phenyl radical adduct.

Interestingly, when APBA was added to the superoxide-generating system in the absence of $^{\bullet}$NO donor, the spectrum of the hydroxyl radical adduct – rather than the EPR spectrum of the superoxide adduct – was detected. The signal was fully inhibitable by SOD; this indicates that the hydroperoxyl adduct is reduced to the hydroxyl adduct by the boronate compound (Scheme 13.8).[49]

This implies that boronates can be used for nonenzymatic conversion of the superoxide spin adduct to hydroxyl radical spin adduct, *e.g.*, for spectral characterization of the hydroxyl adduct and to confirm the identity of the superoxide adduct. This approach was applied recently for a spin trap embedded in mesoporous silica particles.[53] Furthermore, during the spin adduct reduction, boronate undergoes oxidation to the phenolic product, opening up the possibility of detecting the superoxide spin adduct by monitoring SOD-dependent oxidation of fluorogenic boronate probes.[54]

13.2.2 Generation of Superoxide upon One-electron Oxidation or Reduction of Redox Probes

Most spectrophotometric and luminescence-based probes for biologically relevant radicals rely, at least in part, on relatively strong one-electron oxidizing or reducing properties of the radical species.[55–57] Therefore, probe-derived one-electron oxidized or reduced radical species are obligatory intermediates during the conversion of redox probes into the detectable products.[55] It has been demonstrated that numerous probes used to detect biological radicals can react with oxygen to produce superoxide upon

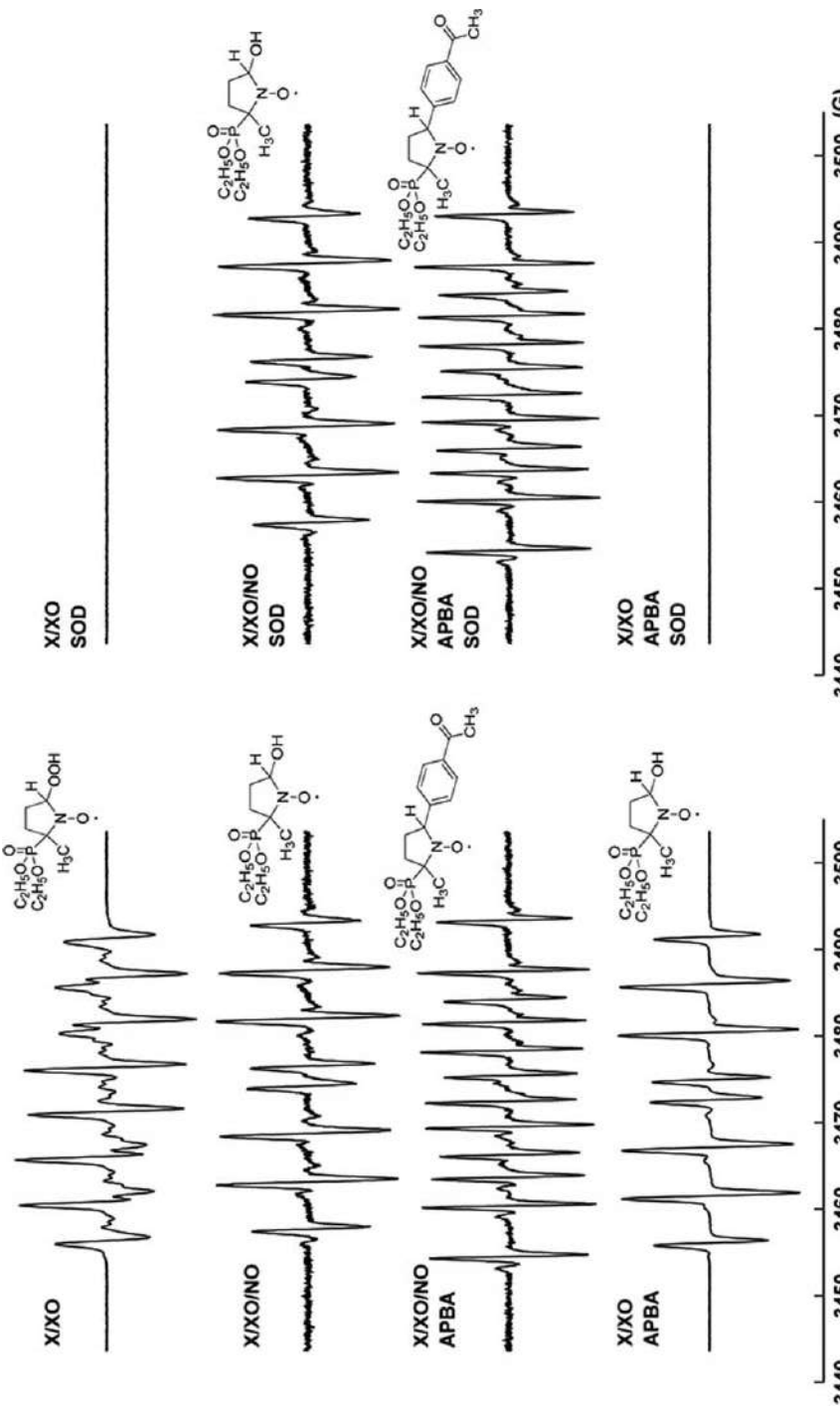

Figure 13.4 EPR spectra of the radical adducts formed during incubation of xanthine/xanthine oxidase (X/XO, enzymatic $O_2^{\bullet-}$ generator) with DEPMPO spin trap, and the effect of $^{\bullet}NO$, boronate (APBA) and superoxide dismutase (SOD). Reproduced from ref. 49 with permission from American Chemical Society, Copyright 2011.

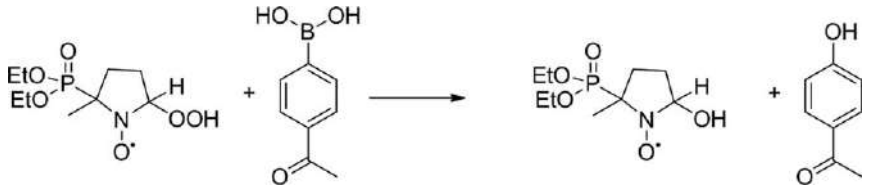

Scheme 13.8 Reduction of the superoxide adduct to DEPMPO by phenylboronate.

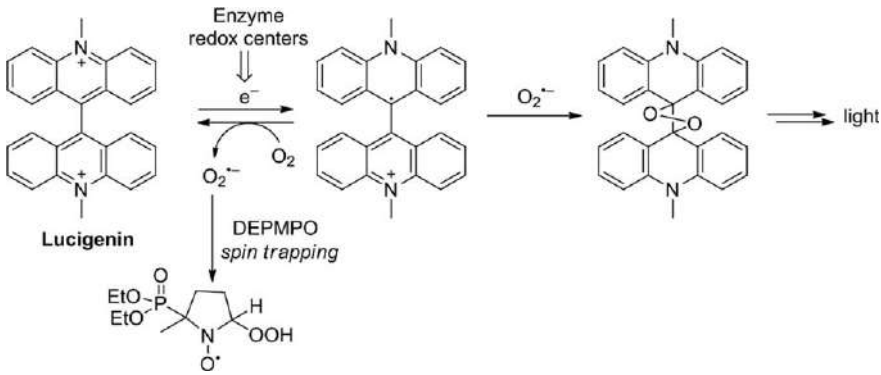

Scheme 13.9 Production and trapping of $O_2^{\bullet -}$ upon one-electron reduction of lucigenin by enzyme redox centers.

one-electron oxidation or reduction.[58–62] This is a significant limitation of the many redox probes for reactive oxygen species (ROS), as ROS-independent probe oxidation/reduction may lead to ROS formation. Determination of the ability of the probe to produce $O_2^{\bullet -}$ is not trivial, leading to controversies regarding the utility of many widely used redox probes. EPR spin trapping of probe-derived radicals and $O_2^{\bullet -}$ was instrumental in the investigation of those phenomena. Among the probes for $O_2^{\bullet -}$, lucigenin and nitroblue tetrazolium (NBT) are cationic compounds, whose ability to detect $O_2^{\bullet -}$ is based on its reducing properties and the reaction of the second $O_2^{\bullet -}$ molecule with the intermediate radical. In the case of lucigenin, the reaction of the probe radical with $O_2^{\bullet -}$ leads to spontaneous emission of blue luminescence. However, it has been demonstrated using DEPMPO-based spin trapping that lucigenin may act as a one-electron redox cycling agent, accepting electrons from redox centers of the proteins and passing them to molecular oxygen to form $O_2^{\bullet -}$ (Scheme 13.9).[63,64] The reaction of the lucigenin radical cation with oxygen has been subsequently confirmed by monitoring the decay of this intermediate in the presence of oxygen using the pulse radiolysis technique.[60]

In the case of the NBT probe, reduction by superoxide results in the formation of a blue-colored formazan, detectable by spectrophotometry. However, with the help of the DEPMPO spin trap, it has been demonstrated that NBT can stimulate $O_2^{\bullet -}$ generation by nitric oxide synthase.[65] This observation

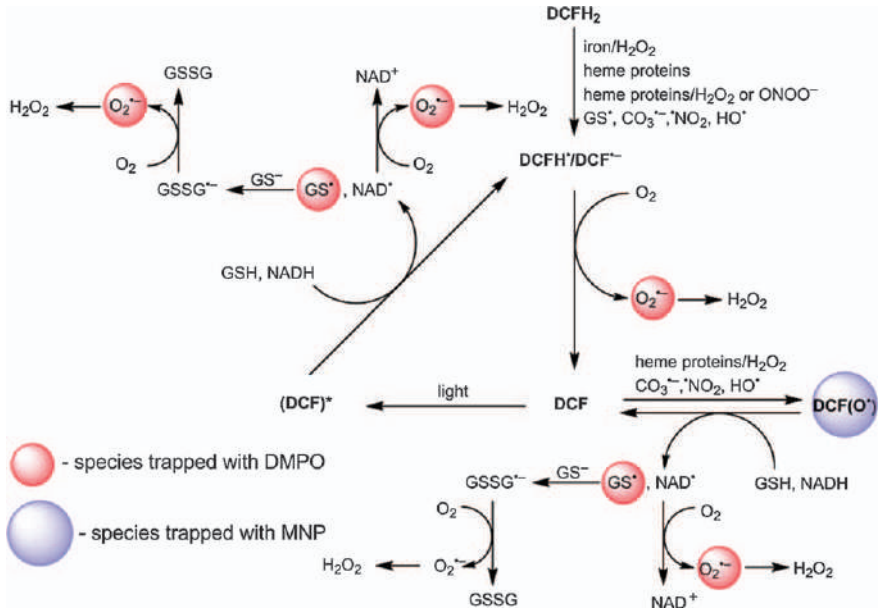

Scheme 13.10 Free radical chemistry of the DCFH probe. The species identified by EPR spin trapping are indicated.

points to the redox cycling ability of the intermediate radical formed upon one-electron reduction of NBT in a reaction similar to that described for the lucigenin radical cation (Scheme 13.10).

Several widely used redox probes (*e.g.*, dichlorofluorescin [DCFH], dihydrorhodamine and hydroethidine) are the products of two-electron reduction of commonly used fluorophores, dichlorofluorescein (DCF), rhodamine 123 and ethidium. Upon reoxidation of those probes, the fluorescent products are formed, providing a fluorescence-based assay for cellular oxidants. Among those probes, the DCFH probe continues to be widely used as a probe for cellular ROS, and multiple reports have focused on its reactivity and applicability for ROS measurements.[66–68] Spin trapping was instrumental in understanding the mechanism of probe oxidation and the possibility of producing superoxide by the probe. Use of the DMPO spin trap has demonstrated that $O_2^{\bullet -}$ is formed upon one-electron oxidation of DCFH by H_2O_2 or $ONOO^-$ in the presence of peroxidase, implicating the ability of the intermediate radical to reduce oxygen.[69,70] This is consistent with the pulse radiolysis report that demonstrated the reaction of DCFH-derived radical with oxygen.[62] The ability of the DCFH radical to produce $O_2^{\bullet -}$, which dismutates into H_2O_2, led to self-propagation of DCFH oxidation in the presence of peroxidase, pointing to a significant limitation in the use of the probe for ROS detection, as any species capable of oxidizing DCFH to its radical would initiate H_2O_2-dependent catalase-inhibitable probe oxidation.[69,70] The same radical can be formed by photoreduction of the

fluorescent product, DCF, in the presence of bioreductants (reduced glutathione [GSH], reduced nicotinamide adenine dinucleotide [NADH]).[71] In such a case, spin trapping with DMPO confirmed the formation of superoxide, which can be formed *via* reduction by the DCF-derived radical and due to radical chemistry of the thiyl radical ($GS^{\bullet}$) and $NAD^{\bullet}$ radical formed.[71] It also has been demonstrated that the fluorescent product, DCF, is a substrate for peroxidase and undergoes oxidation to a phenoxyl radical. The formation of such a radical was confirmed by the detection of the EPR spectrum of the DCF radical adduct to the MNP spin trap.[72] The DCF phenoxyl radical reacts with GSH and NADH to form the corresponding radicals, which in turn reduce oxygen to $O_2^{\bullet -}$, as confirmed by EPR spin trapping using DMPO.[72] While in the presence of GSH, the $GS^{\bullet}$ adduct was observed; in the case of NADH, the superoxide adduct was detected.[72] The overall radical chemistry of the DCFH/DCF system and the spin trapped radical species is shown in Scheme 13.10.

DCFH is not unique in its ability to photosensitize oxidation of bioreductants (*e.g.*, NADH), with the formation of $O_2^{\bullet -}$. For example, resorufin, the product of Amplex Red oxidation, was shown to undergo photoreduction followed by reoxidation in the presence of oxygen. The use of DMPO has demonstrated that $O_2^{\bullet -}$ is formed upon photoreduction of resorufin in the presence of NADH.[73] Also, the Amplex Red probe can serve as an electron donor in place of NADH in an analogous reaction.[74]

13.3 Application of the Spin-trapping Technique to Detect Biologically Relevant Radicals

In biological systems, radicals can be formed as reaction intermediates or end products of enzymatic reactions. In addition, biologically relevant radicals are formed starting from superoxide and/or nitric oxide in a cascade of reactions involving ROS and reactive nitrogen species, and their interaction with biomolecules (Scheme 13.11).

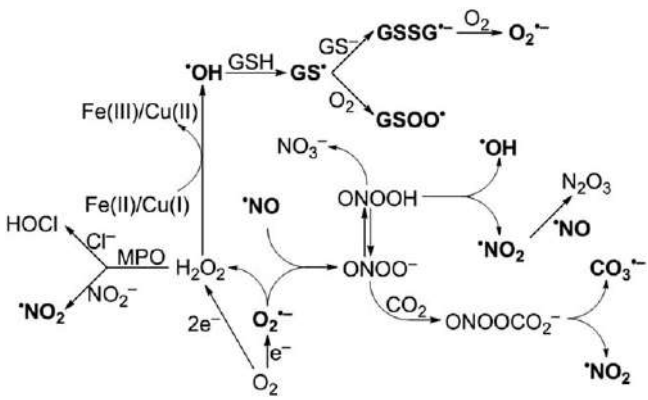

Scheme 13.11 ROS network and radical species formed.

The spin trap to be used for a specific radical species should be chosen based on the kinetics of the reaction of the species with the spin trap, the stability of the adduct formed (*kinetic requirement*) and the spectroscopic properties of the spin adduct, allowing for unambiguous identification of the radical trapped (*spectral requirement*). Recently, application of a cocktail of different spin traps was proposed to trap a wide range of radicals in a single experiment.[75] In the case of biological systems, the cellular/subcellular localization *in vitro* and/or pharmacokinetic properties *in vivo* also should be considered. In any case, the spin trap should not be toxic and should not in other ways perturb the system under investigation. As a general rule, nitroso spin traps are useful for the detection of carbon-centered radicals, while cyclic nitrones traps are choice for studying oxygen- or sulfur-centered radicals.

13.3.1 Superoxide Radical Anion/Hydroperoxyl Radical

Superoxide radical anion ($O_2^{\bullet -}$), a product of the one-electron reduction of molecular oxygen, is not stable and undergoes spontaneous dismutation, involving its protonated form (hydroperoxyl radical [$HO_2^{\bullet}$]) to produce hydrogen peroxide:

$$O_2^{\bullet -} + HO_2^{\bullet} + H^+ \rightarrow O_2 + H_2O_2$$

Therefore, the spin trap has to compete not only with other targets of superoxide (*e.g.*, superoxide dismutases) but also with the self-dismutation reaction. This is a pH-dependent, second-order process, and the lifetime of superoxide can be increased under the conditions of low fluxes of $O_2^{\bullet -}$ and higher pH of the solution. Although initial attempts to spin trap superoxide were done using nitrosoalkyl and linear nitrone spin traps, the short lifetime of the adduct formed[76] makes those spin traps nonpractical. Although the rate constant of the reaction of the DBNBS spin trap with superoxide was determined by pulse radiolysis to equal 4.4×10^7 $M^{-1}\,s^{-1}$, the primary spin adduct decomposes within 1 s in a second-order reaction, with the rate constant of 5.7×10^6 $M^{-1}\,s^{-1}$.[76] On the other hand, although the reaction of cyclic nitrones with $O_2^{\bullet -}$ is significantly slower ($k\sim10^0$–10^2 $M^{-1}\,s^{-1}$),[17,77–82] their good water solubility and the superior stability of the spin adduct make them the spin traps of choice for $O_2^{\bullet -}$ detection (Scheme 13.12).

Due to the slow kinetics of trapping, a high concentration of the spin traps is required (typically ≥50 mM). Initially, DMPO was utilized for the detection of superoxide.[83] However, the superoxide spin adduct to DMPO has a half-life of 50 s,[84] and its decomposition is accompanied by the appearance of a hydroxyl

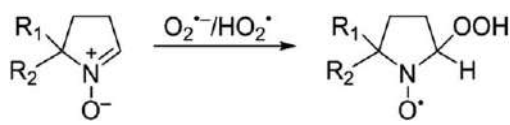

Scheme 13.12 Trapping of superoxide ($O_2^{\bullet -}/HO_2^{\bullet}$) by cycling nitrones.

radical spin adduct, creating a potential for misidentification of the radical trapped. The exact mechanism of the superoxide adduct decay and the extent of its conversion into the hydroxyl radical adduct remain to be established.[17,85–88] Several derivatives and analogs of DMPO have been designed and synthesized, with the aim of increasing the rate of superoxide trapping, extending the lifetime of the spin adduct and avoiding spontaneous conversion into the hydroxyl radical adduct.[89–93] Currently, DEPMPO and DIPPMPO (Scheme 13.4) and their derivatives seem to be the most optimal spin traps for the detection of superoxide.[53,89,90,94–97] The presence of a phosphorus atom leads to an increased (doubled) number of lines in the EPR spectrum, which leads to lower sensitivity; however, this is compensated by an increased lifetime of the radical adduct. Additional hyperfine splitting by phosphorus makes it more straightforward to distinguish adducts of different radicals and deconvolute spectra of the mixture of the adducts. DEPMPO has been extensively used in biochemical studies investigating superoxide production.[42,63,65,98–102] For example, the ''uncoupling'' of nitric oxide synthase leading to the production of superoxide was studied, and the role of the presence/concentration of enzyme cofactors was determined.[42,65,99–102]

The superoxide adduct to cyclic nitrones is subject to the reducing agents and enzymes, including GSH and glutathione peroxidase, respectively. In such cases, the superoxide adduct is converted into the hydroxyl radical adduct, even in the case of spin traps, which avoid the spontaneous conversion. This is an important limitation of all small-molecule spin traps forming hydroperoxyl radical adducts. Embedding cyclic nitrones and/or spin adducts in the macrocyclic structures and particles has been shown as a promising strategy to protect the superoxide radical adduct from the low-molecular-weight and enzymatic reductants.[53,103–111] As a general rule, the detection of superoxide by spin trapping should be accompanied by a demonstration of the sensitivity of the signal to inhibition by superoxide dismutase, a powerful enzymatic scavenger of $O_2^{\bullet -}$.

13.3.2 Hydroxyl Radical

Hydroxyl radical ($^{\bullet}OH$), one of the strongest oxidants generated in biological systems, exhibits high reactivity toward most biomolecules. In addition, in the absence of scavengers, $^{\bullet}OH$ decomposes in a rapid bimolecular reaction to form H_2O_2:

$$2^{\bullet}OH \rightarrow H_2O_2$$

Therefore, a high concentration of the spin trap is required to detect $^{\bullet}OH$ in the presence of other scavengers, and detecting $^{\bullet}OH$ in biological systems remains a challenge. Cyclic nitrones are typically used to detect $^{\bullet}OH$, due to the relatively long lifetime of the adduct formed.[83] However, because of the potential to form the $^{\bullet}OH$ adduct in systems generating other oxygen-centered radicals (*e.g.*, $CO_3^{\bullet -}$), the confirmatory experiments for the presence of $^{\bullet}OH$ always should be performed. Typically, the addition of $^{\bullet}OH$

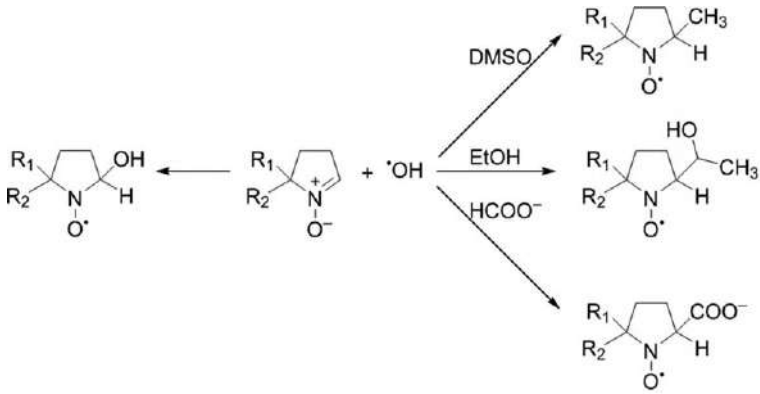

Scheme 13.13 Spin trapping of the hydroxyl radical and the effect of •OH scavengers on the identity of the spin adduct formed.

scavengers, known to produce secondary radicals, which could be trapped and produce characteristic EPR spectra, is the preferred way to identify •OH. Dimethyl sulfoxide (DMSO), ethanol (EtOH) or formate ($HCOO^-$) are most often used for this purpose (Scheme 13.13).

$$^{\bullet}OH + (CH_3)_2SO \rightarrow CH_3SO_2H + {}^{\bullet}CH_3$$

$$^{\bullet}OH + CH_3CH_2OH \rightarrow CH_3{}^{\bullet}CHOH + H_2O$$

$$^{\bullet}OH + HCOO^- \rightarrow CO_2{}^{\bullet -} + H_2O$$

As an example, the incubation of the Fenton reagent with the BMPO spin trap resulted in the appearance of the hydroxyl radical adduct; however, the adduct was not formed in the presence of bromide, and the spectra of $CH_3{}^{\bullet}CHOH$ and $CO_2{}^{\bullet -}$ radical adducts were detected when EtOH or $HCOO^-$, respectively, were present in the solution (Figure 13.5).[112]

13.3.3 Nitrogen Oxides

Nitric oxide (•NO) is a stable radical with an important role in cellular signaling. In the presence of oxygen, it undergoes oxidation *via* ONOO•, $^{\bullet}NO_2$ and N_2O_3 to nitrite. Nitrogen dioxide ($^{\bullet}NO_2$) can be also formed from $ONOO^-$, a product of the reaction of •NO with $O_2{}^{\bullet -}$ or *via* myeloperoxidase-catalyzed oxidation of nitrite anion by H_2O_2 (Scheme 13.11).

EPR spin trapping of •NO, ONOO• and $^{\bullet}NO_2$ is challenging due to the inefficiency of trapping and/or instability of the spin adducts when using nitrones or nitroso spin traps. Alternative approaches have been proposed and used for the detection of nitrogen oxides by EPR spectroscopy both *in vitro* and *in vivo*.[113–116] This includes the development of novel spin traps based on the reaction of *cis*-dienes with •NO or $^{\bullet}NO_2$ to produce stable nitroxides (Scheme 13.14).[117,118] These compounds, called NO cheletropic traps (NOCT), have shown the ability to trap •NO in organic solvents and in some model

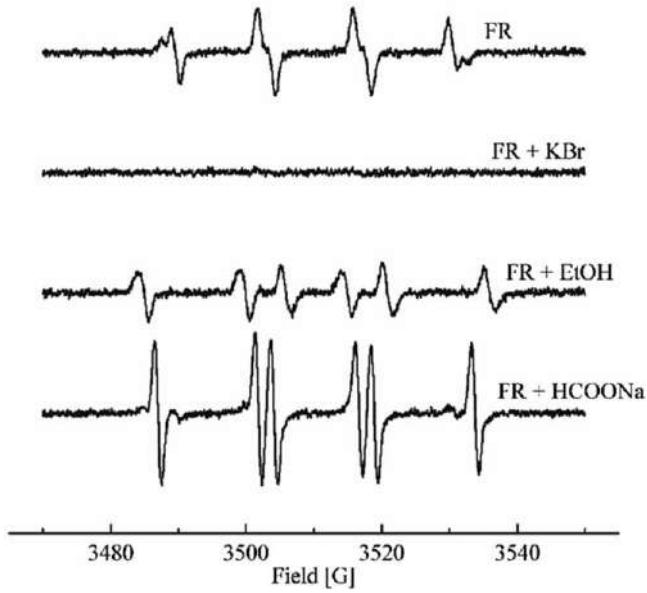

Figure 13.5 Effect of hydroxyl radical scavengers on the EPR spectrum recorded during incubation of the BMPO spin traps with the Fenton reagent (FR). Reproduced from ref. 109 with permission from Elsevier, Copyright 2006.

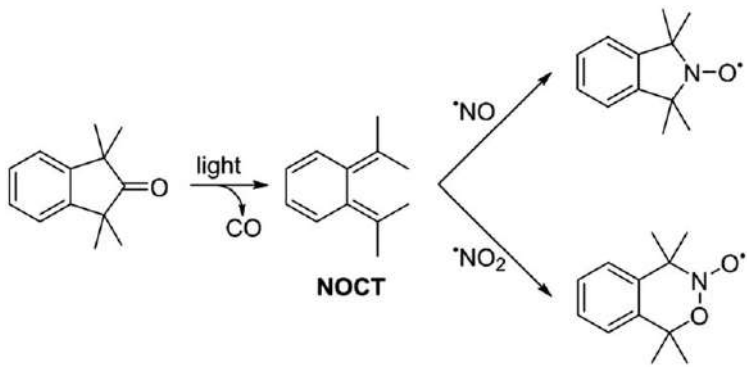

Scheme 13.14 NOCT traps for the detection of •NO and $^{\bullet}NO_2$.

cellular systems, but their wider application was limited due to their poor aqueous solubility and stability. To overcome the low stability issue, NOCT traps are formed *in situ* by photolysis of the carbonyl precursors.[119] Further reports extended NOCT into the fluorescence detection modality,[120–122] and new chemical structures for improved NOCT probes have been proposed, and mechanistic details of the trapping process explored.[123–127]

Also, a spin-trapping approach for •NO and $^{\bullet}NO_2$ using deprotonated nitroalkanes has been reported. Upon deprotonation, nitromethane and

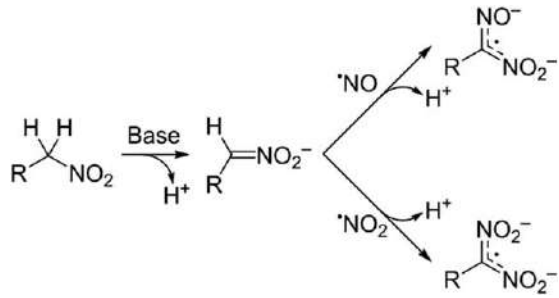

Scheme 13.15 Spin trapping of •NO and $•NO_2$ using nitroalkanes under basic conditions.

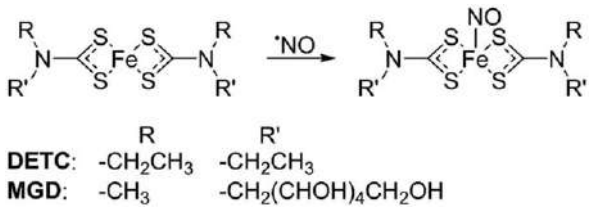

Scheme 13.16 Detection of •NO using iron–dithiocarbamate complexes.

longer chain homologs act as spin traps, reacting, *e.g.*, with •NO and $•NO_2$, forming stable dianionic nitrosonitro or dinitro spin adducts (Scheme 13.15).[128–130] Although this reaction has been used for the detection of $•NO_2$,[131,132] it is limited to strong alkaline solutions (pH > 10) and thus is not suitable for most biological systems.

One of the features of the chemical reactivity of •NO is its rapid reaction with metal complexes. This has been utilized to design iron–dithiocarbamates complexes as spin traps for •NO. As one of the first of such complexes, iron(II) diethyldithiocarbamate $Fe^{2+}(DETC)_2$ (Scheme 13.16) has been synthesized, and its reactivity toward •NO and EPR spectrum of the resulting nitrosylated complex characterized.[133,134] Low aqueous solubility of the $Fe^{2+}(DETC)_2$ complex significantly limits its applicability to detect •NO in biologically relevant systems. Introduction of the carboxylic functionality or glucamine (MGD) into the dithiocarbamate ligand (Scheme 13.16) improves the solubility of the complex, and such probes have been used to detect •NO in cell suspension, isolated tissues and animal models *in vivo*.[135–138]

Another class of spin probes for •NO is nitronyl nitroxides.[139–141] Trapping of •NO, followed by elimination of $•NO_2$, results in the formation of the imino nitroxide product (Scheme 13.17), with a characteristic EPR spectrum.[139,142,143] Linking the nitronyl nitroxide to pyrene fluorophore enabled the detection of •NO by fluorescence spectroscopy, due to differences in the fluorescence quenching capacity between the nitronyl nitroxide and imino nitroxide moieties.[144]

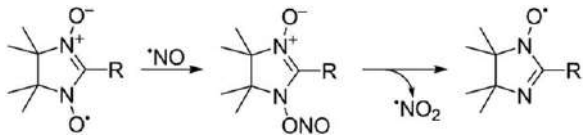

Scheme 13.17 Reaction of •NO with nitronyl nitroxides.

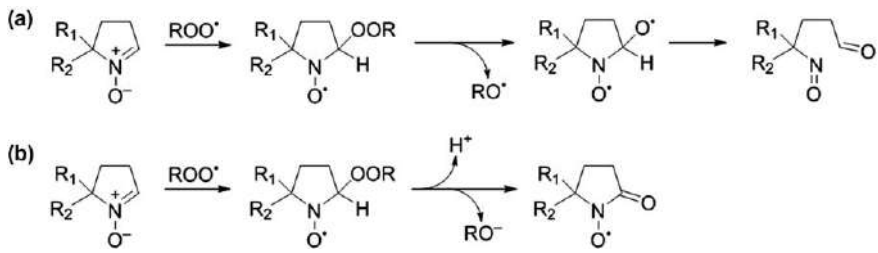

Scheme 13.18 Formation and decomposition of the peroxyl radical adducts to selected spin traps.

13.3.4 Alkyl Radicals

Alkyl radicals are obligatory intermediates of lipid peroxidation. Their detection can be accomplished using both nitrones and nitroso spin traps.[145–150] The choice of the actual spin trap may be affected by the environment of the alkyl radical (*e.g.*, lipophilicity) and the requirement for identification of the radical trapped. Nitroso spin traps typically produce EPR spectra with a stronger influence from the trapped radical, resulting in more pronounced hyperfine splitting (see Figure 13.1 *vs.* Figure 13.4). Like most carbon-centered radicals, alkyl radicals react rapidly with molecular oxygen ($k \sim 10^9$ M^{-1} s^{-1}), forming peroxyl radicals.

$$R^{\bullet} + O_2 \rightarrow ROO^{\bullet}$$

Therefore, the competition between the spin trap and oxygen and/or other scavengers should be considered, and the spin trap concentration appropriately chosen for efficient spin trapping of the species of interest.

13.3.5 Peroxyl Radicals

Efficient trapping of alkylperoxyl radicals and identification of the corresponding spin adducts are challenging tasks due to the instability of the spin adduct. In fact, numerous claims of the detection of the peroxyl radical spin adducts have been revised, and the adducts reassigned to alkoxyl radical adducts.[151,152] A homolytic cleavage of the O–O bond in the peroxyl radical spin adduct results in elimination of the alkoxyl radical and formation of nitrosoaldehyde (Scheme 13.18a).[153] Trapping of the eliminated alkoxyl radical by another molecule of the spin traps results in formation of the radical

adduct, potentially confusing the spectral assignment of the radical adduct detected. Also, the base-catalyzed heterolytic cleavage of the O–O bond in the spin adducts has been reported for the peroxyl radical adducts to DMPO (Scheme 13.18b) and PBN spin traps.[154,155] In those cases, elimination of alcohol results in the formation of EPR-active α-oxo nitroxide.

13.3.6 Thiyl Radicals

Thiyl radicals are formed upon one-electron oxidation of thiols, typically electron transfer from the thiolate anion or hydrogen atom transfer from the thiol. Thiyl radicals can dimerize to form disulfides. In the presence of excess thiols, the thiyl radicals can also form disulfide radical anion, which subsequently reduces oxygen to form superoxide and disulfide (as shown for $GS^{\bullet}$ in Scheme 13.11). The most common class of spin trap used to detect $GS^{\bullet}$ and other thiyl radicals is cyclic nitrones, including DMPO and DEPMPO, due to a high rate constant of trapping reaction and the improved stability of the spin adduct.[91,95,156–160] For both DMPO and DEPMPO, the reversibility of the spin adduct formation was reported, and the possibility of the addition of the thiol to a double bond of the spin trap was investigated.[161] The possibility of spin adduct formation *via* the Forrester–Hepburn mechanism (Scheme 13.4a) was also demonstrated.[161] To avoid the potential occurrence of inverted spin trapping (Scheme 13.4b), DEPMPO may be a preferred spin trap, due to a wider redox window, when strong oxidants are used to generate the thiyl radicals.[156] DEPMPO and its mitochondria-targeted analog, Mito-DEPMPO, also produce more stable spin adducts compared with DMPO.[95,162] Because the spectral patterns of the hydroxyl radical adduct and thiyl radical adducts are similar for both the DMPO and DEPMPO spin traps, the hyperfine splitting constants must be determined and compared with the values of independently prepared thiyl radicals in order to properly identify the radical adducts. A thiol oxidation-independent generation of thiyl radicals *via* photolysis of nitrosothiols or disulfides may be used for spectral characterization of the thiyl radical spin adducts.[156,163]

13.3.7 Protein-bound Radicals

Protein radicals, with the spin located on amino acid residues, are formed as intermediates in the catalytic mechanisms of several enzymes as well as the products of the interaction of proteins with ROS.[164–168] Direct detection has been accomplished in some cases; however, in most cases, the spin-trapping technique had to be applied to detect and identify the protein-bound amino acid radicals.[168,169] The amino acids involved include tyrosine, cysteine, tryptophan, histidine and lysine and represent phenoxyl, thiyl and nitrogen- and carbon-centered radicals.[160,170–174] Both nitroso (MNP, DBNBS) and nitrone (PBN, DMPO) spin traps have been used to detect protein-bound radicals. Interestingly, depending on the spin trap used, different types of spin adducts may be formed from the same amino acid radical. For example, the tyrosyl radical may produce phenoxyl-type (*via* phenolic oxygen) adduct

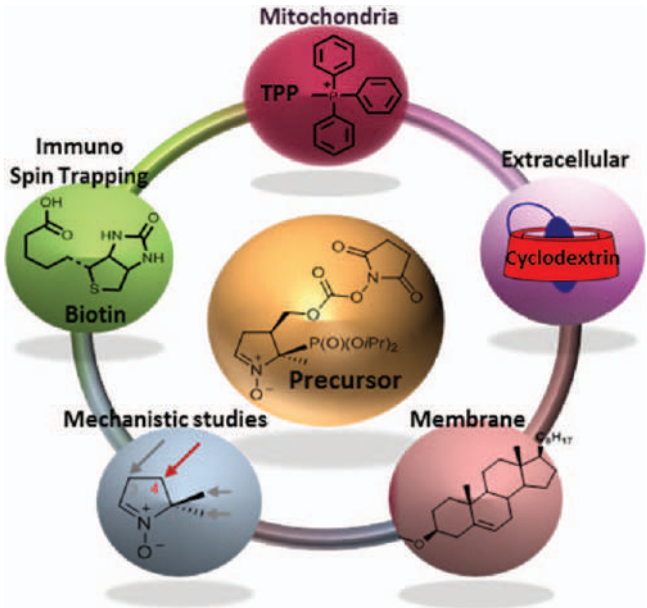

Figure 13.6 Examples of the derivatization strategies of the DIPPMPO spin trap for special applications.

to DMPO, while carbon-centered (*via* benzene ring carbon) radical adduct is formed in the presence of the MNP or DBNBS spin trap.[170,175,176]

Typically, the EPR spectra of protein-bound spin adducts exhibit partial anisotropy due to the limited mobility of the trapped residue(s).[37,38] Although this may limit the sensitivity (line broadening) and make spectral assignment difficult, immobilization of the spin adduct can significantly slow the bimolecular pathways of spin adduct decay, resulting in their improved stability and accumulation. This may help in overcoming the sensitivity issue, as well as in the characterization of the spin adducts by complementary techniques. Furthermore, once a sufficient amount of spin adduct is accumulated, the protein can be subjected to proteolysis to mobilize the spin adduct and minimize line broadening.[37,38]

13.4 Derivatization of the Spin Traps for Specific Applications

Derivatization of spin traps can be realized in different positions for special applications (Figure 13.6), including subcellular targeting or linking to supramolecular structures.

13.4.1 Targeting Spin Traps to Lipophilic Compartments

To study the lipid peroxidation processes, different PBN and EMPO derivatives that accumulate in lipophilic compartments have been prepared

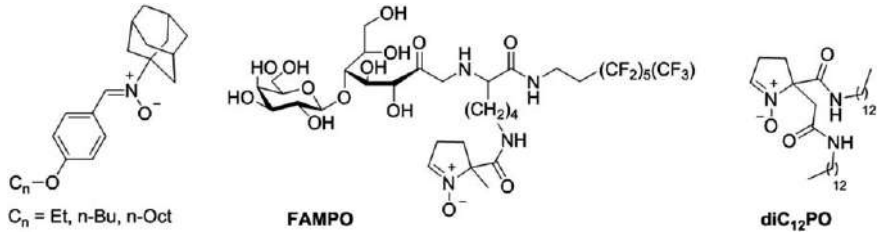

Scheme 13.19 Chemical structures of nitrone spin traps targeted to membranes.

Scheme 13.20 Examples of mitochondria-targeted spin traps.

(Scheme 13.19).[177] To determine the penetration of radicals into the membrane and to trap lipid radicals at a specific depth of the membrane, a series of spin traps were designed with the position of the radical-trapping nitrone moiety at chosen depths.[178] DEPMPO substituted by a cholesteryl group in position 5 was designed to target this spin trap to cholesterol-rich membrane domains, and its ability to trap various radicals including superoxide was reported.[179] Bitailed amphiphilic phenyl-*N*-*tert*-butylnitrone derivatives were designed and evaluated as inhibitors of oxidation of an unsaturated lipid, the 1,2- dilinoleoyl-*sn*-*glycero*-3-phosphocholine.[180] Lipophilic spin traps have been also tested as potential antioxidants for cell protection. FAMPO (Scheme 13.19), a nitrone bearing a fluorinated amphiphilic carrier, has been developed as a potential cytoprotective agent against H_2O_2-, $ONOO^-$- and hydroxynonenal-induced cell death.[181] A membrane-specific spin trap, 5-dodecylcarbamoyl-5-*N*-dodecylacetamide-1-pyroline-*N*-oxide (Scheme 13.19), was developed to selectively target intracellular membranes, with the option of labeling the probe with a fluorescent tag *via* strain-promoted alkyne–nitrone cycloaddition for fluorescence microscopic studies of probe intracellular localization.[182]

13.4.2 Mitochondrial Targeting

Mitochondria are one of the major sources of $O_2^{\bullet -}$ in cells, and development of reliable methods of site-specific detection of free radicals is an active area of research. The first mitochondria-targeted spin trap (Mito-PBN, Scheme 13.20) was reported by Murphy *et al.*[183] to study the mechanisms of $O_2^{\bullet -}$-induced activation of mitochondrial uncoupling proteins. Based on the determined chemical reactivity of the Mito-PBN spin trap, it was concluded that Mito-PBN was able to block $O_2^{\bullet -}$-induced mitochondrial uncoupling protein activation by scavenging carbon-centered radicals. Additional linear nitrones as

mitochondria-targeted antioxidant agents have been subsequently reported.[184] Those spin traps utilized arylpyridinium cations as the mitochondria-targeting moieties. For the purposes of EPR-based detection of mitochondrial free radicals, several cyclic nitrone-based mitochondria-targeted spin traps were developed. Mito-BMPO (Scheme 13.20) was synthesized, its ability to trap biologically relevant radicals confirmed, and the EPR spectra of radical adducts characterized.[185] The first mitochondria-targeted spin trap reported to detect mitochondria-generated $O_2^{\bullet -}$ was Mito-DEPMPO (Scheme 13.20).[94,95] Thereafter, more mitochondria-targeted spin traps bearing triphenylphosphonium were developed and their mitochondrial uptake characterized, but their ability to detect mitochondrial $O_2^{\bullet -}$ or other radicals remains to be established.[96,186] Further studies are needed to confirm the ability of the probes to detect free radicals in respiring mitochondria, and care must be taken to avoid perturbing mitochondrial function by the spin trap and/or targeting moiety. For example, triphenylphosphonium-linked compounds were shown to inhibit mitochondrial complex I.[187–191]

13.4.3 Grafting Spin Traps in the Supramolecular Structures

It was observed that binding of the spin traps to cyclodextrins (CDs) results in increased lifetime of the spin adducts and protects the adducts from bioreduction.[108–110,157,192] For example, a significant increase in the lifetime of the superoxide adduct to the PBN spin trap in the presence of β-cyclodextrin was reported.[110] Determination of the association constant led to the conclusion that the spin adduct (nitroxide) binds to the CDs stronger than the nitrone spin trap.[193] This suggests that although the nitrone may be present outside the CD, upon trapping $O_2^{\bullet -}$, it preferentially forms an inclusion complex, resulting in an increased lifetime of the spin adduct. However, the persistency of the superoxide spin adducts remained modest due to the very short half-life of the unbound spin adduct (PBN–OOH) present in the dynamic equilibrium with the CD-bound adduct. To improve the stabilizing effect of the cyclodextrins on the spin adducts, linear nitrones covalently grafted onto a β-cyclodextrin such as CD–PBN (Scheme 13.21) as spin-traps for $O_2^{\bullet -}$ were developed.[111] Although it was estimated that only

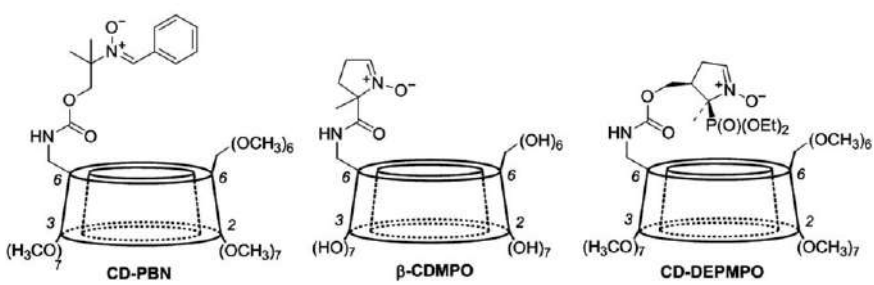

Scheme 13.21 General structures of CD-conjugated spin traps.

25% of the superoxide spin adduct is present as an inclusion adduct at equilibrium, the persistency of the adduct was significantly improved, with the EPR signal easily detectable 10 min after its formation.[111]

To further improve the trapping efficiency of $O_2^{\bullet -}$, cyclic nitrone spin traps such as β-CDMPO[103] and CD–DEPMPO[105] (Scheme 13.21) were covalently bound to β-cyclodextrins. In both cases, the persistency of the superoxide adduct and the rate of trapping were significantly increased, with the DEPMPO–OOH lifetime increased by >2-fold when conjugated to the β-CD (from 17 min for DEPMPO–OOH to 40 min for CD–DEPMPO–OOH).[105] Binding the DEPMPO spin trap to β-CD also resulted in slower nonenzymatic and GPx-catalyzed reduction by GSH. To further improve the spin-trapping behavior of the CD-conjugated cyclic nitrones, various DEPMPO-based spin traps, linked to a β-cyclodextrin with different alkyl chains on the phosphorus atom or with a long spacer arm linking the trap to CD, were synthesized and tested.[97] Although the persistency of the superoxide adducts was close to the value previously reported for CD–DEPMPO,[105] the limit of $O_2^{\bullet -}$ detection was significantly improved. However, no significant improvement was observed with regard to the resistance of the adducts to reduction by ascorbate or GSH. Embedding the traps in CD still afforded significant protection of the superoxide spin adduct from enzymatic reduction by glutathione peroxidase.[97] Additional studies aimed to improve the efficiency of the spin trapping of superoxide by cyclic nitrones, and increased bioavailability included synthesis of the CD–EMPO derivative where the EMPO cyclic nitrone was covalently bound to β-CD while also derivatized using an alkyl dodecyl chain for increased lipophilicity.[104] Another approach was explored by grafting a calix[4]pyrrole on the EMPO spin trap (CalixMPO) in order to improve the rate of trapping of $O_2^{\bullet -}$.[194] It was reported that the rate of trapping of $O_2^{\bullet -}$ in DMF as a solvent can be increased by over two orders of magnitude when compared with the DMPO spin trap.[194] Despite all these advances, only a limited amount of work has been done to determine the applicability of CD-linked spin traps to detect biological radicals. While evaluating the efficiency of different cyclic nitrones to trap extracellular $O_2^{\bullet -}$ generated from RAW 264.7 macrophages, CD–DIPPMPO showed the most improvement in the detection sensitivity of the superoxide adduct.[106] The trapping improvement was attributed not only to the protection of the spin adduct by β-CD but also to the impermeability of the CD-conjugated spin trap, preventing the interaction of the spin adduct with cell components capable of reducing/metabolizing the adduct. The CD–DIPPMPO spin trap enabled the measurement of $O_2^{\bullet -}$ production in unstimulated cells for the first time, with only a low (if any) amount of the hydroxyl adduct formation.[106,195]

An alternative to supramolecular chemistry was proposed by grafting for the first time a DEPMPO derivative on mesoporous silica (Figure 13.7) to enhance the protection of the spin adducts against bioreductants.[53] In addition to resistance to GSH-mediated reduction, the superoxide adduct exhibited an exceptional half-life of 3.5 h.[53] Although it was demonstrated that the trap can be used to detect cell-derived $O_2^{\bullet -}$, the spin adduct was

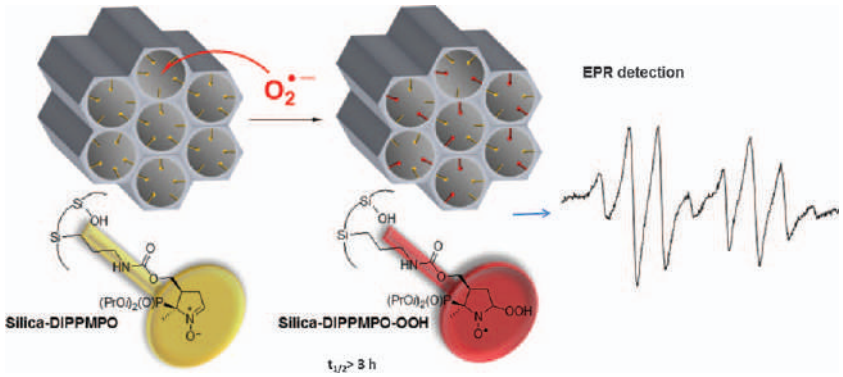

Figure 13.7 Spin trapping of superoxide using the DIPPMPO-based mesoporous silica SBA15 spin trap.
Reproduced from ref. 53 with permission from the Royal Society of Chemistry.

sensitive to the reduction by ascorbate. Future studies should focus on particle structural optimization to limit the ability of ascorbate to reduce the spin adduct and decrease the size of the particles in order to achieve the desired tissue/cell penetration properties.

13.5 Combination of Spin Trapping with Other Detection Modalities

13.5.1 Non-EPR Techniques to Detect Spin Adducts or Their Degradation/Transformation Products

The advantage of EPR spin trapping includes the ability for noninvasive monitoring of the spin adduct formation as well as spectroscopic characterization of the adduct, providing information on the identity of the radical trapped. However, in addition to the requirement of appropriate instrumentation and expertise in EPR, the technique can only report the EPR-active species, which in the case of spin adducts is typically nitroxide. Because nitroxides may undergo reduction or oxidation in EPR-silent species (Scheme 13.14), and because some spin adducts undergo some additional rearrangements, as discussed above, the EPR technique may not be sensitive enough when the rate of spin adduct decay is significantly higher than the rate of its formation. However, in many cases, the covalent bond between the radical trapped and the spin trap is retained during spin adduct degradation/transformation, resulting in the formation of a new product carrying structural information about the radical trapped. Therefore, an array of various detection modalities has been developed to complement and/or replace EPR-based detection, resulting in improved sensitivity and/or more detailed structural characterization of the adducts. These include nuclear magnetic resonance (NMR),[196] high-performance liquid chromatography with absorption,

electrochemical or mass spectrometric detection,[197–205] as well as immunodetection of the spin adducts[206–208] and their *in vivo* imaging by magnetic resonance imaging (MRI).[41] NMR and mass spectrometric[197,209] analyses proved to be especially useful in structural characterization of the adducts and identification of the radicals trapped. Labeling spin traps with NMR-active nuclei other than ^{1}H or ^{13}C provides unique opportunities for NMR spin trapping. In the case of spin traps containing a phosphorus atom (*e.g.*, DEPMPO, DIPPMPO), ^{31}P-NMR spin trapping may be used as a complementary technique to EPR of spin adducts to noninvasively monitor more stable, nonradical metabolites of the spin adducts.[39,196] The immuno-spin-trapping technique provides unparalleled sensitivity in the detection of the spin adducts of biological macromolecule-derived radicals (see Section 13.5.2).[40,207,208] Conjugation of the anti-DMPO antibody with the MRI contrast agents allows the detection of radicals *in vivo* using MRI technology.[41] The most recent development in the *in vivo* application of spin trapping includes the synthesis of the ^{13}C-labeled deuterated DMPO spin trap for *in vivo* free radical detection using the hyperpolarized ^{13}C-MRI technique.[210]

13.5.2 Immuno-spin Trapping

Originally developed in 2002, the immune-spin-trapping (IST) technique provided a novel, rigorous tool to detect free radical formation in biochemical and biological systems, without the requirement of EPR instrumentation and expertise, while providing increased sensitivity due to the stability of the detectable adducts and sensitive immunodetection techniques. IST combines the advantages of the chemistry of cyclic nitrone-based spin trapping of radicals with those of immunological techniques, including sensitivity, higher throughput and the opportunity to choose from several detection modalities. The method is based on the use of a nitrone-specific antibody and takes advantage of the covalent bond formed between the radical trapped and the spin trap and the fate of the spin adducts to cyclic nitrones. Due to the presence of the hydrogen atom in position α to the nitroxide nitrogen atom, nitrone-based spin adducts may undergo one-electron oxidation, forming highly stable nitrones (Scheme 13.22). Although the spin adduct is also subject to bioreduction to the corresponding hydroxylamine derivative, such a process is reversible, and, ultimately, most radical adducts to cyclic nitrones are transformed into the corresponding nitrones.

Nitrones bound to macromolecules (*e.g.*, proteins, DNA) can be recognized using an antibody specific to the nitrone, after separation from the spin trap. Currently, the only commercially available antibody to the cyclic nitrone is anti-DMPO, which has been extensively validated in model biochemical systems, as well as in cells *in vitro* and animal models *in vivo*.[207] The anti-DMPO-based IST technique has been used to detect amino acid radicals produced during exposure of various proteins to H_2O_2, including myoglobin,[211,212] hemoglobin,[213,214] neuroglobin,[215] thyroid peroxidase[216] and Cu,Zn-SOD.[217] In addition to protein radicals, the IST technique has been

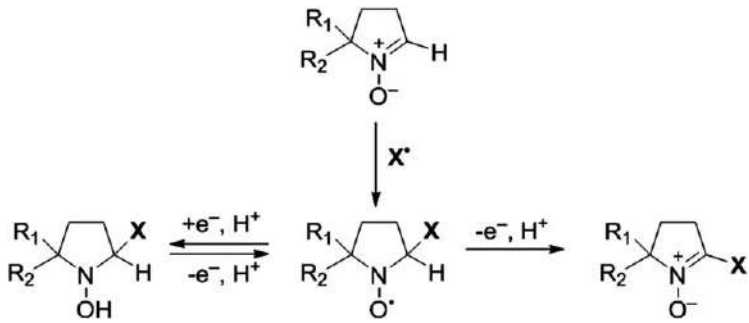

Scheme 13.22 Common metabolic pathways of the radical adducts to cyclic nitrones.

extended to DNA-based radicals.[208,218–223] While the technique does not provide information about the type of radical trapped/detected *per se*, combining IST with other techniques, including EPR, mass spectrometry and modifications in protein amino acid residues, provides a powerful approach for characterization of protein-based radicals.[224,225] The IST technique in combination with the EPR spin-trapping and mass spectrometry techniques has been used to study electron transfer between the tyrosine radical and cysteine amino acid in selected heme proteins exposed to H_2O_2 or $ONOO^-$.[226] IST has been applied to study protein radical formation in cells *in vitro*, including H_2O_2-induced oxidation of hemoglobin in red blood cells,[213] hypochlorous acid-induced catalase inactivation in hepatocytes,[227] xenobiotic-induced protein oxidation in HepG2 cells, modification of MPO in PMA-activated human neutrophils in the presence of sulfite[228] and lipopolysaccharide-induced, $ONOO^-$-mediated protein oxidation in BV2 microglial cells.[229] *In vivo* applications of IST to detect protein radicals include the genetic model ($SOD1^{G93A}$) of amyotrophic lateral sclerosis,[230] the maneb- and paraquat-induced mouse models of Parkinson's disease[231] and the lipopolysaccharide-based mouse model of sepsis.[232,233] Conjugation of the anti-DMPO antibody with MRI contrast agents enabled the IST technique to be combined with MRI-based detection for *in vivo* detection and localization of macromolecule free radicals.[41]

Other approaches for immuno-spin trapping involved the conjugation of the cyclic nitrone (DMPO or DEPMPO) to biotin moiety.[234,235] Although such spin traps are larger, their potential advantage is the insensitivity of the assay to the decomposition of the spin adduct, as long as the biotin moiety is still attached to the macromolecule that formed the radical, and the ability to use streptavidin-based particles to capture, concentrate and characterize the trapped macromolecule.

References

1. B. Halliwell and J. M. Gutteridge, *Free Radicals in Biology and Medicine*, Oxford University Press, USA, 2015.

2. J. F. Wishart and D. G. Nocera, *Photochemistry and Radiation Chemistry: Complementary Methods for the Study of Electron Transfer*, ACS Publications, 1998.
3. G. M. Rosen, B. E. Britigan, H. J. Halpern and S. Pou, *Free Radicals: Biology and Detection by Spin Trapping*, Oxford University Press on Demand, 1999.
4. A. Mackor, T. A. Wajer, T. J. De Boer and J. van Voorst, *Tetrahedron Lett.*, 1966, **7**, 2115–2123.
5. A. Mackor, T. A. Wajer, T. J. De Boer and J. van Voorst, *Tetrahedron Lett.*, 1967, **8**, 385–390.
6. T. A. Wajer, A. Mackor, T. J. De Boer and J. van Voorst, *Tetrahedron*, 1967, **23**, 4021–4026.
7. M. Iwamura and N. Inamoto, *Bull. Chem. Soc. Jpn.*, 1967, **40**, 703.
8. M. Iwamura and N. Inamoto, *Bull. Chem. Soc. Jpn.*, 1967, **40**, 702.
9. M. Iwamura and N. Inamoto, *Bull. Chem. Soc. Jpn.*, 1970, **43**, 860–863.
10. G. Chalfont, M. J. Perkins and A. Horsfield, *J. Am. Chem. Soc.*, 1968, **90**, 7141–7142.
11. G. Chalfont and M. J. Perkins, *J. Am. Chem. Soc.*, 1967, **89**, 3054–3055.
12. E. G. Janzen and B. J. Blackburn, *J. Am. Chem. Soc.*, 1968, **90**, 5909–5910.
13. C. Lagercrantz and S. Forshult, *Nature*, 1968, **218**, 1247–1248.
14. J. M. McCord and I. Fridovich, *J. Biol. Chem.*, 1969, **244**, 6049–6055.
15. B. B. Keele, Jr, J. M. McCord and I. Fridovich, *J. Biol. Chem.*, 1970, **245**, 6176–6181.
16. E. G. Janzen and B. J. Blackburn, *J. Am. Chem. Soc.*, 1969, **91**, 4481–4490.
17. A. Keszler, B. Kalyanaraman and N. Hogg, *Free Radical Biol. Med.*, 2003, **35**, 1149–1157.
18. O. Ouari, M. Hardy, H. Karoui and P. Tordo, in *Electron Paramagnetic Resonance: Volume 22*, The Royal Society of Chemistry, vol. 22, 2011, pp. 1–40.
19. M. D. Wang, T. Wang, D. Wang, W. Jiang and J. J. Fu, *J. Mater. Sci.*, 2019, **54**, 6199–6211.
20. S. M. Opalka, A. R. Longstreet and D. T. McQuade, *Beilstein J. Org. Chem.*, 2011, **7**, 1671–1679.
21. F. Vila, M. Boyer, G. Gronchi, Y. Duccini, O. Santero and P. Tordo, *Tetrahedron Lett.*, 1984, **25**, 2215–2218.
22. N. Song and D. M. Stanbury, *Inorg. Chem.*, 2011, **50**, 12762–12773.
23. G. Gronchi, P. Courbis, P. Tordo, G. Mousset and J. Simonet, *J. Phys. Chem.*, 1983, **87**, 1343–1349.
24. G. L. McIntire, H. N. Blount, H. J. Stronks, R. V. Shetty and E. G. Janzen, *J. Phys. Chem.*, 1980, **84**, 916–921.
25. B. Tuccio, P. Bianco, J. C. Bouteiller and P. Tordo, *Electrochim. Acta*, 1999, **44**, 4631–4634.
26. M. Rosselin, B. Tuccio, P. Pério, F. A. Villamena, P.-L. Fabre and G. Durand, *Electrochim. Acta*, 2016, **193**, 231–239.
27. M. Triquigneaux, B. Tuccio, R. Lauricella and L. Charles, *J. Am. Soc. Mass Spectrom*, 2009, **20**, 2013–2020.

28. K. Ranguelova and R. P. Mason, *Free Radical Biol. Med.*, 2009, **47**, 128–134.
29. F. Leinisch, K. Ranguelova, E. F. DeRose, J. Jiang and R. P. Mason, *Chem. Res. Toxicol.*, 2011, **24**, 2217–2226.
30. F. Leinisch, J. Jiang, E. F. DeRose, V. V. Khramtsov and R. P. Mason, *Free Radical Biol. Med.*, 2013, **65**, 1497–1505.
31. H. Kaur, *Free Radical Res.*, 1996, **24**, 409–420.
32. M. J. Davies, in *Electron Paramagnetic Resonance*, ed. M. J. D. Bruce C. Gilbert and D. M Murphy, Royal Society of Chemistry, vol. 18, 2002, pp. 47–73.
33. T. J. Kemp, *Prog. React. Kinet.*, 1999, **24**, 287–358.
34. C. L. Hawkins and M. J. Davies, *Biochim. Biophys. Acta*, 2014, **1840**, 708–721.
35. F. A. Villamena and J. L. Zweier, *Antioxid. Redox Signaling*, 2004, **6**, 619–629.
36. M. J. Davies, *Methods*, 2016, **109**, 21–30.
37. M. Davies and C. Hawkins, *Free Radical Biol. Med.*, 2004, **36**, 1072.
38. O. Augusto and S. M. Vaz, *Amino Acids*, 2007, **32**, 535–542.
39. L. J. Berliner, V. Khramtsov, H. Fujii and T. L. Clanton, *Free Radical Biol. Med.*, 2001, **30**, 489–499.
40. R. P. Mason, *Redox Biol.*, 2016, **8**, 422–429.
41. R. A. Towner and N. Smith, *Antioxid. Redox Signaling*, 2018, **28**, 1404–1415.
42. J. Vásquez-Vivar, B. Kalyanaraman, P. Martásek, N. Hogg, B. S. S. Masters, H. Karoui, P. Tordo and K. A. Pritchard, *Proc. Natl. Acad. Sci. U. S. A.*, 1998, **95**, 9220–9225.
43. J. Zielonka, A. Sikora, M. Hardy, J. Joseph, B. P. Dranka and B. Kalyanaraman, *Chem. Res. Toxicol.*, 2012, **25**, 1793–1799.
44. A. Sikora, J. Zielonka, M. Lopez, J. Joseph and B. Kalyanaraman, *Free Radical Biol. Med.*, 2009, **47**, 1401–1407.
45. A. R. Lippert, G. C. Van de Bittner and C. J. Chang, *Acc. Chem. Res.*, 2011, **44**, 793–804.
46. R. Michalski, J. Zielonka, E. Gapys, A. Marcinek, J. Joseph and B. Kalyanaraman, *J. Biol. Chem.*, 2014, **289**, 22536–22553.
47. N. Rios, R. Radi, B. Kalyanaraman and J. Zielonka, *J. Biol. Chem.*, 2020, **295**, 6665–6676.
48. C. J. Chang, T. D. James, E. J. New and B. Z. Tang, *Acc. Chem. Res.*, 2020, **53**, 1.
49. A. Sikora, J. Zielonka, M. Lopez, A. Dybala-Defratyka, J. Joseph, A. Marcinek and B. Kalyanaraman, *Chem. Res. Toxicol.*, 2011, **24**, 687–697.
50. J. Zielonka, R. Podsiadły, M. Zielonka, M. Hardy and B. Kalyanaraman, *Free Radical Biol. Med.*, 2016, **99**, 32–42.
51. A. Sikora, J. Zielonka, J. Adamus, D. Debski, A. Dybala-Defratyka, B. Michalowski, J. Joseph, R. C. Hartley, M. P. Murphy and B. Kalyanaraman, *Chem. Res. Toxicol.*, 2013, **26**, 856–867.

52. J. Zielonka, M. Zielonka, L. VerPlank, G. Cheng, M. Hardy, O. Ouari, M. M. Ayhan, R. Podsiadły, A. Sikora, J. D. Lambeth and B. Kalyanaraman, *J. Biol. Chem.*, 2016, **291**, 7029–7044.
53. E. Besson, S. Gastaldi, E. Bloch, J. Zielonka, M. Zielonka, B. Kalyanaraman, S. Aslan, H. Karoui, A. Rockenbauer, O. Ouari and M. Hardy, *Analyst*, 2019, **144**, 4194–4203.
54. J. Zielonka, M. Zielonka, M. Hardy, O. Ouari and B. Kalyanaraman, *Free Radical Biol. Med.*, 2015, **87**, S19–S20.
55. P. Wardman, *Free Radical Biol. Med.*, 2007, **43**, 995–1022.
56. J. Zielonka and B. Kalyanaraman, *Free Radical Biol. Med.*, 2018, **128**, 3–22.
57. B. Kalyanaraman, V. Darley-Usmar, K. J. Davies, P. A. Dennery, H. J. Forman, M. B. Grisham, G. E. Mann, K. Moore, L. J. Roberts 2nd and H. Ischiropoulos, *Free Radical Biol. Med.*, 2012, **52**, 1–6.
58. J. Zielonka, J. D. Lambeth and B. Kalyanaraman, *Free Radical Biol. Med.*, 2013, **65**, 1310–1314.
59. K. Faulkner and I. Fridovich, *Free Radical Biol. Med.*, 1993, **15**, 447–451.
60. P. Wardman, M. J. Burkitt, K. B. Patel, A. Lawrence, C. M. Jones, S. A. Everett and B. Vojnovic, *J. Fluoresc.*, 2002, **12**, 65–68.
61. L. K. Folkes, K. B. Patel, P. Wardman and M. Wrona, *Arch. Biochem. Biophys.*, 2009, **484**, 122–126.
62. M. Wrona and P. Wardman, *Free Radical Biol. Med.*, 2006, **41**, 657–667.
63. J. Vásquez-Vivar, N. Hogg, K. A. Pritchard, Jr, P. Martasek and B. Kalyanaraman, *FEBS Lett.*, 1997, **403**, 127–130.
64. Y. Li, H. Zhu, P. Kuppusamy, V. Roubaud, J. L. Zweier and M. A. Trush, *J. Biol. Chem.*, 1998, **273**, 2015–2023.
65. J. Vásquez-Vivar, P. Martásek, N. Hogg, H. Karoui, B. S. Masters, K. A. Pritchard, Jr and B. Kalyanaraman, *Methods Enzymol.*, 1999, **301**, 169–177.
66. P. Wardman, *Radiat. Res.*, 2008, **170**, 406–407.
67. X. Chen, Z. Zhong, Z. Xu, L. Chen and Y. Wang, *Free Radical Res.*, 2010, **44**, 587–604.
68. M. Karlsson, T. Kurz, U. T. Brunk, S. E. Nilsson and C. I. Frennesson, *Biochem. J.*, 2010, **428**, 183–190.
69. M. G. Bonini, C. Rota, A. Tomasi and R. P. Mason, *Free Radical Biol. Med.*, 2006, **40**, 968–975.
70. C. Rota, C. F. Chignell and R. P. Mason, *Free Radical Biol. Med.*, 1999, **27**, 873–881.
71. E. Marchesi, C. Rota, Y. C. Fann, C. F. Chignell and R. P. Mason, *Free Radical Biol. Med.*, 1999, **26**, 148–161.
72. C. Rota, Y. C. Fann and R. P. Mason, *J. Biol. Chem.*, 1999, **274**, 28161–28168.
73. B. Zhao, K. Ranguelova, J. Jiang and R. P. Mason, *Free Radical Biol. Med.*, 2011, **51**, 153–159.
74. B. Zhao, F. A. Summers and R. P. Mason, *Free Radical Biol. Med.*, 2012, **53**, 1080–1087.
75. V. Marchand, N. Charlier, J. Verrax, P. Buc-Calderon, P. Levêque and B. Gallez, *PLoS One*, 2017, **12**, e0172998.

76. N. B. Nazhat, G. Yang, R. E. Allen, D. R. Blake and P. Jones, *Biochem. Biophys. Res. Commun.*, 1990, **166**, 807–812.
77. R. Michalski, J. Zielonka, M. Hardy, J. Joseph and B. Kalyanaraman, *Free Radical Biol. Med.*, 2013, **54**, 135–147.
78. F. A. Villamena and J. L. Zweier, *J. Chem. Soc., Perkin Trans. 2*, 2002, 1340–1344.
79. F. A. Villamena, S. Xia, J. K. Merle, R. Lauricella, B. Tuccio, C. M. Hadad and J. L. Zweier, *J. Am. Chem. Soc.*, 2007, **129**, 8177–8191.
80. J. Weaver, P. Tsai, S. Pou and G. M. Rosen, *J. Org. Chem.*, 2004, **69**, 8423–8428.
81. S. Goldstein, G. M. Rosen, A. Russo and A. Samuni, *J. Phys. Chem. A*, 2004, **108**, 6679–6685.
82. E. Finkelstein, G. M. Rosen and E. J. Rauckman, *J. Am. Chem. Soc.*, 1980, **102**, 4994–4999.
83. G. R. Buettner and R. P. Mason, in *Methods Enzymol.*, Academic Press, vol. 186, 1990, pp. 127–133.
84. G. R. Buettner and L. W. Oberley, *Biochem. Biophys. Res. Commun.*, 1978, **83**, 69–74.
85. G. R. Buettner, *Free Radical Res. Commun.*, 1993, **19**(Suppl. 1), S79–87.
86. E. Finkelstein, G. M. Rosen and E. J. Rauckman, *Mol. Pharmacol.*, 1982, **21**, 262–265.
87. F. A. Villamena, *J. Phys. Chem. A*, 2009, **113**, 6398–6403.
88. F. A. Villamena, J. K. Merle, C. M. Hadad and J. L. Zweier, *J. Phys. Chem. A*, 2005, **109**, 6089–6098.
89. C. Frejaville, H. Karoui, B. Tuccio, F. Le Moigne, M. Culcasi, S. Pietri, R. Lauricella and P. Tordo, *J. Med. Chem.*, 1995, **38**, 258–265.
90. F. Chalier and P. Tordo, *J. Chem. Soc., Perkin Trans. 2*, 2002, 2110–2117.
91. H. Zhao, J. Joseph, H. Zhang, H. Karoui and B. Kalyanaraman, *Free Radical Biol. Med.*, 2001, **31**, 599–606.
92. F. A. Villamena, A. Rockenbauer, J. Gallucci, M. Velayutham, C. M. Hadad and J. L. Zweier, *J. Org. Chem.*, 2004, **69**, 7994–8004.
93. K. Stolze, N. Udilova, T. Rosenau, A. Hofinger and H. Nohl, *Biol. Chem.*, 2003, **384**, 493–500.
94. M. Hardy, F. Chalier, O. Ouari, J. P. Finet, A. Rockenbauer, B. Kalyanaraman and P. Tordo, *Chem. Commun.*, 2007, 1083–1085.
95. M. Hardy, A. Rockenbauer, J. Vasquez-Vivar, C. Felix, M. Lopez, S. Srinivasan, N. Avadhani, P. Tordo and B. Kalyanaraman, *Chem. Res. Toxicol.*, 2007, **20**, 1053–1060.
96. M. Hardy, F. Poulhes, E. Rizzato, A. Rockenbauer, K. Banaszak, H. Karoui, M. Lopez, J. Zielonka, J. Vasquez-Vivar, S. Sethumadhavan, B. Kalyanaraman, P. Tordo and O. Ouari, *Chem. Res. Toxicol.*, 2014, **27**, 1155–1165.
97. F. Poulhes, E. Rizzato, P. Bernasconi, R. Rosas, S. Viel, L. Jicsinszky, A. Rockenbauer, D. Bardelang, D. Siri, A. Gaudel-Siri, H. Karoui, M. Hardy and O. Ouari, *Org. Biomol. Chem.*, 2017, **15**, 6358–6366.

98. J. Vásquez-Vivar, P. Martasek, N. Hogg, B. S. Masters, K. A. Pritchard, Jr and B. Kalyanaraman, *Biochemistry*, 1997, **36**, 11293–11297.
99. J. Vásquez-Vivar, N. Hogg, P. Martásek, H. Karoui, K. A. Pritchard, Jr and B. Kalyanaraman, *J. Biol. Chem.*, 1999, **274**, 26736–26742.
100. J. Vásquez-Vivar and B. Kalyanaraman, *FEBS Lett.*, 2000, **481**, 305–306.
101. J. Vásquez-Vivar, P. Martásek, J. Whitsett, J. Joseph and B. Kalyanaraman, *Biochem. J.*, 2002, **362**, 733–739.
102. J. Vásquez-Vivar, B. Kalyanaraman and P. Martásek, *Free Radical Res.*, 2003, **37**, 121–127.
103. Y. Han, B. Tuccio, R. Lauricella and F. A. Villamena, *J. Org. Chem.*, 2008, **73**, 7108–7117.
104. Y. Han, Y. Liu, A. Rockenbauer, J. L. Zweier, G. Durand and F. A. Villamena, *J. Org. Chem.*, 2009, **74**, 5369–5380.
105. M. Hardy, D. Bardelang, H. Karoui, A. Rockenbauer, J. P. Finet, L. Jicsinszky, R. Rosas, O. Ouari and P. Tordo, *Chemistry*, 2009, **15**, 11114–11118.
106. K. Abbas, M. Hardy, F. Poulhes, H. Karoui, P. Tordo, O. Ouari and F. Peyrot, *Free Radical Biol. Med.*, 2014, **71**, 281–290.
107. N. Bézière, M. Hardy, F. Poulhès, H. Karoui, P. Tordo, O. Ouari, Y. M. Frapart, A. Rockenbauer, J. L. Boucher, D. Mansuy and F. Peyrot, *Free Radical Biol. Med.*, 2014, **67**, 150–158.
108. D. Bardelang, A. Rockenbauer, H. Karoui, J.-P. Finet, I. Biskupska, K. Banaszak and P. Tordo, *Org. Biomol. Chem.*, 2006, **4**, 2874–2882.
109. H. Karoui, A. Rockenbauer, S. Pietri and P. Tordo, *Chem. Commun.*, 2002, 3030–3031.
110. H. Karoui and P. Tordo, *Tetrahedron Lett.*, 2004, **45**, 1043–1045.
111. D. Bardelang, L. Charles, J. P. Finet, L. Jicsinszky, H. Karoui, S. R. Marque, V. Monnier, A. Rockenbauer, R. Rosas and P. Tordo, *Chemistry*, 2007, **13**, 9344–9354.
112. J. Zielonka, T. Sarna, J. E. Roberts, J. F. Wishart and B. Kalyanaraman, *Arch. Biochem. Biophys.*, 2006, **456**, 39–47.
113. L. B. Maia and J. J. Moura, *Methods Mol. Biol.*, 2016, **1424**, 81–102.
114. N. Hogg, *Free Radical Biol. Med.*, 2010, **49**, 122–129.
115. B. Kalyanaraman, *Methods Enzymol.*, 1996, **268**, 168–187.
116. L. J. Berliner and H. Fujii, *Antioxid. Redox Signaling*, 2004, **6**, 649–656.
117. H.-G. Korth, K. U. Ingold, R. Sustmann, H. de Groot and H. Sies, *Angew. Chem., Int. Ed.*, 1992, **31**, 891–893.
118. H. G. Korth, R. Sustmann, P. Lommes, T. Paul, A. Ernst, H. de Groot, L. Hughes and K. U. Ingold, *J. Am. Chem. Soc.*, 1994, **116**, 2767–2777.
119. T. Paul, M. A. Hassan, H. G. Korth, R. Sustmann and D. V. Avila, *J. Org. Chem.*, 1996, **61**, 6835–6848.
120. M. Bätz, H.-G. Korth and R. Sustmann, *Angew. Chem., Int. Ed.*, 1997, **36**, 1501–1503.
121. P. M. Düppe, P. M. Talbierski, F. S. Hornig, U. Rauen, H.-G. Korth, T. Wille, R. Boese, T. Omlor, H. de Groot and R. Sustmann, *Chem. – Eur. J.*, 2010, **16**, 11121–11132.

122. F. S. Hornig, H.-G. Korth, U. Rauen, H. de Groot and R. Sustmann, *Helv. Chim. Acta*, 2006, **89**, 2281–2296.
123. R. Lauricella, M. Triquigneaux, C. André-Barrès, L. Charles and B. Tuccio, *Chem. Commun.*, 2010, **46**, 3675–3677.
124. A. Rockenbauer and L. Korecz, *J. Chem. Soc., Chem. Commun.*, 1994, 145.
125. W. Adam, S. E. Bottle, I. Darren GCrice, D. Pfeiler and C. Wentrup, *Tetrahedron Lett.*, 1996, **37**, 2113–2116.
126. D. Pfeiler, I. D. Grice, S. E. Bottle and G. R. Hanson, *Free Radical Res.*, 1997, **27**, 377–388.
127. D. R. Kelly, S. Jones, J. O. Adigun, K. S. V. Koh and S. K. Jackson, *Tetrahedron Lett.*, 1997, **38**, 1245–1248.
128. K. J. Reszka, P. Bilski and C. F. Chignell, *Nitric oxide*, 2004, **10**, 53–59.
129. K. J. Reszka, C. F. Chignell and P. Bilski, *J. Am. Chem. Soc.*, 1994, **116**, 4119–4120.
130. K. J. Reszka, P. Bilski and C. F. Chignell, *J. Am. Chem. Soc.*, 1996, **118**, 8719–8720.
131. E. V. Arnold, D. S. Bohle and Y. Hu, *Chem. Res. Toxicol.*, 2000, **13**, 963–966.
132. Y.-Y. Huang, P. J. Rajda, G. Szewczyk, B. Bhayana, L. Y. Chiang, T. Sarna and M. R. Hamblin, *Photochem. Photobiol. Sci.*, 2019, **18**, 505–515.
133. B. A. Goodman, J. B. Raynor and M. C. R. Symons, *J. Chem. Soc. A*, 1969, 2572–2575.
134. A. F. Vanin, *Methods Enzymol.*, 1999, **301**, 269–279.
135. L. A. Shinobu, S. G. Jones and M. M. Jones, *Acta Pharmacol. Toxicol.*, 1984, **54**, 189–194.
136. A. Komarov, D. Mattson, M. M. Jones, P. K. Singh and C. S. Lai, *Biochem. Biophys. Res. Commun.*, 1993, **195**, 1191–1198.
137. C. S. Lai and A. M. Komarov, *FEBS Lett.*, 1994, **345**, 120–124.
138. A. M. Komarov, *Mol. Cell. Biochem.*, 2002, **234**, 387–392.
139. J. Joseph, B. Kalyanaraman and J. S. Hyde, *Biochem. Biophys. Res. Commun.*, 1993, **192**, 926–934.
140. N. Hogg, R. J. Singh, J. Joseph, F. Neese and B. Kalyanaraman, *Free Radical Res.*, 1995, **22**, 47–56.
141. E. A. Konorev, M. M. Tarpey, J. Joseph, J. E. Baker and B. Kalyanaraman, *Free Radical Biol. Med.*, 1995, **18**, 169–177.
142. S. Goldstein, A. Russo and A. Samuni, *J. Biol. Chem.*, 2003, **278**, 50949–50955.
143. T. Akaike, M. Yoshida, Y. Miyamoto, K. Sato, M. Kohno, K. Sasamoto, K. Miyazaki, S. Ueda and H. Maeda, *Biochemistry*, 1993, **32**, 827–832.
144. E. M. Lozinsky, L. V. Martina, A. I. Shames, N. Uzlaner, A. Masarwa, G. I. Likhtenshtein, D. Meyerstein, V. V. Martin and Z. Priel, *Anal. Biochem.*, 2004, **326**, 139–145.
145. O. Toshihiko and H. Akira, *Bull. Chem. Soc. Jpn.*, 1987, **60**, 2304–2306.
146. H. Taniguchi and K. P. Madden, *Radiat. Res.*, 2000, **153**, 447–453.
147. Y. Maeda and K. U. Ingold, *J. Am. Chem. Soc.*, 1979, **101**, 4975–4981.
148. K. Stolze, N. Udilova, T. Rosenau, A. Hofinger and H. Nohl, *Biochem. Pharmacol.*, 2003, **66**, 1717–1726.

149. J. A. North, A. A. Spector and G. R. Buettner, *J. Biol. Chem.*, 1992, **267**, 5743–5746.
150. K. Stolze, N. Udilova and H. Nohl, *Acta Biochim. Pol.*, 2000, **47**, 923–930.
151. S. I. Dikalov and R. P. Mason, *Free Radical Biol. Med.*, 1999, **27**, 864–872.
152. S. I. Dikalov and R. P. Mason, *Free Radical Biol. Med.*, 2001, **30**, 187–197.
153. S. Lescic, H. Karoui, M. Hardy, L. Charles, P. Tordo, O. Ouari, A. Gaudel-Siri and D. Siri, *J. Phys. Org. Chem.*, 2017, **30**, e3677.
154. G. M. Rosen and E. J. Rauckman, *Mol. Pharmacol.*, 1980, **17**, 233–238.
155. J. Van der Zee, D. P. Barr and R. P. Mason, *Free Radical Biol. Med.*, 1996, **20**, 199–206.
156. H. Karoui, N. Hogg, C. Fréjaville, P. Tordo and B. Kalyanaraman, *J. Biol. Chem.*, 1996, **271**, 6000–6009.
157. M. J. Scott, T. R. Billiar and D. A. Stoyanovsky, *Sci. Rep.*, 2016, **6**, 38773.
158. D. N. Polovyanenko, V. F. Plyusnin, V. A. Reznikov, V. V. Khramtsov and E. G. Bagryanskaya, *J. Phys. Chem. B*, 2008, **112**, 4841–4847.
159. M. J. Davies, L. G. Forni and S. L. Shuter, *Chem. – Biol. Interact.*, 1987, **61**, 177–188.
160. O. Augusto, M. G. Bonini and D. Trindade, *Free Radical Biol. Med.*, 2004, **36**, 1224–1232.
161. D. I. Potapenko, E. G. Bagryanskaya, Y. P. Tsentalovich, V. A. Reznikov, T. L. Clanton and V. V. Khramtsov, *J. Phys. Chem. B*, 2004, **108**, 9315–9324.
162. B. Kalyanaraman, H. Karoui, R. J. Singh and C. C. Felix, *Anal. Biochem.*, 1996, **241**, 75–81.
163. I. Osamu and M. Minoru, *Bull. Chem. Soc. Jpn.*, 1984, **57**, 1745–1749.
164. J. Stubbe and W. A. van Der Donk, *Chem. Rev.*, 1998, **98**, 705–762.
165. J. R. Winkler and H. B. Gray, *Chem. Rev.*, 2014, **114**, 3369–3380.
166. M. J. Davies, *Biochim. Biophys. Acta*, 2005, **1703**, 93–109.
167. M. J. Davies, *Biochem. J.*, 2016, **473**, 805–825.
168. G. Jeschke, *Biochim. Biophys. Acta*, 2005, **1707**, 91–102.
169. C. L. Hawkins and M. J. Davies, *J. Biol. Chem.*, 2019, **294**, 19683–19708.
170. M. R. Gunther, *Free Radical Biol. Med.*, 2004, **36**, 1345–1354.
171. M. Ehrenshaft, L. J. Deterding and R. P. Mason, *Free Radical Biol. Med.*, 2015, **89**, 220–228.
172. S. Lopes de Menezes and O. Augusto, *J. Biol. Chem.*, 2001, **276**, 39879–39884.
173. M. R. Gunther, J. A. Peters and M. K. Sivaneri, *J. Biol. Chem.*, 2002, **277**, 9160–9166.
174. C. L. Hawkins and M. J. Davies, *Biochem. J.*, 1998, **332**(Pt 3), 617–625.
175. M. R. Gunther, R. A. Tschirret-Guth, H. E. Witkowska, Y. C. Fann, D. P. Barr, P. R. Ortiz De Montellano and R. P. Mason, *Biochem. J.*, 1998, **330**(Pt 3), 1293–1299.
176. S. Y. Qian, Y. R. Chen, L. J. Deterding, Y. C. Fann, C. F. Chignell, K. B. Tomer and R. P. Mason, *Biochem. J.*, 2002, **363**, 281–288.
177. A. Gamliel, M. Afri and A. A. Frimer, *Free Radical Biol. Med.*, 2008, **44**, 1394–1405.

178. A. Hay, M. J. Burkitt, C. M. Jones and R. C. Hartley, *Arch. Biochem. Biophys.*, 2005, **435**, 336–346.
179. M. Hardy, O. Ouari, L. Charles, J. P. Finet, G. Iacazio, V. Monnier, A. Rockenbauer and P. Tordo, *J. Org. Chem.*, 2005, **70**, 10426–10433.
180. S. Ortial, S. Morandat, M. Bortolato, B. Roux, A. Polidori, B. Pucci and G. Durand, *Colloids Surf., B*, 2014, **113**, 384–393.
181. G. Durand, R. A. Prosak, Y. Han, S. Ortial, A. Rockenbauer, B. Pucci and F. A. Villamena, *Chem. Res. Toxicol.*, 2009, **22**, 1570–1581.
182. C. A. Headley, C. N. Hoffman, J. M. Freisen, Y. Han, J. M. Macklin, J. L. Zweier, A. Rockenbauer, J. Kuret and F. A. Villamena, *Org. Biomol. Chem.*, 2019, **17**, 7694–7705.
183. M. P. Murphy, K. S. Echtay, F. H. Blaikie, J. Asin-Cayuela, H. M. Cocheme, K. Green, J. A. Buckingham, E. R. Taylor, F. Hurrell, G. Hughes, S. Miwa, C. E. Cooper, D. A. Svistunenko, R. A. Smith and M. D. Brand, *J. Biol. Chem.*, 2003, **278**, 48534–48545.
184. L. Robertson and R. C. Hartley, *Tetrahedron*, 2009, **65**, 5284–5292.
185. Y. Xu and B. Kalyanaraman, *Free Radical Res.*, 2007, **41**, 1–7.
186. C. Quin, J. Trnka, A. Hay, M. P. Murphy and R. C. Hartley, *Tetrahedron*, 2009, **65**, 8154–8160.
187. G. Cheng, J. Zielonka, O. Ouari, M. Lopez, D. McAllister, K. Boyle, C. S. Barrios, J. J. Weber, B. D. Johnson, M. Hardy, M. B. Dwinell and B. Kalyanaraman, *Cancer Res.*, 2016, **76**, 3904–3915.
188. J. Zielonka, J. Joseph, A. Sikora, M. Hardy, O. Ouari, J. Vasquez-Vivar, G. Cheng, M. Lopez and B. Kalyanaraman, *Chem. Rev.*, 2017, **117**, 10043–10120.
189. G. Cheng, M. Zielonka, B. Dranka, S. N. Kumar, C. R. Myers, B. Bennett, A. M. Garces, L. G. Dias Duarte Machado, D. Thiebaut, O. Ouari, M. Hardy, J. Zielonka and B. Kalyanaraman, *J. Biol. Chem.*, 2018, **293**, 10363–10380.
190. J. Pan, Y. Lee, G. Cheng, J. Zielonka, Q. Zhang, M. Bajzikova, D. Xiong, S. W. Tsaih, M. Hardy, M. Flister, C. M. Olsen, Y. Wang, O. Vang, J. Neuzil, C. R. Myers, B. Kalyanaraman and M. You, *iScience*, 2018, **3**, 192–207.
191. G. Cheng, Q. Zhang, J. Pan, Y. Lee, O. Ouari, M. Hardy, M. Zielonka, C. R. Myers, J. Zielonka, K. Weh, A. C. Chang, G. Chen, L. Kresty, B. Kalyanaraman and M. You, *Nat. Commun.*, 2019, **10**, 2205.
192. D. N. Polovyanenko, S. R. A. Marque, S. Lambert, L. Jicsinszky, V. F. Plyusnin and E. G. Bagryanskaya, *J. Phys. Chem. B*, 2008, **112**, 13157–13162.
193. D. Bardelang, A. Rockenbauer, H. Karoui, J.-P. Finet and P. Tordo, *J. Phys. Chem. B*, 2005, **109**, 10521–10530.
194. S. U. Kim, Y. Liu, K. M. Nash, J. L. Zweier, A. Rockenbauer and F. A. Villamena, *J. Am. Chem. Soc.*, 2010, **132**, 17157–17173.
195. K. Abbas, M. Hardy, F. Poulhès, H. Karoui, P. Tordo, O. Ouari and F. Peyrot, *Free Radical Res.*, 2015, **49**, 1122–1128.

196. V. V. Khramtsov and T. L. Clanton, *Appl. Magn. Reson.*, 2011, **41**, 305–323.
197. A. Reis, M. R. M. Domingues, M. M. Oliveira and P. Domingues, *Eur. J. Mass Spectrom.*, 2009, **15**, 689–703.
198. D. A. Stoyanovsky, Z. Melnikov and A. I. Cederbaum, *Anal. Chem.*, 1999, **71**, 715–721.
199. D. A. Stoyanovsky and A. I. Cederbaum, *Chem. Res. Toxicol.*, 1999, **12**, 730–736.
200. D. A. Stoyanovsky, A. Maeda, J. L. Atkins and V. E. Kagan, *Anal. Chem.*, 2011, **83**, 6432–6438.
201. H. Iwahashi, *Methods Mol. Biol.*, 2008, **477**, 65–73.
202. J. Towell and B. Kalyanaraman, *Anal. Biochem.*, 1991, **196**, 111–119.
203. J. B. Feix and B. Kalyanaraman, *Arch. Biochem. Biophys.*, 1991, **291**, 43–51.
204. C. P. Novakov, D. Feierman, A. I. Cederbaum and D. A. Stoyanovsky, *Chem. Res. Toxicol.*, 2001, **14**, 1239–1246.
205. D. A. Stoyanovsky and A. I. Cederbaum, *Free Radical Biol. Med.*, 1998, **25**, 536–545.
206. S. E. Gomez-Mejiba, Z. Zhai, M. C. Della-Vedova, M. D. Muñoz, S. Chatterjee, R. A. Towner, K. Hensley, R. A. Floyd, R. P. Mason and D. C. Ramirez, *Biochim. Biophys. Acta*, 2014, **1840**, 722–729.
207. R. P. Mason and D. Ganini, *Free Radical Biol. Med.*, 2019, **131**, 318–331.
208. S. E. Gomez-Mejiba, Z. Zhai, H. Akram, L. J. Deterding, K. Hensley, N. Smith, R. A. Towner, K. B. Tomer, R. P. Mason and D. C. Ramirez, *Free Radical Biol. Med.*, 2009, **46**, 853–865.
209. N. A. Bauer, E. Hoque, M. Wolf, K. Kleigrewe and T. Hofmann, *Free Radical Biol. Med.*, 2018, **116**, 129–133.
210. K. Saito, D. Sail, K. Yamamoto, S. Matsumoto, B. Blackman, S. Kishimoto, J. R. Brender, R. E. Swenson, J. B. Mitchell and M. C. Krishna, *Free Radical Biol. Med.*, 2019, **131**, 18–26.
211. C. D. Detweiler, L. J. Deterding, K. B. Tomer, C. F. Chignell, D. Germolec and R. P. Mason, *Free Radical Biol. Med.*, 2002, **33**, 364–369.
212. C. D. Detweiler, O. M. Lardinois, L. J. Deterding, P. R. de Montellano, K. B. Tomer and R. P. Mason, *Free Radical Biol. Med.*, 2005, **38**, 969–976.
213. D. C. Ramirez, Y. R. Chen and R. P. Mason, *Free Radical Biol. Med.*, 2003, **34**, 830–839.
214. L. J. Deterding, D. C. Ramirez, J. R. Dubin, R. P. Mason and K. B. Tomer, *J. Biol. Chem.*, 2004, **279**, 11600–11607.
215. O. M. Lardinois, K. B. Tomer, R. P. Mason and L. J. Deterding, *Biochemistry*, 2008, **47**, 10440–10448.
216. M. Ehrenshaft and R. P. Mason, *Free Radical Biol. Med.*, 2006, **41**, 422–430.
217. D. C. Ramirez, S. E. Gomez Mejiba and R. P. Mason, *Free Radical Biol. Med.*, 2005, **38**, 201–214.
218. D. C. Ramirez, S. E. Mejiba and R. P. Mason, *Nat. Methods*, 2006, **3**, 123–127.
219. D. C. Ramirez, S. E. Gomez-Mejiba and R. P. Mason, *Nat. Protoc.*, 2007, **2**, 512–522.

220. S. E. Gomez-Mejiba, Z. Zhai, M. S. Gimenez, M. T. Ashby, J. Chilakapati, K. Kitchin, R. P. Mason and D. C. Ramirez, *J. Biol. Chem.*, 2010, **285**, 20062–20071.
221. S. Bhattacharjee, L. J. Deterding, S. Chatterjee, J. Jiang, M. Ehrenshaft, O. Lardinois, D. C. Ramirez, K. B. Tomer and R. P. Mason, *Free Radical Biol. Med.*, 2011, **50**, 1536–1545.
222. S. Chatterjee, O. Lardinois, S. Bhattacharjee, J. Tucker, J. Corbett, L. Deterding, M. Ehrenshaft, M. G. Bonini and R. P. Mason, *Free Radical Biol. Med.*, 2011, **50**, 988–999.
223. F. A. Summers, R. P. Mason and M. Ehrenshaft, *Free Radical Biol. Med.*, 2013, **56**, 64–71.
224. O. M. Lardinois, C. D. Detweiler, K. B. Tomer, R. P. Mason and L. J. Deterding, *Free Radical Biol. Med.*, 2008, **44**, 893–906.
225. T. K. Dalsgaard, M. Triquigneaux, L. Deterding, F. Summers, K. Ranguelova, G. Mortensen and R. P. Mason, *J. Agric. Food Chem.*, 2013, **61**, 418–426.
226. S. Bhattacharjee, L. J. Deterding, J. Jiang, M. G. Bonini, K. B. Tomer, D. C. Ramirez and R. P. Mason, *J. Am. Chem. Soc.*, 2007, **129**, 13493–13501.
227. M. G. Bonini, A. G. Siraki, B. S. Atanassov and R. P. Mason, *Free Radical Biol. Med.*, 2007, **42**, 530–540.
228. K. Ranguelova, A. B. Rice, O. M. Lardinois, M. Triquigneaux, N. Steinckwich, L. J. Deterding, S. Garantziotis and R. P. Mason, *Free Radical Biol. Med.*, 2013, **60**, 98–106.
229. A. Kumar, S. H. Chen, M. B. Kadiiska, J. S. Hong, J. Zielonka, B. Kalyanaraman and R. P. Mason, *Free Radical Biol. Med.*, 2014, **73**, 51–59.
230. P. Cassina, A. Cassina, M. Pehar, R. Castellanos, M. Gandelman, A. de León, K. M. Robinson, R. P. Mason, J. S. Beckman, L. Barbeito and R. Radi, *J. Neurosci.*, 2008, **28**, 4115–4122.
231. A. Kumar, D. Ganini and R. P. Mason, *Mol. Neurodegener.*, 2016, **11**, 70.
232. S. Chatterjee, M. Ehrenshaft, S. Bhattacharjee, L. J. Deterding, M. G. Bonini, J. Corbett, M. B. Kadiiska, K. B. Tomer and R. P. Mason, *Free Radical Biol. Med.*, 2009, **46**, 454–461.
233. S. Chatterjee, O. Lardinois, M. G. Bonini, S. Bhattacharjee, K. Stadler, J. Corbett, L. J. Deterding, K. B. Tomer, M. Kadiiska and R. P. Mason, *J. Immunol.*, 2009, **183**, 4055–4066.
234. O. M. Lardinois, S. Chatterjee, R. P. Mason, K. B. Tomer and L. J. Deterding, *Anal. Chem.*, 2010, **82**, 9155–9158.
235. M. J. Hardy, M. Lopez, B. Kalyanaraman, N. Hogg, O. Ouari and P. Tordo, *U. S. Pat.*, US8143420, 2012.

CHAPTER 14

Biological Applications of Nitroxide Stable Free Radicals

SARWAT NAZ, JOHN A. COOK, MURALI C. KRISHNA* AND JAMES B. MITCHELL

Radiation Biology Branch, Center for Cancer Research, National Cancer Institute, 9000 Rockville Pike, Bethesda, Maryland 20892, USA
*Email: murali@helix.nih.gov

14.1 Introduction

Nitroxyls, more commonly known as nitroxides, are stable organic free radicals. The radical site in a ring structure of piperidinyl (six-membered ring), oxazolydinyl, pyrrolineyl, and pyrrolidiyl (five-membered ring) derivatives are stabilized by the tetra methyl substitutions at the two α-sites to confer stability against conversion to diamagnetic end products. Nitroxide radicals have long been utilized as biophysical tools for electron paramagnetic resonance (EPR) spectroscopic studies such as spin labeling because of their stability and their paramagnetic nature.[1] They are used in stereochemically controlled polymerization,[2] and as probes in distance measurements in large macromolecules.[3] Their diamagnetic precursors such as the nitroso, nitrone, or hydroxylamines find use in detecting, quantifying and characterizing transient free radicals in various chemical, radiolytic and enzymatic reactions.[4] The various types of nitroxides and the possible oxidation states upon redox transformation are shown in Figure 14.1. The oxazolidinyl(I), pyrrolidinyl(II), pyrrolinyl(III) and piperidinyl(IV) are the most commonly used derivatives for the above-mentioned applications (Figure 14.1A). The possible oxidation states of the nitroxides are shown in Figure 14.1B. The nitroxide(VI) can undergo reduction

Nitroxides
Edited by Olivier Ouari and Didier Gigmes

Published by the Royal Society of Chemistry, www.rsc.org

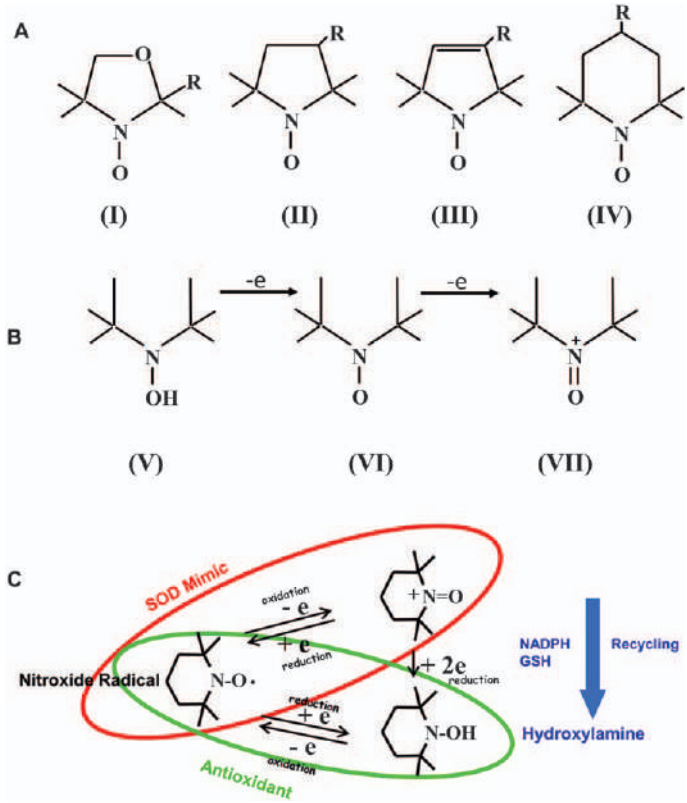

Figure 14.1 (A) Classes of ring nitroxide radicals. Oxazolidinyl(I); purrolidinyl(II); pyrrolynyl(III); piperidinyl(IV). (B) Oxidation states. Hydroxylamine(I); nitroxide(II); oxoammonium(II). (C) Recycling of the nitroxide through redox reactions. The nitroxide can undergo oxidation to the corresponding oxoammonium or reduction to the hydroxylamine. The oxoammonium cation can undergo reduction to the nitroxide by 1-electron or to the hydroxylamine by a two-electron reduction. The hydroxylamine can undergo a one-electron oxidation to the nitroxide radical.

to the hydroxylamine(V) or become oxidized to the corresponding oxoammonium(VII) (Figure 14.1C).

While the chemical and biophysical applications of nitroxides have been actively explored since the 1960s,[5] the anti-oxidant/radioprotective effects of nitroxides have been identified relatively recently when the five-membered oxazolidine nitroxide, OXANO, was shown to have superoxide dismutase (SOD)-mimetic activity although with a significantly lower catalytic rate constant compared to the native enzyme.[6] The SOD-mimetic activity of OXANO (2-ethyl-2,5,5-trimethyl-3-oxazolidinoxyl) was identified when the nitroxide or its one-electron reduction product, the hydroxylamine, were exposed to a flux of superoxide generated by the aerobic xanthine/xanthine oxidase reaction, whereby a steady-state ratio of nitroxide/hydroxylamine

was achieved as detected by monitoring the nitroxide using electron paramagnetic resonance (EPR) spectroscopy. The steady-state ratio of the nitroxide/hydroxylamine was achieved, and when the nitroxide was monitored by EPR it was independent of whether the nitroxide or the hydroxylamine was initially used.[6]

The putative SOD-mimetic activity of this class of nitroxides was consistent with the mechanism:

$$\mathrm{RRNO^{\bullet} + O_2^{-\bullet} + H^+ \rightarrow RRNOH + O_2} \quad (14.1)$$

$$\mathrm{RRNOH + O_2^{-\bullet} + H^+ \rightarrow RRNO + H_2O_2} \quad (14.2)$$

$$\mathrm{O_2^{-\bullet} + 2\ H^+ \rightarrow O_2 + H_2O_2} \quad (14.3)$$

Summing eqn (14.1) and (14.2), yields the superoxide dismutation reactions catalyzed by the nitroxide/hydroxylamine pair (eqn (14.3)).

The SOD-mimetic activity was noticed for other oxazolidinyl nitroxides as monitored by EPR spectroscopy where a steady-state ratio of nitroxide/hydroxylamine was achieved.[6] However, the pyrrolidinyl(II), pyrrolinyl(III) and piperidinyl(IV) nitroxides tested did not show any reduction to the hydroxylamine when exposed to a flux of superoxide generated by the aerobic xanthine/xanthine oxidase reaction as monitored by EPR spectroscopy. The lack of change in nitroxide levels of these derivatives suggested that they lack SOD-mimetic activity unlike the oxazolydinyl nitroxides and were considered as negative controls in cellular studies testing for antioxidant effects. The catalytic rate constants for the SOD-mimetic activity of the oxazolydinyl nitroxides OXANO and cyclohexyl doxyl (CHD) were determined and found to be $\sim 10^3\ \mathrm{M^{-1}\,s^{-1}}$, a rate lower by 6 orders in magnitude than the native enzyme.[7] The smaller molecular weight (~150 Da) of these molecules allows for higher levels of accumulation in cells and thus affords greater protection.[8] When independent chemical assays for superoxide reactivity were used, it was found that the piperidinyl nitroxides displayed 2–3 orders ($\sim 10^6\ \mathrm{M^{-1}\,s^{-1}}$) of magnitude higher catalytic rates of SOD mimetic activity compared to the oxazolydinyl nitroxides OXANO and CHD (cyclohexane doxyl).[7] The higher rate constants in spite of a lack of decrease of nitroxide levels of Tempo and Tempol as monitored by EPR suggested that the hydroxylamine oxidation by superoxide in the SOD-mimetic activity (eqn (14.2)) must proceed at diffusion-limited rates. Independent determination of the kinetics of eqn (14.2) showed that this reaction proceeded at $\sim 10^2\ \mathrm{M^{-1}\,s^{-1}}$.[9] The relatively higher catalytic rate constants for superoxide dismutation for the piperidinyl nitroxides and the relatively slow rate of re-oxidation of the corresponding hydroxylamine were not consistent with the nitroxide/hydroxylamine as the redox pair responsible for SOD mimicking activity and prompted additional studies which identified unique mechanisms of recycling antioxidant reactions.[10] In this chapter, the chemical basis for nitroxide radicals' protective effects in terms of their redox chemistry, recycling nature of the molecule to restore itself *in vivo*, the capability as molecular imaging agents to report on tissue redox status as well as metabolic

modulators influencing body weight and cancer prevention as dietary supplement will be discussed.

14.1.1 SOD Mimetic Activity

The lack of change of levels of the nitroxide radical Tempol when exposed to different fluxes of enzymatically generated superoxide while the catalytic rate constants of $\sim 10^6$ $M^{-1} s^{-1}$ prompted a more detailed study of the redox chemistry of the carbocyclic piperidinyl and pyrrolidinyl nitroxide radicals since the nitroxide/hydroxylamine pair does not explain the high catalytic rate constants of superoxide dismutation. Electrochemical studies using cyclic voltammetry revealed that the nitroxide/oxoammonium pair constitutes a redox couple capable of supporting catalytic reactions such as superoxide dismutation.[9] The hydroxylamine/nitroxide pair is similar to redox pairs such as the classic antioxidants ascorbate/ascorbyl, tocopherol/tocopheroxyl, *etc*. supporting radical-scavenging reactions.

The catalytic superoxide dismutation reaction supported by the nitroxide radical Tempol and its analogs is consistent with an initial univalent oxidation by the protonated form of superoxide to the corresponding oxoammonium cation.

$$RRNO^{\bullet} + HO_2{}^{\bullet} + H^+ \rightarrow RRNO^+ + H_2O_2 \qquad (14.4)$$

The oxoammonium cation undergoes a one-electron reduction to the corresponding nitroxide at diffusion-limited rates.

$$RRNO^+ + O_2{}^{-\bullet} \rightarrow RRNO^{\bullet} + O_2 \qquad (14.5)$$

Summing eqn (14.4) and (14.5), yields the same superoxide dismutation reaction (eqn (14.3)).

Since the initial step of the superoxide dismutation involves oxidation of the nitroxide to the oxoammonium cation by the protonated form of superoxide, the catalytic rate constants were found to be pH dependent ranging from 10^5 $M^{-1} s^{-1}$ to 5×10^7 $M^{-1} s^{-1}$ in the pH range of 7.8 to 6.0.[11] It was also found that the compounds with lower redox mid-point potential for the oxoammonium/nitroxide had higher rate constants for the catalytic dismutation of superoxide.[11]

The redox transformation between the three oxidation states of the piperidine ring, namely the hydroxylamine, nitroxide and oxoammonium in supporting catalytic and stoichiometric antioxidant activity, are shown in Figure 14.1C and can be summarized as follows. The nitroxide/oxoamonim cation pair constitutes a redox couple supporting catalytic reactions to support SOD-mimicking activity. The oxoammonium can be converted to the corresponding hydroxylamine *via* a two-electron reduction with endogenous cofactors such as NADH/NADPH or glutathione. The hydroxylamine can act as a classic antioxidant such as ascorbate by a univalent oxidation by reactive oxygen species to generate nitroxide radicals. Thus, this class of compounds acts as recycling antioxidants participating in catalytic antioxidant defense

as enzyme mimics (Figure 14.1C, red ellipse) as well as classic antioxidants (Figure 14.1C, green ellipse), a property unique to them.[10]

The nitroxide/oxoammonium redox couple was also shown to detoxify hydrogen peroxide and organic peroxides in a manner similar to peroxidases in the presence of any heme group containing protein-identifying additional modes of antioxidant defense in this class of compounds.[12] The mechanism involves the redox cycling of the nitroxide/oxoammonium redox couple with the ferriheme/oxoferryl heme in the process detoxifying hydrogen peroxide and organic peroxides. The low molecular weight, membrane permeability through passive diffusion processes[13] and blood–brain permeability of some of the nitroxides such as Tempol[14] and multiple modes of protection make them effective in protecting against various modes of oxidative stress in live objects globally.

14.2 Nitroxides as Protectors Against Oxidative Stress

The nitroxide radicals' protective effects in various models of oxidative stress and mechanistic aspects have been reviewed.[10,15,16] Based on these studies most research has utilized the six-membered piperidinyl ring nitroxide Tempol for various reasons including low cytotoxicity, high water solubility, oral bioavailability and its ability to cross cell membranes.[8] The toxicologic and pharmacologic information available for this molecule and the large body of preclinical work have shown promise for this as a potential candidate for clinical translation.[17] Tempol exhibits antioxidant activity and reacts with both reactive oxygen species (ROS) and reactive nitrogen species (RNS) *in vitro* and *in vivo*.[10,15] Studies from our laboratory and others have shown beneficial effects of Tempol in animal models of shock, hypertension, diabetes, ischemia–reperfusion injury, spinal cord injury and traumatic brain injury,[18–24] and neurodegenerative models for Parkinson's disease.[25,26] In this chapter, more recent reports on the use of this molecule as an antioxidant/protectant in multiple models will be presented.

14.2.1 Tempol as a Neuroprotector in a Multiple Sclerosis Model

Multiple sclerosis (MS) is a chronic inflammatory and demyelinating neurodegenerative disorder, characterized pathologically by central nervous system (CNS) alterations in the vasculature, inflammatory infiltrates, demyelination, glial scarring, oligodendrocyte loss, and axonal damage and loss.[27] The irreversible axonal loss and neurodegeneration associated with the disease are thought to be major correlates of chronic disability[28] that likely start early in disease.[29,30] Most of the knowledge about the pathogenesis of MS has been derived from murine models, such as experimental autoimmune encephalomyelitis (EAE) and viral encephalomyelitis. In EAE, a mouse model of MS, autoreactive T cells producing pro-inflammatory cytokines such as tumor necrosis factor α (TNFα), interferon-γ (IFNγ), interleukin (IL)-17 and granulocyte macrophage colony stimulating factor (GM-CSF)

travel to the CNS to cause the disease.[31] Both $CD4^+$ and $CD8^+$ T cells have also been implicated in directly contributing to disease pathogenesis.[32] While the results in mouse models have indicated that demyelination and associated axonal loss appear secondary to inflammation,[30] neurodegeneration is seen prior to inflammatory cell infiltration in EAE and the progressive loss of function is seen as a distinct event after the inflammatory phase has subsided.[33,34] Recent studies have also implicated the role of mitochondrial dysfunction indirectly contributing to inflammation associated with MS.[35] Other emerging evidence implicates ROS and RNS, focusing on superoxide, nitric oxide and their intermediates, as contributors to several mechanisms underlying the pathogenesis of MS in the EAE model.[36,37] Studies have shown that ROS drive morphological alterations that promote leukocyte traffic across the blood–brain barrier (BBB) in the MS mouse model.[38,39] Infiltrated leukocytes produce ROS that induce myelin phagocytosis and therein lead to myelin breakdown by macrophages, oligodendrocyte damage, as well as axonal and neuronal injury and loss.[40,41] Microglia and neurons can generate peroxynitrite, a principal mediator of the oxidative stress and excitotoxicity that drive neurodegenerative processes in MS.[37,42] The approved therapies for treating MS fall into two groups: those well tolerated but with partial efficacy, or those with greater efficacy and increased risk profiles.[43,44] Therefore, the development of orally efficacious, safe and well-tolerated therapeutics with immunomodulatory and neuroprotective properties remains a priority for treating patients with MS in the clinic.

A recent collaborative study conducted with our laboratory showed for the first time that oral administration of the antioxidant Tempol, alone, both prophylactically and therapeutically limited CNS autoimmune disease and damage in the most established models of MS.[45] Animals on Tempol chow were spared from severe clinical disease, and showed little evidence of microglial activation, an early indicator of insult to the CNS preceding infiltration and clinical disease in EAE.[46,47] Our studies demonstrated potent immunomodulatory properties of Tempol that have not been described previously. At doses associated with efficacy in a complex disease model, the results indicated immune deviation from an inflammatory phenotype evidenced by cytokine shifts, antibody profile changes and reductions in antigen-presenting molecules. Additionally, Tempol administration brought changes in T cell subsets, most notably an increase in CD4 + regulatory T cell populations. Animals placed on Tempol or control chow for 2 weeks, immunized, and euthanized 10 days later showed (reduced) a form of Tempol at 3.0 ± 1.9 to 5.0 ± 1.5 nmol kg^{-1} tissue in brain and 10.6 ± 4.9 to 40.4 ± 14.5 nmol mL^{-1} (μM) in blood in C57BL/6J and SJL/J animals, respectively ($n = 3$ per group). This suggests that the oral bioavailability of Tempol through the chow allows accumulation to adequate levels and provides defense against inflammatory processes. Interestingly, Tempol reduced the incidence (27% *vs*. 93% in control-diet animals) of MS in EAE models as evidenced by the EAE score (Figure 14.2A). When Tempol was provided after the onset of symptoms (14 days post-immunization), reduced

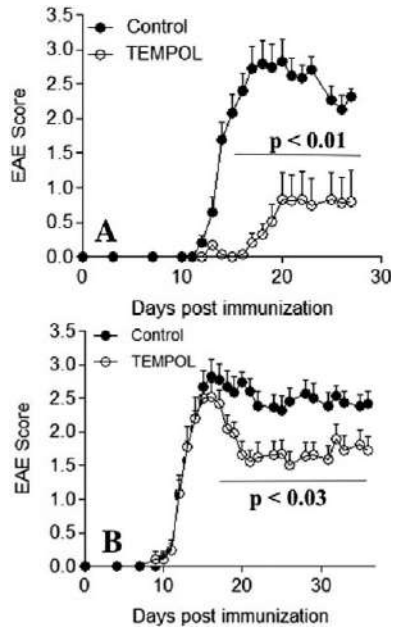

Figure 14.2 (A) EAE severity score of paralysis as a function of time after administration of an immuno-peptide used to induce chronic EAE. Mice were placed on Tempol in the chow two weeks prior to EAE induction. Tempol significantly modulated the severity and onset of disease. (B) EAE severity score when Tempol was administered after the onset of clinical symptoms. Reproduced from ref. 45 with permission from Elsevier, Copyright 2017.

severity in the disease was found in treated animals compared to animals on control food (Figure 14.2B).

Given the evidence for increased levels of ROS and RNS in MS, either prior to or secondary to inflammatory processes, or secondary to mitochondrial dysfunction occurring independent of inflammation,[48] oral Tempol becomes a strong therapeutic candidate in MS as it achieves fully effective concentrations in tissues where it could exert antioxidant and protective actions.[49] Such protective effects at the level of the target tissue may indeed contribute to the ability of Tempol to treat established EAE in both active and passive models of EAE. The fact that Tempol with a molecular weight of 180 Da is not only cell permeable but also penetrates the blood–brain barrier[14] makes it an optimal candidate to provide protection against neuropathologies including MS mediated by inflammatory processes.

14.3 Nitroxide Radioprotection

Ionizing radiation (IR) is an important modality in the treatment of cancer and in some instances may be the single best ''agent'' for treatment. However, for many solid tumors, cure with radiation remains elusive. The success of radiation therapy for cancer patients depends upon achieving a

therapeutic index which is measured by a differential effect between cancer cell cytotoxicity and normal tissue toxicity. Apart from the IR toxicity to normal tissue seen in cancer patients post-radiotherapy, other radiological emergencies such as nuclear power plant disasters or terrorist attacks could place large populations of people exposed to IR doses at risk for a variety of acute effects, including lethality or long-term late effects encompassing organ injury and carcinogenesis. Both situations warrant safe and effective interventions to reduce risks to humans after IR exposure.

Toward this goal, research efforts spanning over more than five decades have been undertaken to develop safe and effective chemical and biologic radiation protectors or mitigators.[50,51] The term radioprotection implies several functions, including the protection of individual cells from death after exposure to radiation. From a clinical perspective, radioprotection can also include protection against the undesired side effects of radiation including fibrosis, alopecia, mucositis, skin damage, and the development of second malignancies. An ideal radioprotective agent would have several characteristics, including minimal toxicity, ease of administration, and selectivity for radioprotection of normal tissues compared with tumor.

14.3.1 Nitroxide Radioprotection: *In Vitro*

After the discovery that nitroxides were SOD mimics and antioxidants capable of protecting cells against oxidative stress-induced by exposure to superoxide and hydrogen peroxide, *in vitro* studies were conducted to determine if nitroxides might protect against ionizing radiation (IR). These studies demonstrated that Tempol could protect against IR-mediated cell killing.[52] For radioprotection, it was necessary that Tempol be applied to cells before IR treatment in high concentrations (mM); if applied after IR no protection was observed. Interestingly, only the oxidized form of Tempol (nitroxide) provided IR protection; the hydroxylamine did not protect. These traits identified Tempol as a chemical radioprotector. IR damages cellular molecules such as DNA predominantly by free radicals ($H^{\bullet}$, $^{\bullet}OH$), e^{-}_{aq}, $O_2^{-\bullet}$ and H_2O_2 resulting from the radiolysis of water.[53–55] Highly reactive $^{\bullet}OH$ radicals generate (in microseconds) longer-lived secondary radicals which are also capable of damaging biomolecules. Since nitroxides and hydroxylamines have similar reactivity with $^{\bullet}OH$, IR protection by nitroxides as opposed to hydroxylamines can be mediated through nitroxide scavenging of secondary radicals.[9] The only FDA-approved radioprotector for clinical use, Amifostine, protects by a similar mechanism. The ability of nitroxides such as Tempol and other derivatives of nitroxides to freely accumulate intracellularly and their ability to participate in radical–radical recombination reactions confer them with unique radioprotective capabilities. While several antioxidants were shown to display antioxidant effects in cellular studies *in vitro*, a feature common with nitroxides and hydroxylamines, only nitroxides were found to be protective against the cytotoxic effects of IR. Thus, nitroxides were identified as being the first case of non-thiol radiation

protectors. It should be noted here that while all radioprotectors can provide antioxidant effects, not all antioxidants (*e.g.*, ascorbate, tocopherol) can provide radioprotective effects. The unique capabilities of radioprotectors may be a result of their efficient reactivity with both highly reactive species such as hydroxyl radicals or secondary radicals with intermediate reactivity at the target site (DNA).[54] This hypothesis was supported by experimental observations that nitroxides with basic substituents accumulate at the DNA site more effectively and scavenge the primary and secondary radicals generated radiolytically.[56] The primary and secondary radicals generated by the more generic oxidants from oxidative stress resulting from exposure to H_2O_2 and $O_2^{-\bullet}$ may be spatially more global in the cell and nitroxides, hydroxylamines and H-atom-donating antioxidants can all be effective in affording protection in such modalities.[57]

The structure–activity relationship of this class of compounds and their oxidation states (hydroxylamine and amine) was studied as radioprotectors and antioxidants. The ring size, ring substituents and oxidation states of the test compounds at fixed concentrations were evaluated for protection against damage induced by exposure to ionizing radiation or hydrogen peroxide in mammalian cells using the clonogenic assay. The study revealed that the main determinants governing protection against hydrogen peroxide exposure were the ring size, redox mid-point potential and oxidation state.[56] In the case of radioprotection, the ring substituents and oxidation state were the main factors. Compounds containing a basic side chain afforded enhanced protection.

The mechanisms underlying radioprotection by nitroxide radicals were understood to be by scavenging secondary radicals of radiolysis by radical–radical recombination reactions. This interpretation was supported by the fact that hydroxylamines were not effective in radioprotection, unlike nitroxide radicals, in spite of similar rates of reaction with the hydroxyl radicals, the primary product of ionizing radiation. However, hydoxylamines were equally effective in protection against oxidative stress induced by exposure to oxidants such as hydrogen peroxide, organic hydroperoxides, *etc*., suggesting that a highly reactive species such as the hydroxyl radical species involved in causing damage in this modality since it reacts equally efficiently with both the hydroxylamine and nitroxide.[57]

14.3.2 Radioprotection: *In Vivo*

The encouraging *in vitro* studies of Tempol as an IR protector were extended to animal models. The toxicity, pharmacology and *in vivo* radioprotective effects of Tempol were studied in C3H mice. Several different concentrations of Tempol were administered to C3H mice *via* intraperitoneal (i.p.) injection, and the pharmacokinetic properties were evaluated.[8,58] The maximum tolerated dose of Tempol administered i.p. (intraperitoneal) was found to be 275 $mg\,kg^{-1}$, which resulted in maximal Tempol levels in whole blood 5–10 min after injection. Five to ten minutes after Tempol injection, mice were exposed to total body irradiation (TBI). The $LD_{50/30}$ (the dose of

radiation that caused 50% lethality at 30 days) for the nontreated mice was found to be 7.84 Gy; whereas the $LD_{50/30}$ for the Tempol-treated mice was significantly higher at 9.97 Gy.[58] The dose-modifying factor (DMF) which is the ratio of $LD_{50/30}$ (treated divided by control) was 1.3. This was the first evidence that Tempol could function as an *in vivo* radioprotector. While Tempol-H (hydroxylamine, reduced form of Tempol) did not protect cells from IR cell killing *in vitro*, it did provide protection *in vivo*. *In vivo*, Tempol-H was rapidly oxidized to Tempol and while its concentration was lower than Tempol given directly, it was high enough to confer protection.[59] In fact, the IR DMF was 1.3 for both Tempol and Tempol-H.

As with any radioprotector of normal tissue there is a concern that systemic administration might protect tumor as well as normal tissue in a clinical setting. Therefore, initial preclinical studies focused on topical application of Tempol with the anticipation that systemic levels of the drug would be low and hence not sufficient to protect tumor tissue. Preclinical studies in guinea pigs and mice revealed that topical application was effective at preventing IR-induced alopecia.[60,61] A phase I clinical trial in brain tumor patients receiving whole-brain radiotherapy suggested that topically applied Tempol may be effective at preventing radiation-induced alopecia.[17] Both the preclinical and clinical studies showed that systemic levels of Tempol were negligible following topical application. To address the issue of tumor radioprotection, preclinical studies evaluated Tempol in tumor-bearing mice.[62] Murine RIF-1 tumors were treated with either PBS or Tempol ($275\ mg\,kg^{-1}$) 10 min before local IR to the tumor at doses ranging from 10 to 60 Gy. Thirty days after IR, tumor growth rates were the same in mice treated with Tempol as in the control group. Furthermore, the radiation dose that resulted in 50% local control at 30 days was 36.7 Gy in Tempol-treated mice compared with 41.8 Gy in the control group and was not statistically different. This study provided evidence that Tempol might be a selective normal tissue radioprotector.[62] Further, studies relating to redox imaging provided additional information as to the selectivity of Tempol for normal tissue radioprotection to be discussed later.

Another significant clinical dose limiting toxicity of IR treatment of head and neck cancers is oral mucositis. Oral mucositis can have adverse effects on patient quality of life and can disrupt radiotherapy continuity, particularly in the setting of chemoradiation with cisplatin. Tempol (systemic or topical application) was evaluated using a murine model for protection against IR- and IR plus cisplatin-induced oral mucositis.[63] Cisplatin combined with IR is the standard of care for head and neck cancer treatment. Fractionated IR (5×8 Gy, daily) resulted in significant large-size lingual ulcers and reduction in epithelial thickness within 10–18 days after initiating IR treatments. For IR + cisplatin, Tempol by both delivery routes essentially nearly completely eliminated ulcers. Tempol given 10 min before each IR fraction by i.p. or topically significantly reduced ulcer size and improved epithelial thickness reduction for IR treatment (see Figure 14.3A,B).[63] To determine if Tempol could protect against IR-mediated oral mucositis

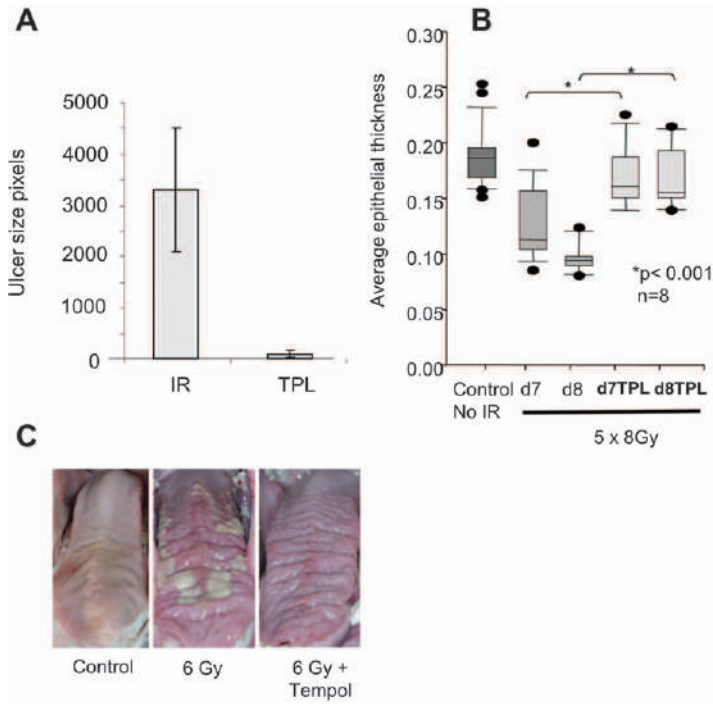

Figure 14.3 Effect of Tempol on ulcer size (A) and epithelial thickness (B) after fractionated IR (5×8 Gy, daily). (A) Mice were euthanized at day 10 after the start of IR and their tongues removed and examined for ulceration with Toluidine Blue. Ulcer size in the two groups was significantly different ($p < 0.001$). (B) Epithelial thickness on the tongue dorsum before frank ulceration (*i.e.*, on days 7 or 8). Data are box plots. The lower boundary of the box represents the 25th percentile of values, whereas the upper boundary represents the 75th percentile. The horizontal line within the box represents the median value. Closed circles above and below the boxes represent out-of-range values. With permission from ref. 63. (C) Lingual mucosal lesions/ulcers from minipigs treated with no treatment (control) or IR (5×6 Gy) with and without Tempol (administered 10 min before each IR fraction). The photographs of the tissues were taken at the 18th day after IR when the inflammation reached a maximum.
Reproduced from ref. 64 with permission from John Wiley & Sons, Copyright 2017 John Wiley & Sons A/S. Published by John Wiley & Sons Ltd.

in a large animal model, miniature pigs were exposed to fractionated IR (5×6 Gy, daily) targeting the entire oral cavity with Tempol being administered 10 minutes before each IR fraction.[64] Tempol provided protection for ulcer size ($p < 0.05$ compared to IR alone; see Figure 14.3C). Since only one concentration of Tempol was used, it remains possible that even better results could have been obtained with a higher Tempol doses.[64]

A concern was examined regarding whether Tempol treatment might interfere with cisplatin-mediated enhancement of IR-induced tumor regrowth delay. Such was not the case as shown in Figure 14.4A,B, where Tempol

provided no protection to control tumor growth nor protected tumors given cisplatin, IR and Tempol.[63] Collectively, our studies suggest that Tempol has promise in helping head and neck cancer patients receiving IR treatment.

14.4 Redox Imaging Using Nitroxide Radicals as Metabolically Responsive MRI Contrast Agents

EPR spectroscopy is the technique of choice to detect and quantify paramagnetic species including nitroxide radicals. EPR can also be used to image paramagnetic species in live objects similar to MRI using magnetic field gradients. EPR imaging was first used to monitor the redox status of tissue and differences in the redox status between normal and tumor tissues using the pyrrolidine 3-carbamoyl nitroxide.[65] The tumor-bearing leg of a mouse was placed in the resonator and projection data to construct EPR images were collected at several time points after administration of the nitroxide. The reconstructed images revealed that there was significant heterogeneity in the nitroxide uptake in the tumor compared to the normal tissue region and further that the rate of reduction of the nitroxide to diamagnetic state proceeded at a faster rate in tumor tissue. Since the reduction rate of a nitroxide agent in a tissue/tumor may depend on the levels of reducing agents such as glutathione (GSH), experiments were conducted in tumor-bearing mice pretreated with L-buthionine sulfoximine (BSO), a GSH-depleting agent.[66] The EPR images revealed that the rate of loss of nitroxide levels in the tumor was significantly retarded in BSO-treated mice, suggesting that the tissue reductant level is one important determinant in nitroxide level as a function of time. EPR imaging however was found to be of inadequate spatial and temporal resolution based on spectral constraints.

Nitroxide radicals having a single unpaired electron are endowed with paramagnetism and can in principle be used as image-intensity-enhancing contrast agents similar to gadolinium (Gd^{3+}) complexes. MRI studies in animal models in the 1980s found them to be less effective in terms of relaxivity and also because of their propensity to be converted to diamagnetic states. The higher relaxivity of Gd^{3+} complexes, their cell impermeability, and the consequent inertness to undergo biological redox reactions made them optimal contrast media for perfusion studies *in vivo* and they are therefore now routinely used in clinical MRI studies. In spite of these negative factors intrinsic to nitroxides for use as contrast agents, their cell-permeability and greater volume distribution are higher than Gd^{3+} complexes (which are essentially extracellular/extravascular agents, partially compensating for lower relaxivity). Their cell permeability and susceptibility to undergo redox reactions can be made use of to report on tissue redox status a capability forming the basis of using these agents for *in vivo* redox imaging. While the bioreduction *in vivo* made them sub-optimal as MRI contrast agents in the 1980s, with the current capabilities of MRI scanners in terms of signal/noise and efficient pulse sequences, nitroxides are once again being evaluated as MRI contrast agents.

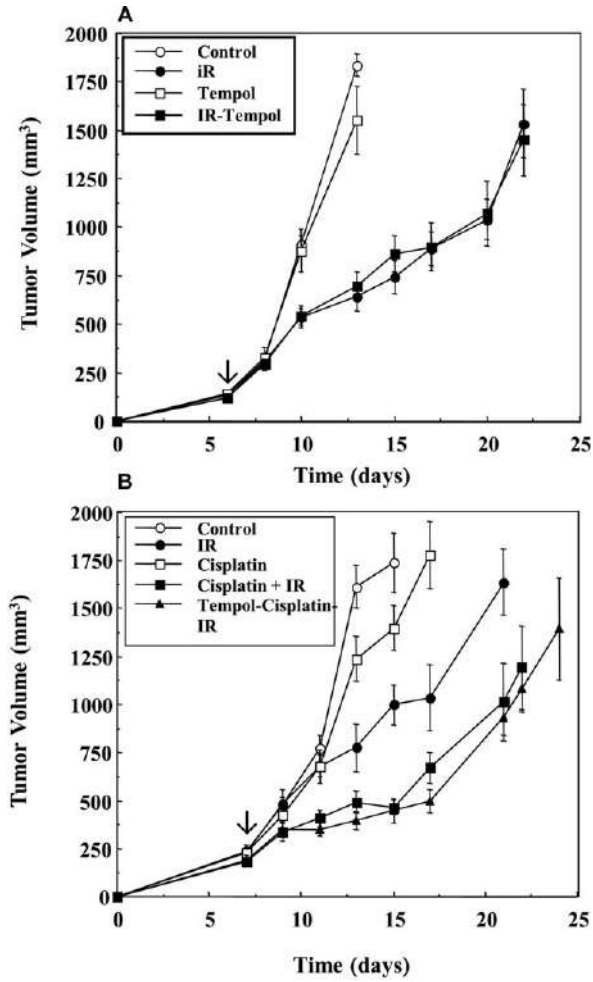

Figure 14.4 Tempol has no effect of SCC VII tumor growth when treated with IR and cisplatin. (A and B) Tumor-bearing mice were treated with IR (5×3 Gy, daily for 1 week), Tempol (275 mg kg^{-1}, i.p., 10 min before each IR fraction) and cisplatin (2.5 mg kg^{-1}, i.p. on days 1, 3, and 5). Arrow marks the day treatment started. There was no effect of Tempol treatment when cisplatin was combined with IR treatment demonstrating lack of tumor radioprotection by Tempol.
Reproduced from ref. 63 with permission from Elsevier, Copyright 2011.

T1-weighted MRI scans at every 20 s for ~20 min after intravenous administration of the nitroxide agent were collected from a mouse with the tumor-bearing leg and contralateral normal leg placed in the resonator. The images showed image intensity enhancement after injection with nitroxide followed by a steady decline.[67] The rate of decline was higher in the tumor region than the normal muscle (Figure 14.5A). The image intensity enhancement can be ascribed to T1 contrast afforded by the paramagnetic state of the

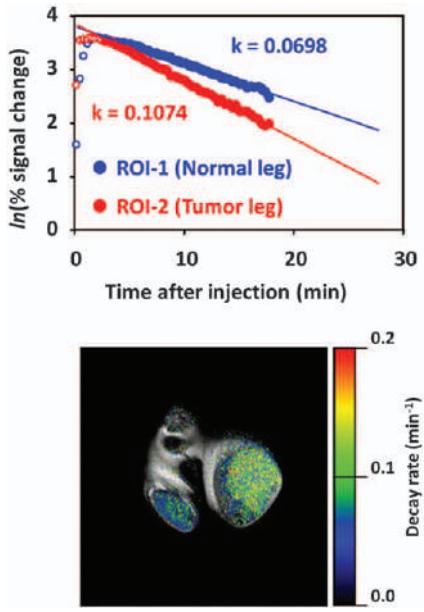

Figure 14.5 (A) Time course of average % signal change in the ROI-1and ROI-2. Logarithmic values of % signal change in the ROIs are plotted with time. Decay rate constants were obtained from the slope of linear decay after peak. (B) Decay rate map overlapped on the corresponding multi-slice multi-echo image shows the distribution of decay rates with clear anatomic information.
Reproduced from ref. 67 with permission from the American Association for Cancer Research, Copyright 2006.

nitroxide, while the time-dependent decrease could be attributed to clearance or bioreduction of the nitroxide. Independent studies verified that the loss of contrast was associated with bioreduction rather than clearance and that the reduction product was predominantly the diamagnetic hydroxylamine.[68] Thus, the kinetics of image intensity loss was understood as representing the tissue redox status. The more reducing the tissue, the faster the signal intensity loss. Since tumors are known to have lower oxygenation (hypoxia) than normal tissue,[69,70] the kinetics of signal intensity loss was higher. A redox map was derived by plotting the rate constants of signal loss in each pixel and displayed in Figure 14.5B. The redox map showed that the reduction rate in the tumor was faster than in the normal leg and further that the tumor regions displayed significant heterogeneity in signal loss. Independent analyses of the tumor tissue revealed that the nitroxide was predominantly converted to the corresponding hydroxylamine. The fact that there was no change in the total (nitroxide + hydroxylamine) during the MRI experiment, but there was a time-dependent loss in signal intensity in a T1-weighted MRI experiment supports the use of redox imaging to reflect the tissue redox status using nitroxide agents as redox-responsive MRI contrast agents.

Nitroxide radicals, but not the corresponding hydroxylamines, were found to be both *in vitro* and *in vivo* radioprotectors. Salivary gland dysfunction is a significant late toxicity following the treatment of head and neck cancers with IR. Using preclinical models, Tempol (both systemic [i.p.] or topical oral gel application) was shown to significantly protect against IR-induced (5 daily treatments) salivary gland damage.[71–73] It is difficult to keep all salivary glands out of the IR field used to treat head and neck tumors. Tempol is paramagnetic, providing the opportunity to monitor tissue levels of Tempol and the rate of its reduction to the hydroxylamine non-invasively using MRI. To monitor tissue levels of Tempol, mice were placed in an MRI resonator such that a traverse slice of 2 mm could be made through the salivary gland area, normal arm muscle and a tumor (SCCVII) implanted in the contralateral arm as shown in Figure 14.6A.[72] Mice were injected with Tempol, and intensity changes of Tempol as a function of time were monitored by MRI as shown in Figure 14.6B. Tempol was clearly reduced to the hydroxylamine (non-paramagnetic) at a two-fold faster rate in tumor as opposed to muscle (normal tissue) and salivary glands. Since the hydroxyamine is not radioprotective, these data suggest that higher levels of Tempol would be available in normal tissue than in tumor to provide radioprotection. In this study two tumor types (SCCVII and HT29) were evaluated for IR tumor regrowth delay where Tempol was administered at the same concentration and timing before each IR fraction as was used in the salivary gland study. No protection by Tempol was observed for either tumor model.[72]

14.5 Tempol and Weight

During the course of studies evaluating Tempol as an *in vivo* chemical radioprotector an interesting study was conducted. The question posed was if mice (female C3H/Hen) were exposed to Tempol for a long period of time (weeks) in their drinking water would this result in any changes in their response to TBI? Due to the unpleasant taste of Tempol in their drinking water mice refused to drink; however, with the addition of sugar, mice readily drank Tempol in the water. The maximum tolerated concentration of Tempol in the sugar-containing drinking water was found to be 58 mM. Mice were placed on sugar water (control) or on sugar/Tempol water for several weeks after which they were exposed to TBI. The response to TBI was the same for both groups, supporting the view that very high systemic concentrations of chemical radioprotectors such as Tempol are required immediately before TBI for protection. Interestingly, the failed experiment yielded an unanticipated result. Expectedly, the weight of control mice on sugar drinking water was substantially increased over time; however, the mice on the sugar/Tempol drinking water did not increase in weight, nor did they exhibit any toxic effects. This finding was confirmed by repeat experiments (Figure 14.7).[74] This study showed that mice on sugar/Tempol drinking water for their lifespan maintained significantly lower weight gain than control mice on sugar water; the sugar/Tempol drinking water was more effective in female as opposed to male mice, Tempol placed in

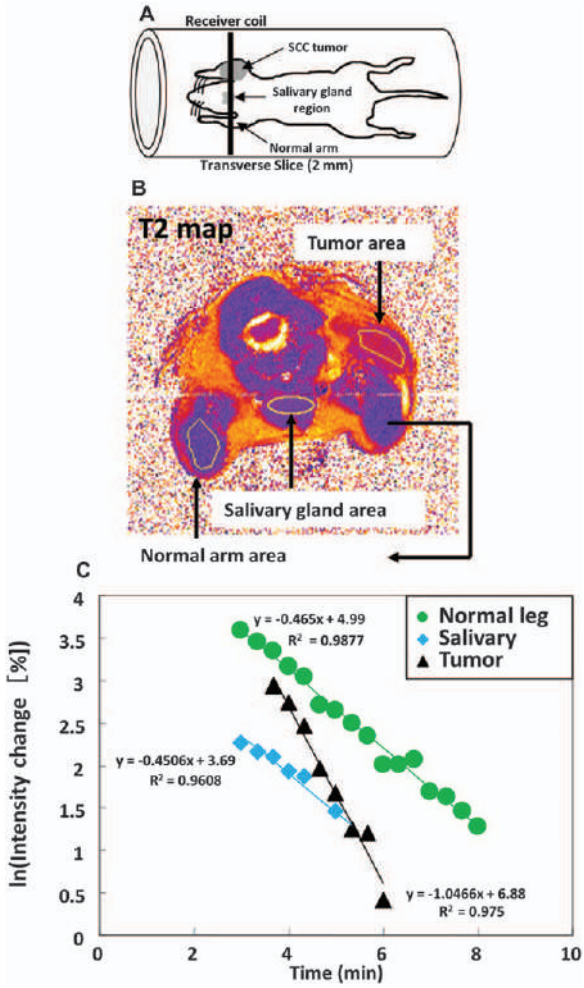

Figure 14.6 (A) Schematic of the placement of the mouse in the resonator and the slice selected for MRI experiments. A transverse slice (2 mm) covering the normal muscle tissue (arm), salivary gland, and the tumor in the contralateral leg were chosen to monitor nitroxide levels as a function of time. (B) T2 map of the slice and the regions of interest chosen in the normal leg, salivary gland and tumor to monitor Tempol decay rates. (C) Representative Tempol decay rates after i.v. injection in a mouse for the selected ROIs shown in (A) and (B). Tempol reduction rate in tumor was statistically different when compared to normal leg ($p < 0.01$) or salivary gland area ($p < 0.001$).
Reproduced from ref. 72 with permission from the American Association for Cancer Research, Copyright 2007.

bacon-flavored chow was as effective as Tempol in drinking water, and overall the Tempol mice were healthy and active. An example of body weights of female C3H/Hen mice on Tempol containing chow for their lifespan is shown

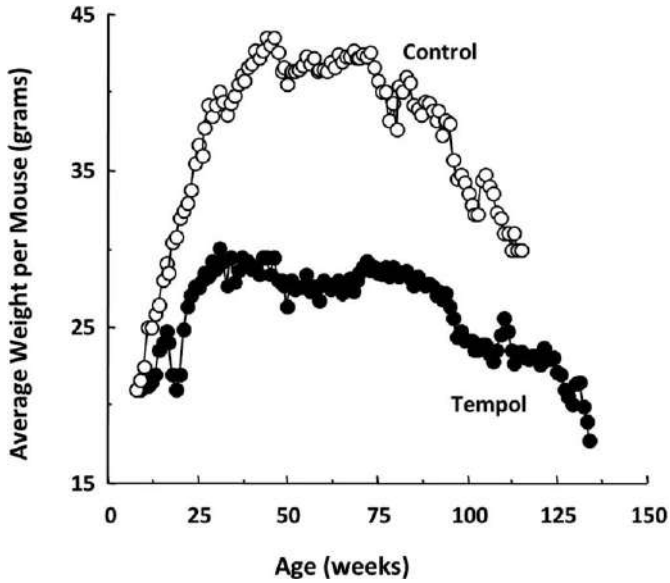

Figure 14.7 Average weight per mouse as a function of time for mice with sugar in their drinking water (Control) or sugar plus Tempol (58 mM) in the drinking water ($n = 10$/group). Reproduced from ref. 74 with permission from Elsevier, Copyright 2002.

in Figure 14.8A.[75] Tempol chow maintained weight in mice approximately 38% lower than mice on control chow. Figure 14.8B shows that throughout the lifespan of these mice, food consumption was very similar between controls and mice on Tempol chow, suggesting that food consumption did not play a role in the reduced weight of the Tempol chow mice.[75] Examination of adipose tissue from these mice revealed that the Tempol-treated mice had much less visceral adipose tissue. These findings led us to examine the mechanism of how a nitroxide antioxidant could exhibit such effects.

To gain a better understanding of the molecular mechanism(s) underlying the influence of Tempol on body weight, the differentiation of mouse 3T3-L1 pre-adipocytes was studied.[76] Tempol inhibited differentiation of 3T3-L1 cells, resulting in a reduction in cellular lipid storage, downregulation of protein levels of key adipogenesis transcription factors (PPARγ and PPARα), downregulation of prolyl hydroxylase, and upregulation of HIF-1α. Gene expression profile studies of selected tissues from mice fed on a Tempol diet indicated early gene expression changes by Tempol in mice before changes in weight (14 days) and later when animal weight gain was reduced by Tempol (60 days). Gene expression (up- and downregulated) in mice treated with Tempol was most prominent in liver (248 genes), muscle (150 genes) and brain (9 genes). In addition, gene expression profiles showed IGF-1 expression levels downregulated after 60 days on the Tempol diet, consistent with the decreased systemic IGF-1 levels.[76] This observation was in agreement with *in vitro*

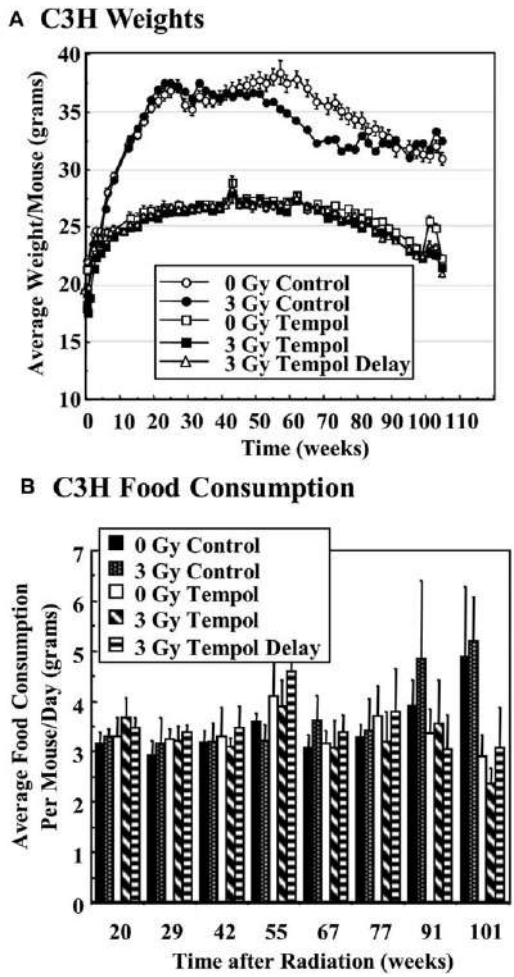

Figure 14.8 Average weight/mouse (grams) of various groups of C3H/Hen mice (A) and average food consumption (grams) per mouse/day (B). CBA mice in this study also demonstrated similar profiles.
Reproduced from ref. 75 with permission from the American Association for Cancer Research, Copyright 2012.

observations in 3T3-L1 cells, showing lower IGF-1 levels as a result of Tempol treatment.[76] IGF-1 regulates tissue growth and metabolism, and elevated levels have been shown to increase the risk of several types of human cancer. Treatment of 3T3-L1 cells with Tempol inhibited the expression of key adipogenesis factors, adipose differentiation and lipid storage, and may be an underlying mechanism, at least in part, of some of the *in vivo* effects of Tempol on body weight.[76]

Obesity is a major health risk which can lead to inflammation, diabetes, cardiovascular disease and cancer.[77–80] Hyperlipidemia coupled with obesity

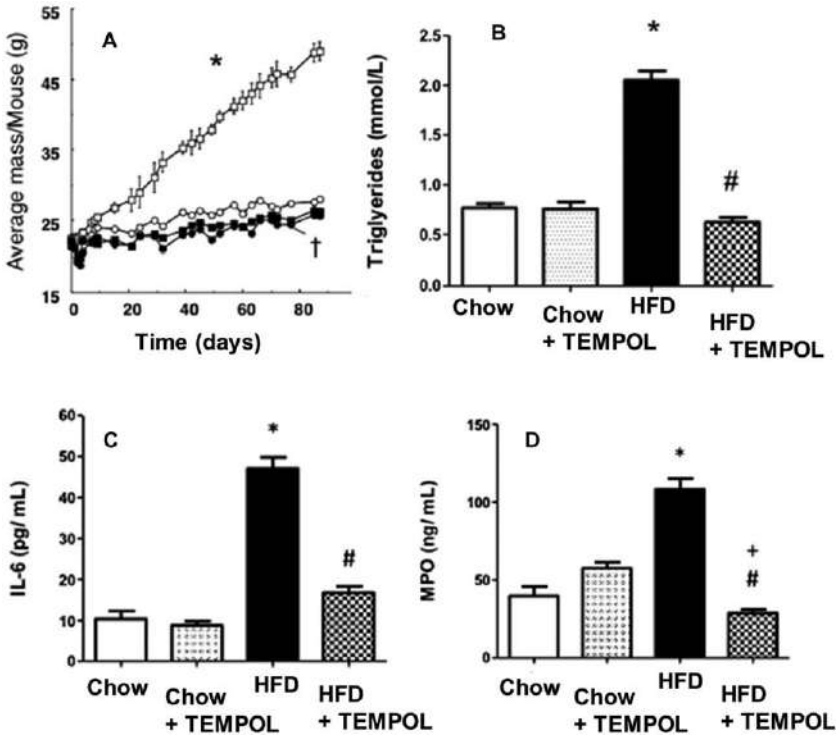

Figure 14.9 Weight and plasma lipid parameters for apoE$^{-/-}$ mice fed either a regular or high-fat diet (HFD) chow with or without Tempol supplementation. (A) Mean body mass (g) of mice over the time course of the study: apoE$^{-/-}$ mice fed HFD (□); apoE$^{-/-}$ mice fed HFD plus added TEMPOL (■); apoE$^{-/-}$ mice fed standard chow (○); apoE$^{-/-}$ mice fed standard chow plus added Tempol (25CF). * $p < 0.001$. (B) plasma triglycerides; (C) plasma interleukin 6 (IL-6), and (D) plasma myeloperoxidase (MPO). Both IL-6 and MPO are inflammatory markers.
Reproduced from ref. 81 with permission from Elsevier, Copyright 2015.

and associated inflammation can result in cardiovascular disease. To study the effects of Tempol on hyperlipidemia, a well-established atherogenesis mouse model, apoE$^{-/-}$ was used to determine if Tempol (in chow) could mitigate any of the factors involved in atherogenesis.[81] A high-fat diet (HFD) resulted in accelerated weight gain in female apoE$^{-/-}$ C57BL6 mice as shown in Figure 14.9A. When Tempol was added to the HFD, there was a significant reduction in weight gain (Figure 14.9A). Interestingly, the weights for apoE$^{-/-}$ mice on a regular diet with or without Tempol were the same, unlike C3H/Hen mice previously reported,[74] underscoring the diversity of strain differences observed in animal models. ApoE$^{-/-}$ mice on the HFD also exhibited higher levels of triglycerides and inflammatory markers, IL-6 and myeloperoxidase (MPO), which were decreased in mice on HFD supplemented with Tempol (Figure 14.9B–D). Decreases were also observed in

HFD/Tempol mice for total cholersterol, LDL and leptin. Mice on HFD/Tempol showed a lower aortic plaque area and the components of the plaques were altered.[81] This study suggests that Tempol may help in controlling obesity, metabolic dysfunction, and perhaps stabilize aortic plaques.

Another potential mechanism of Tempol-mediated weight maintenance dealt with its possible effect on the gut microflora. At a phylum level, obesity has been linked to a high firmicutes to bacteroidetes ratio.[82] Mice placed on a short-term course of Tempol (gavage) or longer term course (drinking water) exhibited a reduction in the firmicutes/bacteroidetes ratio resulting in less weight gain and a reduction in the *Lactobacillus* genus, as shown in Figure 14.10A,B.[83] This reduction was accompanied by significantly lower levels of bile acid hydrolase enzyme activity, which led to an increase of intestinal taurine-linked β-muricholic acid (Figure 14.10C). The T-β-muricholic acid is an antagonist of the farnesoid X receptor (FXR), which is involved in glucose utilization and lipid metabolism, leading to an overall reduction in fat mass (Figure 14.10D,E).[83] Further studies showed that Tempol enhanced liver glucose catabolism by altering several genes involved in glucose and lipid metabolism.[84] These gene alterations were not observed in mice raised in germ-free facilities, thus emphasizing the role of the gut microflora in the Tempol-mediated weight effect.

The initial discovery that a nitroxide free radical such as Tempol would influence in a nontoxic way the weight of an animal was highly unexpected and surprising. There has been considerable progress toward understanding the mechanism(s) responsible for the effect. The mechanism may include Tempol's antioxidant properties, but recent results suggest the interaction of Tempol with the gut microflora may be a predominant mechanism.

14.6 Tempol and Carcinogenesis

In our initial study evaluating Tempol and animal weight, mice on the Tempol for their lifespan were evaluated for spontaneous tumor incidence.[74] Though the number of mice/group was low, there appeared to be fewer tumors in the Tempol group than the control group. This result was somewhat similar in fact to that seen for mice on a caloric-restricted diet.[85–87] To explore the observation with respect to carcinogenesis a series of studies were initiated in genetically modified cancer-prone mouse models including ATM, p53 and Fanconi anemia knockout mice. Atm-deficient mice are an excellent model of the human cancer-prone syndrome ataxia telangiectasia (AT). AT is a pleiotropic syndrome consisting of neuronal degeneration, oculocutaneous telangiectasias, growth retardation, infertility, sensitivity to ionizing radiation (IR) or agents that cause double-stranded DNA breaks, immunodeficiencies and cancer predisposition, particularly lymphomas.[88,89] Tempol was chronically administered (10 mg g^{-1} of bacon-flavored chow) in the diet of these animals. Treated and untreated wild-type mice lived a normal murine lifespan of about 1.5 years. However, the $Atm^{-/-}$ mice were treated with Tempol, and at weaning had significantly

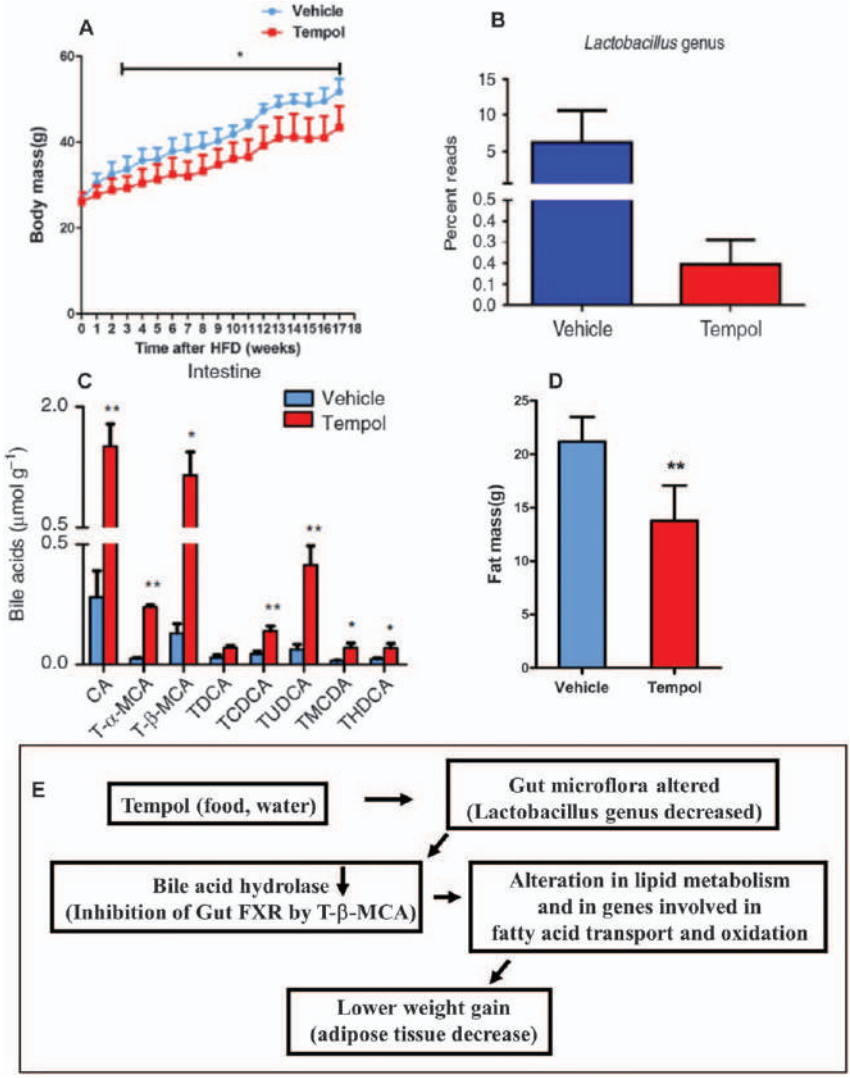

Figure 14.10 (A) Growth curves of mice on vehicle or Tempol receiving a high-fat diet (HFD). (B) Gene sequencing analysis (16S rRNA) of genus *Lactobacillus* cecum content after 5 days of Tempol treatment by gavage clearly showing a substantial decrease in *Lactobacillus* in Tempol-treated mice. (C) Intestinal bile-acid composition of vehicle and Tempol-treated mice on a HFD for 17 weeks. (D) Fat mass (determined by NMR) in vehicle and Tempol-treated mice following 16 weeks on a HFD. (E) Schema showing the effects of Tempol on gut microflora and associated bile acids hydrolase resulting in lower weight gain.
Reproduced from ref. 83 with permission from Springer Nature, Copyright 2013.

increased longevity (62.4 *versus* 30.1 weeks, $p < 0.01$, at the 50% survival level) compared with untreated $Atm^{-/-}$ mice.[90] Tempol treatment prolonged the appearance of thymic lymphomas and also resulted in decreased ROS, oxidative damage and oxidative stress in $Atm^{-/-}$ mice. Furthermore, there was also a significant reduction in weight gain in the $Atm^{-/-}$ mice fed Tempol. These results confirmed that the reduction in weight gain was not a result of decreased food intake, lowered metabolism or physical inactivity.[90] A different nitroxide, 5-carboxy-1,1,3,3-tetramethylisoindolin-2-yloxyl (CTMIO) when placed in the drinking water of $Atm^{-/-}$ mice significantly extended their lifespan (median survival; 379 days *versus* 109 days for treated $Atm^{-/-}$ mice as opposed to untreated $Atm^{-/-}$ mice, respectively) by delaying the onset of thymic lymphomas.[91] Further, it was demonstrated that CTMIO treatment of $Atm^{-/-}$ mice resulted in correction of neurobehavioral deficits and reduction of oxidative damage to Purkinje cells.[91]

Tempol treatment of cancer-prone p53-deficient mice also resulted in a small but significant (25%) increase in lifespan by prolonging latency to tumorigenesis, demonstrating that oxidative stress and damage are not necessary for the chemopreventative effects of Tempol.[92] However, the relatively small effect on latency in p53-deficient mice indicated that Tempol-mediated resistance to oxidative insult was p53-dependent.[92]

Using $Fancd2^{-/-}$ knockout mice as a model of Fanconi anemia (FA), the potential role of Tempol, as a tumor-delaying agent for solid tumors, was studied.[93] FA is a genetic disorder characterized by congenital abnormalities, bone marrow failure and marked cancer susceptibility. FA patients have an elevated risk of developing hematologic malignancies and solid tumors. Dietary Tempol increased the mean tumor-free survival time of $Fancd2^{-/-}$ $Trp53^{+/-}$ mice by 27% ($p < 0.01$), from 308 to 390 days, without changing the overall tumor spectrum.[93] More strikingly, Tempol delayed the onset of epithelial tumors and increased the mean epithelial tumor-free survival time by 38% ($p < 0.0001$), from 312 to 432 days, in $Fancd2^{-/-}$ $Trp53^{+/-}$ mice. These results indicated that Tempol significantly delayed tumor formation in $Fancd2^{-/-}$ $Trp53^{+/-}$ mice. The reduction in oxidative DNA damage in Tempol-treated FA fibroblasts and mice suggested that its tumor-delaying function could possibly be due to its antioxidant activity and independent of p53 pathways as seen in $Atm^{-/-}$ and $p53^{-/-}$ mouse models. Our observation that Tempol can modulate weight gain in C3H mice and from the three cancer-prone murine models established that chronic exposure to Tempol can act as a chemopreventative agent in wild-type C3H mice or genetically modified mouse models of human cancers.

14.7 Radiation Countermeasures

Subsequent to the terror events of 9/11 in the United States, workshop reports and publications questioned the readiness of the United States for terror or accidental events, particularly those involving nuclear weapons or reactor accidents.[94–97] There was a recognized need for further research in

the fields of radioprotection/mitigation and IR dosimetry. The NIH Medical Radiation Countermeasures Program (NIAID) was initiated in 2005 to fund research into these areas (https://www.niaid.nih.gov/research/radiation-nuclear-countermeasures-program). One of the primary missions of the Radiation Countermeasures Program deals with the development of radioprotectors and mitigators to address acute radiation syndrome (ARS), which can cause lethality dependent on IR dose and body coverage. A challenge for this research with respect to ARS is that most chemical radiation protectors, in order to be effective, must be present before or during the actual IR exposure.[50,51] Thus, in a surprise nuclear terror event or an unforeseen nuclear accident, chemical radioprotectors would not be useful. As discussed above, Tempol (and other nitroxides) are chemical radioprotectors and would not be useful in survival protection of an unanticipated IR exposure. However, individuals (or populations) receiving a nonlethal dose of IR would survive, but would be susceptible to future cancer induction.[98,99] Under these conditions, we proposed that Tempol might be an effective chemopreventative agent if administered *after* radiation exposure with respect to reducing or delaying IR-induced carcinogenesis. As chronic administration of Tempol in the diet led to a decrease in weight gain in mice, as discussed above, caloric restriction in rodents leading to decreased weight gain has been shown to decrease IR-induced carcinogenesis.[100,101]

A study was designed to expose two different strains of mice (female C3H/Hen and CBA) to a nonlethal TBI dose of 3 Gy.[75] Immediately after IR, two groups of mice were switched to bacon-flavored chow containing Tempol (0 Gy Tempol, 3 Gy Tempol). An additional group receiving 3 Gy TBI was switched to Tempol chow 1 month after IR (3 Gy delayed Tempol). Mice were maintained on these diets over their entire lifespan. The endpoint for the study was tumor formation (not to exceed 2 cm diameter) or until humane euthanasia criteria were met. Each mouse received a comprehensive necropsy examination and pathology evaluation by a board-certified veterinary pathologist.

As expected, the Tempol diet resulted in reduced weight gain starting at approximately 10 weeks compared with mice on the control diet ($p < 0.001$) (see Figure 14.8).[75] There was no statistical difference in the weights of 0 Gy Tempol or 3 Gy Tempol mice throughout the study. Weights of the 0 Gy control group increased rapidly to 25 weeks, peaked at 60 weeks (37 g), and then slowly decreased as the animals aged. The 0 Gy Tempol group gained weight similar to control animals up to approximately 5 weeks, followed by a plateau in weights to approximately 50 weeks (27 g), and then decreased slowly. The 0 Gy control mice had significantly higher weights ($p < 0.001$) than the 0 Gy Tempol mice from approximately 10–80 weeks with a maximum difference of approximately 38% at 55 weeks. Irradiated mice on the Tempol diet (both those placed on the Tempol diet immediately after IR or 1 month after IR) exhibited near identical weights to 0 Gy controls throughout the study. The decreased weight gain of mice receiving the Tempol diet could not be explained by reduced food consumption. Food consumption monitored from weeks 20 to 101 showed no statistical difference among any of the

groups. The weight and food consumption profiles of the CBA mice were similar to the C3H mice.

Figure 14.11 A shows a Kaplan–Meier survival curve for C3H/Hen mice.[75] There was no significant difference in the lifespan of 0 Gy control *versus* 0 Gy Tempol groups. Overall, chronic Tempol food supplementation was well tolerated by both mouse strains with little untoward toxicity. There was a substantial reduction in the lifespan for the 3 Gy control group compared with unirradiated controls ($p < 0.001$). Tempol diet supplementation initiated immediately after TBI resulted in a significant survival advantage compared with the control diet ($p < 0.001$), representing an extension in survival of approximately 34 weeks for C3H mice. Interestingly, delaying the Tempol diet one month post 3 Gy TBI in C3H mice also provided a significant survival advantage (23 weeks) compared with the 3 Gy control ($p < 0.001$) (Figure 14.11A). There was no statistical difference between the 3 Gy Tempol and 3 Gy Tempol delayed groups. Similar survival profiles were observed with the CBA mouse strain.[75] The cumulative incidence of hematopoietic and solid neoplasms for C3H/Hen mice is shown in Figure 14.11B,C. Both Tempol groups delayed the onset and decreased the incidence of hematopoietic neoplasms (predominantly lymphomas). Though the incidence was low, Tempol provided reduced incidence of hematopoietic neoplasms in unirradiated controls ($p < 0.016$). As for solid neoplasms, Tempol groups exhibited delayed onset, however, by approximately 700 days post-TBI the incidence of solid neoplasms slightly increased over 3 Gy control in both Tempol groups. There were similarities and differences between C3H/Hen and CBA mice with respect to neoplasm induction. The rate of hematopoietic neoplasm incidence was accelerated in C3H mice compared with CBA mice. Tempol also delayed the onset and incidence of hematopoietic neoplasms in CBA mice. Unlike for C3H/Hen mice, Tempol delayed both the onset and incidence of solid neoplasms in CBA mice. These data show that Tempol clearly reduced IR-mediated cancers, leading to an increased lifespan. The mechanism(s) responsible for this finding may involve weight-altering effects, reduction in inflammatory pathways, and antioxidant activity. It is interesting to point out that nitroxides were reported to be mutagens as measured by the *Salmonella typhimurium* assay and likely to induce DNA damage leading to carcinogenesis.[102] Such was certainly not the case when Tempol was used in mammalian systems such as C3H and CBA mice (Figure 14.11A).[75] The lifespan of control mice and mice on Tempol chow for most of their lifespan exhibited no difference in survival or cancer induction. In fact, in mammalian cells, Tempol was found not to be mutagenic or cytotoxic as well as protecting against mutations induced by hydrogen peroxide and superoxide generated by hypoxanthine/xanthine oxidase.[103] More research will be required to further expand upon the mechanism of action of Tempol's influence on carcinogenesis; however, the lifespan study of mice on Tempol chow opens the door toward reducing IR-mediated carcinogenesis and may be useful in a countermeasures situation.

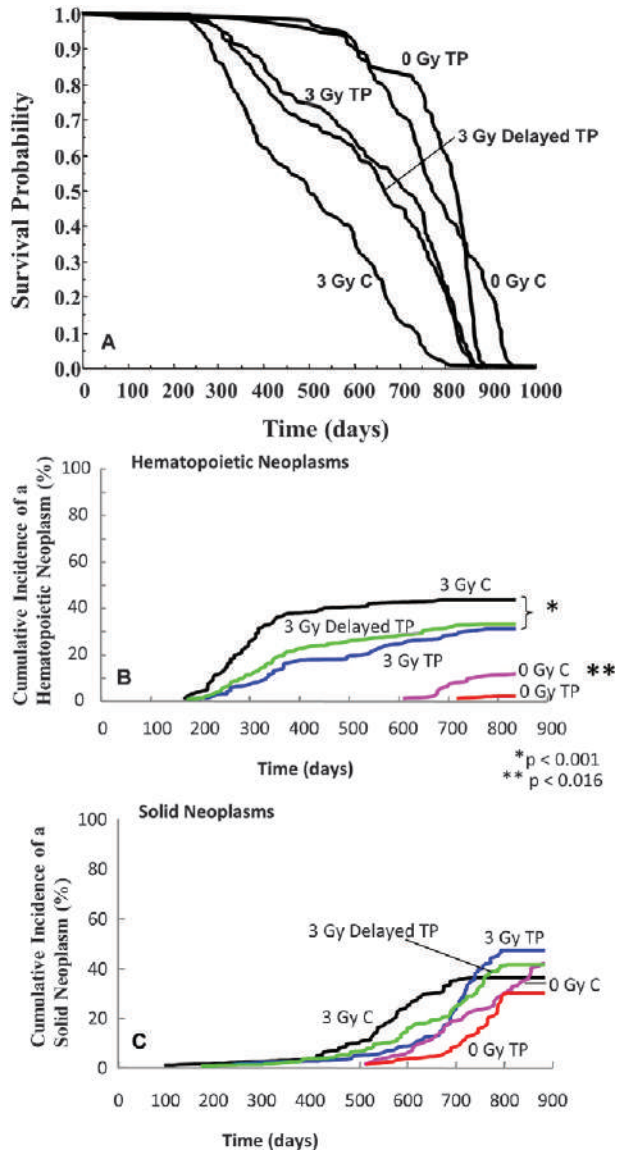

Figure 14.11 (A) Kaplan-Meier survival plots for C3H mice. Mice were exposed to either 0 or 3 Gy TBI with or without Tempol food supplementation initiated immediately after radiation and maintained throughout the lifespan. (B) Cumulative incidence of deaths for various groups shown in (A), hematopoietic neoplasms (B), solid neoplasms (C). The number of mice in each group was 0 Gy $C = 93$; 0 Gy Tempol = 89; 3 Gy control = 170; 3 Gy Tempol = 161; and 3 Gy Tempol delayed = 202. C = Control; TP = Tempol. Statistics using log rank analysis of the survival curves: 0 Gy C *vs.* 0 Gy T ($p = 0.06$); 0 Gy C vs. 3 Gy C ($p < 0.001$); 0 Gy T vs. 3 Gy T ($p < 0.001$); 3 Gy C vs. 3 Gy T ($p < 0.001$); 3 Gy C vs. 3 Gy T delayed ($p < 0.001$); 3 Gy T vs. 3 Gy T delayed ($p = 0.07$).
Reproduced from ref. 75 with permission from the American Association for Cancer Research, Copyright 2012.

14.8 Conclusions

Over 30 years ago the findings of test tube nitroxide chemistry were translated to mammalian cell and animal systems. We had no idea at the time that nitroxides would impact so many diverse mammalian biological systems. Nitroxides have been shown to have broad utility in biomedical research, which is a testament to the involvement of free radical processes in a diverse variety of pathological conditions and the manner in which nitroxides catalytically and/or stoichiometrically interact with ROS and oxidized substrates when oxidative stress is imposed. That nitroxides have been shown to protect against IR-induced lethality, tissue injury and carcinogenesis is noteworthy and could be most beneficial in clinical or countermeasures settings. How nitroxides interact with complex cellular and signal transduction pathways, some of which utilize intra- and extracellular free radicals for initiation will be a future challenge and hopefully will advance the nitroxide and biomedical research field further.

References

1. N. Kocherginsky and H. Swartz, *Terminology, Classification, and Distribution of the Nitroxides in Cells*, CRC Press, Boca Raton, FL, 1995, p. 15.
2. S. Brinkmann, H. F. Sutoris and H. Weiss, Controlled radical polymerization in the presence of N-oxyls, *Macromolecular Symposia*, 2001, **163**, 145.
3. H. M. McConnell, *Molecular Motion in Biological Membranes*, Academic Press, New York, 1976, p. 525.
4. B. Kalyanaraman, E. Perez-Reyes and R. P. Mason, Spin-trapping and direct electron spin resonance investigations of the redox metabolism of quinone anticancer drugs, *Biochim. Biophys. Acta*, 1980, **630**, 119.
5. L. J. Berliner, *Spin Labelling II: Theory and Applications*, Academic Press, New York, 1979.
6. A. Samuni, C. M. Krishna, P. Riesz, E. Finkelstein and A. Russo, A novel metal-free low molecular weight superoxide dismutase mimic, *J. Biol. Chem.*, 1988, **263**, 17921.
7. J. B. Mitchell, A. Samuni and M. C. Krishna, *et al.*, Biologically active metal-independent superoxide dismutase mimics, *Biochemistry*, 1990, **29**, 2802.
8. S. M. Hahn, L. Wilson and C. M. Krishna, *et al.*, Identification of nitroxide radioprotectors, *Radiat. Res.*, 1992, **132**, 87.
9. M. C. Krishna, D. A. Grahame, A. Samuni, J. B. Mitchell and A. Russo, Oxoammonium cation intermediate in the nitroxide-catalyzed dismutation of superoxide, *Proc. Natl. Acad. Sci.*, 1992, **89**, 5537.
10. B. P. Soule, F. Hyodo and K. Matsumoto, *et al.*, The chemistry and biology of nitroxide compounds, *Free Radicals Biol. Med.*, 2007, **42**, 1632.
11. M. C. Krishna, A. Russo, J. B. Mitchell, S. Goldstein, H. Dafni and A. Samuni, Do nitroxides antioxidants act as scavengers of superoxide or as SOD mimics? *J. Biol. Chem.*, 1996, **271**, 26026.

12. M. C. Krishna, A. Samuni, J. Taira, S. Goldstein, J. B. Mitchell and A. Russo, Stimulation by nitroxides of catalase-like activity of hemeproteins, *J. Biol. Chem.*, 1996, **271**, 26018.
13. A. M. Samuni, W. DeGraff, M. C. Krishna and J. B. Mitchell, Cellular sites of H2O2-induced damage and their protection by nitroxides, *Biochim. Biophys. Acta*, 2001, **1525**, 70.
14. R. M. Davis, S. Matsumoto and M. Bernardo, *et al.*, Magnetic resonance imaging of organic contrast agents in mice: capturing the whole-body redox landscape, *Free Radicals Biol. Med.*, 2011, **50**, 459.
15. B. P. Soule, F. Hyodo and K. Matsumoto, *et al.*, Therapeutic and clinical applications of nitroxide compounds, *Antioxid. Redox Signaling*, 2007, **9**, 1731.
16. C. S. Wilcox and A. Pearlman, Chemistry and antihypertensive effects of tempol and other nitroxides, *Pharmacol. Rev.*, 2008, **60**, 418.
17. J. M. Metz, D. Smith and R. Mick, *et al.*, A phase I study of Topical Tempol for the prevention of alopecia induced by whole brain radiotherapy, *Clin. Cancer Res.*, 2004, **10**, 6411.
18. R. Rak, D. L. Chao, R. M. Pluta, J. B. Mitchell, E. H. Oldfield and J. C. Watson, Neuroprotection by the stable nitrioxide Tempol during reperfusion in a rat model of transient focal ischemia, *J. Neurosurg.*, 2000, **92**, 646.
19. N. Kato, K. Yanaka, K. Hyodo, K. Homma, S. Nagase and T. Nose, Stable nitroxide Tempol ameliorates brain injury by inhibiting lipid peroxidation in a rat model of transient focal cerebral ischemia, *Brain Res.*, 2003, **979**, 188.
20. C. G. Schnackenberg, W. J. Welch and C. S. Wilcox, Normalization of blood pressure and renal vascular resistance in SHR with a membrane-permeable superoxide dismutase mimetic: role of nitric oxide, *Hypertension*, 1998, **32**, 59.
21. C. G. Schnackenberg and C. S. Wilcox, The SOD mimetic tempol restores vasodilation in afferent arterioles of experimental diabetes, *Kidney Int.*, 2001, **59**, 1859.
22. C. Thiemermann, Membrane-permeable radical scavengers (tempol) for shock, ischemia-reperfusion injury, and inflammation, *Crit. Care Med.*, 2003, **31**, S76.
23. Y. Deng-Bryant, I. N. Singh, K. M. Carrico and E. D. Hall, Neuroprotective effects of tempol, a catalytic scavenger of peroxynitrite-derived free radicals, in a mouse traumatic brain injury model, *J. Cereb. Blood Flow Metab.*, 2008, **28**, 1114.
24. Z. Sledziński, M. Woźniak and J. Antosiewicz, *et al.*, Protective effect of 4-hydroxy-TEMPO, a low molecular weight superoxide dismutase mimic, on free radical toxicity in experimental pancreatitis, *Int. J. Pancreatol.*, 1995, **18**, 153.
25. T. Lipman, R. Tabakman and P. Lazarovici, Neuroprotective effects of the stable nitroxide compound Tempol on 1-methyl-4-phenylpyridinium ion-induced neurotoxicity in the Nerve Growth Factor-differentiated

model of pheochromocytoma PC12 cells, *Eur. J. Pharmacol.*, 2006, **549**, 50.
26. M. C. Ghosh, W. H. Tong and D. Zhang, *et al.*, Tempol-mediated activation of latent iron regulatory protein activity prevents symptoms of neurodegenerative disease in IRP2 knockout mice, *Proc. Natl. Acad. Sci. U. S. A.*, 2008, **105**, 12028.
27. E. M. Frohman, M. K. Racke and C. S. Raine, Multiple sclerosis–the plaque and its pathogenesis, *N. Engl. J. Med.*, 2006, **354**, 942.
28. C. Bjartmar and B. D. Trapp, Axonal degeneration and progressive neurologic disability in multiple sclerosis, *Neurotoxic. Res.*, 2003, **5**, 157.
29. B. Ferguson, M. K. Matyszak, M. M. Esiri and V. H. Perry, Axonal damage in acute multiple sclerosis lesions, *Brain*, 1997, **120**, 393.
30. B. D. Trapp, J. Peterson, R. M. Ransohoff, R. Rudick, S. Mörk and L. Bö, Axonal transection in the lesions of multiple sclerosis, *N. Engl. J. Med.*, 1998, **338**, 278.
31. M. Sospedra and R. Martin, Immunology of multiple sclerosis, *Annu. Rev. Immunol.*, 2005, **23**, 683.
32. S. L. Hauser, E. Waubant and D. L. Arnold, *et al.*, B-cell depletion with rituximab in relapsing-remitting multiple sclerosis, *N. Engl. J. Med.*, 2008, **358**, 676.
33. M. Hobom, M. K. Storch and R. Weissert, *et al.*, Mechanisms and time course of neuronal degeneration in experimental autoimmune encephalomyelitis, *Brain Pathol.*, 2004, **14**, 148.
34. X. Qi, A. S. Lewin, L. Sun, W. W. Hauswirth and J. Guy, Mitochondrial protein nitration primes neurodegeneration in experimental autoimmune encephalomyelitis, *J. Biol. Chem.*, 2006, **281**, 31950.
35. K. G. Su, G. Banker, D. Bourdette and M. Forte, Axonal degeneration in multiple sclerosis: the mitochondrial hypothesis, *Curr. Neurol. Neurosci. Rep.*, 2009, **9**, 411.
36. Y. Gilgun-Sherki, E. Melamed and D. Offen, The role of oxidative stress in the pathogenesis of multiple sclerosis: the need for effective antioxidant therapy, *J. Neurol.*, 2004, **251**, 261.
37. R. E. Gonsette, Oxidative stress and excitotoxicity: a therapeutic issue in multiple sclerosis, *Mult. Scler.*, 2008, **14**, 22.
38. G. Schreibelt, R. J. Musters and A. Reijerkerk, *et al.*, Lipoic acid affects cellular migration into the central nervous system and stabilizes blood-brain barrier integrity, *J. Immunol.*, 2006, **177**, 2630.
39. A. Van der Goes, D. Wouters and S. M. Van Der Pol, *et al.*, Reactive oxygen species enhance the migration of monocytes across the blood-brain barrier *in vitro*, *FASEB J.*, 2001, **15**, 1852.
40. K. J. Smith, R. Kapoor, S. M. Hall and M. Davies, Electrically active axons degenerate when exposed to nitric oxide, *Ann. Neurol.*, 2001, **49**, 470.
41. M. E. van Meeteren, J. J. Hendriks, C. D. Dijkstra and E. A. van Tol, Dietary compounds prevent oxidative damage and nitric oxide production by cells involved in demyelinating disease, *Biochem. Pharmacol.*, 2004, **67**, 967.

42. F. Torreilles, S. Salman-Tabcheh, M. Guérin and J. Torreilles, Neurodegenerative disorders: the role of peroxynitrite, *Brain Res. Brain Res. Rev.*, 1999, **30**, 153.
43. B. C. Kieseier, H. Wiendl, H.-P. Hartung, V.-I. Leussink and O. Stüve, Risks and benefits of multiple sclerosis therapies: need for continual assessment, *Curr. Opin. Neurol.*, 2011, **24**(3), 238.
44. O. Stüve, Knowns and unknowns in the future of multiple sclerosis treatment, *J. Neurol. Sci.*, 2009, **287**(Suppl 1), S30.
45. S. Neil, J. Huh and V. Baronas, *et al.*, Oral administration of the nitroxide radical TEMPOL exhibits immunomodulatory and therapeutic properties in multiple sclerosis models, *Brain, Behav., Immun.*, 2017, **62**, 332.
46. G. W. Kreutzberg, Microglia: a sensor for pathological events in the CNS, *Trends Neurosci.*, 1996, **19**, 312.
47. E. D. Ponomarev, L. P. Shriver, K. Maresz and B. N. Dittel, Microglial cell activation and proliferation precedes the onset of CNS autoimmunity, *J. Neurosci. Res.*, 2005, **81**, 374.
48. H. E. Andrews, P. P. Nichols, D. Bates and D. M. Turnbull, Mitochondrial dysfunction plays a key role in progressive axonal loss in Multiple Sclerosis, *Med. Hypotheses*, 2005, **64**, 669.
49. C. S. Wilcox, Effects of tempol and redox-cycling nitroxides in models of oxidative stress, *Pharmacol. Ther.*, 2010, **126**, 119.
50. J. F. Weiss and M. R. Landauer, History and development of radiation-protective agents, *Int. J. Radiat. Biol.*, 2009, **85**, 539.
51. D. Citrin, A. P. Cotrim, F. Hyodo, B. J. Baum, M. C. Krishna and J. B. Mitchell, Radioprotectors and mitigators of radiation-induced normal tissue injury, *Oncologist*, 2010, **15**, 360.
52. J. B. Mitchell, W. DeGraff and D. Kaufman, *et al.*, Inhibition of oxygen-dependent radiation-induced damage by the nitroxide superoxide dismutase mimic, Tempol, *Arch. Biochem. Biophys.*, 1991, **289**, 62.
53. C. von Sonntag, *The Chemical Basis of Radiation Biology*, Taylor and Francis, London, 1987.
54. J. F. Ward, DNA damage produced by ionizing radiation in mammalian cells: identities, mechanisms of formation, and reparability, *Prog. Nucleic Acid Res. Mol. Biol.*, 1988, **36**, 95.
55. J. F. Ward, DNA damage and repair, *Basic Life Sci.*, 1991, **58**, 403.
56. M. C. Krishna, W. DeGraff and O. H. Hankovszky, *et al.*, Studies of structure-activity relationship of nitroxide free radicals and their precursors as modifiers against oxidative damage, *J. Med. Chem.*, 1998, **41**, 3477.
57. S. Xavier, K. Yamada and A. M. Samuni, *et al.*, Differential protection by nitroxides and hydroxylamines to radiation-induced and metal ion-catalyzed oxidative damage, *Biochim. Biophys. Acta*, 2002, **1573**, 109.
58. S. M. Hahn, Z. Tochner and C. M. Krishna, *et al.*, Tempol, a stable free radical, is a novel murine radiation protector, *Cancer Res.*, 1992, **52**, 1750.

59. S. M. Hahn, M. C. Krishna, A. M. DeLuca, D. Coffin and J. B. Mitchell, Evaluation of the hydroxylamine Tempol-H as an in vivo radioprotector, *Free Radicals Biol. Med.*, 2000, **28**, 953.
60. T. Goffman, D. Cuscela and J. Glass, *et al.*, Topical application of nitroxide protects radiation induced alopecia in guinea pigs, *Int. J. Radiat. Oncol., Biol., Phys.*, 1992, **22**, 803.
61. D. Cuscela, D. Coffin and G. Lupton, *et al.*, Protection from radiation-induced alopecia with topical application of nitroxides: fractionated studies, *Cancer J. Sci. Am.*, 1996, **2**, 273.
62. S. M. Hahn, F. J. Sullivan and A. M. DeLuca, *et al.*, Evaluation of tempol radioprotection in a murine tumor model, *Free Radicals Biol. Med.*, 1997, **22**, 1211.
63. A. P. Cotrim, M. Yoshikawa and A. N. Sunshine, *et al.*, Pharmacological protection from radiation +/− cisplatin-induced oral mucositis, *Int. J. Radiat. Oncol., Biol., Phys.*, 2012, **83**, 1284.
64. L. Hu, Y. Wang and A. P. Cotrim, *et al.*, Effect of Tempol on the prevention of irradiation-induced mucositis in miniature pigs, *Oral Dis.*, 2017, **23**, 801.
65. P. Kuppusamy, M. Afeworki and R. A. Shankar, *et al.*, In vivo electron paramagnetic resonance imaging of tumor heterogeneity and oxygenation in a murine model, *Cancer Res.*, 1998, **58**, 1562.
66. P. Kuppusamy, H. Li and G. Ilangovan, *et al.*, Noninvasive imaging of tumor redox status and its modification by tissue glutathione levels, *Cancer Res.*, 2002, **62**, 307.
67. K. Matsumoto, F. Hyodo and A. Matsumoto, *et al.*, High-resolution mapping of tumor redox status by magnetic resonance imaging using nitroxides as redox-sensitive contrast agents, *Clin. Cancer Res.*, 2006, **12**, 2455.
68. F. Hyodo, K. Matsumoto, A. Matsumoto, J. B. Mitchell and M. C. Krishna, Probing the intracellular redox status of tumors with magnetic resonance imaging and redox-sensitive contrast agents, *Cancer Res.*, 2006, **66**, 9921.
69. R. H. Thomlinson and L. H. Gray, The histological structure of some human lung cancers and the possible implications for radiotherapy, *Br. J. Cancer*, 1955, **9**, 539.
70. M. Hockel, K. Schlenger, B. Aral, M. Mitze, U. Schaffer and P. Vaupel, Association between tumor hypoxia and malignant progression in advanced cancer of the uterine cervix, *Cancer Res.*, 1996, **56**, 4509.
71. J. M. Vitolo, A. P. Cotrim and A. L. Sowers, *et al.*, The stable nitroxide tempol facilitates salivary gland protection during head and neck irradiation in a mouse model, *Clin. Cancer Res.*, 2004, **10**, 1807.
72. A. P. Cotrim, F. Hyodo and K. Matsumoto, *et al.*, Differential radiation protection of salivary glands versus tumor by Tempol with accompanying tissue assessment of Tempol by magnetic resonance imaging, *Clin. Cancer Res.*, 2007, **13**, 4928.

73. A. Vissink, J. B. Mitchell and B. J. Baum, *et al.*, Clinical management of salivary gland hypofunction and xerostomia in head-and-neck cancer patients: successes and barriers, *Int. J. Radiat. Oncol., Biol., Phys.*, 2010, **78**, 983.
74. J. B. Mitchell, S. Xavier and A. M. DeLuca, *et al.*, A low molecular weight antioxidant decreases weight and lowers tumor incidence, *Free Radicals Biol. Med.*, 2003, **34**, 93.
75. J. B. Mitchell, M. R. Anver and A. L. Sowers, *et al.*, The antioxidant tempol reduces carcinogenesis and enhances survival in mice when administered after nonlethal total body radiation, *Cancer Res.*, 2012, **72**, 4846.
76. Y. Samuni, J. A. Cook and R. Choudhuri, *et al.*, Inhibition of adipogenesis by Tempol in 3T3-L1 cells, *Free Radicals Biol. Med.*, 2010, **49**, 667.
77. D. P. Guh, W. Zhang, N. Bansback, Z. Amarsi, C. L. Birmingham and A. H. Anis, The incidence of co-morbidities related to obesity and overweight: a systematic review and meta-analysis, *BMC Public Health*, 2009, **9**, 88.
78. I. Vucenik and J. P. Stains, Obesity and cancer risk: evidence, mechanisms, and recommendations, *Ann. N. Y. Acad. Sci.*, 2012, **1271**, 37.
79. E. Stolarczyk, Adipose tissue inflammation in obesity: a metabolic or immune response, *Curr. Opin. Pharmacol.*, 2017, **37**, 35.
80. S. Kachur, C. J. Lavie, A. de Schutter, R. V. Milani and H. O. Ventura, Obesity and cardiovascular diseases, *Minerva Med.*, 2017, **108**, 212.
81. C. H. Kim, J. B. Mitchell and C. A. Bursill, *et al.*, The nitroxide radical TEMPOL prevents obesity, hyperlipidaemia, elevation of inflammatory cytokines, and modulates atherosclerotic plaque composition in apoE-/- mice, *Atherosclerosis*, 2015, **240**, 234.
82. R. Mathur and G. M. Barlow, Obesity and the microbiome, *Expert Rev. Gastroenterol. Hepatol.*, 2015, **9**, 1087.
83. F. Li, C. Jiang and K. W. Krausz, *et al.*, Microbiome remodelling leads to inhibition of intestinal farnesoid X receptor signalling and decreased obesity, *Nat. Commun.*, 2013, **4**, 2384.
84. J. Cai, L. Zhang and R. A. Jones, *et al.*, Antioxidant Drug Tempol Promotes Functional Metabolic Changes in the Gut Microbiota, *J. Proteome Res.*, 2016, **15**, 563.
85. R. Weindruch, Caloric restriction and aging, *Sci. Am.*, 1996, **274**, 46.
86. S. D. Hursting, J. A. Lavigne, D. Berrigan, S. N. Perkins and J. C. Barrett, Calorie restriction, aging, and cancer prevention: mechanisms of action and applicability to humans, *Annu. Rev. Med.*, 2003, **54**, 131.
87. J. R. Speakman and S. E. Mitchell, Caloric restriction, *Mol. Aspects Med.*, 2011, **32**, 159.
88. C. Barlow, S. Hirotsune and R. Paylor, *et al.*, Atm-deficient mice: a paradigm of ataxia telangiectasia, *Cell*, 1996, **86**, 159.
89. Y. Shiloh, Ataxia-telangiectasia and the Nijmegen breakage syndrome: related disorders but genes apart, *Annu. Rev. Genet.*, 1997, **31**, 635.

90. R. Schubert, L. Erker and C. Barlow, *et al.*, Cancer chemoprevention by the antioxidant tempol in Atm-deficient mice, *Hum. Mol. Genet.*, 2004, **13**, 1793.
91. N. Gueven, J. Luff, C. Peng, K. Hosokawa, S. E. Bottle and M. F. Lavin, Dramatic extension of tumor latency and correction of neurobehavioral phenotype in Atm-mutant mice with a nitroxide antioxidant, *Free Radicals Biol. Med.*, 2006, **41**, 992.
92. L. Erker, R. Schubert and H. Yakushiji, *et al.*, Cancer chemoprevention by the antioxidant tempol acts partially via the p53 tumor suppressor, *Hum. Mol. Genet.*, 2005, **14**, 1699.
93. Q. S. Zhang, L. Eaton and E. R. Snyder, *et al.*, Tempol protects against oxidative damage and delays epithelial tumor onset in Fanconi anemia mice, *Cancer Res.*, 2008, **68**, 1601.
94. C. N. Coleman, W. F. Blakely and J. R. Fike, *et al.*, Molecular and cellular biology of moderate-dose (1–10 Gy) radiation and potential mechanisms of radiation protection: report of a workshop at Bethesda, Maryland, December 17-18, 2001, *Radiat. Res.*, 2003, **159**, 812.
95. C. N. Coleman and G. W. Parker, Radiation terrorism: what society needs from the radiobiology-radiation protection and radiation oncology communities, *J. Radiol. Prot.*, 2009, **29**, A159.
96. A. L. DiCarlo, C. Maher and J. L. Hick, *et al.*, Radiation injury after a nuclear detonation: medical consequences and the need for scarce resources allocation, *Disaster Med. Public Health Prep.*, 2011, **5**(Suppl 1), S32.
97. C. N. Coleman, J. M. Sullivan and J. L. Bader, *et al.*, Public health and medical preparedness for a nuclear detonation: the nuclear incident medical enterprise, *Health Phys.*, 2015, **108**, 149.
98. A. C. Upton, The dose-response relation in radiation-induced cancer, *Cancer Res.*, 1961, **21**, 717.
99. D. A. Pierce, Y. Shimizu, D. L. Preston, M. Vaeth and K. Mabuchi, Studies of the mortality of atomic bomb survivors. Report 12, Part I. Cancer: 1950–1990, *Radiat. Res.*, 1996, **146**, 1.
100. L. Gross and Y. Dreyfuss, Reduction in the incidence of radiation-induced tumors in rats after restriction of food intake, *Proc. Natl. Acad. Sci. U. S. A.*, 1984, **81**, 7596.
101. K. Yoshida, T. Inoue, K. Nojima, Y. Hirabayashi and T. Sado, Calorie restriction reduces the incidence of myeloid leukemia induced by a single whole-body radiation in C3H/He mice, *Proc. Natl. Acad. Sci. U. S. A.*, 1997, **94**, 2615.
102. H. Sies and R. Mehlhorn, Mutagenicity of nitroxide-free radicals, *Arch. Biochem. Biophys.*, 1986, **251**, 393.
103. W. G. DeGraff, C. M. Krishna, A. Russo and J. B. Mitchell, Antimutagenicity of a low molecular weight superoxide dismutase mimic against oxidative mutagens, *Environ. Mol. Mutagen.*, 1992, **19**, 21.

CHAPTER 15

Introduction to Electron Paramagnetic Resonance (EPR) of Nitroxides

GARETH R. EATON* AND SANDRA S. EATON

University of Denver, Department of Chemistry and Biochemistry,
2101 E. Wesley Ave, Denver, Colorado 80210, USA
*Email: gareth.eaton@du.edu

15.1 Introduction to EPR Spectroscopy

For more than half a century synthesis of nitroxides combined with EPR spectroscopy has enabled new fields of research, especially physical studies of biological molecules and polymers, and animal physiology. The properties of nitroxides that spawned these studies are their persistence through many chemical reactions (see, for example, ref. 1), and the anisotropy of *g*-values and of hyperfine coupling to the nitrogen nuclear spin (see, for example, ref. 2). Reaction chemistry is described in other chapters. This chapter focuses on the EPR spectroscopic properties of nitroxides that make them useful for the applications discussed in other chapters. Spectra are discussed for magnetically dilute samples, such as low-concentration solutions or diamagnetic solids that contain low concentrations of the paramagnetic nitroxide. In these spectra we can measure the properties of individual molecules. In magnetically concentrated samples, which are not discussed in this chapter, spectra are dominated by intermolecular exchange and dipole interactions.

EPR is the resonant absorption of energy from electromagnetic radiation that matches the energy separation between the $m_s = \pm 1/2$ electron spin

Nitroxides
Edited by Olivier Ouari and Didier Gigmes

Published by the Royal Society of Chemistry, www.rsc.org

states in the presence of a magnetic field. The resonance condition is described by eqn (15.1).

$$h\nu = g\beta_e B_0 \tag{15.1}$$

where h is Planck's constant (6.62607×10^{-34} J s), ν is the microwave frequency, g is characteristic of the environment of the unpaired electron, β_e is the electron Bohr magneton (9.2740×10^{-24} J T^{-1}), and B_0 is the external magnetic field. For nitroxides, $g\sim2.006$. If there is no resolved coupling to other nuclear spins, the fluid solution EPR signal is a single line. The g value can be calculated directly from the field position at which the first-derivative signal crosses the baseline (the zero-crossing point) and the known microwave frequency, using eqn (15.1). Although approximate values of g and nuclear hyperfine couplings can be measured directly from the spectra, more accurate values can be obtained by computer simulation using, for example, the software package EasySpin.[3] The spectrum of CTPO (3-carbamoyl-2,2,5,5-tetramethyl-3-pyrroline-1-oxyl) in water (Figure 15.1) is typical of rapidly tumbling nitroxides. There is strong interaction of the unpaired electron with the ^{14}N nucleus, which has nuclear spin $I=1$. The hyperfine interaction, with hyperfine coupling constant designated as A_N, splits the fluid solution EPR signal into three lines that correspond to $m_I=1$, 0, or -1. An individual molecule has a single value of m_I. The observed spectrum is an ensemble average. Each of the three nitrogen hyperfine lines is split into multiple closely

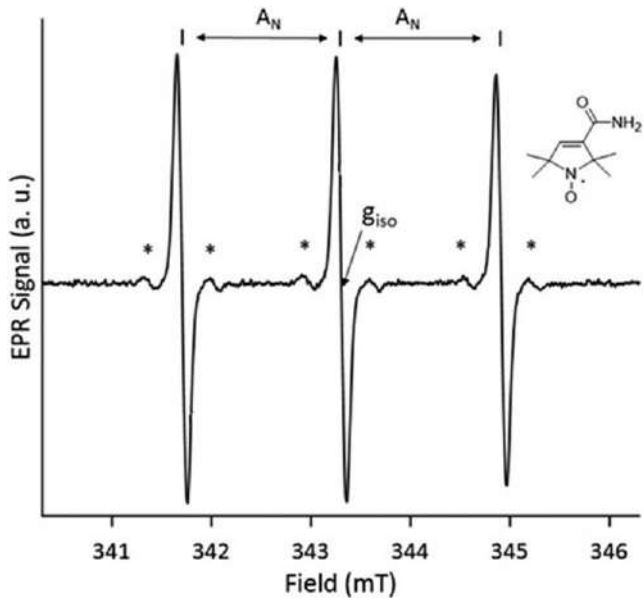

Figure 15.1 X-band (9.6376 GHz) CW spectrum of 0.5 mM CTPO in air-saturated water solution obtained with 0.20 G modulation amplitude at 100 kHz, 1 mW non-saturating microwave power, and single 30 s scan. The positions of the ^{13}C hyperfine lines are marked with *.

spaced lines because of smaller couplings to the protons of the methyl groups. The case of $A_N \ll B_0$ is called the high-field limit and results in equally spaced nitrogen hyperfine lines, as shown in Figure 15.1. When A_N is a significant fraction of B_0 the spacings between the three lines are not equal, which is called the Breit–Rabi effect.[4] For example the splittings between low-field to center-field, and center-field to high-field lines in the spectrum of CTPO in water at 262 MHz ($B_0 = 9.3$ mT) are 1.48 and 1.76 mT, respectively, for a total spacing of 3.24 mT,[5] whereas at X-band both spacings are 1.62 mT with the same total spacing of 3.24 mT as is observed at low field.[6] Also, when the external field is not large relative to the hyperfine couplings, additional "forbidden" transitions may become observable. For example, as many as 10 transitions can be observed in EPR spectra of nitroxides at very low magnetic fields.[7]

The majority of the unpaired electron spin density of the nitroxide is located in the antibonding N–O π^* orbital. Since oxygen is more electronegative than nitrogen, the antibonding orbital has higher electron density on the N than on the O. Changes in geometry of the nitrogen change the relative s and p orbital contribution and thus change both A_N and the orbital angular momentum. The polarity of the environment also changes the electron distribution, and thus changes the magnitude of A_N, which therefore can be used as a probe of local polarity.[8] For many nitroxides, A_N in aqueous solution is about 1.6 mT. The value of A_N also changes when the polarity of substituents is changed. For example, replacement of the typical *gem*-dimethyl groups by four electron-withdrawing carboxymethyl groups decreases A_N to 1.22 mT. To simplify the EPR spectra, nitroxides can be isotopically enriched in ^{15}N, $I = 0.5$, which results in a two-line spectrum.[9]

The linewidths in the spectra are dependent on unresolved hyperfine couplings, collisions with O_2 or other paramagnetic species in the solution, collisions with other nitroxides (concentration effect), restricted motion, and excessive microwave power. Each of these contributions to linewidths is discussed in the following sections.

15.1.1 EPR Methods

Historically, the most common EPR detection technique has been continuous-wave (CW) EPR.[10] In this method a fixed microwave frequency is incident on the sample and the magnetic field is swept slowly through resonance. EPR of nitroxides has been performed at frequencies from very low (hundreds of MHz) to very high (hundreds of GHz) and the associated magnetic fields for $g \sim 2$. The most common frequency is *ca.* 9–10 GHz (X-band), which corresponds to resonance at about 0.35 T for nitroxides. The magnetic field is modulated at kilohertz frequencies, usually 100 kHz, and the EPR signal path includes lock-in detection at this modulation frequency. The output of the lock-in detector is the slope of the absorption signal, yielding the familiar first-derivative EPR spectra as discussed in ref. 10. The detailed hyperfine splittings and lineshapes in the CW signal depend on,

and thus report on, the environment of the nitroxide and its motion. At X-band, samples in non-polar organic solvents such as toluene can be studied in the micromolar concentration range in 4 mm outside diameter sample tubes. Water and other polar solvents require smaller diameter tubes because of the non-resonant absorption of microwaves by the restricted motions of the electric dipoles in the solvent molecules. Hence, sample sizes range from *ca.* 10 to 200 μL of *ca.* 1 to 1000 μM solutions. 10^{14} to 10^{15} spins provide strong signals in X-band spectrometers. The smaller wavelengths for higher frequencies require smaller tube diameters and sample volumes.

Pulsed EPR involves applying short pulses of microwaves at a fixed magnetic field, and observing the response of the spins.[11] There are many versions of pulsed EPR, including sweeping the magnetic field, measuring relaxation times, and measuring spectra at the selected relaxation time. Pulsed EPR has been especially important for measuring distances between spins, which is discussed in Section 15.5.2. T_1 and T_2 for rapidly tumbling nitroxides are about 0.5 μs,[12] which is much shorter than typical NMR relaxation times and limits the complexity of pulse sequences that can be used.

The third major EPR method involves rapid scans of the magnetic field through the spectrum, at fixed microwave frequency, and without the modulation and lock-in detection that characterizes CW EPR. Rapid scan EPR can use higher microwave power than CW, since it is on resonance for very short times, nearly as short as in pulsed EPR. The signal can be averaged thousands of times per second. An example of rapid scan for the center-field line of mHCTPO (3-carbamoyl-2,2,5,5-d_{12}-tetramethyl-3-pyrroline-1-oxyl) is shown in Figure 15.2. The rapid field scan causes oscillations on the trailing edge of the signal, which can be removed by Fourier deconvolution, yielding the absorption spectrum.[13] Differentiation with subsequent filtering provides the familiar first-derivative signal. With modern digital data acquisition and analysis methods, rapid scan EPR of nitroxides in fluid solution provides up to about a factor of 5 improvement in signal-to-noise (S/N) per unit acquisition time relative to CW EPR.[14]

15.1.2 Anisotropy

The electron distribution around most paramagnetic centers has symmetry lower than cubic, so the g and hyperfine values are dependent on the orientation of the molecule relative to the direction of the external magnetic field, which is designated as anisotropy. The axis labeling for nitroxides is shown in Figure 15.3. The axes of the g and hyperfine matrices may not be aligned precisely along the molecular axes, although the assumption of co-linearity is used to simplify this discussion. The g_z value (also called g_{zz}) is the value of g that is observed when the magnetic field is along the molecular z axis, which is the long axis for the nitrogen p orbital in the π^* orbital that contains the unpaired electron. The g and A_N values for tempone in water: $A_x = 0.55$, $A_y = 0.63$, and $A_z = 3.59$ mT and $g_x = 2.0092$, $g_y = 2.0061$, and $g_z = 2.0022$[12] are typical of values for many nitroxides.

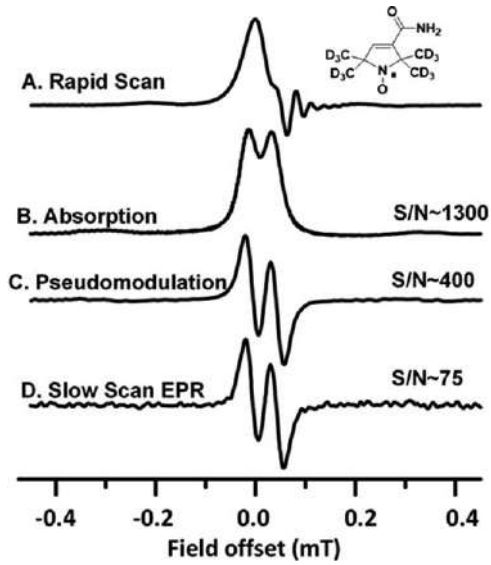

Figure 15.2 X-band rapid scan spectrum of the center line of mHCTPO and comparison of rapid scan and CW EPR spectra of mHCTPO. Magnetic field scans were from low field to high field using 9.5 cm diameter external coils. (A) As-recorded sinusoidal rapid-scan signal obtained with a scan rate of 1.8 MG/s. A total of 1024 averages were recorded in about 0.9 seconds using a Bruker SpecJet II digitizer. The incident microwave power was about 80 mW ($B_1 = 0.014$ mT). (B) Slow-scan absorption spectrum obtained by deconvolution of signal in (A). (C) First derivative spectrum obtained by pseudomodulation of the signal in (B). First derivative spectrum was filtered using a fourth-order Butterworth filter allowing less than 2% broadening of the linewidth. (D) Single scan of a field-modulated first-derivative CW EPR spectrum of the same sample, obtained in 0.9 s using about 5 mW incident microwave power, 10 kHz modulation frequency, 0.9 ms conversion time, 1024 points, 0.013 mT modulation amplitude. Modulation amplitude, power, and fourth-order Butterworth filter were chosen to maximize *S/N* while allowing less than 2% broadening of the linewidth.

15.1.3 Relationship Between Single Crystal, Powder and Fluid Solution Spectra

If a single crystal of a diamagnetic compound doped with a small amount of nitroxide is oriented in a magnetic field, the anisotropy of the g and A_N can be measured. X-band spectra calculated for orientations of a crystal with the magnetic field along the magnetic x, y, or z axes are shown in Figure 15.4. These axes are called the principal axes of the system. The spectra show the differences in positions of the signal and in the hyperfine splittings when the magnetic field is along the three principal axes which arises because of the anisotropy in g and A_N. The center of the three-line patterns is at lower field and A_N is smaller when the magnetic field is along the x or y axes than

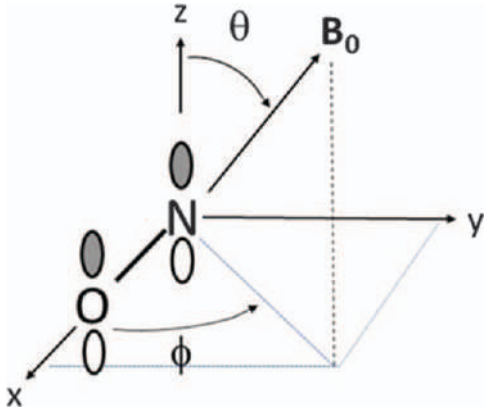

Figure 15.3 Axis definitions used to describe the orientation dependence of molecular g and A_N values. The orbital that contains the unpaired electron has substantial N p_z character.

along the z-axis. For molecules with orientations intermediate between the principal axes, resonance occurs at positions that are intermediate between what is observed when the field is along the axes.

The spectrum of a randomly oriented powder sample of an immobilized nitroxide is the superposition of spectra for all orientations with respect to the magnetic field. A powder sample could be obtained by crushing the single crystal or, more commonly, by dissolving the radical in a solvent mixture that forms a glass when it is cooled below the glass transition temperature. Formation of a glass is important for acquiring powder (immobilized) spectra. If the solvent crystallizes the solute is excluded from the lattice and may become magnetically concentrated, which prevents characterization of the isolated radicals. In the X-band powder spectrum of an immobilized nitroxide the spacing between the low-field maximum and the high-field minimum corresponds to 2 A_z. All other orientations of the molecule have resonances between these two extremes. The most probable orientations are near the x, y plane. At X-band these orientations give resonances near the center of the spectrum, which is why the amplitude of the first derivative spectrum is greatest near the middle of the spectrum.

At higher microwave frequency, B_0 increases so the g anisotropy results in larger spacings between the centers of the hyperfine split multiplets as shown in Figure 15.5 for Q-band (34 GHz) than at X-band (Figure 15.4). At Q-band the higher probability of orientations in which the magnetic field is in the magnetic x, y plane than along the z-axis and the higher g values in the x, y plane shift the maximum amplitude toward the low-field end of the spectrum.

15.1.4 Motion of Nitroxides

The extent to which anisotropy is averaged by molecular tumbling depends on the tumbling correlation time, τ_R. The inequivalent resonant positions

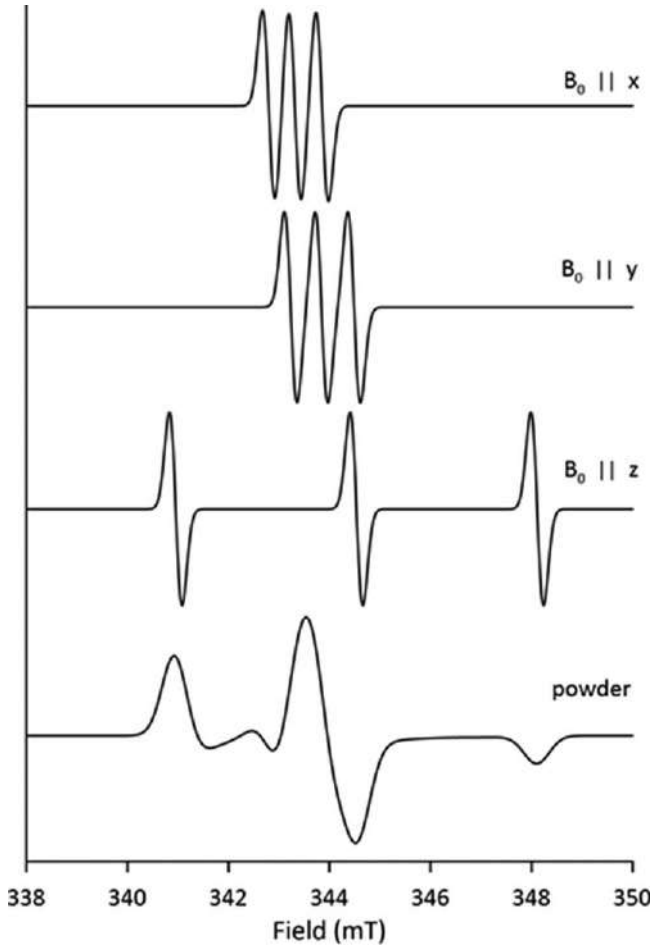

Figure 15.4 Simulated X-band (9.655 GHz) single-crystal spectra of a nitroxide doped into a diamagnetic host. Spectra are shown for the magnetic field along the x, y, and z molecular axes of the radical. The spectra for an oriented crystal are compared with the powder spectrum that could be obtained crushing the crystal to form a randomly oriented powder or by freezing a solution in a solvent that forms a glass. The parameters that were used in the EasySpin simulation were $g_x = 2.0092$, $g_y = 2.0061$, $g_z = 2.0022$, $A_x = 14.8$, $A_y = 17.6$, and $A_z = 100.2$ MHz.

that are averaged by tumbling are the combined effect of the g and A_N anisotropy. At X-band typical nitroxide g and A_N values correspond to a spread in resonance fields of 2.3, 1.2, and 4.3 mT for the $m_I = 1$, 0, and -1 lines, respectively, as sketched in Figure 15.6. The corresponding values in MHz are 64, 34, and 120 MHz for the $m_I = 1$, 0, and -1 lines, respectively. When tumbling correlation rates, $1/\tau_R$, are substantially less than the spread in resonance frequencies that arise from the g and A_N anisotropies, a static limit rigid lattice spectrum is observed. As the tumbling rate increases, there

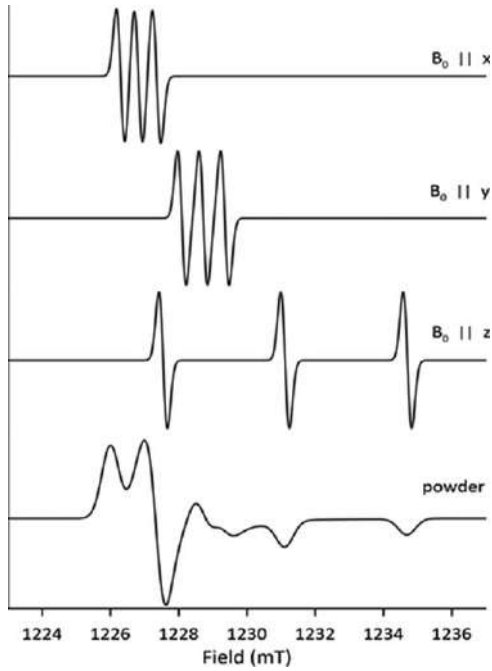

Figure 15.5 Simulated Q-band (9.655 GHz) single-crystal spectra of a nitroxide doped into a diamagnetic host. Spectra are shown for the magnetic field along the x, y, and z molecular axes of the radical. The spectra for an oriented crystal are compared with the powder spectrum that could be obtained crushing the crystal to form a randomly oriented powder or by freezing a solution in a solvent that forms a glass. The parameters that were used in the EasySpin simulation were $g_x = 2.0092$, $g_y = 2.0061$, $g_z = 2.0022$, $A_x = 14.8$, $A_y = 17.6$, and $A_z = 100.2$ MHz, which are the same as in Figure 15.4.

is increasingly effective motional averaging of the anisotropy and the EPR lineshapes become motion-dependent. This motional dependence of the EPR lineshapes of nitroxides provides insights into the motions of spin labels attached to organic polymers and biological molecules on the time scale of τ_R between less than a few ns and about 100 ns, as illustrated in Figure 15.7 for spectra at X-band. In the fast tumbling limit the isotropic g and A_N values are observed. At X-band the spread in rigid lattice resonance frequencies increases in the order $m_I = 0 < m_I = 1 < m_I = -1$ (Figure 15.6), so for a given tumbling rate the effectiveness of averaging decreases in that order and the linewidth increase in the order $m_I = 0 < m_I = 1 < m_I = -1$ (Figure 15.7). Even though the lines are of different width and height, the integrated area under each of the three lines is the same.

At Q-band the anisotropy that is averaged by tumbling (Figure 15.5) increases in the order $m_I = 1 < 0 < -1$ so the low-field line is the narrowest in the intermediate tumbling regime (Figure 15.8). Since the inequivalences

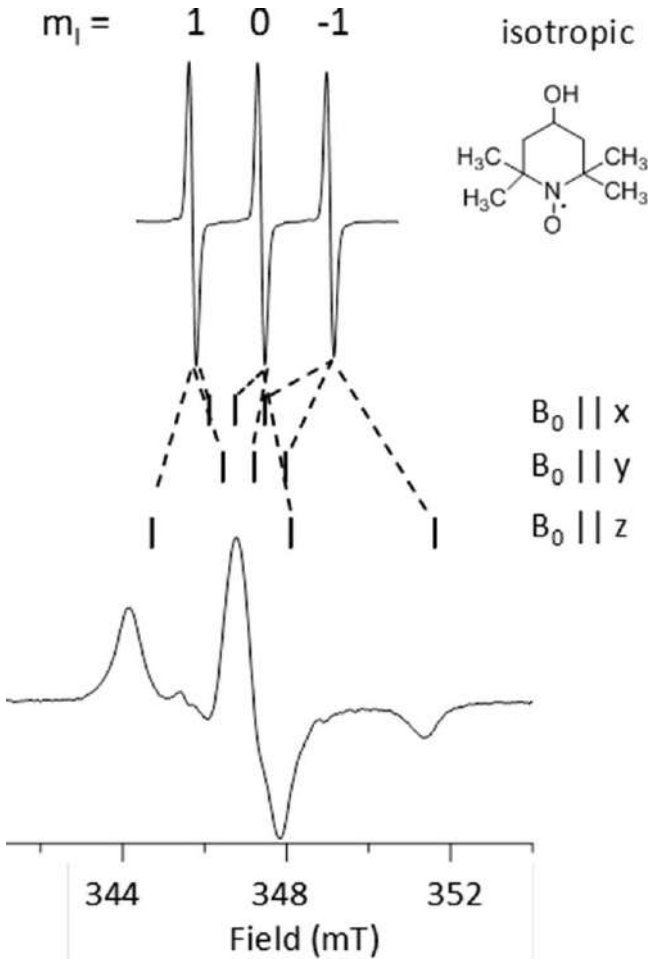

Figure 15.6 In the spectrum for a nitroxide that is rapidly tumbling in fluid solution the g and A_N anisotropy is averaged such that $g_{iso} = 1/3\ (g_x + g_y + g_z)$ and $A_N = 1/3\ (A_x + A_y + A_z)$. The relationship between the average values and the values along the principal axes are marked. The X-band experimental spectra for tempol in water and in glassy trehalose are used as examples.

that are averaged by tumbling are larger at Q-band than at X-band, faster tumbling (shorter values of τ_R) is required to achieve the fast-motional limit.

Spectra shown in Figures 15.4, 15.5, 15.7 and 15.8 were calculated using the shareware program EasySpin,[3] which is available on the web (http://www.easyspin.org) and can be used to simulate many types of EPR spectra, including the slow-motion nitroxides. The software runs on the MatLab platform. If the rigid-lattice parameters are known, the simulations provide values of τ_R. With less precision, one can use the Kivelson model of line width dependence on tumbling[15,16] to find τ_R. Instructions for a student laboratory experiment that uses nitroxides to determine τ_R are provided

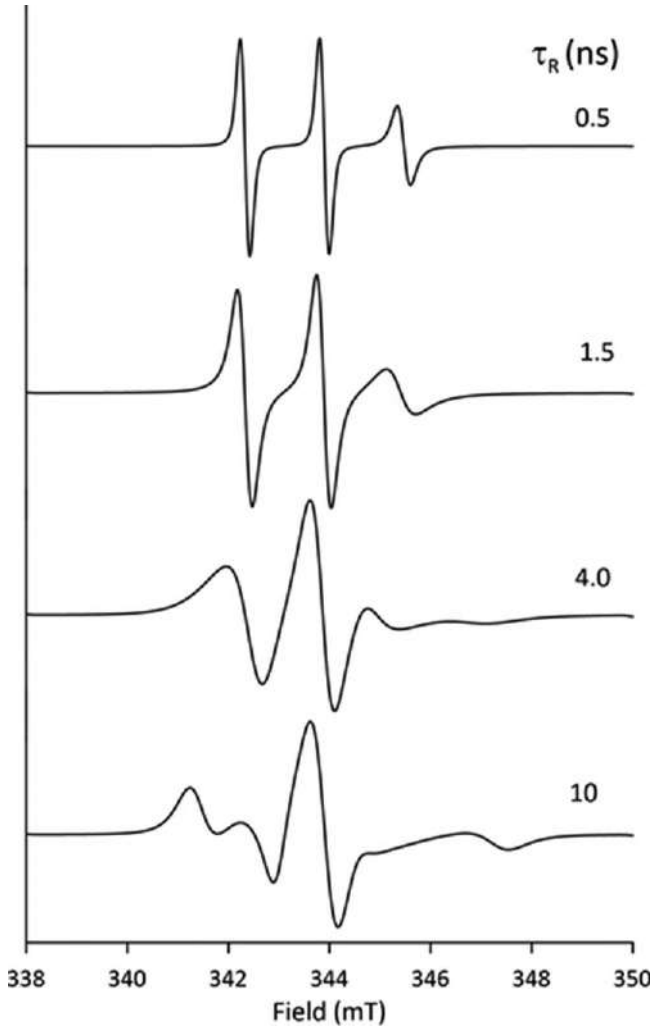

Figure 15.7 X-band intermediate tumbling spectra calculated using the same g and A_N values as for Figures 15.3 and 15.4 with $\tau_R = 0.5$, 1.5, 4.0 and 10 ns. Signal amplitudes are scaled to constant values.

in ref. 17. In the motional regime in which tumbling is fast enough to largely average g and A_N anisotropy, but still leave differences in the widths of the three ^{14}N hyperfine lines, the widths can be expressed as

$$\Delta B_{pp} = A + Bm_I + Cm_I^2$$

A, B and C are coefficients that can be calculated from g and A_N anisotropies, in units of magnetic field. The nuclear magnetic quantum number, m_I, is 0 for the center line, so the width of the center line defines A.

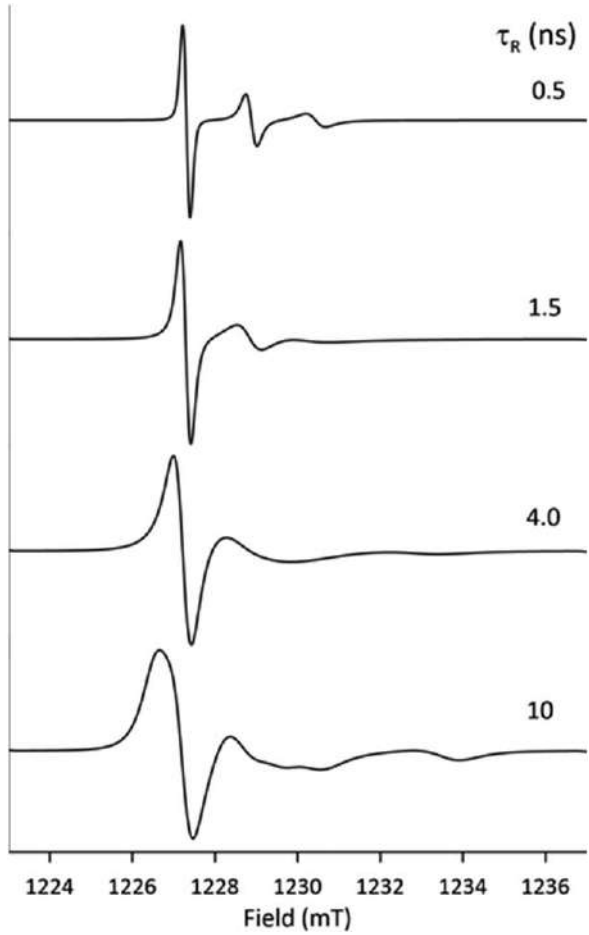

Figure 15.8 Q-band intermediate tumbling spectra calculated using the same g and A_N values as for Figures 15.3 and 15.4 with $\tau_R = 0.5$, 1.5, 4.0 and 10 ns. Signal amplitudes are scaled to constant values.

15.1.5 Half-field Transitions

When there is dipolar interaction between two nitroxides in a rigid lattice (either powder or glassy solution) there can be a spin transition that is describable as an $\Delta m_s = \pm 2$ transition. At fixed microwave frequency, this transition occurs at half the magnetic field of the normal $\Delta m_s = \pm 1$ spin transition, and is commonly called the half-field transition. The ratio of the intensity of the half-field transition to that of the $g \approx 2$ transitions can be used to calculate the distance between the spins up to about 10 Å.[18] Some reports state that this transition is characteristic of a triplet state. However, the transition can be observed in samples containing randomly oriented $S = 1/2$ species, such as monomeric nitroxides,

if the concentration is sufficiently high. If the relative intensity extrapolates to zero at low total spin concentration, the half-field transition is due to intermolecular interactions between monomers, rather than a triplet or triplet-state dimer.[18,19]

15.1.6 Dinitroxides

Nitroxides can be combined with many other free radicals to exploit special spectroscopic characteristics. Of particular interest are molecules that contain two nitroxides, which are called dinitroxides. In fluid solution the EPR spectra are strongly dependent on the ratio of the exchange interaction, J, between the two radicals to A_N (Figure 15.9).[20] As J increases the spectrum evolves from the usual three-line spectrum with equal intensity lines to a multi-line signal. In the strong interaction case with $J \gg A_N$, the dimer exhibits a five-line pattern in which the apparent nitrogen hyperfine coupling is half of the value for the corresponding monoradicals because each unpaired electron is delocalized over both nitrogens. If the exchange interaction is dominated by through-space interactions, motions may vary conformations and modulate J. In flexible dinitroxides lines 2 and 4 for the five-line pattern are broader than lines 1, 3, and 5, which is an example of what is sometimes called ''alternating linewidths.'' Changes in these spectra can be used to monitor dynamics in solution, reaction equilibria, and strengths of orbital interactions.[20] Cleavage of a disulfide linker in a dinitroxide can be used to monitor redox potentials.[21]

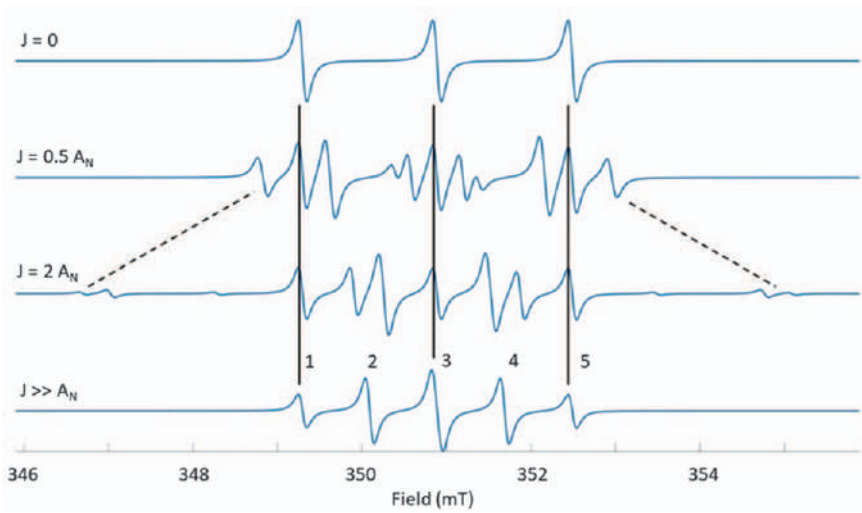

Figure 15.9 Changes in X-band spectra of a dinitroxide as J increases, calculated for $\nu = 9.852$ GHz, $g = 2.006$, $A_N = 16.0$ G, and Gaussian absorption line width of 0.2 G for $J = 0$, $J = 0.5\ A_N$, $J = 2\ A_N$, and $J \gg A_N$.[20]

15.2 Selection of Acquisition Parameters for CW Spectra

Acquisition of CW spectra of nitroxides requires selection of acquisition parameters including incident microwave power, modulation amplitude and time constant, each of which can impact line width and lineshape. In addition, concentration of the sample can affect line width and shape. General guidance is provided in this section. These matters are discussed in greater detail in *Quantitative EPR*[10] and in the manuals provided with spectrometers.

15.2.1 Microwave Power (See Figure 4.5, on p. 47 of ref. 10)

The EPR signal is the net result of absorption and emission of energy at the resonant frequency. The ratio of the equilibrium populations of the upper and lower energy levels ($m_s = \pm 1/2$) can be calculated using the Boltzmann eqn (15.2).

$$\frac{n_{\text{upper}}}{n_{\text{lower}}} = e^{-\Delta E/kT} \tag{15.2}$$

At 9.4 GHz, $\Delta E = 6.228 \times 10^{-24}$ J and $T = 293$ K, which gives $kT = 4.04 \times 10^{-21}$ so $\Delta E/kT \ll 1$ and the ratio of the populations is close to one. The actual ratio of populations at X-band for $T = 293$ K is ~0.998. The almost equal populations of the upper and lower energy levels mean that if energy is absorbed by the spin system at a rate that is faster than electron spin relaxation, the population ratio may become even closer to 1, which decreases signal intensity and is called saturation. The EPR transition is caused by the magnetic field in the resonator, B_1, which is proportional to the square root of incident power

$$B_1 = \Lambda \sqrt{\text{P}} \tag{15.3}$$

where Λ is the resonator efficiency.

When comparing results with the same resonator it is convenient to describe experiments in terms of P. However, when comparing results obtained with different resonators, conversion of P to B_1 is needed. In the absence of saturation, the EPR signal increases linearly with B_1. Well-engineered spectrometers have low-noise sources, so the noise in a spectrum is independent of B_1 except at relatively high power, and S/N increases linearly with B_1. To accurately measure the number of spins in a sample, B_1 should be low enough that the spectrum is in the linear response regime. A power saturation curve is a plot of the signal amplitude *vs.* square root incident power (or B_1), and can be used to determine the linear response range. However, a quick check can be performed by changing the incident power by 6 dB, which is a factor of 4 in power, and a factor of 2 in B_1. If you increase the incident power by 6 dB the signal should double in amplitude. If it does not, the incident power is too high and a lower power should be selected.

The shape of the power saturation curve depends on the relaxation times and the lineshape. If the line is a single spin packet, which has a Lorentzian lineshape, then it is described as homogeneously broadened. If there is unresolved hyperfine splitting, the line is described as inhomogeneously broadened. The peak-to-peak line width, ΔB_{pp}, of a Lorentzian EPR line is given by

$$\left(\Delta B_{pp}\right)^2 = \frac{4}{3}\frac{1}{\gamma^2 T_2^2}\left(1 + \gamma^2 B_1^2 T_1 T_2\right) \tag{15.4}$$

It is helpful to rewrite this in the form:

$$\left(\Delta B_{pp}\right)^2 = \frac{4}{3\gamma^2 T_2^2} + \frac{4B_1^2 T_1}{3T_2} \tag{15.5}$$

which shows that at low microwave power the line width is determined by T_2, but at higher microwave power, and especially with $T_1 > T_2$, the line is power-saturation broadened. In the case of an inhomogeneously broadened line, as a Lorentzian spin packet broadens it adds intensity at the field of the neighboring lines. With enough overlapping lines, the amplitude at a given field may stay approximately constant as the power increases. See, for example, line c in figure 8 in ref. 22. The shape of the curve depends on whether you plot the amplitude at a given magnetic field or the peak of the spectrum. These differ because of the line broadening. If you know the efficiency of a resonator and have approximate values of the relaxation times, you can make an estimate of B_1 that is likely to saturate the signal, using the formula for the saturation factor, S:

$$S = \frac{1}{1 + \gamma^2 B_1^2 T_1 T_2} \tag{15.6}$$

where $\gamma = 1.76 \times 10^8$ rad s^{-1} mT^{-1}. The goal is to have S as close to 1 as is practical. For example, for a rectangular X-band cavity resonator, the efficiency is approximately 0.1 mT/$\sqrt{\text{W}}$ and T_1 and T_2 are about 0.5 μs for low concentrations of small-molecule nitroxides in fluid solution at room temperature. EPR spectrometers typically have a maximum power of *ca.* 200 mW, so 20 dB attenuation provides 2 mW incident on the resonator. Two mW corresponds to 0.0045 mT at the sample. These values give $S = 1/(1 + 0.16)$ which is not a very conservative value, so lower power should be used.

15.2.2 Modulation Amplitude (See Figure 1.11, p. 11 in ref. 10)

Detection of the EPR signal in a CW experiment involves modulation of the magnetic field at a rate is that fast relative to the sweep rate as is described in detail in ref. 10. The most common modulation frequency is 100 kHz. For the most precise lineshapes the modulation amplitude should be less than about 1/10 of ΔB_{pp}. However, modulation amplitudes up to about 1/3 of ΔB_{pp}

cause relatively small broadening, and modulation amplitudes approximately equal to ΔB_{pp} enhance *S/N* at the expense of line broadening.

At the other extreme, if the line is only 0.005 mT wide, then not only do you need a very small modulation amplitude, but there will also be distortion by the 100 kHz modulation. Any pair of frequencies produce $f_1 \pm f_2$ so there are 100 kHz sidebands on the EPR signal when it is detected with 100 kHz modulation. Using the conversion factor of 28 MHz mT^{-1}, 100 kHz corresponds to sidebands that are about 3.5 μT above and below the main signal. Usually, these sidebands are within the hyperfine-broadened EPR line and are not seen, but, with a very narrow line, the sidebands cause observable broadening and may be observable superimposed on the main transition.

To calibrate a spectrometer's modulation amplitude, use a sample with a narrow-line signal, such as particles of LiPc (lithium phthalocyanine), BDPA (1 : 1 α,γ-bisdiphenylene-β-phenylallyl), or a dilute, degassed solution of a trityl radical. With modulation several times ΔB_{pp}, the peak-to-peak separation in the observed spectrum is about 90% of the input modulation. The quantitative lineshape is discussed in Poole (pages 407–408).[23]

Although a large modulation amplitude (up to $\sim \Delta B_{pp}$) distorts the EPR signal, the integrated area remains proportional to signal intensity, so sometimes to get good integrals it is useful to improve *S/N* by overmodulation.

15.2.3 Time Constant (See *Quantitative EPR*[10] Figure 1.12, p. 12, and Figure 4.3, p. 42)

It is good practice to choose a time constant such that the detection system responds in about 1/10 of the time it takes to pass through a line. For more details see eqn (4.1) on page 43 of ref. 10. For example, if the line is 0.1 mT wide, and the scan is 10 mT in 100 s, the field scan will pass through the spectral line in 1 s, so the maximum time constant that would not distort the spectrum would be 0.1 s. To obtain maximum benefit from filtering, the time constant should be set equal to the acquisition time per data point. Selection of a slower scan with a longer time constant may be a more effective strategy for improving *S/N* than signal averaging many scans in the same total acquisition time, especially if lines are very narrow and there is even a small drift in the magnetic field or frequency.

15.2.4 Effect of Concentration on Nitroxide Linewidth

One might assume that if the *S/N* is lower than desired, a strategy to improve the spectrum is to increase the nitroxide concentration. However, lines in EPR spectra may be broadened if the concentration becomes too high. Examples are shown in Figure 15.10. The broadening due to high concentration can be distinguished from the broadening that arises from incomplete motional averaging of anisotropy because the collisions increase

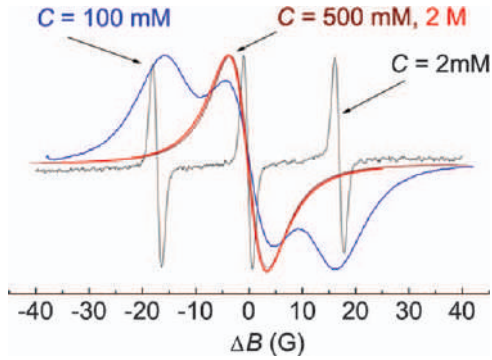

Figure 15.10 Broadening of the spectra of a nitroxide in fluid solution as a function of concentration. ΔB is the offset from the center of the spectrum. 1 Gauss = 0.1 mT.
Reproduced from ref. 68 http://mrsej.ksu.ru/contents.html#13103 under the terms of the CC BY-SA 4.0 license https://creativecommons.org/licenses/by-sa/4.0/.

all linewidths similarly, whereas the impact of incomplete motional averaging is smallest for the central $m_I = 0$ line at X-band or the low-field line at Q-band. Concentration effects on linewidths are greater the lower the viscosity of the solution and the higher the temperature, because both of these factors increase the collision frequency. The concentration effect is also greater the narrower the EPR lines, the larger the hyperfine splittings, and the larger the tendency to aggregate. In fluid solution it usually is necessary to keep concentrations of nitroxides lower than about 1 mM to minimize concentration broadening.

The collisions cause dipolar and exchange interactions between spins. For nitroxides in solution, the primary line-broadening effect is Heisenberg exchange (HE).

$$\frac{1}{T_{1\mathrm{HE}}} = \frac{1}{T_{2\mathrm{HE}}} = \kappa_{\mathrm{HE}}[R] \tag{15.7}$$

where κ_{HE} is the Heisenberg exchange rate constant, and $[R]$ is the concentration of the nitroxide in millimole/liter. Biller *et al.* found $\kappa = ca.$ 2–6 in units of 10^6 $\mathrm{mM^{-1}\,s^{-1}}$ for nitroxides in solution.[24] Thus at 1 mM concentration, HE increases the $1/T_2$ relaxation rate by about a factor of 2. The $1/T_2$ relaxation rate is related to the Lorentzian linewidth by

$$\Delta B_{\mathrm{pp}}(\mathrm{mT}) = \frac{6.56 \times 10^{-9}\ \mathrm{mT\ s}}{T_2(s)} \tag{15.8}$$

A typical nitroxide T_2 of 0.5 μs corresponds to $\Delta B_{\mathrm{pp}} = 0.013$ mT. A small increase in T_2 due to collisions with other nitroxide has a relatively small impact on overall linewidth for a signal with a substantial amount of

unresolved hyperfine interaction, but makes a dramatic difference for narrow lines in the spectra of CTPO (Figure 15.1).

15.2.5 Collisions with Paramagnetic O_2

In fluid solution, collisions with small, rapidly relaxing O_2 enhance the nitroxide relaxation rates *via* Heisenberg exchange, analogous to what occurs when nitroxides collide. Heisenberg exchange between O_2 and the nitroxide is very effective in enhancing relaxation because the T_1 of the O_2 is much less than the T_1 of the nitroxide, and because the transitions of the O_2 extend over a range of *g*-values that are different from that of the nitroxide. This relaxation enhancement may broaden the CW EPR spectra of the nitroxide to the point that line widths are greater than proton hyperfine splittings, and proton hyperfine is not resolved. CTPO provides a good example (Figure 15.11). In air-saturated water the O_2 concentration is about 0.2 mM, and one observes only the three lines due to ^{14}N coupling. Upon purging with N_2, the ^1H couplings to the methyl groups and the proton in the 4-position of the ring become resolved. This highly resolved spectrum is

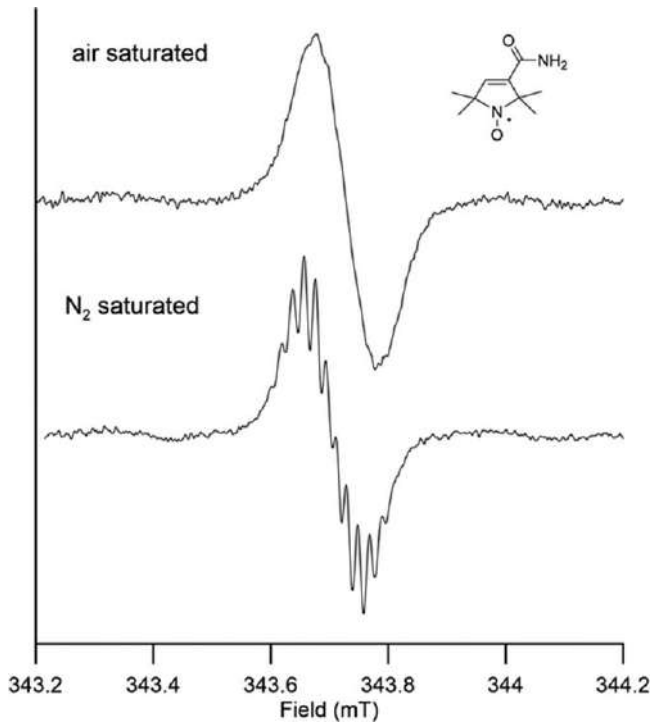

Figure 15.11 X-band (9.651 GHz) spectra of the center line ($m_I = 0$) line for 0.2 mM CTPO in water for air-saturated solution or nitrogen-purged solution at 293 K obtained with 0.05 G modulation amplitude and 0.5 mW microwave power.

sensitive to the microwave power, modulation amplitude, $[O_2]$, temperature, viscosity and concentration of the nitroxide itself. A major application of this phenomenon is *in vivo* oximetry, in which the line width or directly measured relaxation time of trityl, nitroxide or analogues of LiPc can be used to monitor of the concentration of O_2.[25]

15.3 Relaxation Times

A qualitative understanding of electron spin relaxation times is important for selecting parameters for acquiring CW spectra. Understanding of the factors that impact relaxation are crucial to the design and selection of nitroxides for specific applications. A more detailed analysis of relaxation provides insights into dynamic processes and the fundamental nature of the phenomena that are reported by EPR spectra of nitroxides.

15.3.1 Methods to Measure Relaxation Times

Early studies of nitroxide relaxation in fluid solution used CW power saturation (eqn (15.4)). Typically T_2 was estimated from the CW line width based on eqn (15.8). This procedure works well for the nitroxide $(SO_3)_2NO^{2-}$, which is known as Fremy's salt, because there is no unresolved hyperfine splitting. However, for many other nitroxides there is unresolved proton hyperfine splitting which contributes to the linewidth and results in artificially shortened values of T_2 if eqn (15.8) is used. More *et al.*[26] used continuous-wave power saturation together with as complete hyperfine simulation of lineshapes as possible to estimate T_1 and T_2. Calibration was done with Fremy's salt.

For most nitroxides direct measurement of relaxation times by pulsed EPR is needed to get accurate results. Spectrometers for measurement of relaxation times are marketed by Bruker (such as the E580 X-band and E560 W-band spectrometers). For details of pulsed EPR see ref. 11. Briefly, the spectrometer uses a pulse pattern generator to create pulses a few tens of ns long, which are amplified by a high-power microwave amplifier, such as traveling wave tube (TWT) amplifier. The pulses are directed to a resonator that is designed to have high bandwidth. The free induction decay (FID) or echo is detected, amplified and digitized. The time-domain response is then interpreted in terms of the relaxation times. Common sequences are the Hahn echo sequence $\pi/2$–τ–π–τ-echo varying τ to measure T_2 and the inversion recovery sequence π–T–$\pi/2$–τ–π–τ-echo varying T to measure T_1. An FID can be measured instead of an echo. Complexities in the contributions to the decay or recovery time necessitate care in interpretation of the results, as explained in ref. 27. For example, since many factors in addition to T_2 influence the echo decay time constant in solids, the experimental value is usually called T_m, the phase memory time, rather than T_2. In low-viscosity fluid solution T_m typically is $\sim T_2$.

15.3.2 T_1 in Fluid Solution

Typical room-temperature values of T_1 for rapidly tumbling nitroxides at X-band are about 0.5–1.0 μs[12] and increase to 1.7–5 μs for more slowly tumbling spin-labeled lipids.[28] In dilute fluid solution from which oxygen has been removed, a nitroxide is jostled by its neighbors, translates, rotates and undergoes conformational changes which provide a variety of relaxation mechanisms that can be modeled as the sum of contributions from spin rotation, modulation of A_N and g anisotropy, and a thermally activated process eqn (15.9).[12,27,29,30]

$$\frac{1}{T_1} = \frac{1}{T_1^{SR}} + \frac{1}{T_1^{g}} + \frac{1}{T_1^{A}} + \frac{1}{T_1^{\text{therm}}} \tag{15.9}$$

The contribution from spin-rotation (eqn (15.10)) reflects the coupling between rotational and spin angular momenta.[31–33]

$$\frac{1}{T_1^{SR}} = \frac{\sum_{i=1}^{3}(g_i - g_e)^2}{9\tau_R} \tag{15.10}$$

where $i = x, y, z$ and g_e is 2.0023. $\frac{1}{T_1^{SR}}$ is independent of resonance frequency and decreases as τ_R increases. It can be distinguished from other contributions to relaxation in fluid solution by the absence of dependence on microwave frequency.

Modulation of the large anisotropic (dipolar) nitrogen nuclear hyperfine coupling by molecular tumbling (the END process, eqn (15.11)) is a major contributor to nitroxide relaxation in certain motional regimes.[34–36]

$$\frac{1}{T_1^{A}} = \frac{2}{9} I(I+1) \sum_i (A_i - \bar{A})^2 J(\omega) \tag{15.11}$$

where A_i is a component of the nitrogen hyperfine coupling in angular frequency units, $\bar{A}$ is the average nitrogen hyperfine, I is the nitrogen nuclear spin, ω is the resonance frequency, and $J(\omega)$ is the Bloembergen, Purcell, Pound (BPP) spectral density function (eqn (15.12)).

$$J(\omega) = \frac{\tau_R}{1 + (\omega\tau_R)^2} \tag{15.12}$$

In the rapid-tumbling regime the BPP spectral density function is indistinguishable from the Cole–Davidson spectral density function (15.13), which has been found to give better agreement than BPP with the temperature dependence of nitroxide $1/T_1$.[37,38]

$$J_{CD}(\omega) = \frac{1}{\omega} \frac{\sin(\beta \arctan(\omega\tau))}{\left(1 + (\omega\tau)^2\right)^{\beta/2}} \tag{15.13}$$

where β characterizes the distribution of τ_R values. The smaller the value of β, the wider the distribution. For $\beta = 1$, $J_{CD}(\omega)$ reduces to $J_{BPP}(\omega)$. The Cole–Davidson function was developed to interpret dielectric relaxation.

The frequency dependence of $\frac{1}{T_1^A}$ depends on τ_R (eqn (15.12)). For τ_R in the range of 4–50 ps for small nitroxides in low-viscosity solutions, $\omega\tau_R$ changes from <1 at 250 MHz to >1 at 34 GHz. For $\omega\tau_R > 1$, $\frac{1}{T_1^A}$ increases as ω decreases. For $\omega\tau_R \ll 1$, $\frac{1}{T_1^A}$ is independent of ω and increases as τ_R increases. Because $\frac{1}{T_1^A}$ is proportional to $\gamma^2\ I(I+1)$, where γ is the gyromagnetic ratio, the ratio $\left[\left(\frac{1}{T_1^A}\right)\text{for } ^{14}\text{N}\right] \Big/ \left[\left(\frac{1}{T_1^A}\right)\text{for } ^{15}\text{N}\right] = 1.36$. The $^{15}N/^{14}N$ isotope effect on $1/T_1$ can be used to confirm the contribution from the END mechanism.[6,38]

Modulation of g anisotropy by molecular tumbling is described by eqn (15.14).[34,35]

$$\frac{1}{T_1^g} = \frac{2}{5}\left(\frac{\omega}{g}\right)^2 \left\{\frac{(\Delta g)^2}{3} + (\delta g)^2\right\} J(\omega) \tag{15.14}$$

where $\Delta g = g_z - 0.5(g_x + g_y)$, $\delta g = 0.5(g_x - g_y)$. This term is increasingly important at higher microwave frequencies.

For nitroxides in viscous water/glycerol solutions at 1.9, 3.1 and 9.2 GHz at room temperature, $1/T_1$ was larger than predicted by eqn (15.11), (15.12) and (15.14).[29] The additional process dominated relaxation for $\tau_R > \sim 3\times10^{-9}$ s, and the magnitude of the contribution increased with decreasing frequency between 9.2 and 1.9 GHz. This contribution was modeled as a thermally activated process, eqn (15.15).[39,40]

$$\frac{1}{T_1^{\text{therm}}} = C_{\text{therm}}\left(\frac{\omega}{\omega_{\text{ref}}}\right)\frac{\tau_{\text{therm}}}{1 + (\omega\tau_{\text{therm}})^2} \tag{15.15}$$

where $\tau_{\text{therm}} = \tau_c^{\,0}\ \exp(E_a/RT)$, E_a is the activation energy, $\tau_c^{\,0}$ is the pre-exponential factor, C_{therm} is the coefficient for the contribution of the thermally activated process, and $\omega_{\text{ref}} = 9.5$ GHz.

It has also been proposed that modulation of dipolar interaction with solvent nuclei contributes to nitroxide relaxation in fluid solution.[35] Although this relaxation mechanism has been shown to be significant for trityl radicals at 250 MHz when $\omega\tau_R \sim 1$,[41] it has not been observed for nitroxides.

The contribution from spin rotation is independent of ω, and decreases as τ_R increases. The contributions from modulation of *g*- and *A*-anisotropy (END process) depend on both ω and τ_R. The contribution from the thermally activated process depends on ω, but not τ_R. For rapidly tumbling nitroxides, T_1 decreases with decreasing ω between about 34 and 3 GHz because of the frequency dependence of the END process. However, for rapidly tumbling nitroxides, this trend does not continue at lower frequencies because the END process becomes frequency independent. The frequency dependence of $1/T_1$ between 34 and 3 GHz is smaller when $\tau_R = 10$ ps than when $\tau_R = 50$ ps. The thermally activated process has a maximal impact

on T_1 in the range of 1–2 GHz. These three processes are sufficient to model $1/T_1$ over between 250 MHz and 35 GHz. The net effect of the contributions from spin rotation, modulation of anisotropy by tumbling, and the thermally activated process is that for small rapidly tumbling nitroxides there is a maximum in relaxation rate at about 1–2 GHz and relaxation rates become smaller again at lower frequency. Consequently, relaxation rates at very low frequency (*e.g.*, 60 MHz, 250 MHz) are similar to those at ~9.5 GHz, which is fully consistent with the earliest estimates of nitroxide relaxation rates.[12,42]

15.3.2.1 Effect of Collisions on T_1

As discussed in Section 15.2.1, the room temperature populations of the $m_s = \pm 1/2$ spin states at X-band are approximately equal. Thus, half of the spins have one orientation, and half have the other orientation. Upon collision of two free radicals with the same energy, Heisenberg exchange results in the molecules diffusing apart with either the spin with which they came, or with the spin of the other radical. If there is no difference in their resonant fields, there is no spin relaxation. If, however, the radicals had different nuclear spin states, then the effect of the spin exchange is to exchange with the thermal energy of the lattice (the solvent) the energy difference between the two nuclear spin states. This is an HE contribution to the T_1 relaxation mechanism. Because of the nearly equal spin-up spin-down populations, relaxation occurs in only half of the encounters. This is in contrast with T_2, where every exchange involving a different nuclear spin state results in T_2 relaxation, which makes the concentration dependence of T_1 less than for T_2. There is another factor that decreases the effect of collisions on T_1. When radicals diffuse close enough to undergo spin exchange, they have multiple close encounters and reencounters within the solvent cage. There is a roughly 50 : 50 chance that the radical will emerge from the encounter with the same spin that it had before the encounter, even if the other radical with which it collided had the opposite spin. This reencounter phenomenon also helps average out any anisotropy in the spin exchange.[43] The concentration dependence of T_1 and T_2 both depend on the charge on the radical, the type and concentration of counter-ion, the strength of interaction with solvent molecules, including H-bonding ability, and the electron spin density at the periphery of the radical. These factors are all in addition to temperature and viscosity.

15.3.3 T_2 in Fluid Solution

For dilute nitroxide solutions, T_2 is dominated primarily by incomplete motional averaging of g and A_N anisotropy (Figure 15.6), which has been analyzed in detail by the group of Jack Freed.[44] In the limit where the anisotropy is fully averaged T_1 may dominate T_2 and $T_2 \sim T_1$.

If the nitroxide concentration is high enough, the collisions and the exchange rate become fast enough to broaden the spectra (Figure 15.10), and then at very high concentrations, collapse the spectrum into one line, which narrows as the concentration increases further. These patterns are commonly illustrated in

NMR texts under the topic of "dynamic NMR." See, for example, p. 292 in ref. 45. In the intermediate exchange and coalescence regions (where the collapse to a broad line occurs) the lineshape depends on the energy separation and the rate of exchange, but near the slow exchange limit, the onset of broadening depends on the rate of exchange but not on the separation. Thus, in the slow exchange region, the measured T_2 depends on the collision rate, independent of the magnitude of the hyperfine line being averaged. In the intermediate exchange and fast exchange regions, T_2 does depend on the magnitude of the separation.

The observed EPR spectrum of a free radical in solution is a superposition of an ensemble of molecules with all possible combinations of nuclear spin states. Any resolved hyperfine means that electron and nuclear spin relaxation are slow relative to the energy splitting from the hyperfine interaction. If the ^{14}N, for example, were relaxing rapidly, one would see only one line, not three. Consequently, the observation of the nuclear hyperfine tells us that the radicals are in the slow exchange regime. Using the results of the prior paragraph, we know then that each collision between radicals with different nuclear spin states will result in line broadening and T_2 relaxation.

15.3.4 T_1 in Immobilized Samples

For immobilized nitroxides, spin–lattice relaxation is described by the sum of contributions from the direct, Raman, local mode and thermally activated processes.

$$\frac{1}{T_1} = \frac{1}{T_1^{\text{dir}}} + \frac{1}{T_1^{\text{Raman}}} + \frac{1}{T_1^{\text{local}}} + \frac{1}{T_1^{\text{thermal}}} \tag{15.16}$$

The earliest discussions of spin lattice relaxation were at very low temperatures[46] and focused on the direct process (eqn (15.17)) in which there is an exact match of the unpaired electron spin flip energy (the Zeeman energy) with a lattice phonon energy and direct transfer of energy occurs.

$$\frac{1}{T_1^{\text{dir}}} = A_{\text{dir}} B_0^4 T \tag{15.17}$$

where A_{dir} is an experimentally determined adjustable parameter, B_0 is the magnetic field, and T is temperature. The B_0^4 field dependence and the linear dependence on temperature are characteristic of the direct process for a compound with an odd number of electrons, including $S = 1/2$ nitroxides. The direct process typically dominates relaxation at relatively low temperature.

The two-phonon Raman process involves a virtual excited state with an energy that is less than the Debye temperature. The energy that is transferred from the spin system to the lattice is the difference between the energies for absorption to and emission from this virtual excited state.[47] For $S = 1/2$ nitroxides the contribution to T_1 from the Raman process is given by eqn (15.18).[48]

$$\frac{1}{T_1^{\text{Ram}}} = A_{\text{Ram}} \left(\frac{T}{\theta_D}\right)^9 J_8\left(\frac{\theta_D}{T}\right) \tag{15.18}$$

where A_{Ram} is an experimentally determined adjustable parameter, and J_8 is the transport integral eqn (15.19), that was developed to model heat capacity.

$$J_8\left(\frac{\theta_D}{T}\right) = \int_0^{\theta_{D/T}} x^8 \frac{e^x}{(e^x - 1)^2}\,dx \tag{15.19}$$

Well below the Debye temperature, the contribution from the Raman process is proportional to T^9, but above the Debye temperature the limiting temperature dependence is T^2. For nitroxides in glassy organics the T^2 dependence has been observed above about 100 K.[38]

The local mode involves a discrete vibrational frequency, usually for a molecular species. This contribution to relaxation is described by eqn (15.20).[49,50]

$$\frac{1}{T_1^{\mathrm{local}}} = A_{\mathrm{loc}} \frac{e^{\Delta_{\mathrm{loc}}/k_{\mathrm{B}}T}}{(e^{\Delta_{\mathrm{loc}}/k_{\mathrm{B}}T} - 1)^2} \tag{15.20}$$

where A_{loc} is an experimentally determined adjustable parameter, and Δ_{loc} is the energy of the local mode. This contribution typically is greater than the Raman process at higher temperatures.[38]

Thermally activated processes such as rotation of methyl groups, rotation of amino groups, or hopping of a hydrogen-bonded proton can absorb energy from the spin system when the rate of the process is comparable to the resonance frequency of the spin system. The temperature dependence of this contribution is described by eqn (15.21).[51]

$$\frac{1}{T_1} = A_{\mathrm{therm}} \left[\frac{2\tau_{\mathrm{c}}}{1 + \omega^2\tau_{\mathrm{c}}^2}\right] \tag{15.21}$$

where A_{therm} is an experimentally determined adjustable parameter, τ_{c} is the correlation time for the thermally activated process, $\tau_{\mathrm{c}} = \tau_{\mathrm{c}}^{\mathrm{o}} e^{E_a/k_{\mathrm{B}}T}$, E_{a} is the activation energy for the thermally activated process, τ_c^{o} is the pre-exponential factor, and ω is the electron spin Larmor frequency in angular frequency units. Unlike the Raman, local-mode or Orbach processes, this contribution to relaxation depends on the Larmor frequency. It has maximum impact when $\omega\tau_{\mathrm{c}} \approx 1$, so when this process dominates, the relaxation rate exhibits a maximum as a function of temperature that is dependent on the Larmor frequency.

Spin–lattice relaxation rates for nitroxides in glassy solvents have been observed to decrease as the molecular weight increases.[37] Relaxation is faster in low-polarity sucrose octaacetate than in sorbitol which can hydrogen bond to the nitroxide. At temperatures between 100 and 300 K relaxation is independent of frequency between X- and Q-band and is dominated by a combination of the Raman and local-mode processes. The contributions to relaxation from the Raman and local-mode processes are correlated – factors that increase one process also increase the other. There is substantial similarity in the relaxation processes for a variety of nitroxides.[37]

15.3.5 T_m in Immobilized Samples

At temperatures below about 80 K, T_m for nitroxides is largely determined by nuclear spin diffusion of spins in the environment and is in the range of 2–4 μs in most proton-containing lattices. If the solvent is deuterated, T_m increases dramatically.[52] As the temperature is increased toward the glass transition temperature of the solvent, T_m becomes shorter due to increasing motional averaging of g and A_N anisotropy. Above about 80 K, T_m for methyl-containing nitroxides is strongly impacted by rotation of the methyl groups at rates that are comparable anisotropies in the electron–proton couplings. The rates of methyl rotation are determined by local steric effects and do not depend upon the size of the molecule or the properties of the solvent. In spin-labeled proteins, T_m at about 100 K decreases as the local concentration of methyl groups increases.[53]

15.4 Design of Nitroxides for Particular EPR Applications

The synthetic versatility of nitroxides permits tailoring nitroxides for EPR applications. We focus here on two examples. Other examples are in other chapters of this volume.

15.4.1 Nitroxides for *In Vivo* Imaging and Physiology Studies

Applications of nitroxides to *in vivo* physiology and imaging studies require understanding of the mechanisms of spin relaxation of the probes. The calculations in a highly cited paper,[35] convinced many people that nitroxides would not be useful relaxation probes at the low microwave frequencies that are required for *in vivo* experiments. However, the rapid scan estimate of T_2 for a nitroxide at 250 MHz,[54] and subsequent demonstration at NCI of pulsed EPR imaging of nitroxides,[55,56] gave new impetus for development of nitroxides for *in vivo* imaging.

The *in vivo* rate of reduction of nitroxides to diamagnetic analogs is structure dependent.[57] Stability is greater for five-membered rings than for six-membered rings.[58] Nitroxides have been designed, for example, to cross the blood–brain barrier and permit brain imaging.[59–61] *In vivo* stability of nitroxides can be enhanced to permit in cell imaging by replacing *gem*-dimethyls with *gem*-diethyls.[62] Dinitroxides have been designed to monitor *in vivo* redox status.[21,63]

15.4.2 Methyl Rotation and Distance Measurements Using Nitroxides

Double electron–electron resonance (DEER, also called PELDOR) is a powerful technique for measuring distances in proteins and other biomolecules and in polymers. It uses several multiple-pulse methods, some with a

single microwave frequency and some that use two microwave frequencies. For introductions, see Schweiger and Jeschke[11] and Tsvetkov *et al.*[64] Distances have been measured between various free radicals, Cu(II) and Gd(III) labels. The most common label used is the one abbreviated MTSL. This label can be attached to cysteines that are naturally occurring or introduced by site-directed mutagenesis. In a DEER experiment the longer the T_m relaxation time, the longer the interspin distance that can be measured.

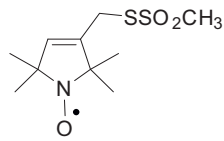

MTSL

As in most nitroxides, MTSL contains *gem*-dimethyl groups adjacent to the N–O moiety. Although these labels are useful for many biomedical applications, they have a disadvantage that limits the distances measurable with DEER. In the temperature range that would otherwise be convenient for measurement of distances between nitroxide spin labels, methyl rotation shortens T_m, (Figure 15.12). The effect of the methyl groups on T_m can be eliminated by using nitroxide derivatives in which the methyl groups have been replaced by cyclohexyl groups as in amino-acid-DICPO or

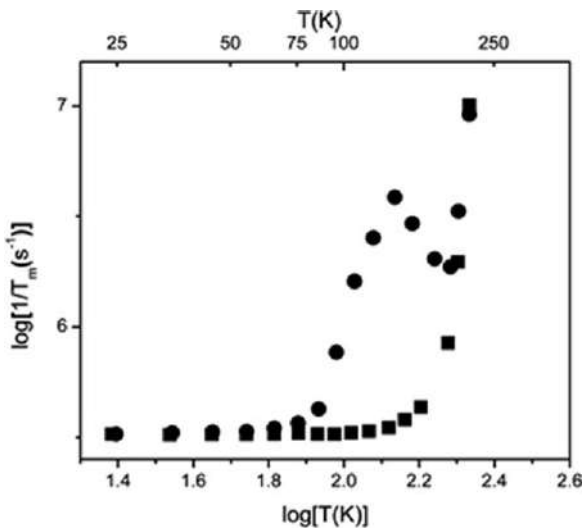

Figure 15.12 Temperature dependence of spin echo dephasing rates $1/T_m$ in 1 : 1 water:glycerol for (■) amino-acid DICPO, or (●) MTSL.
Reproduced from ref. 65 with permission from John Wiley & Sons, Copyright 2010 WILEY-VCH Verlag GmbH & Co. KGaA, Weinheim.

carboxymethyls.[65,66] There is a much smaller effect of coupling to the distant methyl groups of the methyl esters than of the directly attached methyls.[66] The importance of eliminating the methyl group effect on nitroxide relaxation is that the methyl groups shorten T_m in the liquid N_2 temperature region where it would be convenient to perform DEER measurements. Longer T_m facilitates measuring longer distances between spins. Using lower temperature to lengthen T_m requires using He, which is more expensive and less readily available than N_2. Combining the concept of distance measurement with the ideas about anisotropy, DEER measurements at higher microwave frequency permit measurement of the relative orientations of the spin labels. The combined effect of the anisotropy in g and A_N on distribution of intensity in the EPR spectrum results in Q-band (*ca.* 34 GHz) being near optimum for distance measurements using DEER, unless anisotropy and the orientation selection that it enables is the key parameter to study, in which case higher frequency is preferable.

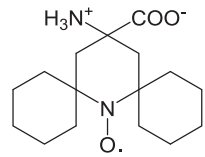

Amino-acid-DICPO

Further Reading

For a general introduction to CW EPR, see *Quantitative EPR*.[10]
The basic references on relaxation are ref. 27 and 67.

References

1. E. G. Rozantsev, *Free Nitroxyl Radicals*, Plenum Press, 1970.
2. O. H. Griffith, D. W. Cornell and H. M. McConnell, *J. Chem. Phys.*, 1965, **43**, 2909–2910.
3. S. Stoll and A. Schweiger, *J. Magn. Reson.*, 2006, **178**, 42–55.
4. G. Breit and I. I. Rabi, *Phys. Rev.*, 1931, **38**, 2082–2083.
5. J. R. Biller, M. Tseitlin, R. W. Quine, G. A. Rinard, H. A. Weismiller, H. Elajaili, G. M. Rosen, J. P. Kao, S. S. Eaton and G. R. Eaton, *J. Magn. Reson.*, 2014, **242**, 162–168.
6. J. R. Biller, V. Meyer, H. Elajaili, G. M. Rosen, J. P. Y. Kao, S. S. Eaton and G. R. Eaton, *J. Magn. Reson.*, 2011, **212**, 370–377.
7. D. Grucker, T. Guiberteau and G. Planinšic, *Res. Chem. Intermed.*, 1996, **22**, 567–579.
8. B. R. Knauer and J. J. Napier, *J. Am. Chem. Soc.*, 1973, **98**, 4395–4400.
9. A. H. Beth and B. H. Robinson, in *Biological Magnetic Resonance: Spin Labeling Theory and Applications*, ed. L. J. Berliner and J. Reuben, Plenum Press, New York , vol. 8, 1989, pp. 179–253.

10. G. R. Eaton, S. S. Eaton, D. P. Barr and R. T. Weber, *Quantitative EPR*, Springer-Verlag, Wien, New York, 2010.
11. A. Schweiger and G. Jeschke, *Principles of Pulse Electron Paramagnetic Resonance*, Oxford University Press, Oxford, 2001.
12. J. R. Biller, H. Elajaili, V. Meyer, G. M. Rosen, S. S. Eaton and G. R. Eaton, *J. Magn. Reson.*, 2013, **236**, 47–56.
13. D. G. Mitchell, R. W. Quine, M. Tseitlin, S. S. Eaton and G. R. Eaton, *J. Magn. Reson.*, 2012, **214**, 221–226.
14. G. R. Eaton and S. S. Eaton, *eMagRes*, 2016, **5**, 1529–1542.
15. D. Kivelson, *J. Chem. Phys.*, 1960, **33**, 1094–1106.
16. R. Wilson and D. Kivelson, *J. Chem. Phys.*, 1966, **44**, 4445–4452.
17. A. Clark, J. Sedhom, H. Elajaili, G. R. Eaton and S. S. Eaton, *Concepts Magn. Reson., Part A*, 2017, **45A**, DOI: 1001/cmr.a.21423.
18. S. S. Eaton, K. M. More, B. M. Sawant and G. R. Eaton, *J. Am. Chem. Soc.*, 1983, **105**, 6560–6567.
19. S. S. Eaton and G. R. Eaton, *J. Am. Chem. Soc.*, 1982, **104**, 5002–5003.
20. S. S. Eaton, L. B. Woodcock and G. R. Eaton, *Concepts Magn. Reson., Part A*, 2018, DOI: 10.1002/cmr.a.21246.
21. B. Epel, S. V. Sundramoorthy, M. Krzykowska-Serda, M. C. Maggio, M. Tseytlin, G. R. Eaton, S. S. Eaton, G. M. Rosen, J. P. Y. Kao and H. J. Halpern, *J. Magn. Reson.*, 2017, **276**, 31–36.
22. S. S. Eaton and G. R. Eaton, in *Ewing's Analytical Instrumentation Handbook*, ed. J. Cazes, Marcel Dekker, New York, 2005, p. 356.
23. C. P. Poole, *Electron Spin Resonance: A Comprehensive Treatise on Experimental Techniques*, Interscience Publishers, New York, 1967.
24. J. R. Biller, J. E. McPeak, S. S. Eaton and G. R. Eaton, *Appl. Magn. Reson.*, 2018, **49**, 1235–1251.
25. B. Epel and H. J. Halpern, *Methods Enzymol.*, 2016, **254**, 501–527.
26. K. M. More, G. R. Eaton and S. S. Eaton, *J. Magn. Reson.*, 1984, **60**, 54–65.
27. S. S. Eaton and G. R. Eaton, *Biol. Magn. Reson.*, 2000, **19**, 29–154.
28. W. K. Subczynski and A. Kusumi, *Biochim. Biophys. Acta*, 2003, **1610**, 231–243.
29. R. Owenius, G. E. Terry, M. J. Williams, S. S. Eaton and G. R. Eaton, *J. Phys. Chem. B*, 2004, **108**, 9475–9481.
30. B. H. Robinson, C. Mailer and A. W. Reese, *J. Magn. Reson.*, 1999, **138**, 210–219.
31. P. W. Atkins, in *Electron Spin Relaxation in Liquids*, ed. L. T. Muus and P. W. Atkins, Plenum Press, New York, 1972, pp. 279–312.
32. P. W. Atkins and D. Kivelson, *J. Chem. Phys.*, 1966, **44**, 169–174.
33. S. K. Rengan, M. P. Khakhar, B. S. Prabhananda and B. Venkataraman, *Pure Appl. Chem.*, 1972, **32**, 287–305.
34. B. H. Robinson, A. W. Reese, E. Gibbons and C. Mailer, *J. Phys. Chem. B*, 1999, **103**, 5881–5894.
35. B. H. Robinson, D. A. Haas and C. Mailer, *Science*, 1994, **263**, 490–493.
36. C. Mailer, R. D. Nielsen and B. H. Robinson, *J. Phys. Chem. A*, 2005, **109**, 4049–4061.

37. H. Sato, V. Kathirvelu, A. J. Fielding, S. E. Bottle, J. P. Blinco, A. S. Micallef, S. S. Eaton and G. R. Eaton, *Mol. Phys.*, 2007, **105**, 2137–2151.
38. H. Sato, S. E. Bottle, J. P. Blinco, A. S. Micallef, G. R. Eaton and S. S. Eaton, *J. Magn. Reson.*, 2008, **191**, 66–77.
39. J. R. Biller, V. M. Meyer, H. Elajaili, G. M. Rosen, S. S. Eaton and G. R. Eaton, *J. Magn. Reson.*, 2012, **225**, 52–57.
40. K. Kundu, D. R. Kattnig, B. Y. Mladenova, G. Grampp and R. Das, *J. Phys. Chem. B*, 2015, **119**, 4501–4511.
41. R. Owenius, G. R. Eaton and S. S. Eaton, *J. Magn. Reson.*, 2005, **172**, 168–175.
42. J. P. Lloyd and G. E. Pake, *Phys. Rev.*, 1954, **94**, 579–591.
43. Y. N. Molin, K. M. Salikhov and K. I. Zamaraev, in *Spin Exchange: Principles and Applications in Chemistry and Biology*, Springer-Verlag, Berlin, 1980, p. 71.
44. J. H. Freed, in *Spin Labeling Theory and Applications*, ed. L. J. Berliner, Academic Press, New York, 1976, pp. 73–75.
45. R. S. Drago, *Physical Methods in Chemistry*, Saunders, 1977.
46. *Spin-Lattice Relaxation in Ionic Solids*, ed. A. A. Manenkov and R. Orbach, Harper & Row, New York, 1966.
47. J. W. Orton, in *Electron Paramagnetic Resonance: An Introduction to Transition Group Ions in Crystals*, Gordon and Breach, 1968.
48. K. J. Standley and R. A. Vaughan, *Electron Spin Relaxation Phenomena in Solids*, Plenum Press, N.Y., 1969.
49. J. G. Castle, Jr. and D. W. Feldman, *Phys. Rev. A*, 1965, **137**, 671–673.
50. J. Murphy, *Phys. Rev.*, 1966, **145**, 241–247.
51. V. A. Atsarkin, V. V. Demikov and G. A. Vasneva, *Phys. Rev. B*, 1997, **56**, 9448–9453.
52. A. Zecevic, G. R. Eaton, S. S. Eaton and M. Lindgren, *Mol. Phys.*, 1998, **95**, 1255–1263.
53. M. Lindgren, G. R. Eaton, S. S. Eaton, B.-H. Jonsson, P. Hammarstrom, M. Svensson and U. Carlsson, *J. Chem. Soc., Perkin Trans. 2*, 1997, 2549–2554.
54. M. Tseitlin, A. Dhami, R. W. Quine, G. A. Rinard, S. S. Eaton and G. R. Eaton, *Appl. Magn. Reson.*, 2006, **30**, 651–656.
55. J. Bourg, M. C. Krishna, J. B. Mitchell, R. G. Tschudin, T. J. Pohida, W. S. Friauf, P. D. Smith, J. Metcalfe, F. Harrington and S. Subramanian, *J. Magn. Reson., Ser. B*, 1993, **102**, 112–115.
56. F. Hyodo, S. Matsumoto, N. Devasahayam, C. Dharmaraj, S. Subramanian, J. B. Mitchell and M. C. Krishna, *J. Magn. Reson.*, 2009, **197**, 181–185.
57. H. M. Swartz and G. Bacic, *eMagRes*, 2007, DOI: 10.1002/9780470034590.emrstm9780470030158.
58. J. F. Keana, S. Pou and G. M. Rosen, *Magn. Reson. Med.*, 1987, **5**, 525–536.
59. M. C. Emoto, Y. Matsuoka, K. Yamada, H. Sato-Akaba and H. Fujii, *Biochem. Biophys. Res. Commun.*, 2017, **485**, 802–806.

60. M. C. Emoto, S. Sato and H. G. Fujii, *Magn. Reson. Chem.*, 2016, **54**, 705–711.
61. H. Fujii, H. Sato-Akaba, K. Kawanishi and H. Hirata, *Magn. Reson. Med.*, 2011, **65**, 295–303.
62. G. Karthikeyan, A. Bonucci, G. Casano, G. Gerbaud, S. Abel, V. Thom, L. Kodjabachian, A. Magalon, B. Guigliarelli, V. Belle, O. Ouari and E. Mileo, *Angew. Chem.*, 2018, **57**, 1366–1370.
63. G. I. Roshchupkina, A. A. Bobko, A. Bratasz, V. A. Reznikov, P. Kuppusamy and V. V. Khramtsov, *Free Radicals Biol. Med.*, 2008, **45**, 312–320.
64. Y. D. Tsvetkov, M. K. Bowman and Y. A. Grishin, in *Pulsed Electron-Electron Double Resonance*, Springer, 2019.
65. A. Rajca, V. Kathirvelu, S. K. Roy, M. Pink, S. Rajca, S. Sarkar, S. S. Eaton and G. R. Eaton, *Chem. - Eur. J.*, 2010, **16**, 5778–5782.
66. S. Huang, J. T. Paletta, H. Elajaili, K. Huber, M. Pink, S. Rajca, G. R. Eaton, S. S. Eaton and A. Rajca, *J. Org. Chem.*, 2017, **82**, 1538–1544.
67. S. S. Eaton and G. R. Eaton, in *Handbook of EPR Spectroscopy: Fundamentals and Methods*, ed. D. Goldfarb and S. Stoll, John Wiley & Sons, Chichester, UK, 2018, pp. 175–192.
68. M. R. Gafurov, *Magn. Reson. Solids*, 2013, **15**, 13103.

Subject Index